The stress-strain-strength anisotropy of a granular medium under general stress conditions

by

Lidija Zdravkovic
CE, BSc, MSc

June 1996

A thesis submitted to the University of London
(Imperial College of Science, Technology and Medicine)
in partial fulfilment of the requirements for the degree of
Doctor of Philosophy in the Faculty of Engineering

BIBL.
LOND N.
CNV.

ABSTRACT

Although principal stress rotation is experienced in almost all geotechnical engineering situations, it is usually neglected in design because of the difficulties in (i) measuring and quantifying the effect experimentally and (ii) formulating theoretical soil models that can realistically account for the observed behaviour. The overall objective of this thesis is to investigate (i) above by performing sophisticated stress path tests using the Imperial College Hollow Cylinder Apparatus. This device enables a variety of stress paths involving different amounts of principal stress rotation to be imposed on soil samples. The research was instigated by recent problems identified with the foundation behaviour of offshore structures which experience large principal stress rotations due to both static and cyclic wave loading. However, such principal stress rotations occur in most geotechnical structures.

The laboratory experiments were performed on an artificial quartz based silt called HPF4, whose grading curve covers the whole silt range of the particle size distribution diagram. This material was chosen for two reasons. Firstly, it has properties similar to those of certain sea-bed sediments and consequently the results have direct relevance to offshore situations. Secondly, little experimental information is available for silt soils and therefore the results provide valuable data spanning the information gap between the behaviour of clay and sand soils.

The research consisted of three main sets of experiments. Each set of experiments was designed to investigate a particular aspect of principal stress rotation:

* The general strength and yielding anisotropy of K_o consolidated HPF4. These tests focused on overall behaviour and are compared with previous studies on sands.

* The directional dependence of the stiffness of lightly overconsolidated HPF4. These tests provide information on the true stiffness anisotropy at small to large strains.

* How the anisotropy established under K_o conditions may be altered by consolidation paths in which the major principal stress direction is rotated. The anisotropy of the "new" material formed this way is compared with that of K_o consolidated HPF4.

The thesis concludes that HPF4 has strong anisotropic strength characteristics after K_o consolidation; that anisotropy plays an important role at small strains as well as large; that different anisotropies may be induced and that there are significant differences between the anisotropies of silts, clays and sands.

ACKNOWLEDGEMENTS

The research work presented in this thesis has been carried out under the supervision of Dr Richard Jardine. He has been a constant source of ideas, guidance and support throughout, continuously struggling with my "the's" and "a's" and my writing of English. I thank him for his persistence.

Financial support during the course of this research was provided by the following organisations:
- PROGRES Company, Belgrade, Yugoslavia
- The Committee of Vice-Chancellors and Principals, UK, through the ORS scheme
- AMOCO exploration company (USA)
- Health and Safety Executive (UK)

Their support is gratefully acknowledged.

I am also thankful to the technicians of the Soil's Laboratory. Without Steve's valuable knowledge of electronics the new HCA system would never have worked. Graham and Alan were always there to grumble about that "bloody woman" and to complain about stretching the O-rings. In addition to this friendly repartee I would like to thank them for the assistance and support that they provided.

I would also like to thank my current and former research colleagues in the Section who made my stay at Imperial so enjoyable and memorable: Federica, Francesca, Fiona, Fernando, Marinos, Achileas, Dennis, Nasha, Esad, Kieran, Mohamed, Trevor, Rob. Special thanks go to Chris who first introduced me to the hollow cylinder and showed me how to drive it. Tim and Reiko shared many long and late hours with me in the laboratory, although Tim always complained of being "abused" by a Serbo-Japo "association". To Jamie go my greatest thanks: for passing to me his knowledge about the laboratory, for always being there for a "little chat", and, most of all, for being my friend.

Other members of staff at Soil's Section have contributed to the successful completion of this study. Prof Potts is specially acknowledged for numerous critical discussions while reading the manuscript. It is to his credit also if this text finally reads as English. I am looking forward to working with him in the future. Dr Skinner spent many lunch breaks discussing my silt particles and elucidating the meaning of "material structure". I would also like to thank Professors Burland and Vaughan for their continual support and moral encouragement.

Without John Baxter and Sue our Section wouldn't be the same. Thanks for lightening the atmosphere and bringing laughter to the laboratory.

At the end, my deepest gratitude goes to my family, my parents Tomislav and Milica and my sister Bilja, for their love, care and support throughout my life.

TABLE OF CONTENTS

Abstract i
Acknowledgements ii
Table of contents iii
List of symbols and abbreviations viii

Chapter 1 - Introduction
1.1. Introduction 1
1.1.1. Importance of investigating principal stress rotation 1
1.1.2. Definition of principal stress rotation and the effect of the intermediate principal stress 1
1.1.3. Practical examples of principal stress rotation 2
1.1.4. Research 4
1.1.5. Choice of testing material 4
1.2. Objectives of this study 5
1.2.1. Previous research with IC HCA 5
1.2.2. Aims of this research 6
1.3. Outline of the thesis 7
Figures for Chapter 1 10

Chapter 2 - Background to soil anisotropy
2.1. Introduction 16
2.2. Laboratory equipment for investigating anisotropy 17
2.3. Previous studies of anisotropy 20
2.3.1. Introduction 20
2.3.2. Effect of α 21
2.3.2.1. Effect of α under plane-strain conditions 21
2.3.2.2. Effect of α under triaxial compression conditions 24
2.3.2.3. Discussion 25
2.3.3. Effect of b on material behaviour 26
2.4. Anisotropic pre-failure parameters 27
2.4.1. Introduction 27
2.4.2. Measurements of anisotropic parameters in laboratory 29
2.4.3. Field measurements of anisotropic parameters 31
2.4.4. Confirmation of anisotropic behaviour at small strains 32
2.5. Factors which influence the magnitude of the anisotropic parameters 33
2.5.1. Porosity 34
2.5.2. Stress level 34
2.5.3. Overconsolidation 35
2.5.4. Strain rate and strain magnitude 35
2.6. Effects of strain level in field tests 38
2.7. Framework for the behaviour of HPF4 39
2.7.1. Constant strain contours 39
2.7.2. The kinematic nature of small strain zones I and II 41
2.7.3. Contours of constant energy 42
2.7.4. Bounding Surface framework 43
2.7.4.1. Behaviour of clays 43
2.7.4.2. Behaviour of materials not obeying Rendulic's principle 44
2.7.4.3. Behaviour of granular materials 45
2.7.5. The role of fabric in granular materials 46
2.7.5.1. Qualitative experimental recognition of granular fabric 46

2.7.5.2. Quantitative experimental recognition of granular fabric 47
2.7.5.3. Numerical consideration of granular fabric 49
2.7.6. Induced anisotropy 49
Figures for Chapter 2 53

Chapter 3 - Test equipment, materials and procedures
3.1. Introduction 95
3.2. Materials tested 96
3.3. Triaxial stress path cell 98
3.3.1. Apparatus 98
3.3.2. Instrumentation 98
3.4. Hollow Cylinder Apparatus 99
3.4.1. Load application and control equations 99
3.4.1.1. Load application 99
3.4.1.2. Stress calculation 100
3.4.1.3. Strain calculation 101
3.4.2. Instrumentation 102
3.4.3. Stress and strain non-uniformities in the HCA 104
3.4.4. Computer control and data acquisition system 109
3.4.4.1. Introduction 109
3.4.4.2. New HCA control system (i.e. hardware) 109
3.4.4.3. Control program (i.e. software) 111
3.4.4.4. The operation with the program 115
3.5. Sample preparation and testing procedures 116
3.5.1. Introduction 116
3.5.2. Sample preparation techniques for granular soils 116
3.5.3. The slurry deposition method adopted for HPF4 samples 117
3.5.4. Setting up procedure for silt samples 118
3.5.5. Testing procedure for triaxial samples 119
3.5.6. Testing procedure for hollow cylinder samples 119
Figures for Chapter 3 121

Chapter 4 - Triaxial tests
4.1. Introduction 144
4.2. Consolidation and swelling characteristics of HPF4 144
4.2.1. Consolidation procedure for triaxial samples 144
4.2.1.1. K_o consolidation 144
4.2.1.2. K_o swelling 145
4.2.2. Compressibility of HPF4 147
4.2.2.1. During virgin K_o consolidation 147
4.2.2.2. During K_o swelling 148
4.3. Undrained triaxial compression tests 148
4.3.1. Description of stress paths 148
4.3.2. Stress-strain behaviour 149
4.3.3. Undrained compression stiffness 150
4.4. Undrained triaxial extension tests 152
4.4.1. Description of stress paths 152
4.4.2. Stress-strain behaviour 152
4.4.3. Undrained extension stiffness 153
4.5. Normalization behaviour of HPF4 153
4.6. Discussion 155
4.6.1. Introduction 155
4.6.2. Compressibility 156

4.6.3. Stress-strain behaviour 156
4.6.4. Stiffness behaviour 158
4.7. Summary 159
Figures for Chapter 4 161

Chapter 5 - Undrained anisotropy of K_o consolidated HPF4
5.1. Introduction 195
5.2. Description of HCA M-Series tests 196
5.3. Consolidation of HPF4 from HCA experiments 198
5.3.1. K_o consolidation 198
5.3.2. Compressibility 199
5.4. Shearing stages of HPF4 in M-test Series 199
5.4.1. b-stage 199
5.4.1.1. Stress paths 199
5.4.1.2. Stress-strain response 199
5.4.1.3. Stiffness response 200
5.4.1.4. Influence of b-change on soil fabric 201
5.4.2. Undrained unloading 201
5.4.2.1. Stress-strain behaviour 201
5.4.2.2. Stiffness behaviour 202
5.4.3. α-rotation stage and shearing with constant α inclination 203
5.4.3.1. Stress-strain response 203
A) α-rotation stage 203
B) Shearing with α=const 204
5.4.3.2. Stiffness behaviour 205
A) α-rotation stage 206
B) Shearing stage 207
5.4.3.3. Directions of the major principal stress and strain 207
5.4.3.4. Undrained strength anisotropy of HPF4 208
5.5. Bounding Surface (BS) for initial anisotropy of HPF4 209
5.5.1. Presentation of the local BS in q-p'-α space 209
5.5.2. Presentation of the local BS in ϕ'-ε_d-α space 211
5.5.3. Uniqueness of the local BS 211
5.6. Discussion 213
5.6.1. Effect of α on soil response, i.e. initial anisotropy due to principal stress rotation 213
5.6.1.1. Apparatus effect 214
5.6.1.2. Strain conditions at b=0.5 214
5.6.1.3. Structural effect 215
5.6.1.4. Particle shape 216
5.6.2. The effect of *b* on soil response 218
5.6.2.1. Effect of *b* on loading behaviour for α=0° 218
5.6.2.2. Effect of *b* on unloading behaviour for α=0° 219
5.6.2.3. Effect of *b* on loading behaviour with α=90° 219
5.7. Summary 220
Figures for Chapter 5 222

Chapter 6 - Directional stiffness anisotropy of lightly overconsolidated HPF4 at small strains
6.1. Introduction 271
6.2. Description of tests 272
6.2.1. Ko consolidation and swelling 272
6.2.2. Shearing behaviour 273

6.3. Discussion of the results 280
6.3.1. Undrained yield 280
6.3.2. Undrained stiffness 281
6.3.3. Undrained failure 282
6.4. Anisotropic stiffness parameters of HPF4 284
6.4.1. Introduction 284
6.4.2. Tests to determine the anisotropic stiffness parameters 284
6.5. Discussion 288
6.5.1. Initial anisotropic parameters 288
6.5.2. The compliance matrix for HPF4 289
6.5.3. Prediction of undrained triaxial stiffness anisotropy from measured drained parameters 290
6.5.4. Prediction of undrained triaxial stiffness anisotropy assuming symmetry 294
6.5.5. Comments on the prediction of undrained triaxial stiffness from drained parameters 296
6.5.6. Prediction of undrained triaxial anisotropy considering loading/unloading stress paths 297
6.5.7 Prediction of the initial inclination of an undrained stress path 300
6.6. Summary 303
Figures for Chapter 6 308

Chapter 7 - Stress induced anisotropy - HPF4 consolidated with inclined σ_1 direction
7.1. Introduction 365
7.2. Description of tests 369
7.3. Drained principal stress rotation 371
7.3.1. Stress-strain behaviour 371
7.3.2. Principal stress and strain increment directions 372
7.3.3. The effects of recent stress history 373
7.3.4. Stiffness behaviour during principal stress rotation 374
7.4. Drained inclined consolidation 374
7.4.1. Stress-strain behaviour 374
7.4.2. Stress and strain increment directions 376
7.4.3. Volumetric behaviour 377
7.4.4. Stiffness behaviour 378
7.5. *b*-change 379
7.5.1. Stress path 379
7.5.2. Stress-strain behaviour 379
7.6. Material behaviour during undrained shearing 380
7.6.1. Introduction 380
7.6.2. Stress-strain behaviour 380
7.6.3. Effective stress paths during undrained shearing 381
7.6.3.1. Comparison of tests M0 and R0 381
7.6.3.2. Comparison of stress paths from R-Series tests 383
7.6.4. Stress and strain increment directions 385
7.7. Anisotropy induced by inclined consolidation 386
7.7.1. Introduction 386
7.7.2. Description of test 386
7.7.3. Comparison of the two stress paths 387
7.7.4. Comparison of the two anisotropies 388
7.8. Summary 389
Figures for Chapter 7 394

Chapter 8 - Summary, practical implications and recommendations for further research
8.1. Summary and conclusions 448
8.1.1. Review of previous work 448
8.1.2. Testing equipment and material 449
8.1.3. Testing programme 450
8.1.4. Consolidation characteristics of HPF4 451
8.1.5. Observed undrained strength anisotropy of HPF4 451
8.1.6. Bounding Surface (BS) 454
8.1.7. Undrained small strain yielding 455
8.1.8. Stiffness 455
8.2. Practical implications 459
8.2.1. Multi stage embankments 460
8.2.2. Behaviour of piles 460
8.2.3. Submarine slopes 461
8.2.4. Tunnels 462
8.3. Future research 462
Figures for Chapter 8 464

Appendix III
III.1. Thin sections 486
III.2. Improvement of electrolevel devices 487
III.2.1. Scatter 488
III.2.2. Spikes 488
III.2.3. Assessment of strain measurement 489
III.3. Computer control and data acquisition system 490
III.3.1. The electronic instrument system 490
III.3.2. Conversion process 491
III.3.3. Data distribution 493
Figures for Appendix III 494

Appendix V
V.1. Principal stress increment direction in α_rotation stage 504
V.2. Simulation of triaxial tests in the HCA 505
V.2.1. Consolidation 505
V.2.2. Stress paths and strength 505
V.3. Undrained triaxial compression of isotropically consolidated HPF4 506
V.3.1. Isotropic consolidation 506
V.3.2. Stress path and strength of isotropically consolidated sample 506
V.4. Mechanism of fabric evolution in granular media 507
V.4.1. Development of Distinct Element Method 507
V.4.2. Extension of program BALL to elliptical particles 508
Figures for Appendix V 510

Appendix VI
VI.1. Anisotropic elasticity 515

Reference list

LIST OF SYMBOLS AND ABBREVIATIONS

σ_1 , σ_2 , σ_3 - major, intermediate and minor principal stresses

σ_z , σ_r , σ_θ - axial, radial and circumferential component stresses

$\tau_{\theta z}$ - torsional shear stress (in the plane with normal *z*, in the direction θ)

σ_{vc}' - vertical effective stress at final consolidation point

σ_{1c}' - major principal effective stress at the final consolidation point

$q = \sigma_1 - \sigma_3$ - deviator stress

$t = (\sigma_1 - \sigma_3)/2$ - half of the deviator stress

$p' = (\sigma_1' + \sigma_2' + \sigma_3')/3$ - current mean effective stress

$p = (\sigma_1 + \sigma_2 + \sigma_3)/3$ - current mean total stress

p_o' - final consolidation mean effective stress

p_c' - mean effective stress at the end of swelling, prior to shearing

$\Delta J = (1/\sqrt{6})[(\Delta\sigma_1 - \Delta\sigma_2)^2 + (\Delta\sigma_2 - \Delta\sigma_3)^2 + (\Delta\sigma_1 - \Delta\sigma_3)^2]^{0.5}$ - incremental deviatoric stress invariant

$\Delta q = (1/\sqrt{2})[(\Delta\sigma_1 - \Delta\sigma_2)^2 + (\Delta\sigma_2 - \Delta\sigma_3)^2 + (\Delta\sigma_1 - \Delta\sigma_3)^2]^{0.5}$ - incremental shear stress

ε_1 , ε_2 , ε_3 - major, intermediate and minor principal strains

ε_z , ε_r , ε_θ - axial, radial and circumferential component strains

$\gamma_{\theta z}$ - torsional shear strain

$\varepsilon_d = (2/\sqrt{6})[(\Delta\varepsilon_1 - \Delta\varepsilon_2)^2 + (\Delta\varepsilon_2 - \Delta\varepsilon_3)^2 + (\Delta\varepsilon_1 - \Delta\varepsilon_3)^2]^{0.5}$ - deviatoric strain

$\varepsilon_s = (\sqrt{2}/3)[(\Delta\varepsilon_1 - \Delta\varepsilon_2)^2 + (\Delta\varepsilon_2 - \Delta\varepsilon_3)^2 + (\Delta\varepsilon_1 - \Delta\varepsilon_3)^2]^{0.5}$ - shear strain

$\varepsilon_{vol} = \varepsilon_1 + \varepsilon_2 + \varepsilon_3$ - volumetric strain

$E_{uz}^{(com)}$, $E_{uz}^{(ext)}$ - undrained Young moduli in compression and extension

$G = \Delta J/\varepsilon_d$ - octahedral shear stiffness

$G_{\theta z} = G_{VH} = \Delta\tau_{\theta z}/\gamma_{\theta z}$ - torsional shear modulus in the vertical plane

$G_{\theta r} = G_{HH}$ - horizontal shear modulus

$E_r' = E_\theta' = E_H'$ - drained horizontal Young modulus

$E_z' = E_V'$ - drained vertical Young modulus

$\nu_{zr}' = \nu_{z\theta}' = \nu_{VH}'$ - Poisson's ratio for strains in horizontal direction due to a vertical stress

$\nu_{rz}' = \nu_{\theta z}' = \nu_{HV}'$ - Poisson's ratio for strains in vertical direction due to a horizontal direct stress

$\nu_{r\theta}' = \nu_{\theta r}' = \nu_{HH}'$ - Poisson's ratio for strains in horizontal direction due to a horizontal direct stress applied at 90° to that direction

ϕ' - mobilised friction angle

ϕ_{CV}' - mobilized friction angle at constant volume

$b = (\sigma_2 - \sigma_3)/(\sigma_1 - \sigma_3)$ - parameter which controls intermediate principal stress

α ($=\alpha_\sigma$) - angle of the principal stress direction with respect to vertical

α_c - angle of the principal stress direction during inclined consolidations and subsequent shearing

α_ε - angle of the principal strain direction with respect to vertical

$\alpha_{\dot{\sigma}}$ - angle of the principal stress increment direction with respect to vertical

$\alpha_{\dot{\varepsilon}}$ - angle of the principal strain increment direction with respect to vertical

θ_α - inclination of the stress path in α-direction

K_o - coefficient of (σ_r'/σ_z') during one dimensional consolidation (no lateral straining)

c_u - undrained 'strength', measured here at Phase Transformation Point

W - external work

A - pore water pressure parameter

PTP - Phase Transformation Point

HRS - Ham River Sand

HK - mixture of Ham River Sand and 10% Kaolin

KSS - mixture of 50% Kaolin, 25% Sand and 25% Silt

PEN - natural silty clay from Pentre

DKS - Dunkirk sand

LCT - Lower Cromer Till

BC - Bothkennar clay

HCA - Hollow Cylinder Apparatus

TXC - Triaxial compression

TXE - Triaxial extension

OCR - overconsolidation ratio

ESP - effective stress path

BS - bounding surface

R^2 - ratio of horizontal to vertical stiffness

MARKS ON FIGURES:

alpha = α ($=\alpha_\sigma$)

alpha(delSIG) = $\alpha_{\dot{\sigma}}$

alpha (STR) = α_ε

alpha(delSTR) = $\alpha_{\dot{\varepsilon}}$

SIGz = σ_z	SIG1 = σ_1	Ez = ε_z	GAMAthz = $\gamma_{\theta z}$	E3 = ε_3
SIGr = σ_r	SIG2 = σ_2	Er = ε_r	E1 = ε_1	
SIGth = σ_θ	SIG3 = σ_3	Eth = ε_θ	E2 = ε_2	

Chapter 1
INTRODUCTION

1.1. Introduction

1.1.1. Importance of investigating principal stress rotation

It has long been recognized that almost all practical geotechnical problems involve rotation of the principal stresses acting in the ground. Only in level, undisturbed sediments is the major principal stress direction found consistently to be either vertical or horizontal. Loading, by natural slope formation or man-made structures, invariably causes not only changes in the magnitudes of the principal stresses, but also rotation of their directions. As a result, the stability of slopes, both on land and underwater, and the foundation behaviour of on-shore and off-shore structures (gravity based and piled), depend on the soil's response to rotation of the principal stress directions. This is important because soil is an anisotropic medium in which properties are directional dependent.

1.1.2. Definition of principal stress rotation and the effect of the intermediate principal stress

In general, the state of stress acting on a soil element can be defined by six components of stress (three normal and three shear stresses), Fig.1.1a. Alternatively, the stress state can be defined in terms of the magnitudes of the three principal stresses and the three angles which define their directions, Fig.1.1b. Angles α, β and γ define the directions of the principal stresses relative to the cartesian axes x, y and z.

The effect of the intermediate principal stress, σ_2, is defined through the parameter *b*:

$$b = \frac{\sigma_2 - \sigma_3}{\sigma_1 - \sigma_3} \qquad (1.1)$$

For the initial in-situ conditions associated with normally consolidated and lightly overconsolidated undisturbed sediments, laid down under level conditions, the horizontal stresses σ_2 and σ_3 are equal and $\sigma_h=\sigma_2=\sigma_3<\sigma_v$, so that the initial *b* is zero. For heavily overconsolidated soils, where $\sigma_h>\sigma_v$, (i.e. K>1.0), the initial b=1.0, as $\sigma_1=\sigma_2>\sigma_3$. When construction or nature (through tectonic activity, mass movement, etc.) modifies the state of stress within the soil, parameter *b* changes between 0.0 and 1.0 according to the stress and strain conditions imposed.

1.1.3. Practical examples of principal stress rotation

a) Vertically loaded foundations

Hight (1983) investigated the amount of principal stress rotation imposed by a vertically loaded flexible circular footing on an isotropic linear elastic foundation (Fig.1.2). He considered two typical elements of the foundation soil: element *A*, located below the centre of the footing on the axis of symmetry, and element *B*, located at the same depth as *A*, but below the edge of the footing. For both elements, the initial stress state in the ground, before placing the footing, was such that the major principal stress, σ_{1i}, was vertical, which is appropriate for normally or lightly over consolidated soil.

When the soil is loaded by the footing, element A experiences changes in principal stress ($\Delta\sigma_1$, $\Delta\sigma_2$ and $\Delta\sigma_3$) such that $\Delta\sigma_1=\Delta\sigma_v$ and $\Delta\sigma_2=\Delta\sigma_3=\Delta\sigma_h$. When these increments are added to the initial in-situ stress distribution, the directions of the principal stresses remain unchanged ($\sigma_1=\sigma_v$ and $\sigma_2=\sigma_3=\sigma_h$).

However, for element *B*, which is away from the axis of symmetry, loading results in principal stress increments that are inclined to the vertical and horizontal and which have $\Delta\sigma_2\neq\Delta\sigma_3$. Adding these changes to the original in-situ stress field, results in the direction of the major principal stress (σ_1) deviating from its initial vertical direction.

Contours of the directions of the major principal stress increment are drawn in Fig.1.3, and show a symmetrical variation about the vertical centre line of the footing from 0°, on the footing centre line, to ±40°, under the footing edge. Also plotted are contours of the incremental *b* (Fig.1.4), defined in terms of the incremental stresses, i.e:

$$\frac{\Delta\sigma_2-\Delta\sigma_3}{\Delta\sigma_1-\Delta\sigma_3} \qquad (1.2)$$

These also show a symmetrical variation about the centre line of the footing, varying from 0.0 on the centre line, to ~0.2 below the edge of the footing.

b) Embankments on soft ground

Another geotechnical structure in which principal stress rotation plays an important role is that of embankment construction on an initially normally or lightly over consolidated clay. Bjerrum (1973) recognised that the directions of principal stress for soil elements along the failure surface beneath an embankment slope rotate from 0° to 90°. Yeats (1983), who performed

finite element analysis of embankment construction, produced the contours of principal stress directions in the foundation soil shown in Fig.1.5. It can be seen that α is 0° under the large central area of the embankment, while rotation starts to occur under the shoulder (α=10°), progressing to 90° at the toe.

Smith (1984) performed finite element analysis of a multi-stage embankment on soft clay. This type of embankment is constructed in stages, with rest periods in between. During the rest periods the soil consolidates with different principal stress inclinations and Smith showed that its undrained strength increases. This gain in undrained strength allows the construction of the next stage of the embankment. The anisotropy induced by "inclined" consolidation is a key factor in controlling multi-stage embankment behaviour.

c) Wave loading

Henkel (1970) recognized the role of waves in causing submarine landslides on very gentle slopes (1:125 at Missisippi Delta). He attributed these landslides to the pressure differences acting on the sea floor due to waves. Their action is oscillatory in nature and causes cyclic loading of a sea bed soil, generating high pore water pressures which remain undissipated and can lead to failure in loose sands due to liquefaction. Pressure differences due to wave action have a large effect on the behaviour of gravity platforms which become subject to combined vertical load and cyclic horizontal loading. Hight (1983) considered this problem for an offshore gravity structure on an isotropic, linear elastic foundation. Fig.1.6 shows the distribution of cyclic forces and moments acting on the foundation of a gravity structure for a sequence of assumed wave positions. Contours of the direction of the major principal stress increment and increments of b are shown in Fig.1.7 and 1.8 respectively, for the loading conditions appropriate to stage II on Fig.1.6. Comparing these plots with those for the vertically loaded foundation shown in Figs.1.3 and 1.4, it can be seen that a similar range of principal stress increment directions is encountered on the "loading " side (α up to 70°) while the values are much lower on the "unloading" side. The distribution of the incremental b parameter (Eq.1.2) is also changed by the addition of horizontal and moment loading with the values being much higher, particularly under the unloaded side of the foundation.

In the above examples the stress changes in the in-situ soil are highly complicated, involving the continuous rotation of the principal stress directions. Such conditions are extremely difficult to simulate in the laboratory. Therefore, only limited investigations have been undertaken to date into the stress-strain-strength anisotropy of soils.

1.1.4. Research

Previous researchers have been hampered by the limited degree of principal stress rotation allowed by their testing apparatus, the inadequate resolution of strain measurement, the non-uniformity of stresses or/and strains within the sample, the lack of control over the intermediate principal stress, σ_2, and other problems. The large Imperial College Hollow Cylinder Apparatus (IC HCA) was developed to overcome the above difficulties and therefore make comprehensive studies of soil anisotropy possible. Using the IC HCA, the magnitude of all three principal stresses can be independently controlled, whilst also varying the direction of σ_1 in a vertical plane at the same time. It is thus possible to study the effect of principal stress rotation and the influence of the intermediate principal stress under a wide range of stress conditions.

1.1.5. Choice of testing material

The main objective of the current research is to broaden the database concerning the anisotropic behaviour of soils and in particular the sort of soils which are potential sea-bed sediments. Most of the research to date, at IC and elsewhere, has concentrated on sands and, to a lesser extent, clays. Pure silts have not received much attention. They have only been considered at IC if they were part of other soils (Pentre clay-silt as a natural material, Connolly (1995); or artificial clay-sand-silt mixture, KSS, Menkiti (1995)). So, from the material behaviour point of view, the choice of the artificial man-made pure silica silt HPF4 for the current research spans an informational gap which exists between the sands and clays previously studied.

Another reason for choosing silt is that geotechnical practice in off-shore engineering often encounters situations where silty material forms the foundation soil for offshore structures, or is involved with submarine landslides which are prone to liquefaction. Toolan (1992), who gave a review of the geographical locations of sea-bed soils, recognized the common occurrence of silt type sediments. Recently, large scale landslides have been identified in the silty deposits of West of Shetland, Paul (1994). Certain major marine sites of Alaska (such as Port Valdez) have very thick (in excess of 60 m) layers of rock flour based silt (Singh & Quigley, 1983), in which landslides have developed on very gentle slopes. Such material consists of very fine unweathered mineral fragments of the predominant rocks in the area. Soil anisotropy and undrained brittleness are key features of behaviour which may explain such phenomena.

For the above reasons, HPF4 has been chosen as an appropriate material for simulating rock flour type sea-bed silts. Independent research is also being carried out at IC (under other research programmes), to investigate the behaviour of a natural laminated clay-silt from a deep glacio-lacustrine deposit at Pentre (near Shrewsbury) and a natural marine shelly sand from Dunkirk (N.W.France). Dunkirk sand is a dense medium size sand, while the grading curve envelope for Pentre sediments falls predominantly in the silt range. So, the behaviour of HPF4 can be directly compared with these two natural soils.

1.2. Objectives of this study

1.2.1. Previous research with IC HCA

The dimensions of the IC HCA sample (outer radius 25 cm, inner radius 20 cm, height 25 cm - Chapter 3), are suitable for testing reconstituted soils. Natural materials have not yet been tested because to do so would require large block samples to meet the specimen dimensions and it would not be easy to trim the samples to the size required. The main research effort over the past 15 years has therefore concentrated on testing artificially prepared sands (Ham River Sand, HRS) and sand-clay mixtures (both of low and high clay content).

The main objective of Symes (1983) research was to establish the initial drained and undrained strength anisotropy, due to principal stress rotation, of isotropically consolidated loose and dense HRS. He also investigated the effect of b on material response and placed the behaviour of HRS into the Bounding Surface framework (defined by Gens, 1982 - Chapter 2). The framework was extended into the α-dimension to account for principal stress rotation.

Shibuya (1985) extended this work by exploring the cyclic behaviour of isotropically consolidated loose HRS. Shibuya and Hight (1996) considered the behaviour of K_o consolidated loose HRS in terms of its initial strength anisotropy. They showed that the Bounding Surface for HRS was unique in that its position was unaffected by the stress path that a soil element followed to reach it.

Menkiti (1995) extended the range of materials tested in the HCA, by investigating the behaviour of two new K_o consolidated materials (HK, a mixture of HRS with 10% kaolin; and KSS, a mixture of 50% kaolin, 25% fine sand and 25% silt). He showed the applicability of the Bounding Surface framework for both of these materials. He also simulated simple shear tests

in the HCA and showed that they agreed with results from simple shear apparatus. His tests, together with a pilot experiment by Shibuya, provided many insights into the otherwise poorly understood simple shear failure stress conditions.

The anisotropy in yielding and stiffness characteristics of these materials at small strains had not been investigated in great detail in the IC HCA, partly because of difficulties with the resolution of the strain measurement devices used in this apparatus to date.

1.2.2. Aims of this research

As stated in the Introduction, the objective of this study was to extend current knowledge concerning the stress-strain and strength anisotropy of soils. The main aims can be conceptually summarized as follows:

a) To establish the initial undrained strength and stiffness parameters (i.e. c_u, ϕ' and G) of a previously unresearched class of materials (silt), through a series of conventional triaxial compression and extension tests on K_o consolidated HPF4, at different OCRs. This information allows the bounding surface hypothesis to be checked with respect to overconsolidation and permits comparisons with the behaviour of clays and sands, so establishing HPF4 silt in the broader context of soil behaviour. The only previous research carried out using HPF4 was that by Ovando-Shelley (1986). He performed a limited number of triaxial tests to provide a comparison with his main research program on Ham River Sand.

b) To establish the more general initial strength anisotropy (c_u, ϕ') of HPF4 in the IC HCA, by undrained shearing of initially K_o normally consolidated samples with different inclinations of the principal stress, keeping the b-value constant. These tests also allow the applicability of the Bounding Surface framework to the behaviour of HPF4 to be investigated.

c) To study the directional dependence of the small strain yield and stiffness characteristics of lightly overconsolidated HPF4. Starting from the same in-situ stress point, K_o consolidated samples with OCR=1.3 were sheared undrained in the IC HCA, with probing stress paths which had different directions in three-dimensional t-p'-α space. Along these stress paths there was a continuous change of α and b. Such stress paths are likely to be observed in practice during undrained construction of a geotechnical structure.

d) To investigate the effects of induced anisotropy of HPF4. This was done by showing how the anisotropy of initially K_o normally consolidated HPF4 could be changed by additional consolidation paths in which the major principal stress direction was rotated away from the vertical. The effects were quantified by investigating the effect of such induced stresses on the behaviour during consolidation and on subsequent undrained shearing. The motivation for this series of tests came from the practical problem of constructing multi-stage embankments on soft ground.

1.3. Outline of the thesis

Chapter 2 presents a general review of investigations in to soil anisotropy (inherent, induced and initial), distinguishing between the influence of α and b on anisotropic material response. Soil is often recognized as a transversely isotropic medium at very small strains and a mathematical framework for such a material is defined. The measurement of the parameters required to define such behaviour is reviewed. In particular methods of establishing the overall shear modulus, G_{max}, at very small strains and the parameters that can influence its magnitude are considered in detail. A global framework in which material behaviour will be presented in later chapters is defined. This involves small strain kinematic yield surfaces and a large strain bounding surface. The role of material fabric, defined by particle shape and the structure of interparticle contacts, on material behaviour and its influence on the global framework is described.

Chapter 3 describes the soils tested and the equipment used in the research (stress path cell and hollow cylinder apparatus). It explains the logic behind the calculation of stresses and strains in the HCA and the principles of a new control and data acquisition system implemented to operate the HCA. Sample preparation and testing procedures are explained for both the stress path cell and HCA. The accuracy and resolution of stress and strain measurements is considered and tabulated to help the reader evaluate the reliability of the test data.

The Appendix to Chapter 3 describes the improvements that have been made to the data acquisition system to enable accurate measurements in the small strain region of soil behaviour. It also gives details of the procedures employed when converting the raw electrical data to give the stress strain response. An overall picture of the operation of the HCA is given, concentrating on the operation and interaction of the various electronic components.

Chapter 4 presents results of a series of undrained triaxial compression and extension tests on K_o consolidated HPF4 for a range of over consolidation ratios (OCR's). From the consolidation stages of these tests both the virgin consolidation and swelling coefficients are determined. The consolidation *e-lnp'* curves and the shearing *t-p'* diagrams indicate that HPF4 behaves very much like a granular material. The undrained stress paths from compression and extension tests performed on normally consolidated HPF4 provide boundaries for the initial Bounding Surface (BS). The stress-strain and stiffness behaviour of HPF4 are compared to those of other soils, both clays and granular soils, previously tested at IC. This comparison enables the behaviour of HPF4 to be established within the general framework of soil behaviour.

Chapter 5 presents the results of the first Series of tests performed in the HCA (M-Series). The objective of these tests was to investigate the initial anisotropy of HPF4 after K_o normal consolidation. Samples were initially K_o normally consolidated, the *b* value was then changed to either 0.3 or 0.5 under drained conditions, the direction of the major principal stress, α, was then adjusted to have a value between 0° and 90° before the samples were sheared undrained, maintaining this value of α. The results from these tests enable the initial anisotropy of HPF4, when sheared with different inclinations of the major principal stress, to be quantified in terms of "undrained strength"[1], c_u, and mobilized angle of shearing resistance, ϕ'. The effect of *b* is investigated by comparison of tests with α=0° performed in the stress path cell under triaxial conditions (b=0.0) with those with α=0° from the M-Series (b=0.5 and b=0.3). The high values of the angle of shearing resistance, ϕ', observed when α<20°, are explained by considering the particle shape of HPF4 and the material structure formed by interparticle contacts.

The Appendix to Chapter 5 presents a detailed discussion of the possible reasons for the high ϕ' values observed in the Hollow Cylinder tests with α<20° and *b=0.5*. By comparing results from triaxial tests performed on Ham River Sand in the HCA with similar tests performed in a conventional stress path cell it is shown that there is unlikely to be an apparatus effect. The main reason for the high ϕ' values is particle shape and the material structure that is formed by particle contacts under the different stress conditions. Results from isotropically and anisotropically consolidated samples are used to illustrate this point.

The first part of Chapter 6 investigates the initial yield and stiffness anisotropy of lightly

[1]"Undrained strength" throughout the thesis is the maximum value of *t* achieved at Phase Transformation.

overconsolidated HPF4 (OCR=1.3), when sheared undrained with different $\Delta t/\Delta\alpha$ directions, from the same stress state. The tests simulated the effects of anisotropy that may be observed during the undrained construction of a geotechnical structure when the state of stress in the soil changes from its initial triaxial in-situ conditions towards plane strain conditions. The test results enable the three-dimensional shape of the Y_2 and Y_3 yield surfaces[2] in t-p'-α space to be determined. The second part of the Chapter presents results of drained tests from which the initial anisotropic parameters necessary to define the cross-anisotropy of the material, are determined. These parameters are then used to investigate whether or not the undrained stiffness and inclination of the undrained stress path can be predicted from drained material parameters.

The Appendix to Chapter 6 gives the theory behind an elastic transversely isotropic (or cross-anisotropic) material and the derivation of the compliance matrix to represent such a material.

Chapter 7 considers the effects of induced anisotropy. Initially, samples were K_o normally consolidated, the direction of the principal stress was then changed so that each sample had a different value of α between 0° and 90°, the samples were then subjected to further consolidation (to double the value of p') with these inclined principal stress directions, i.e. with $\alpha=\alpha_c\neq 0°$. The value of b was then changed to 0.5 before the samples were sheared undrained maintaining b and α constant. By shearing α_c-consolidated samples with a constant α_c under undrained conditions it is possible to investigate by how much the stress-strain-strength behaviour differs from that observed in K_o material sheared with $\alpha=0°$. Tests were also performed in which the direction of the major principal stress was changed after α_c-consolidation, but prior to undrained shearing. These results enable a comparison to be made between the initial anisotropy existing after K_o consolidation and the anisotropy induced by the additional α_c-consolidation. The results of these tests have direct relevance to many practical problems, including the construction of multi-stage embankments on soft ground.

Chapter 8 summarises the results from the previous Chapters and presents the main conclusions of the research. The practical application of these to engineering practice is discussed. Recommendations for future research are made.

[2] Y_2 and Y_3 yield surfaces are defined by Jardine (1985) and are presented in Chapter 2.

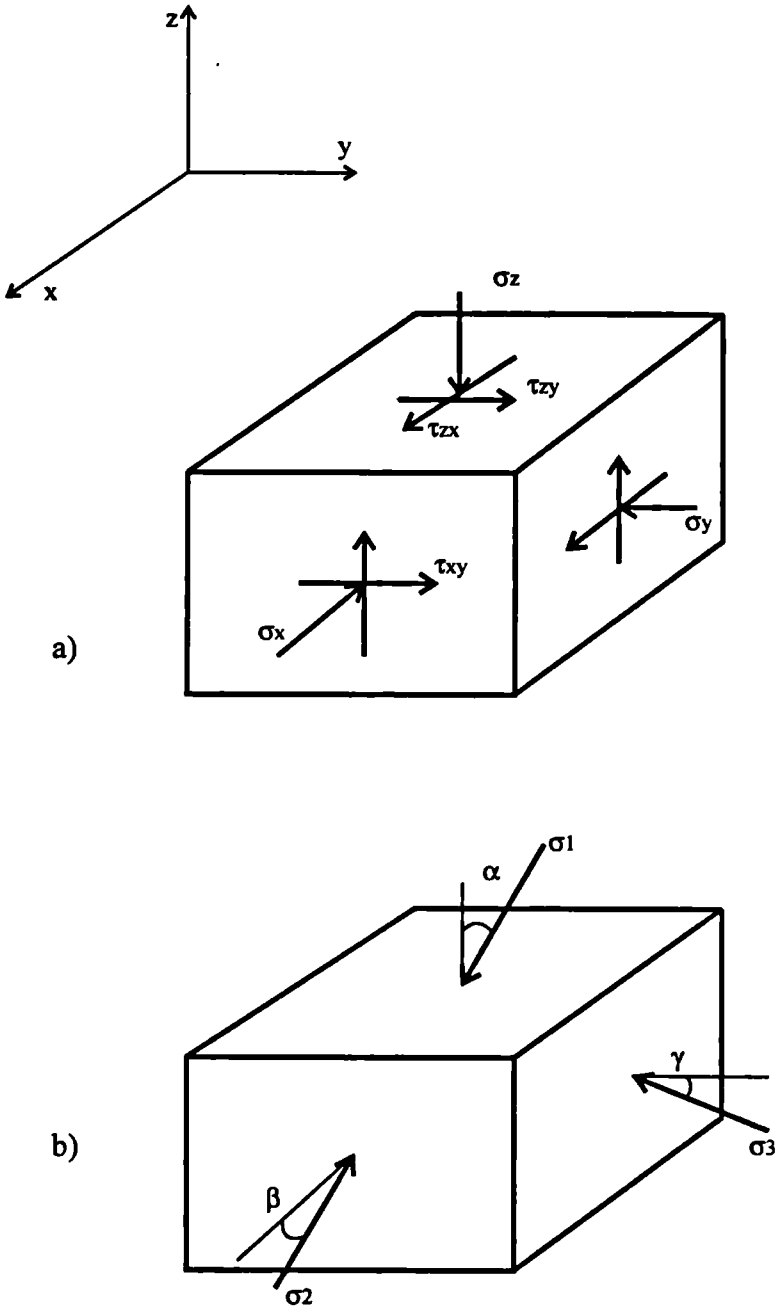
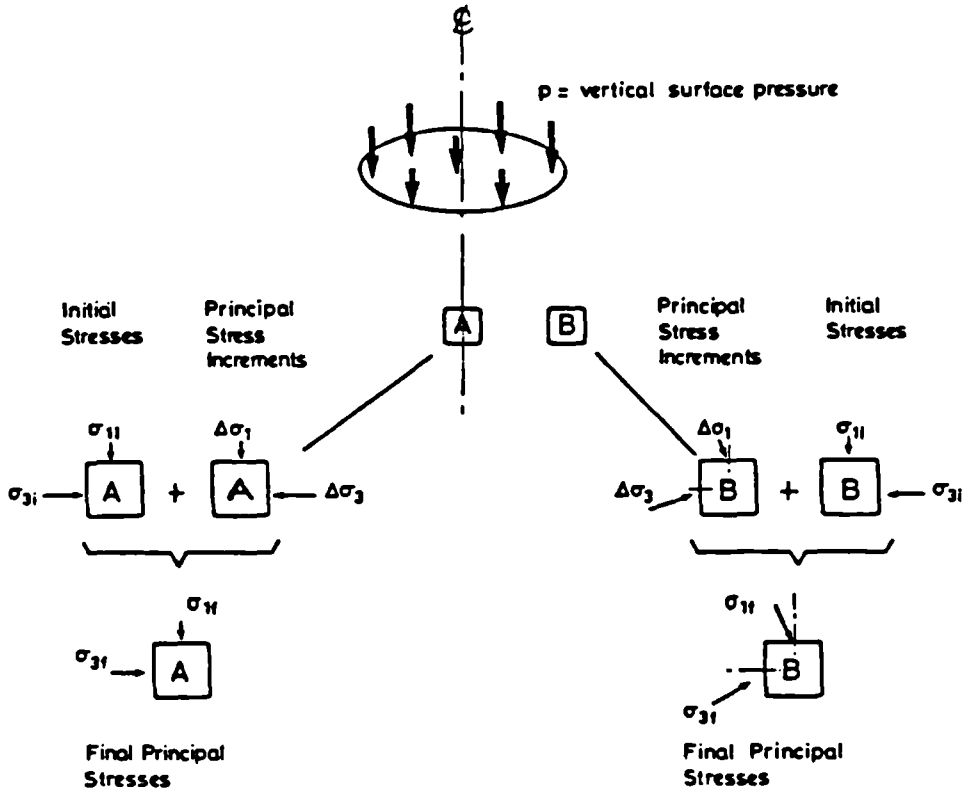


Fig.1.1 - Component stresses acting in the ground



(a) Principal stress directions on and off the axis of symmetry.



(b) Influence of shear stress direction on rotation of principal stresses.

Fig.1.2 - Principal stress rotation beneath a vertically loaded circular footing (Hight, 1983)

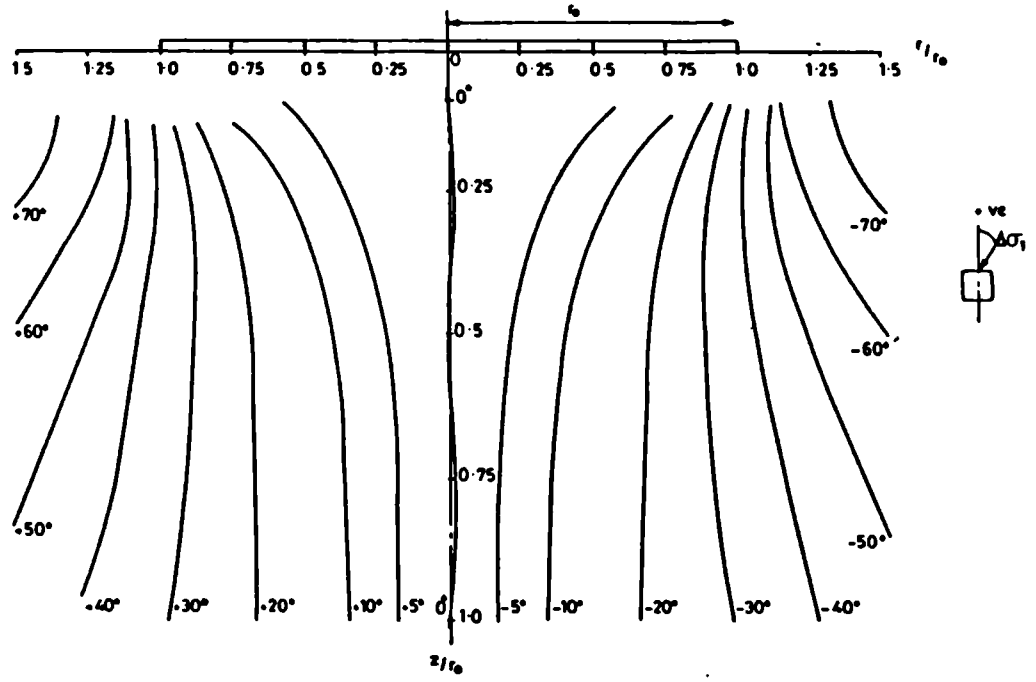


Fig.1.3 - Contours of principal stress increment direction beneath vertically loaded circular footing on isotropic linear elastic foundation (Hight, 1983)

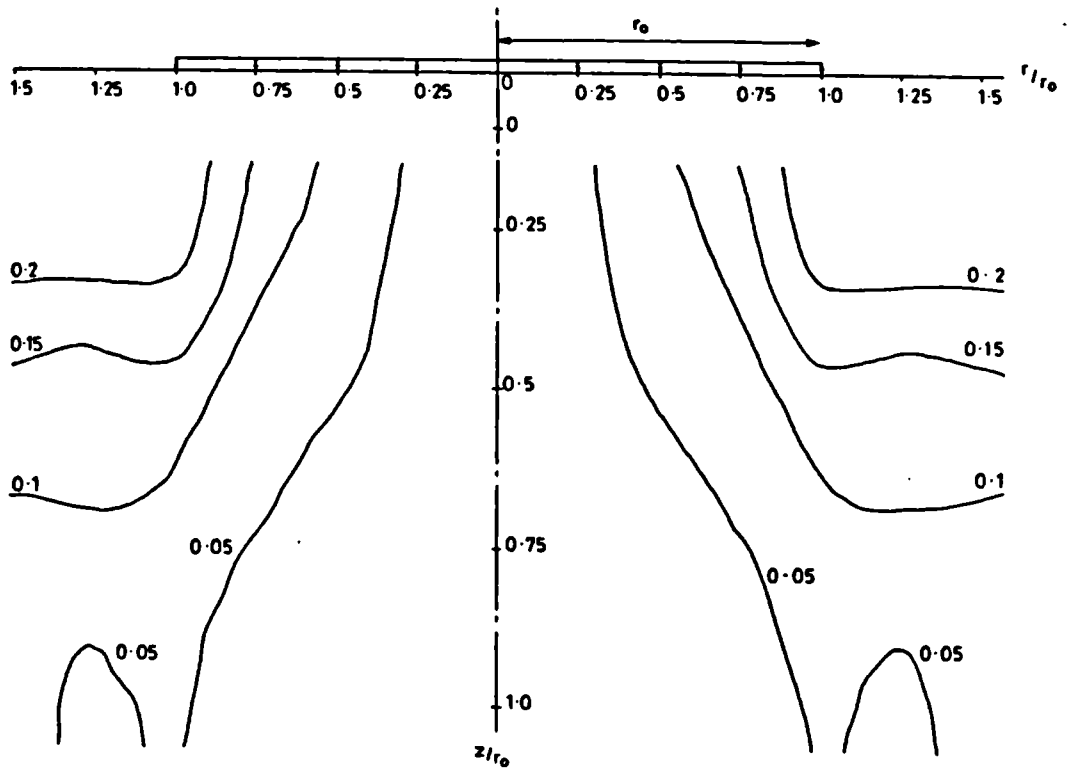


Fig.1.4 - Contours of $(\Delta\sigma_2-\Delta\sigma_3)/(\Delta\sigma_1-\Delta\sigma_3)$ beneath vertically loaded circular footing on isotropic linear elastic foundation (Hight, 1983)

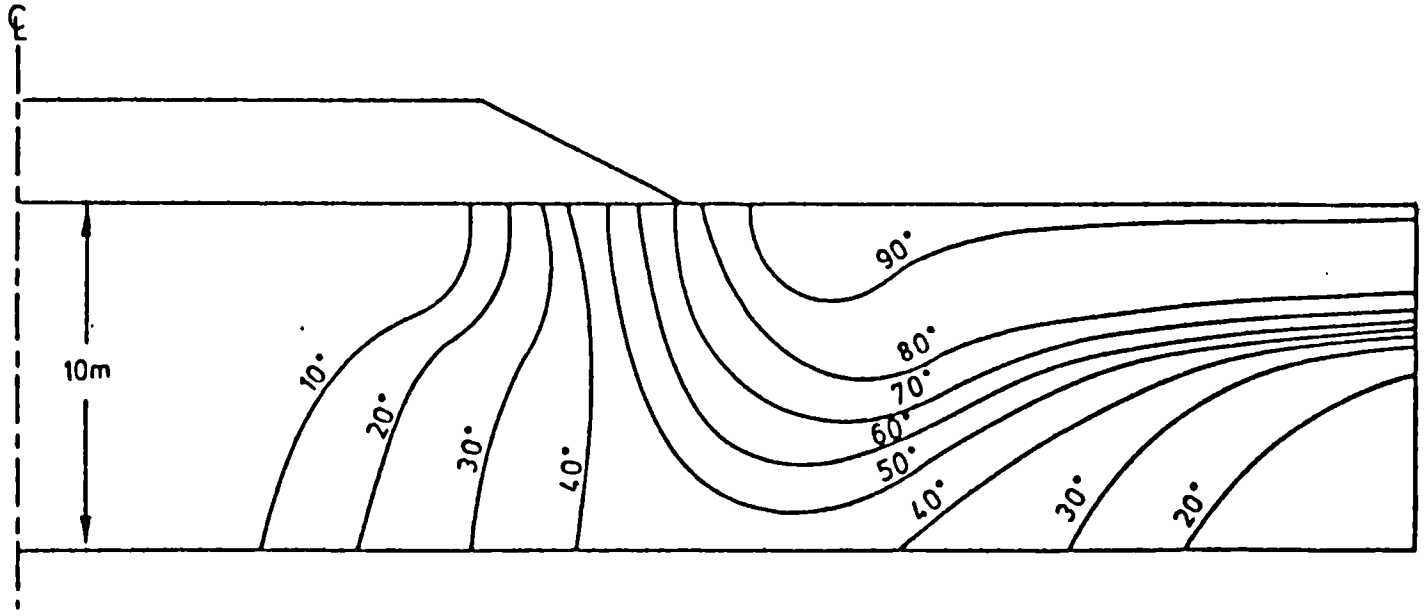


Fig.1.5 - Contours of principal stress directions beneath embankment (Yeats, 1983)

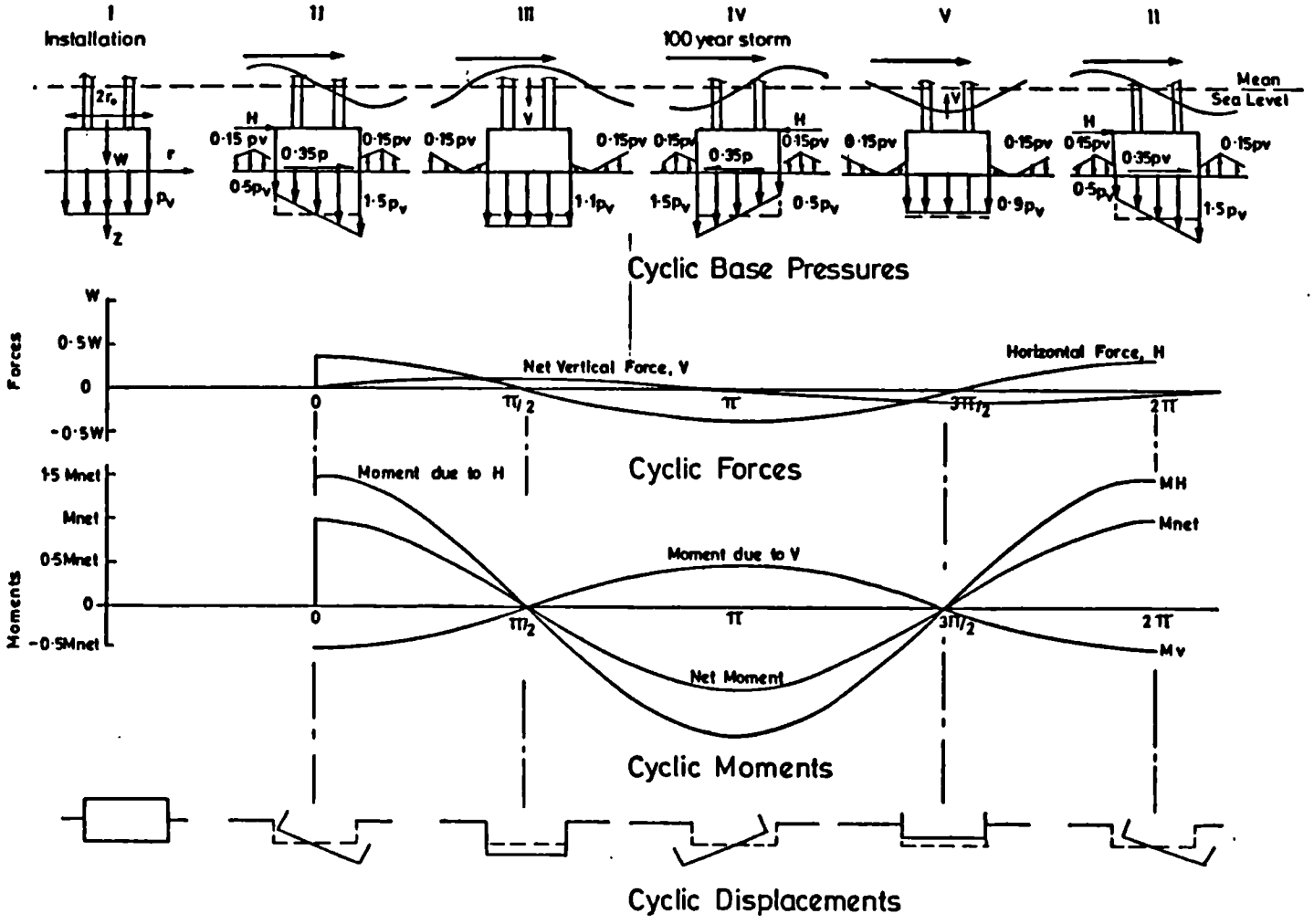


Fig.1.6 - Cyclic forces, base pressures, moments and displacements for a typical gravity structure under design storm wave loading (Hight, 1983)

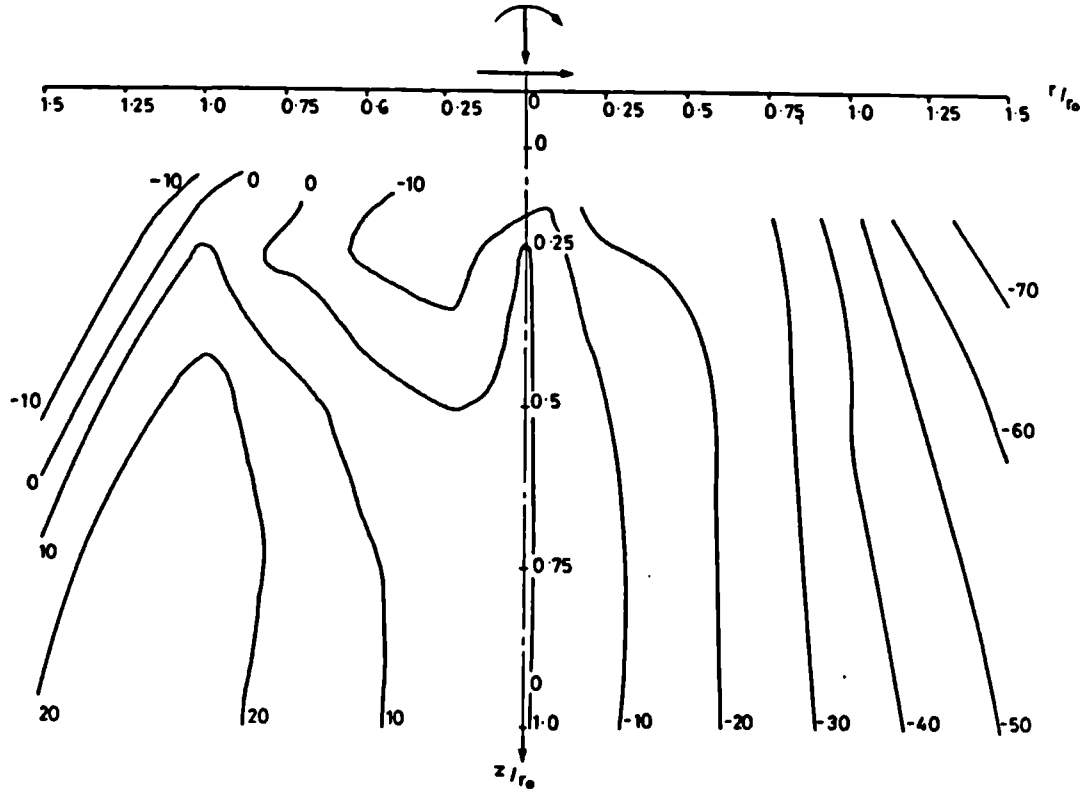


Fig.1.7 - Contours of rotation of principal stress increments in foundation to typical gravity structure (Hight, 1983)

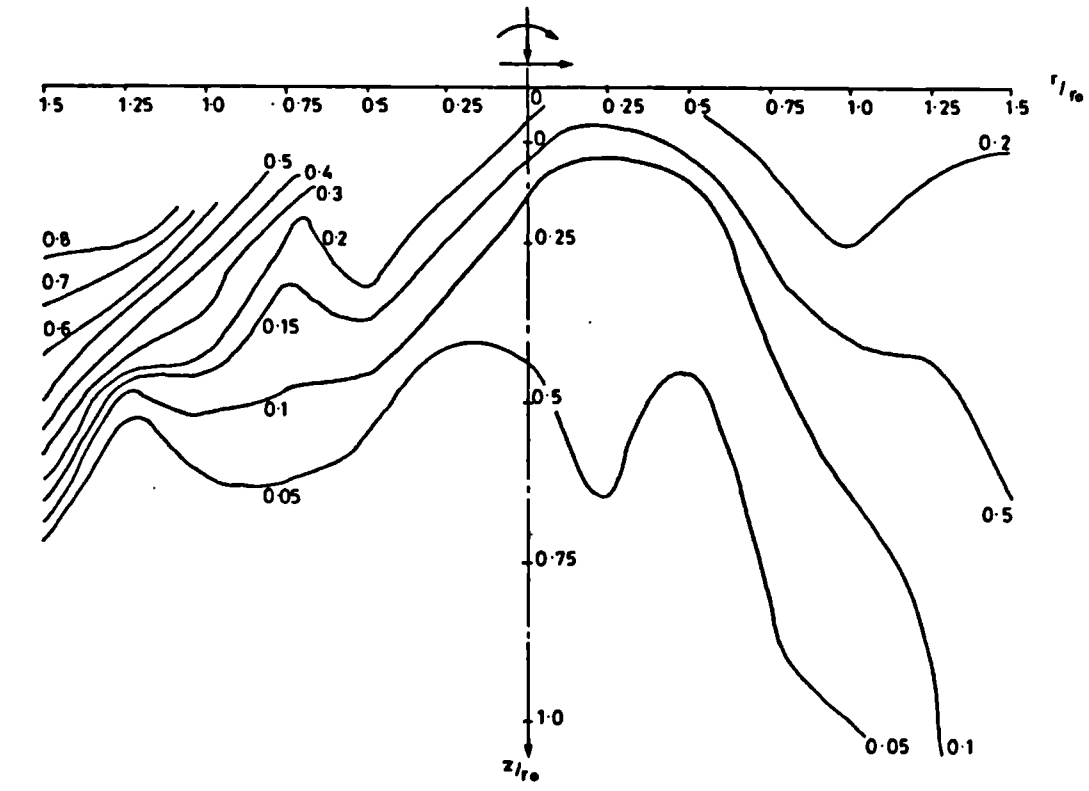


Fig.1.8 - Contours of $(\Delta\sigma_2-\Delta\sigma_3)/(\Delta\sigma_1-\Delta\sigma_3)$ in foundation to typical gravity structure (Hight, 1983)

Chapter 2
BACKGROUND TO SOIL ANISOTROPY

2.1. Introduction

A material is said to be anisotropic if its properties are directional dependent. Soil is, generally, anisotropic because of the processes involved in its deposition, its previous stress history and its composition. The first considerations of soil anisotropy are dated back to 1944, when Casagrande and Carillo characterised soil anisotropy into two constituent parts:

a) *inherent* anisotropy, defined as "a physical characteristic inherent in the material and entirely independent of the applied strains" and

b) *induced* anisotropy defined as "due exclusively to the strains associated with the applied stresses".

The anisotropy possessed by a soil element existing in situ under a set of applied stresses, after being subjected to a particular stress history, is a combination of both *inherent* and *induced* anisotropy and is called *initial* anisotropy.

The first investigations into soil anisotropy were performed using a range of standard laboratory testing devices. However, it was difficult in many of these devices to realistically simulate field conditions (Bishop & Henkel, 1962; Hight, 1983; Jamiolkowski et al, 1985; Arthur & Menzies, 1972). The main difficulty was to achieve a controlled rotation of the principal stresses so that the directional response of a material could be investigated.

Early studies by Bishop (1966), Green & Reades (1975), also showed that the intermediate principal stress, σ_2, plays an important role in soil behaviour. Shibuya (1985) and Symes (1983) showed that σ_2, expressed in terms of b $[=(\sigma_2'-\sigma_3')/(\sigma_1'-\sigma_3')]$, has a significant effect on soil anisotropy. For example, the effect of the direction of the major principal stress is much larger if $b=0.5$ than if $b=0$ or $b=1$. In most practical situations the effects of principal stress rotation and changes in b are usually coupled. It is, therefore, necessary to consider the b-effect when examining soil anisotropy (Symes, 1983; Tatsuoka et al., 1986; Menkiti, 1995).

2.2. Laboratory equipment for investigating anisotropy

Menkiti (1995) gives a detailed summary of the available laboratory equipment for studying soil anisotropy, highlighting both the shortcomings and advantages of each. Consequently, only a brief review of the more relevant pieces of equipment will be presented here.

A) The Direct Shear Box Device (DSB)

The DSB has been reviewed by Saada & Townsend (1981), Hight (1993) and more recently by Shibuya et al. (1993). The latter reported improvements in instrumenting the DSB with additional load cells to measure both vertical load and side friction stresses. The DSB enables a soil sample to be K_o consolidated vertically and then sheared horizontally, by sliding the upper part of the sample container over the lower part. The direction of the major principal stress, σ_1, therefore rotates away from the vertical as shearing progresses. However, this rotation is uncontrollable and varies throughout the sample because of the high degree of non-uniformity of stresses that exist in the DSB, making the device unsuitable for studying anisotropy of soils. The non-uniformity arises due to the stress concentrations which occur at the front and back end of the shearing plane and is a direct consequence of the way in which the apparatus works. The stress distributions within the sample have been studied theoretically by Potts, Dounias and Vaughan (1987) and Dounias and Potts (1993).

B) Triaxial Cell

The triaxial cell is, nowadays, a standard piece of equipment in most soil mechanics laboratories. It is described in detail by Bishop & Henkel, 1962. Strength and stiffness parameters obtained from triaxial testing are the main parameters used in geotechnical design.

The triaxial soil sample is subjected to stress and strain non-uniformities arising from the rigid end platens which transmit load through the sample. However, these non-uniformities are dependent on the aspect ratio of the sample and are thought to be insignificant for samples with a height to diameter ratio of two.

The triaxial test is severely restricted in its ability to investigate soil anisotropy. The sample can either be sheared in compression (where σ_1 is vertical, i.e. $\alpha=0°$) or in extension

(where σ_1 is horizontal, i.e. α=90°). However, the *b* values associated with these two stress paths are different: *b=0.0* when α=*0°* and *b=1.0* when α=*90°*, so the contribution of each of the parameters (α and *b*) cannot be distinguished.

Attempts have been made for inclined cylindrical samples (i.e. samples trimmed under a different angle to the axis of deposition) to be tested for anisotropy in the triaxial cell, but such samples are prone to errors due to end bending, which will be discussed in Section 2.3. They also suffer from the fact that initial K_o conditions in the ground can not be applied to the sample.

C) Simple Shear device (SS)

Several types of SS device have been used in laboratory research. The Roscoe type device, known as the Cambridge Simple Shear Apparatus (CSSA), used a prismatic sample, whereas the device developed at the Norwegian Geotechnical Institute (NGI) (Bjerrum & Landva, 1966) and a version developed by the Royal Swedish Geotechnical Institute (SGI) (Kjellman, 1950) both use a short cylindrical sample. These SS devices were designed to offer improvements to the DSB device and in particular to avoid the stress concentrations at the leading and trailing parts of the shear surface. However, these devices still promote non-uniformities in the sample which make them difficult to interpret. This is particularly true for the NGI and SGI devices, in which the cylindrical samples are sheared with a constant perimeter boundary condition and no complimentary shear stresses applied on the vertical sides of the sample (Jefferson, 1994).

K_o consolidation is possible in these devices and σ_1 rotates away from the vertical as shearing progresses. However, σ_2' cannot be measured in most devices and due to the non-uniformities the calculation of the inclination of σ_1' is uncertain. These restrictions render the device unsuitable for investigating soil anisotropy.

D) The True Triaxial Apparatus (TTA)

Several different versions of this device are available (Saada & Townsend, 1981; Arthur, 1988). Common to all of them is that the three principal stresses can be independently applied to the sides of a prismatic sample, via either rigid or flexible boundaries. Consequently, the TTA is ideal for investigating the effect of *b* on soil response, but σ_1 cannot be rotated and so anisotropy cannot be easily investigated unless inclined samples are used.

E) The Plane Strain device (PS)

Many versions of the PS device have been developed: Cornforth (1964), Green & Reades (1975), Marachi et al (1981), Arthur (1988). In this device prismatic samples are constrained to keep the intermediate principal strain, ε_2, equal to zero. Direct stresses or strains are then applied to the other boundaries of the sample. The intermediate principal stress, σ_2, cannot be measured in some devices and therefore the state of stress in the apparatus is not fully defined. Consequently, the b value cannot be evaluated. Samples can be tested in either vertical compression or extension, giving only a restricted view of the material stress-strain-strength anisotropy. To overcome some of these restrictions some researchers have attempted to test samples which have been either cut or sedimented in different directions, so that they can be placed in the apparatus with their axis of deposition at an angle to the testing platens. However, the results from such tests are vulnerable to significant end effects. Similar as with inclined triaxial samples, stress state other than isotropic consolidation cannot be investigated. It may be concluded that the PS device is not fully suitable for investigating soil anisotropy.

F) The Directional Shear Cell (DSC)

The DSC was developed at University College London (UCL) by Arthur et al (1977a), for testing sand samples under plane strain conditions. The plane strain conditions are imposed on two opposite faces of the sample by end platens. On the other four sides, both direct and shear stresses are applied via flexible membranes so that σ_1 can be rotated in a controlled manner. Therefore, the DSC applies relatively uniform stresses and strains to the specimen, σ_1 can be rotated in a controlled manner and b can be measured, but not fully controlled. On the other hand, strain measurement, which has to be performed via photometry and/or radiography, is laborious and prevents the testing from being conducted using servo-control. This can be a serious restriction when attempting to study material anisotropy. In addition, facilities are not available to provide cell or back pressures. Consequently only drained tests can be performed. In summary, although the DSC can be used to study soil anisotropy, its operation is cumbersome and great care must be exercised when performing the tests.

G) The Hollow Cylinder Apparatus (HCA)

The history of testing hollow cylinder soil specimens goes back to Cooling and Smith (1936) who applied torque to unconfined samples. Since then, more sophisticated apparatuses

have been developed. Hight et al. (1983) give a review of hollow cylinder equipment.

The main characteristic of the HCA is that four loads can be applied to the specimen and independently controlled. These are the internal and external pressures on the curved sides of the sample, the vertical load and a torque. This in turn implies the independent control of both the intermediate principal stress, expressed through b, and rotation of the direction of the major principal stress, σ_1. The key point is that the K_0 consolidation is possible, so that samples can be tested with initial stress states which resemble in-situ field conditions. Both drained and undrained shearing can be performed.

Non-uniformities in stress and strain conditions exist in the HCA due to the curvature of the sample and due to end restraints arising from the rigid top and bottom platens. The philosophy behind the design of the HCA was to accept the existence of these non-uniformities, but to reduce their magnitude by careful choice of sample geometry. Hight et al. (1983), Symes (1983) and Sayao & Vaid (1991) addressed this problem by using finite element analyses and came up with conclusions about the sample dimensions and allowable limits for stress and strain distributions across the sample wall. Menkiti (1995) interpreted these non-uniformities from the aspect of engineering significance and concluded that they were negligible for the IC HCA. Similar analysis was performed by Porovic (1995), for hollow cylinder sample in resonant column device, only with another geometry. A review of the non-uniformities in the IC HCA, together with more details about its operation and instrumentation, are given in Chapter 3. Although complex in its operation and interpretation the HCA provides a valuable tool for investigating stress-strain-strength anisotropy of soil.

The conclusion of this short review is that among the available laboratory equipment, only well designed DSC's and HCA's can be used to investigate soil anisotropy.

2.3. Previous studies of anisotropy

2.3.1. Introduction

The first attempts to explore anisotropic soil behaviour involved tests on tilted samples subjected to conventional triaxial tests. Duncan & Seed (1966) cut vertically consolidated samples of kaolin at different inclinations to the direction of consolidation and tested them in a triaxial apparatus. Arthur and Phillips (1975) made "inclined" samples by pouring sand into

a tilting mould to get different inclinations of the bedding plane. These samples, however, can not be K_o consolidated and, therefore, do not represent initial in-situ ground conditions, or reproduce the strength anisotropy which occurs in situ. In addition to the above limitation, Saada (1970) and later Saada & Bianchini (1975) demonstrated that undesirable end bending moments and deformed shapes of the sample develop when cylindrical samples with inclined bedding planes are tested between rigid end platens (Fig.2.1). Such samples generate highly non-uniform stresses in the mid-section and these non-uniformities change with the sample inclination, so that accurate evaluation of anisotropy cannot be made from such tests. Jamiolkowski et al. (1985) supported this view and also noted that, with regard to natural samples, there was also the additional influence of the variable degree of sample disturbance, which tends to mask anisotropy. From the above it may be concluded that only triaxial tests on vertical or horizontal samples can be considered reliable for studies of anisotropy.

To investigate the influence of both α and b on soil response, many researchers have tested cubical (or prismatic) "inclined" samples under both plane strain and true triaxial conditions, by using flexible boundaries which, in principle, overcame Saada's non-uniformity criticism: Lade & Duncan (1973), Arthur & Assadi (1977), Ochiai & Lade (1983), Wong & Arthur (1985), Tatsuoka et al. (1986), Lam & Tatsuoka (1988).

The subsequent discussion of the effects of α and b on the behaviour of different granular materials will focus only on findings using hollow cylinder or prismatic specimens (either Plane Strain, True Triaxial or Directional Shear Cell). The main parameters for each of the sands which are referenced in this discussion are summarized in Table 2.1.

2.3.2. Effect of α

2.3.2.1. Effect of α under plane-strain conditions

a) Leighton Buzzard sand (LBS) has been intensively tested by Arthur and his co-workers at University College, London (UCL), in the Directional Shear Cell (DSC, Section 2.2). Sand is poured through air into a 10x10x10 cm mould so that it is initially very dense. An initial isotropic stress of 100 kPa is applied via suction to the sample so that it can be handled and placed in the DSC. The sample can be orientated with its axes of deposition either perpendicular or parallel to the plane of subsequent shearing (Fig.2.2). If the perpendicular orientation is used then the sample is initially isotropic in the plane of subsequent shearing and tests can be performed to investigate induced anisotropy. In comparison, if the parallel orientation is used

then the sample will be anisotropic in the plane of shearing and the behaviour on subsequent shearing will involve the effects of both inherent and induced anisotropy. Once the sample is in the DSC an all round pressure of 14 kPa is applied and then the suction is released. The samples are therefore over consolidated and are subjected to an isotropic stress of 14 kPa at this stage. The samples are then sheared drained in plane strain, with a prescribed value for the orientation of the major principal stress, α, in the plane of shearing.

Principal stress rotations of α=0°, 70° and 90° were applied to samples of LBS prior to shearing. The samples were then sheared drained with these values of α, to evaluate their inherent anisotropy (Wong & Arthur, 1985). Peak mobilized ϕ' values varied from 49.8° for α=0° to 45.5° for α=90°, while the initial stiffness reduced as α increased from 0° to 90°. This variation in ϕ' is shown in Fig.2.4, along with data from other similar studies. In Fig.2.4, the horizontal axis represents both, α, the degree of principal stress rotation from the vertical when the bedding plane is horizontal, and δ the inclination of the bedding plane from the vertical (Fig.2.3). They are compatible in that α=90°-δ.

b) Toyoura sand has been intensively investigated in Japanese laboratories and its behaviour is well documented. Oda et al. (1978) performed an extensive study into the anisotropy of Toyoura sand, using both plane strain and triaxial equipment. Samples were initially dense, with e_o=0.66 and D_r=91%. In the plane strain device the sample was 4.4 cm wide, 6 cm high and 8 cm long. During testing the 4.4 cm by 6 cm sides of the sample where prevented from moving insuring plane strain conditions. Sand was poured in a mould so that when mounted in the testing apparatus the bedding plane of the sample could have an orientation to the vertical, ranging from 0° to 90°. After pouring the dry specimen was soaked in water and then frozen so that it could be trimmed and placed into the testing device. Samples were tested under different cell pressures (50, 100, 200 and 400 kPa).

The stress-strain curves showed distinct peaks in deviator stress, but at the final strain level of ε_z=6% the tests did not indicate that ϕ_{cv}' had been reached. Fig.2.4 presents the distribution of peak ϕ' values for different bedding plane inclinations, for samples tested with a cell pressure of 100 kPa. The minimum ϕ' value is obtained for δ between 20° and 30°, and the maximum difference in ϕ' over the range of δ values tested (i.e. maximum anisotropy) is ~5°. This difference is more pronounced at larger cell pressures (i.e at a cell pressure of 400 kPa $\Delta\phi$'~8°), but the maximum ϕ' still occurs when δ=90° and the minimum ϕ' when δ~30°. The variation of ϕ' with cell pressure is presented in Fig.2.5 for samples tested with a horizontal

bedding plane, i.e. δ=90° (α=0°). This figure shows the reduction in ϕ' with increasing cell pressure.

The initial stiffness for a particular cell pressure is virtually the same for all tests, up to 0.5% strain. Subsequently the stiffness decreased progressively with δ, that is the test with δ=90° gave the stiffest response while the test with δ=0° gave the softest response.

c) Tatsuoka et al. (1986) and Lam & Tatsuoka (1988a, b), at the Institute of Industrial Science (IIS), Tokyo, performed sets of plane strain tests on Toyoura sand in a true triaxial apparatus using prismatic samples. In some of these tests, not reported here, they varied the aspect ratio of the sample and concluded that cubical samples gave accurate results. The results presented here are for samples 76x76x76 mm in size. Both loose and dense samples were tested, with e_o varying between e_o=0.8, (D_r=53%) and e_o=0.7, (D_r=81%), at a cell pressure σ_3=100 kPa. Sample preparation was similar to that reported by Oda and discussed above.

Fig.2.6 presents the variety of loading conditions applied in plane strain tests. A range of *b* values was investigated, with different bedding plane inclinations, as shown in Fig.2.7. In the figure, *n* is the direction of deposition and is normal to the bedding planes. In three dimensional space, the bedding plane inclination is defined by the angles ξ and ω. The largest variations in strength and stiffness occurred when ω changed from 0° to 90°, at ξ=90°. This corresponds to the situation when the bedding plane changes orientation from 0° to 90° to the vertical, in the plane of shearing (i.e. plane perpendicular to σ_2), Fig.2.7. These results are therefore compatible with the other results presented here and can be used for comparison. The angle ω is equivalent to (90°-δ) or α (Fig.2.3).

Stress-strain curves for dense samples show distinct peaks in the deviator stress and after 10% axial strain they seem to have reached ϕ_{cv}'. Fig.2.4 presents the variation of the peak ϕ' for dense samples with different bedding plane inclinations. The IIS tests show a similar trend to the other sands: maximum ϕ' occurs when δ=90° and minimum ϕ' occurs for δ between 20° and 30°, making the maximum $\Delta\phi$'~8°. A similar trend is also seen for loose samples in Fig.2.8, where the maximum $\Delta\phi$' reduces to 5°. The plane strain constant volume value of ϕ' is apparently ϕ_{cv}'=~36°.

The same anisotropic trend in behaviour is observed at all of the confining stress levels considered (5 to 400 kPa). The variation of peak ϕ' for tests with a horizontal bedding plane,

δ=90°, with increase in cell pressure, is presented in Fig.2.5. The variation of peak ϕ', again for samples with a horizontal bedding plane, with the sample's initial density is shown in Fig.2.9. The values of b at failure were observed to be between 0.3 and 0.5 for these tests.

d) Plane strain compression tests on granular materials, with horizontal bedding planes (δ=90°), have been performed by many researchers. The results of these studies by Cornforth (1964), Marachi et al. (1981), Leusink & Wittke (1964) are included in Figs.2.4, 2.5, 2.8 and 2.9. Most of these tests were performed drained.

Cornforth (1964) tested Brasted sand, with the characteristics as shown in Table 2.1, in states between loose (D_r=15%) and dense (D_r=80%). The peak ϕ' values are plotted in Figs.2.4 to 2.9. A constant volume ϕ' of ~33° seems to be reached at the end of all tests and is independent of initial density.

Marachi et al. (1981) performed a study into the plane strain behaviour of Monterey No.20 sand, at different densities and cell pressures. Again the samples were tested with the bedding planes horizontal. Figs.2.4 to 2.9 show the peak ϕ' distributions, while a ϕ_{cv}' of ~38° seems to have been achieved at the end of tests. It is interesting to note that the values of ϕ_{cv}' shown on Fig.2.4 range from 33° to 38°.

2.3.2.2. Effect of α on strength under triaxial compression conditions

Conventional triaxial devices are commonly used in geotechnical practice to obtain design parameters for soil strength. However, many geotechnical failures develop under plane strain conditions and it is of interest to know the difference in results obtained for these two testing conditions. Consequently, results from triaxial compression tests performed on isotropically consolidated tilted samples of the sands discussed above are presented below.

a) Dense Leighton Buzzard sand (LBS) has been tested in drained triaxial compression in a true triaxial apparatus (Arthur & Menzies, 1972). Samples were formed by pouring sand into a tilting mould so that samples with bedding plane inclinations to the vertical covering the range 0° to 90° could be achieved. An isotropic effective cell pressure of 55 kPa was applied. A maximum difference of only 2° in the peak mobilized ϕ' was seen between samples with bedding plane inclinations of δ=0° and δ=90°, Fig.2.10.

b) A set of drained triaxial tests on prismatic samples of tilted dense Toyoura sand, with different bedding plane inclinations, has been performed by Oda et al (1978). The samples were prepared with the same freezing technique as described in Section 2.3.2.1.b. The samples were sheared after normal consolidation to an isotropic effective stress of 100 kPa. The stress-strain curves are generally more ductile than those observed in plane strain tests and exhibit less pronounced anisotropy when δ changes from 0° to 90°. Fig.2.10 shows the variation of peak mobilized ϕ' with δ. There is only a maximum difference in ϕ' of 3° over the range of δ values considered. The maximum ϕ' was observed in the test with δ=90° and the minimum in the test with δ=0°. Similar trends occur for tests conducted at other cell pressures and Fig.2.11 presents the variation of ϕ' with cell pressure, for samples with a horizontal bedding plane.

c) Drained triaxial tests on prismatic tilted samples of dense Toyoura sand (e_o=0.66) were performed by Tatsuoka et al. (1986) and Lam & Tatsuoka (1988). Again the samples were prepared by the freezing technique so that the bedding plane inclination varied from 0° to 90°. The variation of the peak ϕ' value with α is shown in Fig.2.10 The samples were not strained sufficiently to show that ϕ_{cv}' had been reached. The variation of peak ϕ' with initial density is presented in Fig.2.12.

d) Cornforth (1964) and Marachi et al. (1981) performed standard drained triaxial tests on samples of Brasted sand and Monterey No.20 sand with horizontal bedding planes, respectively. The changes in peak ϕ' values for the range of densities and cell pressures investigated are presented in Fig.2.10 to 2.12.

2.3.2.3. Discussion

Sections 2.3.2.1 and 2.3.2.2 presented studies of drained anisotropy of sand in both triaxial and plane strain conditions. Most of these studies tested prismatic samples prepared using techniques such that the samples could be tested with their bedding plane orientated at angle (0° to 90°) to the vertical principal stress. The samples did not experience a K_o consolidation history, but were sheared drained after application of an isotropic cell pressure.

All the studies showed that samples tested with a horizontal bedding plane (i.e. δ=90°) gave the highest peak mobilized ϕ'. In plane strain conditions, the minimum ϕ' was observed in tests in which 20°<δ<30°. The maximum anisotropy in ϕ' for the same sample density and the same cell pressure is ~8° (Tatsuoka et al., 1986), ~6° (Oda et al., 1978) and ~5° (Arthur &

Assadi, 1977.). In triaxial compression conditions the minimum ϕ' was observed in tests with δ=0°, and the maximum observed difference in ϕ' between tests with δ=0° and δ=90° is less pronounced than in the plane strain tests. It is ~4° (Tatsuoka, 1986), ~3° (Oda et al., 1978) and only ~2° (Arthur & Menzies, 1972).

Although little accurate stiffness data was presented in the above studies, the stress-strain plots in both triaxial and plane strain compression generally indicate a softer response as δ decreases, i.e. as the bedding plane changes inclination from horizontal to vertical.

2.3.3. Effect of b on material behaviour

Comparing the triaxial and plane strain behaviours of a soil tested under the same initial density and initial stress conditions, provides a first indicator of the influence of the intermediate principal stress parameter *b*. In this respect, it should be noted that b=0 for triaxial compression and b is typically 0.3 to 0.5 for plane strain compression. Generally, plane strain conditions develop higher peak strengths for all bedding plane inclinations than triaxial compression conditions. The differences obtained in the studies discussed above are summarized in Table 2.2.

Table 2.2: Difference in peak ϕ' between triaxial and plane strain tests

Author	ϕ_{PS}'-ϕ_{TX}' dense	ϕ_{PS}'-ϕ_{TX}' loose
Cornforth (1964)	4.5°	1°
Marachi et al. (1981)	7°	3°
Oda et al. (1978)	5°	/
Tatsuoka et al. (1988)	7°	5°

In addition, many studies have been carried out, mainly using cubical triaxial samples, to investigate the influence of *b* over its full range from 0 to 1. Fig.2.13 summarizes data from some of the studies involving isotropically consolidated samples sheared under drained conditions.

Notable in this data set are the curves for dense Toyoura sand (Lam & Tatsuoka, 1988b) tested with bedding plane inclinations of 0°, 30°, 60° and 90° to the vertical (δ=90° is horizontal).

The sample preparation and material characteristics were as described in Section 2.3.2.

Lade & Duncan (1973) tested isotropically consolidated Monterey No.0 sand under drained conditions with a horizontal bedding plane, in both dense (e_o=0.57) and loose states (e_o=0.78). Under similar conditions, but with an initial e_o=0.53, Ochiai & Lade (1983) tested Cumbria Sand to investigate the influence of *b* on its response.

Symes (1983) performed a set of isotropically consolidated drained tests on dense HRS in the HCA to investigate the influence of both *b* and α on the material response. He performed tests with b=0, 0.14, 0.5 and 1.0, while α changed from 0° to 90° for each *b*-value. As a result, he obtained the three-dimensional surface shown in Fig.2.14. Part of this surface, when α=45° and b=0.0 to 1.0, is shown in Fig.2.13.

Two observations are drawn from Figs.2.13 and 2.14:

(i) For all the results obtained from isotropically consolidated samples, the peak ϕ' value (and the stress ratio σ_1'/σ_3') increases when *b* changes from 0.0 to ~0.5 and remains constant, or slightly decreases, at b~0.9 to 1.0.

(ii) Both Tatsuoka's and Symes' results show that the σ_1'/σ_3' *vs. b* curve becomes flatter at higher α inclinations, i.e. the effect of *b* reduces when the bedding plane changes inclination from horizontal to vertical: for Toyoura sand, maximum $\Delta\phi$' of ~5° (between b=0 and b~0.5) for the horizontal bedding plane decreases to $\Delta\phi$'~1° when δ=0°; for Ham River Sand $\Delta\phi$' decreases from 8° to 1° when principal stress inclination changes from 0° to 90° at the horizontal bedding plane.

2.4. Anisotropic pre failure parameters

2.4.1. Introduction

Soil is predominantly a non-linear material because of its particulate nature and is anisotropic because of its particle shape, depositional environment and stress history. The parameters to describe its stress-strain behaviour depend critically on the stress history and direction of loading. Even at very small strains (less than 10^{-3} %), where soil is considered to be elastic, more than two elastic parameters (E and ν, which describe isotropic elastic materials) are required to describe its behaviour. This Section reviews the theory behind the anisotropic elasticity of soils and whether and how the required parameters for its description can be

measured.

Because soil is often horizontally layered, its initial structure is frequently isotropic in the horizontal bedding plane. This implies that the initial elastic parameters might not vary with direction in the horizontal plane and that the vertical axis (i.e. the direction of deposition) may be an axis of symmetry. This type of anisotropy is known as transverse isotropy, or cross-anisotropy, or orthotropy. As will be shown in Chapter 6, a perfectly transversely isotropic elastic material requires five independent elastic parameters to fully describe its behaviour: Young modulus in the vertical direction, E_V'; Young modulus in the horizontal direction, E_H'; Poisson's ratio for strains in the horizontal directions due to a vertical direct stress, ν_{VH}'; Poisson's ratio for strain in one horizontal direction due to a horizontal direct stress applied at 90° to that direction, ν_{HH}'; and the modulus of shear deformation in the vertical plane, G_{VH}. The Poisson's ratio for strain in the vertical direction due to a horizontal direct stress, ν_{HV}, and the horizontal shear modulus, G_{HH}, are, according to anisotropic elasticity theory (Love, 1927), not independent and are given by:

$$\nu_{HV} = \frac{E_H}{E_V}\nu_{VH} \tag{2.1}$$

$$G_{HH} = \frac{E_H}{2(1+\nu_{HH})} \tag{2.2}$$

With these parameters, the link between the strain and stress vectors, i.e. the anisotropic compliance matrix, is of the form given by Eq.2.3. In this equation, z is vertical while x and y are orthogonal horizontal axes. A more detailed discussion of this mathematical expression of anisotropy is given in Chapter 6.

Until comparatively recently, most analyses of soil pre-failure deformation have assumed elastic behaviour and the problem as how to measure the anisotropic elastic parameters, either in the field or laboratory, was debated widely. Hardin (1978) and later Hardin & Blandford (1989), who performed triaxial tests on sand, suggested that the Young modulus for elastic compressive strains in a certain direction is a unique function of the direct stress in that direction and it is therefore possible to express the deformation moduli at small strains by means of the following equation:

$$E_{ij} = S_{ij} F(e) p_a^{1-2n} (\sigma_i' \sigma_j')^n \tag{2.4}$$

where: F(e) - void ratio function

S_{ij} - dimensionless anisotropic modulus constant

σ_i', σ_j' - principal effective stresses

p_a - reference (atmospheric) pressure

$$\begin{bmatrix} \varepsilon_x \\ \varepsilon_y \\ \varepsilon_z \\ \gamma_{xz} \\ \gamma_{yz} \\ \gamma_{xy} \end{bmatrix} = \begin{bmatrix} \frac{1}{E_H'} & -\frac{\nu_{HH}'}{E_H'} & -\frac{\nu_{VH}'}{E_V'} & 0 & 0 & 0 \\ -\frac{\nu_{HH}'}{E_H'} & \frac{1}{E_H'} & -\frac{\nu_{VH}'}{E_V'} & 0 & 0 & 0 \\ -\frac{\nu_{HV}'}{E_H'} & -\frac{\nu_{HV}'}{E_H'} & \frac{1}{E_V'} & 0 & 0 & 0 \\ 0 & 0 & 0 & \frac{1}{G_{VH}} & 0 & 0 \\ 0 & 0 & 0 & 0 & \frac{1}{G_{VH}} & 0 \\ 0 & 0 & 0 & 0 & 0 & \frac{1}{G_{HH}} \end{bmatrix} \begin{bmatrix} \sigma_x \\ \sigma_y \\ \sigma_z \\ \tau_{xz} \\ \tau_{yz} \\ \tau_{xy} \end{bmatrix} \qquad (2.3)$$

Also Roesler (1979) and Yu & Richart (1984), by means of resonant column tests on clean sands, and Lee (1985), Jamiolkowki et al. (1991) and Lo Presti & O'Neil (1991), by measuring body wave velocities in a large sand specimen, showed that the elastic shear stiffness of sand depends on the effective stresses in the directions of propagation and particle motion, but is independent of the stress normal to the plane of particle motion. This implies that full three-dimensional control over stress conditions is necessary when attempting to measure stiffness anisotropy at small strains and that the shear and Young moduli, usually determined in torsional and triaxial tests at small strains, can be written as a function of stress components as shown below:

$$G_{vh} = S_{vh} F(e) p_a^{1-2n} (\sigma_v' \sigma_h')^n$$
$$E_v' = S_v F(e) p_a^{1-2n} (\sigma_v')^{2n} \qquad (2.5)$$

2.4.2. Measurements of anisotropic parameters in the laboratory

Special equipment is required to measure all five elastic parameters in laboratory tests. Assuming that stresses and strains can be measured precisely, the conventional triaxial

compression test, with its cylindrical sample and constant radial stress, can be used to determine only E_V' and ν_{VH}' from samples with the bedding planes positioned horizontally (Fig.2.15a). If sample is prepared such that the bedding planes are vertical (Fig.2.15b), then it is unlikely to behave uniformly in the horizontal plane, because of the non-symmetrical fabric and particle contact structures in the circular cross-section of the sample. It is, therefore, not possible to isolate straining in the direction of the bedding plane (i.e. ν_{HH}'), from that perpendicular to the bedding plane (i.e. ν_{HV}').

The use of more sophisticated true triaxial apparatus, in which a cubical specimen is subject to independent control of three direct stress components, and which is locally instrumented to measure the corresponding direct strains, can be used to measure four of the five elastic parameters: E_V', E_H', ν_{VH}', ν_{HH}' (Kirkgard & Lade, 1991). To achieve this, it is necessary to perform at least two tests in which $\Delta\sigma_2=\Delta\sigma_3=0$: one in which the bedding planes of the sample are positioned perpendicular to the direction of the major principal stress and the other in which they are positioned parallel to the direction of the major principal stress (Fig.2.16).

Neither the conventional triaxial test, nor the true triaxial test enable G_{VH} to be established.

King (1970) developed a 10x10x10 cm true triaxial cell in which, using the propagation of both shear (S) and compressional (P) waves, he was able to measure all five elastic constants on rock samples, under dynamic conditions, using the expressions developed from elasticity theory. The tests consisted of P and S wave velocity measurements made parallel, perpendicular and at 45° to the rocks' predominantly horizontal macro-fabric. Horizontal Young modulus was measured from the velocity of compressional (P) waves in the direction parallel to the direction of bedding plane ($E_H=\rho V_{PH}^2$, where ρ is the density of the rock); E_v from the velocity of (P) waves in the direction perpendicular to the bedding plane ($=\rho V_{PV}^2$); G_{VH} from the velocity of shear (S) waves perpendicular to the bedding plane ($=\rho V_{SV}^2$). Poisson's ratios ν_{HH} and ν_{VH} were calculated from expressions dependent on all velocity components (V_{PH}, V_{PV}, V_{SH}, V_{SV} and V_{PQ}, where V_{PQ} is the velocity of compressional (P) waves in a direction of 45° to the horizontal). A similar approach has recently been used by Bellotti et al. (1996) to determine the anisotropic properties of Ticino sand.

Recently, the bender element technique has been developed for shear stiffness measurements. Bender elements are made of a piezoelectric material which has a capability to

convert an applied electric voltage into mechanical motion. By placing these devices onto a sample it is possible to generate shear waves which propagate through the soil. From the measured velocity of these waves it is possible to estimate values of the elastic shear moduli. Early references go back to Shirley & Hampton (1978) and Shirley (1978), who tested sand in a special chamber, with bender elements placed horizontally at opposite ends. Schultheiss (1981) was the first to install bender elements in triaxial and oedometer cells, and after him Lo Presti et al. (1993), Jamiolkowski et al. (1994), Viggiani (1992), Porovic (1995), Jovicic (1995). Viggiani (1992) and Jovicic (1995) developed improved techniques for filtering and measuring the received signals. For triaxial samples with the bedding planes positioned horizontally, the shear modulus G_{VH} can be measured by propagating vertical shear waves which oscillate in the horizontal direction, Fig.2.17a. When the sample is trimmed and positioned such that the bedding planes are vertical, then there are only two positions in which the bender elements can be placed to measure the G_{HH} and G_{HV} moduli, Fig.2.17b, c (Jovicic, 1995). The use of bender elements in a conventional triaxial test therefore allows only three shear moduli to be determined (only two of which are independent), without giving any data on the Poisson's ratios. G_{VH} and G_{HV} are, for a cross-anisotropic elastic medium, equal; G_{HH} contains two unknowns, E_H' and ν_{HH}', which cannot be determined directly from the bender element measurements.

In principle, the inclusion of bender elements into a true triaxial apparatus (which is equipped for local strain measurements), would allow all five elastic parameters to be determined. This would work under the assumption that dynamic and static stiffnesses at small strains are equivalent.

The hollow cylinder device, with complete local instrumentation and independent control of the three direct stresses and one torsional shear stress, allows direct static measurement of the soil's stiffness characteristics under any combination of stress changes involving $\Delta\sigma_v'$, $\Delta\sigma_r'$, $\Delta\sigma_\theta'$ and $\Delta\tau_{\theta z}$, including tests to determine the five cross-anisotropic elastic parameters. Results from such tests will be presented in Chapter 6.

2.4.3. Field measurements of anisotropic parameters

To date it has not been possible to measure all five anisotropic parameters in the field. Dynamic methods involving the measurement of the propagation of shear waves have been used to obtain values of the shear moduli. The various field techniques that are available are described in detail by Tani (1994).

Geophysical exploration from the ground surface using reflection, refraction or surface waves techniques have been used to obtain an equivalent isotropic shear stiffness. Geophysical borehole logging and seismic cone penetration tests, using downhole techniques, have been used to obtain estimates of G_{VH}. Such equipment can also be employed using the crosshole approach to obtain estimates of G_{HH} or G_{HV} ($=G_{VH}$), depending on the direction of polarisation of the shear waves.

2.4.4. Confirmation of anisotropic behaviour at small strains

In order to check whether soil is cross anisotropic elastic at small strains, several researchers have attempted to predict the initial behaviour of undrained triaxial tests using elastic parameters obtained from drained tests.

Henkel (1971) considered the degree of anisotropy in London clay, using results from conventional undrained triaxial compression tests on vertical and horizontal specimens. He assumed that the elastic compliance matrix, Eq.2.3, was symmetric by substituting Eq.2.1 and that, although Poisson's ratio ν_{HH}' is an independent parameter, $\nu_{HH}'=1/2(\nu_{HV}'+\nu_{VH}')$. He also noted that for an ideal triaxial test there are no shear stresses or strains in the vertical, circumferential and radial directions.

For an undrained triaxial test on a vertical sample, from the requirements that $\Delta\sigma_{H1}'=\Delta\sigma_{H2}'$ and $\varepsilon_{vol}=0$, he obtained the following expression for the stress path inclination as a function only of the stiffness ratio $R^2=E_H'/E_v'$ and Poisson's ratio ν_{VH}':

$$\frac{\Delta\sigma_v'}{\Delta\sigma_h'}=-2\frac{(1-2\nu_{VH}\frac{1+3R^2}{2})}{R^2(1-2\nu_{VH})}=M_I \tag{2.6}$$

For the undrained Youngs modulus, E_u, the expression is:

$$\frac{E_u}{E_H'}=\frac{1}{R}\left[\frac{M_I-1}{M_I-2\nu_{VH}}\right] \tag{2.7}$$

For London clay, Henkel used values of $\nu_{VH}\approx 0.12$ and $R^2\approx 1.6$, deduced by Wroth (1971). With these parameters he managed to predict the undrained behaviour of London clay in triaxial compression.

Graham & Houlsby (1983), adopted a variation of Henkel's approach to propose a method for prediction of the undrained triaxial stress path inclination. The theory was checked using the results from monotonically loaded drained triaxial tests on Winnipeg clay (Graham et al. (1983)). Considering a symmetric compliance matrix and the conditions appropriate to ideal triaxial tests, they expressed the system of equations given by Eq.2.3 in terms of triaxial invariants (this will be shown in detail in Chapter 6):

$$\begin{bmatrix} \delta p' \\ \delta q \end{bmatrix} = \begin{bmatrix} K^* & J \\ J & 3G^* \end{bmatrix} \begin{bmatrix} \delta \varepsilon_{vol} \\ \delta \varepsilon_d \end{bmatrix} \tag{2.8}$$

All three parameters of the compliance matrix, K^*, G^* and J are functions of E_H', E_V', ν_{HH}' and ν_{HV}'. Letting $R^2=E_H'/E_V'$ and $\nu_{HV}'=\nu^*/R$, where $\nu^*=\nu_{HH}'$, they reduced the number of parameters to two: the stiffness ratio, R^2, and the Poisson's ratio, ν^* (similar to Henkel). From several drained triaxial tests (with different $\delta q/\delta p'$ ratios), they used the measured stress and strain increments $\delta p'$, δq, $\delta\varepsilon_{vol}$ and $\delta\varepsilon_d$ to calculate, from Eq.2.8, K^*, G^*, and J, and from them R^2 and ν^*. For Winnipeg clay, this calculation gave $R^2\approx1.8$ and $\nu^*\approx0.2$, which is similar to those estimated for London clay. The expression for the stress path inclination can be found by setting $\delta\varepsilon_{vol}=0$ in Eq.2.8. This gives an expression for $\delta q/\delta p'$ which is a function only of R^2 and ν^* (similar to Henkel).

The above theories were shown to give good predictions of the inclinations of the undrained stress paths for London clay and Winnipeg clay, respectively, and concluded that these materials could be approximated as being cross anisotropic elastic. However these results may have been fortuitous as anisotropic elasticity exists only in the range of recoverable elastic strains. This strain range is very small and is extremely difficult to characterise in static laboratory tests. It is probably the case that overconsolidated clays have a more extended linear elastic zone than more granular soils. Consequently, if the above approaches were applied to granular soils they may not work.

2.5. Factors which influence the magnitude of the anisotropic parameters

Due to the limitations of testing devices and the difficulties in estimating all five cross anisotropic elastic parameters at very small strain levels, little research has been done to specifically evaluate these parameters or investigate the factors which influence their magnitude. Most of the research that has been done in the past has implicitly assumed the soil to be

isotropic and has either considered the equivalent Youngs modulus, E_{max}, or Shear modulus, G_{max}, (Triaxial or Plane strain devices), or has expressed the stiffness in terms of G_{VH} (Torsional shear devices). Such studies have, however, investigated the factors which effect the magnitude of these equivalent moduli and some of the findings are presented below.

2.5.1. Porosity

The soils' porosity influences the equivalent small strain shear stiffness, G_{max}, such that it increases systematically as e_o decreases. Fig.2.18 shows this relation for Ticino and Quiou sands (Lo Presti et al., 1993). The authors fitted a linear relation through the data, marked as Eq.1, which is of the form:

$$G_{max}=C_g F(e)(p')^n p_a^{(1-n)} \tag{2.9}$$

where C_g=710 - a dimensionless soil constant

$F(e)=(2.27-e)^2/(1+e)$ - void ratio function

n=0.43

p_a - atmospheric pressure

p' - mean effective stress

Also fitted to this data is an expression given by Jamiolkowski et al. (1991), which is valid at p'=100 kPa:

$$G_{max}=\frac{60}{e^{1.3}} \tag{2.10}$$

Both curves fit the data with ±12% tolerance.

Porovic & Jardine (1994) presented results from resonant column tests on Ham River sand, where the relative density varied from D_r~18% to D_r~70% (Fig.2.19). The effect of the initial void ratio on G_{max} is evident. However as the strain level increases the effect of the initial void ratio diminishes and the three curves given on Fig.2.19 coincide from ~0.1% shear strain.

2.5.2. Stress level

Generally, G_{max} increases with an increase of stress level. Hardin & Richart (1963) showed that shear wave velocities for dry round and angular sands depend on the level of confining stress such that V_S increases with increasing cell pressure (Fig.2.20). This figure also reinforces the statement given in (a) above that shear wave velocity (i.e. G_{max}) increases with a

reduction in void ratio.

Jamiolkowski et al. (1994) show similar trends of G_{max}-p' for six Italian clays.

Porovic (1995) tested HRS at different stress levels and different consolidation histories (Fig.2.21). It is evident that samples either consolidated isotropically or anisotropically to the same p_o' have similar stiffness, i.e. consolidation history is not very influential on G_{max}.

2.5.3. Overconsolidation

The effect of overconsolidation seems to be dependent on material type. Tatsuoka & Shibuya (1992) and Porovic & Jardine (1994) used resonant column torsional shear tests to show that the normalized initial G_{max} for sands is insensitive to OCR.

On the other hand, Viggiani (1992) found that isotropic overconsolidation has a significant effect on G_{max} obtained from bender element tests on clay. She recommended the expression:

$$G_{max}=[G_{max}]_{nc}R_o^m \tag{2.11}$$

where R_o is the OCR in terms of p' and m=0.2 for kaolin. However, Jamiolkowski et al. (1994) argue that m is close to zero and OCR has little effect on G_{max}.

Porovic & Jardine (1994) plotted G_{max} of Ham River sand at different OCR's against p' in a log-log plot, and showed that all results fall on a single straight line. Plotting this relation for higher strain levels they again observed that the results fell on a single line, the slope of which increased with strain level. They proposed a suitable dimensionally consistent equation to present data, in the form:

$$G_{sec}=A\left[\frac{p'}{p_a}\right]^n \tag{2.12}$$

where A and n are functions of strain, as presented in Fig.2.22.

2.5.4. Strain rate and strain magnitude

The stiffness of an elastic material does not depend on loading rate (stress or strain) or

the type of loading (monotonic or cyclic). It is generally regarded that soil behaviour is both highly nonlinear and loading rate dependent. Differences in strain rate, the number of loading cycles and strain level among various types of testing methods, have been shown to influence soil behaviour. However, when the stiffness is measured at very small strains (less than 0.001%), the effects of strain rate are thought to be negligible and the soil can be considered truly elastic. Consequently, the stiffness at very small strains required for the analysis of low level of dynamic loading (such as for foundations for gently vibrating machinery and low-level environmental loading of offshore gravity structures) can be evaluated from stiffnesses obtained from static laboratory tests. In the past 20 years several researchers have shown that stiffnesses at very small strains, measured under static monotonic loading conditions and under dynamic loading conditions, including those from field seismic surveys, are similar.

Among the first, Hardin & Drnevich (1972) and Drnevich & Massarsch (1979) examined the effect of strain rate on the stiffness of cohesionless and cohesive soils using a static torsional apparatus (monotonic and cyclic) and a resonant column apparatus. They reported that for a range of frequencies from 0.1 Hz to 260 Hz (Hardin & Drnevich, 1972) and from 0.1 Hz to 30 Hz (Drnevich & Massarch, 1979), the effect of frequency on stiffness under cyclic loading conditions was not significant for a range of strain less than 0.001%.

Bolton & Wilson (1989) tested Leighton Buzzard sand (LBS) on solid cylindrical samples in both static and dynamic conditions in a torsional shear apparatus. The dynamic tests were conducted with an alternating torque over the range 20 to 120 Hz, while the static tests were performed at a frequency of 0.001 Hz. The test results presented in Fig.2.23, as torque-strain curves, show that for this range of frequencies the behaviour of soil was independent of the frequency of applied load for strains up to 0.07%.

Shibuya et al. (1990) showed first that Young's moduli obtained from static monotonic loading (ML) and cyclic loading (CL) triaxial tests, on Hime gravel, are essentially the same for strains less than 0.001% (Fig.2.24). The modulus E_{eq} for a cyclic loading test then becomes greater than the secant stiffness (E_{sec}) from a monotonic test. The definitions of the moduli are presented in Fig.2.26.

Tatsuoka and Shibuya (1992) made a similar comparison of the shear moduli between dynamic tests (i.e. resonant column, RC) and static ML and CL tests for Toyoura sand (Fig.2.25). Curve (1) shows the stiffness from monotonic loading in a torsional simple shear

(TSS) test; curve (2) is from a static cyclic loading TSS test; curve (3) is a combination of results from a RC test and a static CL test in which the shear stresses were cycled 10 times at each stage and the average results taken. Again, coincidence of all three curves is seen up to 0.001% shear strain.

Recent results from Kim & Stokoe (1995) on granular materials show that shear moduli from both RC and TS tests are constant and equal to G_{max} at or below the elastic strain limit γ_t^e=0.001% (Fig.2.27). The strain range between γ_t^e and γ_t^c(~0.01%) represents a transition zone where shear modulus is independent of number of cycles, but decreases as shearing strain increases. Beyond the γ_t^c limit, shear modulus is affected by the number of loading cycles, and the difference between moduli increases as strain increases (Fig.2.27).

Porovic & Jardine (1994) made a summary showing that G_{max} was the same from triaxial, RC and BE tests, but varied strongly with the level of mean effective stress, p' (Fig.2.28).

Apart from laboratory static and dynamic stiffness measurements, Kohata et al. (1995) showed broad agreement of the elastic stiffness from field shear wave velocities, G_f ($=\rho V_S^2$), and that obtained from laboratory monotonic and cyclic loading tests, G_{max}, for the range of materials: sedimentary soft rock, cement-treated sandy soil, pleistocene clay (Fig.2.29).

Soga et al. (1995) reported the same behaviour for two cohesive materials: San Francisco Bay mud and Pisa clay, using a torsional shear device run at different frequencies. However, from tests on dispersed and flocculated kaolin, they obtained an increase in G_{max} with an increase in frequency (Fig.2.30), which they believed is a characteristic of the material and not due to experimental error. However, normalized curves of G/G_{max}, were not affected with change in frequency, Fig.2.31.

So, recent research shows that the perceived difference between static and dynamic moduli is decreasing as the accuracy of static measurements at small strains is improving. It has been postulated that the stiffness available at any given set of conditions is upper-bounded by a strain rate independent elastic limiting line.

2.6 Effect of strain level in field tests

One way of evaluating equivalent shear stiffnesses in the field is from static loading tests: a) bore-hole loading or pressuremeter test (G_{BHLT}) and b) plate loading tests (G_{PLT}). These tests are essentially boundary value problems and therefore the magnitude of the stresses and strains in the soil vary from place to place. As the soil stiffness depends on both these quantities this also varies spatially. However, most of the theories which are used to obtain the stiffness value from the test data are based on a constant isotropic value of stiffness. This shortcoming means that in most cases they do not take into account the strain level dependency of stiffness when selecting the design stiffness value. Consequently, when the strain level in the ground under designed loading is less than that from pressuremeter and plate load tests, the deformation of soil and structure estimated by using G_{BHLT} or G_{PLT} would be larger than the actual value. Jardine et al. (1986), Burland (1989) and Tatsuoka & Shibuya (1992) showed how non-linear stress-strain data can be obtained when the field tests include measurements of displacements within the soil mass.

Jardine (1992b) also proposed a method which accounts for the equivalent secant shear stiffness varying with strain level when interpreting pressuremeter tests. Only when the strain level dependency of stiffness is taken into account, can field stiffness values be properly linked to the true soil properties.

The field measurement of elastic shear wave velocity V_S is one of the most reliable methods for evaluating the in situ stiffness at very small strains. To take into account the strain level dependency of stiffness, field measurements need to be related to laboratory results. Tatsuoka & Shibuya (1992) suggested that the in-situ stiffness at very small strains can be obtained as $(G_{max})_{field}=G_f=\rho V_S^2$; next, the relationship between $(G_{eq}/G_{max})_{lab}$ (Fig.2.26), with corresponding strain, γ, is evaluated from relevant laboratory tests using undisturbed samples, Fig.2.32. Combining the results of these two measurements, the in-situ stiffness is estimated as a function of strain level by the following relationship:

$$(G_{eq})_{field} = \left[\frac{G_{eq}}{G_{max}}\right]_{lab} \times G_f \qquad (2.13)$$

This method assumes that the strain level dependency observed in the laboratory is similar to that in-situ, whereas the G_{max} measured in the laboratory element test may not be equal to the field value because of possible sample disturbance, non-uniformity of the ground, etc.

2.7. Framework for the behaviour of HPF4

2.7.1. Constant strain contours

The framework for soil behaviour shown in Fig.2.33 was presented by Jardine (1985, 1992). In this thesis this framework is extended to three-dimensional t-p'-α stress space to include considerations of anisotropy and principal stress rotation (Hight et al., 1987).

The framework tends to describe soil stress-strain behaviour by defining, in normalized stress space (p_e' is defined subsequently), an outer Bounding Surface (BS) and three Zones which subdivide the space inside the BS. The projection of the boundary of each zone on the t/p_e'-p'/p_e' plane is presented in Fig.2.33b, while the estimated projections on the t-α plane are shown in Fig.2.33c (from Hight & Higgins, 1994). The Zone boundaries, or Sub Yield Surfaces (SYS), are mobile and may be re-positioned by changing the current stress state. They have been found to model very well the kinematic nature of soil behaviour in terms of ground movement predictions and soil-structure interaction problems. Mathematically, the framework forms a soil model incorporating kinematic yield surfaces (Mroz, 1967; Simpson et al., 1979). Improvements in laboratory instrumentation now allow the behaviour of this framework to be experimentally determined.

The stress-strain characteristics of each of the Zones are described by considering the stress path shown in Fig.2.34, where an element of soil is located in triaxial space at point A, and then loaded monotonically. Four distinct phases of the stress path are engaged:

A) Linear elastic Zone I

This is a zone of true linear elastic behaviour, where strains are fully recoverable. The boundary of this zone is usually identified as a contour of strain, using either ε_1 or the total length of the strain vector. Its size can be better estimated in cemented materials than in most other soils. However, its range is believed to be between 0.0001% and 0.001% strain. While it is generally accepted that the stiffness is constant in this zone it is often difficult to make measurements at these small strain levels, especially when γ<0.0001%. The strain boundary of Zone I is marked as Y_1.

Soil behaviour within the elastic region can be anisotropic. Shear wave tests on laboratory specimens have shown that the measured G_{max} depends on the stresses acting in the directions of wave propagation and particle motion, and therefore varies with direction for an

anisotropic stress state (Jamiolkowski et al., 1991). Small strain anisotropy has also been interpreted from correlations between resonant column and triaxial tests on clays (Jardine, 1985).

B) Recoverable Zone II

The stress-strain behaviour in Zone II is non-linear and hysteretic, but fully recoverable in load-unload cycles. The energy dissipated in a hysteretic loop is thought to have gone into local yielding at particle contacts. The strain boundary of the Zone II is marked as Y_2. It can be determined more easily than the Y_1 boundary. Undrained triaxial compression and extension tests allow the upper and lower extent of the boundary Y_2 to be determined (Fig.2.35), while drained probing tests are necessary to map out the rest of the region. Values of axial strain at the Y_2 boundary, ε_{crit}, for a variety of soils are listed in Table 2.3 (after Jardine et al., 1991).

Table 2.3: Value of ε_{crit} for some soils

Soil type	PI	ε_{crit} (%)	Research
Loose clayey sand	3	0.007	Georgiannou (1988)
Magnus till	18	0.01	Jardine (1985)
London clay	45	0.04	Takahashi (1981)
Bothkennar clay	70	0.025	Smith (1990)
Intact chalk	/	0.065	Jardine (1985)

Behaviour of material in Zone II is marked with rapid loss of stiffness. Also in this zone, static (monotonic) and dynamic shear stiffness curves start to diverge from each other. In addition, the direction of the major principal strain increment, $\Delta\varepsilon_1$, is dependent on the direction of the major principal stress increment , $\Delta\sigma_1$, so that $\alpha_\varepsilon=\alpha_\sigma$.

C) Plastic Zone III

Zone III starts after the Y_2 boundary, where irrecoverable plastic straining begins. The amount of plastic straining increases as the stress path approaches the Bounding Surface. It is thought that soil particles start to slide relative to each other in Zone III, with load columns breaking and reforming continuously. Soils do not show a great tendency to either dilate or contract in this zone, so that undrained effective stress paths show a constant inclination. Shear stiffness continues to decay with strain development, but not so abruptly as in Zone II. Boundary

of Zone III is marked as Y_3.

D) Bounding Surface

The changes in the particle packing which started in Zone III, with the initiation of plastic straining, become more pronounced as the stress path approaches the local BS. After the Y_3 yield, material can behave in two ways, depending on the type, initial density and stress level: (i) it shows contraction and reaches a stable stress point; (ii) following the initial contraction it reaches Phase Transformation and continues further dilation, where particles start to override each other. More about the BS will be given in Section 2.7.4.

2.7.2. The kinematic nature of small strain zones I and II

It was suggested by Skinner (1975) and shown in tests on Magnus till (Jardine, 1985), that when the Y_2 boundary is engaged, it follows the stress state as the stress path transverses stress space. If the stress path is then sharply redirected so that it goes back through Zone II, the material will show stiffer behaviour.

Fig.2.36 shows how the Zone II boundary, Y_2, of K_o consolidated Magnus till is realigned and changed in shape by K_o swelling. A suite of tests performed from points A, B, C and D were used to estimate the Y_2 boundary. It should be noted that during swelling the Y_2 boundary is probably coincident with the stress state, however, during the ageing period which was allowed before the samples were sheared the surface expands (or moves) slightly, such that resumption of swelling would initially invoke a higher stiffness than observed prior to the ageing period. The top and bottom limits of the Y_2 boundary at each OCR level are determined from undrained triaxial compression and extension tests (i.e. ε_{crit}=0.01%). The remaining parts of the boundaries are drawn from the contours of ε_1=0.01% found from drained probing tests at each of the OCR points. Triaxial compression and extension test from OCR=1.0 also map the major part of the local BS, shown in Fig.2.36. Therefore, it is evident that the Y_2 boundary at OCR=1.0 is constrained by the proximity of the BS.

The kinematic Sub Yield Surfaces (KSYS) are not symmetrical about their local stress origins (i.e. points A, B, C and D), so that the stiffness in Zone II is strongly influenced by recent stress history. For overconsolidated states of stress the sharp change in the direction of the stress path from that in swelling to that in undrained triaxial compression results in quite a large proportion of the Y_2 yield surface to be covered. In contrast, there is a much less severe

change in direction of the stress path when changing from swelling to triaxial compression and consequently a much smaller part of the Y_2 yield zone is transversed.

Similarly, Fig.2.37 shows how the Y_2 boundary moves and changes when the soil element is subjected to undrained unloading. Undrained extension radically alters the soil stiffness: under "in-situ" K_o conditions (point A) $E_{u,0.01}{}^{com}/E_{u,0.01}{}^{ext}=0.7$, but this ratio rises to ~4 after perfect sampling (point B) (i.e. reduction of deviator stress to zero). With $E_{u,0.01}$ is marked a value of undrained Young modulus at $\varepsilon_{crit}=0.01\%$.

The factors affecting the stress-strain response of soil inside the Y_2 boundary are identified in Fig.2.38 (after Hight & Higgins, 1994). In this figure, the stiffness-strain relationship for various stress path directions with respect to the current Y_2 boundary are considered. The stiffness is expressed in terms of an equivalent triaxial Young's modulus defined as $\Delta\sigma_a/\Delta\varepsilon_a$. In Fig.2.38a the effect of changing the stress path direction with a fixed inclination of the major principal stress is considered. The stiffest behaviour is associated with the greatest rotation of the stress path. Fig.2.38b shows the effect of different stress path directions which include principal stress rotation, while Fig.2.38c and Fig.2.38d consider the effect of recent stress history. All figures show that the stiffest response is associated with the greater distance that the stress path must cover to reach the Y_2 boundary.

A simple constitutive model, based on Fig.2.36 and which accommodates many of the above facets of soil behaviour at small strains, has been developed by Jardine (1985), and incorporated into the Imperial College Finite Element program (Potts, 1986). Analyses performed with this program on practical problems experiencing ground movements have shown excellent agreement between predicted and observed behaviour, Jardine et al. (1991). Recently, several new models have been proposed that deal more explicitly with the kinematic and inelastic nature of soil behaviour at small strains (Simpson, 1992).

2.7.3. Contours of constant energy

An alternative approach to defining the Y_1 and Y_2 boundaries by constant strain contours, is to associate these boundaries with contours of constant work (Burland, 1989; Burland & Georgiannou, 1991). These authors investigated the small strain behaviour of two soils: Ham River sand sedimented into a kaolin suspension (HK) and a natural clayey sand from the North Sea (Gulfaks), at OCR=1.0 and 1.3. The stress space around each of the initial stress

points (after consolidation) was probed by undrained, triaxial compression and extension, and drained stress paths. The work applied from the initial stress points σ_{rc}' and σ_{zc}' (radial and axial stress prior to shearing), was calculated as:

$$U=\sum_{0}^{\varepsilon_z}(\sigma'_z-\sigma'_{zc})\delta\varepsilon_z+2\sum_{0}^{\varepsilon_r}(\sigma'_r-\sigma'_{rc})\delta\varepsilon_r \qquad (2.14)$$

It was shown that the work contours were approximately elliptical in shape (Fig.2.39), with the major axis vertical. This shape is similar to the constant strain contours seen previously for normally and lightly overconsolidated soils. From Fig.2.39 it can be observed that for NC soil, the portion of the Y_2 surface lying above the initial stress point is shorter than for the OC soil. This implies that the undrained stiffness in compression is higher for OC than for NC material. In contrast, the initial undrained stiffness in extension is higher for NC soil than for soil with OCR=1.3. The shape of the constant work contour also reflects the anisotropy of the soil skeleton which is stiffer in the axial than in the radial direction.

So, as was the case for the constant strain contours, Section 2.7.2, it has been demonstrated that the shape and spacing of constant work contours, together with the location of the initial stress state within them, give a quantitative measure of the stiffness and anisotropy of the soil. Puzrin & Burland (1996a, b) have developed a theoretical constitutive model based on the above ideas. This too has been incorporated into the Imperial College Finite Element Program and used to investigate soil behaviour due to twin tunnel construction (Addenbrooke, 1996).

2.7.4. Bounding Surface framework

The bounding surface framework was originally introduced to unify the presentation of a soil's response as observed in different tests (Rendulic, 1936). Originally, it was defined in *q-p'-e* space, as in conventional critical state soil mechanics theory. Rendulic's principle states that there exists a unique relationship between effective stress and void ratio for normally consolidated soil, i.e. any change in void ratio due to an increment of effective stress is uniquely determined by the magnitude of the effective stress increment and is independent of the stress path followed.

2.7.4.1. Behaviour of clays

The idealised picture of behaviour of most clays under one dimensional consolidation and swelling is presented in *e-lnp'* space in Fig.2.40. On loading from a slurry, the soil will travel down the virgin consolidation line (VCL). If subsequently unloaded, it will then travel up a swelling line (SL). If reloaded, it will travel back down the swelling line until it reaches its maximum previous applied vertical stress (i.e. intersection of the swelling and virgin consolidation lines), from where it will once again travel down the VCL with any further increase in loading. The VCL and SL are often assumed to be straight lines in *e-lnp'* space, of slope λ and $\varkappa$ respectively. The VCL is considered to be unique for a material and its position is fixed. Therefore, for any value of void ratio, *e*, there is a unique value of the mean effective stress on the VCL. This value is called p_e' (Fig.2.40):

$$p_e' = \exp\left[\frac{(e-e_1)}{\lambda}\right] \tag{2.15}$$

where: e_1 - void ratio of an isotropically consolidated sample at p'=1.0

e - current void ratio

The application of Rendulic's principle then results in all the effective stress paths, experienced by a normally consolidated soil (under drained or undrained triaxial conditions), plotting on a single curve in normalized t/p_e'-p'/p_e' stress space. This further leads to the prediction of a unique State Boundary Surface (SBS) for a particular soil, which separates possible and impossible stress state (Fig.2.43).

2.7.4.2. Framework for materials not obeying Rendulic's principle

Testing reconstituted low plasticity clay (Lower Cromer Till) Gens (1982) noticed large differences between undrained normalised effective stress paths (ESPs) for triaxial and plane strain samples consolidated with different stress ratios and then sheared from normally consolidated states. These paths are presented in normalized t/p_e'-p'/p_e' space in Fig.2.44. Clearly none of these paths could be taken as a unique State Boundary Surface (SBS) which separates possible and impossible stress states. Gens postulated a new framework in which the SBS was taken as the outer locus of undrained ESPs for all normally consolidated specimens. In addition, he showed that the undrained ESP forms what has since been termed a local bounding surface (BS) for a particular consolidation stress ratio. Any sample that has been normally consolidated with this same stress ratio, but unloaded, will if subsequently loaded undrained, engage this local BS and "travel" along it, but not pass outside it. Only drained stress paths can take the stress

state outside the local BS and possibly bring it to the SBS, Fig.2.45. For the special case of materials obeying Rendulic's principle, these two surfaces, the SBS and the local BS, coincide.

2.7.4.3. Behaviour of granular materials

The behaviour of granular materials is still more complex (Vesic & Clough, 1968; Skinner, 1975; Coop, 1990, 1993). Their behaviour may be idealised as shown in Fig.2.41, which shows the consolidation characteristics for two samples of the same sand: one initially in a dense state, the other in a loose state. It should be noted that when attempting to set up a set of ideally identical sand samples, it is difficult to achieve exactly the same initial void ratio every time, either for a loose or dense state. There is, therefore, a multiplicity of initial void ratios of sand for the same stress point, and sands, therefore, do not obey Rendulics principle (Ishihara et al, 1975). If these samples are now compressed one-dimensionally, they will follow normal consolidation lines (NCL) which, at high values of effective stress, may approach a straight virgin consolidation line. As samples have a different initial void ratio, the NCL's will not be coincident. The VCL is approached when the sand particles start to crush and therefore the magnitude of the vertical stress at which this occurs is dependent on the strength of the soil particles (Coop, 1990). For loose HRS, for example, which consists of quartz-based particles, the VCL may be reached only at about 10 MPa mean effective stress (Fig.2.42, after Coop). Consequently, for the stress levels associated with most geotechnical structures, behaviour is restricted to the early parts of the normal consolidation curves.

The difficulty for sand is that the VCL and its slope λ are difficult to establish, as tests are required to be performed at high pressures. Also, the determination of e_1 at p'=1.0 kPa is difficult to accurately establish because of the multiplicity of normal compression lines, and p_e' determined from Eq.2.15 is therefore a not suitable parameter for normalization in sands.

Gens' framework has been applied when describing the behaviour of granular materials, although it is difficult to define the SBS because of the requirement of high pressure testing equipment. Symes (1983) and Shibuya (1985) extended the framework from the scheme developed for the t-p' plane by introducing principal stress rotation, α, and the effect of the intermediate principal stress (i.e. b). Using hollow cylinder experiments they defined the local BS for pluviated isotropically consolidated Ham River sand in t-p'-b-α space. From undrained tests they deduced three-dimensional surfaces in t-p'-α space, for different b-values (Fig.2.46). Shibuya & Hight (1996), Menkiti (1995) and Porovic (1995) showed that the same framework

holds for K_o consolidated soils, including HRS, a low clay content-sand mixture (HK), and a silty sandy clay (KSS).

2.7.5. The role of fabric in granular materials

It has been shown in Section 2.7.4.2 that the VCL for granular materials is far beyond the engineering level of stresses, and that granular materials are normally well on the "dry" side of the critical state line. It is, therefore, difficult to demonstrate the existence of the critical state line (CSL) for granular materials. To reach the CSL in undrained tests, dense granular materials must mobilize a very high deviator stress level and develop significant negative pore water pressures. Such tests therefore require the use of high pressure testing equipment. On the other hand, drained tests involve considerable dilation and large strains. This usually results in non-uniformities in the samples making their interpretation difficult.

2.7.5.1. Qualitative experimental recognition of granular fabric

The reason for such behaviour follows from the particulate nature of the granular material where the particles' shape and depositional method determine its initial fabric. The initial fabric of the granular assembly results in columns of contacts between the particles, which transfer external load through the sample. Contacts whose normals are parallel to the σ_1 direction are the most effective in supporting the axial load. Konishi (1972) and later Oda & Konishi (1974), conducted an experiment with photoelastic rods to show the construction of such particle columns (Fig.2.47). As the photoelastic material shows the patterns of stress concentration, chains of contacts become clearly visible. The main mechanism for sustaining a higher stress ratio with increasing axial strain is the continuous reconstruction of the initial fabric. At an early stage of shearing, the process of strain hardening may be understood as the collapse of individual load columns in the weaker parts of the granular mass, transferring load to the adjacent particles, so that the granular fabric steadily becomes more homogeneous throughout the specimen. At a later stage, the frictional resistance of the grains is overcome and the granular particles move to dilate, overriding each other to make grain contacts normal to the maximum principal stress direction. The deformation of the sample is concentrated into local shear bands. The rest of the sample, apart from the soil close to the end platens, forms a dilated domain - a large unstable mass with high void ratio. Particles at the ends of the specimen, in the vicinity of the end platens, are restrained from movement by the radial friction forces and therefore little fabric reconstruction occurs during deformation of the specimen. It can therefore be concluded that the

rolling of soil particles is a significant factor in controlling the mechanism of fabric reconstruction during the progressive deformation up to the critical state (Oda, 1972c).

A similar experiment on photo-elastic discs of different diameters was performed by De Josselin de Jong & Verruijt (1969), Fig.2.48. The assembly of discs was placed between two vertical plexiglass plates and loaded by means of two horizontal and two vertical rigid beams on the side boundaries, so that the ratio of horizontal to vertical force at the boundaries could be controlled. The results shown in Fig.2.48a and Fig.2.48b are for F_H/F_V=0.39 and 0.33 respectively. The results provide a qualitative picture of force-vector plots, i.e. the distribution of boundary forces through the particle contacts.

2.7.5.2. Quantitative experimental recognition of granular fabric

Subsequent to these initial qualitative experimental results showing the role of granular fabric, extensive experimental work was carried out by Oda in the early seventies to explain the particulate nature of granular materials and find a mechanism of fabric change. His work was mainly based on studying, under the microscope, thin sections of resin-fixed sand fabrics from different stages of triaxial tests. For him, the concept of fabric includes two main subconcepts: a) orientation of an individual particle and b) position of the particle and its mutual relationship to other particles. These characteristics of fabric are closely related to the shape of particles, especially to the average flatness or slenderness.

a) To find an orientation of an individual particle, Oda (1972a) defined the "axial ratio method" to measure the shape factor of grain particles, in the following form:

$$\bar{n} = \frac{1}{f} \sum_{i=1}^{f} \left[\frac{L_2}{L_1} \right] \qquad (2.16)$$

where: L_1 - is the apparent long axis of a grain

L_2 - is the apparent short axis of a grain

f - is the total number of grains measured (Fig.2.49)

These measurements were made on sand grain images projected from thin sections on to a screen. If $\bar{n}$ approaches 0, the grains are elongated, while if is 1.0 they are more spherical.

To define the orientation of an individual grain in the structure, Oda produces "frequency histograms". He measures the orientation, θ_i, of the longest axis of a grain to the horizontal, x,

on both vertical and horizontal thin sections of the sample (Fig.2.50). The histogram is usually a result of about 200 measurements from each thin section and presents a percentage of that number appearing at orientations from $\theta=0°$ to $\pm 90°$. Fig.2.51 is an example of the frequency histograms for two sands: sand B has $\bar{n}=0.605$ (relatively elongated particles) while sand D has $\bar{n}=0.706$ (more spherical particles). For sand D, both the V and H distributions of θ are uniform, as expected, while for sand B the vertical distribution shows a concentration of horizontally layered elongated particles (i.e. $\theta \sim 0°$).

b) When defining the mutual relation of particles to each other, Oda (1972a) considered the normals to planes tangential to particle contacts. The position of the normal is defined by angles α and β as in Fig.2.52. Measurements can again be plotted as a concentration of normals, $E(\beta)$, versus angle β. Clearly, specimens which have a concentration of normals close to $\beta=0°$ (i.e. vertical), posses more stable fabric than the other specimens.

With these definitions of the main fabric characteristics Oda (1972b) examined several granular materials to show the mechanism of fabric change during vertical compressional deformation. To do this he used thin sections at different stages during a test. Fig.2.53 is one example of sand initially prepared by a tapping method. It shows that the concentration of the normals to particle contacts ($E(\beta)$) becomes closer to $\beta=0°$ (i.e. vertical) as the deformation of the sample increases. The number on each diagram denotes the percentage of axial strain reached at that stage. For the normals to the particle contacts to realign some rolling of the soil particles must occur. The results therefore imply that particle rolling becomes the mechanism of deformation at a later stage of shearing, when particles start to override each other to sustain further loading.

To evaluate these changes in terms of material strength, he projected the area of a particle contact, ΔS_i, onto the horizontal and vertical cross-sectional planes (Fig.2.54), i.e. ΔS_z and ΔS_x, so that the sum of the vertical projections is S_x and the sum of the horizontal projections is S_z. Measuring these areas at different stress ratios (σ_1/σ_3) during the test, he found the relation between (σ_1/σ_3) and S_z/S_x shown in Fig.2.55. It clearly shows an increase of the horizontally projected area (i.e. orientation of contact normals closer to the vertical) with an increase of stress ratio. Considering later Rowe's dilatancy theory, Oda developed the following expression for the relation between (σ_1/σ_3) and S_z/S_x:

$$\frac{\sigma_1}{\sigma_3} = \frac{4}{\pi}\frac{S_z}{S_x}\tan\left[\frac{\pi}{4} + \frac{\phi_\mu}{2}\right] \qquad (2.17)$$

where ϕ_μ is an angle of interparticle friction. It should be noted that Skinner (1975) proved that mobilized friction angle, ϕ', is not a function of interparticle friction, ϕ_μ.

2.7.5.3. Numerical consideration of granular fabric

A numerical consideration of the fabric of granular materials is the next step in exploring the behaviour of granular materials. A Discrete Element Method was developed by Cundall (1978) and Cundall & Strack (1979), which considered an assembly of ideal discs under biaxial test conditions. Using Newton's second law and a force-displacement law they developed a computer program BALL which was able to calculate interparticle forces and their vectors, so that the development of force chains through an assembly could be evaluated. They validated the method (i.e. DEM) and program BALL by reproducing the experimental results of De Josseling de Jong & Verruijt (1969).

In an extension of this work, Rothenburg & Bathurst (1992) treated elliptical planar particles with the Discrete Element Method and showed that material frictional resistance increases with changes in particle shape (i.e. from circular to elongated). Numerical results were confirmed with biaxial tests on such assemblies. More detail about the DEM will be given in Chapter 5, when the particle shape of HPF4 is discussed.

Both experimental and numerical work have demonstrated the mechanism of the development of anisotropic granular fabrics during loading and their importance in explaining material behaviour.

2.7.6. Induced anisotropy

The outline of the concept of the local Bounding Surface in Section 2.7.1 showed that the shape of the local BS for normally consolidated material reflects the initial anisotropy of that material, since the same normally consolidated samples are sheared with different orientation of principal stress axes.

Rodriguez (1977) examined the effect of induced stresses on the drained response of

BIBL. LONDIN.

Leighton Buzzard sand (LBS) in the Directional Shear Cell (DSC). As described in Section 2.2, the DSC is a plane strain device in which the method of material deposition gives an isotropic shearing plane. Rodriguez first tested LBS in a series of tests where the direction of the major principal stress (α) was maintained constant for each test and the sample loaded monotonically to failure. Fig.2.56 shows that all tests can be presented with a single line in an R-ε_1 plot, which means that the samples had similar yield, stiffness and failure parameters.

In the second set of tests, he loaded all samples initially to $\sigma_1'/\sigma_3'=4.0$, with $\alpha=0°$, and then unloaded back to $\sigma_1'/\sigma_3'=0$. Subsequent loading was performed with α varying from 0° to 90°. The effect of the induced first stress cycle was that stiffness and yield in reloading reduced as α increased (Fig.2.57). However, final failure points were similar.

A similar effect was shown by Symes (1983) on isotropically consolidated dense HRS samples, sheared in drained conditions. Initially two tests were performed with monotonic shearing with $\alpha=0°$ and $\alpha=45°$ (b=0). In Fig.2.58, the results of these tests have been used to construct the $\sigma_1'/\sigma_3'=2.6$ boundary in ε_{vol}-ε_{oct} strain space. Two further tests were then performed. In both these tests the samples were first loaded to $\sigma_1'/\sigma_3'=2.6$ and then unloaded back to an isotropic state with $\alpha=0°$ throughout. One of the samples was then reloaded to failure with $\alpha=0°$. In the other test the direction of the major principal stress was first rotated to give $\alpha=45°$ before being loaded with this α value to failure. The results of these tests are shown in Fig.2.58. It is evident that the sample sheared to failure with $\alpha=0°$ experienced Y_3 yielding when $\sigma_1'/\sigma_3'=2.6$, because the stress state at that point exactly matched that of the previously applied cycle. For the sample sheared with $\alpha=45°$, this yielding occurred at a much lower stress level.

Chapter 7 of this thesis explores the effects of anisotropy induced in K_o consolidated samples, by further consolidating these samples with the same t/p' ratio developed during K_o loading, but with different inclinations of the direction of the major principal stress, α_c, (Fig.2.59). If the initial anisotropy of the K_o soil is such that the soil shows a massive reduction in material strength when sheared undrained with $\alpha\neq0°$ (Fig.2.60; Menkiti, 1995; Shibuya & Hight, 1996), two questions become of interest:

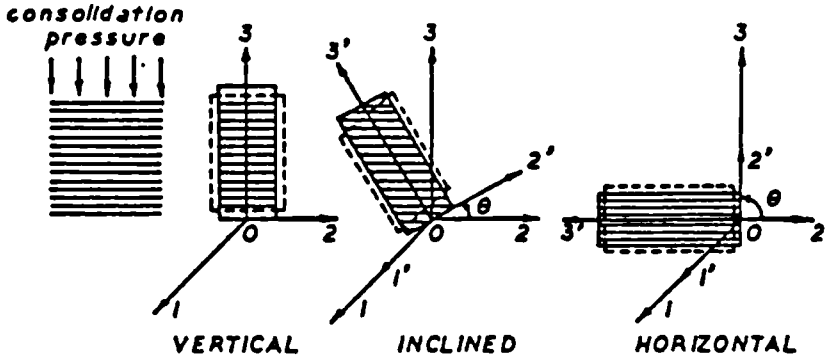
a) whether the inclined consolidation with $\alpha=\alpha_c$ will form a "new" material which will sustain a similar strength as that of K_o consolidated material (i.e. will the anisotropy of Fig.2.60 become a dashed line)

b) will such "new" material have the same anisotropy as that of K_o consolidated soil, i.e. could the dotted lines be drawn in Fig.2.60.

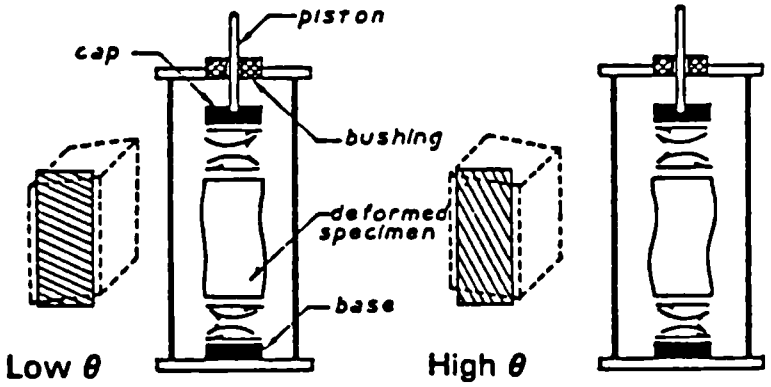
A review of the work done on this topic (Smith, 1992; Porovic, 1995) to date is given in the Introduction to Chapter 7.

Table 2.1: Classification characteristics of some sands

SOIL	d_{50}	U	e_{min}	e_{max}	MINERALOGY			particle shape
					quartz	feldspar	magnetit	
Toyoura sand	0.18	1.5	0.63	0.99	75%	22%	3%	subangular
Monterey No.20 sand	0.55	1.25	0.53	0.83	90%	10%		rounded to subrounded
Brasted sand	0.25	3	0.475	0.792				
Monterey No.0 sand	0.43	1.53	0.565	0.860	90%	10%		subangular subrounded
Cambria sand			0.51	0.80				
Leighton Buzzard sand								rounded



(a) Trimming inclination



(b) End effects and deformed shapes.

Fig.2.1 - Limitations of inclined triaxial tests between rigid platens (Saada, 1970)

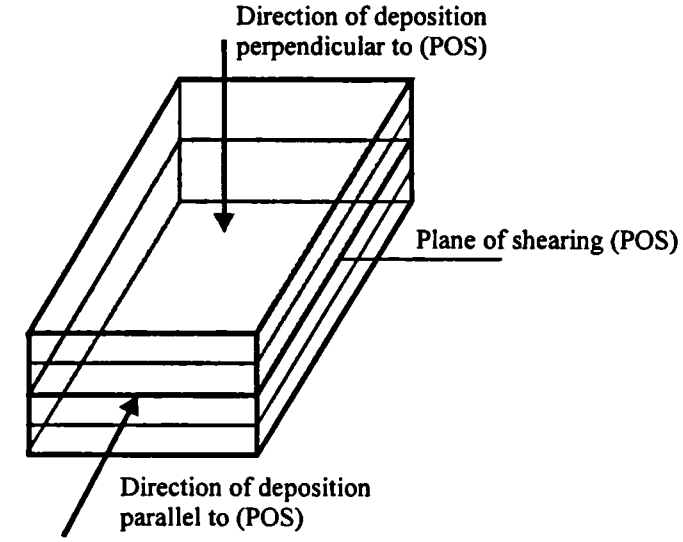


Fig. 2.2 - Possibilities for sample preparation in Directional Shear cell

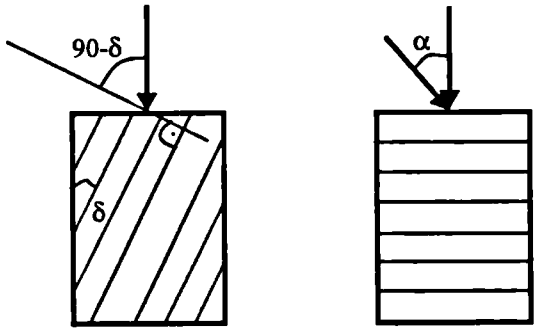


Fig.2.3 - Definition of angles α and δ for investigating anisotropy

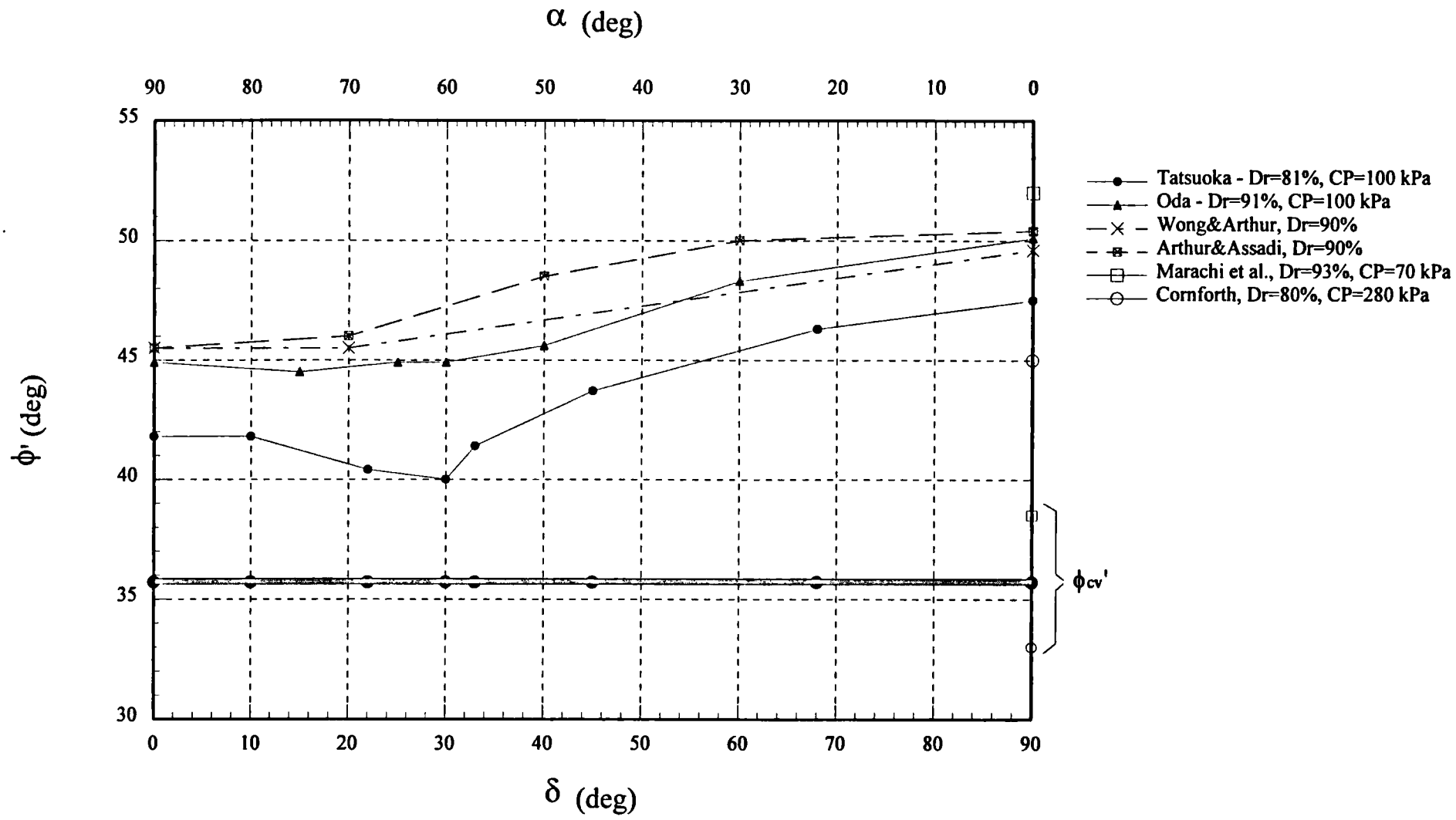


Fig.2.4 - Anisotropy of peak ϕ' values for isotropically consolidated dense sands, in drained plane strain shearing

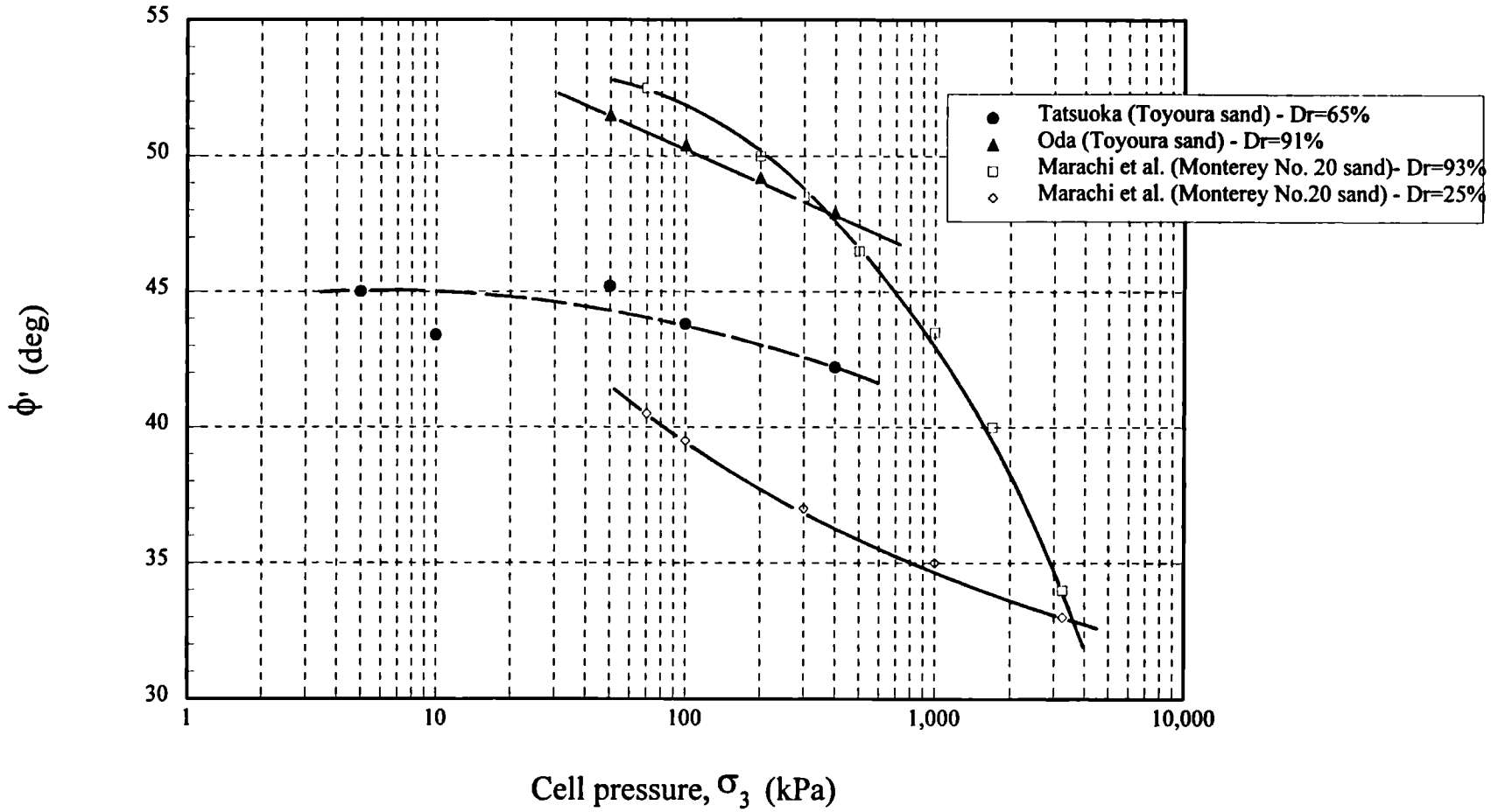


Fig.2.5 - Dependance of peak ϕ' on cell pressure, plane strain conditions (horizontal bedding plane, i.e. δ=90)

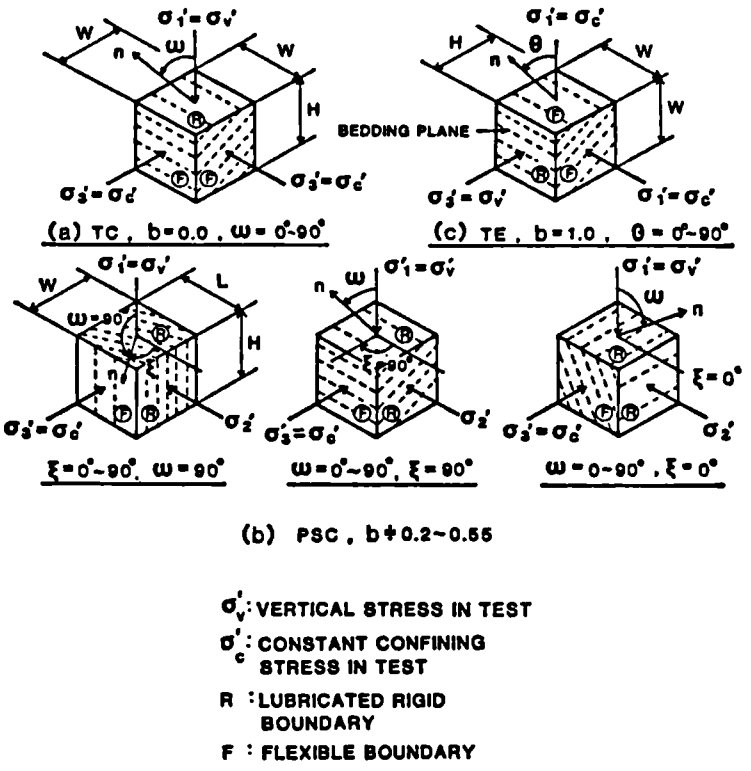


Fig.2.6 - Inclinations of bedding planes in cubical device
(Lam & Tatsuoka, 1988)

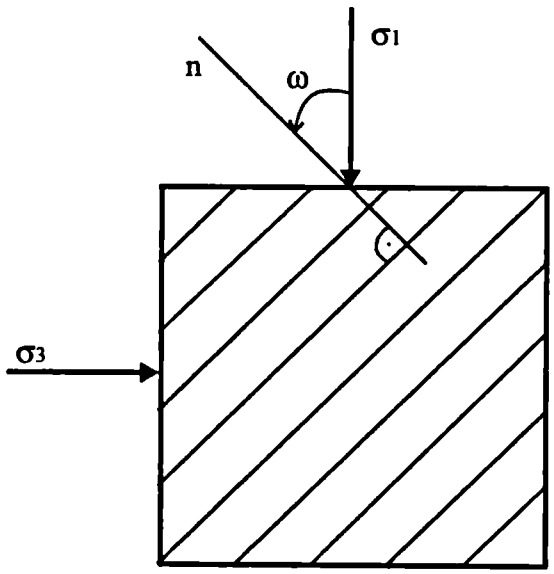


Fig.2.7 - Definition of angle ω for the inclination of bedding plane
(Lam & Tatsuoka, 1988)

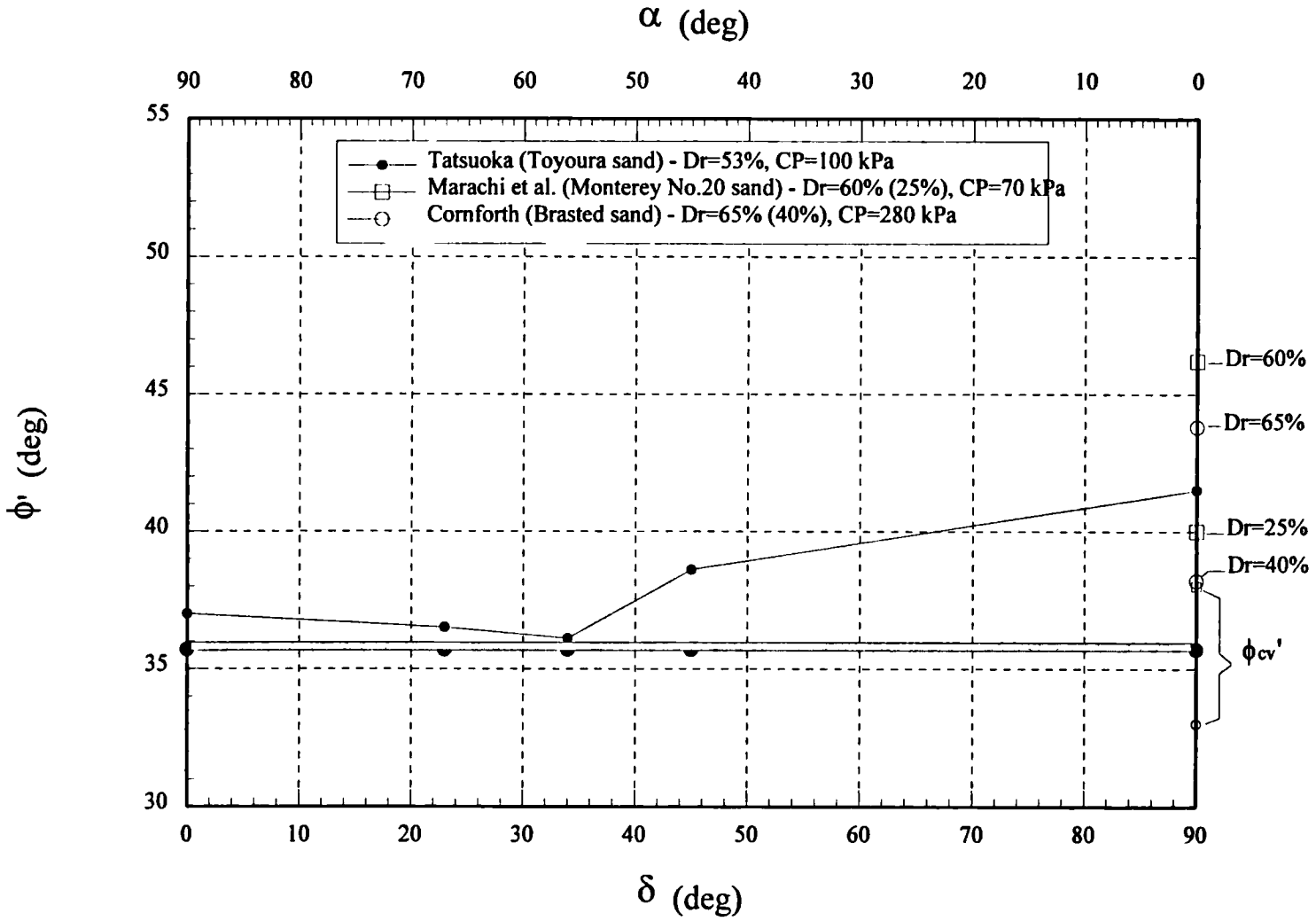


Fig.2.8 - Anisotropy of peak ϕ' values for loose sands in drained plane strain shearing

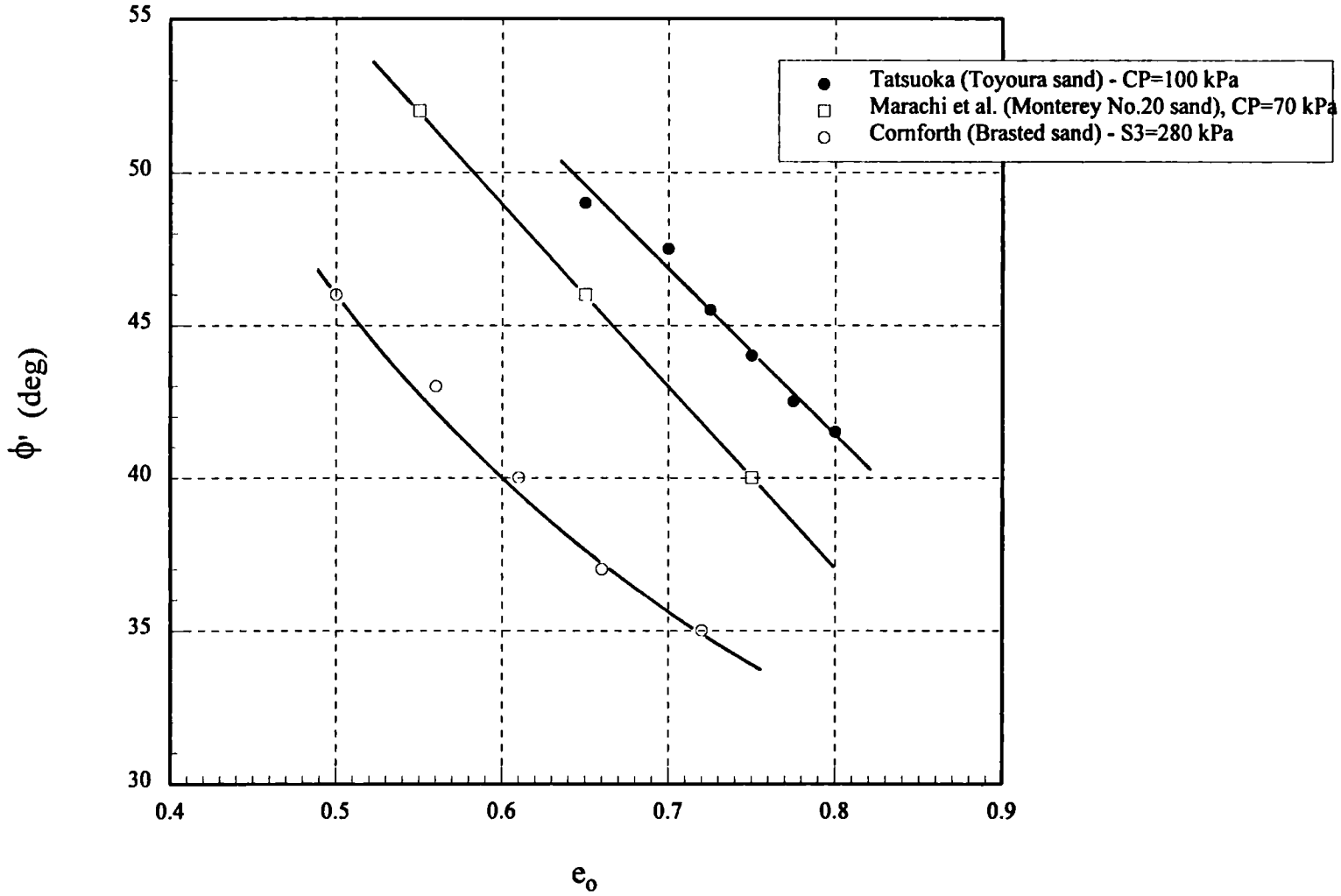


Fig.2.9 - Dependance of peak ϕ' on e_o, plane strain conditions
(horizontal bedding plane, i.e. δ=90)

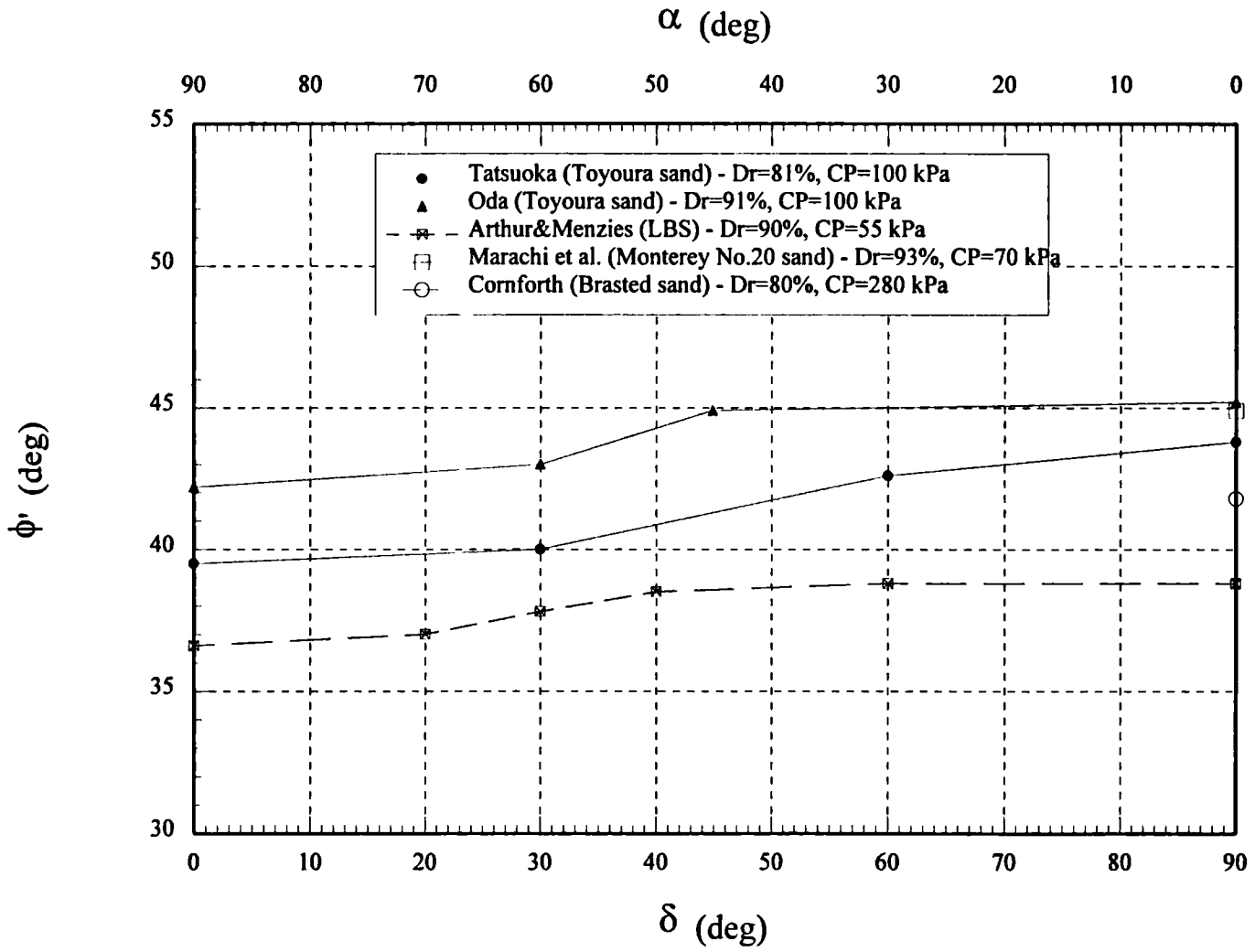


Fig.2.10 - Anisotropy of peak ϕ' values for dense sands in drained triaxial compression

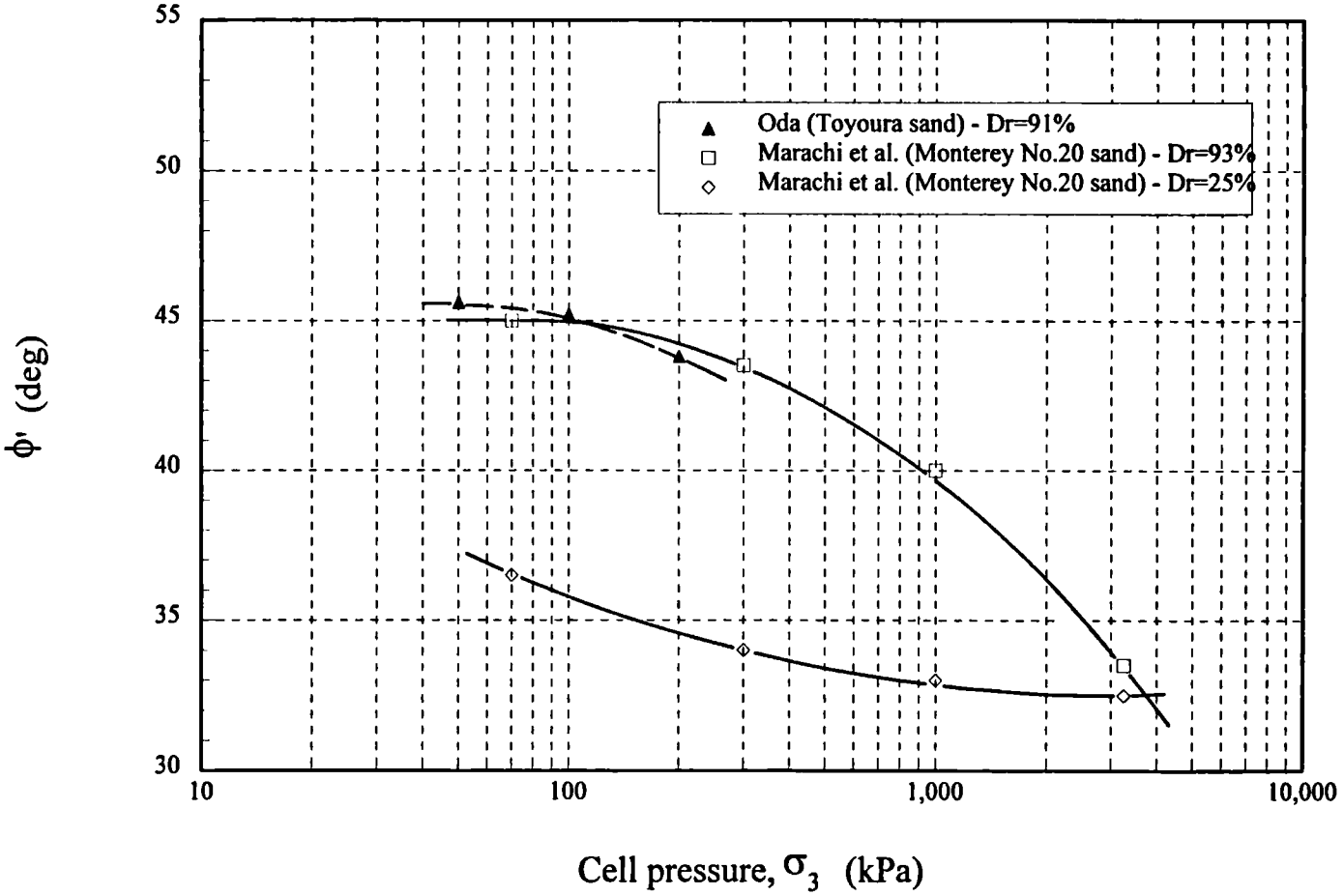


Fig.2.11 - Dependance of peak ϕ' on cell pressure in triaxial conditions (horizontal bedding plane, i.e.δ=90)

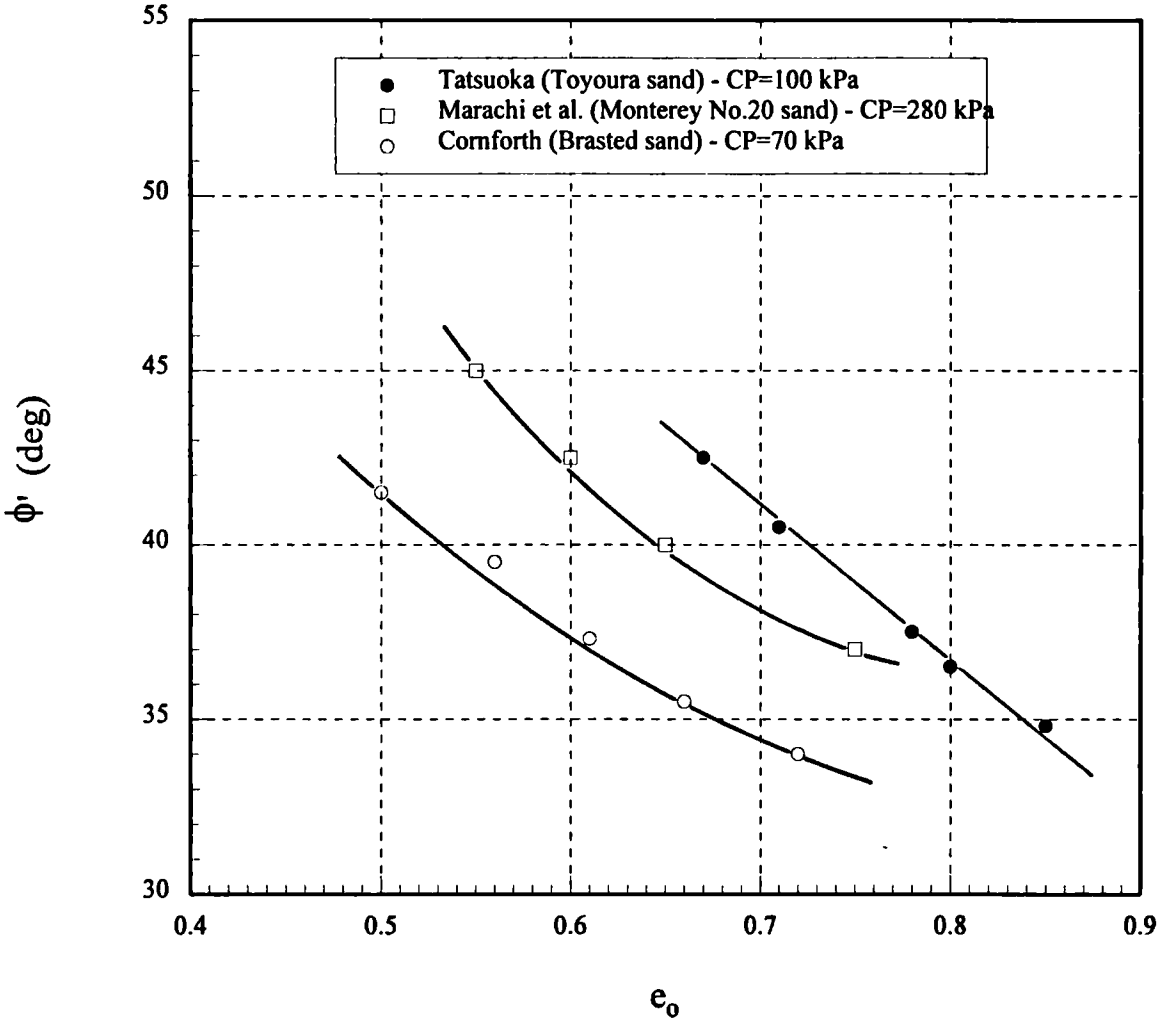


Fig.2.12 - Dependance of peak ϕ' on e_o, triaxial conditions (horizontal bedding plane, i.e. δ=90)

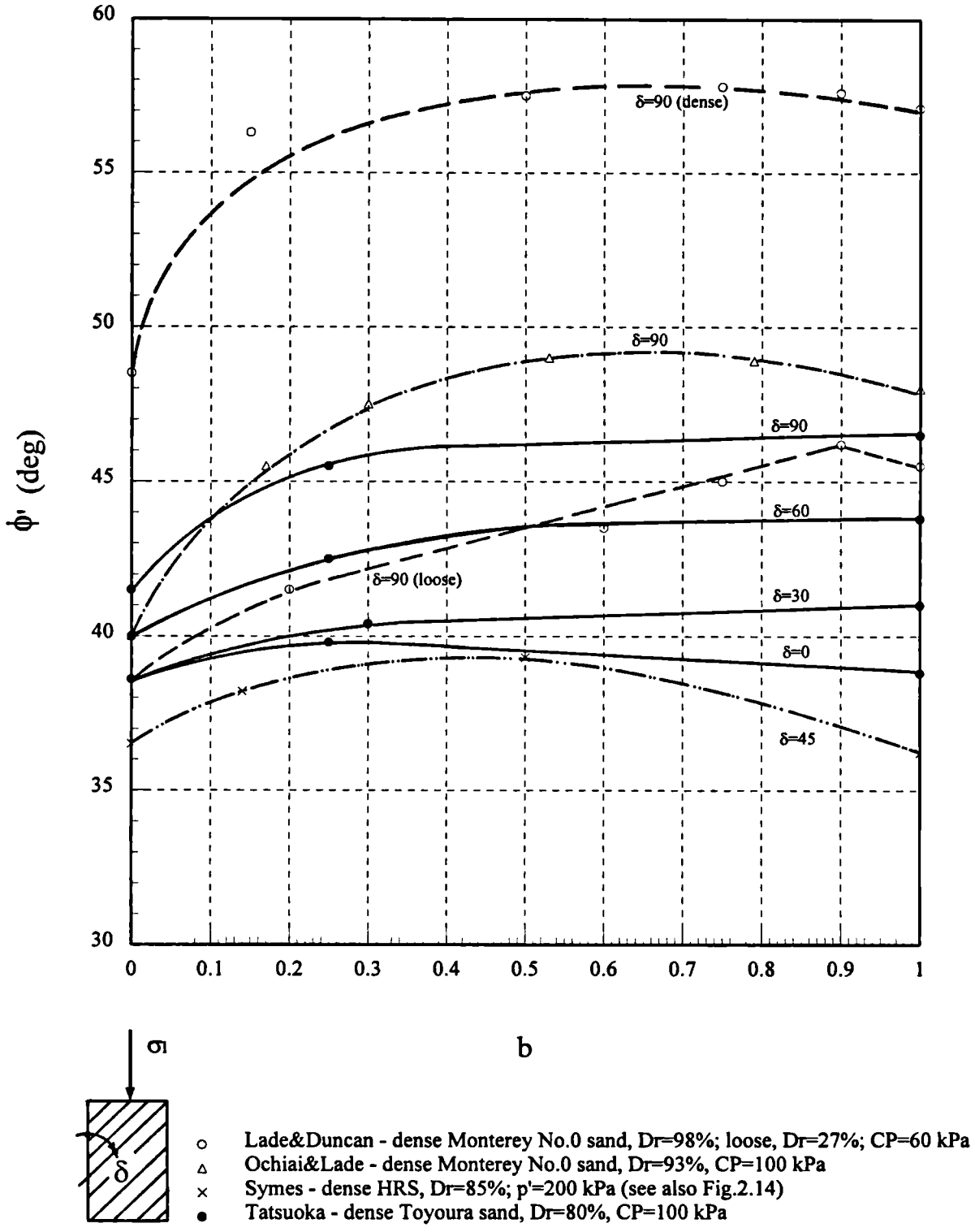


Fig.2.13 - Dependance of peak ϕ' on intermediate principal stress

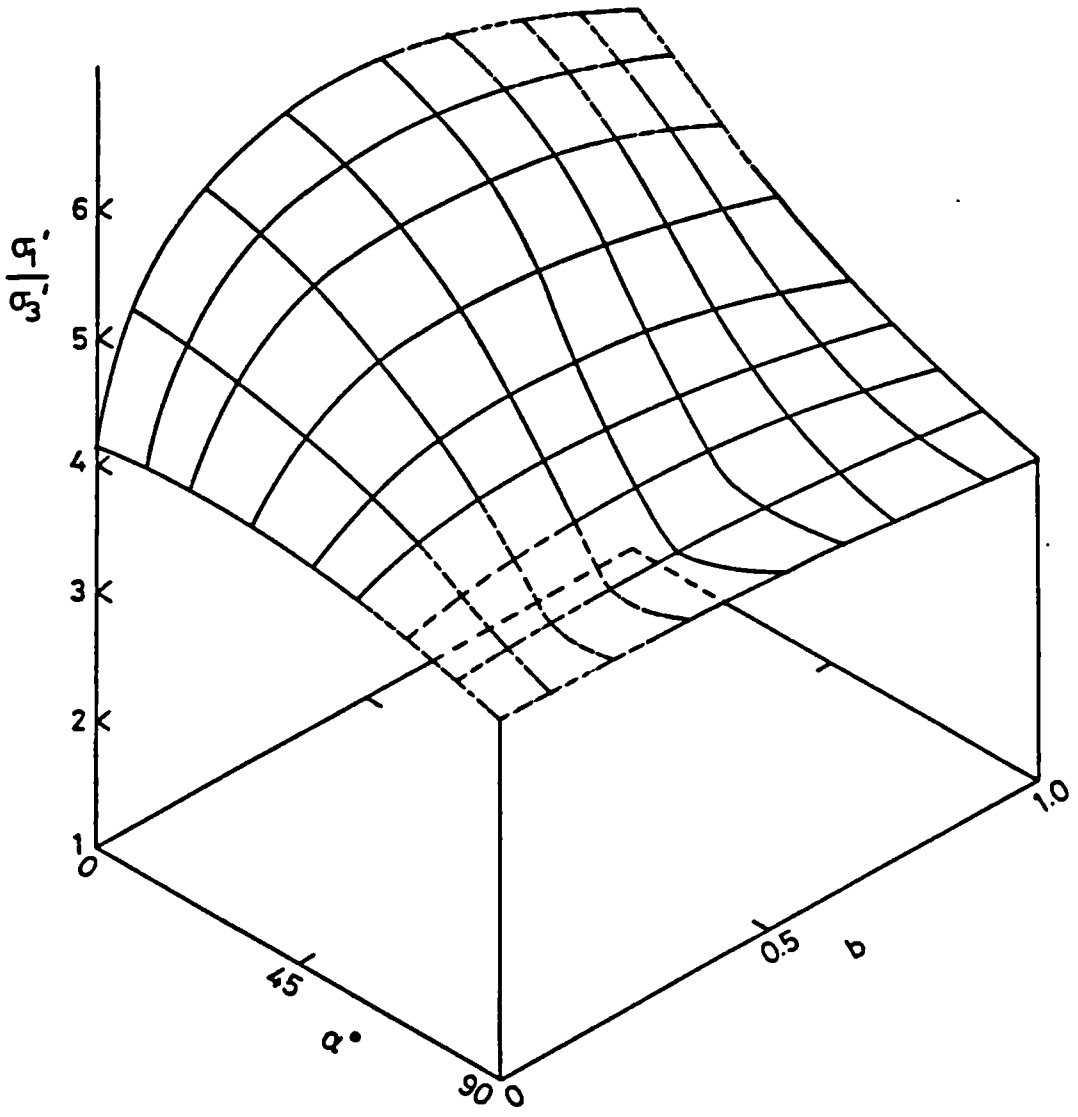


Fig.2.14 - The dependency of σ_1'/σ_3' on both b and α (Symes, 1983)

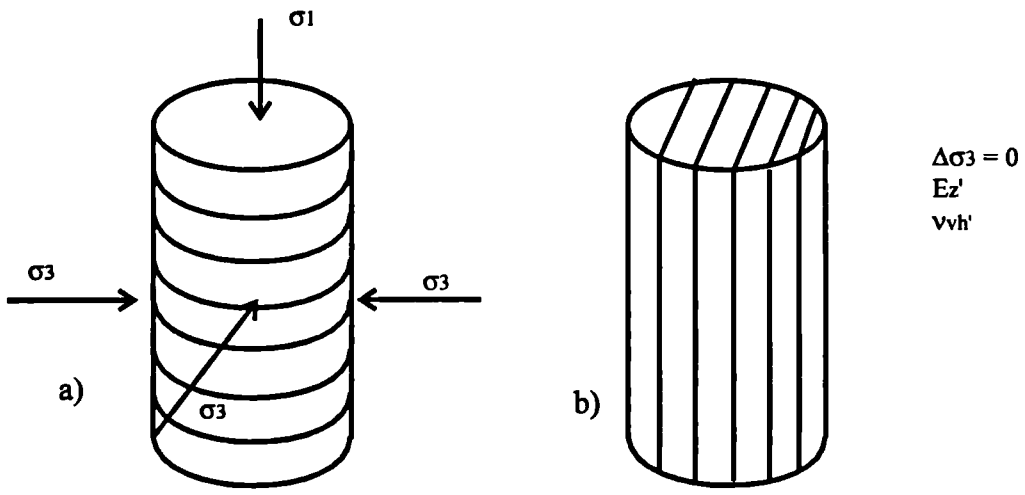


Fig.2.15 - Anisotropic elastic parameters from triaxial test with cylindrical sample

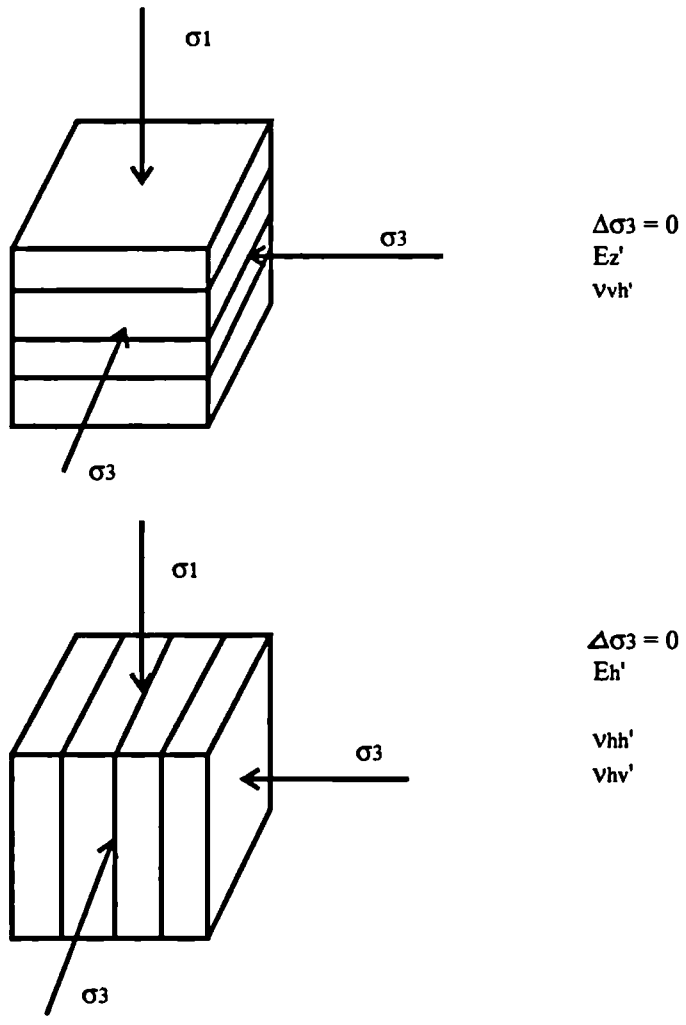


Fig.2.16 - Anisotropic elastic parameters from triaxial tests with cubical sample

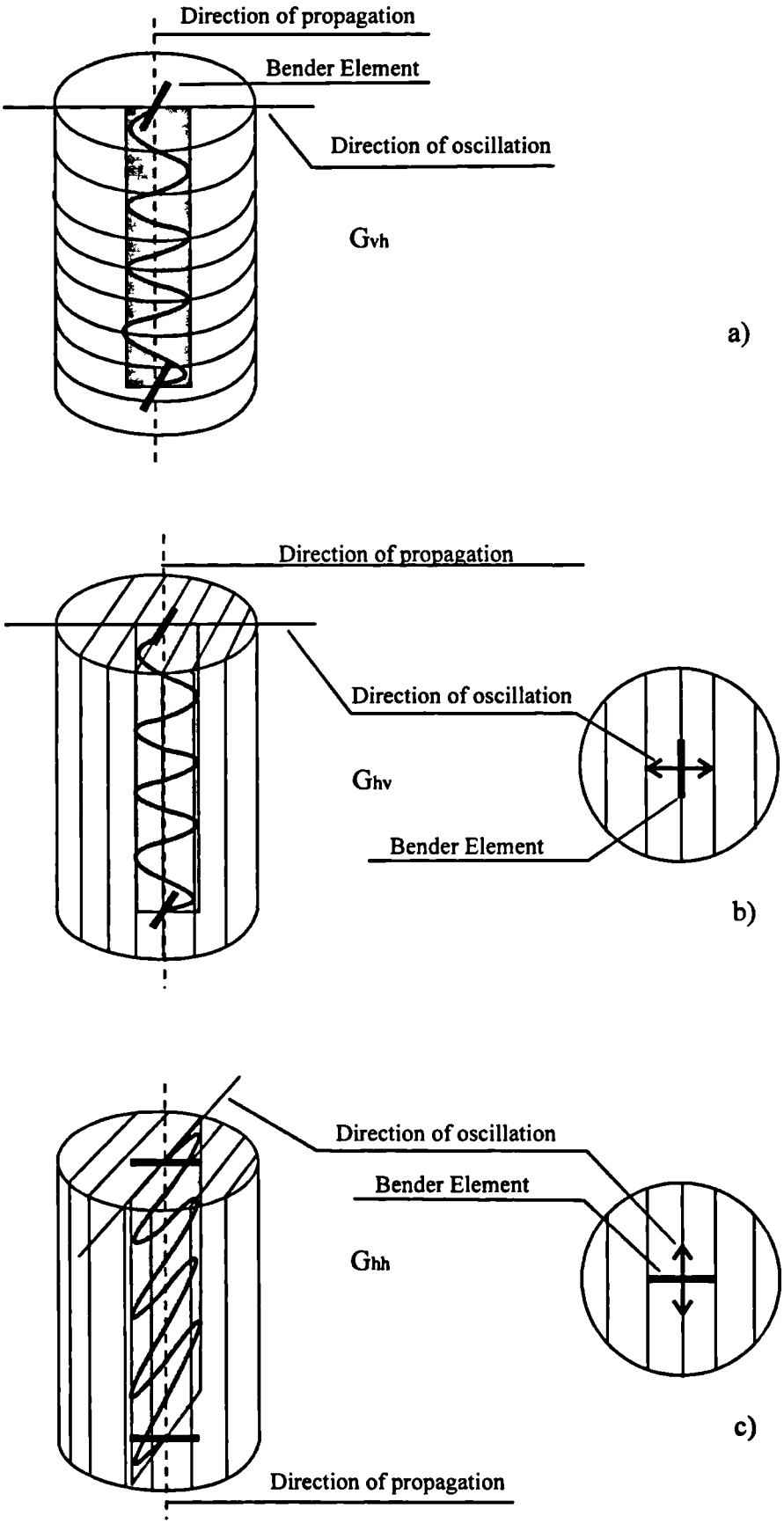


Fig.2.17 - Measurement of G-moduli using Bender Elements in triaxial sample

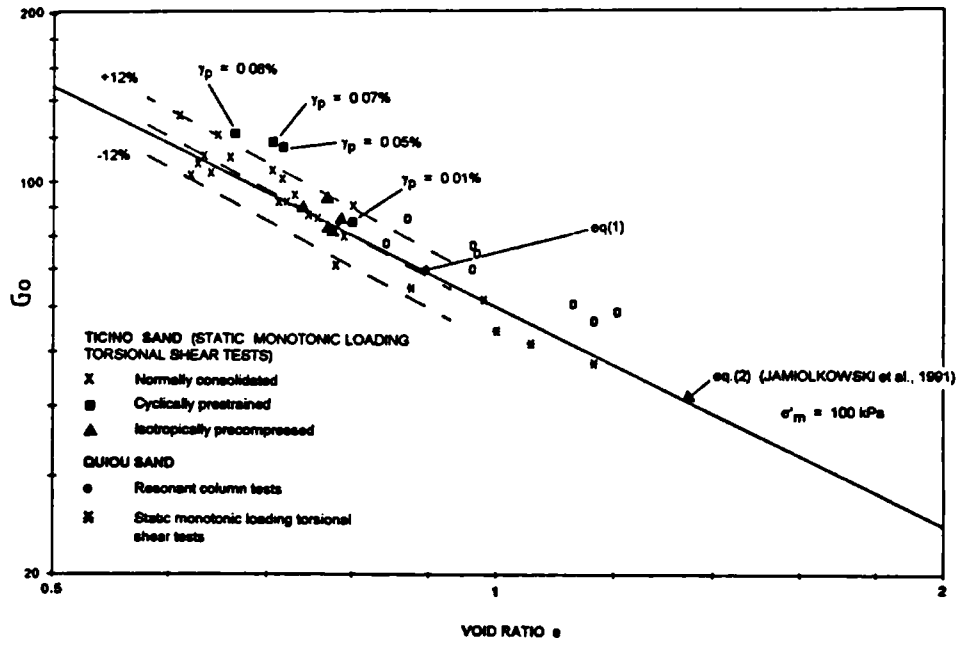


Fig.2.18 - Maximum shear modulus of Ticino and Quiou sands vs. void ratio (Lo Presti et al., 1993)

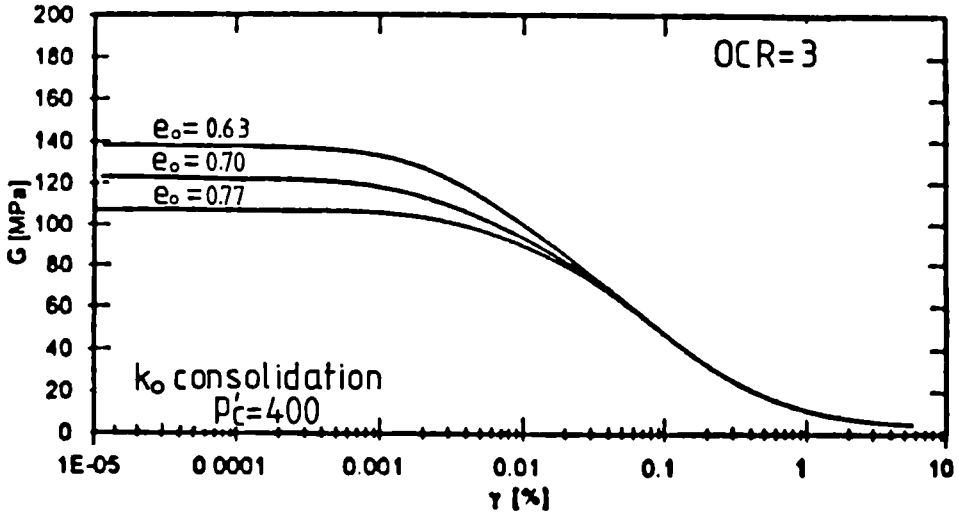


Fig.2.19 - Effect of initial void ratio on G-γ curves for Ham River Sand (K_o consolidation to p_c'=400 kPa, OCR=3; Porovic & Jardine, 1994)

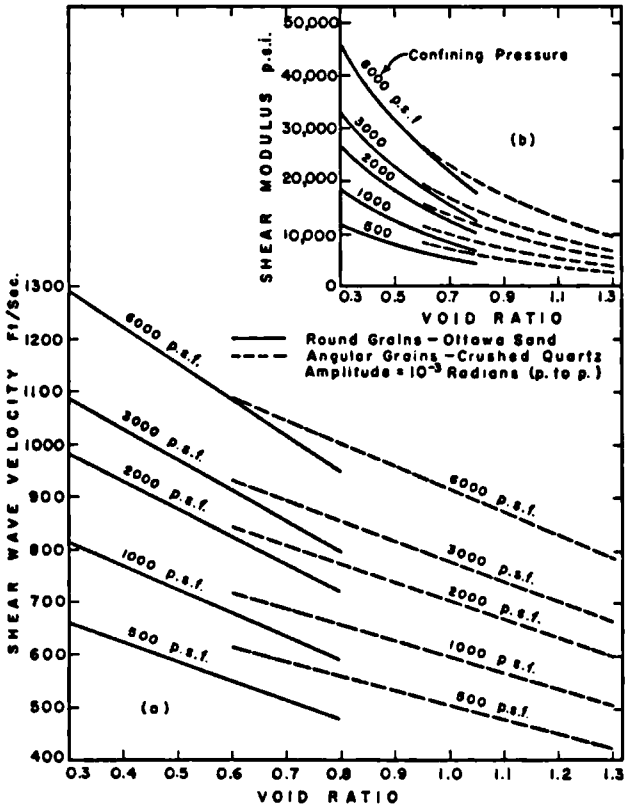


Fig.2.20 - Variation of shear wave velocity with void ratio and confining pressure in dry sand (Hardin & Richart, 1963)

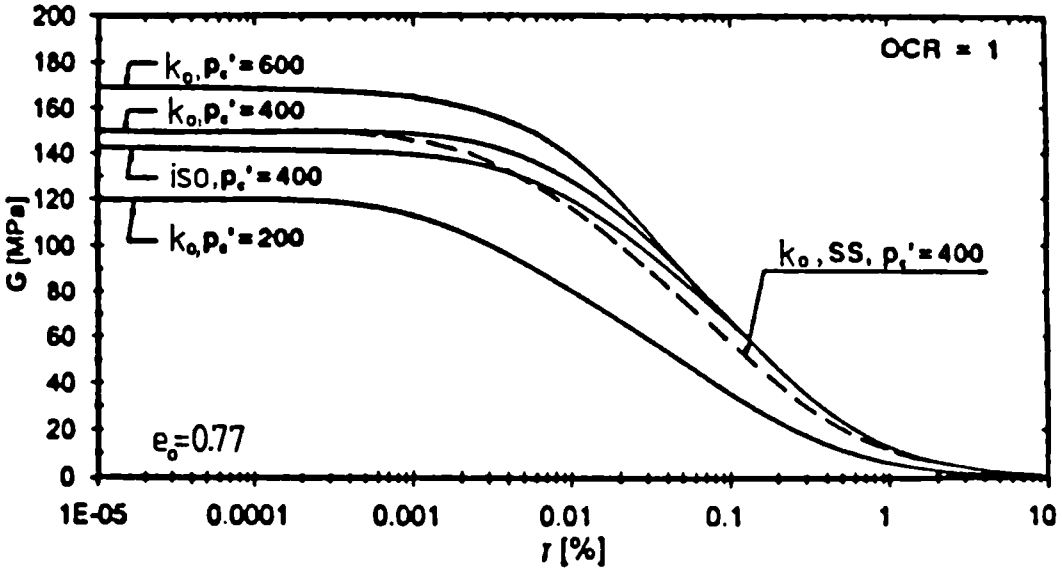


Fig.2.21 - Dependence of G_{max} on stress level in Ham River Sand (Porovic & Jardine, 1994)

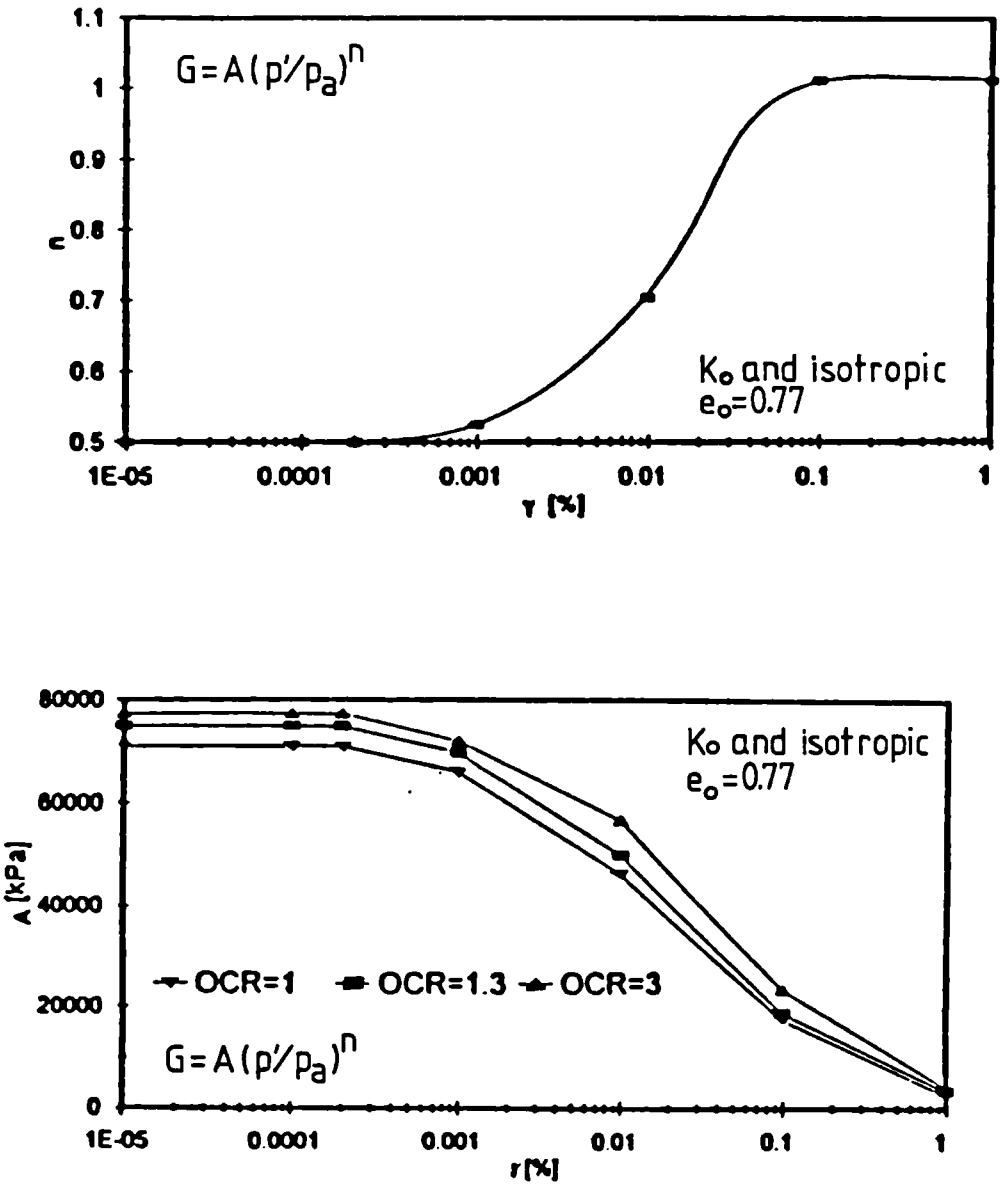


Fig.2.22 - Variation of parameters a) n and b) A with strain level, Ham River Sand (Porovic & Jardine, 1994)

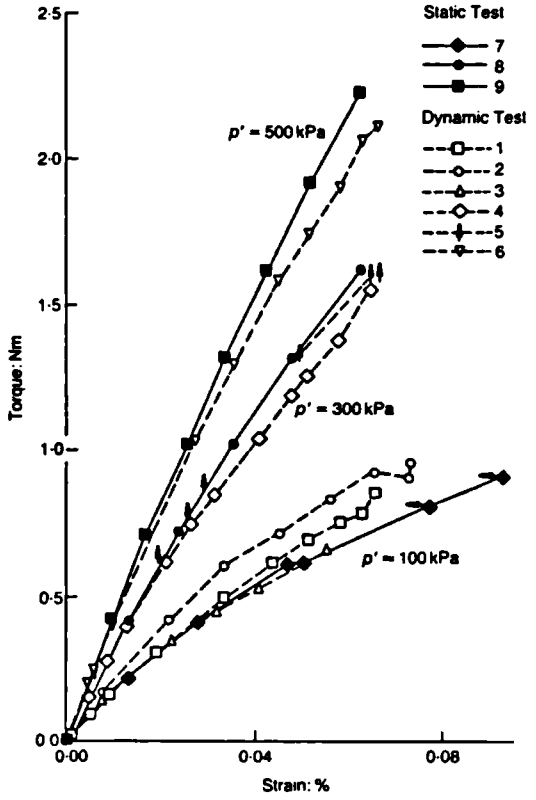


Fig.2.23 - Static and dynamic torque-strain curves (Bolton & Wilson, 1989)

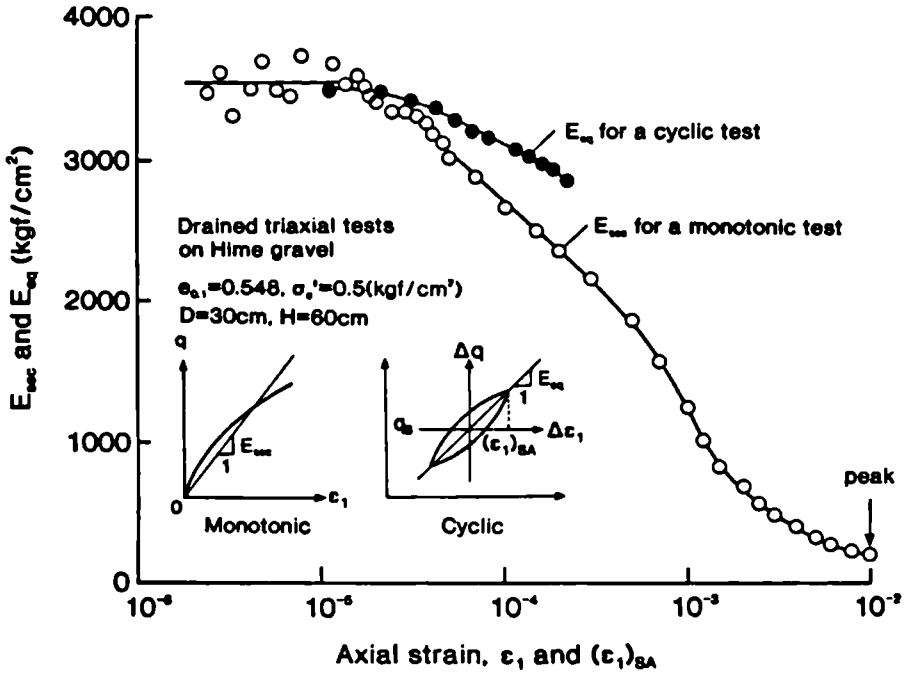


Fig.2.24 - Comparison of stiffness between static monotonic (ML) and cyclic (CL) triaxial tests on Hime gravel (Shibuya et al., 1990)

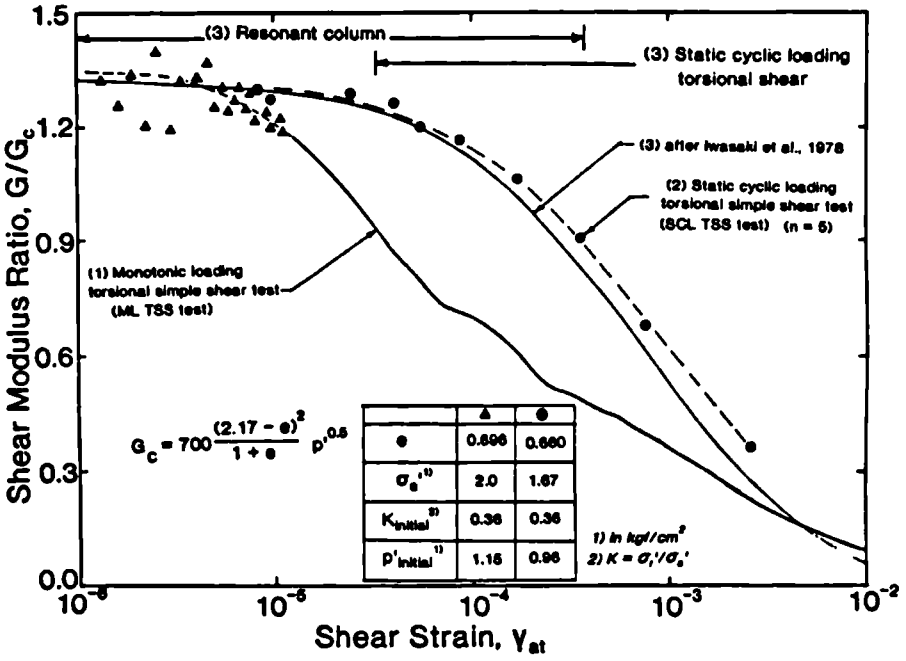


Fig.2.25 - Comparison of shear modulus between resonant column (RC) and static monotonic (ML) and cyclic (CL) tests on Toyoura sand (Tatsuoka & Shibuya, 1992)

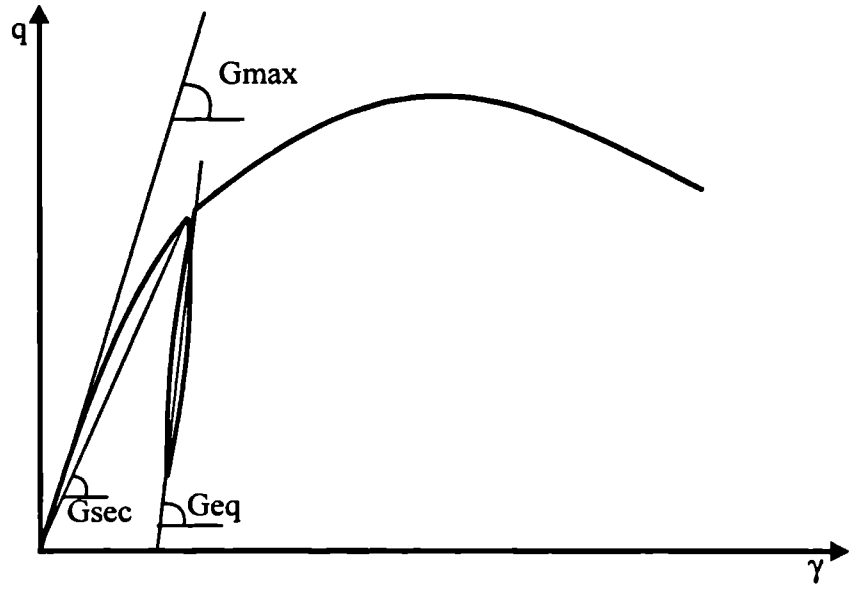


Fig.2.26 - Definition of different stiffness components

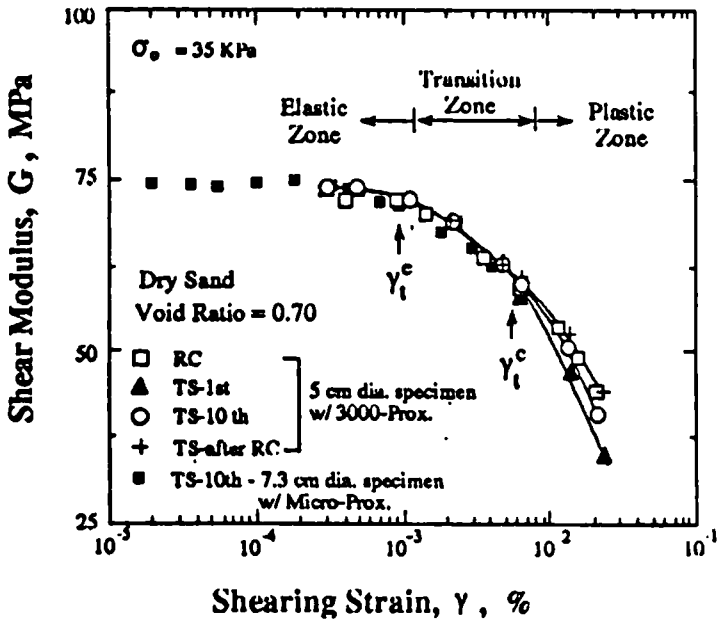


Fig.2.27 - Comparison of shear modulus between resonant column (RC) and torsional shear (TS) cyclic tests on sand (Kim & Stokoe, 1995)

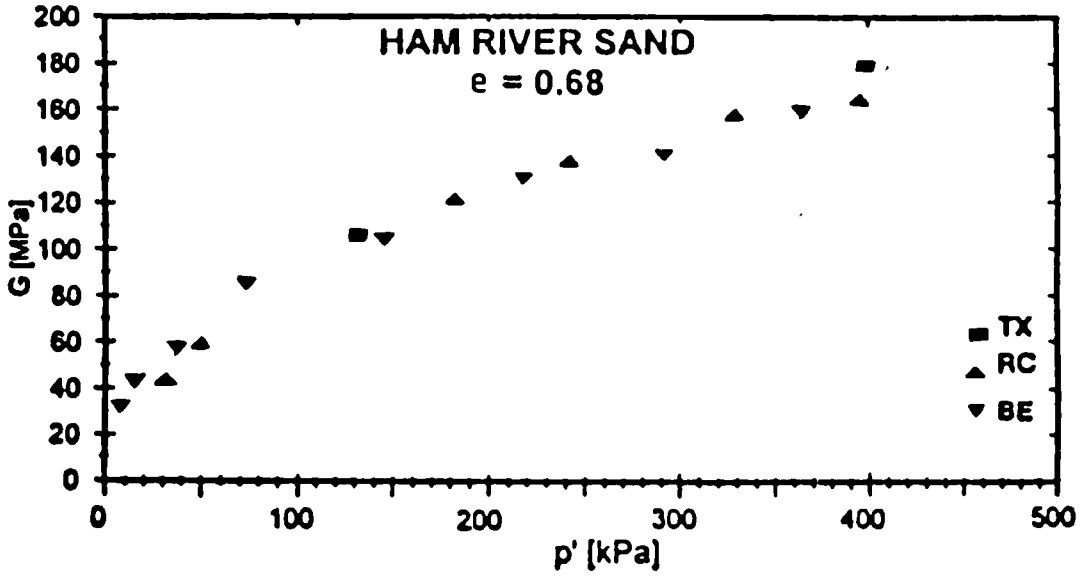


Fig.2.28 - Comparison of G_{max} from triaxial (TX), resonant column (RC) and Bender Element (BE) test on Ham River Sand (Porovic & Jardine, 1994)

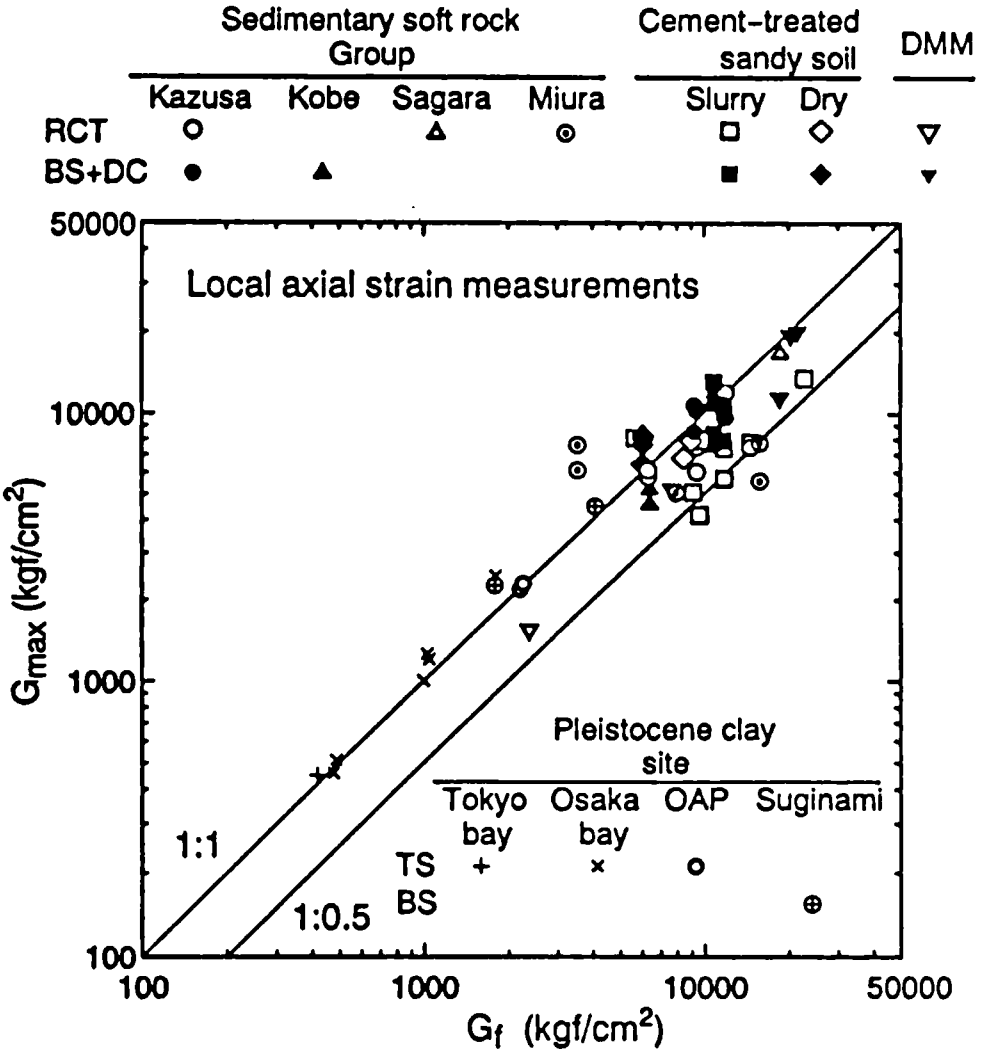
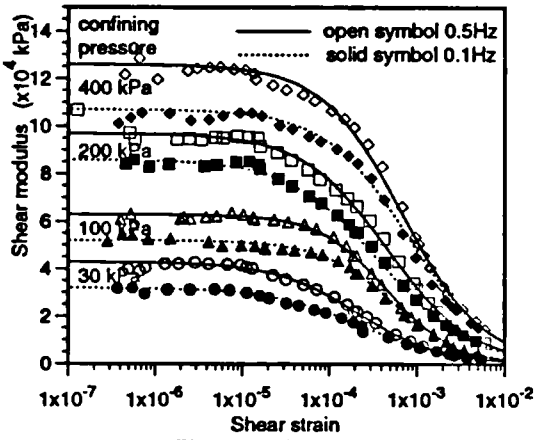
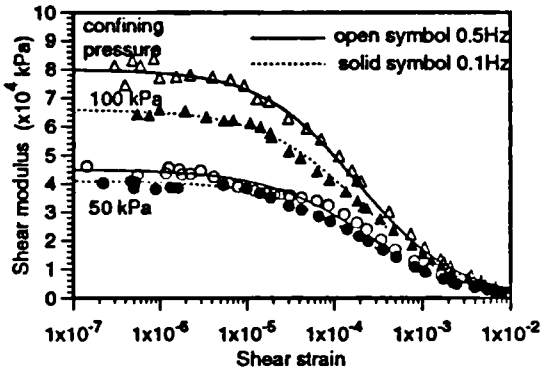


Fig.2.29 - Comparison between G_{max} from cyclic triaxial tests and G_f from field shear wave velocity (Kohata et al., 1995)

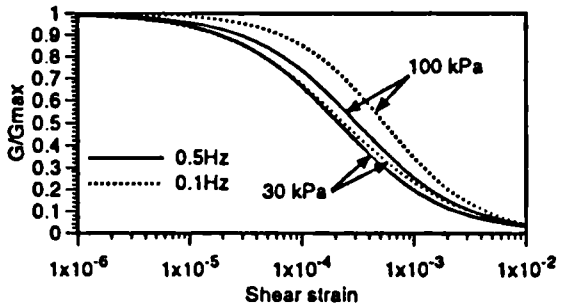


(a) Flocculated Kaolin

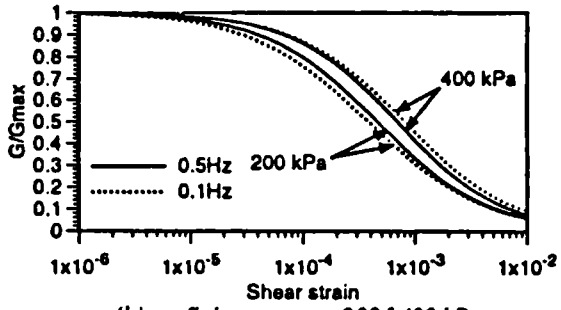


(b) Dispersed Kaolin

Fig.2.30 - Frequency dependence of shear modulus for Flocculated and Dispersed Kaolin (Soga et al., 1995)



(a) confining pressure 30&100 kPa



(b) confining pressure 200&400 kPa

Fig.2.31 - Effect of frequency on normalized stiffness degradation curves on flocculated kaolin (Soga et al., 1995)

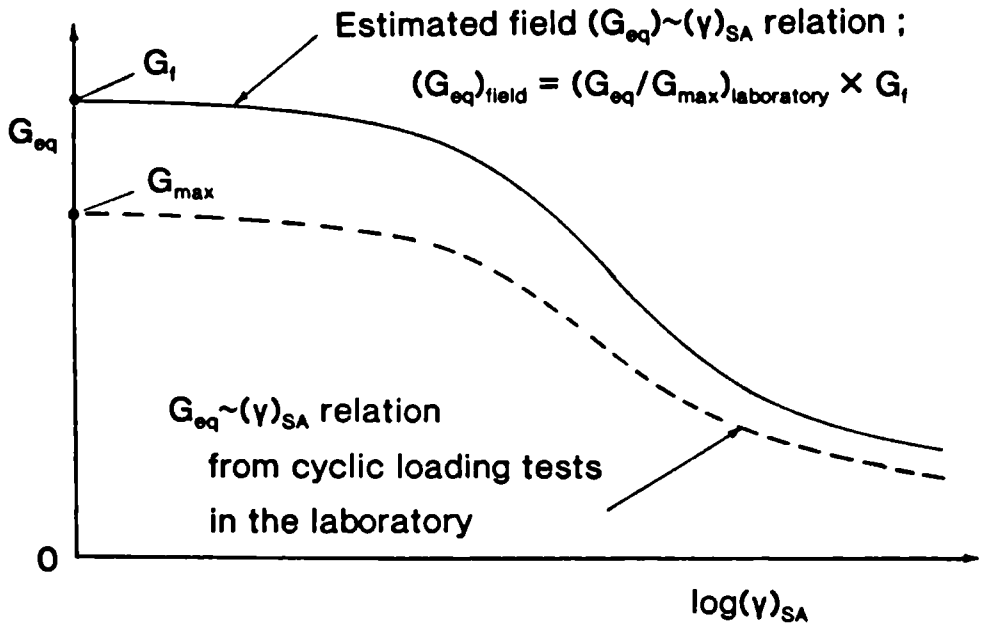


Fig.2.32 - A method to estimate the in situ stiffness as a function of strain

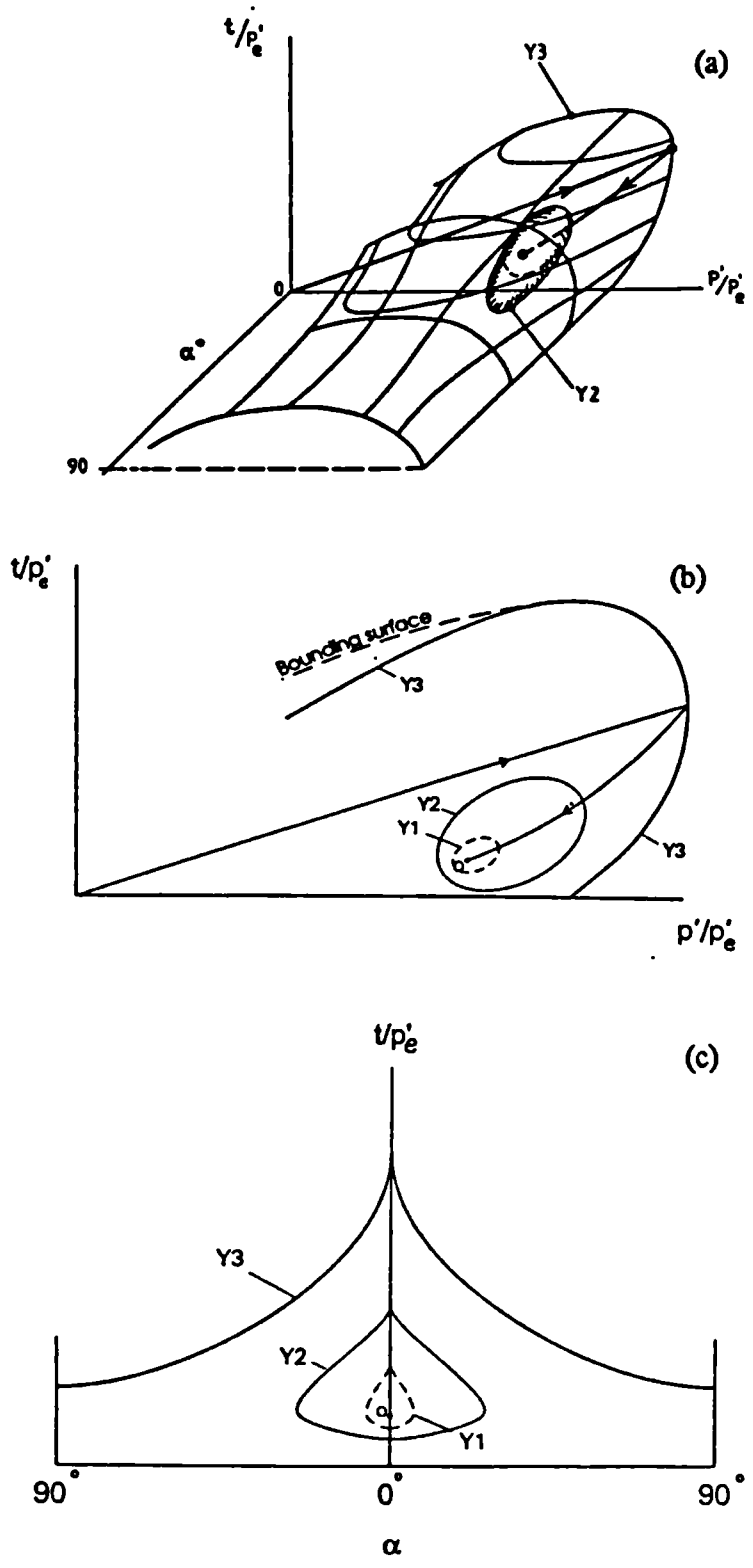


Fig.2.33 - Framework for soil behaviour (Jardine, 1985; Hight et al., 1987)
a) 3D presentation in t/p_e'-p'/p_e'-α space
b) Projection on t/p_e'-p'/p_e' plane
c) Projection on t/p_e'-α plane

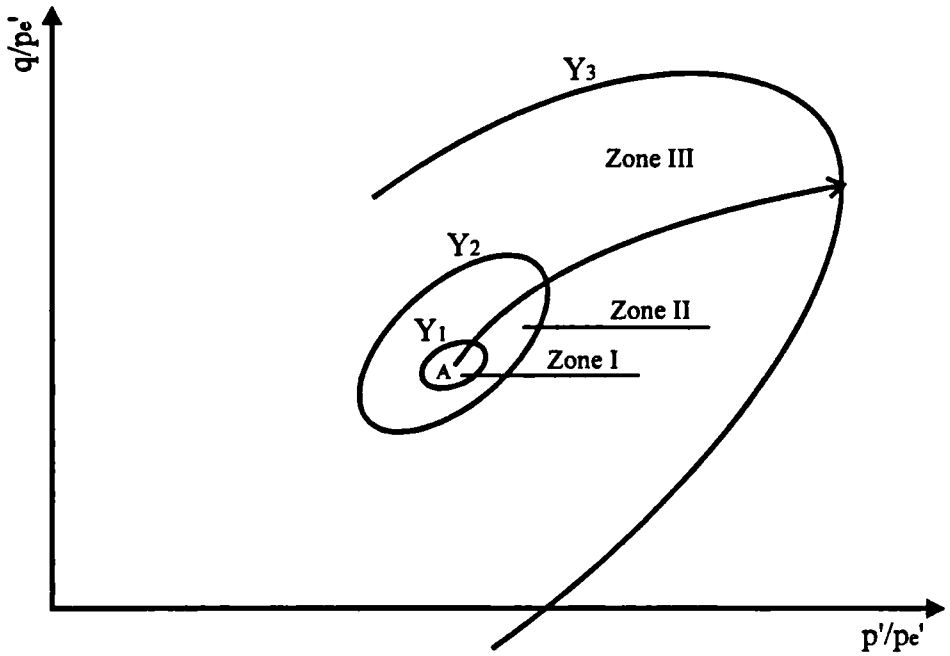


Fig.2.34 - Identification of Zones I, II and III in triaxial stress space (Jardine, 1992)

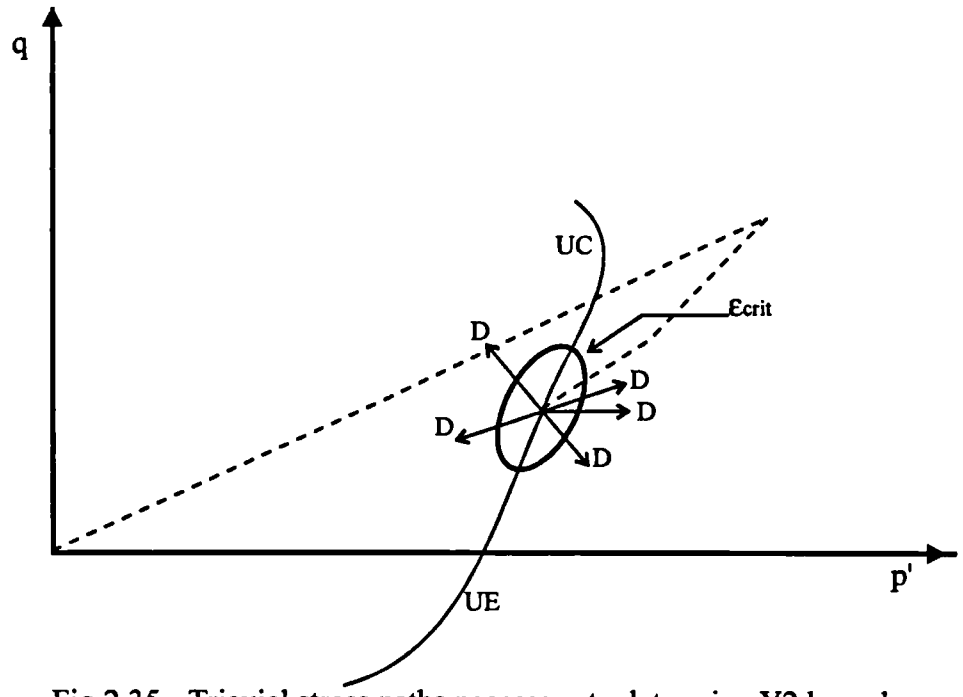


Fig.2.35 - Triaxial stress paths necessary to determine Y2 boundary

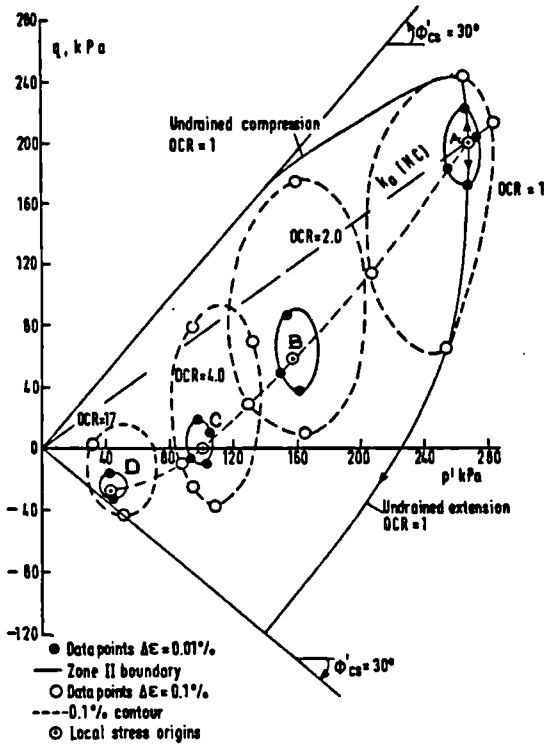


Fig.2.36 - Movement and evolution of small strain regions due to K_o swelling, Magnus till (Jardine, 1992)

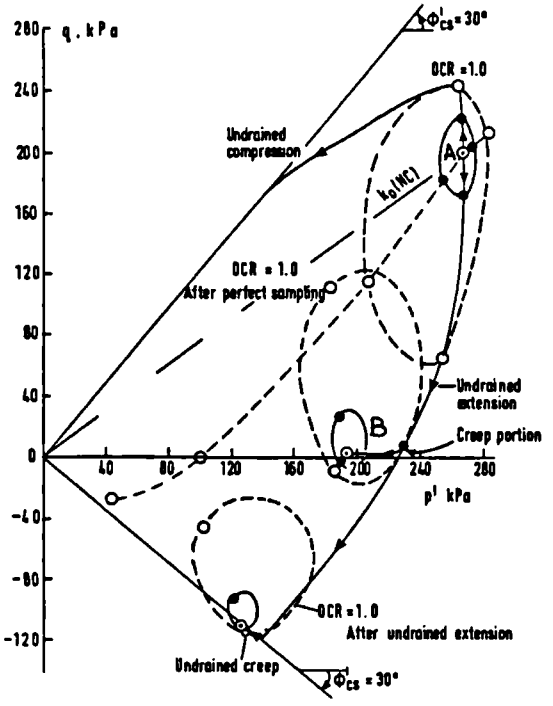


Fig.2.37 - Movement and evolution of small strain regions due to undrained shearing, Magnus till (Jardine, 1992)

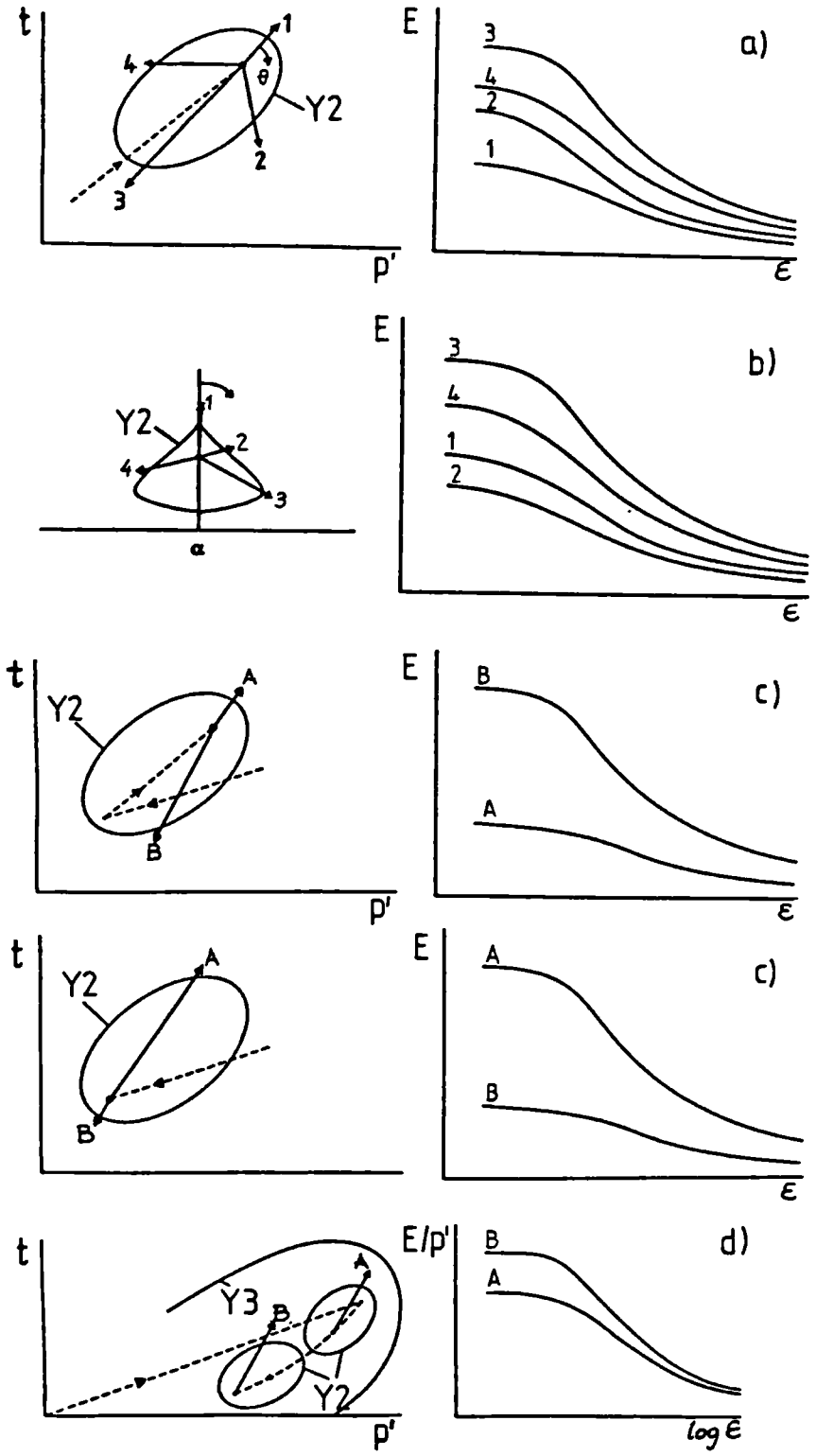


Fig.2.38 - Factors affecting stress-strain response inside the Y_2 surface (Hight, 1994)

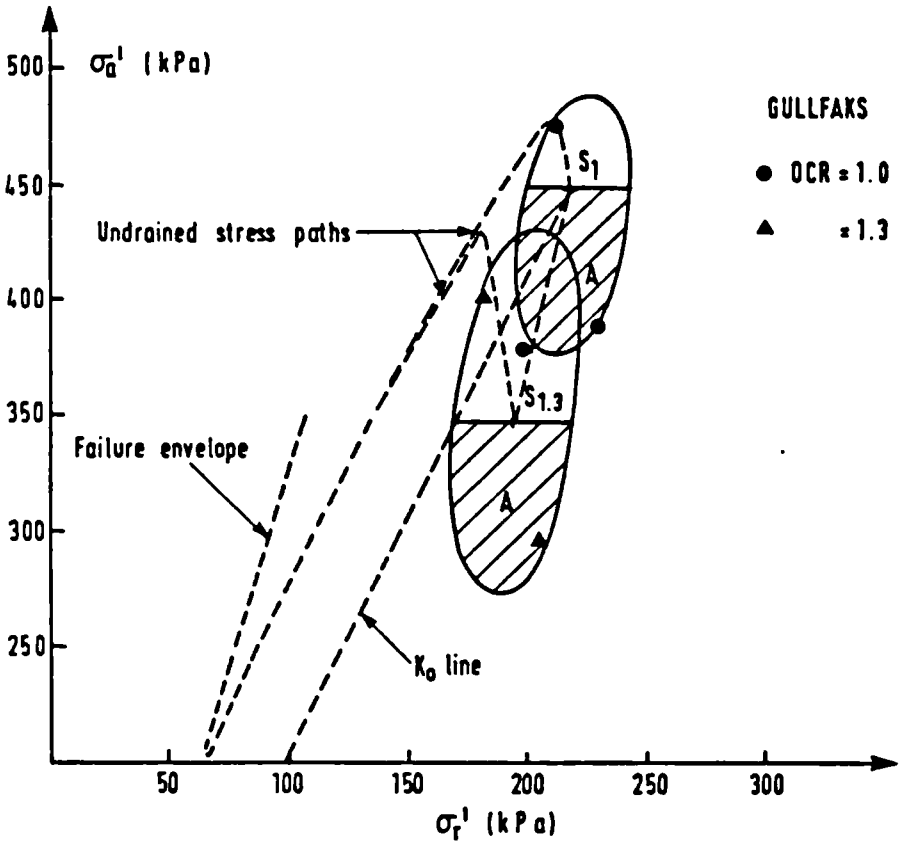


Fig.2.39 - Comparison of the strain energy contours at OCR=1.0 and 1.3 for Ham River Sand-kaolin samples (Burland & Georgiannou, 1991)

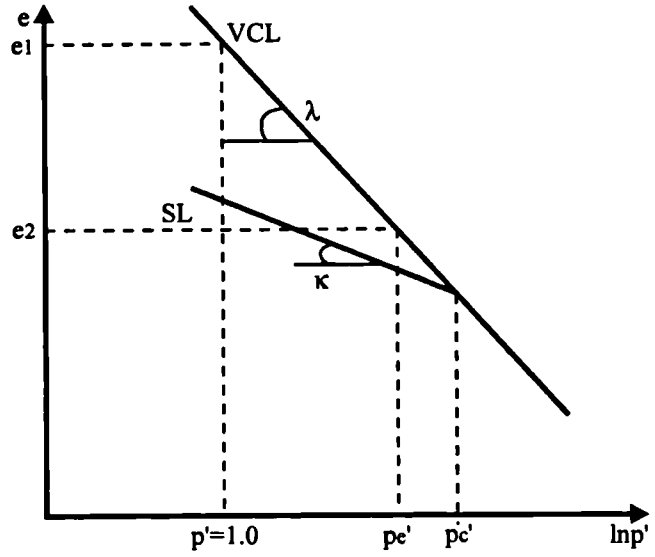


Fig.2.40 - Idealized consolidation behaviour of clays

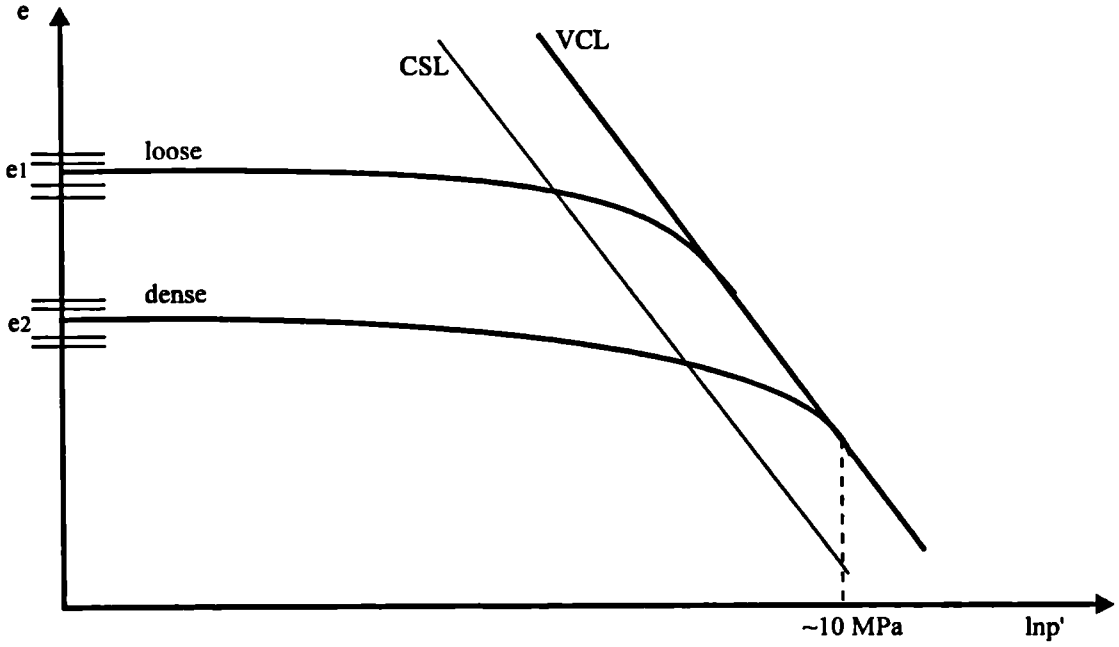
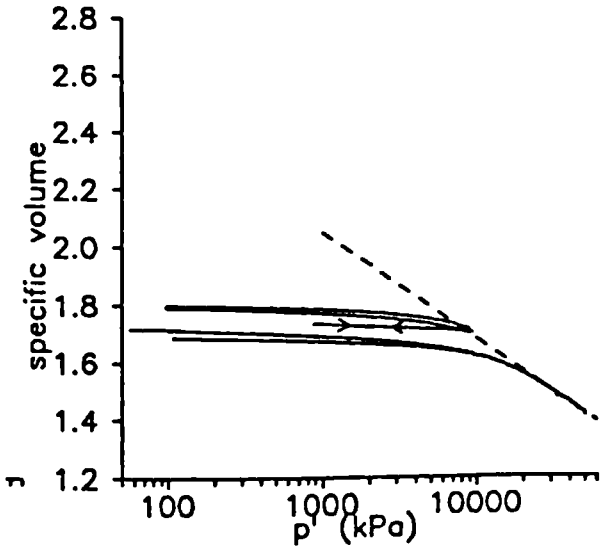
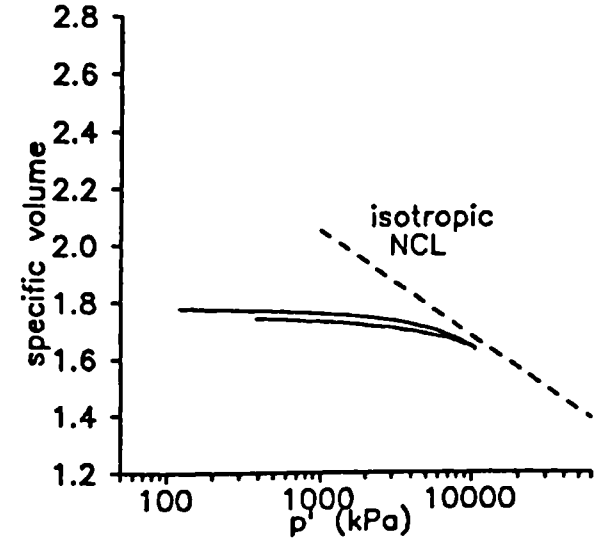


Fig.2.41 - Consolidation behaviour of sands



(c) Ham River Sand

isotropic consolidation



(b) Ham River Sand

one-dimensional consolidation

Fig.2.42 - Isotropic and one-dimensional consolidation of Ham River Sand (Coop, 1990)

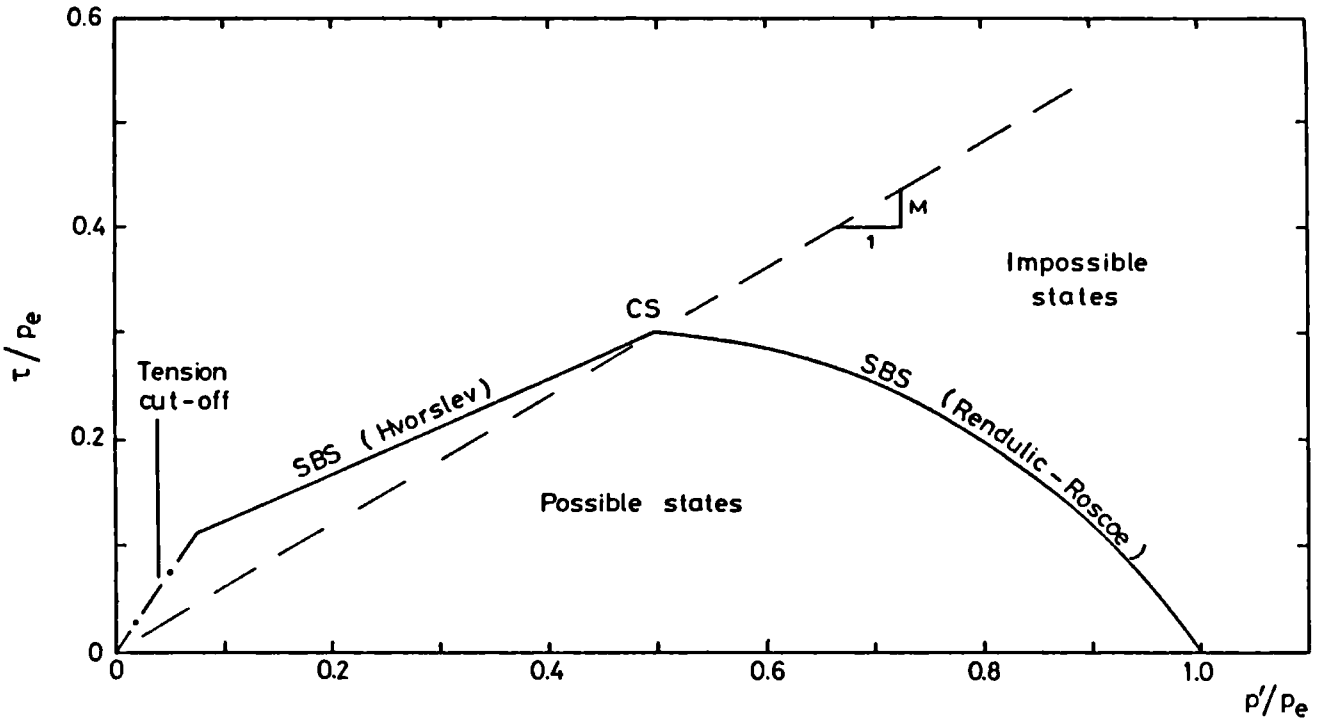


Fig.2.43 - State Boundary Surface for a classical critical state framework (Gens, 1982)

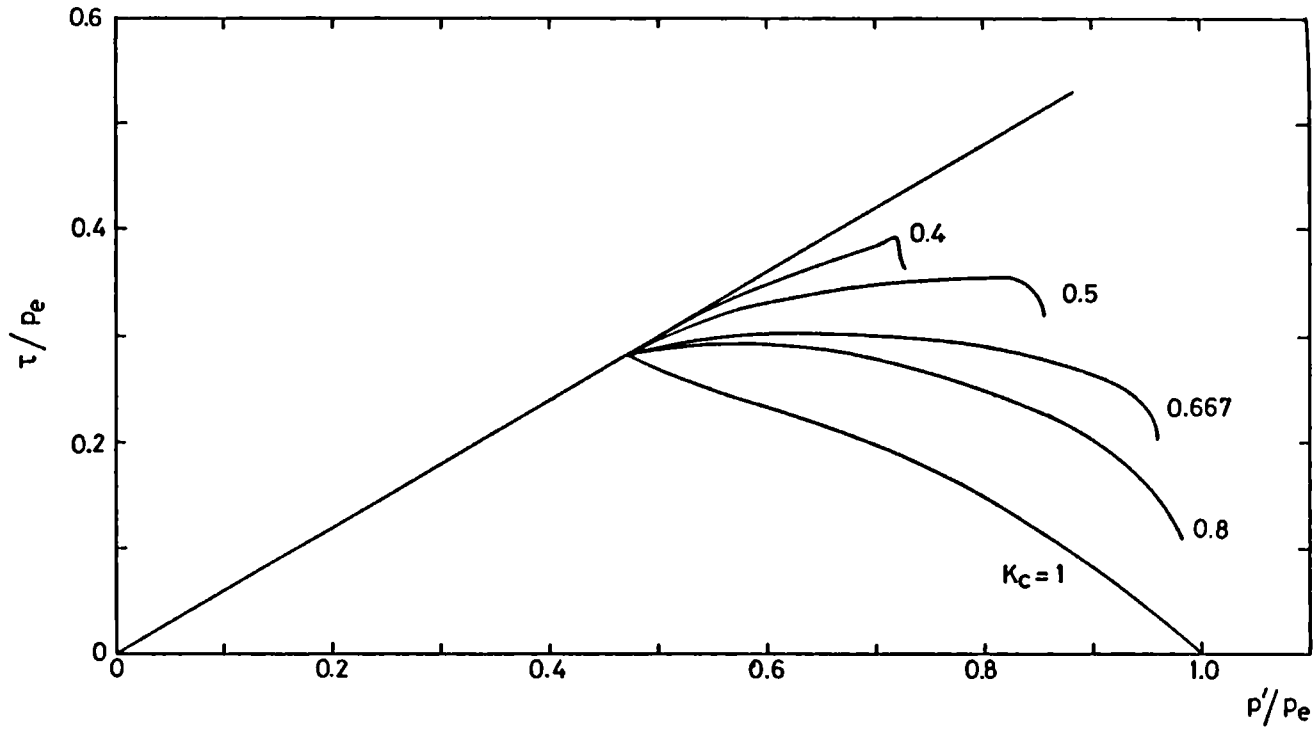


Fig.2.44 - Normalized undrained stress paths for triaxial compression tests on samples consolidated at different values of K (Gens, 1982)

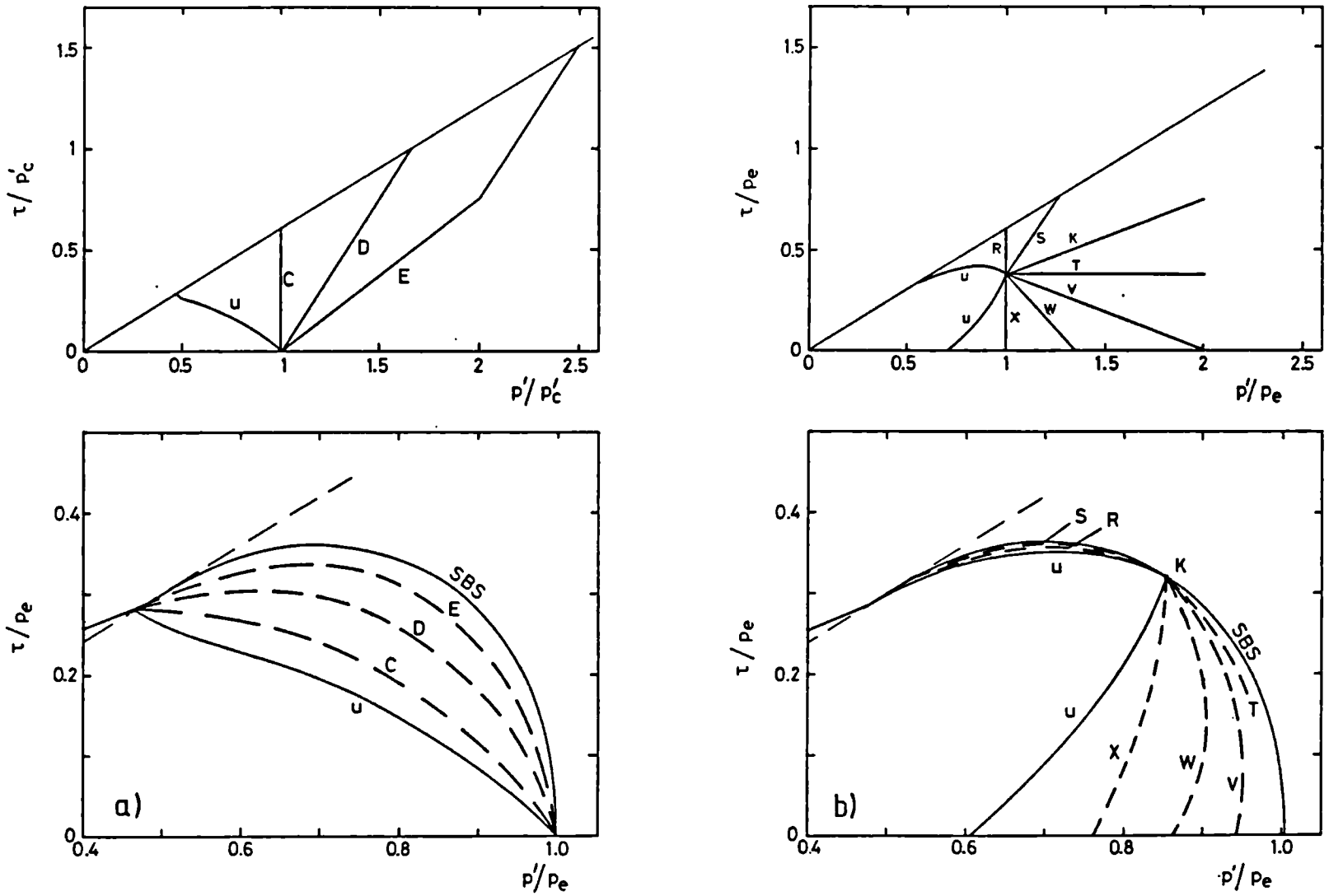


Fig.2.45 - a) Stress paths on isotropically normally consolidated samples and normalized stress paths predicted by the framework
b) Stress paths on anisotropically normally consolidated samples and normalized stress paths predicted by the framework

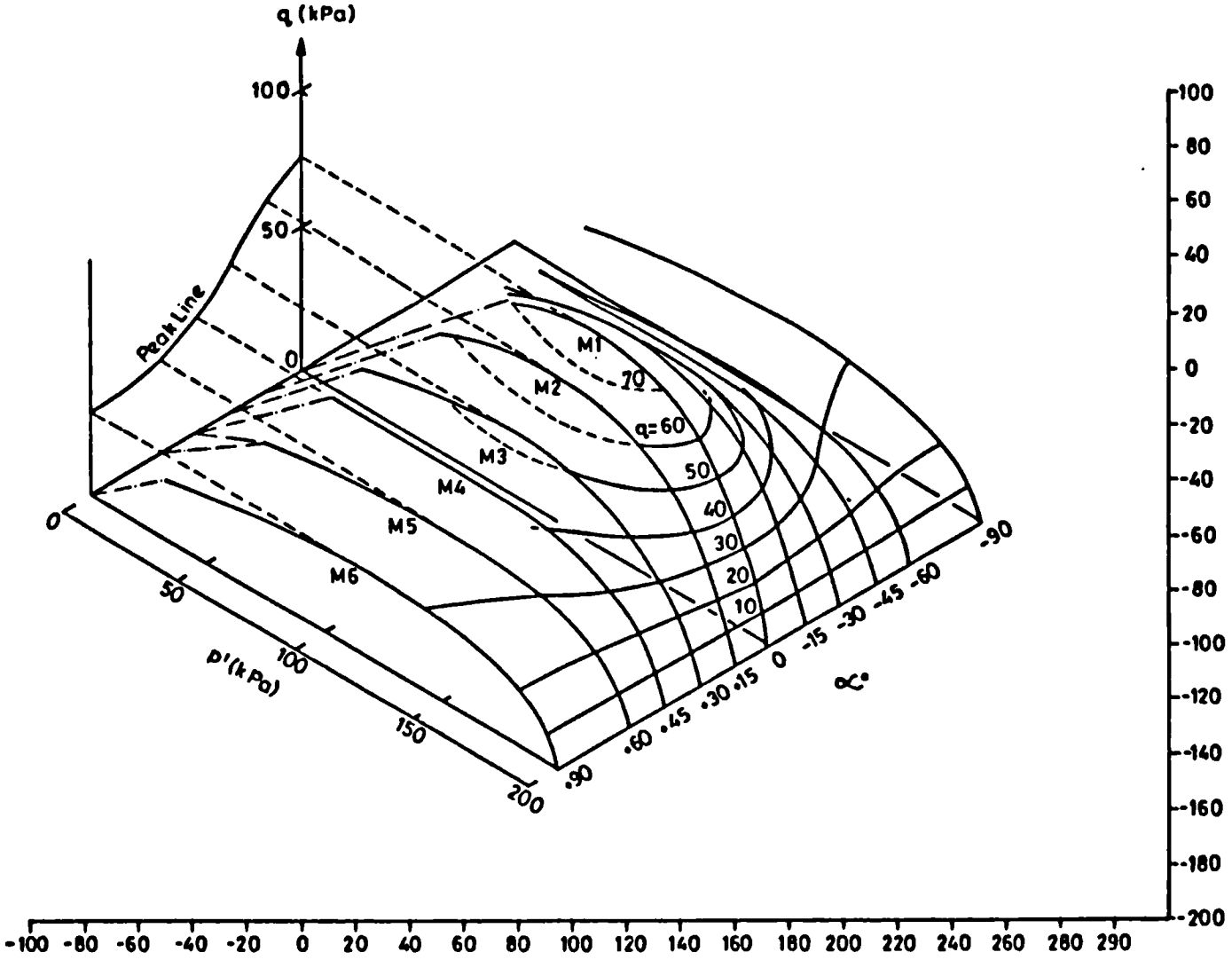


Fig.2.46 - Undrained Bounding Surface for isotropically consolidated loose Ham River Sand at b=0.5 (Shibuya, 1985)

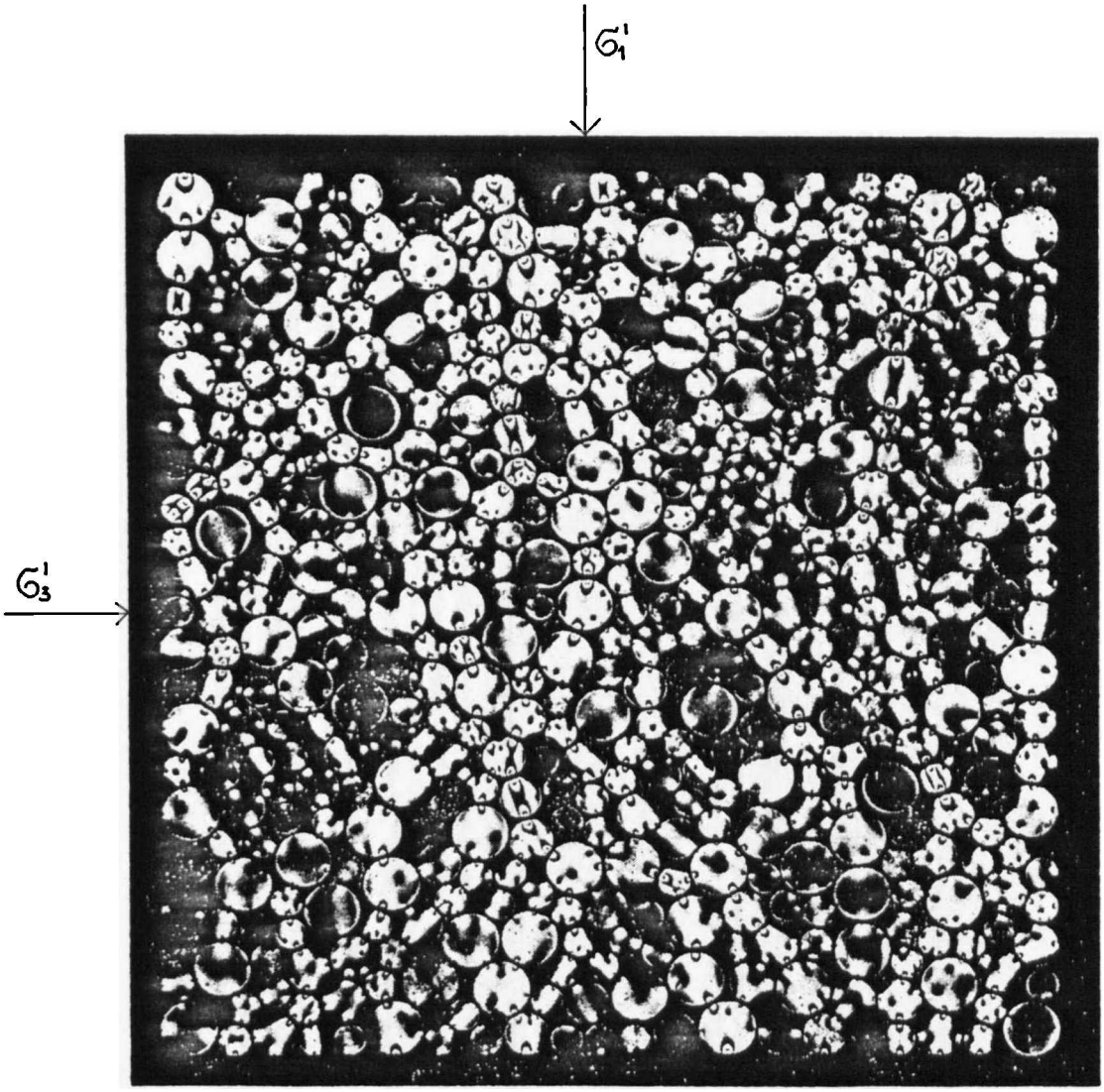


Fig.2.47 - Photoelastic test to show the construction of columns in a granular assembly (Oda & Konishi, 1974)

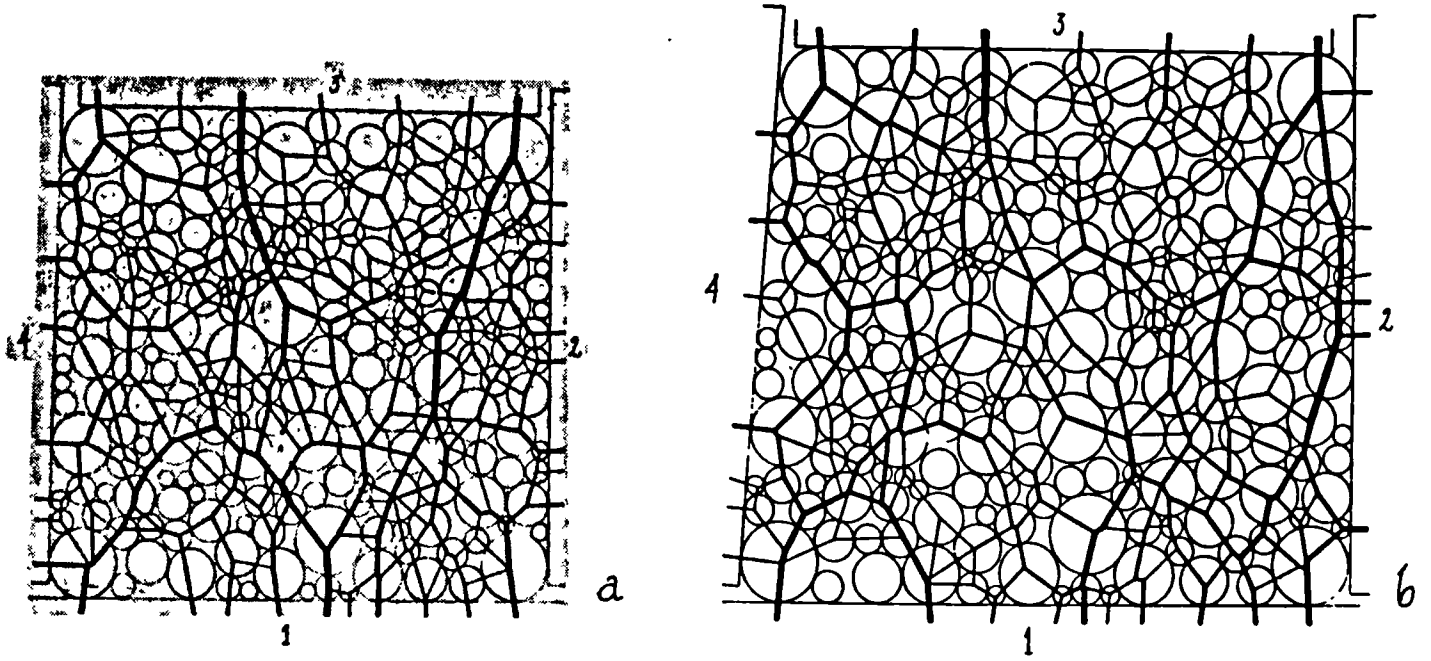


Fig.2.48 - Force vectors in a test on photoelastic discs: a) $F_H/F_V=0.39$;
b) $F_H/F_V=0.33$ (de Jong & Verruijt, 1969)

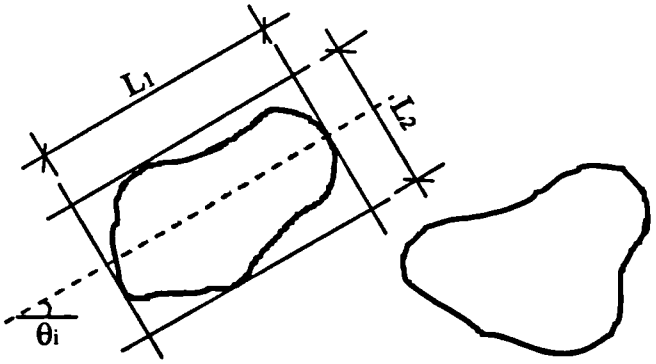


Fig.2.49 - Measurement of particle size and orientation (Oda, 1972a)

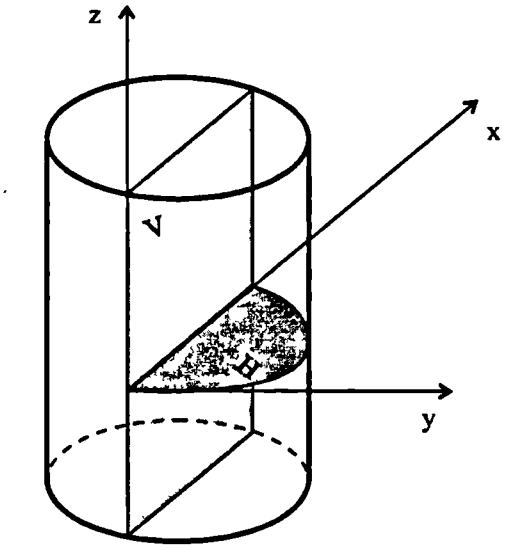


Fig.2.50 - Vertical and horizontal thin sections cut from triaxial samples (Oda, 1972a)

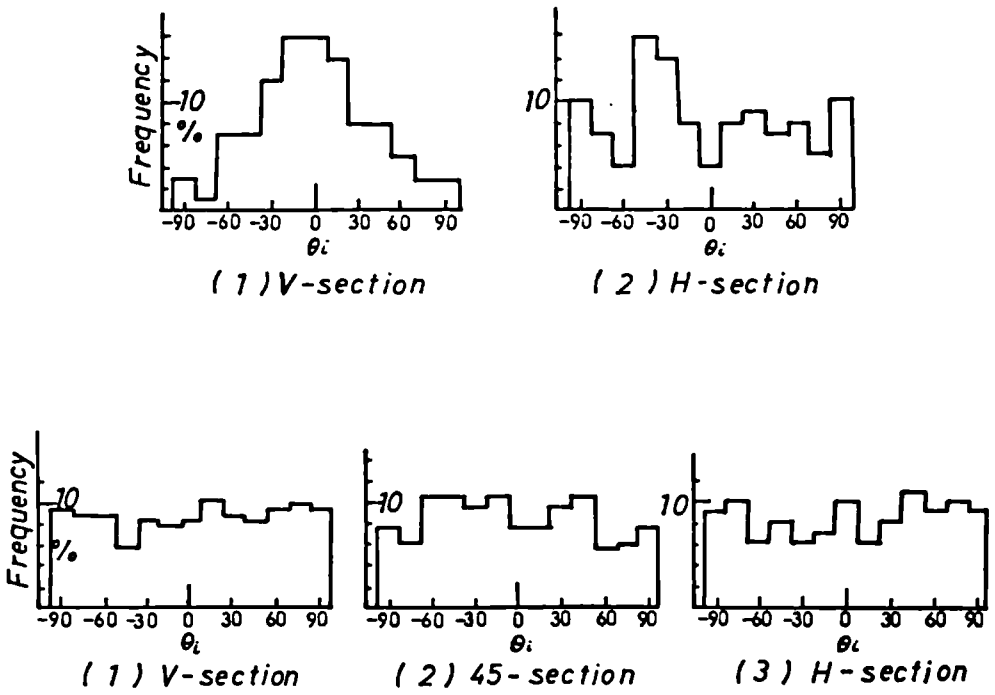


Fig.2.51 - Frequency histograms of θ_i in various sections of a) Sand B and b) Sand D (Oda, 1972a)

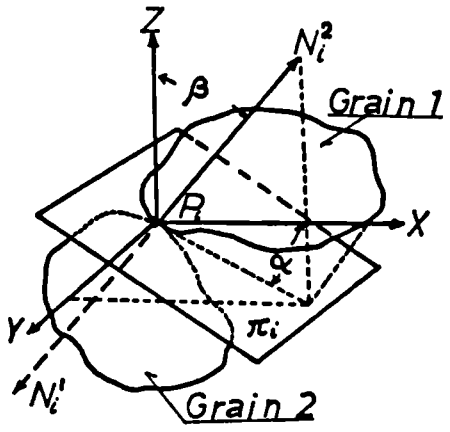


Fig.2.52 - Measurement normals to planes tangential to particle contacts (Oda, 1972a)

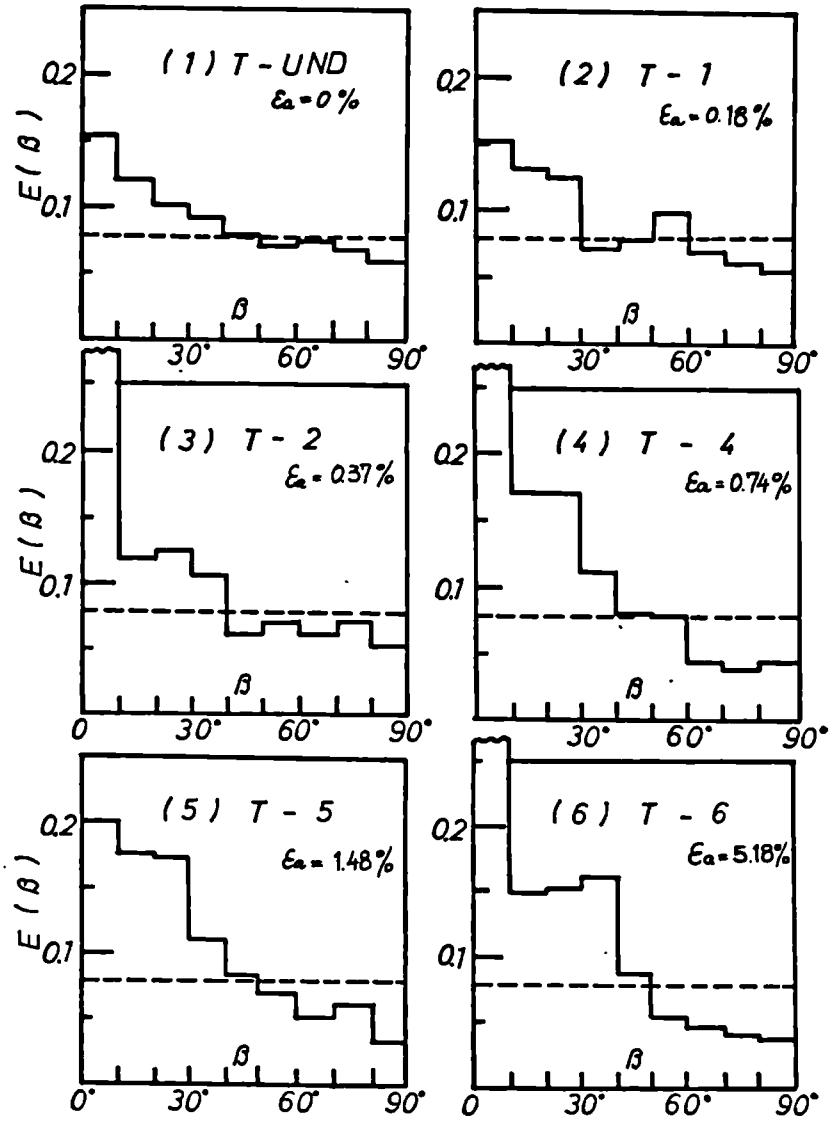


Fig.2.53 - Orientation of normals to particle contacts during progression of triaxial compression test (Oda, 1972b)

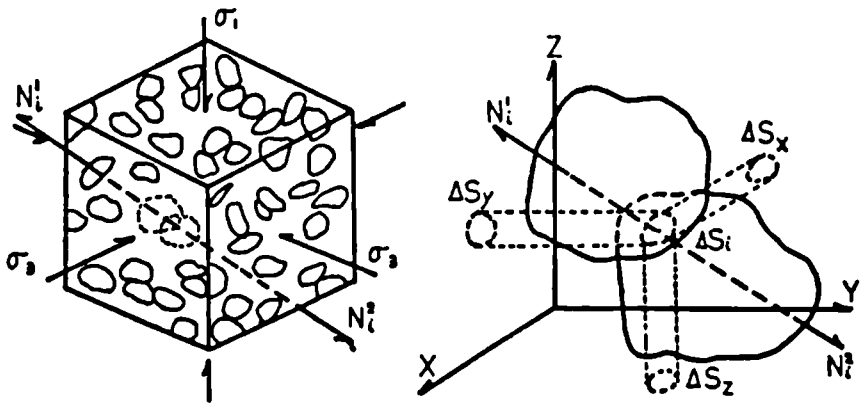


Fig.2.54 - Determination of fabric index, S_z/S_x, for sand (Oda, 1972b)

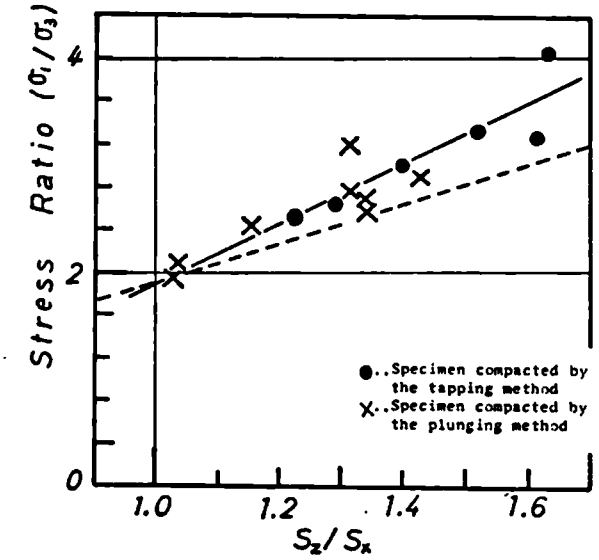


Fig.2.55 - Relation between mobilized stress ratio σ_1/σ_3 and fabric index S_z/S_x (Oda, 1972b)

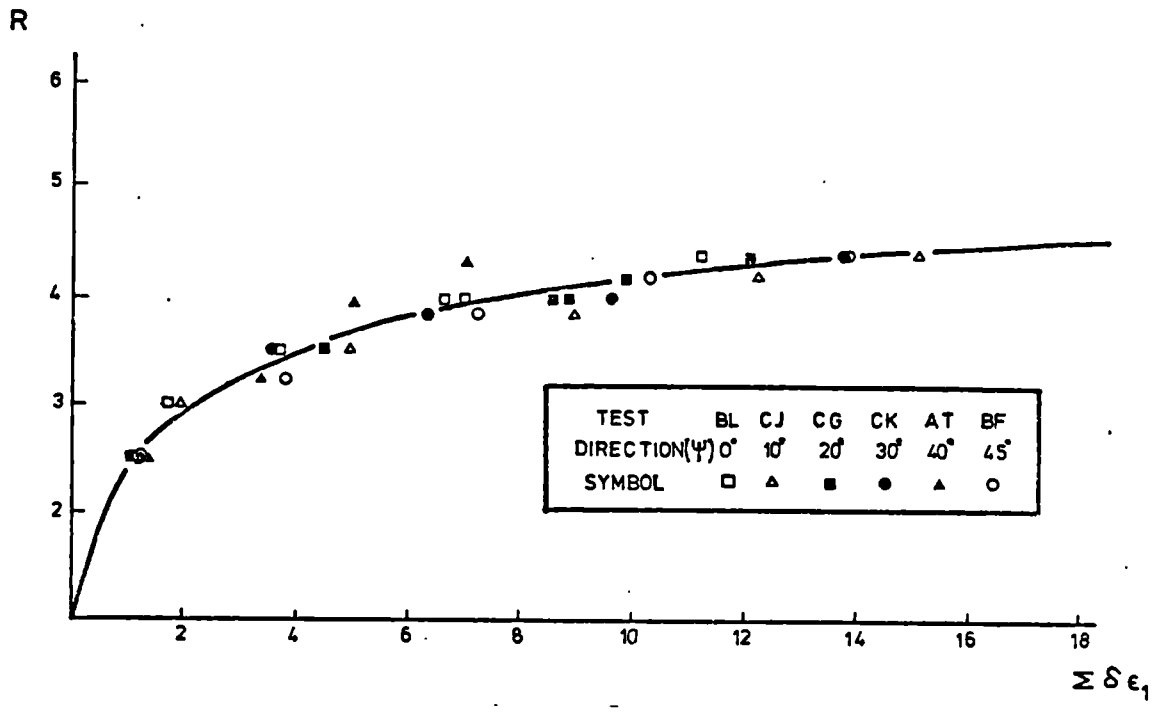


Fig.2.56 - Monotonic loading of isotropic plane with different but constant value of α (Rodriguez, 1977)

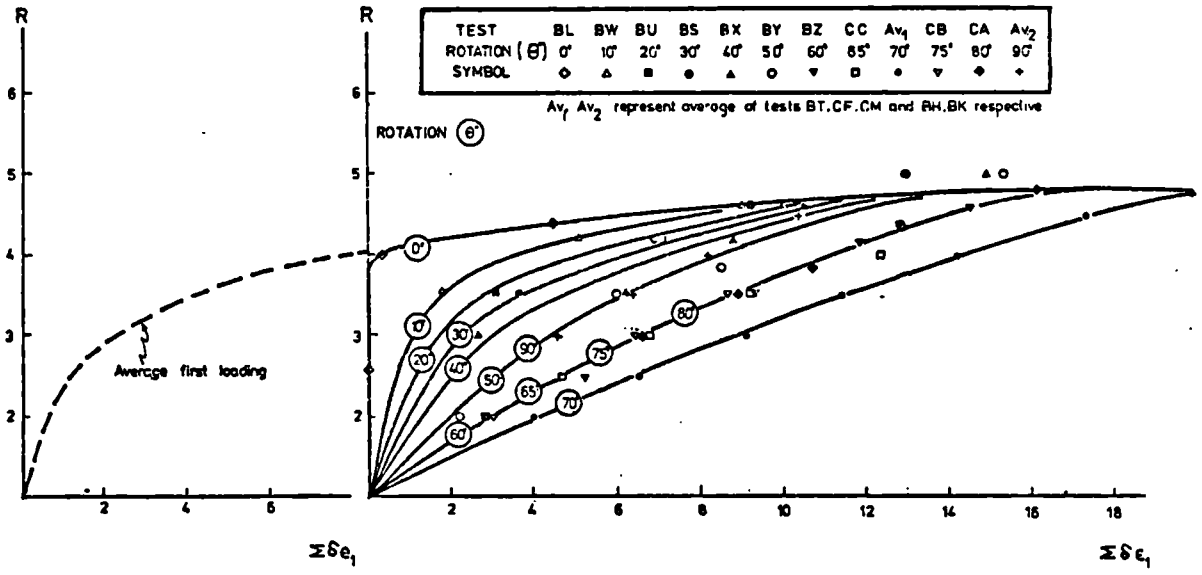


Fig.2.57 - First loading of isotropic plane with α=0° and second loading with α=0° to 90° (Rodriguez, 1977)

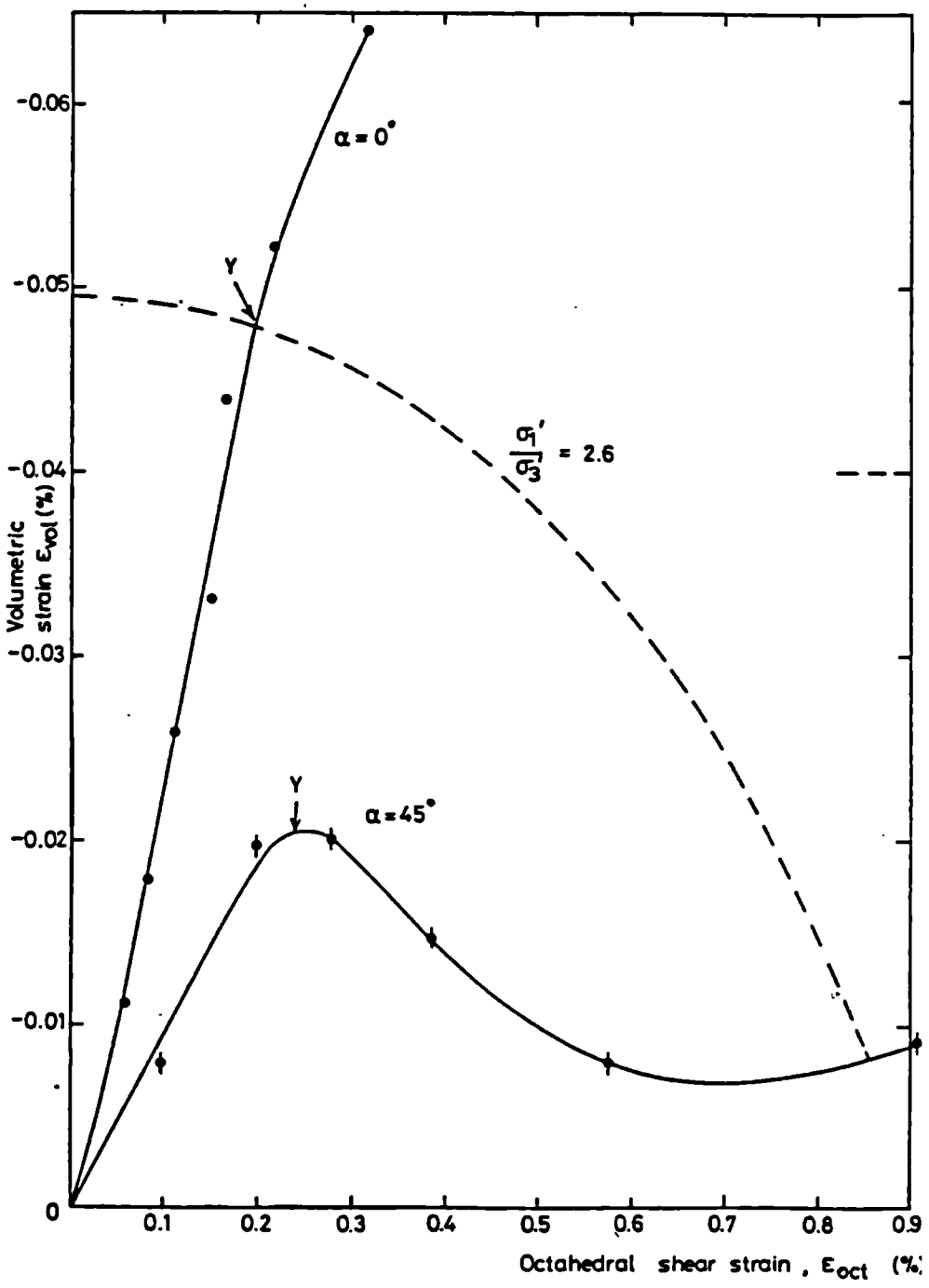


Fig.2.58 - Influence of the first loading cycle with α=0°, on subsequent yielding when α=0° and α=45° (Symes, 1983)

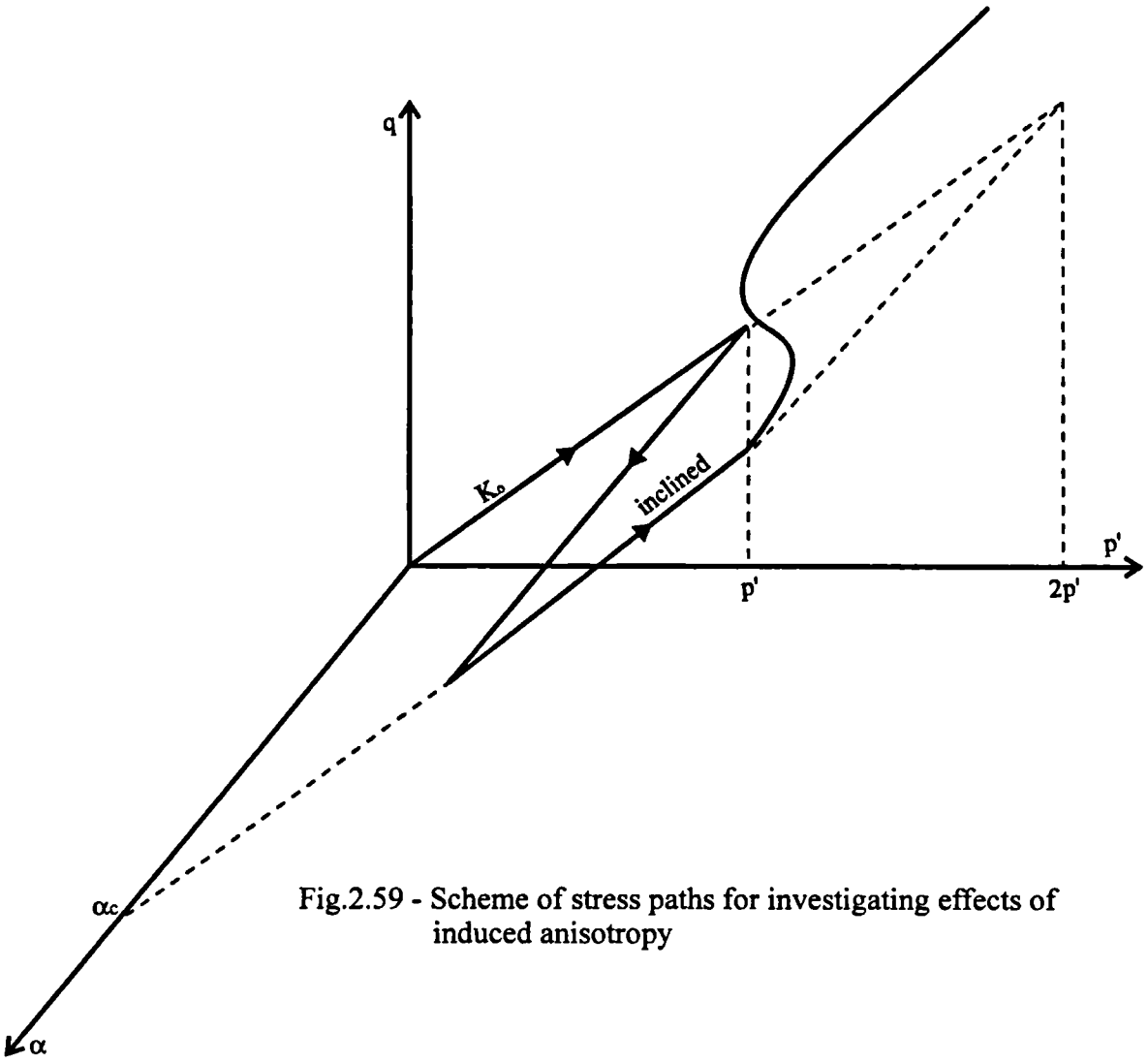


Fig.2.59 - Scheme of stress paths for investigating effects of induced anisotropy

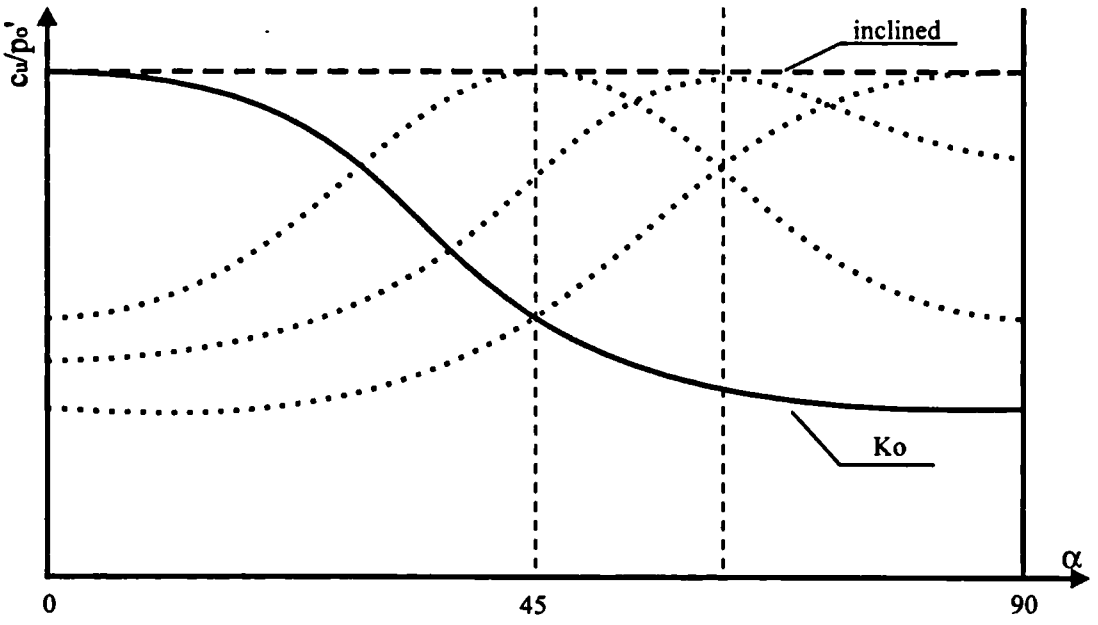


Fig.2.60 - Probable responses of induced anisotropy

Chapter 3

TEST EQUIPMENT, MATERIALS AND PROCEDURES

3.1. Introduction

To meet the objectives of the current research programme, experiments have been performed using both a Bishop & Wesley (1975) triaxial stress path cell and the large Imperial College Hollow Cylinder Apparatus (HCA).

The soil tested was an artificial (i.e. man made) quartz based silt called HPF4. This was chosen because of its similarities with certain sea bed sediments. It also adds to the data bank of materials tested at Imperial College, filling the gap between the clay and sand materials previously tested.

At the start of the present research, the only data that existed for HPF4 silt was a limited set of undrained triaxial stress path tests on loose samples (e_0=0.95), performed by Ovando-Shelley (1986). These tests were performed in order to check the framework postulated for his main research on Ham River Sand (HRS). Everton (1991) performed some shear box tests on different granular materials, including HPF4, as a part of a study of frictional shearing resistance between non-cohesive soils and construction materials. Parathiras (1994) also tested HPF4 in the ring shear apparatus. The mobilized friction angles, obtained in ring shear and triaxial tests, are summarized in Table 3.1. The ring shear results are residual strengths obtained after, on average, 80 cm of shear displacement, which remained unchanged for the total shear displacement of ~150 cm. The triaxial compression and extension results are ultimate values measured after ~5% axial strain. Also shown are the normal effective stresses (σ_n'), at which ring shear tests were performed, and the mean effective stresses (p_0'), to which triaxial samples were K_0 consolidated. HPF4 was also used as a constituent material in the research on silty sand (Hellings, 1988) and sand-silt-clay mixtures (Rossato, 1992; Menkiti, 1995).

The data in Table 3.1 shows an extreme range of ultimate ϕ' values: from ~50° to ~25°. This spread of results suggests either strong anisotropy or/and high sensitivity to *b* changes (ring shear tests impose plane strain conditions where b>0 and α=0°, while in triaxial compression b=0, α=0°, and in triaxial extension b=1, α=90°).

Table 3.1: Mobilized friction angles of HPF4, seen in previous studies

apparatus	RING SHEAR									TRIAXIAL	
type	NC non submerged			NC submerged			OC submerged			com	ext
σ_v' or p_c'	50	100	300	50	100	200	50	100	250	200	200
ϕ'	44.4	44.4	45.2	49.2	47.2	47.2	49.5	45.8	47.7	33.2	24.6

The triaxial stress path tests performed in this study were incorporated into the main testing programme in order to obtain basic information about the behaviour and stress-strain-strength parameters of HPF4 and, in particular, how they varied with OCR. It was necessary to have such information before more complex HCA testing was carried out.

3.2. Materials tested

HPF4

The principal material used in this study was an artificial High Pure Silica silt, commercially marketed by "Minerals Ltd." as HPF4. It is produced by crushing quartz stone and its mineralogical content is 100% quartz. The Author found the silt to have the following classification characteristics:

a) A grain size distribution curve which covers the whole range of silt-size particles (Fig.3.1), plus about 30% of the fine sand grain size.

b) A specific gravity of 2.65, the same as for HRS.

c) A liquid limit of 27% (from cone penetrometer tests), and a plastic limit close to zero (non-plastic).

d) The maximum and minimum void ratios estimated by the Kolbuszewski (1948) method are 1.332 and 0.563.

The maximum void ratio, e_{max} (i.e. the loosest packing), was obtained by the following procedure: 1000 g of HPF4 was placed in a 2000 cc cylinder (76 mm diameter) with the stopper at the end. The cylinder is tipped upside down and then quickly tilted back to its original position; the volume of the particle arrangement after sedimentation is measured and e_{max} calculated to be 1.332. A peculiarity of HPF4 is its compressibility which causes the material column in the cylinder to creep gradually from e=1.764, immediately after placing it on the pedestal, to e=1.332 when it stabilizes (after 1 hour).

The minimum void ratio, e_{min}, was estimated by hand tamping and vibrating the material in a glass cylinder: HPF4 was tamped dry in 100 cc layers by hand (100 times per layer) and vibrated by hand (10 times per layer). The volume of the final material column was measured and e_{min} calculated to be 0.563.

f) The grain shapes correspond to a roundness range 0.0 to 0.2 and sphericity range 0.45 to 0.8 (Appendix III). The roundness of a particle is a measure of the curvature of its edges and corners and is expressed as the ratio of the radius of the curvature of the corners to the radius of the inscribed circle on a particle's projection. Sphericity is defined as the ratio of the volume of a particle to the volume of its circumscribing sphere.

Roundness is most conveniently defined by Krumbein's projection method: The projection of the particle is compared with standard images of known roundness (see Chart III.1; after Krumbein, 1941).

Sphericity is defined by Rittenhouse's projection method where again projections of grains are compared with standard images of known sphericity (see Chart III.2; after Rittenhouse, 1944).

By inspection of ~50 grains from thin sections (Appendix III, Plates III.1, III.2), it is estimated that the average roundness of HPF4 is 0.11 and average sphericity 0.625. These numbers characterize HPF4 as both highly angular and elongated. This is not surprising as it is obtained by crushing quartz stone. Ham River Sand, for example, with grain size and shape as in Plate III.3, was characterized as subrounded and subspherical with 0.4 roundness and 0.772 sphericity (Kolbuszewski, 1948).

HRS

The second material tested in this research programme was Ham River Sand (HRS). This material has been extensively tested at Imperial College. It was used at the beginning of the current research programme to:

a) test the new control system for the HCA (Section 3.4.4) by repeating tests from some of the previous research on HRS in the HCA (Symes, 1983; Shibuya, 1985).

b) check how the test equipment influences the HRS strength characteristics. This was achieved by comparing results from triaxial tests performed in the stress path cell and triaxial tests simulated in the HCA.

The characteristics of HRS have been reported elsewhere (Skinner, 1975; Symes, 1983; Shibuya, 1985; Ovando-Shelley, 1986; Georgiannou, 1988; Porovic, 1995).

3.3. Triaxial stress path cell

3.3.1. Apparatus

The Bishop & Wesley (1975) stress path cell has become a standard piece of laboratory equipment and the apparatus used currently at Imperial College is described in detail by Smith (1992) and others. Consequently, only a brief summary of the main features of the apparatus and instrumentation will be given here.

A cross-section drawn through the apparatus used for 76x38 mm samples is presented in Fig.3.2 (Bishop & Wesley, 1975). The pedestal for the sample is mounted on top of a loading ram. This in turn is connected to a piston and pressure chamber. Vertical load is applied by moving the sample pedestal upwards or downwards from below. The reaction at the top of the sample is provided by an upper (stationary) load cell. Downward stretching of a sample (i.e. extension) is realised by means of a suction cap which bridges the physical gap between the load cell and the sample's top cap.

The water pressures within the perspex test chamber (cell pressure), loading ram and back pressure lines are controlled by air-valves acting through air water interfaces. By varying these pressures any desired triaxial stress path can be easily applied to a sample. During shearing tests to failure, the ram pressure is controlled by a constant rate of displacement pump, enabling shearing stages to be performed with a controlled rate of strain.

Because HPF4 is a granular material, a venturi suction system was attached to the apparatus for the application of a small effective stress during the sample setting up procedure.

3.3.2. Instrumentation

An Imperial College immersible load cell was used for measuring the deviator force. This had a capacity of 4.5 kN and its output was insensitive to changes in cell pressure.

Standard "Bell and Howell" pressure transducers, with a capacity of ~1.0 MPa, were used to measure the water pressures in the cell, loading ram and back pressure lines. As HPF4 samples gave an immediate equalisation of pore pressure when tested undrained, a mid-height pore pressure transducer (Hight, 1983) was not required.

Soil strains were measured by three means. Firstly, a standard displacement transducer, with a maximum travel of 25 mm, was mounted on a crosshead to provide external axial strain measurement. Secondly, an Imperial College volume gauge, with ~50 cc capacity, was used to measure water flow in and out of the samples, i.e. volume strain. Thirdly, two pendulum local axial strain devices, with a resolution of 0.002% strain, were mounted on each sample (Ackerley et al., 1987). The interpretation of raw stress-strain data obtained from these gauges is demonstrated in Appendix III.

The equipment was controlled via a computer system developed by Toll (1988). All data was recorded and stored on the computer's hard disk before being transferred to floppy disks for subsequent reduction and processing.

3.4. Hollow Cylinder Apparatus

3.4.1. Load application and control equations

3.4.1.1. Load application

The layout of the large Imperial College Hollow Cylinder Apparatus is given in Fig.3.3 (Shibuya, 1985). It is described in detail by Hight et al. (1983), Symes (1983), Shibuya (1985) and Menkiti (1995). Consequently only a brief description will be given here.

The dimensions of the HCA sample are 200 mm inner diameter, 254 mm outer diameter and 254 mm height.

The apparatus' design allows four load components to be independently applied and controlled (Fig.3.4). These are the inner and outer cell pressures (p_i and p_o respectively), axial load (W) and torque (M_T). Cell pressures are applied through flexible latex membranes, while axial load and torque are applied via rough, rigid top platen. As with the triaxial system, air-water interfaces convert air pressure into hydraulic pressure, which is then applied onto the sample.

Unlike the triaxial system, a rigid connection is made between the sample's top cap and load cell. Both axial and torque load applications are controlled by means of pairs of pneumatic pistons: any difference in pressure between the upper and lower chambers of the two axial pistons (P1 and P2 in Fig.3.3) moves the load cell up and down (causing the sample to extend

or compress), while pressure differences between the two torque pistons (P3 and P4, Fig.3.3) rotate the sample's top.

If the inner and outer cell pressures are different, then the stresses and strains induced in the sample will vary across the sample thickness. As with all the previous work performed using this apparatus, average values of the stresses and strains are used to interpret the test results. These are defined below.

3.4.1.2. Stress calculation

The stress components acting on the HCA specimens are calculated as the average values resulting from the pressures and forces applied at the boundaries (Hight et al.,1983). This gives:

Average axial stress, σ_z:

$$\sigma_z = \frac{W}{\pi(r_o^2 - r_i^2)} + \frac{p_o r_o^2 - p_i r_i^2}{r_o^2 - r_i^2} \tag{3.1}$$

Average radial stress, σ_r:

$$\sigma_r = \frac{p_o r_o + p_i r_i}{r_o + r_i} \tag{3.2}$$

Average circumferential stress, σ_θ:

$$\sigma_\theta = \frac{p_o r_o - p_i r_i}{r_o - r_i} \tag{3.3}$$

Average shear stress, $\tau_{\theta z}$:

$$\tau_{\theta z} = \frac{3M_T}{2\pi(r_o^3 - r_i^3)} \tag{3.4}$$

where r_i and r_o are the current inner and outer radii of the sample, respectively. The principal stresses are then calculated as:

$$\sigma_1 = \frac{\sigma_z + \sigma_\theta}{2} + \sqrt{\left(\frac{\sigma_z - \sigma_\theta}{2}\right)^2 + \tau_{\theta z}^2} \tag{3.5}$$

$$\sigma_2 = \sigma_r \tag{3.6}$$

$$\sigma_3 = \frac{\sigma_z + \sigma_\theta}{2} - \sqrt{(\frac{\sigma_z - \sigma_\theta}{2})^2 + \tau_{\theta z}^2} \tag{3.7}$$

According to the standard soil mechanics convention, compressive stresses are considered positive.

3.4.1.3. Strain calculation

The average strain components are calculated from the boundary deformations. This gives:

The average axial strain, ε_z:

$$\varepsilon_z = \frac{w}{l_o} \tag{3.8}$$

where w is the axial deformation of the initial local reference length, l_o, determined by the measuring device.

The average radial strain, ε_r:

$$\varepsilon_r = - \frac{u_o - u_i}{r_{oz} - r_{iz}} \tag{3.9}$$

where u_o and u_i are outer and inner wall displacements respectively, and r_{oz} and r_{iz} are the initial outer and inner radii, respectively.

The average circumferential strain, ε_θ:

$$\varepsilon_\theta = - \frac{u_o + u_i}{r_{oz} + r_{iz}} \tag{3.10}$$

The average shear strain, $\gamma_{\theta z}$:

$$\gamma_{\theta z} = \frac{2\theta(r_o^3 - r_i^3)}{3H_o(r_o^2 - r_i^2)} \tag{3.11}$$

where θ is the circumferential angular displacement and H_o is the initial sample height.

The corresponding principal strains are:

$$\varepsilon_1 = \frac{\varepsilon_z + \varepsilon_\theta}{2} + \sqrt{\left(\frac{\varepsilon_z - \varepsilon_\theta}{2}\right)^2 + \left(\frac{\gamma_{\theta z}}{2}\right)^2} \tag{3.12}$$

$$\varepsilon_2 = \varepsilon_r \tag{3.13}$$

$$\varepsilon_3 = \frac{\varepsilon_z + \varepsilon_\theta}{2} - \sqrt{\left(\frac{\varepsilon_z - \varepsilon_\theta}{2}\right)^2 + \left(\frac{\gamma_{\theta z}}{2}\right)^2} \tag{3.14}$$

3.4.2. Instrumentation

The load cell, which measures both axial load and torque, is an advanced form of the Imperial College load cell, originally developed for use in triaxial apparatus. It is located inside the cell (i.e. under water) and is oil-filled, water proofed and pressure compensated. Because of its double action (i.e. it applies both axial load and torque), there is a small cross-sensitivity between axial and torque action (typically 0.06% to 0.75% for the effect of the axial load on the torque output and 0.5% to 1.47% for the effect of the torque on the axial load output). The HCA load cell is calibrated by applying combinations of axial load and torque, as shown in Fig.3.5, and the best fit matrix of calibration coefficients includes some minor off-diagonal terms. The axial capacity of the load cell in compression is 9.0 kN, and in extension 7.5 kN. The torque capacity is 0.8 kNm.

The inner and outer cell pressures, back pressure and pore pressure (at the base of the sample) are measured by a set of standard pressure transducers, the capacity of which is about 1.0 MPa.

A volume gauge of 100 cc capacity is used to measure the volume of pore fluid leaving and entering the sample.

A range of local displacement transducers are mounted on, or near to, the sample's inner and outer wall surfaces. The radial displacements are measured using encapsulated Kaman proximity transducers. A proximity transducer is a non-contacting displacement transducer which operates on the principle of impedance variation. The sensor induces an eddy current in a remote metal foil target attached to the sample wall, which in turn interacts with a coil within the sensor. The output is a function of the gap between target and sensor. Two sets of proximity

transducers are employed: 3 outer and 3 inner devices, in the arrangement shown on Fig.3.6. The range of wall movement is 6 mm.

Axial and torsional shear deformations are measured locally by means of electrolytic tilt transducers. These devices were first developed at Imperial College for use in the HCA by Burland and Symes, (1982), and their design was modified subsequently by Shibuya (1985). The heart of the device is a glass capsule, half filled with an iodine based electrolyte, and containing a set of three electrodes (Fig.3.7). When the sensor is at its zero position, the electrical resistance of the fluid from the central electrode to each outside electrode is equal. Tilting the sensor disturbs this balanced condition and the resistance changes, in proportion to the angle of tilt. Such devices can be either of the single axis type (with one set of electrodes), measuring only torsional shear displacement, or the double axis variety (with two orthogonal sets of electrodes), which measure both axial and torsional displacement.

Fig.3.8 shows the general construction and modes of deformation of the double-axis devices employed on the HCA. The transducer consists of two glass capsules encased in stainless steel protective cylinders. The two cylinders have a joint connection, with only one degree of freedom for axial strain measurement. In the twisting mode of deformation the transducer behaves as a rigid body. Transducers which measure only torsional shear displacement consist of only one single axis capsule incased in a stainless steel cylinder, Fig.3.9.

Problems experienced previously with these electrolytic devices included a large scatter and random "spikes" in the devices' output voltage. In the present study it was intended to explore the soils' small strain properties as accurately as possible, and such problems had to be rectified. To meet this aim, a complete redesign of the system's electrical connections was carried out (see Appendix III), along with the implementation of a new computer control and data logging system, described in the next section. This increased the resolution of the devices from ~0.01% strain (Menkiti, 1995), to ~0.001% strain.

Both the proximity and electrolevel local strain sensors are mounted on the central part of the sample as far away as possible from the top and bottom platens where certain restraints occur. Displacement transducers are also mounted outside the cell, on the loading frame, to record the external overall measurements of axial and torsional shear strain.

Table 3.2 summarizes the ranges, stability and accuracy of the HCA transducers. Standard calibration techniques, developed at Imperial College during last 30 years, have been used for all transducers. All calibrations and tests were performed in the IC Research Laboratory,

which is temperature controlled to 20°±2°. Symes (1983), Hight (1983), Shibuya (1985) and Menkiti (1995) all give comprehensive descriptions of the instrumentation calibration for the IC HCA. Consequently, this section will not consider calibration of instrumentation.

Table 3.2: Summary of ranges, accuracy and stability of transducers employed in the HCA

TRANSDUCER TYPE	RANGE	ACCURACY*	STABILITY**
External Displacement	0 to 25 mm	0.01 mm	±0.002 mm
Volume Gauge	0 to 100 cc	0.03 cc	±0.015 cc
Load Cell	-7.0 to 9.0 kN -0.8 to 0.8 kNm	0.04 kN 0.004 kNm	±0.006 kN $\pm 3.2 \times 10^{-4}$ kNm
Proximity transducer	0 to 6.0 mm	0.008 mm	0.001 mm
Electrolevel	-30° to 30° -15 to 15 mm	0.02% ($\gamma_{\theta z}$) 0.02% (ε_z)	0.001% ($\gamma_{\theta z}$) 0.001% (ε_z)
Pressure transducer	0 to 1000 kPa	0.3 kPa	0.1 kPa

* Accuracy is based on the mean deviation from regression line obtained during calibration.

** Stability is based on the scatter observed over a period of 24 hours in the atmosphere, prior to calibration

3.4.3. Stress and strain non-uniformities in the HCA

The question of stress and strain non-uniformities in the Imperial College HCA has been addressed in the past by many researchers: Hight et al. (1983), Hight (1983), Symes (1983), Gens & Potts (1984) and Menkiti (1995). Contributions have also been made by Vaid et al. (1990) and Sayao & Vaid (1991), who have analyzed their hollow cylinder device (University of British Columbia, Vancouver), which has different dimensions to that of the Imperial College apparatus. Porovic (1995) also presented analyses of the smaller hollow cylinder device used at IC. A summary of the results from these investigations is presented below.

In the design of the IC HCA, Hight et al. (1983) considered three sources of sample non-uniformities when choosing the final dimensions of the sample. These are:

a) Due to the curvature of the specimen wall when different inner and

outer cell pressures are applied.

b) Due to the manner in which the torque is applied to the sample. Because of the rigid nature of the top cap, a constant angular rotation is applied to the top of the sample. This results in a linear variation of the applied shear strain, $\gamma_{z\theta}$, across the wall of the sample.

c) Due to the friction between the top and bottom platens and the soil sample. This restricts any radial movement of the top and bottom of the sample.

When evaluating these non-uniformities they defined three parameters that should be considered (Fig.3.10):

- The real distribution of stresses across the sample wall, $\sigma(r)$;
- The average value of the real distribution, named as a "real average", $\bar{\sigma}^*$;
- The calculated average stress from Eq.3.1 to 3.4, $\bar{\sigma}$.

To quantify the level of non-uniformity of stresses, the parameter:

$$\beta_3 = \frac{\int_{r_i}^{r_o} |\sigma(r) - \bar{\sigma}^*| \, dr}{(r_o - r_i)\sigma_L}$$

was defined, where σ_L is the normalising stress level, taken in general as $(|\sigma_r|+|\sigma_\theta|+|\sigma_z|)/3$, and r_o and r_i are the outer and inner sample radius, respectively.

To show the accuracy of the interpreted data another parameter, β_1, was defined as follows:

$$\beta_1 = \frac{|\bar{\sigma}^* - \bar{\sigma}|}{\sigma_L}$$

i.e. the difference between the "real" average and the interpreted (calculated) average normalised by σ_L.

The parameters β_1 and β_3 have been examined theoretically, assuming that the hollow cylinder sample was either isotropic linear elastic or behaved according to the Modified Cam

Clay model (MCC). Various stress paths were investigated but only non-uniformities due to (a) and (b) above were simulated. Small differences were obtained from these two sets of analyses and based on the results the final dimensions for the sample were selected such that $r_i/r_o=0.8$, while a restriction was imposed on the ratio p_o/p_i (the ratio of outer and inner cell pressure) such that $0.9<p_o/p_i<1.2$. For the dimensions of the IC HCA this implies that $\beta_3<11\%$ is acceptable. They defined two "no-go" areas in terms of stress space, where samples would experience excessive non-uniformities because of the large difference in inner and outer cell pressure. These areas are centred around $\alpha=0°$, b=1.0 and $\alpha=90°$, b=0.0 (Fig.3.11).

Further analyses in which stress non-uniformities due to (a) and (c) above were investigated (Hight et al., 1983) were also carried out using both elastic and the MCC model. A test was simulated in which the inner and outer cell pressures were maintained constant at 350 and 400 kPa, respectively, while the axial stress was increased from its initial value of 400 kPa to failure. Torque was omitted so that axisymmetric conditions were maintained and therefore the complexity of the analysis reduced (this implies that non-uniformities due to (b) above were absent). The analysis showed that the distribution of σ_r is not significantly affected by end restraint, so only plots of contours of σ_z and σ_θ are presented at $q=2/3(q_f)$ and $q=q_f$ (Fig.3.12). Both linear elastic and Modified Cam clay (elasto-plastic) analyses, showed that the central part of the specimen (with IC HCA dimensions) has a reasonably uniform stress distribution at $q=2/3(q_f)$. The stress distributions are less uniform at failure when $q=q_f$, especially for the analysis using Modified Cam clay. At first sight it may seem surprising that the elastic analysis shows changes in the uniformity of stresses with loading. This arises because the plots are in terms of accumulated stresses and therefore are a combination of the uniform initial stress conditions (any effects of non-uniformities ignored) and those due to shearing (which simulated the effects of non-uniformities (a) and (c)).

More recently, Vaid et al. (1990) and Sayao & Vaid (1991) re-examined the stress distributions in a hollow cylinder specimen, as part of the design of a new HCA for the University of British Columbia, Vancouver. They used an isotropic elastic soil model and suggested that the contribution of all stress components to sample non-uniformities should be considered together and therefore, the non-uniformities should be evaluated in terms of principal stresses. They proposed a new coefficient of non-uniformity, β_R, defined as:

$$\beta_R = \frac{R_{max} - R_{min}}{R_{ave}}$$

where R_{max}, R_{min} and R_{ave} are the maximum, minimum and average stress ratios (Fig.3.13). They

concluded that β_R<20% was an acceptable level for stress non-uniformities and this led them to define a new "no-go" zone around the α=45° line in b-α space (Fig.3.11). However, they also admitted that they would anticipate different results if more realistic soil models were used to represent the sample. They confirmed this in subsequent paper by Wijewickreme & Vaid (1991), using incremental elastic hyperbolic soil model proposed by Duncan & Chang (1970).

Gens & Potts (1984) developed a quasi-axisymmetric finite element formulation for the use of a 2D finite element mesh for the analysis of some three dimensional problems in which the geometry is axisymmetric, but the loads and displacements are not truly axisymmetric in the conventional sense. Such an approach enables non uniformities due to (a) and (b) above, but not those due to (c), to be considered. Analyses with non associated and associated plastic soil models were considered for a HCA stress path in which $p_i=p_o$=const (no non-uniformities due to the samples curvature), $\varepsilon_z=0$ and undrained torsional shear was applied. Their results are presented in Fig.3.14, showing that for associated plasticity a high degree of stress uniformity exists and the usual assumption that $\sigma_r=\sigma_\theta$ when $p_i=p_o$ is valid. For non-associated plasticity, non-uniformity increases in the sample and the assumption that $\sigma_r=\sigma_\theta$ is no longer valid when $p_i=p_o$.

All the above studies give an insight into the distribution of stresses across the wall of the sample for different geometries of the hollow cylinder sample. However, they do not consider the influence of the non-uniformities on engineering properties that result from hollow cylinder testing, i.e. the global effect on the interpreted stress-strain and stiffness response.

Menkiti (1995) considered this question first, by using finite element analyses. He adopted the same elasto-plastic soil model and testing conditions as Gens & Potts (1984). Consequently, he ignored any non-uniformities due to (c) above, assuming that these are negligible for the geometry of the IC HCA. To perform the hollow cylinder analysis the finite element mesh shown in Fig.3.15 was used. In addition an analysis was performed using a single finite element to which the same stress path was applied. As such an element behaves uniformly, the results provide the "true" response of the soil model to the applied stress path, which can then be compared with the results from the hollow cylinder analyses. Figs.3.16 and 3.17 present the stress paths and stress-strain curves from these analyses. The curves with solid circles and marked "uniform conditions" are the results from the single element analysis and therefore represent the "true" behaviour. The following points are noted:

- The open circles represent calculated "average" values from loads and displacements

applied at the boundaries of the hollow cylinder analyses (calculated from Eqs.3.1 to 3.14). Both the stress-strain and stress path response show good agreement with the "true" behaviour.

- The curves marked with crosses represent the real averages, calculated by averaging the shear stress and shear strain distributions across the sample wall from the hollow cylinder analyses. These curves represent the response that could be derived from a hollow cylinder test, if the stress distribution within the specimen could be measured during the test. Again the curves show good agreement with the "true" behaviour.

Both plots show a very good agreement of all three paths, indicating a negligible influence of stress non-uniformities. It also indicates that the equations 3.1 to 3.14 are sufficiently accurate for interpreting hollow cylinder tests.

Menkiti also compared the secant octahedral shear stiffness response for the different analyses (Fig.3.18). The shear stiffness, G_{sec}, variation with shear strain calculated from the real average $\gamma_{\theta z}$ and the real average $\tau_{\theta z}$, is shown as open squares. This is the response that could be obtained from the HCA if the stresses and strains within the specimen could be measured during the test. It plots very close to the "true" behaviour obtained from the uniform element analysis (solid circles). The remaining curves are derived from the calculated average $\gamma_{\theta z}$ and $\tau_{\theta z}$ (i.e. from boundary loads and displacements). If $\gamma_{\theta z}$ is taken in the middle of the sample, then the shear stiffness plots as the curve with open circles, which is again very close to the "true" behaviour. If $\gamma_{\theta z}$ is taken as the value on the outer wall (which is, actually, the quantity measured in the HCA tests), then the shear stiffness plots as crosses, giving ~10% underestimation of the "true" stiffness. Menkiti (1995) therefore concluded that the measured strains in the HCA represent deformation of the outer wall and they should be recalculated for the centre of the wall, by multiplying the measured values by the ratio of the average $((r_o+r_i)/2)$ to outer (r_o) radii. All the results presented in this thesis have been calculated in this manner. Also, from the engineering point of view, he concluded that the stress and strain non-uniformities in the IC HCA sample do not influence significantly the interpretation of the effective stress paths and stiffnesses of tested soils[1].

[1]- Porovic (1995) came to similar conclusions in similar study of small HCA.
- Further research with different soil models and 3D-analysis of HCA is under way by Author in collaboration with Prof. Potts.

3.4.4. Computer control and data acquisition system

3.4.4.1. Introduction

One of the main tasks at the beginning of this research programme was to introduce a new computer control and data acquisition system for the HCA. The old "System 35", which had been in use for over 15 years, was obsolete and unreliable. The new system involved a completely new combination of computer, data acquisition system and control programs. Appendix III.3 describes the general elements of electronic instrument systems, the conversion of signals and the transfer of data within the system. This Section will present some specific elements and characteristics of the new data acquisition and control system.

3.4.4.2. New Hollow Cylinder control system (i.e. hardware)

The layout of the new system is illustrated in Fig.3.19. The main parts of it are:

- a 486 PC computer with an Input/Output (I/O) card
- a data acquisition system, consisting of two analogue to digital (A/D) converters and two modulator/demodulator (M/D) boxes
- range of transducers
- a sample of HPF4

The system runs as a closed loop. The process starts when the computer operator sets the desired stress path. The program then reads all transducers, calculates the sample's current states of stress and strain and then calculates incrementally the stress targets which should be achieved to follow the desired stress path. The computer then drives the stepper motors which control the loading (through air-water interfaces) to achieve these targets. After a short interval, the computer re-reads all the transducers and up-dates the instructions sent to the stepper motors. The process continues as a closed loop until the final targets are met.

A) Datascan

Two Datascan 7220 series modules, manufactured by Measurement System Ltd., are employed for monitoring the HCA transducers. These are networked together and connected to the computer via an RS232 interface (Appendix III.3). Each of the Datascans consists of a 16-channel module so that the combined system can monitor 32 channels in total. It can be extended to provide up to 256 channels by networking 16 modules together.

Each module has its own analog-to-digital conversion unit (Appendix III.3) to convert measured analog voltage into digital code suitable for further processing. It is programmed for each channel to provide 16-bit resolution, with high noise rejection (Appendix III.3). The two modules are organized so that one supports DC (direct current) energised transducers, while the other supports AC (alternating current) energised transducers. The first group represents the strain gauged transducers (load cell, displacement and pressure transducers). The second group consists of the proximity and electrolytic transducers, both of which require a Modulator/Demodulator (M/D) box to develop the necessary AC energisation signals and transmit the AC return signals to an A/D convertor.

B) Modulator/Demodulator (M/D) box

An electrolytic transducer, whose working principle has already been described in Section 3.4.2, is a resistance potentiometer with a liquid resistance element. To avoid electrolytic erosion, it requires alternating current (AC) excitation. The electrolytic capsules used for the HCA transducers are a product of the FREDERICKS Company (USA) and their excitation voltage normally ranges from 0 to 12.5 VAC. The supply frequency may have a square, triangular or sine wave shape, with a range from 25 Hz to 20 kHz, with a standard value of 400±10 Hz.

A proximity transducer, on the other hand, is a sensor with one active coil driven at a very high frequency of 1 MHz, which generates a magnetic field between the sensor and a metal foil target (i.e. conducting material), Fig.3.20. The unit used in the HCA is produced by Kaman (USA). When magnetic flux lines from the sensor intersect with the surface of the conducting material, eddy currents are induced at the conducting surface, whose strength varies with the sensor-to-foil distance. The eddy currents generate a magnetic field of their own which, in turn, affects an inactive coil set in the sensor unit. The active and inactive coils are connected into an impedance bridge, whose output gives a direct measure of the sensor-to-target gap distance. While the induced eddy currents have high frequency, the Kaman transducers include signal conditioning circuits which produce an output signal with a typical frequency of 20 kHz.

When transferring such high frequency data further through the system, *modulation* of the signal is applied which is, basically, a form of data transmission that enables a transducer signal to be filtered from electrical noise. However, such signal is not suitable for display and interpretation and has to go through *demodulation* process. Such a conditioned output signal is still in an analog form and must pass through an A/D converter before any further digital

processing can be performed (Fig.3.19).

Both M/D boxes employed in the HCA control system (for electrolevels and proximity transducers) have separate data transmission cards for each of the sensors, i.e. 6 cards in the M/D box for the proximity transducers and 6 cards in the M/D box for the electrolevels.

The HCA control system has 4 double axes and two single axis electrolevel devices. A relay switch is mounted on each of the 4 double axes data transmission cards to enable sequential reading of both axial and torsional shear strains.

C) Computer with an I/O card

The 8255 I/O card is a programable input/output interface for IBM PC compatible computers. It has been installed for two purposes:
- to address and drive stepper motors for load application
- to operate relay switching in the electrolevel's M/D box.

This card has 48 programable I/O lines, housed in two 40-pin ports (note: only 24 pins in each port are actually used). Each port has three groups of programable pins: PA0 to PA7, PB0 to PB7 and PC0 to PC7, which can be addressed via 3 subports: 1A, 1B and 1C for the main PORT1, and 2A, 2B and 2C for the main PORT2, Fig.3.21. The address of each subport is also marked in Fig.3.21.

For the operation of each stepper motor a pair of pins is used; one for signalling that the motor must turn by a single pulse and the other for controlling the direction that the motor turns. As there are 4 stepper motors operating the HCA load application, pins PA0 and PA1 are used to drive the stepper motor for the inner cell pressure, PA2 and PA3 the outer cell pressure, PA4 and PA5 the torque application and PA6 and PA7 the axial load application.

The relay operation in the M/D box is linked to the 1C subport and uses PC0 and PC1 pins for its operation.

This makes a total of 5 lines from the I/O card to operating elements of the system (Fig.3.19).

3.4.4.3. Control program (i.e. software)

The control program which operates the HCA tests has been written by the Author in the QBASIC program language, developed for IBM PC compatible computers. The code is

~10000 lines big and is structured to cover all operations which are necessary for HCA testing (Fig.3.22), including:

- CALIBRATION procedures for all transducers
- MONITORING of all channels
- all activities during the SETTING UP procedure, such as monitoring and adjustment of initial positions for all transducers, taking sample dimensions, sample saturation, etc
- CONSOLIDATION as the first part of the applied stress path, which can involve either isotropic or anisotropic stress conditions
- SHEARING which, generally, consists of :
  - a *b-change* subroutine to vary the intermediate principal stress (σ_2). Different *b* values, from 0 to 1, can be applied at the end of the consolidation stage.
  - an *unloading* subroutine.
  - an *α-change* subroutine where the directions of the principal stresses can be rotated from 0° to 90°, at constant deviator stress level.
  - a subroutine with incremental deviator stress increasing under the constant rotation of the direction of principal stresses.
  - a subroutine where both α and *b* can change simultaneously.

Four control parameters are chosen to drive the desired stress path:

$$b = \frac{\sigma_2 - \sigma_3}{\sigma_1 - \sigma_3} \tag{3.15}$$

$$t = \frac{\sigma_1 - \sigma_3}{2} \tag{3.16}$$

$$p = \frac{1}{3}(\sigma_1 + \sigma_2 + \sigma_3) \tag{3.17}$$

$$\alpha = \arctan\left(\frac{2\tau_{\theta z}}{\sigma_z - \sigma_\theta}\right) \tag{3.18}$$

where α is the angle between the major principal stress axis and the vertical.
With these control parameters, target stresses are calculated as:

$$\sigma_z = p - t\left(\frac{2b-1}{3} - \cos 2\alpha\right) \tag{3.19}$$

$$\sigma_r = p - t[2(1-2b)/3] \tag{3.20}$$

$$\sigma_\theta = p - t\left(\frac{2b-1}{3} + \cos 2\alpha\right) \tag{3.21}$$

$$\tau_{\theta z} = t \sin 2\alpha \tag{3.22}$$

$$p_o = [\sigma_r(r_o + r_i) + \sigma_\theta(r_o - r_i)]\frac{1}{2r_o} \tag{3.23}$$

$$p_i = [\sigma_r(r_o + r_i) - \sigma_\theta(r_o - r_i)]\frac{1}{2r_i} \tag{3.24}$$

The algorithm for one increment of a stress path implementation is given on Fig.3.23. First of all, a leading control parameter is selected. For the *consolidation* and *shearing* stages of a test this is t, for a *b_change* stage it is b and for an *α_rotation* stage it is α. A small change to this lead parameter is then specified, namely 0.5 kPa, 0.05 or 0.1° for Δt, Δb or $\Delta\alpha$ respectively. The associated changes in the remaining three control parameters are then calculated so that the desired stress path is followed. These values are then translated into the required pressure changes that must be applied to the relevant air-water interfaces and pneumatic pistons and appropriate instructions sent to the stepper motors. The sample response is then read on the transducers and the new stresses and strains calculated. This data is then plotted on the computer screen and saved on the computer's hard disk. A time delay is imposed before the next load step. The process is repeated until the required stress path is completed.

The time delay that is imposed between the application of the load steps is used to ensure that the strain rate is suitable for a certain stage, i.e. consolidation, shearing, b_change or α_rotation. The values used were determined from calibration tests performed at the beginning of the current research programme.

In the program structure, two subroutines are crucial to the success of the control system. They communicate with the Datascan units and with the stepper motors and relays.

A) Subroutine for Communicating with the Datascan units

This subroutine is the first executable subroutine at the beginning of the program. It opens communication with the Datascan units, defines the communication protocol and initialises the channels for all transducers. It is not called again during a test.

To operate the Datascans, it is necessary to open the communication port COM1 of the computer, where the RS232 9-pin connection is plugged in. The line of code which does this, further defines baud rate, parity, data bits, stop bit, request to send signal, clearance to send, data set, data carrier, length of communication file (see Appendix III.3). The code line is of the form:

OPEN "COM1:9600,N,8,1,RS,CS0,DS0,CD0" FOR RANDOM AS #1 LEN=800

The data is sent in a frame with 1 start bit, 8 data bits and 1 stop bit (Appendix III.3). Therefore, the time to transmit each frame, for the baud rate of 9.6k, can be calculated as

$$t = 10 \times \frac{1}{\text{baud rate}}$$

and is equal 1.042 ms. While this is relatively slow it is acceptable for the current test program in which the shearing strain rate is approximately 5.0 %/day.

This subroutine also defines the 'echo' and 'handshake' status. The handshake mode is used for high baud rates (i.e. high transmission speeds), but it needs different computer settings to be applied. For the present research 'no echo' and 'no handshake' modes are used, and the code line is:

PRINT #1, "TI".

Data report mode is set to ASCII packed format (mode 1):

PRINT #1, "RM1".

Channel types are defined in two lines:

a) PRINT #1, "CT1,32,1"

which sets channels 1 to 32 to give readings in microvolts (1);

b) PRINT #1, "CS1,32,0,1"

which sets all 32 channels to autorange (0) and 16-bit resolution (1).

B) Subroutine for Communicating with stepper motors and relays

The structure of the I/O card and its physical link with the stepper motors and relays was described in Section 3.4.4.2.

The subroutine for driving a stepper motor (Appendix III) first addresses the port on the card which has the pair of pins for that motor. For all stepper motors that is port 1A, which is addressed as port=&H1B0 in the code (Fig.3.21). Then, one pin in a pair is used to define the direction in which the motor will drive by using binary bits 0 and 1. If it is set to 0 the motor will drive backwards (i.e. unloading) and if it is set to 1 it will go forwards (i.e. loading). The remaining pin is used to instruct the stepper motor to rotate by a single pulse.

Although there are 4 relay switches in the electrolevel M/D box they all have to be open or closed at the same time. Hence only one pair of pins on the I/O card is used to operate all of them. Since port 1C is used for relay operation, its address in the code is port=&H1B2 (Fig.3.21). Only the direction pin is used to operate the relays: when it is set to 0, the relays are closed and enable the torsional pair of electrolevel axes to be read; when it is set to 1, the relays are open and the axial pair of electrolevel axes can be read.

3.4.4.4. The operation with the program

To apply a desired stress path to a HCA specimen, the operator needs to undertake the following steps:

- input sample dimensions (r_i, r_o and H); at the beginning of stress path, these are values as measured during set-up procedure; for later stages, they are calculated at the end of the previous stage, from radial and axial strain measurements during that stage;
- take a 'zero' readings of all transducers at the beginning of each stage; these are starting points for stress increment application and strain measurement for that stage;
- input values of control parameters that remain constant in that stage;
- input values of the increments of parameters which are changing;
- input final (target) values for parameters which are changing;
- input time delay to ensure desired strain rate for the application of a particular stage (because apparatus is stress, and not strain, controlled);
- start the operation.

Apart from this initial input, the program is organized such that the operator can interact during its execution, in the case of the unexpected progression of the stress path. For example, if the desired strain rate is not being followed, the operator can change the time delay to keep strain rates within the required limits.

3.5. Sample preparation and testing procedures

3.5.1. Introduction

Granular materials are usually tested as reconstituted samples because it is difficult to obtain undisturbed samples out of the ground. However, techniques do exist for sampling undisturbed granular specimens, such as special tube sampling methods (Hight, 1993), or the in-situ freezing method (Yoshimi et al., 1989, 1994; Shibuya et al., 1995; Yamashita et al., 1995).

A preparation technique for reconstituted samples needs to fulfil the following criteria:
a) The samples must have uniform void ratio throughout, which means that no particle segregation should occur.
b) The samples must be fully saturated.
c) The sample preparation method should simulate the natural mode of soil deposition as closely as possible.

This Section will first make a review of possible sample preparation techniques for reconstituted granular materials and then describe the technique adopted for HPF4 samples for both triaxial and hollow cylinder devices. The testing procedures for both devices will then be described.

3.5.2. Sample preparation techniques for granular soils

A) Moist tamping

This reconstitution technique consists of pouring moist soil layers into a sample mould and tamping each layer with a suitable frequency to achieve the desired void ratio. This method may be suitable to model the soil fabric of some construction fills.

Granular samples prepared by this method can have larger void ratios than it is possible to achieve by pluviation, because of the action of water tension forces between the soil grains. These forces are larger in finer grained material and samples may be assembled in such a loose state that they may undergo large strains during the saturation process due to the removal of water tension forces between the grains (Casagrande, 1976; Chang et al., 1982).

B) Air Pluviation

The air pluviation technique is a procedure of pouring granular material into a sample mould through air. The major factors that affect relative density of air pluviated samples are

height of particle drop (Vaid & Negussy, 1984) and rate of deposition (Miura and Toki, 1982).

Air pluviation best models the natural deposition process of wind blown aeolian deposits. The process of sample saturation can be rather long compared to the length of the whole test and may disrupt initial material fabric, specially if the granular material has a considerable percentage of fines.

C) Water Pluviation

This technique is similar to the air-pluviation technique, but sand is rained through de-aired water rather than air, ensuring better initial saturation of the samples. The velocity of particles falling through water is lower than that of particles falling though air and thus the energy of settlement and relative density of water pluviated granular materials are generally lower than for air pluviated samples. The water pluviation technique simulates the deposition of sand through water, that is found in many natural environments.

However, both air and water pluviation techniques are prone to particle segregation when well-graded granular materials are tested.

3.5.3. The slurry deposition method adopted for HPF4 samples

To avoid problems of particle segregation associated with pluviation techniques (Kuerbis & Vaid, 1988; Kuerbis et al., 1988), the Author adopted a slurry deposition method for the well-graded HPF4 silt.

The silt slurry was prepared for both triaxial and HCA specimens by the following procedure:

a) The necessary amount of dry silt was mixed with 33% water (by weight) in a vacuum mixer. This ensured that the material was thoroughly mixed and formed a uniform de-aired slurry.

b) The sample mould(s) was set on the apparatus' base pedestal with membrane(s) stretched over it. The gap formed by the mould(s) was filled with de-aired water.

c) Slurry was then poured into the mould through a tube. Initially the outlet of this tube was positioned close to the base porous stone and is lifted up as the cavity filled with slurry. For HCA samples, the tube was both lifted and moved around the annular cavity, ensuring that the cavity was evenly filled up with slurry. Pouring slurry through water ensures high saturation and reduces the time for the subsequent saturation process to only a few hours.

To prove the uniformity of samples along their height, (i.e. uniform void ratio), especially for the hollow cylinder samples, two checks were made.

First, a dummy perspex mould for the HCA sample was made and filled with slurry in the manner described above. As this mould was transparent the condition of the sample could be viewed. No layering of material was observed due to segregation, apart from the top ~30 mm of the sample, which was very soft and milky (due to fines). Therefore, extension perspex rings were manufactured for both the triaxial and HCA sample moulds so that the slurry could extend above the top end of the original moulds. This ensured that the soft layer of fines was above the top end of the final test sample which was obtained by trimming the excess material contained in the perspex extension rings. The final sample then had a uniform structure (Fig.3.24).

Another way of testing the uniformity of a sample was to check the grain size distribution along the height of the sample. Three specimens were taken from the top, middle and bottom part of a HCA sample and grain size distribution curves were determined. All three curves are presented in Fig.3.25, showing that the adopted sample preparation method produces uniformly graded samples.

This sample preparation method produced samples with a typical void ratio of 0.65±0.03, which is actually a dense structure (Dr=88.7%) compared to the maximum and minimum limits (Section 3.2). Ovando-Shelley (1986) obtained loose samples of HPF4 (e_0=0.95) by the moist tamping technique, but, as discussed above, this technique does not represent the sedimentation process of natural soil deposits and also introduces a higher degree of sample non-uniformity.

3.5.4. Setting up procedures for silt samples

The setting up procedures for both triaxial and hollow cylinder samples were similar. The following description is therefore applicable to both types of sample. When there are differences they will be highlighted.

a) A de-aired base porous stone is placed on the sample pedestal.
b) The sample mould is placed around the pedestal to form the shape and size of the sample. For triaxial samples a 3-piece metal mould which forms a cylindrical 38x76 mm (diameter x height) sample is used. For HCA samples there are 2 wooden moulds: a 6-piece inner mould and 3-piece outer mould. Together they form a 25 mm wide annular cavity.
c) A latex membrane is stretched around the mould to hold the HPF4 after the mould is removed. The HCA samples have both inner and outer membranes to form the inner and outer

walls of the sample.

d) A mould extension is added for the reasons described in Section 3.5.3.

e) Slurry is poured into the mould and its extension and left to sediment.

f) The mould extensions are removed and the sample is trimmed to the top end of the mould.

g) The top porous stone is positioned at the top of the sample and the membrane(s) stretched and fixed with O-rings around it.

h) A suction of 30 kPa is applied so that the sample has a sufficient initial effective stress to support itself when the moulds are removed. With the moulds removed the sample dimensions are taken and local instrumentation attached.

i) The perspex test chamber is placed over the sample, fixed to the pedestal and filled with water.

j) Full saturation is achieved by applying a back pressure of 400 kPa and cell pressure of 450 kPa. These pressures are applied in steps of 50 kPa.

3.5.5. Testing procedure for triaxial samples

All samples were K_o consolidated, with the K_o value determined from a series of trial tests performed such that there were no radial strains. This condition is realised if $\varepsilon_z=\varepsilon_{vol}$ (see Chapter 4). After K_o consolidation, some samples were swelled back to overconsolidation ratios of 1.3, 2.0 or 4.0.

Undrained compression and extension shearing stress paths were then applied from the final consolidation state at a controlled rate of axial strain (5 %/day). This was applied by a constant rate of strain pump. Further details about the triaxial stress paths are given in Chapter 4.

The calculations to obtain stresses and strains were performed assuming that the samples deformed as right cylinders (Bishop & Henkel, 1962). During undrained tests, ε_r was taken as $(-\varepsilon_a/2)$. The initial porosity was calculated from the volume of the samples immediately after the sample dimensions had been taken.

3.5.6. Testing procedure for hollow cylinder samples

All HCA samples were K_o consolidated, with the same K_o value as determined from triaxial tests. However, in these tests all strains (axial, radial, circumferential and torsional) were directly measured. In Chapter 5 plots of ε_r and ε_θ are plotted, which confirm the validity of the applied K_o value.

All HCA tests were stress controlled and the applied stress paths are described in detail in Chapters 5, 6 and 7. The shearing strain rate was also maintained at approximately 5 %/day. This was achieved through the control program by changing the length of the time delay between two successive stress steps (Menkiti, 1995).

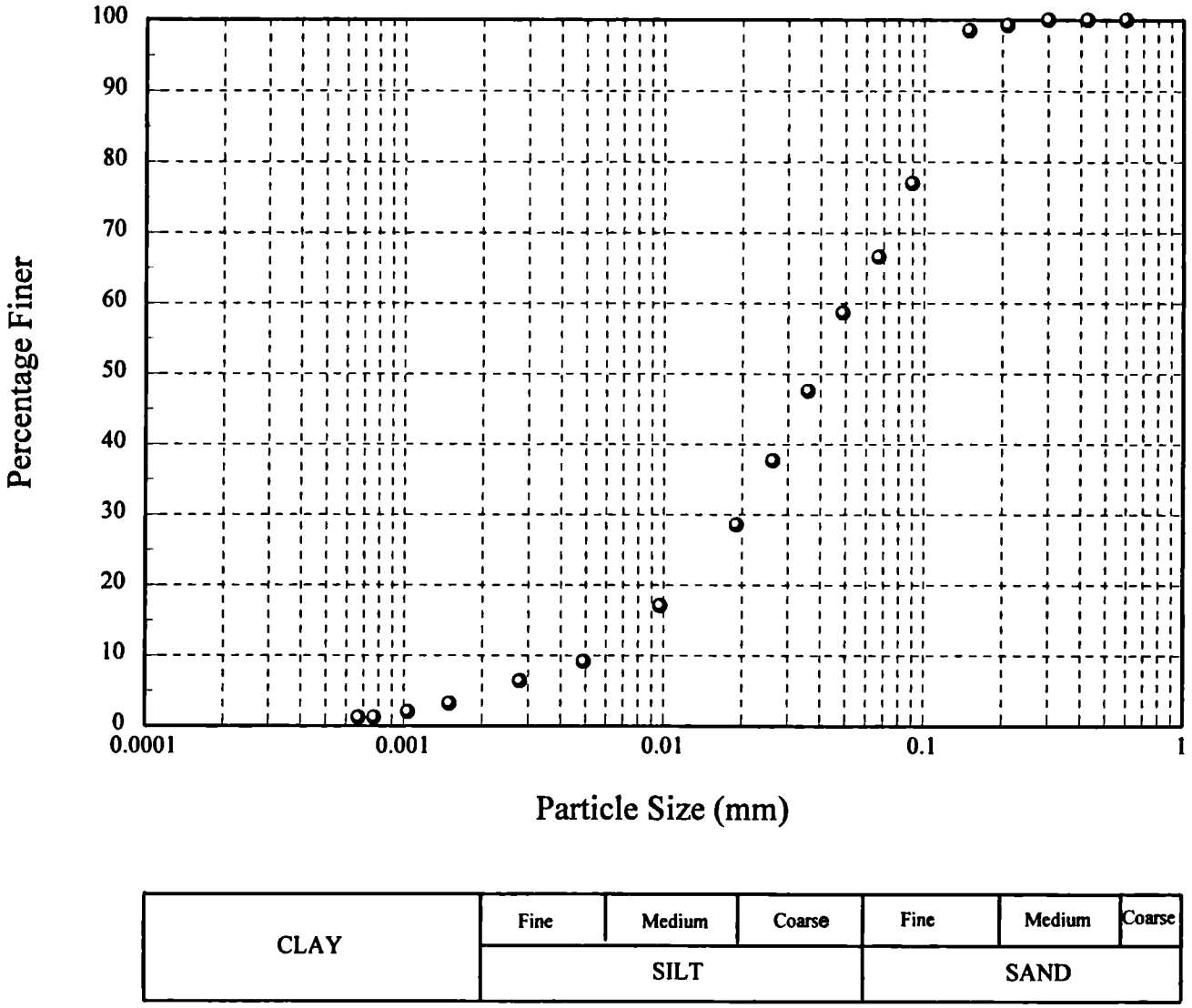


Fig. 3.1 - Grain size distribution curve for silt HPF4

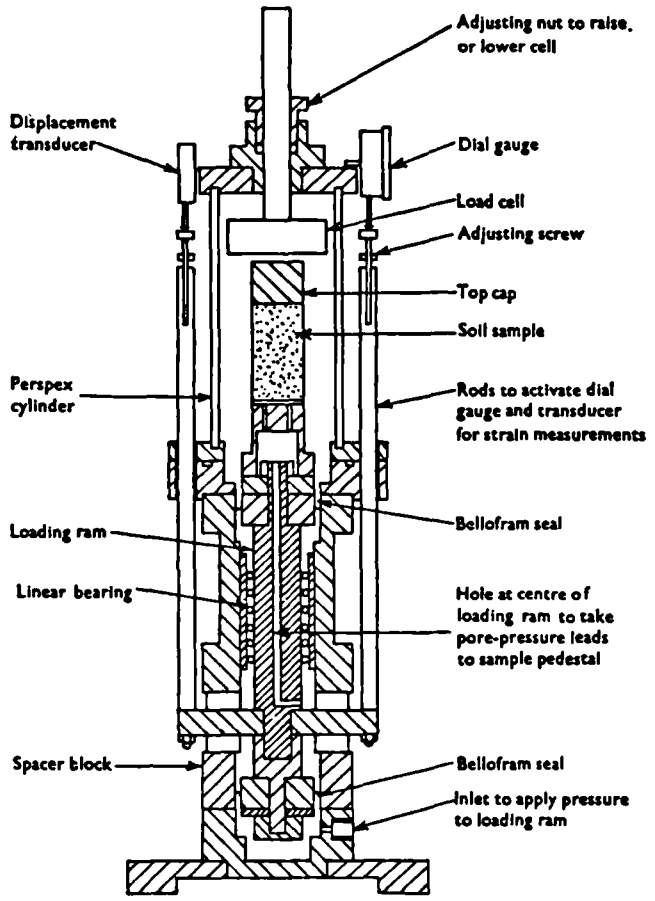


Fig.3.2 - General layout of the triaxial stress path cell (Bishop & Wesley, 1975)

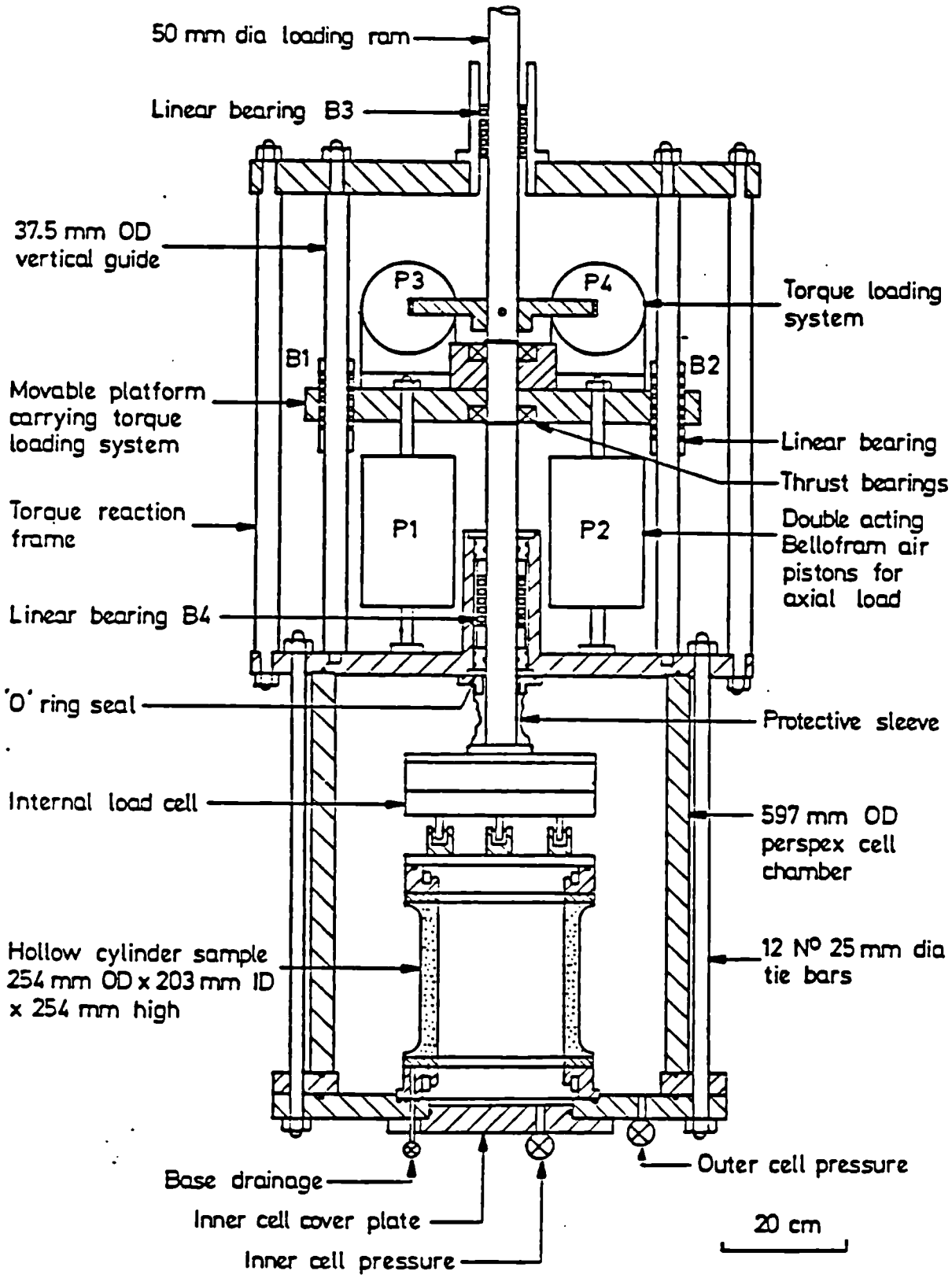


Fig.3.3 - General layout of the Imperial College Hollow Cylinder Apparatus (Shibuya, 1985)

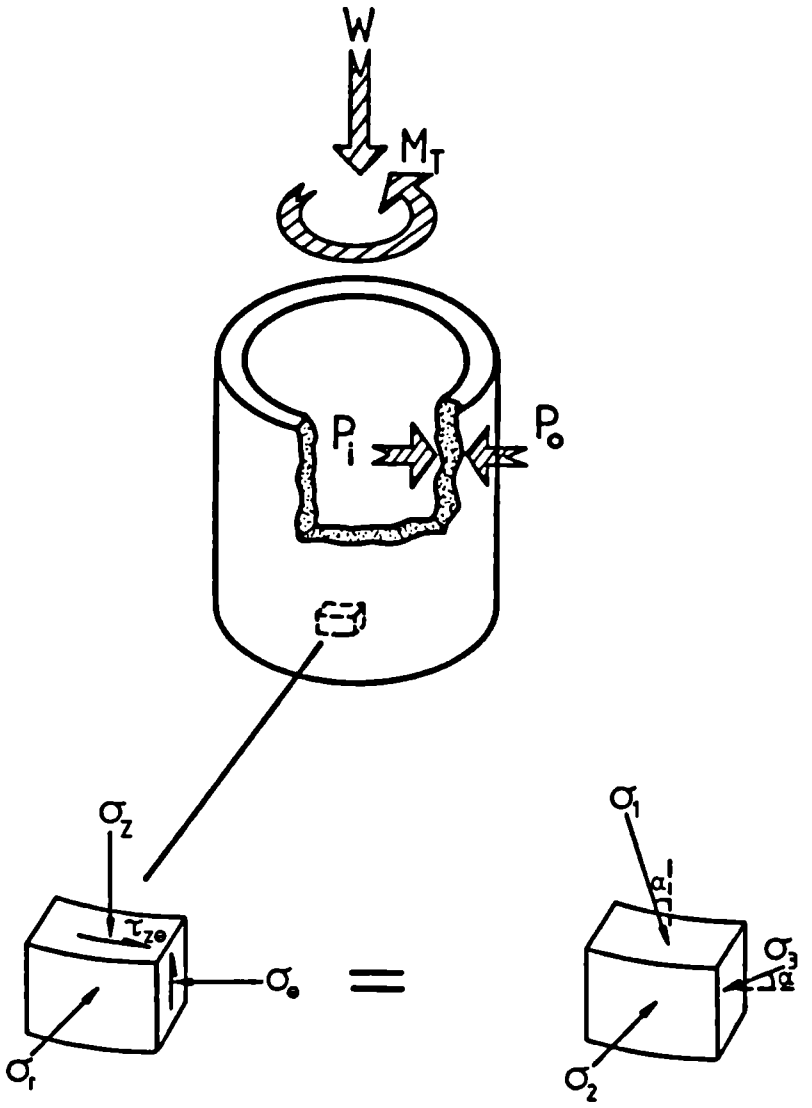


Fig.3.4 - Idealized stress conditions in a hollow cylinder element

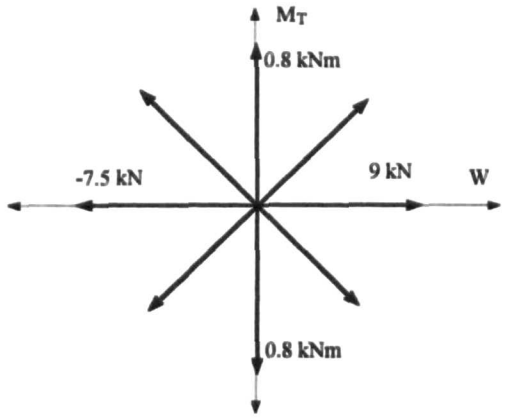


Fig.3.5 - Load paths for the calibration of the HCA load cell

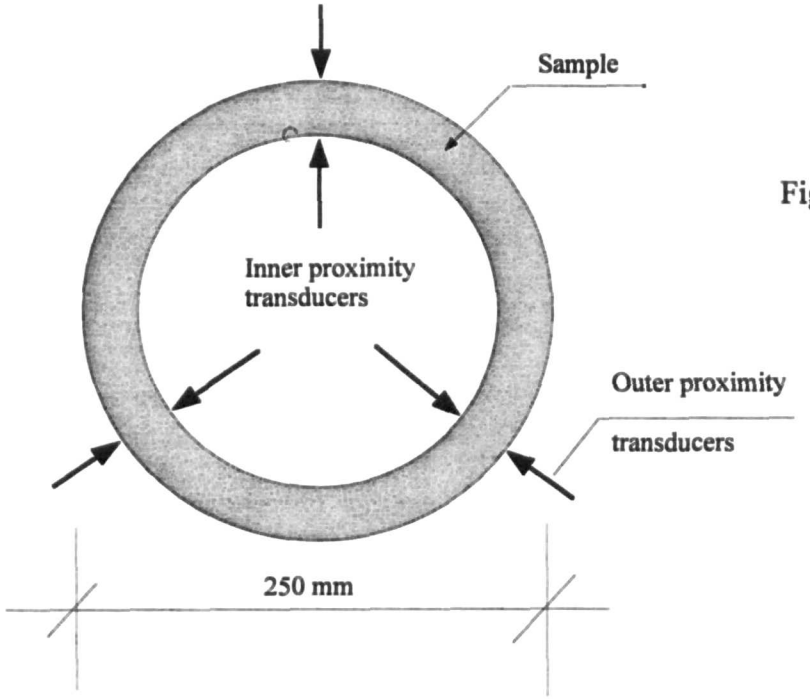


Fig.3.6 - Proximity transducers on a HCA sample

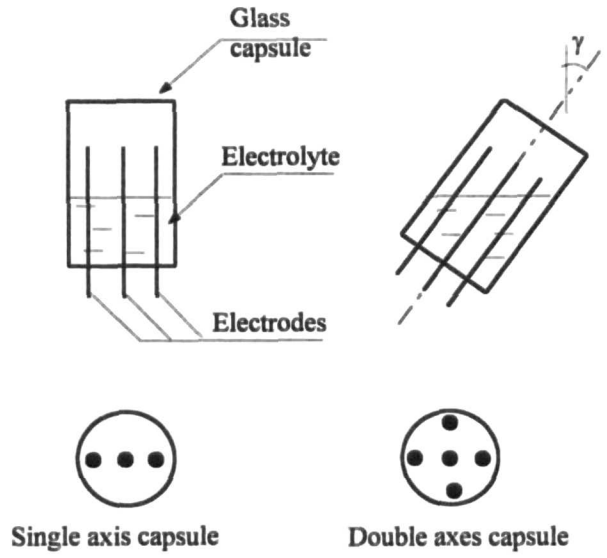
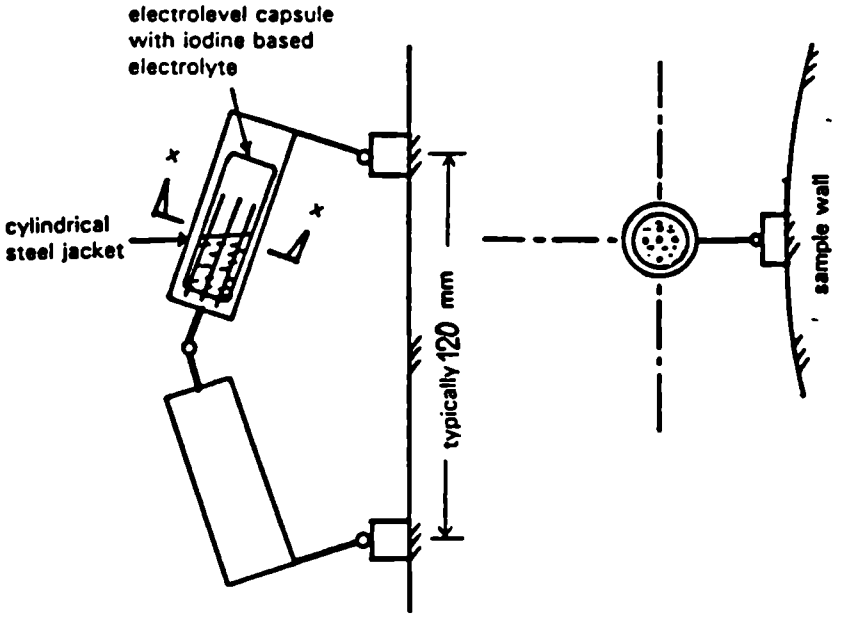
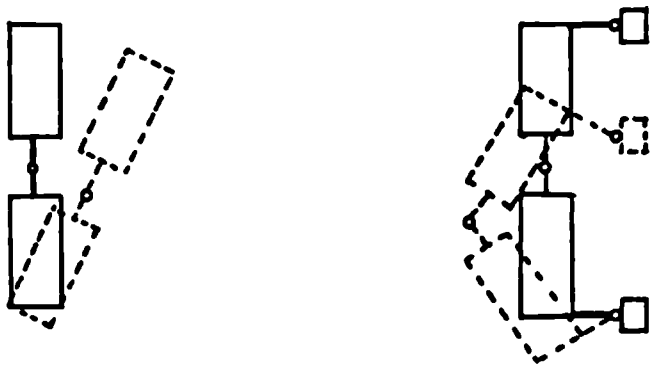


Fig.3.7 - Capsules for the electrolytic type transducer



Side elevation Section x-x

(a) General construction



Deformed shape, pure twist.
Front elevation

Deformed shape, pure compression.
Side elevation

(b) Modes of deformation

Fig.3.8 - The combined strain electrolevel

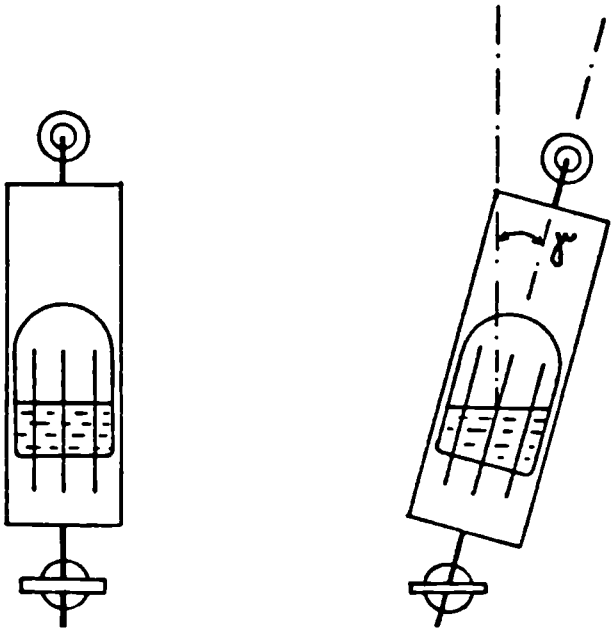


Fig.3.9 - Single axis torsional shear strain electrolevel

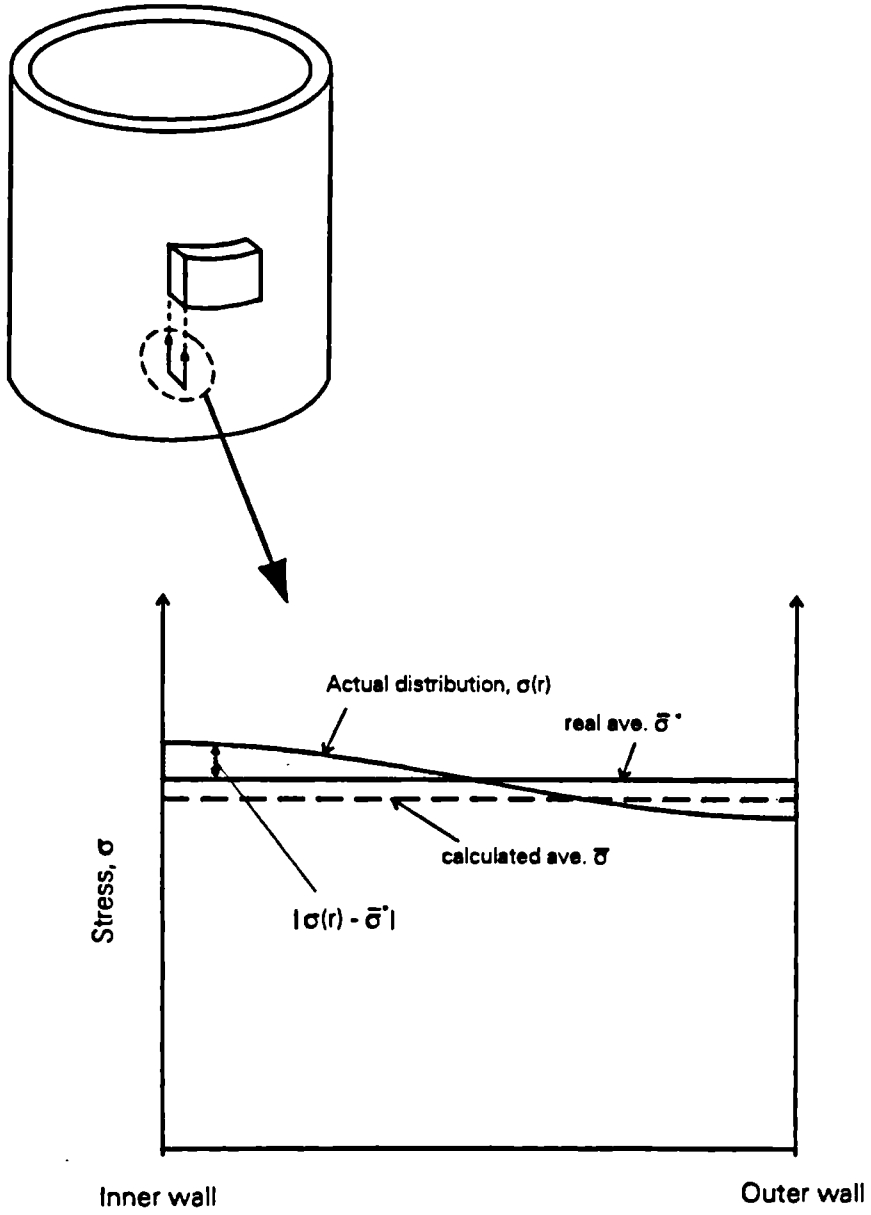
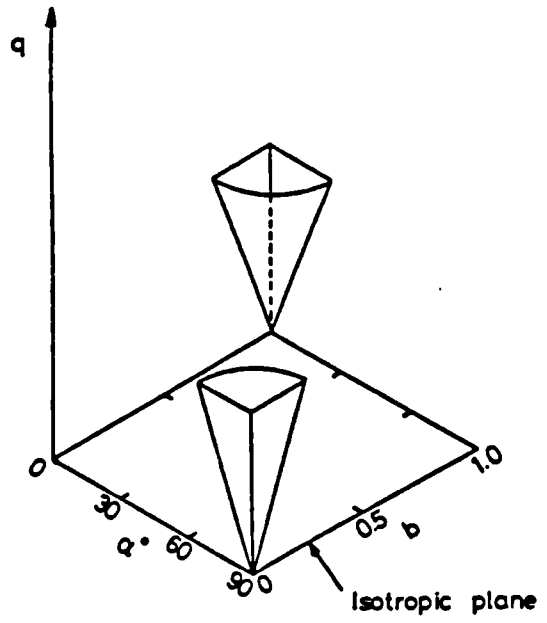
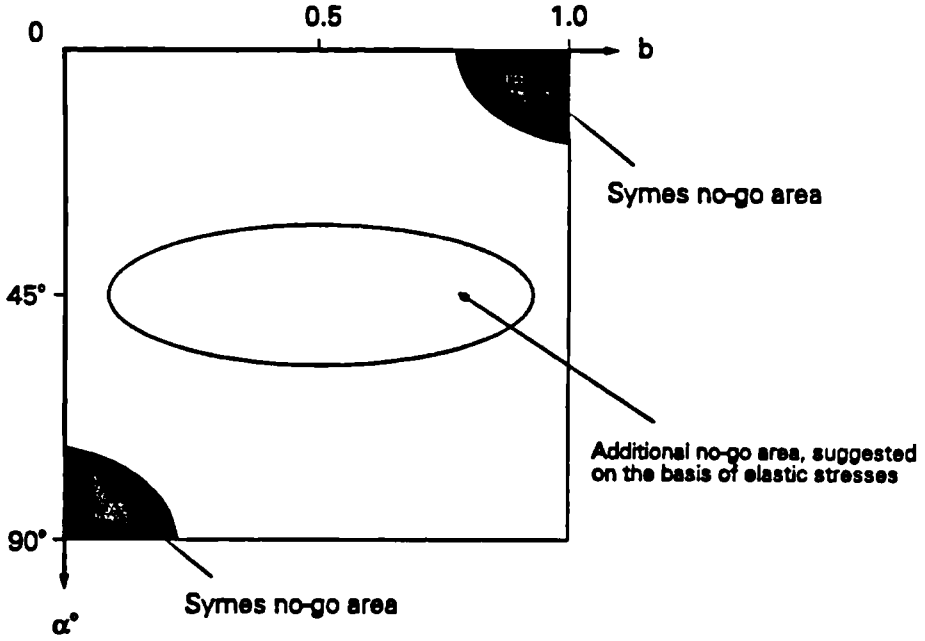


Fig.3.10 - Schematic view of the stresses within the wall of a hollow cylindrical specimen (Hight et al., 1983)



(a) "No-go" areas in stress space, from elasto-plastic analyses (Symes, 1983)



(b) Schematic representation of suggested "no-go" areas by Symes (1983) on the basis of elasto-plastic analyses and Vaid et al (1990) on the basis of elastic analyses

Fig.3.11 - 'No-go' areas suggested by previous workers

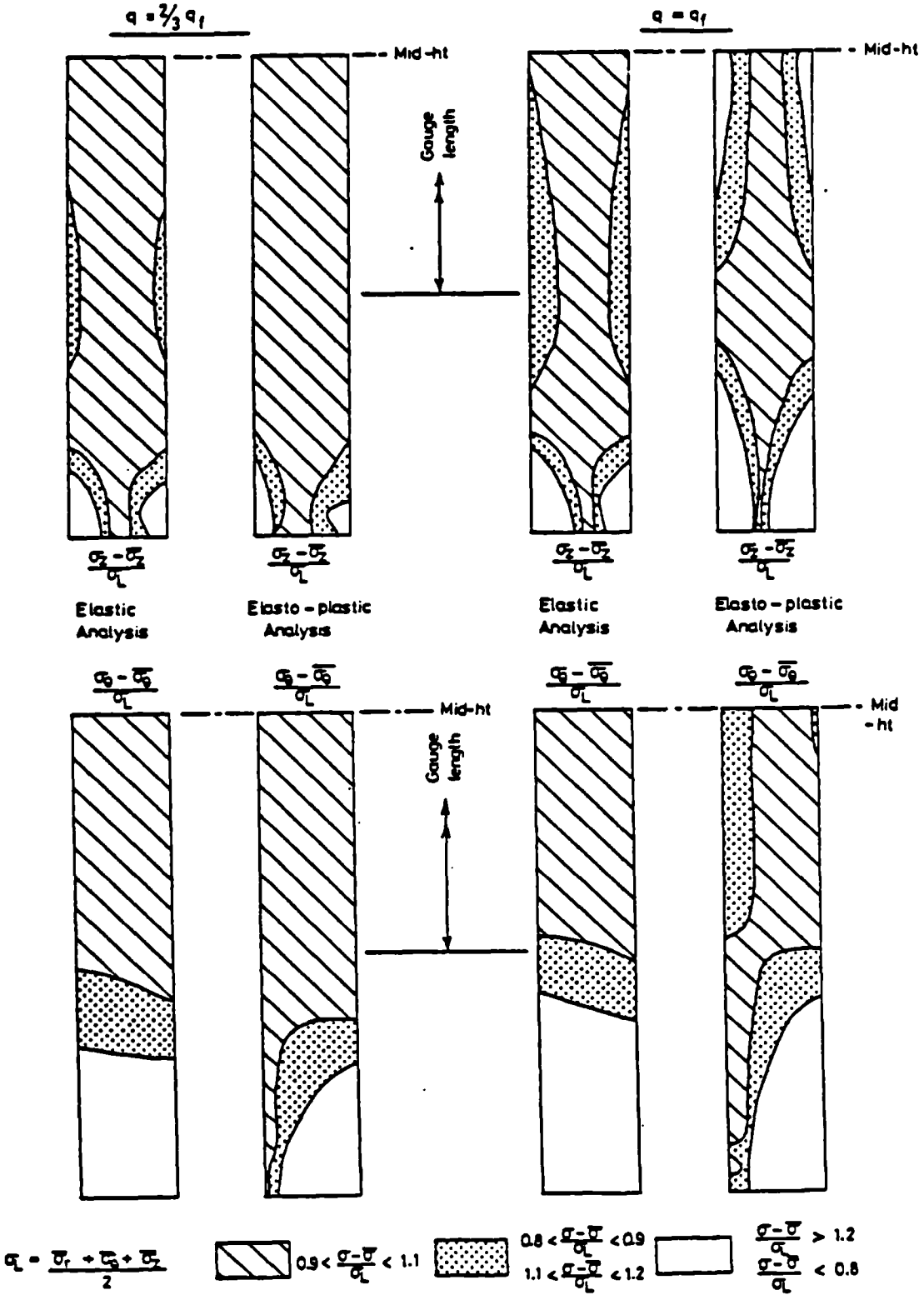


Fig.3.12 - Elasto-plastic and elastic analyses of fixed-end hollow cylinder samples (Hight et al., 1983)

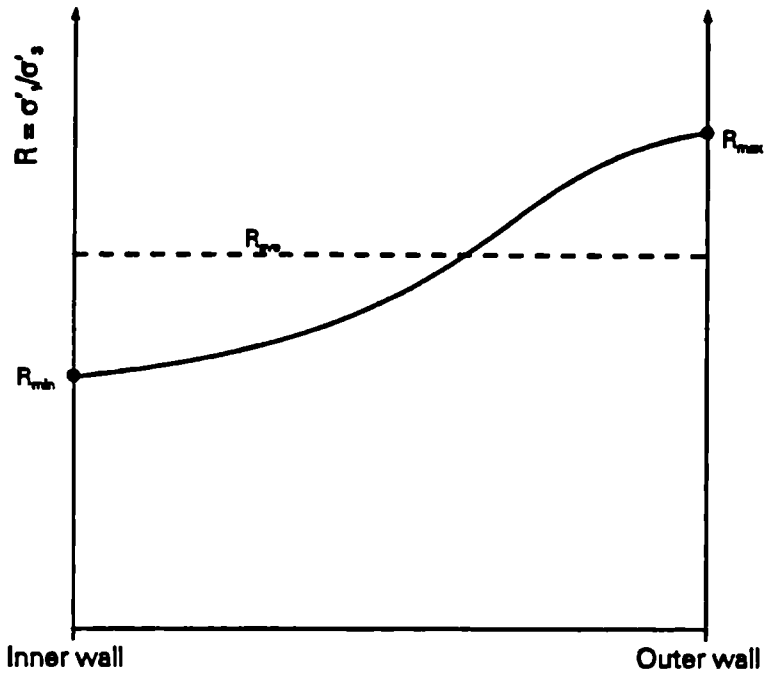


Fig.3.13 - Variation of stress ratio across the wall of a hollow cylinder sample (Vaid et al., 1990)

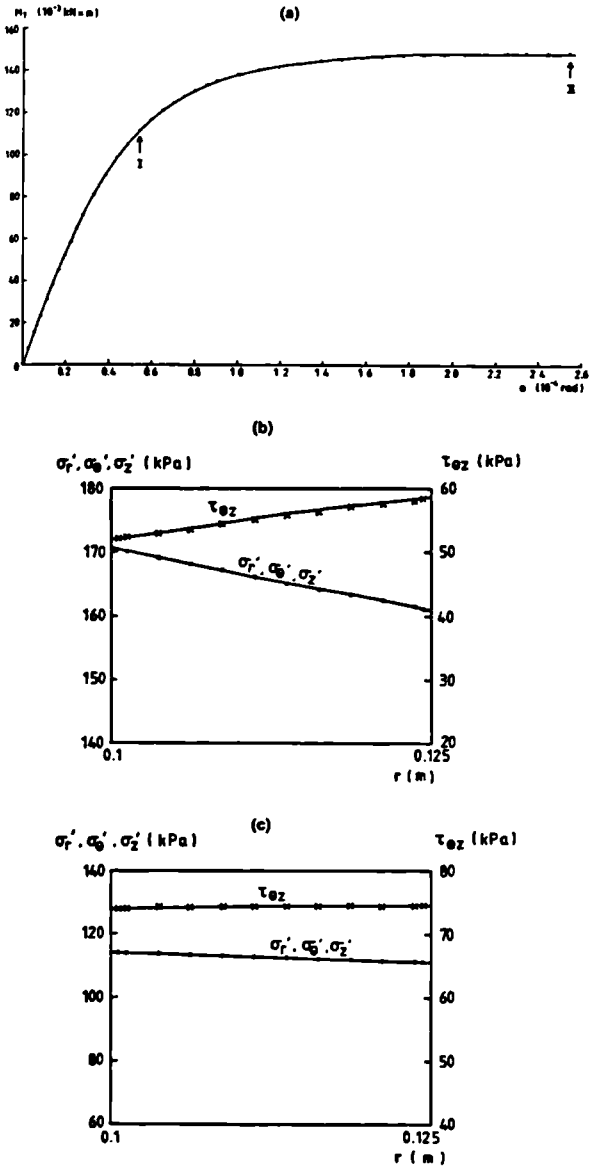


Figure 7 Hollow cylinder subjected to torsion—associated plasticity model. (a) Torque *versus* rotation angle; (b) stress distributions at stage I; (c) stress distributions at stage II

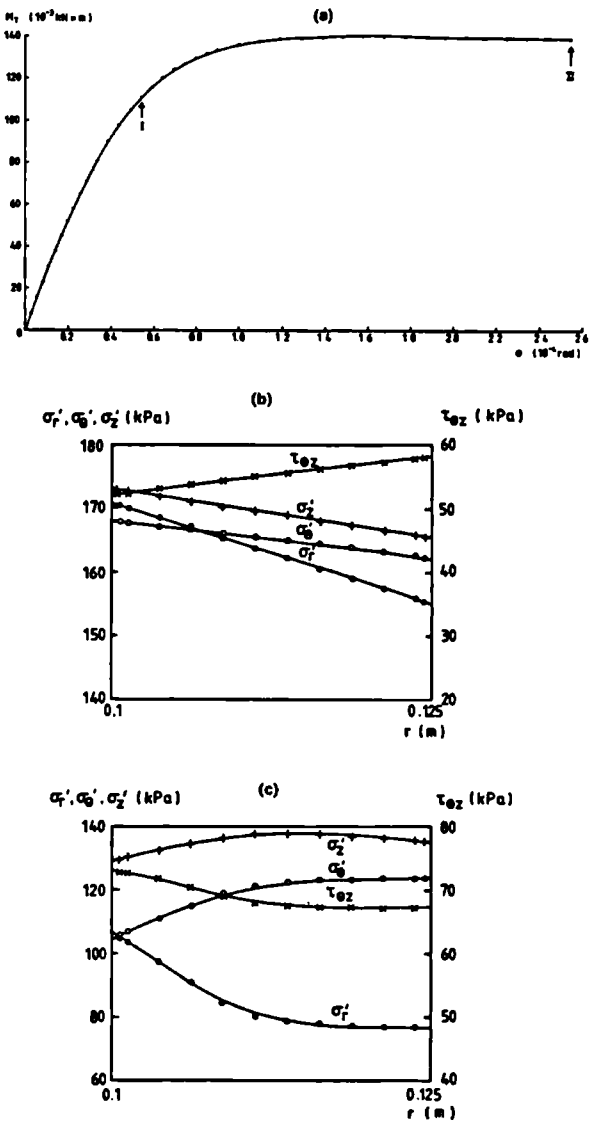
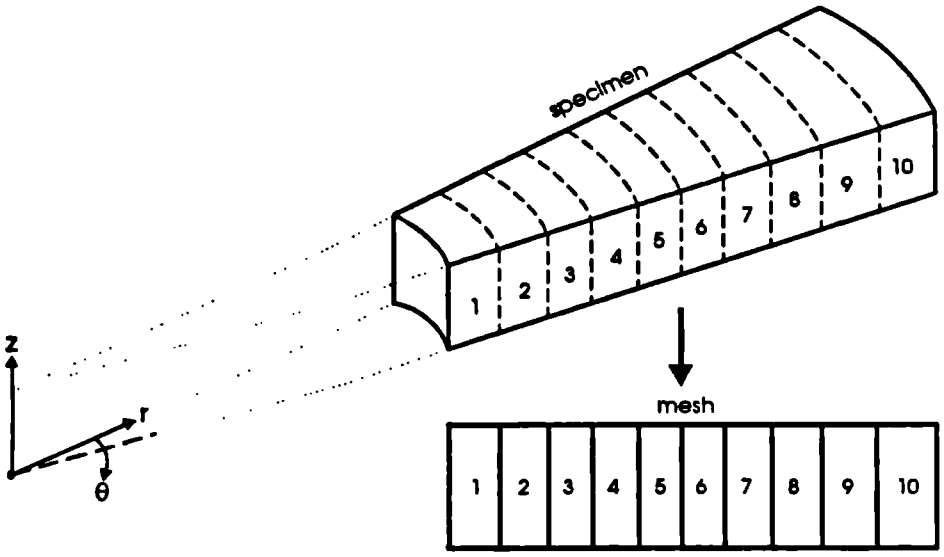
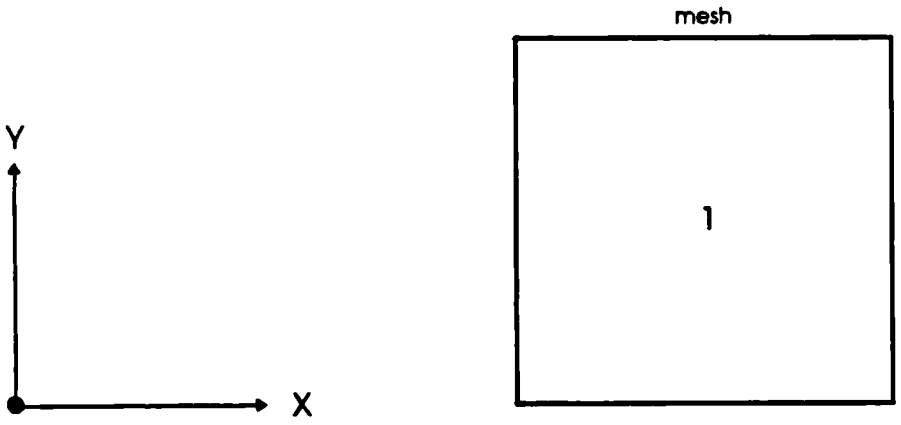


Figure 8 Hollow cylinder subjected to torsion—non-associated plasticity model. (a) Torque *versus* rotation angle; (b) stress distributions at stage I; (c) stress distributions at stage II

Fig.3.14 - Analyses of hollow cylinder nonuniformities using assoiciated and non-associated plasticity model (Gens & Potts, 1984)



(a) Finite element mesh for hollow cylinder problem



(b) Finite element mesh for uniform soil element

Fig.3.15 - Finite element meshes for the analyses of the curvature for hollow cylinder samples (Menkiti, 1995)

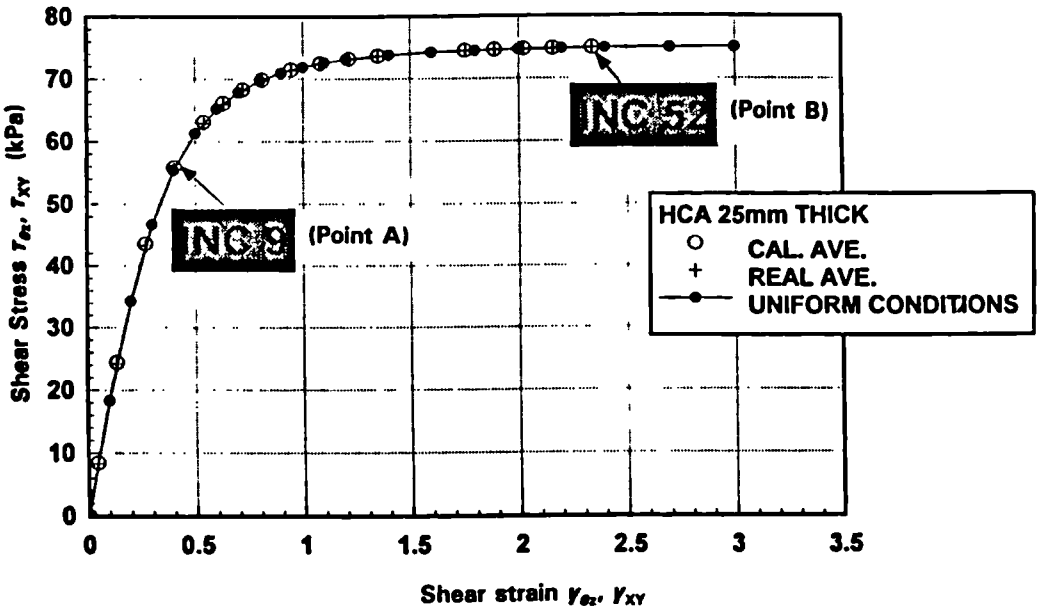


Fig.3.16 - Interpreted stress-strain responses from elasto-plastic finite element analysis (Menkiti, 1995)

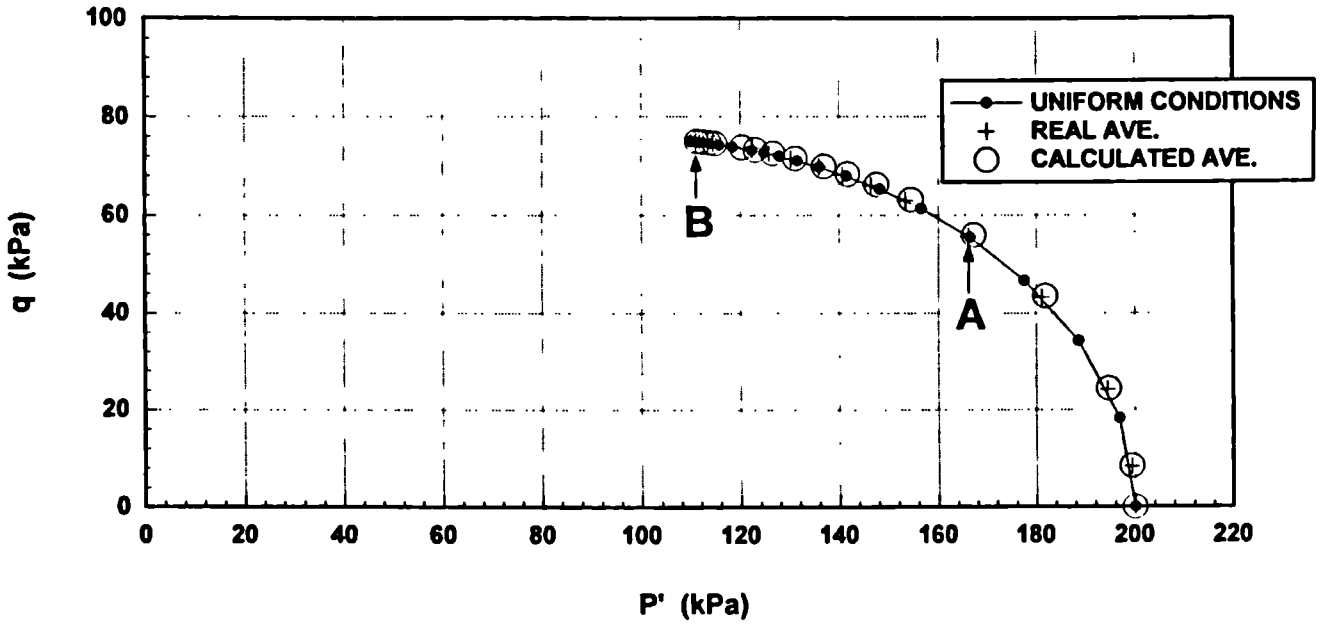


Fig.3.17 - Interpreted stress paths from elasto-plastic finite element analysis (Menkiti, 1995)

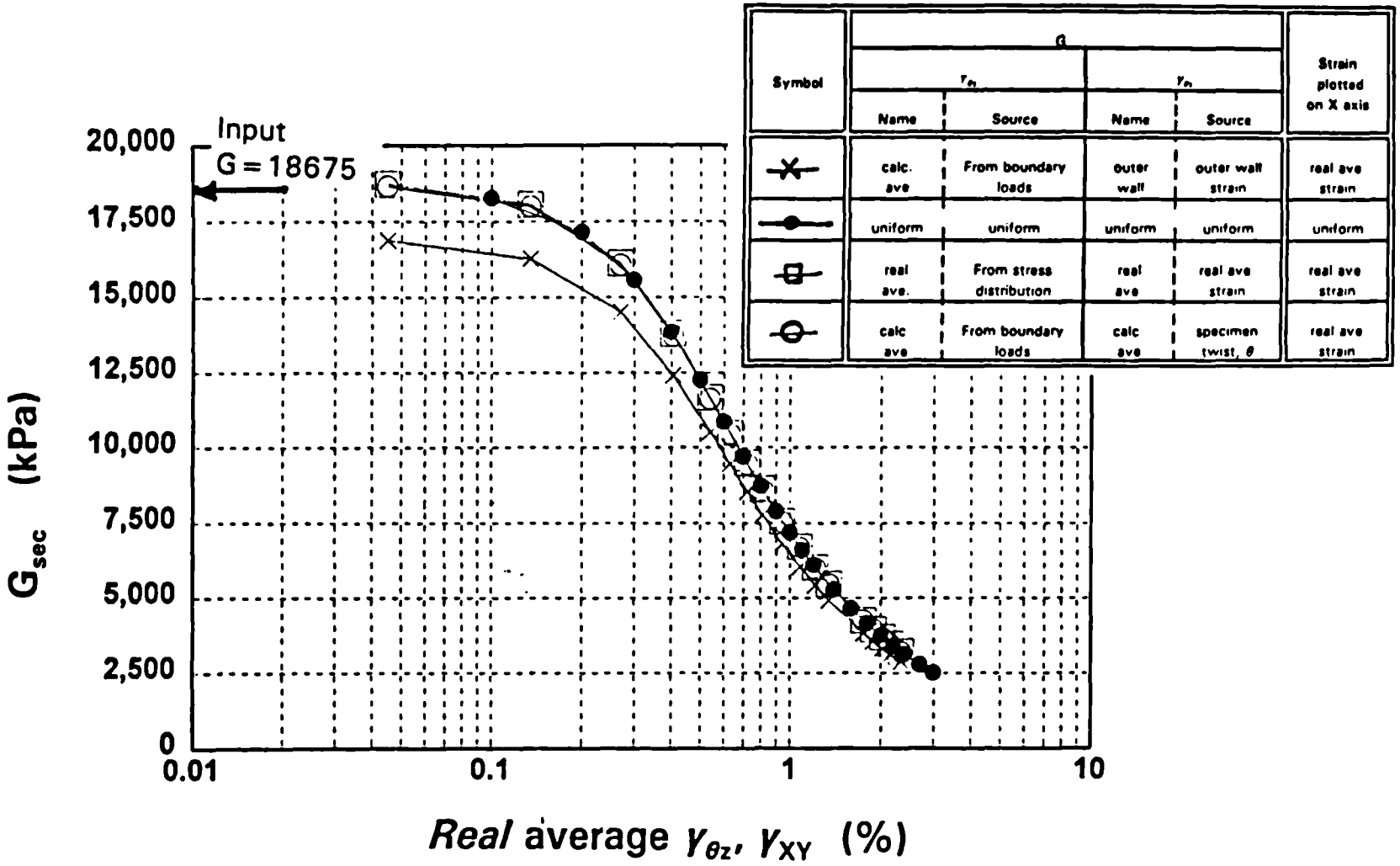


Fig.3.18a - Interpreted stiffness decay curves from elasto-plastic finite element analyses: HCA data plotted against real average $\gamma_{\theta z}$ (Menkiti, 1995)

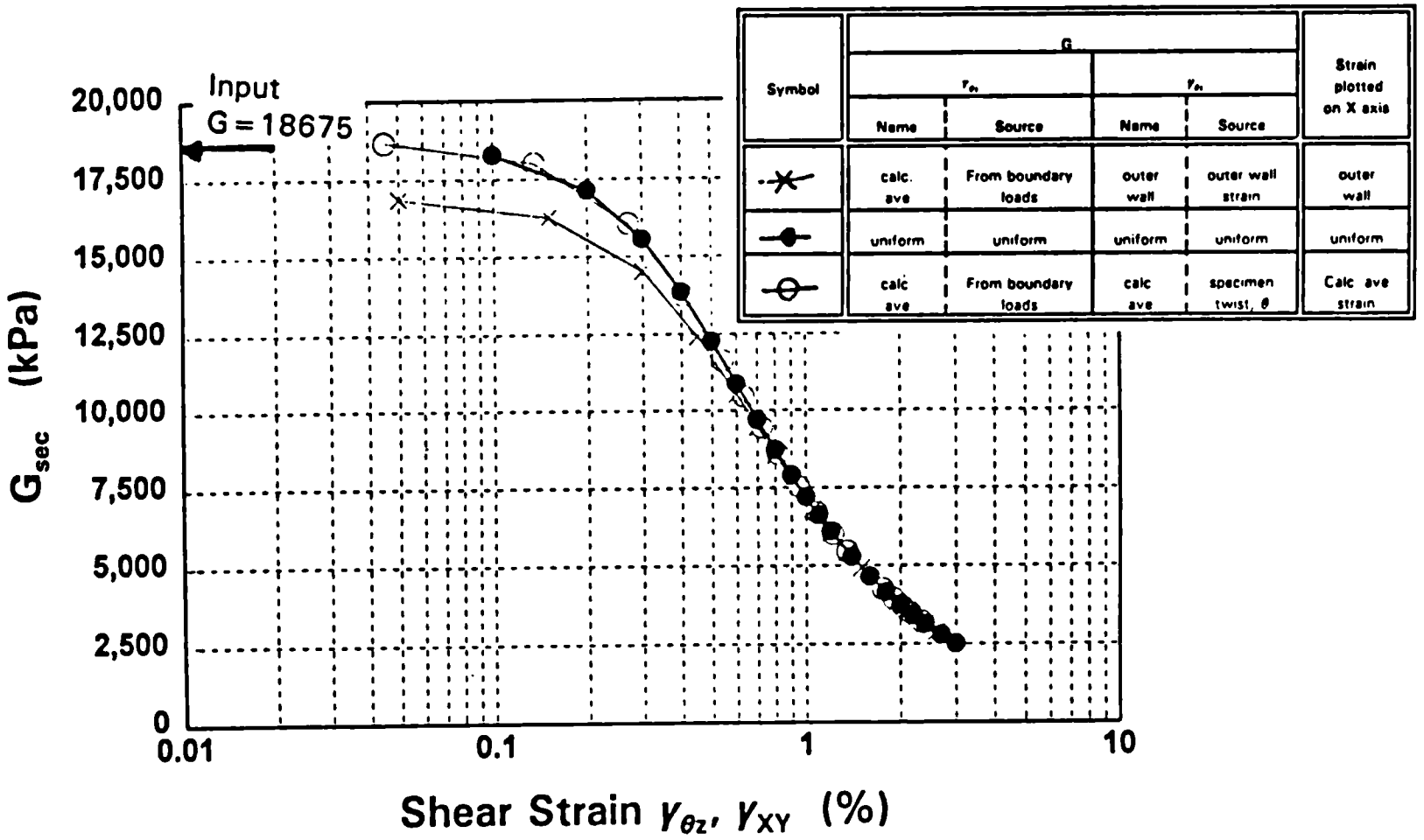


Fig.3.18b - Interpreted stiffness decay curves from elasto-plastic finite element analyses: HCA data plotted as interpreted in real test (Menkiti, 1995)

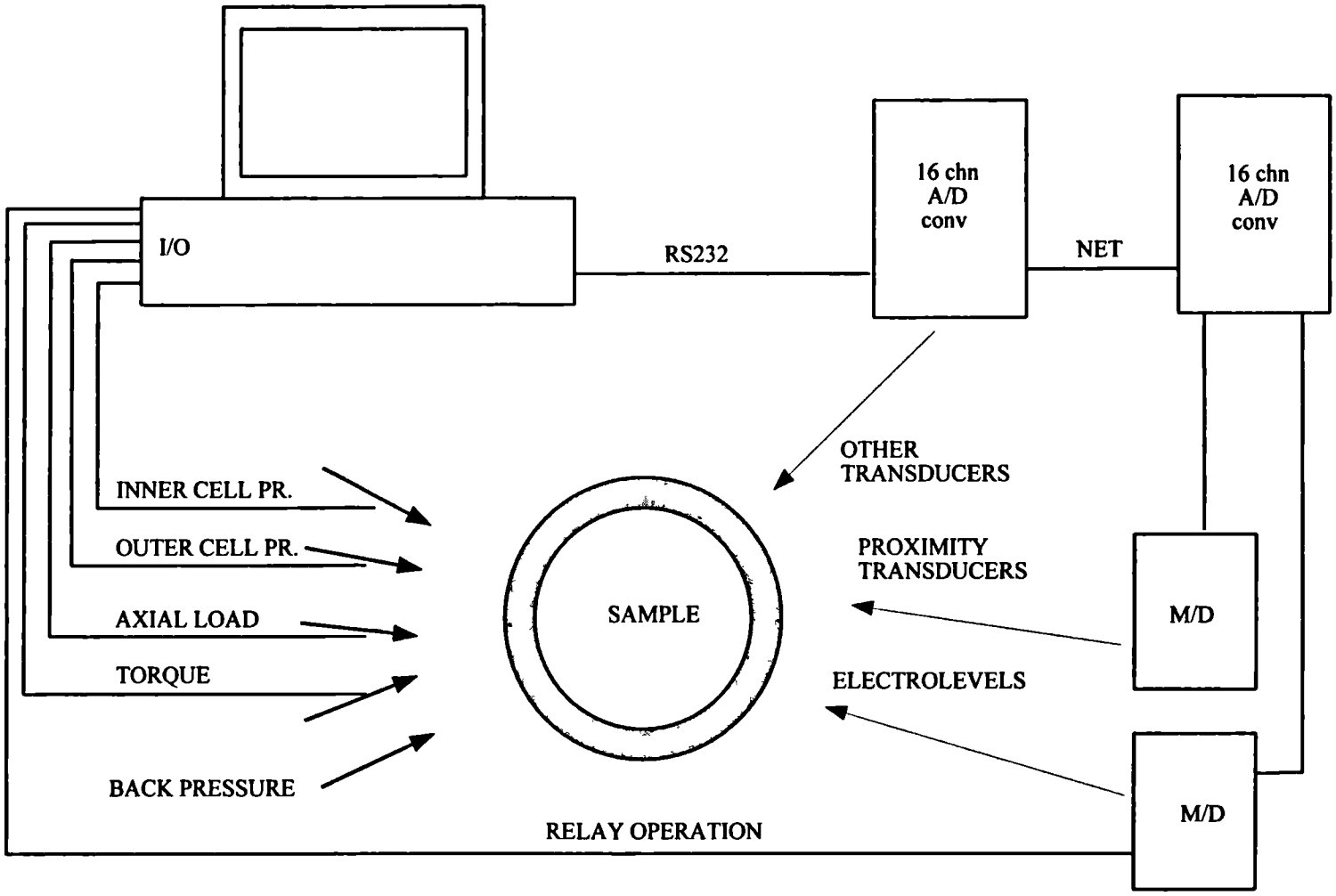


Fig.3.19 - HCA control and data acquisition system

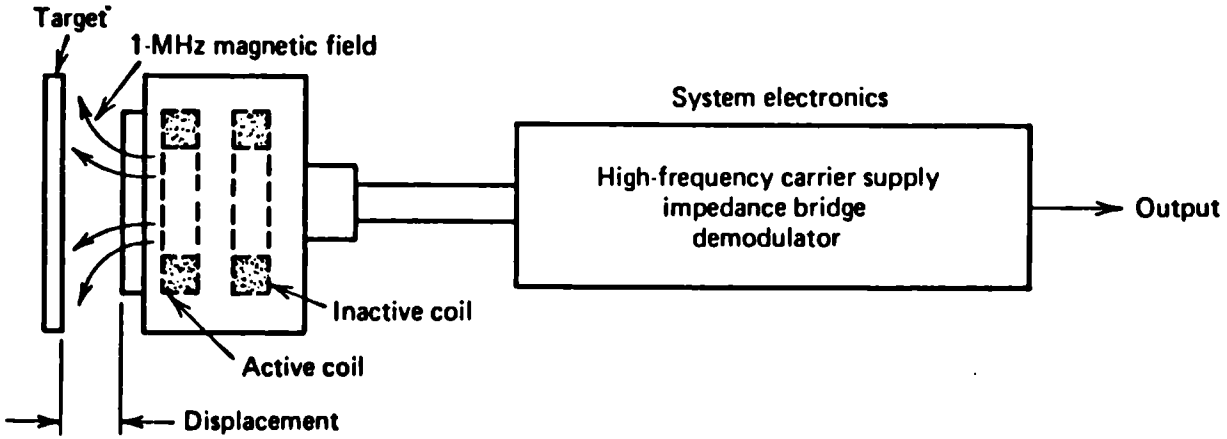
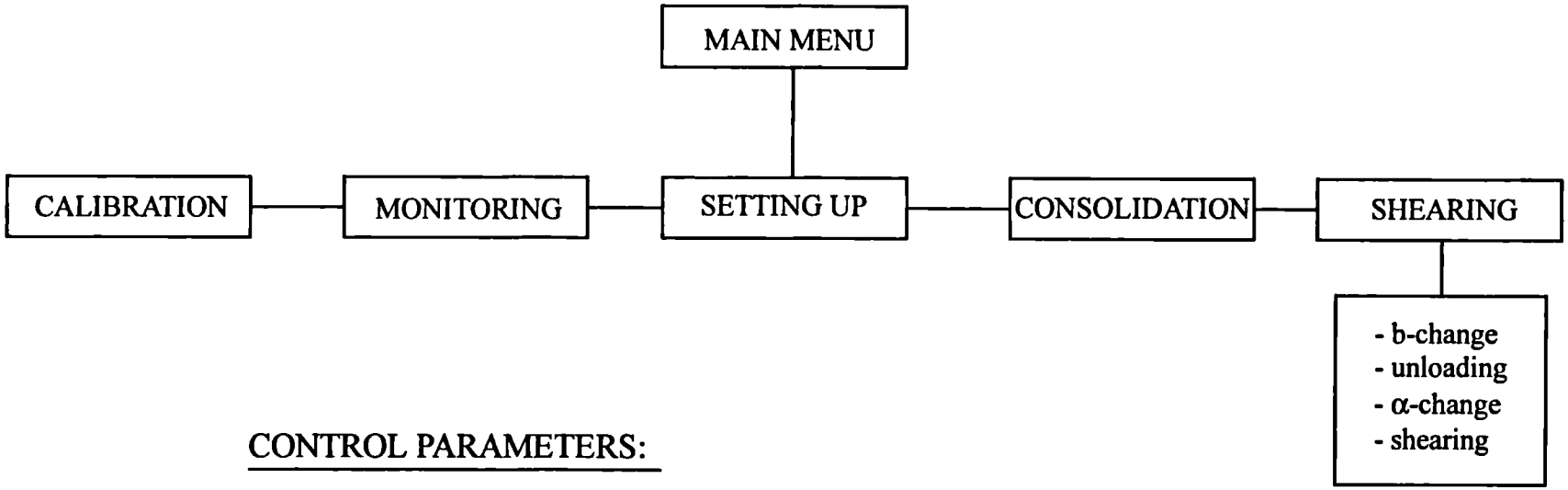


Fig.3.20 - Layout of a proximity transducer

	PORT 1			PORT 2		
	1A	1B	1C	2A	2B	2C
	PA0	PB0	PC0	PA0	PB0	PC0
	PA1	PB1	PC1	PA1	PB1	PC1
	PA2	PB2	PC2	PA2	PB2	PC2
	PA3	PB3	PC3	PA3	PB3	PC3
	PA4	PB4	PC4	PA4	PB4	PC4
	PA5	PB5	PC5	PA5	PB5	PC5
	PA6	PB6	PC6	PA6	PB6	PC6
	PA7	PB7	PC7	PA7	PB7	PC7
address	$1B0	$1B1	$1B2	$1B4	$1B5	$1B6

Fig.3.21: Port distribution on 8255 I/O card

Program structure



CONTROL PARAMETERS:

$b = (\sigma_2 - \sigma_3)/(\sigma_1 - \sigma_3)$

$t = (\sigma_1 - \sigma_3)/2$

p_{tot} - mean total stress

α - angle of principal stress rotation

Fig.3.22 - Schematic presentation of program structure

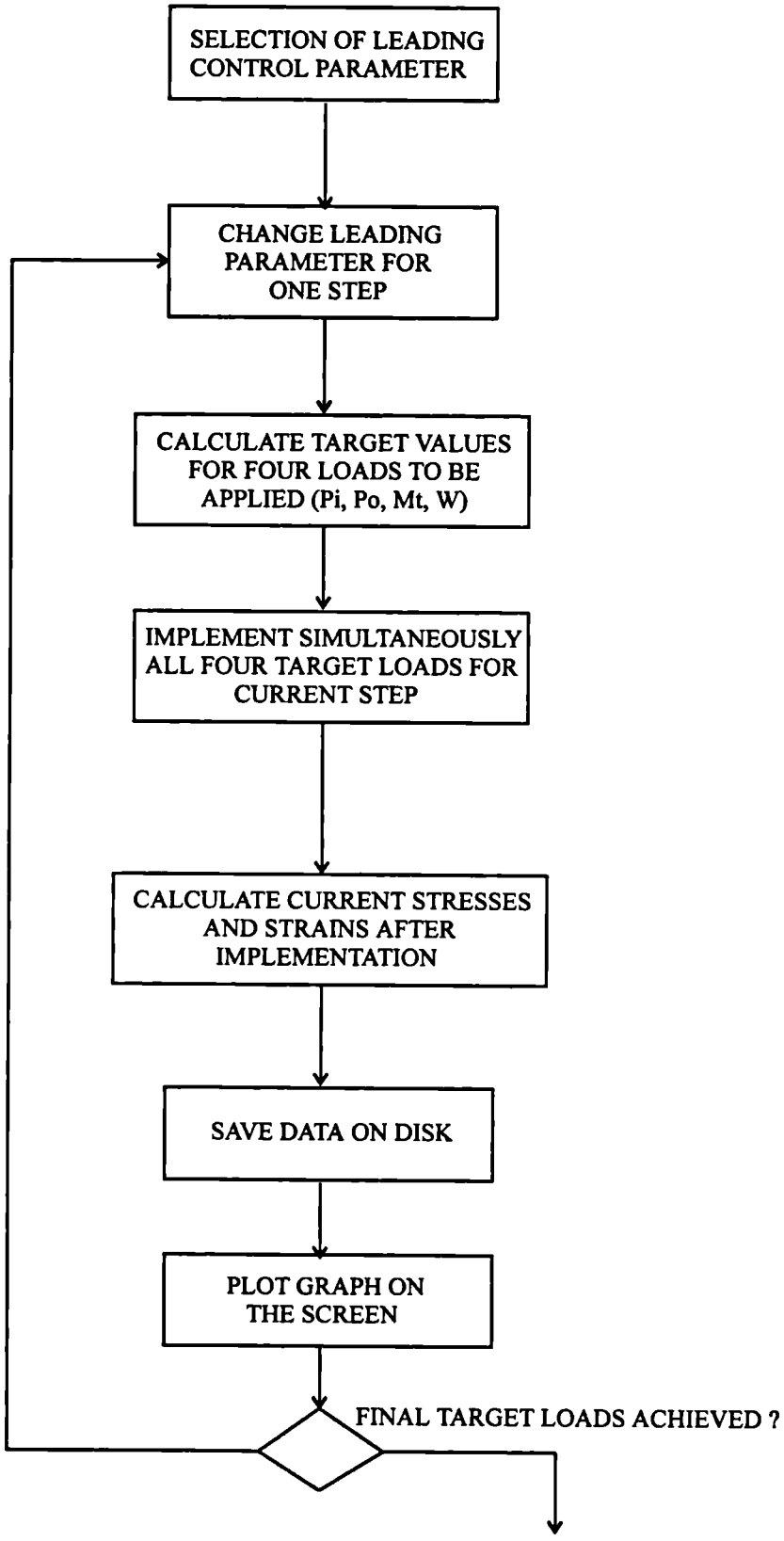


Fig.3.23 - Algorithm for load application

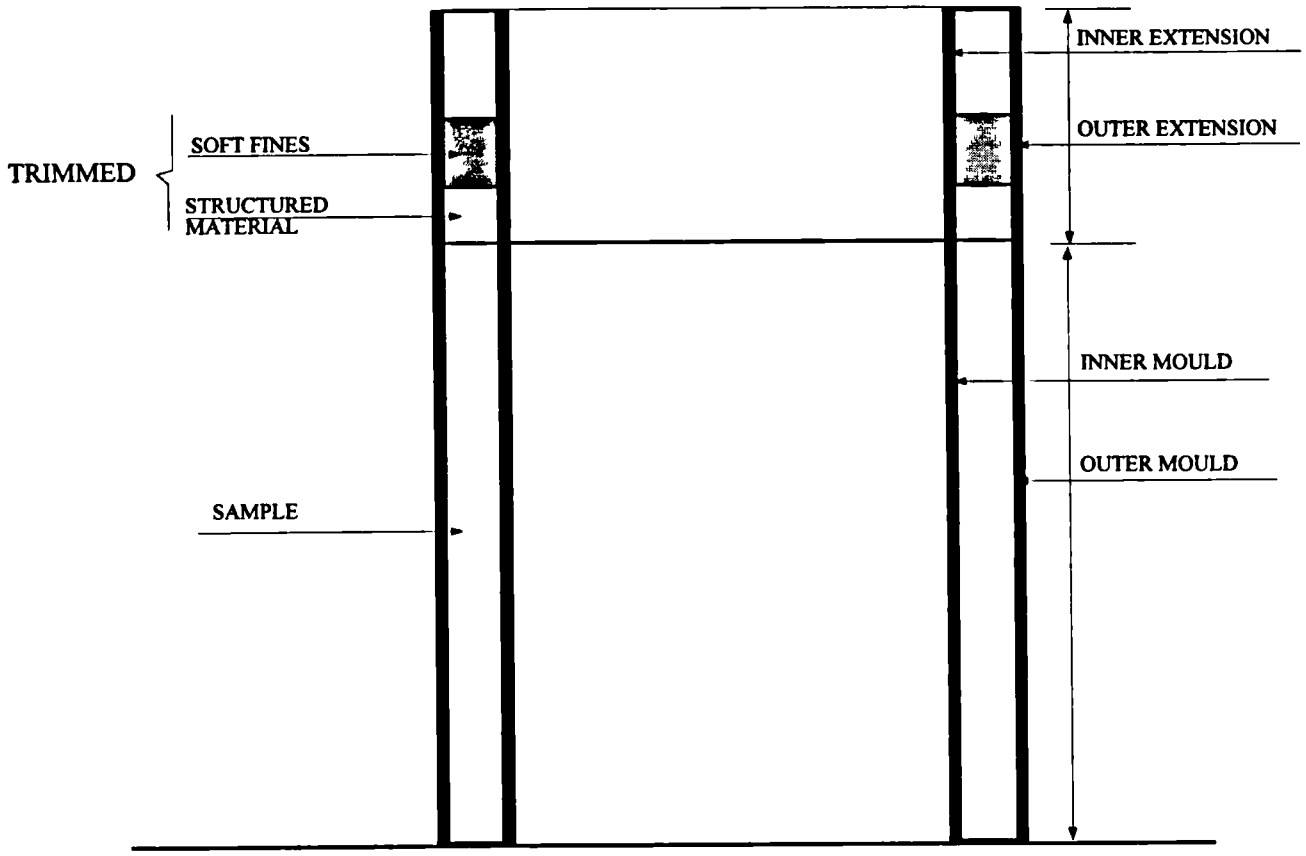
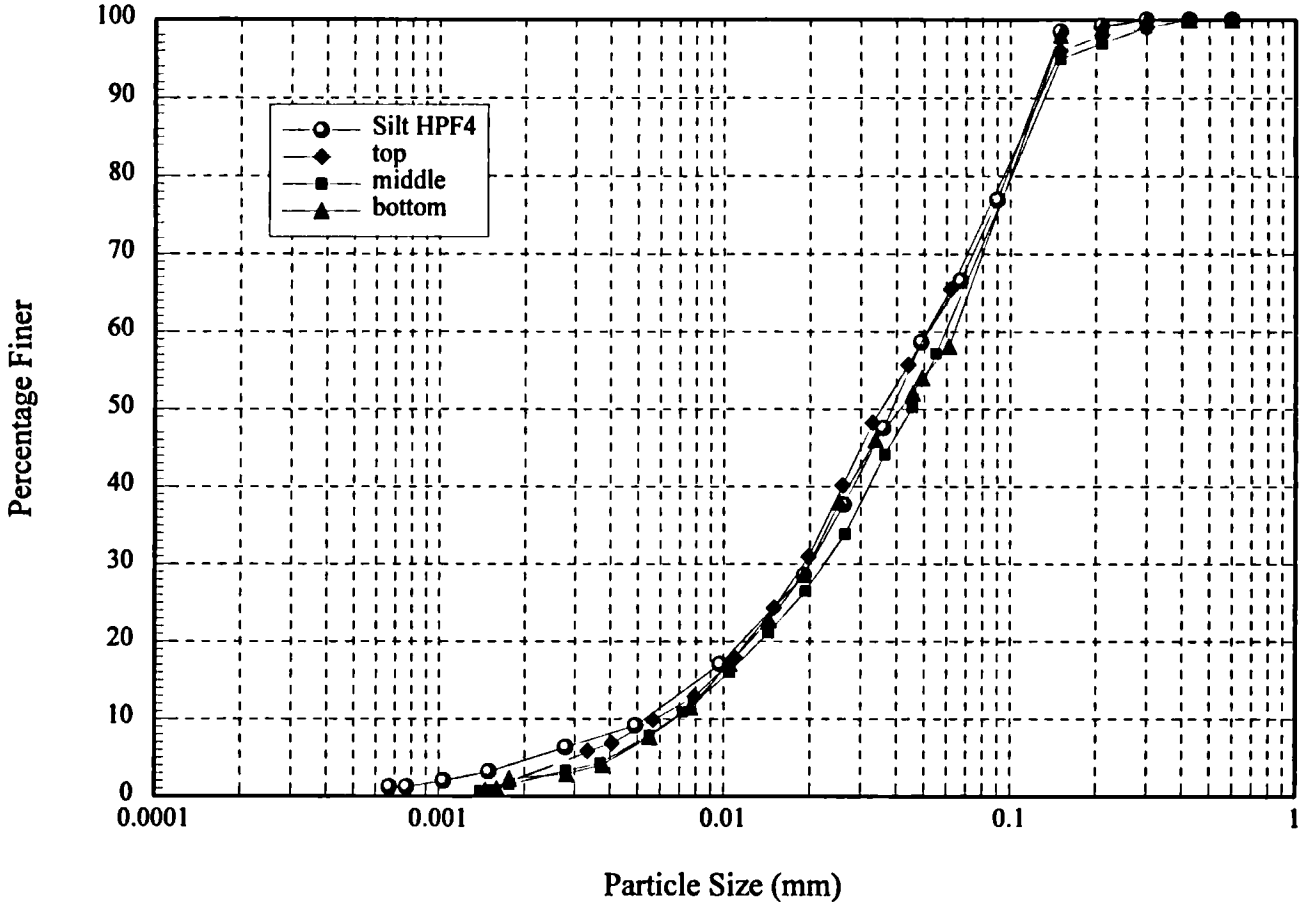


Fig.3.24 - Preparation of HPF4 samples in HCA moulds



CLAY	Fine	Medium	Coarse	Fine	Medium	Coarse
	SILT			SAND		

Fig. 3.25 - Grain size distribution curves for silt HPF4 from three parts of a sample

Chapter 4

TRIAXIAL TESTS

4.1. Introduction

In this Chapter results from a series of undrained triaxial stress path tests on HPF4 are presented. These tests were performed in the stress path cell described in Chapter 3. They were undertaken to provide basic information on the behaviour of HPF4. Such data was necessary before the more complex testing to be performed in the HCA could be planned and undertaken.

The suite of tests consisted of four compression and four extension tests. These were performed on K_o consolidated samples with overconsolidation ratios (OCR's) of 1.0, 1.3, 2.0 and 4.0. As shown in Fig.4.1, samples consolidated to an OCR of 4 have their final stress state on the isotropic axis. These OCRs were chosen so that the material behaviour could be investigated for normally consolidated to moderately overconsolidated states. These values are also typical of those used by other researchers when testing other types of reconstituted soil. Such consistency allows direct comparison of results for different soils.

Results from the K_o consolidation and K_o swelling stages of the tests are presented first. Then the results from the shearing stages of the tests are given. The undrained triaxial compression and extension effective stress paths are discussed and the small strain behaviour and yielding characteristics are considered. Finally the behaviour of HPF4 is compared with the behaviour of some other soils tested recently at Imperial College.

4.2. Consolidation and swelling characteristics of HPF4

4.2.1. Consolidation procedure for triaxial samples

4.2.1.1. K_o consolidation

As stated in Section 3.5, both triaxial and hollow cylinder samples were K_o consolidated, as this simulates the in-situ state of most soils before they are subjected to any engineering construction. Methods for estimating K_o values for a given material have been summarized and described elsewhere (Gens, 1982; Menkiti, 1995). The normally consolidated K_o values for HPF4

used in this study were determined using a trial and error procedure to control zero lateral straining during the consolidation of trial triaxial samples. Figures 4.2 and 4.3 illustrate this iterative procedure. The first part of the *t-p'* diagram in Fig.4.2 is a normal consolidation stress path for a K ($=\sigma_r'/\sigma_z'$) value of 0.45. This gave a $\varepsilon_{vol}/\varepsilon_z$ ratio of about 0.6, Fig.4.3. As zero radial strain corresponds to $\varepsilon_{vol}/\varepsilon_z=1$, this indicates that the confining pressure was too small and therefore the K value too low. The strain origin for this first consolidation path was at t=30 kPa and p'=70 kPa, which is the stress state at which the sample first experienced K=0.45. When K was increased to 0.5, the $\varepsilon_{vol}/\varepsilon_z$ ratio came close to unity, see Fig.4.3, and consequently this value was adopted as K_o for all subsequent tests. The strain origin for this K_o path was at t=56 kPa and p'=146 kPa which is the stress state at which the sample first experienced K=0.5. Figure 4.4 summarizes the relation between volumetric and axial strain during normal consolidation for all subsequent triaxial compression and extension tests (with strain origins at t=25 kPa and p'=70 kPa). All curves follow very well the line $\varepsilon_z = \varepsilon_{vol}$ ($\varepsilon_r = 0$) and therefore confirm the choice of K_o=0.5.

The duration of K_o consolidation was 24 hours, so that the applied strain rate was, on average, 1.0 %/day for both axial and volumetric strains (Fig.4.5a, b). Subsequently a drained creep period of 24 hours, in which the effective stresses on the sample were held constant, was allowed to enable strains to stabilize. A creep strain rate of 0.05 %/day (i.e. 0.002 %/hour), which is 1/100 of the shearing strain rate, was adopted as a criterion for stabilization. Plots of typical strain rates during K_o consolidation, calculated as $\Delta\varepsilon/\Delta t$ (where t is the time), are given in Fig.4.6a, b. The initial creep rate, immediately after K_o consolidation (24 hours), was 0.035%/hour, Fig.4.6a. It dropped to the desired value of 0.002%/hour, or less, during the last five hours of the creep period (see enlarged view in Fig.4.6b).

The mean effective stress at the end of normal consolidation was 200 kPa, under a back pressure of 400 kPa. The consolidation stress paths for all samples are presented in Fig.4.7. These show the excellent repeatability of the consolidation procedure.

4.2.1.2. K_o swelling

As some tests were to be performed on overconsolidated HPF4 (OCR's of 1.3, 2 and 4) some samples were subjected to K_o swelling after initial consolidation. The K_o values applied to swell samples to these OCRs were calculated from the Mayne & Kulhawy (1982) formula:

$$(K_o)_{OC} = (K_o)_{NC}(OCR)^{\sin\phi} \quad (4.1)$$

where:

$(K_o)_{OC}$ - swelling coefficient

$(K_o)_{NC}$ - coefficient in normal consolidation (=0.5)

ϕ' - angle of shearing resistance, taken as ϕ'=32° at the Phase Transformation Point observed in undrained compression tests on normally consolidated samples of HPF4.

The variation of K_o with OCR is presented in Fig.4.8. It shows an increase of $(K_o)_{OC}$ with overconsolidation. During the swelling stages, the effective stress paths followed linear sections in *t-p'* space between stress points calculated with $(K_o)_{OC}$ at OCRs 1.0, 1.3, 2.0 and 4.0.

The maximum duration (24 hours) of the swelling phase was for OCR=4.0, which swelled back to the isotropic axis. For other OCR's, swelling was achieved in proportionally shorter times. In the same manner as after K_o-consolidation, a creep period was allowed after swelling was completed, for strains to stabilize. As a total period of 48 hrs was allowed for the swelling phase and creep period, the creep period was longer for the samples with lower OCR's. Typical strain-time curves are presented in Fig.4.9a, b, for both axial and volumetric strain. Strain rates of both these strains during K_o-swelling and subsequent creep are plotted in Fig.4.10. These plots show that the creep strains reduced to the target value of 0.002%/hour or less within around 10 hours. Also evident is the non-linearity in strain rate vs. time curve during swelling and the swelling tangent bulk modulus K' ($=\Delta p'/\Delta\varepsilon_{vol}$) is shown in Fig.4.11. In these plots the strain origin for swelling is taken at the end of the K_o-consolidation stage, i.e. at t=75 kPa and p'=200 kPa.

The ratio of volumetric and axial strains during swelling for all tests is presented in Fig.4.12, where the strain origin is defined at the end of the creep period after K_o consolidation, (t=75 kPa and p'=200 kPa). This diagram indicates a spread of results, with $\varepsilon_z/\varepsilon_{vol}$ varying by about ±0.2 from a trend line, for which $\varepsilon_z/\varepsilon_{vol}\approx 0.8$. It appears that the path followed led to slightly excessive volumetric swelling, that is K_o should have increased marginally more rapidly with OCR. However, the differences are relatively small (0.04% strain at most) and were considered to be acceptable.

The swelling effective stress paths followed by all overconsolidated samples, are presented in Fig.4.13. These show the excellent repeatability of the swelling procedure.

4.2.2. Compressibility of HPF4

4.2.2.1. During virgin K_o consolidation

Fig.4.14a presents the set of *v-lnp'* traces found during K_o consolidation and swelling to different OCRs in all the triaxial tests on HPF4. The same data are plotted in *e-log*σ_v' space in Fig.4.14b. These plots show the recognized difficulties inherent in trying to set up granular samples to exactly the same initial void ratio. The average value of the initial void ratio, e_o, was 0.65, with a scatter of ±0.03, which was considered as acceptable. As outlined in Chapter 2, granular materials exhibit a multiplicity of normal consolidation lines, each line corresponding to a given initial void ratio and fabric. For the range of stresses applied to the samples in this study, which covers the usual engineering range (up to 1.0 MPa mean effective stress), the normal consolidation curves are parallel to each other and do not converge onto a unique, steeper, straight virgin consolidation line (Fig.4.14a, b). However, they are non-linear and become steeper with increasing effective stresses: for the applied mean effective stress of 200 kPa, the compression index, C_C *(=*$\Delta e/\Delta(\log\sigma_v')$*)*, varies, as an average from all tests, from 0.0264 for $100<\sigma_v'<200$, to 0.03586 for $200<\sigma_v'<300$ kPa (see Fig.4.15b - for the OCR=4.0 consolidation path). In the same way, λ *(=*$\Delta v/\Delta(lnp')$*)* varies from 0.0121 for $100<p'<150$ to 0.01575 for $150<p'<200$ kPa (Fig.4.15a). The typical Δe during the creep period is 0.0015, which is ~(1/10) of the volumetric change during K_o consolidation.

Following the ideas reviewed in Chapter 2, concerning the position of the virgin consolidation line for granular materials, a high pressure oedometer test was performed on HPF4. The maximum axial force that could be achieved in the high pressure oedometer (Cotecchia, 1996) was 50 kN, giving a maximum vertical effective stress of ~20 MPa. The sample was set up from slurry using the same technique as for the triaxial and hollow cylinder specimens (see Chapter 3). The resulting *e-*σ_v' curve is presented in Fig.4.16. Coop (1990) showed that K_o for sand does not change with increasing consolidation stresses. Therefore, if K_o=0.5 (as measured in triaxial one-dimensional consolidation test) is taken, Fig.4.16 can be replotted in *v-lnp'* plot (i.e. $p'=2/3\sigma_v'$, Fig.4.17). The curves are significantly non-linear and clearly the maximum vertical stress of 20 MPa is not sufficient for any conclusions to be made as to whether or not a unique VCL has been reached. Even when plotted in log-log diagram (Fig.4.18a, b), the non-linearity persists.

It can be concluded that the one dimensional behaviour of HPF4 agrees with the generally accepted framework for sands, but does not tend to a unique log-linear virgin

consolidation line at σ_v'<20 MPa.

4.2.2.2. During K_o swelling

The swelling paths in *e-lnp'* and *e-logσ_v'* diagrams shown in Fig.4.14 are parallel to each other for different OCRs. The initial part of a typical swelling line (Fig.4.15) is almost flat, while the rest of the line follows an upward trending curve (as seen in Fig.4.10). However, the average value of swelling index, C_S, is 0.00708 and the average value of the inclination of the *e-lnp'* swelling path, $\varkappa$, is 0.004282.

4.3. Undrained triaxial compression tests

4.3.1. Description of stress paths

The effective stress paths followed during triaxial compression tests performed on samples consolidated and swelled under K_o conditions to OCR levels of 1.0, 1.3, 2.0 and 4.0, are presented in Fig.4.19a, b. The difference between these figures is that the former has the slopes of the various parts of the stress paths marked, whereas the latter has contours of axial strain superimposed. Both figures show the earlier parts of the stress paths. The complete stress paths are shown in Fig.4.20. Several significant features of behaviour can be observed:

i) None of the samples reached a well defined peak deviator stress condition. Instead, all stress paths rose to a line inclined at t/p'=0.75, equivalent to ϕ'=37°, and then travelled up this line, (Fig.4.20). Tests were stopped after 10% to 20% axial strain was reached because of limitations in the travel of the loading piston, or premature detachment of the local strain devices. At this time the effective stress paths (Fig.4.20), were still climbing steeply, without reaching a stable, critical, state. As noted in Chapter 2, dense granular materials dilate to very high mean effective stresses before critical state conditions are reached.

ii) The effective stress paths show at least four distinct phases, Fig.4.19a.

For the samples with low OCR's, the stress paths rise at an almost constant initial slope (labelled as 'slope 1') from their final consolidation stresses (O), until the axial strains exceed ~0.02%.

After reaching this strain, the effective stress paths of overconsolidated samples turn clockwise, whilst that of the normally consolidated sample rotated in the opposite sense. The

paths again tend towards constant gradients ('slope 2'), until a distinct anti-clockwise rotation of the effective stress path occurs at a yield point marked as Y_3 on Fig.4.19a. The normally consolidated sample does not have the well defined second phase observed in the tests on overconsolidated samples. The angular rotation of the effective stress paths reduced with increasing OCR.

The third distinct phase of behaviour (which again corresponded to a stage with nearly constant $\Delta t/\Delta p'$ gradient, i.e. 'slope 3') spans the range from the Y_3 yield point to the Phase Transformation Point (PTP). This stage involves a contractant response with p' decreasing as t increases. The tendency to contract reduces with OCR and completely diminishes at OCR=4.0. The fourth stage commences at the PTP, where the effective stress paths undergo clockwise rotation again and show a highly dilatant response as the value of t increases.

Table 4.1 gives the values of the gradients shown over the first three phases, while Fig.4.21 shows how these gradients varied with OCR. The initial slope of the undrained effective stress path ('slope 1') increases with OCR, becoming nearly vertical for OCR=4.0. The slope of phase 2 (i.e. 'slope 2') decreases with OCR and that of phase 3 ('slope 3)', which is a measure of the contraction of the stress path, reduces from OCR=1.0 and even changes sign at OCR=4.0.

Table 4.1: Slope $\Delta t/\Delta p'$ at different stages of the undrained compression ESPs

OCR	slope 1 (0 to Y_2)	slope 2 (Y_2 to Y_3)	slope 3 (Y_3 to PTP)
1.0	2.35	∞	-1.50
1.3	3.30	2.37	-1.10
2.0	3.71	1.45	-4.00
4.0	∞	1.20	2.43

4.3.2. Stress-strain behaviour

The stress strain curves, t-ε_z, are presented in Fig.4.22. As noted above, tests were terminated after 10% to 20% axial strain was reached. Fig.4.22a shows that at these large strains all samples were sustaining positive gradients $\Delta t/\Delta\varepsilon_z$. This is consistent with the stress paths shown in Fig.4.20 and clearly indicates that critical state conditions had not been reached. The

reason for such behaviour follows from the particulate nature of the granular HPF4 material where the particles' shape and depositional method determine the initial fabric which continuously changes to sustain external stresses. This has been discussed in detail in Chapter 2.

Since the undrained compression tests on HPF4 did not indicate distinct peaks, the t_{max} values are arbitrary, depending only on the maximum strain permitted. Instead, deviator stresses at the Phase Transformation Points (PTP's) will be used as gauges of "undrained shear strength" when comparing the material characteristics at different OCR's (Tatsuoka & Ishihara 1974, Ishihara et al. 1975). The PTP on an undrained stress path is defined as the position where the gradient $\Delta u/\Delta\varepsilon_z=0$ and after that point increases rapidly (Fig.4.23). The PTP's are marked on the stress paths presented in Fig.4.19. It can be seen that the deviator stress, t, at the PTP's reduces systematically with OCR, from 120 kPa at OCR=1.0 to 87 kPa at OCR=4.0. The values of axial strain at which the PTP's were reached are plotted in Fig.4.24 and show a steady increase with OCR. The stress ratios (t/p') at the PTP's are very close to the line t=0.63p', which corresponds to an angle of shearing resistance of ϕ'=32°. The mobilised ϕ' value increases after passing the PTP's to reach a maximum of 37°.

While critical state conditions were not reached in these tests, ϕ_{cs}' can be roughly estimated from the undrained triaxial tests by Ovando-Shelley (1986), where for loose HPF4 (e_o=0.95) ultimate ϕ' values of 34° were achieved after around 10% axial strain.

4.3.3. Undrained compression stiffness

Curves of secant undrained Young modulus, E_u (=$\Delta q/\varepsilon_z$), against axial strain, normalized by the mean effective stress after consolidation, p_c', are presented in Fig.4.25a. The overconsolidated samples show a consistent trend for E_u/p_c' to increase with OCR. However, the normally consolidated sample is much softer than this trend would suggest. The reason for this is that overconsolidation moves the current effective stress points inside the local Bounding Surface developed as a result of the large strain consolidation history. The Kinematic Sub Yield Surfaces move with the effective stress point and become reoriented away from the virgin consolidation stress path towards the direction of the swelling path (see Chapter 2). On shearing, the compression test stress path direction deviates more sharply from the swelling paths, than it does from the normal consolidation path. The overconsolidated samples track across a far more extensive portion of their small strain Kinematic Sub Yield Surface.

The influence of the overconsolidation ratio on stiffness, for different strain levels, is presented in Figs.4.26 and 4.27. The plots show three trends:

a) The marked difference in normalised stiffness between OCR=1.0 and 1.3 remains evident for strains between 0.001% and 0.1%, from the slopes of the $logE_u/p_c'$-$logOCR$, or $logE_u$-$logp_c'$ lines constructed for equal strain values. The value of $(E_u/p_c')_{OCR=1.0}$ is about 45% smaller than $(E_u/p_c')_{OCR=1.3}$. When $\varepsilon_z \geq 1.0\%$, the difference reduces and the normalised stiffnesses for all OCR's plot on a single line in $logE_u/p_c'$-$logOCR$ space.

b) The compression E_u/p_c' values of overconsolidated samples (OCR≥1.3) are not constant for any given strain level, but increase with OCR and decrease with mean effective stress level.

c) Excluding the OCR=1.0 data, the stiffnesses deduced at fixed strain levels appear to plot as straight lines in $logE_u$-$logp'$ space in Fig.4.27. The gradients $\Delta(logE_u)/\Delta(logp_c')$ increase with strain level from 0.717 at ε_z=0.001%, to 0.848 at ε_z=0.1%, as summarized in Table 4.2.

Table 4.2:

ε_z (%)	$\Delta logE_u/\Delta logp'$
0.001	0.717
0.01	0.763
0.1	0.848

This trend is in agreement with what has been shown recently by Porovic (1995), that the power n in logarithmic relation between stiffness and mean effective stress, $G=A(p')^n$, increases with strain level. However, this range of p' values (88 to 200 kPa) is not extensive and as OCR varied as well as p', the values of n may not be exact. It should be noted here that normalization for different values of initial e_o was not carried out (Hardin & Richart, 1963; Jamiolkowski et al., 1991; Lo Presti et al., 1993), because the variations in e_o were small.

The variation in stiffness is also shown in terms of axial strain contours in Fig.4.19b. The contours appear to rotate slightly as strains increase, from a direction approximately parallel to the K_o swelling line, to a direction parallel to the effective stress failure envelope.

Fig.4.25b shows relation of tangent and secant Youngs moduli for OCR=1.0 and 1.3.

As expected, the tangent values decrease more steeply with strain.

4.4. Undrained triaxial extension tests

4.4.1. Description of stress paths

The effective stress paths developed in undrained extension tests on K_o consolidated samples are presented in Fig.4.28. As with compression tests, at least four stages can be identified, although it is more difficult to divide the extension paths into distinct linear segments. On moving away from their final consolidation points (O), the effective stress path directions $\Delta t/\Delta p'$ initially follow practically the same gradients as those quoted in Table 4.1 (i.e. 'slope 1'). Once an axial strain of about 0.01% has been reached, the paths show gradual clock-wise rotations. Tentative Y_3 points are marked on the effective stress paths, although the yielding process is clearly progressive rather than abrupt. The response is markedly contractant between the marked Y_3 points and the clear PTPs, with samples dilating strongly when they reach the latter.

The large strain shearing process is unstable in extension and three out of the four specimens underwent a premature necking failure (point U) at relatively low values of p'. The value of the mobilised angle of shearing resistance at the end of the tests just prior to necking failure was $\phi'=30^0$. This compares to 37° observed in the compression tests.

The mobilised ϕ' value at the PTP's is 25°, which compares with 32° in triaxial compression.

4.4.2. Stress-strain behaviour

As with the compression tests, the Phase Transformation Points will be used to compare material undrained "strength" at different OCR's. The first point to note is that deviatoric stress t at the PTP's again reduces with OCR: from 31 kPa at OCR=1.0 to 24 kPa at OCR=4.0. This decrease of 22% in deviator stress from OCR=1.0, compares with the decrease of 27% seen in compression tests.

The stress-strain curves are presented in Fig.4.29. All curves are smooth and orderly up to 2% axial strain. As indicated on these curves all samples reached the PTP at an axial strain

of 1.0%.

4.4.3. Undrained extension stiffness

The extension secant stiffness-strain curves are presented in Fig.4.30. In comparison with the compression data, a greater spread of results is seen among the overconsolidated samples. Also, in contrast to the compression data, the normalised stiffness (E_u/p_c') now decreases with increase in OCR and the normally consolidated sample shows the stiffest response.

The influence of OCR on stiffness, at different strain levels, is presented in Fig.4.31. Unlike compression tests, the plot shows a gradual decrease of normalised stiffness, E_u/p_c', with OCR at all strain levels and all $log(E_u/p_c')$-$log(OCR)$ slopes are nearly parallel.

Similar behaviour can be seen when the data is plotted in $logE_u$-$logp_c'$ space, Fig.4.32. The $\Delta(logE_u)/\Delta(logp_c')$ gradients vary less strongly with strain level than in the compression tests.

Strain contours are plotted in Fig.4.28b. As with the compression data, a gradual rotation, with increasing strain, of the contours can be seen from the swelling line towards the failure line.

As in compression tests, tangent extension stiffness decays more rapidly with strain than secant stiffness (Fig.4.30b).

4.5. Normalization behaviour of HPF4

Rendulic's principle has been discussed in detail in Chapter 2. If this principle is true then material behaviour can be normalised by dividing the effective stress variables by p_e', the mean effective stress on the virgin consolidation line corresponding to the current void ratio. Such normalisation depends on there being a unique virgin consolidation line. This principle has been found to work well for soils like clays and clay-silts.

As discussed in Chapter 2, the behaviour of granular soils is more complex. At engineering levels of stress the position of the normal consolidation line depends on the initial voids ratio and fabric of the soil. This results in a whole suite of normal consolidation curves,

even though the soil is currently being subjected to the maximum effective stress it has ever sustained (Fig.4.14). Such normal consolidation lines are therefore not unique. Only when the soil is subject to extremely large effective stresses, where soil particles begin to crush, do these normal consolidation lines merge to form a unique virgin consolidation line. As noted in Chapter 2, some researchers claim this virgin consolidation line is straight in *e-log*σ_v' space. If this is correct, then the virgin consolidation line and its extension to lower stress levels could be used to evaluate p_e'. Other researchers (Juarez-Badillo, (1963, 1977), Ovando-Shelley, (1986)) used the normal consolidation line obtained in engineering stress ranges to determine p_e'.

From the results presented in this Chapter, it is clear that HPF4 behaves like a granular material and therefore the two options described above for calculating p_e' are possible. As shown in Fig.4.16, the high pressure oedometer test on HPF4 did not generate enough vertical stress to show a convincing yield point after which the soil followed a straight virgin consolidation line. Fig.4.33 shows a tentative critical state line (CSL) and VCL, estimated from Ovando-Shelley's data on loose HPF4: point A is a starting point of his tests, with e_0=0.95; point B is estimated from the ratio of the final consolidation mean effective stress (p_o') and p' where the failure line is reached. Even if this line was straight, the results shown in Fig.4.33 indicate that there would be two serious problems in using it to calculate p_e'. Firstly the values of p_e' would be at least an order of magnitude greater than the engineering stresses used in the triaxial tests and any normalisation would be prone to slight inaccuracies in the values of p_e'. Secondly, the variations in the initial void ratios of the triaxial samples, when combined with the small range of the consolidation stresses used, would lead to illogical values of p_e'. For example, the extension sample with OCR=4 has a p_e' value greater than that of the extension sample with OCR=2. No attempt has therefore been made to normalise the current results using this approach.

The second option discussed above has been used to evaluate p_e' for the normalised effective stress paths (NESP's) presented in Fig.4.34. For each sample p_e' has been calculated from the normal consolidation curve observed on that sample. An example of the procedure used is shown for a sample with OCR=4 in Fig.4.35. From this figure it can be seen that the slope of the swelling line is roughly constant and that there is a measurable change in specific volume during the creep period at the end of K_o consolidation. In order to eliminate the effect of the creep strains, the swelling line is re-positioned (moved upward in Fig.4.35) so that it intersects the NCL prior to the onset of creep. The value of the mean effective stress on the NCL at the same void ratio as that at the end of the re-positioned swelling line (OCR=4) is taken as p_e'.

Inspection of the NESP's for both the compression and extension tests given in Fig.4.34 indicates that the curves for the normally consolidated samples do not provide a truly unique bounding surface (BS) for the behaviour of the overconsolidated samples. The NESP's for the overconsolidated samples do not follow a single curve after Y_3 yielding. They only approach those of the normally consolidated samples when they reach the failure line, after the PTPs have been passed.

4.6. Discussion

4.6.1. Introduction

In this Section the observed behaviour of HPF4 will be compared to the triaxial response observed in other soils tested recently in the IC laboratory. In particular the behaviour will be compared to that of the following materials;

- Ham River Sand (HRS) (Ovando-Shelley, 1986). This is a quartz based sand that was prepared in a loose state with an initial void ratio e_o=0.8.

- Dunkirk Sand (DKS) (Kuwano, 1995). This is a quartz based sand with approximately 10% calcareous shell fragments, prepared in a dense state with an initial void ratio e_o=0.65.

- HRS+10% Kaolin Mixture (HK) (Georgiannou, 1988). This was prepared in loose state with an initial void ratio e_o=0.8.

- HPF4 (Ovando-Shelley, 1986). This is the same material as used in the present research but was prepared in a loose state with an initial void ratio e_o=0.95. In the present study dense samples with e_o=0.65 were tested.

- Artificial Clay (KSS) (Rossato, 1992). This material was prepared by mixing 50% kaolin with 25% fine sand and 25% silt and consolidating it from a slurry.

- Lower Cromer Till (LCT) (Gens, 1982). This is reconstituted low plasticity boulder clay which was consolidated from a slurry.

- Pentre Clay (PEN) (Connolly, 1995). This is a natural silty clay.

- Bothkennar Clay (BC) (Smith, 1992). This is a natural high plasticity clay.

The grading curves for these materials are compared in Fig.4.36. All soils have been tested after K_o consolidation followed by K_o swelling to a range of OCR's. In all cases, tests were performed covering the usual range of stresses encountered in engineering problems (i.e. mean effective stresses between 200 kPa to 450 kPa).

4.6.2. Compressibility

Fig.4.37 compares the compressibility, under K_o conditions, of HPF4 with that of some of the materials listed above. The volume change of dense HPF4 silt during K_o consolidation appears to be about 50% greater than for coarser granular materials like HRS and HK, but much smaller than for clayey materials such as the KSS mixture. The dense HPF4 is also far less compressible than the low plasticity natural clay-silt from Pentre (PEN), or the more plastic Bothkennar clay-silt (BC). The Pentre materials show a spread of volume change behaviour, depending on whether the samples were relatively silty or clayey, or had laminated or marbled macro-structures.

4.6.3. Stress-strain behaviour

The effective stress paths (ESP's) observed in undrained triaxial compression and extension tests following K_o consolidation and swelling to a range of OCR's are presented in Fig.4.38 for several of the materials listed above.

The results for LCT and KSS show the typical behaviour associated with clay soils. The normally consolidated ESP's all indicate contractant behaviour when sheared. This tendency diminishes with OCR and after a critical OCR of about 3.0 is exceeded, samples tend to dilate. All ESP's indicate a well defined final stress state which corresponds to the critical state. The effective stress paths shown in Fig.4.38 indicate that samples prepared with a common maximum p' value almost conform to a unique local bounding surface. When normalised by p_e' to take account of water content changes during swelling, the local BS becomes even more well defined. The behaviour of natural Pentre clay-silt (PEN), when consolidated to effective stresses well above its in-situ p', also follows the general behaviour associated with clay soils.

The behaviour of sand is illustrated by the results from HRS and DKS. With dense DKS the shearing in compression leads to p' increasing at all OCR's, while the response in extension is initially contractant and then dilatant. The effective stress paths travel along an inclined failure line to high values of mean effective stress. Within the range of engineering stresses they show no sign of reaching a well defined final stress state. This is in agreement with general behaviour of granular materials discussed in Chapter 2. If the stress paths are normalised with respect to their current normal overconsolidation lines, those from the normally consolidated samples do not provide a bounding surface that applies to the overconsolidated ones. The large strain behaviour of loose HRS is similar. However, the samples tested in compression show strongly contractant behaviour before they reach Phase Transformation Line. Unlike dense sand, the effective stress paths tend towards a more well defined BS when normalised with respect to current NCL, although the phase transformation points do not coincide (Ovando-Shelley, 1986; Porovic, 1995).

It is interesting to compare the results from the tests on HRS and HK in more detail. HK consists of 90% HRS mixed with 10% kaolin. Both soils had an initial void ratio of 0.8. It is evident that the addition of the small quantity of kaolin has a marked effect on the shape of the stress paths. For the compression tests, the onset of contraction is abrupt and is so intense that it results in a drop in deviatoric stress. Quite large positive pore water pressures are generated before the material undergoes phase transformation and begins to dilate. The effective stress paths then travel up the failure line to large values of mean effective stress in a similar manner to loose sands. As with clays, the behaviour of normally consolidated samples provide a bounding surface for the overconsolidated ESP's.

Comparing the behaviour of HPF4 with the other materials it is evident that it follows the general pattern established for sands. Loose samples of HPF4 behave similarly to loose HRS, and dense HPF4 responds in the same way as dense DKS. The dense HPF4 shows a strongly dilatant response in compression and does not reach a clear peak resistance or critical state in either compression or extension. A far more contractive response is observed in extension, with p' falling by up to 50% before reaching the Phase Transformation Point. In a similar fashion to that observed for dense sands, the dense HPF4 exhibits a weaker 'memory' of its past stress history than do most clay soils. Consequently, when tested in an overconsolidated state, its yielding characteristics appear to be less clearly associated with those shown by normally consolidated samples. This can be seen from the overconsolidated stress paths which show yielding (i.e. effective stress path rotation) well inside the bounding surface corresponding to

normally consolidated behaviour.

4.6.4. Stiffness behaviour

In the light of the simplified model for pre-failure behaviour, described in Chapter 2, undrained tests after K_o overconsolidation are special cases from the general set of possible combinations of perturbing stress paths and recent stress histories. The effective stress paths on Fig.4.38 show that at the beginning of the undrained tests, the stress path abruptly changes its direction, causing the current effective stress points to re-enter the Y_1 and Y_2 zones, (Chapter 2).

In the series of triaxial tests presented in this Chapter, the instrumentation used for local strain measurement could not reliably resolve strains within the elastic region (i.e. Zone I). The stiffness in this region can therefore not be quantified and the effect of OCR on the value of G_{max} for HPF4 was not established. In the literature there are arguments to whether overconsolidation influences the relationship between G_{max} and p' or not, with evidence being quoted to support both statements (Porovic,1995; Jamiolkowski, 1991; Viggiani, 1995).

In agreement with Porovic (1995) the HPF4 triaxial test data show that the effects of overconsolidation become marked beyond the linear range. If 0.01% strain level is taken as a boundary for the Y_2 sub-yield surface at each of the final swelling points, then from the strain contours in Fig.4.39 it can be seen that the KSYSs are not located symmetrically about their local stress origins. For OCR=1.0 the unloading response is stiffer than that in loading, while the opposite is true for overconsolidated samples. This is illustrated in Fig.4.40 where the ratio of E_u in compression and E_u in extension, at $\varepsilon_z = 0.01\%$, is plotted for different materials:

$E_u^{(com)} / E_u^{(ext)} < 1.0$ for OCR = 1.0 and

$E_u^{(com)} / E_u^{(ext)} > 1.0$ for OCR > 1.0

The broken line represents the dense HPF4 tested for this thesis.

In Fig.4.41 the ratio of (E_u/p_c') for overconsolidated samples and (E_u/p_c') for normally consolidated samples in compression, at ε_z=0.01%, is plotted for different soil types tested over a similar stress range. The broken line again represents HPF4. For all materials this ratio can rise or fall between OCR= 2.0 and 10.0, but common for all soils is the extremely low compression stiffness at 0.01% strain for OCR<1.5.

The general picture, therefore, clearly shows that K_o swelling relocates the Y_1 and Y_2 sub-yield surfaces and the overconsolidated shearing stress paths in compression represent a much larger change in effective stress path direction than was the case for NC samples, or is experienced by samples tested in extension. That is the "directional" response can be seen as a function of stress history/perturbing stress path direction, rather than a truly inherent anisotropy.

4.7. Summary

The suite of triaxial tests identifies some of the main parameters for HPF4:

- The coefficient of earth pressure at rest, K_o, for dense normally consolidated HPF4 (e_o=0.65), was found to be 0.5.

- As for all granular materials, a multiplicity of normal consolidation lines was evident, with *v-lnp'* and *e-log*σ_v*'* curves being non-linear over the engineering range of stresses. The compression index, C_c, varies from 0.0264 for $100<\sigma_v<200$ kPa, to 0.03586 for $200<\sigma_v<300$ kPa and 0.255 for $10<\sigma_v<20$ MPa. The value of λ varies from 0.0121 for $100<p'<150$ kPa to 0.1575 for $150<p'<200$ kPa. The swelling behaviour is such that swelling indices, C_s=0.00708 and $\varkappa$=0.004282.

- Effective stress paths developed during shear show a highly dilatant large strain response, without a clearly defined peak deviator stress being obtained.

- The undrained strength, taken as the deviator stress at the Phase Transformation Points, decreases with OCR in both compression and extension. The maximum difference is 25% on average, between OCR=1.0 and OCR=4.0.

- The mobilized ϕ' value at the PTPs is 32° in compression and 25° in extension.

- The maximum mobilized ϕ' value is 37° in compression and 30° in extension.

- Compression stiffness, E_u/p_c', increases with OCR, while extension stiffness decreases with OCR.

HPF4 follows a similar pattern of stress-strain behaviour to that seen previously with

dense granular soils. It appears to show strong anisotropy in the two types of undrained tests that can be performed in the triaxial cell: triaxial compression, where $\alpha=0°$, and triaxial extension, where $\alpha=90°$. However, the results give no information concerning behaviour at intermediate values of α and are not strictly representative of anisotropy, because during triaxial compression b is equal 0.0, while in extension it is 1.0. The effects of principal stress rotation and intermediate principal stress changes (i.e. b values) are therefore combined and the contribution of each of these parameters cannot be separated through triaxial testing alone.

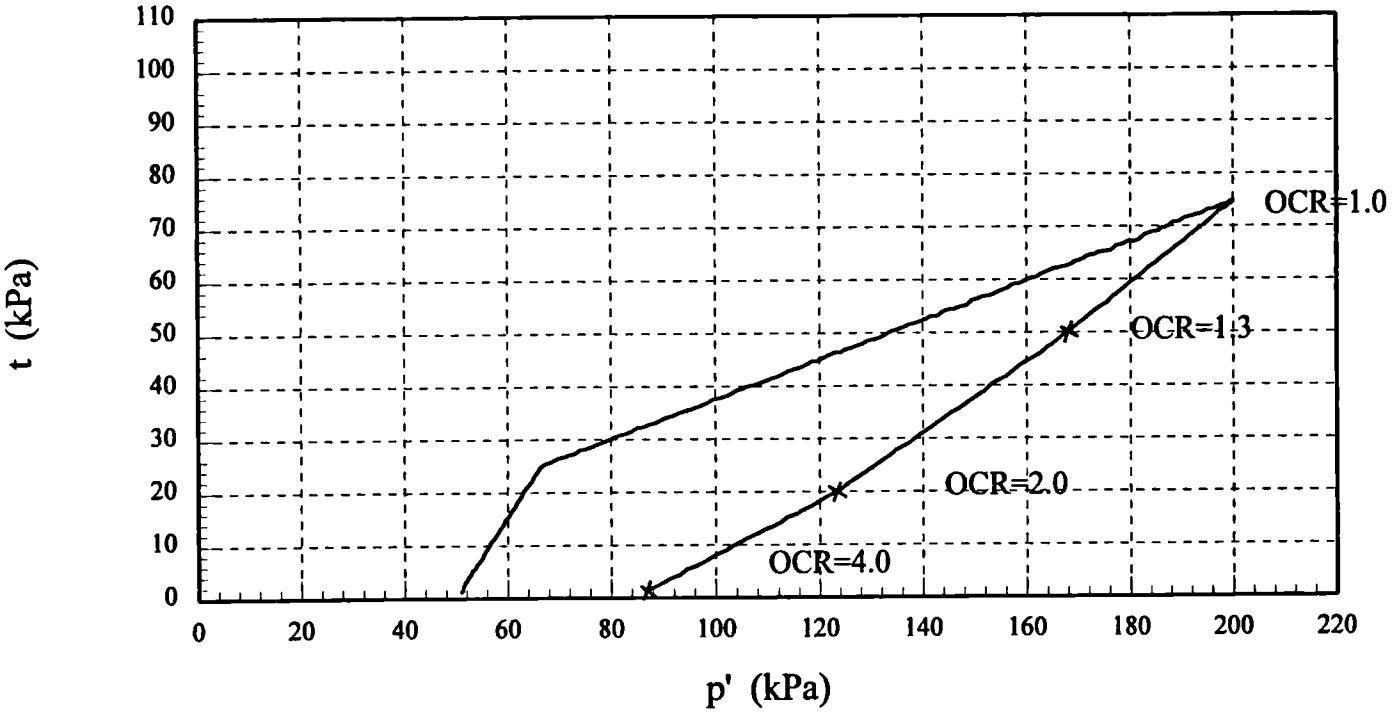


Fig.4.1 - Consolidation paths planned for triaxial test Series

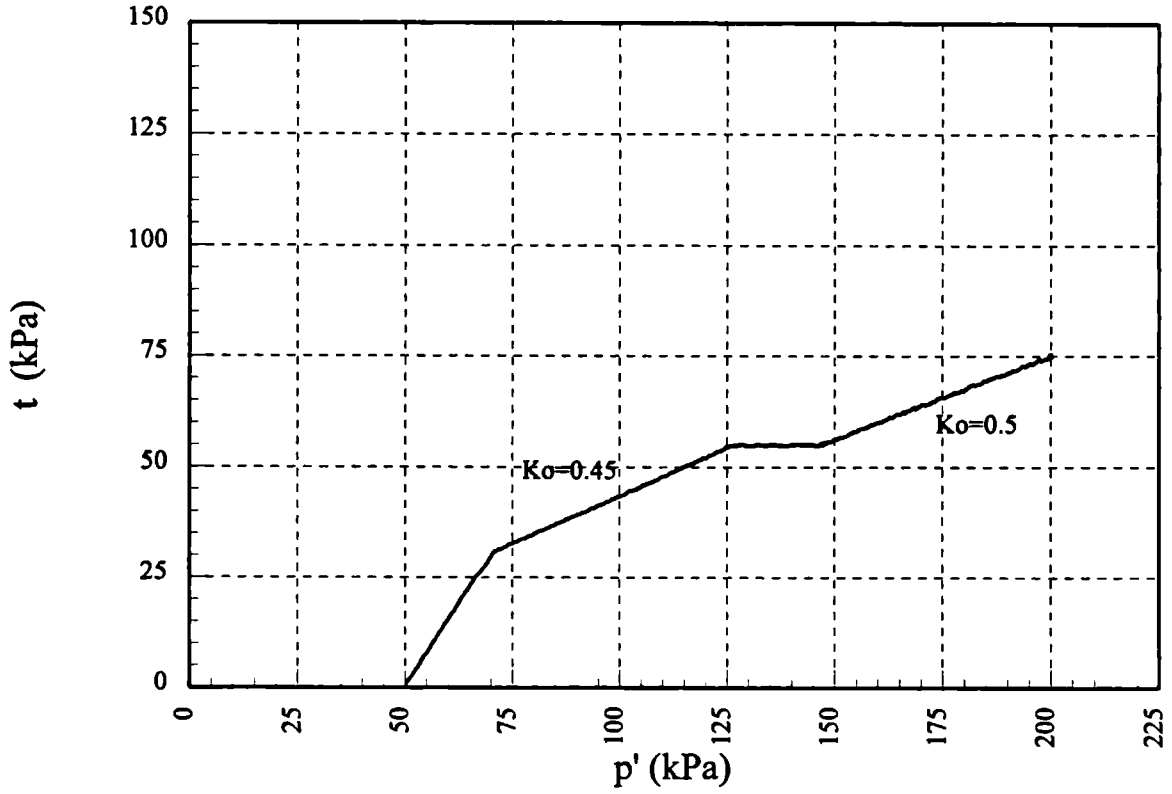


Fig.4.2 - Trial and error procedure for estimating Ko value for one-dimensional consolidation

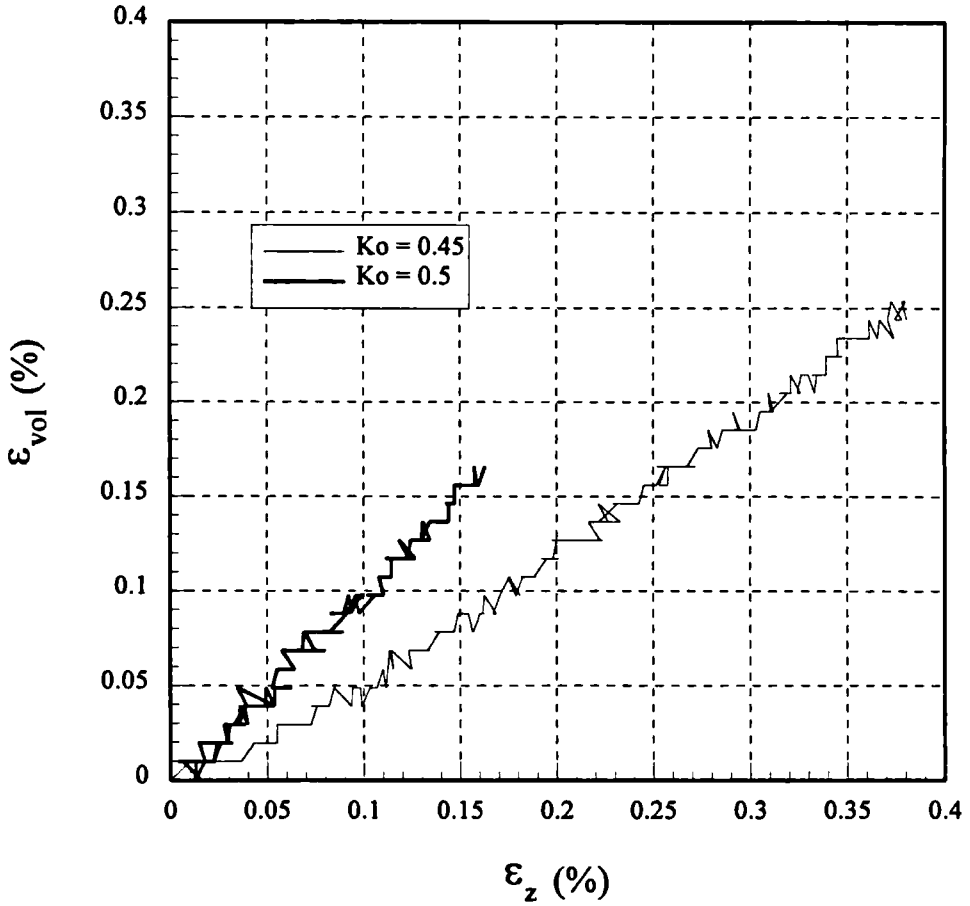


Fig.4.3 - Volumetric vs. axial strain during K-consolidation for different K values

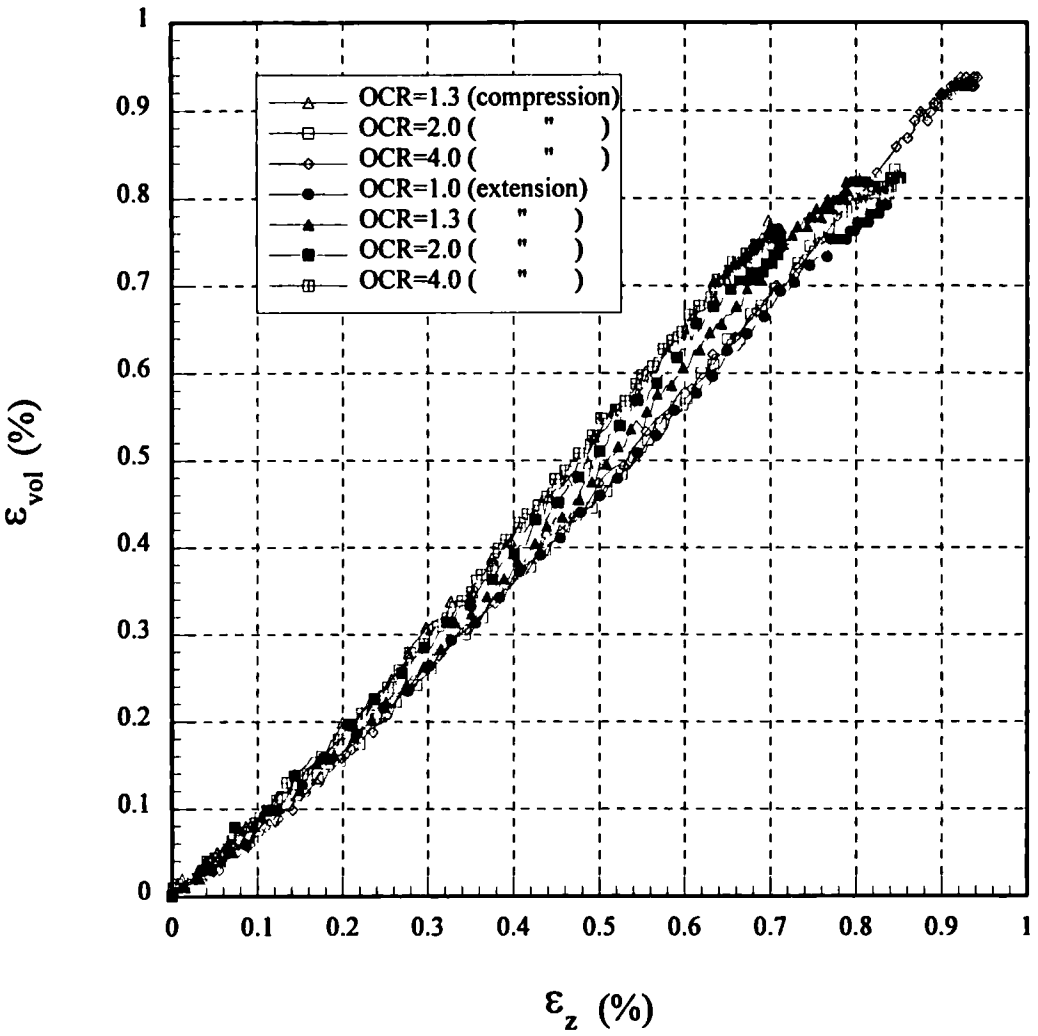


Fig.4.4 - Volume change vs axial strain during Ko consolidation of HPF4 silt in triaxial apparatus

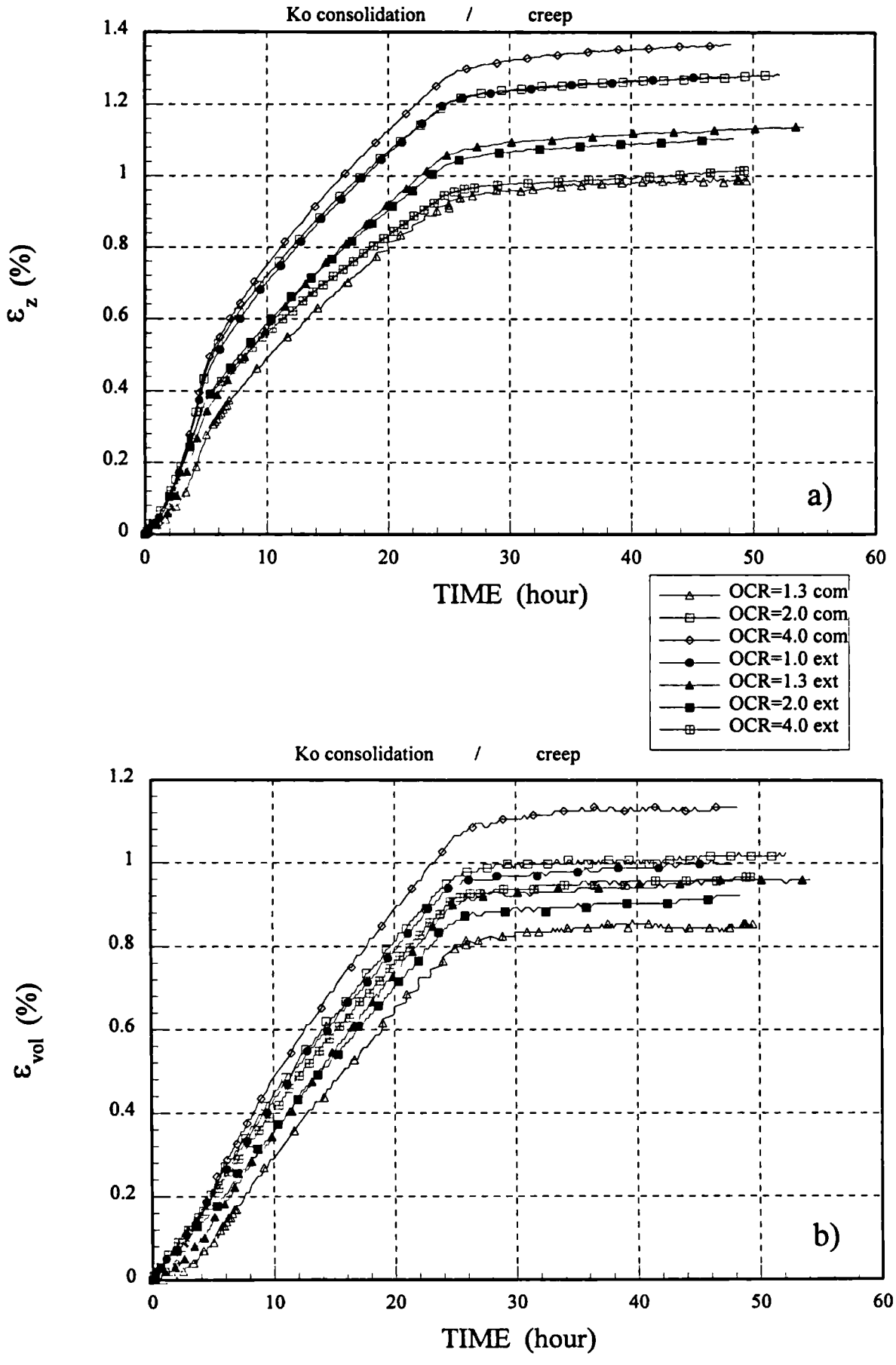


Fig.4.5 - Time dependance of strains during Ko consolidation:
a) axial and b) volumetric

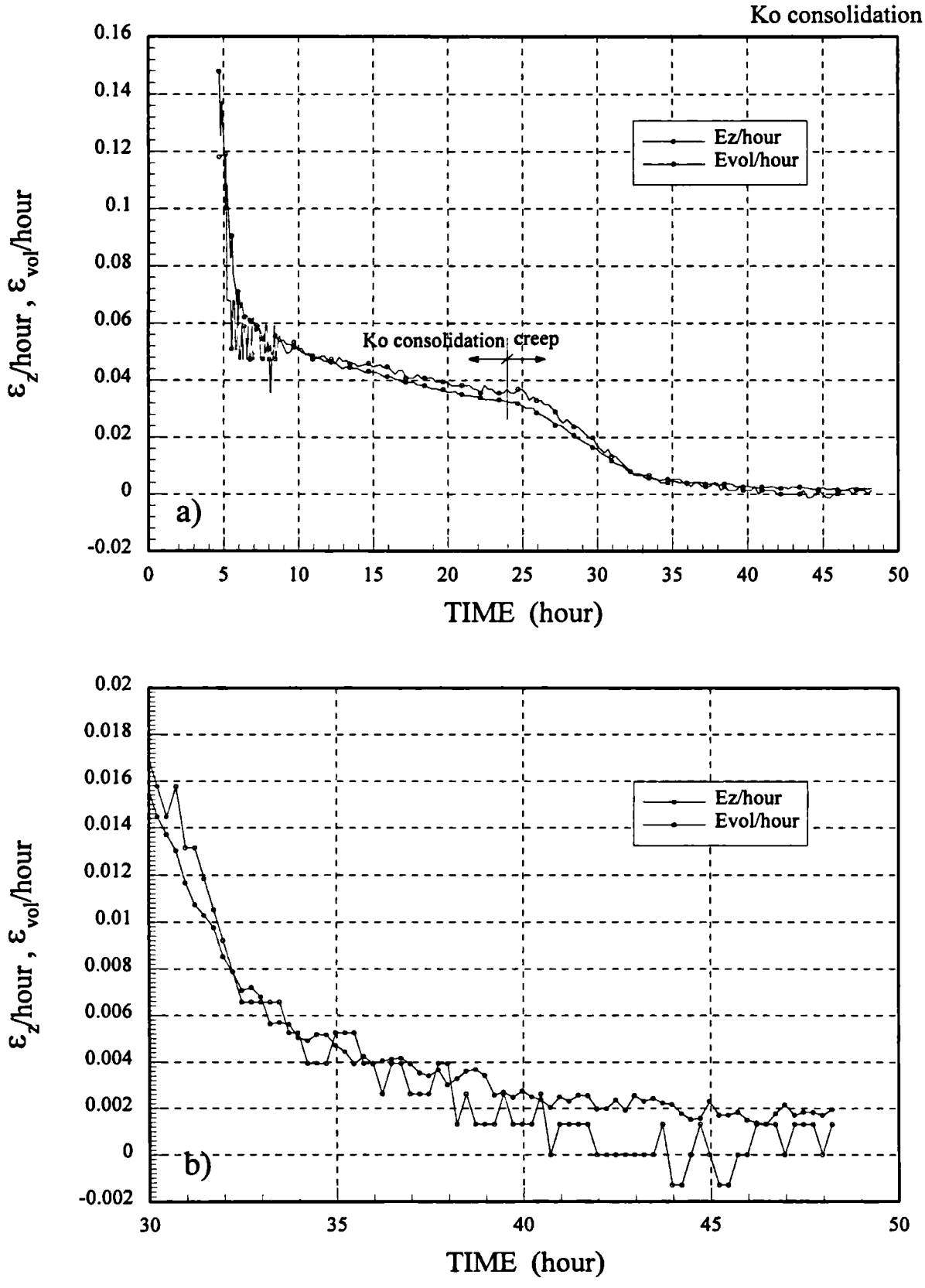


Fig.4.6 - a) Volumetric and axial strain rate during Ko consolidation
b) Enlarged view of creep strain rate

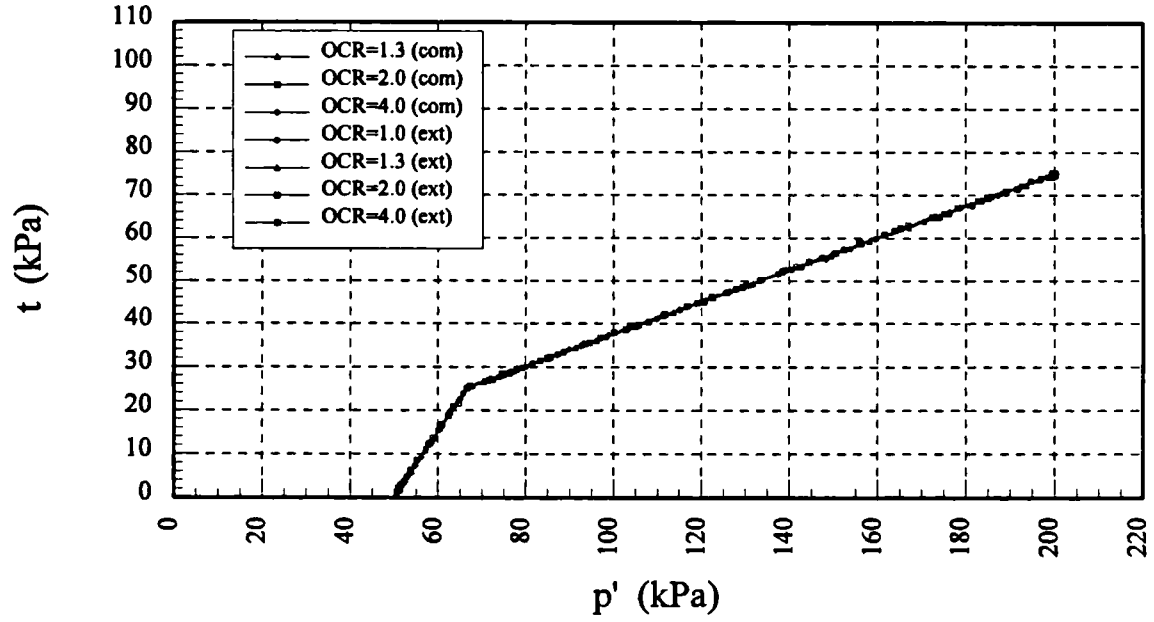


Fig.4.7 - Performed Ko consolidation paths for triaxial test Series

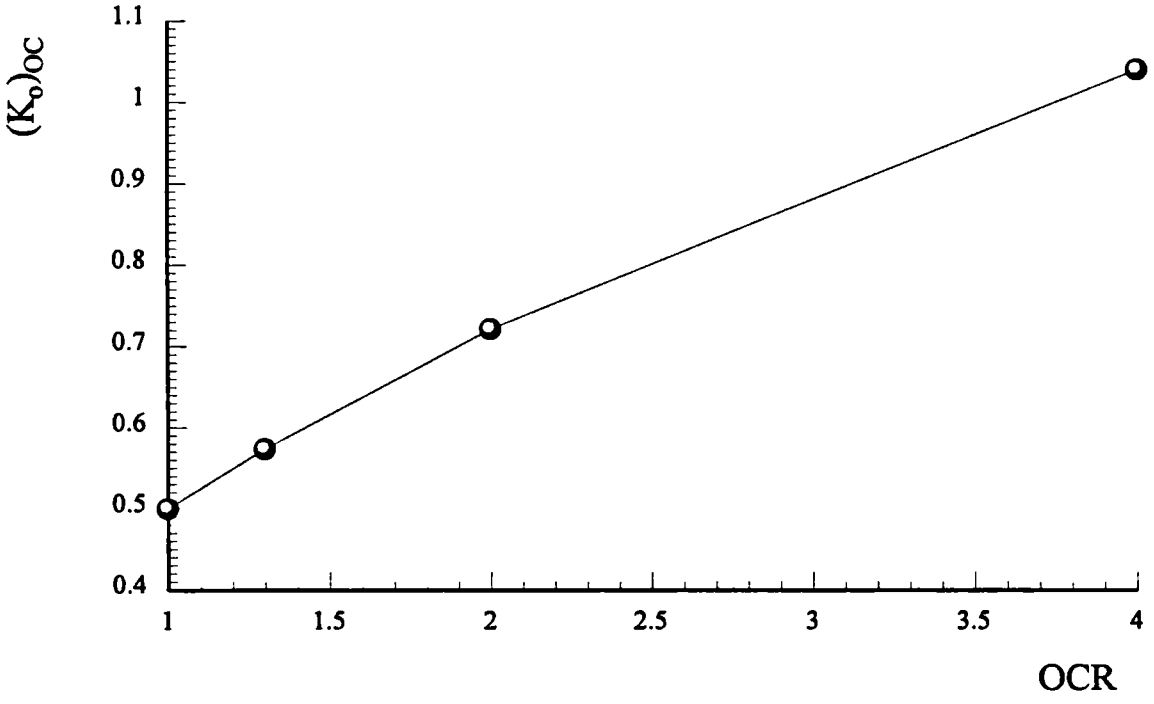


Fig.4.8 - Variation of overconsolidation swelling ratio with OCR

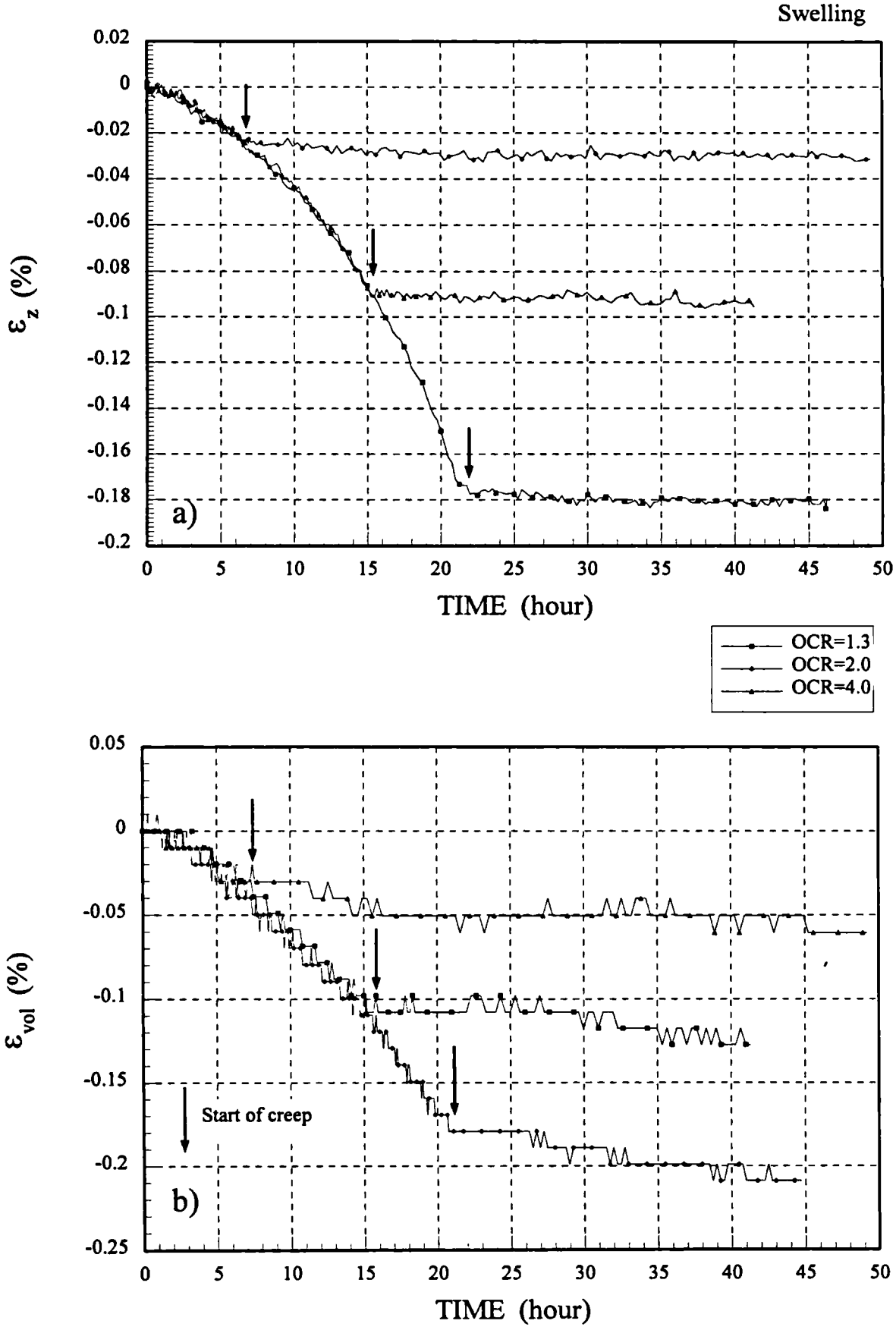


Fig.4.9 - Time dependance of strains during Ko swelling for different OCR: a) axial and b) volumetric strain

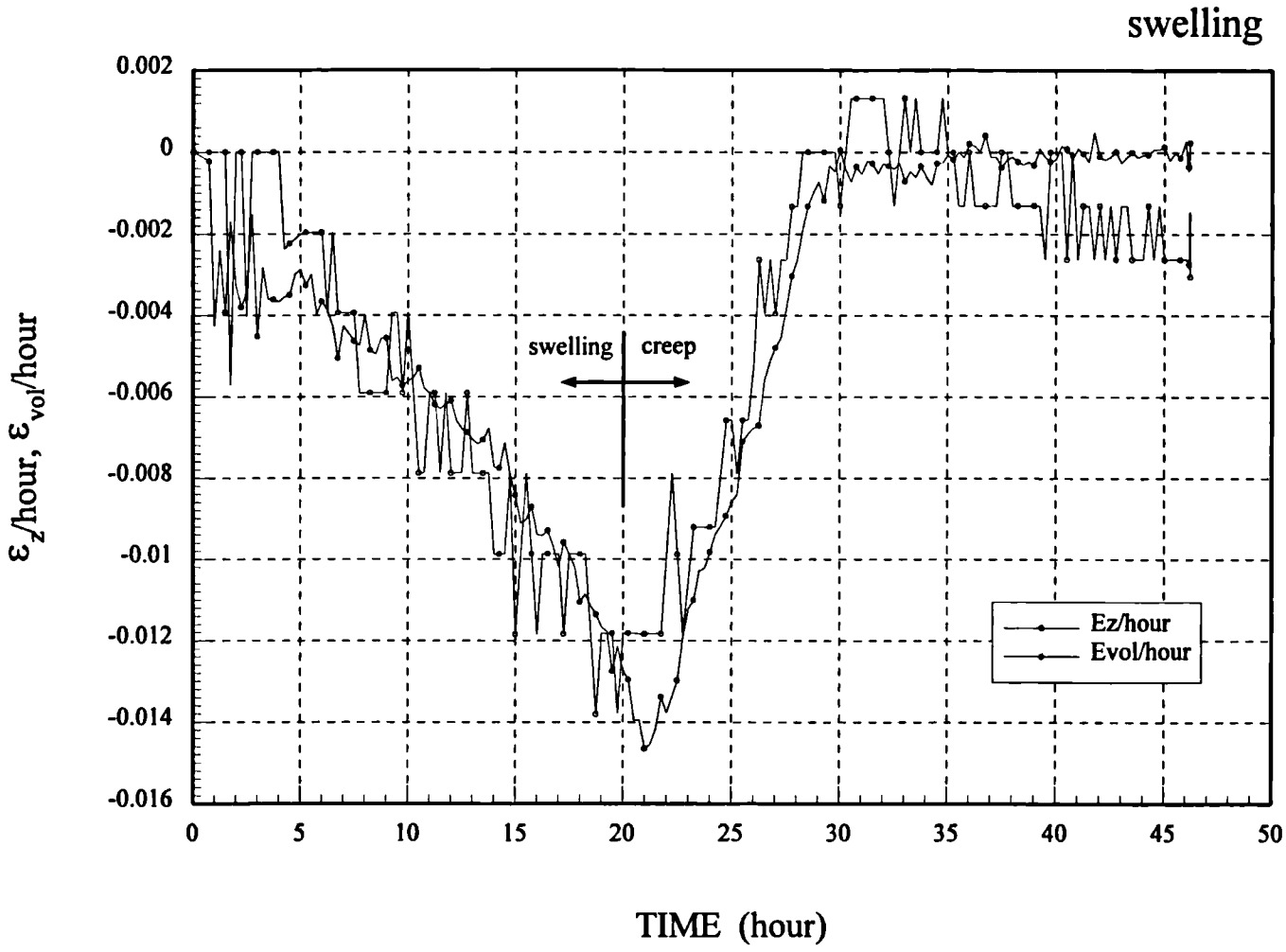


Fig.4.10 - Axial and volumetric strain rates during Ko swelling and creep

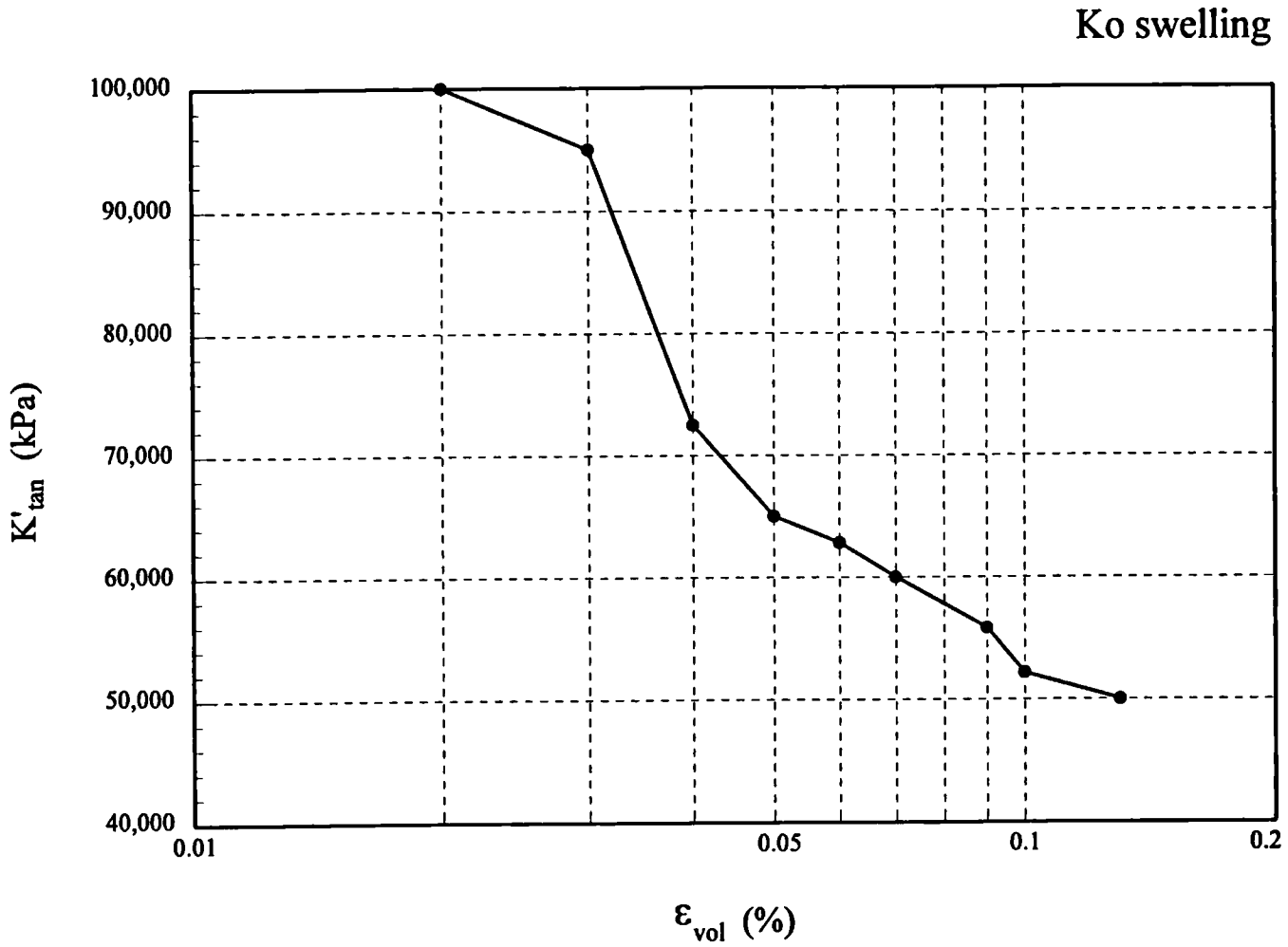


Fig.4.11 - Bulk modulus from Ko swelling

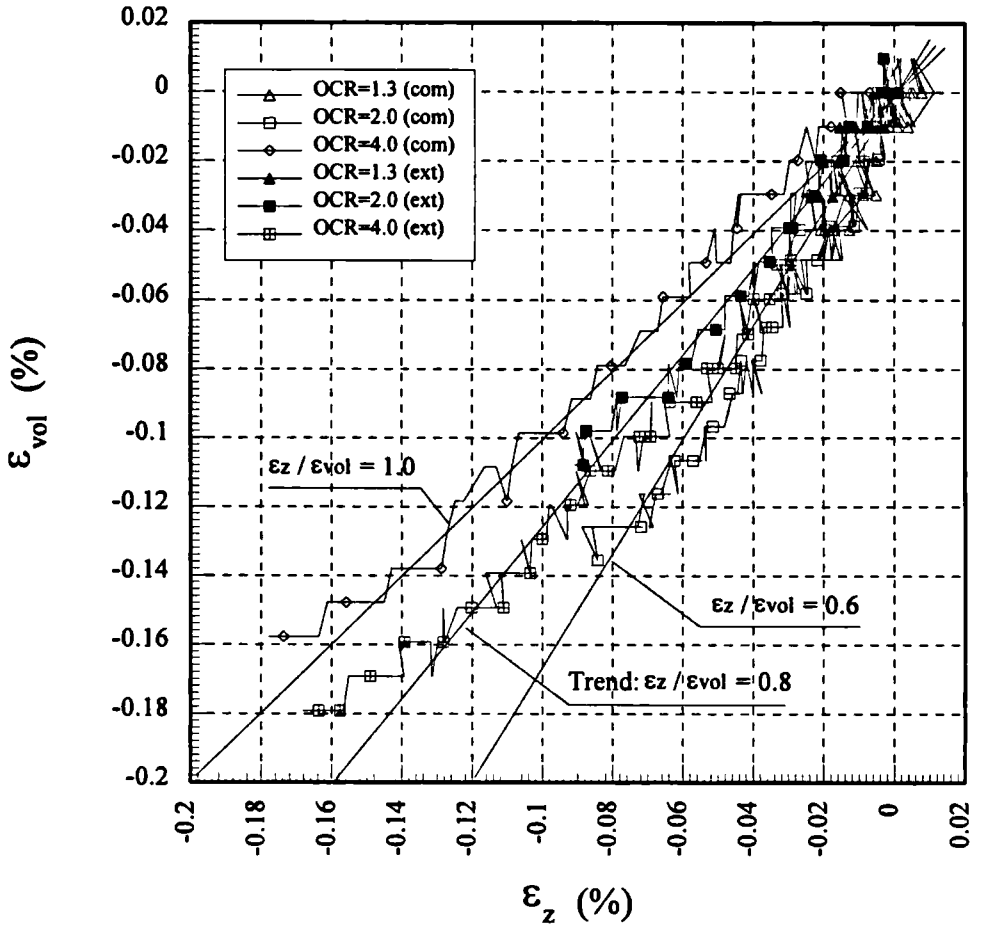


Fig.4.12 - Relation between axial and volumetric strain during Ko swelling

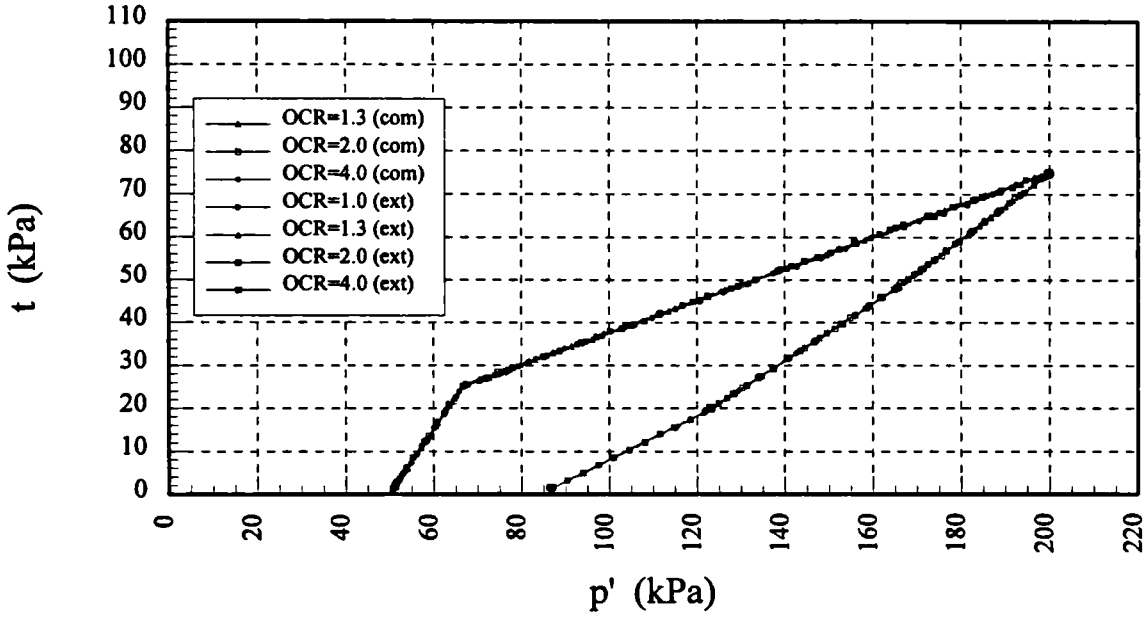
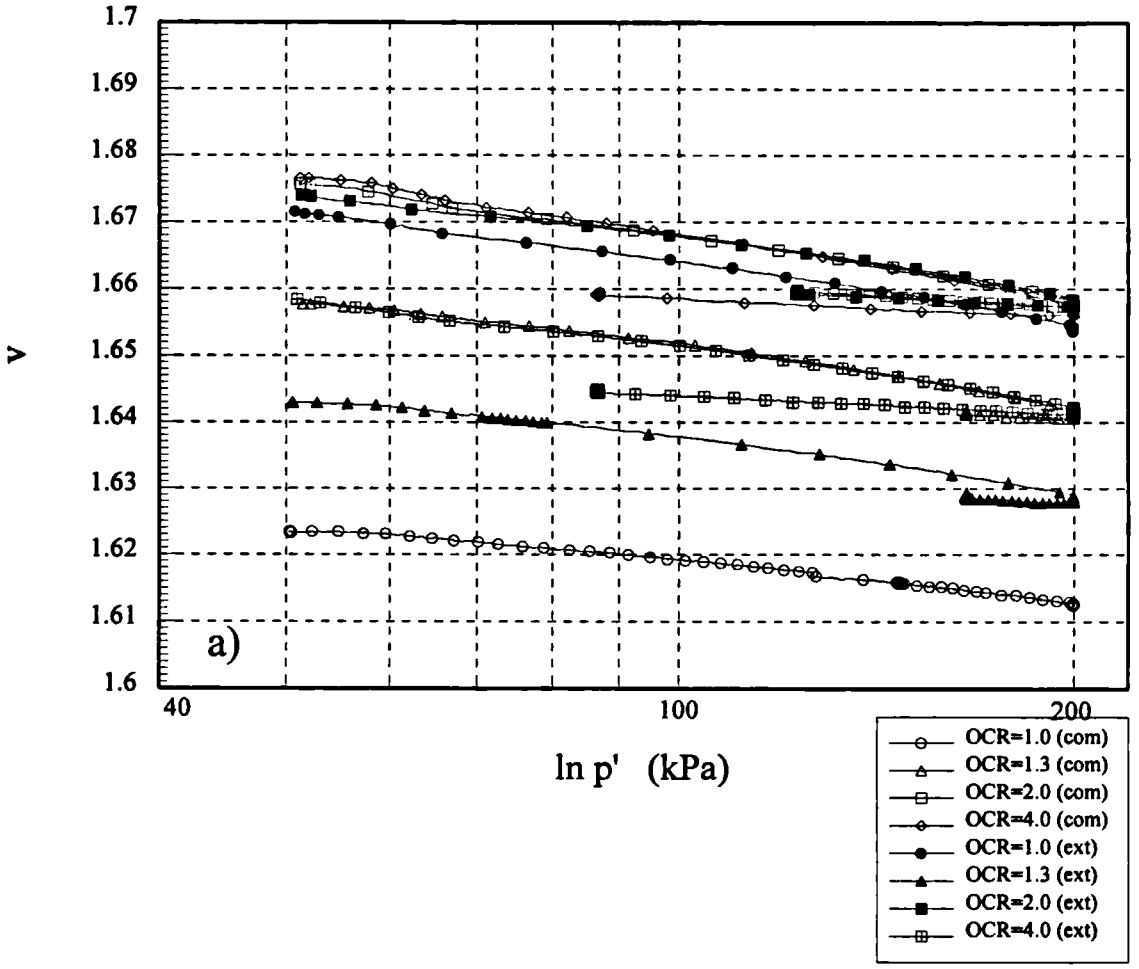


Fig.4.13 - Stress paths followed during Ko swelling in triaxial test Series



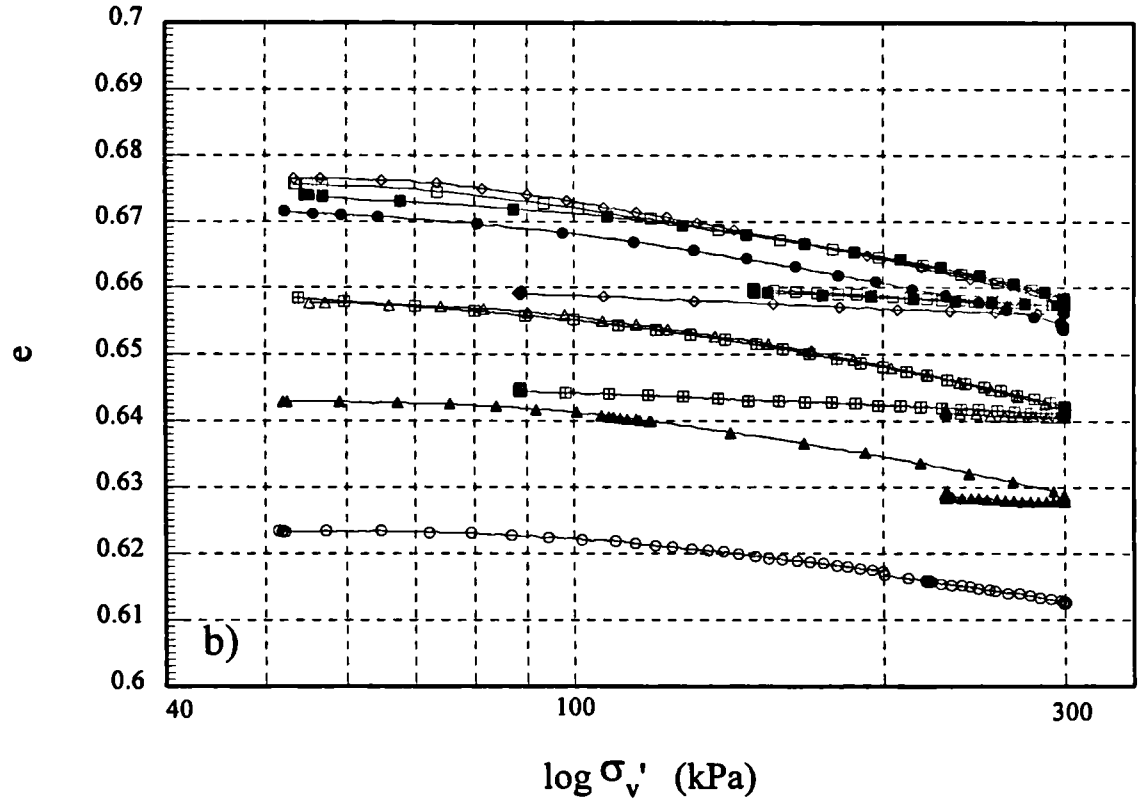
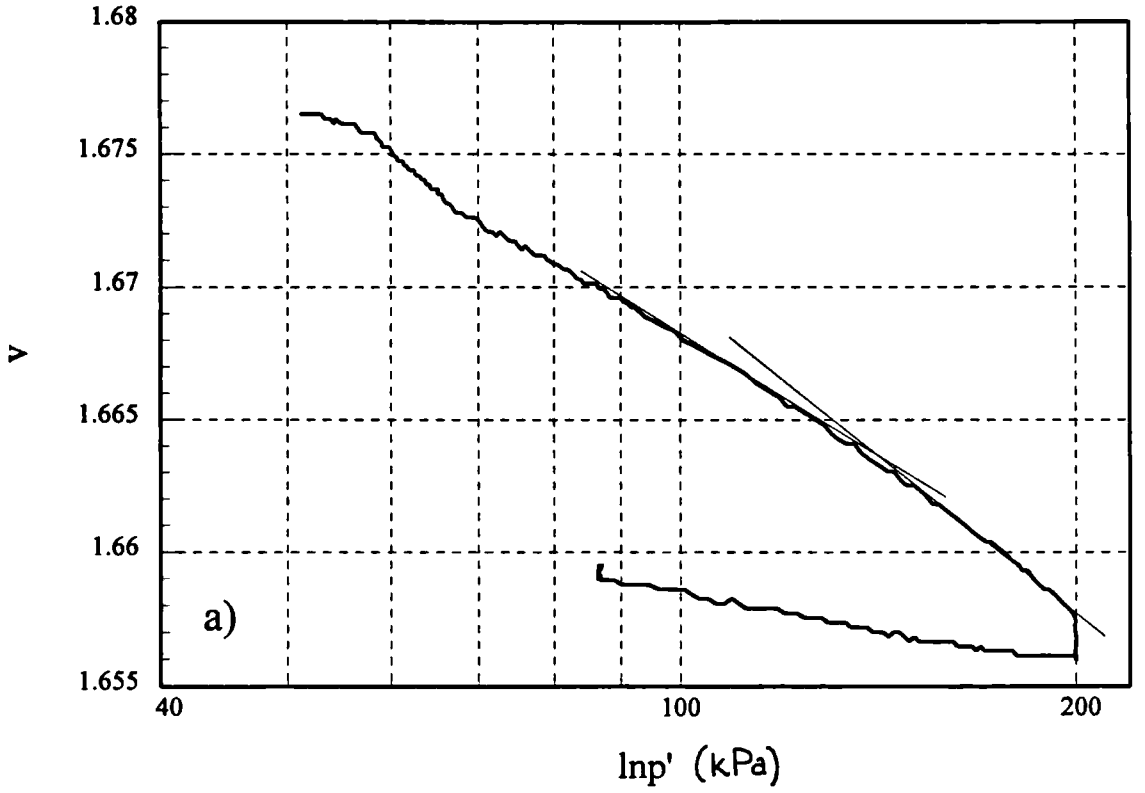


Fig.4.14 - Compresibility of Ko consolidated HPF4:
a) v - lnp' b) e - logσv'



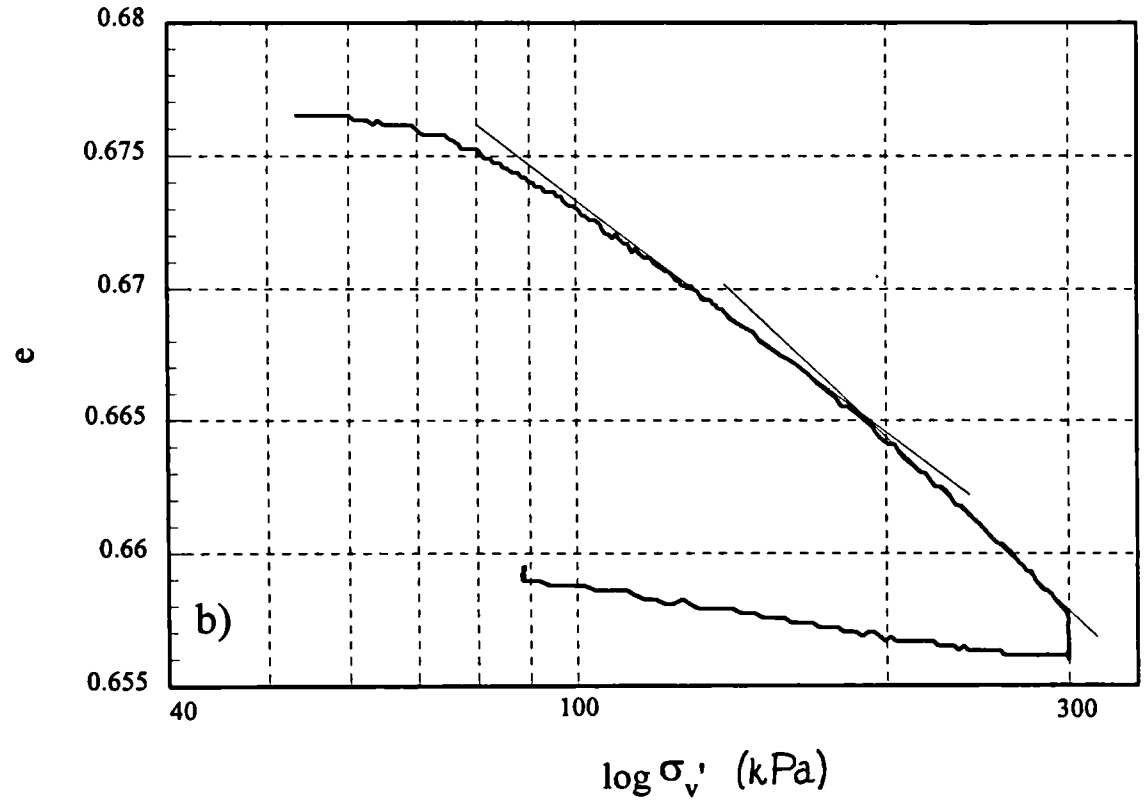


Fig.4.15 - Non-linearity of compression curves in:
a) v-lnp' plane
b) e-log σv' plane

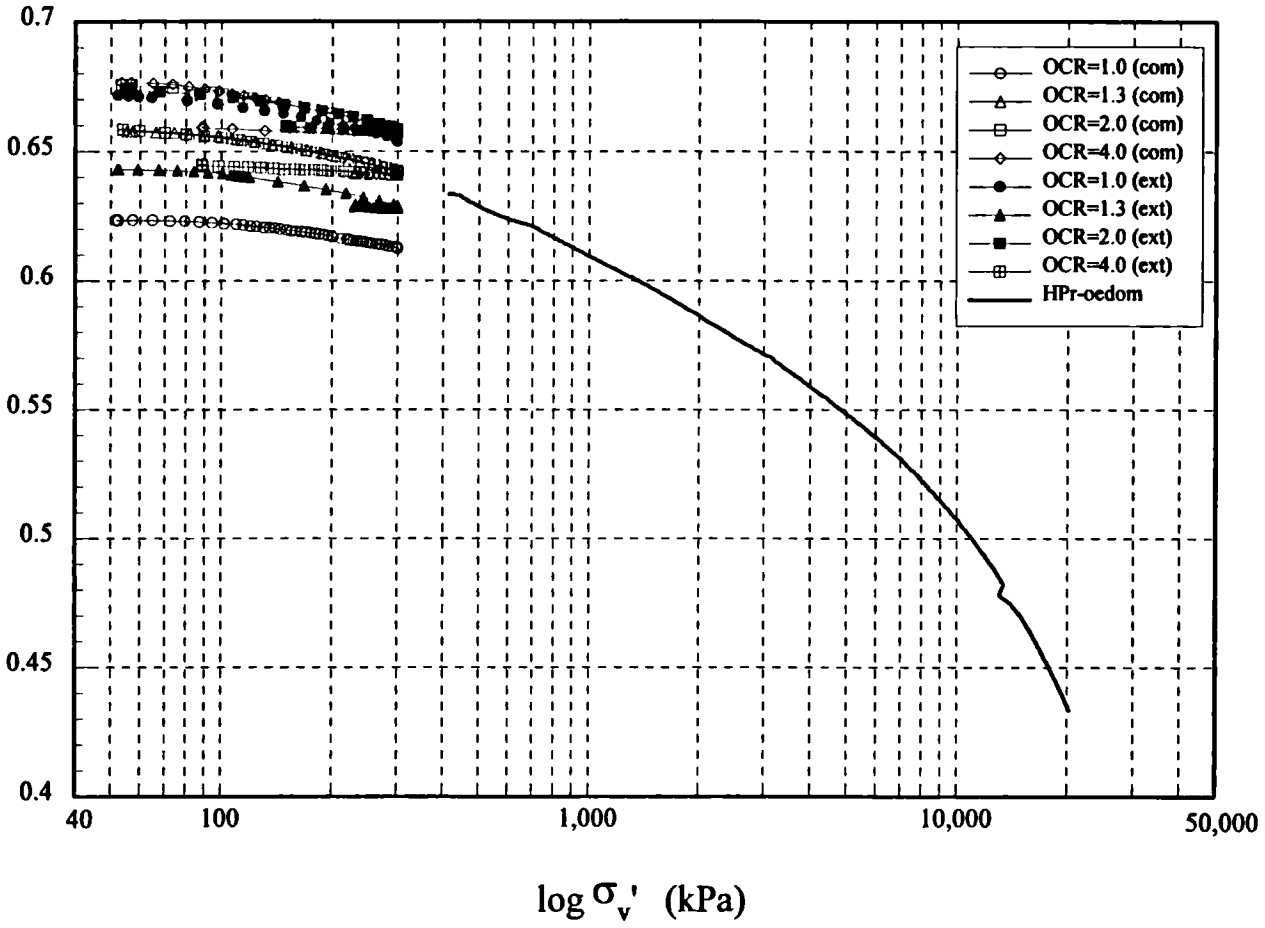


Fig.4.16 - High pressure oedometer compression curve in e-log σ_v' plane

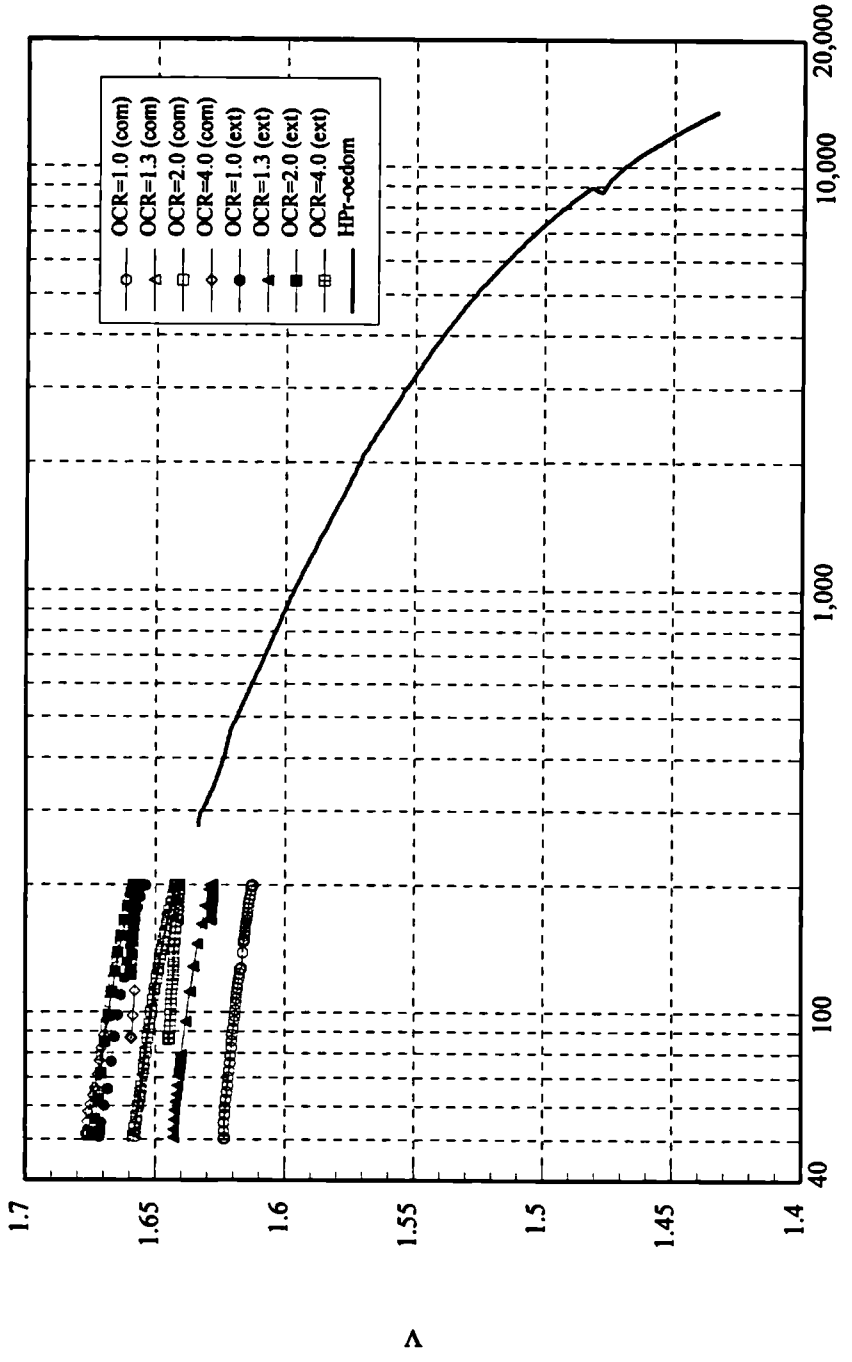


Fig.4.17 - High pressure oedometer compression curve in v-lnp' plane

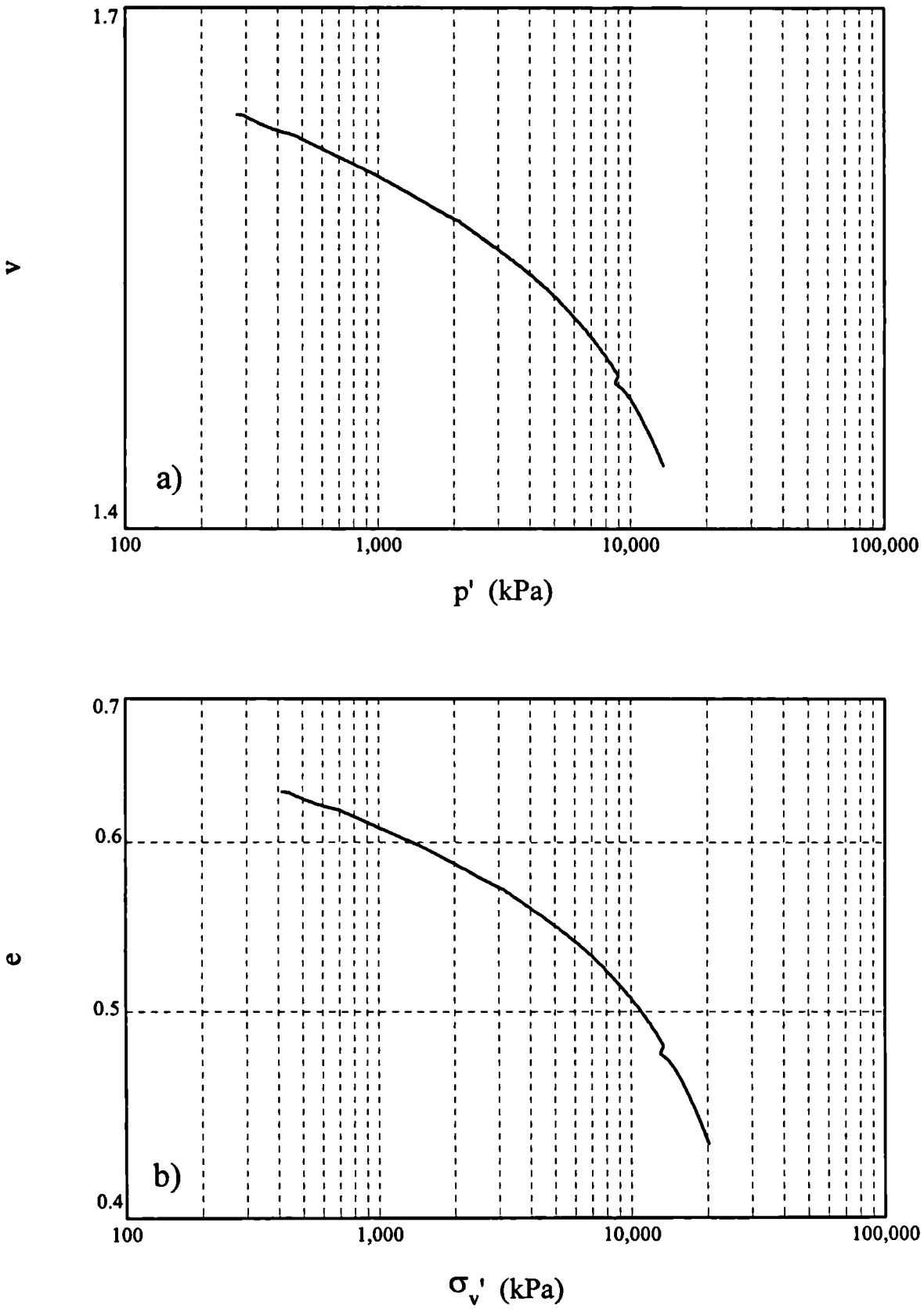
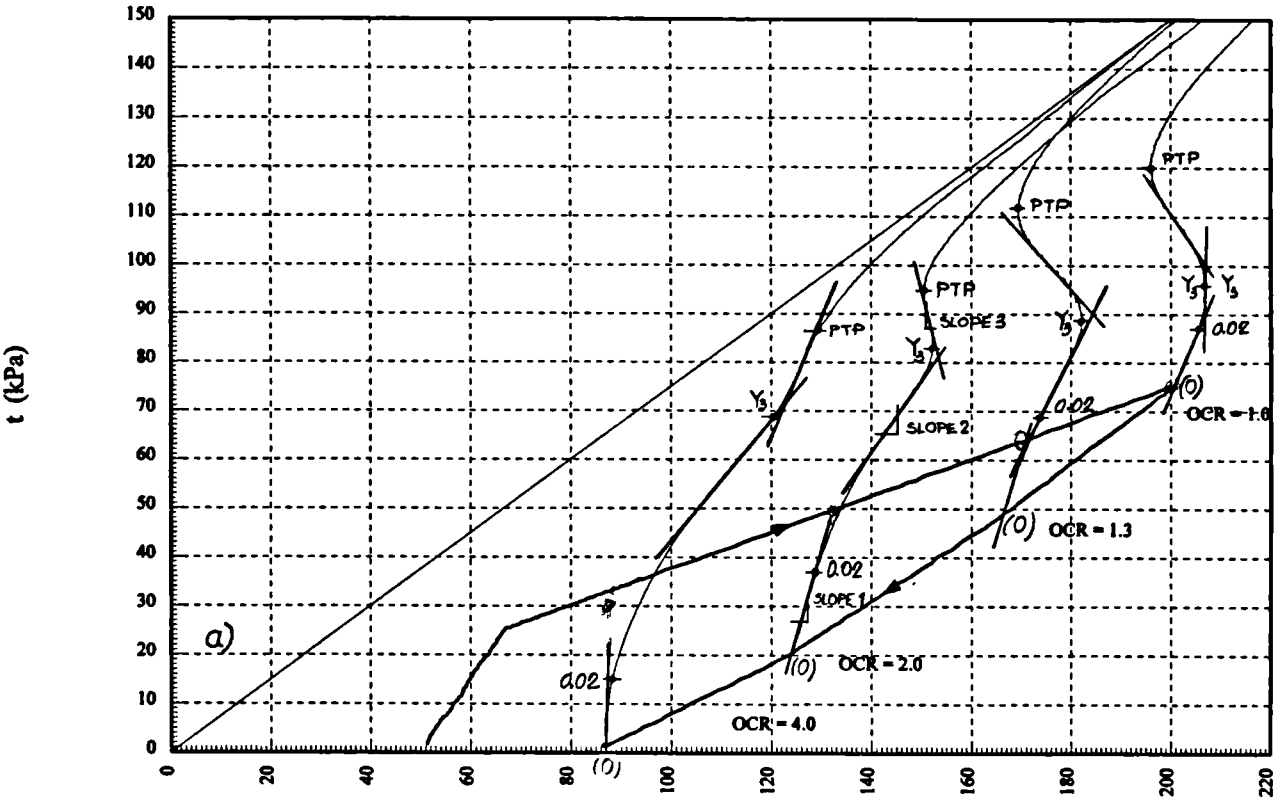


Fig.4.18 - Log - log plots of normal consolidation line in a) v-lnp' plane; b) e-logσv' plane



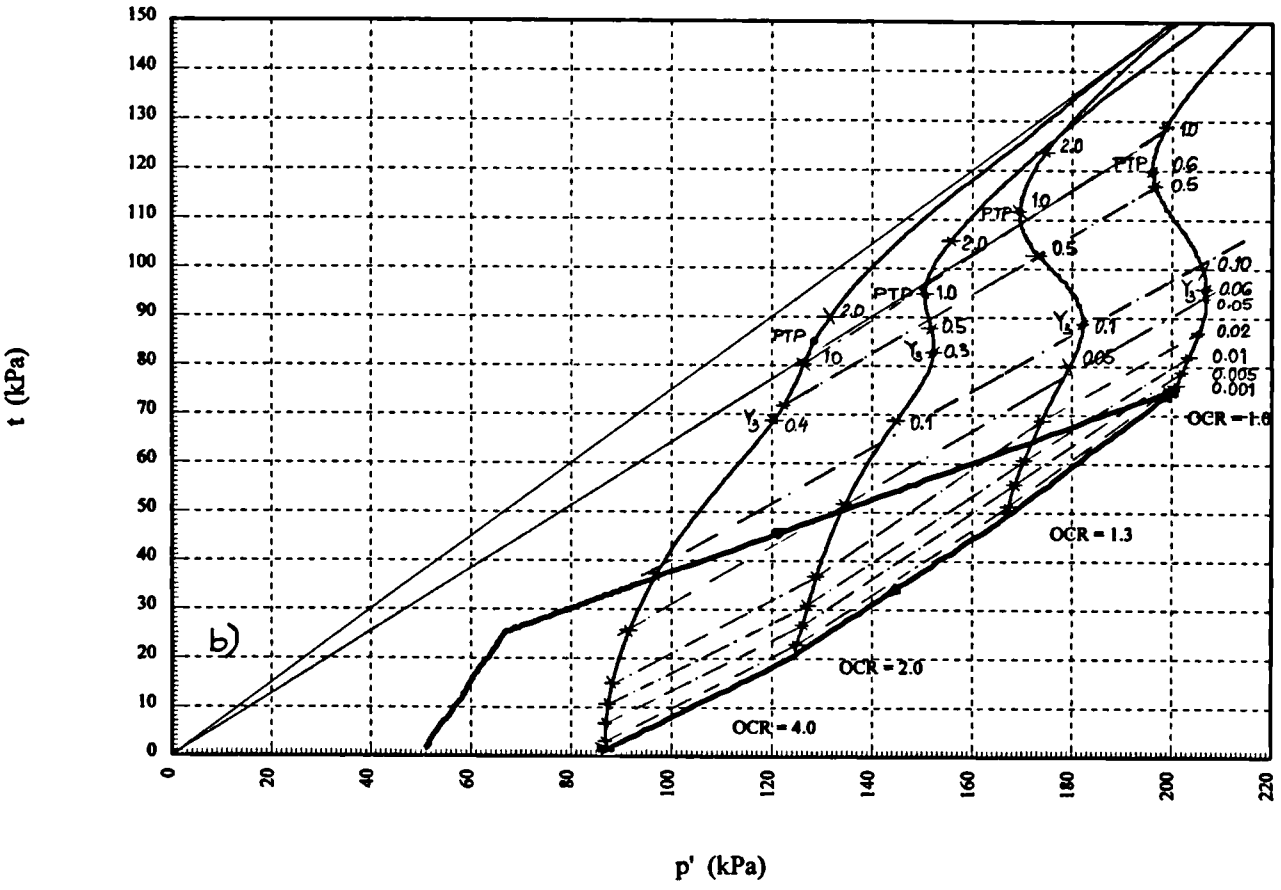


Fig.4.19 - a) Slopes and b) Strain contours of the effective stress paths in undrained triaxial compression

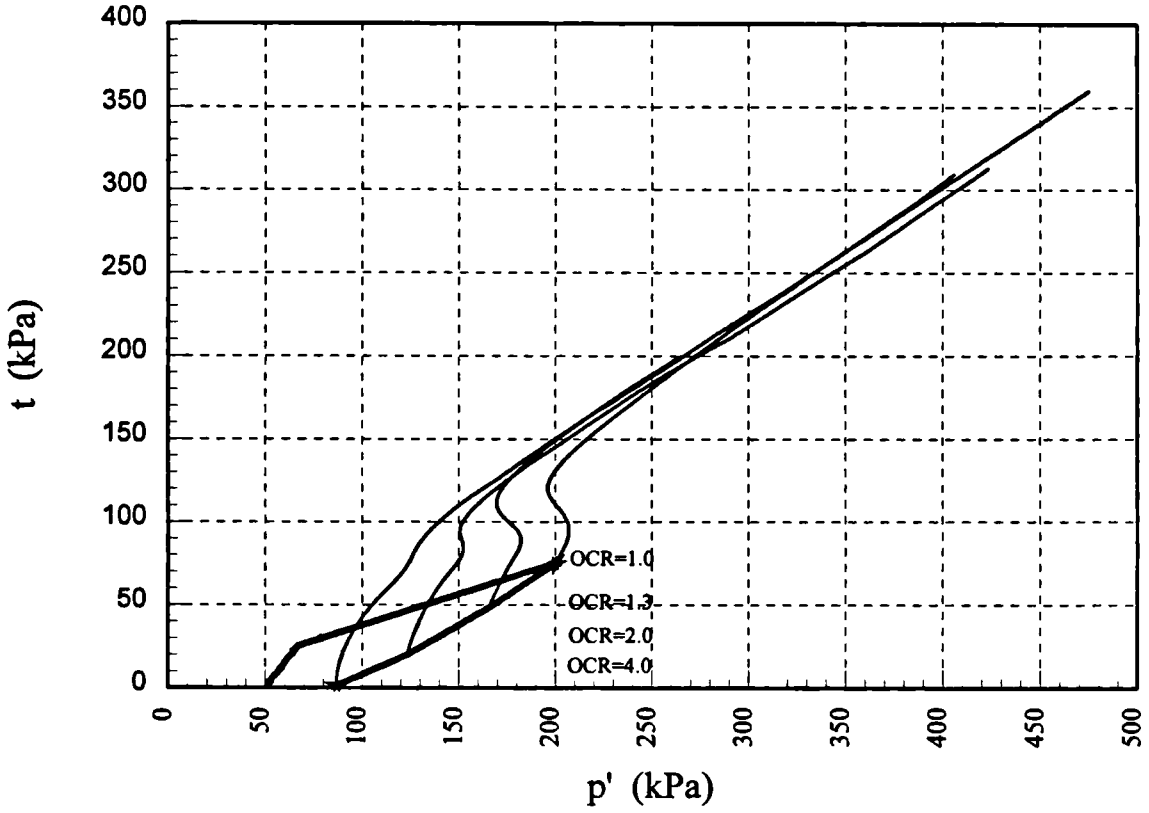


Fig.4.20 - Effective stress paths for triaxial compression tests on HPF4

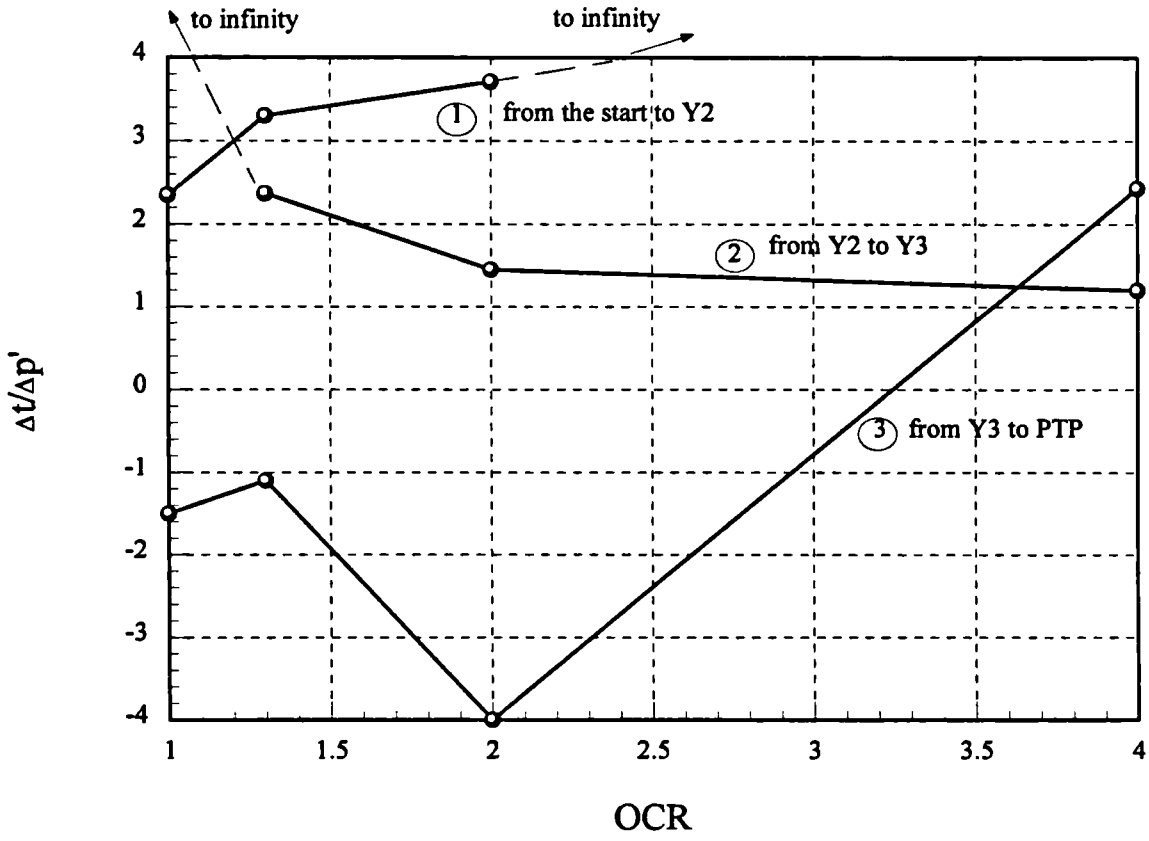


Fig.4.21 - Variation of effective stress path's slopes with OCR

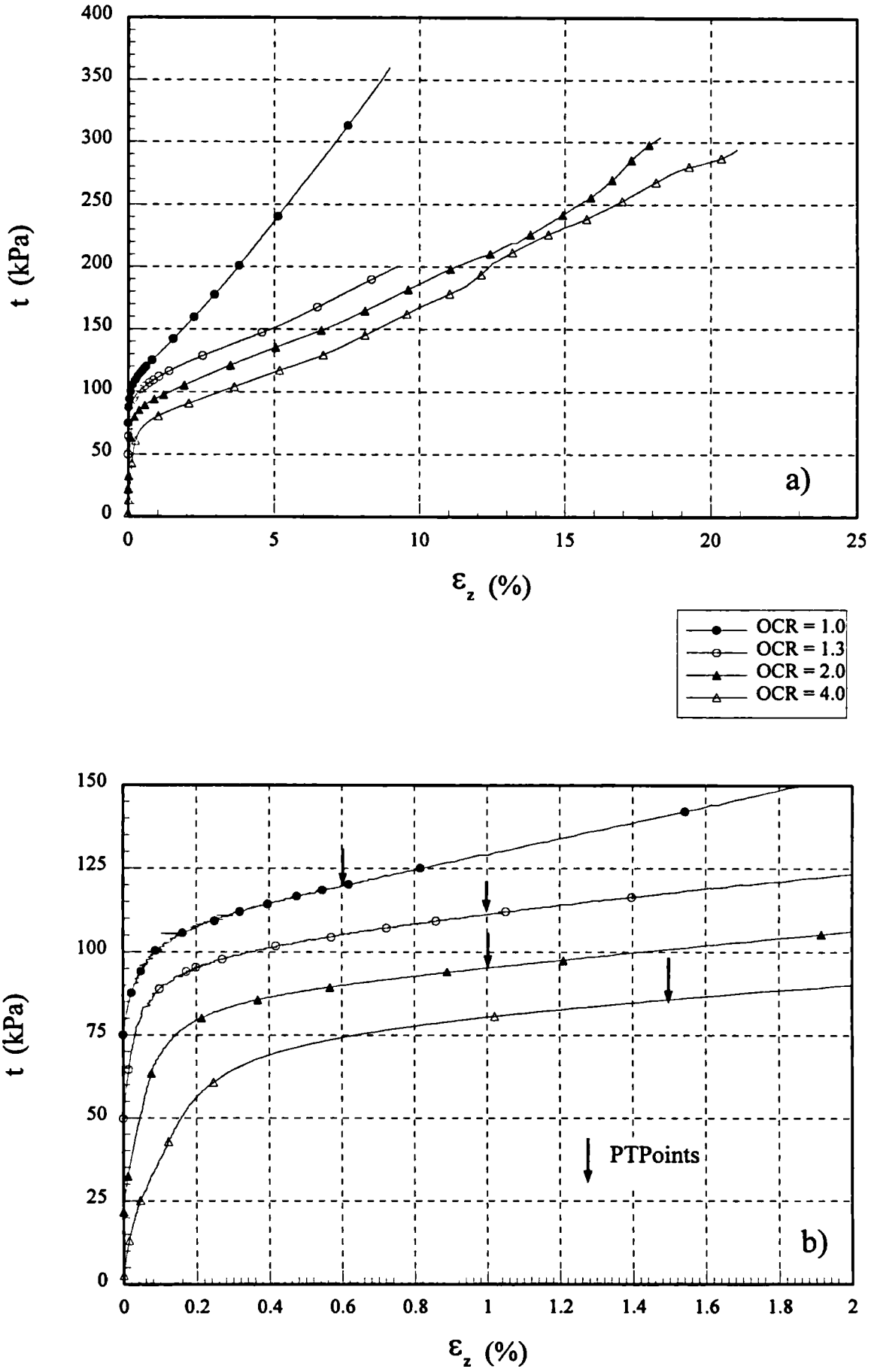


Fig. 4.22 - a) Stress-strain curves for triaxial compression test;
b) Small strain view

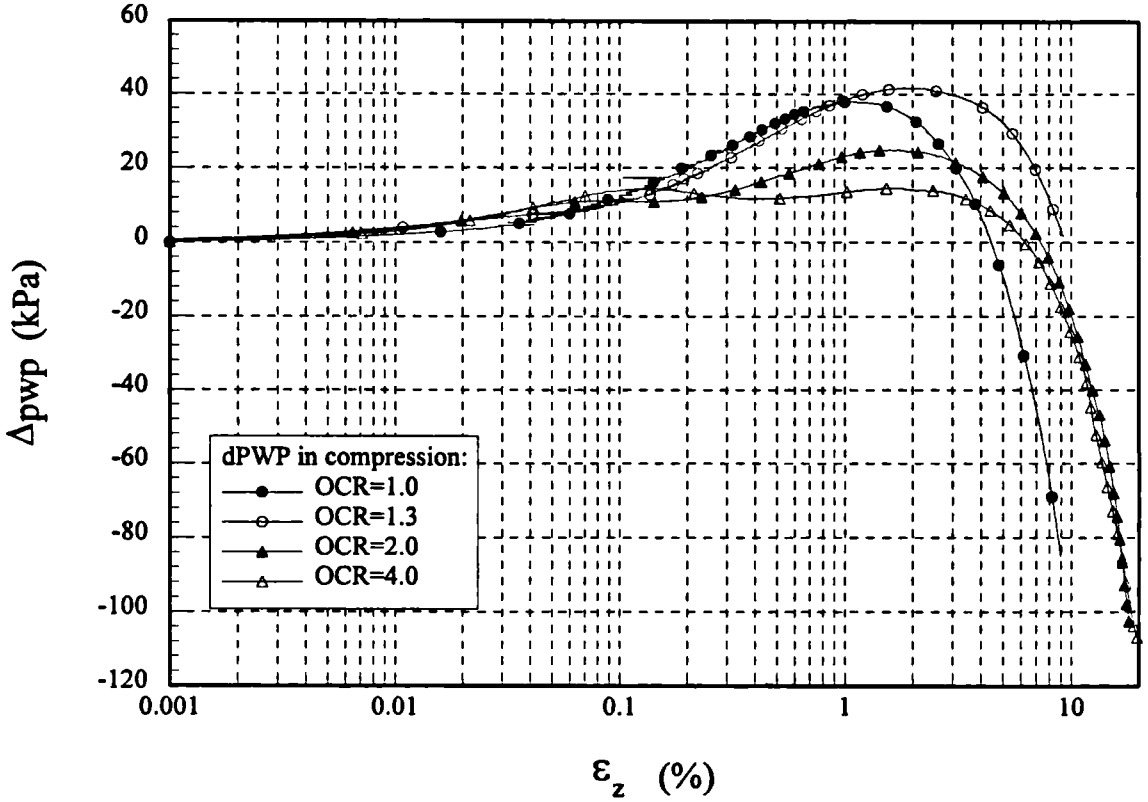


Fig.4.23 - Generation of pore water pressure during triaxial compression tests from different OCR points

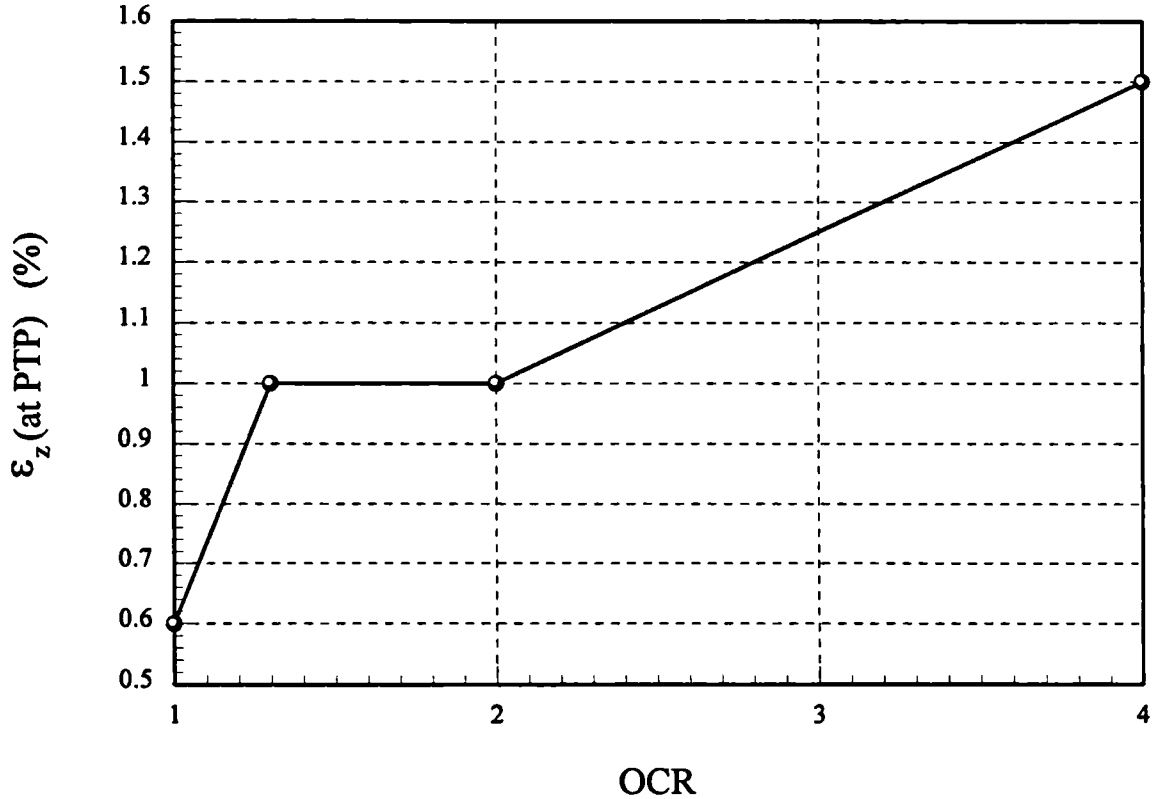


Fig.4.24 - Generated axial strain at the Phase Transformation Point for different OCRs

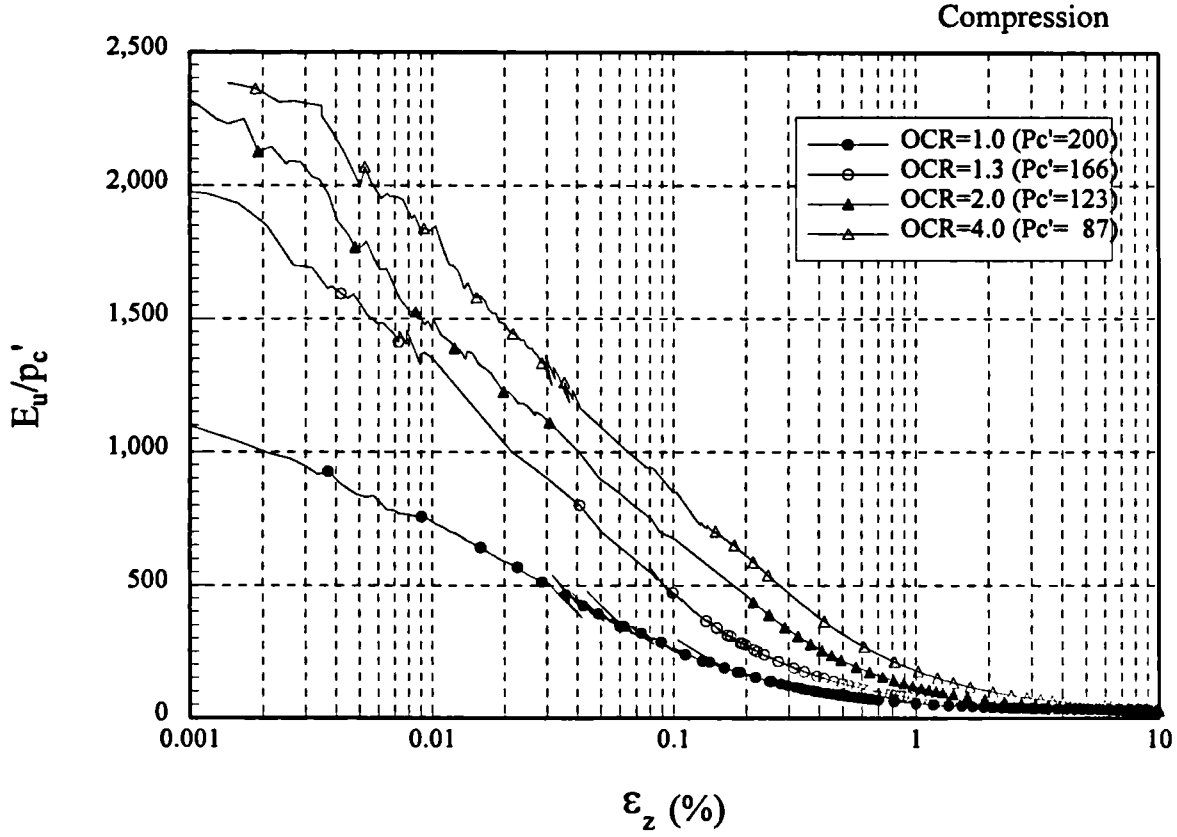


Fig.4.25a - Undrained compression Young moduli of Ko consolidated HPF4 for different OCRs, normalized with the p' prior to shearing

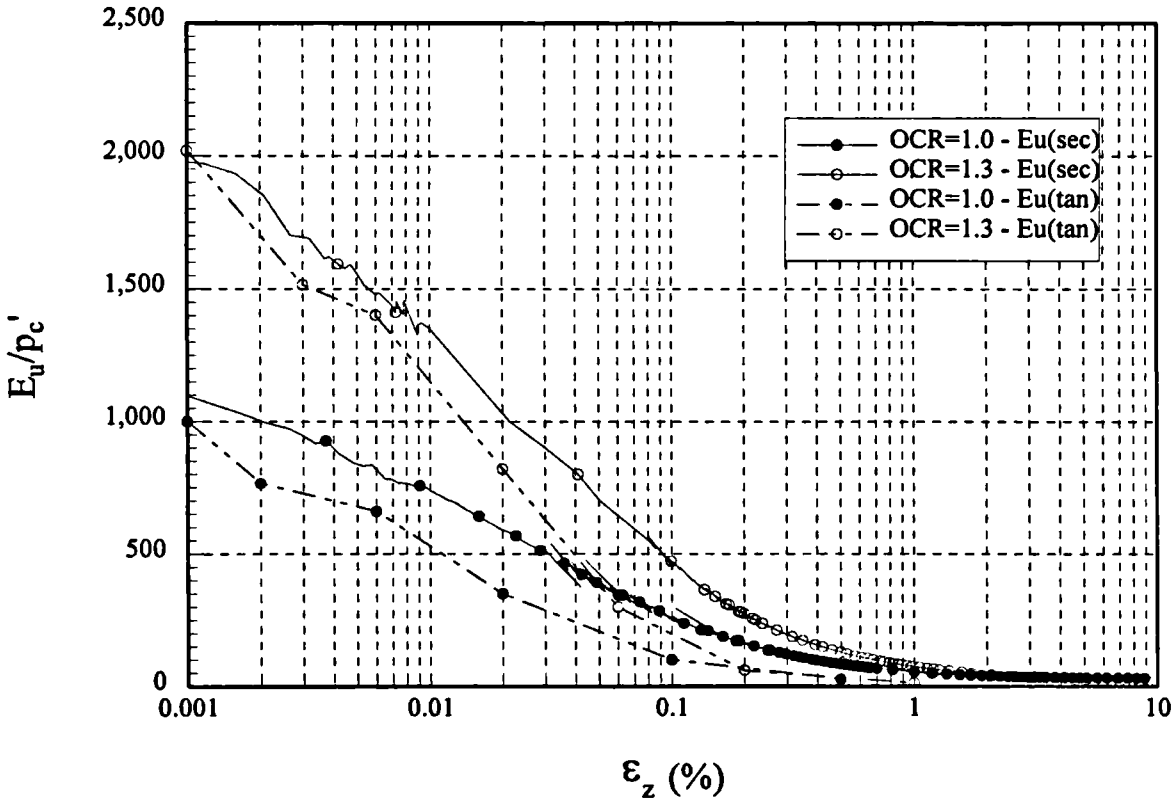


Fig.4.25b - Comparison of secant and tangent Young moduli of Ko consolidated HPF4 for OCR=1.0 and 1.3, normalized with the p' prior to shearing

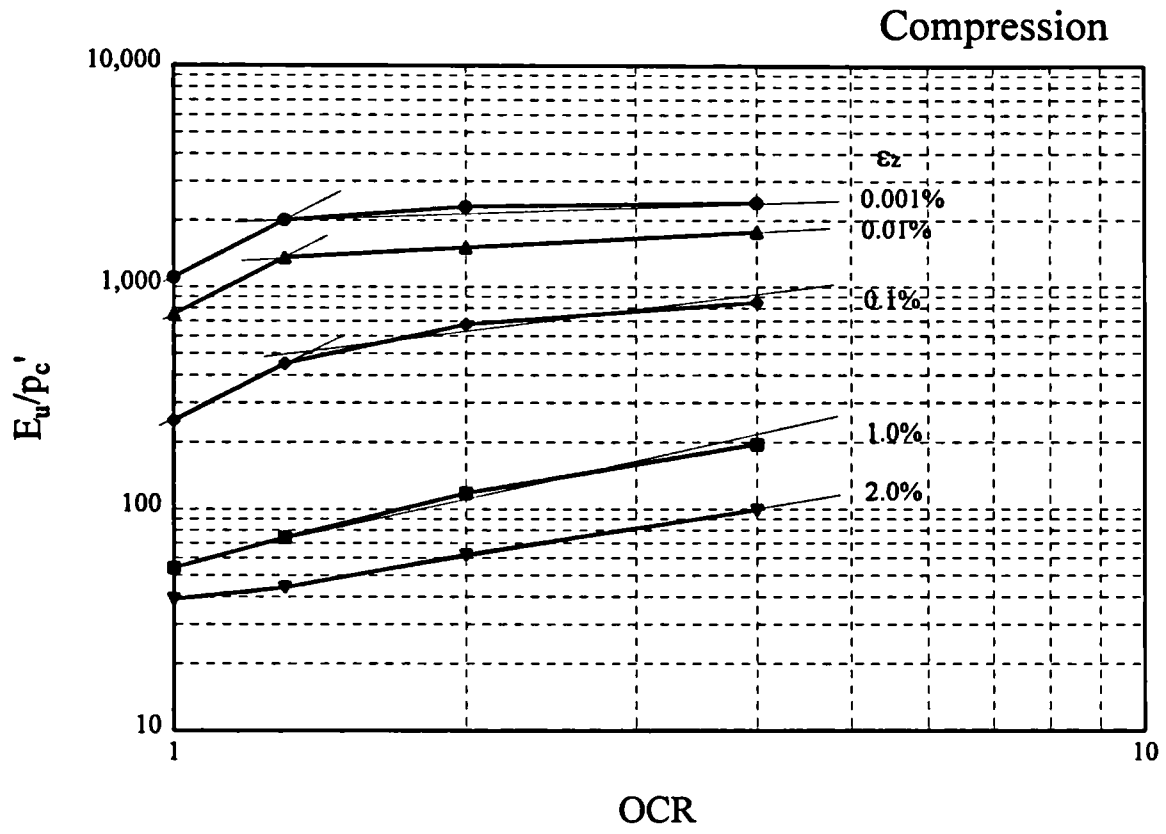


Fig.4.26 - Variation of Young modulus with OCR at different strain levels

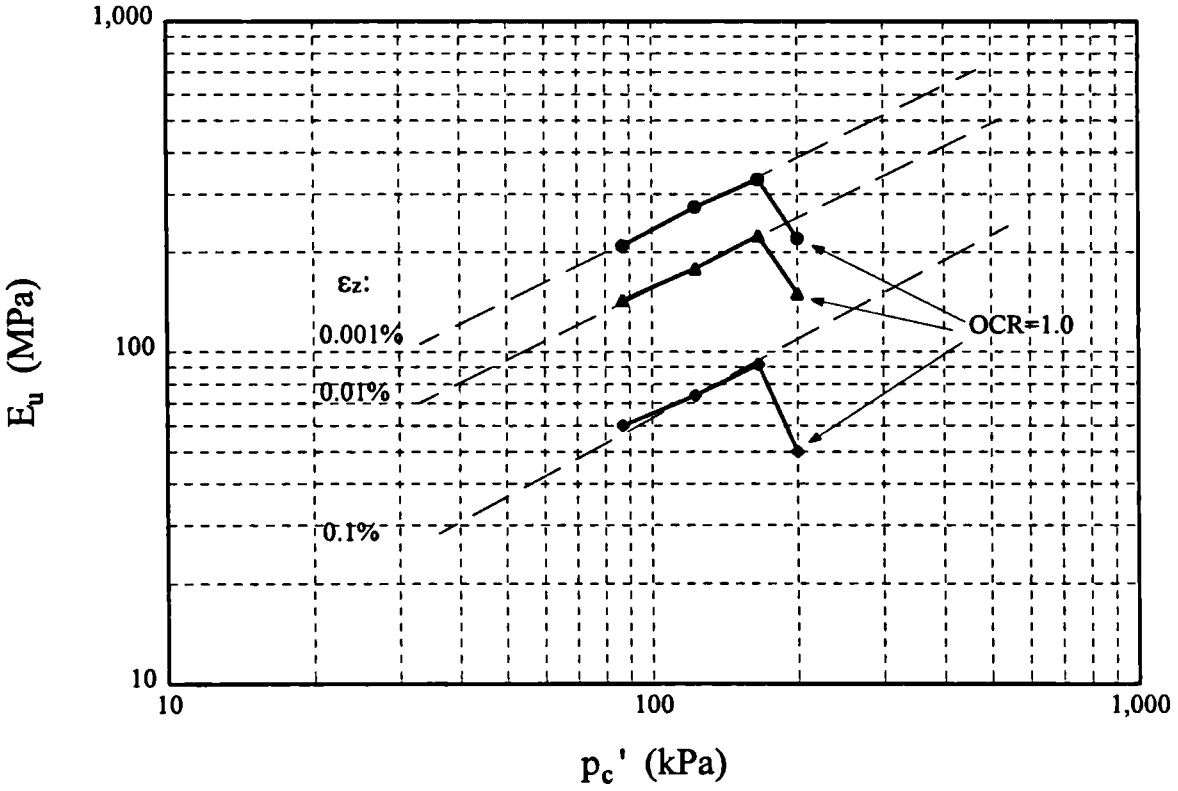


Fig.4.27 - Dependance of Young modulus on p' at different strain levels

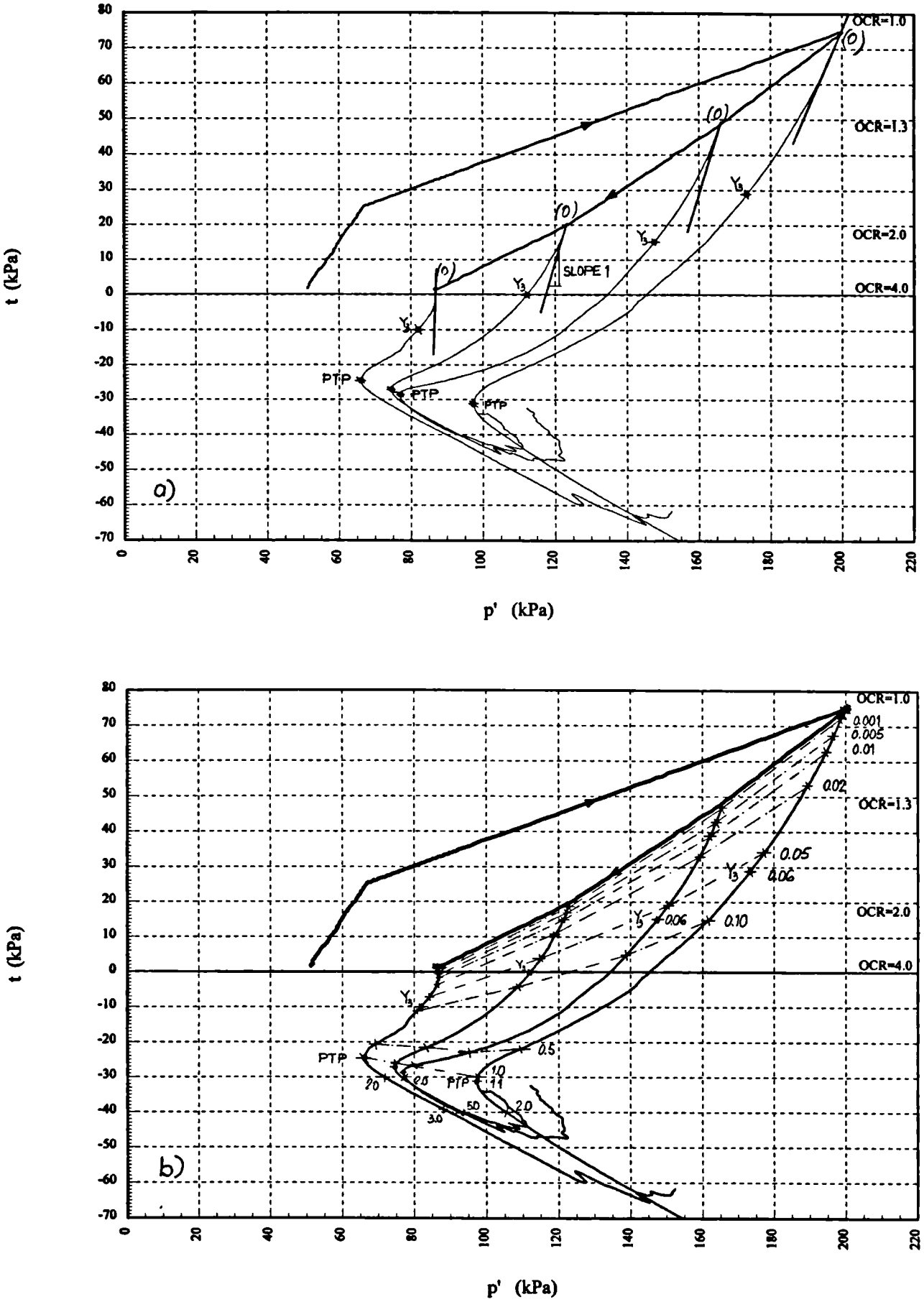


Fig.4.28 - a) Slopes and b) Strain contours of the effective stress paths in undrained triaxial extension

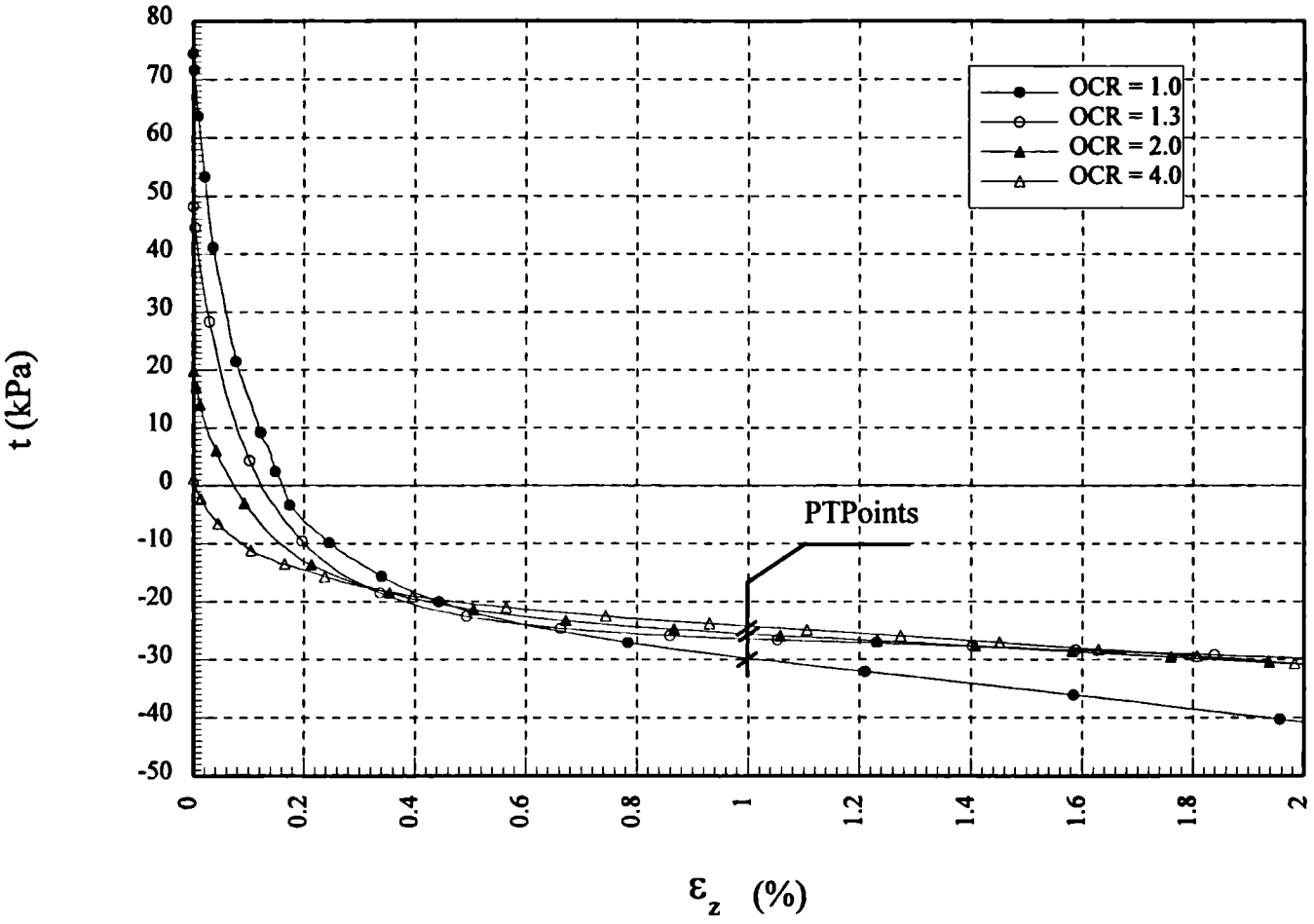


Fig.4.29 - Stress-strain curves for triaxial extension tests performed at different OCRs

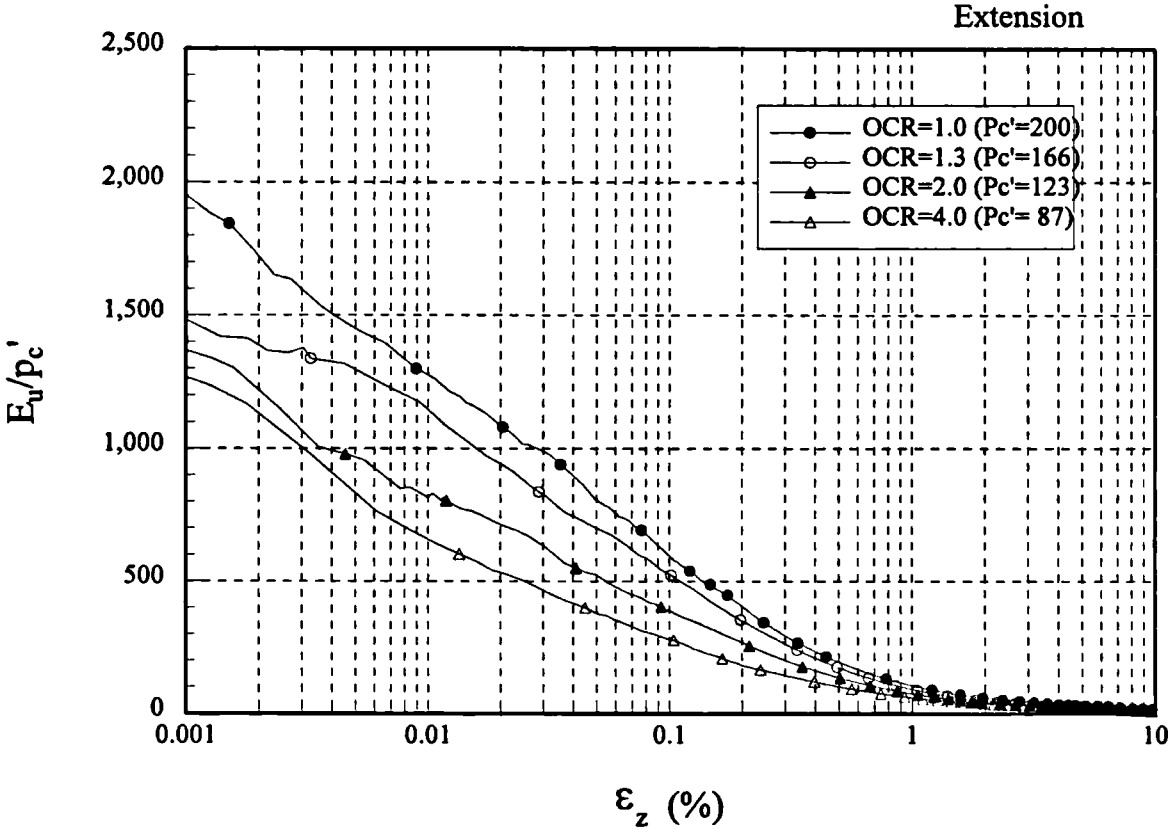


Fig.4.30a - Undrained extension secant Young moduli of Ko consolidated HPF4 for different OCRs, normalized with p' priror to shearing

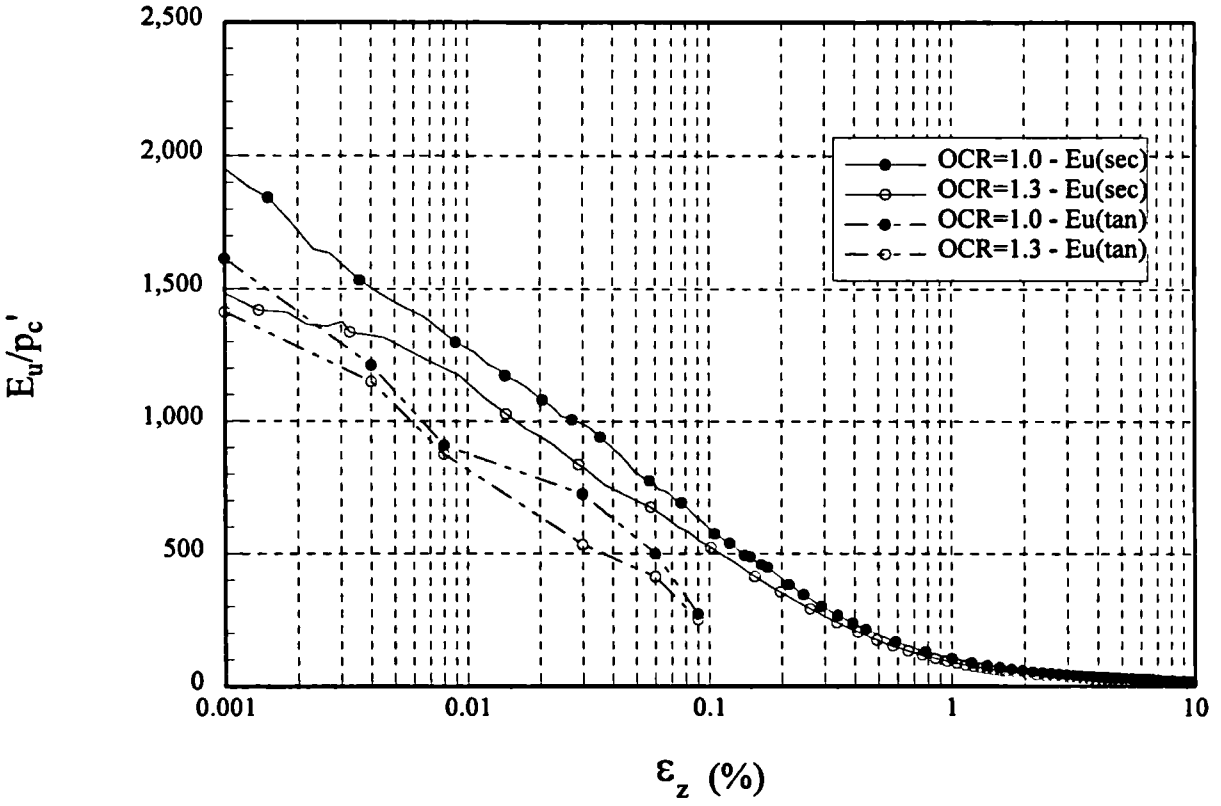


Fig.4.30b - Comparison of secant and tangent Young moduli of Ko consolidated HPF4 for OCR=1.0 and 1.3, normalized with the p' prior to shearing

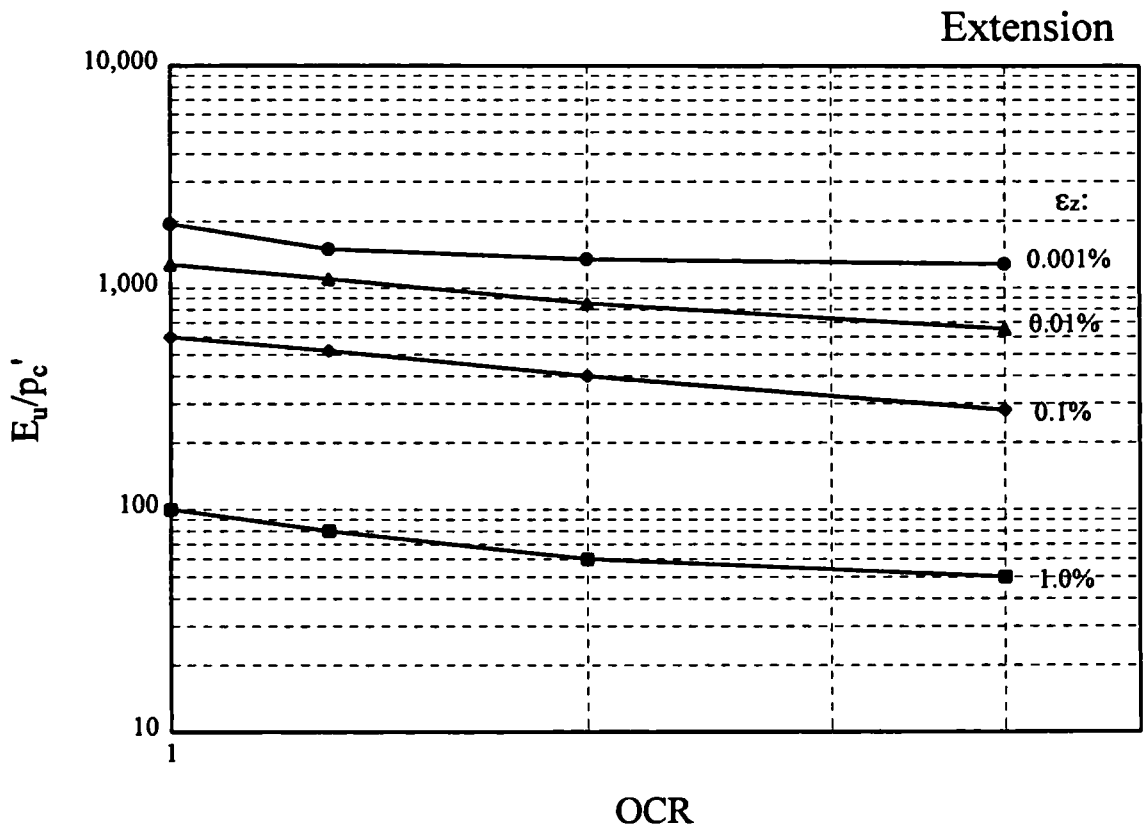


Fig.4.31 - Variation of Young modulus with OCR at different strain levels

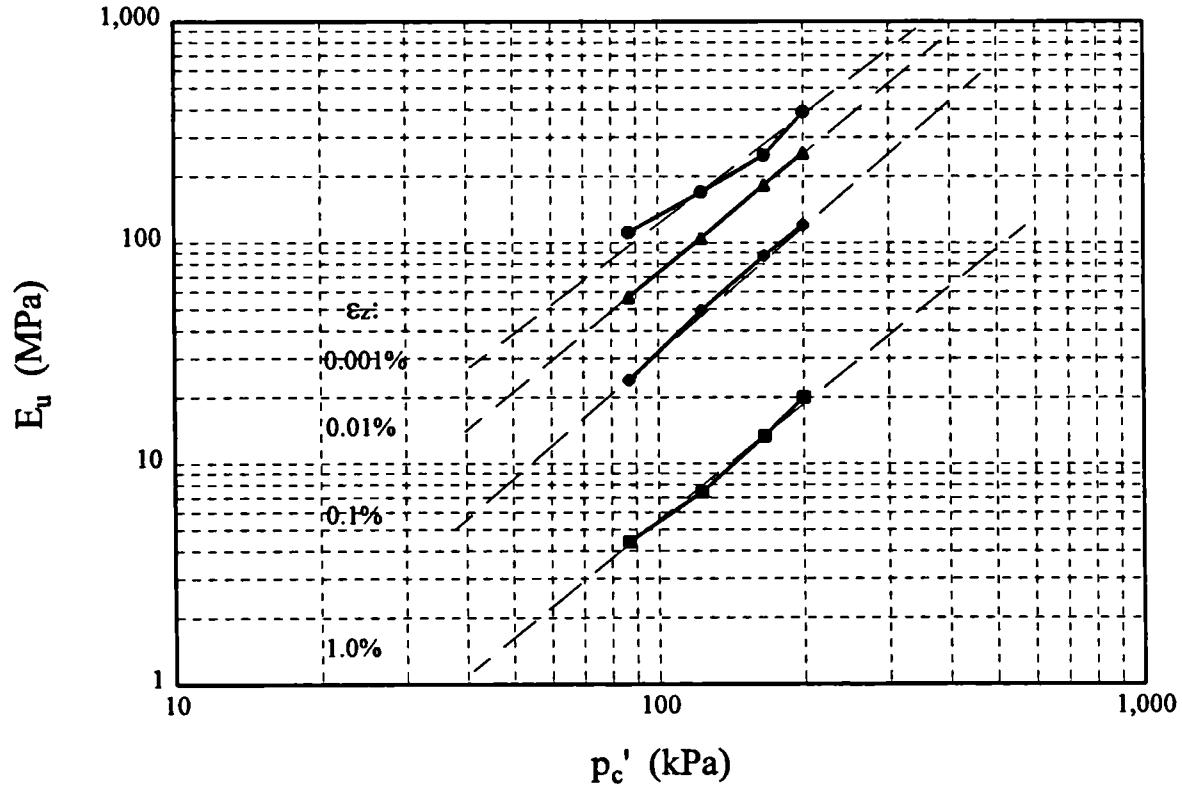


Fig.4.32 - Dependance of Young modulus on p' at different strain levels

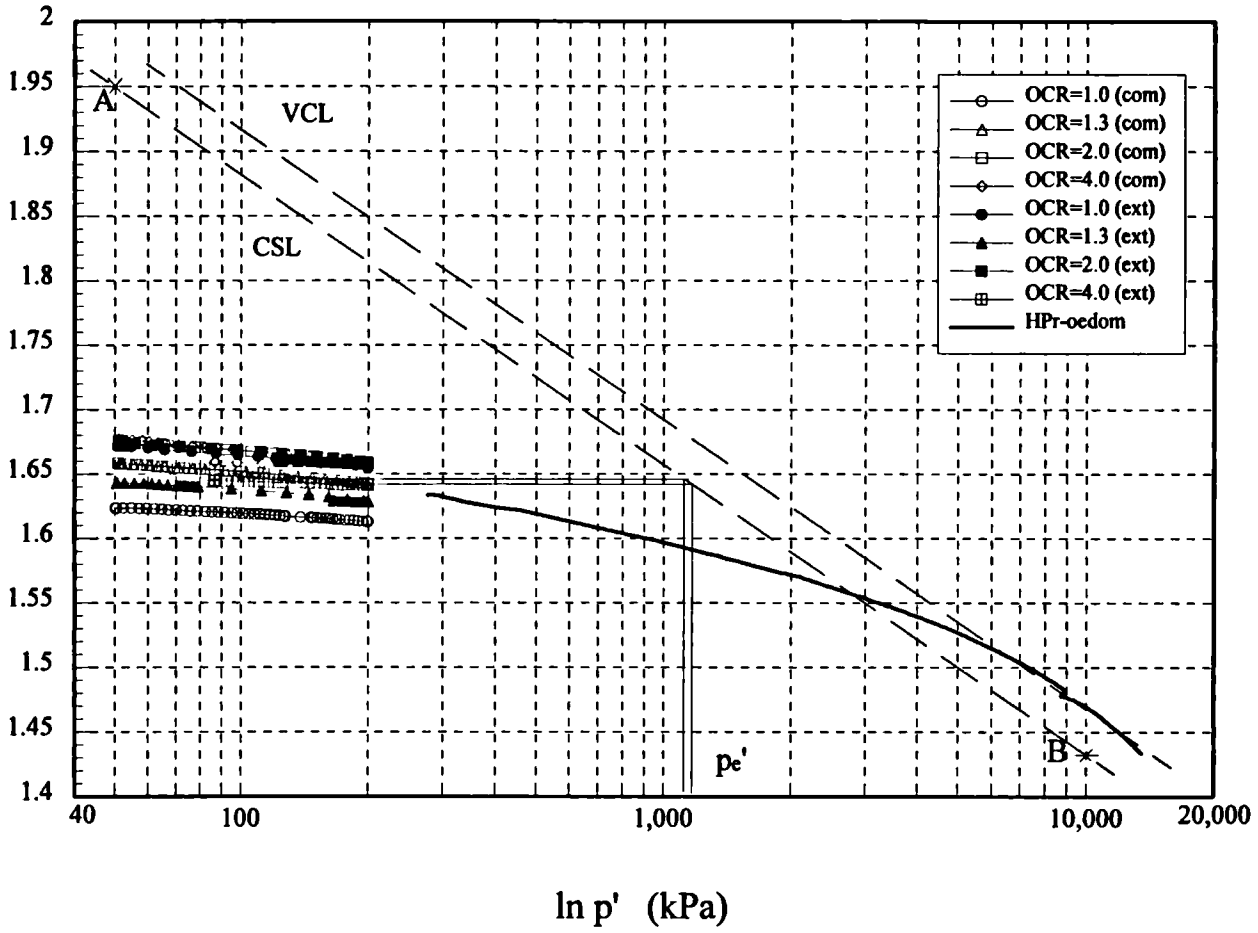


Fig.4.33 - Estimation of a tentative critical state line and virgin consolidation line for normalization

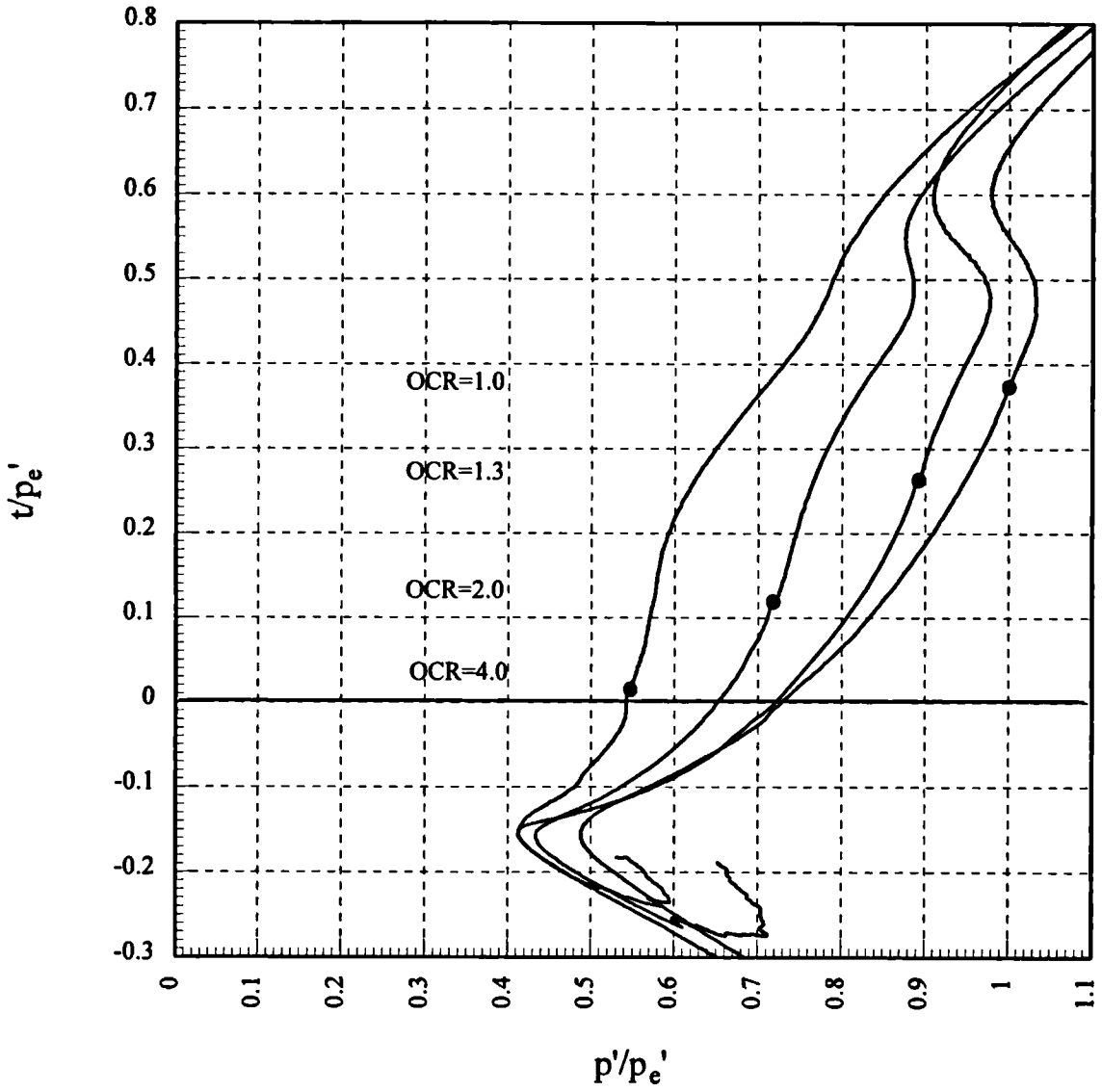


Fig.4.34 - Normalized effective stress paths from undrained triaxial compression and extension

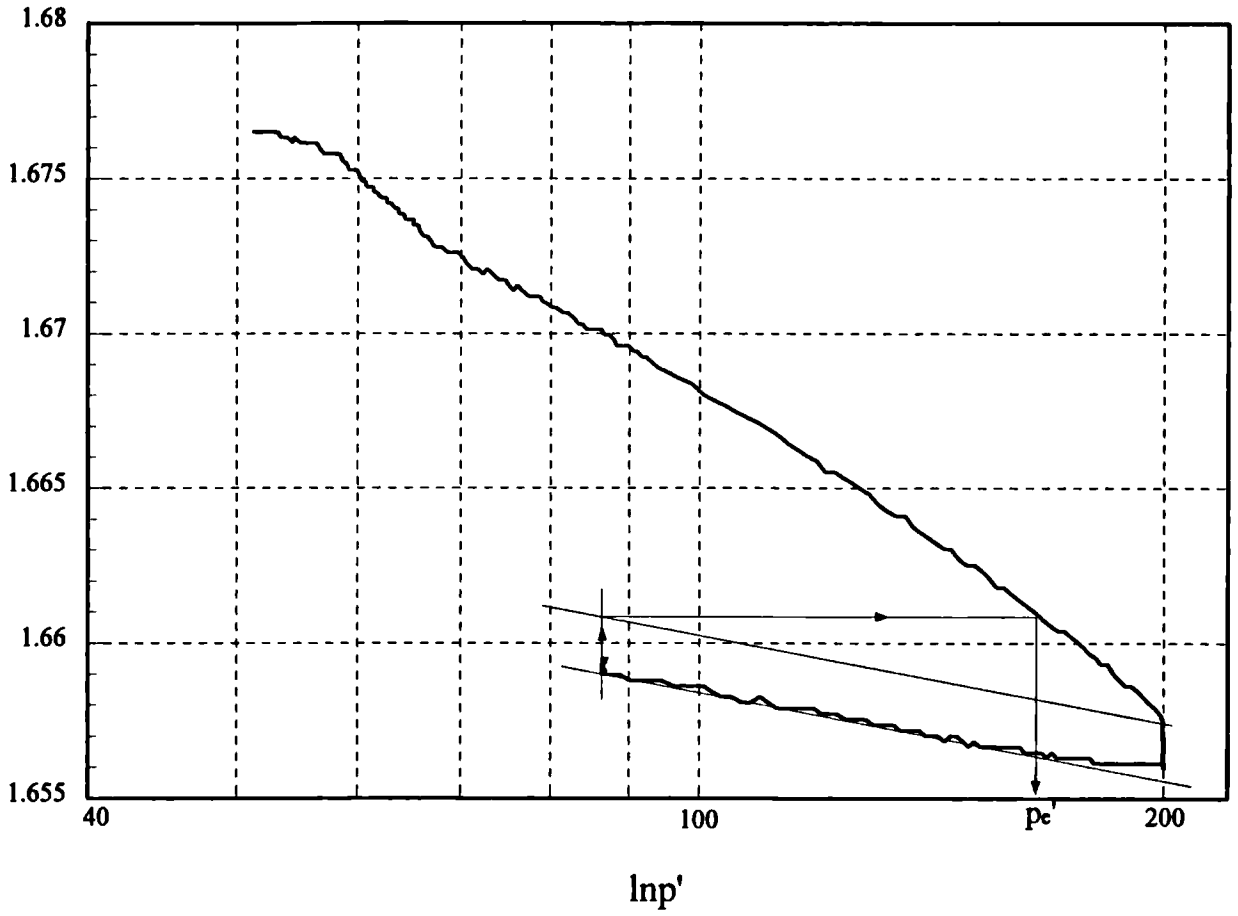


Fig.4.35 - Determination of the normalizing p_c'

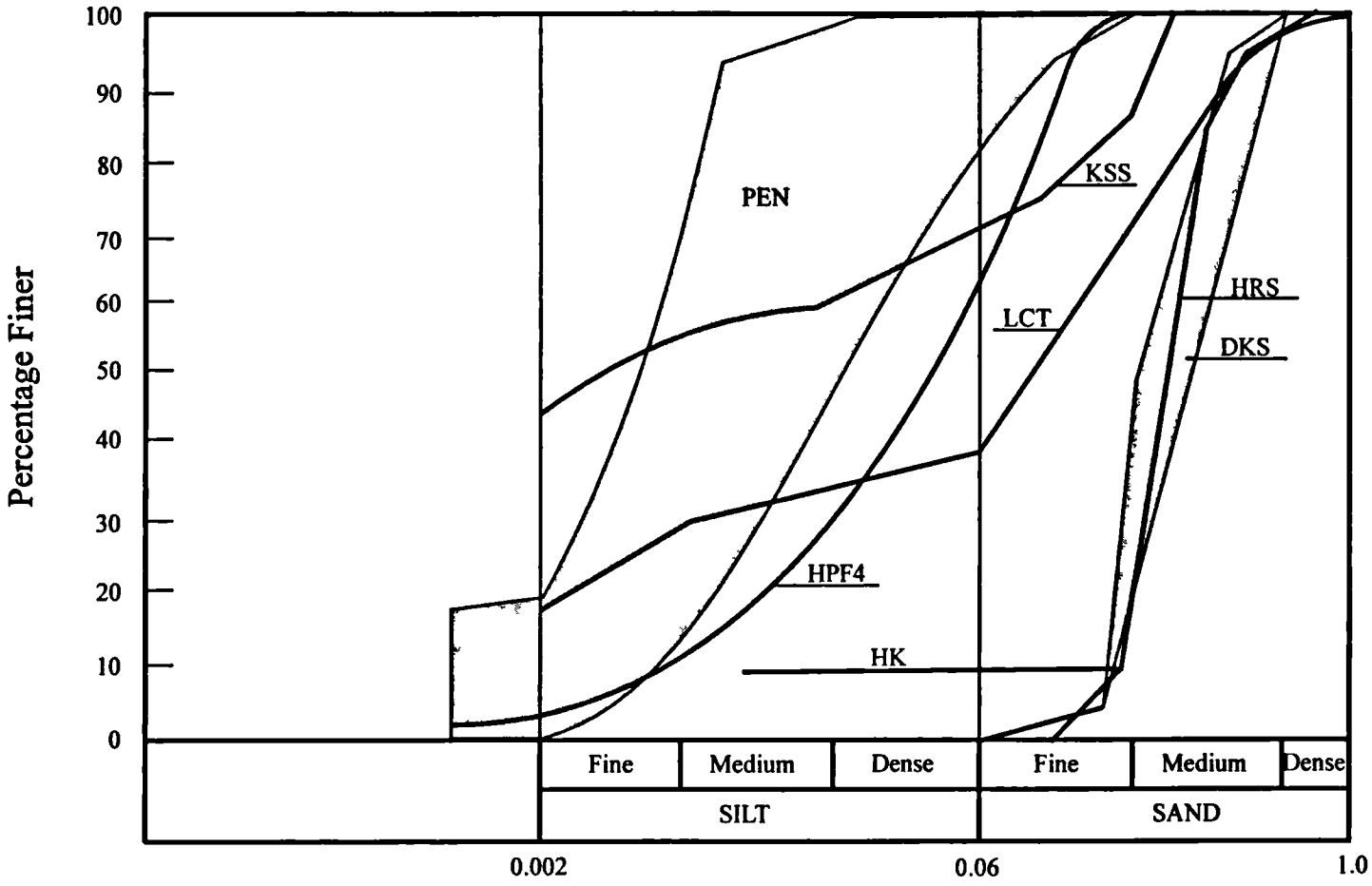


Fig.4.36 - Grain size distribution curves for different materials

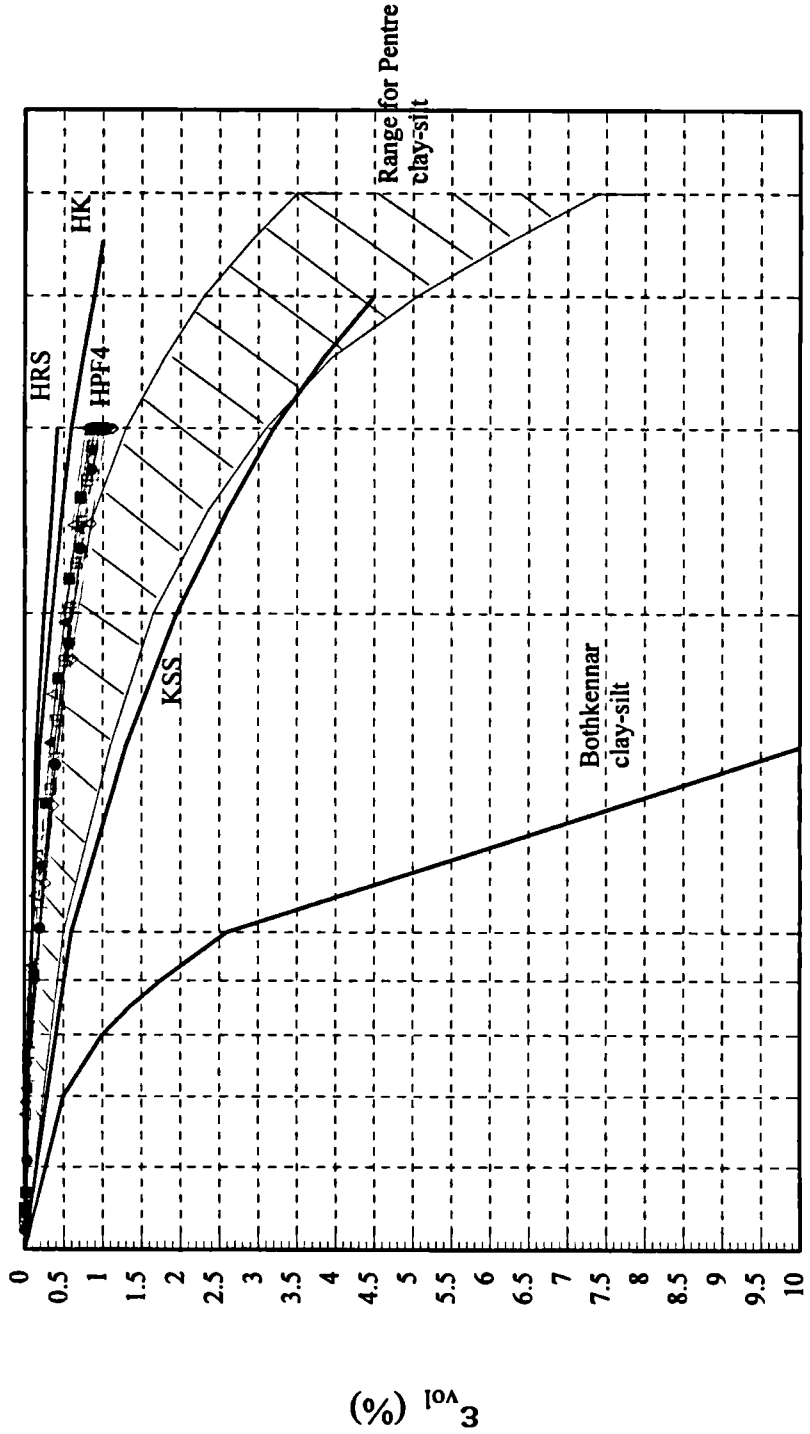
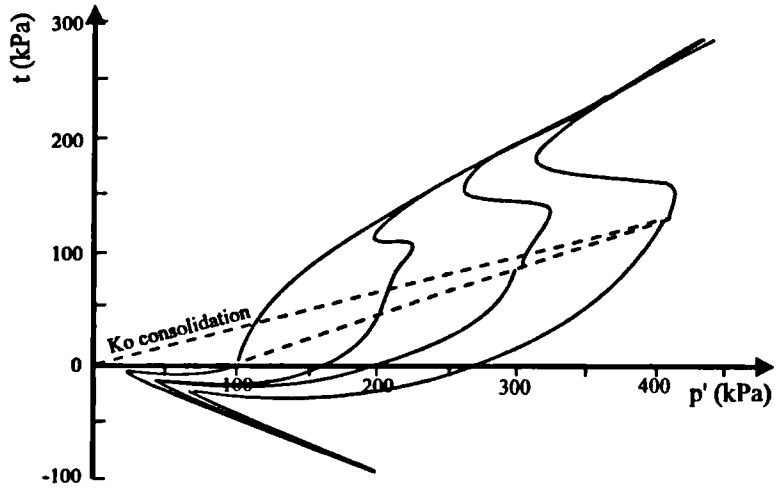
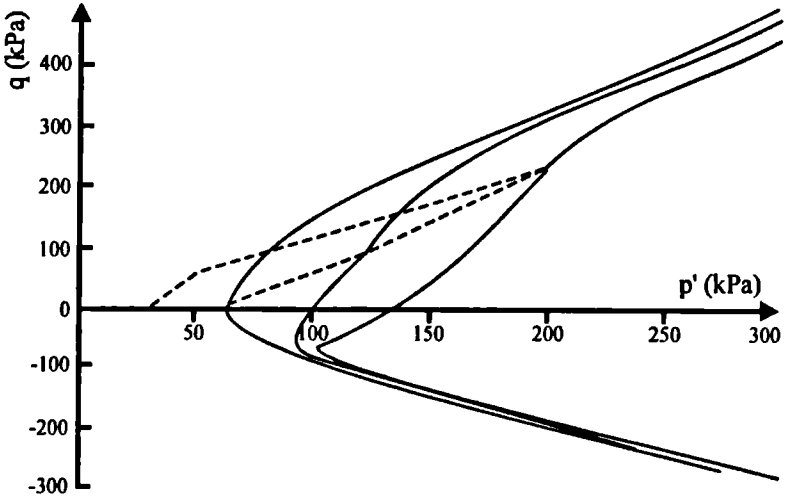


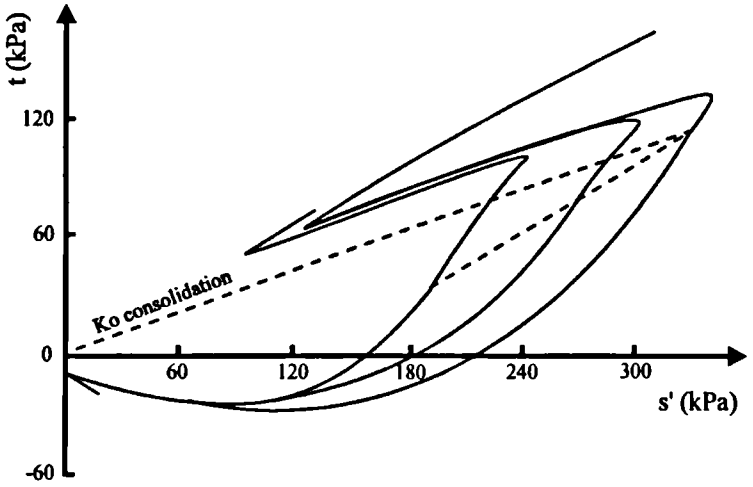
Fig.4.37 - Stress-volumetric curves for different materials tested at IC



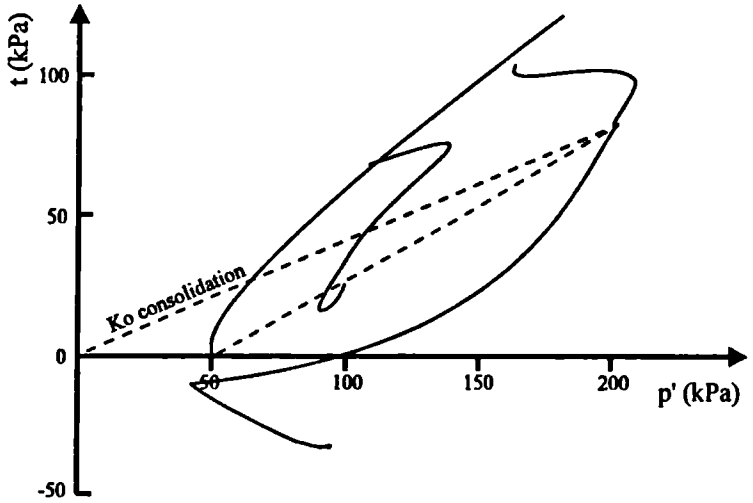
Loose Ham River Sand (Ovando-Shelley, 1986)



Dense Dunkirk Sand (DKS) (Kuwano, 1995)

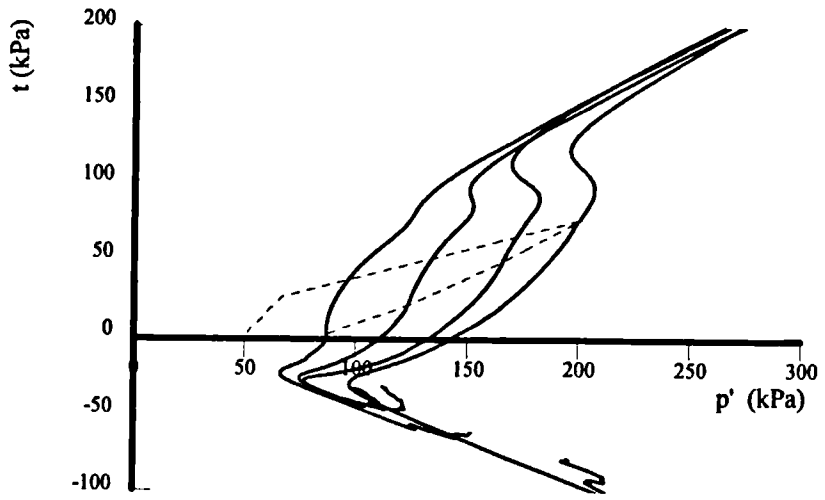


Loose Ham River Sand + Kaolin (HK) (Georgiannou, 1988)

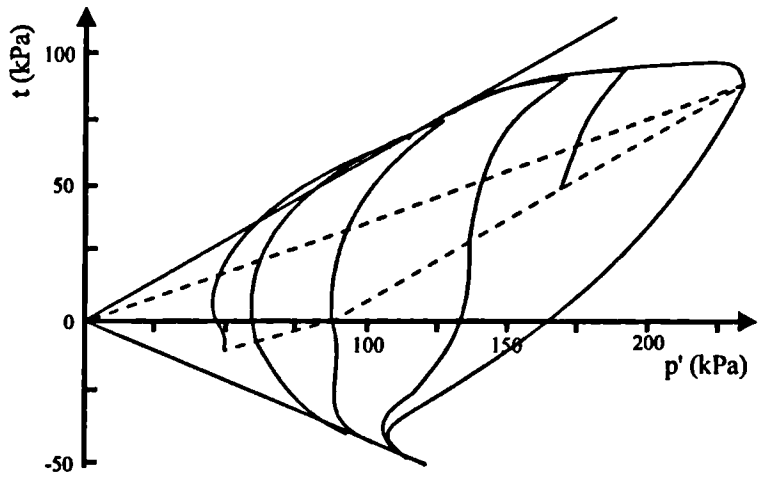


Loose HPF4 (Ovando-Shelley, 1986)

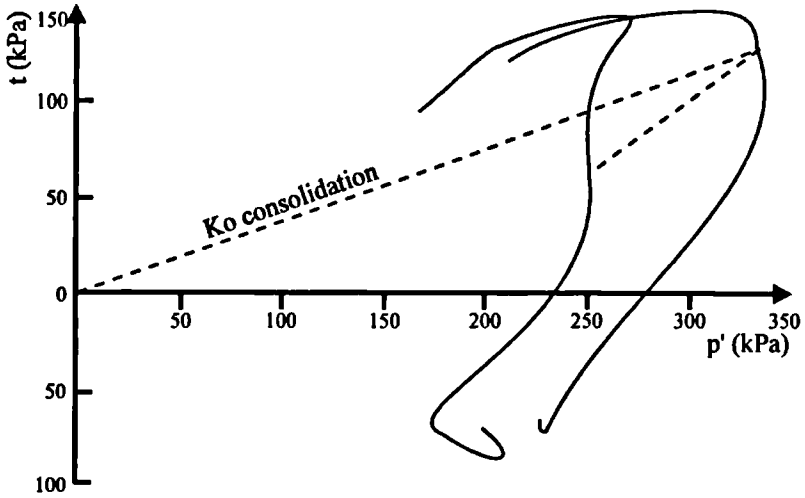
Fig.4.38 - The effective stress paths for different normally consolidated and overconsolidated materials



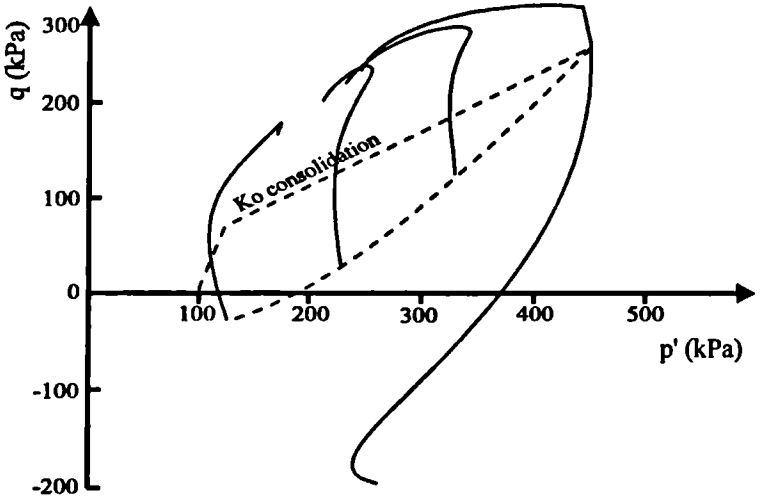
Dense HPF4 (this study)



Lower Cromer Till (LCT) (Gens, 1982)



Natural Pentre clay-silt (PEN), (Connolly, 1995)



Kaolin-silt-sand (KSS) (Rossato, 1992)

Fig.4.38 - (...cont) The effective stress paths for different normally consolidated and overconsolidated materials

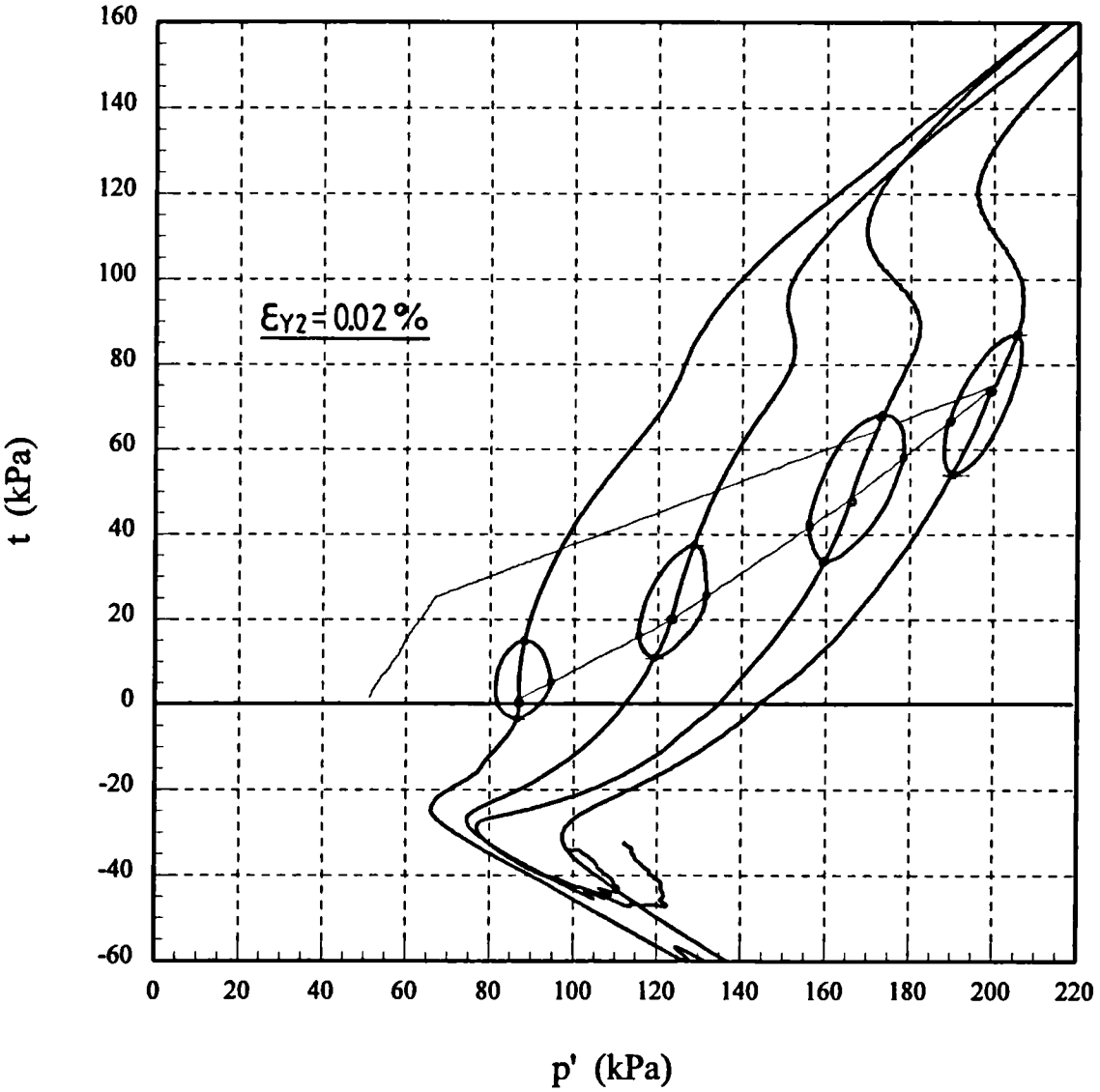


Fig.4.39 - Kinematic Yield Surfaces formed during Ko swelling of HPF4

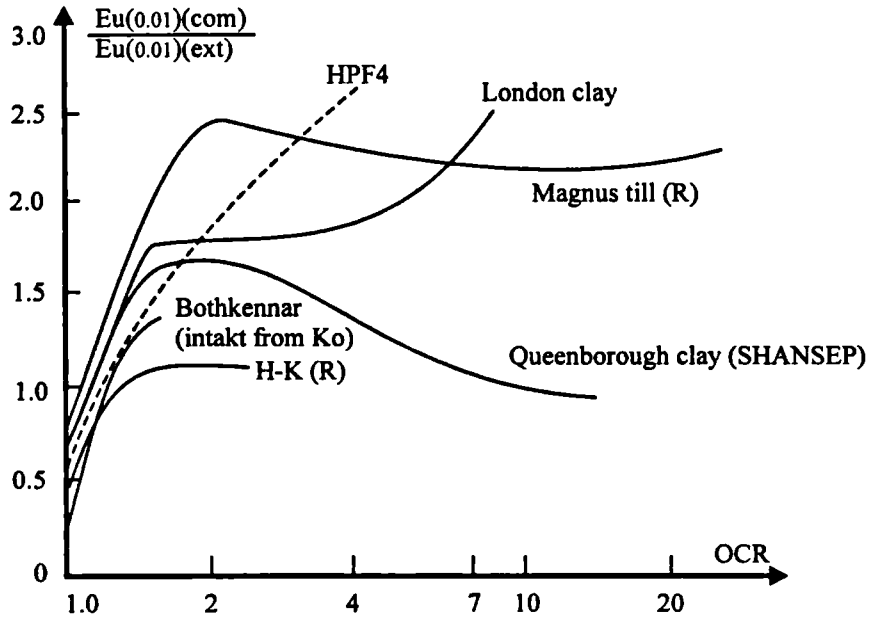


Fig.4.40 - Effect of loading sense on Eu(0.01) in CUKo tests (Jardine, 1994)

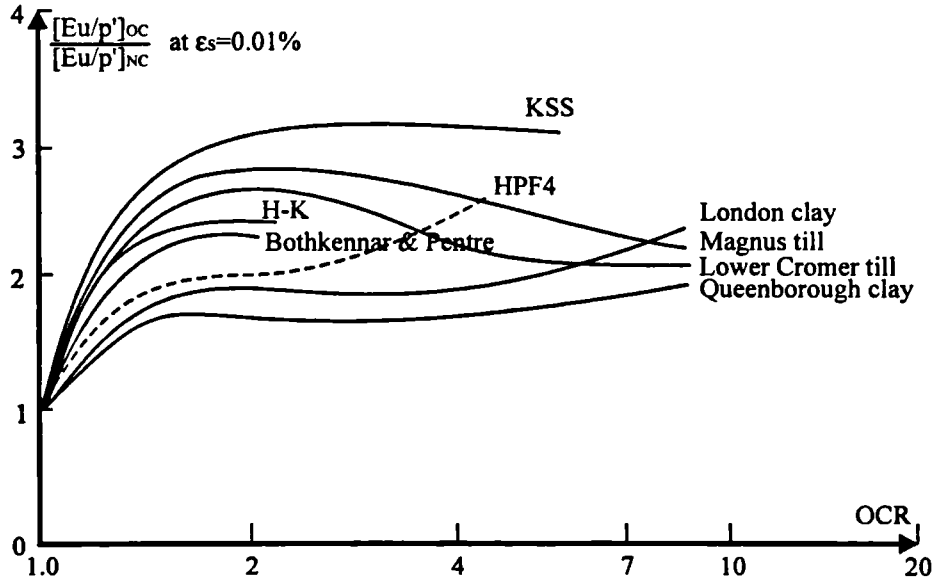


Fig.4.41 - Ratio of Eu(0.01) in overconsolidation and normal consolidation (Jardine, 1994)

Chapter 5

UNDRAINED ANISOTROPY OF K_o CONSOLIDATED HPF4

5.1. Introduction

This chapter presents results from a series of tests (named the M-Series) which was performed in the Hollow Cylinder Apparatus (HCA) to investigate the anisotropy of normally, K_o, consolidated HPF4. In particular, the tests were performed to identify:

i) The influence of the direction of the major principal stress on material behaviour. Tests were performed on K_o consolidated samples in which the direction of the major principal stress, α, was varied while the intermediate principal stress parameter *b* was held equal to 0.5.

(ii) The effects on material behaviour of varying *b*. This was achieved by comparing HCA results with b=0.5 and α=0° or 90° with results from triaxial tests presented in Chapter 4, where *b* was 0.0 when α=0° and b=1.0 when α was 90°.

The HCA tests were performed under nominal plane strain conditions. Ideally, this should involve zero radial strain. But, it was more convenient to maintain a constant *b* value and to ensure that all samples followed consistent effective stress paths. A value of b=0.5 was chosen for the following reasons:

- Plane strain failures (which are relevant to many practical geotechnical problems) often develop with b=0.3 to 0.5. In combination with triaxial results they cover a broad range of *b*-α combinations (Fig.5.1).

- The anisotropic shear strength of granular soils, resulting from the anisotropic alignment of particle contacts due to the depositional process, can be observed more clearly under plane strain conditions (ε_2=0) than under symmetrical triaxial conditions, where ε_2=ε_3 (Oda et al., 1978; Cornforth, 1964).

- The b=0.5 region of *b*-α space is free of the "no go" areas defined by Symes (1983), where large differences between the inner and outer cell pressure lead to significant

stress non-uniformities across the HCA sample wall (Fig.5.1).

This Chapter begins by presenting the undrained stress-strain-strength response of HPF4 when sheared with different orientations of the major principal stress, α=0° to 90°. All samples were initially K_o normally consolidated with α=0° and therefore had similar particle alignments. The value of *b* was set to 0.5 under drained conditions, while the values of *t* were reduced and the directions of the principal stresses were rotated undrained, before the samples were subjected to their final undrained shearing paths to failure. It will be seen that the initial micro-structure of the material formed during K_o consolidation significantly influences its subsequent response to shearing.

The results of the tests are then used to assess the applicability, to low OCR conditions, of the Bounding Surface framework, described in Chapter 2, for HPF4.

By comparing results from tests in the HCA with those from the stress path cell presented in Chapter 4, the effect of the *b* value on the behaviour of normally consolidated HPF4 will be evaluated. This relation between triaxial and HCA (b=0.5, i.e. nominal plane strain) characteristics of HPF4 is then compared with existing studies on triaxial vs. plane strain behaviour of granular materials.

5.2. Description of HCA M-Series tests

This Series of tests was designed to study the strength and yielding characteristics of K_o normally consolidated HPF4. The advantage of the HCA is that all samples can be prepared with the same "undisturbed in-situ" initial conditions, i.e. K_o consolidation, and then be sheared with different orientations of the major principal stress. Therefore, the response of the K_o consolidated structure of HPF4, when sheared with different orientations of the major principal stress, can be investigated without having to form, unload and then tilt the sample before re-loading, as is the case with some other experimental apparatus (Oda et al., 1978; Tatsuoka et al., 1986; Lam & Tatsuoka, 1988).

The Series consisted of six tests on normally consolidated samples, each sheared undrained with a different orientation of the major principal stress. The effective stress paths are presented in Fig.5.2. Each test is identified by a code *M*α, where the numerical value of α denotes the degree of principal stress rotation applied during undrained shearing. For example in the test labelled M30 the principal stress acted at 30° to the vertical. Hollow cylinder tests on

anisotropically consolidated HRS (Shibuya & Hight, 1996), high clay content mixture (KSS) and low clay content mixture (HK) (Menkiti, 1995) showed that major changes in material response occurred if sheared with the direction of the major principal stress between 0° and 45°. The change in response was much less marked for major principal stress directions greater than 45°. Consequently, in the M-Series more tests were performed with α in the range 0° to 45° (M0, M15, M30 and M45) than in the range 45° to 90° (M70, M90).

All samples were first K_o normally consolidated with K_o=0.5, to a mean effective stress p'=200 kPa, after saturation under a 400 kPa back pressure. The value of K_o was the same as that used for the triaxial tests presented in Chapter 4. At the final K_o consolidation point, *A* (Fig.5.2), the *b* value was changed from 0.0 to 0.5 under fully drained conditions. This "b-stage" plots as a single point (A) in *t-p'* space at the end of the K_o line (Fig.5.2). The rest of the test was performed under undrained conditions. After bringing all samples to a final common point *A* with b=0.5, then ideally the direction of the principal stress should be rotated by the required amount before shearing. However, hollow cylinder tests on anisotropically consolidated Ham River Sand (Shibuya & Hight, 1996), KSS and HK (Menkiti, 1995) showed that only a small amount of principal stress rotation (~20°) can be applied to a sample in this condition before it engages the local Bounding Surface, yields, and then experiences failure. So, to be able to apply the desired range of principal stress directions to the samples, it was necessary to bring the samples inside the local BS before applying the required rotation. This was achieved by reducing the deviator stress, *t*, while keeping b=0.5 (points B_α in Fig.5.2), before gradually rotating α from zero to the desired angle, while keeping *t* constant (stage B_α to C_α, Fig.5.2). After rotating α and allowing a suitable pause period for creep (for octahedral shear strain to reduce to 0.05 %/day), each sample was sheared by increasing the deviator stress from point C_α, whilst keeping α, *p* and *b* constant.

The effective stress paths developed are shown in Fig.5.2. None of the applied stress paths led to a distinct peak in the shearing resistance of the relatively dense HPF4. This behaviour is similar to that reported in Chapter 4 for the triaxial tests. All samples underwent Phase Transformation after reaching certain limiting effective stress conditions, after which they attempted to dilate steadily, generating negative pore water pressures. The HCA tests had to be aborted after smaller deviatoric strains than the triaxial experiments (ε_d~8% compared with up to 20%), because of the potential problems of damaging the HCA's proximity transducer local strain instrumentation.

5.3. Consolidation of HPF4 from HCA experiments

The K_o consolidation and swelling characteristics of HPF4 were established from the suite of triaxial tests described in Chapter 4. The same value of K_o (=0.5) was adopted for K_o consolidation of the hollow cylinder samples. In both test series normal consolidation was performed to the same final effective stresses (p'=200, t=75 kPa) and under the same back pressure (400 kPa). In this Section the consolidation characteristics of HPF4 from the two different devices will be compared. In this respect it should be noted that radial strains (which are supposed to be zero in K_o consolidation) are directly measured in the HCA.

5.3.1. K_o consolidation

The consolidation stress paths followed by all HCA samples are presented in Fig.5.3. They show that the consolidation process is well controlled and followed the same effective stress paths as the triaxial tests (Fig.4.7).

Plots of volumetric versus axial strain (ε_{vol} vs. ε_z) and radial versus axial strain (ε_r vs. ε_z) are presented in Fig.5.4 for all M-Series tests. All strain components are measured independently in the HCA. The strain origin is taken at p'=65 kPa and t=24 kPa (Fig.5.3) for these plots. The plots show (i) good repeatability and (ii) that K_o conditions were well satisfied ($\varepsilon_{vol} \approx \varepsilon_z$ and $\varepsilon_r \sim 0$) in the HCA with the adopted K_o value of 0.5. The radial strain ε_r obtains a maximum value of only 0.03% (on average) at the end of consolidation, when ε_z=1.0%.

The same consolidation and creep strain rates were applied as in the triaxial tests performed in the stress path cell. Consolidation was completed in 24 hours, giving a strain rate of ~1.0 %/day. A 24 hour creep period was then allowed for axial and volumetric strain rates to stabilize to 0.05 %/day (=0.002 %/hour), see Section 4.2.1. Typical strain-time curves are presented in Fig.5.5a, b and the corresponding axial and volumetric strain rates are shown in Fig.5.6a,b. These strain rates are similar to those obtained in the triaxial tests (Fig.4.6). The initial creep rate (~0.035 %/hour) immediately after K_o consolidation was the same in both sets of tests. Fig.5.6b is an enlarged view of Fig.5.6a, showing only the creep strain rates. It shows that the creep strain rate reduces to the desired 0.002 %/hour in the last 5 to 7 hours of the creep period.

Swelling behaviour measured in the HCA will be presented in Chapter 6, where samples were swelled back to OCR=1.3.

5.3.2. Compressibility

The compressibility of K_o normally consolidated HPF4 in the HCA is shown in *e-log*σ_v' and *v-lnp'* planes in Fig.5.7a, b. The non-linearity seen with triaxial tests is observed again, and similar compressibility parameters obtained. The compression index, C_c, varies from 0.02628 for $100<\sigma_v'<200$ to 0.039 for $200<\sigma_v'<300$, compared to 0.0264 and 0.03586 from triaxial tests. The slope of the normal compression line, λ, varies from 0.014 for $100<p'<150$ to 0.017 for $150<p'<200$, which is ~10% steeper than observed in the triaxial tests.

The repeatability of the initial void ratio of the samples was better than in the triaxial tests, with the average value being $e_o=0.637\pm0.007$. Only the sample for the M30 test was slightly looser, with $e_o=0.66$. However, considering the range of the minimum and maximum void ratio of HPF4 (Chapter 3), it can be concluded that both triaxial and hollow cylinder samples were of very similar initial relative density (average $D_r=88.7\%$).

5.4. Shearing stages of HPF4 in M-test Series

5.4.1. b-stage

5.4.1.1. Stress paths

After K_o consolidation, all samples were subjected to stress changes such that *t*, *p* and α (the main control parameters for stress path application, Chapter 3) remained constant, while *b* changed gradually from 0 to 0.5. This stage of the tests was performed under fully drained conditions and therefore *p'* also remained constant.

All samples in the Series underwent the same changes of the direct stresses (σ_z', σ_r' and σ_θ'), shown in Fig.5.8a, to achieve the *b* change. The vertical (σ_z') and circumferential (σ_θ') effective stresses reduce linearly, at the same rate, with increase in *b*, while the radial (σ_r') effective stress increases linearly at twice the rate. The torsional shear stress, $\tau_{\theta z}$, remains zero as α is not rotated. Figures 5.8b, c show that *p'* and *t* remain constant at all times during the *b* change.

5.4.1.2. Stress-strain response

Fig.5.9 shows the generation of volumetric strain with change in *b* for all tests. The

following points can be noted:

- The volumetric strain, ε_{vol}, is small, typically 0.06% during the complete *b*-change from 0 to 0.5, but increases very significantly (by a further 0.1%) during the subsequent creep period. The total volume change is about 15% of that generated during K_o consolidation.

- The results obtained are highly repeatable. The scatter in strain measurements between tests is less than ±0.005%.

- The initial material response is non-linear. The gradient $\Delta b/\Delta\varepsilon_{vol}$ is at least three times steeper at b=0.2 than at b=0.5.

- The typical variations of the stress components (σ_z', σ_r' and σ_θ') with deviatoric strain (ε_d) are presented in Fig.5.10. These plots show that a clear reduction in material stiffness occurs at about 0.05% deviatoric strain, when b≈0.2. This change mirrors the volumetric "yielding" seen in Fig.5.9, at ε_{vol}≈0.012% and b≈0.2.

A positive volumetric strain during the b-change indicates compression of the sample. It also shows that the HPF4 is not behaving as an isotropic linear-elastic material. If it were, then the volumetric strain should be zero if there is no change in mean effective stress, *p'*, (i.e. if $\Delta p'=0$).

5.4.1.3. Stiffness response

The variation of the direct strains (ε_r, ε_θ and ε_z) with *b* and deviatoric strain, ε_d, are presented in Fig.5.11a, b respectively. The strains presented are the direct response to the stress changes presented in Figs.5.8 and 5.10. Both ε_z and ε_θ are tensile, while ε_r is compressive. However, although σ_z' and σ_θ' reduce by the same amount, the reduction in circumferential strain (ε_θ) is twice that of the axial strain (ε_z), i.e. $\varepsilon_\theta/\varepsilon_z$≈2.0. From the equations of linear elasticity (Menkiti, 1995), this implies that the vertical unloading stiffness of HPF4 is at least double that applicable to horizontal unloading, i.e. $E_z'^{unld}/E_\theta'^{unld}$=2.0. In contrast, isotropic linear elasticity predicts equal vertical and circumferential strains during a *b*-change. However, the observed ratio for $\varepsilon_r/\varepsilon_z$ is ~4.5. Noting that $\Delta\sigma_r=-2\Delta\sigma_z$, this implies $E_z'^{unld}/E_r'^{load}$=2.25, and suggests that at least the horizontal plane in reconstituted HPF4 can be considered as isotropic.

5.4.1.4. Influence of *b*_change on soil fabric

The volume changes that occur during the b-change are a result of a structural adjustment of the soil fabric to the new stress conditions. Since the measured volumetric strains are relatively small (15%) compared to the volumetric strains during K_o consolidation, only minor structural changes can occur and subsequent material behaviour will still be governed by the initial K_o fabric.

Menkiti (1995) considered in greater detail the effect of a *b*-change on the fabric of KSS and HK mixtures. He concluded that an increase in radial stress σ_r' results in new particle contacts and an increase in the area of existing contacts perpendicular to the radial direction, while an unloading in σ_z' and σ_θ' results in a small loss of contacts perpendicular to the vertical and circumferential directions. The overall fabric after the *b*-change is thought to be very similar to the initial K_o structure, but with more particle chains in the radial, σ_r ($=\sigma_2$) direction. These chains are anticipated to provide additional lateral support to the vertical force chains during subsequent vertical loading. Overall, Menkiti (1995) concluded that the *b*-stage resulted in an increase of material strength. As will be shown in later sections, this *b*-change has a particularly strong influence on the behaviour of HPF4.

5.4.2. Undrained unloading

As noted above (Section 5.2), any attempt to rotate the direction of the major principal stress by more than 20°, after applying K_o consolidation and the *b*-change, is likely to lead to failure. It was therefore necessary to unload the samples before applying the desired change in direction of the major principal stress.

All samples from the M-test Series, apart from that for test M0, were therefore unloaded under undrained conditions to a prescribed deviatoric stress level, holding constant the values of *p*, α (=0°) and *b* (=0.5) and reducing *t* before attempting to rotate the direction of the major principal stress. In Fig.5.2 this stage is represented by the stress paths from A to B_α which show the excellent repeatability followed by all samples.

5.4.2.1. Stress-strain behaviour

Fig.5.12 is a summary plot showing deviatoric stress, *t*, versus deviatoric strain for all samples during undrained unloading; the strain measurements are, generally, repeatable to within

±10%. The maximum generated deviatoric strain, ε_d, is only ~0.25% for unloading down to the isotropic axis (test M90), because the previous K_o consolidation formed strong vertical particle chains which develop small strains when initially unloaded. Relatively small strains were developed during the creep period after undrained unloading (Fig.5.12).

The variations of direct stresses (σ_z, σ_r and σ_θ) and direct strains (ε_z, ε_r, and ε_θ) with deviatoric strain (ε_d) are presented in Fig.5.13 and Fig.5.14 respectively, for test M90 which underwent unloading to the isotropic axis. The trends shown in these plots are similar for all other tests, except that they experienced only partial unloading. Unloading instigates vertical extension, circumferential compression and almost no change in radial strain (Fig.5.14).

Creep period was allowed after this stage for axial and circumferential strains to reduce to 0.05 %/day (0.002 %/hour), and pore pressure generation to reduce to 0.1 kPa/hour.

5.4.2.2. Stiffness behaviour

The variation of the octahedral shear stiffness, *G*, with deviatoric strain, ε_d, for the unloading stage of each test is presented in Fig.5.15. The shear stiffness, *G*, is defined as $\Delta J/\varepsilon_d$ and the stress and strain components are defined in relation to the local origin at point *A* in Fig.5.2. So,

$$\Delta J = \frac{1}{\sqrt{6}}((\Delta\sigma_1 - \Delta\sigma_2)^2 + (\Delta\sigma_2 - \Delta\sigma_3)^2 + (\Delta\sigma_1 - \Delta\sigma_3)^2)^{0.5} \qquad (5.1)$$

$$\varepsilon_d = \frac{2}{\sqrt{6}}((\Delta\varepsilon_1 - \Delta\varepsilon_2)^2 + (\Delta\varepsilon_2 - \Delta\varepsilon_3)^2 + (\Delta\varepsilon_1 - \Delta\varepsilon_3)^2)^{0.5} \qquad (5.2)$$

$$G = \frac{\Delta J}{\varepsilon_d} \qquad (5.3)$$

The plots show stiffness curves that are repeatable to within ±5 MPa of the mean curve for all six samples. The stiffness values represent behaviour under plane strain vertical unloading and are taken in later Sections of this Chapter to provide one of the 'limit' curves to be compared with shear stiffnesses derived from the rotational and shearing stages of the tests. Another 'limit' curve used for later comparisons is the undrained shear stiffness in nominal plane strain vertical compression (i.e. that observed in test M0).

5.4.3. α_rotation stage and shearing with constant α inclination

After undrained unloading and subsequent creep, samples were exposed to a principal stress rotation from 0° to α° (paths B_α-C_α in Fig.5.2). During this rotation of the direction of the major principal stress, the values of *t*, *p*, and *b* were kept constant.

Subsequent undrained shearing from point C_α was performed by increasing *t*, while keeping α, *b* (=0.5) and *p* constant.

5.4.3.1. Stress-strain response

A) α_rotation stage

The variation of the direct stresses (σ_z, σ_r and σ_θ) with deviatoric strain (ε_d) and the torsional shear stress ($\tau_{\theta z}$) with torsional shear strain ($\gamma_{\theta z}$) are presented in Fig.5.16a and Fig.5.16b, for tests M15, M30, M45 and M70. The plots in Fig5.16a show that the samples undergo unloading in terms of the axial deviator stress (σ_z-σ_θ), with σ_z reducing and σ_θ increasing. While (σ_z-σ_θ) reduces, the absolute value of torsional shear stress, $\tau_{\theta z}$, gradually builds up as α increases (Fig.5.16b), until α reaches 45°, after which $\tau_{\theta z}$ starts to reduce. It should be noted here that $\tau_{\theta z}$ is drawn negative, as it acts in clock-wise direction on the element of sample's wall. The dominant mode of deformation during α_rotation is torsional shearing plus vertical extension of the sample (continuing from the previous undrained unloading stage), as can be seen from Fig.5.17 which shows the variation of strain components with deviatoric strain. For this plot the strain origin is taken at the beginning of this stage, i.e. from point B_α for each individual test (Fig.5.2). Negative values of ε_z indicate axial extension, while positive values of ε_θ indicate a reduction in the sample's circumference. The radial strain, ε_r (=ε_2), varies around the zero value. This is to be expected as a *b* value of 0.5 was imposed to implement nominal plane strain conditions.

The variation of the shear strain components, (ε_z-ε_θ) and $\gamma_{\theta z}$, with deviatoric strain (ε_d) are compared in Fig.5.18a, where it can be seen that the component (ε_z-ε_θ) becomes more dominant as rotation progresses. The early parts of these curves are shown in the enlarged view given in Fig.5.18b. Inspection of this figure suggests that during the initial stages of rotation all samples experienced a sharp change in the strain ratio $\Delta(\varepsilon_z$-$\varepsilon_\theta)/\Delta\varepsilon_d$ when ε_d reached ~0.02%. The strain ratio $\Delta(\varepsilon_z$-$\varepsilon_\theta)/\Delta\varepsilon_d$ then increased to values between ~0.8 (for test M15 rotation) and ~1.0 (for test M70 rotation), Fig.5.19.

This change in strain increment direction can be identified as a Y_2 yield point and is associated with a similar deviatoric strain to that seen under triaxial conditions (see Chapter 4). On reaching this yield point, the strain increment direction changed from that applying under the pseudo-elastic pre-Y_2 conditions, to that set by the previous unloading stress path.

The standard creep regime was applied (over a period of 12 hours) for strains to diminish to 0.002 %/hour and excess pore water pressure change rates to diminish to 0.1 kPa/hour. Mean effective stress, p', reduced further for ~15 kPa, on average, during the creep period.

B) Shearing with α=const

The effective stress paths associated with the final shearing stages of the tests start from their final rotational point C_α in Fig.5.2. These effective stress paths show a steep increase in deviatoric stress, t, almost without any change in mean effective stress, p', until the Y_3 yield point is reached.

After the Y_3 yield point, the samples attempt to contract, generating reductions of p' with increasing t, until the Phase Transformation Point, PTP, is reached. This contraction, which manifests itself as a decrease in p' from the start of shearing (C_α) to the PTP in Fig.5.2, increases systematically with α. The values of t and p' at which the PTP's are reached are not unique, but fall dramatically as α increases.

After the PTP is reached the effective stress paths turn clockwise and the samples attempt to dilate generating negative pore water pressures. This behaviour is similar to that observed in the triaxial compression tests presented in Chapter 4.

The variation of all strain components with deviatoric strain, ε_d, for the shearing stages of all the tests in the M series are presented in Fig.5.20. The strains plotted are the changes from the beginning of the shearing stage (i.e. points C_α in Fig.5.2). If these tests were modelling precisely plane strain conditions, then the radial strains, (ε_r=ε_2), should all be zero. However, at the beginning of shearing for tests M0 and M15, the radial strain is compressive and nearly equal to the axial strain, although ε_r becomes less significant as ε_d increases, Fig.5.21. This indicates that for these tests the use of b=0.5 does not produce plane strain conditions. For the remaining tests, the radial strains are very small throughout. The b=0.5 state does approximate to plane strain conditions, but it is clear that the true plane strain tests would develop a range of b-values between 0.0 and 0.5 at different stages.

The strain data are re-plotted in Fig.5.22 in the form of (ε_z-ε_θ) and $\gamma_{\theta z}$ against ε_d for tests

M15, M30, M45 and M70. These show that tests M15 and M30 undergo a predominantly compressive mode of deformation, while test M45 experiences mainly a torsional shear and test M70 an extensive mode of shearing.

Plots of mean effective stress, p', against deviatoric strain, ε_d, are presented in Fig.5.23. Initially there is no change in p' as the deviatoric strain increases. The points at which the p'-ε_d curves show slight non-linearity are tentatively identified as Y_2 yield points. Such points are marked on Fig.5.23. The Y_3 yield points are associated with a sudden changes in stress-strain gradients. The strains associated with the Y_2 and Y_3 yield points and the PTP's for the shearing stages of all tests are listed in Table 5.1.

Fig.5.24 presents the deviator stress-deviator strain plots for the shearing stage of each test. The strains presented are the changes from the start of the shearing stage.

Table 5.1: Strain levels associated with the Y_2 and Y_3 yield points during shearing stage

TEST	Y_2 (%)	Y_3 (%)	PTP (%)
M0	0.01	0.15	2.0
M15	0.01	0.12	1.85
M30	0.01	0.05	1.9
M45	0.01	0.03	1.6
M70	0.01	0.03	1.5

5.4.3.2. Stiffness behaviour

The secant octahedral shear stiffness, G, for both the α-rotation and constant-α shearing stages is defined as $\Delta J/\varepsilon_d$ (Eq.5.3), where the stress and strain components are defined in relation to the beginning of each stage, i.e. from origins B_α and C_α (Eqs.5.1 and 5.2). If this is not done, and ΔJ is calculated from the accumulated values ($= J_i - J_o$), then the α_rotation stages (from B_α to C_α) appear to be absurdly soft, because J is constant along these paths.

The torsional shear stiffness, $G_{\theta z}$, is calculated from the direct measurements of torsional shear stress, $\tau_{\theta z}$, and torsional shear strain, $\gamma_{\theta z}$, as

$$G_{\theta z} = \frac{\Delta \tau_{\theta z}}{\gamma_{\theta z}} \qquad (5.4)$$

Tests M0 and M90 do not undergo principal stress rotation and therefore represent nominal plane strain compression and extension. The secant shear stiffness curves for these two tests conform with the trends shown in Figs.4.25 and 4.30, showing that the normally consolidated HPF4 is generally half as stiff in undrained compression as it is in extension. These two curves will be used as a 'limit' curves for comparison with the shear stiffnesses from the other tests.

The variation of secant shear stiffness with deviatoric strain for both the α-rotation, constant *t* (G(alpha)) and the constant α, *t* increasing shearing (G(shear)) stages of tests M15, M30, M45 and M70 are shown in Fig.5.25. Also plotted are the 'limit' curves G(M0) and G(M90) from tests M0 and M90. At first sight, it appears that undrained plane strain extension gives a much stiffer response (i.e. G(M90)), than torsional shearing in both the α-rotation and the shearing stages. The curves from the latter fall towards the stiffness obtained in undrained plane strain compression (i.e. G(M0)). The octahedral stiffness seen during α rotation stages tend to fall systematically with the value of *t* at which they were performed. Tests M15 and M30 gave similarly stiff α-rotation curves (with t=60 and 45 kPa, respectively), while M70 gave the softest (t=20 kPa). However, to gain a more meaningful picture of material stiffness, the observed behaviour has to be decoupled into its directional components.

A) α_rotation stage

As observed in Section 5.4.3.1, during the α_rotation stage two sets of stress changes take place. The torsional shear stress, $\tau_{\theta z}$, gradually increases, while $(\sigma_z-\sigma_\theta)$ reduces (Fig.5.16). The sample therefore continues to unload in terms of the axial deviator stress. The secant shear stiffness response can now be resolved into two similar components. Firstly, $G_{\theta z}(alpha)=\Delta\tau_{\theta z}/\Delta\gamma_{\theta z}$, which represents the torsional shear stiffness in the α-rotation stage. The variation of $G_{\theta z}(alpha)$ with deviatoric strain is compared with the data presented on Fig.5.25 in Fig.5.26. In all four tests the curve lies above that for undrained extension (i.e.G(M90)), indicating that this component is very stiff. The second stiffness component, $G_{\Delta\sigma}$, is associated with the continuing deformation of the sample in 'plane strain' extension and is calculated from the shear stresses and strains corresponding to this mode of deformation:

$$G_{\Delta\sigma} = \frac{\sigma_z - \sigma_\theta}{2(\varepsilon_z - \varepsilon_\theta)} \qquad (5.5)$$

The variations of both these stiffness components with deviatoric strain are shown in Fig.5.27 for the α_rotation stage of each test. Also shown on these figures are the octahedral shear stiffness variations (*G(alpha)*). In all tests $G_{\Delta\sigma}$ reduces abruptly with increase in deviatoric strain and becomes relatively soft compared to both *G(alpha)* and $G_{\theta z}$*(alpha)*. Inspection of Fig.5.18, which shows the variation of the shear strain components with deviatoric strain, shows that the $(\varepsilon_z-\varepsilon_\theta)$ component suddenly increases its rate of change after Y_2 yield occurs, becoming far larger in relation to the $\gamma_{\theta z}$ component. This explains the acceleration in the reduction of $G_{\Delta\sigma}$ observed in Fig.5.27.

B) Shearing stage

The shearing stage, performed after α-rotation, also involves coupling of torsional shear and axial strains. The variations of secant shear stiffness, *G(shear)*, and secant torsional shear stiffness, $G_{\theta z}$*(shear)* with deviatoric strain, are presented in Fig.5.26 for each test, together with those from the α_rotation stage. The $G_{\theta z}$*(shear)* and *G(shear)* values are much softer than those observed during the α_rotation stage with the values of *G(shear)* falling close to or below those associated with undrained plane strain compression (i.e. G(M0), Fig.5.25).

5.4.3.3. Directions of the major principal stresses and strains

Fig.5.28 presents the changes in the major principal stress, stress increment and strain increment directions with deviatoric strain (i.e. α_σ, $\alpha_{\dot\sigma}$ and $\alpha_{\dot\varepsilon}$ respectively), seen during both the α-rotation and the shearing stages of tests M15, M30, M45 and M70. The deviatoric strain, ε_d, is calculated from the beginning of the α-rotation stage. To avoid cluttering the figure with data points, only every third point is plotted. During the α-rotation stage the control parameters (*p, q, b* and α) are applied in such a way that they impose a constant difference between α_σ and $\alpha_{\dot\sigma}$, such that $\alpha_{\dot\sigma}=\alpha_\sigma\pm45°$ (see Appendix V). This can clearly be seen in Fig.5.28. The major principal strain increment direction, $\alpha_{\dot\varepsilon}$, shows a change in orientation between ε_d=0.01% and ε_d=0.02%, which can be associated with the interception of the Y_2 yield surface (as observed on the strain plots in Fig.5.18). Generally, the major principal strain increment direction, $\alpha_{\dot\varepsilon}$ does not coincide with the major principal stress increment direction, $\alpha_{\dot\sigma}$, at the beginning of the α-rotation stage. They do, however, tend to merge with each other at the end of the α-rotation stage, when creep effects move the effective stress point inside the local bounding surface.

During the shearing stage of each test α is maintained constant and this in turn fixes $\alpha_{\dot{\sigma}}$ to be equal to α_{σ}. Inspection of the results presented in Fig.5.28 shows that this is generally the case although there is some variation in the $\alpha_{\dot{\sigma}}$ values due to slight experimental scatter combined with the incremental calculation procedure. At the beginning of the shearing stage the major principal strain increment and stress increment directions coincide. This can be seen better on a separate plot where incremental changes are presented only for the shearing stage (Fig.5.29). They remain coincident until the new Y_2 yield point is reached (data points plot above α_{σ} line), where the major principal strain increment direction changes. The manner in which it changes depends on the mode of deformation of each sample. For the M15 and M30 tests, $\alpha_{\dot{\varepsilon}}$ switches to a predominantly compressive mode of deformation (data points plot below the α_{σ} line) and remains approximately constant in relation to α_{σ} and $\alpha_{\dot{\sigma}}$. In test M15, $\alpha_{\dot{\varepsilon}} \approx \alpha_{\sigma}$-5°, while in test M30 $\alpha_{\dot{\varepsilon}} \approx \alpha_{\sigma}$-10°. The ($\alpha_{\dot{\sigma}}$-$\alpha_{\dot{\varepsilon}}$) value is smaller in test M15 than in test M30 because compression is more dominant in the former than in the latter case. Test M45 is special because both ε_z and ε_{θ} are close to zero, while the direct stresses σ_z, σ_r, and σ_{θ} are equal and constant during the shearing stage. The sample therefore undergoes only torsional shearing, $\gamma_{\theta z}$. In this case α_{σ} , $\alpha_{\dot{\sigma}}$ and $\alpha_{\dot{\varepsilon}}$ all coincide with α_{σ}=45°. In test M70 the predominant shearing mode is extension (Fig.5.20). The major principal stress increment direction $\alpha_{\dot{\sigma}}$ again coincides with α_{σ}, while $\alpha_{\dot{\varepsilon}}$ remains constant, at $\alpha_{\dot{\varepsilon}} \approx \alpha_{\sigma}$+10°, continuing the extension mode of deformation started during the previous α-rotation stage.

So, it appears that in both the α_rotation and the subsequent shearing stage major strain increment directions are initially set by the sample's recent stress history and that a period of adjustment is required until the current Y_2 surface becomes re-aligned with the new stress path direction (Fig.5.29a).

5.4.3.4. Shear strength anisotropy of HPF4

Since the effective stress paths followed by the M-Series tests do not exhibit distinct peaks, the values of t associated with the Phase Transformation Points (PTP's) are used to evaluate the influence of principal stress rotation on the engineering strength available under undrained conditions. In general, the stress-strain curves of HPF4 become relatively flat after reaching PTP; furthermore, in geotechnical structures shear bands could form where shear strains are concentrated and dilation is accommodated without p' increasing, by inflow of water from surrounding soil. In this respect, the PTP is not a totally arbitrary boundary and the following points are noted:

- From Fig.5.2 it is clear that the deviator stress, t, available to K_o consolidated HPF4, at the PTP's drops as α increases. These values of t are plotted against α in Fig.5.30a and show a drop of 65% when α is rotated from 0° to 90°. Most of this reduction occurs for α between 0° and 45° and only small reductions occur for α between 45° and 90°. Associating these values of t with the undrained strength, c_u^{PTP}, and normalising by the initial effective stress prior to shearing, p_o', gives the variation of c_u/p_o' with α shown in Fig.5.30b. Also plotted on these figures are results from the triaxial compression (TXC) and triaxial extension (TXE) tests presented in Chapter 4.

- The variation of the mobilized angle of shearing resistance, ϕ', at the PTP's with α is presented in Fig.5.31. These results also indicate a high degree of anisotropy, with ϕ' dropping from a maximum of 53°, for α=0°, to a minimum of 36°, for α=70°. An interesting feature is the high ϕ' values for α=0° and 15° (53° and 52° respectively), compared to the lower values of ϕ' between 41° and 36° for $\alpha \geq 30°$. Also plotted on this figure are ϕ' values at the PTP's from the triaxial compression (TXC) and triaxial extension (TXE) tests presented in Chapter 4. The meaning of the "plane strain" envelope will be described later in this Chapter.

- The high ϕ' values observed in tests M0 and M15 may be partly explained by the fact that torsional shearing ($\tau_{\theta z}$) had little effect on their mode of failure. Their predominant collapse mode involved vertical compression and circumferential bulging. At higher values of α, the torsional shear component, $\tau_{\theta z}$, increases in importance and ϕ' reduces. In the tests with higher values of α distinct spiral failure mechanisms were observed and the effective stress paths indicate more contractant behaviour (Fig.5.2).

5.5. Bounding surface (BS) for initial anisotropy of HPF4

5.5.1. Presentation of the local BS in q-p'-α space

In Chapter 4 the definition of the local BS for K_o normally consolidated samples of dense HPF4 under triaxial compression and extension conditions was discussed, that is to say for b=0.0, α=0° and b=1.0, α=90°. It was shown that the normalized local BS shrinks during overconsolidation, so that the BS for normally consolidated samples does not apply to overconsolidated states.

From the M-Series of tests described in this chapter it is possible to construct the local BS for K_o normally consolidated HPF4 under conditions where α varies, but with b held equal to 0.5. This variation in α provides a third dimension to the BS in addition to the triaxial (q-p') plane (or α=0° plane). The results of the M-Series tests, along with the constructed local BS are plotted in t-p'-α space in Fig.5.32. The projections of these effective stress paths and local BS onto the t-p' plane are presented in Fig.5.33. It should be noted that all samples are of nominally identical initial void ratio.

The BS in the α=0° plane is defined in a similar manner to that for the triaxial tests presented in Chapter 4. The effective stress path from the shearing stage of test M0 (nominal plane strain compression) defines the local BS above the final consolidation point A. The initial unloading (from point A down to the isotropic axis) part of the effective stress path from the shearing stage of test M90 (nominal plane strain extension) defines the local BS below point A. The remaining part of the stress path from the shearing stage of test M90 gives the local bounding surface for α=90°.

The local BS for other constant α-sections were constructed using the following information:

- The post Y_3 portions of the stress paths from the shearing stages (constant α-sections) of the other M-Series tests were assumed to follow the local BS.

- All constant α-sections of the BS must pass through point C, on the isotropic axis (Fig.5.32 and Fig.5.33), because α can take any value between 0° and 90° when t=0 and therefore point C is common for all constant α-sections.

- The post Y_3 portion of the α_rotation stages of each test (i.e. portions B_α-C_α on Fig.5.2, where α denotes the final value of rotation at that stress level) give further points for constant-α sections of the BS. In Fig.5.34a the projections of the α-rotation stress paths onto the p'-α plane are shown. As noted previously, after unloading to reach points B_α and prior to the α_rotation stage, the samples were allowed to creep under undrained conditions with (p, t, b=0.5 and α=0 kept constant). As a result, the mean effective stress, p', reduced and the effective stress state moved inside the local BS for α=0. The reduction in p' marked at the top right hand corner of Fig.5.34a is the total change from point A (p'=200 kPa), due to both unloading and subsequent creep. The values of p'

plotted at α=0° are therefore those after the creep period, just prior to the α_rotation stage. When the α_rotation stage began, the samples' initial response was to maintain an almost constant *p'*, without any excess pore pressure generation. However, a clear Y_3 yielding condition was reached in each test (see enlarged view in Fig.5.34b), after which the effective stress paths travelled on the *t-p'*-α bounding surface until reaching the final desired α value. The samples were again allowed to creep at constant volume, before starting the shearing stage in which t increased with α held fixed. The points identified as S_α^t, where the subscript denotes a particular α value and the superscript *t* denotes the level of $(\sigma_1-\sigma_3)/2$ in kPa, give the stress conditions associated with different values of α during each α_rotation stage. As all these points correspond to post Y_3 points on the constant *t* paths, they are on the local bounding surface for that particular α value.

- In Fig.5.32 and Fig.5.33 the constant-α sections of the BS are shown passing through point C, the relevant S_α^t points and the post Y_3 portions of the constant α effective stress paths. On the three-dimensional plot of the local BS, Fig.5.32, these points are marked for the α=45° section.

5.5.2. Presentation of the local BS in ϕ'-ε_d-α space

The local BS for normally consolidated HPF4 can also be presented in terms of the mobilised angle of shearing resistance ϕ', providing diagrams that may be compared more easily with published data. The ϕ'-*deviatoric strain* curves for each of the M-Series tests are presented in Fig.5.35 where the deviatoric strain is calculated from the strain changes occurring from point A (Fig.5.2). It should be noted that the tests show no distinct peak in ϕ', and that the maximum angles depend strongly on α, ranging from a remarkably high 57° for α=0° to 41° for α=70°.

In Fig.5.36, the projection of the Bounding Surface determined in the *q-p'* plane is mapped through the corresponding points in the ϕ'-ε_d plane, using the strains associated with point C, the relevant S_α^t points and the post Y_3 portions of the constant α effective stress paths. Its three-dimensional image is presented in Fig.5.37.

5.5.3. Uniqueness of the local BS

Having established the local BS for normally consolidated HPF4, the question arises as whether this surface can be used to predict the behaviour of samples subjected to different stress paths, provided they have a similar density and consolidation history to those used to construct

the BS.

The stability of the local BS for anisotropically consolidated medium loose Ham River Sand (HRS), under different principal stress rotations, was checked by Shibuya & Hight (1996), with b held at 0.3. They performed a variety of undrained stress paths which showed that the behaviour of HRS can be well predicted by the initial BS, even for stress paths with many cycles of principal stress rotation.

In this study, only one test in addition to the M-Series was performed to check the uniqueness of the local BS defined for HPF4. This test has a code name of BS30 and its stress path is shown in Fig.5.2. It was performed in the same way as test M30, until reaching the C_{30} point (i.e. the end of the creep period after the α-rotation stage at a constant deviator stress level of 45 kPa). From this point, the BS30 sample was unloaded undrained down to the isotropic axis, with α held at 30°, before being subjected to the shearing stage. Shearing from this point, with α=30°, generated negligible changes in p' and pore pressure, until the Y_3 yield point was reached (Fig.5.2). The unloading stress history applied to BS30 brought the sample inside the initial BS and on reloading the Y_3 yield point fell inside the previously defined BS for α=30°. However, the two effective stress paths (M30 and BS30) have similar values of t, p', ϕ' and ε_d at their PTP's, and a common effective stress path after Phase Transformation.

So, it may be concluded that for normally consolidated dense HPF4, with $b=0.5$, the local normalised BS under undrained conditions has the following properties:

- it defines a region outside which no state is possible without developing relatively large volume strains;

- if the stress state is on the BS, the subsequent normalised effective stress path will either remain on the BS and develop relatively large strains, or move inside the BS, developing relatively small strain increments;

- the normalized initial BS contracts inwards if the soil is unloaded under either undrained or drained conditions.

Generally, the BS portrays the soil's initial yielding anisotropy, so it will have a modified shape if any of the following change:

a) preparation technique

b) initial density

c) consolidation history (t/p', α, OCR)

d) value of *b* (i.e. restriction of axisymetric straining)

5.6. Discussion

5.6.1. Effect of α on soil response, i.e. initial anisotropy due to principal stress rotation

The data presented in this Chapter show that K_o normally consolidated HPF4 exhibits high strength anisotropy when sheared undrained with the major principal stress direction varying between 0° and 90° to the vertical. In particular, the value of the deviator stress at the PTP reduces by up to 65% when α changes from 0° to 90° (i.e. from t=130 kPa for α=0°, to t=45 kPa for α=90°, Fig.5.30). In addition, the mobilised angle of shearing resistance, φ', at the PTP obtains a maximum value of 53° for α=0° and a minimum value of 36° for α=70°, while the ultimate angles observed varied between 57° and 41° over the same range.

In Fig.5.38 the undrained strength anisotropy of HPF4, in terms of the deviator stress at the PTP ($t=c_u^{PTP}$), is compared with that of other soils tested in the IC HCA (Shibuya & Hight, 1996; Menkiti, 1995). Although dense HPF4 is stronger, its variation of c_u/p_o' with α is comparable to that of Ham River Sand. The curve for the clay material KSS is much flatter.

The plane strain drained anisotropy of isotropically consolidated dense Toyoura sand was examined in a cubical triaxial device by Oda and Tatsuoka (Chapter 2). Their tests also showed that the maximum peak mobilized φ' value was reached for α=0° (i.e. horizontal bedding plane), while the minimum peak φ' was observed for α=70°. However, the maximum difference of 8° between the two values was much smaller than that observed for HPF4. Menkiti (1995) performed a similar set of undrained Hollow Cylinder tests on KSS and HK, varying α from 0° to 90°. The maximum difference in peak mobilized φ' between 0° and 90° was 2° for KSS (29.5° falling to 27.5°) and 7° for the HK mixture (from 39° to 31°).

The two most striking features arising from the data presented in this Chapter, which may appear unusual when compared with earlier studies of plane strain behaviour of granular materials, are:

a) The high value of φ' at the PTP for the test without principal stress rotation, M0, (φ'=53°), and

b) The sharp difference between the behaviour of the two tests, M0 and M15, when compared to that of the other tests at higher α values, both in terms of the mobilized ϕ' and shapes of their effective stress paths (Fig.5.2).

Some of the possible reasons for this unusual behaviour of HPF4 are discussed below.

5.6.1.1. Apparatus effect

It is important to consider whether the HCA design was responsible for the very high ϕ' values seen with HPF4 when α was low.

At the beginning of this research, a set of triaxial tests on K_o consolidated Ham River Sand were performed in the HCA and compared with conventional triaxial tests on HRS performed by Ovando-Shelley (1986) in the triaxial stress path cell (see Appendix V). The original purpose of the tests was to prove the new computer control and data acquisition system developed for the HCA. However, comparison of the results from the two different test devices does enable any apparatus effects acting at low α values to be quantified at b=0.0 and b=1.0. Such a comparison showed that the HCA triaxial stress paths were slightly more contractant, with larger reductions in p' being generated than those obtained in the stress path cell. However, tests in both apparatus mobilised the same deviatoric stress, t, and angle of shearing resistance, ϕ', at the PTP (i.e. t=75 kPa and ϕ'=32.8° in compression, and t=20 kPa and ϕ'=26° in extension).

It may therefore be concluded that there is no obvious apparatus restraining effect contributing to the high value of the angle of shearing resistance at b=0.5 measured in the Hollow Cylinder Apparatus.

The Author's recent numerical research suggests that the restraining action of the rough platens could raise ultimate friction angles marginally under certain conditions, but not by the amount required to explain the M-Series test data.

5.6.1.2. Strain conditions at b=0.5

It was shown in Section 5.4.3 that, while near plane strain conditions were achieved with b=0.5 in tests with α>15°, they were not satisfied at failure for the tests with α=0° and 15°. In these tests the radial strain (also the intermediate principal strain) was compressive and approximately equal in magnitude to the axial strain at the beginning of shearing (Fig.5.21). As

triaxial compression tests, where b=0 (and α=0°), produce a negative radial strain, plane strain conditions for α=0° must involve 0<b<0.5. To provide further information on the effect of *b*, an additional test was performed, similar to test M0, but with *b* held at 0.3, (i.e. test M0-03).

The variations of the direct strains (ε_z, ε_r and ε_θ) with deviatoric strain (ε_d) are presented in Fig.5.39. This shows that the radial strains remain very small and therefore that at PTP the sample was deforming under almost completely plane strain conditions. The mobilized ϕ' value at the PTP for this test was markedly lower - 44° compared to 53° at b=0.5. This gives a maximum difference in ϕ' of 8° over the range 0°<α<90°, which compares favourably with data obtained for other granular materials (Lam & Tatsuoka, 1988; Tatsuoka et al., 1986; Oda et al., 1978).

The anisotropy in ϕ' due to principal stress rotation, presented previously in Fig.5.31, can be, therefore, viewed in terms of two envelopes. Firstly a b=0.5 envelope, which joins the PTP values of ϕ' for all tests performed at b=0.5 (i.e. M0, M15, M30, M45, M70 and M90) and secondly a 'plane strain' envelope, which joins the PTP values of ϕ' for all tests that exhibited plane strain conditions (M0-03, M30, M45, M70 and M90).

It is postulated that the difference in mobilised ϕ' for the three tests performed with different b-values but all with α=0°, is influenced by the strain conditions existing in each test. This can be explained by considering the relative values of the direct stresses for each tests as shown in Fig.5.40:

- Under axisymmetric triaxial stress conditions axial loading can be sustained by particles moving and rearranging both radially and circumferentially.

- When b>0, with σ_r>σ_θ, radial movements are restricted and particles have a greatly reduced freedom of movement which helps to build up greater frictional resistance at particle contacts. The b=0.5 condition is more restrictive than b=0.3 since σ_r is much higher than σ_θ.

5.6.1.3. Structural effect

Fig.2.13 (Chapter 2) summarized the relation between drained peak mobilized ϕ' values and *b*, obtained mainly with isotropically consolidated granular materials. A common trend of increasing ϕ' with *b*, up to b~0.5, was seen in all curves. With further increase in *b* up to 1.0, ϕ'

did not change, or dropped slightly. This behaviour is in contrast to that observed in the present tests where ϕ' decreases dramatically with b>0.5. This happens because K_o consolidation induces a different initial structure in the material to that formed under isotropic consolidation, making the vertical (depositional) direction stronger and more resistant to further compression loading. When such an anisotropic structure is sheared in the opposite (extension) direction, its frictional resistance reduces significantly.

The influence of K_o consolidation on the structure of HPF4 is particularly strong because of its particle shape (see next Section, 5.6.1.4). Fig.5.41 compares triaxial compression effective stress paths for isotropically and K_o normally consolidated HPF4 (this study) and Ham River Sand (Ovando-Shelley, 1986) (see Appendix V for details of the isotropic test). It can be seen that at PTP the mean effective stress, p', in the isotropically consolidated HPF4 sample has reduced by ~40%, while the interlocked K_o consolidated sample has hardly any change in p' before reaching its PTP. The K_o consolidated HRS sample, with more rounded particles, exhibited a much larger change in p' during compressive shearing.

5.6.1.4. Particle shape

Some numerical, experimental and particulate analyses will be reviewed here to help to explain the influence of particle shape on frictional resistance of a granular material.

A) A numerical model of the mechanism of fabric evolution in granular media was developed by Cundall & Strack (1979), by representing particles as ideal circular discs (see Appendix V). Rothenberg & Bathurst (1989, 1992) extended this approach by changing the shape of the discs from being circular to being elliptical (see Appendix V). Fig.5.42 (from Rothenberg & Bathurst, 1992) presents results from both a numerical model and experimental biaxial tests, obtained by using elliptical discs with three eccentricities (Appendix V): e=0.0, 0.05 and 0.20 (0.0 stands for circular disc). It is evident that ideal circular particles have the lowest strength and that the strength increases as the ellipses become more elongated (i.e. e increases).

B) Bishop (1969) compared data on the critical state angle of shearing resistance, ϕ_{cv}', of glass ballotini (Skinner, 1969), mudstone and granite (Tombs, 1969). The latter two materials had particles which were angular to subangular, giving ϕ_{cv}'~40°, as compared to the spherical particles of glass ballotini which gave ϕ_{cv}'~25°. Bishop concluded that

"the shape factor plays a very important part in the inter-particle friction (ϕ_μ) - strength relationship and cannot be ignored or simplified".

C) Frossard (1979) examined the strength of two types of minerals with different surface asperities, in drained triaxial tests. One was a calcareous sand: a) very angular, made of crushed limestone and b) well rounded, worn away by a stream; and the other was a quartz sand: c) very angular, resulting from the crushing of hard quartz stone and d) sub-rounded, from a coastal pond. To define the morphological state of each of these grains, he related the well known index of particle roundness, R_w (Krumbein, 1941), defined from Krumbein's chart (Chart III.1, Appendix III), to the asperity index *Ia*. This latter index is defined as the ratio of a projected particle's surface area without asperities, to the total projected particle surface area. The relationship between these two indicators of particle roundness (or angularity) is presented in Fig.5.43. Test results for both minerals show an increase in the interparticle friction angle with reduction in the asperity index (Fig.5.44). This implies that rougher particles, with smaller asperity indices, have an increased interlocking potential which can sustain higher loads and generate higher frictional resistance. This helps explain the increase in ϕ' of HPF4 when changing from triaxial to plane strain conditions (Section 5.6.1.2) as the particles' have a very poor roundness (~0.1, Chapter 3) and, consequently, very low asperity index (Ia<0.5), which results in a large amount of interlocking.

D) Oda (1972a) used an "axial ratio method" to measure the shape factor of the grain particles for four sands. From a thin section photograph he measured the ratio of the apparent short axis, L_2 to the apparent long axis, L_1, for a number of particles (Chapter 2) and defined the axial ratio as:

$$\bar{n} = \frac{1}{f} \Sigma \left(\frac{L_2}{L_1}\right)_i \qquad (5.6)$$

where *f* is the total number of measurements. When $\bar{n}$ approaches unity the projections of sand grains are mainly circular, and when it is close to zero, particles are elongated. Tests performed on these materials consisted of a set of drained triaxial tests on cubical specimens, with bedding plane inclinations to the vertical of 90°, 60°, 30° and 0°. All samples were set to the same initial relative density. Sand B presented here had an axial ratio of 0.605 (Eq.5.6) and was characterized to consist of elongated particles; in comparison, sand D had an axial ratio of 0.706 and consisted of relatively spherical

particles. Test results in Fig.5.45 (from Oda, 1972a) show that the peak deviator stress for each of the bedding plane inclinations was higher for sand B than for sand D. They also show that the difference in the deviator stress between shearing of the horizontal and vertical bedding plane (i.e. material anisotropy) is higher when the more elongated particles of sand B are tested, than in the case of the more spherical particles of sand D. Again, elongated and angular particles are more prone to interlocking and therefore increase both the frictional resistance of the material and its anisotropy.

As discussed in Chapter 3, HPF4 shows an $\bar{n}$ value of 0.484, indicating a far stronger shape factor than either of Oda's sands. It is therefore reasonable to expect a more pronounced effect of particle shape on material anisotropy for HPF4.

5.6.2. The effect of b on soil response

While studying the influence of b on the soil's response was not a primary objective of the M-Series HCA experiments, comparisons with the triaxial tests presented in Chapter 4 allow the effects of σ_2 to be assessed for α=0° and α=90° for normally consolidated HPF4. Effective stress paths, secant stiffness curves and ϕ'-ε_s curves from the relevant tests are compared in Figs.5.46 to 5.48. To be able to compare stiffnesses from these different stress conditions, E_u is calculated as $\Delta q/\epsilon_s$, where:

$$\Delta q = \frac{1}{\sqrt{2}}[(\sigma_1 - \sigma_2)^2 + (\sigma_2 - \sigma_3)^2 + (\sigma_1 - \sigma_3)^2]^{0.5} \quad (5.7)$$

$$\varepsilon_s = \frac{\sqrt{2}}{3}[(\varepsilon_1 - \varepsilon_2)^2 + (\varepsilon_2 - \varepsilon_3)^2 + (\varepsilon_1 - \varepsilon_3)^2]^{0.5} \quad (5.8)$$

Inspection of Figs.5.46 to 5.48 leads to the following observations.

5.6.2.1. Effect of b on loading behaviour for α = 0°

- As shown from the stress paths in Fig.5.46, HPF4 is least contractant when sheared with b=0.0. The mean effective stress p' reduces gradually with increasing b, being ~15% lower at the PTP for b=0.5 than for b=0.0. The deviator stresses developed at the PTP when b=0.3 and b=0.5 are similar, both being ~10% greater than for b=0.0.

- The undrained shear stiffness (E_u-ε_s) curves for compression (α=0°) with three different values

of *b* are broadly similar, as shown in Fig.5.47, although the stiffness available at small strains gradually reduces with increase in *b*. Stiffness values for b=0.3 are approximately 15% lower than those for b=0.0 and those for b=0.5 are approximately 25% lower than the triaxial result.

- The magnitude of the angle of shearing resistance is strongly affected by the change in *b* (Fig.5.48). Considering α=0°, the triaxial compression PTP angle is 12° lower than that for b=0.3 and 20° lower than for b=0.5. The ultimate values are also dependent on the value of b increasing from 37° at b=0 to 52° at b=0.3 and 57° at b=0.5. Slow drained ring shear tests, which approximate to plane strain conditions, gave ultimate values between 44° and 49°, depending on the test conditions (Parathiras, 1994; as summarized in Section 3.1, Chapter 3).

The studies summarized in Chapter 2, concerning the relation between drained triaxial (TX) and plane strain (PS) strengths of granular materials, reported maximum differences in ϕ' values between PS and TX conditions, for isotropically consolidated dense samples, of about 4° (Cornforth, 1964), 6° (Oda et al.1978), 7° (Tatsuoka et al., 1986), 8° (Marachi et al., 1981), 11° (Leussink & Wittke, 1964). The trends seen in the HPF4 tests with b=0.3 are more compatible with the published plane strain results than those found with b=0.5.

5.6.2.2. Effect of *b* on unloading behaviour for α=0°

-As shown in Figs.5.46 and 5.48, the unloading response of HPF4 with α=0° is approximately 10% less contractant in the HCA tests with b=0.5, than when b=0.0 in the triaxial test.

-The (E_u-ε_s) stiffness responses with b=0.0 and b=0.5 are comparable (Fig.5.47), both being markedly stiffer than the corresponding compression curves. The triaxial test was again ~25% stiffer at small strains.

5.6.2.3. Effect of *b* on loading behaviour with α=90°

-The stress paths shown on Figs.5.46 and 5.48 show that the response to loading with α=90° is also more contractant under b=0.5 conditions then when b=1.0. The value of *p'* at the PTP is ~25% lower than in triaxial extension. The value of the deviator stress at the PTP is about 30% greater for b=0.5, compared to that obtained in triaxial extension.

-As with α=0°, a far larger angle of shearing resistance is developed for b=0.5 at the PTP than

for triaxial extension, the difference being ~15°.

5.7. Summary

This chapter has investigated the undrained anisotropy of K_o normally consolidated HPF4. The following conclusions arise:

A) The K_o consolidation characteristics of HPF4 observed in HCA testing are similar to those already seen in triaxial tests (Chapter 4). This implies that the HCA apparatus does not have an undue effect on the test results. This was also confirmed by comparing the results of triaxial tests performed in sand in both the HCA and stress path cell.

B) Shearing of K_o normally consolidated HPF4 with the orientation of the major principal stress varying from 0° to 90° to the vertical, and with *b* held at 0.5, showed significant anisotropy in undrained material strength. The deviator stress at the PTP reduced by ~65% from α=0° to 90°, while the mobilized angle of shearing resistance at the PTP reduced dramatically by up to 17° from a maximum of 53° (at α=0°) to a minimum of 36° (at α=70°).

C) Close inspection of the M-Series stress paths, which consisted of undrained unloading, principal stress rotation at constant deviator stress and undrained shearing with constant α, showed the influence of the previous stress history (i.e. previous stress path) on the material behaviour in the subsequent path. It was seen that in the α-rotation stage, after previous undrained unloading, and in the shearing stage, after previous α-rotation, the stress-strain response of HPF4, after reaching Y_2 yield, was determined by its previous mode of deformation. This pattern was changed as the Y_2 yield surface became gradually realigned with the new stress path direction.

D) The radial strain response due to the shearing stages of tests M0 and M15 showed that the b=0.5 condition does not simulate plane strain conditions perfectly, although it applies very well for principal stress rotations greater than 15°. An additional test proved that b=0.3 modelled plane strain conditions more satisfactorily at α=0°. The 'plane strain' envelope plotted on Fig.5.31 is a combination of the b=0.3 and b=0.5 test results.

E) For normally consolidated HPF4 the shape of the local BS depends on the value of *b* (Fig.5.46). In particular:

- the BS is more contractant under plane strain conditions than under triaxial conditions (in both compression and extension);

- the deviator stresses mobilised at the PTP are greater in 'plane strain' tests than in the comparable triaxial cases;

- the samples sheared in the HCA after changing from b=0 to b=0.3 or 0.5 give a marginally softer shear stiffness at small strains than those sheared triaxially from K_o conditions;

F) The shape of the local Bounding Surface depends critically on the direction of the major principal stress axis so that the permissable values of *t* reduce with increase in α. Constant α-sections of the BS tend to rotate and distort about a common point on the isotropic axis, because the degree of contraction prior to Phase Transformation increases with α (Figs.5.32 and 5.33).

I) The particle shape of HPF4, which is highly angular, is probably responsible for the strong influence on the frictional resistance of the parameter *b*.

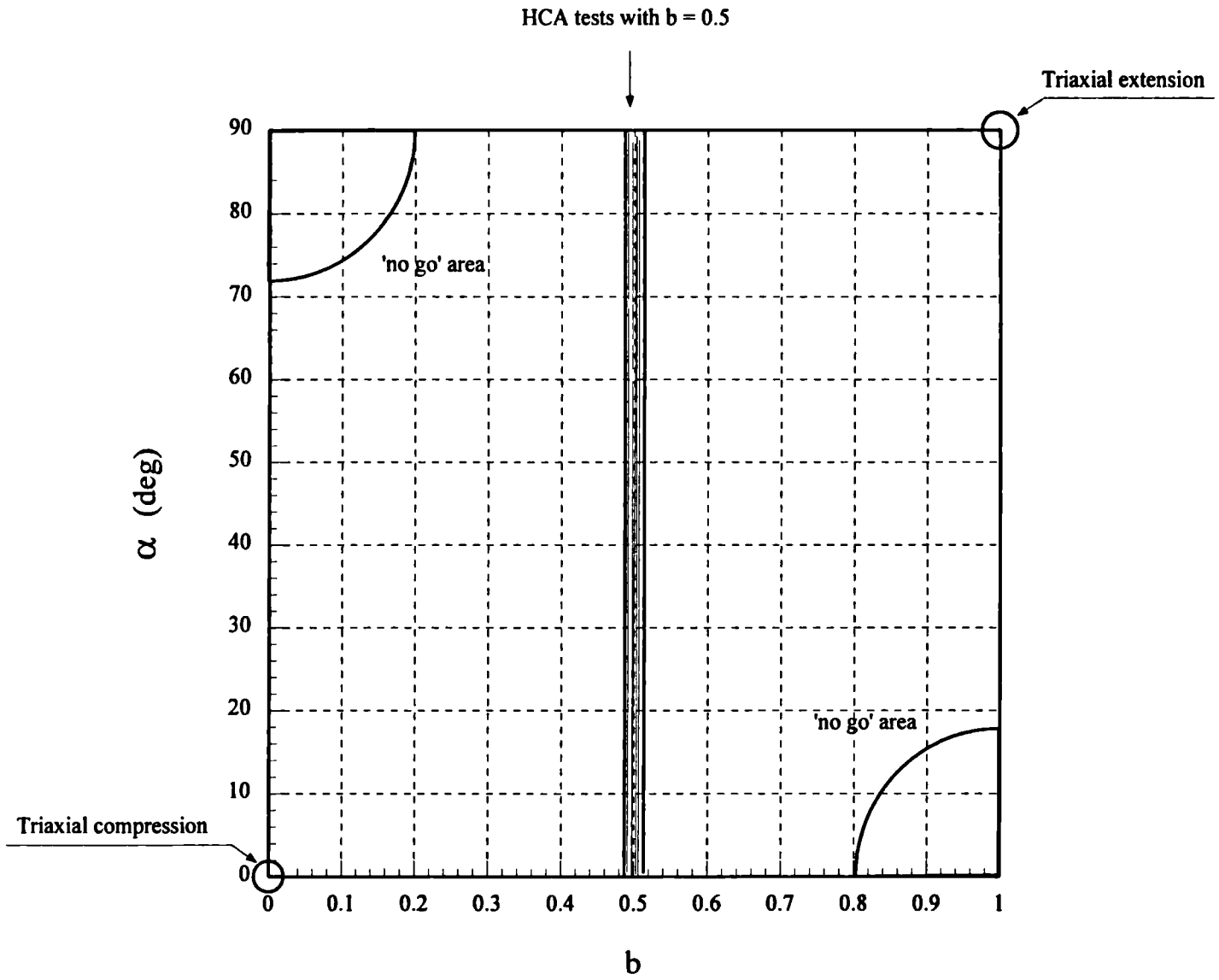


Fig.5.1 - 'b - α' space for tests in the HCA

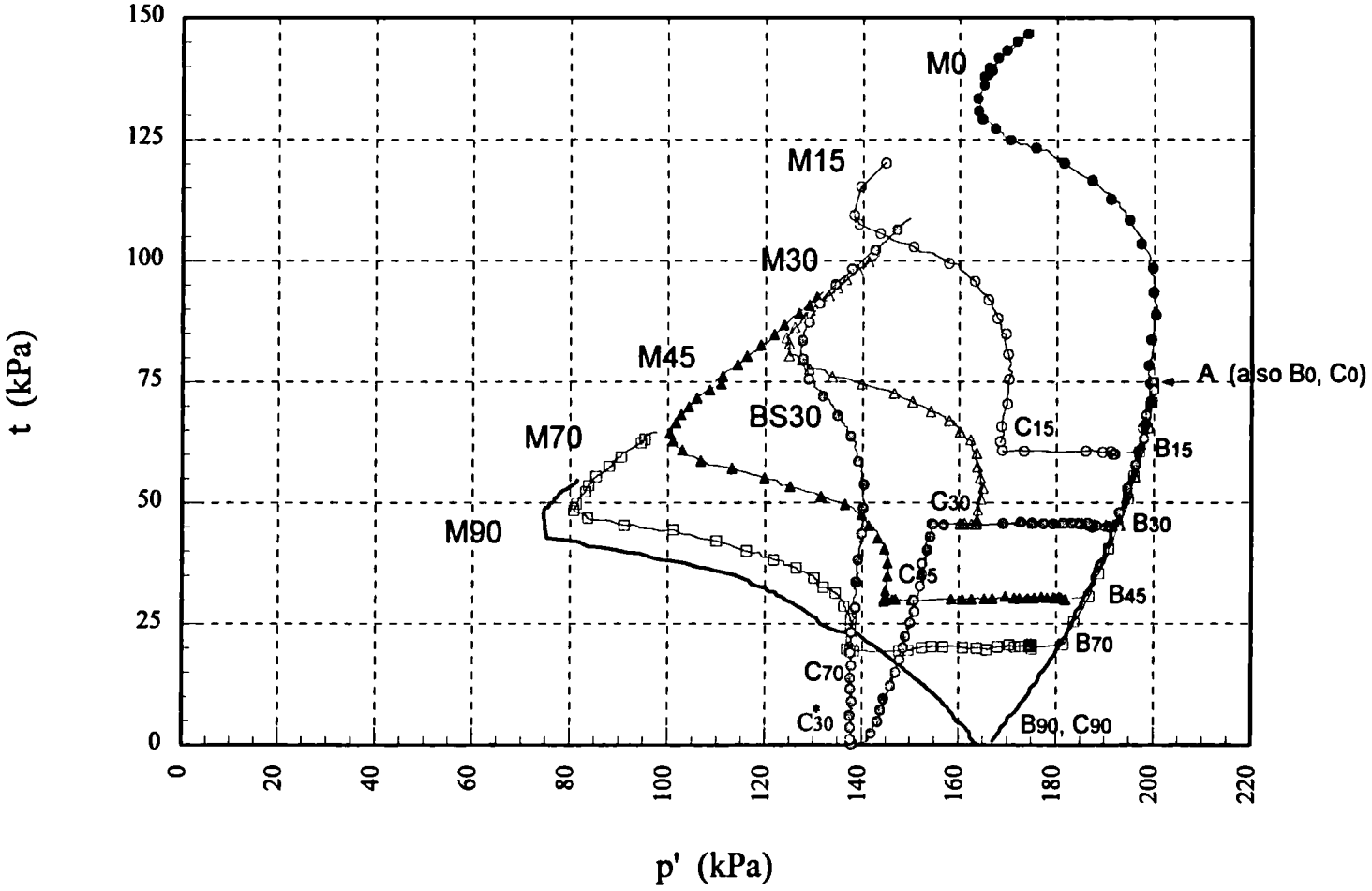


Fig.5.2 - Effective stress paths for the Series M of HCA tests

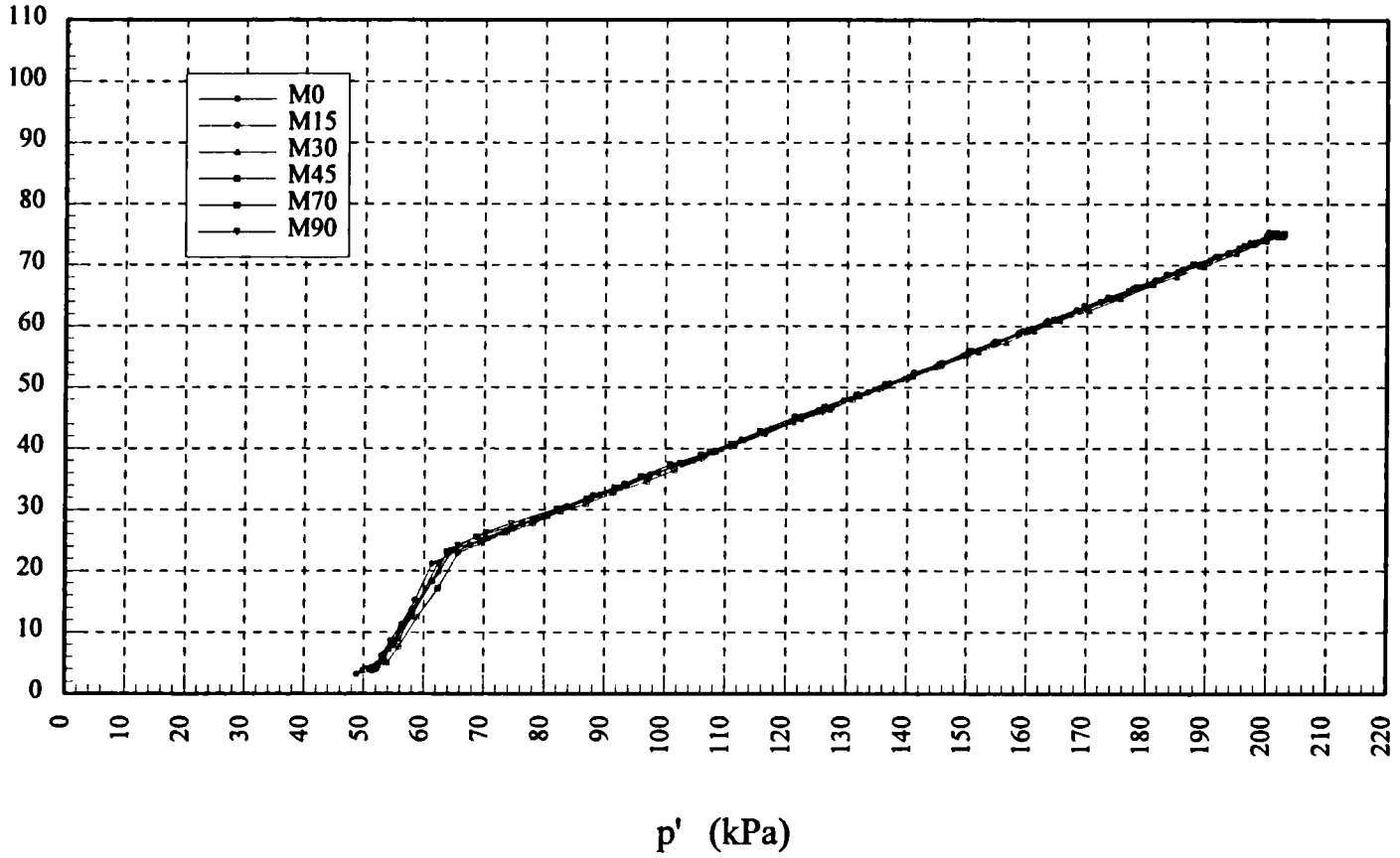


Fig.5.3 - Ko consolidation stress paths followed in M-Series tests

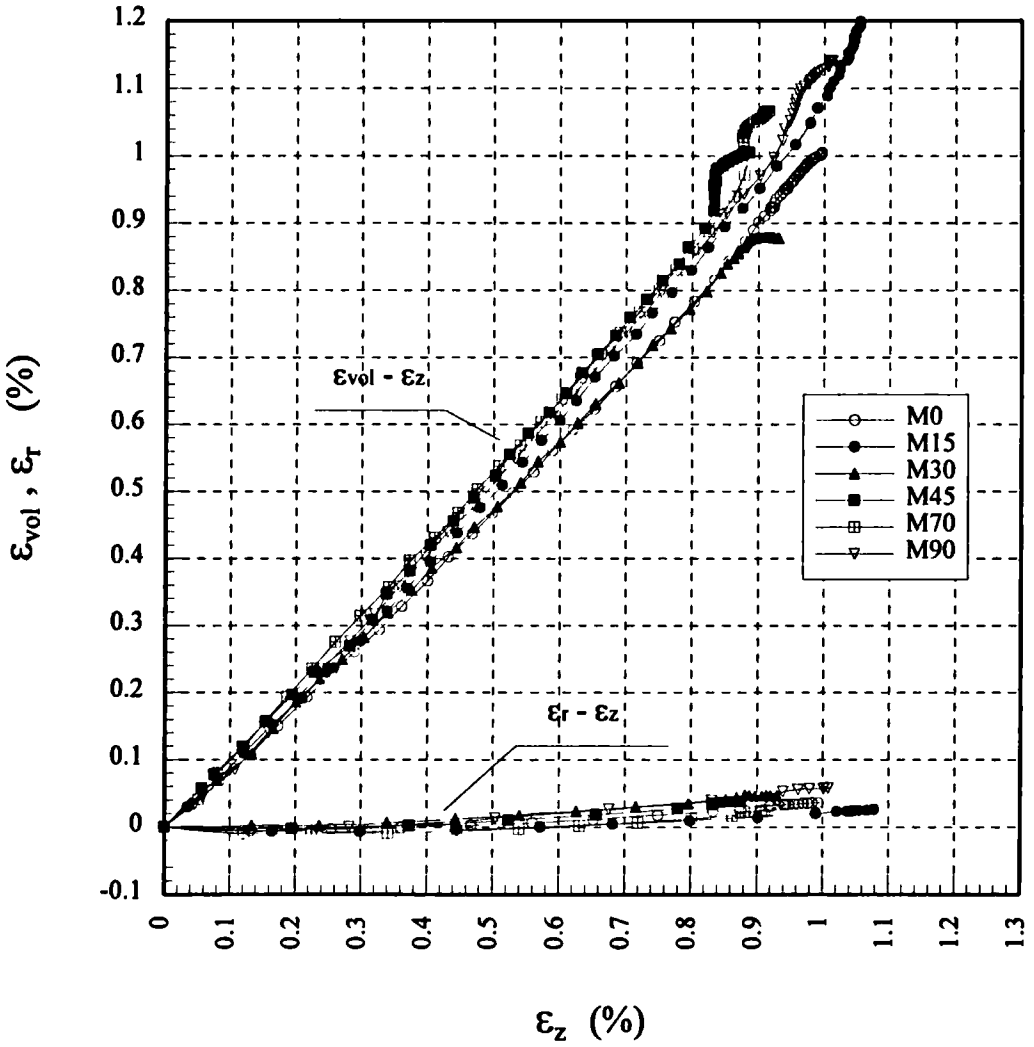
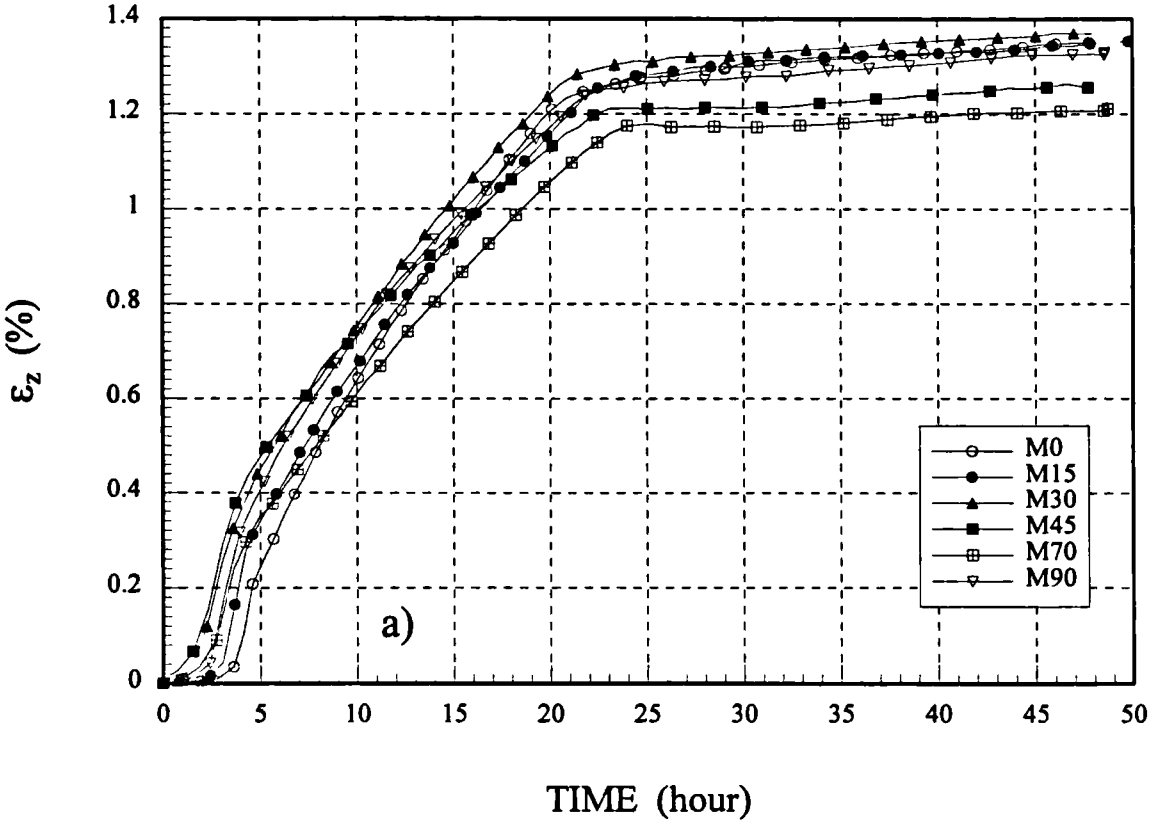


Fig.5.4 - Development of strains during Ko consolidation



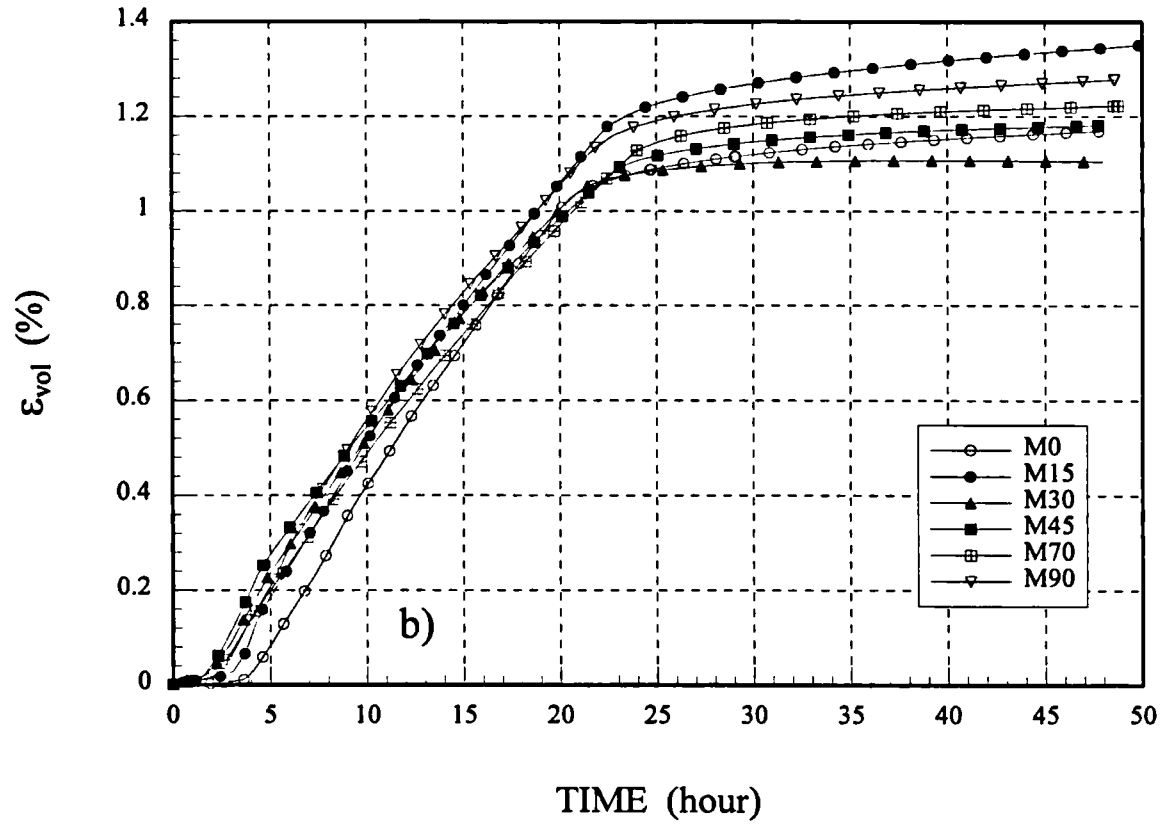


Fig.5.5 - Ko consolidation strains in time: a) axial and b) volumetric

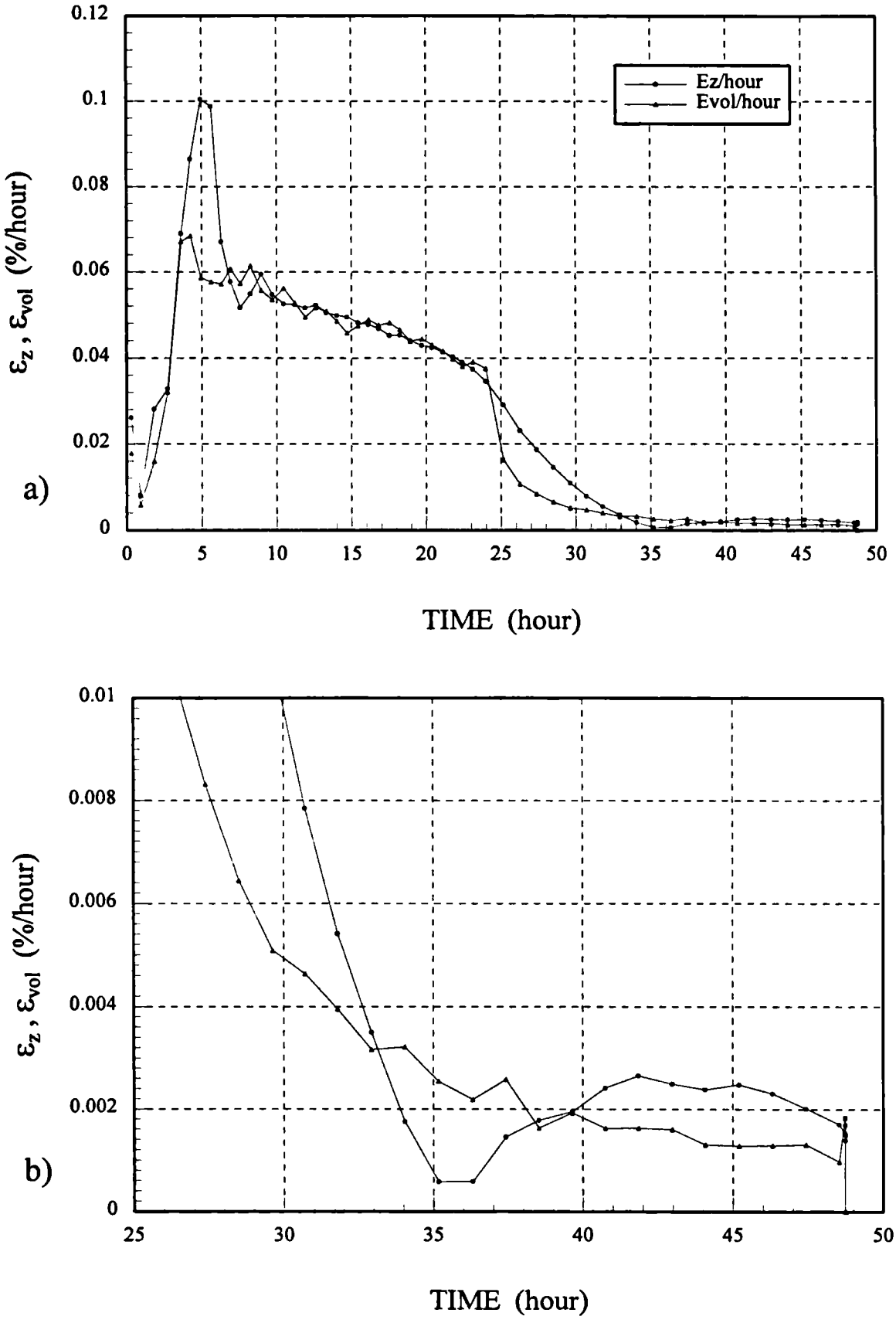


Fig.5.6 - Axial and volumetric strain rates during a) Ko consolidation and b) enlarged view during creep period

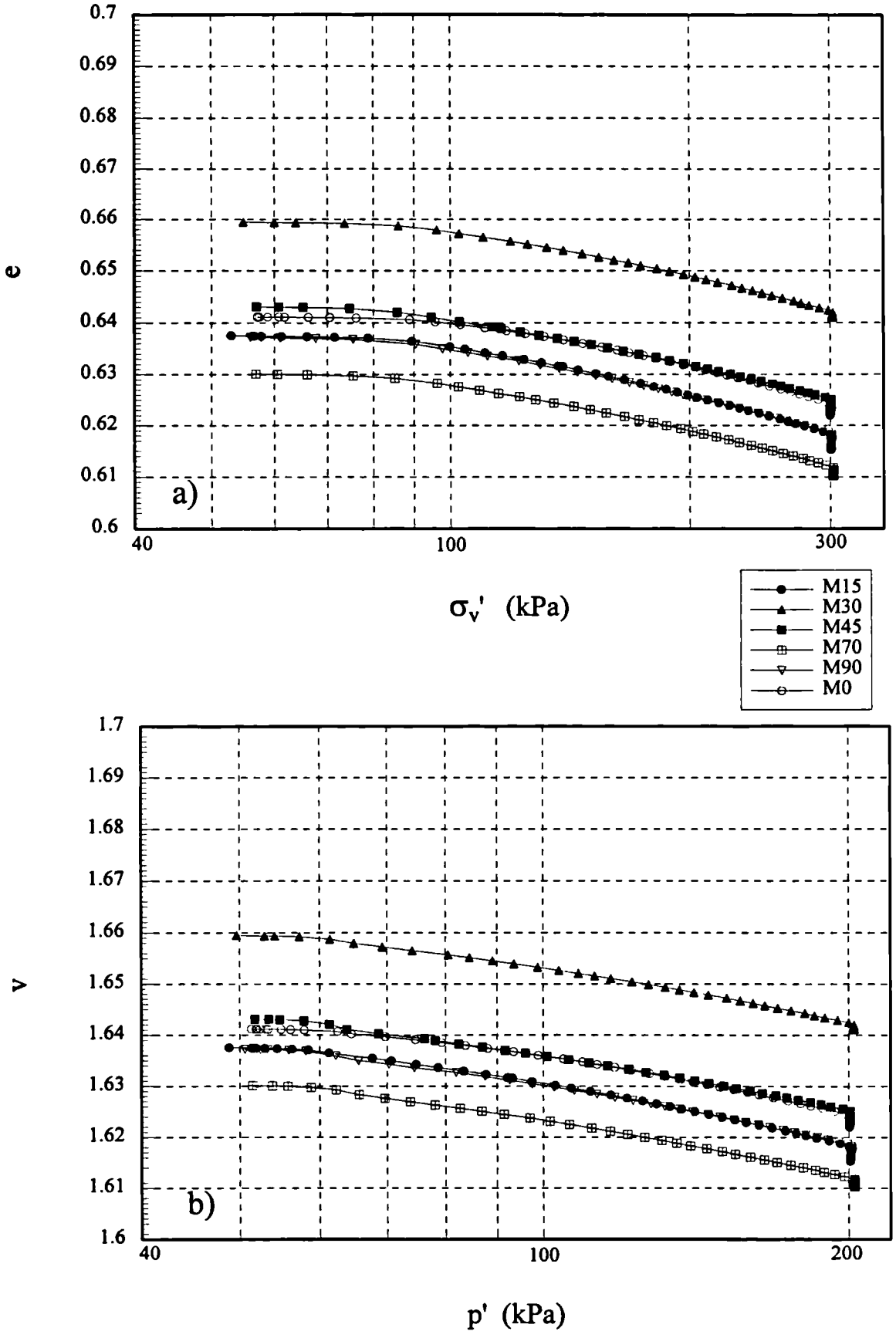


Fig.5.7 - Compressibility curves of Ko consolidated HPF4:
a) e -log σ_v'
b) v - lnp'

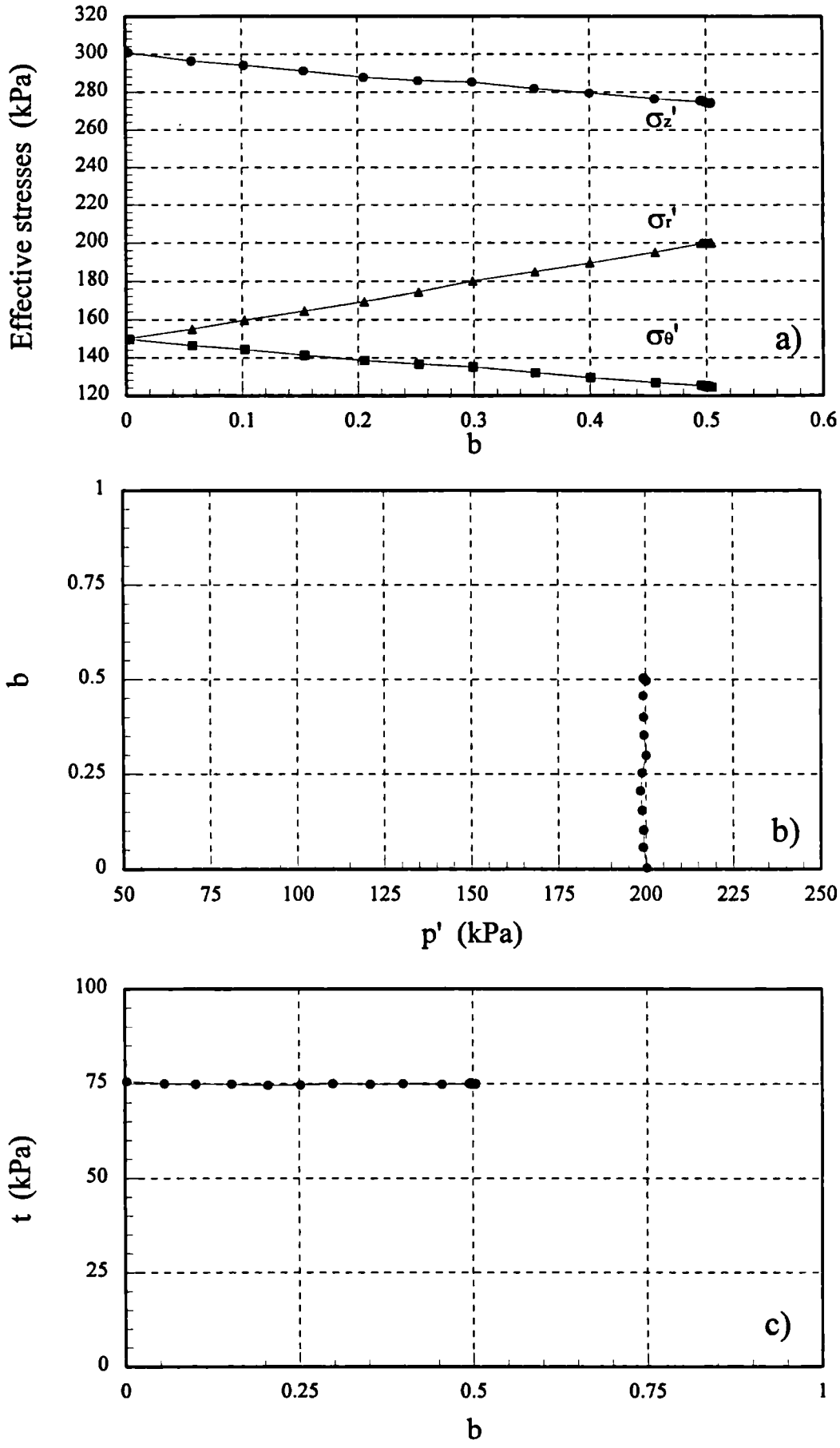


Fig.5.8 - Development of stresses during b-change from 0 to 0.5:
a) direct effective stresses
b) mean effective stress, p'
c) deviator stress, t

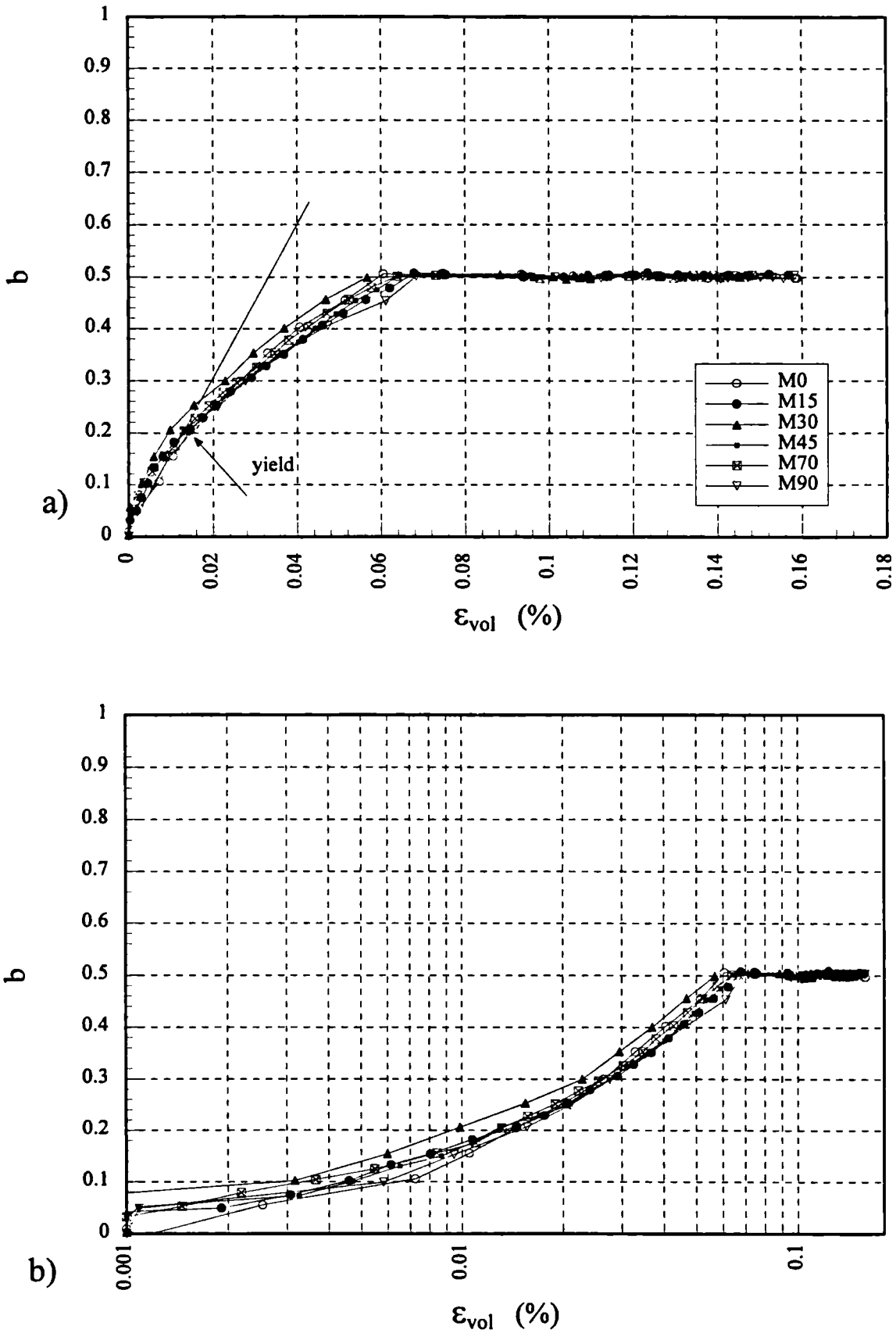


Fig.5.9 - a) Volume strain development during b-change
b) Enlarged view in the logharitmic scale

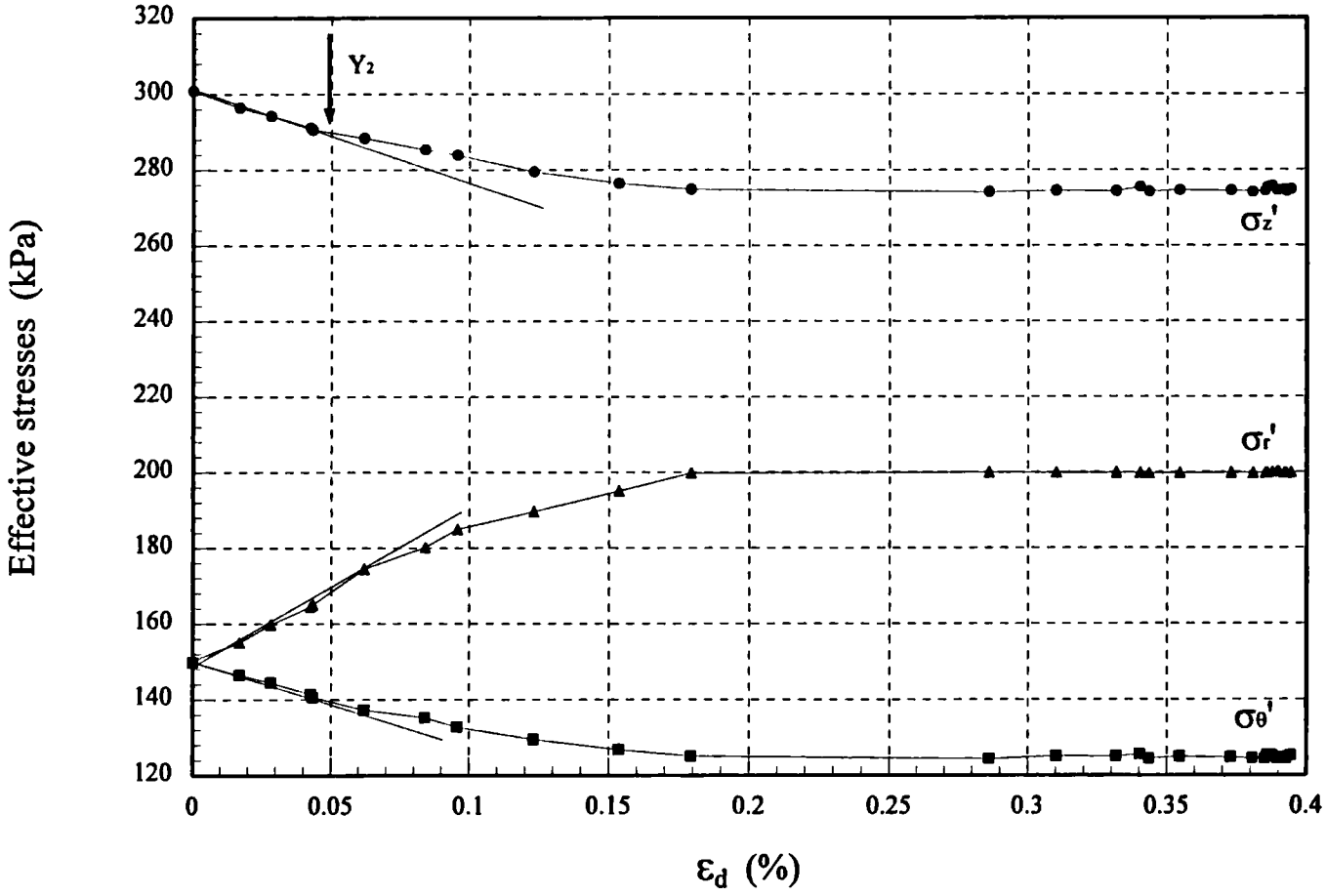
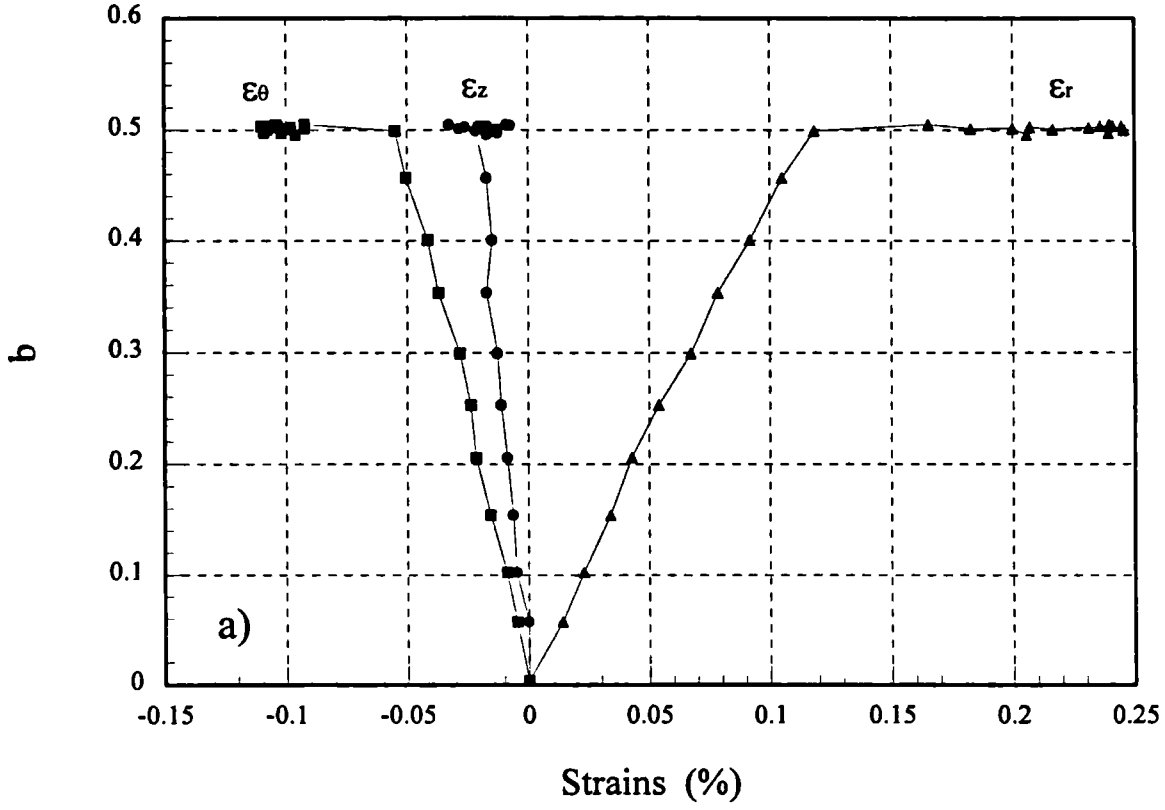


Fig.5.10 - Effective direct stresses versus deviator shear strain



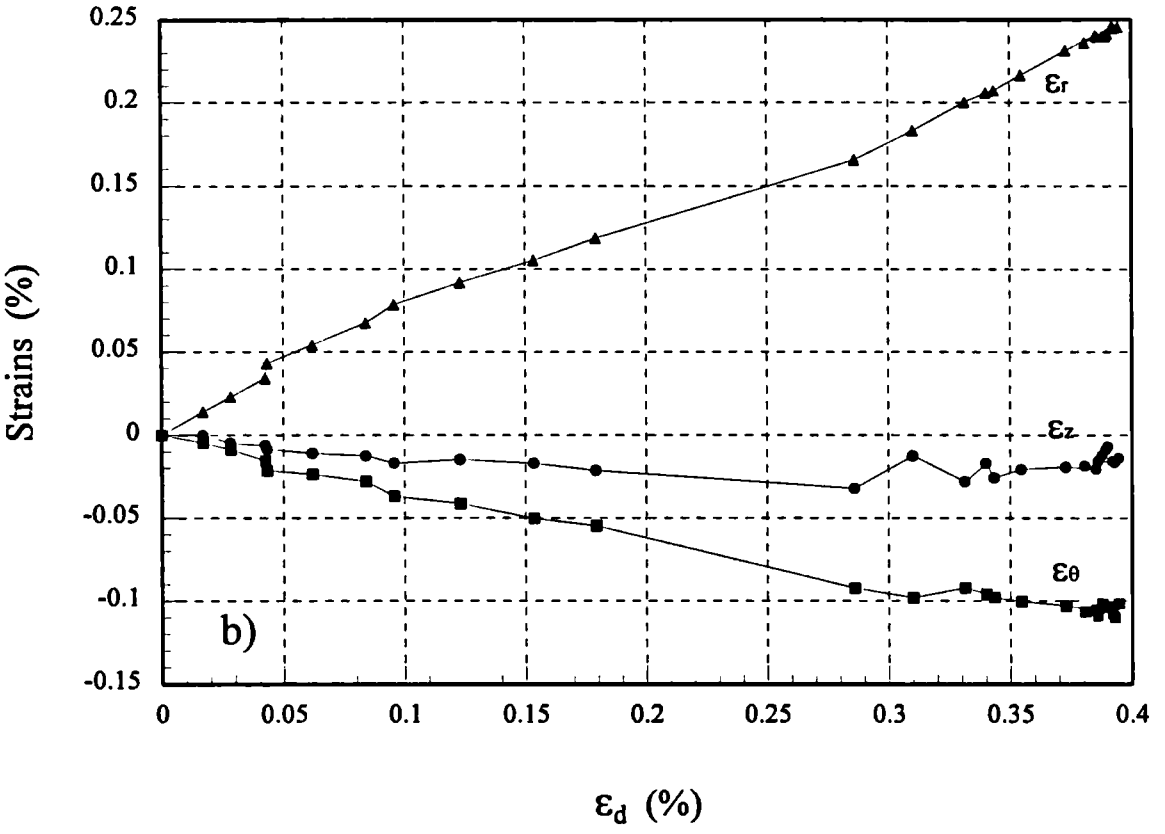


Fig.5.11 - a) Development of component strains during b-change
b) Variation of component strains with the deviator strain

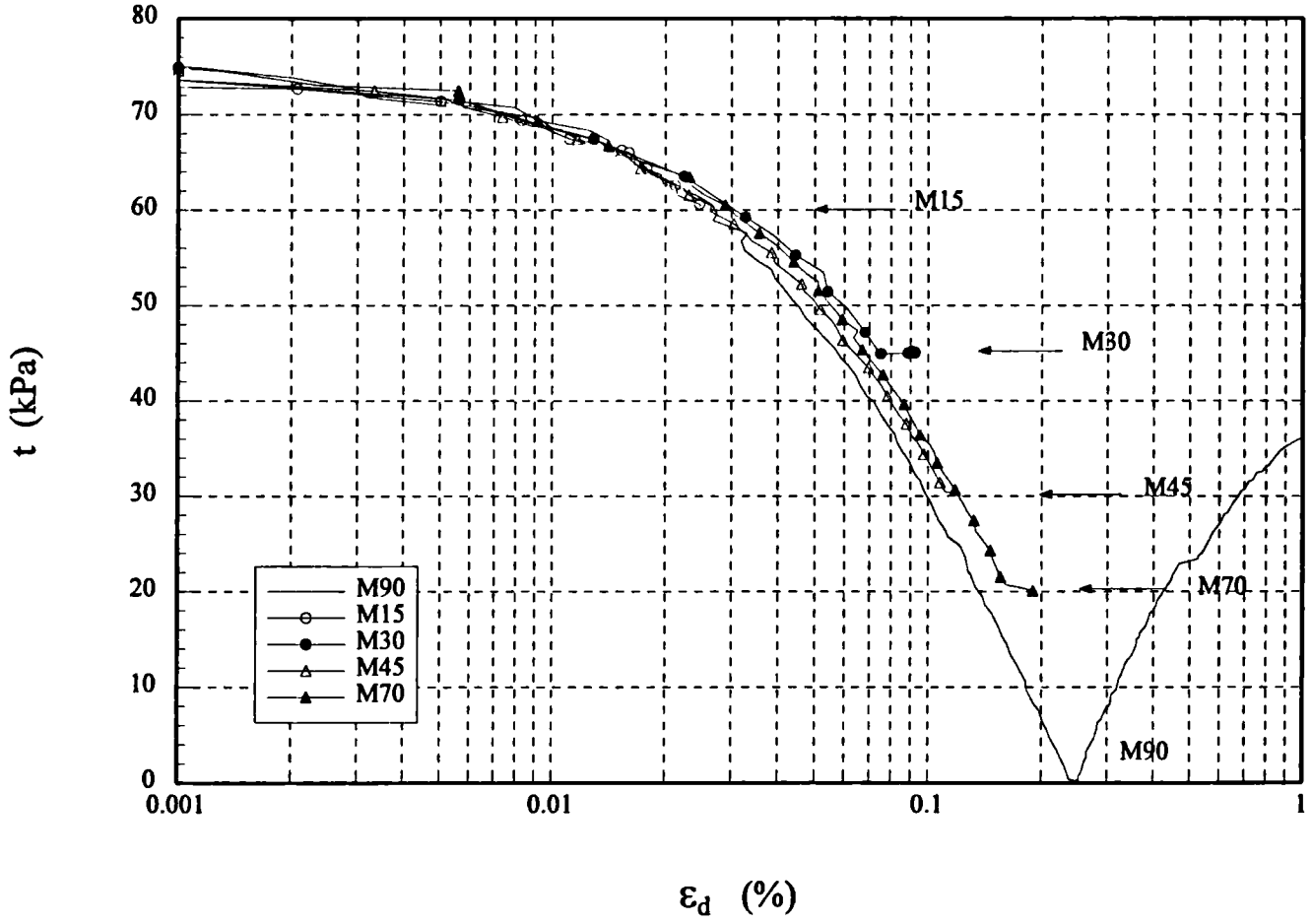


Fig.5.12 - Development of deviatoric strain during undrained unloading

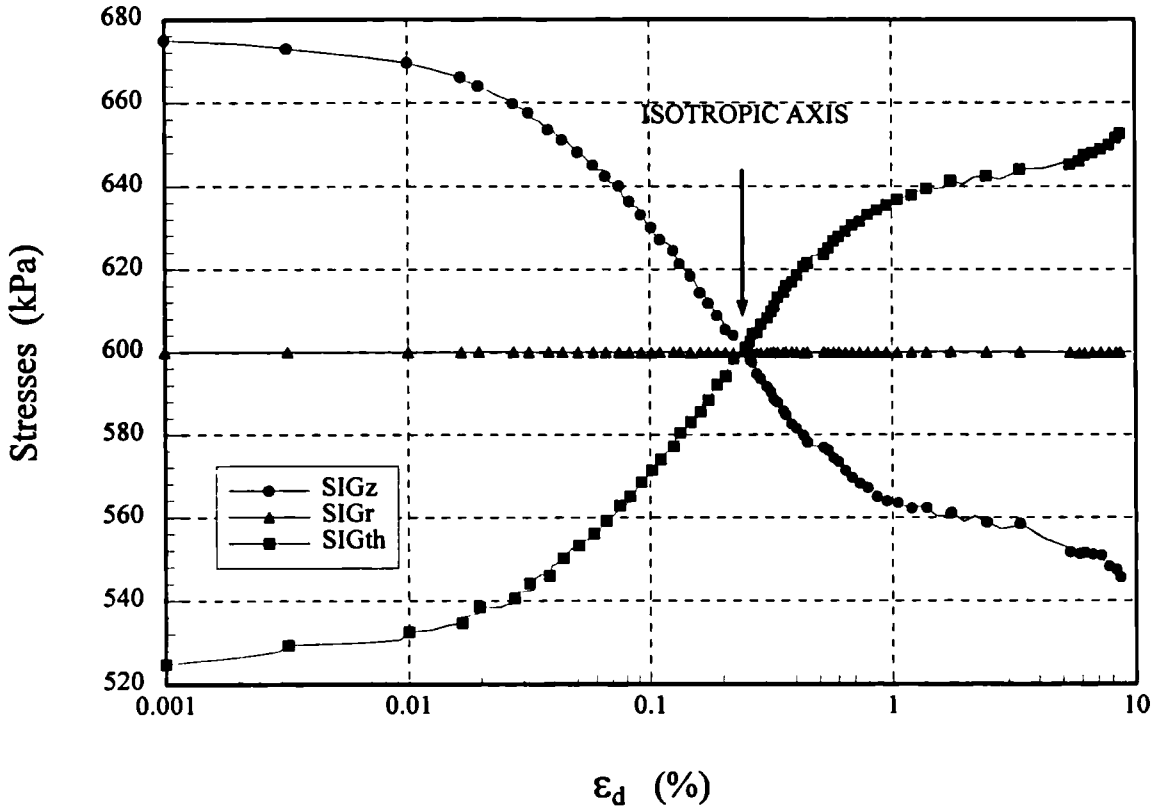


Fig.5.13 - Direct stresses during undrained unloading

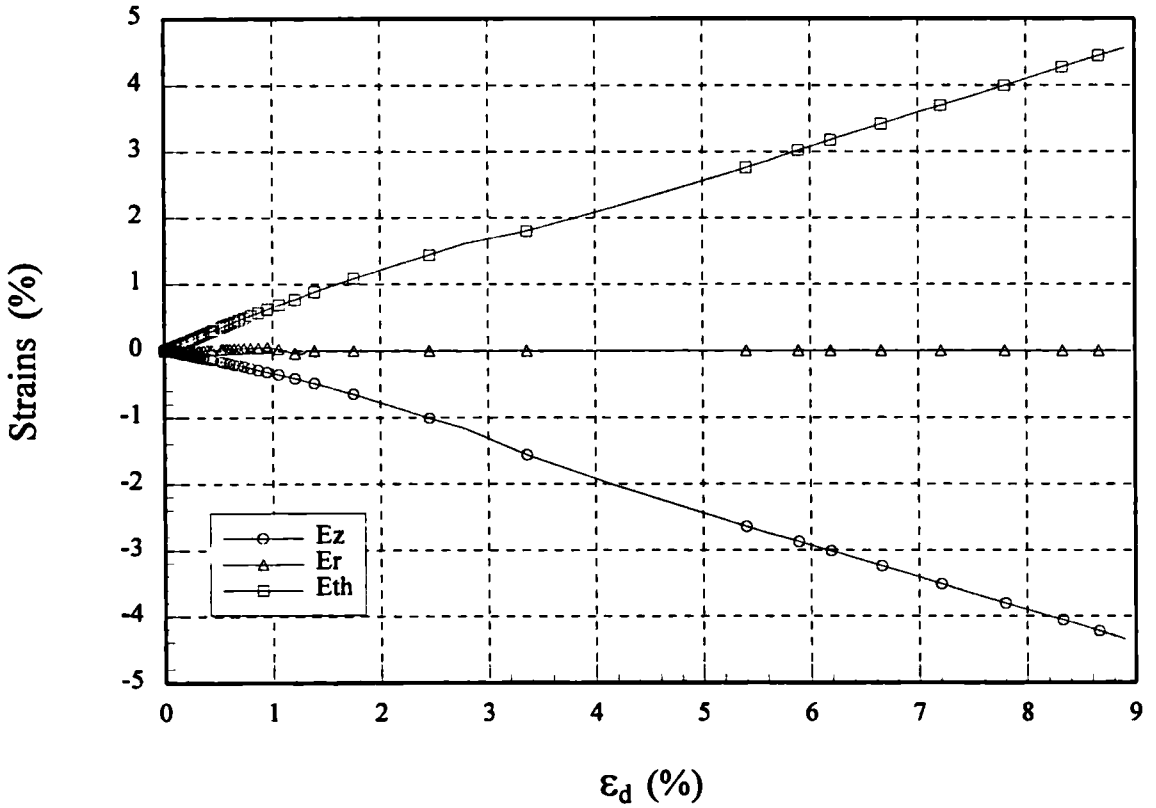


Fig.5.14 - Strain components during undrained unloading

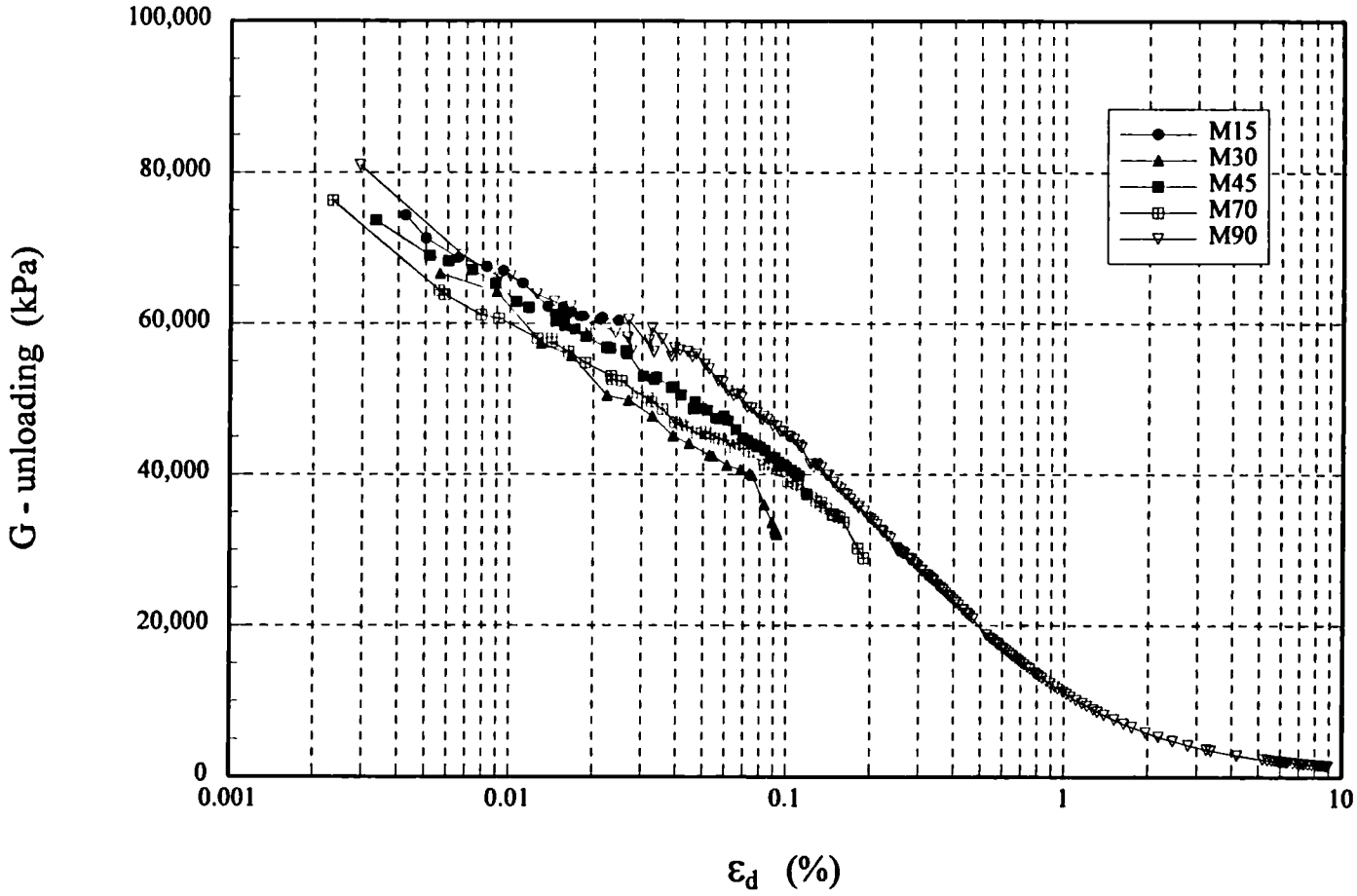


Fig.5.15 - Octahedral shear stiffness, G, during undrained unloading

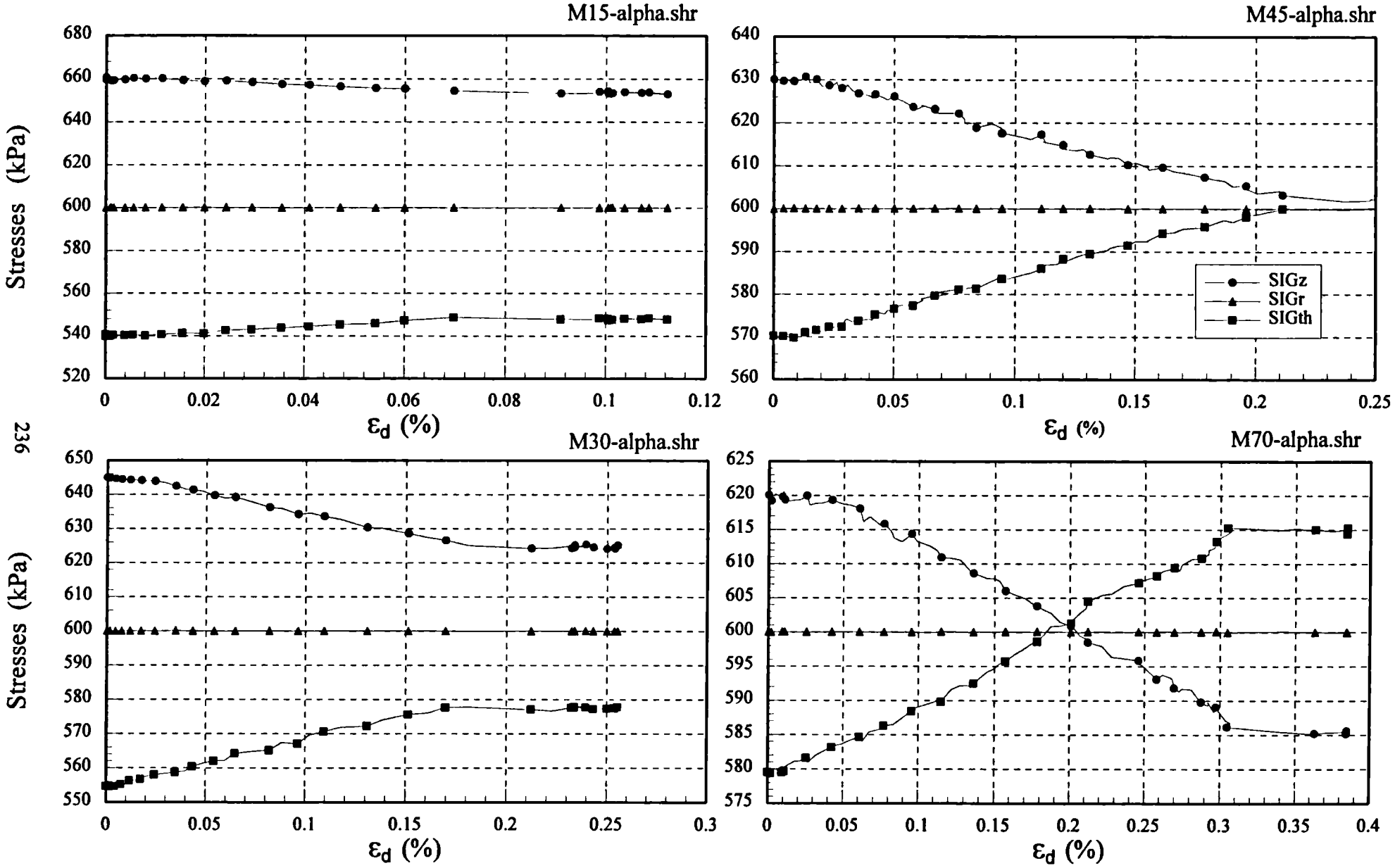


Fig.5.16a - Development of direct component stresses during undrained principal stress rotation at constant 't'

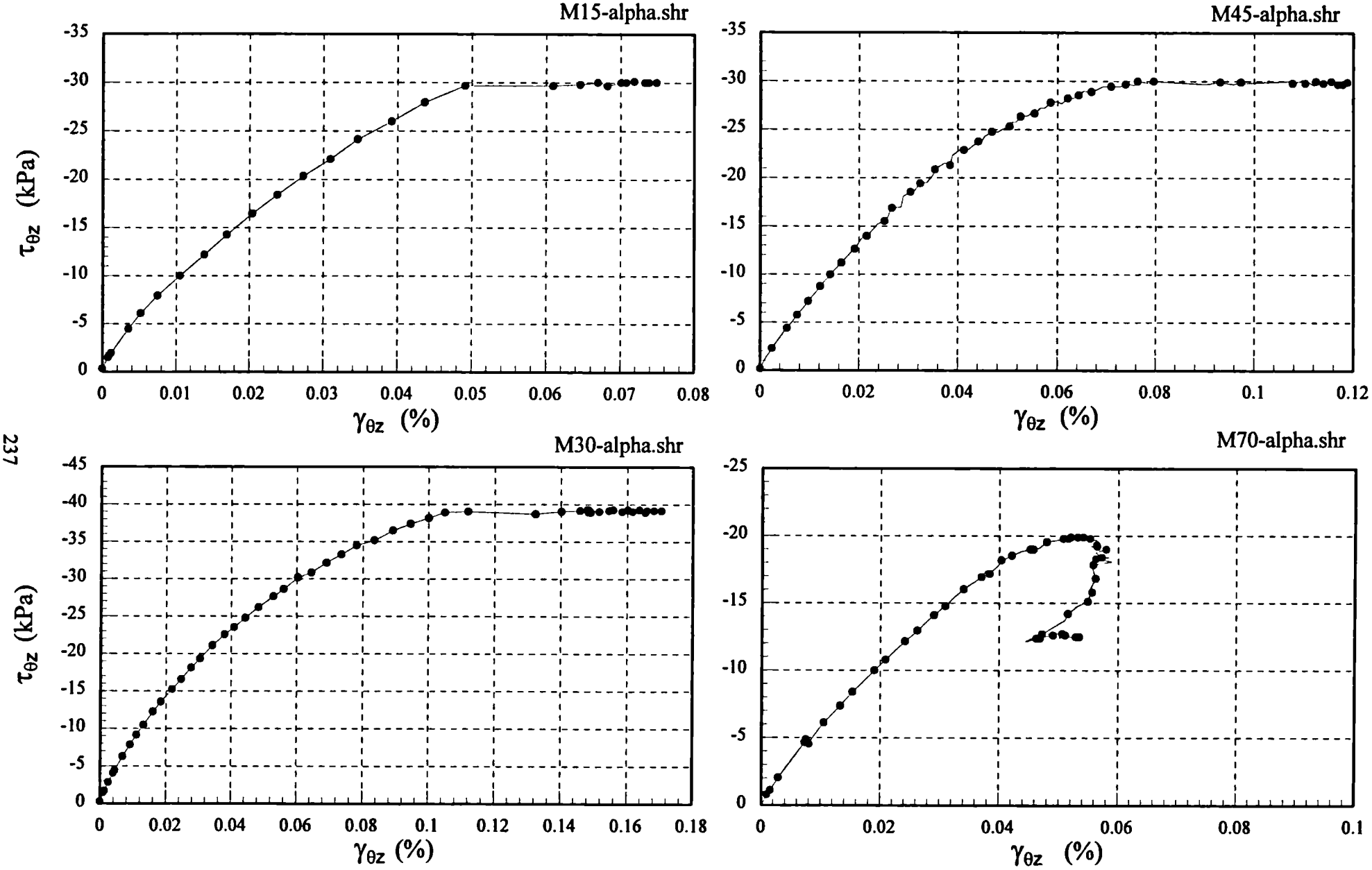


Fig.5.16b - Development of torsional shear stress during undrained principal stress rotation at t=const

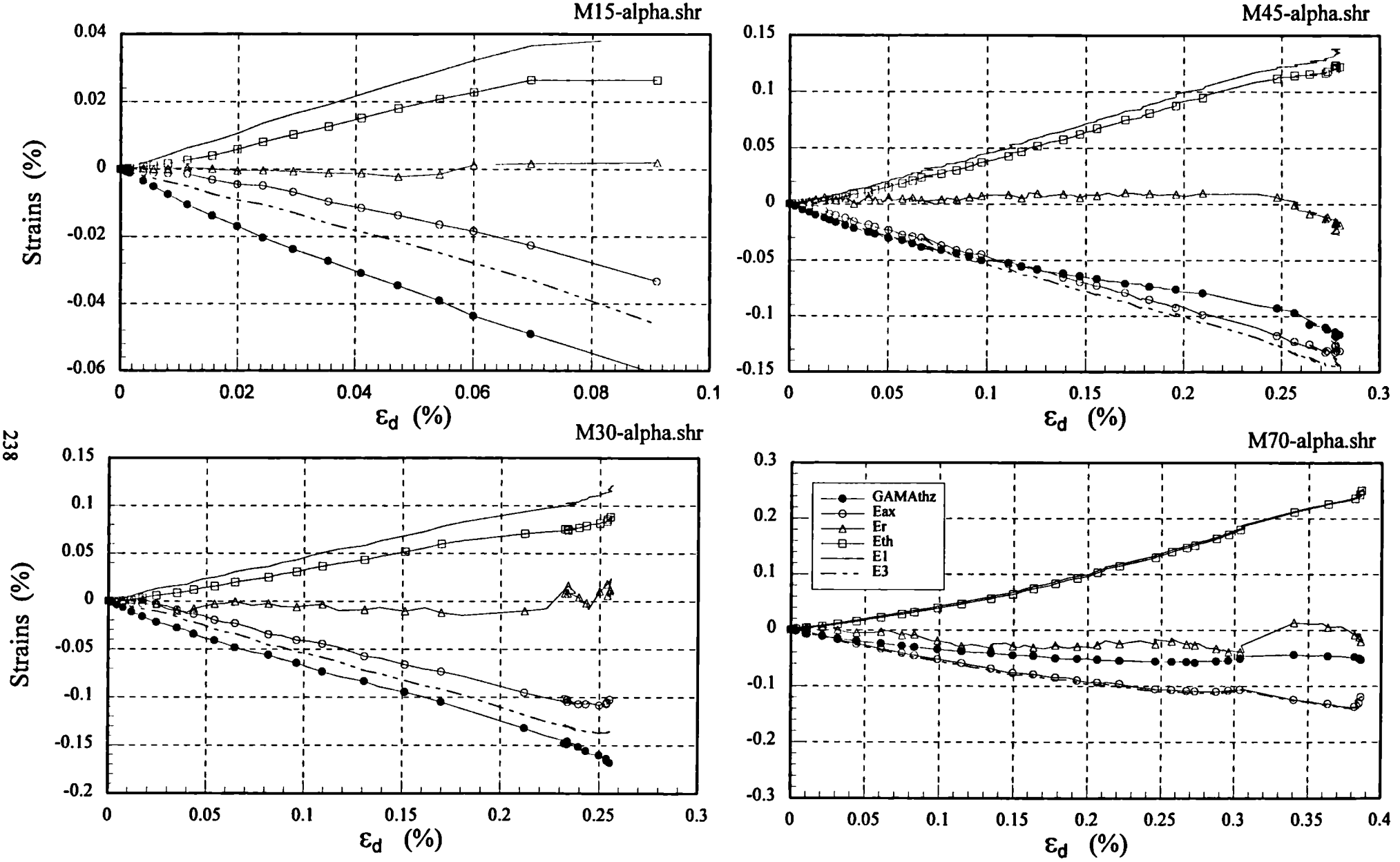


Fig.5.17 - Strain components during undrained principal stress rotation at b=0.5 and t=const

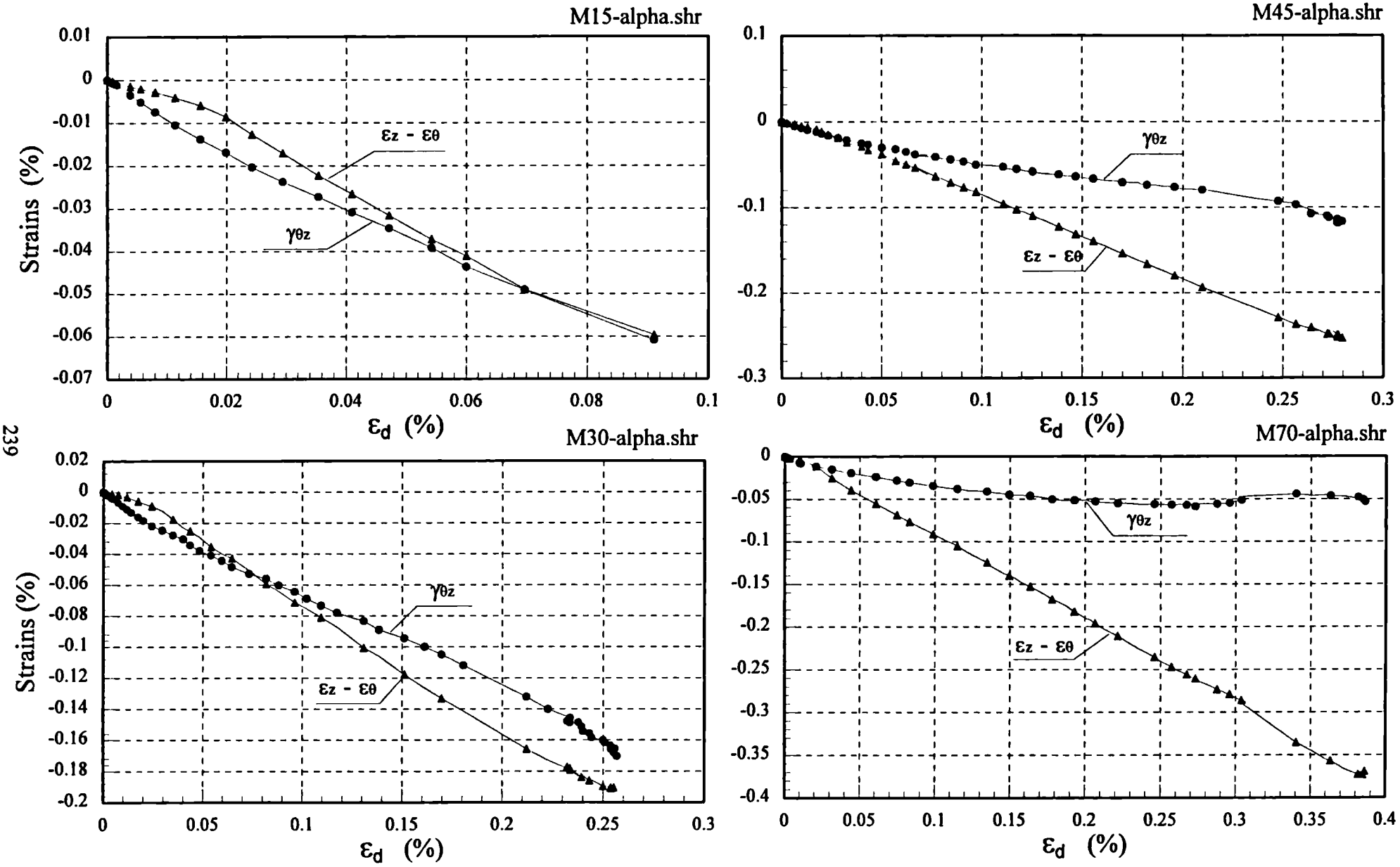


Fig.5.18a - Torsional shear strains developed during undrained principal stress rotation at t=const

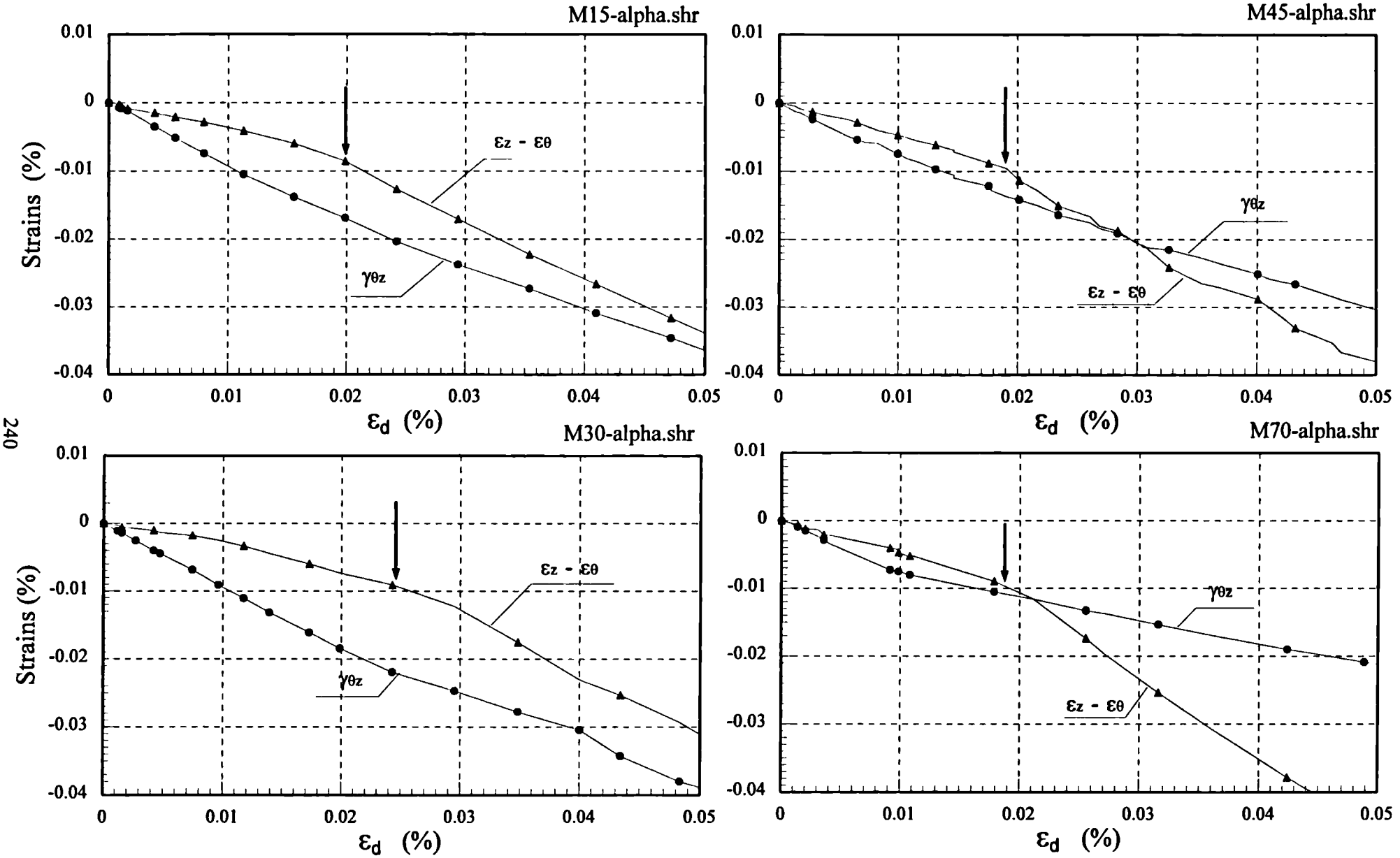


Fig.5.18b - Torsional shear strains developed during undrained principal stress rotation at t=const, small strain view

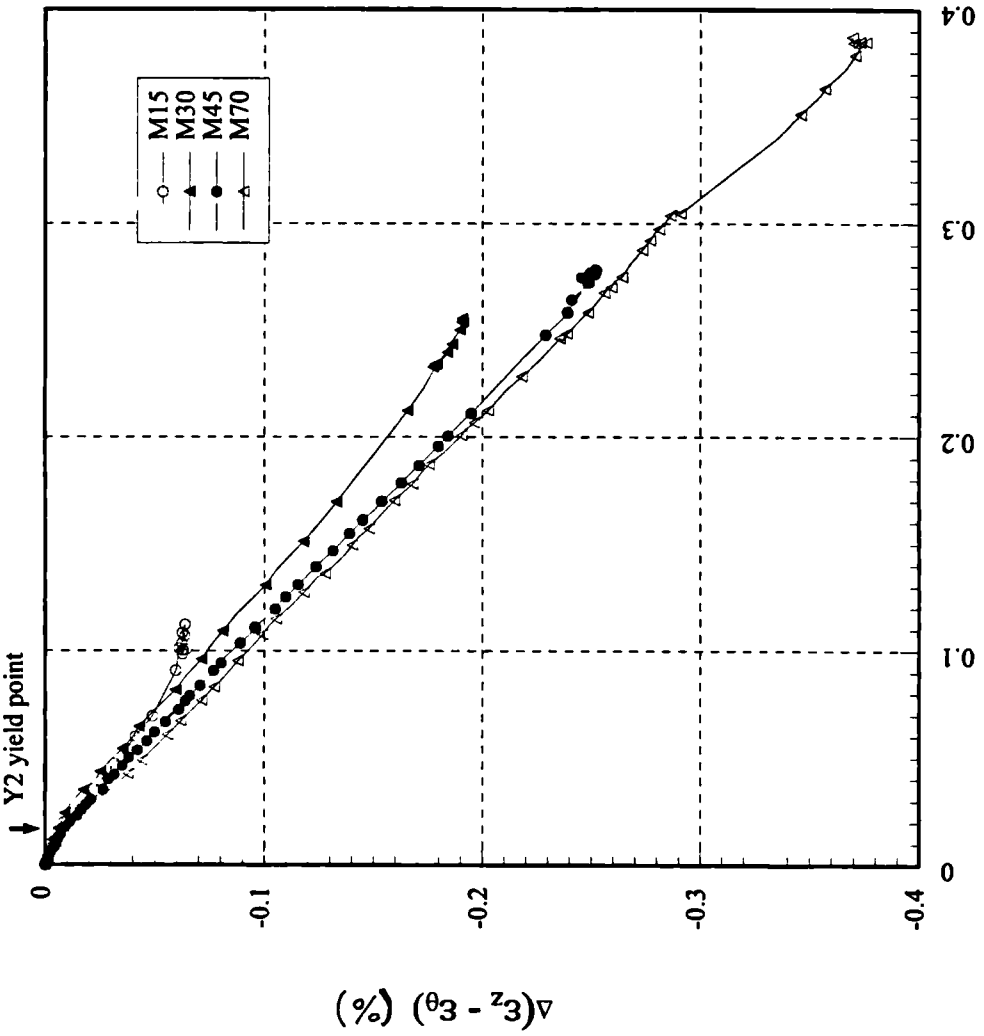


Fig.5.19 - Shear strain rate during α-rotation stage

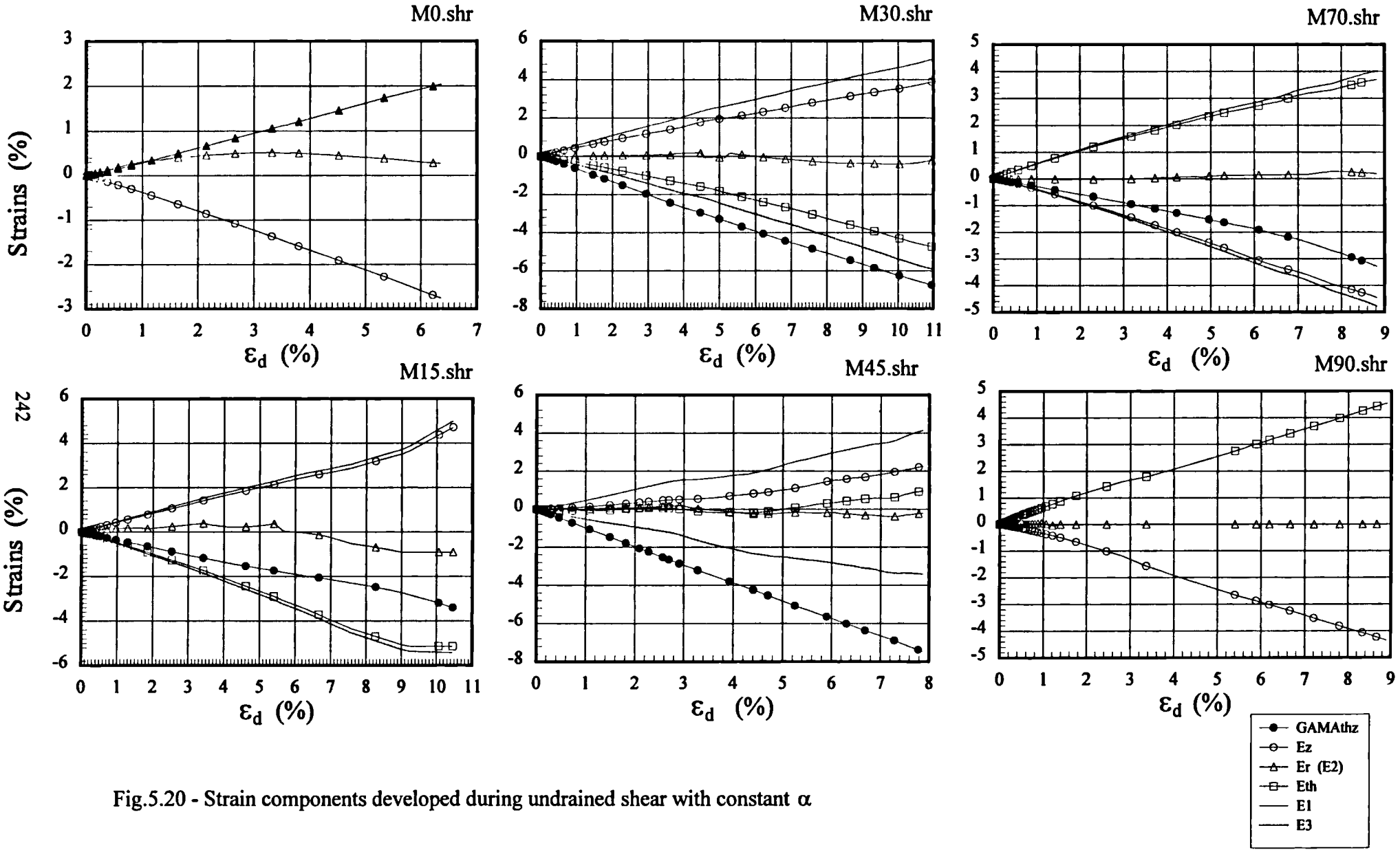
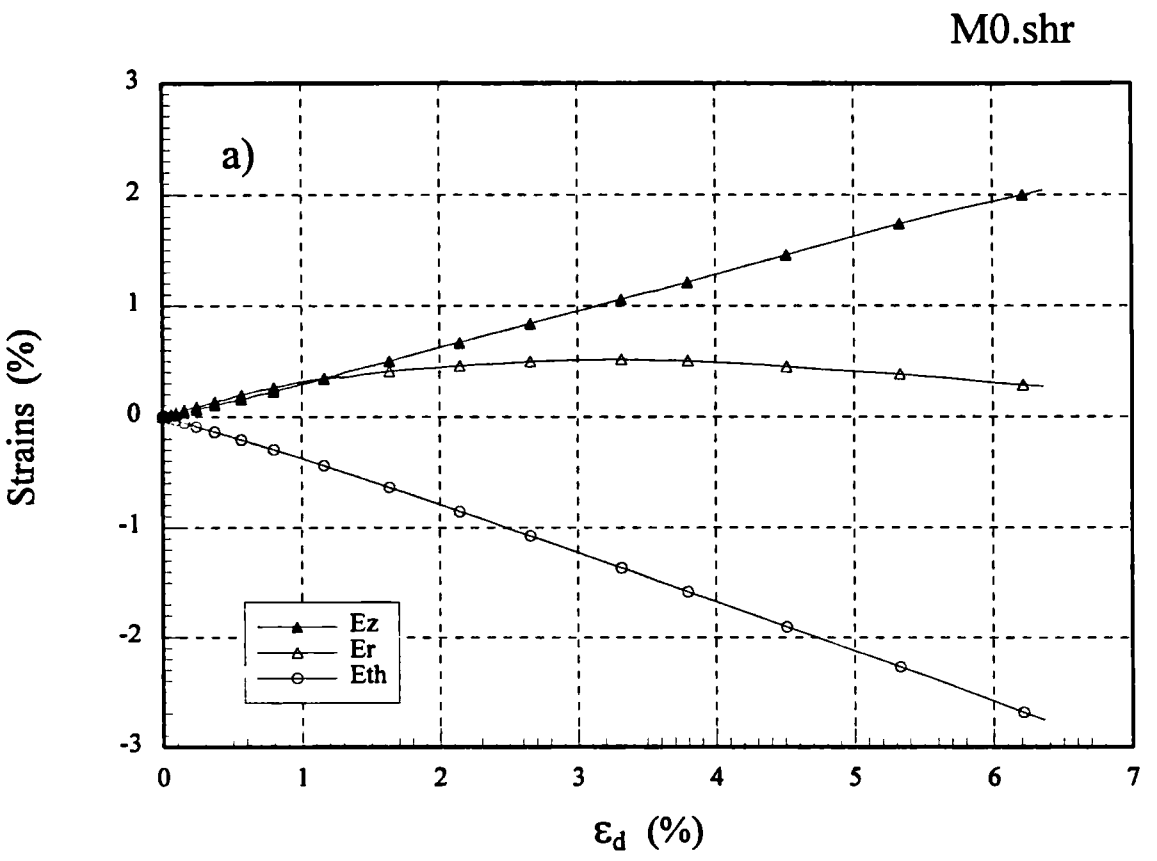


Fig.5.20 - Strain components developed during undrained shear with constant α



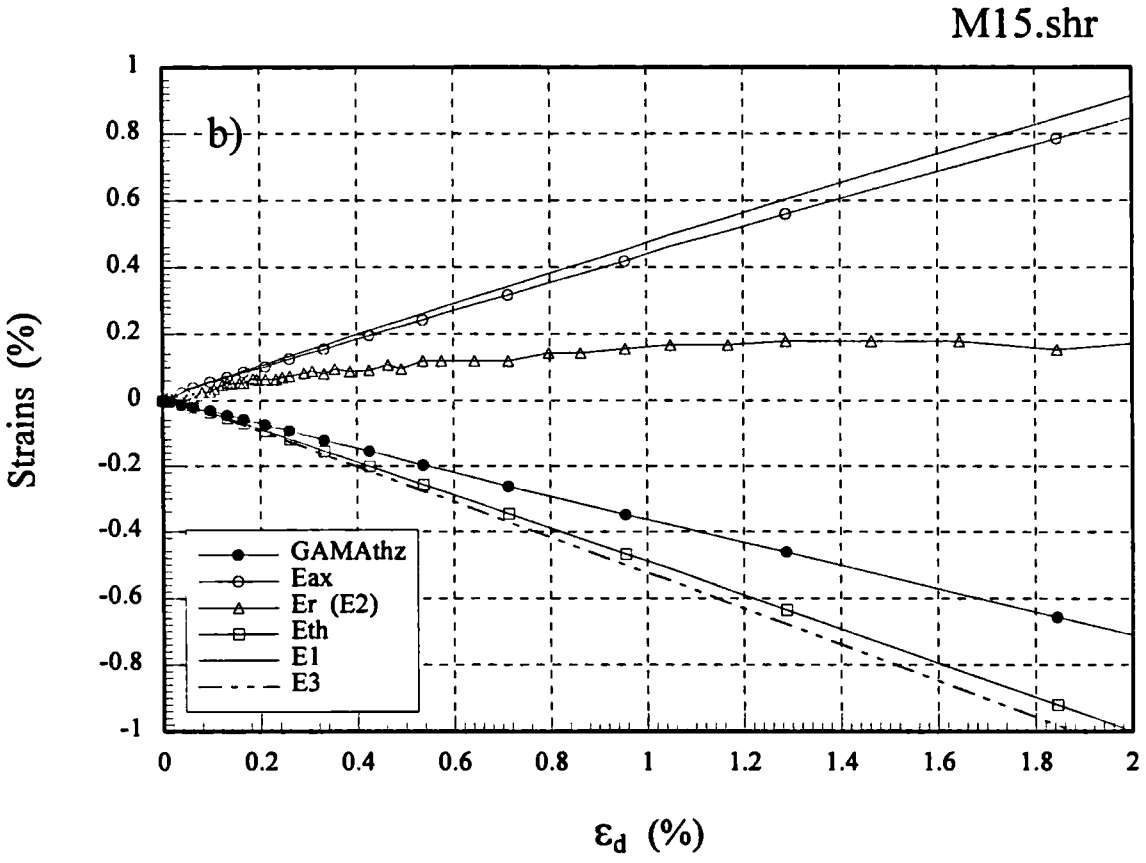


Fig.5.21 - a) Strain components during undrained shearing of test M0
b) Strain components during undrained shearing of test M15

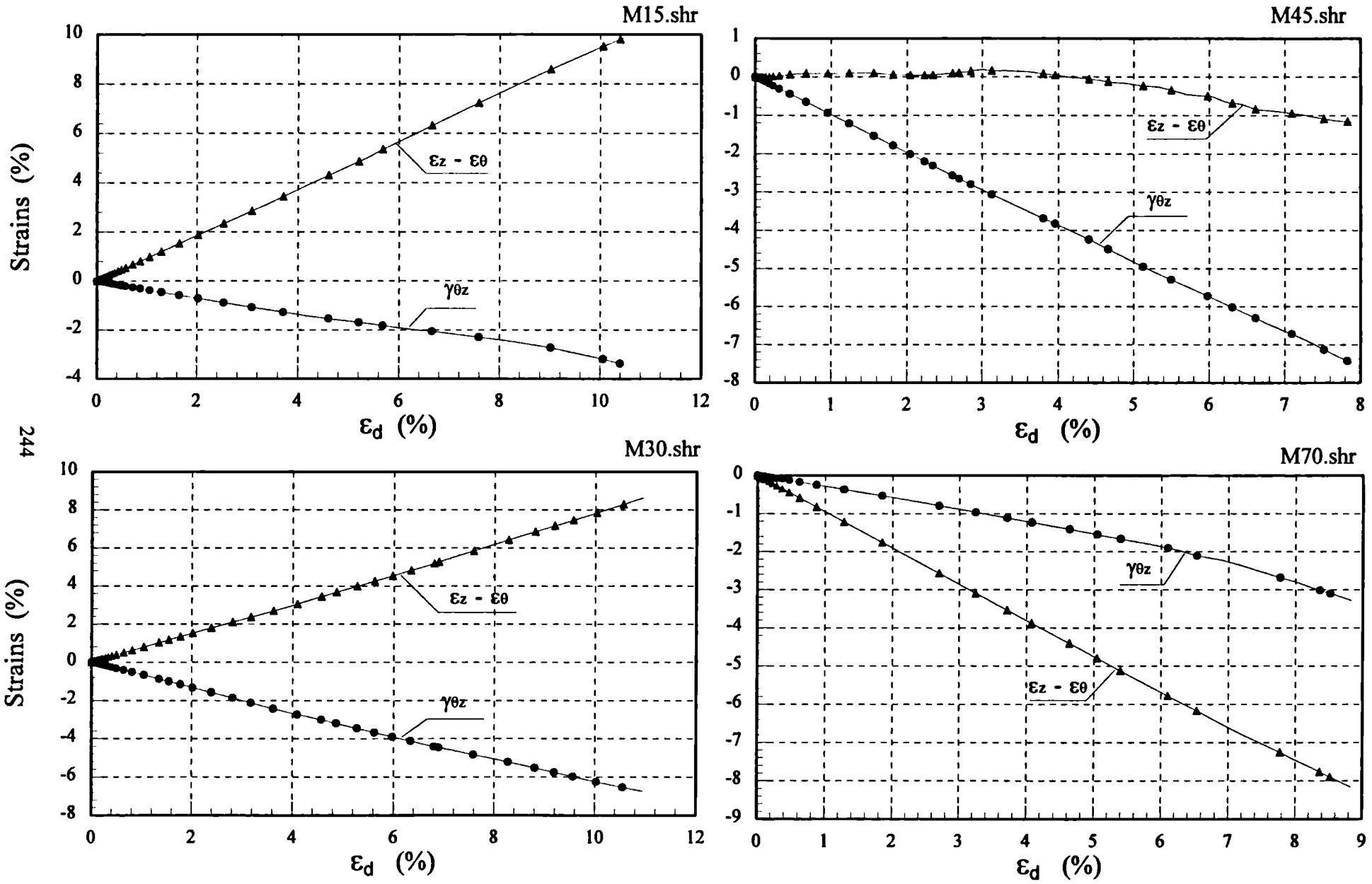


Fig.5.22 - Torsional shear strains developed during undrained shearing with constant α

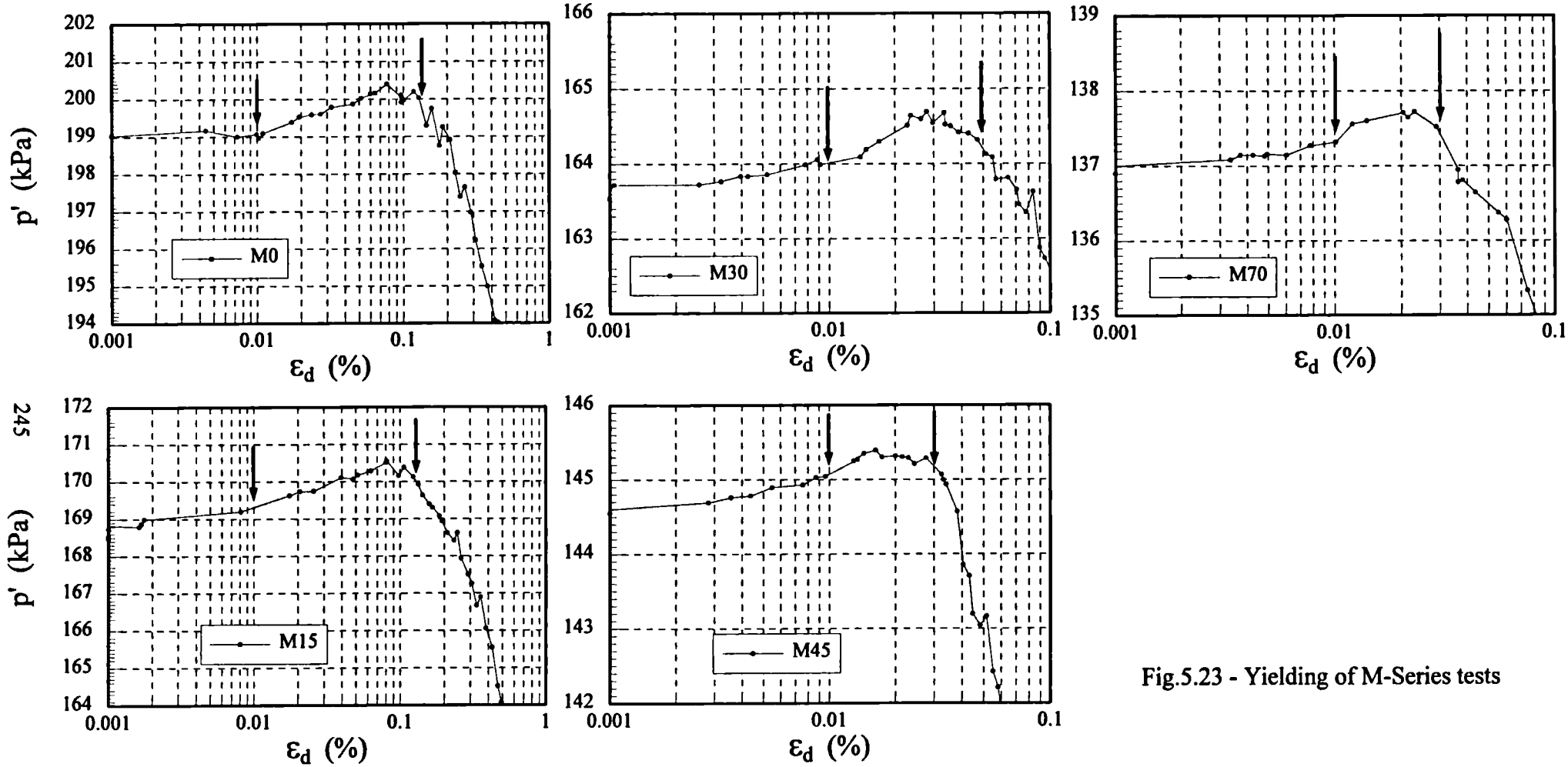


Fig.5.23 - Yielding of M-Series tests

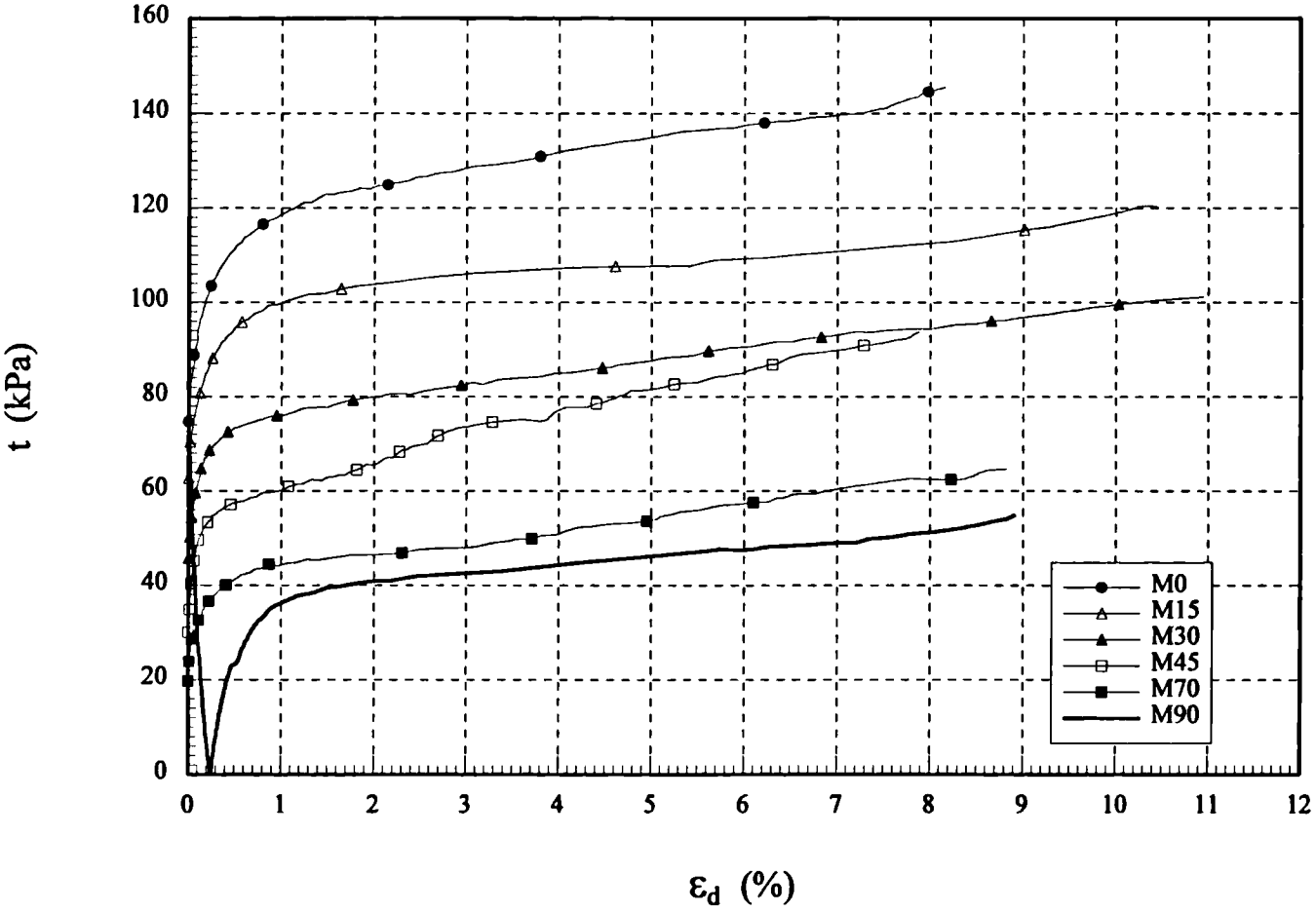


Fig.5.24 - Deviator strain during undrained shearing of M-Series tests

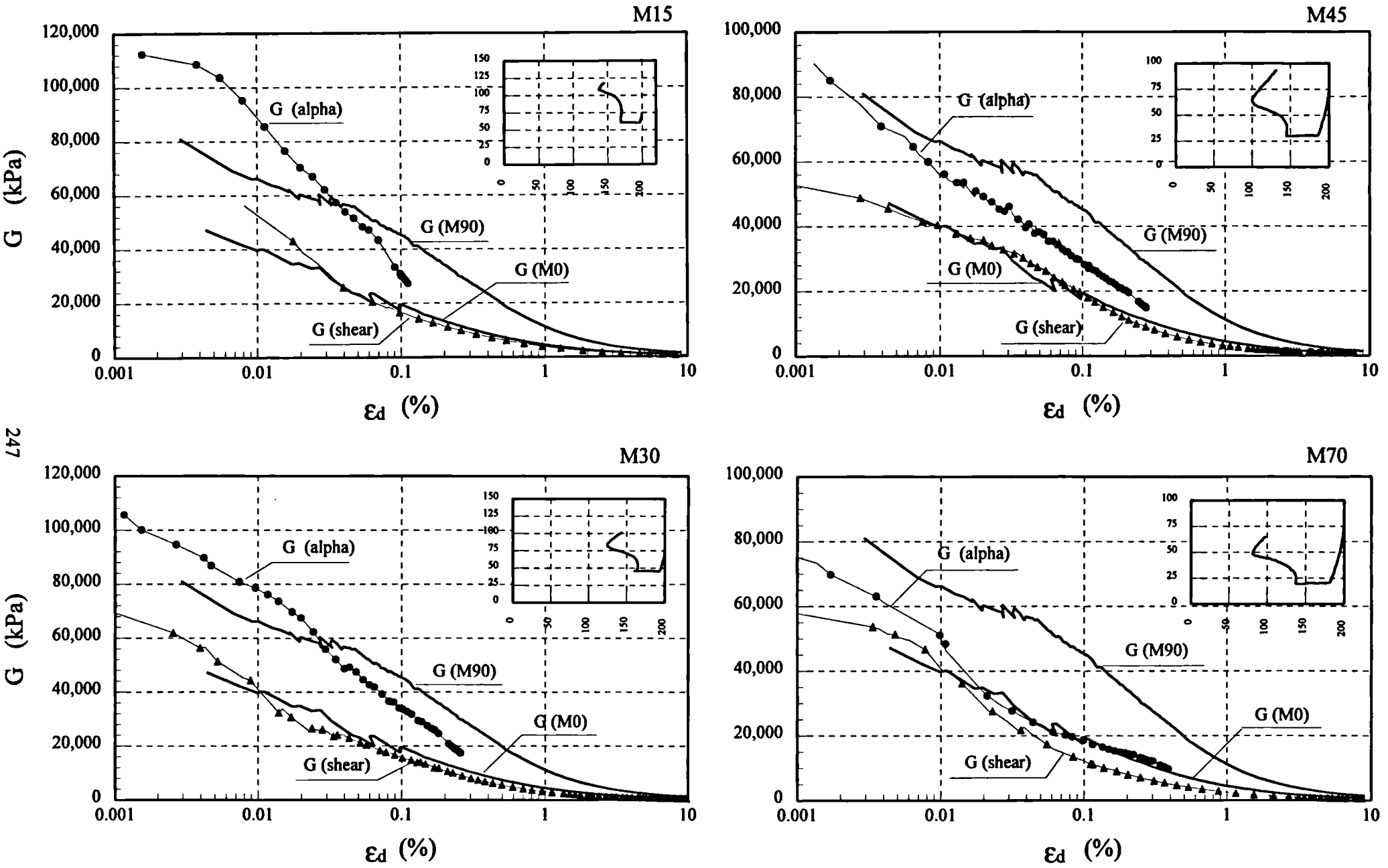


Fig.5.25 - Octahedral shear stiffness for rotational and shearing stages of M-Series tests

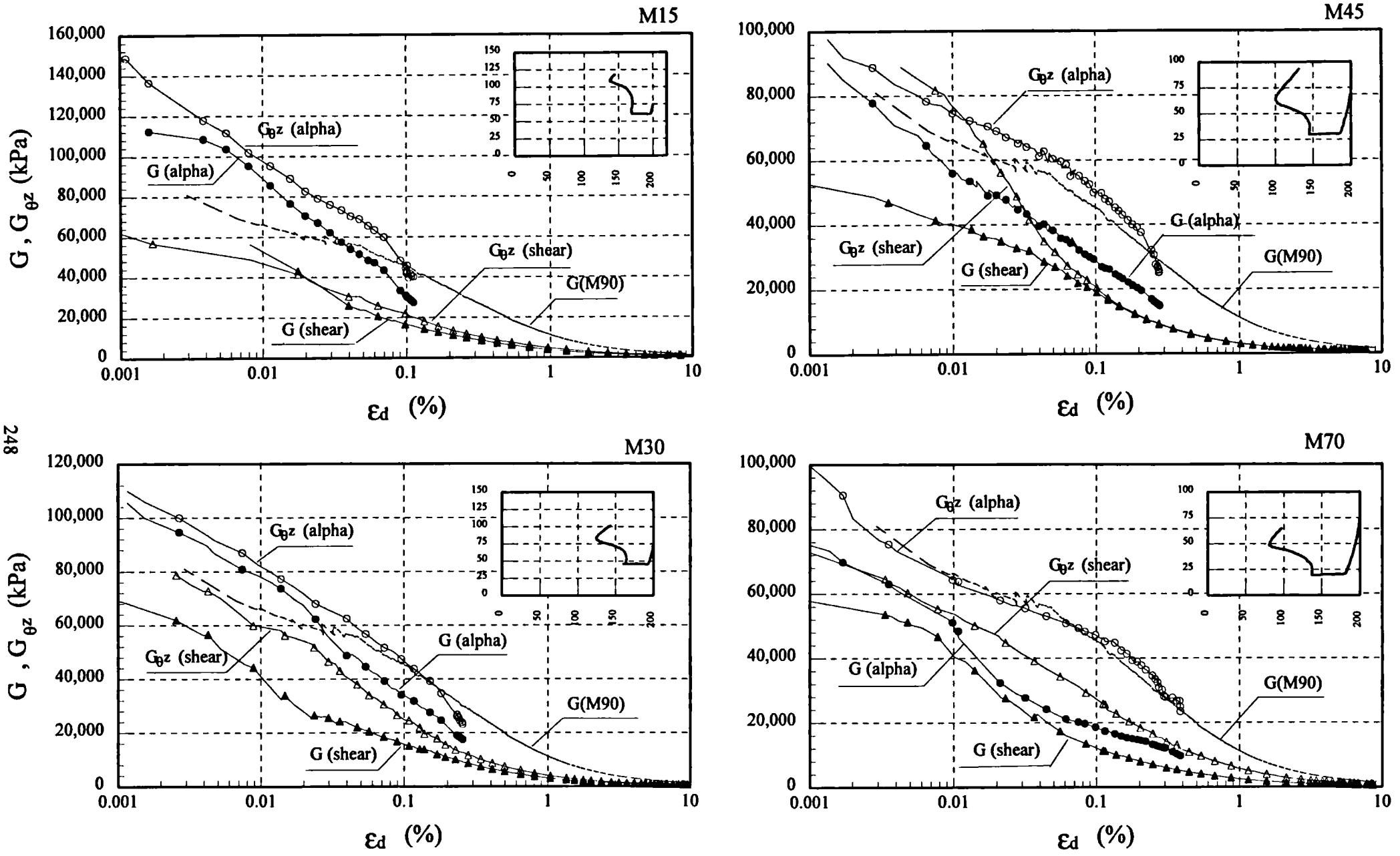


Fig.5.26 - Comparison of torsional shear stiffness, $G_{\theta z}$, with other stiffness components

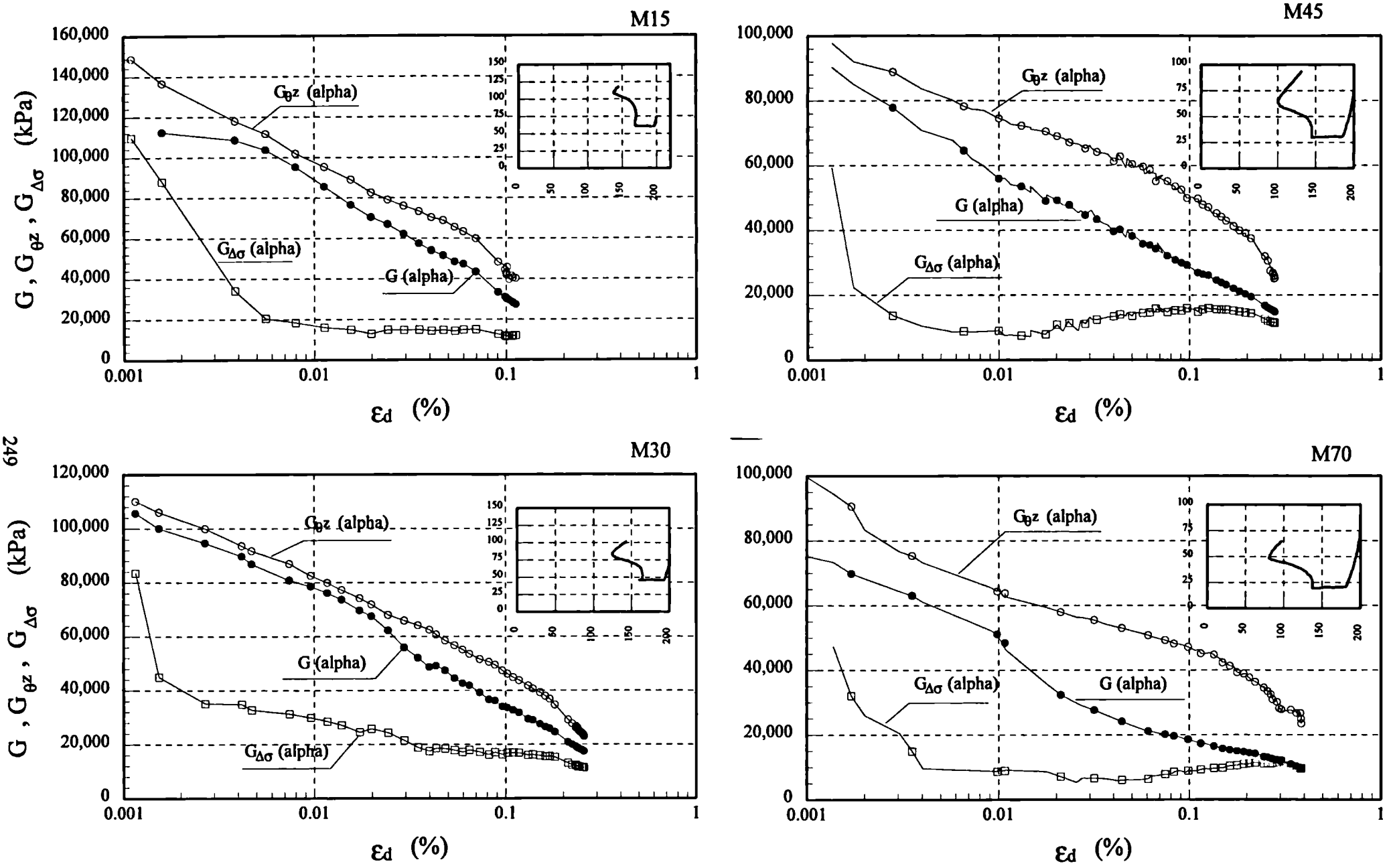


Fig.5.27 - Summary of component stiffnesses for rotational stage

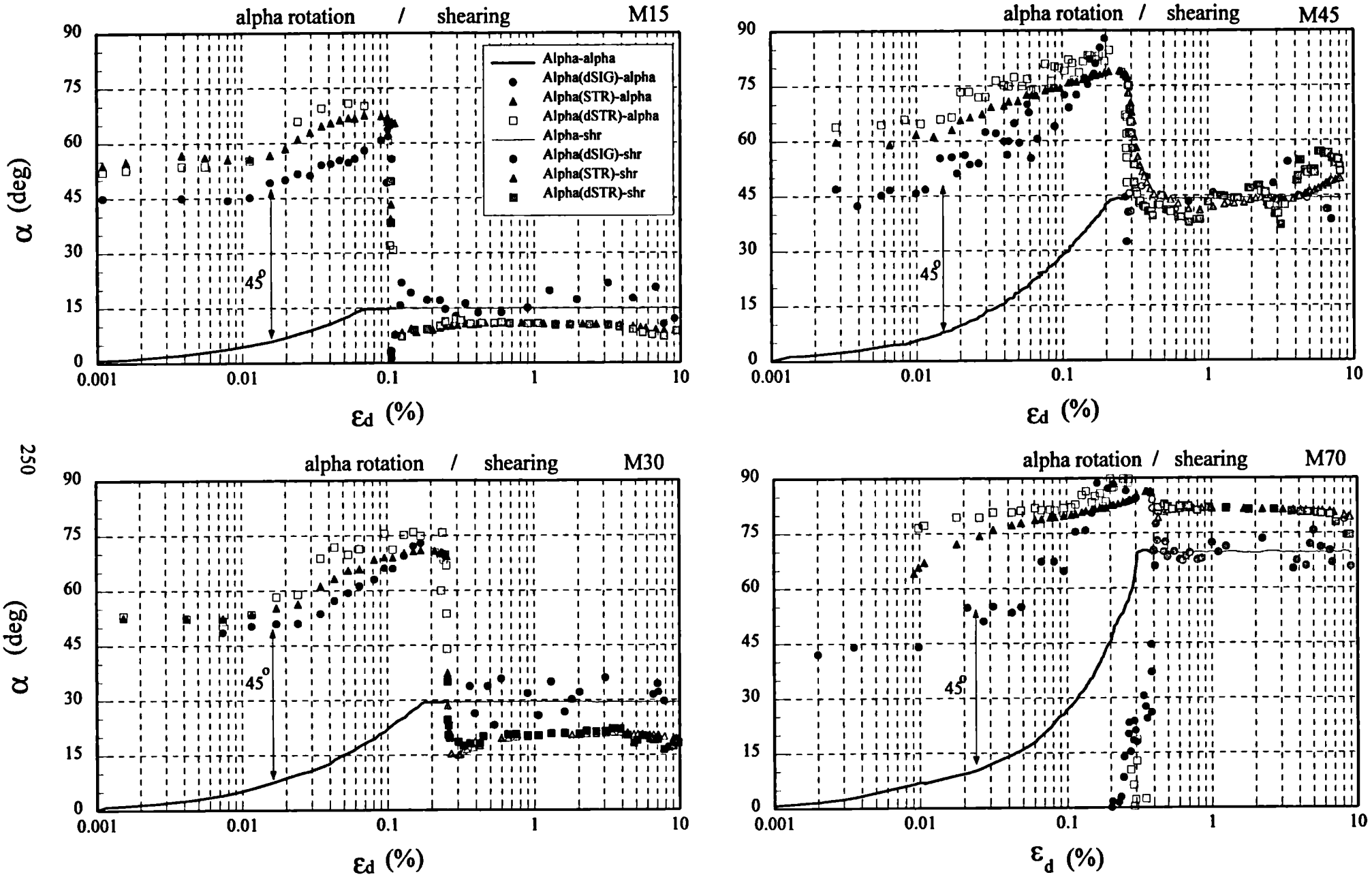


Fig.5.28 - Directions of principal stress and strain and their increments during α-rotation and shearing stages

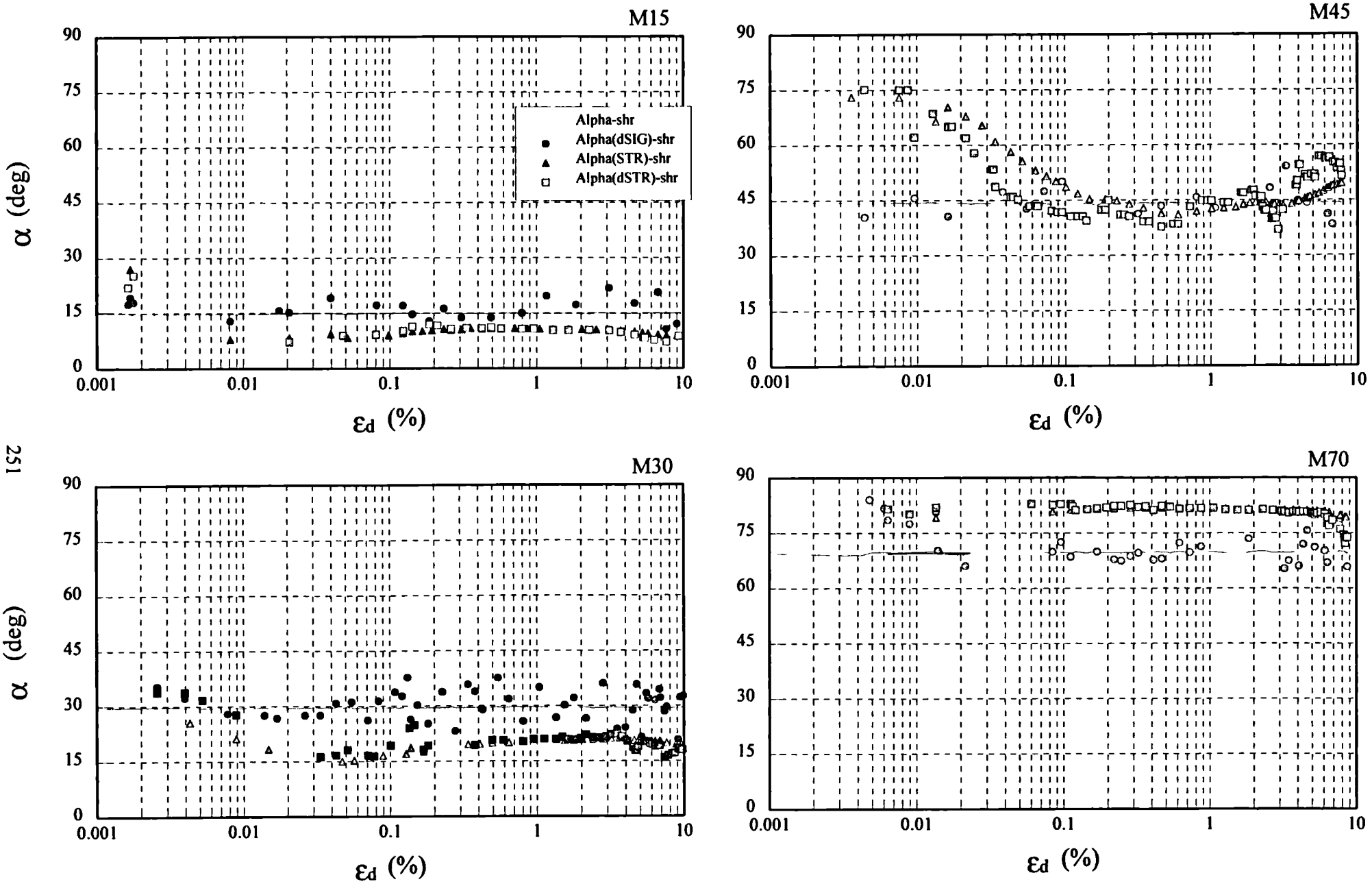


Fig.5.29 - Directions of principal stress and strain and their increments during shearing stage

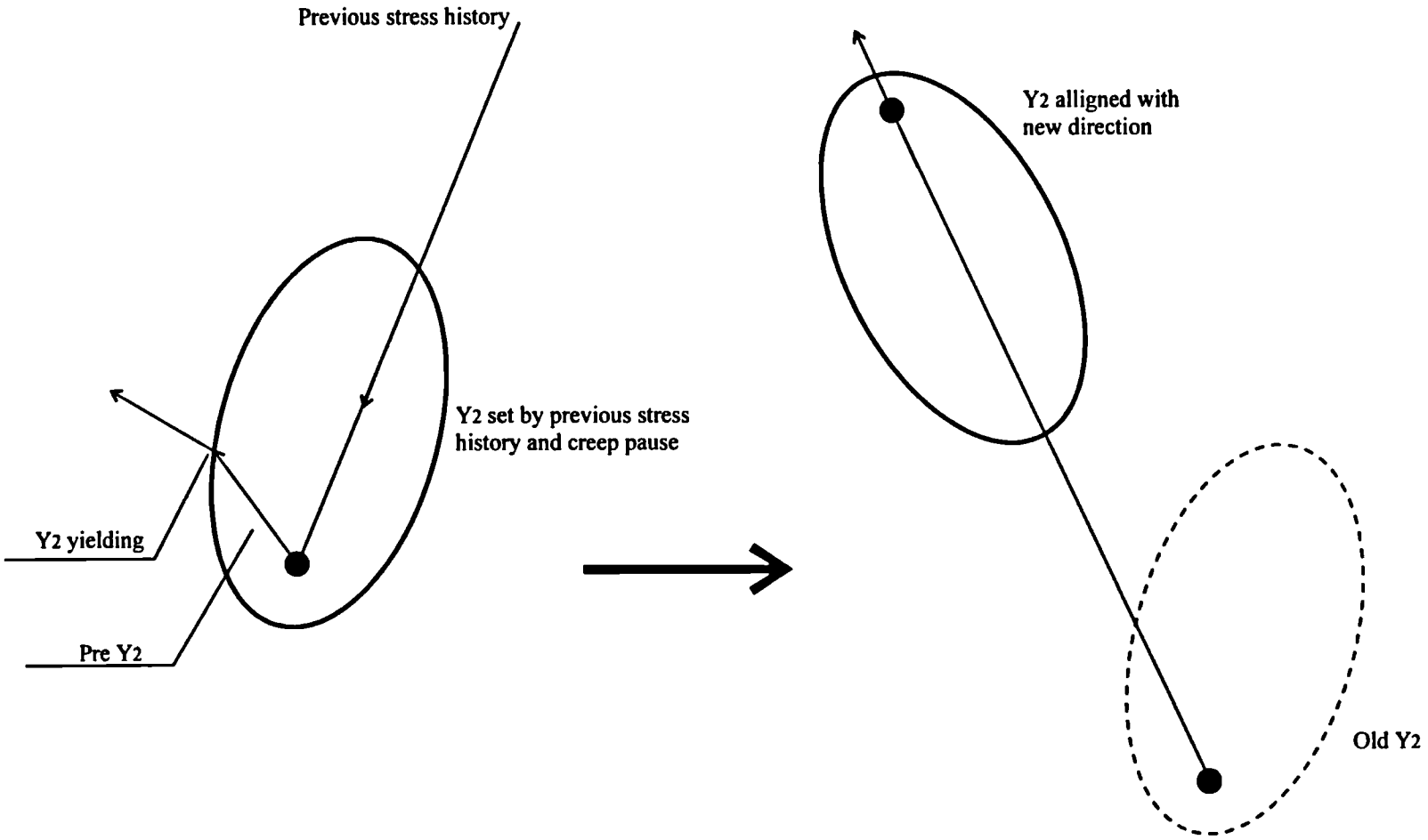


Fig.5.29a - Recent stress history

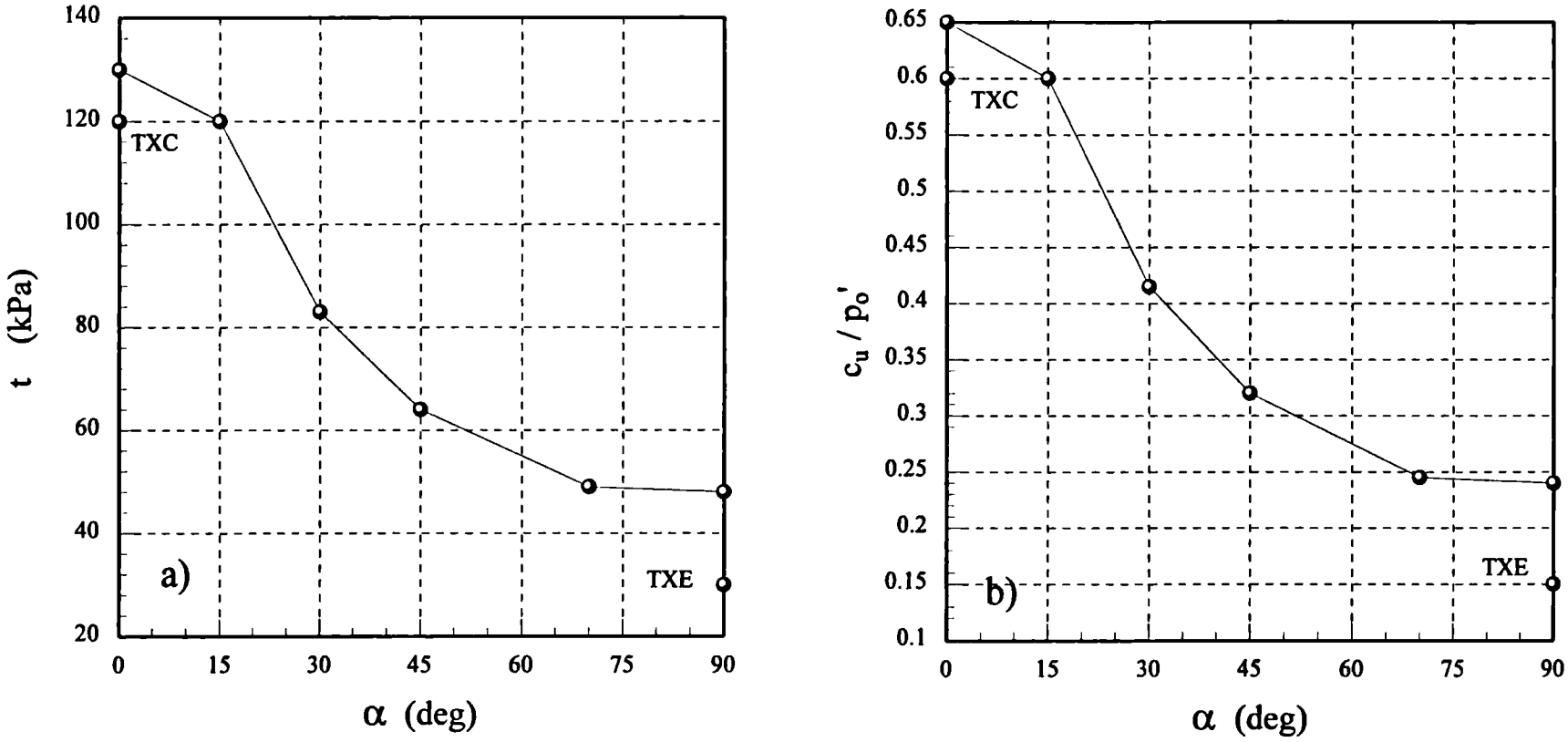


Fig.5.30 - a) Reduction of Phase Transformation value of 't' with principal stress rotation, α
b) Normalization of the PTP value of 't' with the consolidation mean effective stress, po'

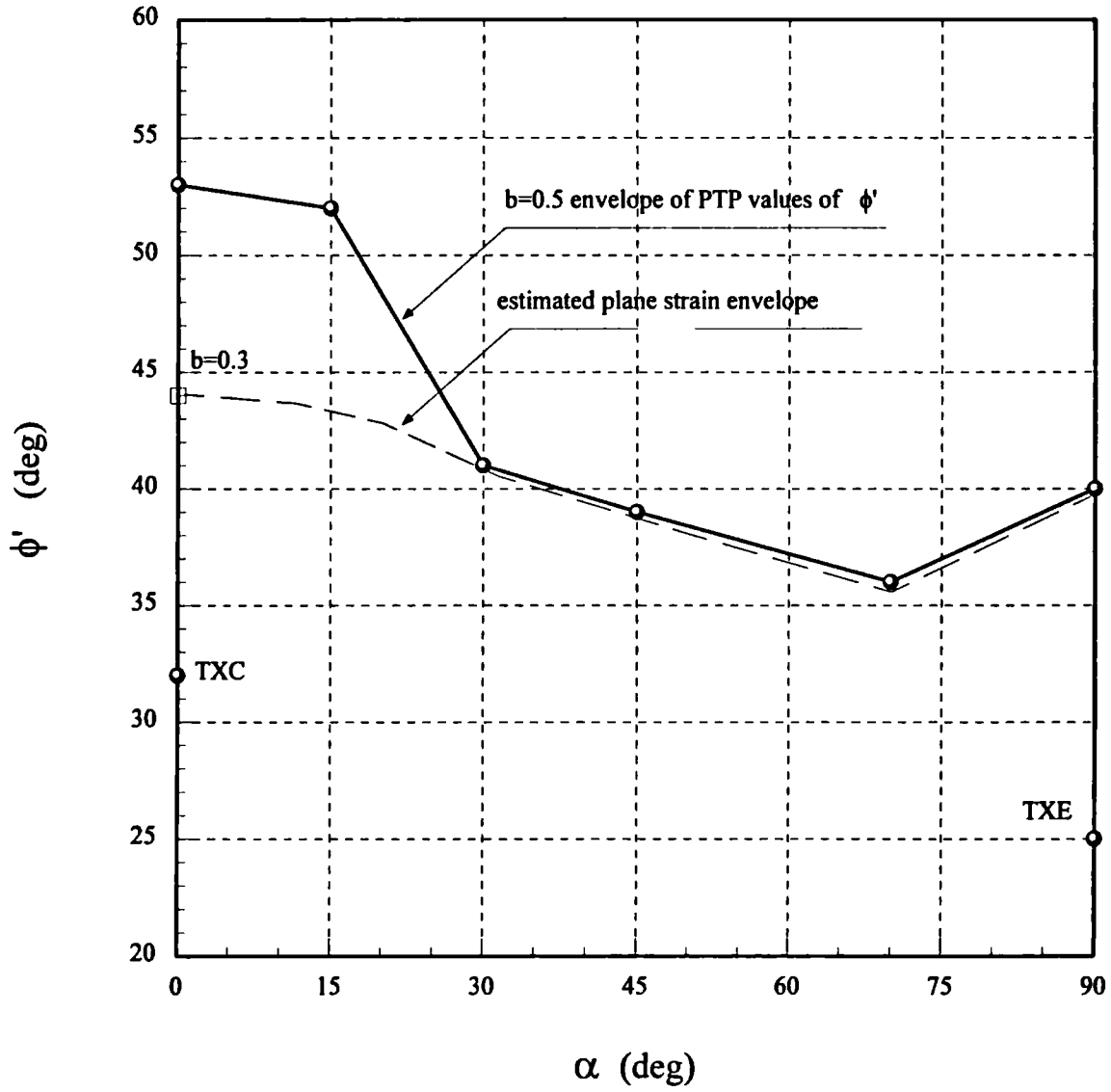


Fig.5.31 - Anisotropy of mobilized friction angle at the PTP due to principal stress rotation

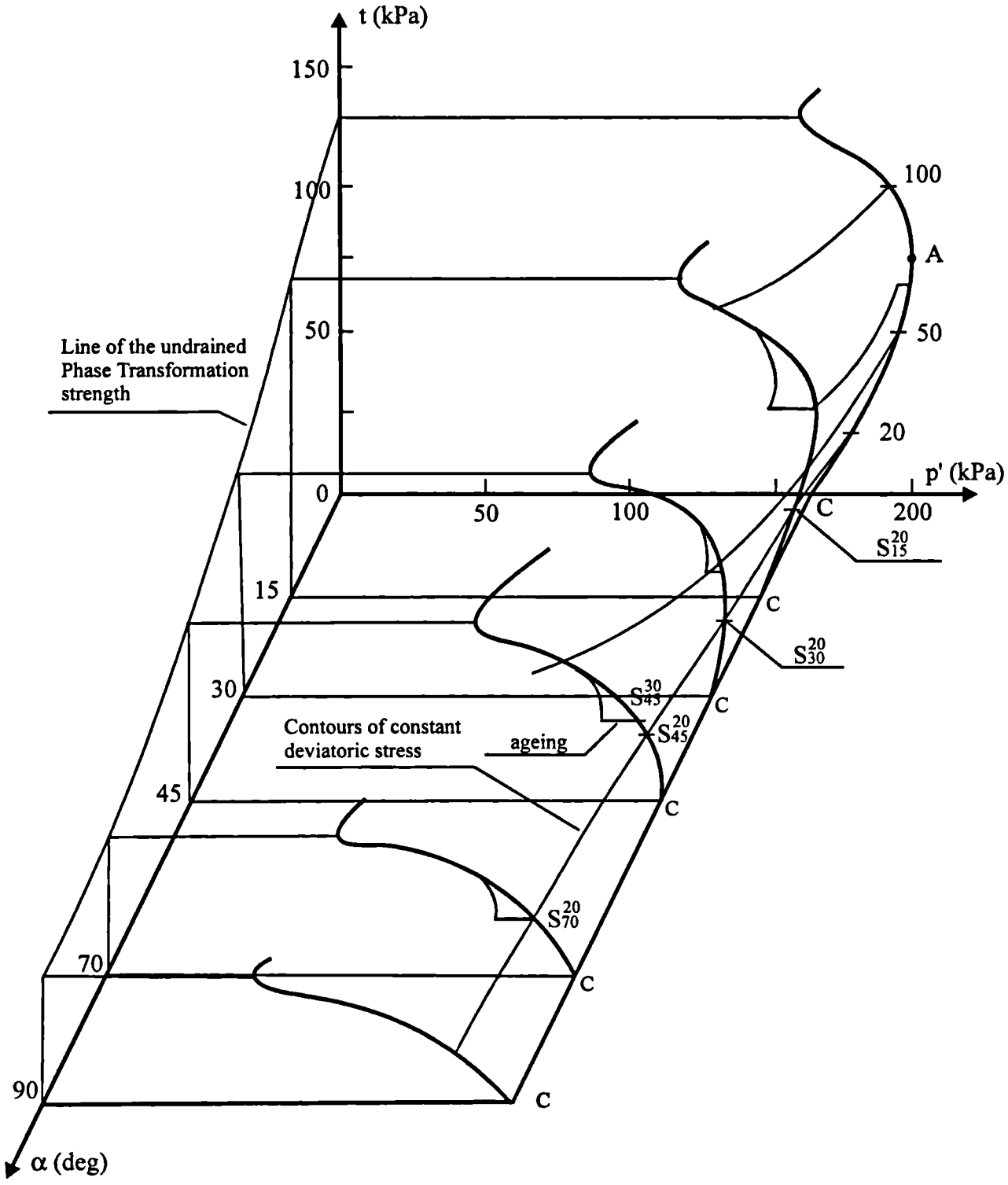


Fig.5.32 - Bounding surface for dense HPF4 in t-p'-α space

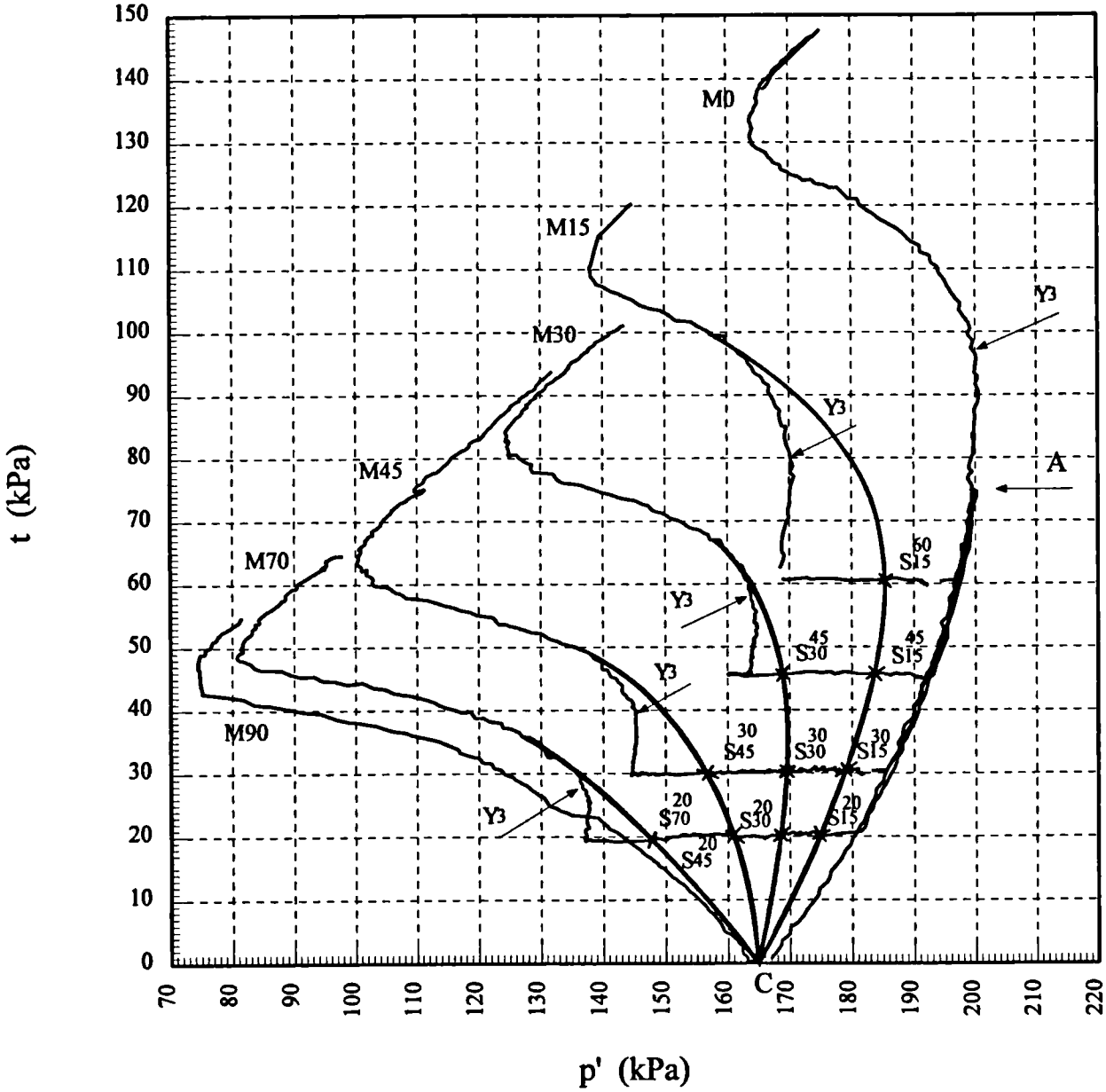


Fig.5.33 - Construction of the bounding surface for normally consolidated HPF4

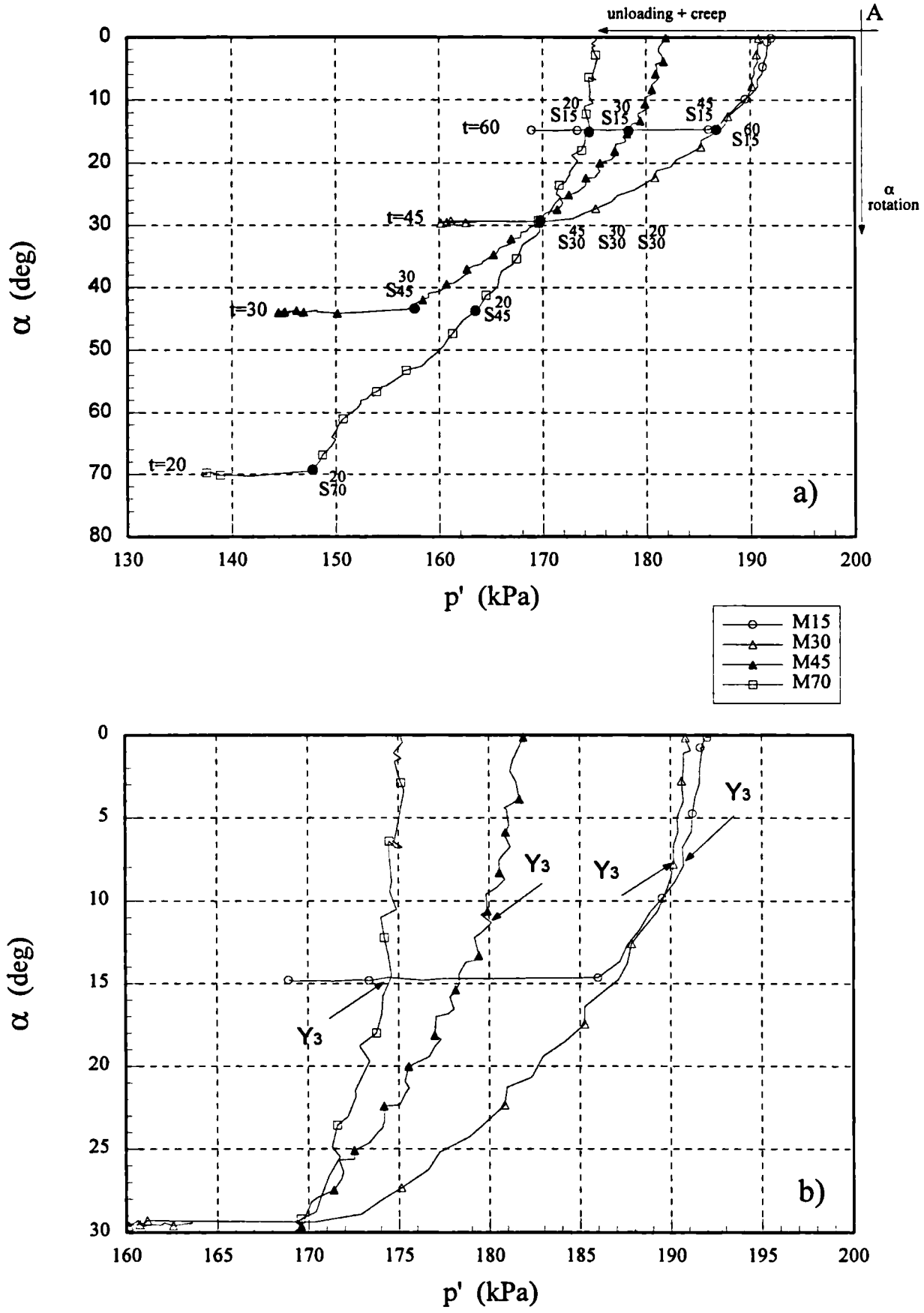
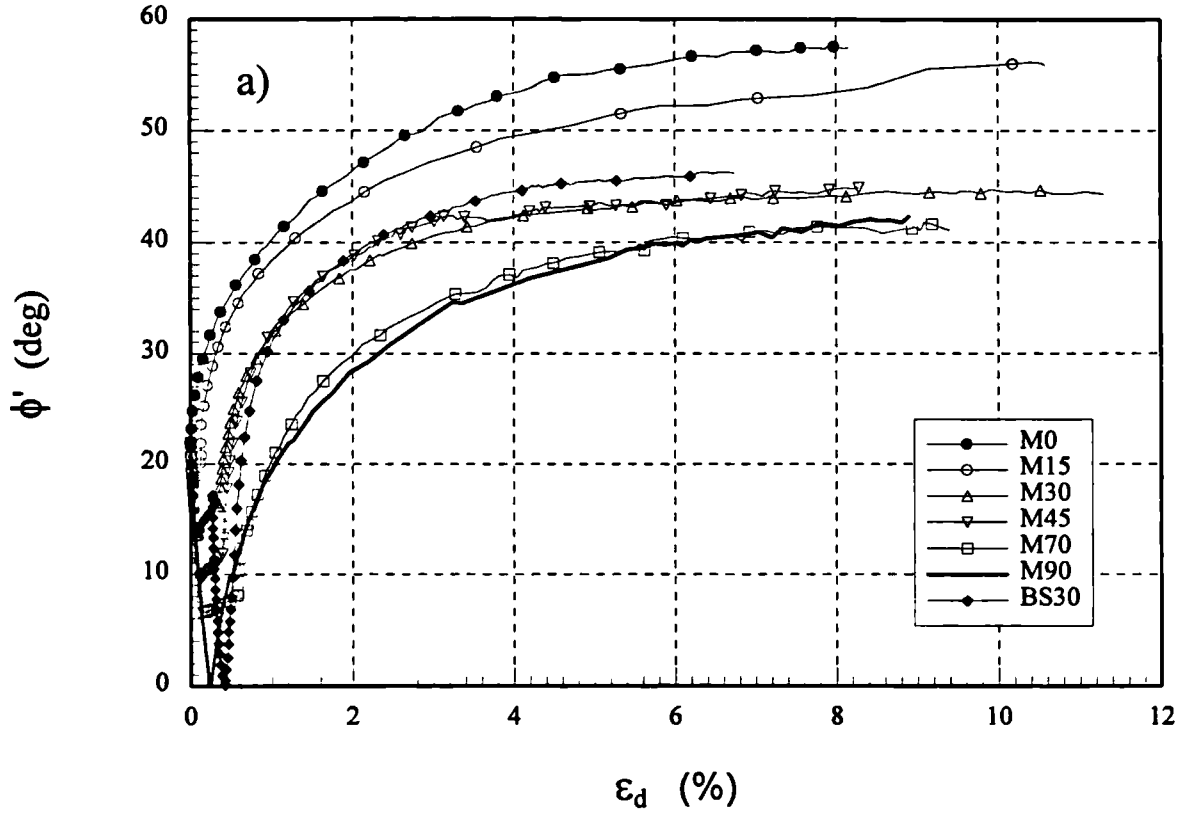


Fig.5.34 - a) Projection of the bounding surface on p'-α plane
b) Enlarged view



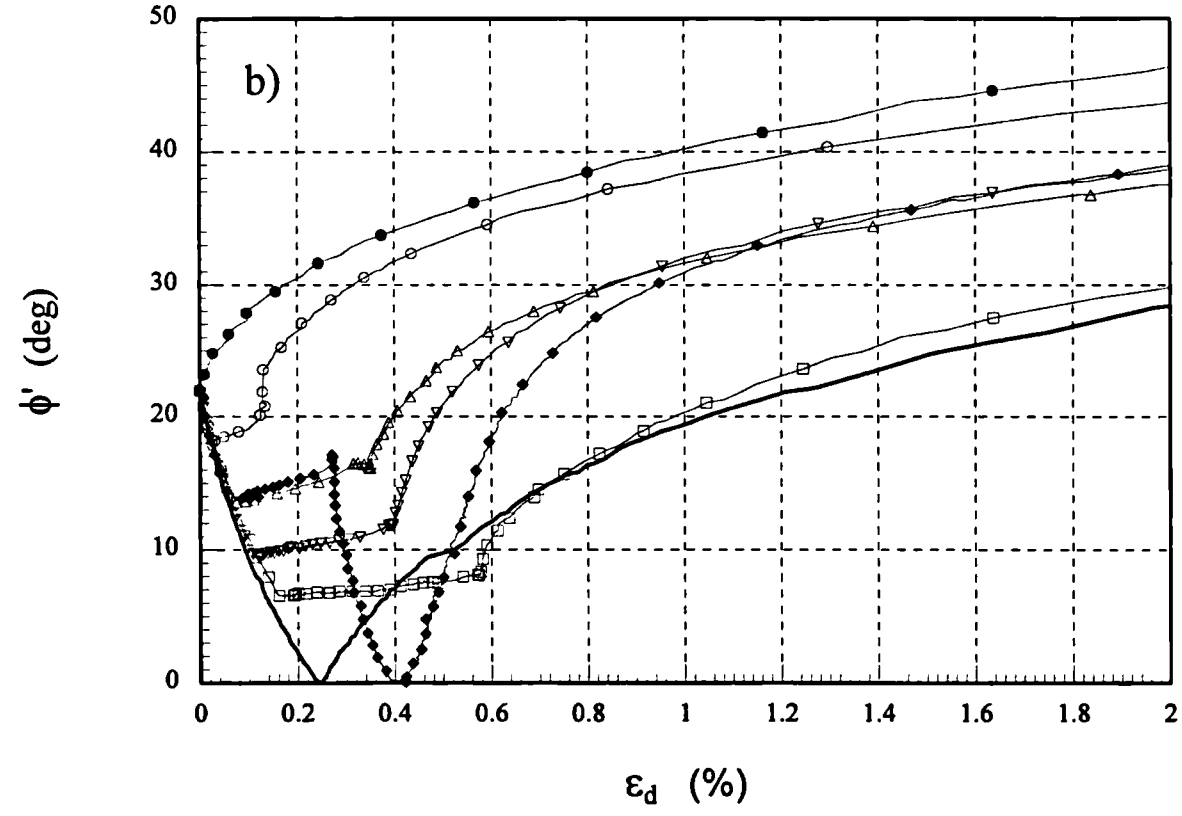


Fig.5.35 - Projection of the stress paths on ϕ'-ε_d plane

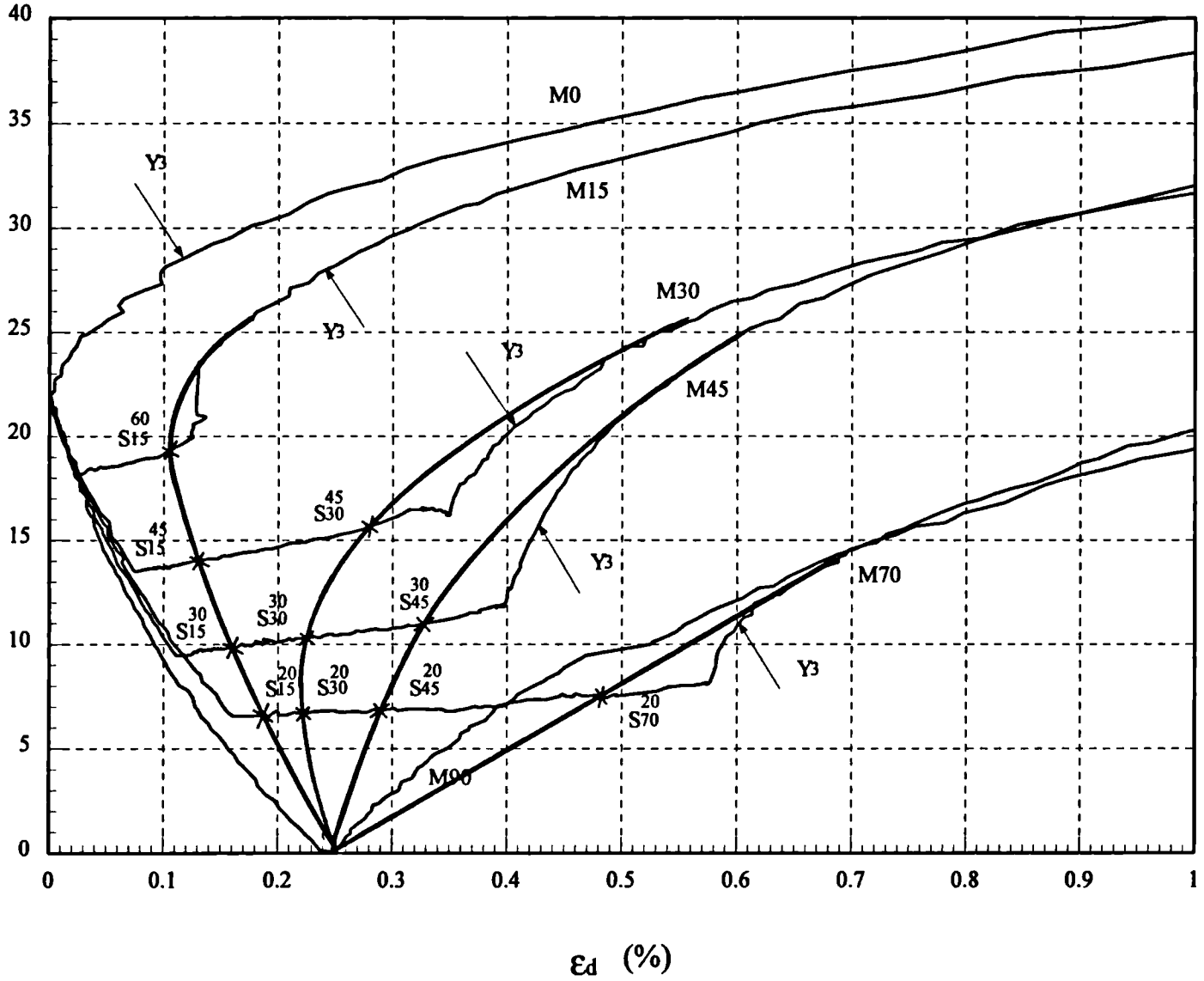


Fig.5.36 - Projection of the bounding surface on ϕ' - ε_d plane

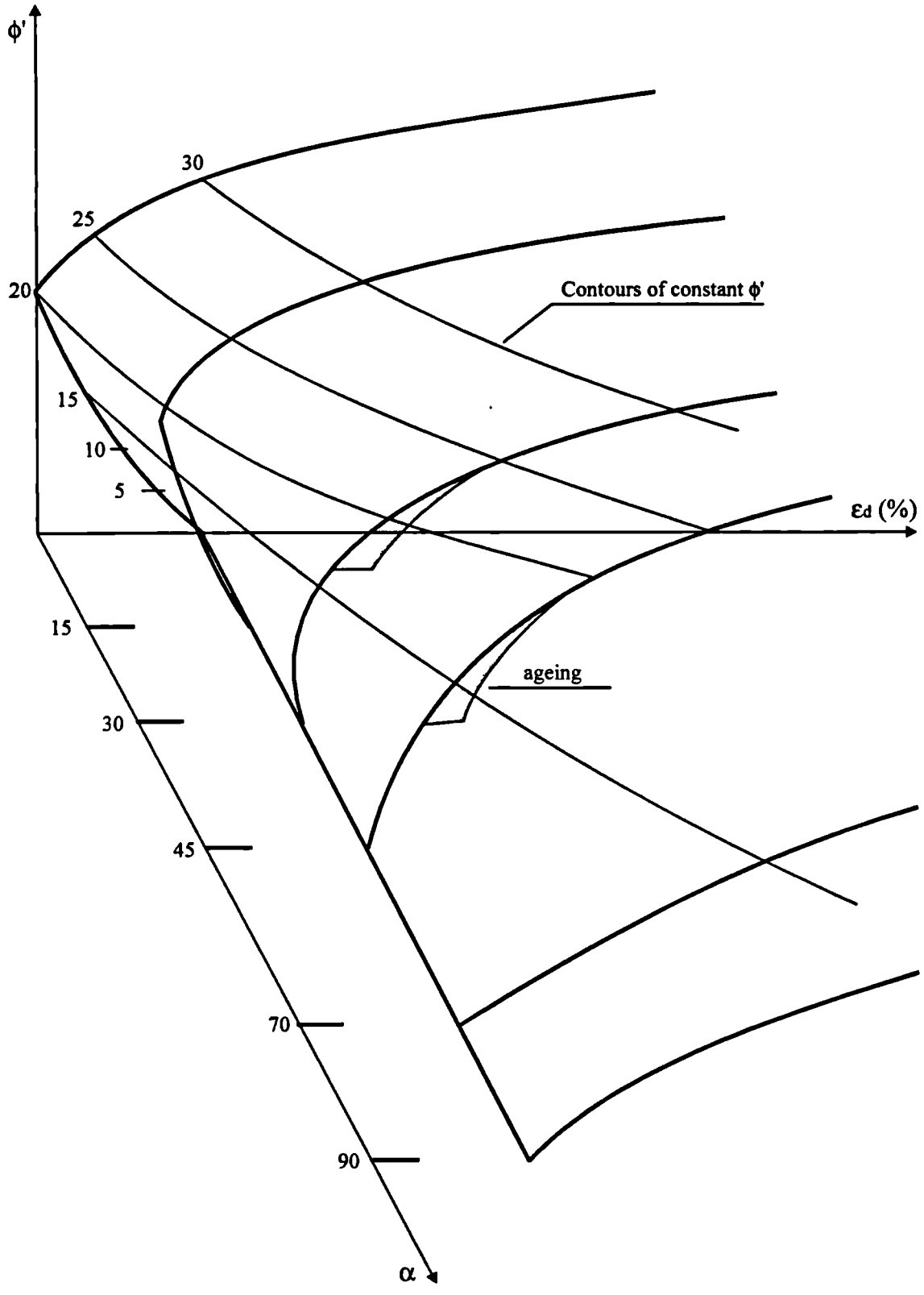


Fig.5.37 - Presentation of local BS in ϕ'-εd-α space

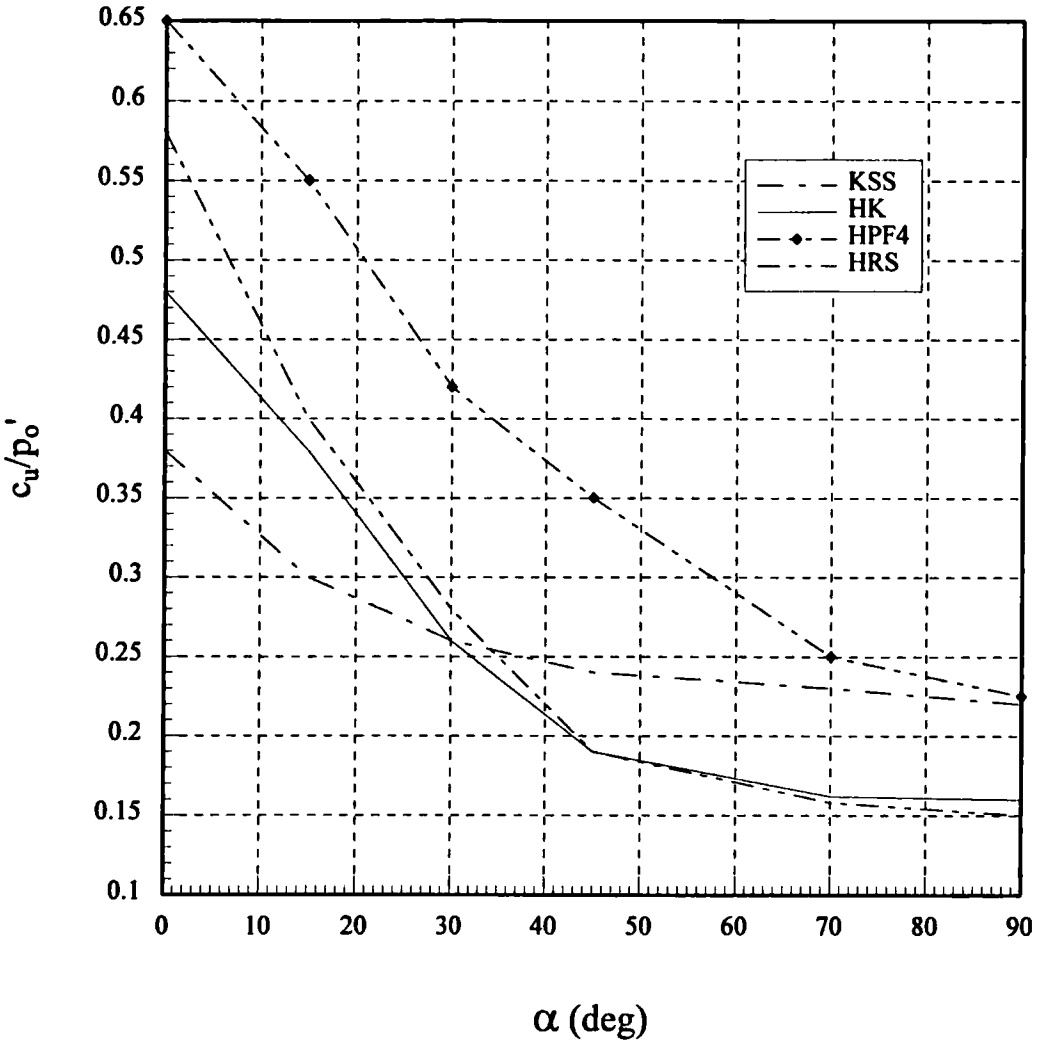


Fig.5.38 - Comparison of HPF4 'strength' anisotropy with other materials

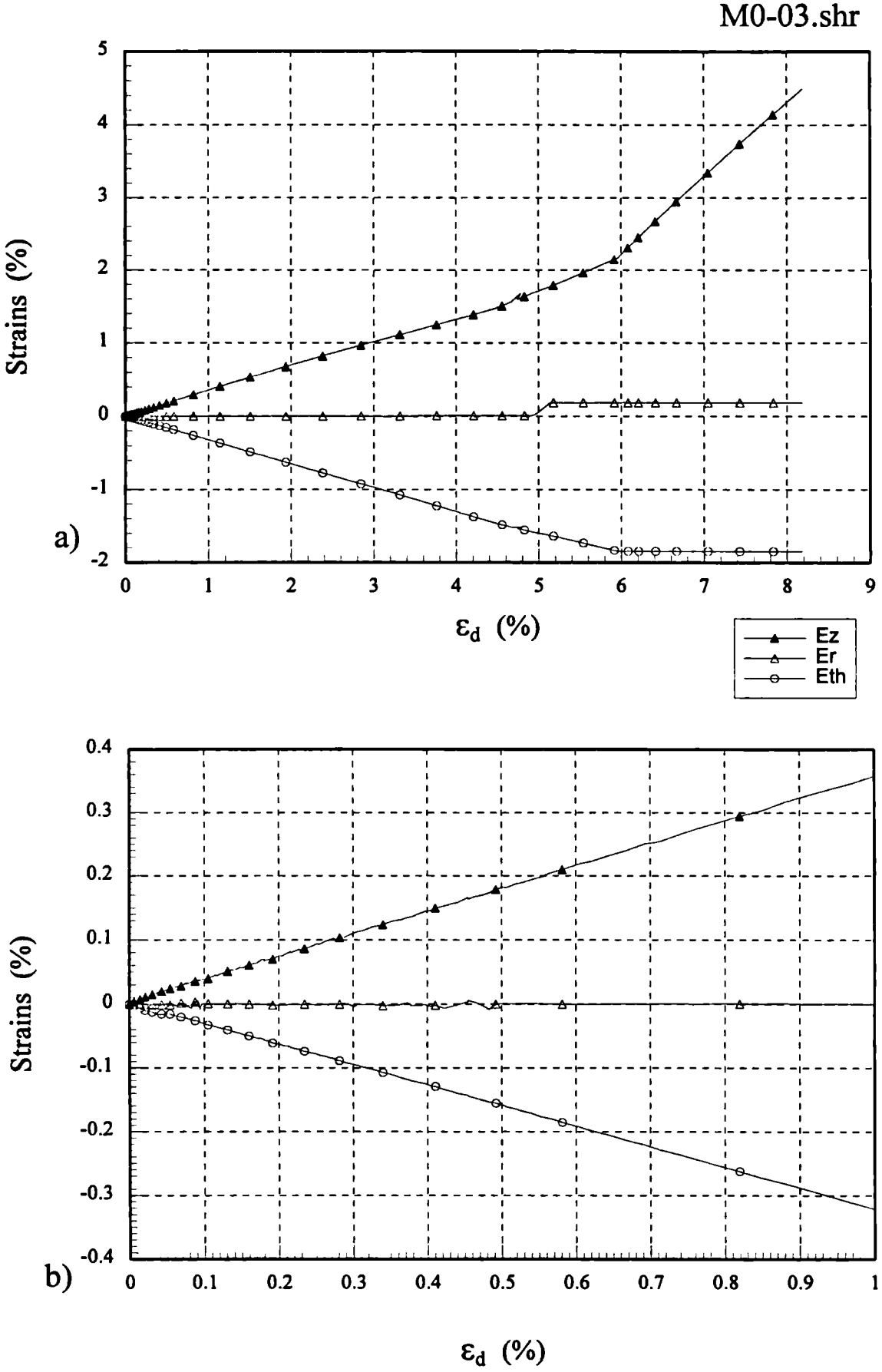


Fig.5.39 - a) Strain components for shearing with α=0 and b=0.3
b) Enlarged view into a small strain region

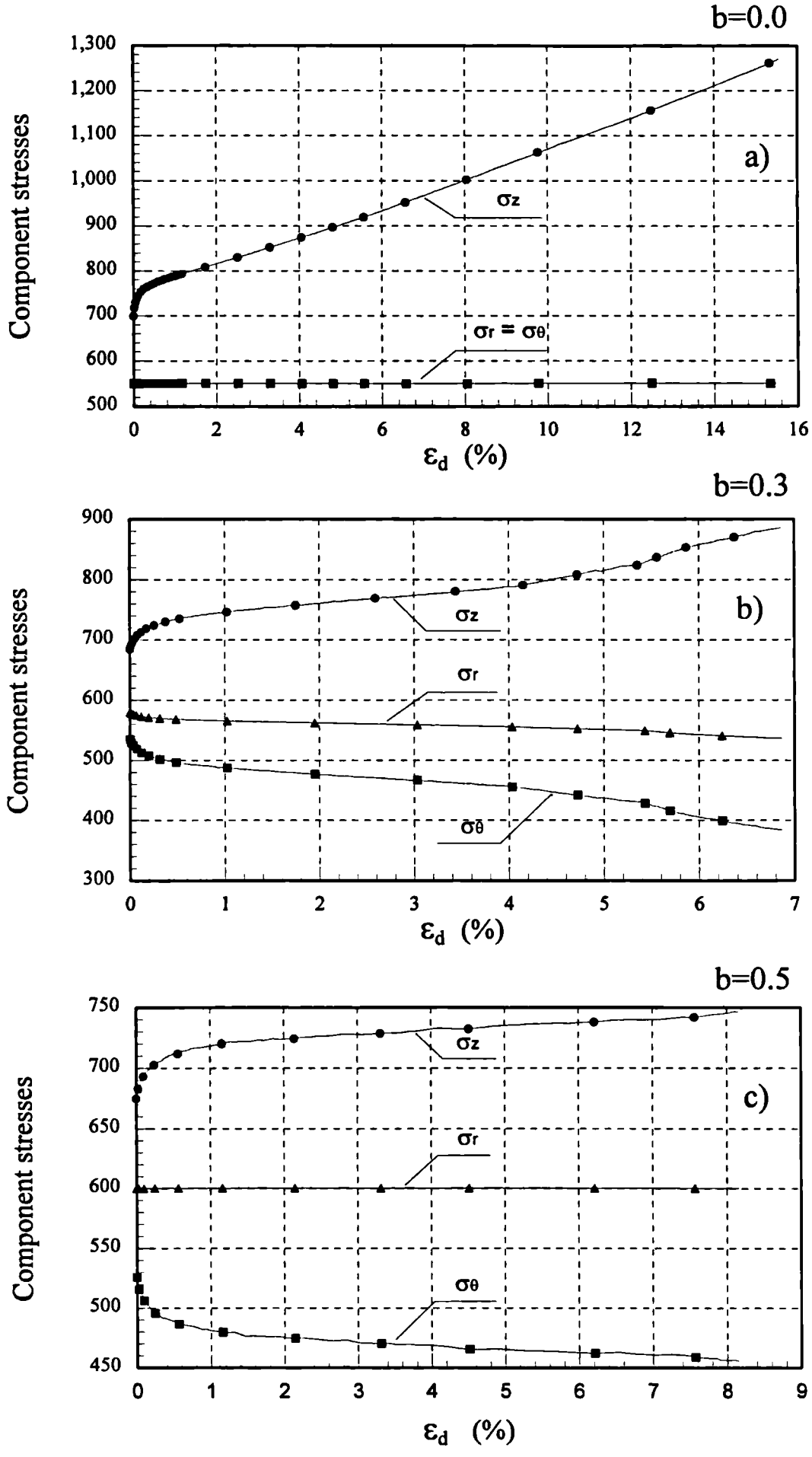


Fig.5.40 - Direct stress components developed for shearing with α=0 and different values of 'b'

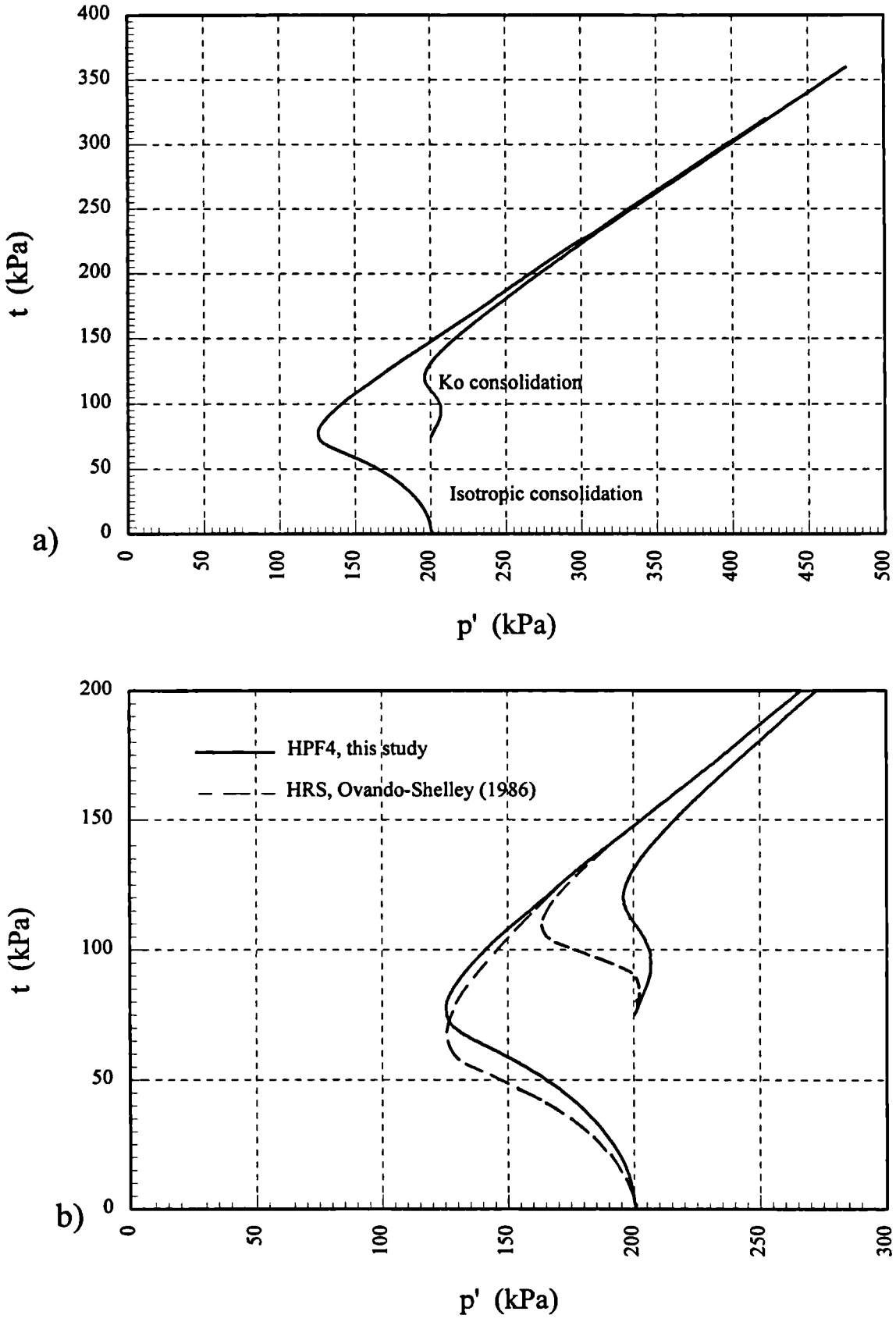
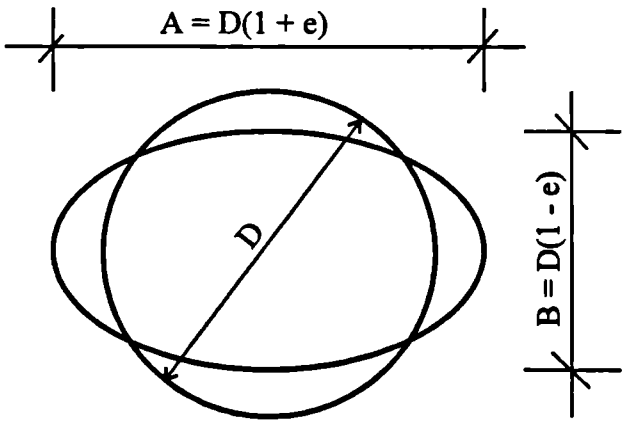


Fig.5.41 - a) Triaxial compression effective stress paths on isotropically and Ko consolidated HPF4
b) Comparison with the same set of stress paths on HRS



Transformation of circular into elliptical disk

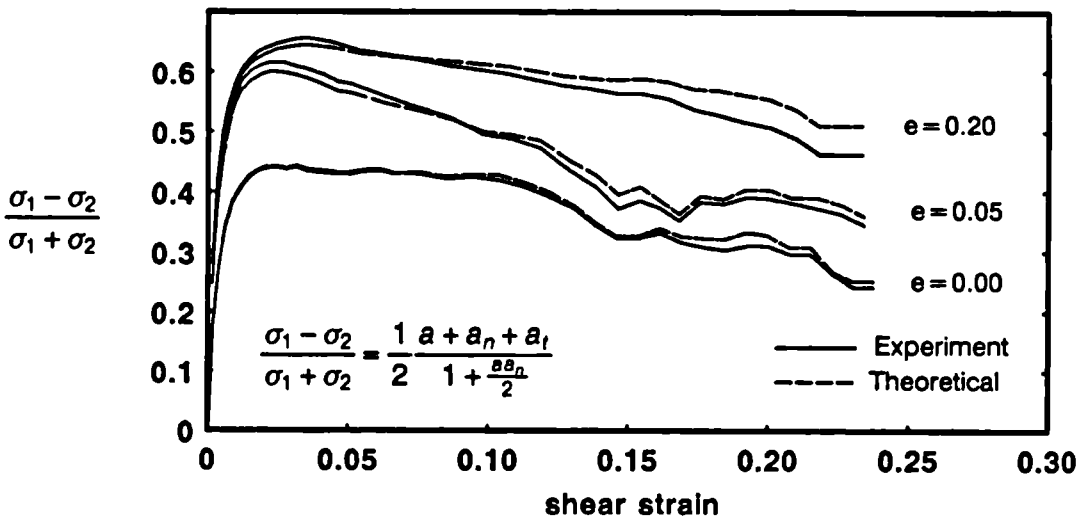


Fig.5.42 - Verification of stress-force-fabric relationship for plane assemblies of elliptical particles (Rothenberg & Bathurst, 1992)

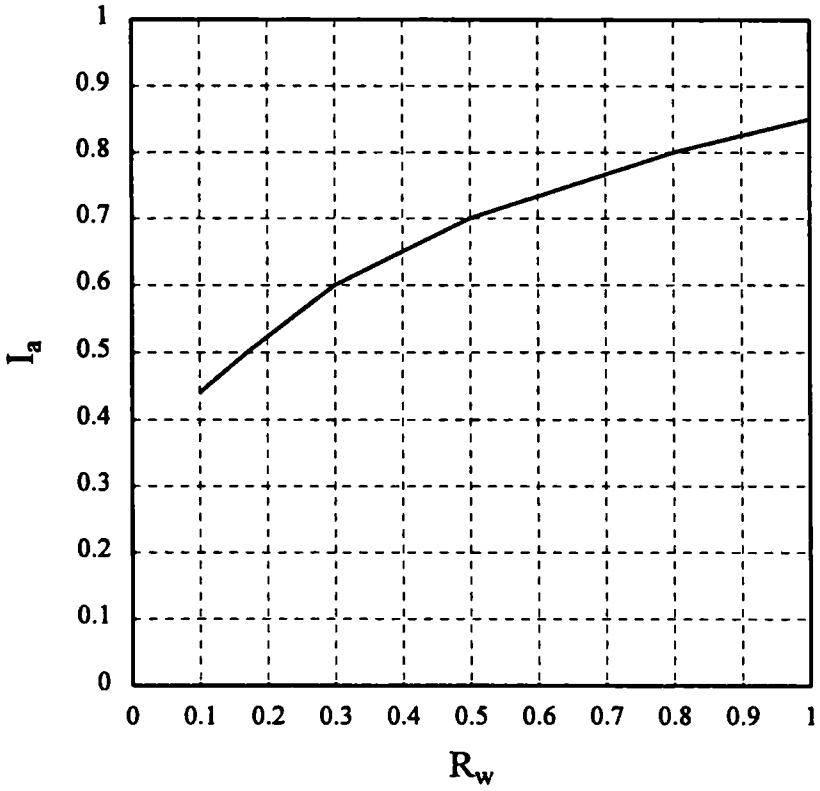


Fig.5.43 - Correspondence between roundness index, Rw, and asperity index, Ia, (after Frossard, 1979)

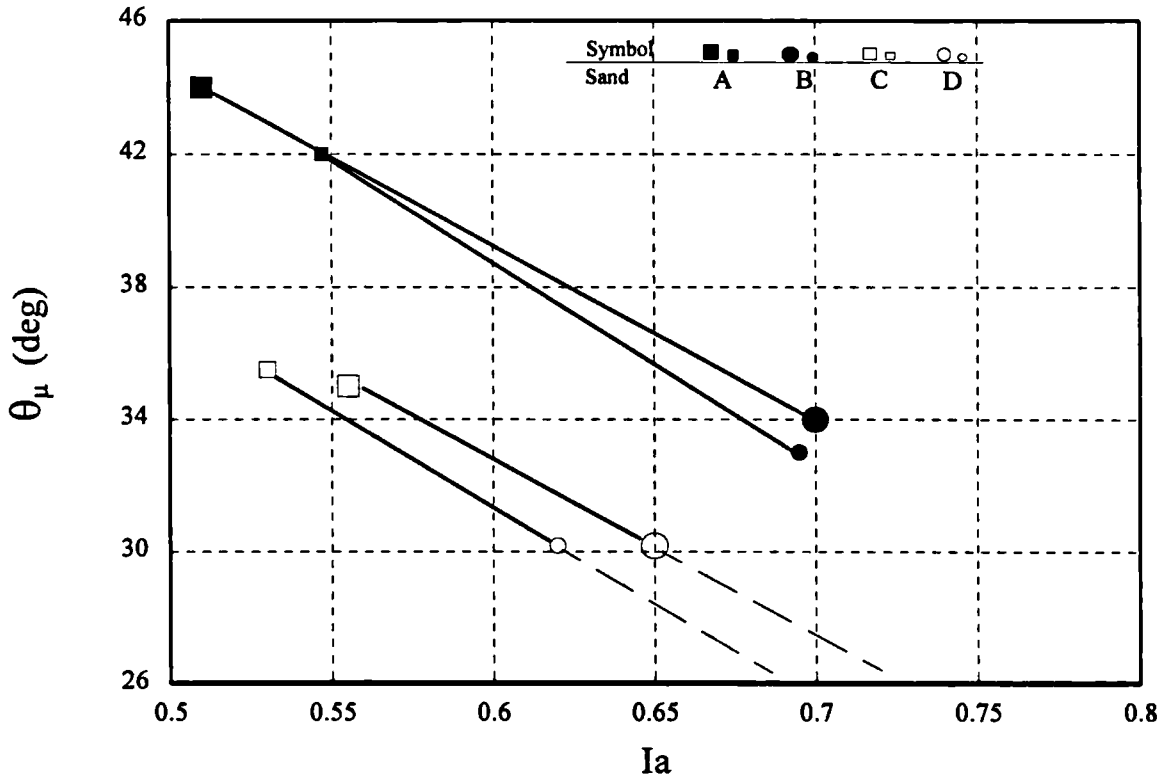
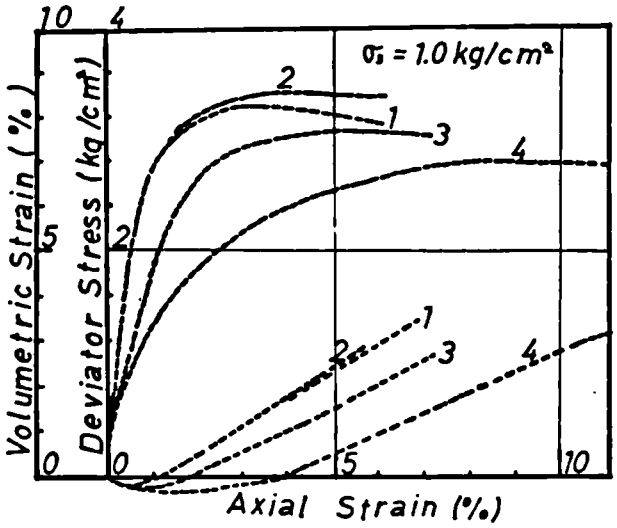
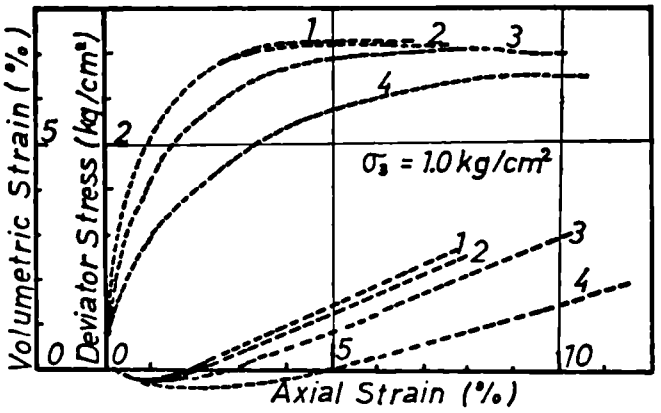


Fig.5.44 - Correspondence between interparticle friction and asperity index Ia (after Frossard, 1979)



(1) Sand B

Specimen	Initial Void Ratio	Angle φ°
(1)	0.722	90°
(2)	0.715	60°
(3)	0.718	30°
(4)	0.728	0°



(2) Sand D

Specimen	Initial void Ratio	Angle φ°
(1)	0.861	90°
(2)	0.854	60°
(3)	0.867	30°
(4)	0.860	0°

Fig.5.45 - Effect of particle shape on stress-strain behaviour of sand (Oda, 1972a)

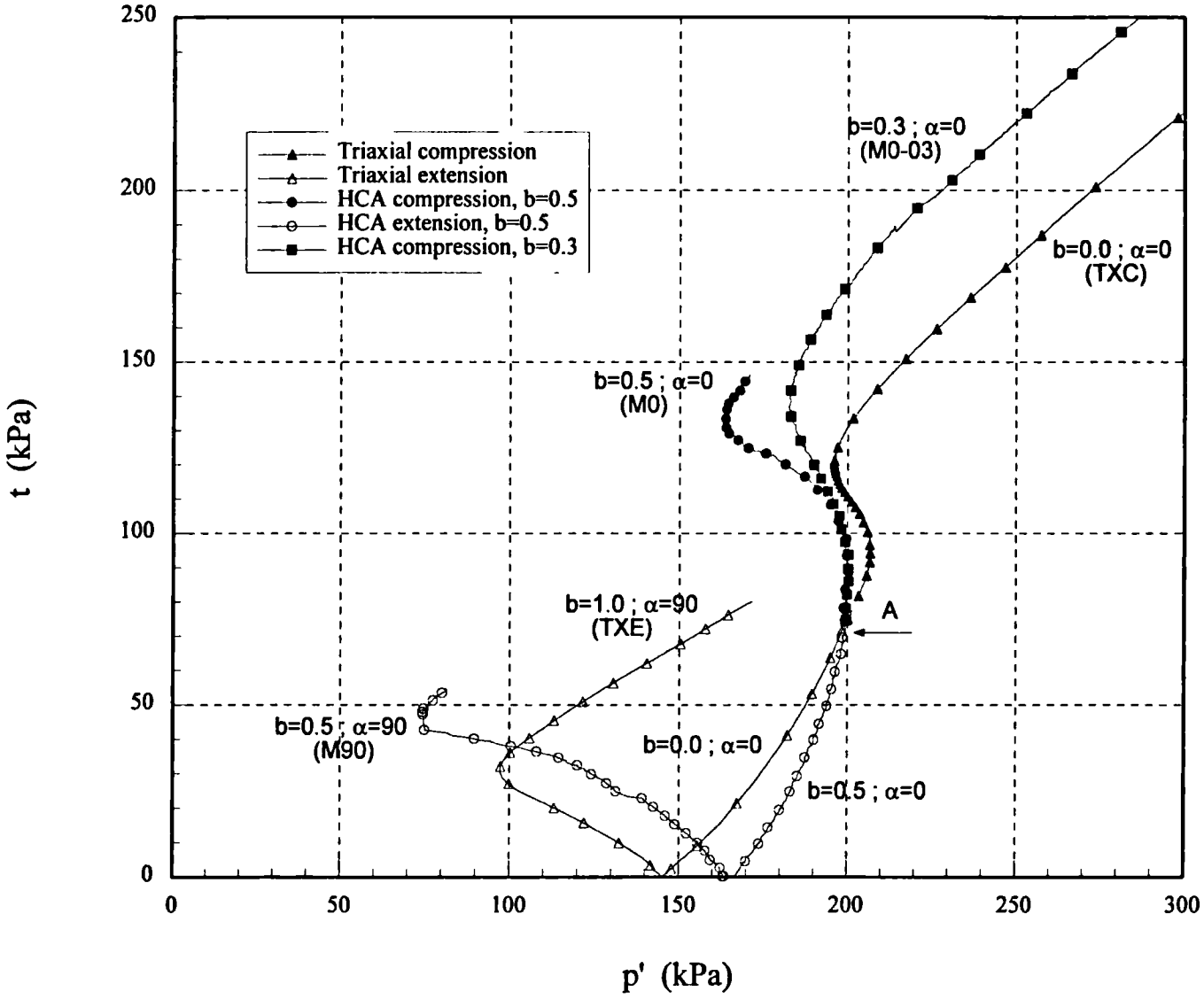


Fig.5.46 - Mobilised undrained strength for different combinations of b and α

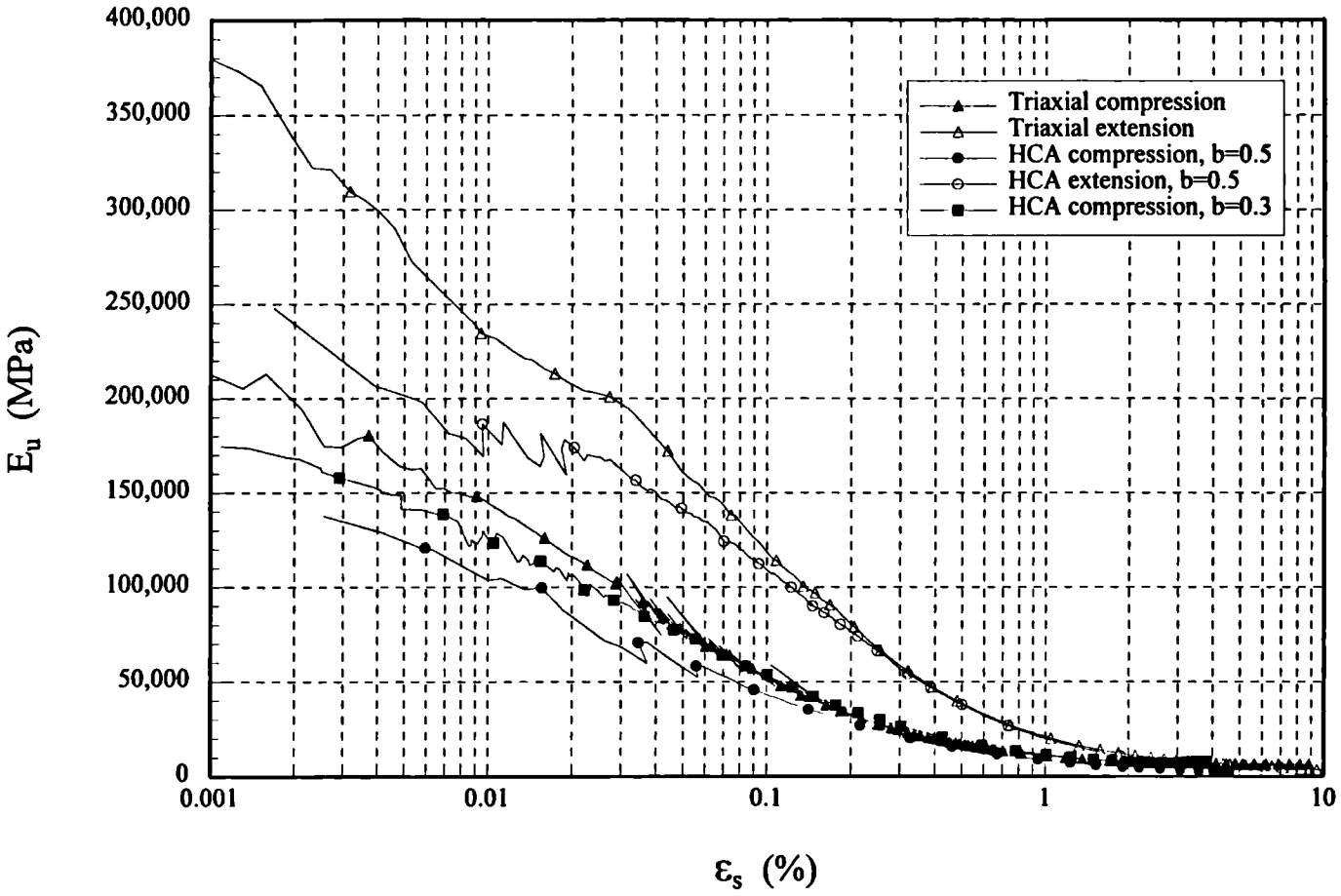


Fig.5.47 - Undrained Young modulus for different combinations of b and α

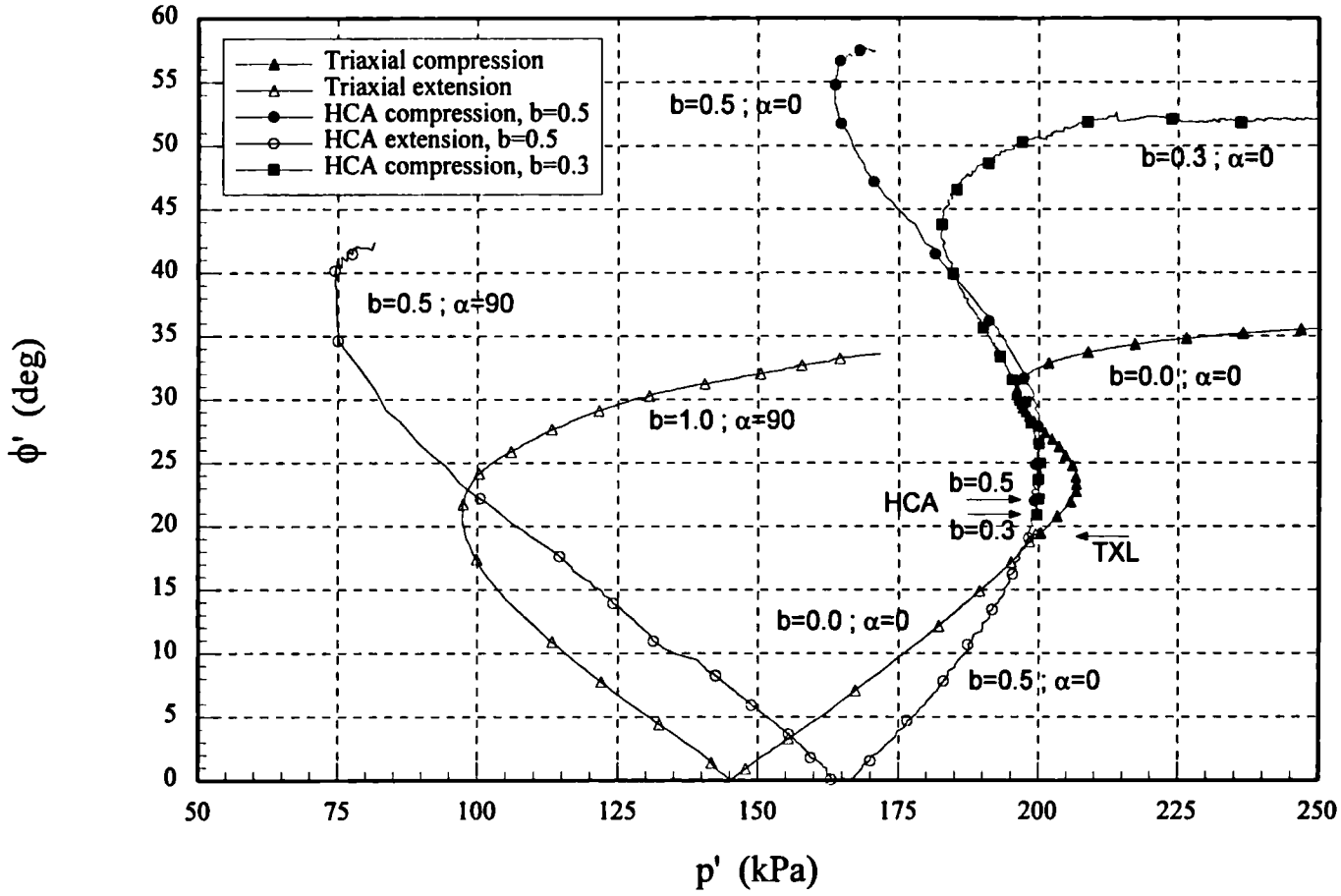


Fig.5.48 - Mobilized frictional resistance for differet combinations of b and α

Chapter 6

DIRECTIONAL STIFFNESS ANISOTROPY OF LIGHTLY OVERCONSOLIDATED HPF4 AT SMALL STRAINS

6.1. Introduction

The two Series of tests presented in this Chapter (called the Q-A and D Series) were designed principally to investigate the directional yielding and stiffness anisotropy of low OCR HPF4.

The stress paths applied in the tests are shown schematically in t-α space in Fig.6.1. The Q-A Series tests approximately simulate the response of soil elements in the field, initially under K_o conditions, which are loaded undrained towards plane-strain failure, following a range of stress paths that involve gradually changing α values.

Sharp changes in b do not generally occur in nature and it was decided to keep the incremental b value (Δb) constant and equal to 0.5, so that the differences in material response could be considered purely as a consequence of the inclination ($\Delta t/\Delta\alpha$) of the applied stress path. The total b value, of course, changed along the applied stress paths. All tests started from the same stable stress state at OCR=1.3.

The first part of this Chapter presents the Q-A tests and their interpretation follows the framework of Y_1, Y_2 and Y_3 yield surfaces postulated in Chapter 2. The conventional consideration of yield in a two-dimensional t-p' stress space is extended into a third, α, dimension. The small strain undrained stiffness is considered in terms of the stress-path inclination (i.e. $\Delta t/\Delta\alpha$). The stability of the bounding surface, determined in the M-Series tests, is examined further by considering the post-Y_3 behaviour of the Q-A-Series tests.

The Series D experiments involved drained tests designed to assess the HPF4 silt's basic anisotropic stiffness parameters. Data from the D-Series is presented in part 2 of this Chapter. It is subsequently used to make predictions for undrained behaviour which may be compared with HCA and triaxial test data.

6.2. Description of tests

All tests in Series Q-A and D were initially K_o consolidated to a mean effective stress of 200 kPa and then swelled back to a OCR=1.3. Such an initial stress state provided adequate space for the probing tests to be performed well inside the bounding surface estimated from the normally consolidated M-Series tests (Fig.6.1). A low OCR also ensures that the shrinkage of the initial bounding surface (which was shown to happen with increasing OCR in triaxial tests) is not too marked, and that the tests can be interpreted as being constrained initially by the normally consolidated (OCR=1.0) bounding surface.

The numerical part of the code used to identify each Q-A Series test signifies the particular $\Delta t/\Delta\alpha$ ratio followed. Thus Q-A33 stands for a loading test in which $\Delta t/\Delta\alpha$=3.33 kPa/degree, Q-A0 a test with $\Delta t/\Delta\alpha$=0 and Q-A33ext an unloading test in which $\Delta t/\Delta\alpha$=-3.33. Data from conventional undrained triaxial tests performed in the stress path cell (compression, where $\Delta t/\Delta\alpha=\infty$ and b=0.0; and extension, where $\Delta t/\Delta\alpha=-\infty$ and b=1.0) and a hollow cylinder test which involved undrained torsion, test G0 (where Δt has a nonlinear relationship with $\Delta\alpha$, and Δb=0.5), are also shown.

6.2.1. K_o consolidation and swelling

All samples were K_o consolidated to a mean effective stress of 200 kPa, under a back pressure of 400 kPa, in a similar manner to that of the M-Series tests. The same consolidation strain rate of 1.0 %/day was applied and the target stable strain rate at the end of the creep period was also 0.05 %/day. Results of the stress-strain behaviour during K_o consolidation, as measured in the HCA, were presented in Chapter 5.

For the swelling stage the K_o value was determined from the Mayne-Kulhawy formula (Chapter 4) to be 0.57 and the samples were swelled back to an OCR=1.3 (t=49 kPa and p'=166 kPa). Again, the same swelling and creep strain rates were applied as for the normal consolidation stage.

Fig.6.2 presents the variation of ε_{vol} and ε_r with ε_z during the swelling stage of Q-A Series tests. The ratio $\varepsilon_{vol}/\varepsilon_z$ is generally in the range 0.7 to 1.0, while the radial strain, ε_r, deviates from zero by only 0.01% towards the end of swelling. Typical strain-time curves are presented in Fig.6.3 for axial and volumetric strains, while the corresponding strain rates plotted

in Fig.6.4 show that both strains reach the target creep rate of 0.002 %/hour during the last 5 hours of the creep period. The curves are similar to those presented in Chapter 4 for the swelling stages of triaxial compression and extension tests performed in the stress path cell.

6.2.2. Shearing behaviour

A three-dimensional (*t-p'-α* space) composite plot of the undrained effective stress paths followed by the tests during undrained shearing is presented in Fig.6.5. All effective stress paths start from the common stress state associated with OCR=1.3. Projections of these stress paths onto the *t-p'* plane and the *t-α* plane are shown in Fig.6.6 and Fig.6.7 respectively.

A standard shearing strain rate of 5.0 %/day was applied for all stress paths. A summary plot of deviatoric stress, *t*, versus deviatoric strain, ε_d, for all tests is presented in Fig.6.8. The strains plotted are the changes that have occurred during undrained shearing from the OCR=1.3 stress point, i.e. from p'=166 kPa and t=49 kPa.

The following part of this Section describes the small strain yielding and stiffness characteristics and the large strain yielding and undrained strength characteristics developed along each of the probing stress paths.

Test Q-A33

a) Stress path

This test was performed with $\Delta t/\Delta\alpha$=3.33 kPa/degree and Δb=0.5. As expected from the M-Series tests, the gradual rotation of α during shearing led to a more contractant response than was observed in triaxial compression. Fig.6.6 shows the effective stress path in *t-p'* space where it can be noted that the initial effective stress path inclination, $\Delta t/\Delta p'$, is almost vertical. Figures 6.7 and 6.8 show the variations of *t* with α, and *t* with ε_d.

b) Stress-strain response

The variations of the individual strain components with deviatoric strain, ε_d, are presented in Fig.6.9a. The mode of deformation was one of continuous axial compression combined with torsional shearing. The enlarged small strain view (Fig.6.9b) shows that the initial radial strain, ε_r, which is also the intermediate principal strain, ε_2, is compressive and nearly equal to ε_z. As shearing progresses, the radial strain decreases towards zero and remains small

in comparison with the principal strains ε_1 and ε_3, indicating near plane strain conditions at Phase Transformation and beyond. This strain response is a consequence of the action of the componential stress changes, Fig.6.10. Increasing σ_z and decreasing σ_θ impose axial compression and circumferential extension. Torsional shear strain, $\gamma_{\theta z}$, is a direct consequence of the torsional shear stress, $\tau_{\theta z}$.

c) Yielding

The Y_3 yielding point is clearly identified from the p'-ε_d plot given in Fig.6.11a, b, as occurring when ε_d=0.1%. Before the Y_3 yield point the effective stress path is nearly vertical, whereas afterwards the stress path gradient $\Delta t/\Delta p'$ falls to a minimum of -0.9, before reaching the Phase Transformation Point at a deviatoric strain, ε_d, of ~2%.

The enlarged view of the small strain p'-ε_d response shown in Fig.6.11a indicates that at ε_d=0.02% a slight change occurs in the $\Delta p'$-ε_d gradient. This feature is tentatively associated with the Y_2 yield point.

The Y_2 and Y_3 yield points, expressed above in terms of generated strains, can also be expressed in terms of the angle of principal stress rotation. The Y_2 yield point corresponds to α=2.5°, while α=8° when the Y_3 yield point is engaged and α=17° at the PTP, (Fig.6.12).

The existence of Y_2 yielding can also be inferred from the plots of stress, stress increment and strain increment directions (Fig.6.13). At the beginning of shearing, it can be seen that α_σ and α_ε coincide up to approximately 0.01% deviatoric strain, indicating a region where the directions of the major principal strain increments are coincident with those of the stress increments. Beyond this point, α_ε remains practically constant (~10°), while α_σ increases continuously. Only after reaching the PTP (ε_d~2.0%) does α_ε start to fall towards the α_σ direction.

Another way to assess the yielding of soil is to consider the external work required to change its state (Graham et al., 1983; Burland & Georgiannou, 1991; Smith, 1992; Smith et al., 1992). The energy required to bring a sample to a certain stress level is the area underneath the stress-strain curve:

$$W = \int (\sigma_1 d\varepsilon_1 + \sigma_2 d\varepsilon_2 + \sigma_3 d\varepsilon_3) \qquad (6.1)$$

The expression is integrated between the limits of the initial in-situ stress point (σ_{1o}, σ_{2o}, σ_{3o}) existing at OCR=1.3 and the current stress state (σ_1, σ_2, σ_3). The change in work, W, is plotted

against mean effective stress, p', in Fig.6.14a, b. The ΔW-p' curve indicates changes in gradient near to the Y_2, Y_3 and PTP points, established earlier from the stress-strain curves. Energy changes of 0.06 kJ/m^3, 2.0 kJ/m^3 and 60 kJ/m^3 are required to achieve Y_2, Y_3 and PTP yielding respectively. The energy defining the limit of the linear range (Y_1 yielding) appears to be smaller than 1.0 J/m^3.

d) Change in b

The development of b throughout the test, in relation to p' and ϕ', is considered in Fig.6.15. Towards the end of shearing, when near plane strain conditions are established, b tends towards 0.3. At the same time, the mobilized ϕ' value is stable at 45°, with $\alpha \approx 25°$. At the Phase Transformation Point (PTP) b reached a value of 0.26 and the mobilized ϕ' value was 41°, with α=17°. The progression of b with change in the principal stress inclination, α, is presented in Fig.6.16.

Test G0

a) Stress path

The torsional shear test G0 was performed such that all three components of direct stress, σ_z, σ_r and σ_θ, were kept constant, while applying a torsional shear stress, $\tau_{\theta z}$. The variations of the component stresses with deviatoric strain are presented in Fig.6.17. As a result of these applied stress changes the stress path in t-α space, Fig.6.7, is curved. Initially the incremental inclination, $\Delta t/\Delta\alpha$, is horizontal, becoming nearly vertical at the end of the test. The projection of the stress path in the t-p' plane, Fig.6.6, shows that the sample underwent Y_3 yielding at an early stage, with the stress path turning sharply to the left after a short initially vertical portion, and achieving a minimum gradient $\Delta t/\Delta p'$ of ~-0.55 before the Phase Transformation Point was reached.

b) Strains

In ideal elasticity, the application of pure torsion, with all direct stress components kept constant, should generate only a shear strain, $\gamma_{\theta z}$. In test *G0* this condition was only met at the beginning of shearing, prior to Y_2 yielding (see Fig.6.18b). Further shearing led to a structural collapse, with axial compression and circumferential extension of the sample, while the intermediate principal strain, $\varepsilon_2=\varepsilon_r$, remained close to zero, indicating plane strain conditions.

c) Yielding

The Y_2 and Y_3 yielding boundaries are estimated firstly from the p'-ε_d plot given in Fig.6.19. This gives ε_d=0.02 % and ε_d=0.1 % at the Y_2 and Y_3 boundaries respectively. At these boundaries the directions of the major principal stress are α=8.5° and α=19° (Fig.6.20). Phase transformation occurs at ε_d=2.0%, with α=27°.

The stress, stress increment and strain increment data plotted in Fig.6.21 indicate a slightly higher strain level for the Y_2 boundary (ε_d~0.03 %). The directions of the major principal stress increment, α_σ, and strain increment, α_ε are both 45° up to ε_d=0.03 %. The value of α_ε then falls as the sample undergoes compression (see Chapter 5) becoming coincident with α_σ at ε_d≈0.6%.

From the energy plots shown in Fig.6.22, it is estimated that changes in work, ΔW, of 0.05 kJ/m^3, 0.7 kJ/m^3 and 40 kJ/m^3 are necessary to reach the Y_2, Y_3 and PTP boundaries, respectively.

d) b-change

Failure develops under near plane strain conditions, with b approaching 0.3 (Fig.6.23). The mobilized ϕ' value reaches 44° with α=32° at the end of the test, while it is 39° at the Phase Transformation Point where b=0.21 and α=27° (Fig.6.24).

<u>Test Q-A0</u>

a) Stress path

Test Q-A0 was controlled so that $\tau_{\theta z}$ and $(\sigma_z$-$\sigma_\theta)$ rose and fell in such a way that Δt remained zero (Fig.6.25). The sample responded by straining in a continuous, but not monotonic manner and sustained 135° total rotation of the direction of the major principal stress, before its inner wall came into contact with the inner set of proximity transducers and the test was terminated. The effective stress path involved an initial increase of p' of ~3.0 kPa, followed by a continuous reduction at constant t (Fig.6.6).

b) Strains

The variation of the component strains with deviatoric strain are presented in Fig.6.26a-d. This sequence of plots shows how the sample's deformational mode changes throughout shearing. During the α_rotation stage from 0° to 45°, (with $\tau_{\theta z}$ being positive clockwise), the sample compresses axially and extends radially as it twists (Fig.6.26a, b). However, the ε_z

increments start to become tensile after α=35° is reached (i.e. ε_d=0.2 %), Fig.6.26c. As rotation continues to α=90° (ε_d=3.0 %), the sample undergoes continuous axial extension (Fig.6.26d), while the torsional shear strain, $\gamma_{\theta z}$, tends to reverse once α>65°. At α=90°, σ_θ becomes σ_1 and $\sigma_z=\sigma_3$, Fig.6.25a. After this point the sign of both $\tau_{\theta z}$ and $\gamma_{\theta z}$ changes (to counter clockwise, Fig.6.26d). The sample continues to extend vertically for some time after α=90° is reached, because of the lag in the sample's response, and increments of vertical strain only become compressive at ε_d=5.0 %.

The mobilized ϕ' was still increasing monotonically (Fig.6.27) when the test was halted prematurely, before failure was reached. At the end of the test the mobilised ϕ' was 34°, and the strain component plots show that the conditions were far from those of plane strain.

c) Yielding

The stress-strain and strain component plots shown in Figs.6.28a and 6.26 suggest that the Y_2 boundary is engaged at a deviatoric strain of ~0.015 %. The sharp change in the gradient of the stress-strain curve at ε_d=0.07 % locates the Y_3 boundary. No phase transformation point was reached (i.e. p' reduced continuously). In terms of principal stress rotation, α, the Y_2 and Y_3 boundaries occur when α=7° and α=18° respectively (Fig.6.29).

The plots of major principal stress, stress increment and strain increment directions in Fig.6.30 again show initial coincidence of the principal stress increment and strain increment directions until ε_d=0.015%, after which $\alpha_\sigma > \alpha_\varepsilon$. It should be noted that α_i values greater than 90° are plotted as α_i-90° in Fig.6.30. Once α exceeds 90°, α_σ and α_ε coincide, i.e. from about 3.0% deviatoric strain.

The changes in work associated with the Y_2 and Y_3 yield boundaries are estimated as 0.04 kJ/m^3 and 0.6 kJ/m^3, respectively.

Test Q-A33ext

a) Stress path

This stress path (in t-α space) is a mirror image of that for test Q-A33, as it was performed with a $\Delta t/\Delta\alpha$ inclination of -3.33 (Fig.6.7). The sequence of stress changes is followed in Fig.6.31.

The projection of the effective stress path onto the p'-t plane (Fig.6.6) shows that the unloading part of the stress path is almost coincident with the unloading part of the undrained triaxial extension test. The stress-strain plots in Fig.6.8 also show that the unloading stress-strain paths for the two tests are similar, and that very little deviatoric strain (ε_d~0.2%) is generated. This coincidence of the two paths in unloading indicates that the initial overconsolidated volumetric behaviour in unloading is not strongly dependent on α. On further loading the stress path in test Q-A33ext is much steeper and only small deviatoric strains, or changes in p', are developed until a sharp counter clockwise rotation of the stress path occurs at the level of t=49 kPa (which is the value of t at which the test started).

The requirement to keep the incremental b value constant, together with an unloading stress condition, caused the total b value to change gradually from 0.0 to 1.0 in unloading from point A to B and move back from 1.0 to 0.0 during loading from B to C (Fig.6.38a). From point C, the total b changes again from zero to develop a certain value at the end of the test. Only the first part of the whole stress path will be considered (A-B) when assessing the initial response of HPF4, while the failure response will be considered referring only to portion C-D.

b) Strains

The initial unloading path (A-B) develops only about 0.2% deviatoric strain and the strain components indicate an extension mode of deformation (Fig.6.32a). During subsequent loading from B to C the change in deviatoric strain is small (Fig.6.33) and the axial strain changes sign so that part C-D of the stress path is initially in axial compression (Fig.6.32b). The increments of axial strain become tensile once again towards the end of the test, after a principal stress rotation of α=45°. The radial strain, ε_r (=ε_2), becomes close to zero towards the end of the test, indicating plane strain conditions (Fig.6.32b).

c) Yielding

The Y_2, Y_3 and PTP boundaries appear to occur at deviatoric strains of ε_d≈0.02 % (α=2.5°), ε_d≈0.08 % (α=7.5°) and ε_d≈1.2 % (α=37°), respectively (Figs.6.34 and 6.35). Work changes of 0.05 kJ/m^3, 0.6 kJ/m^3 and 15 kJ/m^3 are necessary to reach the Y_2, Y_3 and PTP yield points (Fig.6.36).

Plots of the major principal stress, stress increment and strain increment directions for the whole stress path are presented in Fig.6.33. This shows that α changes by 15° during unloading from A to B (i.e. to ε_d≈0.2%). Subsequent loading from B to C generated a further

15° of principal stress rotation, with practically no change in deviatoric strain. Values of α_σ and α_ε start to coincide after $\varepsilon_d \approx 2.0$ %.

d) b_change

The change of *b* is presented only for the C-D part of the stress path (Fig.6.37). The value of *b* tends towards 0.3 at the end of the test, having mobilised ϕ' of 43°. At the Phase Transformation Point, b=0.17, with ϕ'=35° and α=37° (Fig.6.38).

The strains, work, amount of principal stress rotation and level of deviatoric stress, at yield points Y_2 and Y_3 and the PTP are summarized in Table 6.1.

Table 6.1: Y_2 and Y_3 yielding in terms of strain, work and principal stress rotation

TEST	Δv/Δ α	ε_d (%)			Work (kJ/m³)			t (kPa)			α (deg)		
		Y_2	Y_3	PTP	Y_2	Y_3	PTP	Y_2	Y_3	PTP	Y_2	Y_3	PTP
TXC	+ ∞	0.020	0.2	0.6	0.1	5	70	62	90	110	0	0	0
Q-A33	+ 3.33	0.020	0.1	2.0	0.06	2	60	58	78	108	2.5	8	17
Q-A0	0	0.015	0.07	/	0.04	0.6	/	49.5	49.5	/	7	18	/
G0	0	0.020	0.10	2.0	0.05	0.7	40	52	64	89	8.5	19	27
QA33e	- 3.33	0.020	0.08	1.2	0.05	0.6	15	42	27	78	2 5	7.5	37
TXE	- ∞	0.01	0.07	1.0	0.02	0.7	150	45	25	30	0	0	90

6.3. Discussion of the results

The tests described in the previous Section were aimed to give an insight into the directional undrained yield and stiffness anisotropy of HPF4, when loaded in different directions from a common stress point. The tests were performed with different $\Delta t/\Delta\alpha$ inclinations and, as the incremental *b* was kept constant and equal 0.5, the anisotropy of different parameters will be quantified in terms of different stress path inclinations.

6.3.1. Undrained yield

Three-dimensional plots of the developed effective stress paths in t-p'-α space are shown in Fig.6.39a-d for all tests of the Q-A_Series. These plots differ in that the t-p'-α space is viewed from four different perspectives to show better the 'depth' of the yield surfaces in the α dimension. Also presented are the undrained triaxial compression and extension stress paths obtained from tests performed in the stress path cell. The locations of the Y_2 and Y_3 yield boundaries for each test have been estimated from the stress-strain and stress-energy diagrams, as described in the previous Section, and summarized in Table 6.1. These are marked on Fig.6.39 and have tentatively been joined to form surfaces in t-p'-α space. The projection of these surfaces on to the t-p' and t-α planes are shown in Fig.6.40 and Fig.6.41, respectively.

The values of the deviatoric strain, ε_d, at the Y_2 boundary all seem to fall between 0.01% and 0.02 %. When plotted on the t-p' plane (Fig.6.40a), the Y_2 surface contour is irregular and elongated in the t direction, as it is associated with small or no change in p'. The projection on the t-α plane, (Fig.6.41a), shows that the Y_2 boundary involves a spread of α values. Tests with $\Delta t/\Delta\alpha$ inclinations close to the vertical (i.e. 3.33, -3.33) engage only up to 2.5° principal stress rotation before reaching the Y_2 boundary, while the rotation increases to 8.5° when the stress path decreases in inclination and becomes initially more horizontal (which is the case in both the Q-A0 and G0 tests). Similar behaviour is observed for the Y_3 boundary which is elongated in the deviatoric stress direction in the t-p' plane, but covers a wide range of α values, as the initial inclination of stress path, $\Delta t/\Delta\alpha$, becomes closer to zero.

Burland & Georgiannou (1991) proposed that the Y_2 boundary was a contour of constant work. If an average value of 0.05 kJ/m^3, from data in Table 6.1, is adopted, then the alternative surface shown in Fig.6.40b and Fig.6.41b is obtained. This surface is very similar to that obtained using the observed experimental values, although its t-dimension is slightly reduced and

its α-dimension slightly increased. Instead of defining the Y_2 boundary as a contour of constant work, Jardine (1985) assumed that it is a contour of constant major principal strain. From presented experimental data it is adopted that octahedral shear strain, ε_d, determines the Y_2 boundary and it is seen that it varies from 0.01% to 0.02%. However, in four of the tests ε_d=0.02% and if this constant value is adopted to define the Y_2 boundary, then the surface so obtained agrees quite well with that observed. From the presented data both approaches provide a reasonable fit to the data.

6.3.2. Undrained stiffness

The influence of the stress path inclination ($\Delta t/\Delta\alpha$) on the shape and size (specially the α-dimension) of the yield boundaries, reflects the stiffness behaviour of HPF4 at small strains. Fig.6.42a presents the variation of secant octahedral shear stiffness, G, with the change in deviatoric strain, ε_d, from the beginning of shearing, for the Q-A test series, while Fig.6.42b presents the same data but with the shear stiffness, G, normalised by the current mean effective stress, *p'*. Plot 6.43 shows the change in normalised stiffness G/p' with the $\Delta t/\Delta\alpha$ inclination, for different strain levels. It is clear that both the G0 and Q-A0 tests experienced significantly higher stiffness at small strain levels ($0.001\%<\varepsilon_d<0.01\%$) than the other tests, while this difference diminished at higher strain levels. It should be noted that the inclination ($\Delta t/\Delta\alpha$) of the G0 stress path changes during the test. The results from the triaxial compression, TXC, and extension, TXE, tests are not strictly comparable to the others, as these tests did not have $\Delta b=0.5$.

Ignoring the results from the triaxial tests it can be concluded that the small strain stiffness decreases as the gradient of the stress path in *t*-α space rotates from 0 kPa/degree (i.e. horizontal) to ±∞ kPa/degree (i.e. vertical). This can also be seen from Fig.6.44 which shows the variation of ΔJ with α. At the Y_2 boundary the α value for tests G0 and Q-A0 was approximately 8.5°, whereas for tests Q-A33 and Q-A33ext it was 2.5°. The corresponding values of ΔJ are ~15 kPa and ~8 kPa respectively. As the deviatoric strain at this boundary is ~0.02% for all tests, then clearly the secant stiffness G ($=\Delta J/\varepsilon_d$) will be greater in the tests with the larger value of α as these have the greater ΔJ. This trend is a direct result of the strain cross coupling that occurs with steeper $\Delta t/\Delta\alpha$ inclinations. Plots of the componential strains for tests G0 and Q-A0 (Fig.6.18b, 6.26a) have already shown that the initial deformation for these samples was one of torsional shear, $\gamma_{\theta z}$, while for samples Q-A33 and Q-A33ext all direct strain components (ε_z, ε_r, ε_θ) developed from the beginning of the test. The stiffness of samples Q-A33 and Q-A33ext can be resolved into components $G_{\Delta\sigma}$ and $G_{\theta z}$ (Eq.5.4, 5.5). The variation of these

components with deviatoric strain for these two tests are presented in Figs.6.45 and 6.46. It can be seen that $G_{\theta z}$ has the greatest magnitude being twice the value of $G_{\Delta\sigma}$, which itself is approximately equal to G ($=\Delta J/\varepsilon_d$).

The distribution of the torsional shear moduli, $G_{\theta z}=G_{VH}$, for different stress path inclinations is presented in Fig.6.47. Although there is some scatter in the results at a strain level of ε_d=0.001%, it can be concluded that the initial value of $G_{\theta z}$ is approximately the same for all stress paths. With further shearing in the small strain region, the stiffness curves begin to deviate, as cross-coupling terms affect the distribution of $G_{\theta z}$, with a maximum difference of 20% between the $G_{\theta z}$ from tests Q-A0 (maximum value) and Q-A33ext (minimum value).

6.3.3. Undrained failure

The projection of the effective stress paths in the *t-p'* plane, given in Fig.6.6, shows that a gradual decrease of the $\Delta t/\Delta\alpha$ inclination leads to more contractant behaviour. No clear peak was observed in *t* as the samples failed (as in the M-Series tests, Chapter 5). For convenience, the behaviour will again be compared at the Phase Transformation Points. As test Q-A0 did not exhibit Phase Transformation, only tests Q-A33, Q-A33ext and G0 will be considered in detail in this section. The aim is to check the post Y_3 behaviour from these tests against the Bounding Surface determined in the M-Series tests (for b=0.5, OCR=1.0).

Two plots, Fig.6.48 and Fig.6.49, are provided to show the progression of principal stress rotation, α, during the tests. Fig.6.48 presents the variation of *b* with *p'* for each test. Values of the direction of the major principal stress, α, at various stages of the tests are marked at the appropriate positions on these curves. It may be noted that horizontal stress paths (i.e. those with $\Delta t/\Delta\alpha$ close to zero) engage substantially higher principal stress rotations for the same level of *b*. For test Q-A33ext only the latter C-D portion of the stress path is presented. Prior to point C this test has undergone a change in α of 29° and *b* has varied from 0 to 1 and back to 0 again. In Fig.6.48, the α values in brackets denote the actual inclination of the major principal stress in Q-A33ext, while the second column of values denotes the change in major principal stress inclination from point C, when *b* starts to change again from zero. This same α-notation is used in Fig.6.49 in which the results are plotted in *t-p'* space. The following two observations are made concerning these plots:

A) The strain plots for each test discussed in Section 6.2 showed that during shearing, the mode

of deformation gradually changed from one of triaxial conditions to that of plane strain as the tests progressed. At the end of the tests the radial strain, ε_r, (also the intermediate principal strain), became close to zero. Fig.6.48 shows that the *b*-value reached at the end of tests was between 0.28 and 0.31. The maximum principal stress rotations, α, achieved at this stage were between 22° and 25°, with a mobilized angle of shearing resistance, ϕ', of between 43° and 45°.

This average failure data is compared to the failure envelope determined from the M test Series (Chapter 5), in Fig.6.50. In Chapter 5 it was shown that the M-Series tests conducted with b=0.5 did not achieve plane strain conditions when sheared with α between 0° and approximately 20°. It was also shown that the condition of b=0.3 for α=0° is a closer approximation to plane strain failure and consequently the plane strain envelope was estimated as the dotted line from α=0° to α=30°, Fig.6.50. The average condition at the end of the current series of tests (with values ϕ_{av}' = 43°, b_{av}= 0.29, α_{av}= 23° as summarized above) is plotted on Fig.6.50 as a single point and it can be seen that it agrees with the estimated plane strain envelope obtained from the M-Series tests. It can therefore be concluded that the plane strain failure of HPF4, while undergoing undrained shearing with a major principal stress inclination $0° \leq \alpha < 30°$ involves $b \approx 0.3$, while for $30° \leq \alpha \leq 90°$ a *b*-value of 0.5 is more appropriate.

B) Phase Transformation for each test was reached at different *b* and α values (Fig.6.48 and 6.49). The values of the deviator stress at the PTP are plotted against the corresponding value of α and compared to the b=0.5 envelope for PTP values obtained from the M-Series tests in Fig.6.51. It should be noted that the b=0.5 envelope was derived from tests on normally consolidated HPF4, while the present data is from samples sheared from an OCR=1.3. Also, the present tests did not involve constant α shearing (as was the case for the M-Series tests), but α was continuously changing from the beginning of the stress path to the PTP. From this figure it can be inferred that for α values between 15° to 45°, the mobilized strength at the PTP is insensitive to the value of *b*.

However, *b* does have a significant influence on the mobilised angle of shearing resistance, ϕ'. If the Phase Transformation values of ϕ' from the Q-A series are added to the envelopes established in Fig.6.50 (see Fig.6.52), it is seen that ϕ' decreases as *b* decreases. Some tentative ϕ' envelopes are drawn on Fig.6.52 for *b* changing from 0.5 to 0.0.

6.4. Anisotropic stiffness parameters of HPF4

6.4.1. Introduction

The Q-A and M test series described earlier have demonstrated several features of the undrained behaviour of HPF4. In particular they have shown non-linearity in stress-strain behaviour, strain coupling when principal stress rotation is involved, the existence of Y_2, Y_3 and PTP yield boundaries, small strain stiffness anisotropy, and large strain strength anisotropy. It is now of interest to investigate whether HPF4, with its depositional history, exhibits the pattern of behaviour associated with transversely isotropic materials, as described in Chapter 2. Some additional tests have been performed in the HCA, to determine, if possible, the basic anisotropic parameters of HPF4. The results of these tests are used to provide answers to the following two questions: a) can the undrained triaxial stiffness parameters be predicted at small strains, using measured drained parameters; b) can the initial directions of the undrained effective stress paths be predicted from the measured drained anisotropic parameters.

6.4.2. Tests to determine the anisotropic stiffness parameters

The preparation and consolidation procedures for K_o consolidated Hollow Cylinder (HC) HPF4 samples, which involve one-dimensional compression after vertical deposition of particles through water (Chapter 3), forms a structure with horizontal bedding planes, similar to that formed by natural deposition over a flat sediment basin. The Hollow Cylinder Apparatus has the advantage, compared to conventional triaxial equipment, of being able to control independently four stress components, so that identical samples, experiencing the same initial stress conditions, can be loaded directly in either of two independent horizontal directions, or in vertical or torsional modes. Series D tests (D0, E0 and G0) were performed in the HCA, the results from which are sufficient to determine the five basic effective stress parameters of a transversely isotropic elastic porous material.

The compliance matrix for such a material is presented in Eq.6.2 (see Appendix VI) where z is the depositional (vertical) direction and r and θ are horizontal directions (Fig.6.53a). For an ideal transversely isotropic elastic material, $\nu_{\theta z}'=\nu_{rz}'=\nu_{HV}'$; $\nu_{\theta r}'=\nu_{r\theta}'=\nu_{HH}'$; $\nu_{zr}'=\nu_{z\theta}'=\nu_{VH}'$; $E_z'=E_V'$; $E_\theta'=E_r'=E_H'$; and $G_{\theta z}=G_{HV}$. Tests D0, E0 and G0 provide direct evidence as to whether the very small strain behaviour of HPF4 can be described by the above model.

$$\begin{bmatrix} \varepsilon_z \\ \varepsilon_r \\ \varepsilon_\theta \\ \gamma_{\theta z} \end{bmatrix} = \begin{bmatrix} \frac{1}{E_z'} & -\frac{\nu_{rz}'}{E_r'} & -\frac{\nu_{\theta z}'}{E_\theta'} & 0 \\ -\frac{\nu_{zr}'}{E_z'} & \frac{1}{E_r'} & -\frac{\nu_{\theta r}'}{E_\theta'} & 0 \\ -\frac{\nu_{z\theta}'}{E_z'} & -\frac{\nu_{r\theta}'}{E_r'} & \frac{1}{E_\theta'} & 0 \\ 0 & 0 & 0 & \frac{1}{G_{\theta z}'} \end{bmatrix} \begin{bmatrix} \Delta\sigma_z' \\ \Delta\sigma_r' \\ \Delta\sigma_\theta' \\ \Delta\tau_{\theta z} \end{bmatrix} \qquad (6.2)$$

In the presentation of the results that follow, drained stiffness parameters E_z', E_r', ν_{zr}', ν_{rz}' and $\nu_{r\theta}'$ are plotted versus shear strain, ε_s, as opposed to deviatoric strain, ε_d. This is done so that undrained stiffness parameters, E_u, from undrained triaxial tests (Chapter 4), which are calculated as $\Delta q/\varepsilon_s$, can be compared with the drained stiffness at the same strain level. Strain ε_s is defined as:

$$\varepsilon_s = \frac{\sqrt{2}}{3}\sqrt{(\Delta\varepsilon_1-\Delta\varepsilon_2)^2+(\Delta\varepsilon_2-\Delta\varepsilon_3)^2+(\Delta\varepsilon_1-\Delta\varepsilon_3)^2} \qquad \text{and}$$

$$\Delta q = \frac{1}{\sqrt{2}}\sqrt{(\Delta\sigma_1-\Delta\sigma_2)^2+(\Delta\sigma_2-\Delta\sigma_3)^2+(\Delta\sigma_1-\Delta\sigma_3)^2}$$

It should be noted that $\varepsilon_d = \sqrt{3}\,\varepsilon_s$.

A) Test D0

-Stress path:

Test D0 was a drained triaxial compression test, performed from the initial state represented by stress point A on Fig.6.54. The horizontal stresses σ_r and σ_θ were maintained constant throughout the test (i.e. $\Delta\sigma_r=0$, $\Delta\sigma_\theta=0$), while loading was applied in the vertical direction, $\Delta\sigma_z$ (Fig.6.53b). No shear stress, $\tau_{\theta z}$, was applied. This procedure enables the vertical stiffness and the material's response in the horizontal direction to a vertical direct stress change to be estimated. Provided the response can be resolved adequately under very small changes in stresses and strains, the following elastic parameters can be calculated from Eq.6.2:

$$E_z' = \frac{\Delta\sigma_z'}{\varepsilon_z}$$

$$\nu_{zr}' = -\frac{E_z'}{\Delta\sigma_z'}\varepsilon_r = -\frac{\varepsilon_r}{\varepsilon_z}$$

$$\nu_{z\theta}' = -\frac{E_z'}{\Delta\sigma_z'}\varepsilon_\theta = -\frac{\varepsilon_\theta}{\varepsilon_z}$$

where equality of ν_{zr}' and $\nu_{z\theta}$' is expected if the material is isotropic in the horizontal plane.

- Stress-strain behaviour:

Fig.6.55a presents the measured strain components versus the applied vertical stress. Viewed in the small strain region, ε_z, ε_r, ε_θ<0.01% (Fig.6.55b), the first key feature to note is that the response is only gently non-linear until $\varepsilon_z \approx 0.005\%$, with little or no overall volume change. The initial value of E_z' is close to 200 MPa. The data also show that the two horizontal strain components, ε_r and ε_θ, are practically equal until they reach 0.005 %, at which point they start to deviate from each other. This initially transversely isotropic response gives a single parameter for the influence of vertical stress on horizontal straining, i.e. $\nu_{zr}'=\nu_{z\theta}'=\nu_{VH}'$. The value of ν_{VH}' (calculated from ε_θ) is plotted on Fig.6.56 versus shear strain ε_s and can be approximated, for the small strain region ($0.001\% \le \varepsilon_s \le 0.01\%$), as 0.46. As expected, no torsional shear strain was observed.

The volumetric strain in Fig.6.55b shows a slight initial contraction at the beginning of shearing, with ε_{vol} reaching a maximum of 0.002% when ε_z=0.015% and σ_z'=255 kPa, and then dilating continuously until a drained failure was reached (Fig.6.57).

- Yield characteristics:

The stress-strain plot p'-ε_d in Fig.6.58a indicates that the Y_2 yield boundary occurs at $\varepsilon_d \sim 0.015\%$, while the Y_3 yield point is engaged at $\varepsilon_d \sim 0.7\%$. From energy considerations, the change in work necessary to mobilize Y_2 and Y_3 is ~0.1 kJ/m^3 and ~20 kJ/m^3 respectively (Fig.6.58b). Compared to the undrained triaxial compression results summarized in Table 6.1, it appears that the Y_2 yield boundary is the same for both tests, while the Y_3 boundary for the drained test exceeds the undrained one.

B) Test E0

- Stress path:

Drained test E0 was performed such that the sample was loaded horizontally in the σ_θ direction, while the other stress components were kept constant, i.e. $\Delta\sigma_r'=\Delta\sigma_z'=0$, $\tau_{\theta z}=0$ (Fig.6.53c). These conditions enable the horizontal direct stiffness and the material's response in both the horizontal and vertical directions due to a horizontal direct stress, to be determined.

Again, from Eq.6.2, the following elastic parameters can be calculated:

$$E_\theta' = E_H' = \frac{\Delta\sigma_\theta'}{\varepsilon_\theta}$$

$$\nu_{\theta z}' = \nu_{HV}' = -\frac{E_H'}{\Delta\sigma_\theta'}\varepsilon_z = -\frac{\varepsilon_z}{\varepsilon_\theta}$$

$$\nu_{\theta r}' = \nu_{HH}' = -\frac{E_H'}{\Delta\sigma_\theta'}\varepsilon_r = -\frac{\varepsilon_r}{\varepsilon_\theta}$$

- Stress-strain response:

The strain response to the applied stress condition is presented in Fig.6.59, with the strain components plotted against circumferential stress, σ_θ'. In this case the response was more clearly non-linear at an earlier stage (ε_θ>0.003%) and the volume change response was markedly compressive throughout the test, Fig.6.59a. Both circumferential strain, ε_θ, and axial strain, ε_z, are compressive, while radial strain, ε_r, is tensile from the very beginning of the test. The initial values of Poisson's ratio show some scatter, but give ν_{HH}' of ~0.4 for 0.001%≤ε_s≤0.01%, while ν_{HV}' is negative and can be estimated to be -0.3 over the same strain range (Fig.6.60). The initial value of E_H' is ~100 MPa and no torsional shear strain was observed during horizontal loading.

Yield:

The yield boundaries Y_2 and Y_3 are reached at ε_d~0.02% and 0.13% respectively (Fig.6.61a), while the change in work required to reach these boundaries is estimated as 0.1kJ/m^3 and 2kJ/m^3 respectively (Fig.6.61b). However, these boundaries are not so well defined as in test D0 and the previous undrained tests from the Q-A Series.

C) Test G0

Test G0 has already been described in Section 6.2, where its results were considered in the context of the directional anisotropy of HPF4 when sheared undrained along different t-α stress path inclinations. With respect to the basic anisotropic parameters, this test allows the evaluation of the torsional shear modulus G_{VH} (=$G_{z\theta}$). In this test, all three components of direct stress, σ_z, σ_r and σ_θ, were kept constant, while applying a torsional shear stress $\tau_{\theta z}$ (Fig.6.53d). The initial response was such that the sample showed no change in p', i.e. no change of pore water pressure (Fig.6.62), or strain cross-coupling (Fig.6.18), until ε_d exceeded ~0.03%. Consequently, the small strain value of torsional shear modulus, $G_{\theta z}$, and shear modulus, G, obtained from this undrained test, can be considered to be the same as the equivalent drained parameters. The initial value of $G_{\theta z}$ was 110 MPa.

6.5. Discussion

6.5.1. Initial anisotropic parameters

The purely vertical loading ($\Delta\sigma_z>0$) of K_o consolidated HPF4, with constant horizontal stresses ($\Delta\sigma_r=\Delta\sigma_\theta=0$, test D0), demonstrated that the material has the same initial response in two orthogonal horizontal directions (r and θ). In this sense, the material is initially transversely isotropic, with $\nu_{zr}'=\nu_{VH}'\approx0.46$ and $E_z'\approx200$ MPa.

The response to horizontal loading ($\Delta\sigma_\theta>0$ and $\Delta\sigma_r=\Delta\sigma_z=0$, test E0), on the other hand, is more difficult to interpret. While the value of $\nu_{r\theta}'$ (=ν_{HH}') is not surprising (~0.4), and the initial value of $E_r'=E_\theta'=100$ MPa is comparable to E_z', the value of $\nu_{rz}'=\nu_{\theta z}'$ (=ν_{HV}') is quite different to that expected theoretically. For example Eq.2.1 predicts ν_{HV}', from the condition of the symmetry of the compliance matrix, to be ~0.23, while the value of -0.3 was recorded. HPF4 appears to show a strongly in-elastic response during horizontal loading. As noted in Chapter 5, the highly angular nature of the particles which constitute HPF4 form an anisotropic structure of particle contacts during deposition and K_o consolidation. It happens that an increase in the direct (horizontal) circumferential stress ($\Delta\sigma_\theta>0$) causes the structure to collapse radially, giving a high expansive horizontal radial strain accompanied by a compressive vertical strain (Fig.6.59). Plastic strains may develop almost immediately.

Fig.6.63 presents the variation of drained secant Young's moduli, E_z' (vertical) and E_r' (horizontal) with shear strain, obtained from tests D0 and E0 respectively. The same plot also

shows undrained secant Young's moduli for compression and extension, $E_u^{(com)}$ and $E_u^{(ext)}$, obtained from triaxial tests presented in Chapter 4. All four stiffness parameters were obtained by shearing from OCR=1.3. The drained stiffness parameters indicate that lightly overconsolidated HPF4 is nearly twice as stiff when loaded in the vertical than in the horizontal direction, in the small strain region (i.e. $0.001\% \le \varepsilon_s \le 0.1$). Both compression and extension undrained stiffnesses are greater than the drained vertical stiffness.

Fig.6.64 shows the variation of secant octahedral shear stiffness, *G*, for tests D0, E0 and G0, against the deviatoric shear strain ε_d (Eq.5.3). Globally, the torsional shear mode, G0, with G~110 MPa, appears to be the stiffest, while the sample loaded in the horizontal direction gives the softest response. A similar plot showing the variation of secant bulk moduli is given in Fig.6.65 where it is seen that K(E0) is much softer then K(D0).

6.5.2. The compliance matrix for HPF4

Adopting values of the elastic parameters associated with a strain level $\varepsilon_s \approx 0.001\%$ results in the following form of Eq.6.2:

$$\begin{bmatrix} \varepsilon_z \\ \varepsilon_r \\ \varepsilon_\theta \\ \gamma_{\theta z} \end{bmatrix} = 10^{-3} \begin{bmatrix} \frac{1}{200} & +\frac{0.30}{100} & +\frac{0.30}{100} & 0 \\ -\frac{0.46}{200} & \frac{1}{100} & -\frac{0.40}{100} & 0 \\ -\frac{0.46}{200} & -\frac{0.40}{100} & \frac{1}{100} & 0 \\ 0 & 0 & 0 & \frac{1}{110} \end{bmatrix} \begin{bmatrix} \Delta\sigma_z' \\ \Delta\sigma_r' \\ \Delta\sigma_\theta' \\ \Delta\tau_{\theta z} \end{bmatrix} \qquad (6.3)$$

The experimental compliance matrix is not symmetrical and therefore violates the condition of ideal elasticity (see Appendix VI). However, a negative Poisson's ratio ν_{rz}' does not necessarily violate the more absolute thermodynamic requirement for the positive strain energy of the material. Pickering, 1970, suggested that the necessary and sufficient condition for this requirement to be fulfilled is that the compliance matrix is positive definite. This occurs if all the principal minors of the matrix are positive. From Eq.6.3 the four principal minors can be shown to have the following values:

$$D_1 = \frac{1}{E_z'} = \frac{1}{2 \cdot 10^5} > 0 \qquad (6.4)$$

$$D_2 = \frac{1}{E_z' E_r'}(1 - \nu_{zr}'\nu_{rz}') = \frac{10^{-6}}{200 \cdot 100}[1 - (-0.3)\,0.46] > 0 \tag{6.5}$$

$$\begin{aligned} D_3 &= \frac{1}{E_z' E_r'^2}[1 - 2\nu_{zr}'\nu_{rz}'(1 + \nu_{r\theta}') - \nu_{r\theta}'^2] \\ &= \frac{10^{-9}}{200 \cdot 100}[1 - 2 \cdot 0.46 \cdot (-0.3) \cdot (1 + 0.4) - 0.4^2] > 0 \end{aligned} \tag{6.6}$$

$$D_4 = D_3 \frac{1}{G_{\theta z}} > 0 \tag{6.7}$$

As all the above values are positive, the thermodynamic requirements are satisfied.

It may be concluded from the above discussion that HPF4 is not truly elastic but behaves in a plastic manner when loaded horizontally.

6.5.3. Prediction of undrained triaxial stiffness anisotropy from measured drained parameters

In this Section the small strain anisotropic parameters measured in the drained tests and presented in Section 6.4 are used to predict undrained triaxial stiffness parameters $E_u^{(com)}$ and $E_u^{(ext)}$. These predictions are then compared to the observed behaviour. The approach adopted is based on Henkel's theory (1971), Chapter 2, the only difference being that all anisotropic parameters are measured, and not assumed as in Eq.2.7.

i) Pore water pressure parameter A

From the matrix equation 6.2 the following relationships can be obtained:

$$\begin{aligned} \varepsilon_z &= \frac{1}{E_z'}\Delta\sigma_z' - \frac{\nu_{rz}'}{E_r'}\Delta\sigma_r' - \frac{\nu_{\theta z}'}{E_\theta'}\Delta\sigma_\theta' \\ \varepsilon_r &= -\frac{\nu_{zr}'}{E_z'}\Delta\sigma_z' + \frac{1}{E_r'}\Delta\sigma_r' - \frac{\nu_{\theta r}'}{E_\theta'}\Delta\sigma_\theta' \\ \varepsilon_\theta &= -\frac{\nu_{z\theta}'}{E_z'}\Delta\sigma_z' - \frac{\nu_{r\theta}'}{E_r'}\Delta\sigma_r' + \frac{1}{E_\theta'}\Delta\sigma_\theta' \end{aligned} \tag{6.8}$$

Assuming that the material is transversely isotropic results in a reduction of the number of drained anisotropic parameters: $\nu_{rz}'=\nu_{\theta z}'$; $\nu_{zr}'=\nu_{z\theta}'$; $\nu_{\theta r}'=\nu_{r\theta}'$; $E_\theta'=E_r'$.

Considering undrained triaxial conditions, the following is true:

$$\begin{aligned}\Delta\sigma_r'&=\Delta\sigma_\theta'\\ \varepsilon_{vol}&=\varepsilon_z+\varepsilon_r+\varepsilon_\theta=0\end{aligned} \tag{6.9}$$

Substituting Eq.6.8 into the later of the above two equations gives:

$$\frac{\Delta\sigma_z'}{E_z'}(1-2\nu_{zr}') + 2\frac{\Delta\sigma_r'}{E_r'}(1-\nu_{rz}'-\nu_{r\theta}')=0 \tag{6.10}$$

Using Skempton's expression (1954) for the generation of pore pressure:

$$\Delta u=B[\Delta\sigma_r+A(\Delta\sigma_z-\Delta\sigma_r)] \tag{6.11}$$

in which B=1 for a fully saturated material with an incompressible pore fluid, and noting that in a conventional triaxial test $\Delta\sigma_r=0$, gives $\Delta u=A\Delta\sigma_z$. The changes in effective stress are then given by:

$$\begin{aligned}\Delta\sigma_z'&=(1-A)\Delta\sigma_z\\ \Delta\sigma_r'&=-A\Delta\sigma_z\end{aligned} \tag{6.12}$$

Substituting Eq.6.12 into Eq.6.10 and rearranging gives the ratio of drained horizontal to vertical Young's moduli expected in an undrained triaxial test:

$$\frac{E_r'}{E_z'}=\frac{2A(1-\nu_{rz}'-\nu_{r\theta}')}{(1-A)(1-2\nu_{zr}')} \tag{6.13}$$

Rearrangement of this equation provides the following expression for the pore water pressure parameter A:

$$A=\frac{1}{1+2\dfrac{E_z'}{E_r'}\dfrac{1-\nu_{rz}'-\nu_{r\theta}}{1-2\nu_{zr}'}} \tag{6.14}$$

ii) Ratio of E_z'/E_{uz} in undrained triaxial test

The ratio between drained and undrained vertical Young's moduli is estimated using

Eq.6.8a, which is the expression for axial strain in terms of drained parameters:

$$\varepsilon_z = \frac{1}{E_z'}\Delta\sigma_z' - \frac{\nu_{rz}'}{E_r'}\Delta\sigma_r' - \frac{\nu_{\theta z}'}{E_\theta'}\Delta\sigma_\theta' \qquad (6.15)$$

Substituting Eq.6.10 in 6.15 and noting that for undrained conditions:

$$\varepsilon_z = \frac{\Delta\sigma_z}{E_{uz}} \qquad (6.16)$$

gives the ratio E_z'/E_{uz} in the form:

$$\frac{E_z'}{E_{uz}} = (1-A)\left[1 + \frac{\nu_{rz}'(1-2\nu_{zr}')}{1-\nu_{rz}'-\nu_{r\theta}'}\right] \qquad (6.17)$$

As the initial conditions, Eq.6.9, are the same in both triaxial compression and extension, both the parameter A in Eq.6.14 and E_{uz} in Eq.6.17 are predicted to have the same magnitudes in either test. The Young's moduli E_r' and E_z' and Poissons ratios ν_{zr}', $\nu_{r\theta}'$ and ν_{rz}', were measured in tests D0 and E0 and had the following values: E_r'=100 MPa, E_z'=200 MPa, ν_{zr}'=0.46; $\nu_{r\theta}'$=0.40 and ν_{rz}'=-0.30.

These drained parameters are now used with the above equations to predict the behaviour in undrained shearing. Several different approaches have been considered:

a) Substituting these values into Eq.6.14 gives a predicted value of A=0.0217. The observed pore water pressure factor, A ($=\Delta u/\Delta\sigma_z$), can be obtained from the measured pore water pressure changes in the undrained triaxial tests. At the beginning of both the undrained triaxial compression and extension tests the stress path has the same slope, Chapter 4, implying that the parameter A is the same in compression and extension. Fig.6.66 shows the development of A with shear strain for both undrained triaxial compression and extension from an OCR=1.3. The initial value of A is 0.18 in both cases. This is much larger than the value predicted above.

Substituting the predicted value of A into Eq.6.17 gives E_z'/E_{uz}=0.952 which implies that there is very little difference between E_z' and E_{uz}. The results shown in Fig.6.63 indicate a much bigger difference.

b) Adopting the observed value of A=0.18 and the measured values of the Poisson's ratios, Eq.6.13 gives E_r'/E_z'=4.94. This indicates that the sample is far stiffer in the horizontal

than vertical direction. This does not agree with the test observations where $E_r'/E_z'=0.5$.

Substitution of this value of A into Eq.6.17, with all other parameters as measured, enables value of E_z'/E_{uz} to be predicted. Table 6.2 summarizes the difference between predicted and measured undrained moduli for both triaxial compression and extension, in the small strain region.

Table 6.2: Prediction of E_{uz} when measured A and drained parameters are adopted

ε_s	0.001 %	0.005 %	0.01 %
measured E_z' (MPa)	200	175	165
predicted E_{uz} (MPa)	250	219	207
measured $E_{uz}^{(com)}$ (MPa)	320	260	225
	22 % lower	16 % lower	8 % lower
measured $E_{uz}^{(ext)}$ (MPa)	235	215	190
	6.4 % higher	2 % higher	8.8 % higher

* The percentage shown in the shaded cells indicates by how much the predicted E_{uz} is either lower or higher than the measured E_{uz}.

Overall, the predictions are better for the undrained triaxial extension stiffness, being less than 10% higher than measured. For triaxial compression, the prediction is, on average, about 15% lower than that observed.

c) Combining Eq.6.13 with Eq.6.17 gives the following relationship between E_r'/E_z' and E_z'/E_{uz}:

$$\frac{E_z'}{E_r'} = \frac{1}{2Av_{rz}'}\left[\frac{E_z'}{E_{uz}} - 1\right] \tag{6.18}$$

Taking E_z'/E_{uz} as ~2/3, which is in agreement with the observations, Fig.6.63, and A and v_{rz}' as measured, then Eq. 6.18 gives $E_r'/E_z'=0.325$. This is less than that measured in drained tests, where $E_r'/E_z'=0.5$, and for typical observed values of E_z' predicts values of E_r' about 30% lower than measured.

6.5.4. Prediction of undrained triaxial stiffness anisotropy assuming symmetry

In the preceding Section undrained triaxial behaviour was predicted using parameters obtained from drained tests. This involved using the measured negative value of the Poisson's ratio ν_{rz}'. If it is considered that such a value is unrealistic for other stress paths and that the compliance matrix, Eq.6.2, should be symmetric, then ν_{rz}' can be expressed in terms of the other drained parameters as (Appendix VI):

$$\nu_{rz}' = \frac{E_r'}{E_z'} \nu_{zr}' \tag{6.19}$$

As before, several different approaches to predict undrained behaviour have been considered:

a) Substituting Eq.6.19 into Eq.6.14 produces a value of A=0.0512. This is again much lower than the value observed in the experiments, i.e. A=0.18. Using the predicted value of A in Eq.6.17 gives E_z'/E_{uz}=0.996, which again does not agree with the experimental observations.

b) Adopting the observed value of A=0.18, combining Eq.6.19 with Eq.6.13, rearranging and substituting the measured Poisson's ratios produces a E_r'/E_z' of 0.934. If this value is then used in Eq.6.19 with the measured value of ν_{zr}', a value of ν_{rz}'=0.43 is obtained. Substituting this value into Eq.6.17 gives E_{uz}/E_z'~1.014 and the difference between the predicted E_{uz} and measured $E_{uz}^{(com)}$ and $E_{uz}^{(ext)}$ is summarized in Table 6.3.

Table 6.3: Prediction of E_{uz} when symmetry of compliance matrix is assumed

ε_s	0.001 %	0.005 %	0.01 %
measured E_z' (MPa)	200	175	165
predicted E_{uz} (MPa)	203	178	167
measured $E_{uz}^{(com)}$ (MPa)	320	260	225
	36 % lower	32 % lower	26 % lower
measured $E_{uz}^{(ext)}$ (MPa)	235	215	190
	13 % lower	17 % lower	12 % lower

On average, this procedure predicts undrained compression stiffnesses ~30% lower, and undrained extension stiffnesses ~15% lower, than those observed.

c) An alternative approach is to assume symmetry of the compliance matrix, Eq.6.19, but instead of using Eq.6.13 to calculate E_r'/E_z', to use the measured value of this ratio from the drained tests, i.e. $E_r'/E_z'=0.5$. Using this value with the measured value of ν_{zr}', a value of $\nu_{rz}'=0.23$ is obtained form Eq.6.19. Substituting $\nu_{rz}'=0.23$ into Eq.6.17 gives $E_z'/E_{uz}=0.861$ and the predicted undrained moduli are summarized in Table 6.4.

Table 6.4: Prediction of E_{uz} using measured drained stiffness ratio, E_r'/E_z'

ε_s	0.001 %	0.005 %	0.01 %
measured E_z' (MPa)	200	175	165
predicted E_{uz} (MPa)	232	203	192
measured $E_{uz}^{(com)}$ (MPa)	320	260	225
	27 % lower	22 % lower	15 % lower
measured $E_{uz}^{(ext)}$ (MPa)	235	215	190
	1 % lower	5.4 % lower	1 % higher

On average, the undrained compressive stiffness is ~21% lower than that observed, while the undrained extension stiffness agrees well with the observations having only ~2.5% error.

d) Substituting the symmetry condition given by Eq.6.19 into Eq.6.17 gives the following relationship between E_r'/E_z' and E_z'/E_{uz}:

$$\frac{E_r'}{E_z'}=\frac{(1-\nu_{r\theta}')\left[\frac{E_z'}{E_{uz}}\frac{1}{1-A}-1\right]}{\frac{\nu_{zr}'}{1-A}\frac{E_z'}{E_{uz}}-2\nu_{zr}'\nu_{zr}'} \qquad (6.20)$$

Taking E_z'/E_{uz} as ~2/3, which is in agreement with observations, Fig.6.63, and A and ν_{rz}' as measured, then Eq.6.20 gives $E_r'/E_z'=2.3$. This is again opposite of what has been measured in drained tests, where $E_r'/E_z'=0.5$.

6.5.5. Comments on the prediction of undrained triaxial stiffness from drained parameters

In the previous two sections the drained anisotropic parameters were initially used to predict the pore water pressure coefficient, A, and the undrained Youngs moduli in triaxial compression and extension. This procedure gave very small values of A and indicated that the undrained stiffnesses in both triaxial compression and extension were approximately equal to the drained vertical stiffness. Such predictions are not in agreement with the experimental observations.

In an attempt to improve the predictions, the measured value of A=0.18 was adopted and various approaches were presented to predict the undrained Young's moduli in triaxial compression and extension, on the basis of measured drained anisotropic parameters, ν_{zr}', $\nu_{r\theta}'$ and ν_{rz}'.

Initially, the measured value of ν_{rz}'=-0.3 was used which implied that the compliance matrix was non-symmetric. These results showed that:

a) The ratio of drained horizontal to vertical Young's moduli, E_r'/E_z', at small strains, predicted for the undrained triaxial compression tests, indicates a far stiffer response in the horizontal than vertical direction. This is the opposite to that observed in drained tests where E_r'/E_z'=0.5.

b) The predicted ratio of drained to undrained vertical Young's moduli at small strains was in better agreement with the results of the extension tests, with an average maximum error of ~6%. The agreement between the predictions and the observations for the compression tests was less good, with a maximum error of 15%.

If it is considered that the negative value of ν_{rz}' observed in the drained tests was inappropriate for undrained stress paths then an alternative value of ν_{rz}' can be found by considering the condition of symmetry of the compliance matrix. Such an approach led to Eq.6.19 and a value of ν_{rz}'=0.43. With this new value of ν_{rz}' the following results were obtained:

a) The predicted ratio E_r'/E_z'=0.934 for an undrained test, indicating nearly the same horizontal and vertical stiffness. Again this differs from that observed in the drained tests.

b) The predicted ratio of drained to undrained moduli, E_z'/E_{uz}, is not in as good agreement with

the experimental observations as that obtained with the measured negative value of ν_{rz}'.

A third approach, using the measured $E_r'/E_z'=0.5$ from drained tests with the symmetrical condition, gave ν_{rz}' =0.23 and a E_z'/E_{uz} ratio which agreed better with the extension test data than the prediction using the negative ν_{rz}'. However, the agreement with the compression test data was worse.

Overall, using the measured value of ν_{rz}' of -0.3 seems to provide the best fit for both compression and extension stiffnesses.

6.5.6. Prediction of undrained triaxial anisotropy considering loading/unloading stress paths

In the above discussion the behaviour of HPF4 in loading and in unloading has been assumed to be the same. A conventional undrained triaxial compression test experiences vertical loading and horizontal unloading in terms of effective stress, while the opposite is true for a triaxial extension test. In this Section the behaviour in loading and unloading is investigated and taken into account for predicting undrained moduli. It is assumed that in triaxial compression tests:

$$E_u^{com}=\frac{\Delta q}{\Delta \varepsilon_z} \tag{6.21}$$

and in triaxial extension tests:

$$E_u^{ext}=\frac{\Delta q}{\Delta \varepsilon_z} \tag{6.22}$$

An undrained triaxial compression test, performed with $\sigma_z>\sigma_r$ and σ_r=const, exhibits vertical loading and horizontal unloading in terms of effective stresses. From Eqs. 6.12, 6.15 and 6.16, the undrained Young modulus in compression can be written as:

$$E_{uz}^{com}=\frac{1}{\frac{1-A}{E_z^{/load}}+\frac{2\nu_{rz}^{/}A}{E_r^{/unld}}} \tag{6.23}$$

where the superscripts 'load' and 'unload' distinguish between loading and unloading mode.

For a conventional undrained triaxial extension test, performed with $\sigma_z<\sigma_r$ and σ_r=const the sample undergoes vertical unloading and the above equation becomes:

$$E_{uz}^{ext} = \frac{1}{\frac{1-A}{E_z^{/unld}} + \frac{2\nu_{rz}^{/} A}{E_r^{/load}}} \tag{6.24}$$

Alternative expressions for the undrained stiffnesses can be found by considering the analogous test conditions in which a compression test is performed with $\sigma_r<\sigma_z$ and σ_z=const, with the sample undergoing lateral unloading, and an extension test is performed with $\sigma_r>\sigma_z$ and σ_z=const, with the sample undergoing lateral loading. This is possible if it is assumed that the strains ε_z and ε_r are a unique function of the deviatoric stress. Considering the second case of an extension test performed with lateral loading, the expression for radial strain (6.8b) is:

$$\varepsilon_r = -\frac{\nu_{zr}^{/}}{E_z^{/unld}}\Delta\sigma_z^{/} + \frac{1-\nu_{\theta r}^{/}}{E_r^{/load}}\Delta\sigma_r^{/} \tag{6.25}$$

and expressing:

$$\begin{aligned} \Delta\sigma_z^{/} &= (A-1)\Delta\sigma_r \\ \Delta\sigma_r^{/} &= A\Delta\sigma_r \end{aligned} \tag{6.26}$$

the following expression for E_{uz}^{ext} can be written:

$$E_{uz}^{ext} = \frac{1}{2}\frac{1}{A(1-\nu_{\theta r}^{/})\frac{1}{E_r^{/load}} + \nu_{zr}^{/}(1-A)\frac{1}{E_z^{/unld}}} \tag{6.27}$$

This expression can be shown to be identical to Eq.6.24 if A is defined in a consistent manner. It should be noted that, theoretically, A has the same value in both Eq.6.24 and 6.27. If on the other hand A is obtained from the experimental observations, then it is unlikely that Eq.6.24 and Eq.6.27 will give the same values of E_{uz}^{ext}, unless A happens to be in agreement with the theoretical value given by Eq.6.14.

Provided that we assume Poisson's ratios do not change between loading and unloading, equations 6.23 and 6.24 may be used to evaluate values of $E'_r{}^{unld}$ and $E'_z{}^{unld}$. Dealing first with Eq.6.23 and considering a shear strain level of 0.001%, the available test data gives E_{uz}^{com}=320 MPa and A=0.18 (from triaxial test), $E_z{}'^{load}$=200 MPa and ν_{rz}'=-0.3 (from D0 and E0 tests). Substituting these values into Eq.6.23 and re-arranging gives $E'_r{}^{unld}$=110 MPa. Comparing this with the $E_r{}'^{load}$ measurement made in test E0 gives:

$$\frac{E_r'^{load}}{E_r'^{unld}} = \frac{100}{110} = 0.91 \qquad (6.28)$$

Turning then to the undrained Young's modulus expression given by Eq.6.24 and considering again a shear strain level of 0.001%, the triaxial test data gives E_{uz}^{ext}=235 MPa and A=0.18, while E0 test gave $E_{r\text{-}load}'$=100 MPa and ν_{rz}'=-0.3. Substituting these values into Eq.6.24 and re-arranging gives $E_z'^{unld}$=153 MPa. So, in comparison with the loading value:

$$\frac{E_z'^{load}}{E_z'^{unld}} = \frac{200}{153} = 1.307 \qquad (6.29)$$

This result is unrealistic because the same analysis as in the following step, summarized in Table 6.5, gives $E_u^{com}/E_u^{ext} \approx 2.0$.

An alternative approach is to obtain $E_z'^{unld}$ from Eq.6.27. The drained horizontal Young's modulus, $E_r'^{load}$ and the Poisson ratio, $\nu_{\theta r}'$ are obtained from test E0. Poisson's ratio ν_{zr}' is not known for vertical extension, but is assumed to be the same as in test D0. Substituting the measured values of these parameters at a shear strain of 0.001% (i.e. $E_r'^{load}$=100 MPa, $\nu_{\theta r}'$=0.4 and ν_{zr}'=0.46) along with the observed values of E_{uz}^{ext}=235 MPa and A=0.18, into Eq.6.27 gives $E_z'^{unld}$=360 MPa. So:

$$\frac{E_z'^{load}}{E_z'^{unld}} = \frac{200}{360} = 0.556 \qquad (6.30)$$

The values of Young's moduli at a strain level of 0.001% can be summarised as:

$E_z'^{load}$=200 MPa	(measured)
$E_z'^{unld}$=360 MPa	(estimated)
$E_r'^{load}$=100 MPa	(measured)
$E_r'^{unld}$=110 MPa	(estimated)
E_{uz}^{com}=320 MPa	(measured)
E_{uz}^{ext}=235 MPa	(measured)

An expression for the predicted value of the ratio E_u^{com}/E_u^{ext} can be obtained by dividing Eq.6.23 by Eq.6.27 giving:

$$\frac{E_u^{com}}{E_u^{ext}} = 2\frac{A(1-\nu'_{\theta r})\frac{1}{E_r^{'load}} + \nu'_{zr}(1-A)\frac{1}{E_z^{'unld}}}{\frac{2\nu'_{rz}A}{E_r^{'unld}} + \frac{1-A}{E_z^{'load}}} \qquad (6.31)$$

The conclusion from the above exercise is that the vertical and horizontal drained Young's moduli differ in loading and unloading and it is not possible to accurately predict values of E_{uz}^{com} and E_{uz}^{ext} from drained parameters derived from tests involving direct *compressive (loading)* stress conditions. For HPF4 at OCR=1.3, the ratios of the loading to unloading stiffnesses are given by Eq.6.28 and Eq.6.30. Values for the ratios of loading to unloading secant Young's moduli for three levels of strain are shown in Table 6.5. It can be seen that while the ratio $E_z^{'load}/E_z^{'unld}$ remains approximately constant, this is not so for the ratio $E_r^{'load}/E_r^{'unld}$, which reduces over the strain range considered. However, taking the average of both sets of ratios, using this to establish unloading moduli values from those measured in drained loading, and substituting these into Eq.6.31 gives estimates of E_u^{com}/E_u^{ext} that are in agreement with the observed values, Table 6.5.

6.5.7. Prediction of the initial inclination of an undrained stress path

When presenting the framework for material behaviour in Chapter 2, two theories were described that predict the undrained Young's moduli and the stress path inclination of triaxial samples, using the principles of transverse isotropy, i.e. Henkel, 1971 and Graham & Houlsby, 1983. Both theories assume a symmetrical compliance matrix (Appendix VI). In this Section, the results obtained with HPF4 are checked against the recommendations of Graham & Houlsby (1983).

Graham & Houlsby (1983) proposed a procedure which used drained monotonic triaxial stress paths to estimate a soil's anisotropic elastic parameters. These were then used to predict the initial inclination of undrained stress paths. The method was demonstrated using results from monotonic triaxial tests on lightly overconsolidated Winnipeg clay (Graham et al, 1983), on the assumption that it is transversely isotropic and linearly elastic within the yield locus.

The stiffness matrix for such a material, following the considerations given in Appendix VI, is symmetrical and of the form:

$$\begin{bmatrix} \delta p' \\ \delta q \end{bmatrix} = \begin{bmatrix} K^* & J \\ J & 3G^* \end{bmatrix} \begin{bmatrix} \delta \varepsilon_{vol} \\ \delta \varepsilon_d \end{bmatrix} \tag{6.32}$$

All three parameters K^*, G^* and J are functions of E_H', E_V', ν_{HH}' and ν_{HV}', see Eq.VI.9. Letting $R^2=E_H'/E_V'$ and assuming that $\nu_{HV}'=\nu^*/R$, Graham & Houslby reduced the number of parameters from four to two, namely, R and ν^*. It should be noted that the parameter ν^* is equal to ν_{HH}', which cannot be measured directly in a conventional triaxial cell. Taking several drained triaxial stress paths (with different $\delta q/\delta p'$ ratios) Graham & Houlsby used measured values of stress and strain increments δq, $\delta p'$, $\delta \varepsilon_{vol}$ and $\delta \varepsilon_d$ and Eq.6.32 to first calculate the K^*, G^* and J moduli, from which the parameters ν^* and R were then evaluated. For Winnipeg clay they found ν^* is about 0.2, and the stiffness ratio $R^2 \approx 1.8$, indicating that the soil is stiffer in the horizontal direction than in the vertical direction.

To obtain the initial inclination of an undrained stress path, $\delta \varepsilon_{vol}=0$ is substituted in Eq.6.32, giving the following expression:

$$\frac{\delta q}{\delta p'} = \frac{3G^*}{J} \tag{6.33}$$

which, in terms of parameters ν^* and R^2, becomes:

$$\frac{\delta q}{\delta p'} = 3\left[\frac{(1-\nu^*) - 2R\nu^* + R^2/2}{(1-\nu^*) + R\nu^* - R^2}\right] \tag{6.34}$$

Using the values of R^2 and ν^* obtained from the drained tests on Winnipeg clay it was shown that Eq.6.34 gave a good match to the initial inclination of the undrained stress path.

Equation 6.34 is now used to predict the inclination of an undrained stress path for HPF4, using the measured drained parameters obtained from tests D0 and E0. These tests were also monotonic as were the tests on Winnipeg clay. The stiffness ratio $R^2=E_H'/E_V'$ equals 0.5 and $\nu^*=\nu_{HH}'$ equals 0.4 in the small strain region. On substitution in Eq.6.34 these give a value of $\delta q/\delta p'=2.22$, which does not agree with the slope obtained from the undrained triaxial test described in Chapter 4 (Fig.4.19) where $\delta q/\delta p'=6.4$ over the range of $0<\varepsilon_d<\sim 0.1\%$.

In the above approach the elastic stiffness matrix is assumed to be symmetric. An attempt is now made to estimate the initial inclination of an undrained stress path using the drained non-symmetric stiffness matrix (Eq.6.2). Following a similar procedure to that outlined

in Appendix VI, the following equation is obtained:

$$\begin{bmatrix} \varepsilon_z \\ \varepsilon_r \end{bmatrix} = \begin{bmatrix} \frac{1}{E_z'} & -2\frac{\nu_{rz}'}{E_r'} \\ -\frac{\nu_{zr}'}{E_z'} & \frac{1-\nu_{r\theta}'}{E_r'} \end{bmatrix} \begin{bmatrix} \Delta\sigma_z' \\ \Delta\sigma_r' \end{bmatrix} \tag{6.35}$$

and in terms of invariants:

$$\begin{bmatrix} \delta p' \\ \delta q \end{bmatrix} = \begin{bmatrix} K^{**} & J_1 \\ J_2 & 3G^{**} \end{bmatrix} \begin{bmatrix} \delta\varepsilon_{vol} \\ \delta\varepsilon_d \end{bmatrix} \tag{6.36}$$

Here, the stiffness moduli K^{**}, G^{**}, J_1 and J_2 are of the form:

$$K^{**} = \frac{1}{9}\frac{2E_r'(1+\nu_{zr}') + E_z'(1-\nu_{r\theta}'+2\nu_{rz}')}{1-\nu_{r\theta}'-2\nu_{zr}'\nu_{rz}'}$$

$$3G^{**} = \frac{1}{2}\frac{E_r'(1-2\nu_{zr}') + 2E_z'(1-\nu_{r\theta}'-\nu_{\theta z}')}{1-\nu_{r\theta}'-2\nu_{zr}'\nu_{rz}'}$$

$$J_1 = \frac{1}{3}\frac{E_z'(1-\nu_{r\theta}'-\nu_{rz}') - E_r'(1-2\nu_{zr}')}{1-\nu_{r\theta}'-2\nu_{zr}'\nu_{rz}'} \tag{6.37}$$

$$J_2 = \frac{1}{3}\frac{E_z'(1-\nu_{r\theta}'+2\nu_{rz}') - E_r'(1+\nu_{zr}')}{1-\nu_{r\theta}'-2\nu_{zr}'\nu_{rz}'}$$

If $\delta\varepsilon_{vol} = 0$ (representing undrained conditions) is substituted in Eq.6.36, the initial inclination of the undrained stress path becomes:

$$\frac{\delta q}{\delta p'} = \frac{3G^{**}}{J_1} \tag{6.38}$$

while a further transformation gives:

$$\frac{\delta q}{\delta p'} = \frac{3}{2} \frac{\left[(1 - 2\nu'_{zr}) + 2\frac{E'_z}{E'_r}(1 - \nu'_{r\theta} - \nu'_{rz}) \right]}{\left[\frac{E'_z}{E'_r}(1 - \nu'_{r\theta} - \nu'_{rz}) - (1 - 2\nu'_{zr}) \right]} \qquad (6.39)$$

Substitution of measured parameters: $E_r'/E_z' = 0.5$; $\nu_{zr}=0.46$; $\nu_{r\theta}=0.4$ and $\nu_{rz}=-0.3$ gives the inclination of the undrained stress path of $\delta q/\delta p' = 3.2$, which, while better than before, still does not agree with the observation that $\delta q/\delta p'=6.4$.

However, a set of parametric calculations is summarised in Table 6.6, which shows how the key variables affect the $\delta q/\delta p'$ predictions:

- Firstly, it can be noted that the anisotropy in stiffness, i.e. whether the material is stiffer horizontally or vertically, changes the orientation of the stress path. It is positive for $E_z'/E_r' > 1.0$ and negative for $E_z'/E_r' < 1.0$. This was also shown by Graham & Houlsby (1983).

- Secondly, once the orientation of the stress path is known (positive in the case of HPF4), the inclination is not significantly affected by changes in the values of E_z'/E_r', $\nu_{r\theta}'$ or ν_{rz}'. The inclinations in Table 6.6 for these changes are all around 3.2.

- The controlling parameter for the stress path inclination is Poisson's ratio ν_{zr}'. To fit the observed inclination of the undrained stress path, a value of $\nu_{zr}' \approx 0.1$ is required if the other parameters remain unchanged.

The above study shows that the combination of elastic theory and drained parameters from monotonic tests leads to unreliable predictions for undrained effective stress path inclinations. The true elastic range for granular soils is very small (Tatsuoka and Shibuya, 1992; Porovic, 1995), and as each monotonic test progresses a new anisotropy is evolving in terms of E_z', E_r', ν_{zr}, ν_{rz} and $\nu_{r\theta}$ throughout the test (once the Y_1 region has been crossed).

6.6. Summary

In this Chapter two facets of the behaviour of HPF4 have been examined. Firstly, the behaviour of HPF4 when subjected to undrained shearing with different values of

$\Delta t/\Delta\alpha$ and with Δb=0.5 has been considered. These tests were performed to simulate the response of a soil element in the field which is loaded in plane strain from an initial K_o conditions. Secondly, the initial small strain behaviour of HPF4 has been investigated to see whether or not it can be classified as a transversely isotropic elastic material. The following conclusions arise from these investigations:

A) Effect of $\Delta t/\Delta\alpha$

a) For all undrained Q-A tests the deviatoric strain, ε_d, or the change in work, ΔW, required to reach Y_2 yield boundary were approximately constant. This boundary was determined from stress-strain diagrams, at points where the change in strain increment gradient occurred. In terms of deviatoric strain, the Y_2 boundary occur at ε_d~0.02%. The corresponding value for the change in work is ~0.05 kJ/m^3.

b) The stiffness depends on the $\Delta t/\Delta\alpha$ ratio such that it decreases as $\Delta t/\Delta\alpha$ rotates from 0° to ±∞.

c) The above is also linked with the amount of principal stress rotation engaged at the Y_2 boundary, such that shear stiffness increases with the amount of stress rotation required to reach the Y_2 boundary.

d) The tests (apart from Q-A0) all approached failure with zero increments of radial strain, indicating plane strain conditions. The *b*-value in all tests at failure was approximately 0.3. This agrees with the results of the M-Series tests.

e) The ultimate angles of shearing resistance, ϕ', were approximately 43° and occurred at α~23°. Again, the value is in agreement with the M-Series tests.

B) Initial anisotropic parameters

a) Drained vertical loading of HPF4 indicated transversely isotropic behaviour. When interpreted in terms of anisotropic elastic parameters, the small-strain Poisson's ratio relating the vertical response to direct horizontal loading was negative. This resulted in a non-symmetric compliance matrix. However, this matrix was shown to be thermodynamically acceptable.

b) When the drained elastic parameters were used to predict the behaviour of undrained tests, poor agreement was found with the measured behaviour.

c) If no distinction is made between the drained Young's moduli in loading and unloading, the elastic theory predicts equal undrained vertical Young moduli, E_{uz}, for compression and extension tests. Using the measured drained parameters the predicted value of E_{uz} was closer to the observed value in extension, E_{uz}^{ext}, than in compression, E_{uz}^{com}.

d) To improve the prediction of the undrained stiffness ratio, $E_{uz}^{com}/E_{uz}^{ext}$, a distinction should be made between loading and unloading modes of behaviour.

e) Using the measured drained anisotropic elastic parameters it was not possible to accurately predict the inclination of the undrained stress path. Further investigations as to the sensitivity of this inclination to the magnitude of the anisotropic parameters indicated that the Poisson's ratio ν_{zr}' was the only influential parameter.

f) Following from above, transverse anisotropic elastic theory is not an adequate model for predicting the behaviour of granular HPF4 soil, even at small strains.

Table 6.5: $E_{uz}^{com}/E_{uz}^{ext}$ at three strain levels, when load/unload modes are taken into account

strain level (%)		0.001	0.005	0.01	average	
Measured	E_{uz}^{com} (MPa)	320	260	225		
	E_{uz}^{ext} (MPa)	235	215	190		
	$E_z^{'load}$ (MPa)	200	175	165		
	$E_r^{'load}$ (MPa)	100	90	80		
Measured	$E_{uz}^{com}/E_{uz}^{ext}$	1.36	1.21	1.18	1.25	
Prediction when $E^{'load}=E^{'unld}$	from Eq(6.23)/(6.27)	1.96	1.92	2.01	1.96	
Prediction from Eq.(6.23) Eq.(6.27)	$E_r^{'unld}$ $E_z^{'unld}$	110 360	129 335	206 294		
Predicted	$E_r^{'load}/E_r^{'unld}$	0.90	0.70	0.39	0.66	0.6
Predicted	$E_z^{'load}/E_z^{'unld}$	0.55	0.52	0.56	0.54	
Prediction when $E^{'load}/E^{'unld}=0.6$	from Eq.(6.31) $E_{uz}^{com}/E_{uz}^{ext}$	1.29	1.26	1.32	1.29	
error (%), in $E_{uz}^{com}/E_{uz}^{ext}$ considering load/unload		-5.5	4.5	11	3	
error (%), in $E_{uz}^{com}/E_{uz}^{ext}$ without considering load/unload		44	59	70	57	

Table 6.6: Prediction of the inclination of undrained stress path

E_z'/E_r'	$\nu_{r\theta}'$	ν_{zr}'	ν_{rz}'	dq/dp'
Stiffer vertical direction				
2	0.4	0.46	-0.3	3.21
1.5	0.4	0.46	-0.3	3.28
2.5	0.4	0.46	-0.3	3.16
2	0.2	0.46	-0.3	3.17
2	0.3	0.46	-0.3	3.18
2	0.5	0.46	-0.3	3.24
2	0.4	0.3	-0.3	4.28
2	0.4	0.2	-0.3	5.25
2	0.4	0.1	-0.3	6.6
2	0.4	0.46	-0.2	3.24
2	0.4	0.46	-0.5	3.17
2	0.4	0.46	0.1	3.39
Stiffer horizontal direction				
0.5	0.4	-0.3	0.46	-1.71

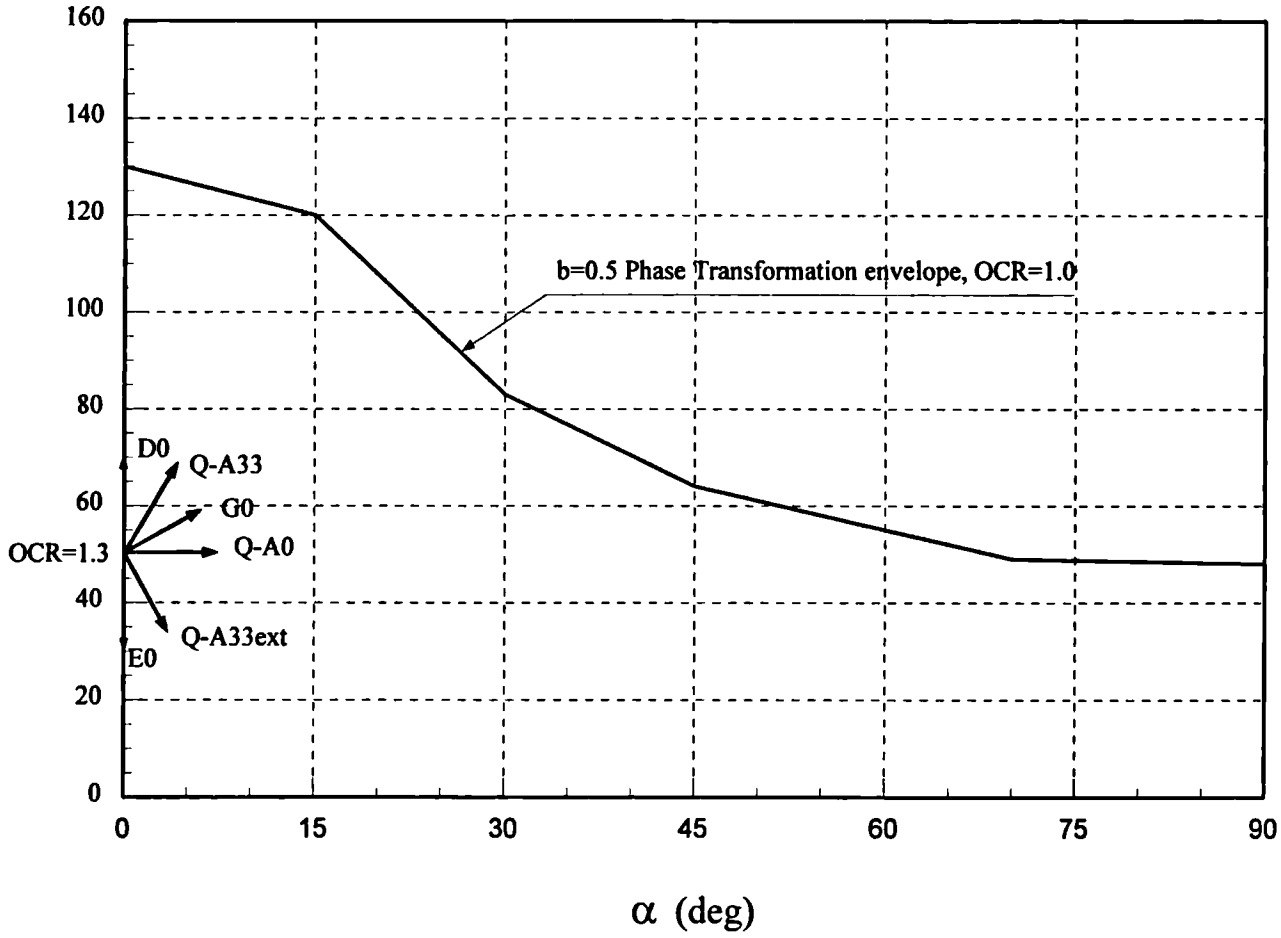


Fig.6.1 - Schematic presentation of Q-A and D stress paths

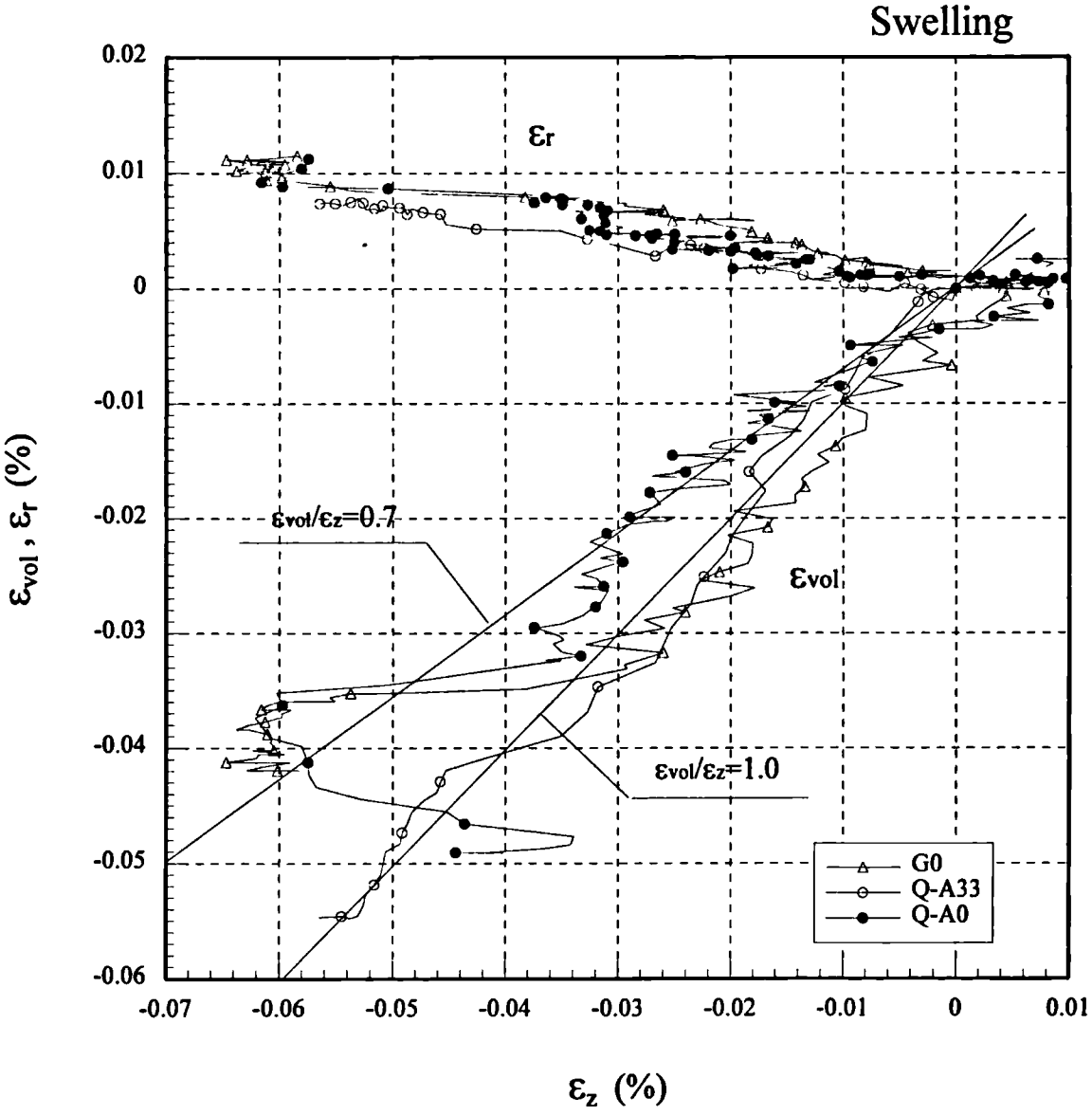


Fig.6.2 - Radial and volumetric strains vs. axial strain during Ko swelling, as measured in HCA tests

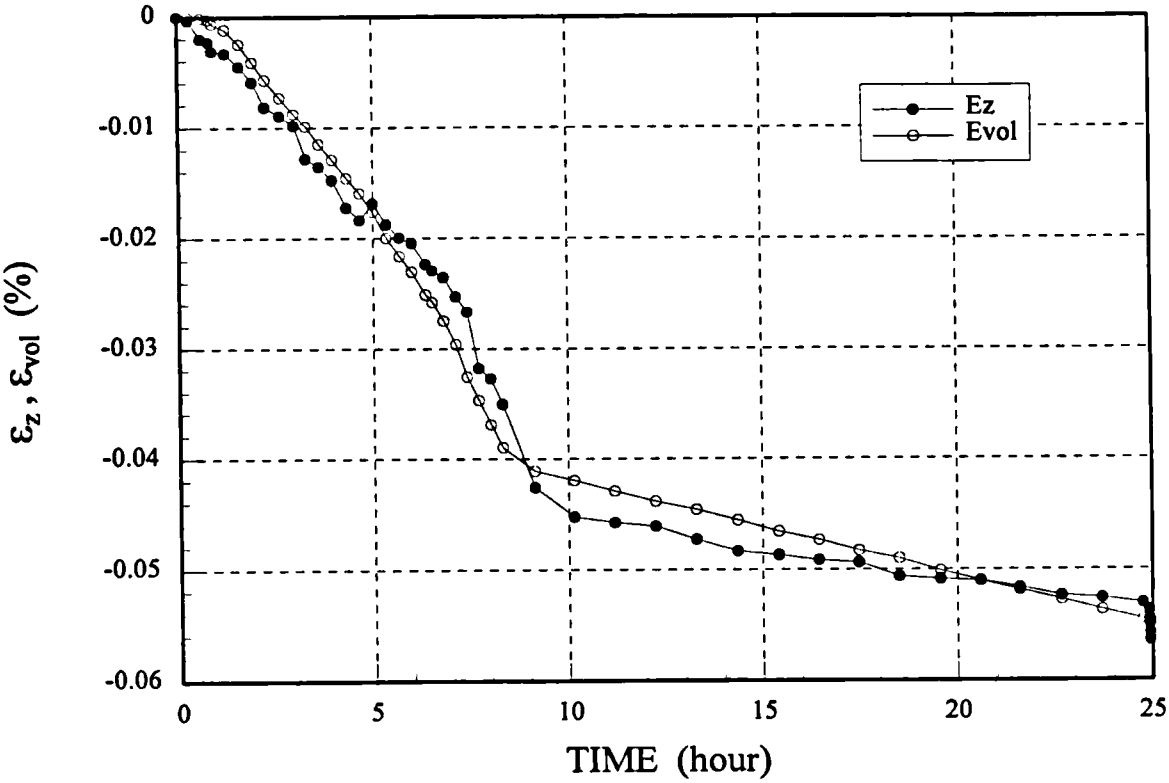


Fig.6.3 - Time development of axial and volumetric strains during Ko swelling, as measured in the HCA

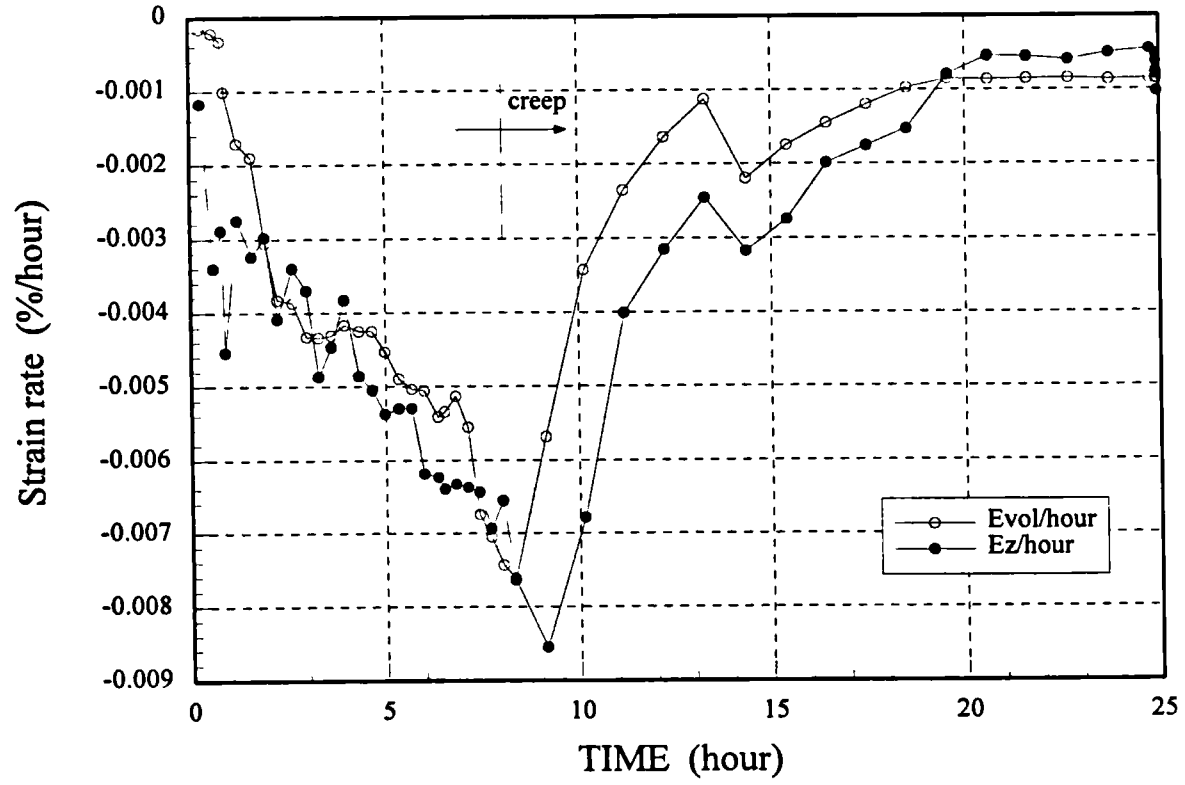


Fig.6.4 - Volumetric and axial strain rate during Ko swelling, as measured in the HCA

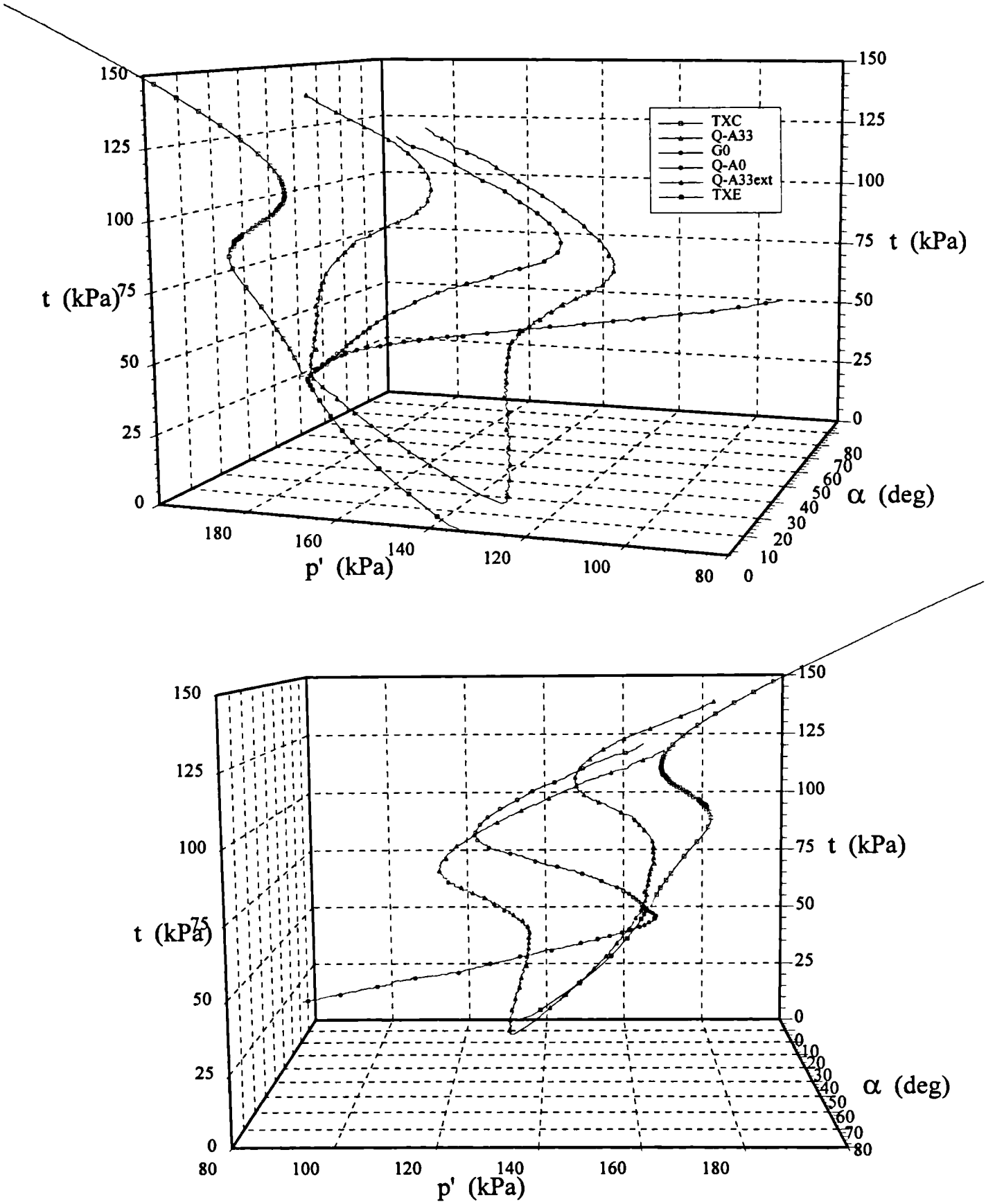


Fig.6.5 - a), b) Effective stress paths of undrained tests from Q-A Series, in two different perspectives

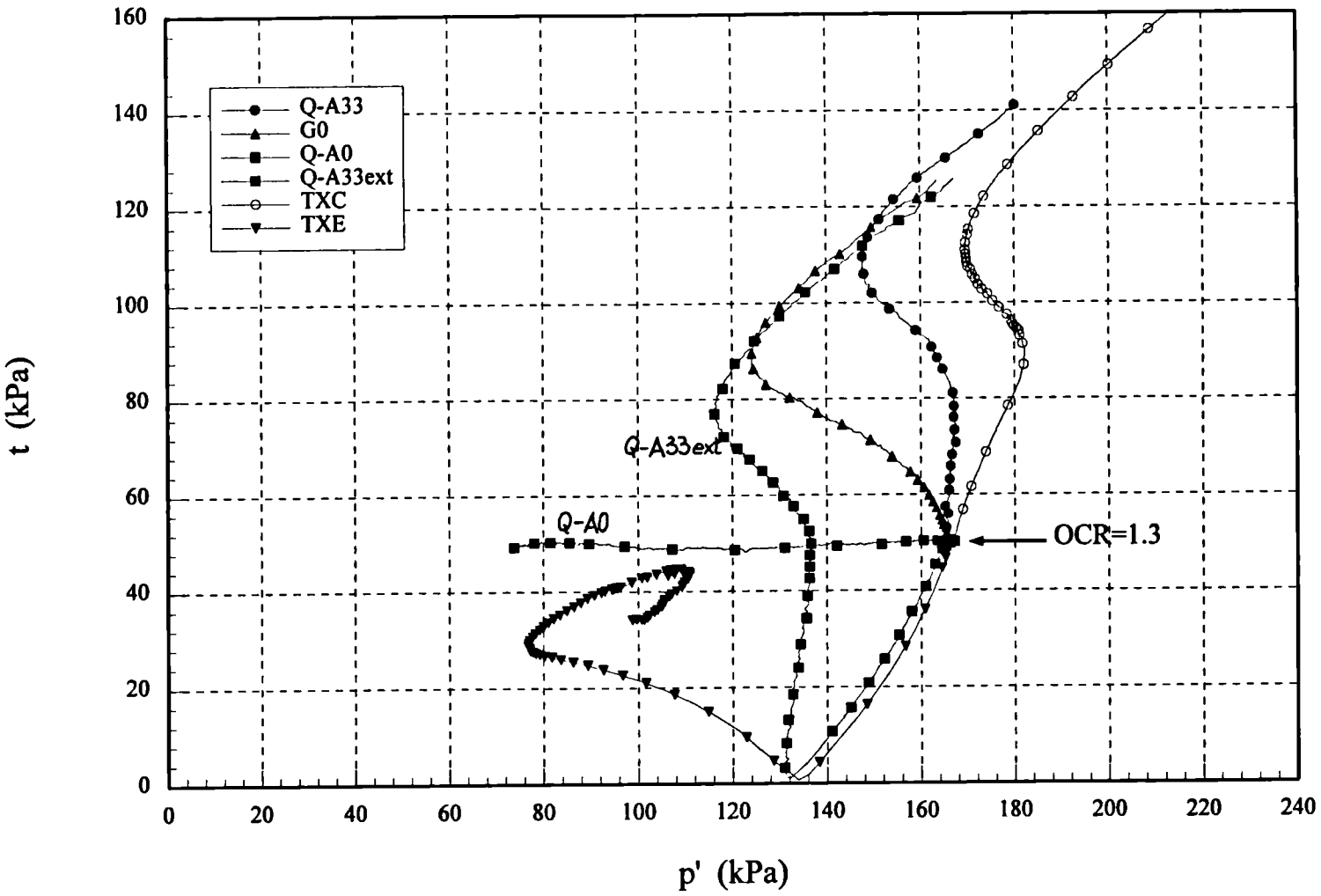


Fig.6.6 - Effective stress paths from Q-A Series projected on t-p' plane

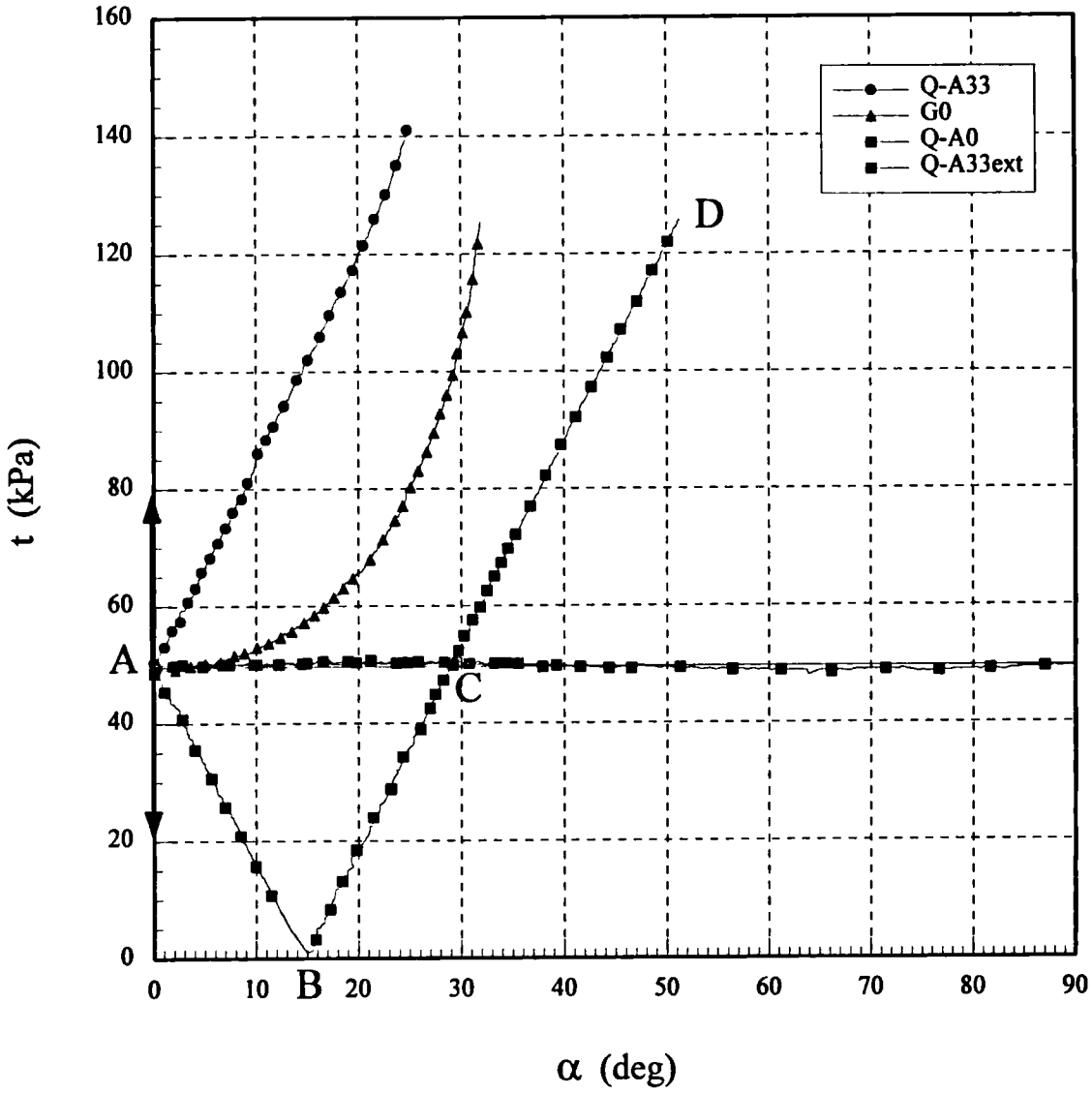


Fig.6.7 - Projection of the effective stress paths from Q-A Series on t-α plane

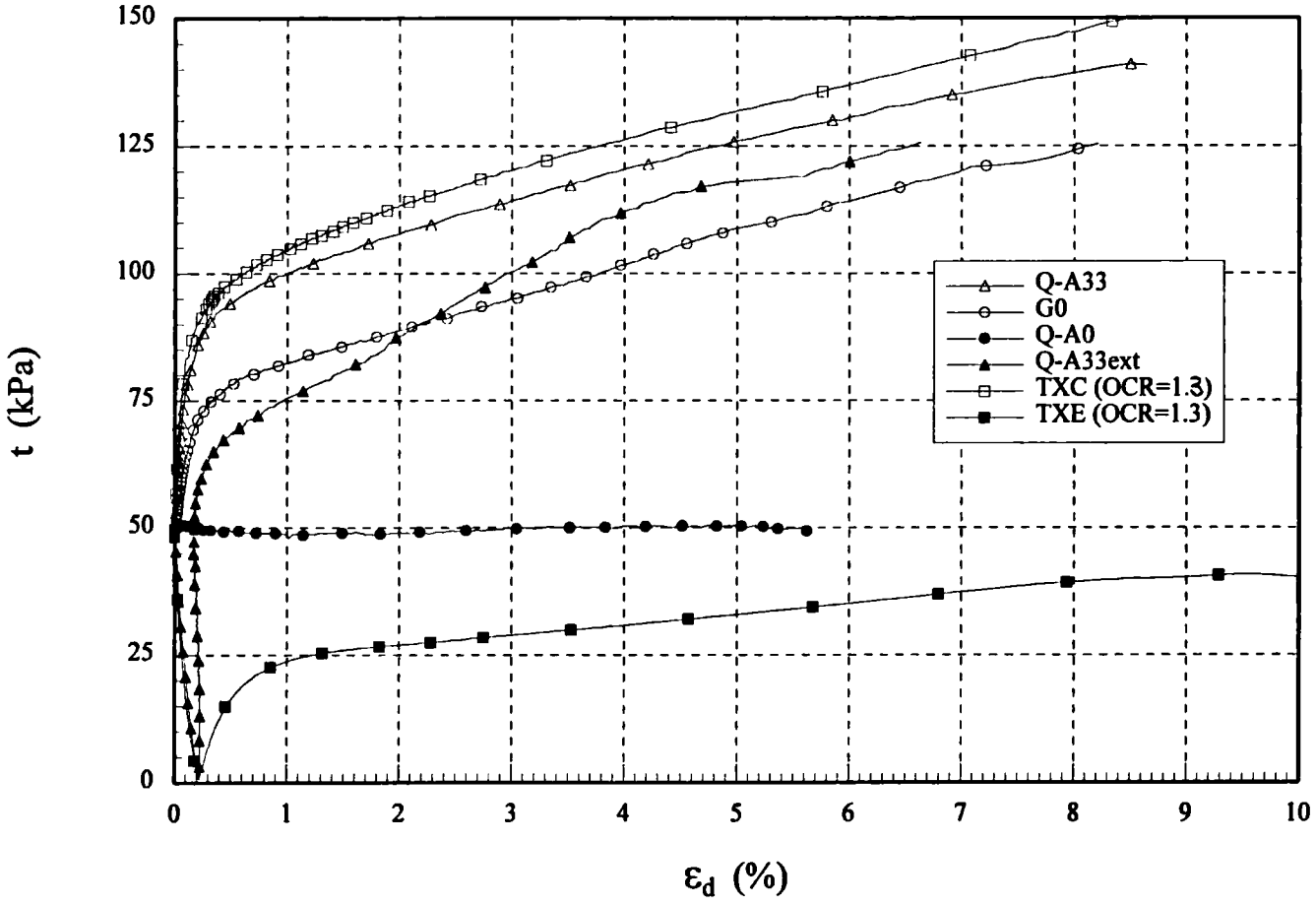


Fig.6.8 - Stress-strain curves developed during undrained shearing paths of Q-A Series

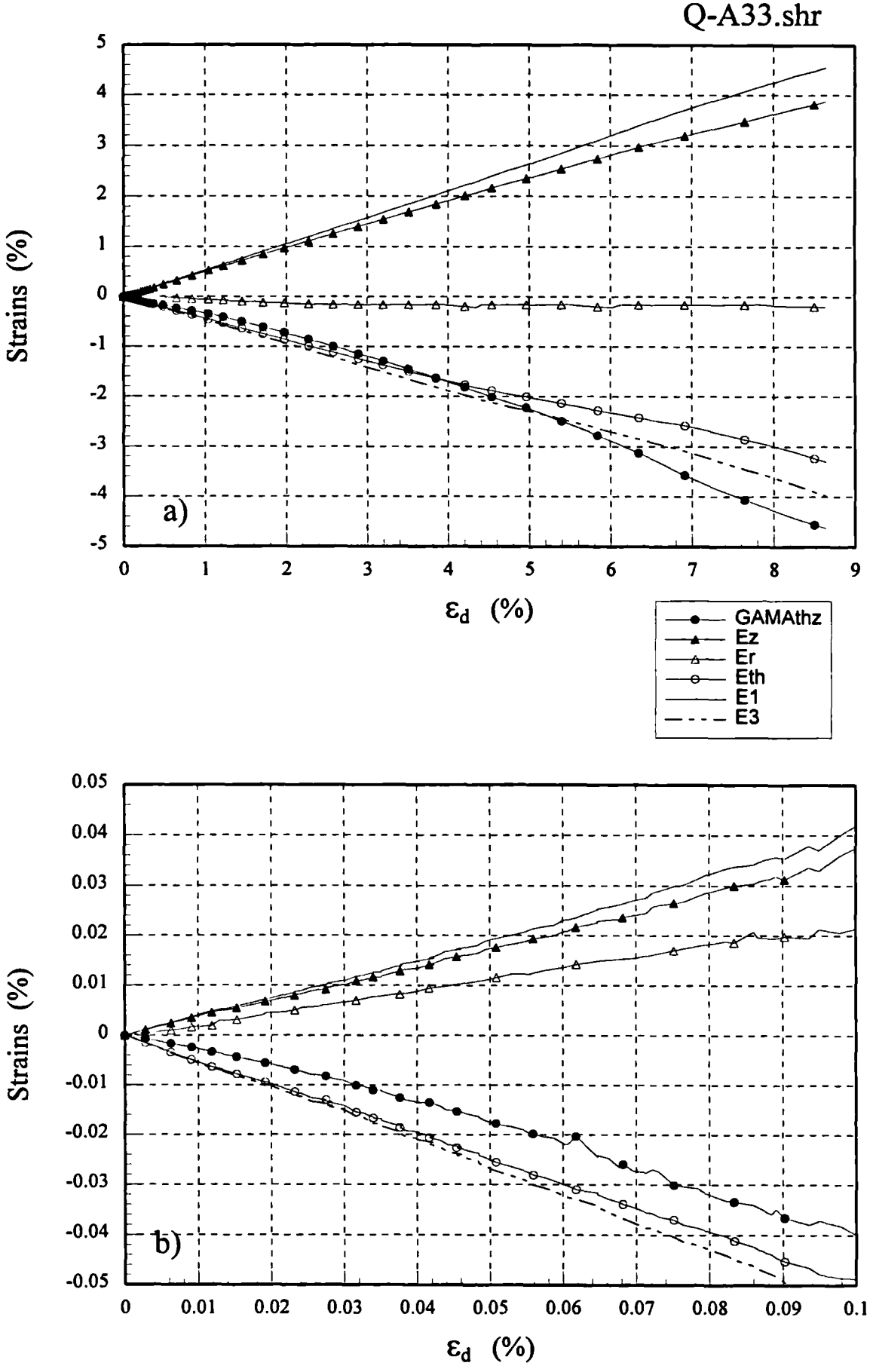


Fig.6.9 - a) Strain components for Q-A33 shearing stress path
b) Small strain region

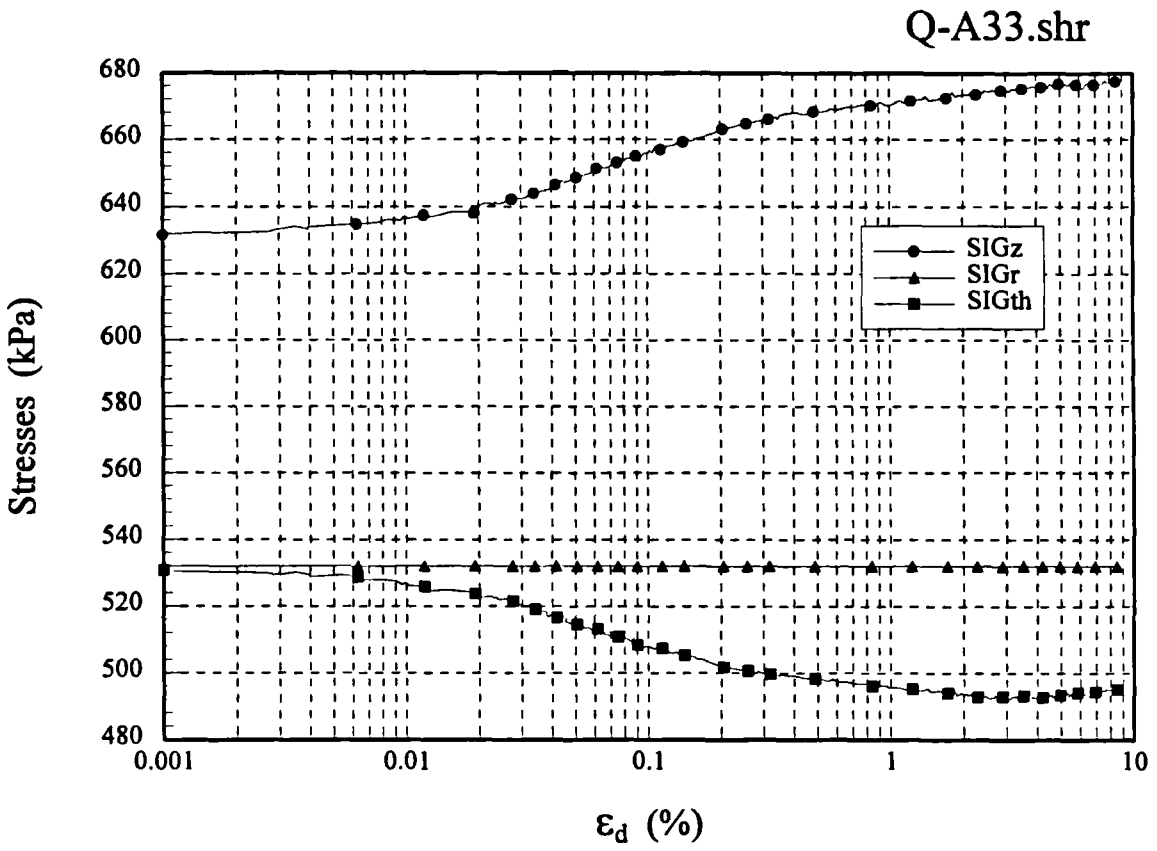


Fig.6.10a - Direct component stresses for shearing stress path Q-A33

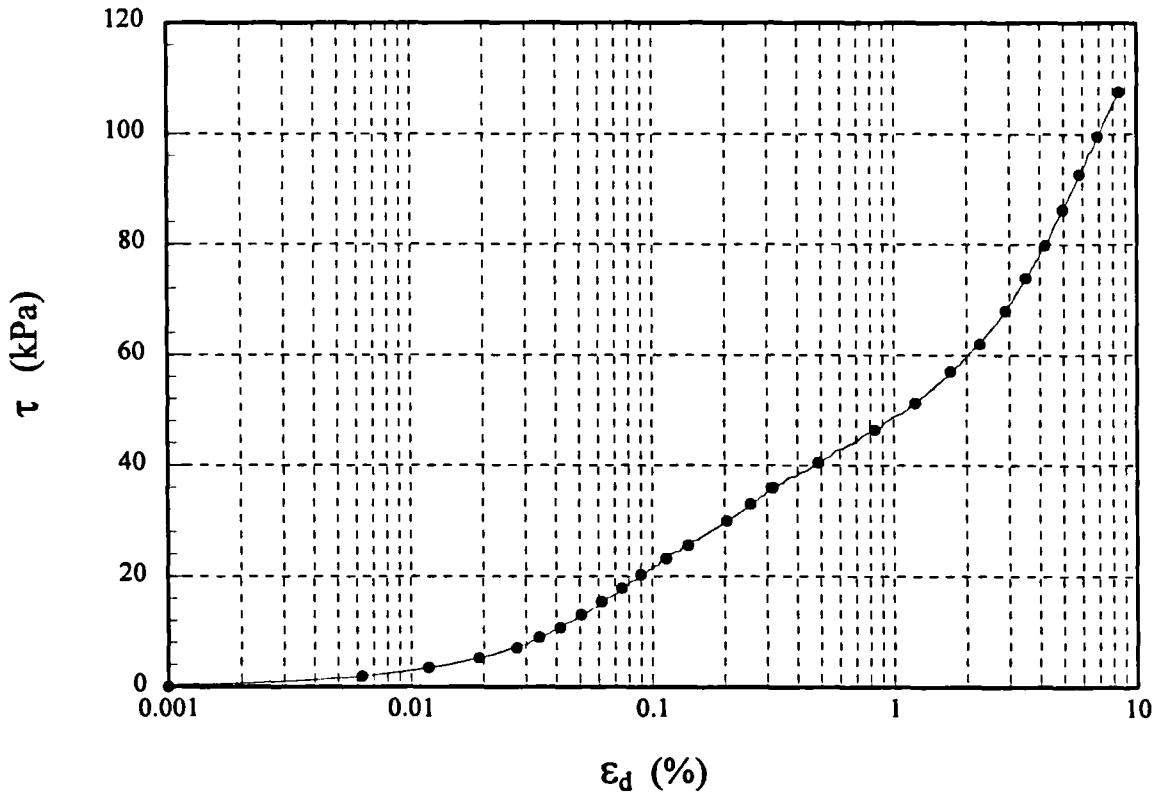
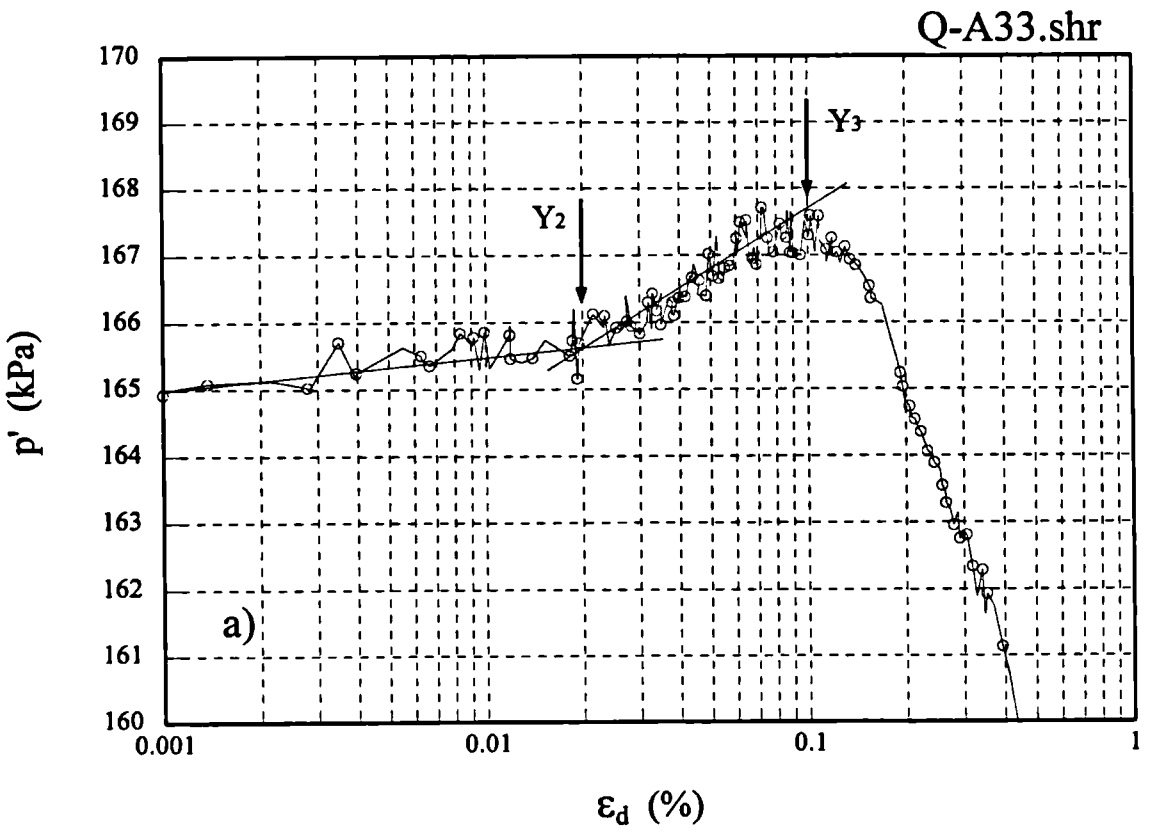


Fig.6.10b - Torsional shear stress during shearing stress path Q-A33



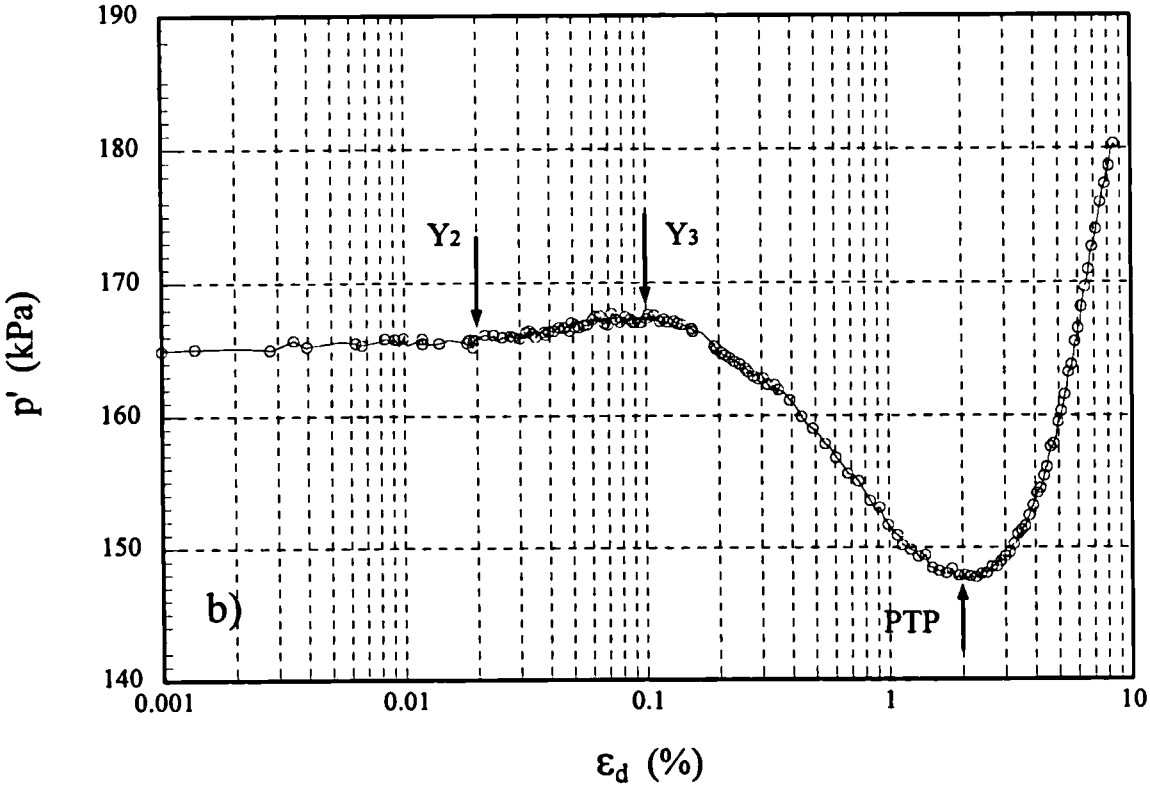


Fig.6.11 - a) Determination of small strain yield
b) Large strain yield

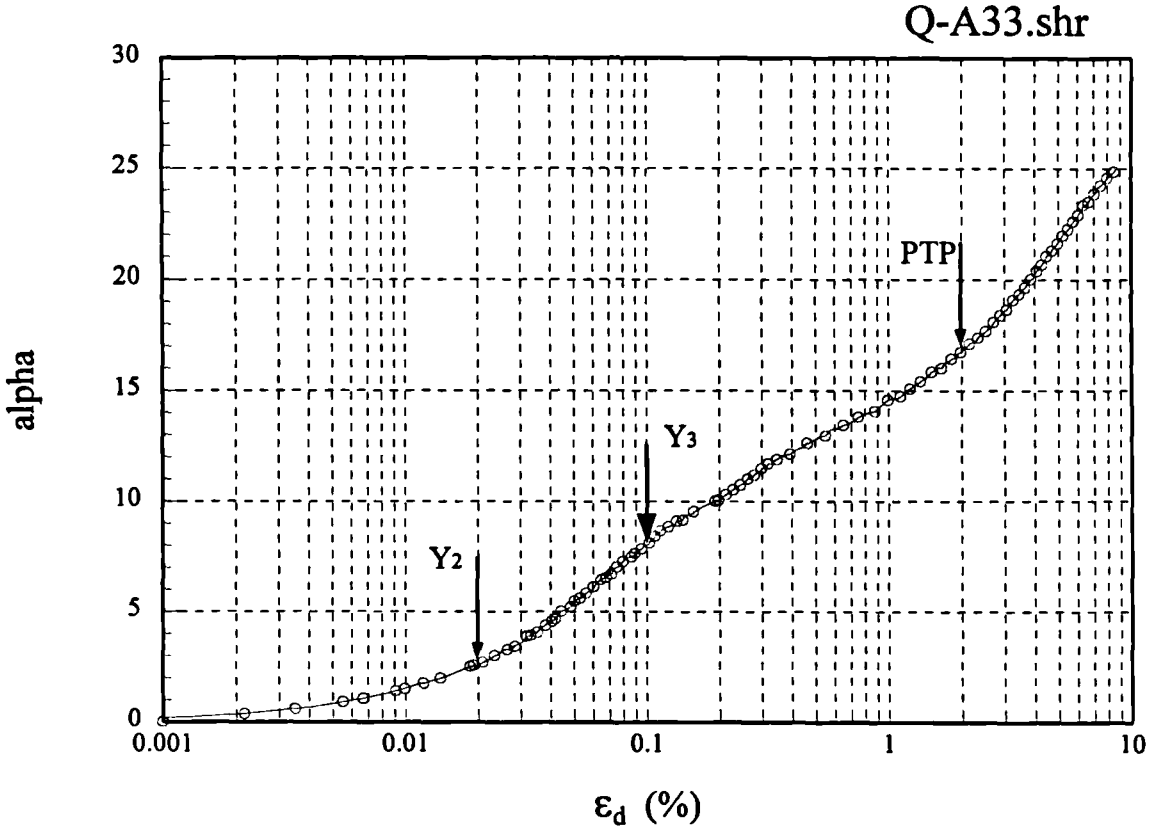


Fig.6.12 - Yield points in respect to α for Q-A33 shearing path

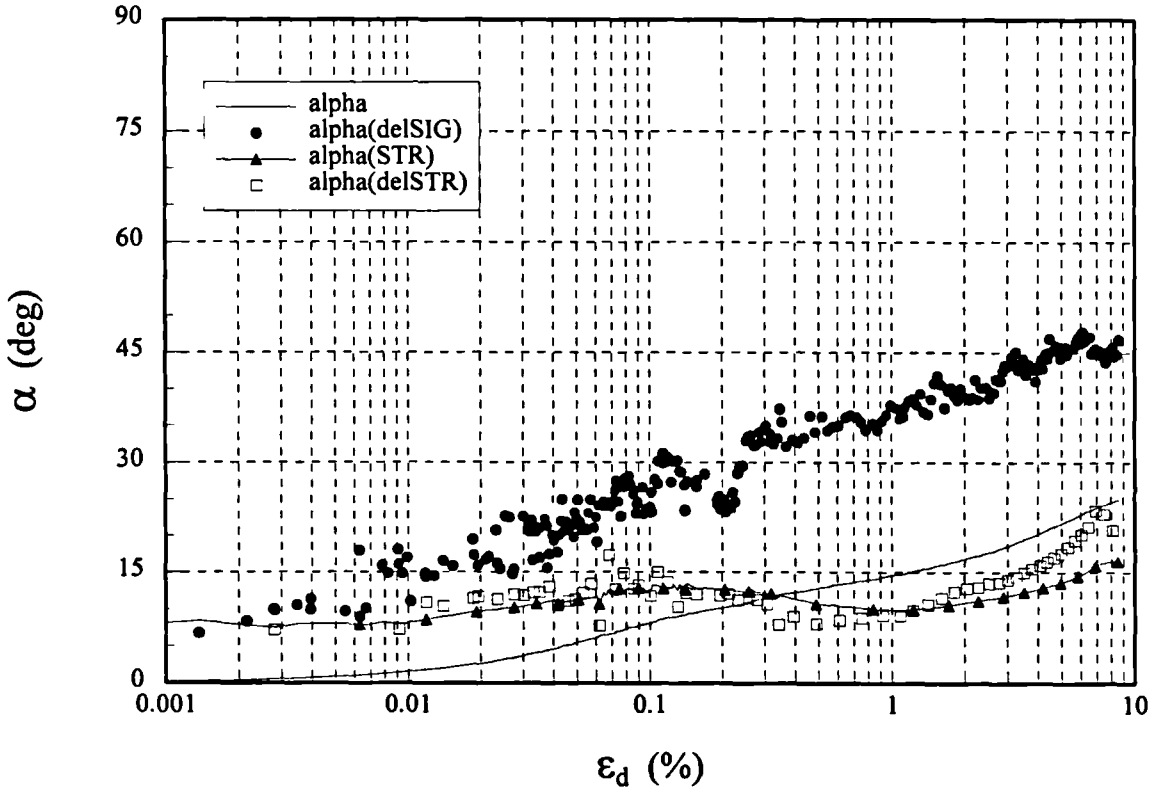
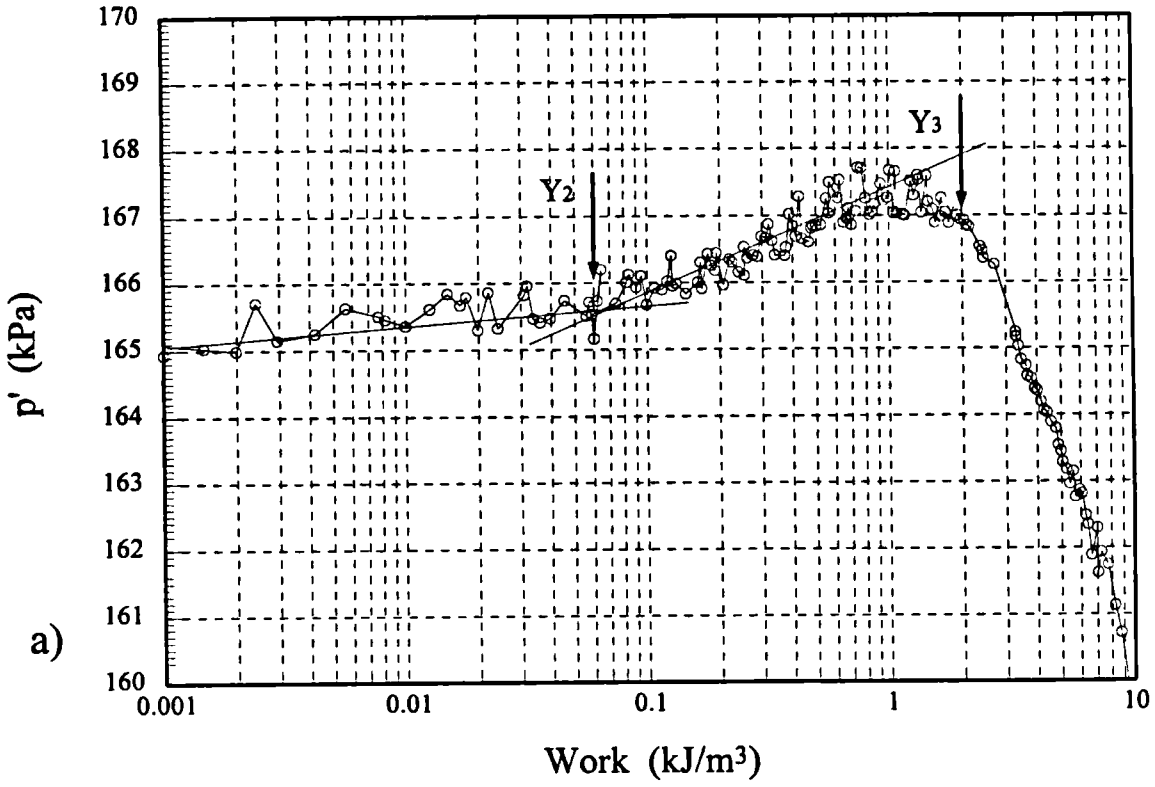


Fig.6.13 - Directions of stresses and strains and their increments for Q-A33 shearing path



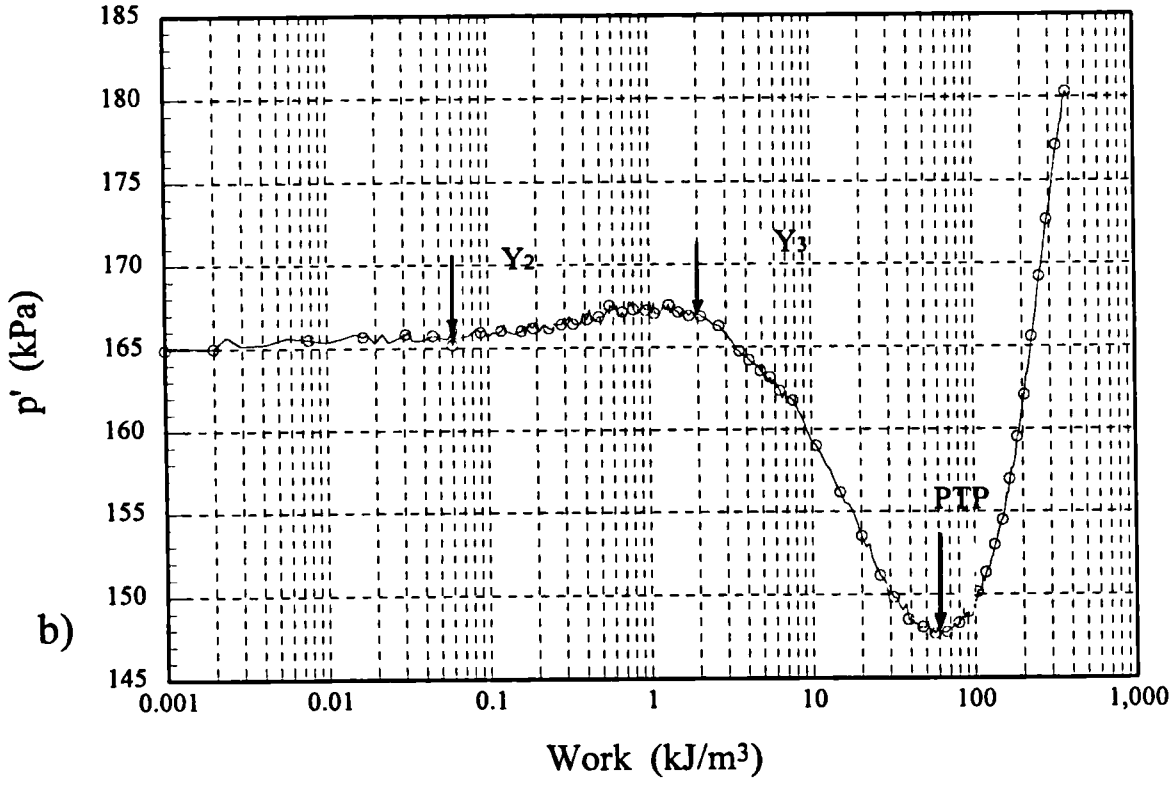


Fig.6.14 - a), b) Determination of yield points in respect to work

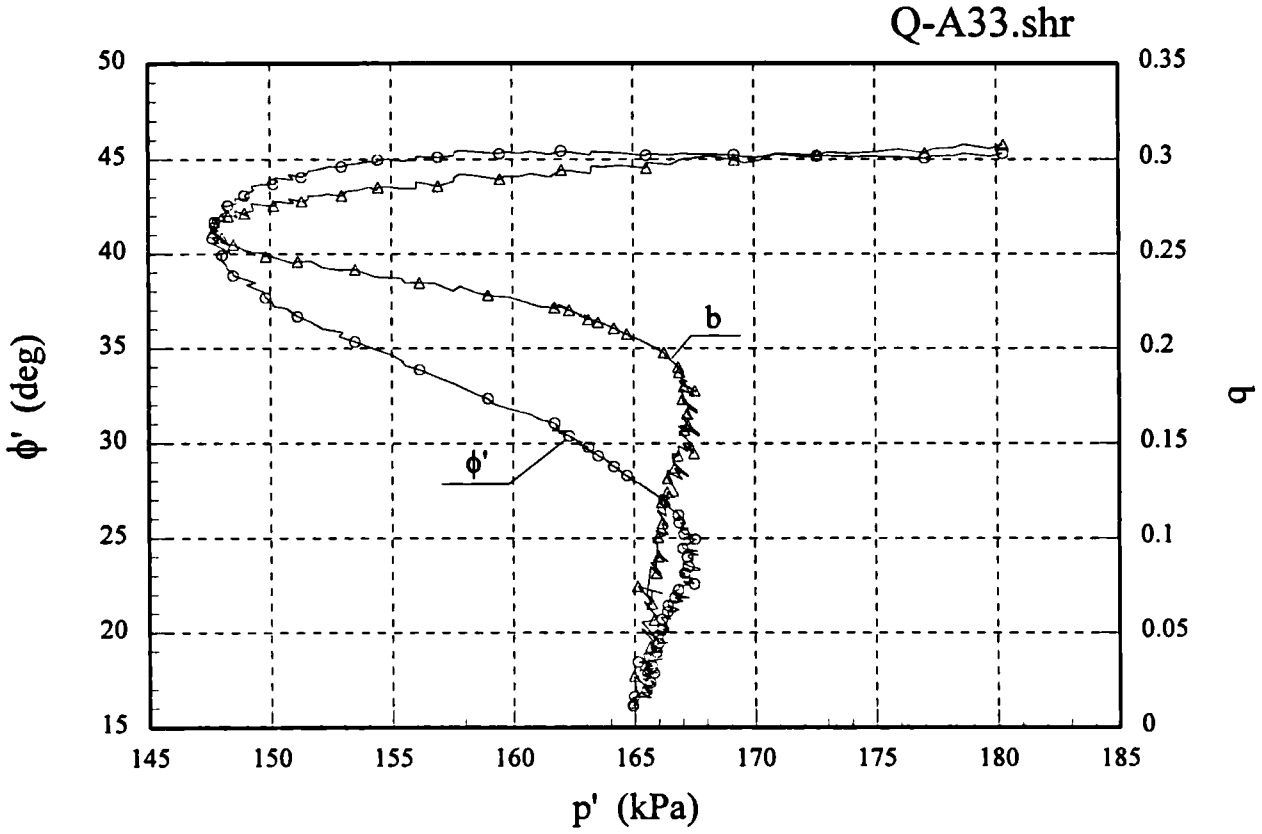


Fig.6.15 - Generation of b and ϕ' during Q-A33 shearing stress path

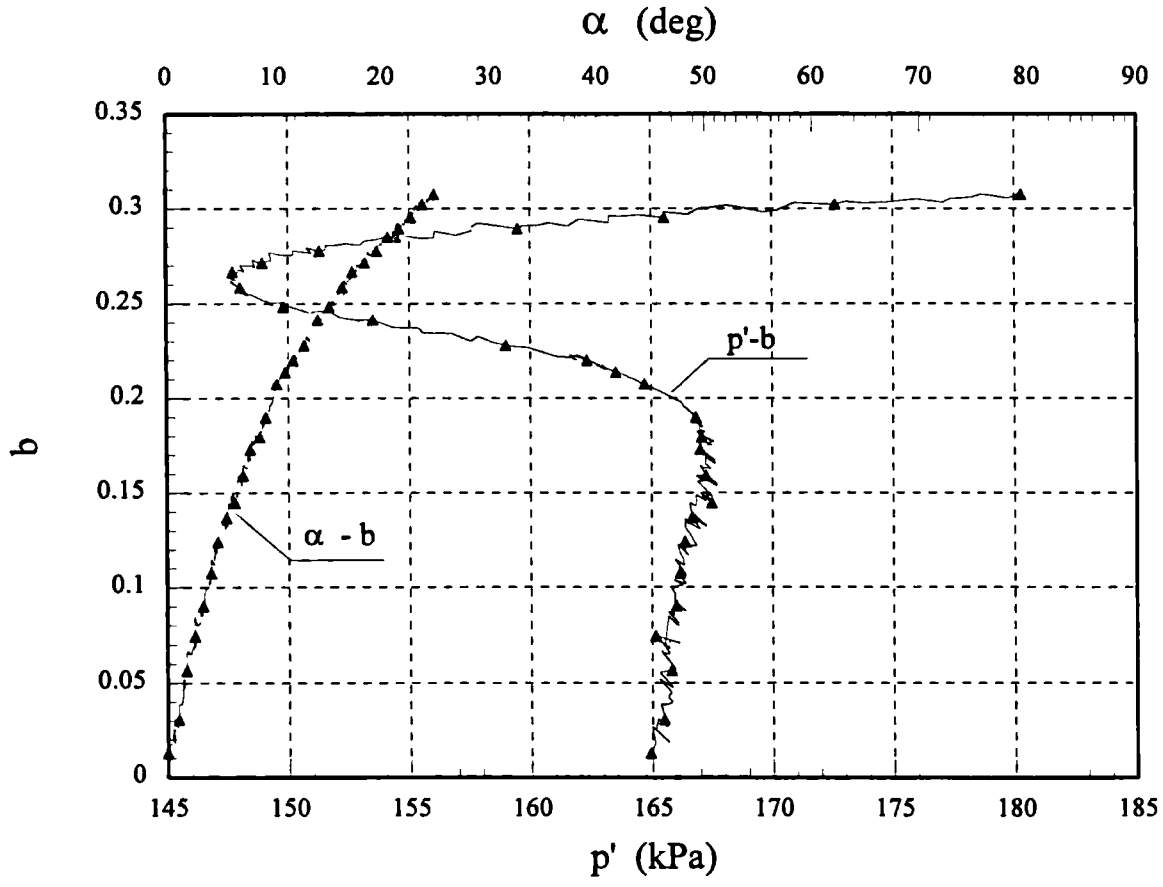


Fig.6.16 - Generation of b and α during Q-A33 shearing stress path

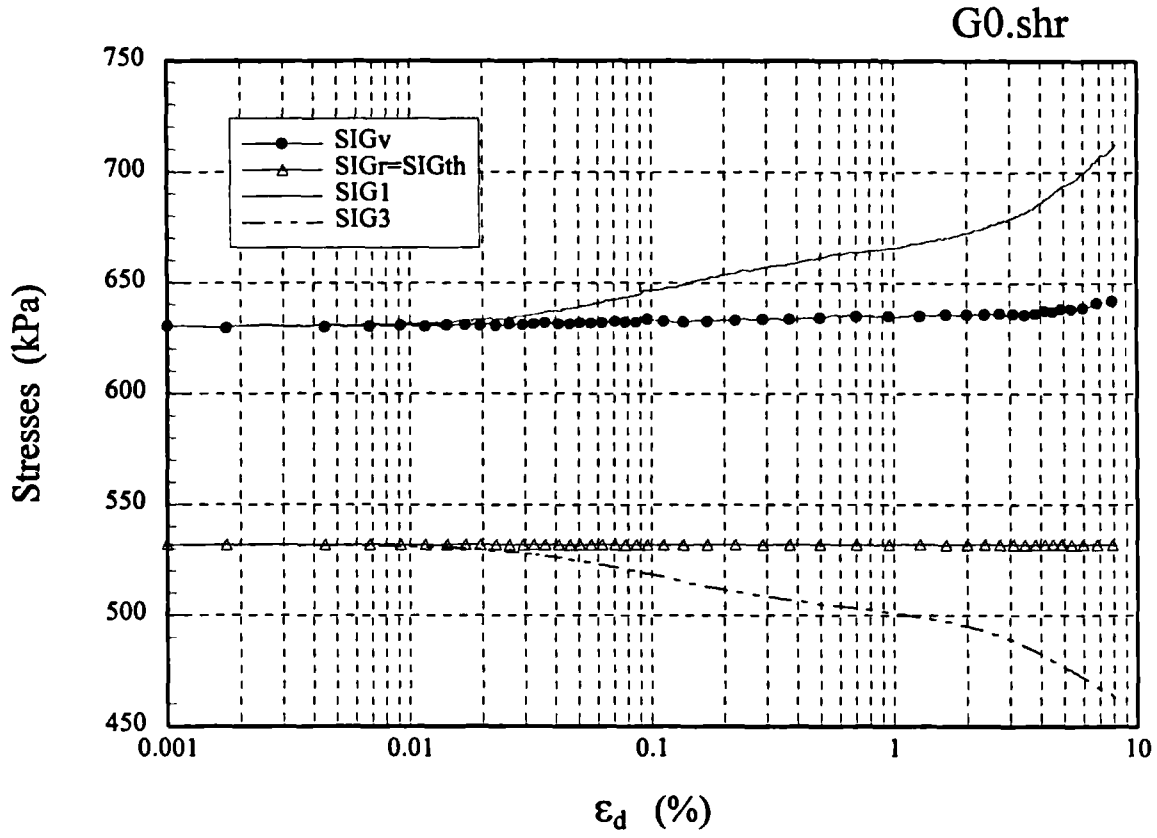


Fig.6.17a - Direct component stresses for shearing stress path G0

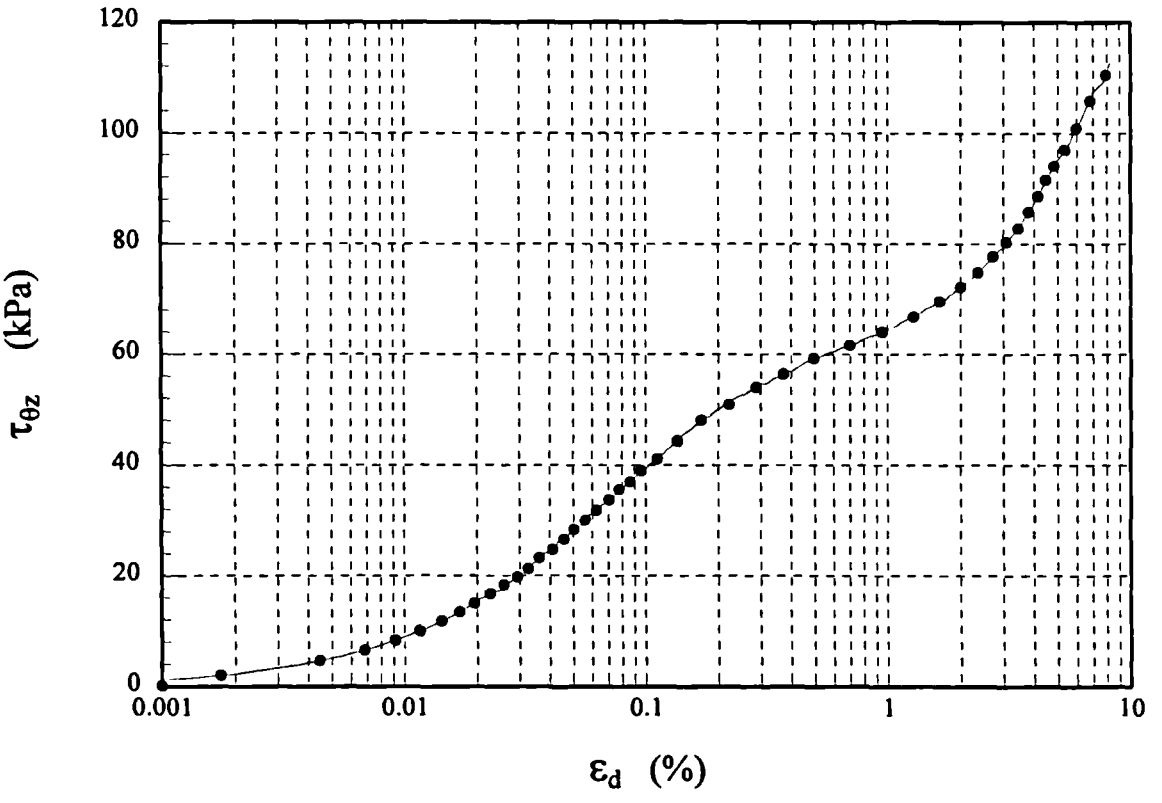


Fig.6.17b - Torsional shear stress during shearing stress path G0

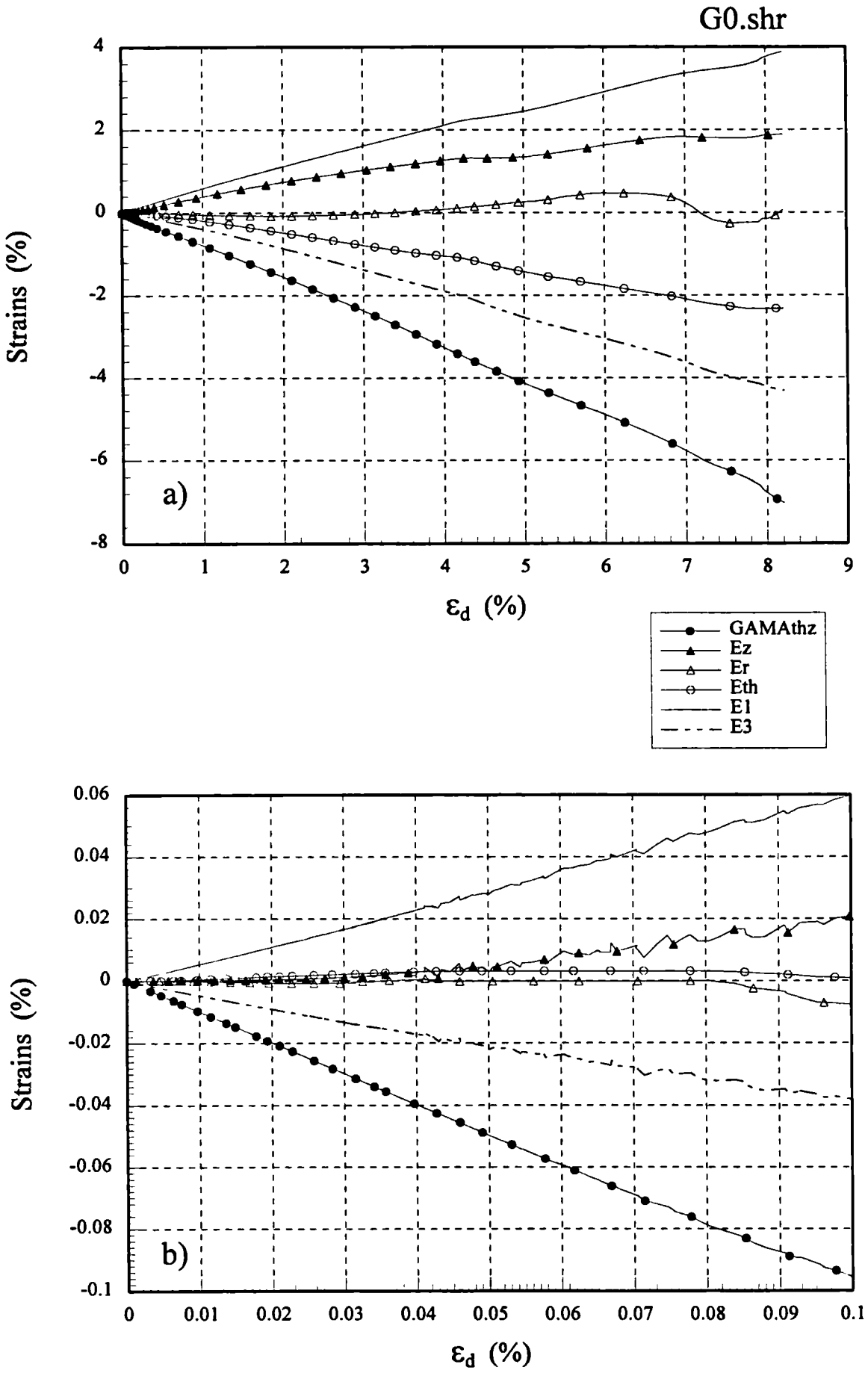


Fig.6.18 - a) Strain components for G0 shearing stress path
b) Small strain region

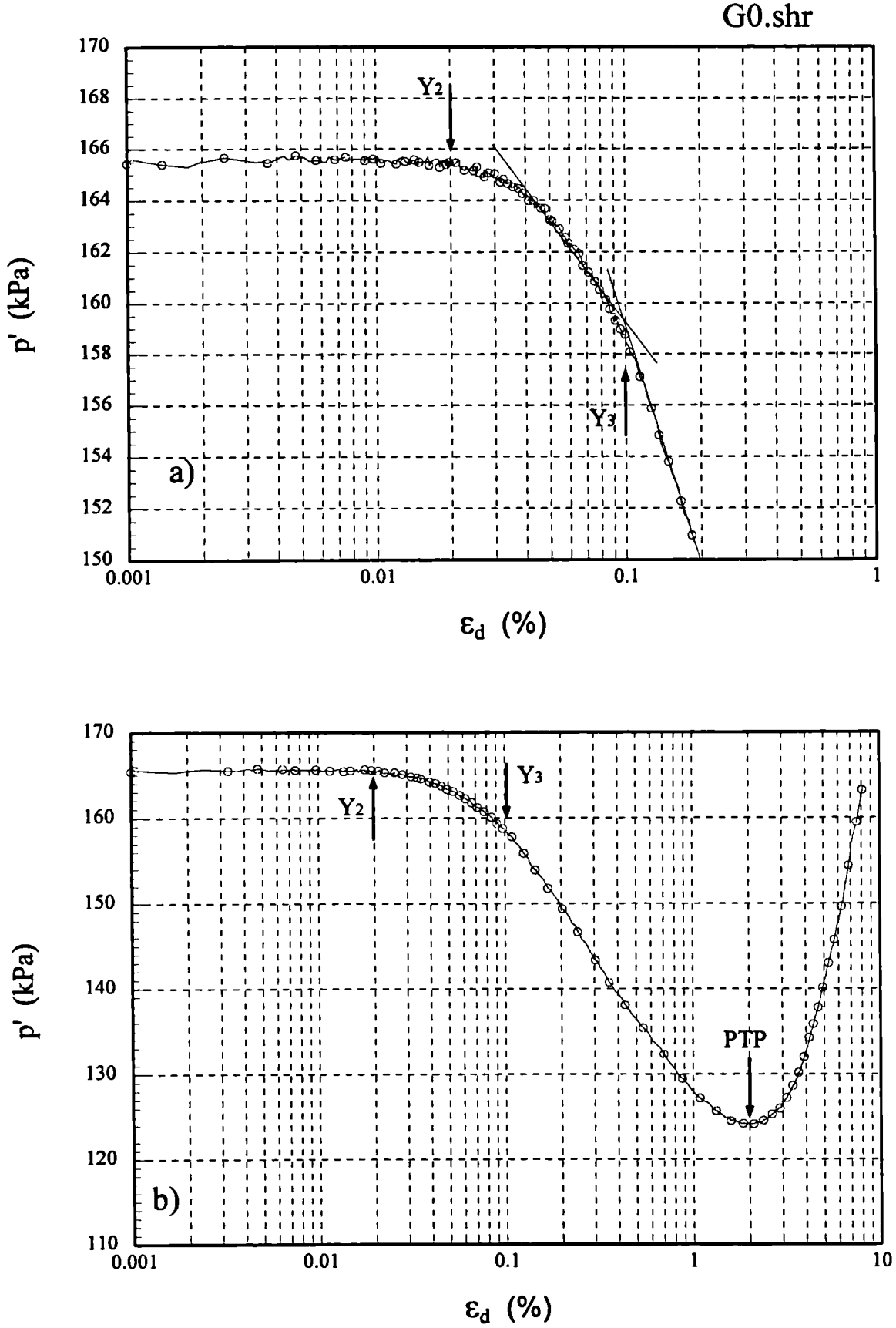


Fig.6.19 - a) Determination of small strain yield
b) Large strain yield

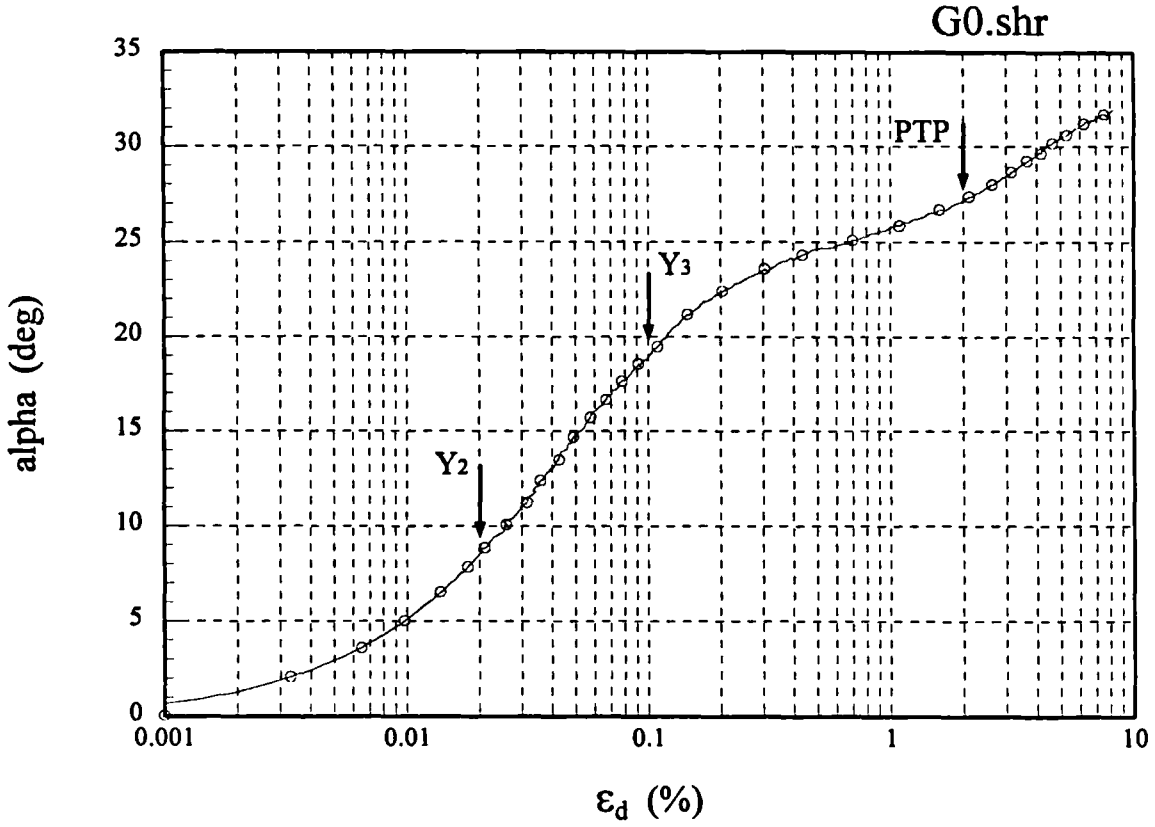


Fig.6.20 - Yield points in respect to α for G0 shearing path

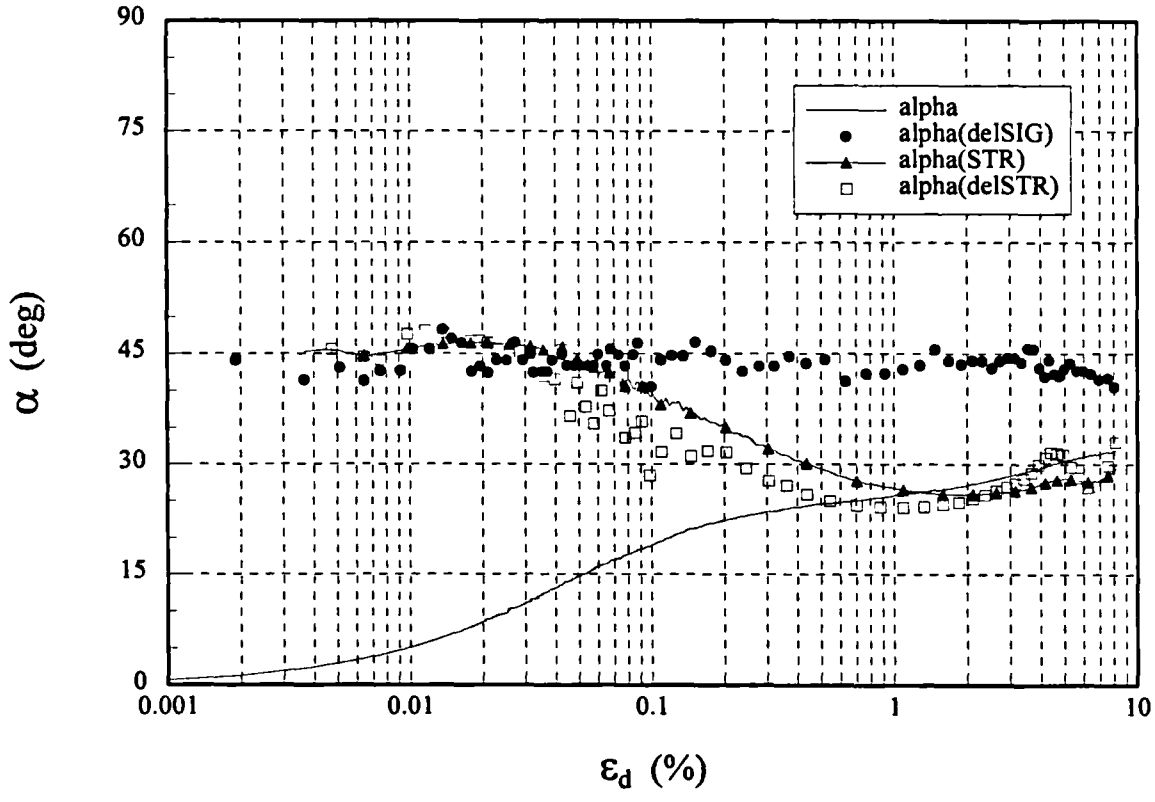
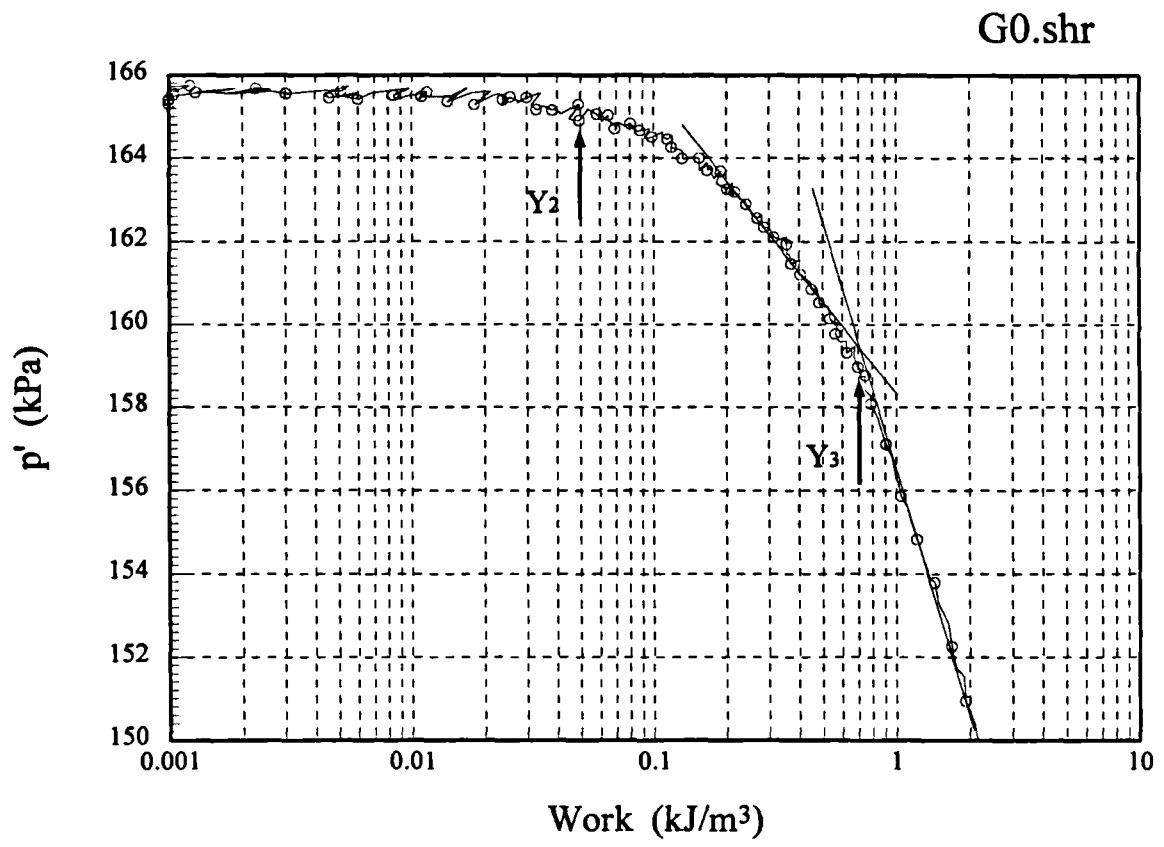


Fig.6.21 - Directions of stresses and strains and their increments for G0 shearing path



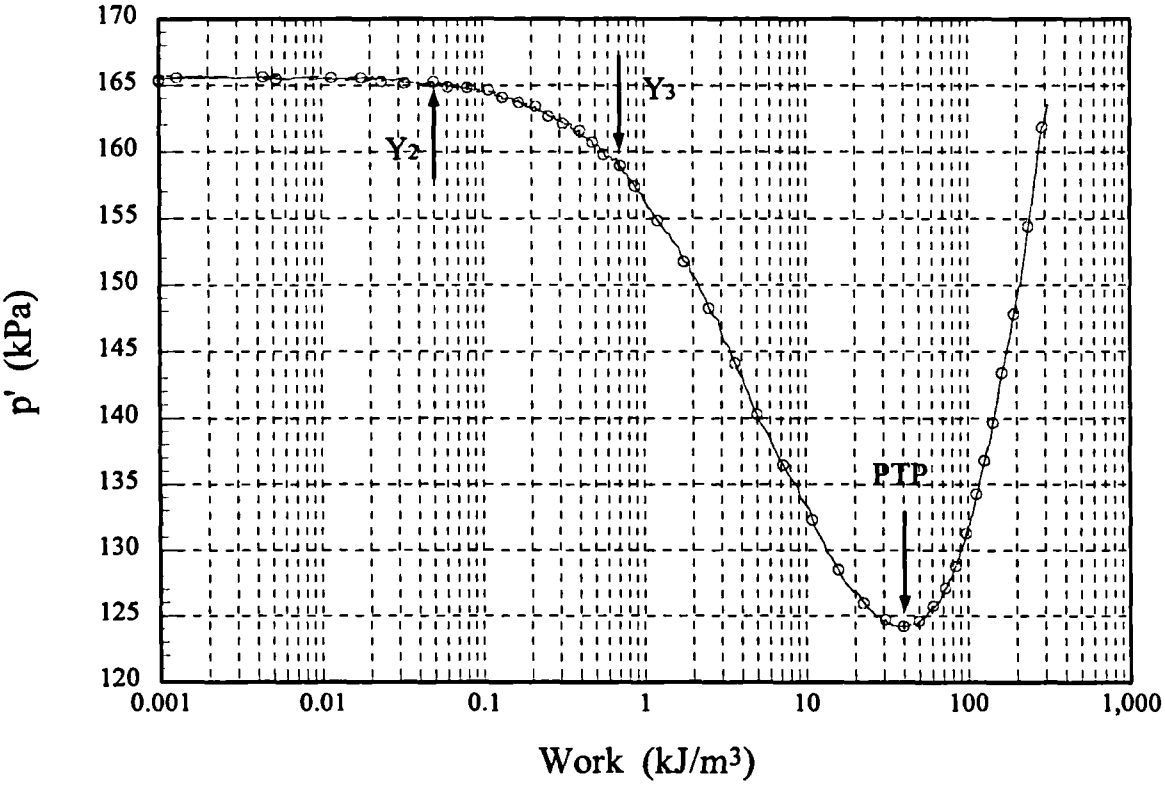


Fig.6.22 - a), b) Determination of yield points in respect to work

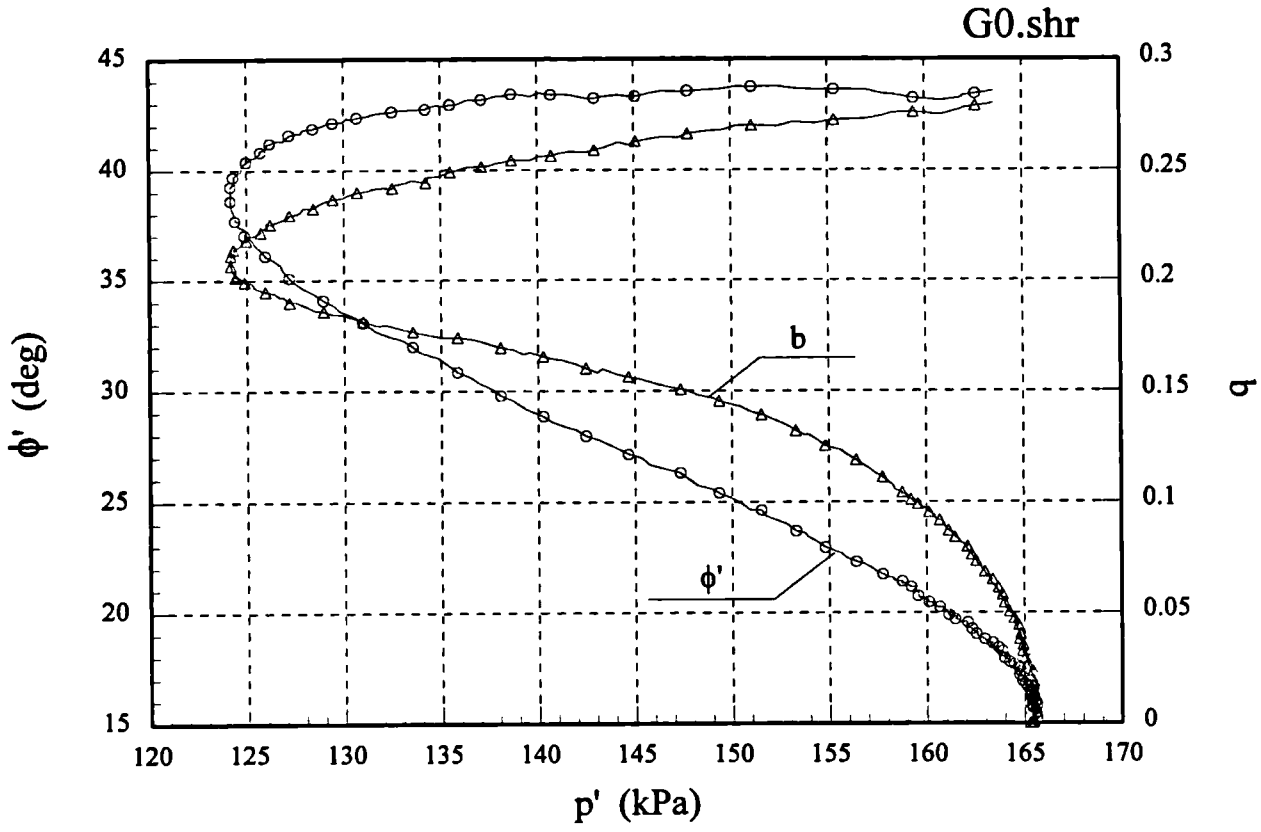


Fig.6.23 - Generation of b and ϕ' during G0 shearing stress path

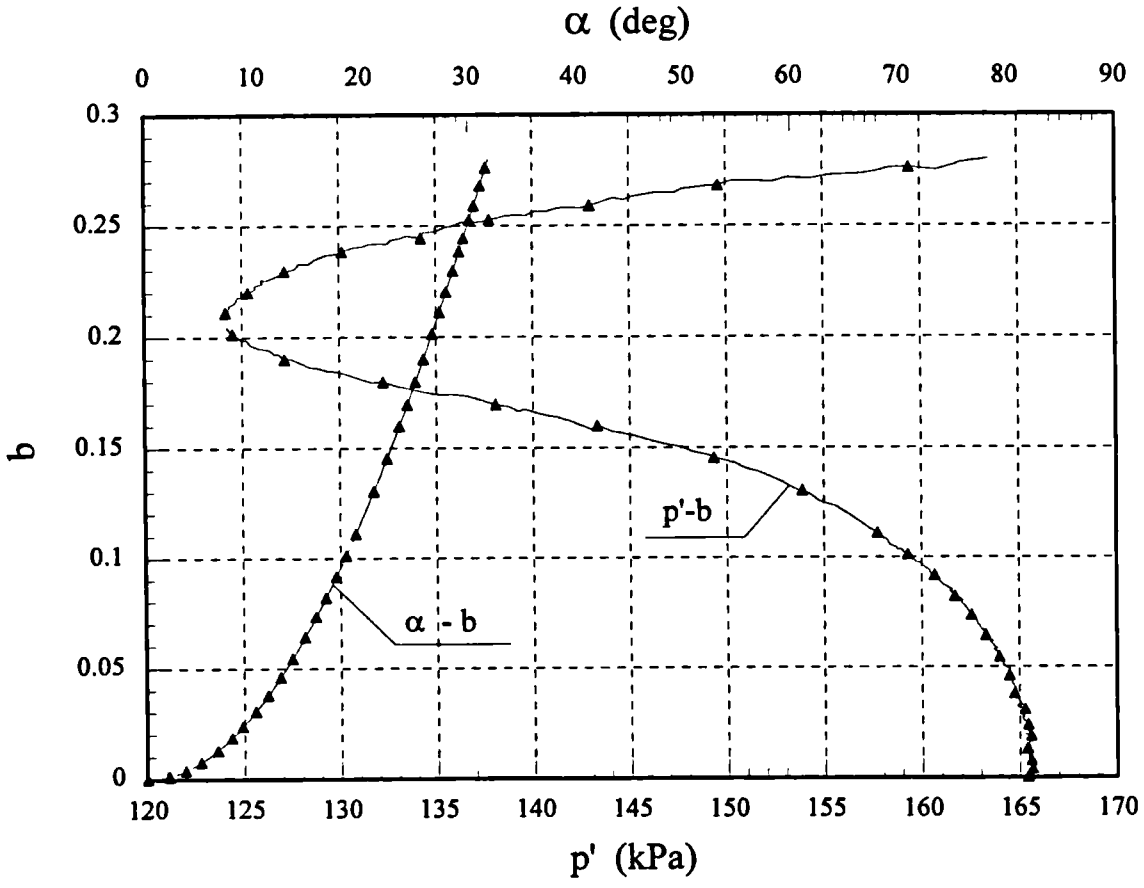


Fig.6.24 - Generation of b and α during G0 shearing stress path

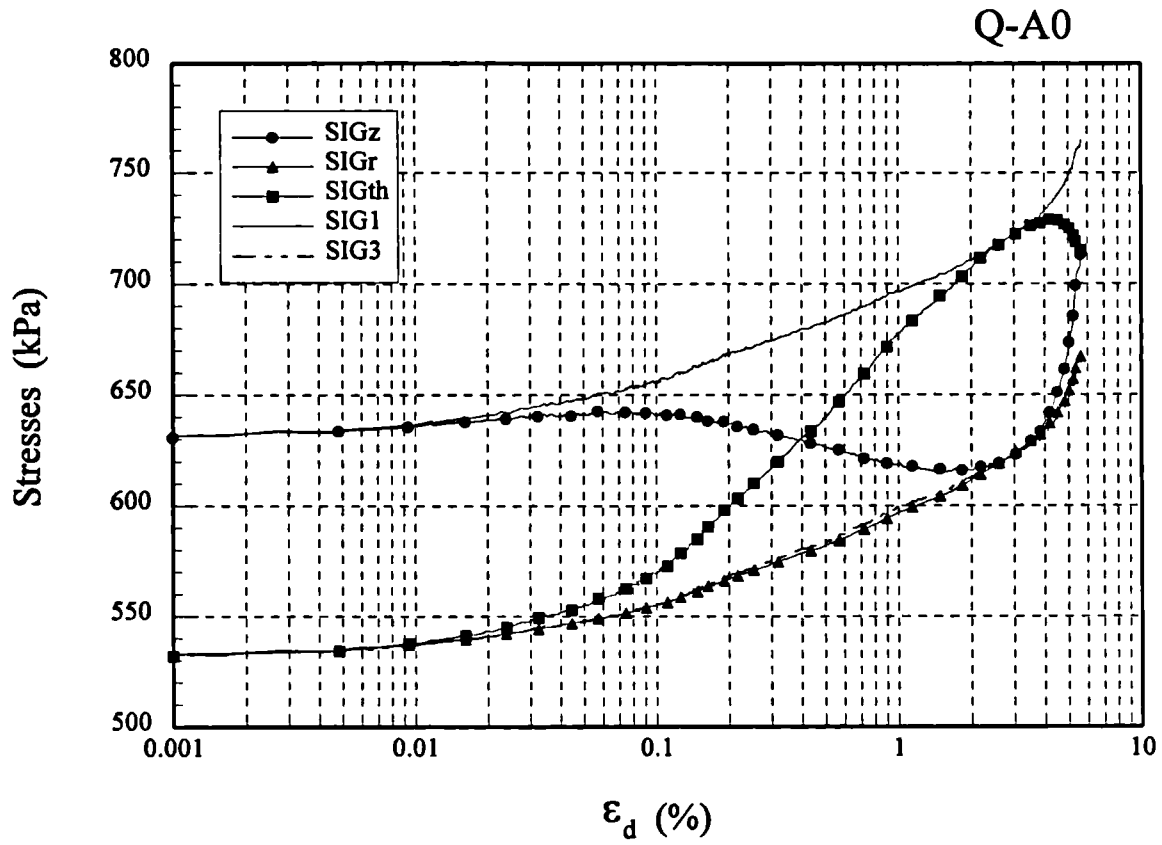


Fig.6.25a - Direct component stresses for shearing stress path Q-A0

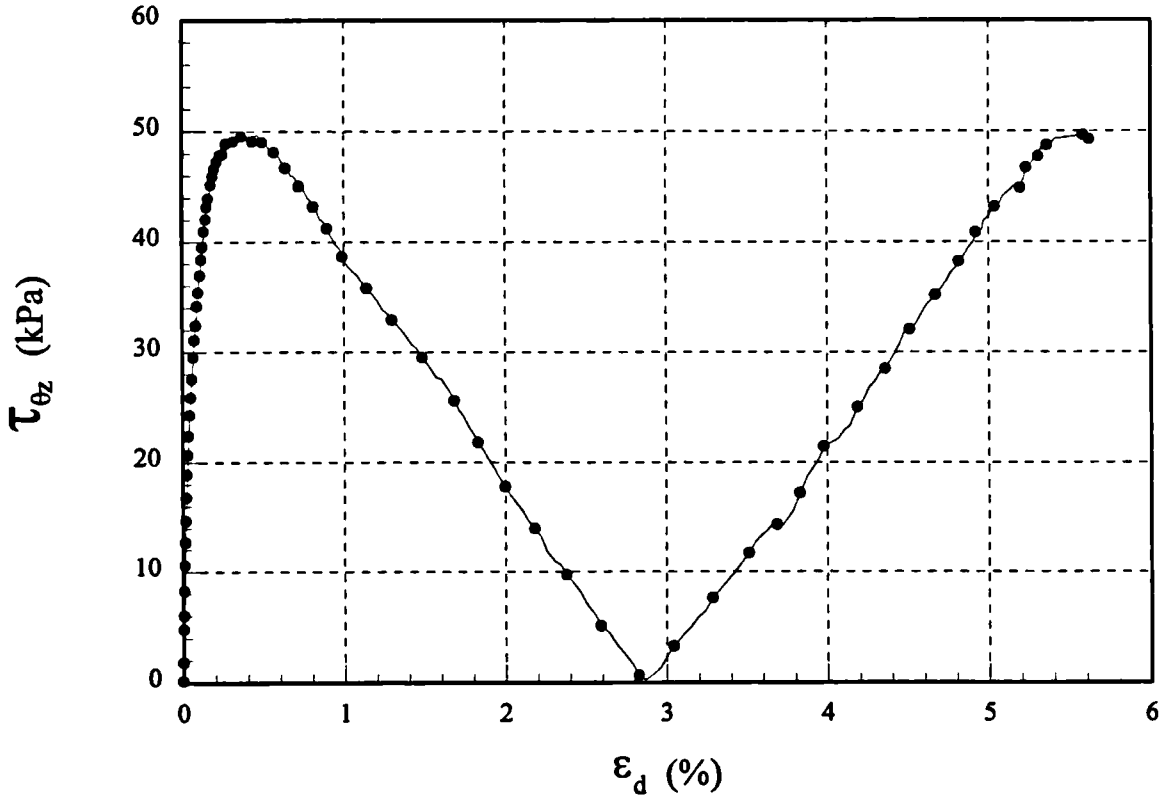


Fig.6.25b - Torsional shear stress during shearing stress path Q-A0

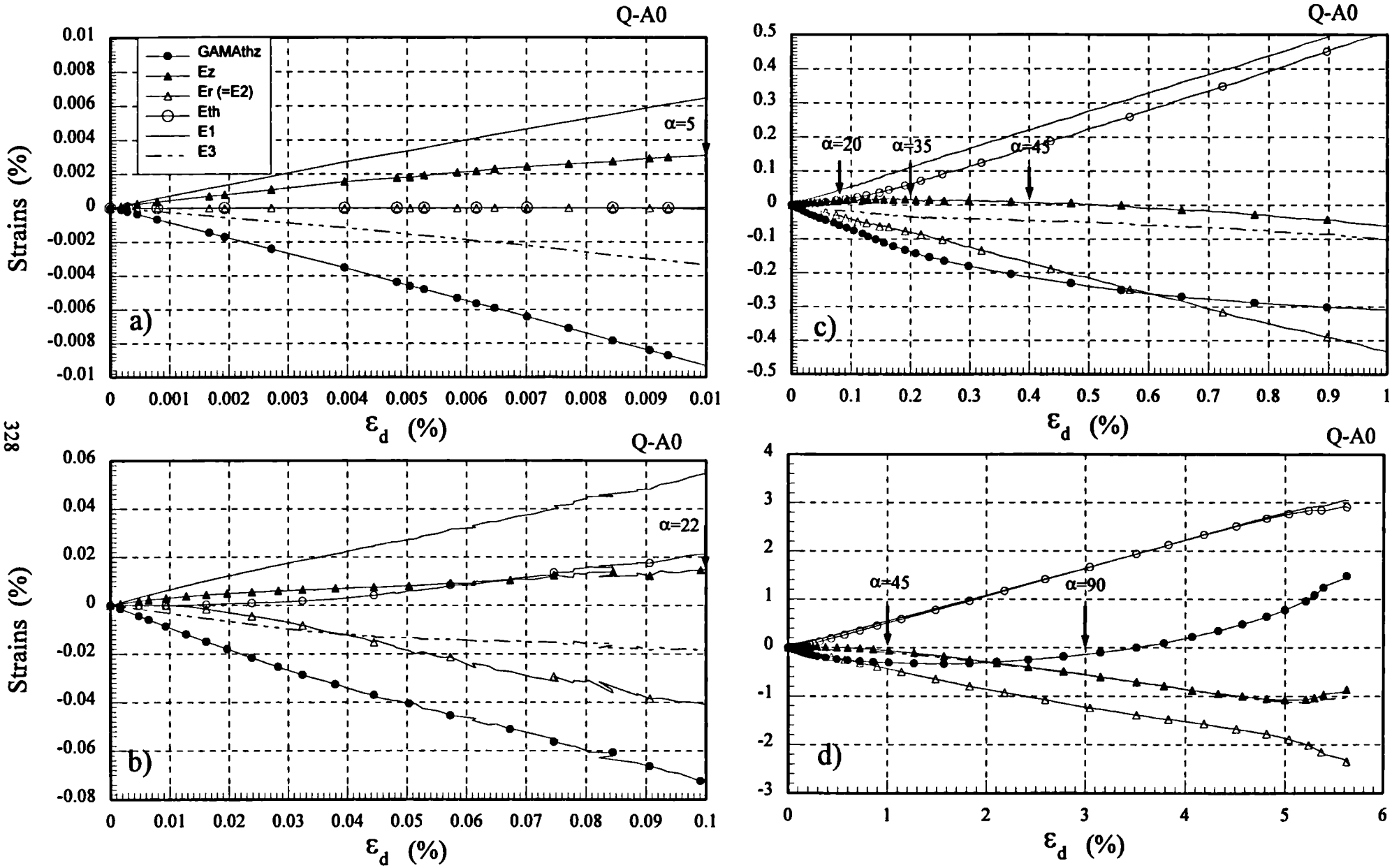


Fig.6.26 - Strain components for Q-A0 shearing stress path

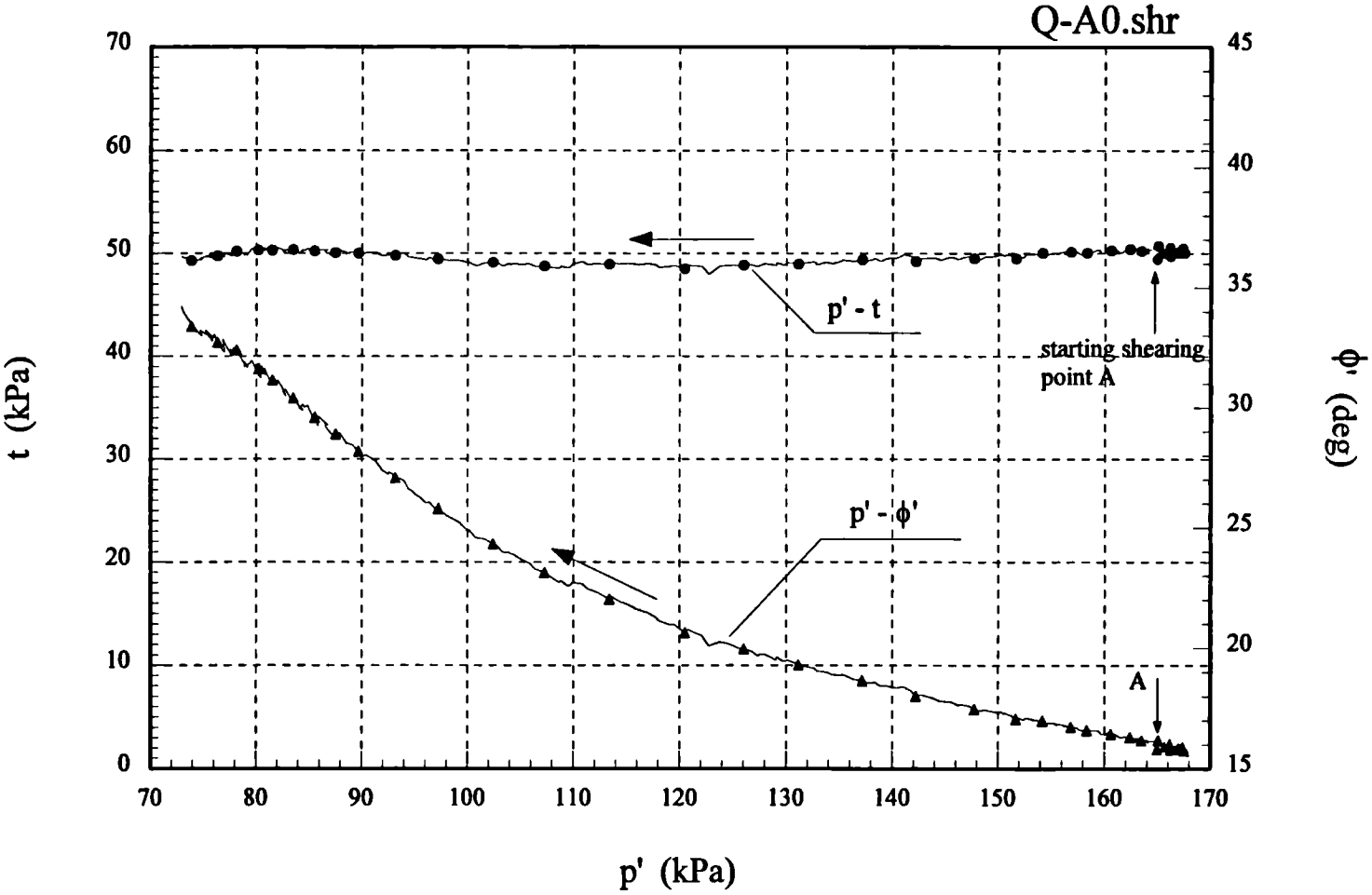


Fig.6.27 - Development of ϕ' with t and p' along Q-A0 stress path

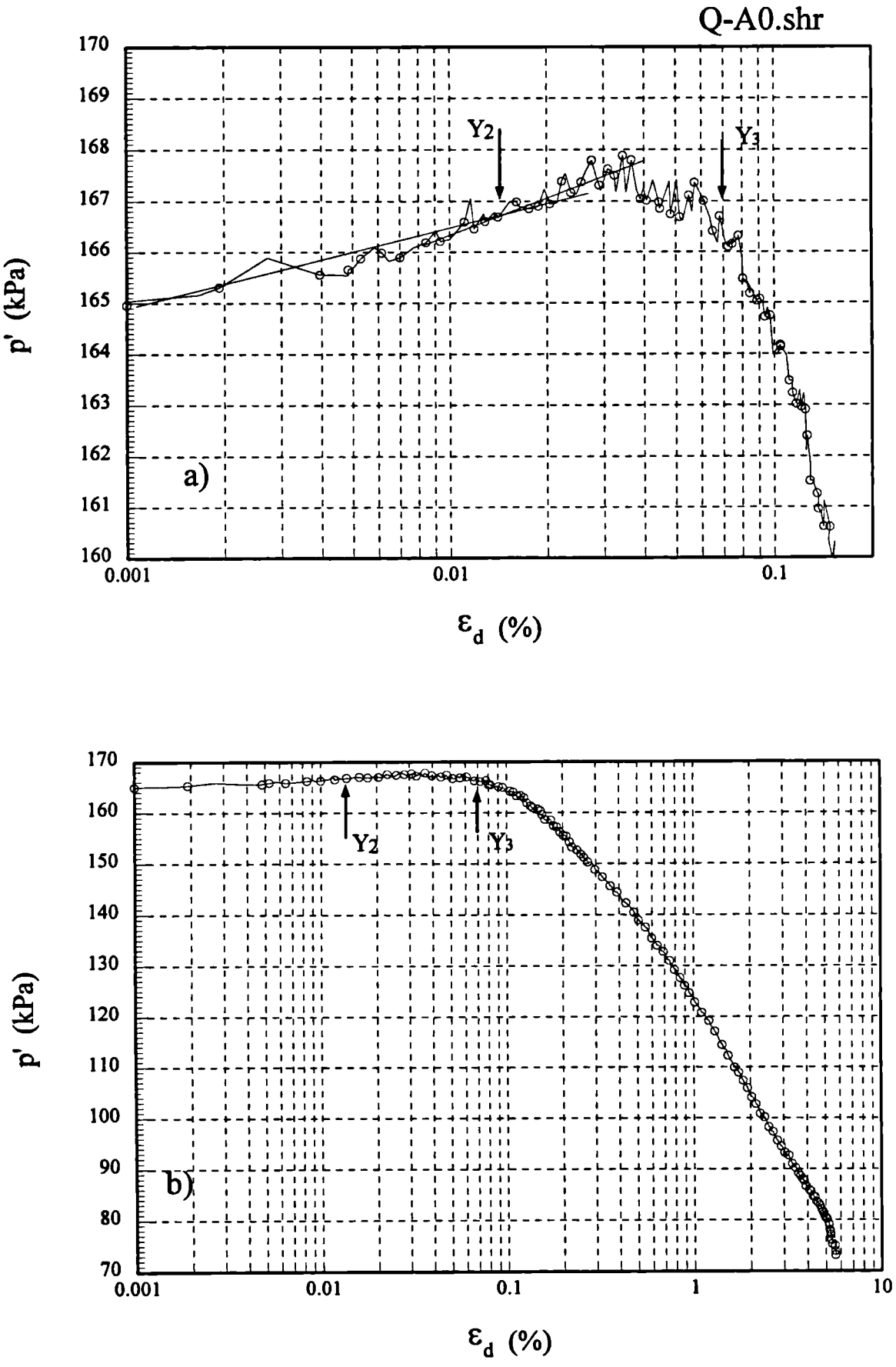


Fig.6.28 - a) Determination of small strain yield
b) Large strain behaviour

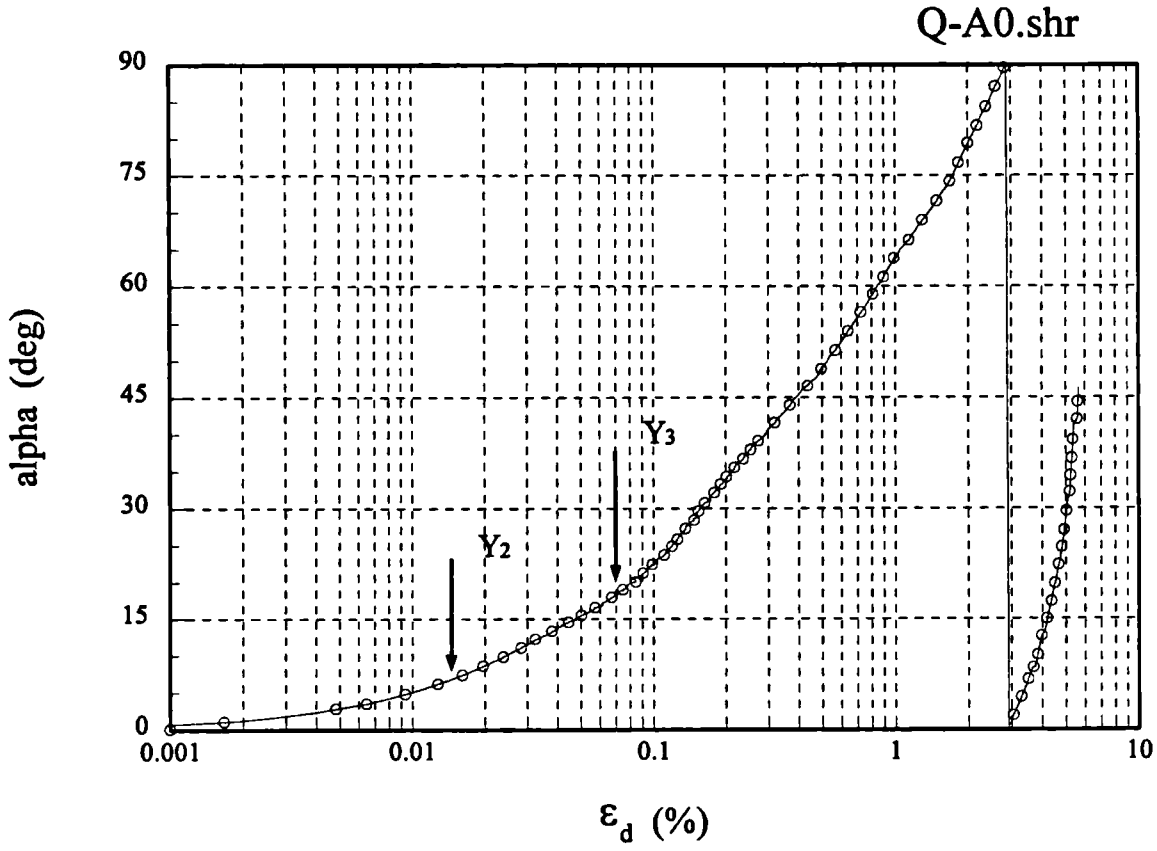


Fig.6.29 - Yield points in respect to α for Q-A0 shearing stress path

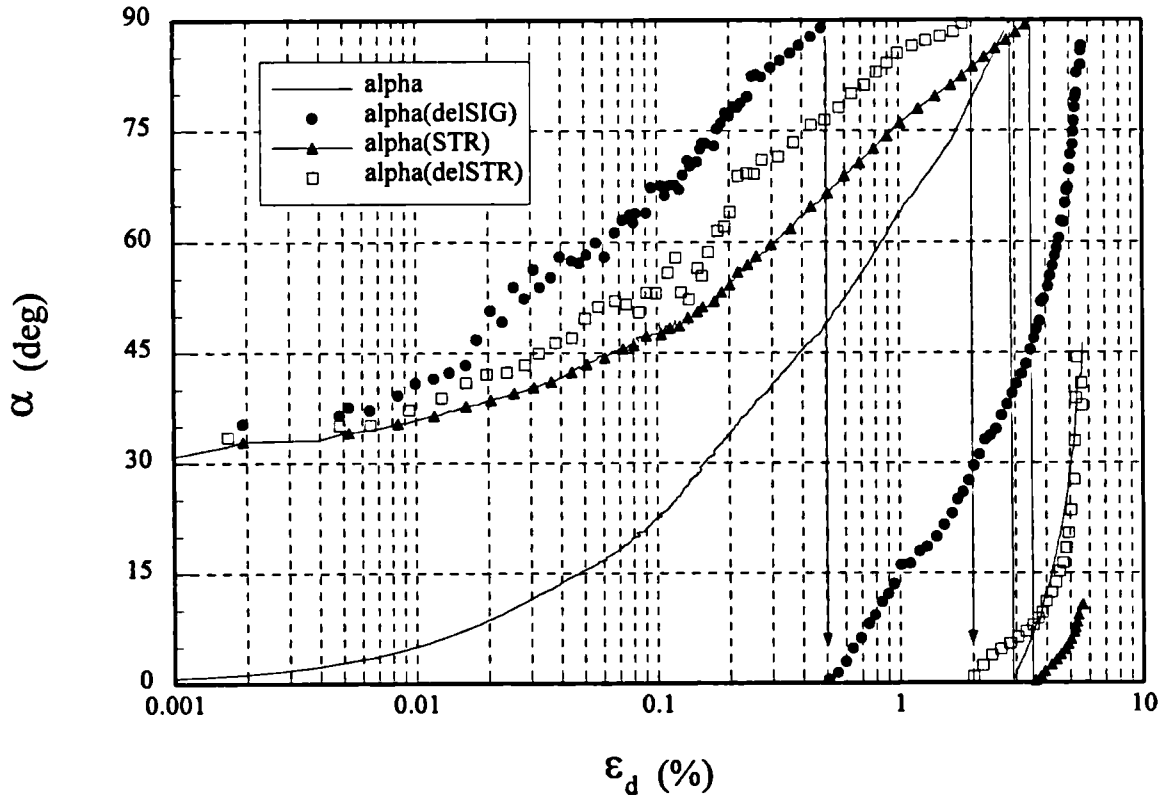


Fig.6.30 - Directions of stresses and strains and their increments for Q-A0 shearing stress path

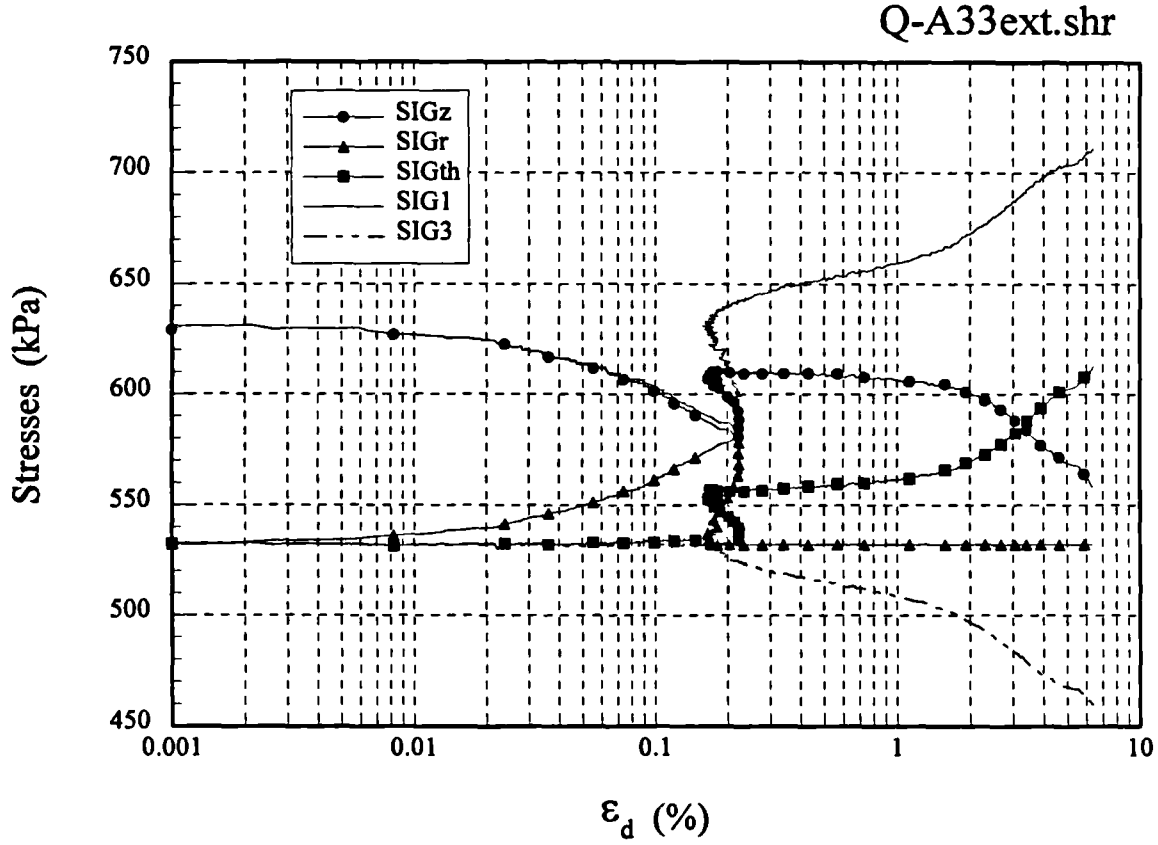


Fig.6.31a - Direct component stresses for shearing stress path Q-A33ext

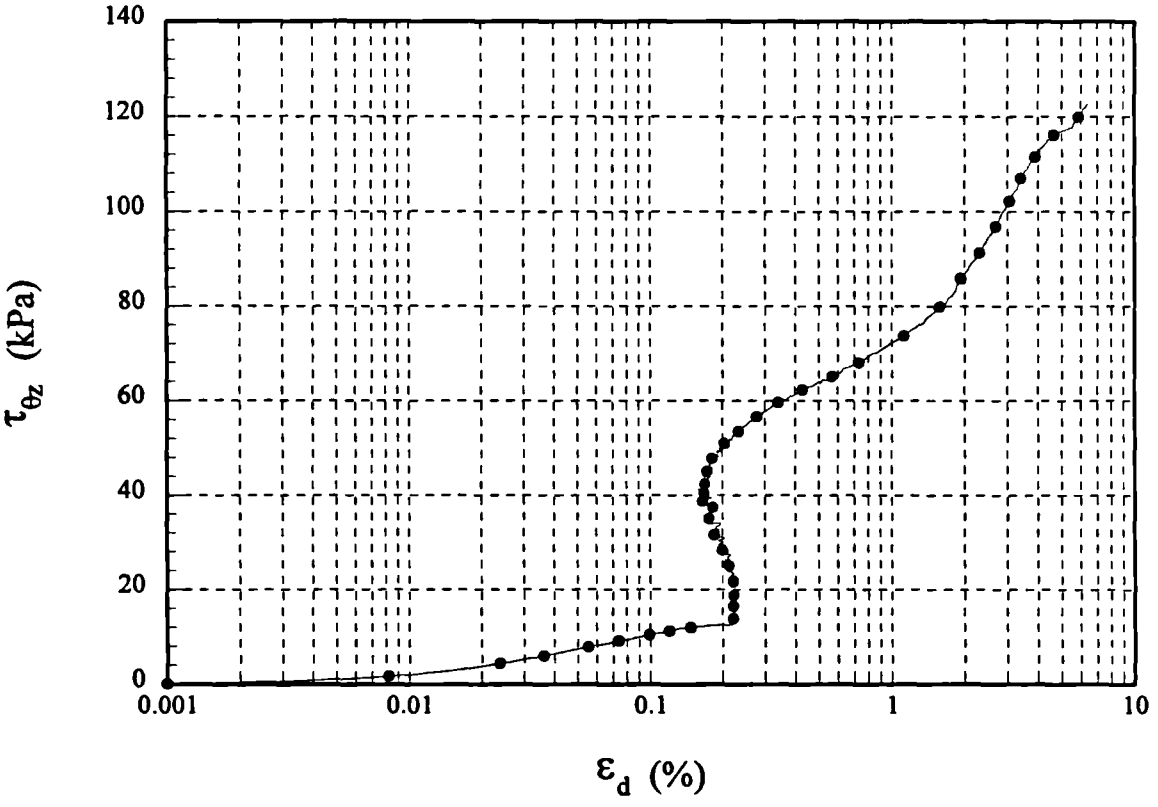


Fig.6.31b - Torsional shear stress during shearing stress path Q-A33ext

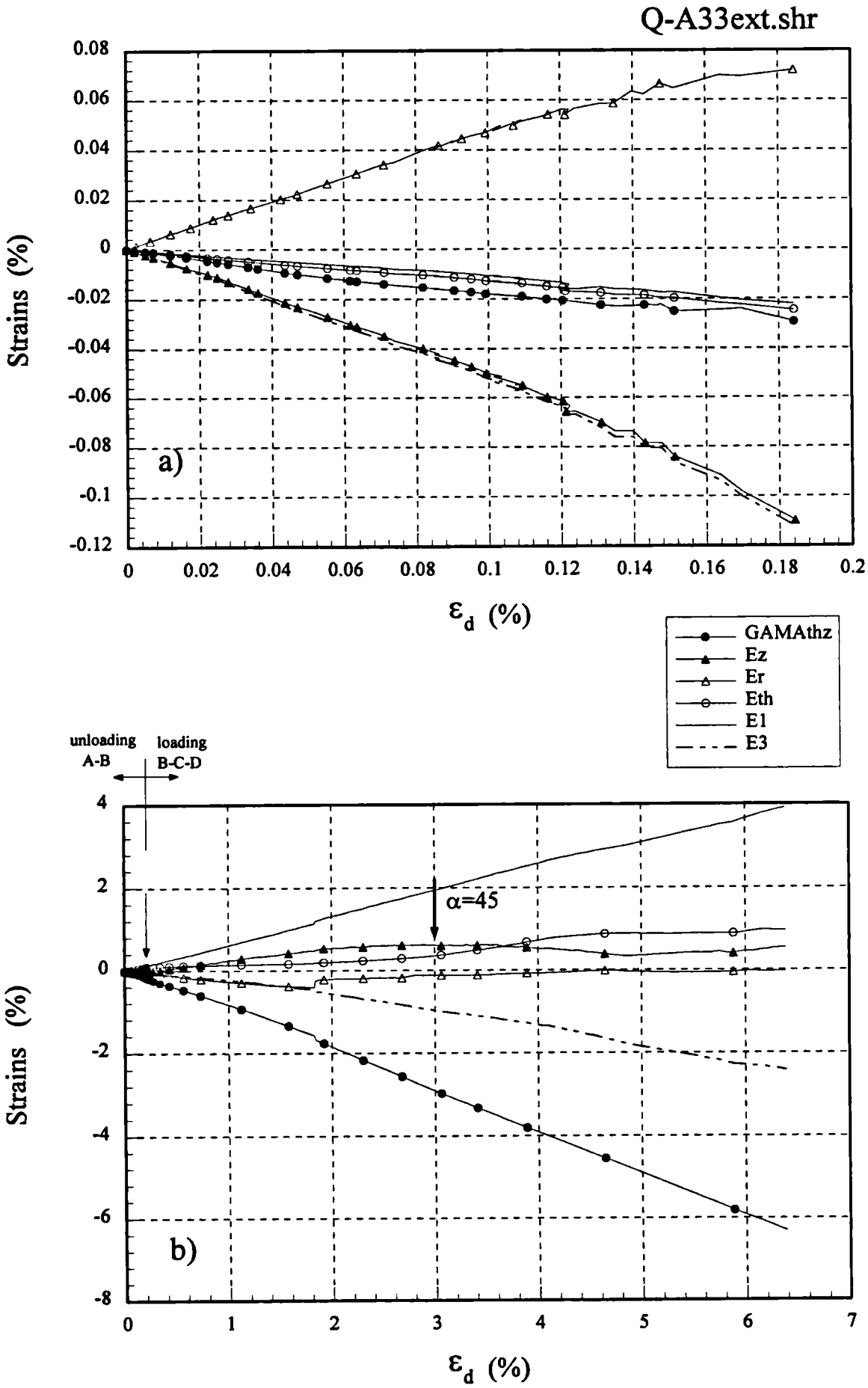


Fig.6.32 - a) Strain components for the initial unloading path A-B
b) Strain components for the total Q-A33ext stress path

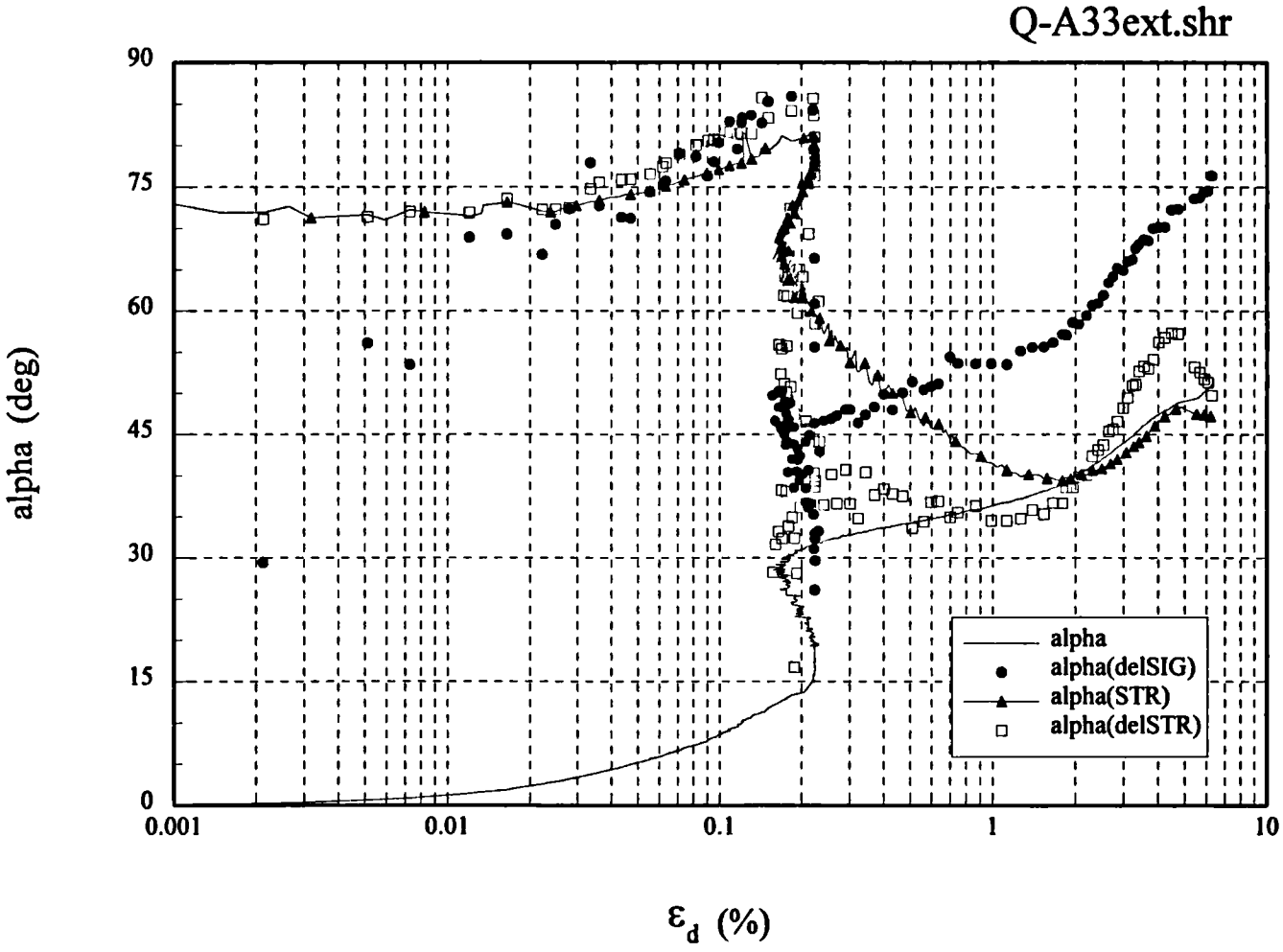


Fig.6.33 - Directions of principal stresses and strains and their increments

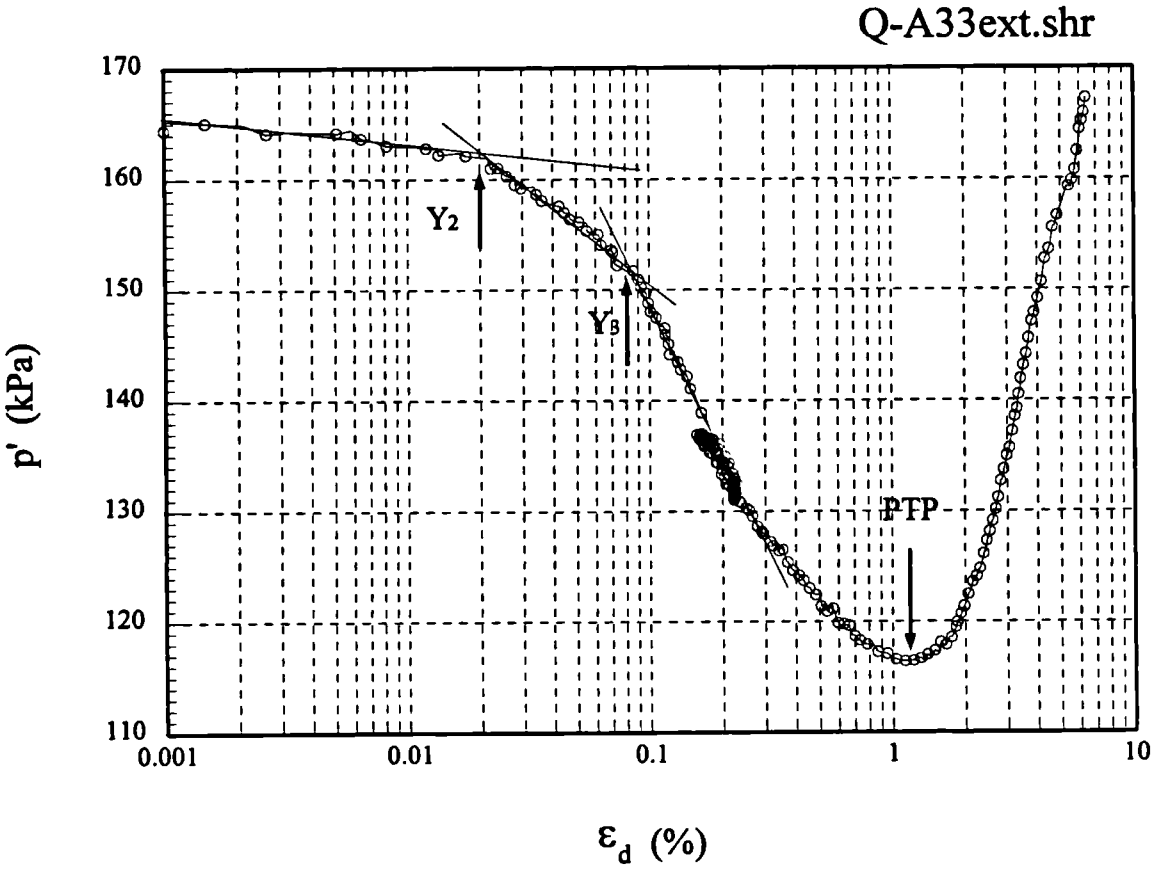


Fig.6.34 - Determination of yielding points

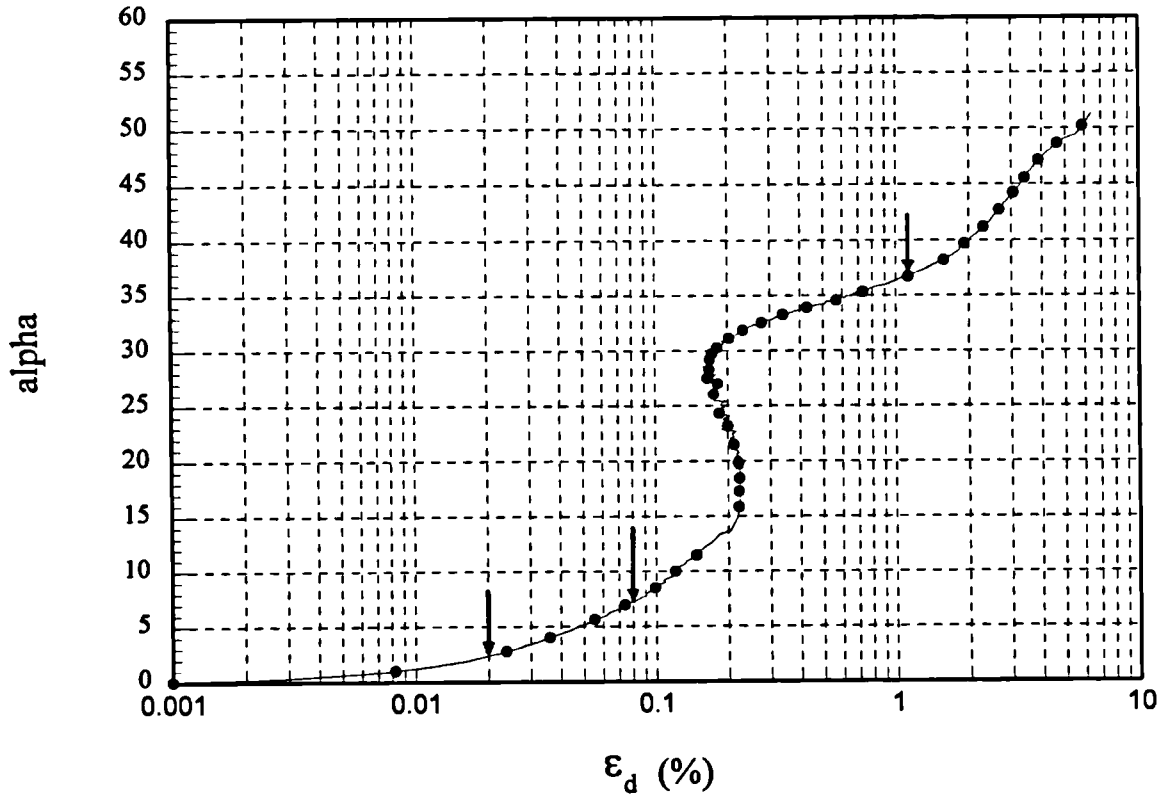


Fig.6.35 - Yield points in respect to α for Q-A33ext shearing path

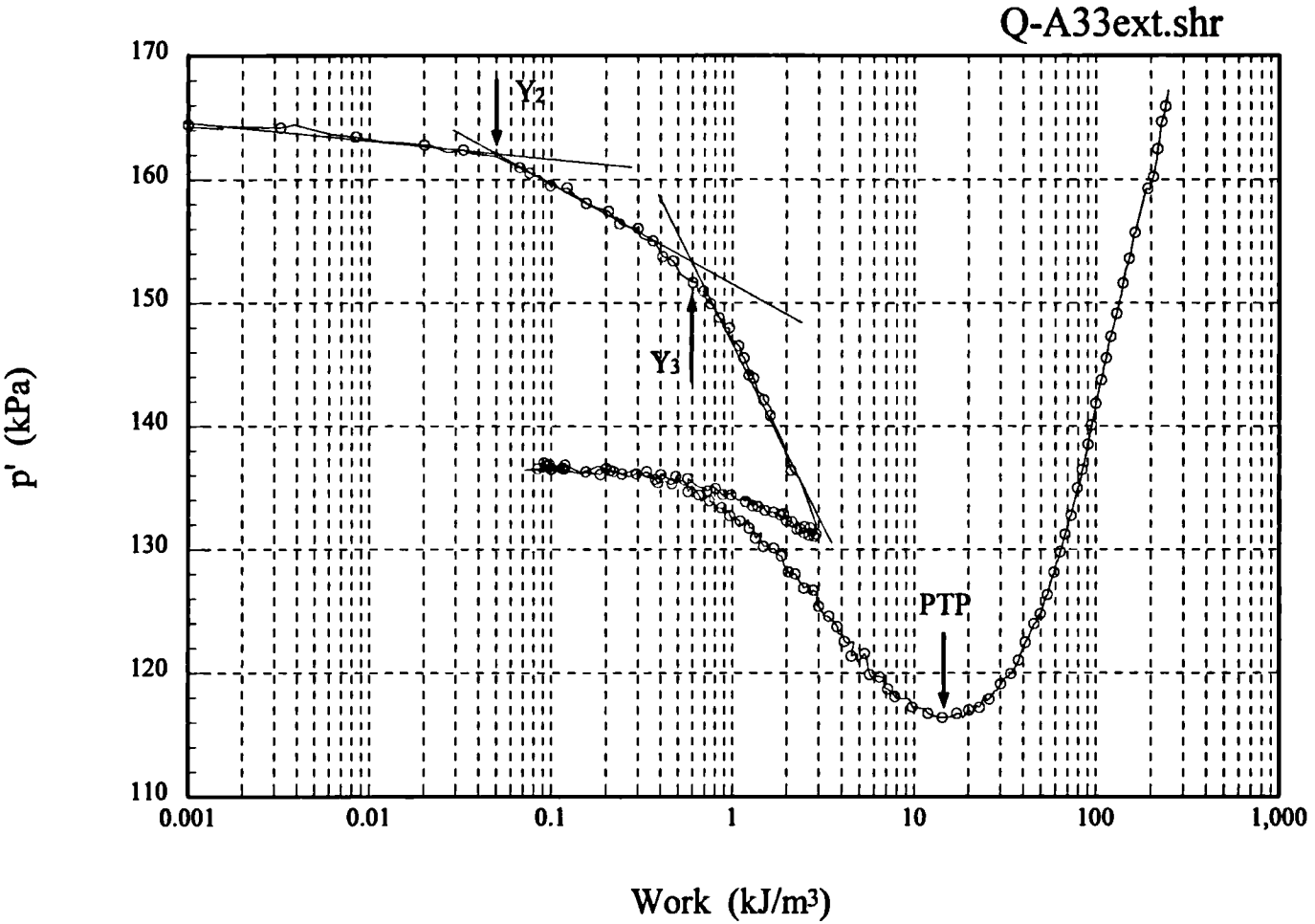


Fig.6.36 - Determination of yield points in respect to work

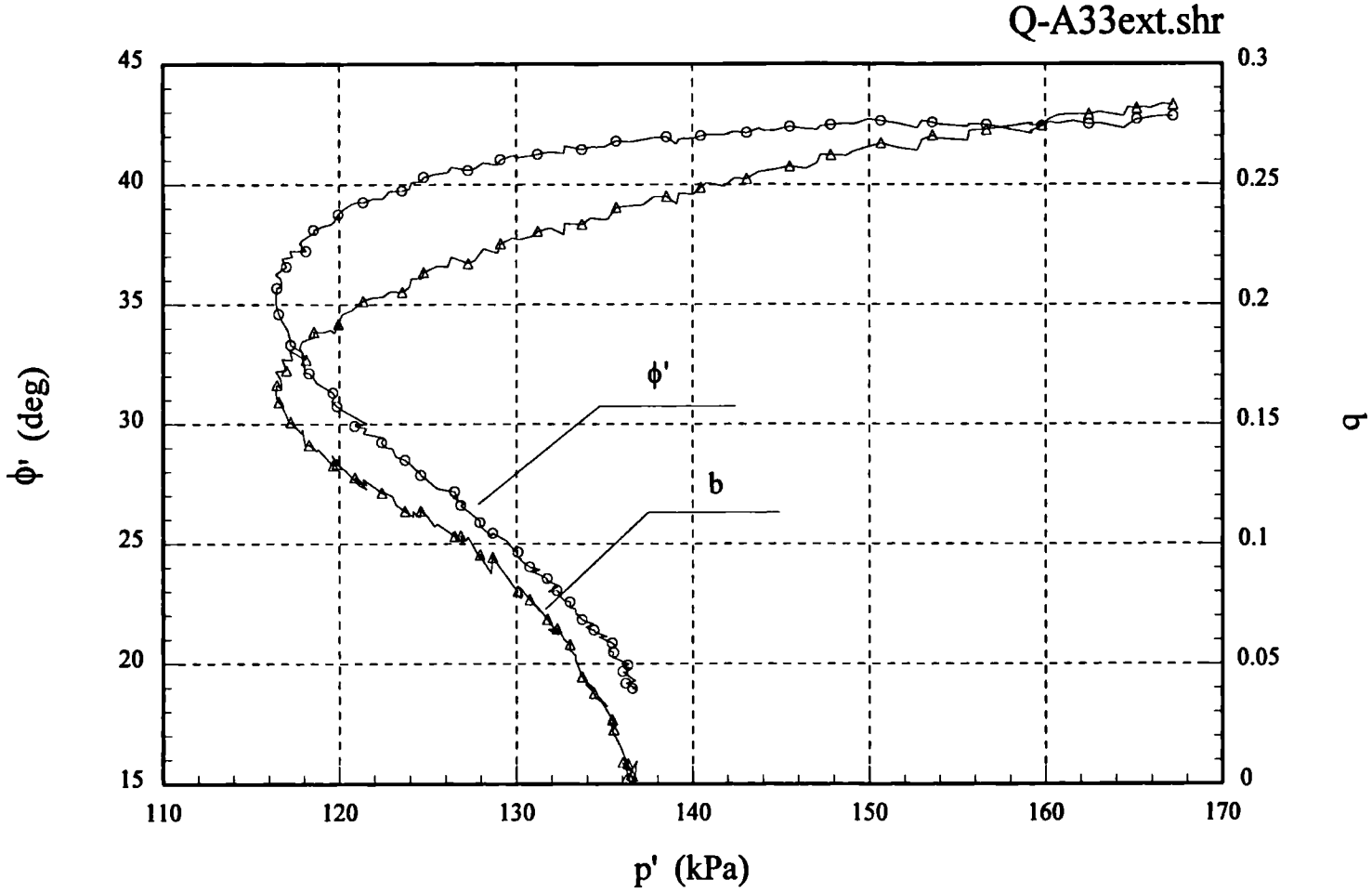


Fig.6.37 - Generation of b and ϕ' during 'Q-A33ext' shearing stress path, part C-D

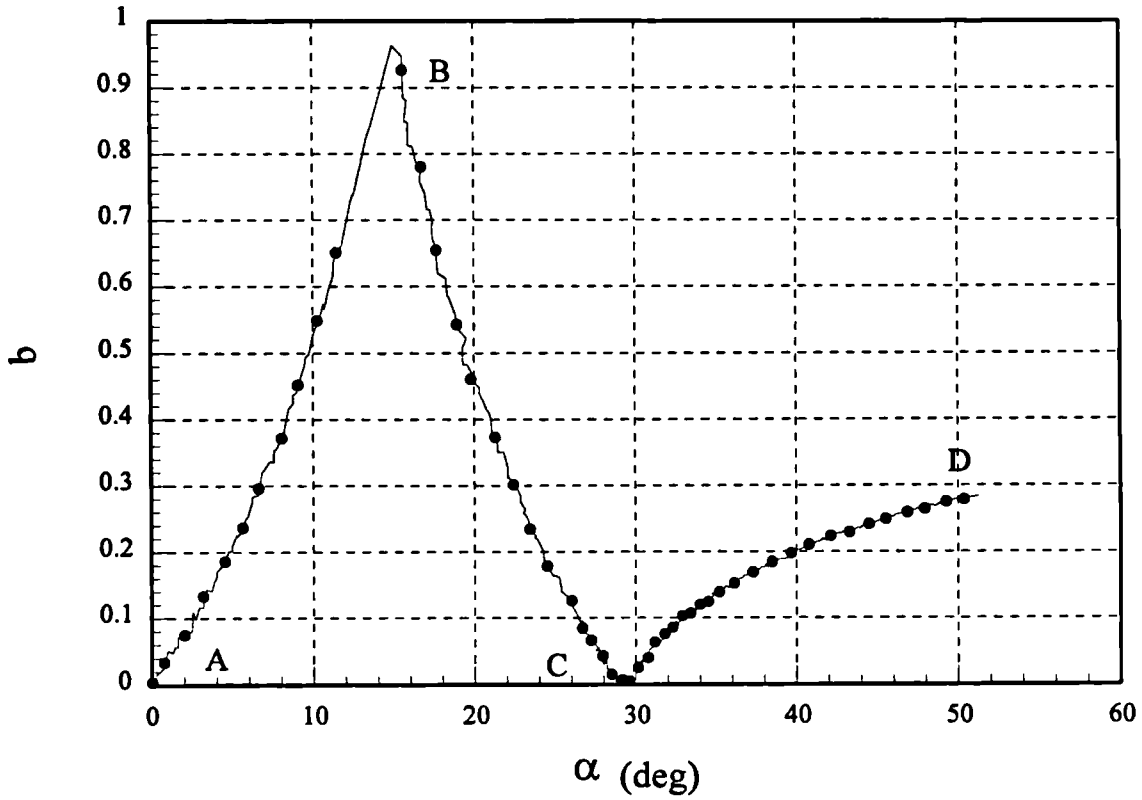


Fig.6.38a - Generation of b during 'Q-A33ext' shearing stress path

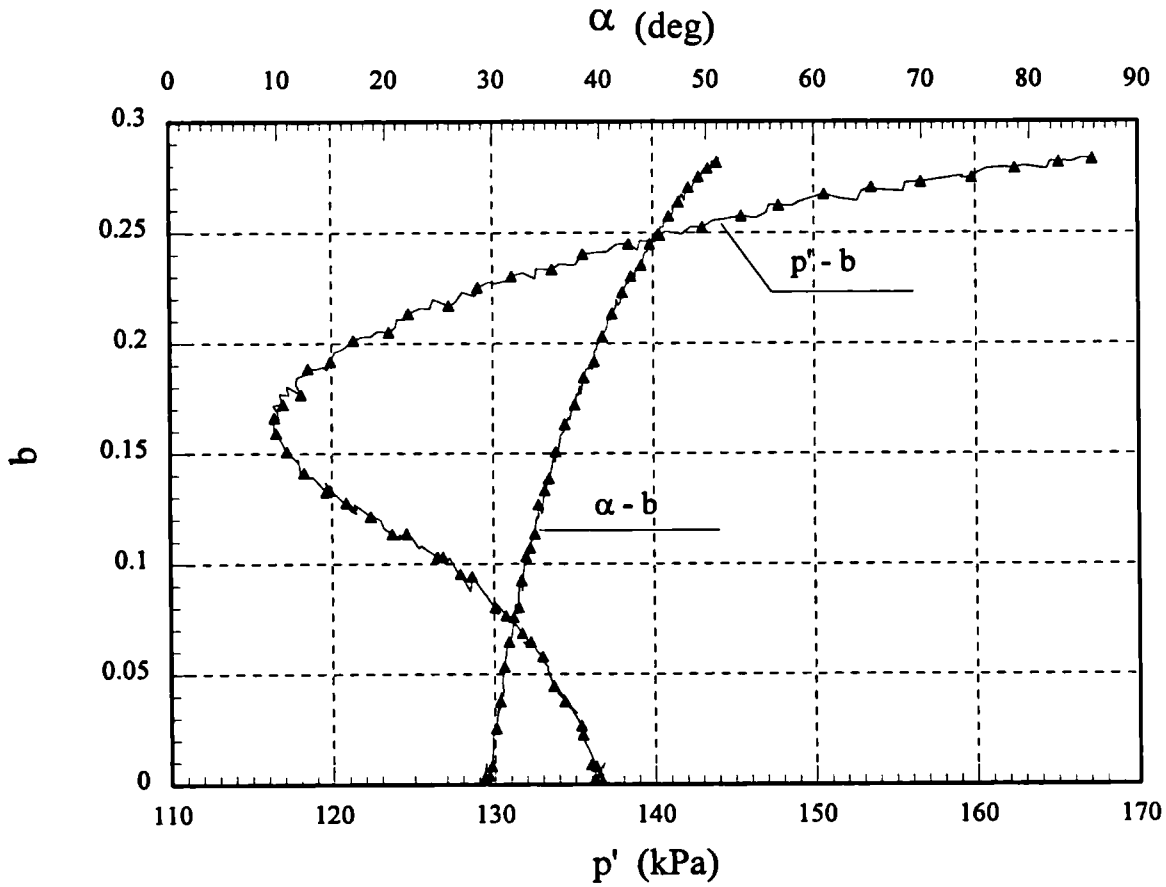


Fig.6.38b - Generation of b and α during 'Q-A33ext' shearing stress path, part C-D

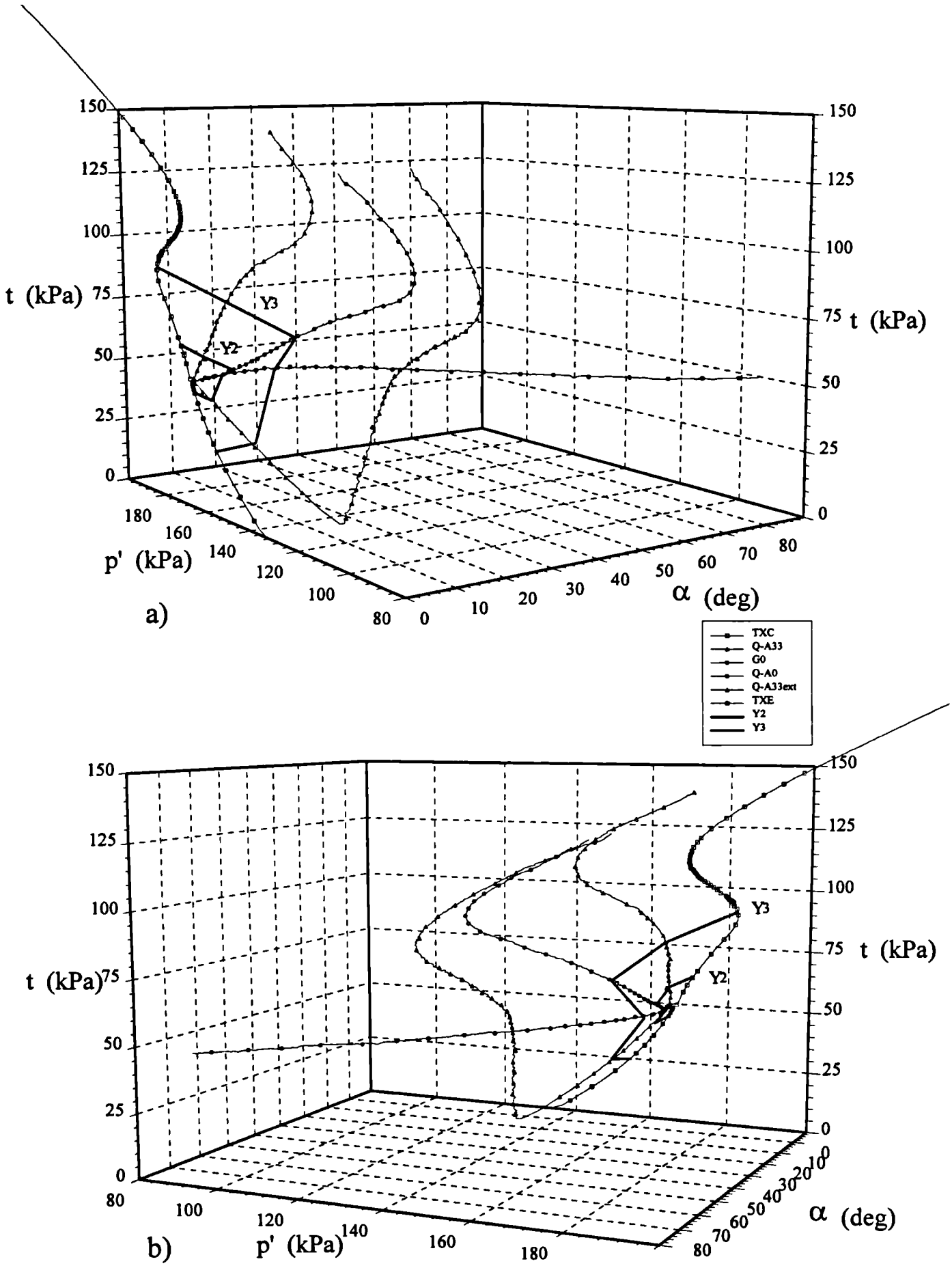


Fig.6.39 - a), b) Y2 and Y3 yield surfaces determined from undrained shearing in Q-A test Series, presented in two different perspectives

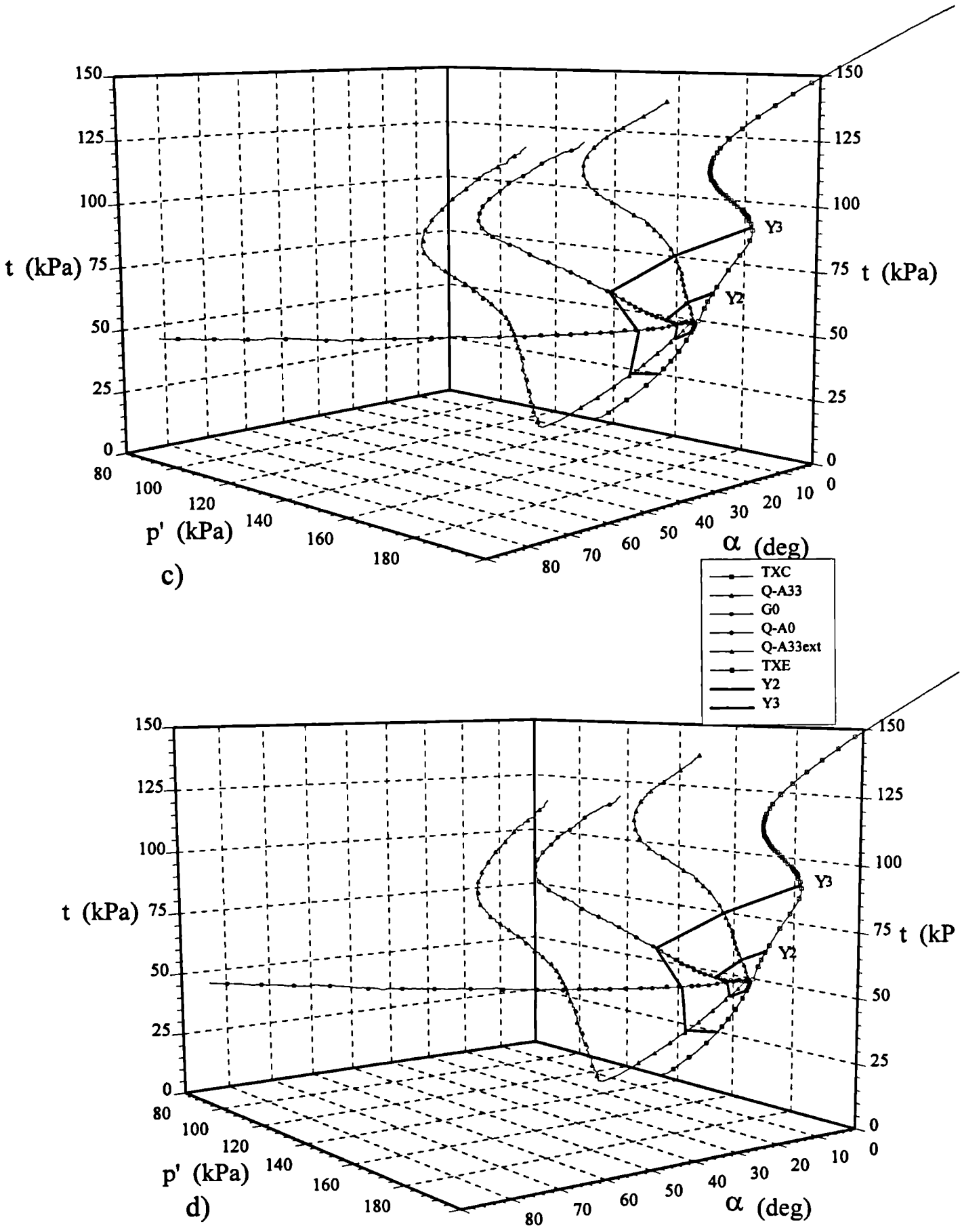
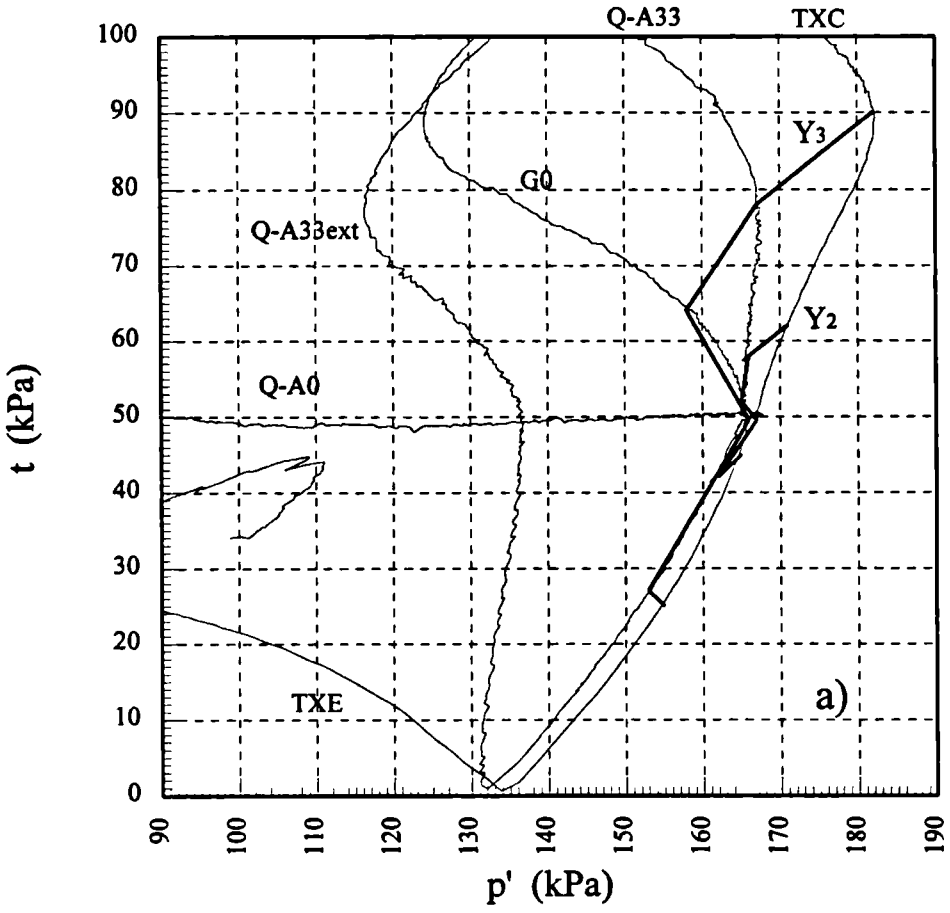


Fig.6.39 - c), d) Y2 and Y3 yield surfaces determined from undrained shearing in Q-A test Series, presented in two different perspectives



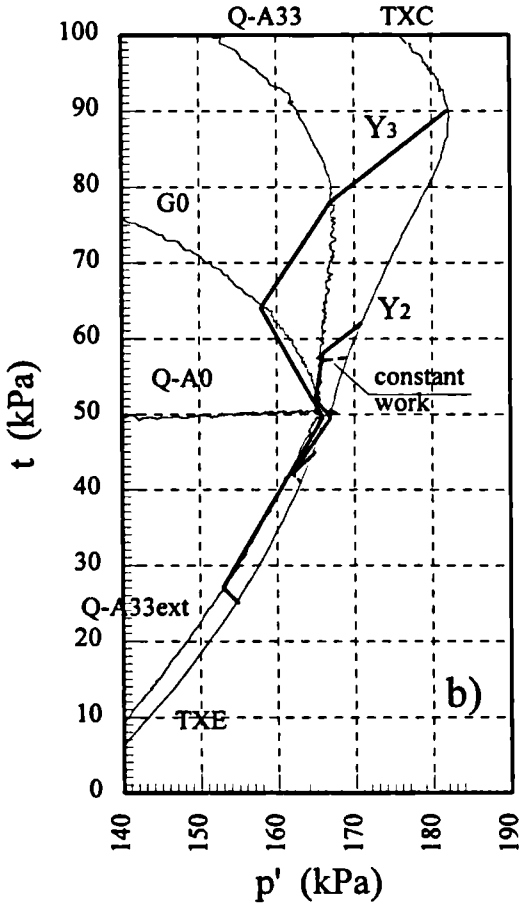
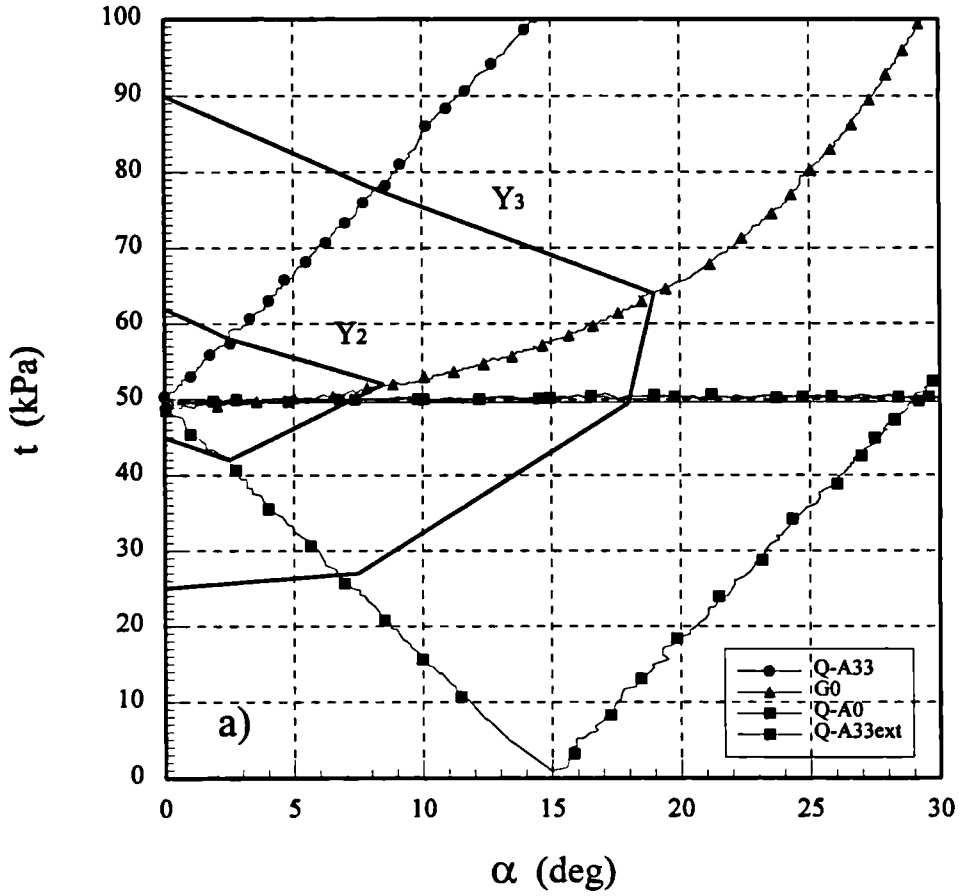


Fig.6.40 - a) Contours of Y2 and Y3 strain boundaries in t-p' plane
b) Contour of Y2 constant work boundary in t-p' plane



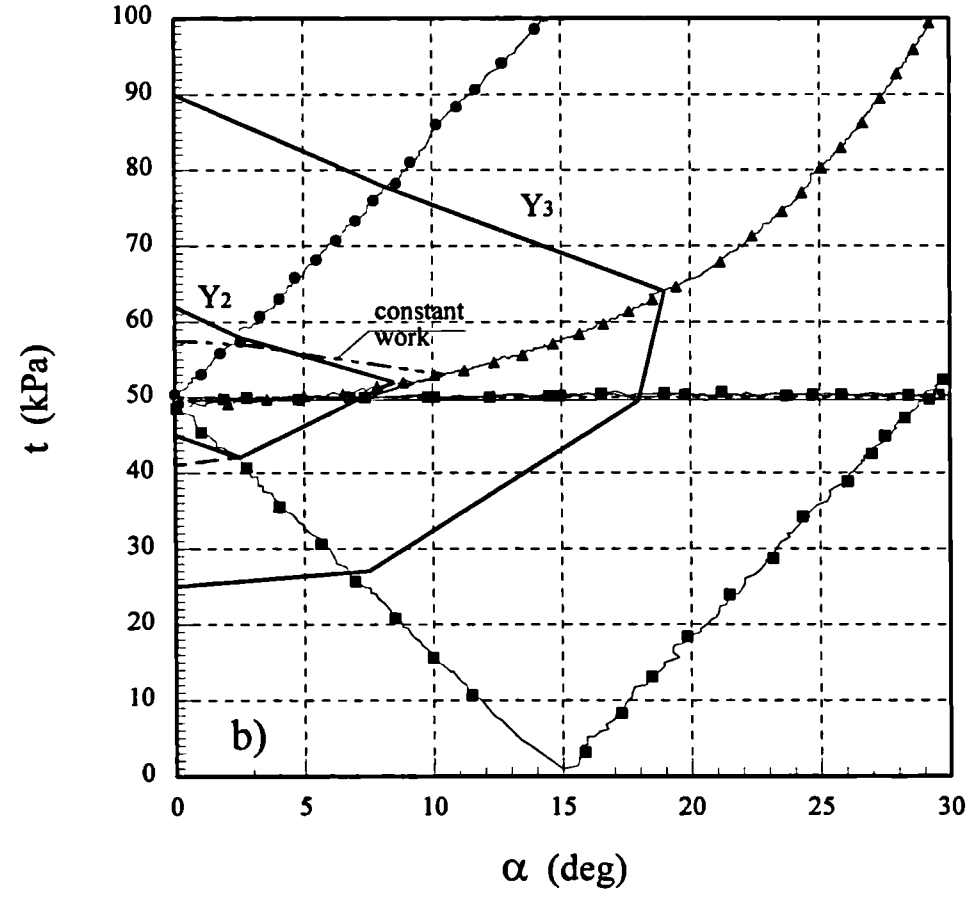


Fig.6.41 - a) Contours of Y2 and Y3 strain boundaries in t-α plane
b) Contour of Y2 constant work boundary in t-α plane

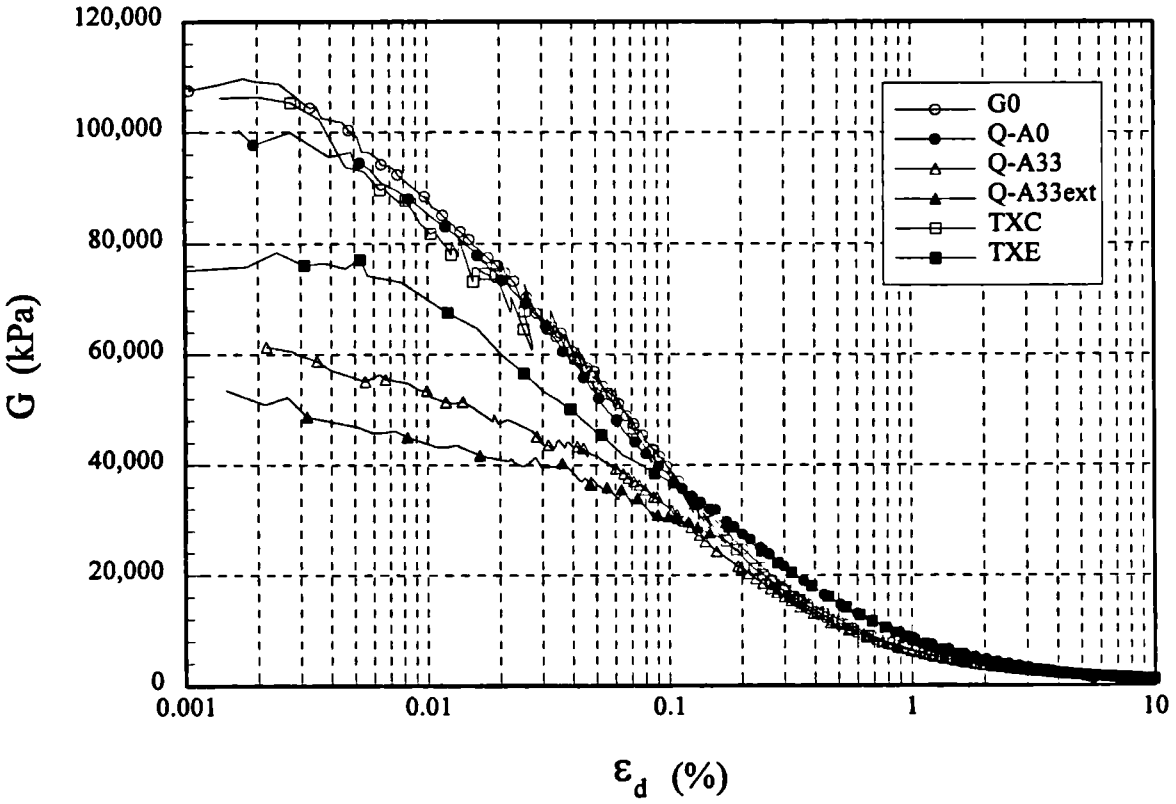


Fig.6.42a - Octahedral shear modulus for Q-A shearing stress paths

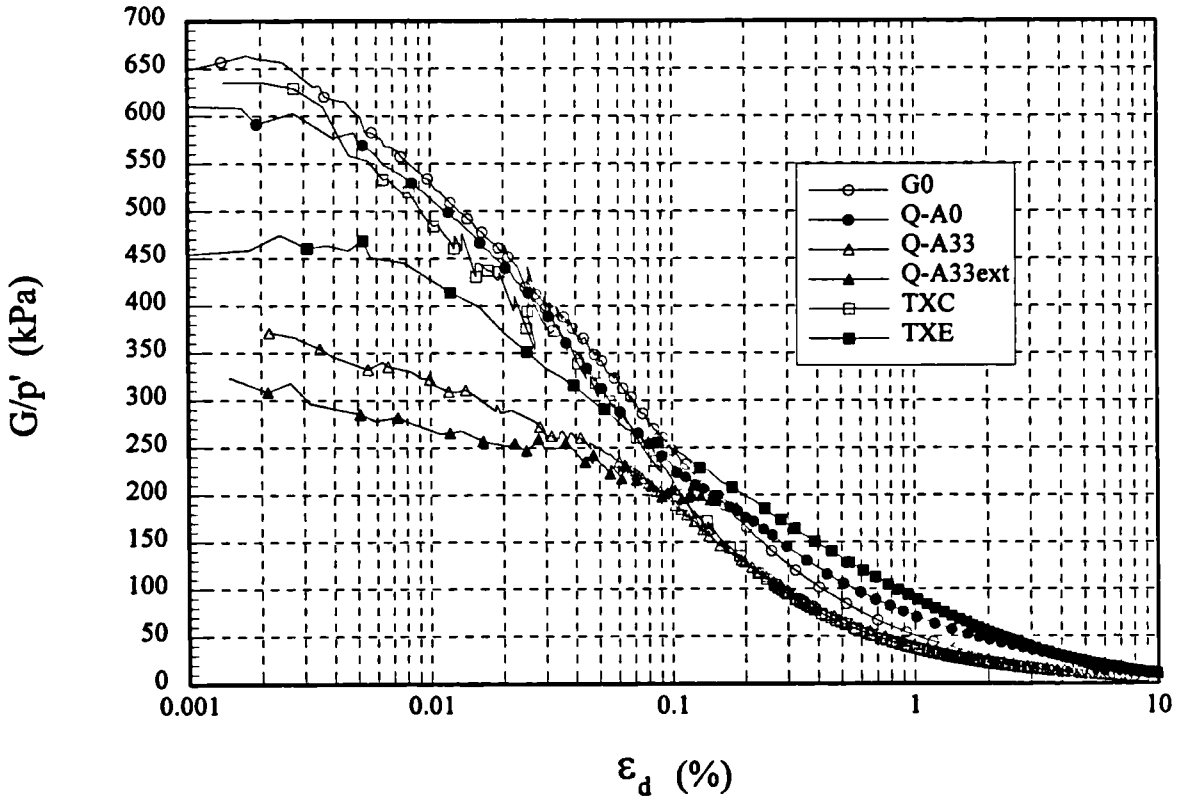


Fig.6.42b - Octahedral shear modulus normalized by the current p'

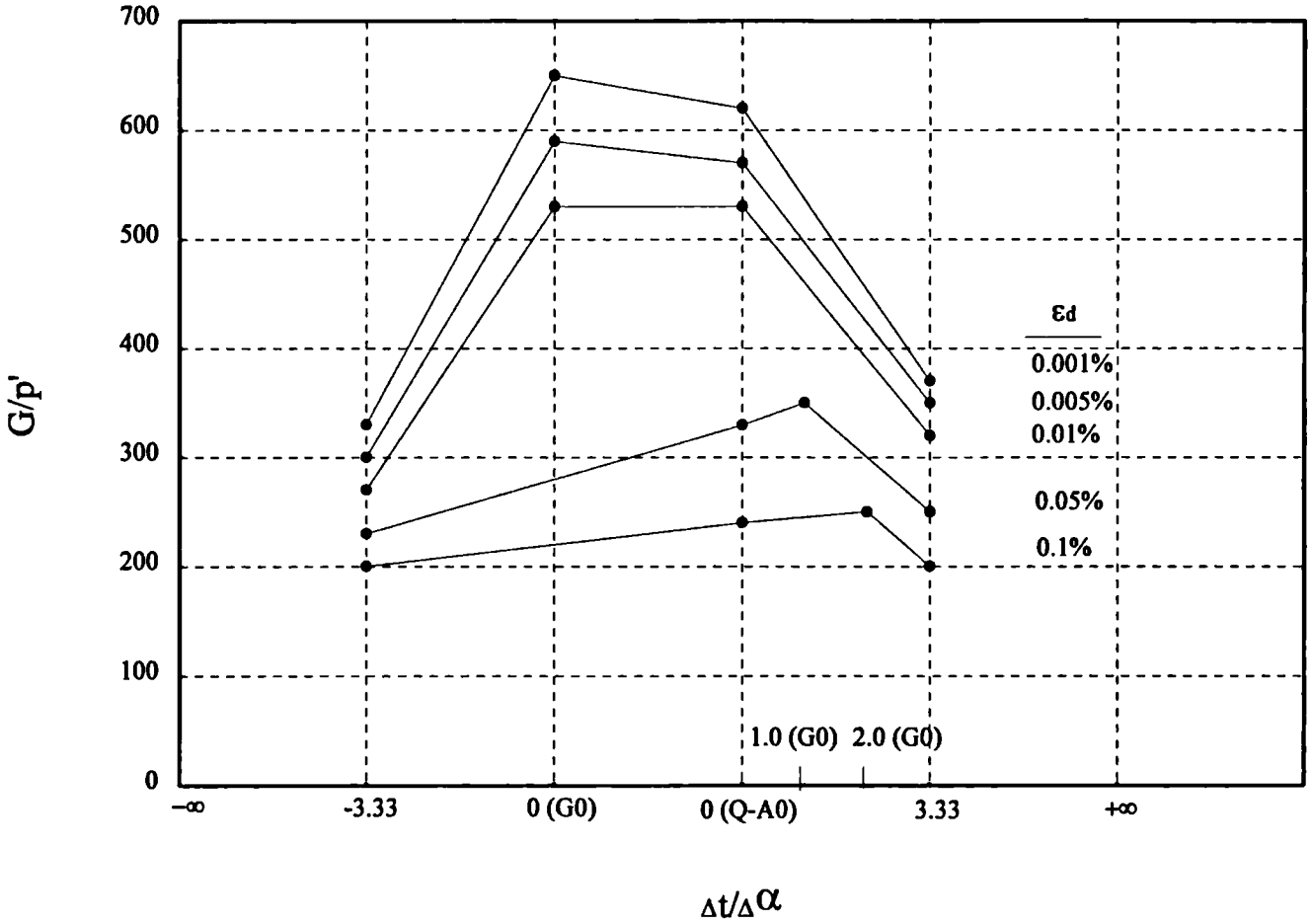


Fig.6.43 - Dependance of G on the inclination of stress path, at different strain levels

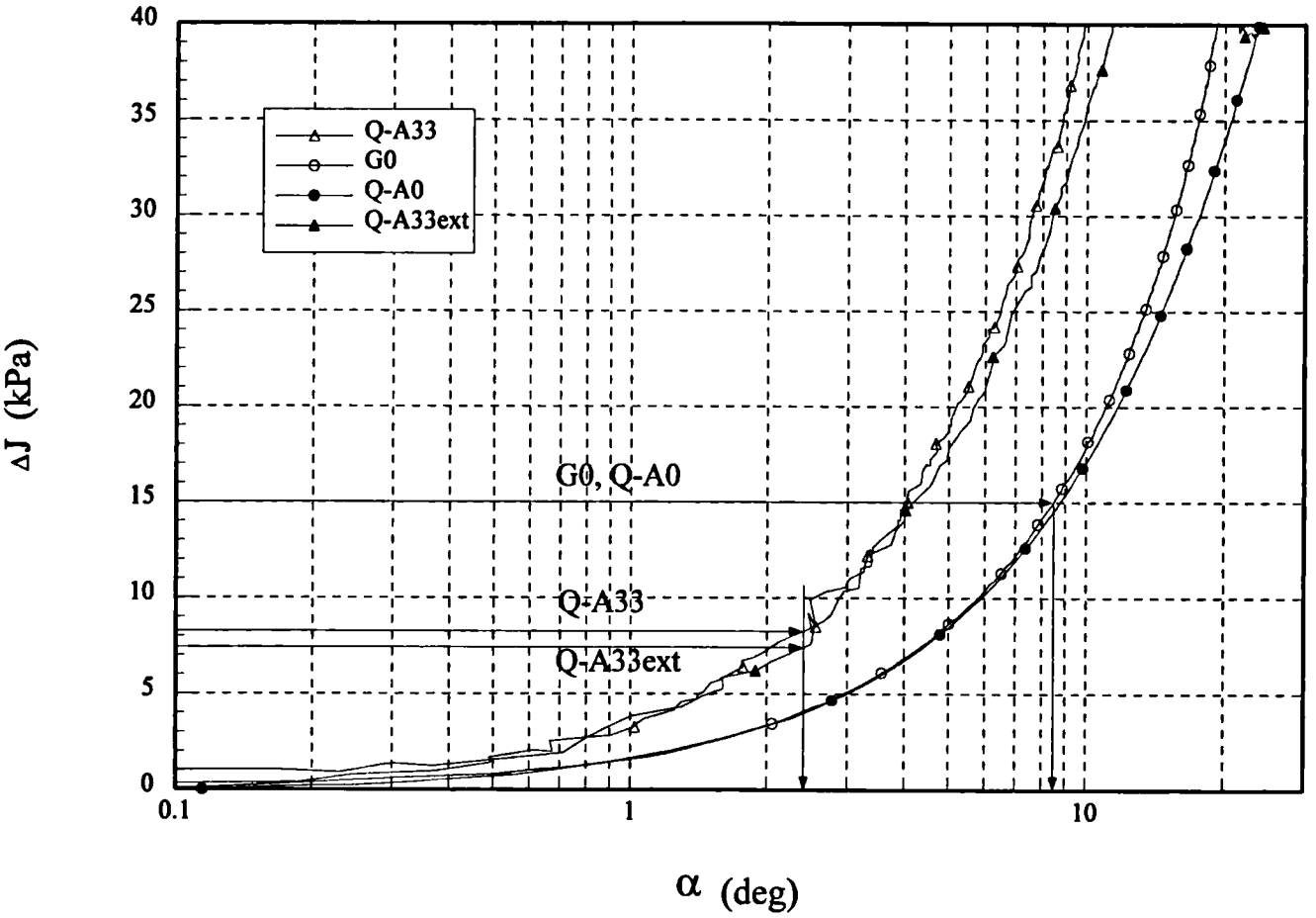


Fig.6.44 - Values of ΔJ corresponding to α

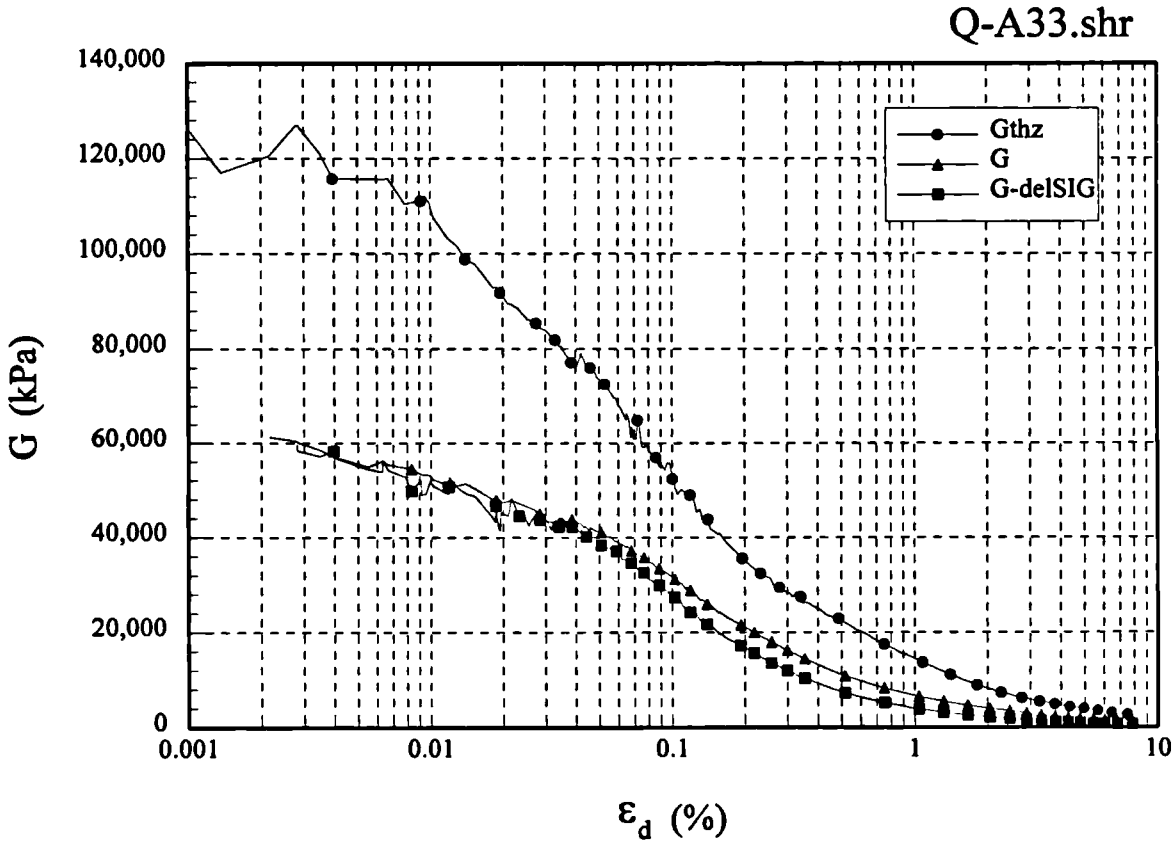


Fig.6.45 - Components of shear moduli for test Q-A33

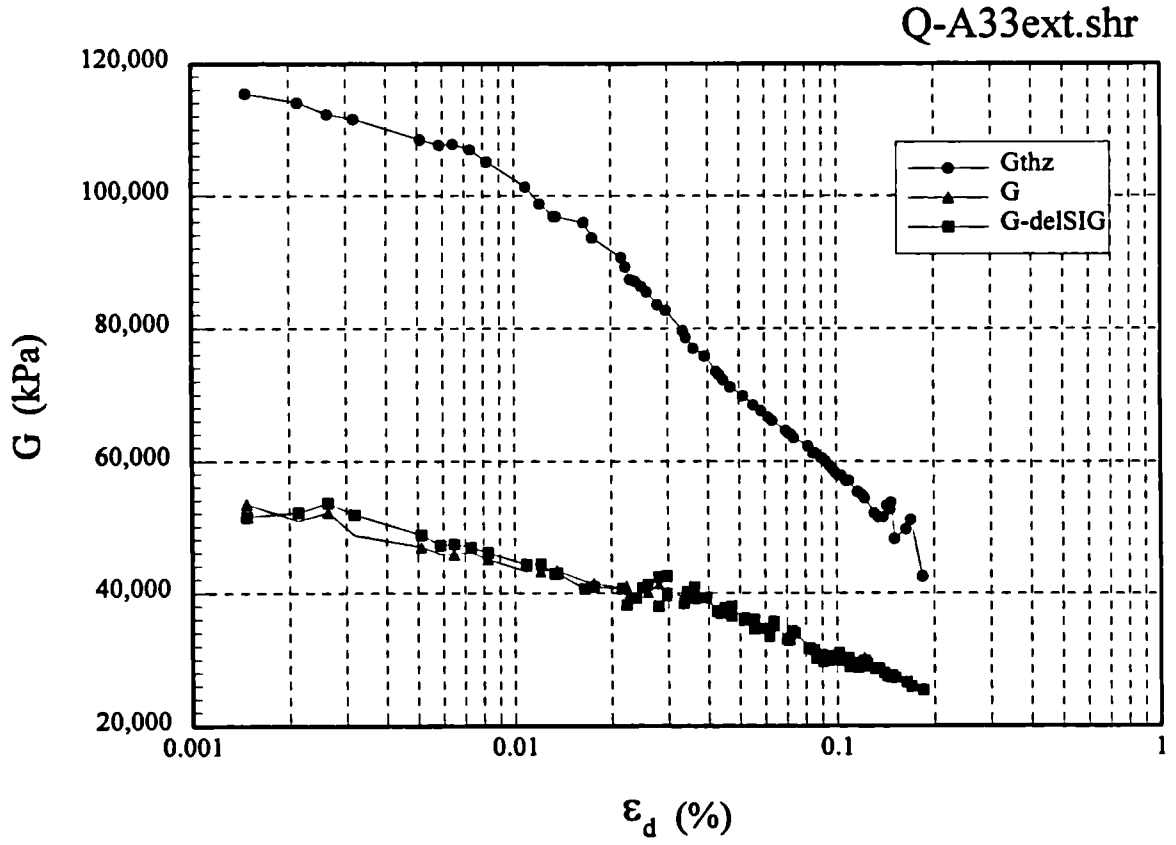


Fig.6.46 - Components of shear moduli for test Q-A33ext

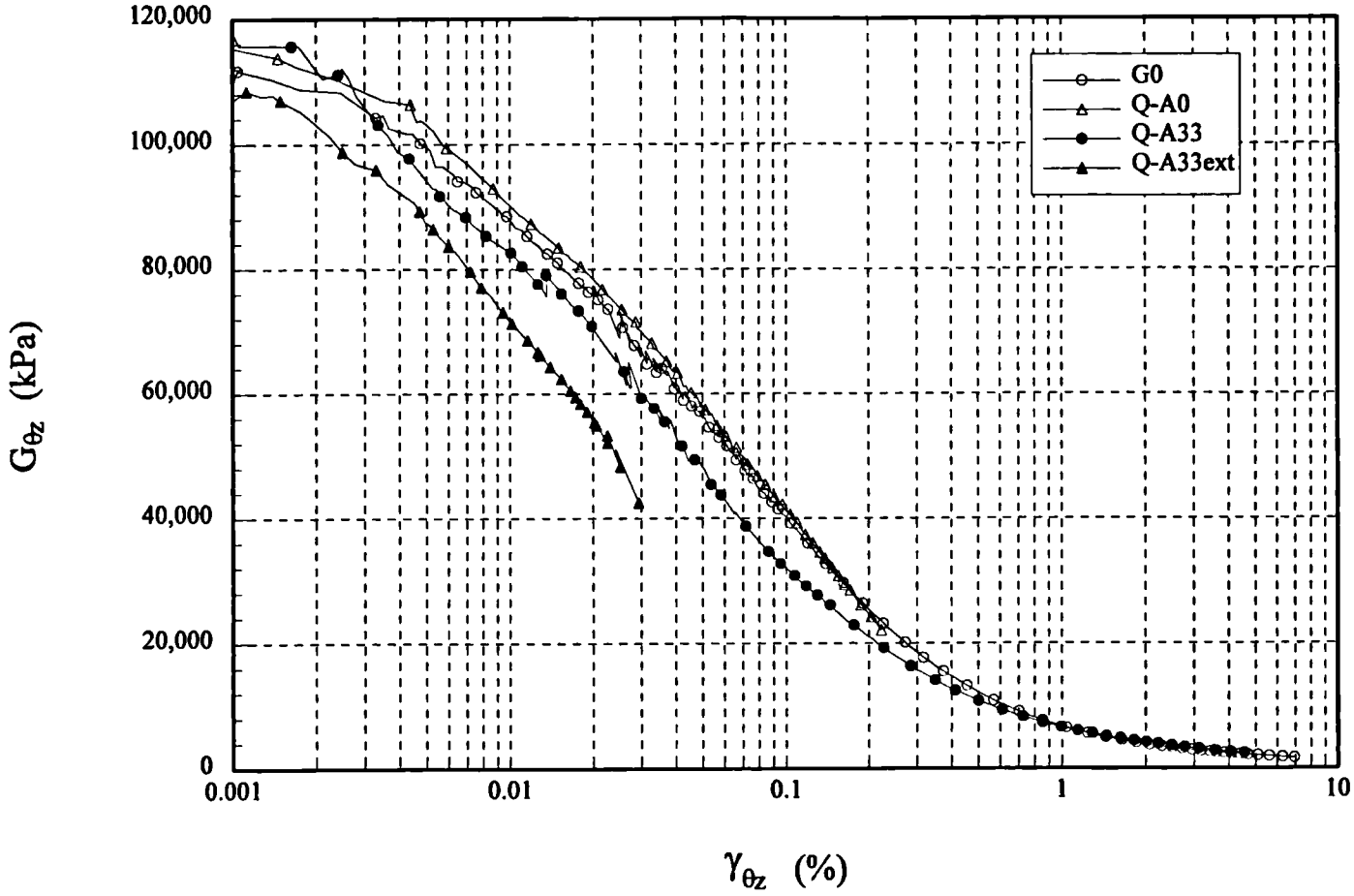


Fig.6.47 - Torsional shear moduli for probing tests from OCR=1.3

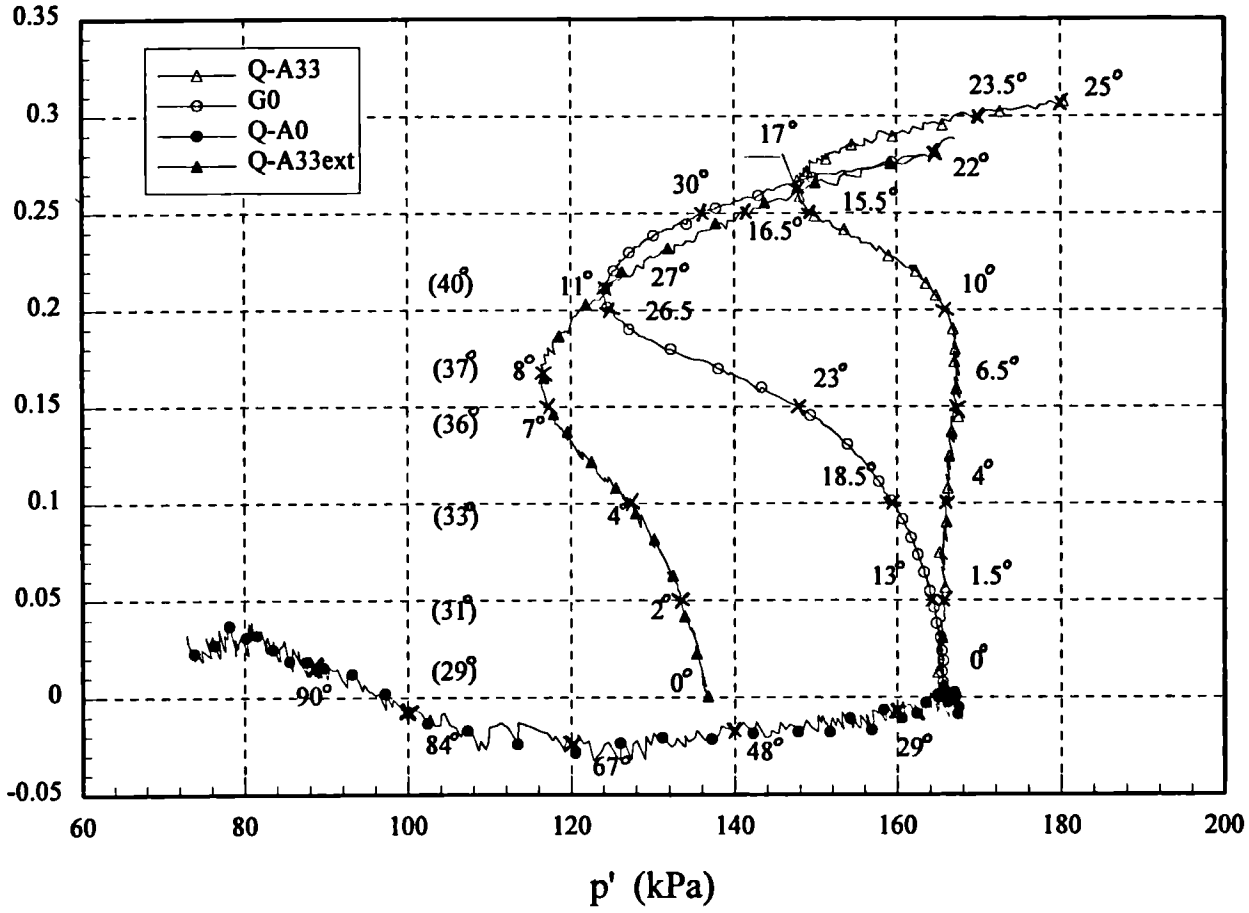


Fig.6.48 - Summary plot of development of b with p'
(numbers denote generated principal stress rotation)

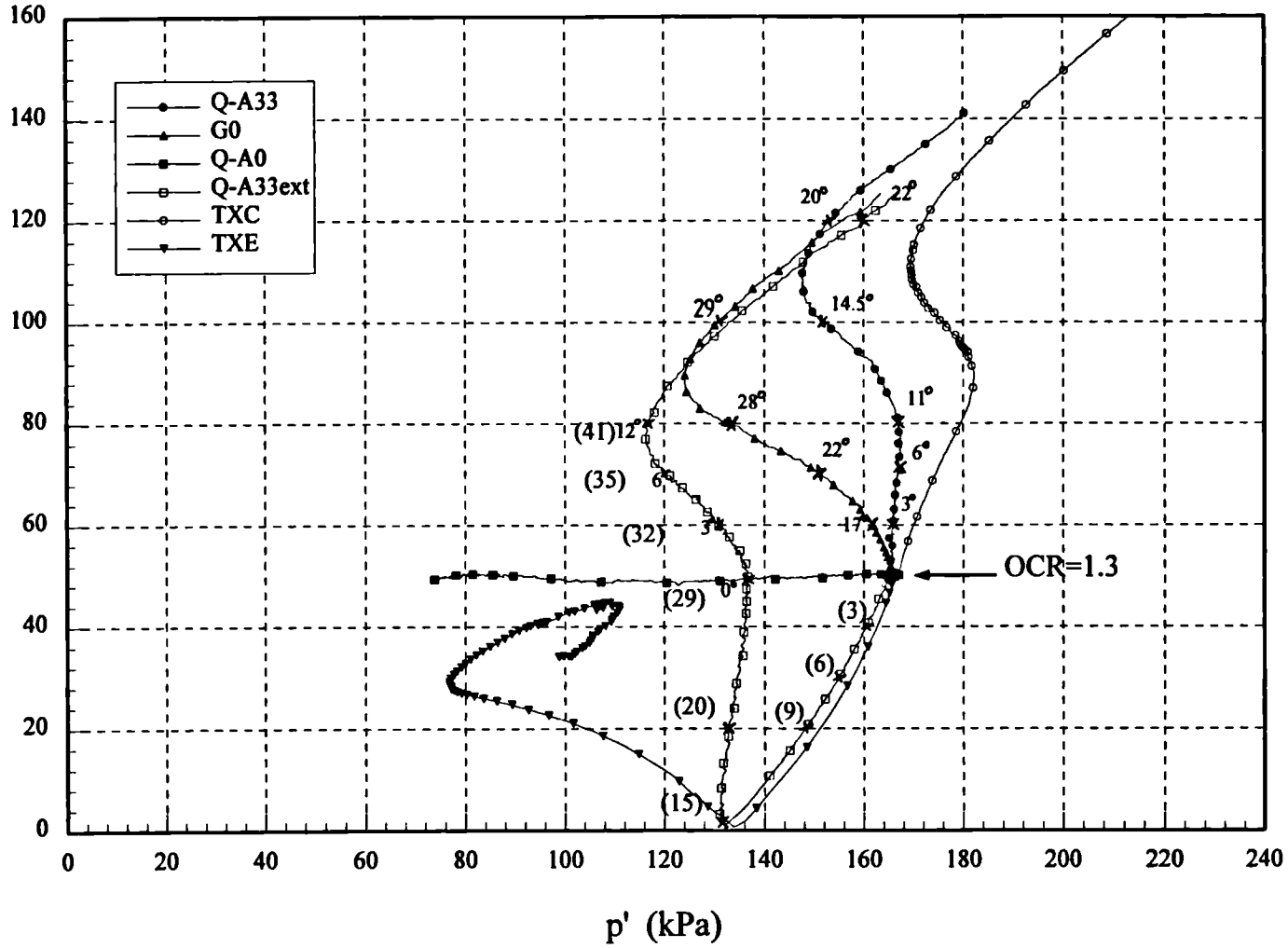


Fig.6.49 - Effective stress paths from Q-A Series projected on t-p' plane
(numbers denote generated principal stress rotation along paths)

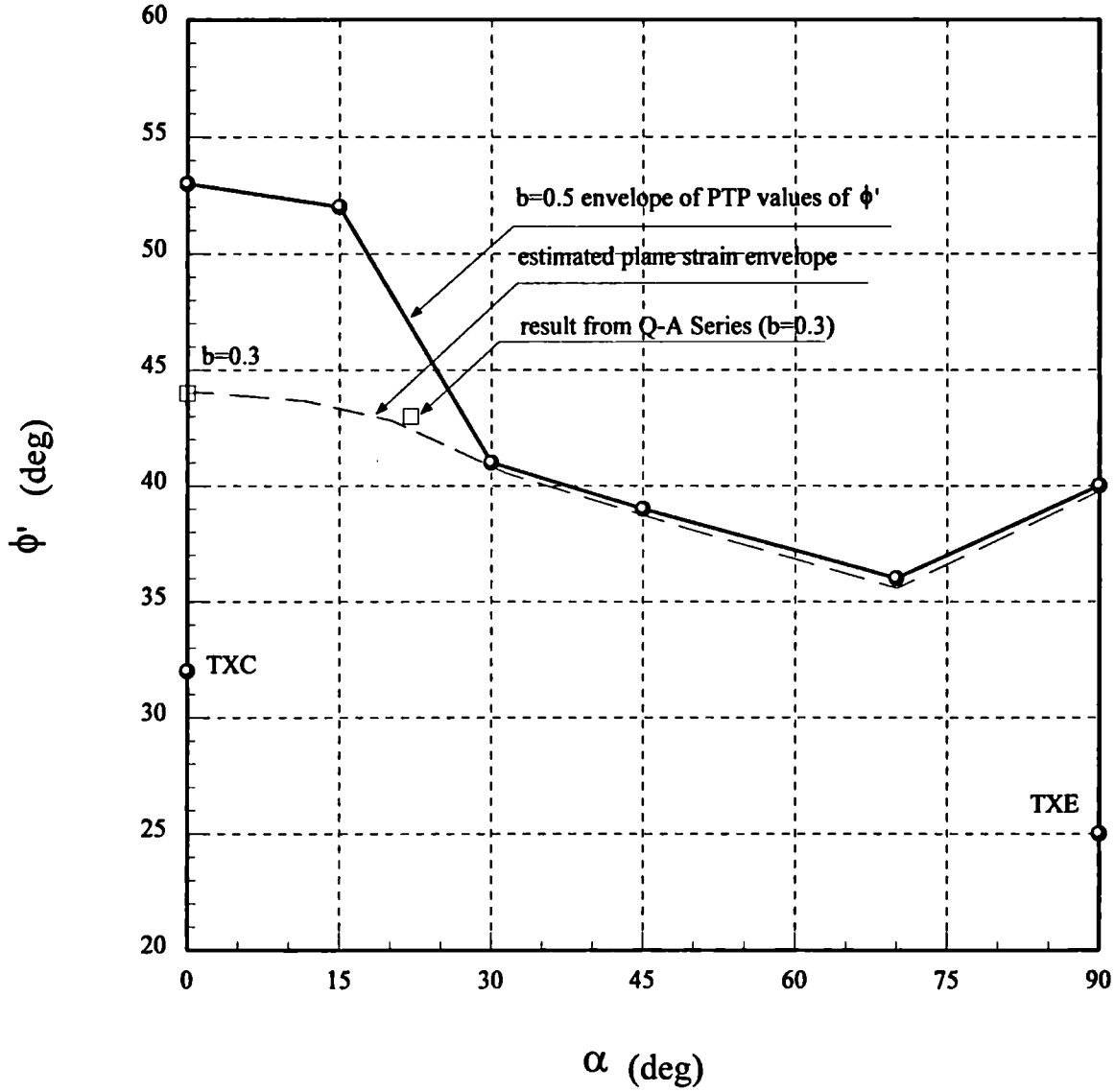


Fig.6.50 - Anisotropy of PTP mobilized friction angle, due to principal stress rotation

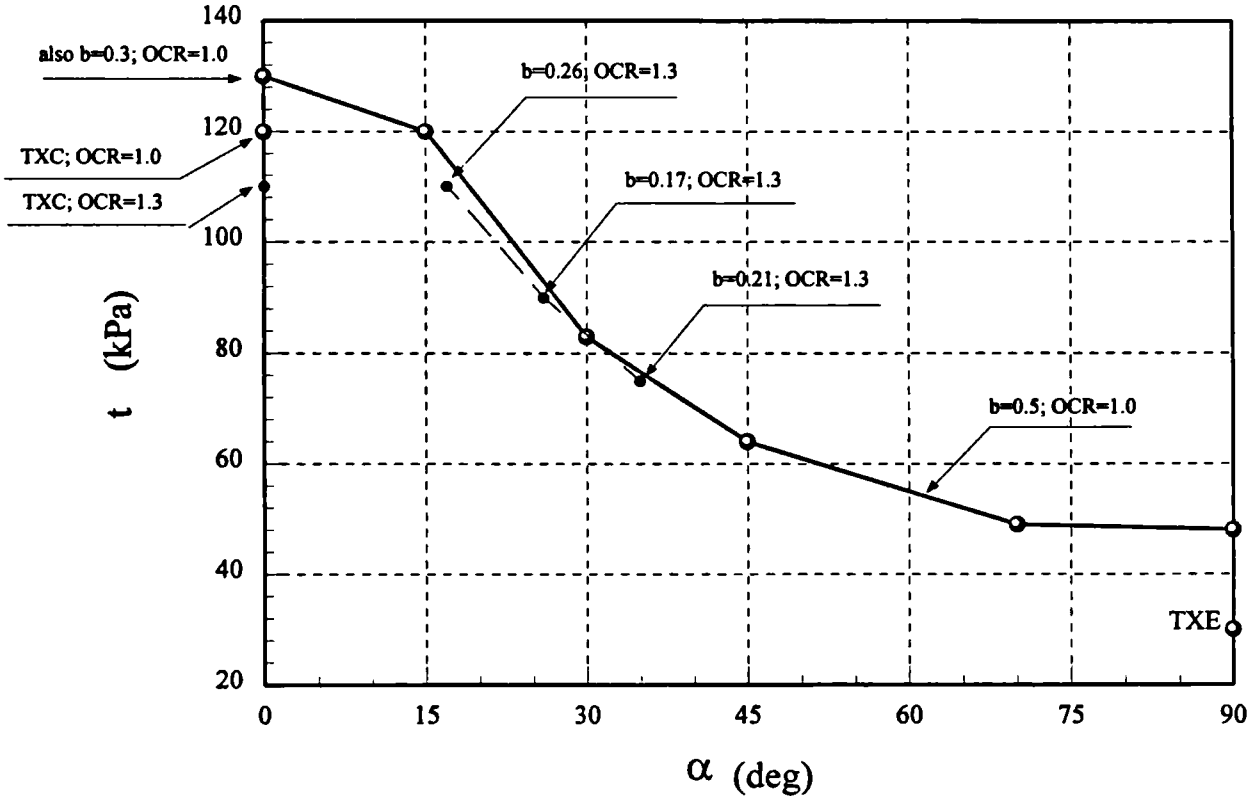


Fig.6.51 - Comparison of the t values at the PTP for M and Q-A Series

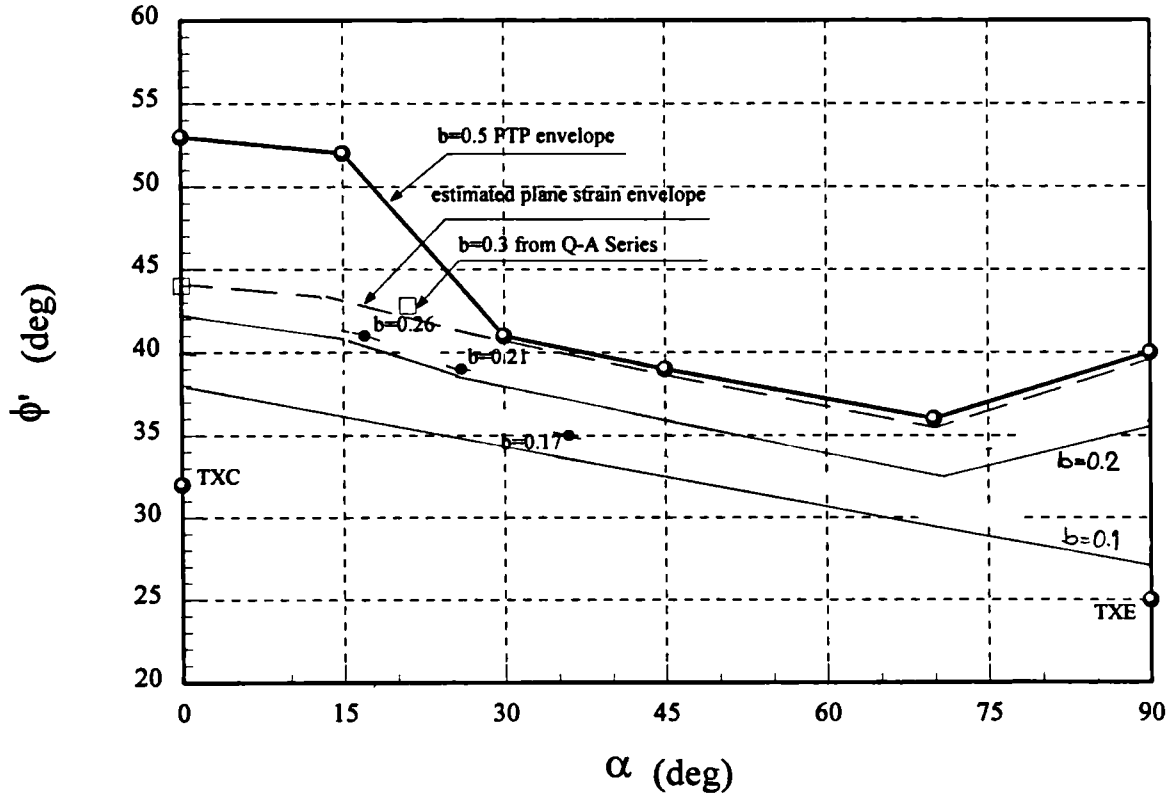


Fig.6.52 - Comparison of the ϕ' values at the PTP for M and Q-A Series

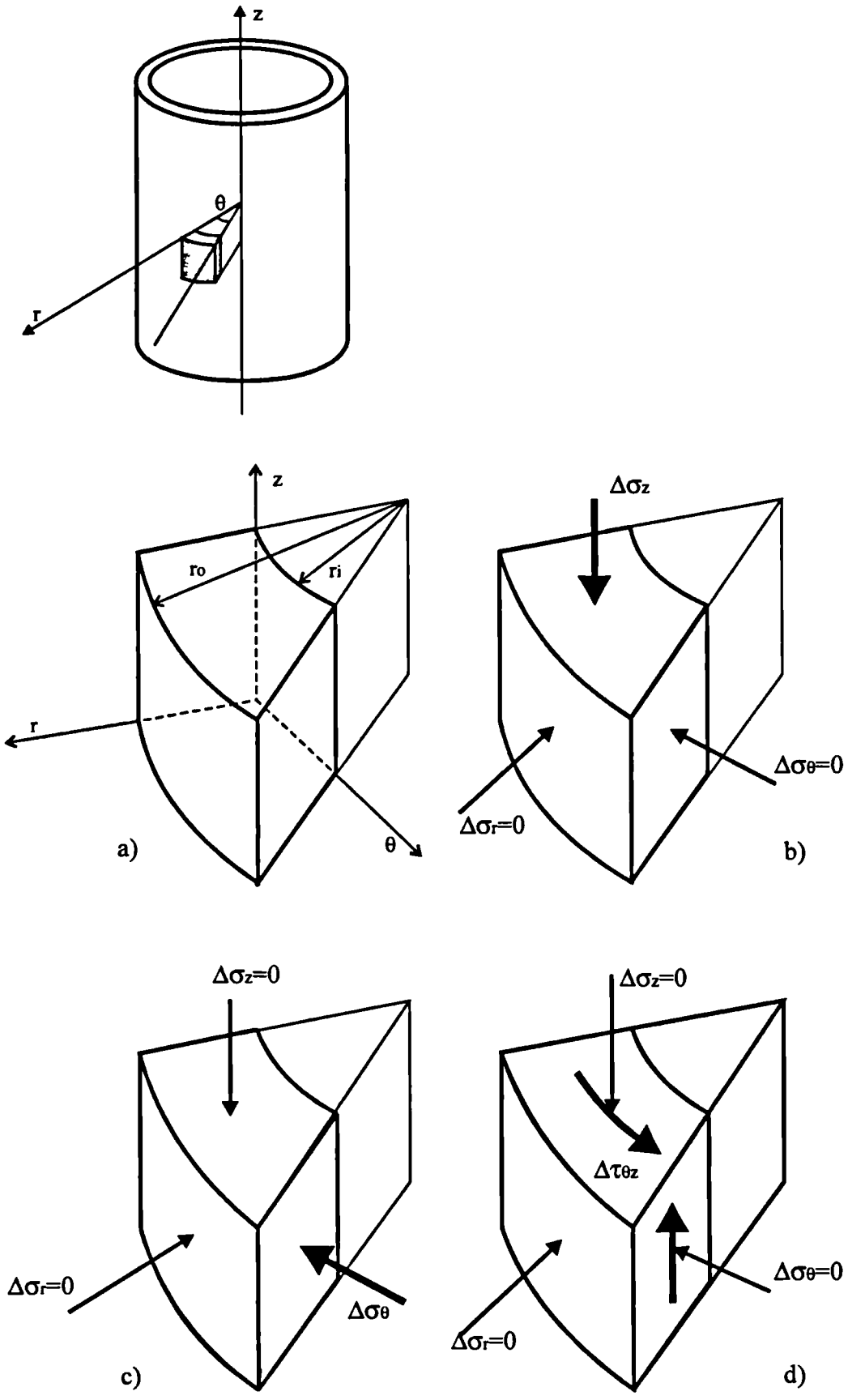


Fig.6.53 - Scheme of stress applications to determine anisotropic elastic parameters

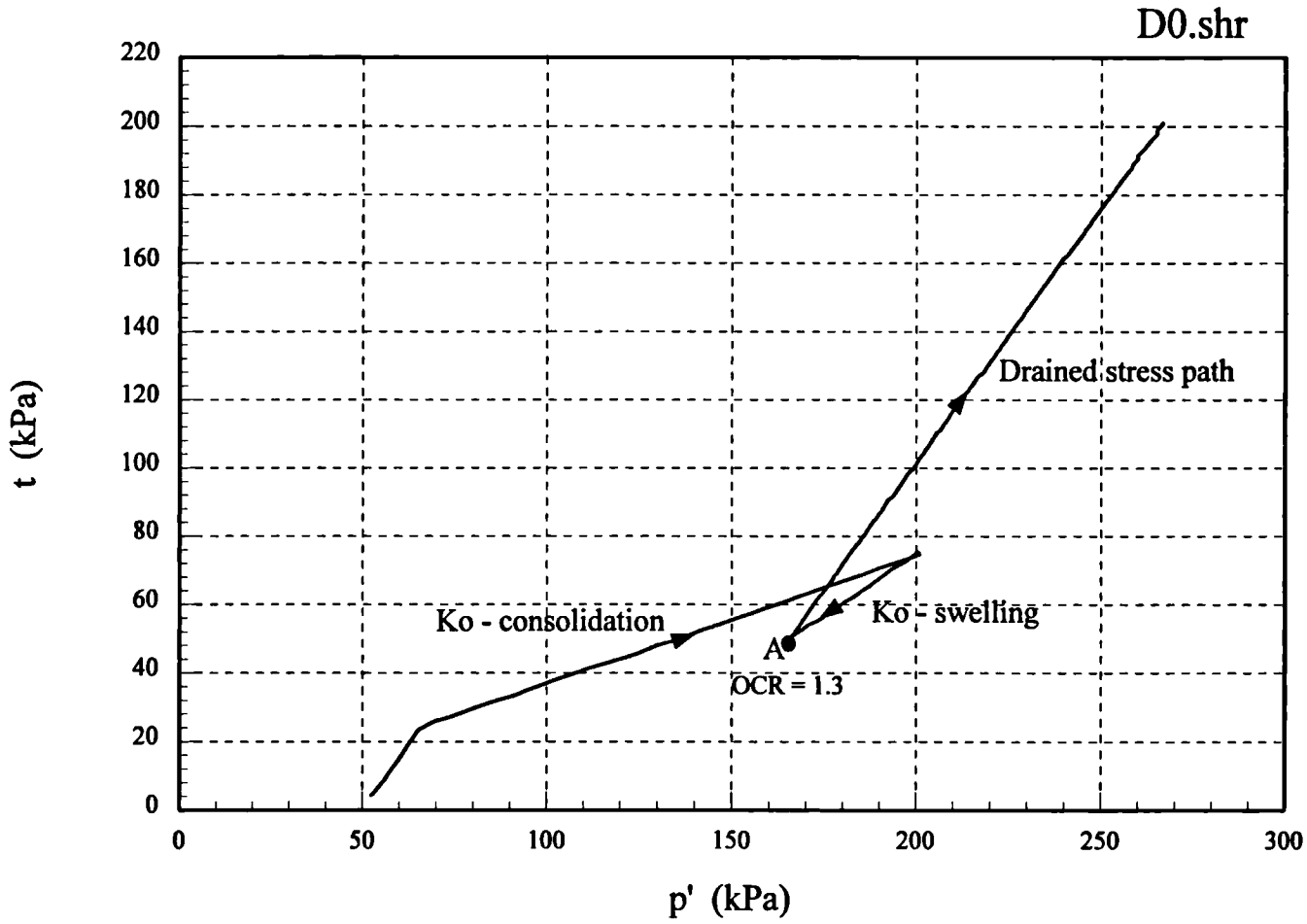


Fig.6.54 - Drained stress path followed during direct vertical loading

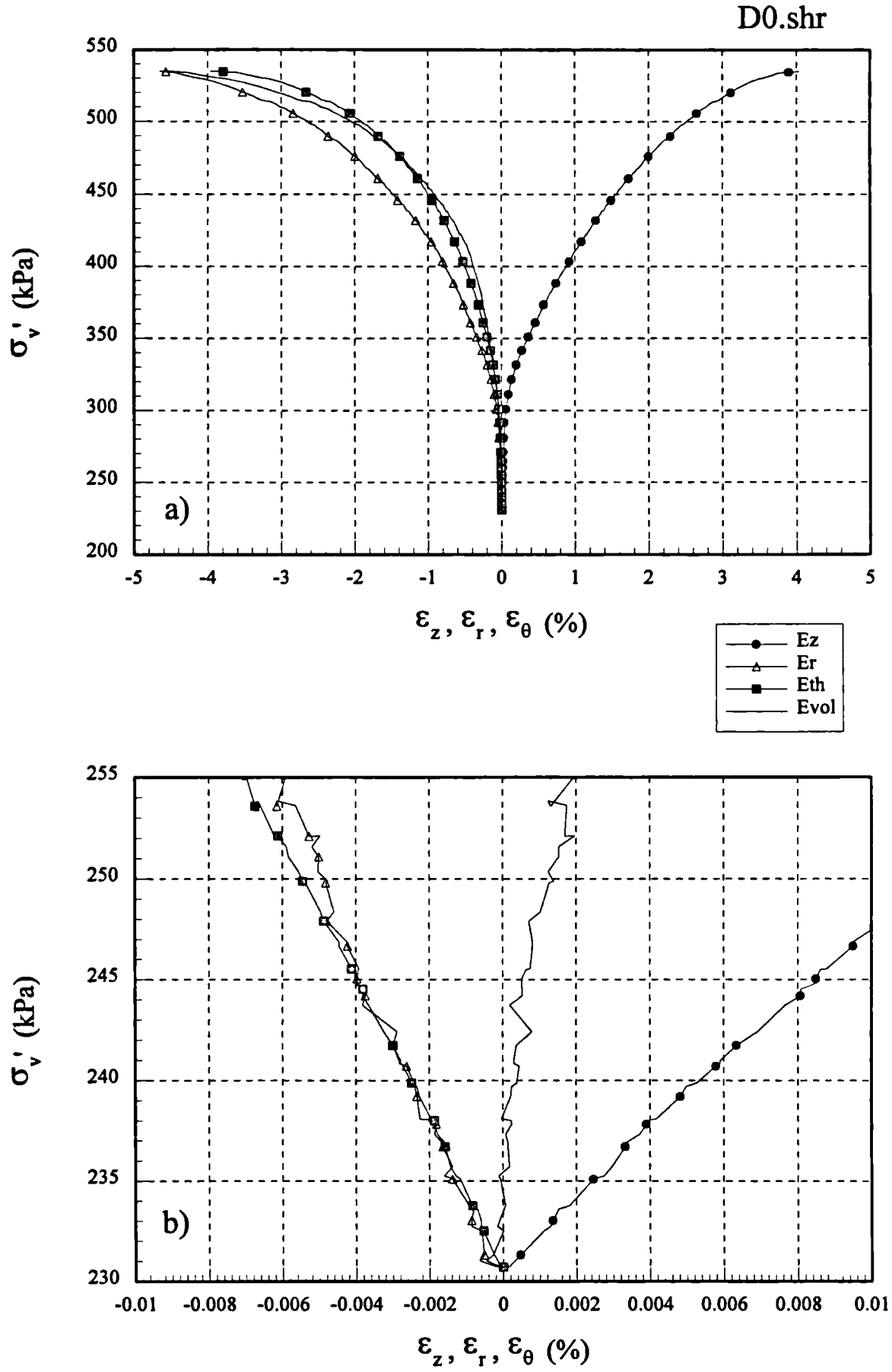


Fig.6.55 - a) Strain components developed during drained direct vertical loading
b) Small strain view

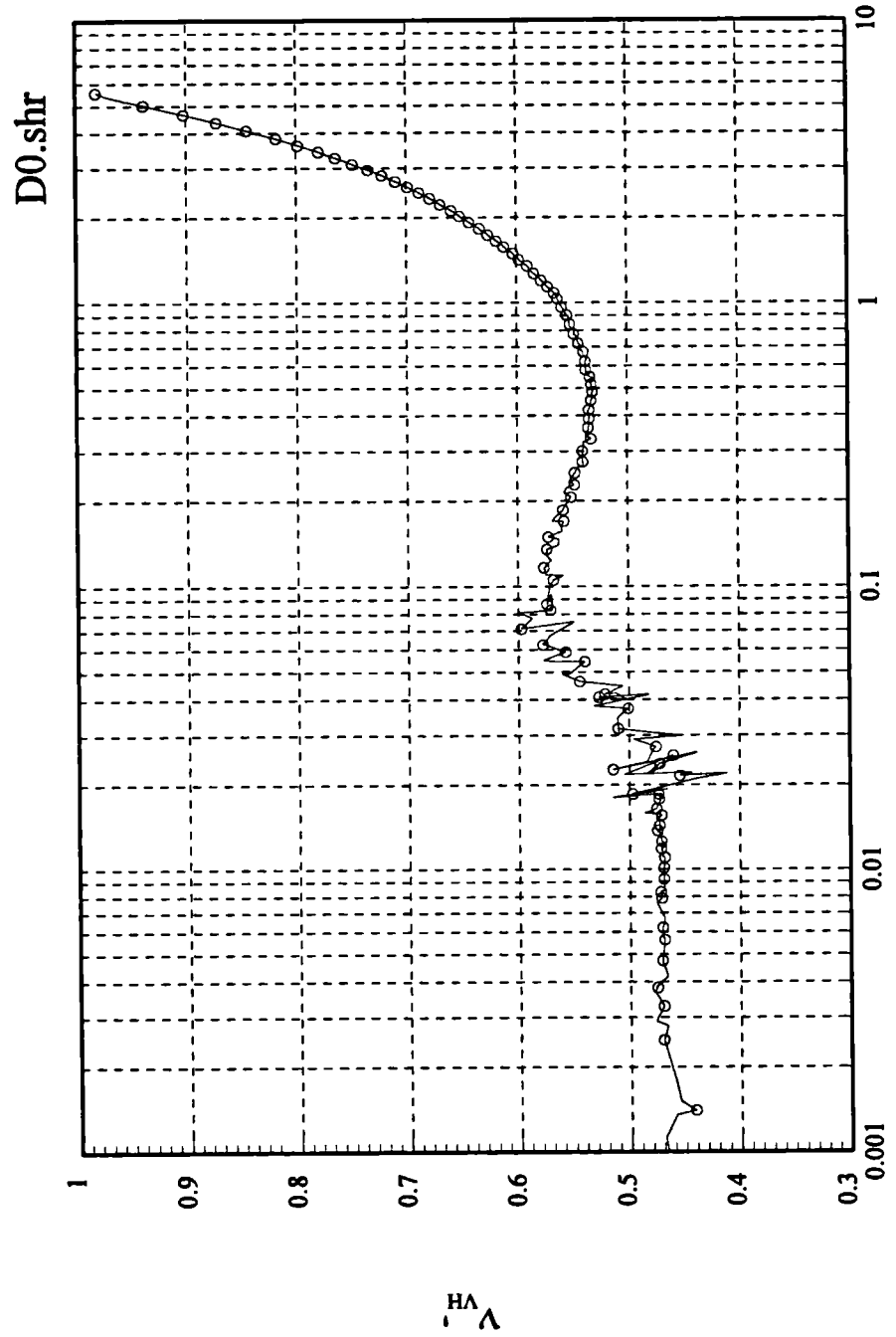


Fig.6.56 - Poisson's ratio for horizontal strain due to vertical direct stress

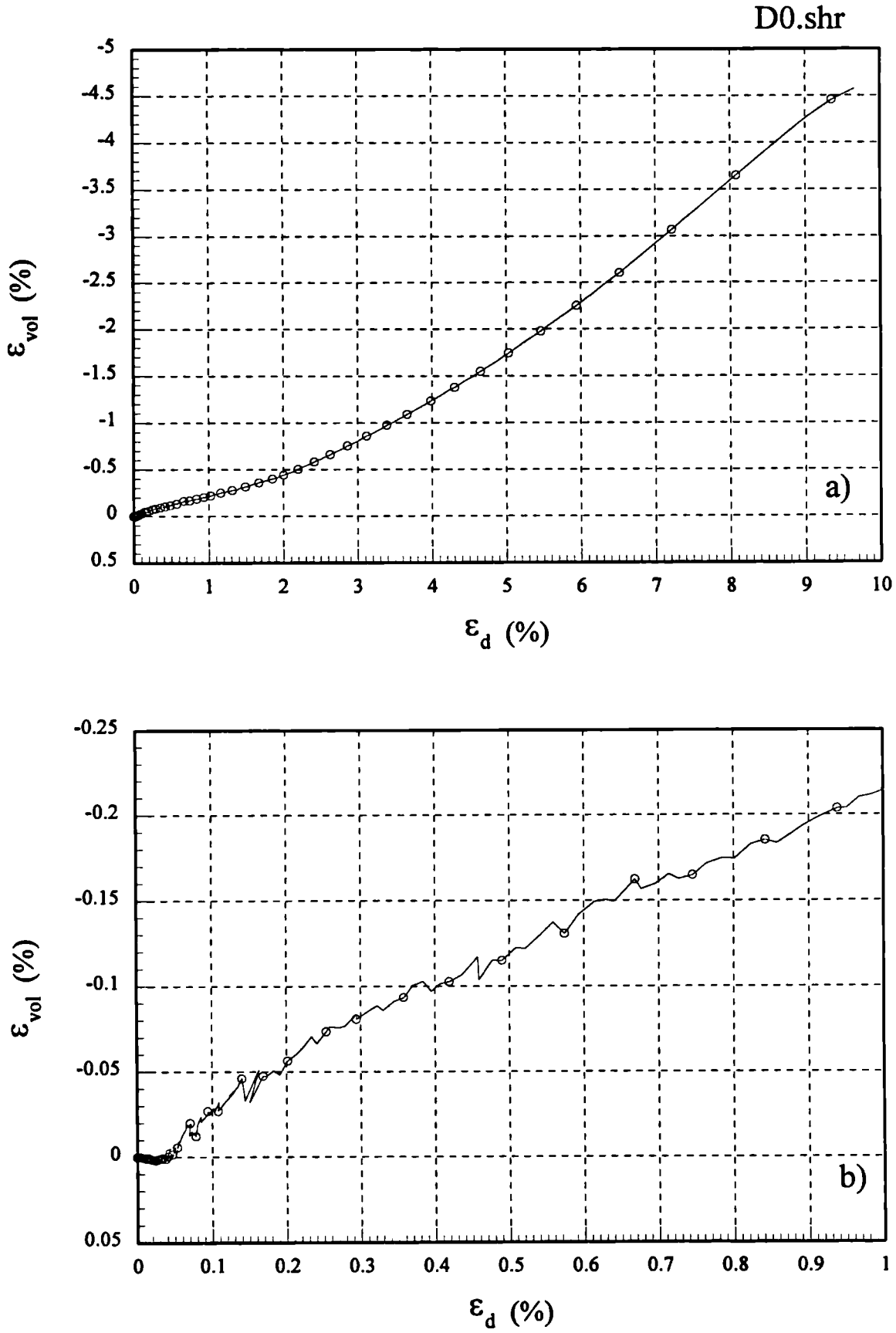


Fig.6.57 - a) and b) Development of volumetric strain during drained direct vertical loading

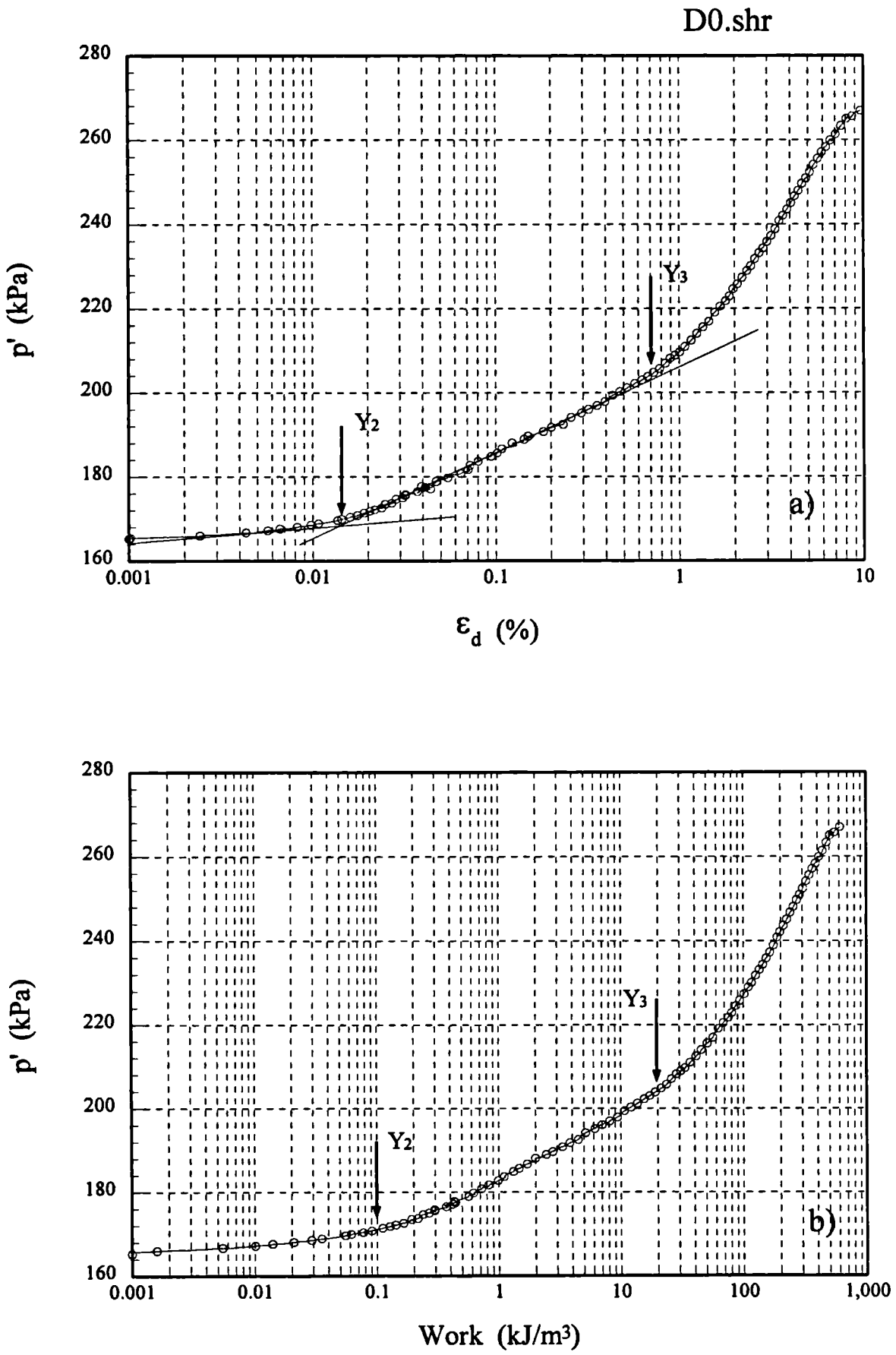


Fig.6.58 - a) Determination of yield boundaries from stress-strain curve
b) Determination of yield boundaries from work

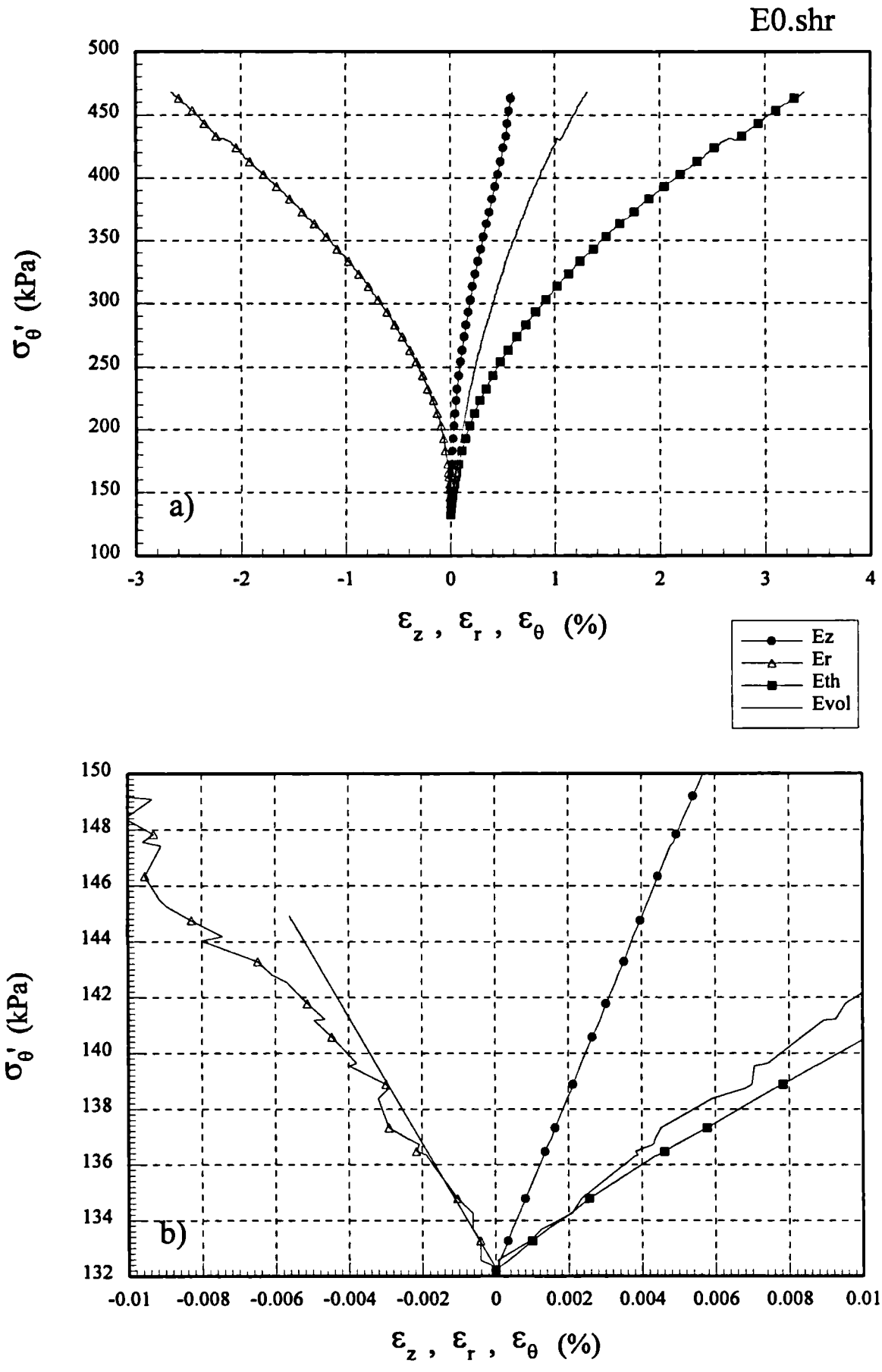


Fig.6.59 - a) Strain components developed during drained direct horizontal loading
b) Small strain view

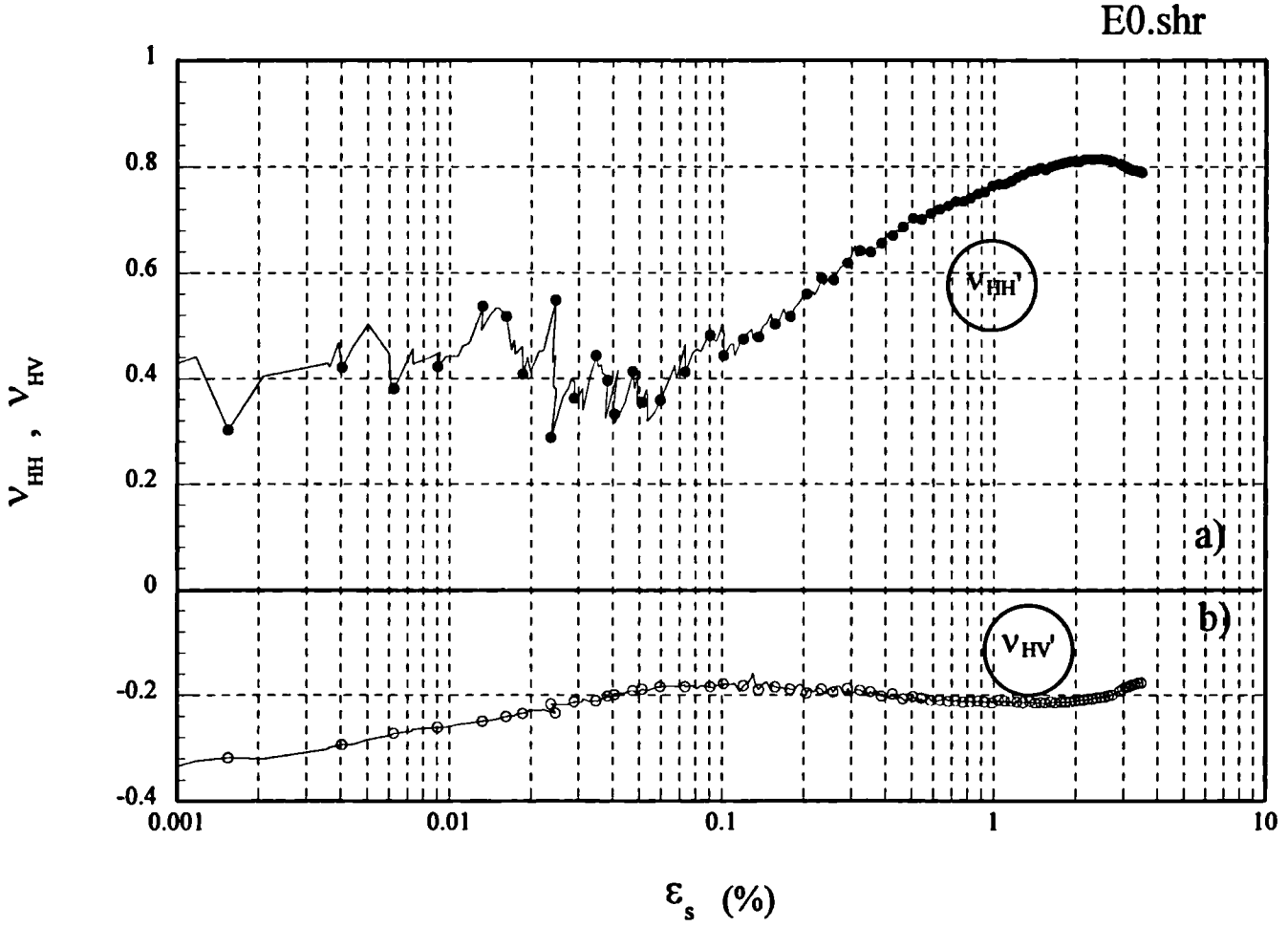
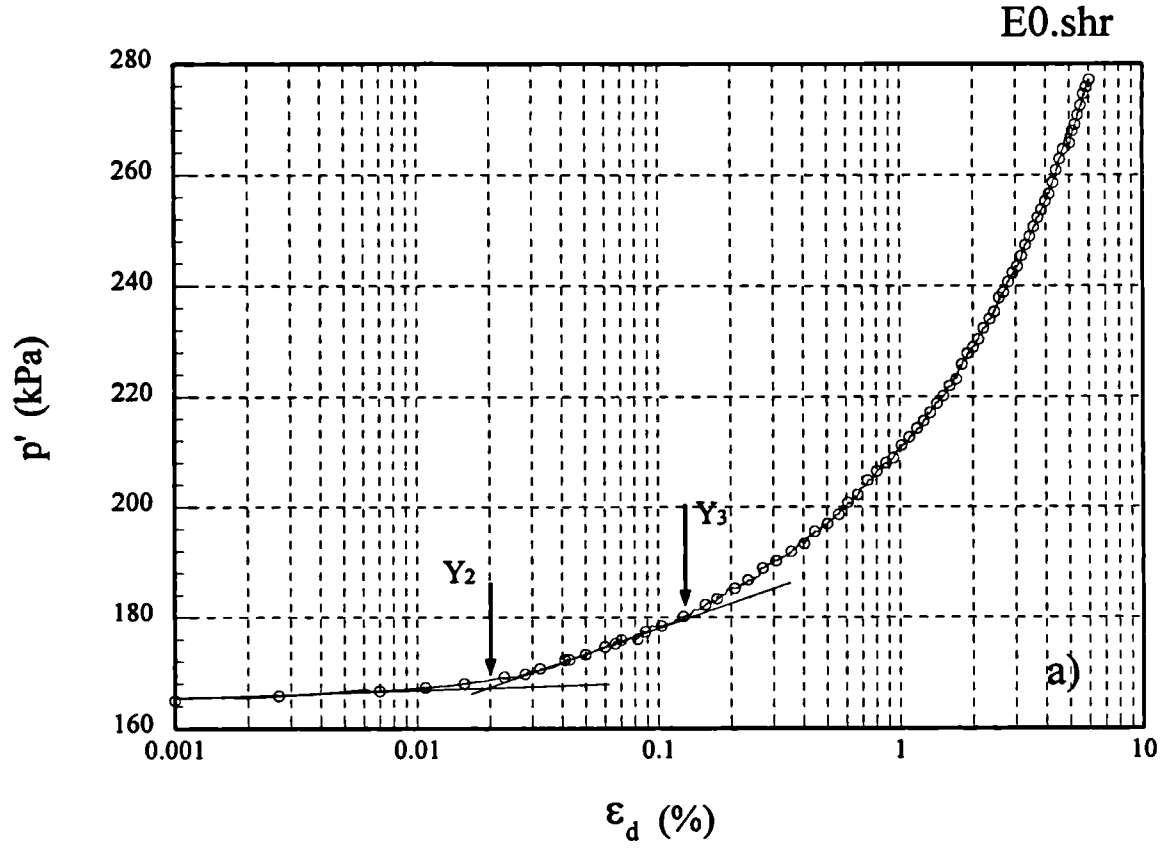


Fig.6.60 - a) Poisson's ratio for horizontal strain due to the horizontal direct stress
b) Poisson's ratio for vertical strain due to the horizontal direct stress



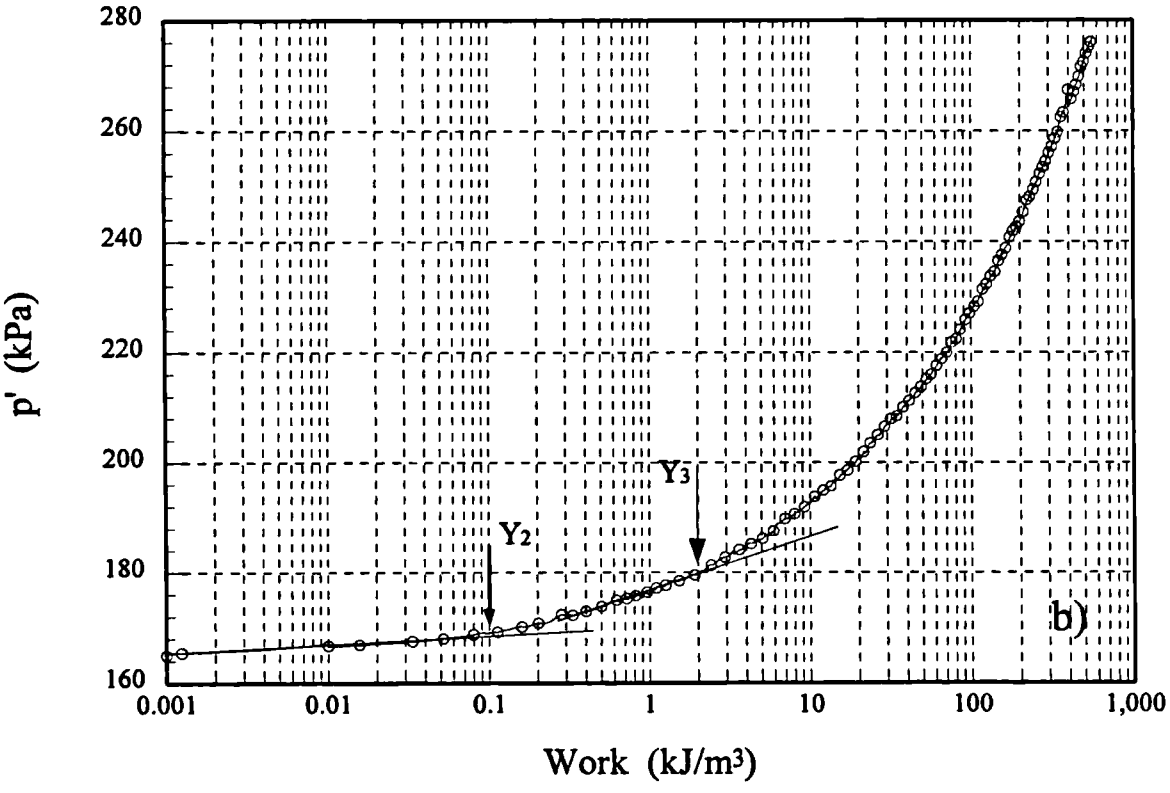


Fig.6.61 - a) Determination of yield boundaries from stress-strain curve
b) Determination of yield boundaries from work

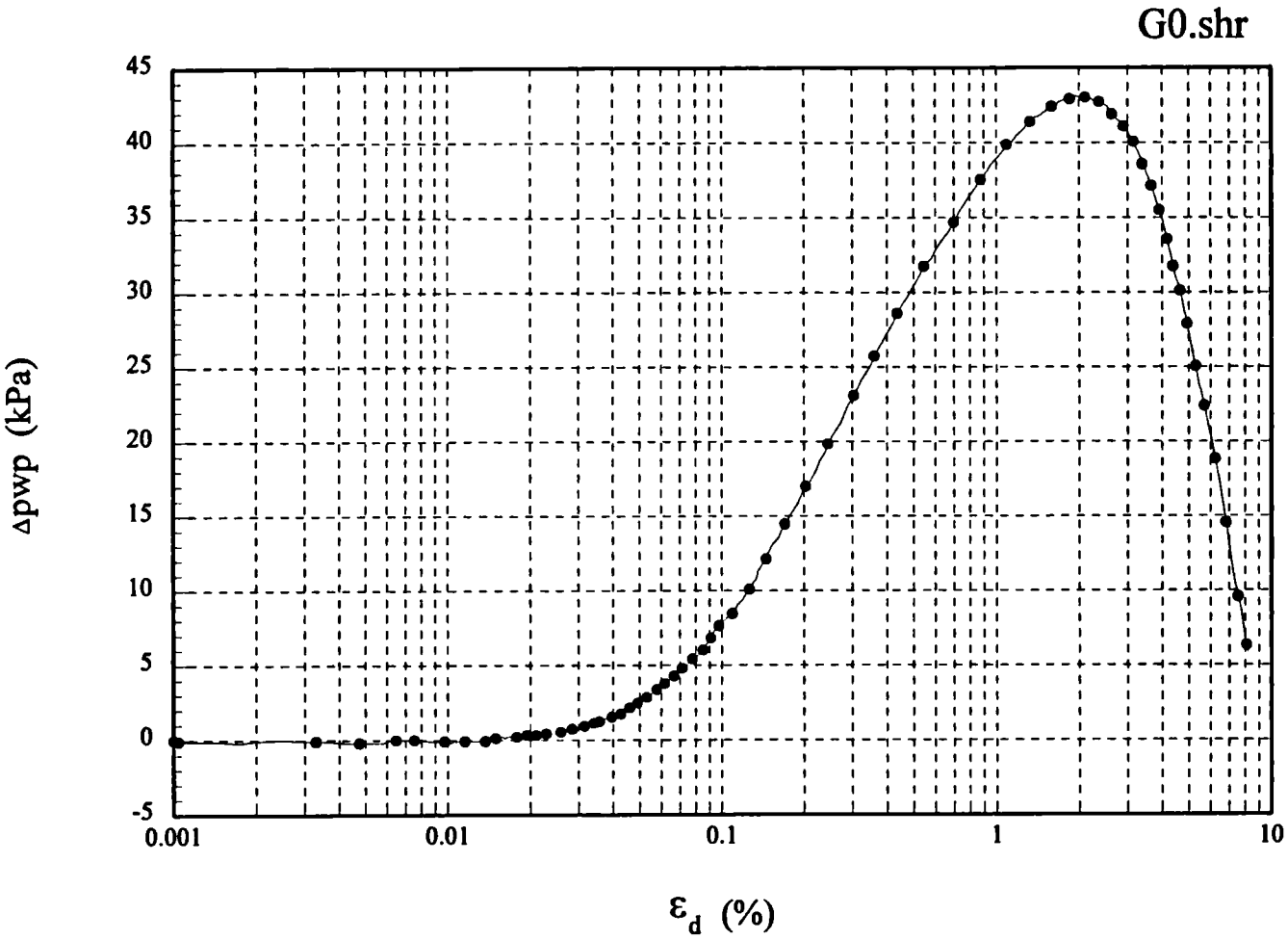


Fig.6.62 - Generation of pore water pressure during pure torsional shearing

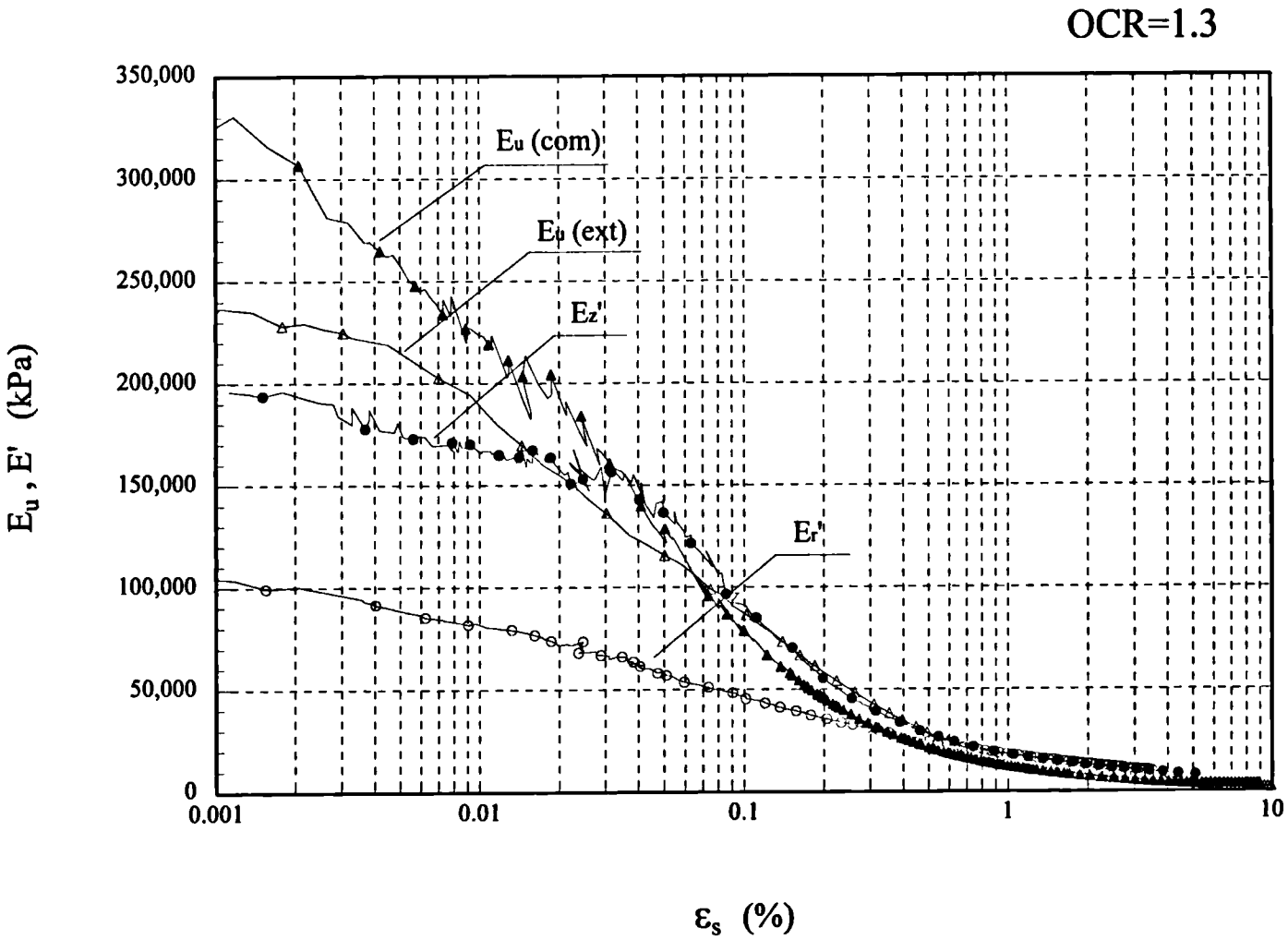


Fig.6.63 - Summary of drained and undrained Young's moduli

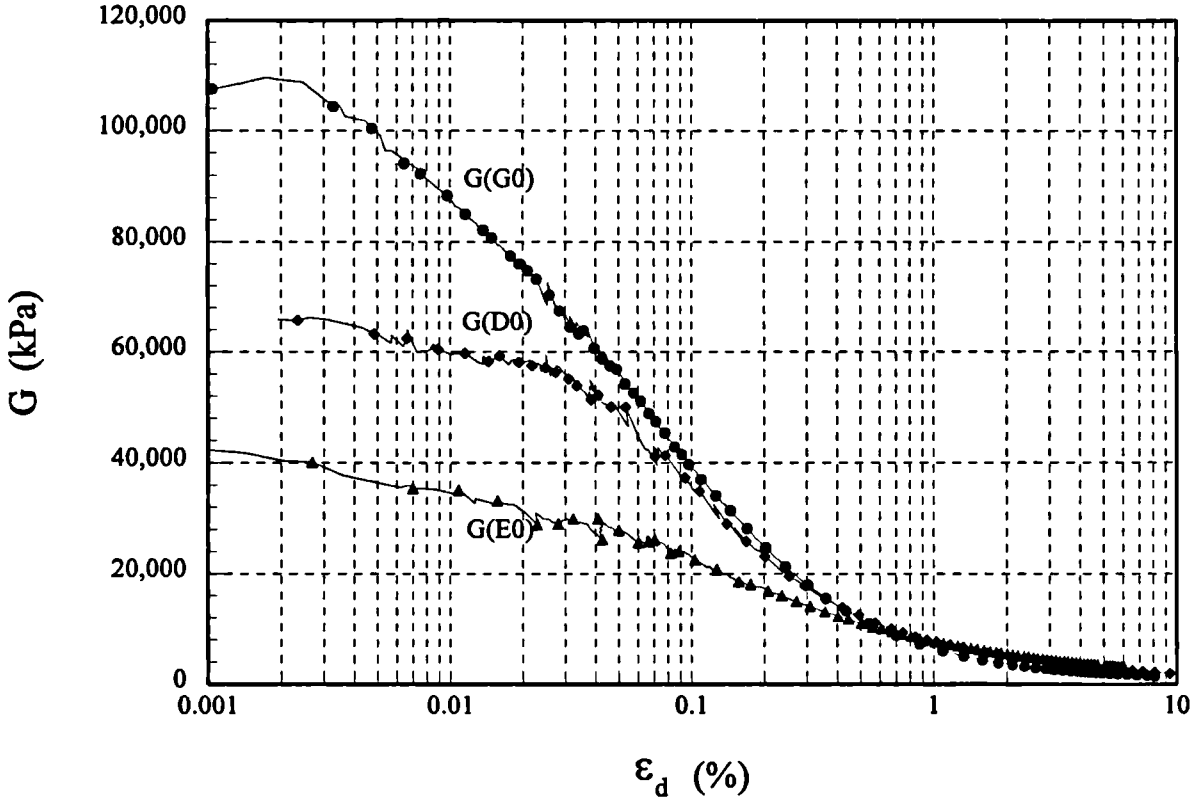


Fig.6.64 - Octahedrah shear modulus

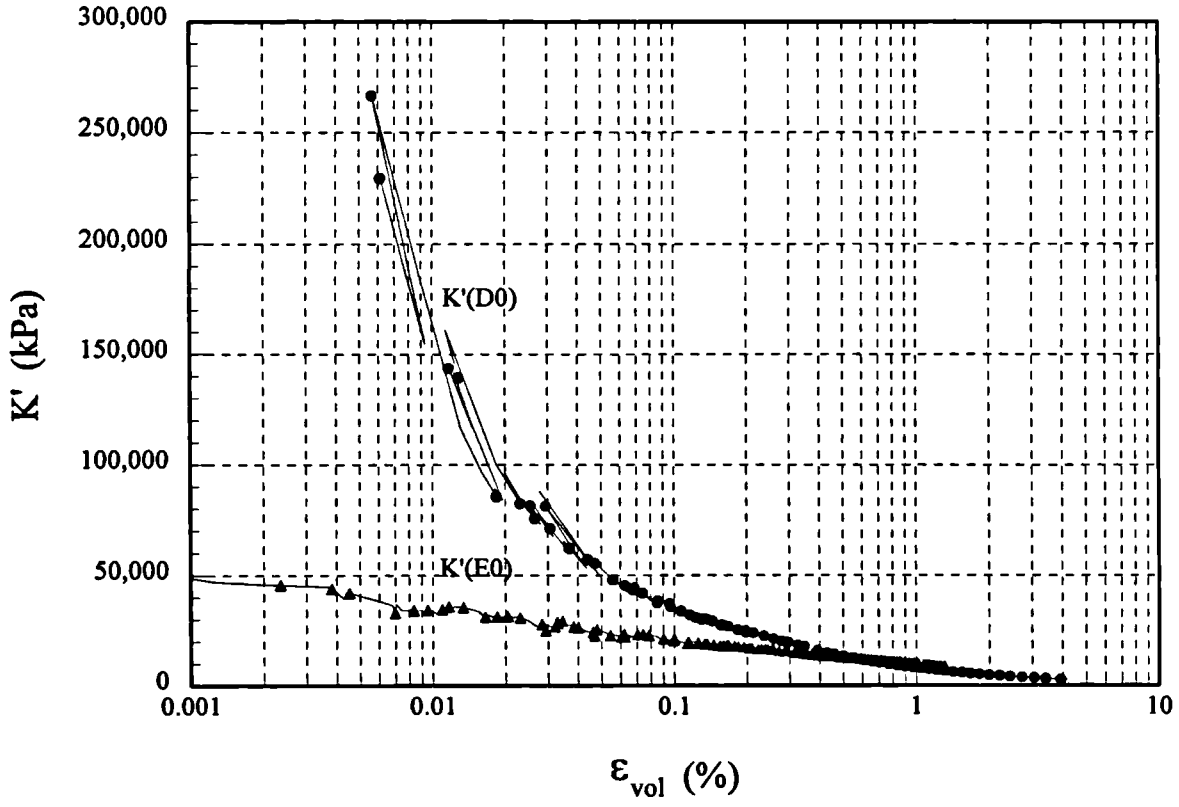
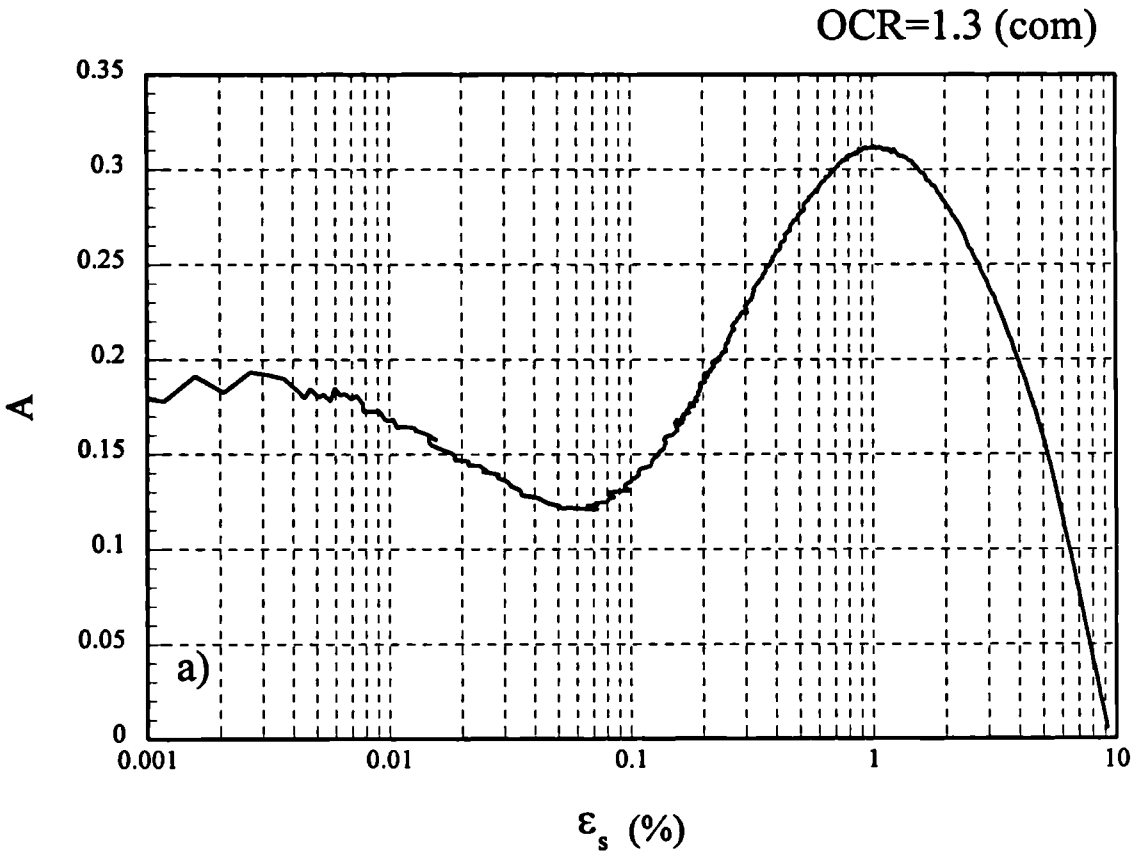


Fig.6.65 - Bulk modulus



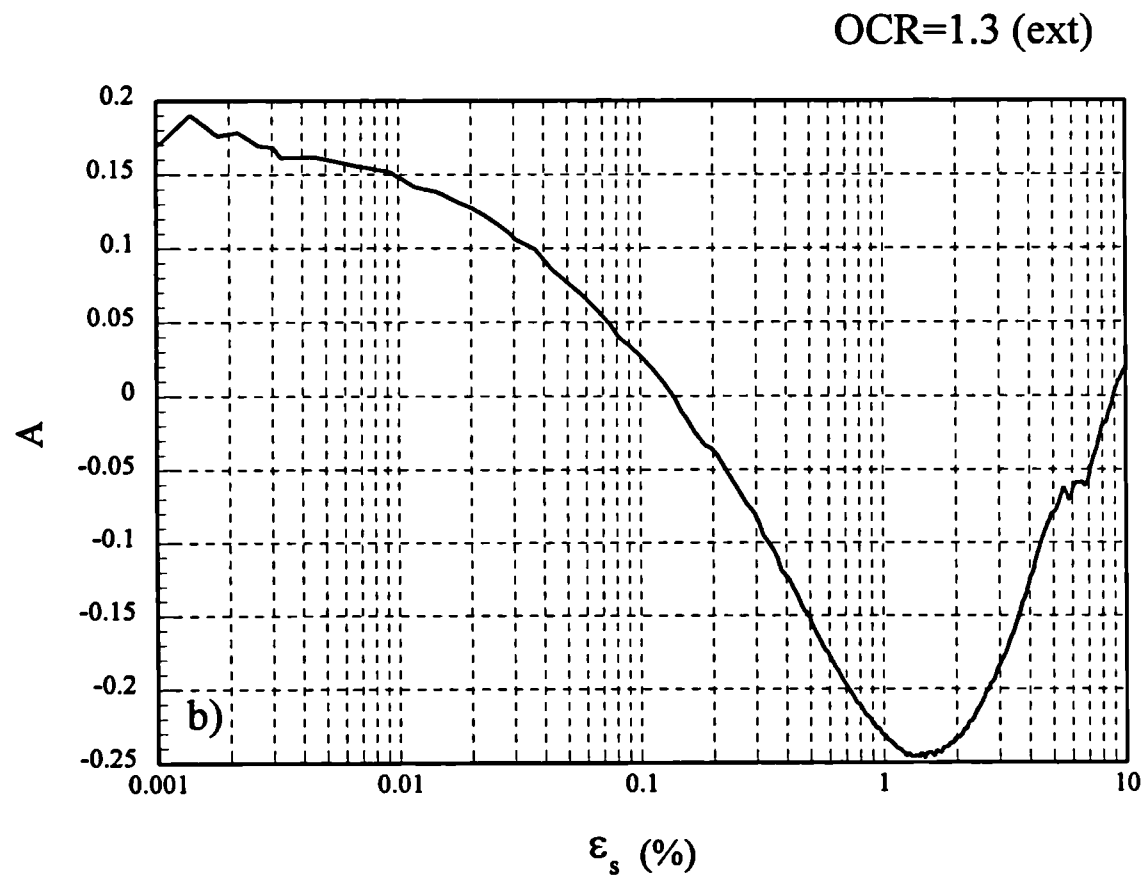


Fig.6.66 - Pore water parameter A in a) undrained triaxial compression and b) undtrained triaxial extenison

Chapter 7

STRESS INDUCED ANISOTROPY - HPF4 CONSOLIDATED WITH INCLINED σ_1 DIRECTION

7.1. Introduction

The test Series described in previous Chapters investigated the anisotropy developed by HPF4 after K_o consolidation. For the range of OCR's considered, the major principal stress direction was always vertical during consolidation. However, in many practical situations geotechnical structures are designed so that the foundations consolidate during construction, under stress conditions with the major principal stress direction rotated away from the vertical. The intermediate principal stress parameter *b* can also hold values between the extremes of zero and unity.

One example of a practical boundary value problem involving "inclined consolidation" is that of multi-stage embankment construction on soft clay (Burland, 1971; Yeats, 1983; Jardine & Hight, 1987a; Jardine & Smith, 1991; Ladd, 1991; Smith, 1992). In this approach the embankment is constructed in stages with rest periods in between. During the rest periods the soil consolidates and its undrained strength increases. This gain in undrained strength allows the construction of the next stage of the embankment. By using this, embankments can be constructed to much greater heights than if construction was attempted in a single stage without any rest periods. The embankment loading imposes a range of different stress paths on the foundation soils, which depend on the location of the soil element relative to the embankment. The anisotropy induced by "inclined" consolidation is a key factor in controlling multi-stage embankment behaviour.

Yeats (1983) performed Finite Element analyses of a *single-stage* embankment using the Modified Cam-Clay (MCC) model to represent the foundation soil. The embankment was constructed quickly so that the foundation soil behaved undrained. Contours of the inclination (α) of the major principal stress direction from the vertical, predicted in the foundation just before failure, when the embankment height was 3m, are presented in Fig.7.1. Prior to construction of the embankment the major principal stress acted in a vertical direction in the foundation. From Fig.7.1, it can be inferred that the major principal stress direction remains nearly vertical over the central area under the embankment. Rotation of the major principal stress

direction occurs mainly under the side slopes of the embankment, being about 10° under the shoulder, about 45° under the mid-side slope and rising to 90° at the toe. To determine the variation of strength of the foundation soil along a potential failure surface under a single-stage embankment, plane strain compression, simple shear and plane strain extension tests on K_o consolidated samples are often considered appropriate, over the portions identified in Fig.7.2.

For *multi-stage* embankment construction, it is important to evaluate the gain in soil strength due to the consolidation which occurs in the rest periods between the stages of construction. Smith (1984) performed an elasto-plastic FE analyses of a multi-stage embankment[1] to predict the stress paths developed during both the construction and rest periods. The isotropic MCC model was used for this study and the simulated embankment was built up in layers to a final height of 7.0 m, as shown in Fig.7.3. Eight construction stages were modelled. In the first stage the embankment was constructed to a height of 3m, in the second stage a further 1m of fill was added and in each of the subsequent stages 0.5m of fill was added. Between each construction stage a rest period was allowed for partial consolidation. This sequence of partial dissipation and loading phases approximately followed that of the Queenborough case history. The predicted effective stress paths *(t, s')* are presented in Fig.7.4, for soil elements located at positions 1, 3, 5 and 1', 3', 5' under the embankment, Fig.7.3. These stress paths confirm that the first lift of 3.0m in thickness brought the soil elements close to failure. During the following rest period consolidation occurred and the stress paths all moved away from failure. At points away from the centre-line of the embankment consolidation took place with $\alpha>0$. This sequence of events was followed for subsequent construction and rest periods. During the construction stages the effective stress paths approach failure but move away from failure during the rest period. The variation of the inclination of the major principal stress, α, with embankment height, for soil elements located at points 1, 2, 3, 4 and 5, are given in Fig.7.5. For soil under and adjacent to the toe of the embankment, a large rotations in the direction of the major principal stress occur during the first stage of construction. Only small changes in this direction occur during subsequent construction stages and rest periods and consequently the soil is subjected to large strain consolidation with an approximately constant α value. For soil under the shoulders of the embankment the direction of the major principal stress, α, rotates gradually from 0° to 30° as the embankment height rises from 0 to 7 m. This soil is therefore subjected to consolidation with slowly changing α values.

[1]Based loosely on the Queenborough Bypass case history described by Nicholson & Jardine (1981).

The scope for simulating such conditions in ordinary laboratory equipment is limited. Smith (1992) performed suites of triaxial stress-path tests to help elucidate the effects of multi-stage construction on soft clays. These tests gave an insight into the strength gain for active (α=0°) and passive (α=90°) strength zones (ignoring the possible effects of *b*). However, he could not examine soil behaviour under different inclinations, α, of the major principal stress. Ladd & Edgers (1972) simulated the behaviour of the foundation soil under *multi-staged* embankments using the Geonor Direct Simple Shear apparatus (DSS).

Although limited, the results from these triaxial and DSS tests provide the following important indications about the behaviour of foundation soils under multi-stage embankments:

- Smith (1992) performed passive consolidation tests (i.e. consolidation with α=90°) on Bothkennar and Queenborough clays. In these tests the same ratio of σ_1'/σ_3' was used during consolidation as in the K_o consolidated tests, but the horizontal stress was greater than the vertical stress. In terms of the multi-staged embankment problem such tests approximately resemble the consolidation behaviour of soil elements under the embankment toe. The effective stress path (ESP) from his Bothkennar clay test, together with compression and extension ESPs for K_o consolidated samples and a compression ESP for an isotropically consolidated sample, are presented in Fig.7.7. Results are summarized (as shown in Table 7.1) for all tests in the form of the undrained peak strength, c_u, normalized by either σ_{vc}' (vertical effective stress at the final consolidation point), or σ_{1c}' (major principal effective stress at the final consolidation point). For all but the passive consolidation test $\sigma_{1c}'=\sigma_{vc}'$. The observed value of c_u/σ_{vc}' in the passive consolidation test was 2.5 times larger than that of the extension test performed on the K_o consolidated material (SUD1). The equivalent number for the ratio c_u/σ_{1c}' is 1.5. These results imply that adopting either the c_u/σ_{vc}' or c_u/σ_{1c}' ratios derived from conventional extension tests (in which consolidation occurs with the major principal stress acting vertically) will be conservative for soil which undergoes consolidation and shearing with the same inclined direction of the major principal stress.

- Ladd & Edgers (1972) performed a series of experiments on initially similar samples of Boston Blue clay which were consolidated while being subjected to a gradually increasing horizontal shear stress, τ_h. This procedure results in a gradual change in the direction of the major principal stress during consolidation. As noted above soil under the shoulders of a multi-staged embankment is subjected to such conditions. The samples were then sheared undrained. The results of these tests are shown in Fig.7.6. Three trends can be observed from these results.

Firstly, the stress-strain curves, which are ductile in tests on K_o consolidated samples, become more brittle with increasing α_c (where α_c is the amount of rotation of the principal stress direction during consolidation). Secondly, the initial stress-strain response during undrained loading becomes progressively stiffer as the value of α_c increases. Thirdly, the peak undrained strength ratio τ_h/σ_{vc}' increased significantly with α_c. For example, an estimated rotation of α_c=*16.7°* at the end of consolidation resulted in an increase in peak τ_h/σ_{vc}' by a factor of 1.65 over that obtained for the K_o consolidated sample (α_c=*0°*). Jardine and Hight (1987) estimated that this is equivalent to an increase in the ratio c_u/σ_{1c}' of about 30%.

Table 7.1: Summary of c_u/σ_{vc}' and c_u/σ_{1c}' ratios for tests done by Smith (1992)

TEST	DESCRIPTION	c_u/σ_{vc}'	c_u/σ_{1c}'
LUD1	K_o consolidated, compression (OCR=1.0)	0.347	0.347
SUD1	K_o consolidated, extension (OCR=1.0)	0.241	0.241
SUD2	Isotropic consolidation, compression	0.372	0.372
LCD315	Passive consolidation, extension	0.597	0.372

To examine the effects of inclined consolidation in a systematic way, a more sophisticated device with controlled principal stress rotation, such as a hollow cylinder apparatus, is necessary. Porovic (1995) performed a set of three tests in such equipment, on Ham River Sand (HRS), with an initial e_o=0.77. "Inclined" consolidation, following an initial K_o consolidation to p'=200 kPa, was performed with α_c varying from 0° to 22.5°, 0° to 30° and 0° to 45°, with each sample reaching a final *p'* of 400 kPa, while keeping *t/p'* constant. These samples were then sheared undrained, by applying only $\tau_{\theta z}$, which led to failure with nearly constant values of α. Normalized undrained shearing effective stress paths for the three tests are presented in Fig.7.8a. They suggest that samples consolidated in this manner to a range of α_c values, develop similar undrained effective stress paths and similar undrained strength, when sheared to failure with $\alpha \approx \alpha_c$. The variations of secant torsional shear stiffness, $G_{\theta z}$, with shear strain, $\gamma_{\theta z}$, for all three tests are presented in Fig.7.8b. This figure shows that the initial, small strain stiffness, is also nearly the same for all three inclinations of the major principal stress, but that the values of $G_{\theta z}$ differ for $\gamma_{\theta z}$ greater than 0.001%. When compared to the results from the DSS presented above, these finding may seem contradictory. However, the two sets of experiments are not directly comparable. In the hollow cylinder tests all samples were consolidated with the same *t/p'* ratio, whereas in the DSS

each sample had a different (and unquantifiable) *t/p'* ratio during consolidation. Consequently, in the DSS tests two effects, different α_c and *t/p'* ratios, are operating during consolidation which then contribute to the observed differences in subsequent shearing behaviour.

However, it is clear from the above triaxial, DSS and HCA experiments that consolidation with $\alpha_c>0$ induces a new anisotropy of strength and stiffness that differs considerably from that normally expected in K_o consolidated sands and clays. This Chapter reports a more extensive set of HCA tests (named the R-Series), which were performed on HPF4 silt, to study how strength and stiffness anisotropy might be induced by a stress regime such as that developed under a multi-stage embankment. First, the consolidation behaviour will be considered, comparing "inclined" and K_o consolidation. Then the undrained shearing response observed at the end of consolidation will be analyzed with respect to the anisotropy induced by the preceding "inclined" consolidation.

7.2. Description of tests

Fig.7.9a presents the effective stress paths, in *t-p'*-α space, applied in the R-Series Hollow Cylinder tests. All samples were initially K_o consolidated with K_o=0.5, from an initial void ratio of approximately 0.65 (as in the previous test series) to a mean effective stress p'=200 kPa, under a back pressure of 400 kPa (path OA). At point A (p'=200 kPa and t=75 kPa), drained rotation of the direction of the major principal stress was applied. Each test in the series was subjected to a different amount of stress rotation and ended at either points B, C, D, E and F for tests R15 to R90 respectively, where the number in this test identifier denotes the final value of α. During this rotation of the direction of the principal stress, the stress point in the *t-p'* plane remains unchanged and the projection of the rotational stress path in this plane remains at point *A* (Fig.7.9b). After rotation of the major principal stress direction, the samples were allowed to age for 12hrs (i.e. over night). Then further consolidation was continued with a constant inclination of α, to a mean effective stress p'=400 kPa, under the same back pressure of 400 kPa. Test R0 was performed without any principal stress rotation, i.e. it was continuously K_o consolidated to 400 kPa. It was anticipated that consolidation to double the initial effective stress level would establish conditions where the initial K_o history would be substantially replaced by new, induced anisotropy (Gens, 1982). This was later confirmed by the experimental observations made in this test series. The inclination of the effective stress path in the *t-p'* plane during inclined consolidation was the same as that for the previous K_o consolidation path,

namely $\Delta t/\Delta p'=0.375$, Fig.7.9b. A pause-period of 24hrs was allowed after "inclined" consolidation for strains to stabilize to 0.05 %/day.

An additional test R45f was performed such that α rotated continuously during the "inclined" phase, starting from $\alpha=0°$ at point *A*, and reaching $\alpha=45°$ at the final consolidation point, *J*. The purpose of performing this test was to assess the effective stress path dependence of the consolidation and subsequent shearing characteristics, by comparing consolidation paths of tests R45 (where α=const=45°, path ADJ) and test R45f (path AJ). The projection of the stress path for test R45f on the *t-p'* plane is of the same slope as the others: $\Delta t/\Delta p' = 0.375$. In the following text, these paths will be referred to as the 'constant_α' and the 'increasing_α' consolidation paths, respectively. Table 7.2 gives a summary of all parts of the consolidation history for each test in this Series.

At the end of inclined consolidation and the subsequent creep period, the *b* value was changed from 0 to 0.5, maintaining constant *p*, *t* and α values for all samples in the test series. A further creep period was then allowed before the samples were sheared under undrained conditions with a deviatoric strain rate of approximately 5%/day. During this shearing stage *p*, *b* and α were kept constant.

Table 7.2: Consolidation stress paths for R-Series tests

TEST	K_o consolidation	PSR* at t=75 kPa	"inclined" consolidation	b-change at
R0	O-G	/	O-G (α=0°)	G
R15	O-A	A-B (0°-15°)	B-H (α=15°)	H
R30	O-A	A-C (0°-30°)	C-I (α=30°)	I
R45	O-A	A-D (0°-45°)	D-J (α=45°)	J
R70	O-A	A-E (0°-70°)	E-K (α=70°)	K
R90	O-A	A-F (0°-90°)	F-L (α=90°)	L
R45f	O-A	/	A-J (α=0°-45°)	J

* Principal Stress Rotation at constant *t*

The paths followed in the R-test Series are an idealised and systematic form of those

predicted by Smith (1984) for soil underneath a multi-stage embankment on soft clay. As mentioned earlier, he showed for soil under and adjacent to the toe of the embankment, that marked principal stress rotation developed during the single-stage loading of initially K_o consolidated soil, while subsequent multi-stage construction leads to relatively slight further changes in α (Fig.7.5). The R-test Series did not simulate the first stage of undrained embankment construction, but included drained changes in α, followed by constant α "inclined" consolidation.

One of the dilemmas when planning this series of tests was at what stage should the *b* value be changed. Strictly speaking, if the tests were intended to simulate soil behaviour after the first construction stage of an embankment then the logical place to change *b* would have been after K_o consolidation, either before or after the direction of the principal stress was changed. However this would have impeded comparisons with the M-Series tests (Chapter 5) where *b* was changed to 0.5 after consolidation was complete. On balance, it was decided that the latter requirement was more important and therefore the *b* change was imposed after the inclined consolidation stages were complete in the R-Series tests.

7.3. Drained principal stress rotation

7.3.1. Stress-strain behaviour

As noted above, slow drained principal stress rotation was applied to samples R15 to R90, after initial K_o consolidation to p'=200 kPa. During this rotation the effective stress point remained at p'=200 kPa and t=75 kPa, while α increased monotonically. In Fig.7.9a these stress paths are labelled AB, AC, AD, AE and AF.

The stress path directions imposed during the α_rotation stages are common to all tests and the material response to the different values of α_c is summarized in Fig.7.10, where the stress components are plotted against deviator strain ε_d. In all cases the axial stress, σ_z, reduces, while the radial stress, σ_r, remains constant and the circumferential stress, σ_θ increases. The torsional shear stress, $\tau_{\theta z}$, initially increases as α increases from 0° to 45° (point C), but then reduces as α increases further, Fig.7.11. The application of the torsional shear stress is fully repeatable at small strains (to ~0.15% ε_d, see logarithmic plot in Fig.7.11b), but deviates by as much as ~10% at higher values of principal stress rotation, α. This deviation is not thought to have a significant effect on the sample's subsequent responses.

Although the applied stress changes all involve unloading in (σ_z-σ_θ), the measured strain components indicate compressive axial strain increments, $\Delta\varepsilon_z$, until $\alpha\approx60°$ (Fig.7.12a). The circumferential strains, ε_θ, increase monotonically with α, while the radial strains are expansive and relatively large. As with ε_z, the torsional shear strains $\gamma_{\theta z}$ increase with α until they reached a maximum when $\alpha\approx60°$. A similar pattern of strain behaviour was seen in test E0 of the D-Series (Chapter 6), where the response to drained horizontal circumferential loading was observed (Fig.6.59). In test E0, σ_z and σ_r were kept constant while σ_θ was increased in drained shearing, following K_o consolidation. In contrast, in the R-Series tests drained principal stress rotation was applied with σ_r=const, σ_z decreasing and σ_θ increasing, after K_o consolidation. It may therefore be concluded that the structure formed in HPF4 by K_o consolidation is collapsible in the radial direction when loaded circumferentially under drained conditions.

The relationship between axial and volumetric strains during principal stress rotation is presented in Fig.7.13. The two strains follow roughly linear relationships up to ε_{vol}~0.05%, (which corresponds to ε_d~0.15% and α~15°), reflecting the trend from the previous K_o consolidation where $\varepsilon_z=\varepsilon_{vol}$. The volumetric strains become relatively large once α>30° and ε_z fails to keep pace with volumetric strains once this limit has been exceeded. The axial strain remains in compression during the α_rotation stage in all tests except test R90. In test R90 it underwent slight extension during the creep period.

Strain-time curves for strain components ε_{vol}, ε_z and $\gamma_{\theta z}$ for each test are presented in Fig.7.14. It can be noted that the absolute magnitudes of the strains developed during the creep period do not depend on α, with $\varepsilon_{vol}^{(creep)}$~0.1%, $\varepsilon_z^{(creep)}$~0.05% and $\gamma_{\theta z}^{(creep)}$~0.05% for all of the tests. The variation of the associated strain rates with time are presented in Fig.7.15. These plots show that the creep strain rates for all three strain components reduced to the desired 0.05 %/day (or 0.002 %/hour) before the end of the creep period.

7.3.2. Principal stress and strain increment directions

The progressive change of the mode of straining, observed in Fig.7.12a, is also evident in the trends of the changes in the directions of σ_1, $\Delta\sigma_1$, ε_1 and $\Delta\varepsilon_1$ shown in Fig.7.16. Due to the manner in which the stress changes are imposed during the α_rotation stage, the direction of the incremental principal stress, $\alpha_{\dot{\sigma}}$, is always inclined at 45° to the direction of the major principal stress, α_σ, i.e. $\alpha_{\dot{\sigma}}=\alpha_\sigma+45°$. The major principal strain increment direction, $\alpha_{\dot{\varepsilon}}$, starts with an inclination of ~25° and lags approximately 15° behind $\alpha_{\dot{\sigma}}$ for the most part of

all tests. For tests R70 and R90, $\alpha_{\dot{\sigma}}$ changes from a compression to an extension mode at α=47° (point C), when $\varepsilon_d \approx 1.4\%$ (see also Fig.7.10). The major principal strain increment direction, $\alpha_{\dot{\varepsilon}}$, changes mode at point D, after a lag of $\varepsilon_d \sim 1.0\%$ (or 23° lag in α) from point C. The Mohr circles of strain increment for the situations prior to and after point D are presented in Fig.7.17. Prior to point D (α<47+23°) both $\Delta\varepsilon_z$ and $\Delta\varepsilon_\theta$ are compressive, Fig.7.17a. After point D (α>47+23°) $\Delta\varepsilon_z$ becomes tensile and $\Delta\gamma_{\theta z}$ changes sign, Fig.7.17b. As indicated in Fig.7.17b the direction of the major principal strain increment direction, $\alpha_{\dot{\varepsilon}}$, exceeds 90° after point D. For convenience, such values have had 90° subtracted before being plotted in Fig.7.16.

In general, while α_σ, $\alpha_{\dot{\sigma}}$ and $\alpha_{\dot{\varepsilon}}$ coincided during K_o consolidation, the relationships during drained principal stress rotation were: $\alpha_{\dot{\sigma}} = \alpha_\sigma \pm 45°$ and $\alpha_{\dot{\varepsilon}} = \alpha_{\dot{\sigma}} - 15°$.

7.3.3. The effects of recent stress history

The effects of recent stress history on the response of HPF4 at small strains were recognized in earlier test series. For example in the M-Series (Chapter 5), the applied stress stages consisted of K_o consolidation, *b*_change, undrained unloading in *t* (with α=0°, b=0.5), principal stress rotation (with t=const, b=0.5), and shearing (with α=const, b=0.5), with pause periods in between to allow the creep strain rates, resulting from the previous stage, to stabilize before the application of the next stage. During each stage of loading, a set of particle contacts developed in the sample that corresponded to the applied stress conditions of that stage. It was seen that the previous stress path, together with ageing, formed an Y_2 yield boundary which influenced the strain increment direction for the new stress path.

The variation of the strain components with deviatoric strain observed at the start of the α-rotation stages of the R-Series tests (Fig.7.12b), indicates a similar influence of the recent stress history. The applied stress path consisted of increasing $\tau_{\theta z}$ and decreasing $(\sigma_z - \sigma_\theta)$, with σ_r=constant. The samples responded by developing $\gamma_{\theta z}$, as expected. However, ε_z continued to increase in compression, while ε_r and ε_θ remained close to zero. At $\varepsilon_d \approx 0.02\%$, a marked change in behaviour occurred, with ε_r and ε_θ developing significant strains (which were tensile and compressive respectively). These counter-acting trends in ε_r and ε_θ mask the effect of Y_2 yielding at ε_d=0.02%, in the ε_z versus ε_{vol} plot given in Fig.7.13, which appears to show a constant strain increment direction up to ε_z=0.05%.

7.3.4. Stiffness behaviour during principal stress rotation

The variation of secant torsional shear stiffness, $G_{\theta z}$, with torsional shear strain, $\gamma_{\theta z}$, during the principal stress rotation stages of all five tests is presented in Fig.7.18. The data all fall very close together, indicating the excellent repeatability of the test procedures. The only difference is the maximum value of $\gamma_{\theta z}$ in each test, which depends directly on the amount of principal stress rotation applied. Similarly, the corresponding secant octahedral shear stiffness, *G*, versus deviatoric shear strain, ε_d, curves all fall very close to a single curve (Fig.7.19). As in Section 5.4, *G* octahedral is calculated as $\Delta J/\varepsilon_d$, where ΔJ and ε_d are evaluated from the changes in stresses and strains occurring from the beginning of this α_rotation stage (Eq.5.1, 5.2). If instead the change in the accumulated *J* had been used to evaluate ΔJ, the curves would show an absurdly soft response because *J* remained constant during the constant *t* principal stress rotation phases.

7.4. Drained inclined consolidation

7.4.1. Stress-strain behaviour

After completion of the α_rotation stage and the subsequent creep period the R-Series samples were further consolidated with *b*, α and $\Delta t/\Delta\alpha$ constant as shown in Fig.7.9a, where the paths are identified as AG, BH, CI, DJ, EK and FL. The paths all start at p'=200 kPa and t=75 kPa, and end at p'=400 kPa and t=150 kPa. The inclination of the stress path in t-p' space ($\Delta t/\Delta p'$=0.375), and the rate of consolidation (i.e. ε_{vol}=1.0 %/day, with a total duration of 24hrs) was the same as that for K_o consolidation.

Summary plots of the stress-strain diagrams are presented in Fig.7.20. For test R0 stresses σ_z, σ_r and σ_θ increase monotonically, with $\sigma_r'=\sigma_\theta'=0.5\sigma_z'$, during K_o consolidation. The "inclined" consolidation stress paths for tests R15, R30, R45, R70 and R90 are also monotonic, with $\tau_{\theta z}$, σ_z, σ_r and σ_θ increasing at the particular rates required to keep the specified α and $\Delta t/\Delta p'$ values.

The changes in the strain components, ε_z, ε_r, ε_θ and $\gamma_{\theta z}$ during inclined consolidation with deviatoric strain, ε_d, are shown in Fig.7.21. As tabulated below (Table 7.3), the strain components reflected the applied stress paths: the ratio $\Delta\varepsilon_z/\Delta\varepsilon_d$ fell with α, while the ratio $\Delta\varepsilon_\theta/\Delta\varepsilon_d$ increased. The ratio $\Delta\gamma_{\theta z}/\Delta\varepsilon_d$ was zero at α=0° and achieved its maximum value when α=45°,

after which it decreased again and became zero at α=90°. In all cases $\Delta\varepsilon_z/\Delta\varepsilon_d$ remained positive, i.e. samples were sustaining further compression. The magnitude of the deviatoric shear strain, ε_d, that developed over the inclined consolidation paths, (excluding the creep period), grew from 0.8% in test R0 to a maximum of 1.4% in test R90 (while ε_d=0.84% in R15; ε_d=0.9% in R30; ε_d=1.0% in R45; and ε_d=1.3% in R70). The axial strain developed at the final consolidation points reduced by 75% from test R0 to test R90. These differences are consistent with the stress changes imposed in the different tests during inclined consolidation.

Test R45f

Test R45f was performed such that α changed continuously from 0° to 45° as *t* increased during inclined consolidation (Fig.7.9a). The variations of the stress components with deviatoric strain, ε_d, for test R45f are shown in Fig.7.22. These show that stress path AJ (Fig.7.9a) also involved a continuous increase in the component stresses. However, different patterns of straining are detected when comparing the component strains in Fig.7.21 and 7.23. In the test involving constant α=45° consolidation, ε_z and ε_θ develop with approximately similar gradients (Fig.7.21). In comparison, in test R45f which involved increasing_α consolidation, ε_z initially increased at a faster rate than ε_θ (i.e. $\Delta\varepsilon_z/\Delta\varepsilon_d > \Delta\varepsilon_\theta/\Delta\varepsilon_d$), however towards the end of consolidation this trend reversed and $\Delta\varepsilon_\theta/\Delta\varepsilon_d > \Delta\varepsilon_z/\Delta\varepsilon_d$ (Fig.7.23).

Table 7.3: Development of stress increments during inclined consolidations

"inclined" consolidation	$\Delta\varepsilon_z/\Delta\varepsilon_d$	$\Delta\varepsilon_\theta/\Delta\varepsilon_d$	$\Delta\gamma_{\theta z}/\Delta\varepsilon_d$
0°	0.944	0.083	0
15°	0.800	0.125	0.2
30°	0.625	0.285	0.367
45°	0.375	0.417	0.367
70°	0.293	0.492	0.138
90°	0.114	0.543	0

7.4.2. Stress and strain increment directions

Plots showing how the major principal strain increment directions develop during "inclined" consolidation are shown in Fig.7.25. Because α is constant, α_σ and $\alpha_{\dot{\sigma}}$ coincide along the entire consolidation stress paths, while the strains develop according to the response of the sample. The following observations are made from Fig.7.25:

- In test R15, the direction of the axis of the major principal strain increment, $\alpha_{\dot{\varepsilon}}$, slowly increases from around 5° at the beginning, to 10°±5° towards the end of inclined consolidation. The scatter in the observed values towards the end of consolidation reflects the incremental way in which $\alpha_{\dot{\varepsilon}}$ is evaluated. Axial straining is dominant in this test and the response towards the end of consolidation is such that $\alpha_{\dot{\varepsilon}}$ approaches $\alpha_{\dot{\sigma}}$.

- Test R30 showed a similar trend. ε_z was greater than ε_θ throughout and while $\alpha_{\dot{\varepsilon}}$ lagged 20° to 25° degrees behind α_σ at the beginning of inclined consolidation, $\alpha_{\dot{\varepsilon}}$ and $\alpha_{\dot{\sigma}}$ tended to coincide at the end of the consolidation process.

- In tests R45 and R70, ε_z was no longer dominant. In both cases $\alpha_{\dot{\varepsilon}}$ exceeded α_σ during the early stages, but settled to give $\alpha_{\dot{\varepsilon}} \approx \alpha_{\dot{\sigma}} \approx \alpha_\sigma$ towards the end of inclined consolidation.

- For tests R15, R30, R45 and R70 $\alpha_{\dot{\varepsilon}}$ and $\alpha_{\dot{\sigma}}$ become approximately coincident after 0.6% deviatoric strain.

- In test R90, the direction of $\Delta\varepsilon_1$ was always circumferential, so that $\alpha_\sigma = \alpha_{\dot{\sigma}} = \alpha_{\dot{\varepsilon}} = 90°$.

In summary, the condition $\alpha_{\dot{\varepsilon}} \approx \alpha_{\dot{\sigma}} \approx \alpha_\sigma$ was achieved in all tests once ε_d had exceeded ~0.6%. It is likely that such a condition reflects the development of a new material structure which overwhelms that created during K_o consolidation. This is substantiated later in this Chapter.

Test R45f

In test R45f, α varied continuously during inclined consolidation and consequently the directions of the major principal stress and stress increment did not coincide as they did for the other tests (Fig.7.24). For this test the manner in which the stresses were applied resulted in $\alpha_{\dot{\sigma}} = \alpha_\sigma + 30°$ along the entire inclined consolidation stress path. The major principal strain

increments and stress increments have similar directions ($\alpha_{\dot{\varepsilon}}$ and $\alpha_{\dot{\sigma}}$) at the start of inclined consolidation. However, $\alpha_{\dot{\varepsilon}}$ lags behind $\alpha_{\dot{\sigma}}$ by up to ~15° when 0.1%<ε_d<1.0% (Fig.7.24) and it tends again to coincide with $\alpha_{\dot{\sigma}}$ after about 1.5% shear strain. This coincidence was observed at an earlier stage in the constant α consolidation test (ε_d~0.6%), (see test R45 in Fig.7.25).

7.4.3. Volumetric behaviour

The variations of axial strain with volumetric strain during inclined consolidation, for tests R0 to R90 and test R45f are given in Fig.7.26. As expected, the results for test R0 fall close to the initial K_o line of equality (ε_z=ε_{vol}), while the curves for the other tests tend to move progressively away from this limit as α increases. The overall volumetric strains developed during inclined consolidation are approximately the same - about 1%.

A summary plot of void ratio, *e*, against *p'* for all tests in the R-Series is given in Fig.7.27. During the K_o consolidation stage of each test, the *e-p'* curves (to p'=200 kPa) are all parallel. For the constant_α inclined consolidation stage of tests with α>0, the *e-p'* curves are initially almost flat (after the principal stress rotation), but reach constant, mutually parallel slopes, after p'=250 kPa. The amount of volume change occurring during the α-stage of each test increases with α, as detailed below, but the volume change during constant_α inclined consolidation (p'=200 to 400 kPa) is hardly affected by α, with Δe~0.01 for tests R15 to R90, while that observed during K_o consolidation is slightly larger (Δe=0.016).

A comparison of the results from tests R45 and R45f during total consolidation over their respective paths OADJ and OAJ (Fig.7.9), indicates that both tests experienced approximately the same accumulated volumetric strain. Test R45 developed ε_{vol}≈1.0% during K_o consolidation (OA), ε_{vol}≈0.2% during α-rotation to 45° (AD), Fig.7.13, and ε_{vol}≈0.7% during the subsequent constant α (=45°) consolidation, Fig.7.26, giving an accumulated volume strain of 1.9%. Test R45f developed the same volumetric strain (ε_{vol}≈1.0%) during K_o consolidation and ε_{vol}≈0.9% during subsequent increasing α consolidation, Fig.7.26, again making an accumulated volumetric strain of 1.9%.

It therefore appears that for a given final α, the volumetric strain developed in reaching the final (*t, p', b*) consolidation point, does not depend on whether a constant α or an increasing α stress path is followed during inclined consolidation. However, the accumulated volume strains

developed at the final effective stress points of the R-Series tests (where t, p' and b were all equal, but α varied) increased systematically with α, having values of 1.8%, 1.85%, 1.95%, 2.0%, 2.20% and 2.45% in tests R0 to R90. Fig.7.28a shows a change of volumetric strain, $\Delta\varepsilon_{vol}(Ri)-\Delta\varepsilon_{vol}(R0)$, from 0° to 90°; Fig.7.28b shows the corresponding change in void ratio. These differences were mainly due to the volumetric strains generated during the principal stress rotation phase.

7.4.4. Stiffness behaviour

The variation of secant torsional shear stiffness, $G_{\theta z}$, with shear strain $\gamma_{\theta z}$, calculated from the beginning of the inclined consolidation stage for each R-Series test, is given in Fig.7.29. The results from the tests in which α was constant during inclined consolidation (i.e. R15 to R90) indicate a common initial $G_{\theta z}$ value of about 120 MPa. Values of $G_{\theta z}$ at various values of $\gamma_{\theta z}$ are plotted against the value α for these tests in Fig.7.30. It can be seen from these plots that test R45 gives the stiffest response. Cross-coupling action in the other tests led to 25% lower $G_{\theta z}$ values at the same $\gamma_{\theta z}$ levels.

Also shown on Fig.7.29 is the shear stiffness curve observed in test R45f, where α varied during the inclined consolidation stage, as indicated by the α values marked on the stiffness curve. The stiffness in this test at $\gamma_{\theta z}$=0.001% is ~30% softer than that recorded for the constant α consolidation tests, even though all tests started the inclined consolidation stage from the same (p_o', t, b) stress point. For $\gamma_{\theta z}$>0.02% (α>4°) the $G_{\theta z}$ values agree with those observed in test R45.

If compared with the $G_{\theta z}$ curves for the α-rotation stage (also indicated on Fig.7.29), which also start from the same (p_o', t, b) stress point, it is clear that the stiffnesses observed in the constant-α consolidation stages (including test R45f) are lower than those observed during the α-rotation stage. The reason for these differences can be explained by considering the strain coupling which is connected with the development of the other stress components along each of the stress paths considered:

- During the α rotation stage, t is constant and the sample is being unloaded in terms of $(\sigma_z-\sigma_\theta)$, but loaded in terms of $\tau_{\theta z}$, making $\gamma_{\theta z}$ the dominant strain component;

- For the two inclined consolidation paths, constant_α and increasing_α, both

$\tau_{\theta z}$ and $(\sigma_z-\sigma_\theta)$ are increasing and there is cross-coupling and mutual re-enforcement between the consequent $(\varepsilon_z-\varepsilon_\theta)$ and $\gamma_{\theta z}$ strain components. This appears to be strongest in test R45f, because it combines the strains associated with the constant α and constant t phases, which are separated into two distinct stages in tests R15 to R90. During constant_α consolidation the sample fabric has already been modified by the earlier α_rotation phase, such that the interparticle contacts are aligned to offer the maximum resistance to straining with the same ε_1 axis orientation. In increasing_α consolidation, on the other hand, α_δ deviates from α_σ because the sample is constantly re-aligning the contact distribution to accommodate the ongoing changes in α (Fig.7.31).

The corresponding secant octahedral shear stiffness curves, G $(=\Delta J/\varepsilon_d)$ versus ε_d, are presented in Fig.7.32. Since ΔJ is the same for all tests, the stiffness curves reflect the development of shear strain, ε_d, which is a minimum in test R45 (stiffest response and least strain coupling for ε_d<0.5%) and a maximum in test R90 (softest response), Fig.7.33.

7.5. b-change

7.5.1. Stress path

After completion of consolidation (including K_o consolidation, α_rotation and inclined consolidation) all samples were subjected to drained stress changes such that t, p' and α remained constant, while b changed from 0 to 0.5. During this stage, the direct effective stress components, σ_z', σ_r' and σ_θ', all changed linearly with b (Fig.7.34). As for the b_change stage of the M-Series tests, which occurred at the lower stress level (p'=200 kPa) after K_o consolidation, $\tau_{\theta z}$ remains constant, at the value which was reached at the end of the inclined consolidation stage. While the effective stresses have different magnitudes due to the different α values developed in each test, the stress changes $\Delta\sigma_z'$, $\Delta\sigma_r'$ and $\Delta\sigma_\theta'$, necessary to change b, are the same for all tests ($\Delta\sigma_z'$=-50, $\Delta\sigma_r'$=+100 and $\Delta\sigma_\theta'$=-50 kPa).

7.5.2. Stress-strain behaviour

Fig.7.35 presents the generation of volumetric strain during the b-change from 0 to 0.5 for all tests. The following points are noted:

- The volume strains are positive. This agrees with the volumetric strains observed during the

b-change after K_o consolidation for the M-Series tests.

- All samples, with the same t and p', but different α values, experienced the same volume change. This means that α does not bear any influence on the volumetric strain while changing b from 0 to 0.5.

- The volumetric strains are relatively small, typically 0.09%, increasing by a relatively large additional 0.13% during the creep period. This is about 50% greater than ε_{vol} observed during the b-change after K_o consolidation at half the stress level, in the M-Series tests.

- The volumetric strains during the b-change are about 10% of the accumulated volumetric strains measured up to the p'=400 kPa and t=75 kPa stress point.

So, compared to the b-change stage of the M-Series tests which was performed at half the stress level (p'=200 kPa compared to p'=400 kPa) and with α=0°, similar volumetric behaviour is observed which is independent of α, but with strains ~50% greater in magnitude.

7.6. Material behaviour during undrained shearing

7.6.1. Introduction

After following the consolidation history described above and shown in Fig.7.9a, the R-Series samples had b=0.5, p'=400 kPa and t=150 kPa. The only difference between the samples was the inclination of their major principal stress, α. The samples were then sheared undrained, with α held constant at the value achieved at the end of inclined consolidation. Results from the shearing stage of test R45 are not presented here because this sample developed an internal leak (probably due to a hole in one of the membranes) after completion of the b-change and had to be sheared under drained conditions. However, the results from test R45f (subjected to increasing α inclined consolidation) which was sheared undrained with α=45° are presented.

7.6.2. Stress-strain behaviour

The stress changes applied during the undrained shearing stages of the R-Series tests are presented in Fig.7.36 and involve a similar pattern of stress changes to those applied during the constant α consolidation stage (t increasing, α fixed). The principal difference is that p was held

constant, no drainage was allowed and b was equal to 0.5. The radial stress, σ_r, is the intermediate principal stress, σ_2, and is held mid-way between σ_z and σ_θ. In the predominantly compression tests (R0, R15 and R30), the σ_z component increases while σ_θ decreases in a symmetric fashion keeping σ_r constant. In the predominantly extension tests (R70 and R90), the opposite occurs with σ_θ increasing while σ_z decreases symmetrically so that σ_r remains constant. In test R45f all direct stress components are equal and held constant while $\tau_{\theta z}$ increases.

Stress-strain curves in the form of t-ε_d plots for all tests are presented in Fig.7.37. All curves show a continuous increase in t with increase in strain up to the maximum deviatoric strain, ε_d, of ~8%. The most striking observation is the initial coincidence (up to ε_d~0.2%) of all the stress-strain curves, which indicates similar octahedral shear stiffnesses in all tests. This point will be discussed subsequently.

The strain response from these tests is presented in Fig.7.38. As in the M-Series, maintaining b=0.5 led to nominally plane strain conditions, with the development of relatively small radial strains, except when $\alpha<20°$. As expected, the axial strains, ε_z, are compressive in tests R0, R15, R30 and R45, and tensile in tests R70 and R90. The circumferential strains, ε_θ, show broadly the opposite behaviour. In test R45f, $\gamma_{\theta z}$ is the dominant strain component and ε_z, ε_r and ε_θ are initially equal to zero. However, towards the end of shearing this sample undergoes slight compression with the axial strain, ε_z, obtaining a maximum value of about 10% of the maximum shear strain, $\gamma_{\theta z}$.

7.6.3. Effective stress paths during undrained shearing

The effective stress paths followed during undrained shearing are given in Figs.7.39, 7.40. Fig.7.40b shows these stress paths normalized by the final consolidation mean effective stress, p_o'=400 kPa. Recalling the wide differences seen between tests performed at different α values following K_o consolidation (M-Series, see Fig.5.2), the much closer similarity of the shearing stress paths is striking. The paragraphs below offer a more detailed comparison between the M and R series data.

7.6.3.1. Comparison of tests M0 and R0

Tests M0 and R0 were both performed on samples that were K_o consolidated and then

sheared undrained with b=0.5 and α=0°. The only difference between them was the mean effective stress level: M0 was consolidated to p'=200 kPa, while R0 was consolidated to p'=400 kPa (Fig.7.41).

A) Consolidation

The consolidation characteristics of the two samples were fully compatible, with $\varepsilon_{vol} \approx \varepsilon_z$ (Fig.7.42), except that R0 was taken to ε_{vol}~1.8%, while M0 developed around 1.0% volumetric strain. Both samples had the same initial void ratio of 0.64 and similar Δe=0.015 on the common path to p'=200 kPa. Test R0 had a similar reduction of Δe~0.016 over the rest of its consolidation path (Fig.7.43).

B)Stress paths

The shearing effective stress paths for the two tests are shown in Fig.7.44, normalized by their respective final consolidation mean effective stresses, p_o'. In this plot, the paths practically coincide, showing a maximum divergence of around 2% in p'/p_o'. This indicates that the local Bounding Surface of K_o consolidated samples, formed with e_o~0.65, keeps virtually the same shape and grows in proportion to changes in the mean effective consolidation stress (Fig.7.41).

Regarding the failure conditions, the R0 stress path developed a slightly lower value of ϕ'=51° at the Phase Transformation Point, compared to test M0 which mobilised a value of 53°. This high value for the angle of shearing resistance was discussed earlier in Chapter 5.

Turning to shear stiffness, the octahedral secant stiffness curves shown in Fig.7.45 confirm earlier findings (Jamiolkowski et al., 1991; Porovic, 1995) concerning the dependency of stiffness on initial mean effective stress. Porovic (1995) proposed a relationship between the secant shear modulus G and mean effective stress, p', for Ham River Sand, in the form

$$G = A\left[\frac{p'}{p_a}\right]^n \qquad (7.1)$$

where A and n are functions of the shear strain. Substituting in this equation G values from both tests R0 and M0 at various values of the deviatoric strain, ε_d, enables the variation of the exponent, n, with ε_d to be evaluated. This variation is shown in Fig.7.46. With shearing n increases from approximately 0.5 to 1.0. Also shown on this figure are results from Porovic (1995) who tested Ham River Sand in torsional shear, at an initial e_o=0.77. There is broad

agreement between the present results and those of Porovic, although a deviatoric strain, ε_d, of 1% has to be applied before n=1 for HPF4, whereas only 0.1% is needed for Ham River Sand.

7.6.3.2. Comparison of stress paths from R-Series tests

Figs.7.40a, b, which present the effective stress paths followed in the R-Series tests, show the following trends:

a) The first feature is the general similarity in shape of all the undrained shearing stress paths. The following detailed observations are made in this respect:

- Tests R0 and R15 show effective stress paths that rise above the others, giving t values at the Phase Transformation that are ~15% higher than observed in tests R30 to R70. It will be recalled from Chapter 5, for the M-Series, that rotation of the direction of the major principal stress to α=15° (test M15) did not significantly alter the material response in comparison with the test with α=0° (M0), giving a similar deviator stress and ϕ' value at the PTP. In the same way, the consolidation paths of R0 and R15 showed similar volume change characteristics and it is not surprising that inclined consolidation with α=15° results in a similar structure to K_o consolidation, and the two subsequent undrained shearing stress paths are similar in shape and size.

- Tests R30 to R90 involved more significant principal stress rotations and developed higher volume losses during consolidation. Except for test R90, which developed less pore water pressure in shearing than the other tests, the samples all developed a similar reduction in p' (13% to 17%) at the PTP.

- The yield boundaries Y_2, Y_3 and the PTP were estimated from the p'-ε_d plots shown in Fig.7.47. The Y_3 yield points are marked on the t-p' plots given in Fig.7.48. The strains corresponding to each of these points are summarized in Table 7.4. The Y_2 boundary appears to be reached in all tests at ε_d~0.015% to 0.02%. The deviatoric strains at the Y_3 yield points are broadly similar, ranging from ε_d~0.04% to 0.08%, and, apart from test R90, all have approximately similar deviatoric stress levels (t~170 to 180 kPa). The PTP's, apart from test R45, are all reached at ε_d~3.0%.

Table 7.4: Values of ε_d at three yield points

TEST	Y_2 (%)	Y_3 (%)	PTP (%)
R0	0.02	0.08	3.0
R15	0.02	0.04	3.0
R30	0.015	0.06	3.0
R45	0.015	0.04	1.5
R70	0.015	0.07	3.0
R90	0.015	0.4	3.0

- With respect to the stiffness response, the G-ε_d curves shown for tests R30, R45, R70 and R90, in Fig.7.49a and 7.49b all fall within 10% of each other at small strains, while the G-ε_d curves from tests R0 and R15 are ~20% softer. It should be noted that R0 and R15 curves become stiffer than the others when ε_d>0.5%.

b) Overall, the R-Series samples all showed closely comparable undrained stress-strain, stiffness and yielding behaviour, the principal difference between the tests being the spread of initial effective stress path inclinations.

The deviator stress values developed at the PTP among the R-Series tests differed at most by 15%. The associated values of "undrained strength ratio" (calculated from the t values at the PTP's) are presented in Fig.7.50, superimposed on the equivalent plot for the M-Series tests (where K_o consolidated HPF4 was sheared with different α inclinations). The strong association between principal stress rotation and low strength is dramatically reduced when the samples are consolidated with the principal stress directions rotated to the same inclination under which they were eventually brought to undrained failure. The systems of particle contacts developed during inclined consolidation can sustain nearly the same degree of shear loading as that formed by K_o consolidation with α=0°. A maximum difference of 15% in strength is observed between R0 and the group R30 to R70 tests. It is interesting that R90 is comparatively strong.

It is clear from Fig.7.50 that allowing HPF4 to consolidate with an inclined σ_1 axis, α>0, leads to large potential gains in strength for specimens that are to be failed with this same α value. These gains range from 5% for α=15°, to 140% for α=90° (Fig.7.50). These results are

presented in terms of the parameters used for assessing multi-stage embankment construction, i.e. c_u/σ_{vc}' and c_u/σ_{1c}' (Jardine & Hight, 1987; Smith, 1992), in Figs.7.51, 7.52. The ratio c_u/σ_{vc}' increases 5 times for the case of a sample subjected to passive consolidation, α=90°, compared to a K_o consolidated sample.

c) The third point to emerge from the R-Series was that the anisotropy in PTP ϕ' values is only weakly affected by "inclined" consolidation. The ϕ' values mobilized at the PTP's from the R-Series tests are superimposed on the envelope obtained from the K_o consolidated tests of the M-Series in Fig.7.53. For tests R0 and R15 the values of ϕ' are similar to those for the K_o structure. The high values mobilised are a consequence of the strain conditions and initial depositional particle assembly of HPF4, as discussed in Chapter 5. These ϕ' values are much larger than those observed in tests R30, R45f, R70 and R90. Inclined consolidation has therefore not erased the initial anisotropy of the silt's large strain shearing behaviour (as was the case with small-strain stiffness and PTP values of *t*). However, for the tests with $\alpha \geq 30°$, the variations in the ϕ' values at the PTP's are reduced compared to those observed for K_o consolidated samples, and range from 41° to 39°, compared to 41° to 36°.

d) The torsional secant shear stiffness, $G_{\theta z}$, curves developed in tests R15 to R70 (Fig.7.54), show similar patterns to those observed during inclined consolidation (Fig.7.29). The effective stress paths for each test start from the same initial stress point (p_o'=400 kPa, t=150 kPa, but with different α values) and undergo the same loading conditions with $\alpha_\sigma=\alpha_{\dot{\sigma}}$ (Fig.7.56). The results indicate that they have the same initial value of stiffness, $G_{\theta z}$, of ~150 MPa (at $\gamma_{\theta z}$=0.001%), but show slight differences in $G_{\theta z}$ at different strain levels (Fig.7.55). Test R45f with α=45° produces the stiffest response. In this mode there is no cross-coupling between $\gamma_{\theta z}$ and the changes in σ_z, σ_r and σ_θ. The smallest stiffness is again for test R15, being ~20% lower than for R45f.

7.6.4. Stress and strain increment directions

The stress increment and strain increment directions reported in Fig.7.56 for tests R15, R30, R45f and R70 all confirm the α=constant condition, with stress and stress increment directions coinciding throughout the shearing path (i.e. $\alpha_\sigma=\alpha_{\dot{\sigma}}$)[2]. At the beginning of shearing, $\alpha_i=\alpha_{\dot{\sigma}}$ and this holds true up to $\varepsilon_d \approx 0.02\%$ in all shearing paths. The

[2]Note also that $\alpha_\sigma=\alpha_{\dot{\sigma}}=\alpha_\varepsilon=\alpha_i=0°$ in R and 90° in R90, throughout each shearing stage.

previous inclined consolidation and creep period appear to have established a new structure which does not "remember" the original K_o consolidated structure when sheared at small strains. After Y_2 yielding occurs at $\varepsilon_d \approx 0.02\%$, further shearing leads to strain increment directions that lag slightly behind $\alpha_{\dot{\sigma}}$ in the compression mode (5° in R15 and 15° in R30) tests respectively, and lead $\alpha_{\dot{\varepsilon}}$ in the extension shearing mode (by 5° in R70).

7.7. Anisotropy induced by inclined consolidation

7.7.1. Introduction

It has been shown in the previous sections of this Chapter that consolidation with σ_1 inclined at an angle, α_c, to the vertical, forms 'new' material structures whose axes of anisotropy (with respect to pre-failure behaviour) are aligned with α_c in a comparable way to those of K_o consolidated HPF4. By analogy, we might suppose that when the new structure is sheared undrained with α inclinations different to α_c, it will exhibit a new induced anisotropy comparable to that seen after K_o consolidation in the M-Series tests. Test R90/45 was performed to assess whether this is true.

7.7.2. Description of test

The sample was consolidated to point, L (Fig.7.9a), (α=90°) by inclined consolidation, and then sheared undrained in a similar manner to test M45 (Chapter 5). The effective stress paths for both this new test and test M45 are compared in Fig.7.57. Point L (p'=400 kPa, t=150 kPa) is the final point of the consolidation path OAFL (Fig.7.9a). After consolidation and a subsequent rest period, the *b*-value was gradually changed from 0.0 to 0.5 under drained conditions, so that the stress point remained at L. Undrained unloading was then performed from points L to M, keeping α=90° so as to bring the stress point inside the anticipated α=90° local Bounding Surface. As in the M-Series tests, this unloading was necessary so that the major principal stress direction could be rotated to α=45° under undrained conditions, without failure occurring. It was originally intended to unload the sample to the same *t/p'* value as in test M45. However, on unloading the effective stress path showed a lower gradient $\Delta t/\Delta p'$ than was observed in test M45, producing proportionally greater reductions in p'. This led to the concern that if the sample was unloaded to the desired *t/p'* value and subjected to α rotation that it would have travelled so far below the local Bounding Surface that, when sheared, the PTP would not be well defined. Consequently the unloading was stopped prematurely. Undrained principal stress

rotation from α=90° to α=45°, at constant deviatoric stress level (t=90 kPa) was then applied. During this stage positive pore water pressures were developed and the stress state moved from M to N in Fig.7.57. The large change in p' (from 400 kPa at L to 265 kPa at N) is an early indication of a strong anisotropy. Undrained shearing was then applied from point N by increasing t while keeping p, b and α constant. Suitable pause periods were allowed at the end of the unloading and α_rotation stages for the strain rate to reduce to 1/100 of the shearing strain rate (which was 5%/day, as before).

7.7.3. Comparison of the two stress paths

The normalized effective stress paths for tests M45 and R90/45, together with those for tests M0 and R90 are presented in Fig.7.58. During the unloading stage test R90/45 (α=90°) generated a larger reduction in p'/p_o' than test M45 (α=0°). The gradients (Δt/Δp') of the stress paths for this unloading stage are ~1.7 and ~5.0 for tests R90/45 and M45 respectively. This indicates that the α=90° consolidated structure is less stable than that formed under K_o consolidation.

During the 45° α-rotation stage, test M45 experienced a change in $\Delta p'/p_o'$=-0.18, while test R90/45 showed a larger reduction of -0.24. However, the K_o consolidated sample (test M45) gave a more contractant response when sheared with α=45°, leading to lower value of t/p_o' and p'/p_o' at the PTP, as tabulated in Table 7.5.

The mobilized φ' value at the PTP fell to 34° in test R90/45 from 39° in test M45. The former value is lower than any of the values observed in both the M and R series tests, Fig.7.53. However, both tests seem to have reached similar ultimate values of φ'.

Table 7.5: Comparison of K_o and R90 anisotropy

at PTP	ultimate	M45	R90/45
t/p_o'		0.31	0.36
p'/p_o'		0.50	0.64
φ'		39°	34°
	ϕ'_{cv}	45°	43°

7.7.4. Comparison of the two anisotropies

In this Section, the anisotropy generated at b=0.5, after α=0° (i.e. K_o) consolidation, and that induced at b=0.5 after α=90° (i.e. inclined) consolidation will be compared. They will be referred to in the following text as "K_o anisotropy" and "α=90° anisotropy", respectively.

The effective shearing stress path of test M0 and the undrained unloading portion of the stress path of test M45 at α=0° identify a part of the local "K_o" Bounding Surface (BS) in the *t-p'* plane. Likewise the shearing stress path of test R90 and the undrained unloading portion of the stress path of test R90/45 at α=90° give a part of the local BS for α=90° anisotropy in the *t-p'* plane (Fig.7.58). The following features are observed for these two Bounding Surfaces:

- The K_o BS is more contractant than the α=90° BS, giving 15% to 20% lower *p'* values at the PTP's.

- The inclination of the initial effective stress path for undrained loading and unloading with α=0° is $\Delta t/\Delta p'$=5.0, whereas for undrained loading and unloading with α=90° it is $\Delta t/\Delta p'$=1.7.

- The difference in the *t* value (i.e "undrained strength") at the PTP's for "K_o anisotropy" tests M0 (α=0°) and M45 (α=45°) is ~50%, whereas for "α=90° anisotropy" tests R90 (α=90°) and R90/45 (α=45°) the difference is ~40% (Fig.7.59).

- The difference in the mobilized ϕ' values at the PTP for tests R90 and R90/45 is $\Delta\phi'$=5°. In contrast the difference for tests M0 and M45 is $\Delta\phi'$=14°. However, as noted in Chapter 5, b=0.5 does not produce plane strain conditions in test M0. The equivalent plane strain test was M0-03 which had b=0.3. If the mobilised ϕ' value at the PTP of this test is compared with that of test M45, a difference $\Delta\phi'$=5° is obtained (Fig.7.60). The plane strain difference in ϕ' is therefore the same under both "K_o anisotropy" and "α=90° anisotropy".

So, it can be concluded that both K_o and inclined consolidation produce material with similar, but not strictly identical, degrees of anisotropy.

7.8. Summary

This Chapter attempts to explore what happens when the ground is loaded slowly enough for a new anisotropy to be induced during consolidation. The classical example of this process in geotechnical practice is multi-stage embankment construction on soft foundations (Burland, 1971; Yeats, 1983; Jardine & Hight, 1987; Smith, 1992), but "inclined" consolidation happens under many other types of foundation and in natural slopes.

Earlier studies of this phenomenon have been performed using triaxial (Smith, 1992), and Direct Simple Shear equipment (Ladd & Edgers, 1972), but these were limited by the capabilities of the test apparatus. Porovic (1995) was able to extend the scope of such studies considerably, by using a Hollow Cylinder Apparatus. However in none of these tests was it possible to control the direction of the major principal stress during undrained shearing.

This Chapter has shown that further refinements are possible if a Hollow Cylinder Apparatus, equipped with independent stress control and a full local strain measurement capability, is available. The R-Series performed by the Author enabled the following to be investigated:

a) Stress-strain and stiffness characteristics developed by inclined consolidation stress paths with constant α and increasing α inclinations, which may be compared with the behaviour observed during K_o consolidation.

b) The influence of such induced consolidation stress paths on subsequent undrained shearing behaviour in constant α tests.

c) The anisotropy induced by inclined consolidation and how it compares to the anisotropy generated by K_o consolidation.

The following can be concluded:

a1) Drained rotation of the direction of the major principal stress, α, generates volumetric strains which increase systematically as α increases from α=0° to α=90°.

a2) Subsequent consolidation along similar effective stress paths (t/p') at a variety of constant

values of α, generates similar incremental Δe-p' curves, irrespective of α.

a3) A limited check suggested that the volume change developed in reaching a given normally consolidated t, p', α, b point is independent of the path followed to reach it.

a4) In the α=constant consolidation phases, following drained α_rotation, the stress and strain increment directions tend to be mutually aligned once a deviatoric shear strain of about 0.6% has been exceeded. This may indicate that a new material structure, with re-oriented and stable sets of interparticle contacts, has been fully formed, which is analogous to that developed under K_o conditions where α_σ, $\alpha_{\dot{\sigma}}$ and $\alpha_{\dot{\varepsilon}}$ all coincide.

a5) Consolidation paths involving continuous changes in α impose a constant difference between α_σ and $\alpha_{\dot{\sigma}}$. In such tests $\alpha_{\dot{\varepsilon}}$ approaches α_σ when strains become large (~1.5% deviatoric strain).

a6) The initial torsional secant shear stiffness, $G_{\theta z}$, developed over drained stages of all tests, appears to depend not only on p_o' (i.e. the mean effective stress at the beginning of the stage), but also on the recent stress history and the imposed accumulated stress path up to that stage. As the stress paths during inclined consolidation considered in the R-Series tests all plot as a single line when plotted in t-p' space, any variation in the initial $G_{\theta z}$ value depends on the orientation of the stress path in the α-dimension of t-p'-α space. This orientation is defined by the angle θ_α in Fig.7.61. The initial $G_{\theta z}$ values for the α-rotation and α-constant consolidation stages of the tests are similar because both stress paths during these stages have an orientation of θ_α=90° to the stress path followed during the previous stage. That is the angle between the stress paths for the *α-rotation* and *K_o consolidation* stages and the *constant-α consolidation* and *α-rotation* stages are both θ=90°. In comparison, the initial $G_{\theta z}$ value for the increasing-α consolidation stage is softer because for this stage the stress path makes an angle θ_α<90° to that followed during the previous K_o consolidation stage, (Fig.7.61). Such behaviour can be seen in Fig.7.29 which shows the stiffness curves during inclined consolidation. The stiffness values for test R45f, which underwent increasing-α consolidation, are initially significantly smaller than those observed in the other R-Series tests which underwent constant-α consolidation. Also shown in this figure is the average stiffness curve obtained for the *α-rotation* stage of tests R15, R30, R45 and R70. It can be seen that this curve is only slightly stiffer than that observed at the start of the constant-α consolidation stage of these same tests.

a7) The volumetric strain generated during the *b*-change at the end of "inclined" consolidation is not influenced by the value of α.

b1) Undrained shearing with t increasing, $\alpha=\alpha_c$ and b=0.5, generates broadly similar effective stress paths, G-ε_d curves and deviatoric stresses at the PTP for all values of α_c. Consolidation with $\alpha>0°$ tends to over-write the anisotropy seen at small to moderate strains in tests on K_o consolidated material.

b2) From a4) and b1) it can be concluded that the inclined consolidation forms a new material structure in which new particle contacts are aligned so that they are perpendicular to the direction of the major principal stress. This is similar to that of the K_o structure where horizontal contacts are perpendicular to the vertical direction of the major principal stress. This new structures can, therefore, take the same loading as the K_o structure.

b3) Considering the undrained shearing tests in more detail, samples consolidated with $\alpha\geq30°$ (R30, R45, R70 and R90) produced slightly smaller values of t and ϕ' at the PTP compared to samples with $\alpha<30°$ (R0 and R15). The latter samples have a predominately K_o structure which appears to be marginally stronger than that developed under inclined consolidation with $\alpha>30°$.

b4) Because of the increasing volume change which occurs with the higher degree of principal stress rotation, stress paths other than $\alpha=0°$ and $\alpha=15°$ generate larger negative pore water pressures at the beginning of shearing.

c1) Samples consolidated with α inclined retain a large-strain ϕ' anisotropy, which is a similar, but muted, version of that seen with K_o consolidated samples. The specific characteristics of HPF4, in particular its particle shape and angularity, lead to a degree of inherent anisotropy that remains from the soil's original deposition as a slurry. This can be seen in Fig.7.59. If such inherent anisotropy did not exist, then curves A and C would be symmetrical about $\alpha=45°$.

c2) The initial inclination of the Bounding Surface for K_o consolidated HPF4 (i.e. inclination of undrained loading and unloading stress paths in $\alpha=0°$ plane) is $\Delta t/\Delta p'=5.0$. For all samples subjected to inclined consolidation with $\alpha\geq30°$ the subsequent undrained shearing stress paths are inclined with $\Delta t/\Delta p'=1.7$ (Fig.7.40a). Consequently the inclination of the BS in the α_c plane, in t-p'-α space, for $\alpha_c\geq30°$ can be reasonably considered the same and equal to $\Delta t/\Delta p'=1.7$.

c3) The soil structure developed under inclined consolidation is less stable than that developed under K_o consolidation. Samples subjected to inclined consolidation generate more pore water pressure in undrained unloading and undrained α rotation, but are then more dilatant in subsequent undrained shearing.

The main practical conclusion to draw from this Chapter is that, in terms of undrained strength, soil that is consolidated with constant, or slightly changing α, and then sheared undrained with a similar σ_1 axis inclination is likely to be much stronger than similar soil that is sheared with α differing significantly from α_c. This is evident from Fig.7.51 where the value of the ratio c_u/σ_{vc}' for a soil consolidated and sheared with α=90° is 5 times larger than for the same soil consolidated with α=0° and then sheared with α=90°. From Fig.7.52 the equivalent increase in strength in terms of the ratio c_u/σ_{1c}' is 2.5 times. These gains are much higher than those obtained by Smith (1992) for the far less anisotropic Bothkennar clay, as quoted in section 7.1: c_u/σ_{vc}' for passively consolidated clay sheared in extension was 2.5 times larger than for K_o consolidated clay sheared in extension; the equivalent increase in terms of c_u/σ_{1c}' was 1.54. This clearly has practical implications for the design and construction of works such as multi-stage embankments. The use of standard laboratory triaxial and simple shear tests in which the soil is consolidated with one value of α and then sheared with another are likely to underpredict the undrained strength that is available for later stages of embankment construction.

The results show that the ratio c_u/σ_{1c}' remains approximately constant with α_c, Fig.7.52, whereas this is not the case for c_u/σ_{vc}', Fig.7.51. This implies that the value of c_u/σ_{1c}' obtained from a conventional laboratory compression test with α=0° may be applicable as an upper bound to soil subjected to inclined consolidation and sheared with α>0°. This single parameter could therefore be used to estimate changes in undrained strength in the foundation soil below an embankment. Table 7.6 summarizes c_u/σ_{vc}' and c_u/σ_{1c}' ratios obtained from tests presented and discussed in this Chapter: Bothkennar clay (Smith, 1992), HRS (Porovic, 1995) and HPF4 (this study).

Table 7.6: Summary of c_u/σ_{vc} and c_u/σ_{1c} ratios for different tests and materials

α_c	α	Bothkennar clay			HRS			HPF4		
		b	c_u/σ_{vc}	c_u/σ_{1c}	b	c_u/σ_{vc}	c_u/σ_{1c}	b	c_u/σ_{vc}	c_u/σ_{1c}
0°	0°	0	0.347	0.347	0	0.46	0.46	0.5	0.43	0.43
15°	15°							0.5	0.43	0.42
*22°	22°				0.15	0.30	0.28			
*30°	30°				0.28	0.33	0.29	0.5	0.42	0.37
*45°	45°				0.5	0.41	0.30	0.5	0.49	0.37
70°	70°							0.5	0.66	0.37
90°	90°	1.0	0.597	0.372				0.5	0.8	0.4

* α_c is the value of α at the end of consolidation: for HRS and Bothkennar clay it is also a constant value during consolidation; for HRS it is a final value after rotation from 0°

These ratios are broadly similar for all three materials, for the comparable α and *b* values, although those for HPF4 are higher than the others.

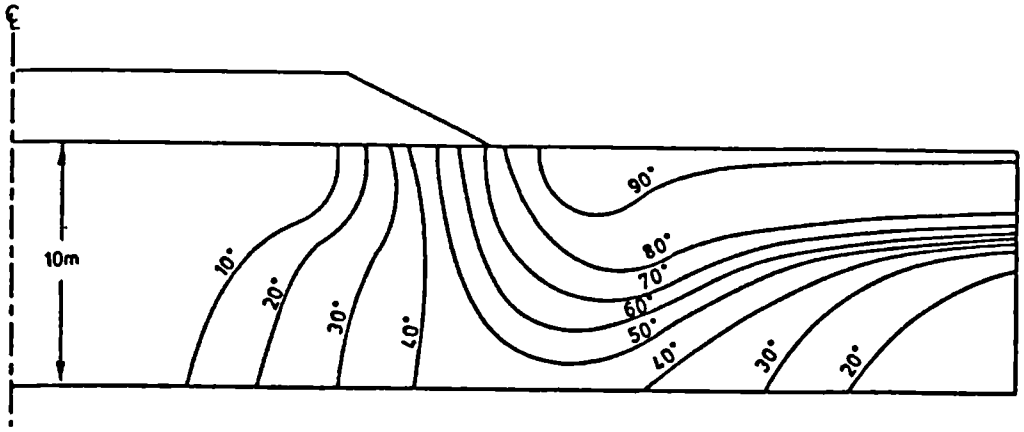


Fig.7.1 - Rotation of the principal stress direction under emankment (Yeats, 1983)

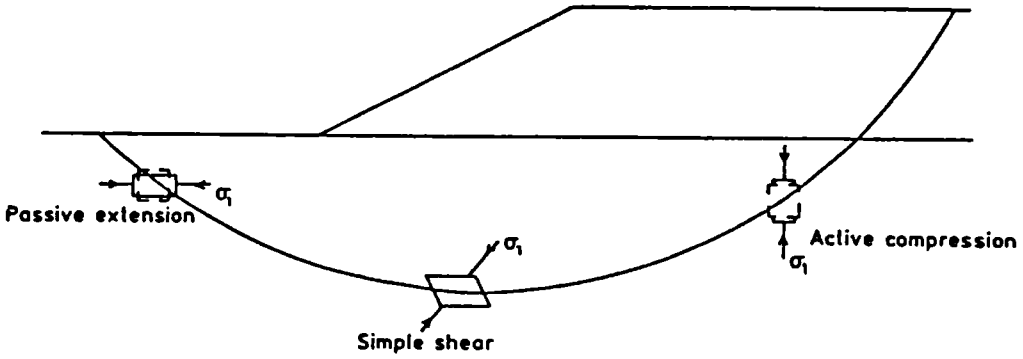


Fig.7.2 - Stress states in a potential failure surface

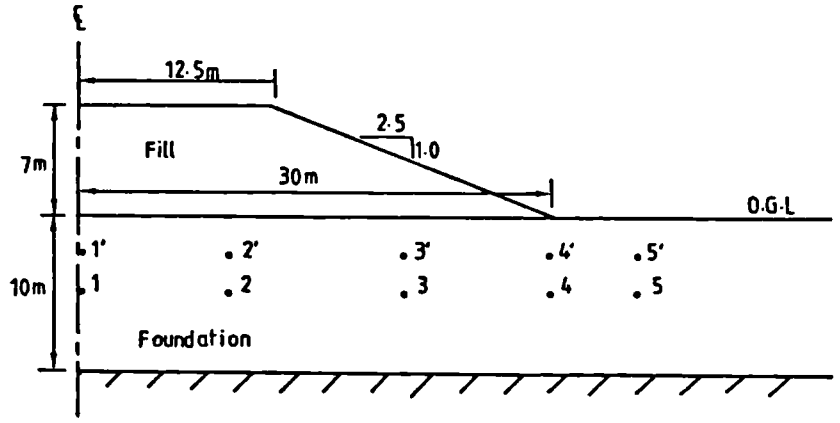
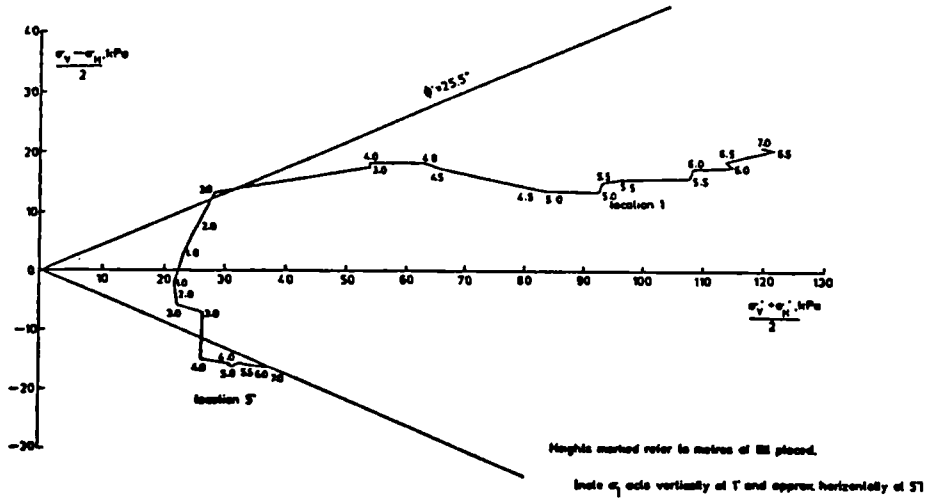
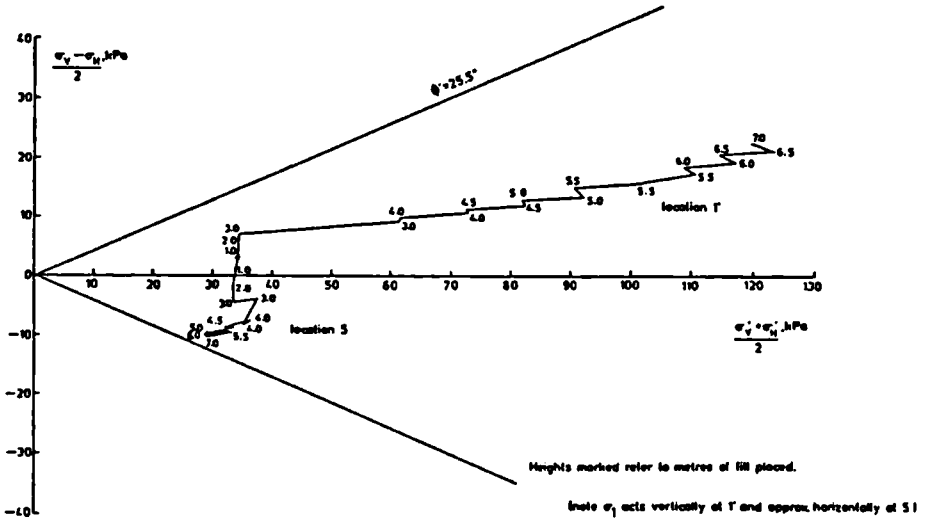


Fig.7.3 - Embankment geometry and initial soil profile adopted for finite element study (Smith, 1984)

(a)



(b)



(c)

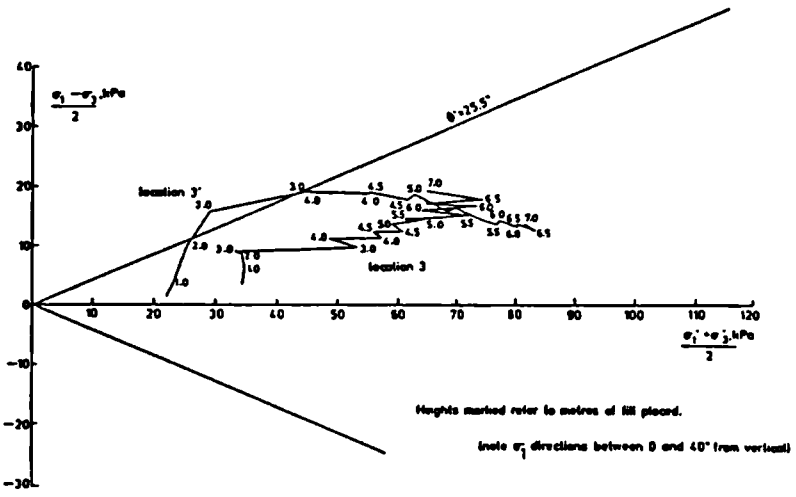


Fig.7.4 - Effective stress paths predicted during multi-stage emankment construction (Smith, 1984); the figures alongside the stress paths correspond to embankment height

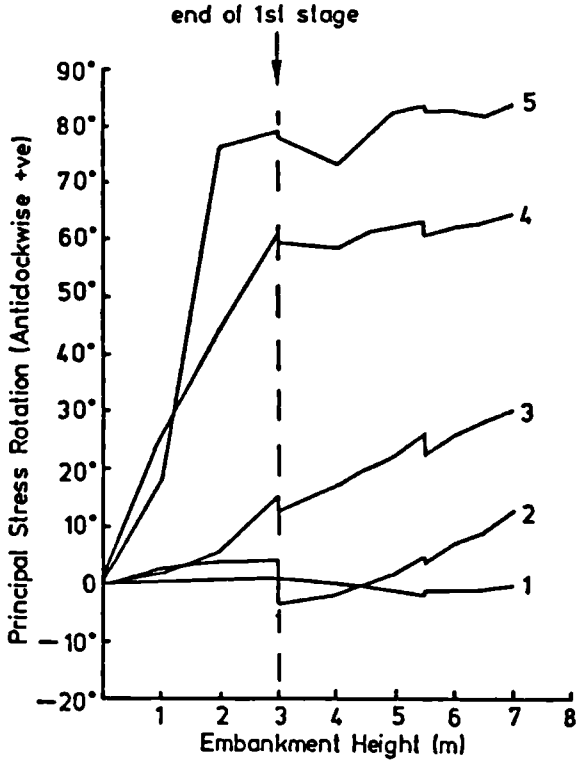


Fig.7.5 - Predicted orientations of the σ1 direction during multi-stage construction (Smith, 1984)

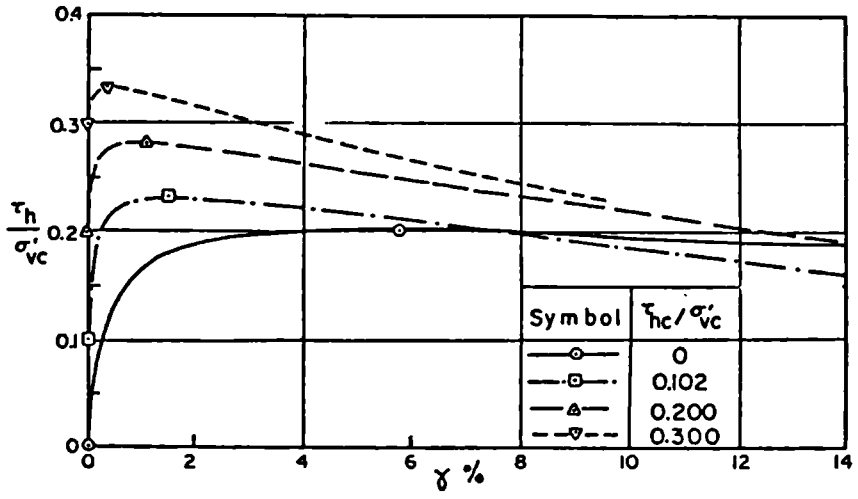


Fig.7.6 - Variation of normalized shear strength with shear strain for DSS tests on Boston Blue Clay, with shear stresses applied during consolidation (Ladd & Edgars, 1972)

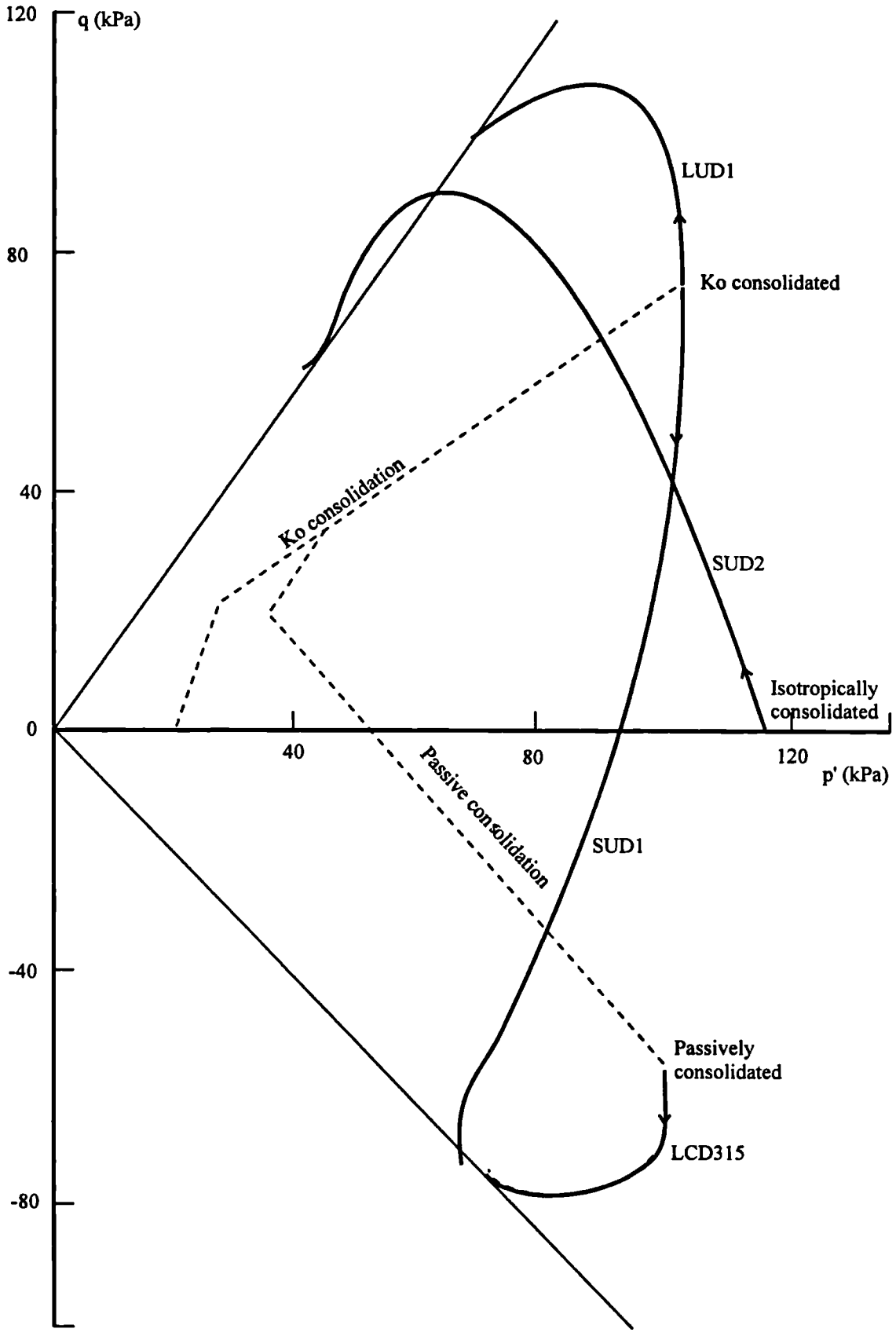


Fig.7.7 - Undrained effective stress paths followed by Bothkennar clay samples (Smith, 1992)

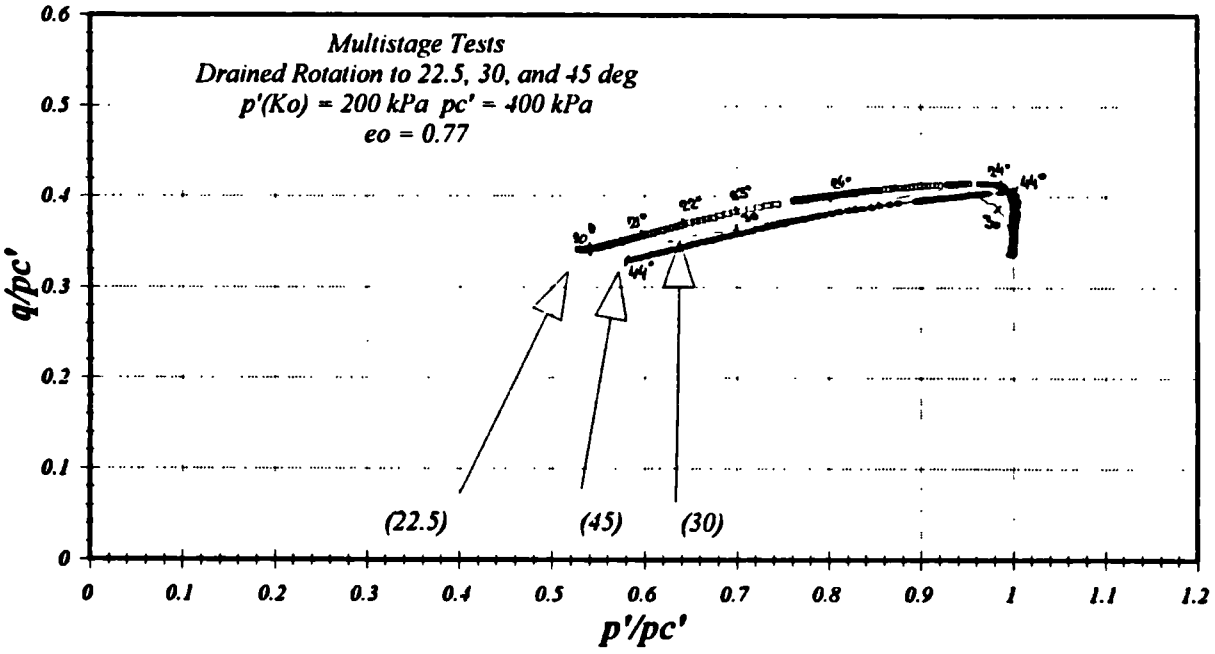


Fig.7.8a - Normalized undrained effective stress paths for samples sheared after inclined consolidation (Porovic, 1995)

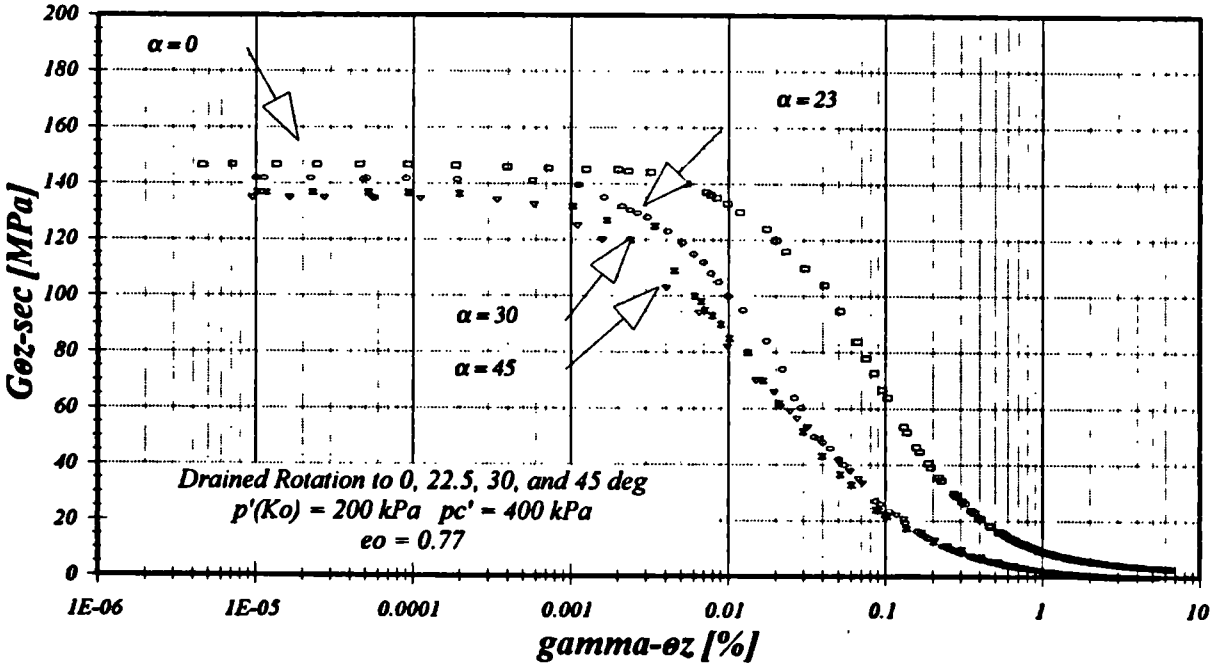


Fig.7.8b - Torsional shear stiffness during undrained shear of inclined consolidated samples (Porovic, 1995)

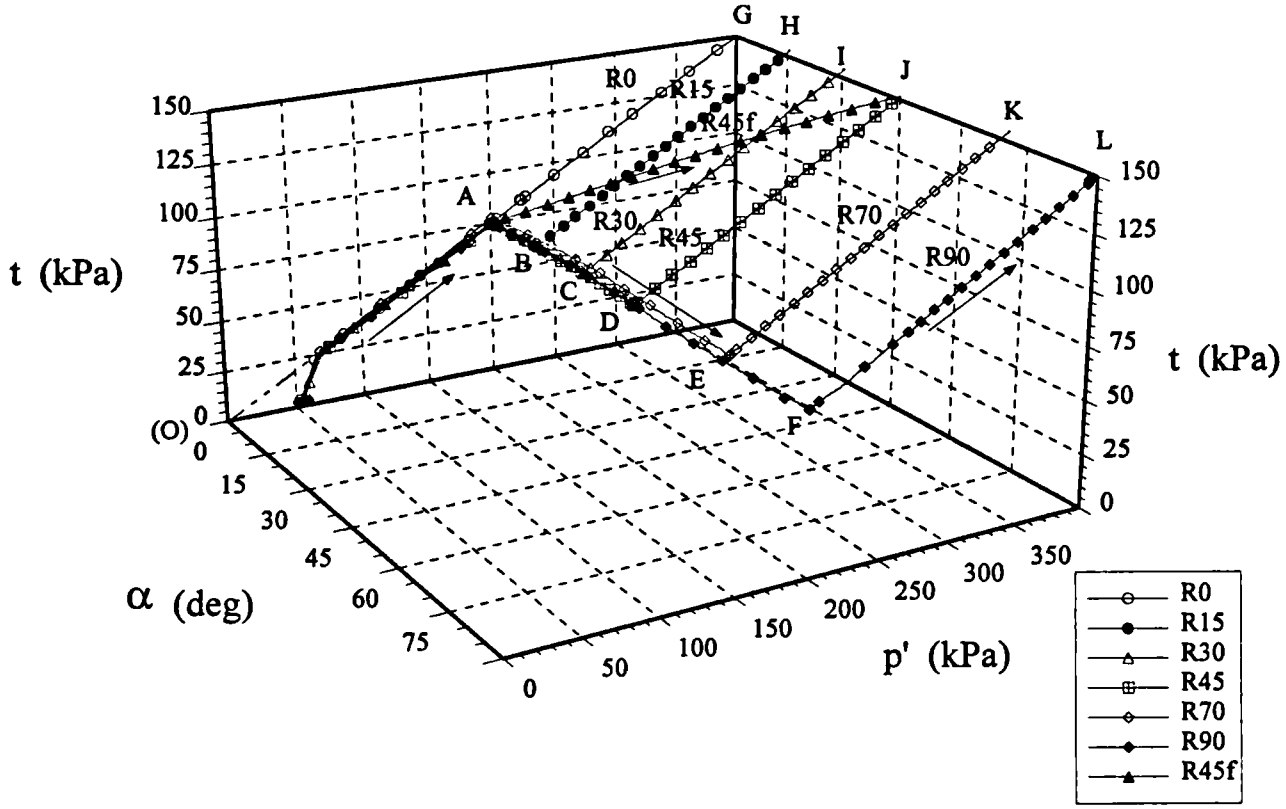


Fig.7.9a - Consolidation stress paths for R-Series tests

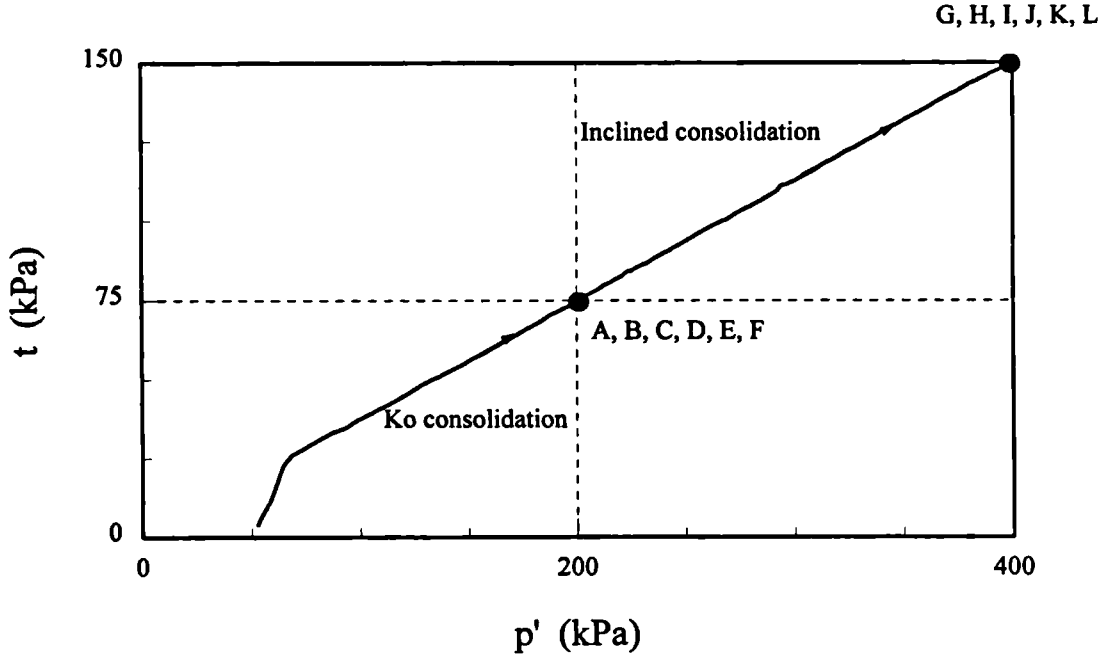


Fig.7.9b - Projection of the consolidation stress paths onto p'-t plane

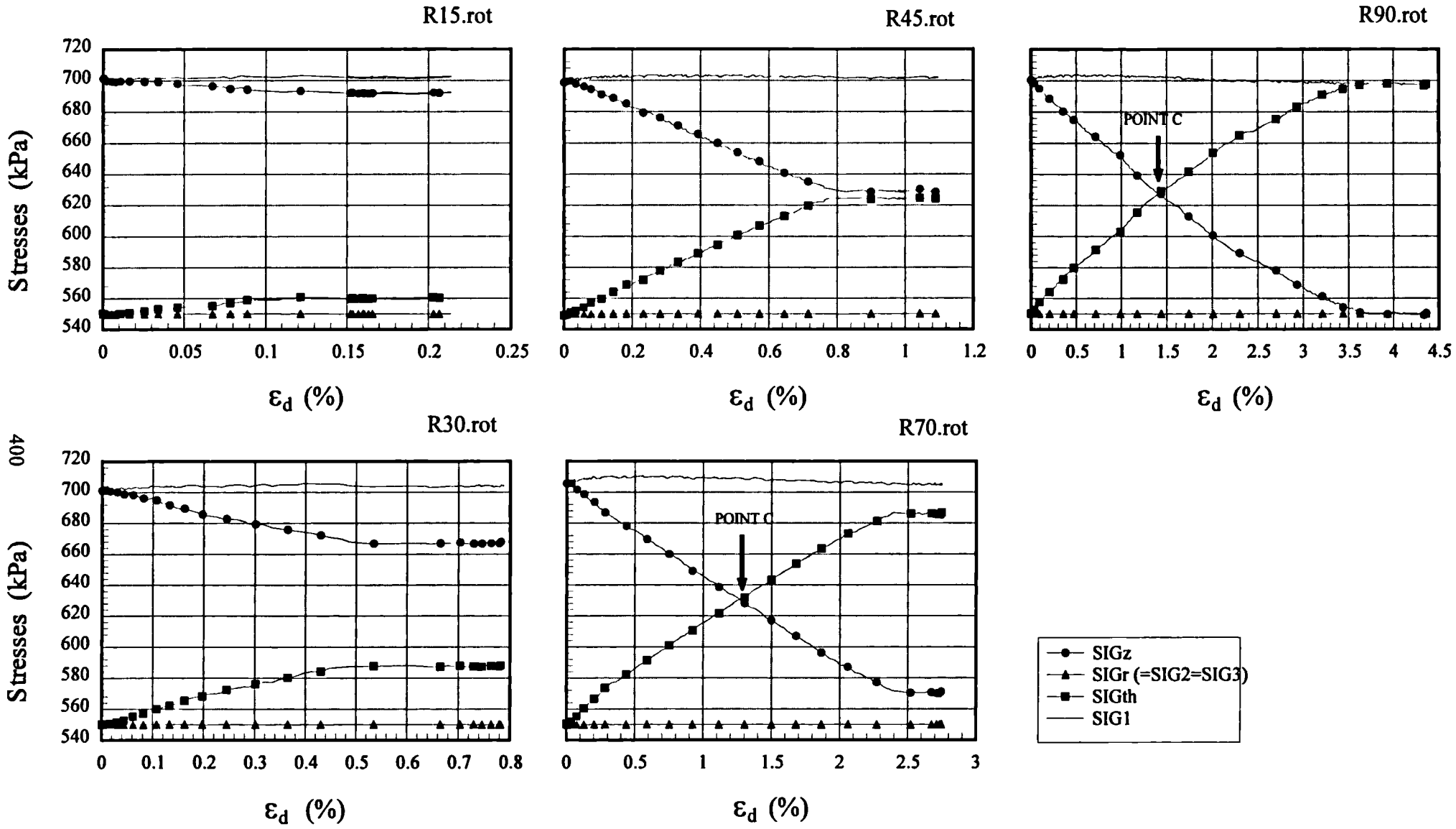


Fig.7.10 - Distribution of direct stresses during rotation stage

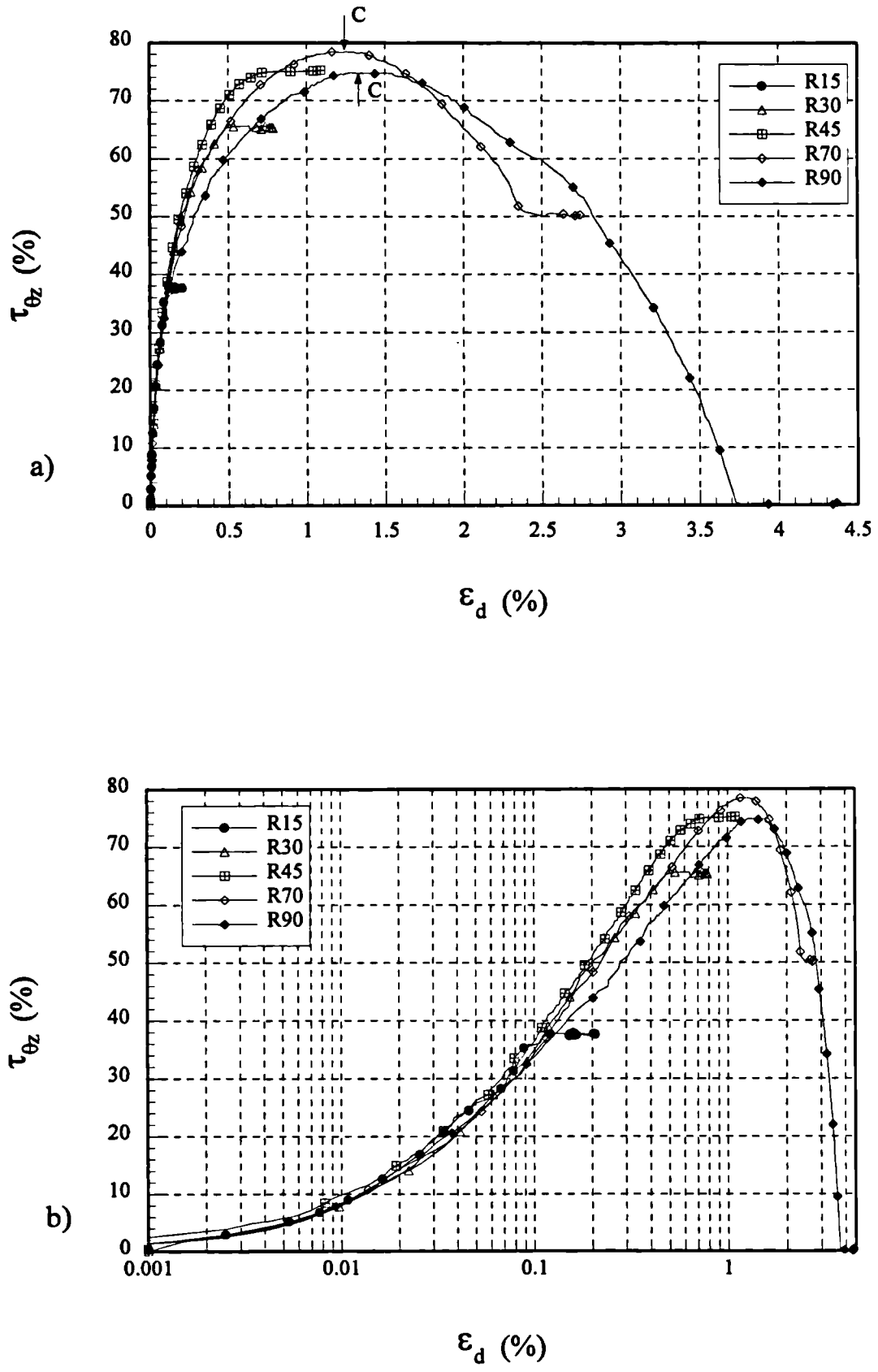


Fig.7.11 - a) Development of torsional shear stress during α rotaion stage
b) View into small strain range

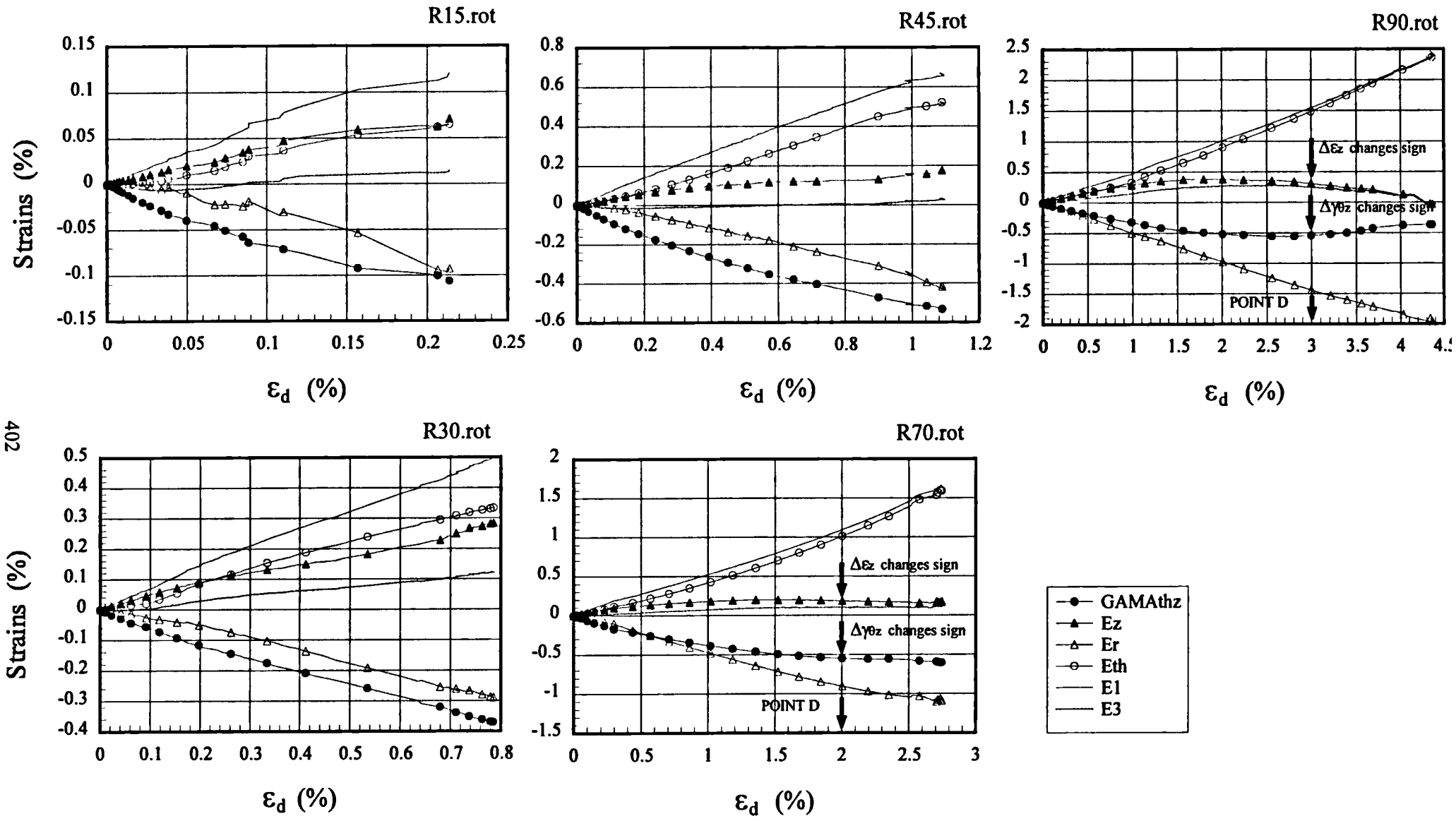


Fig.7.12a - Component strains during principal stress rotation stage

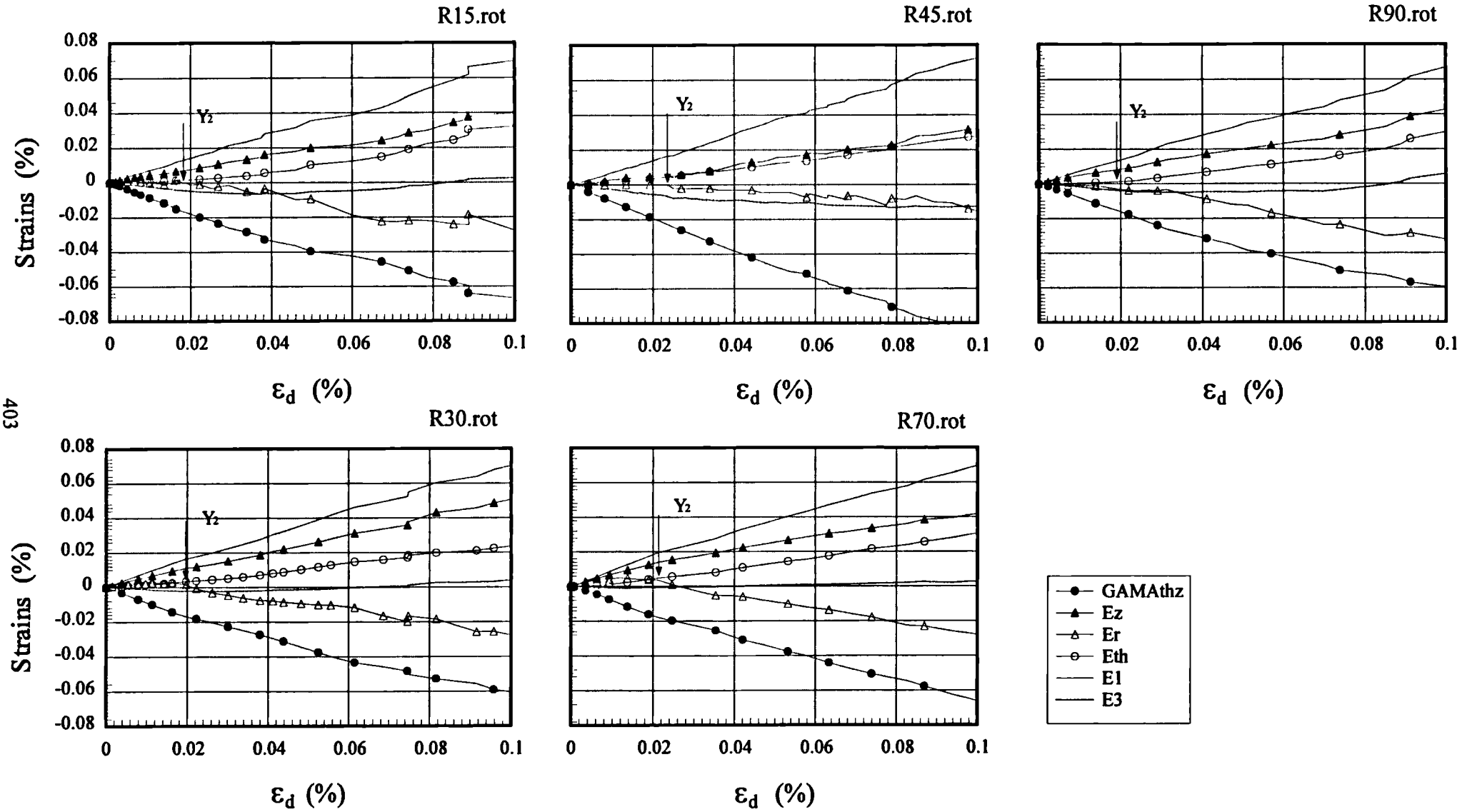


Fig.7.12b - Component strains during principal stress rotation - small strain view

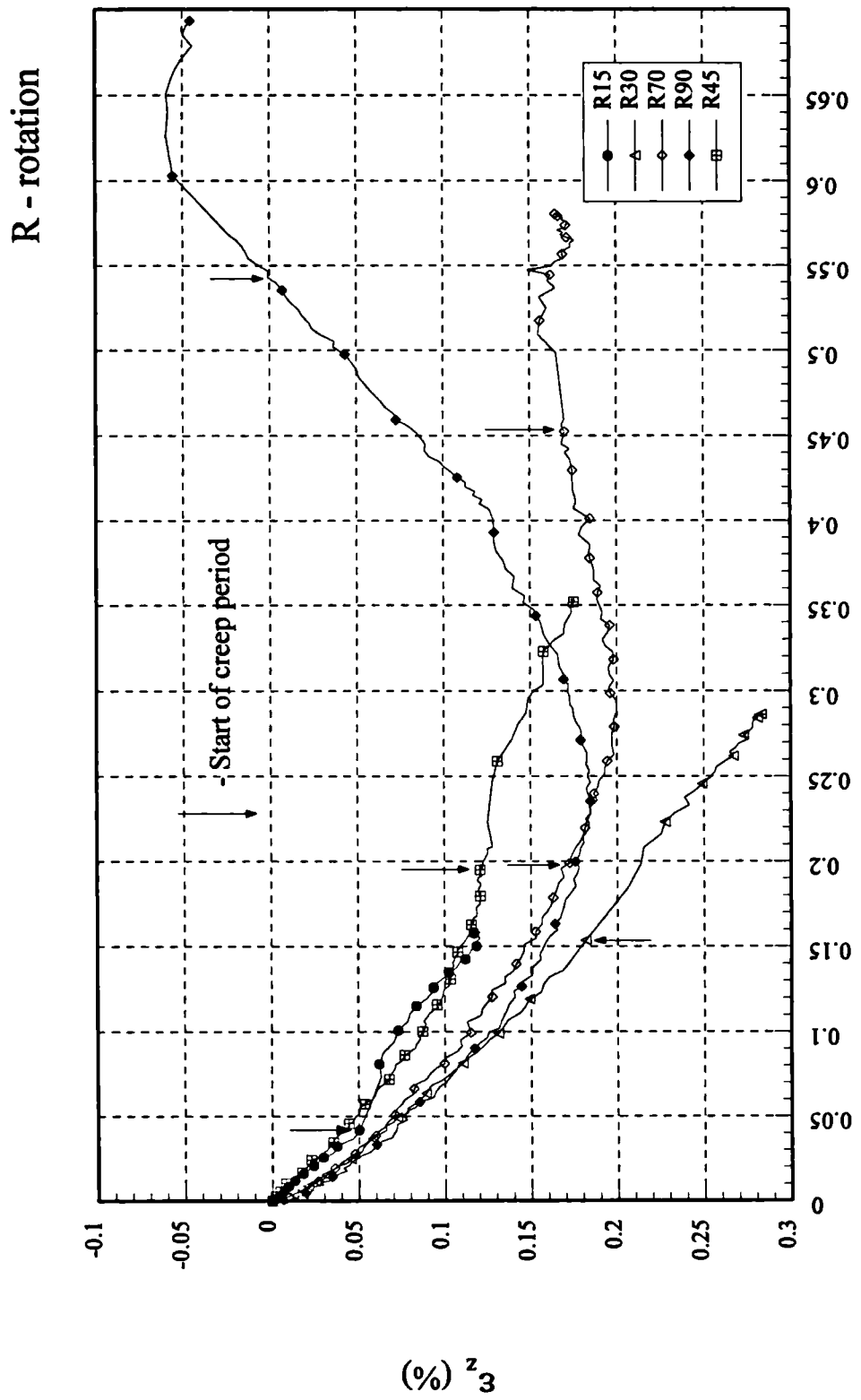


Fig.7.13 - Relation between axial and volumetric strain during α rotation stage

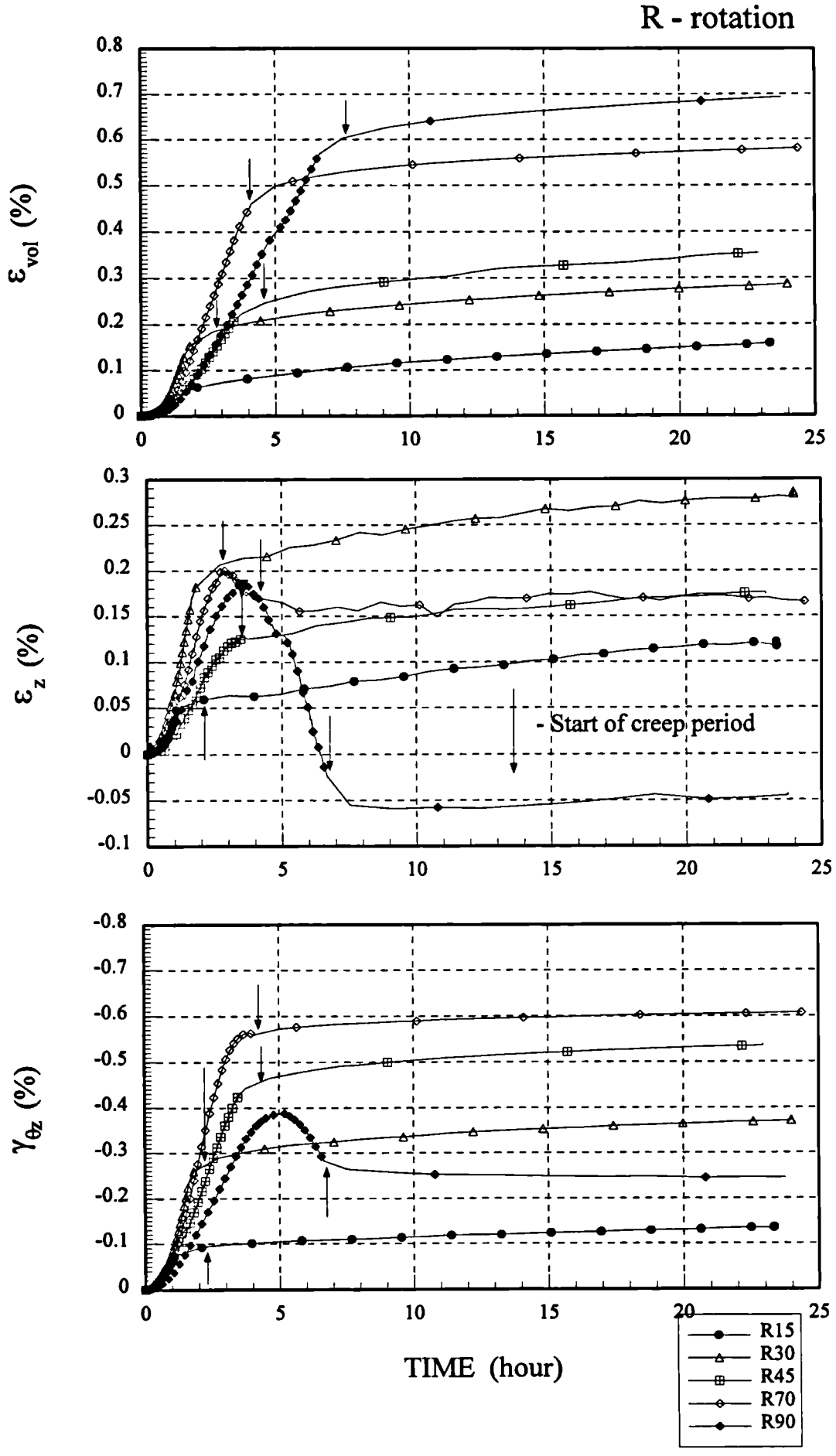
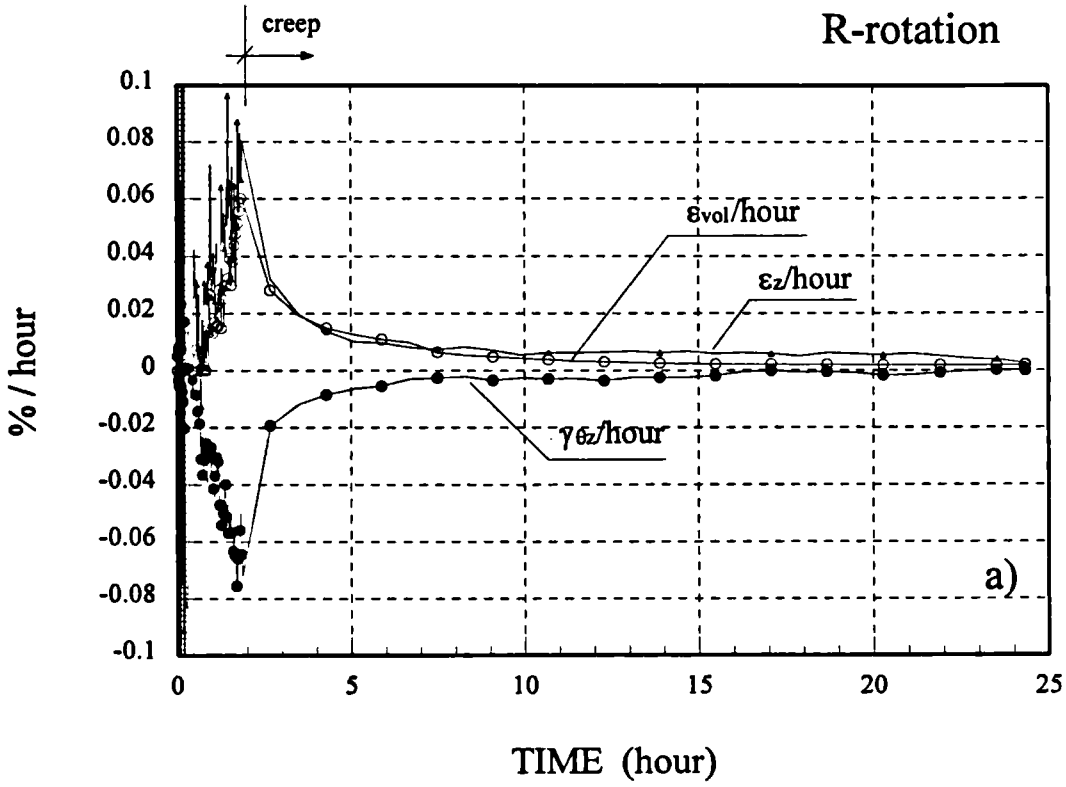


Fig.7.14 - Time distribution of axial, radial and torsional strains during drained principal stress rotation



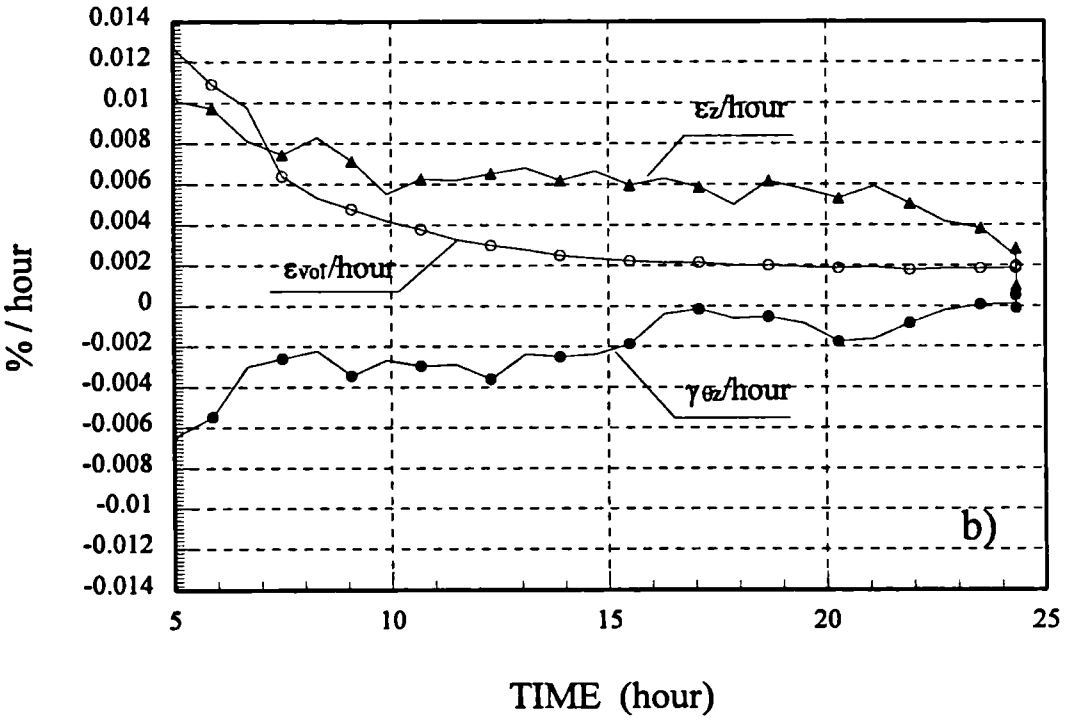


Fig.7.15 - a) Strain rate during drained principal stress rotation
b) Enlarged view into a creep stage

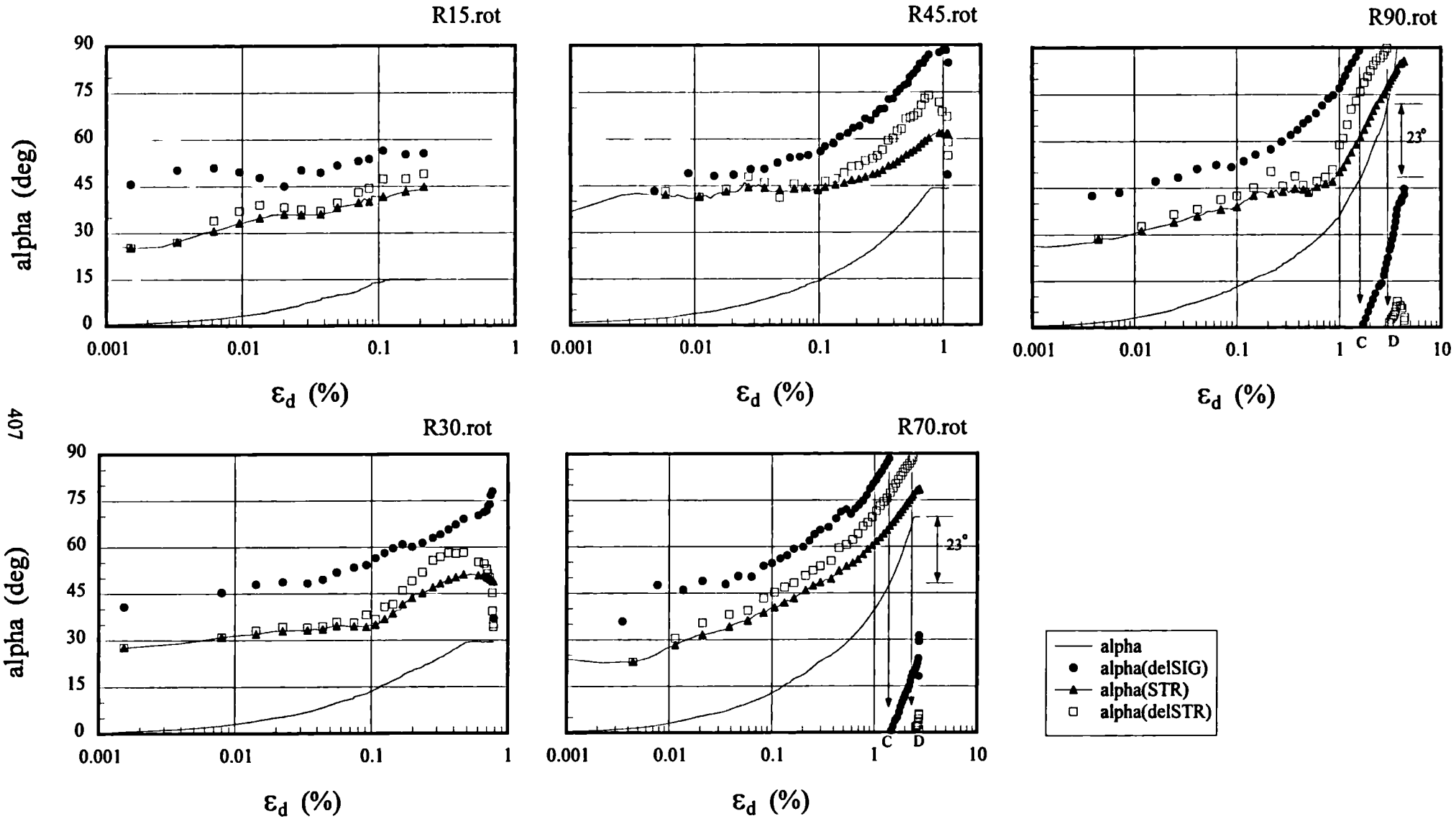


Fig.7.16 - Directions of stresses and strains and their increments during rotation stage

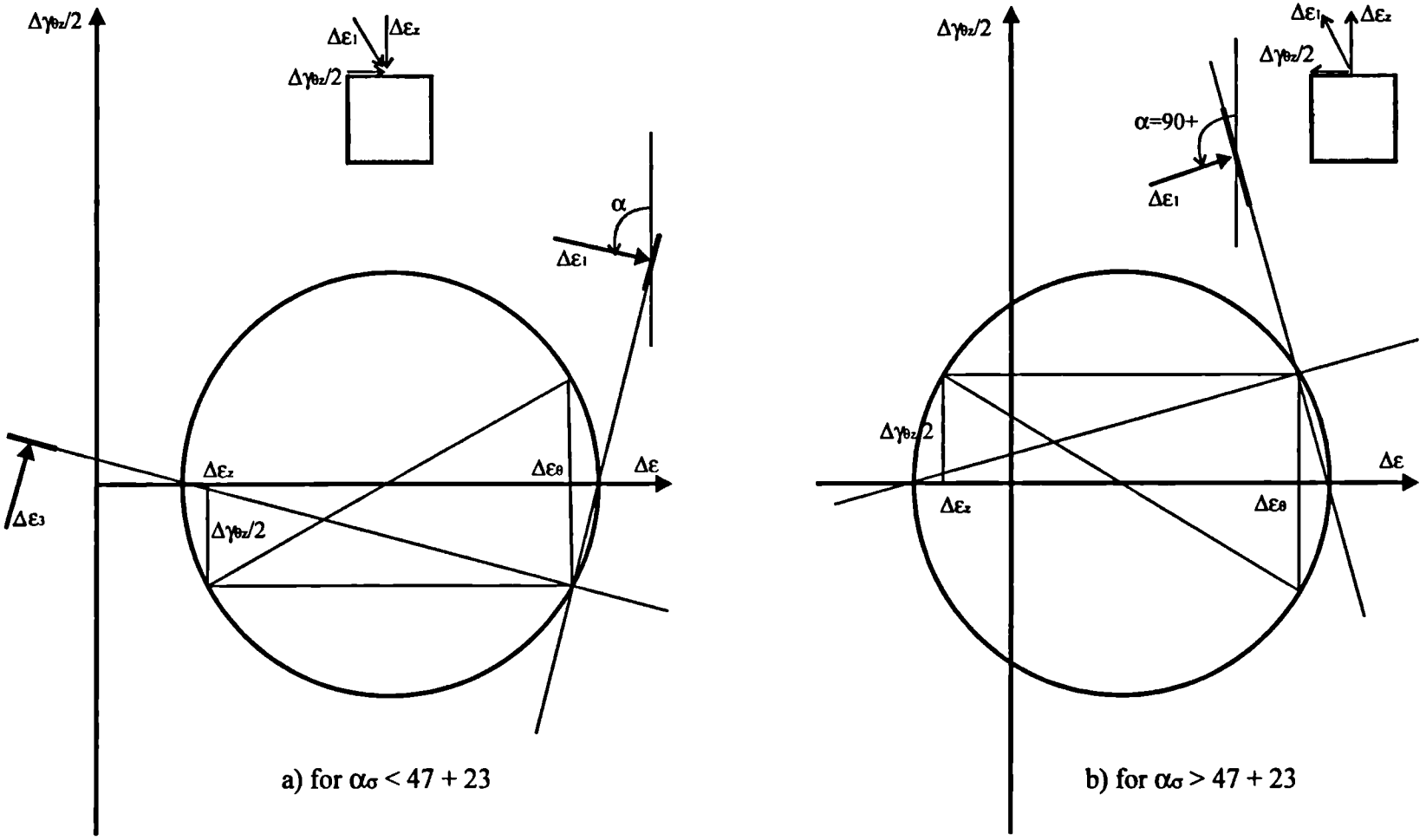


Fig.7.17 - Strain increment direction a) before point D and b) after point D

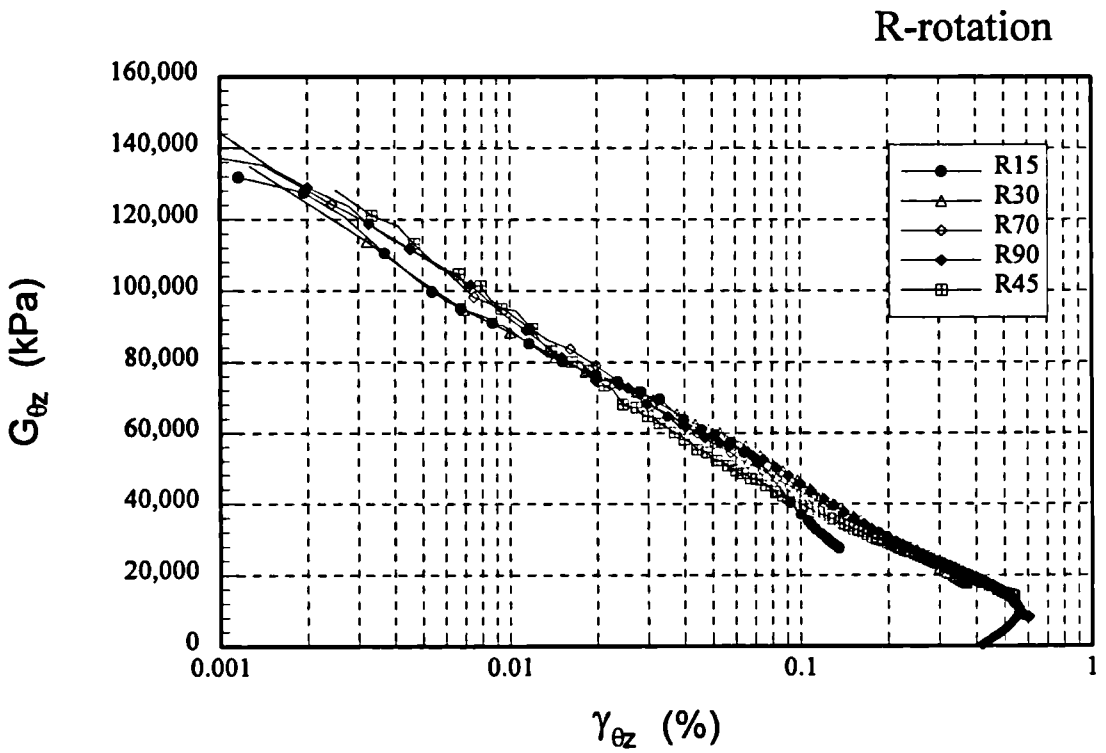


Fig.7.18 - Torsional shear stiffness vs. torsional shear strain in drained principal stress rotation

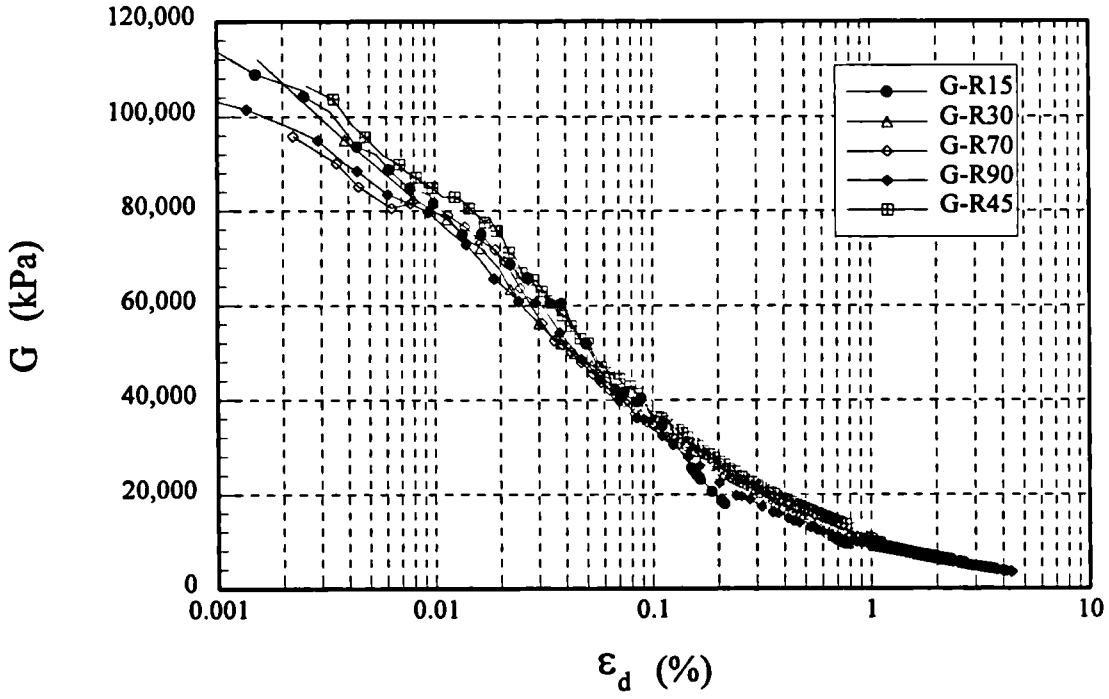


Fig.7.19 - Octahedral shear stiffness vs. deviatoric shear strain in drained principal stress rotation

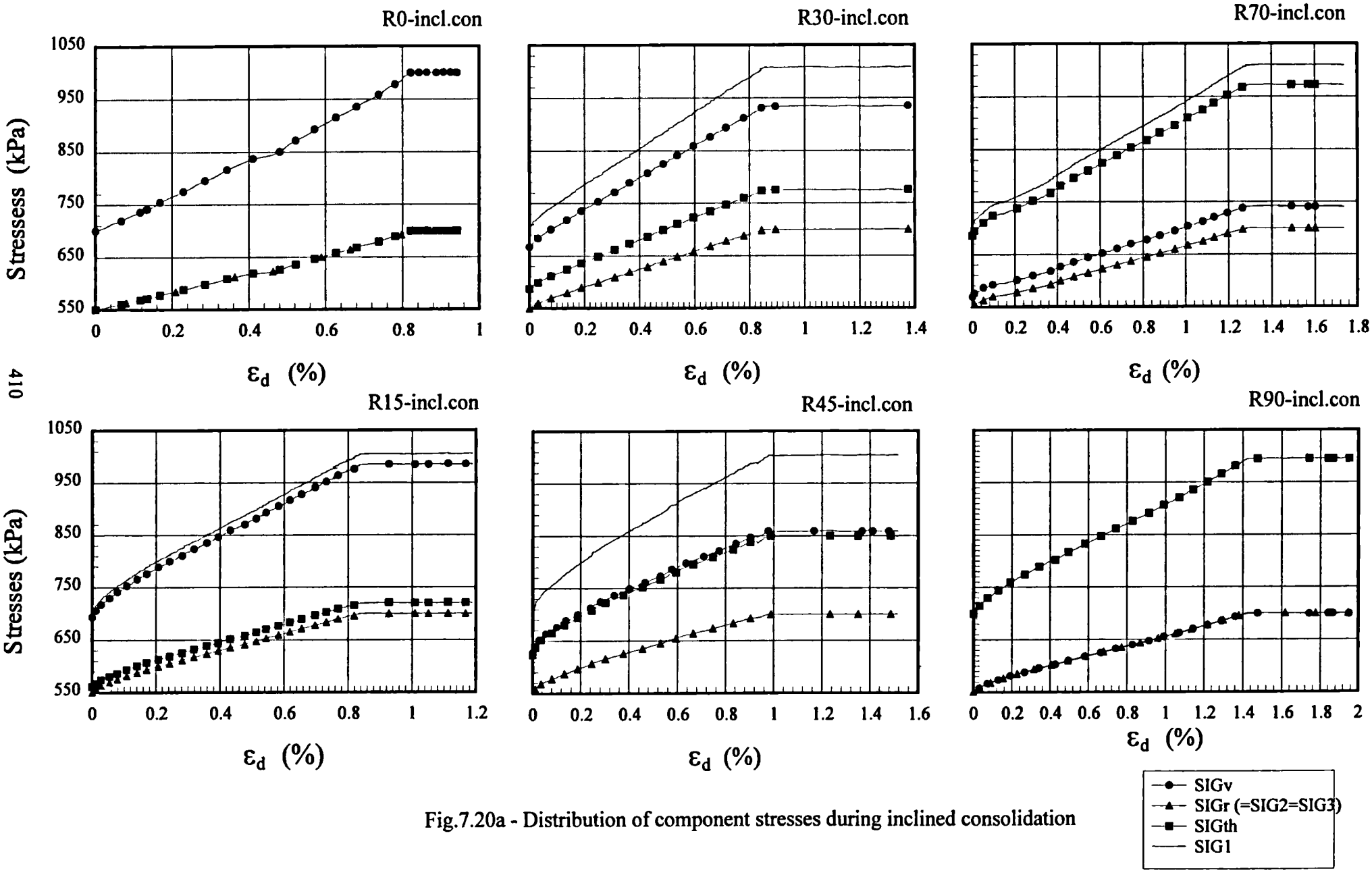


Fig.7.20a - Distribution of component stresses during inclined consolidation

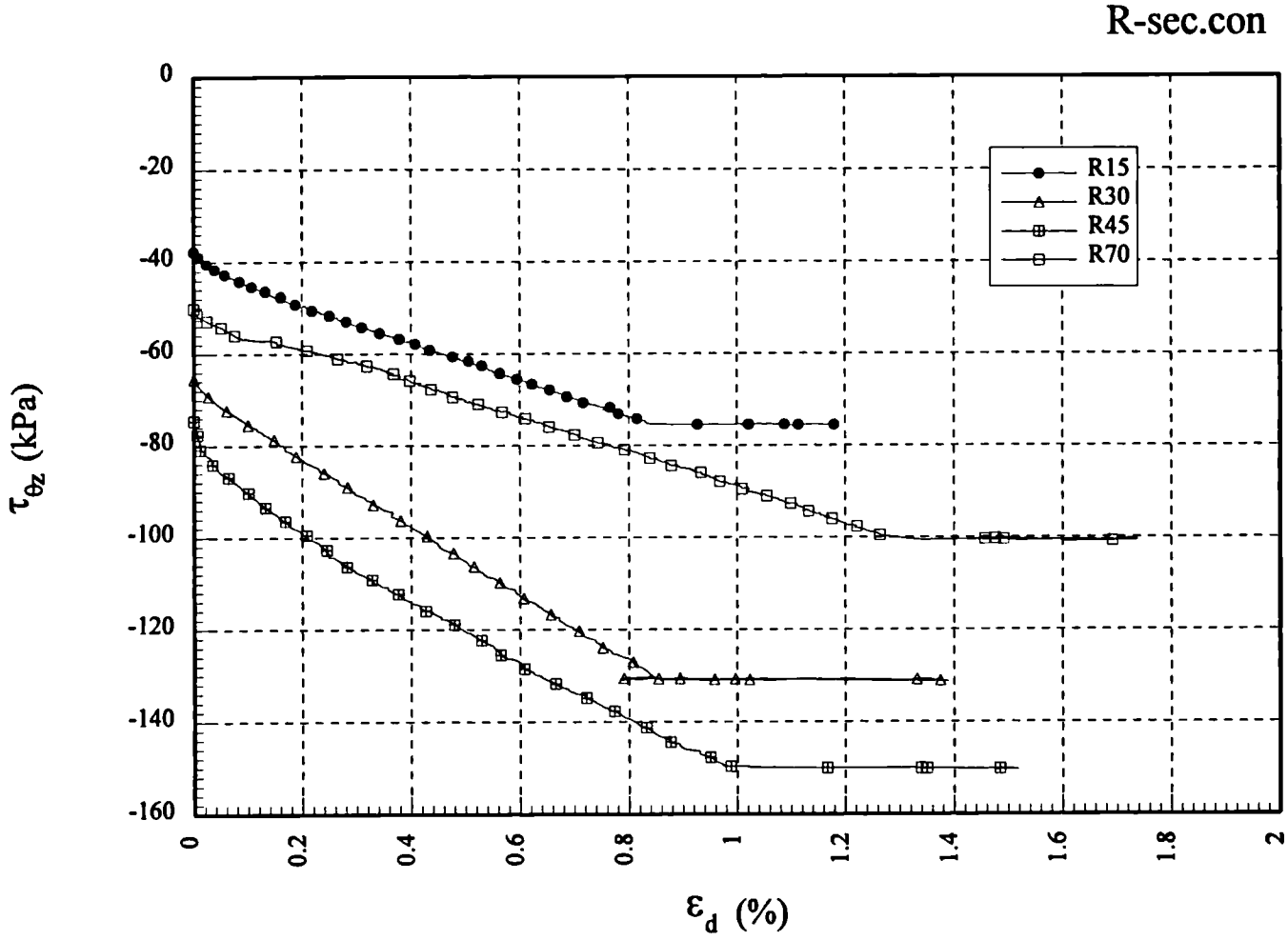


Fig.7.20b - Development of torsional shear stress during inclined consolidation

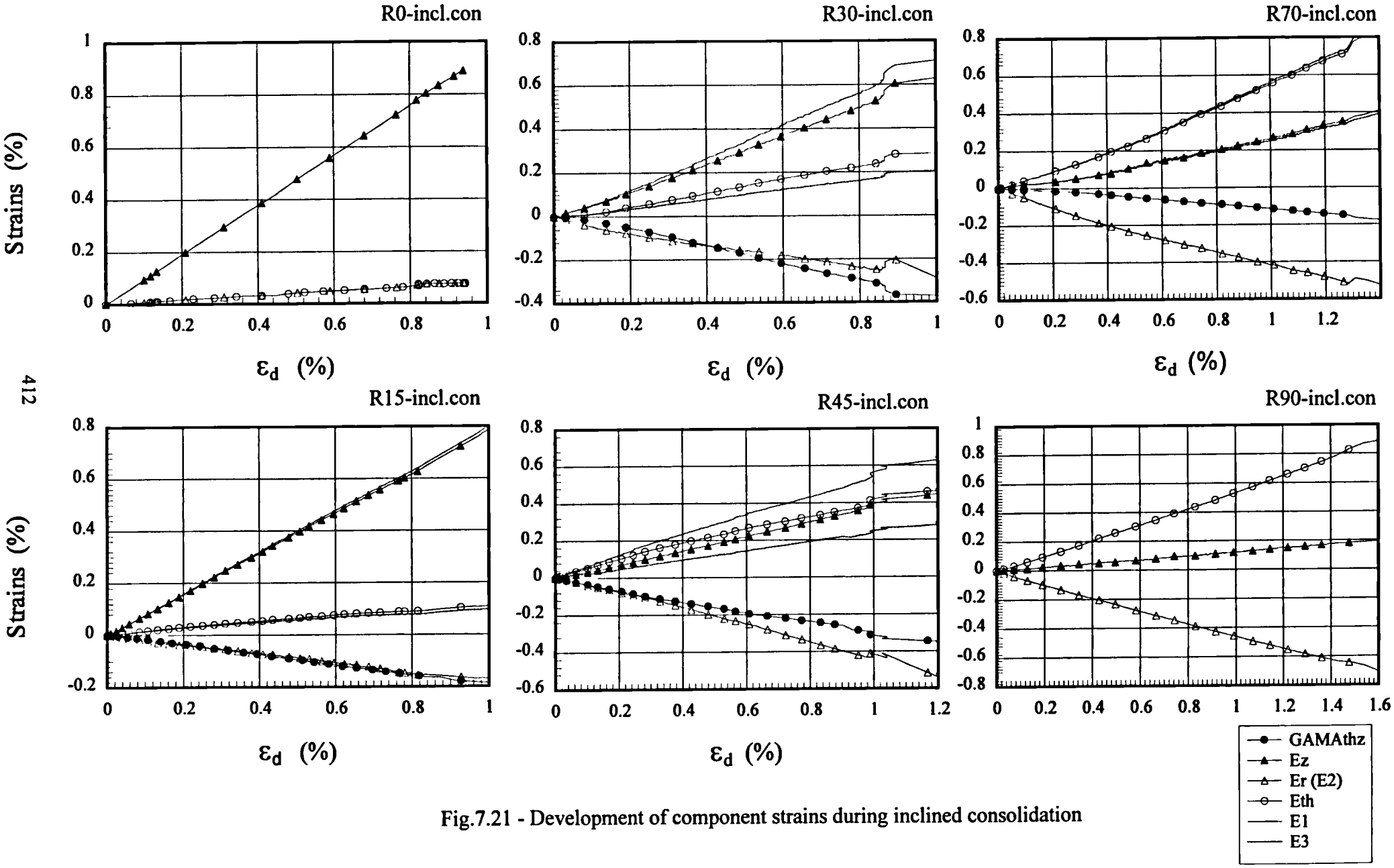


Fig.7.21 - Development of component strains during inclined consolidation

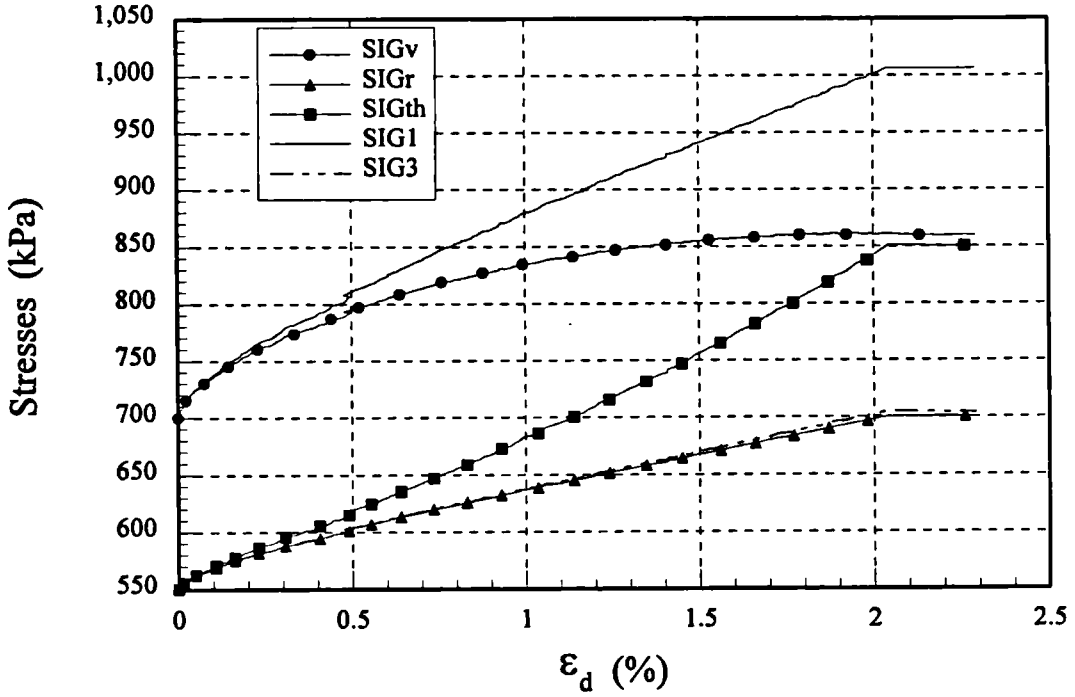


Fig.7.22a - Development of direct component stresses during inclined consolidation, when α continuously increases

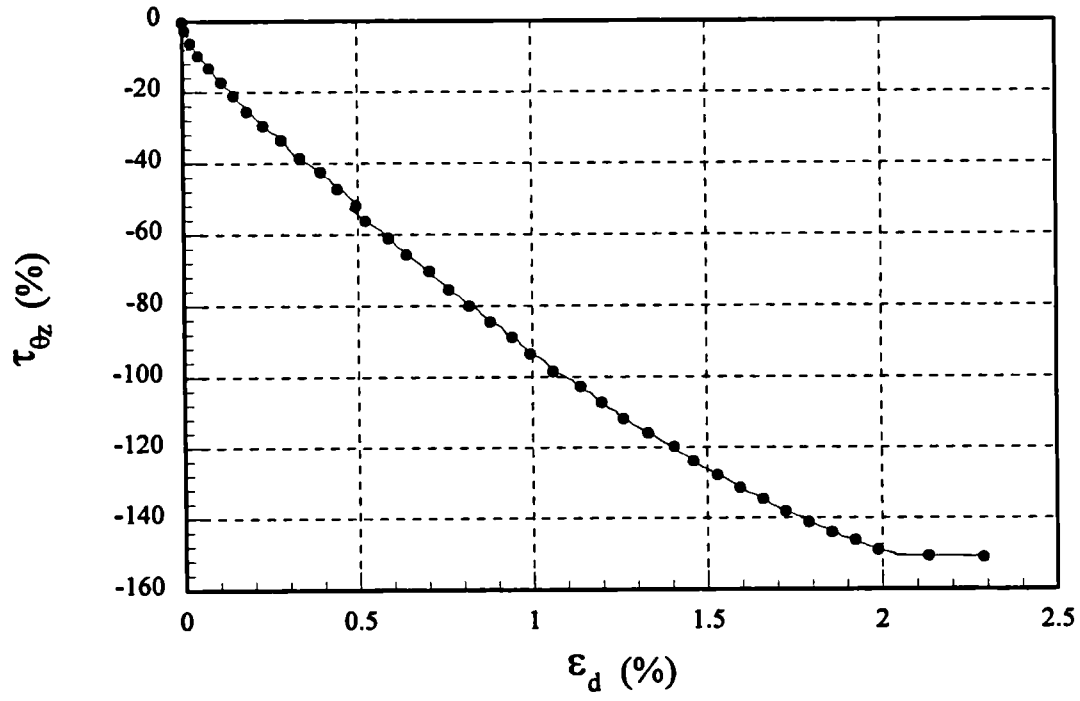


Fig.7.22b - Development of torsional shear stress during inclined consolidation, when α continuously increases

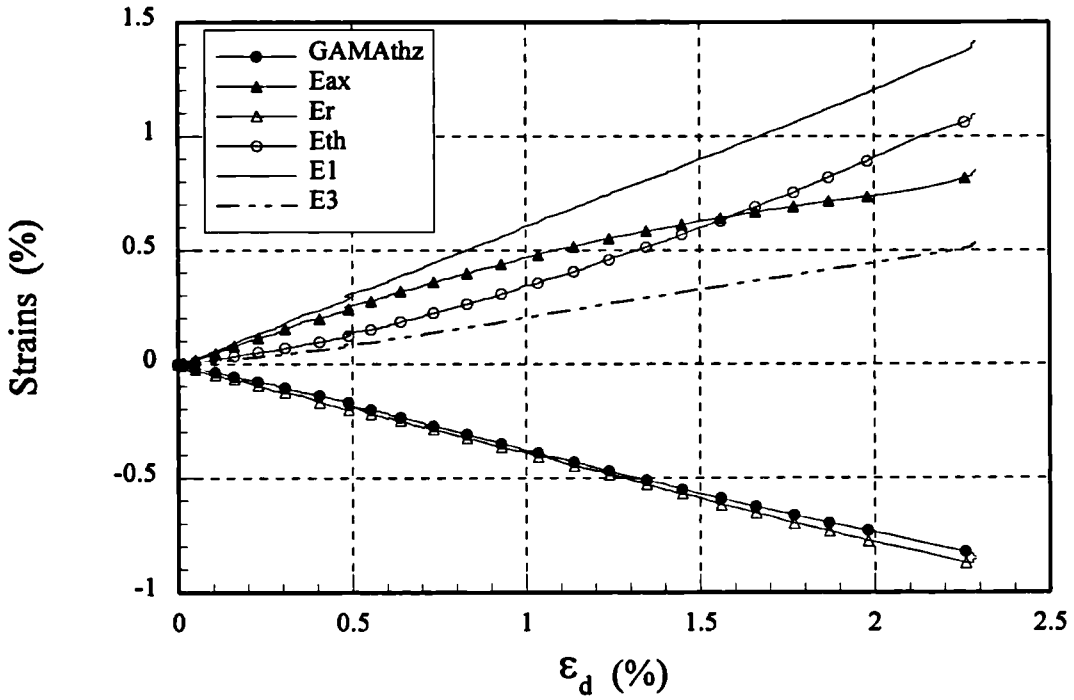


Fig.7.23 - Strain components developed during inclined consolidation, when α continuously increases

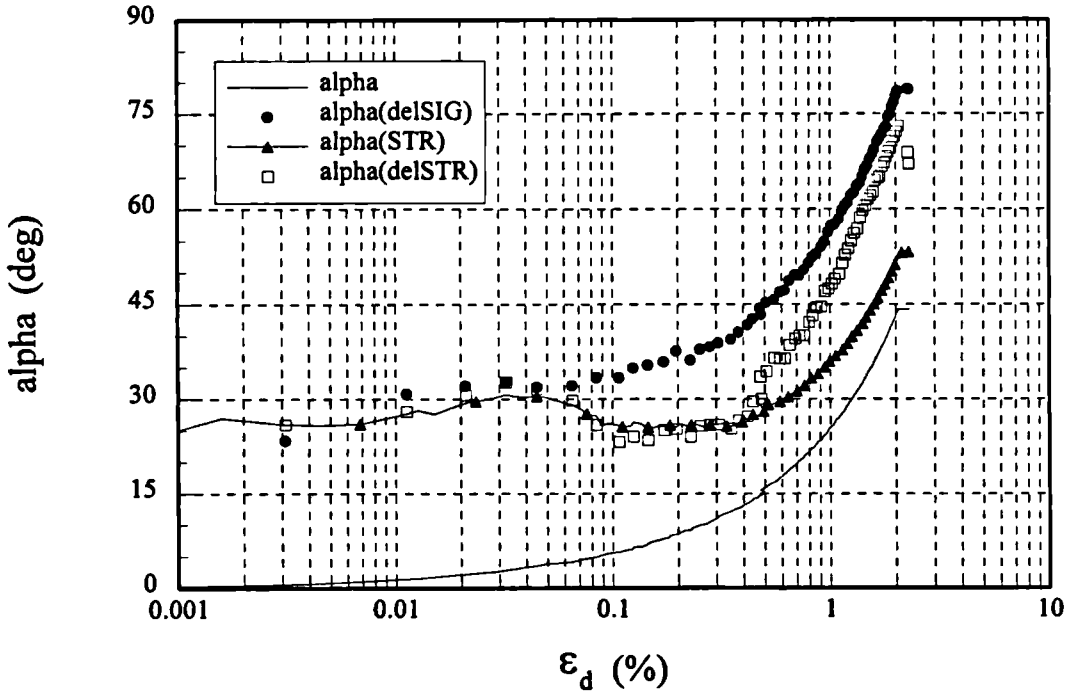


Fig.7.24 - Variation of major principal stress, stress increment, strain and strain increment directions, when α continuously increases

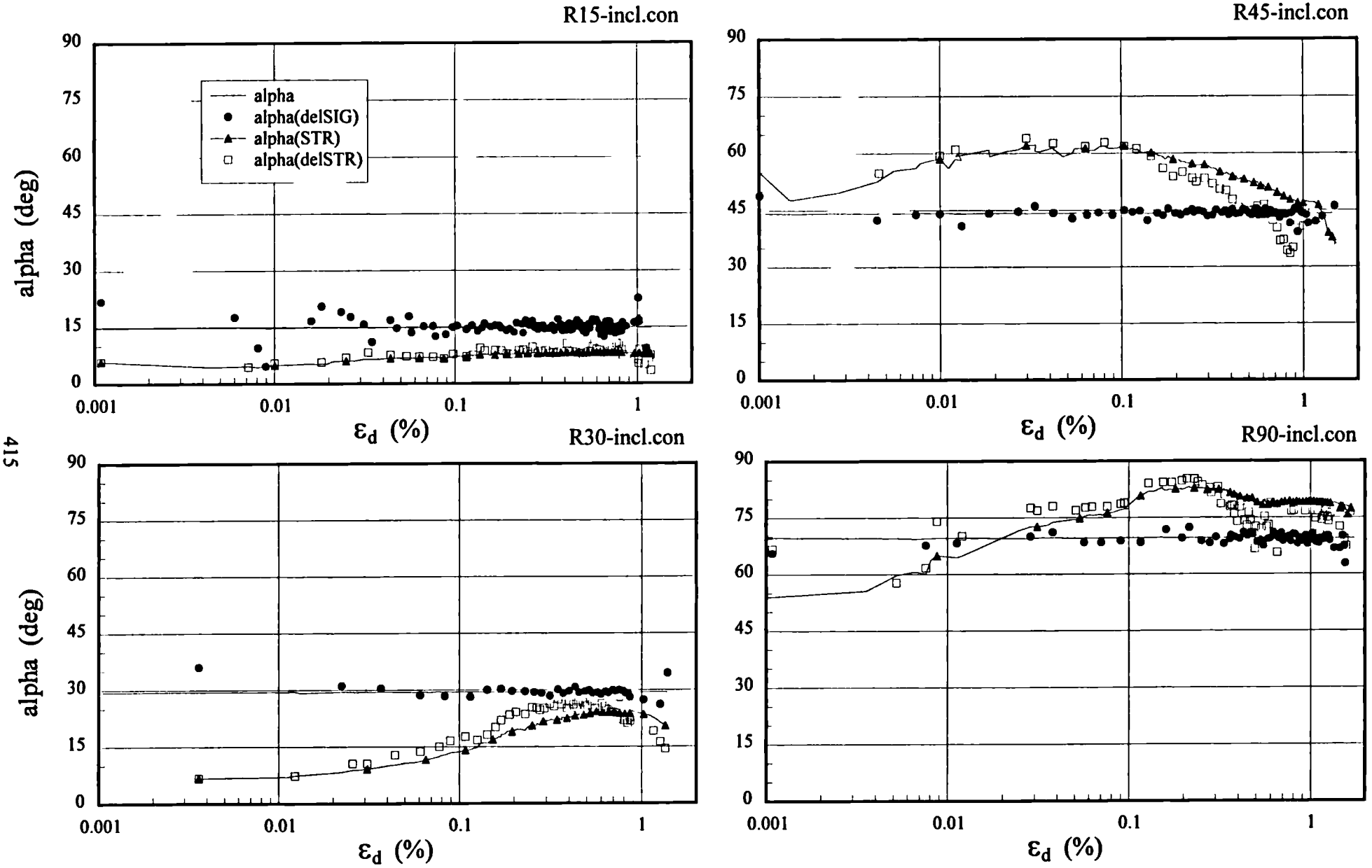


Fig.7.25 - Directions of stresses and strains and their increments during inclined consolidation

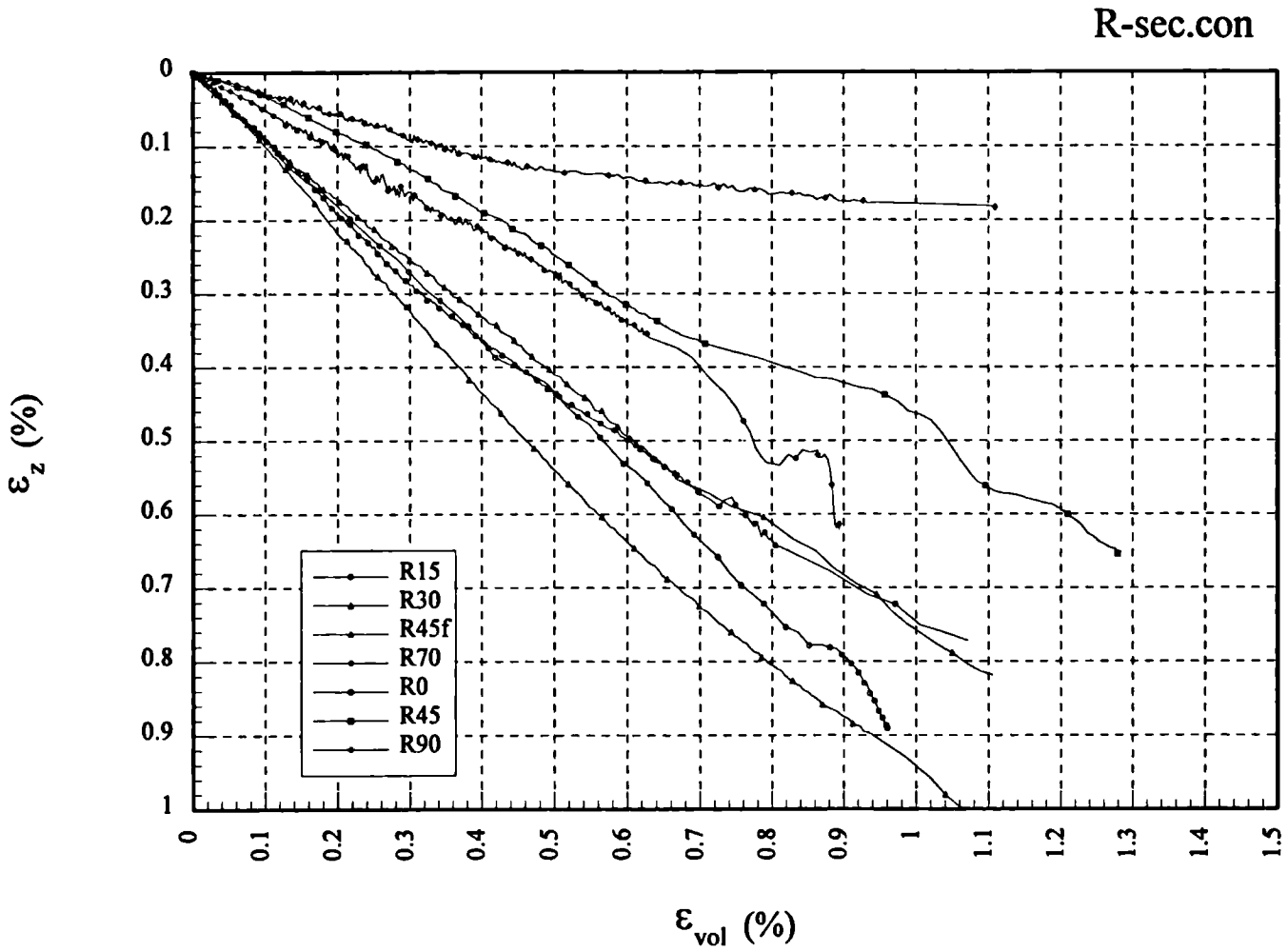


Fig.7.26 - Relation of axial and volumetric strain during inclined consolidation, with α rangeing from 0 to 90

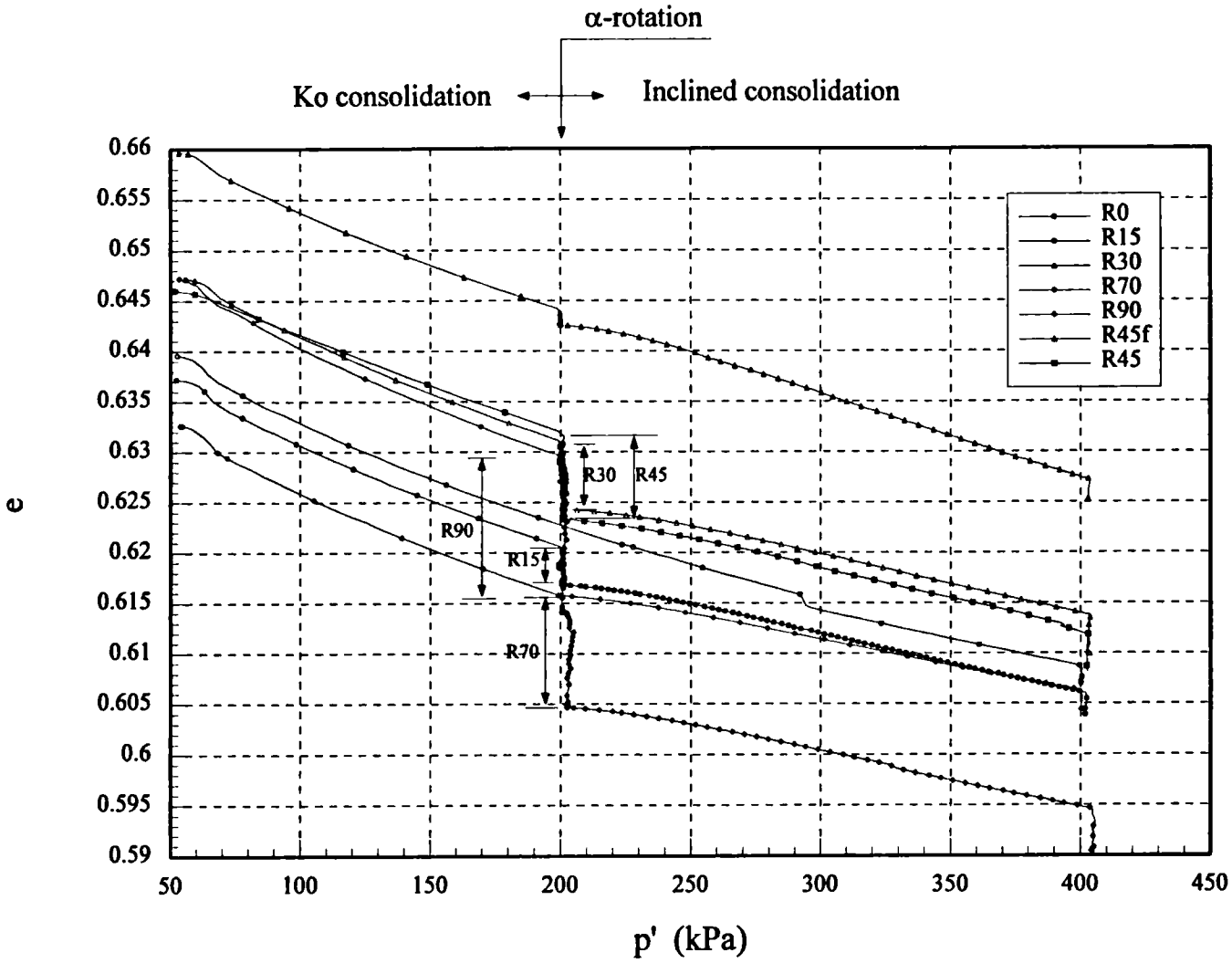


Fig.7.27 - Summary plot for the change in void ratio, e

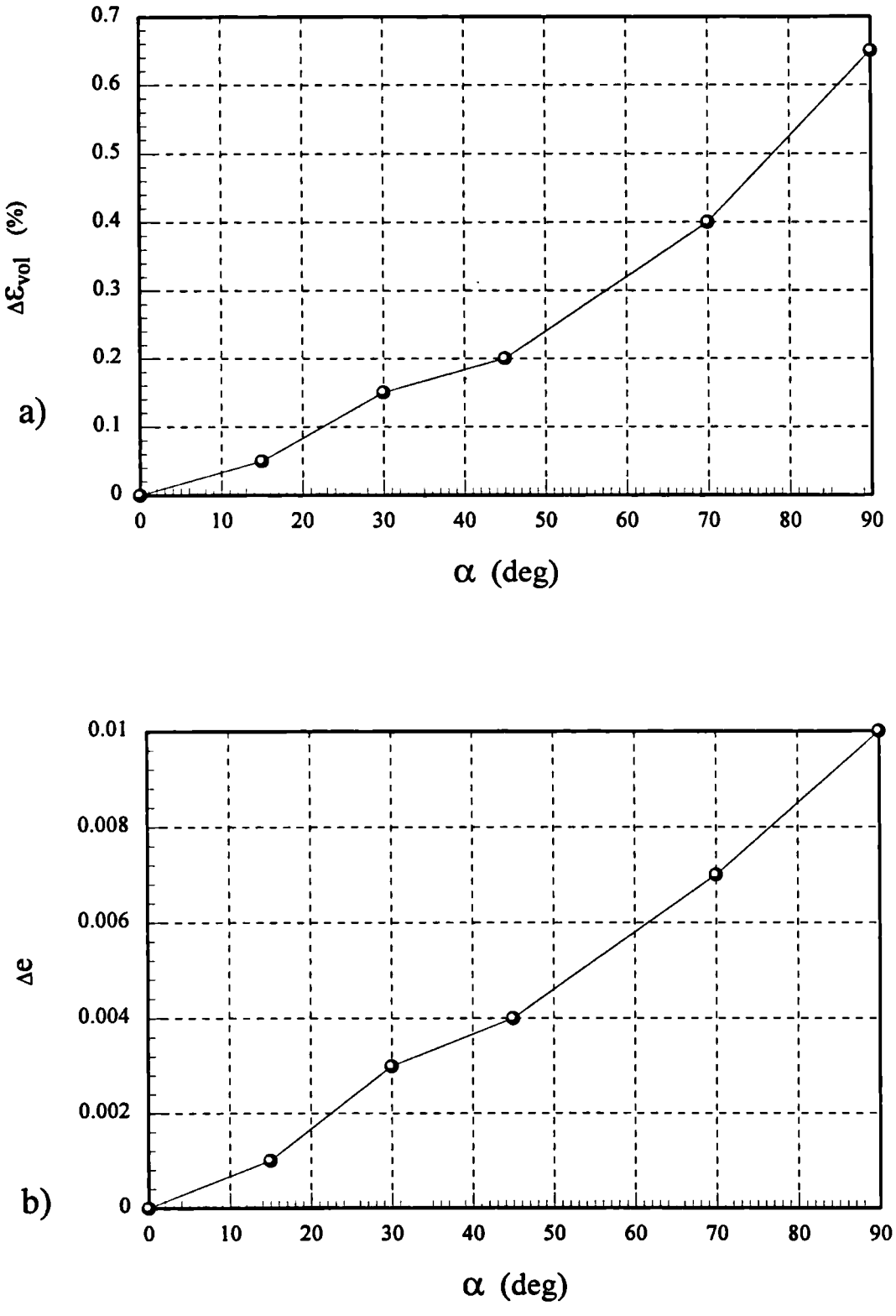


Fig.7.28 - a) Change in volumetric strain and b) change in void ratio, after subtracting R0 test, when α = const during inclined consolidation

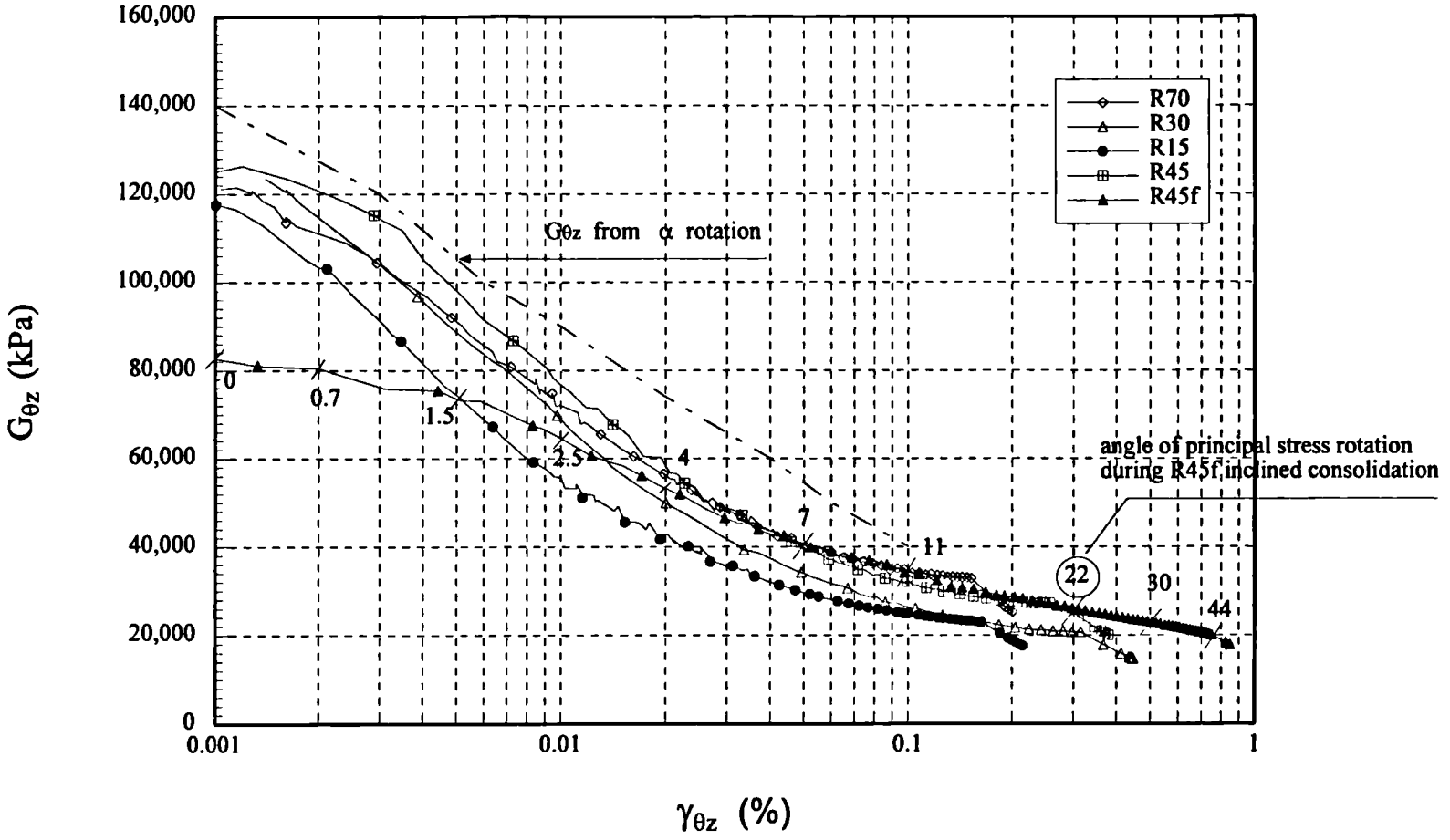


Fig.7.29 - Variation of torsional shear stiffness during inclined consolidation

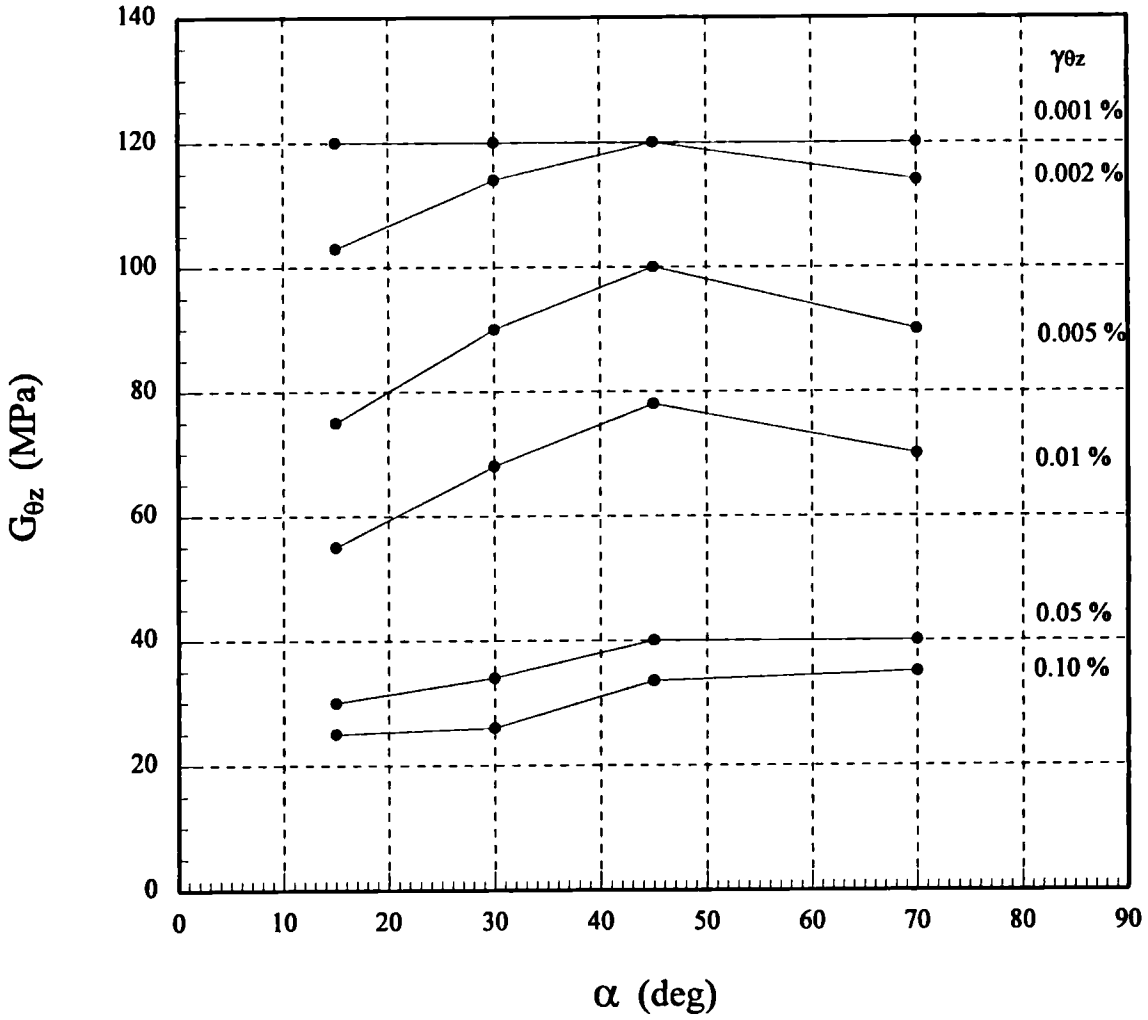


Fig.730 - Distribution of $G_{\theta z}$ with α, at different strain levels

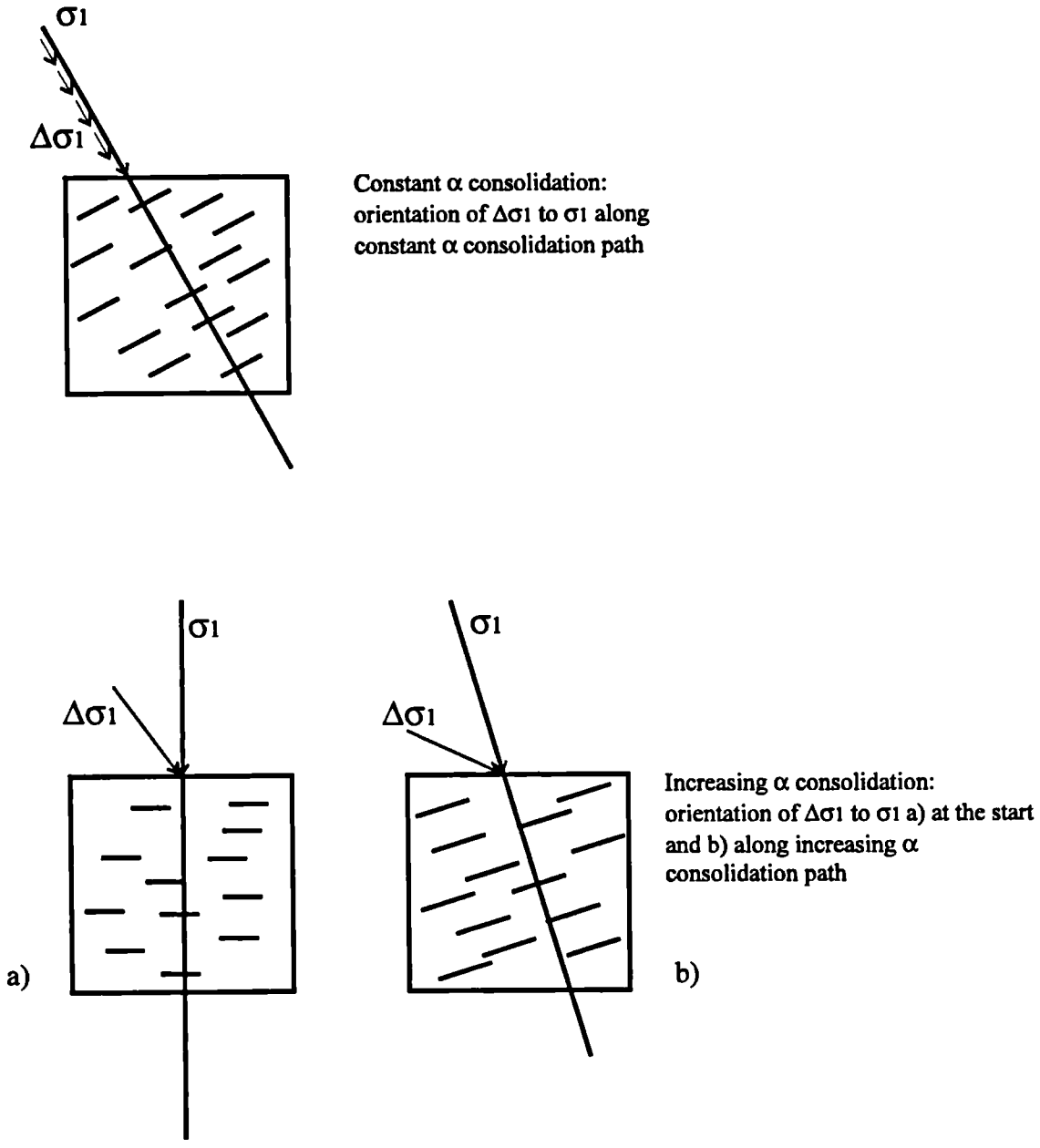


Fig.7.31 - Probable particle arrangements along different consolidation paths

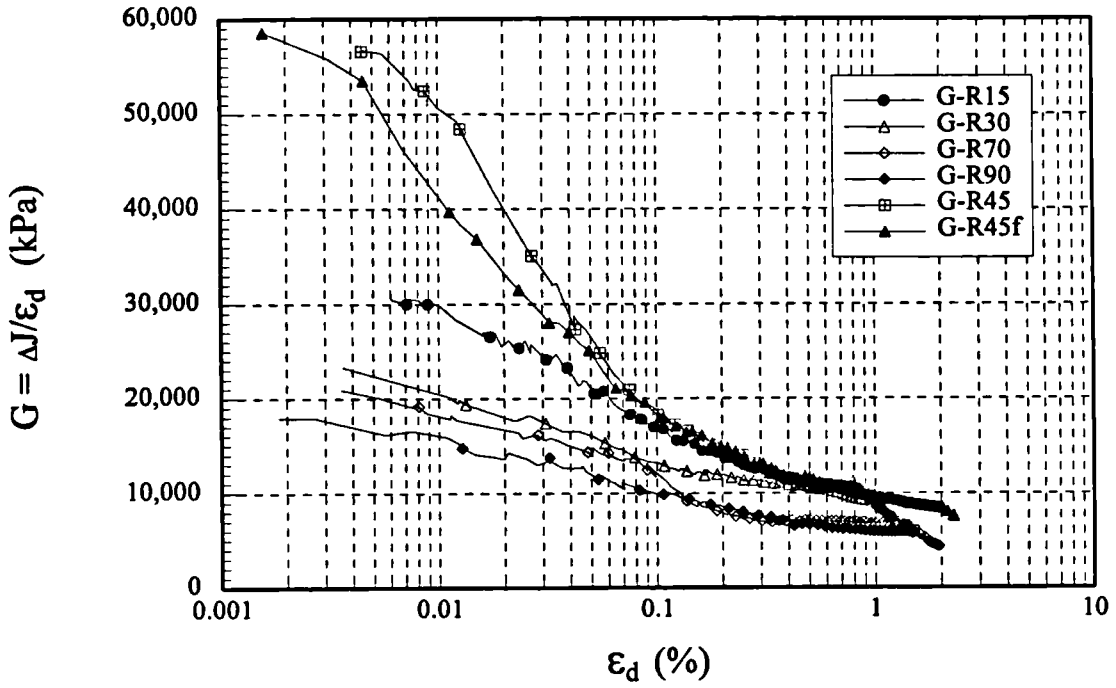


Fig.7.32 - Octahedral shear stiffness generated during inclined consolidation

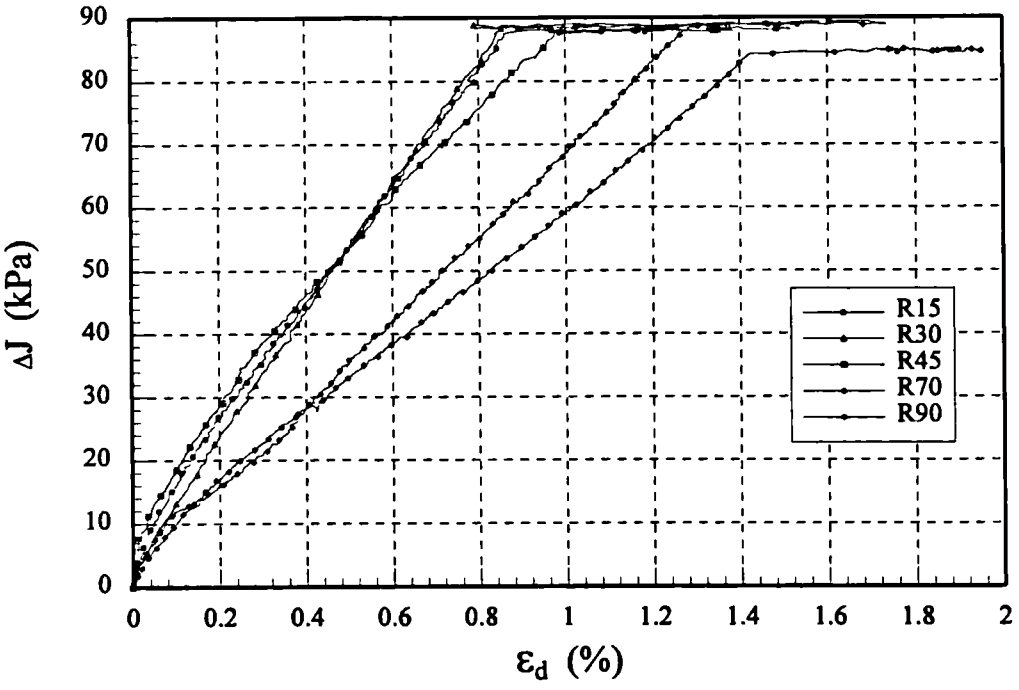
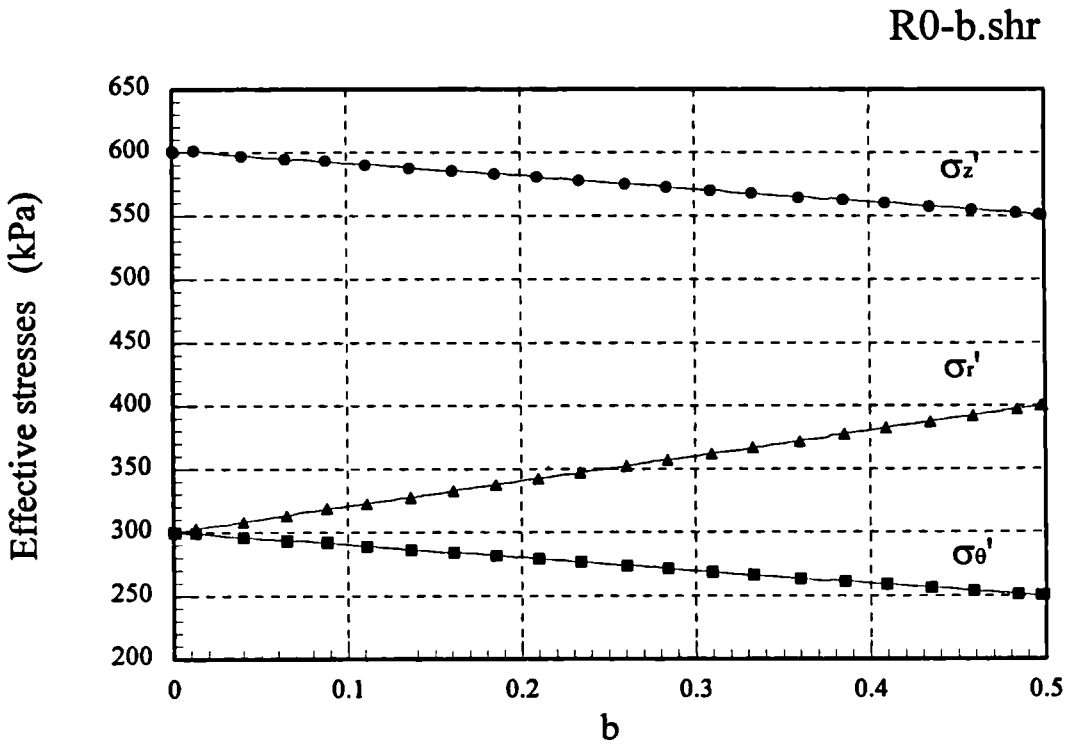


Fig.7.33 - Invariant deviatoric stress



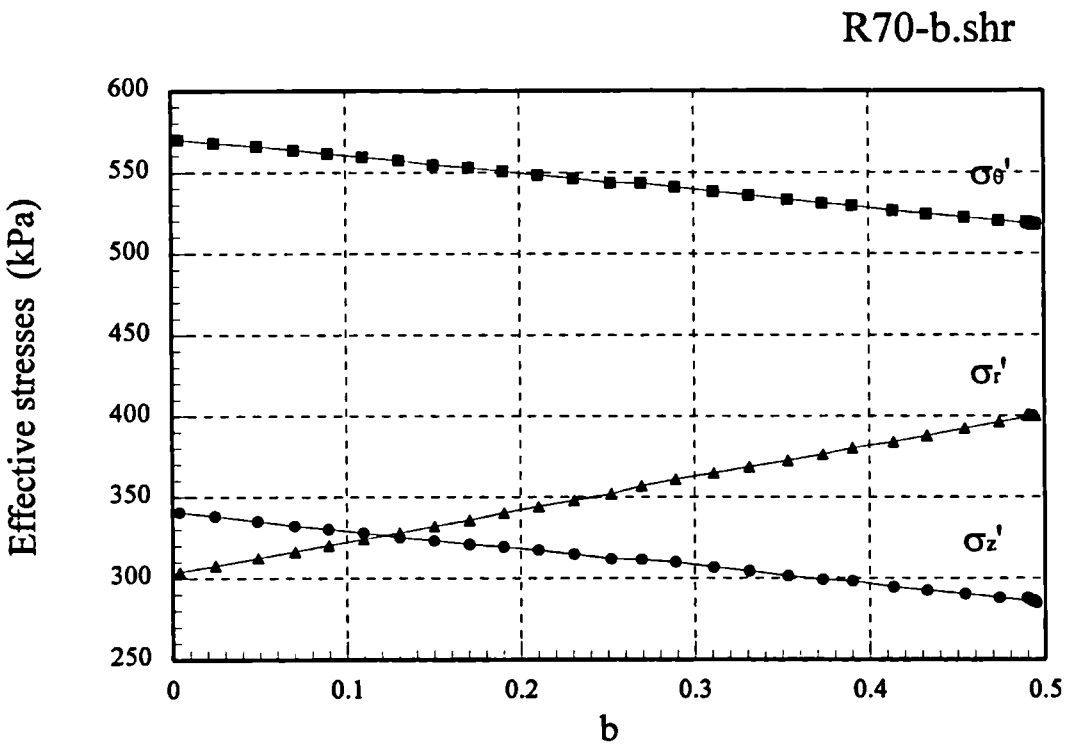


Fig.7.34 - Changes of direct component stresses during b-stage

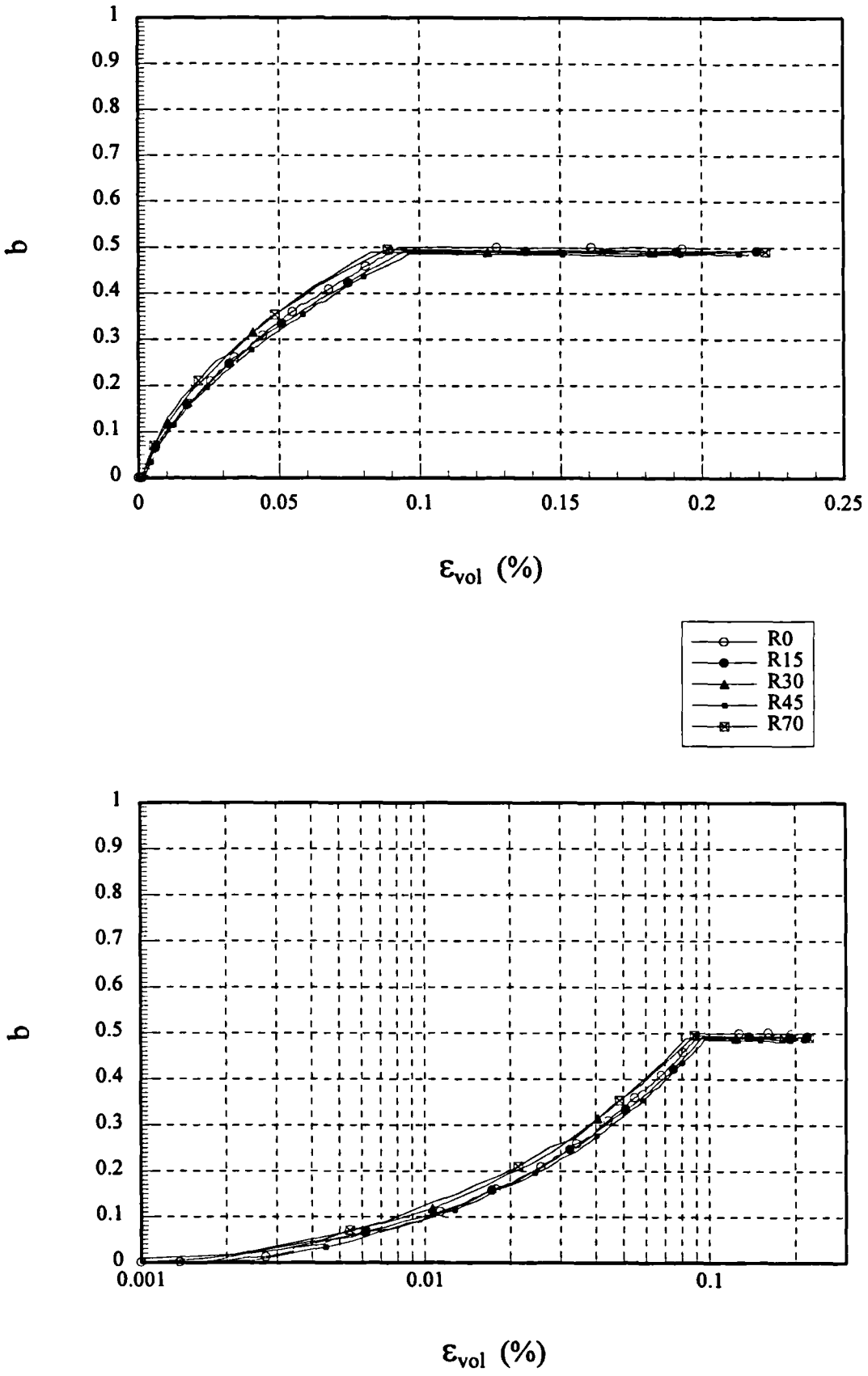


Fig.7.35 - Generation of volumetric strain during the b-stage

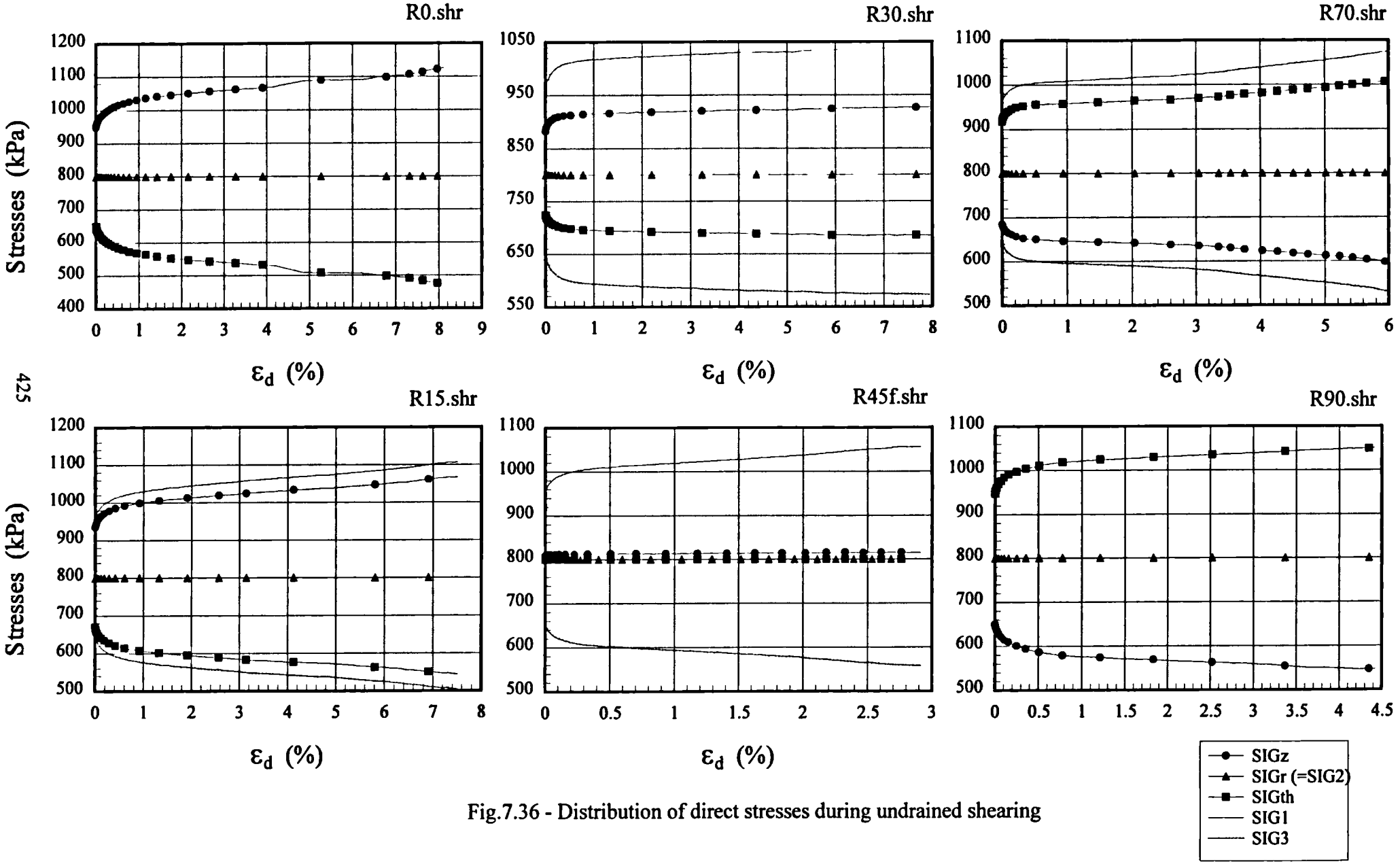


Fig.7.36 - Distribution of direct stresses during undrained shearing

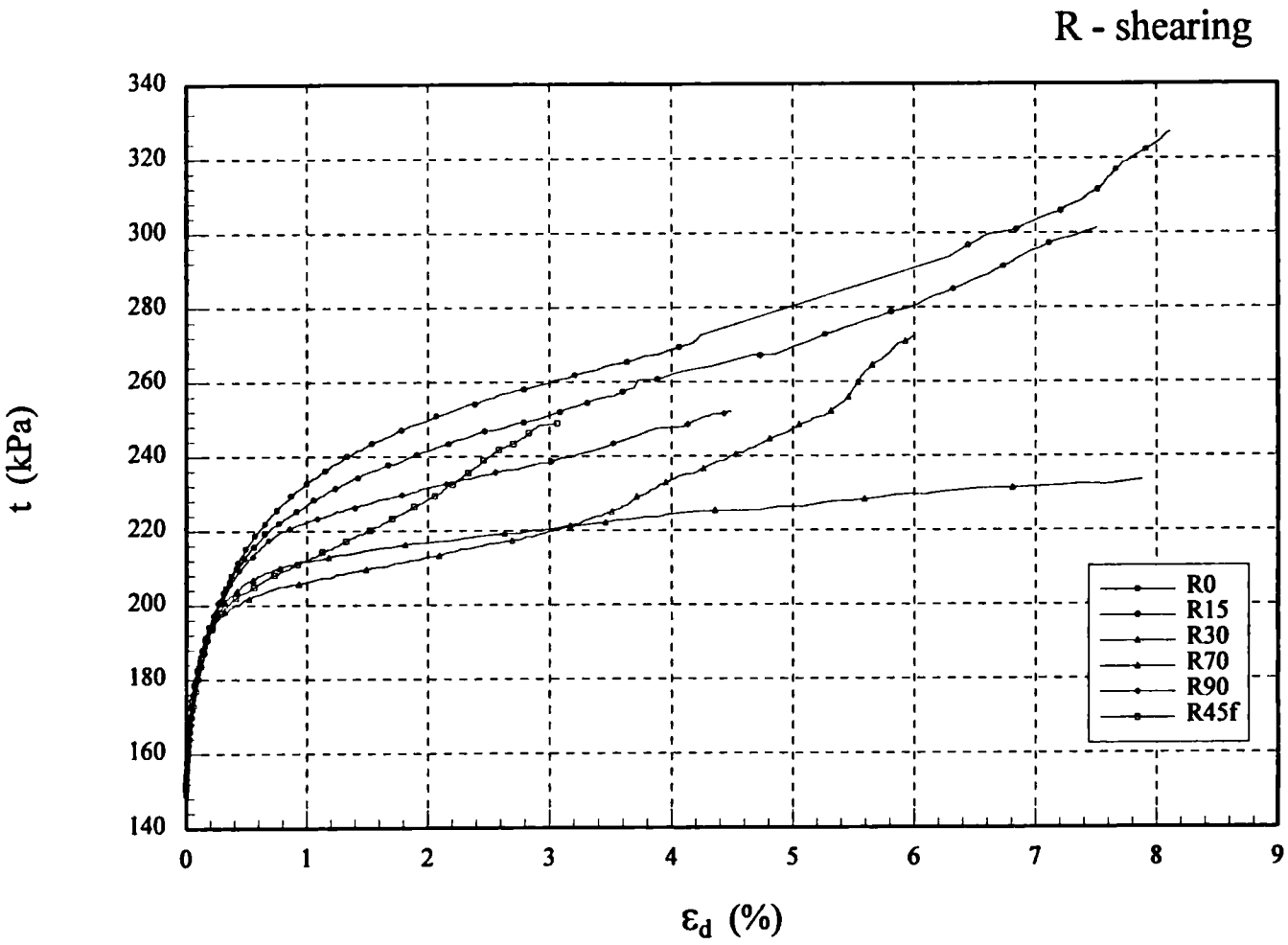


Fig.7.37 - Stress-strain curves for shearing stage of R-Series tests

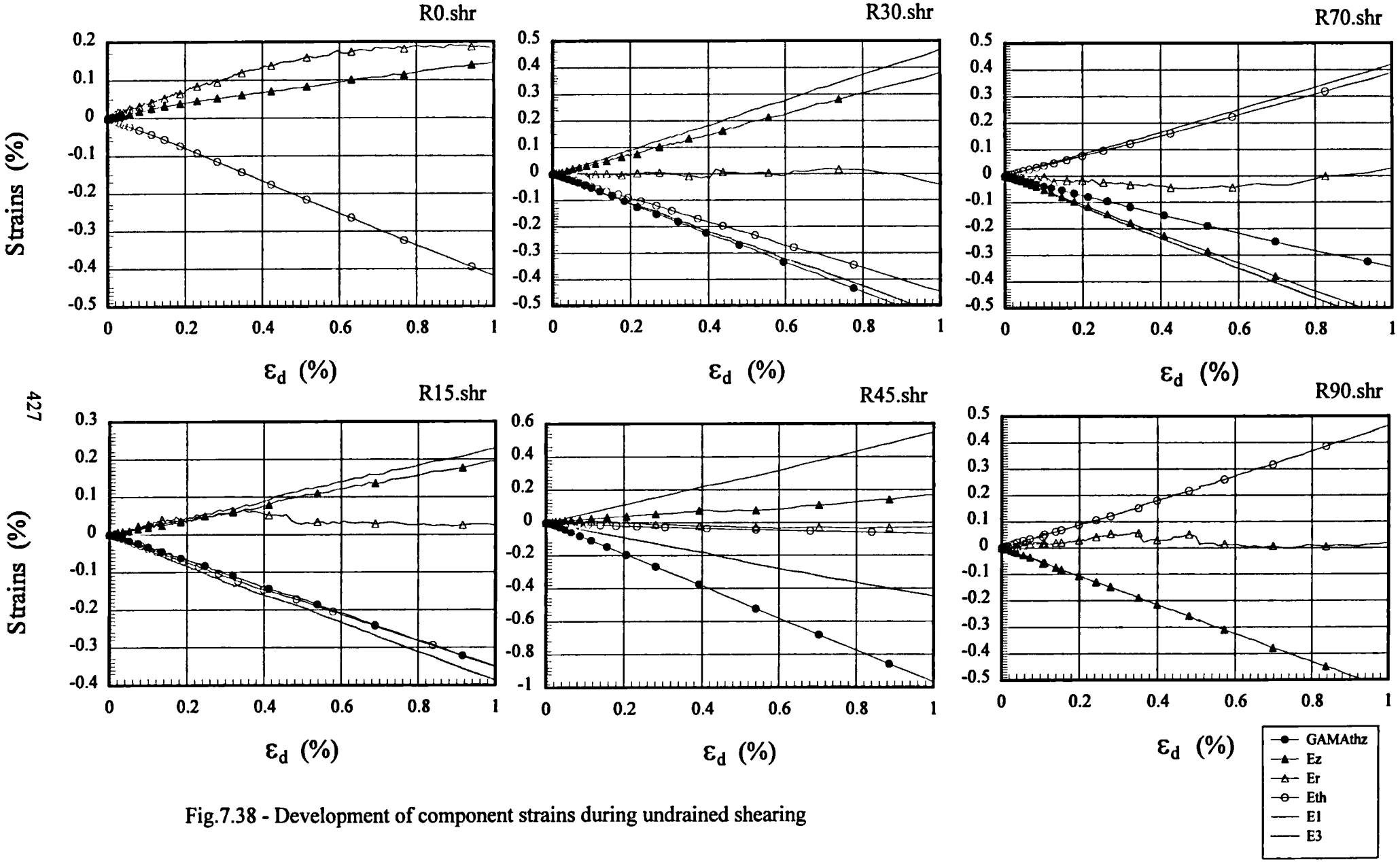


Fig.7.38 - Development of component strains during undrained shearing

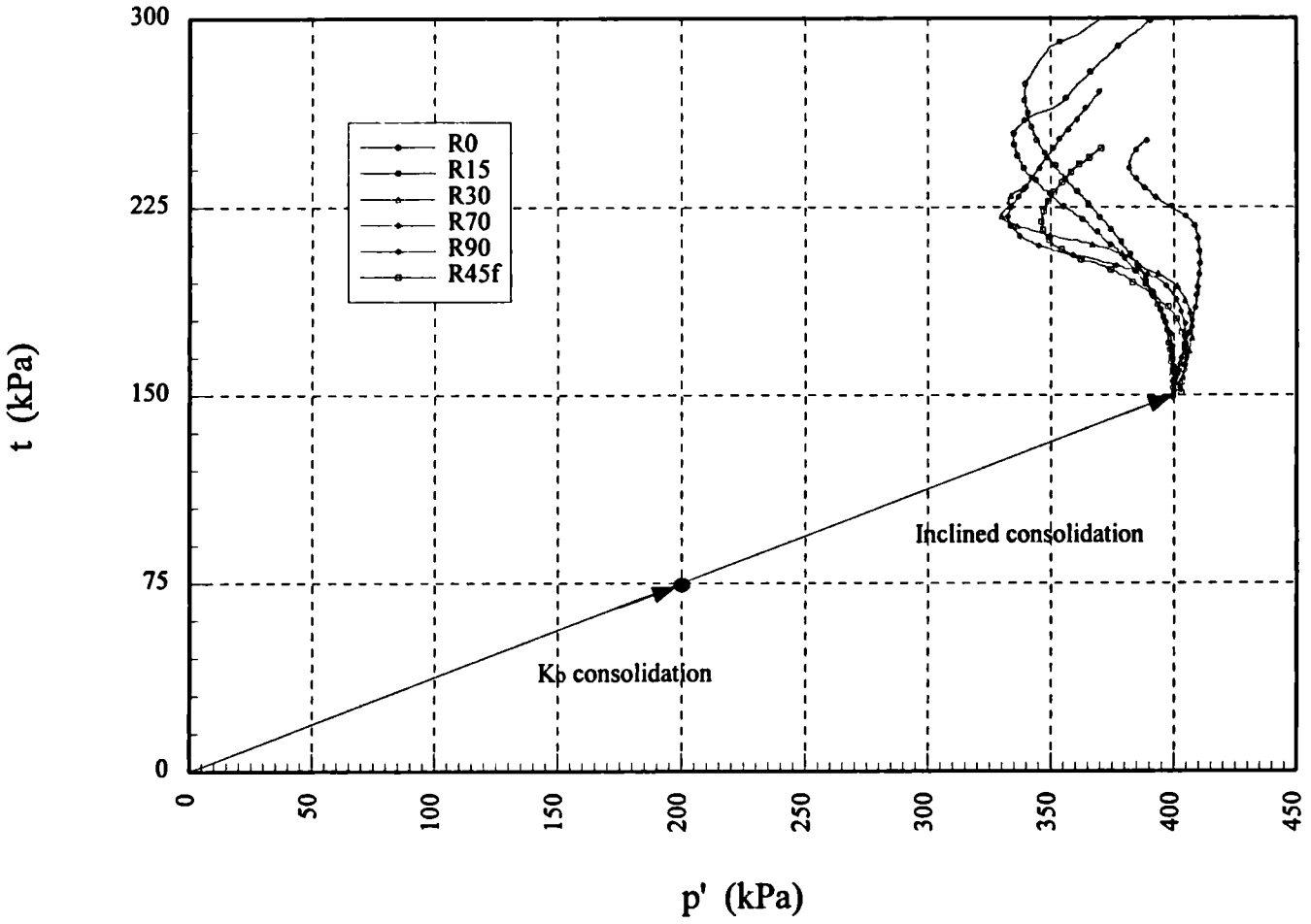


Fig.7.39 - The effective stress paths followed during undrained shearing of R-Series tests

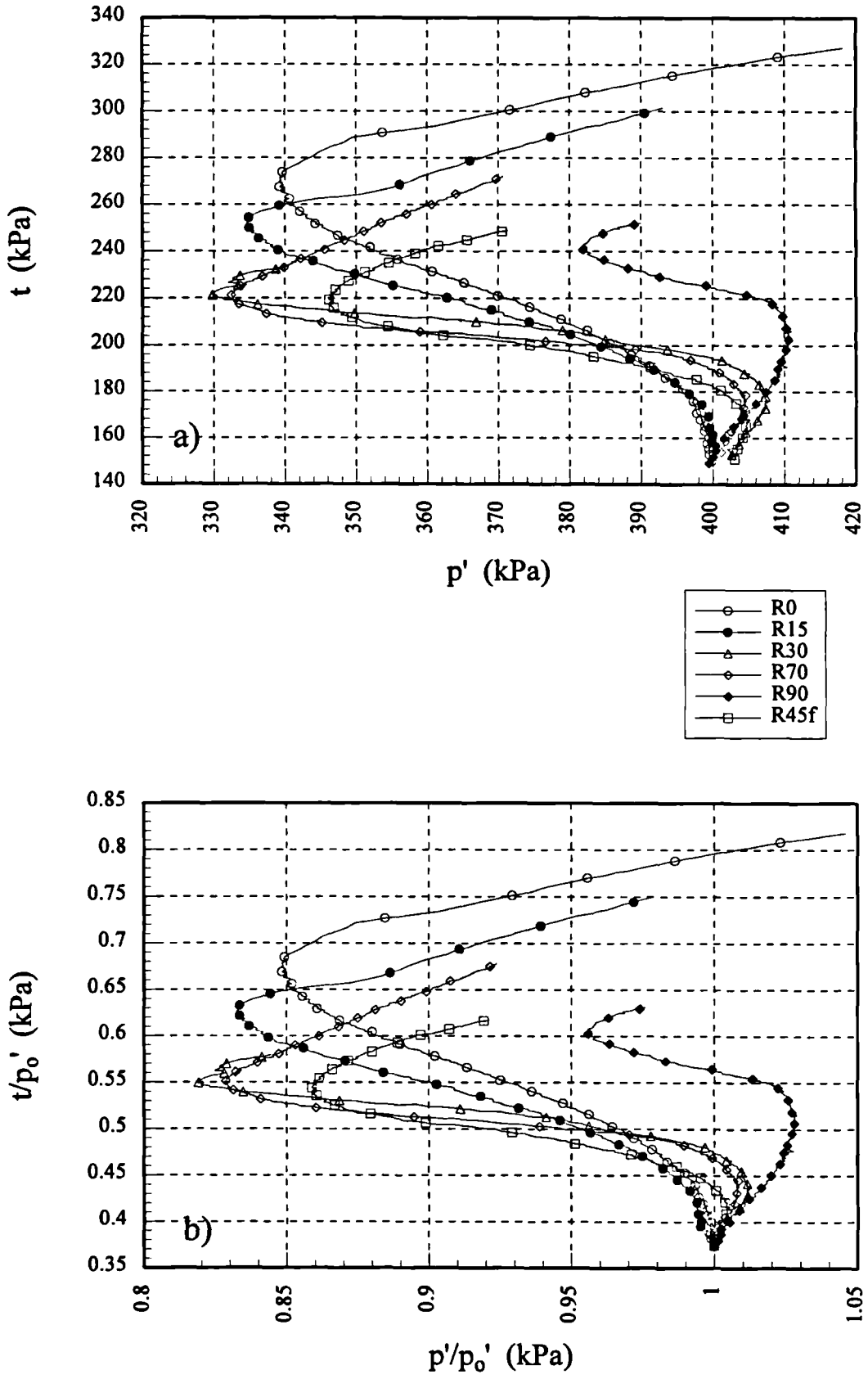


Fig.7.40 - a) Enlarged view of the effective stress paths followed in undrained shearing;
b) Normalized effective stress paths

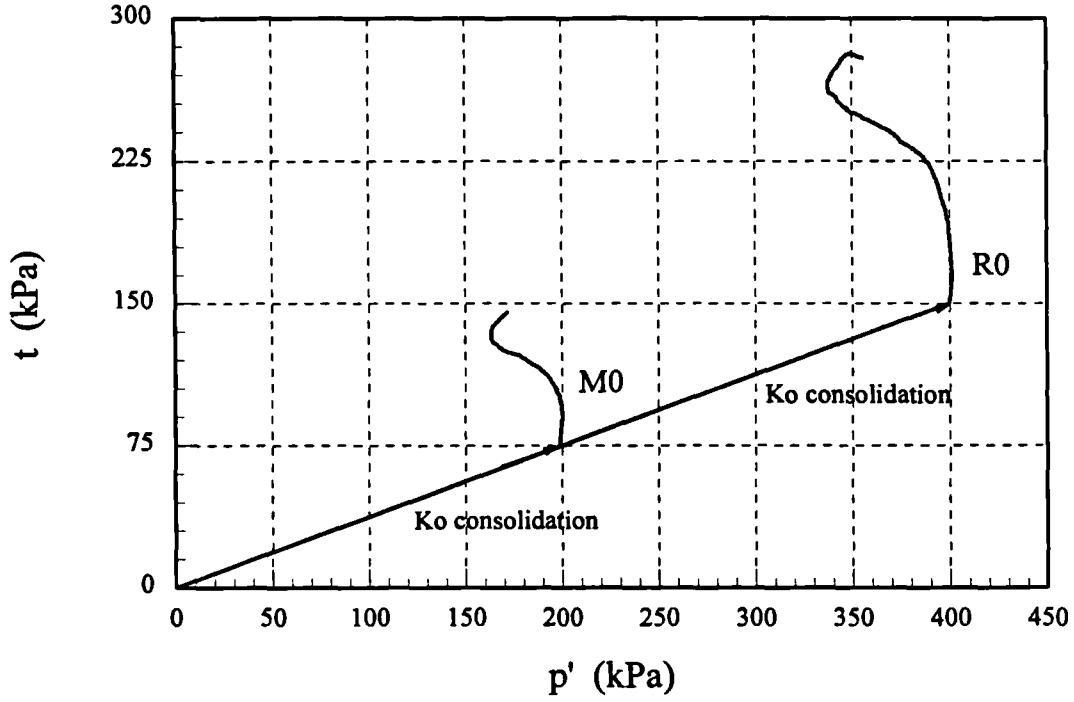


Fig.7.41 - Effective stress paths for M0 and R0 tests

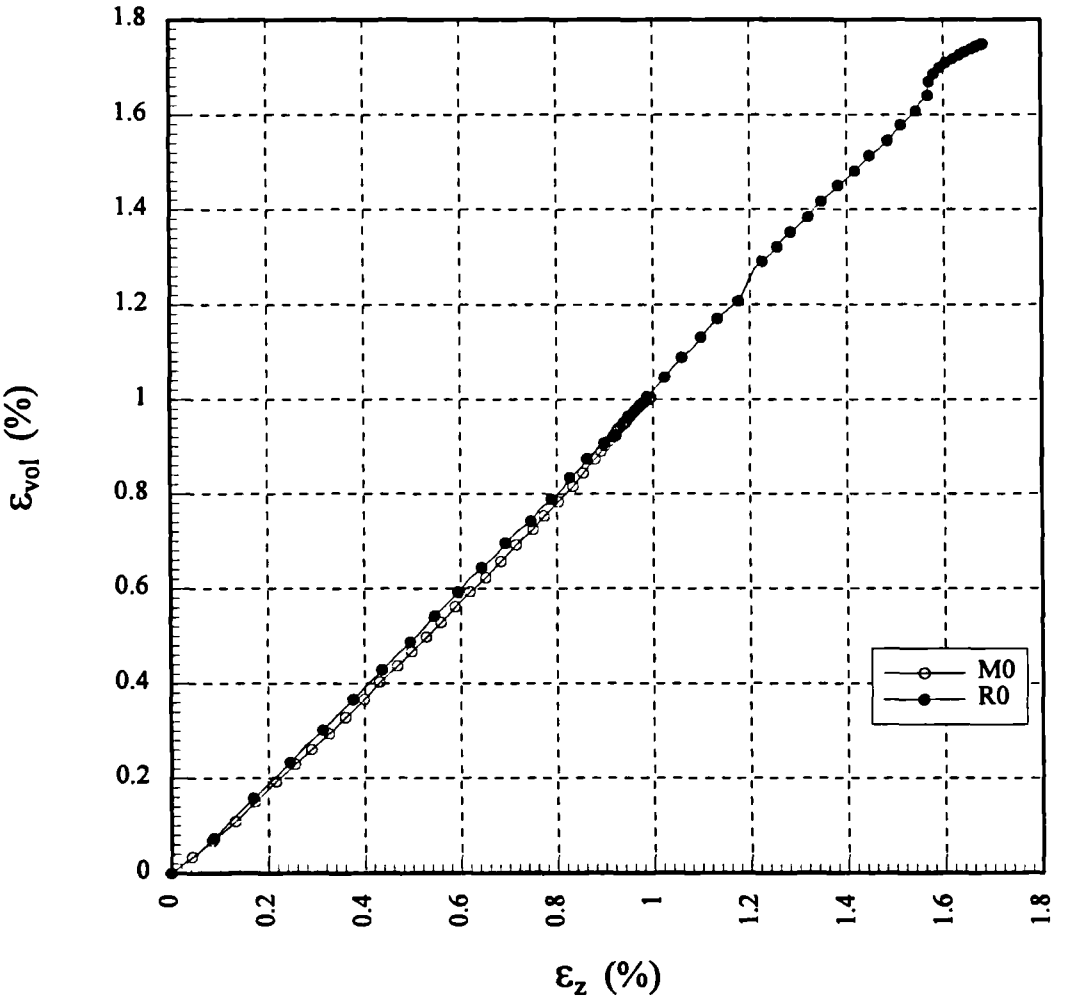


Fig.7.42 - Volumetric vs. axial strain during Ko consolidation of samples R0 and M0

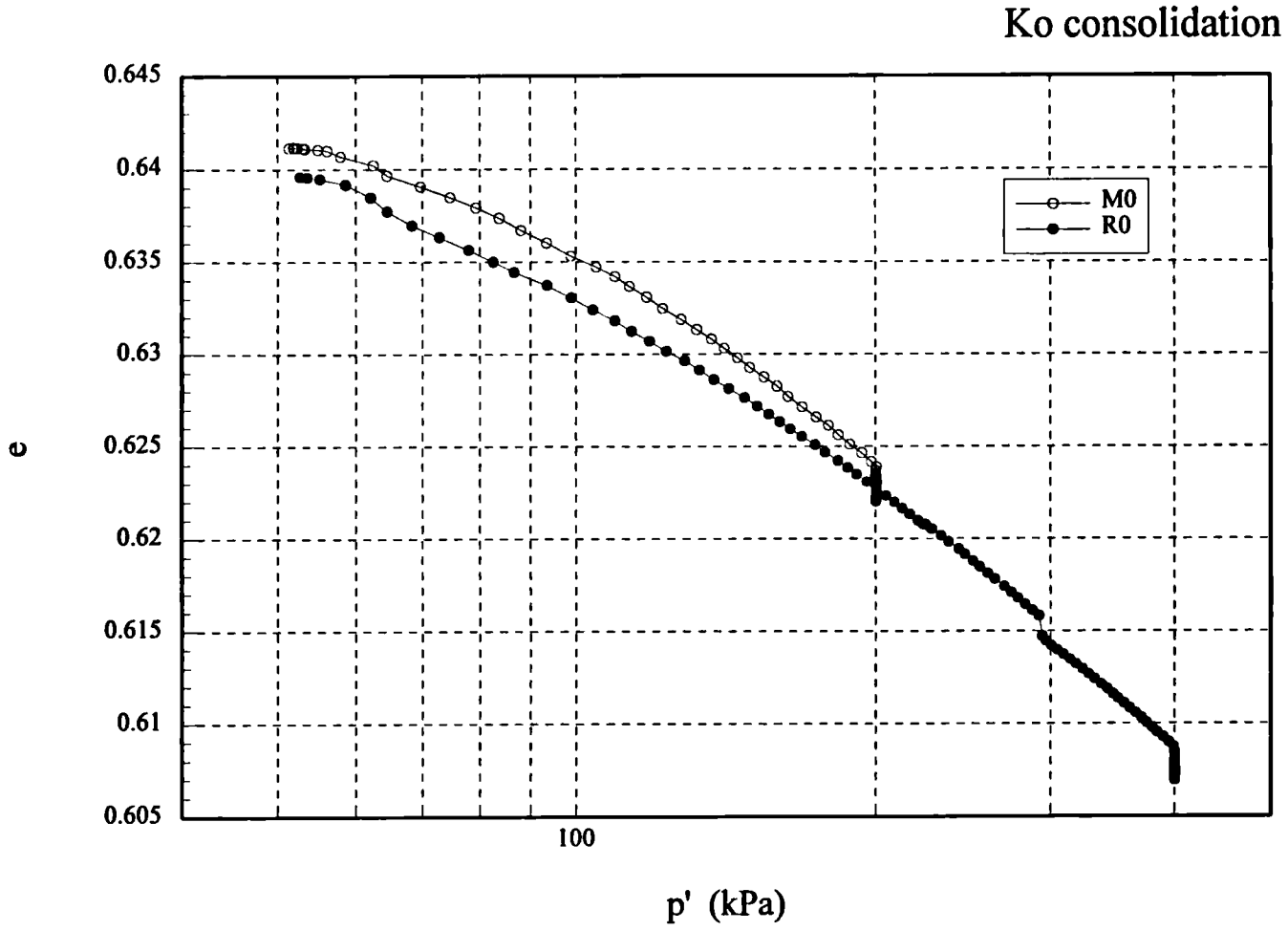


Fig.7.43 - Change of the initial void ratio during Ko consolidation of samples M0 and R0

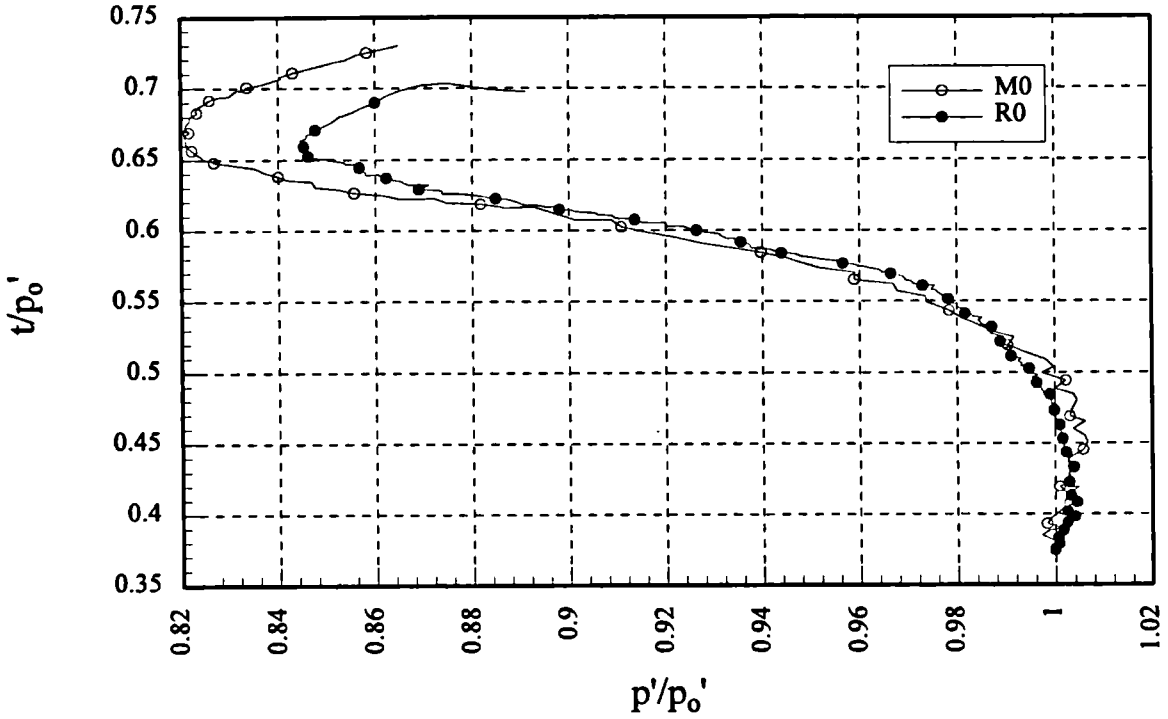


Fig.7.44 - Normalized effective stress paths for tests M0 and R0

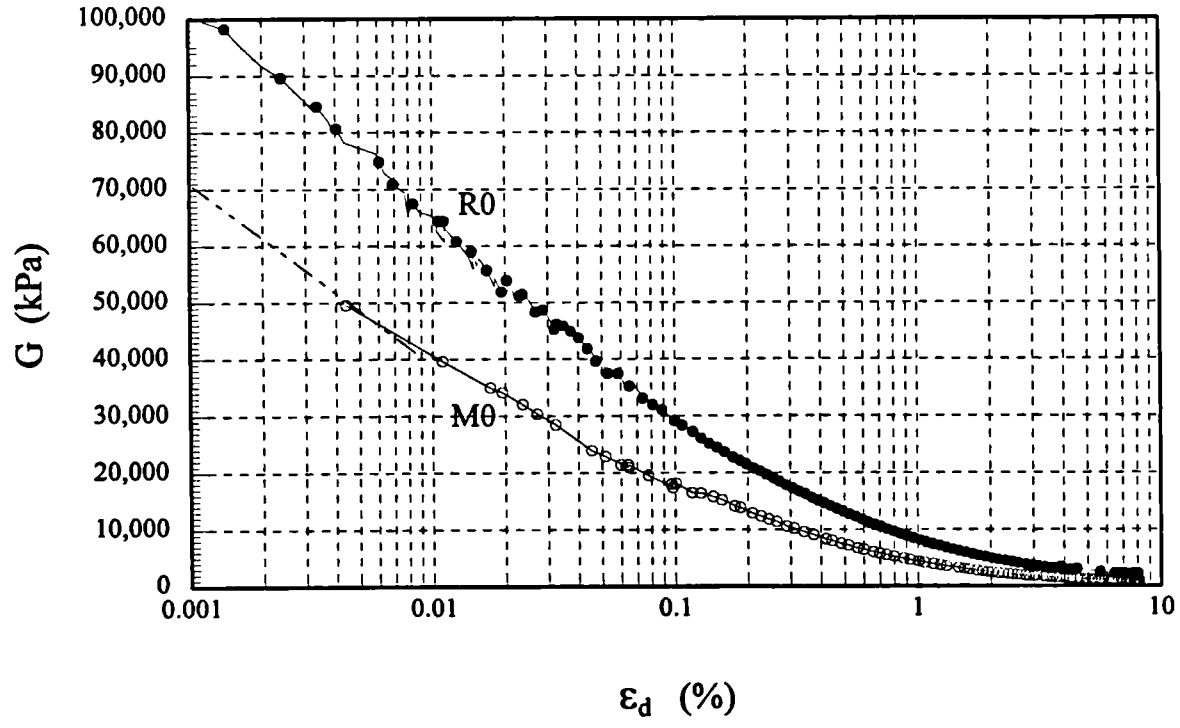


Fig.7.45 - Octahedral shear stiffness for tests R0 (p_o'=400 kPa) and M0 (p_o'=200 kPa)

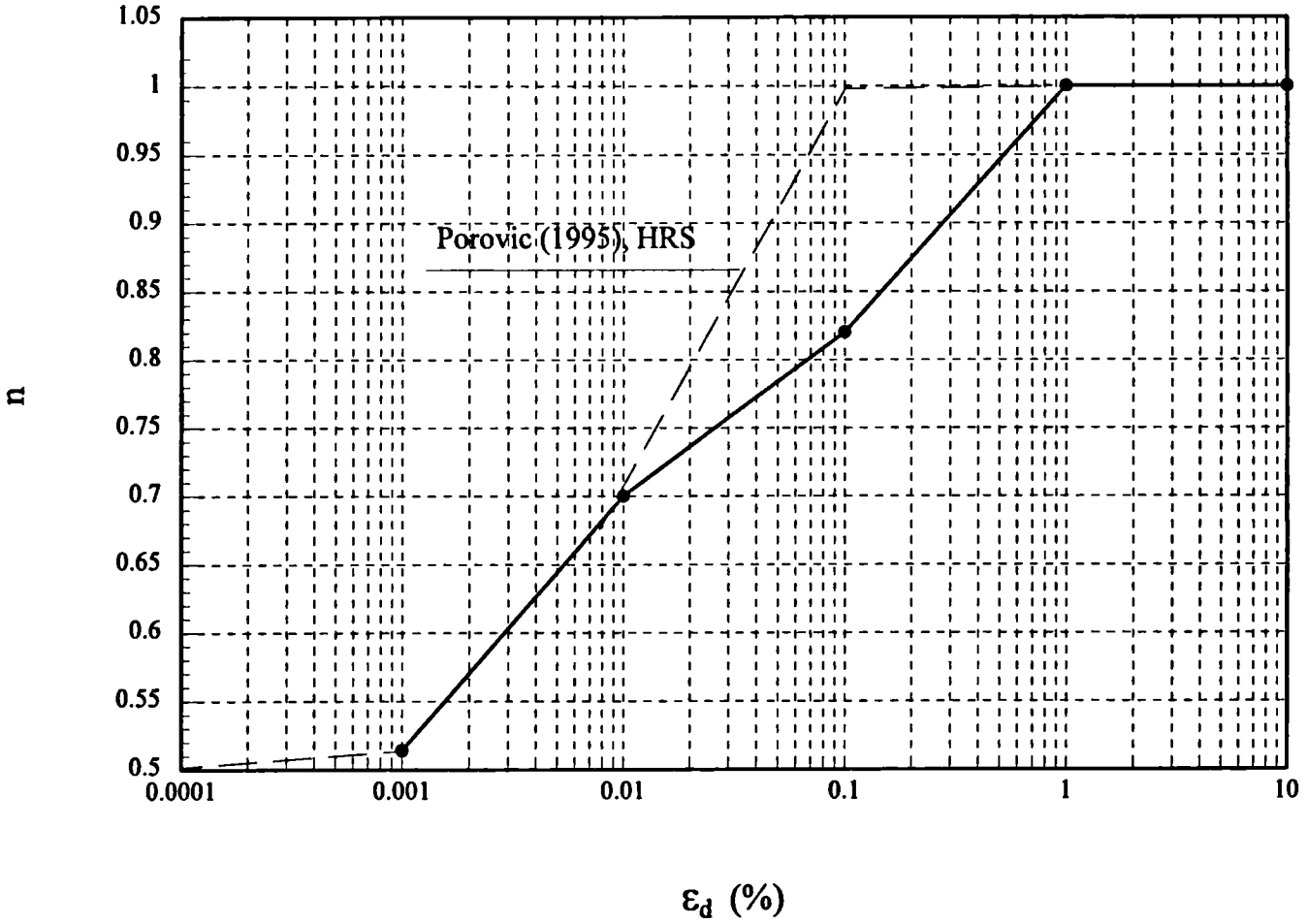


Fig.7.46 - Dependence of 'n' on the strain level

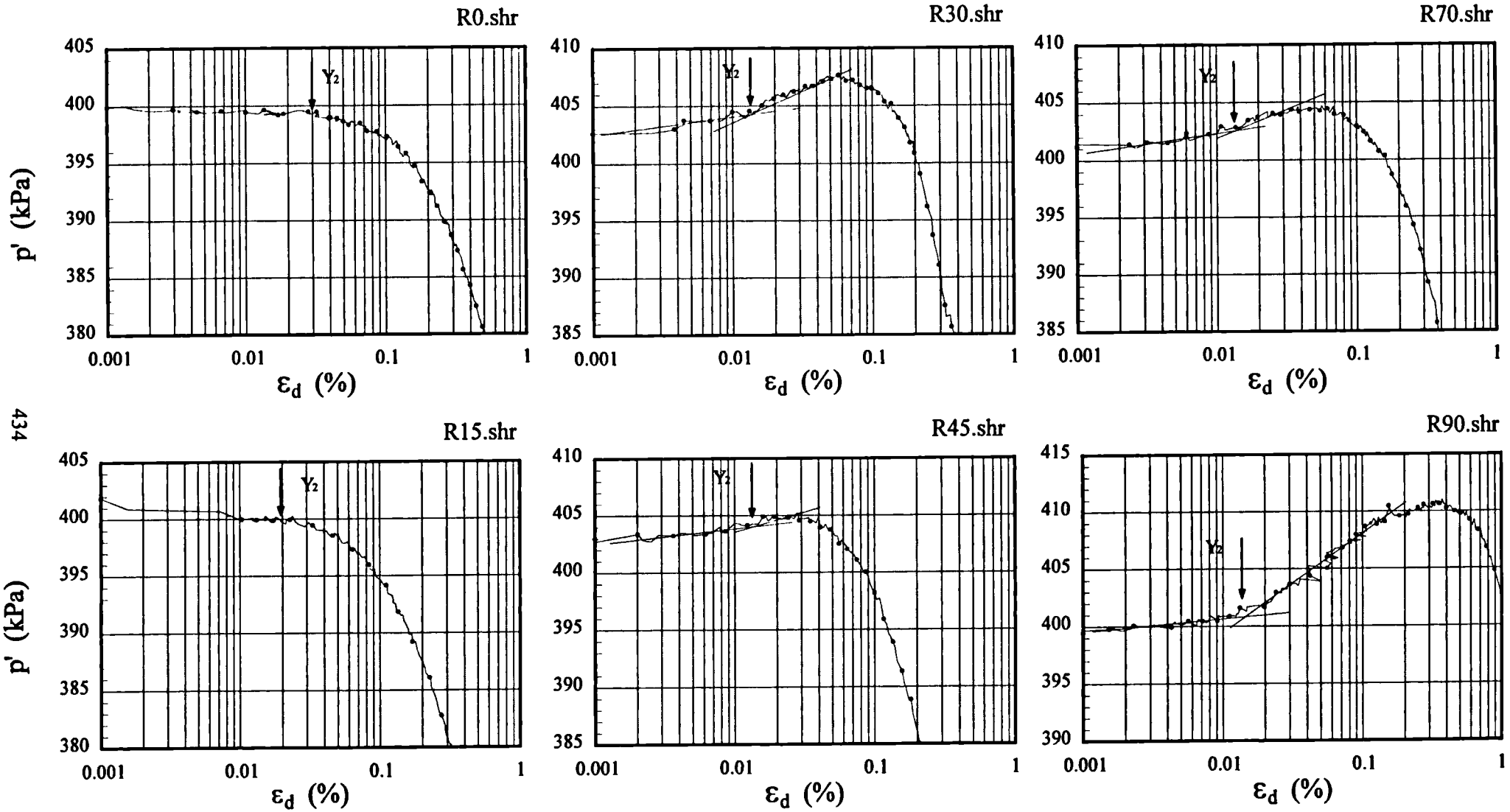


Fig.7.47 - Y2 yield of undrained shearing stress paths of R-Series tests

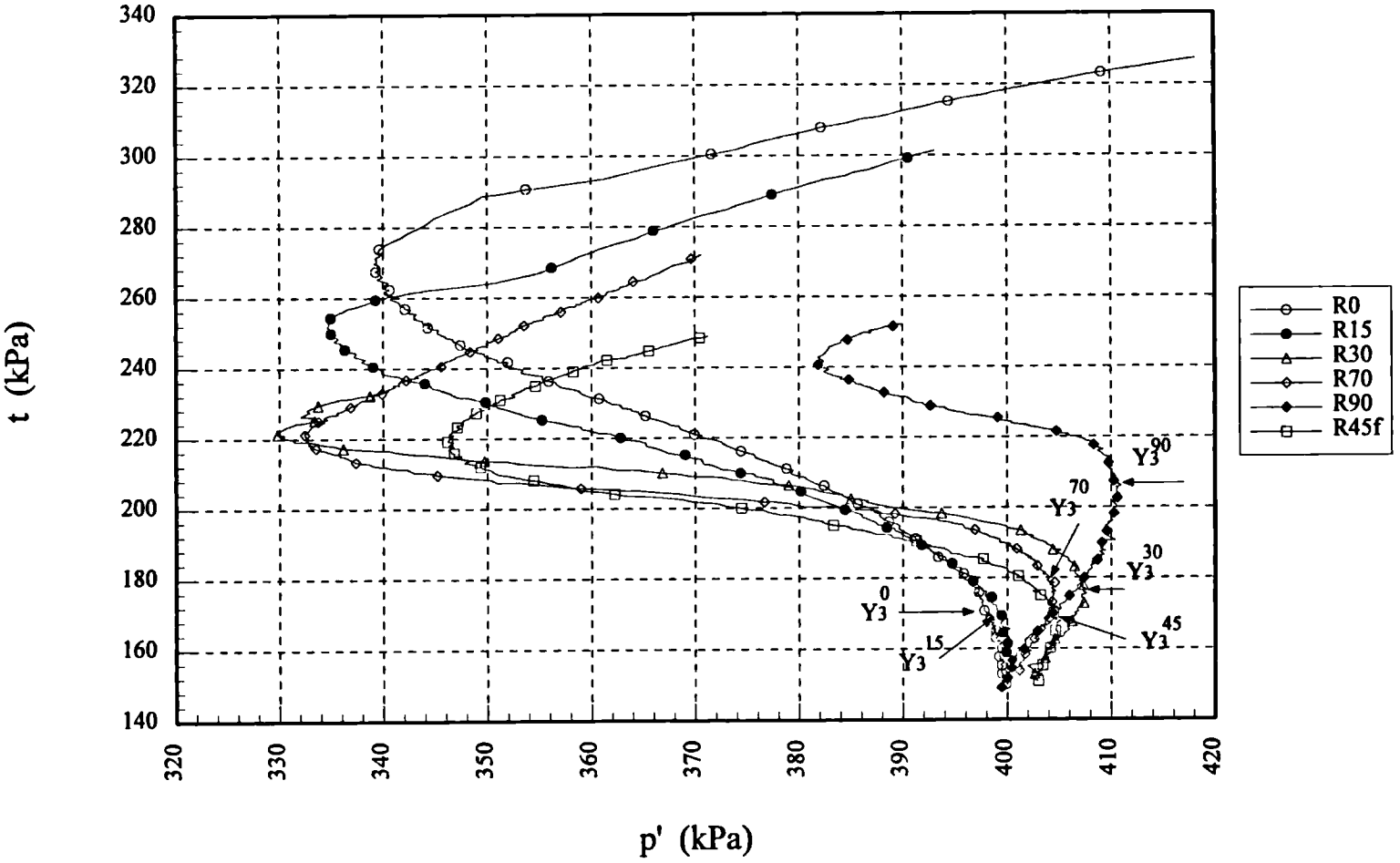


Fig.7.48 - Y_3 yield points of the shearing stage, R-Series tests

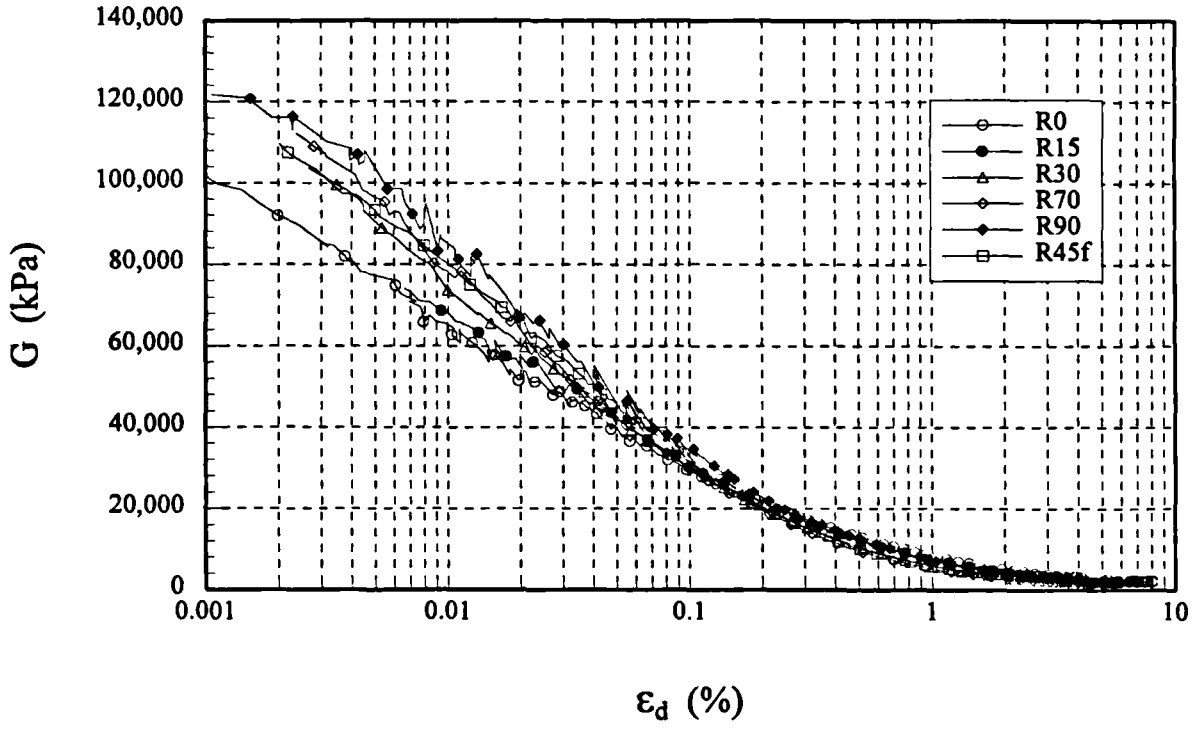


Fig.7.49a - Octahedral shear stiffness for all R-Series tests

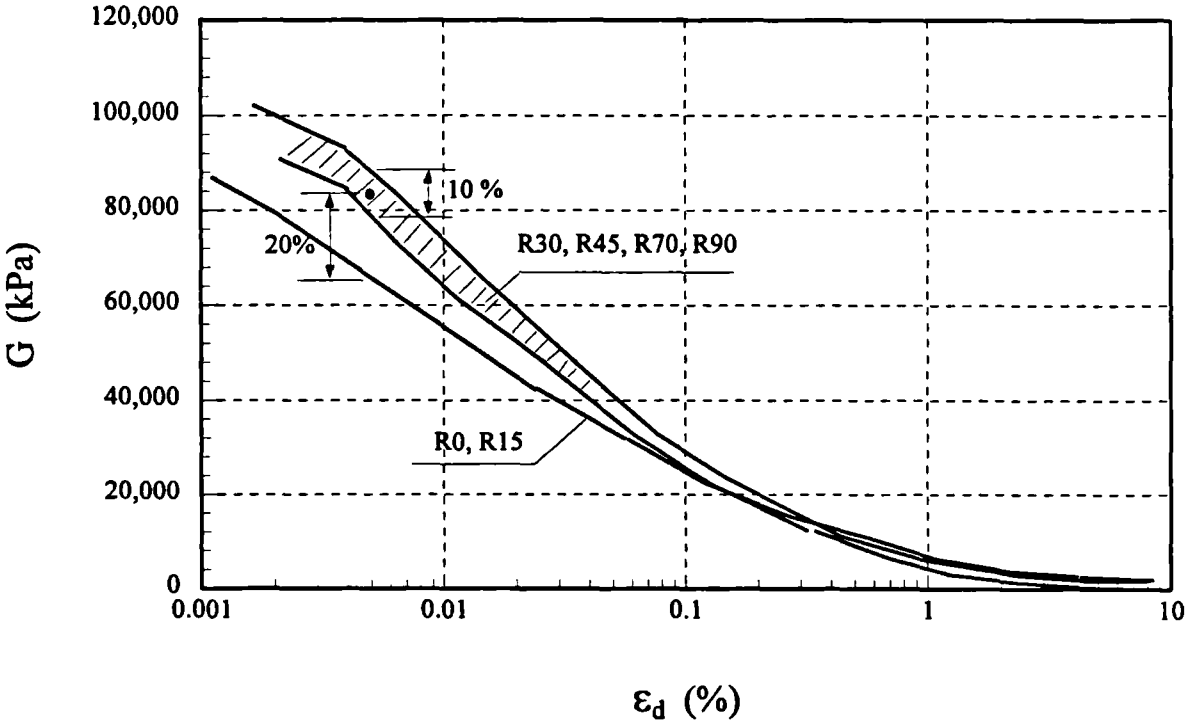


Fig.7.49b - Envelope of stiffnesses for R-Series tests

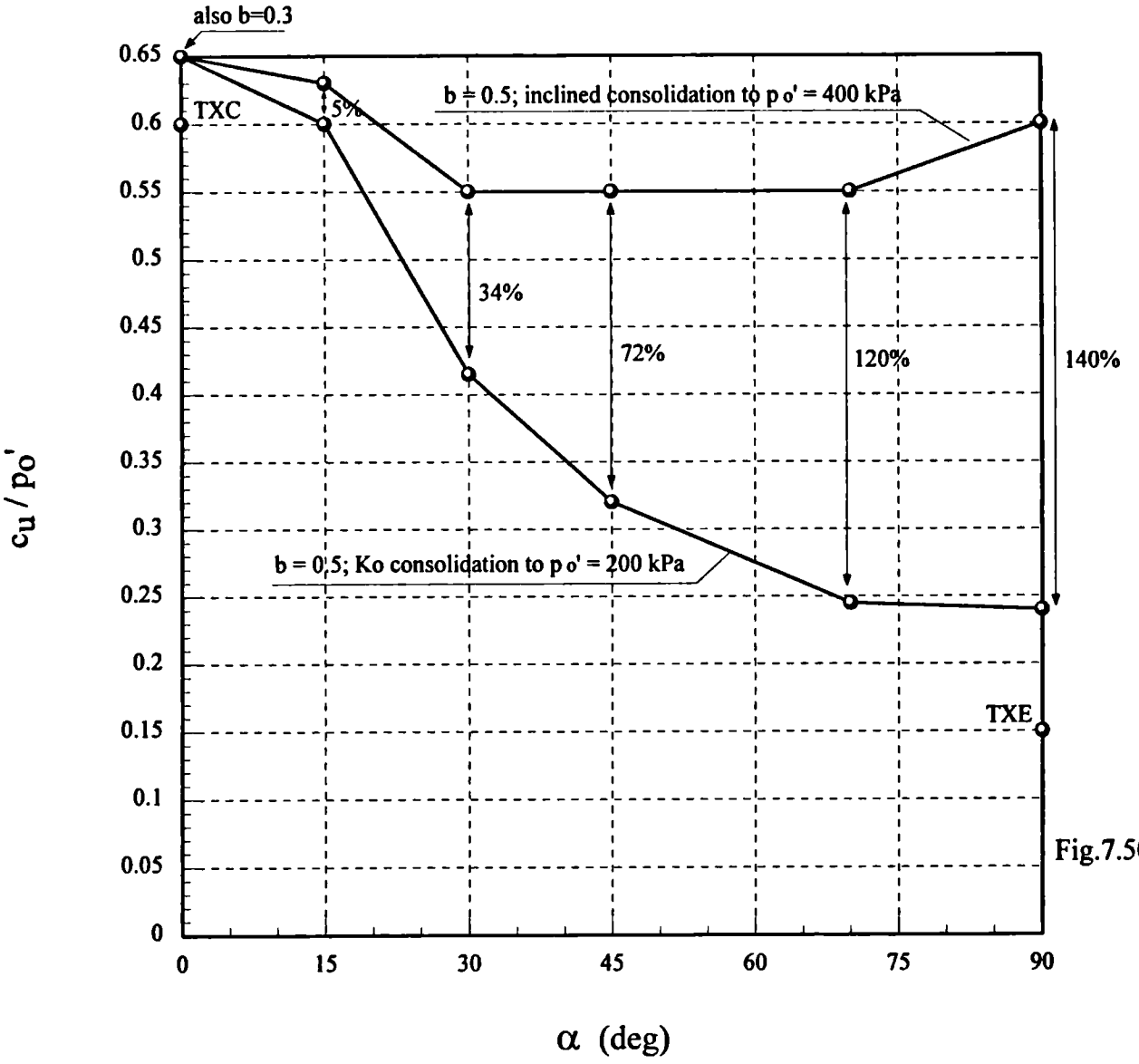


Fig.7.50 - Gain in undrained strength because of inclined consolidation

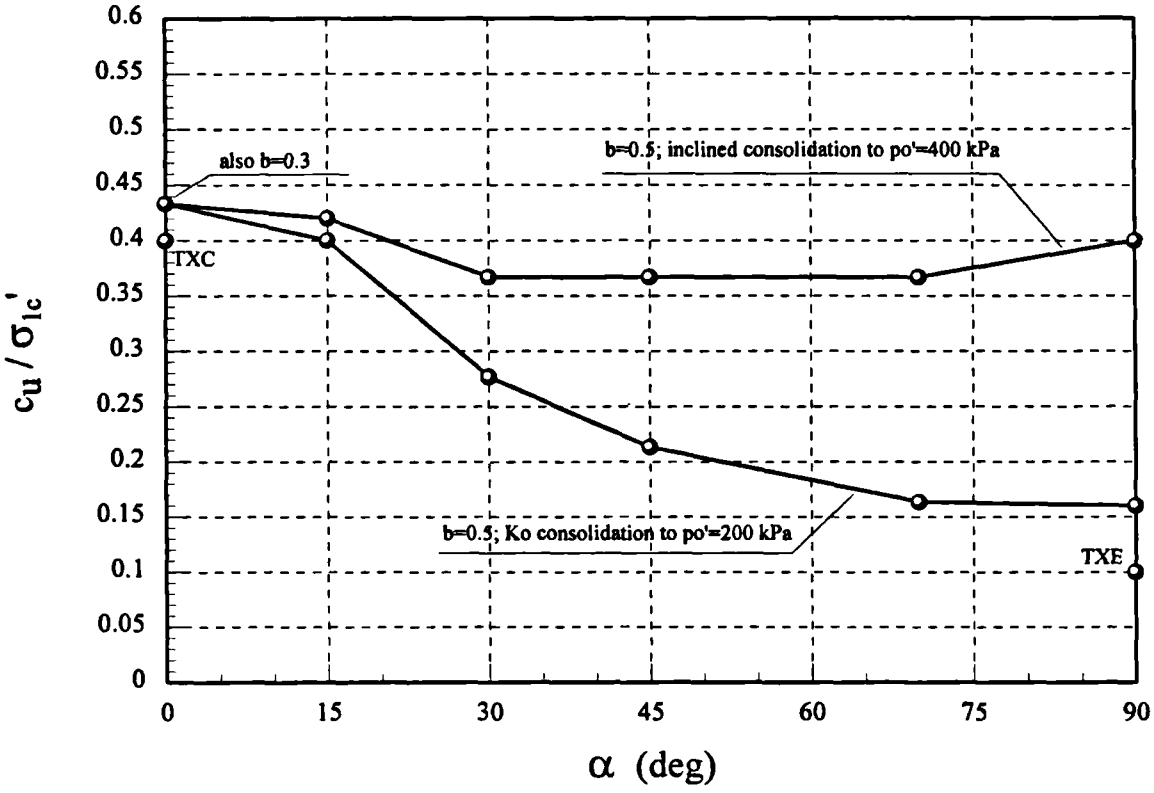


Fig.7.51 - Gain in strength because of inclined consolidation
(normalized by the major principal stress at the end of consolidation)

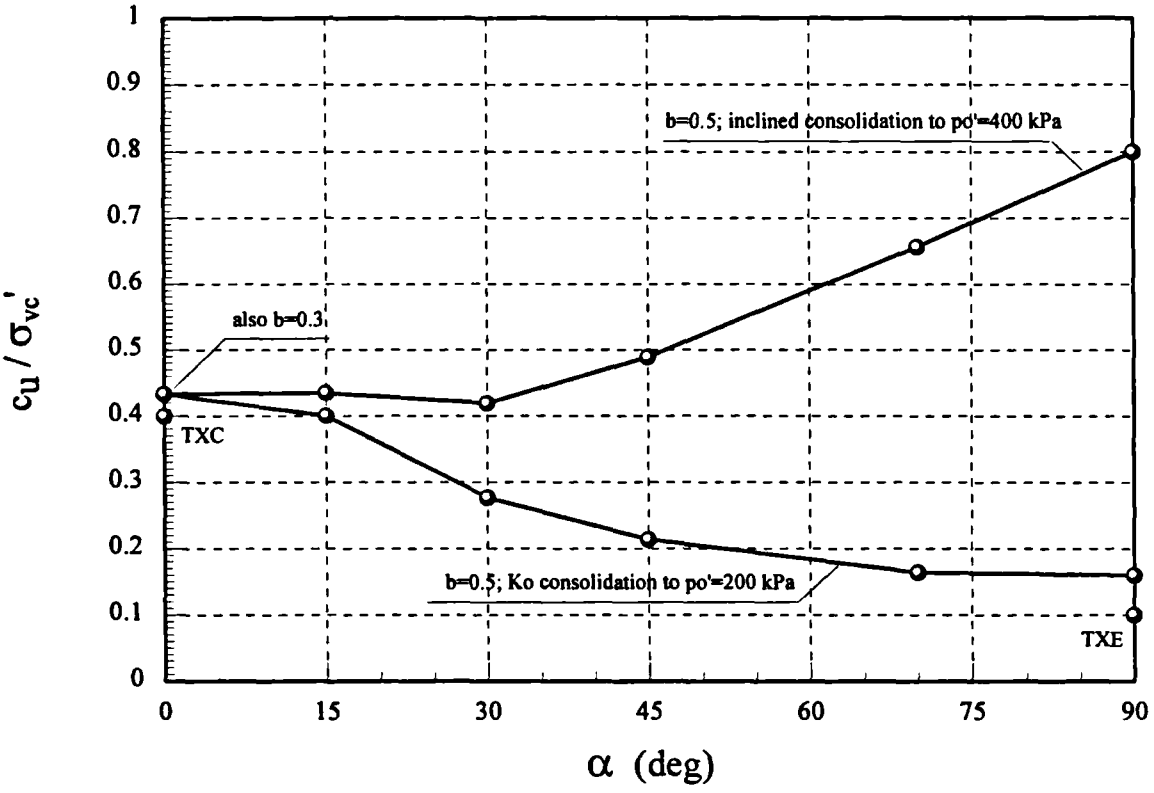


Fig.7.52 - Gain in strength because of inclined consolidation
(normalized by the vertical effective stress at the end of consolidation)

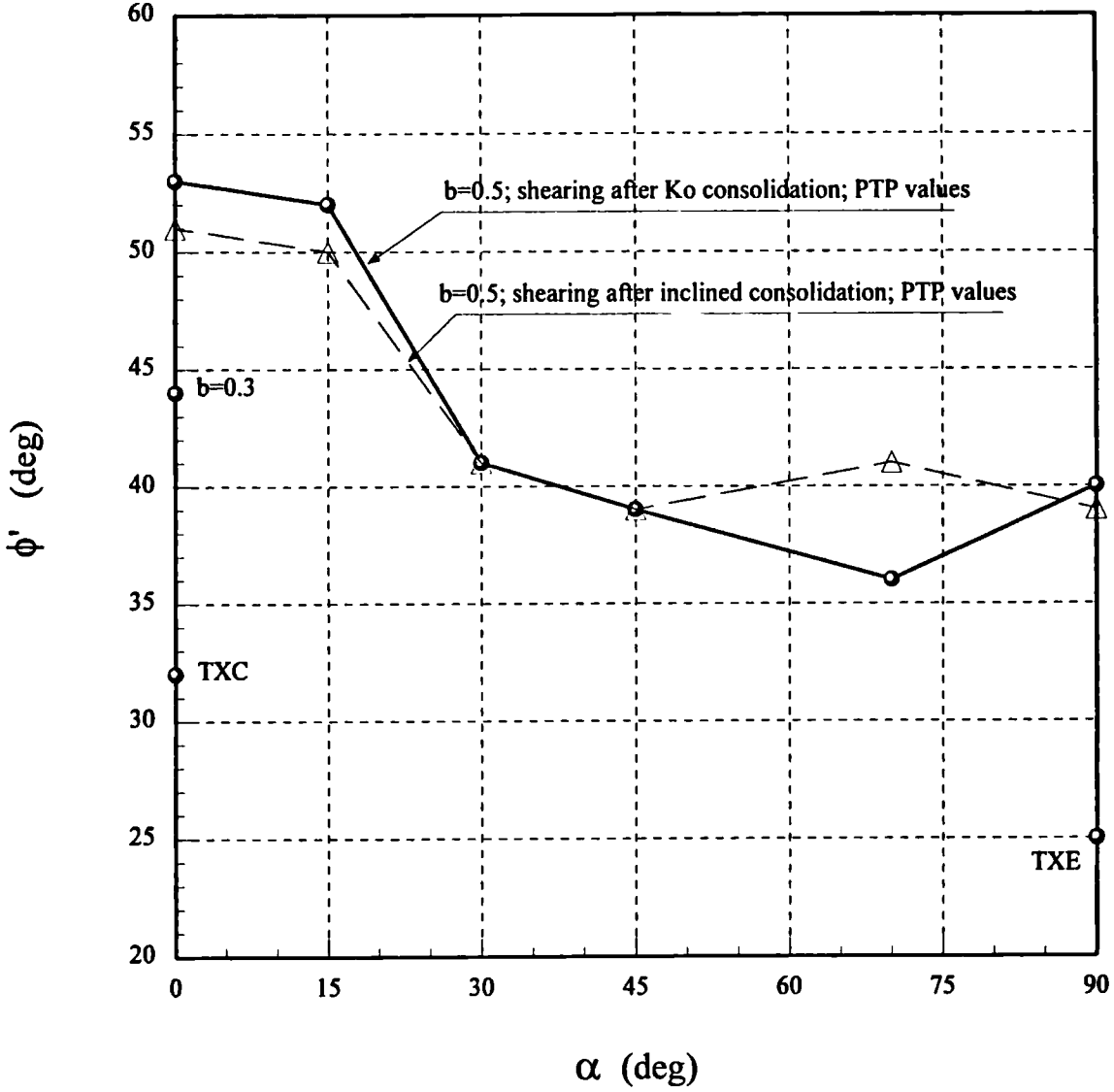


Fig.7.53 - Mobilized ϕ' after inclined consolidation

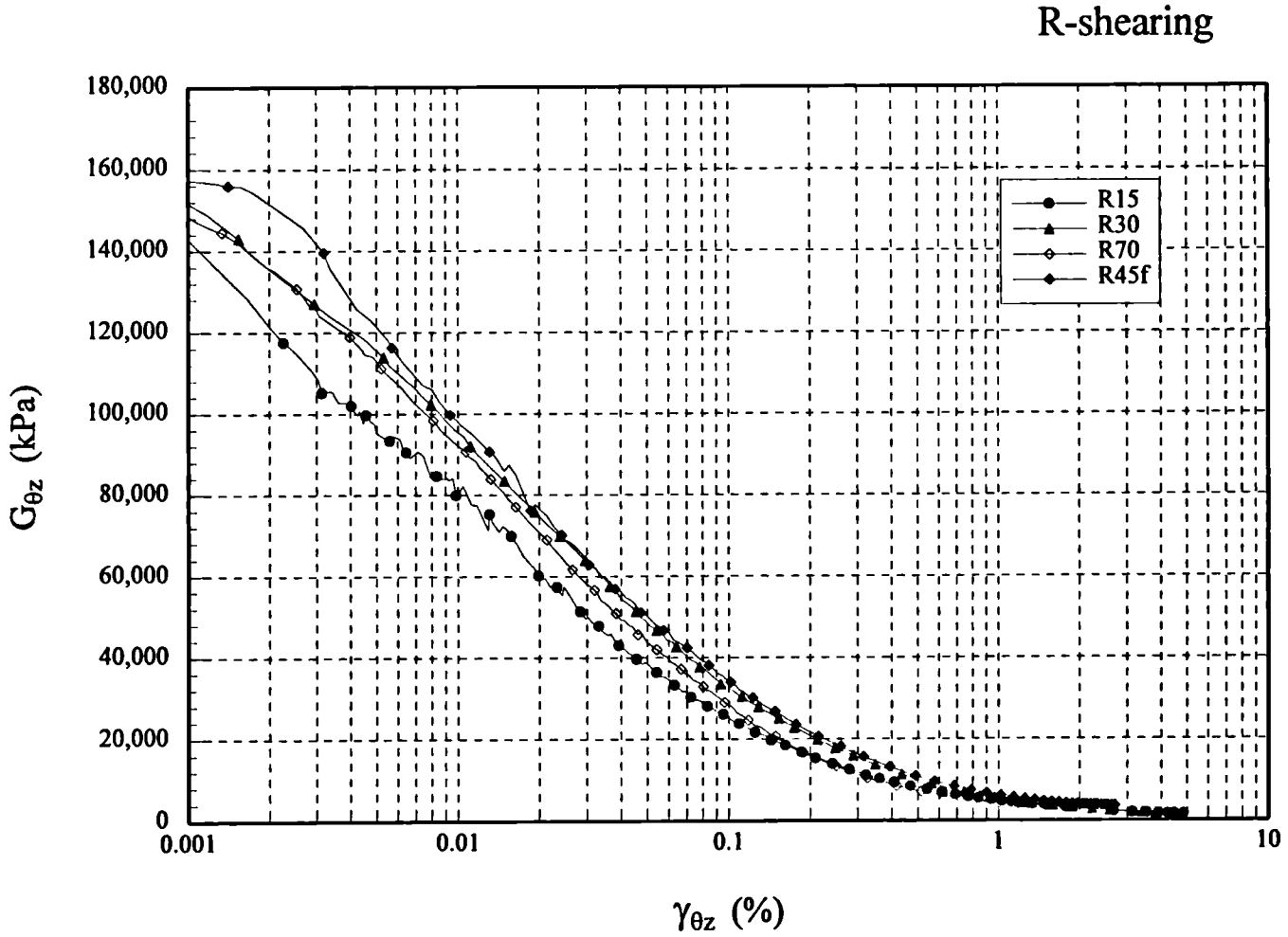


Fig.7.54 - Variation of torsional shear stiffness during shearing stage of R-Series tests

Fig.7.55 - Distribution of $G_{\theta z}$ with α, at different strain levels

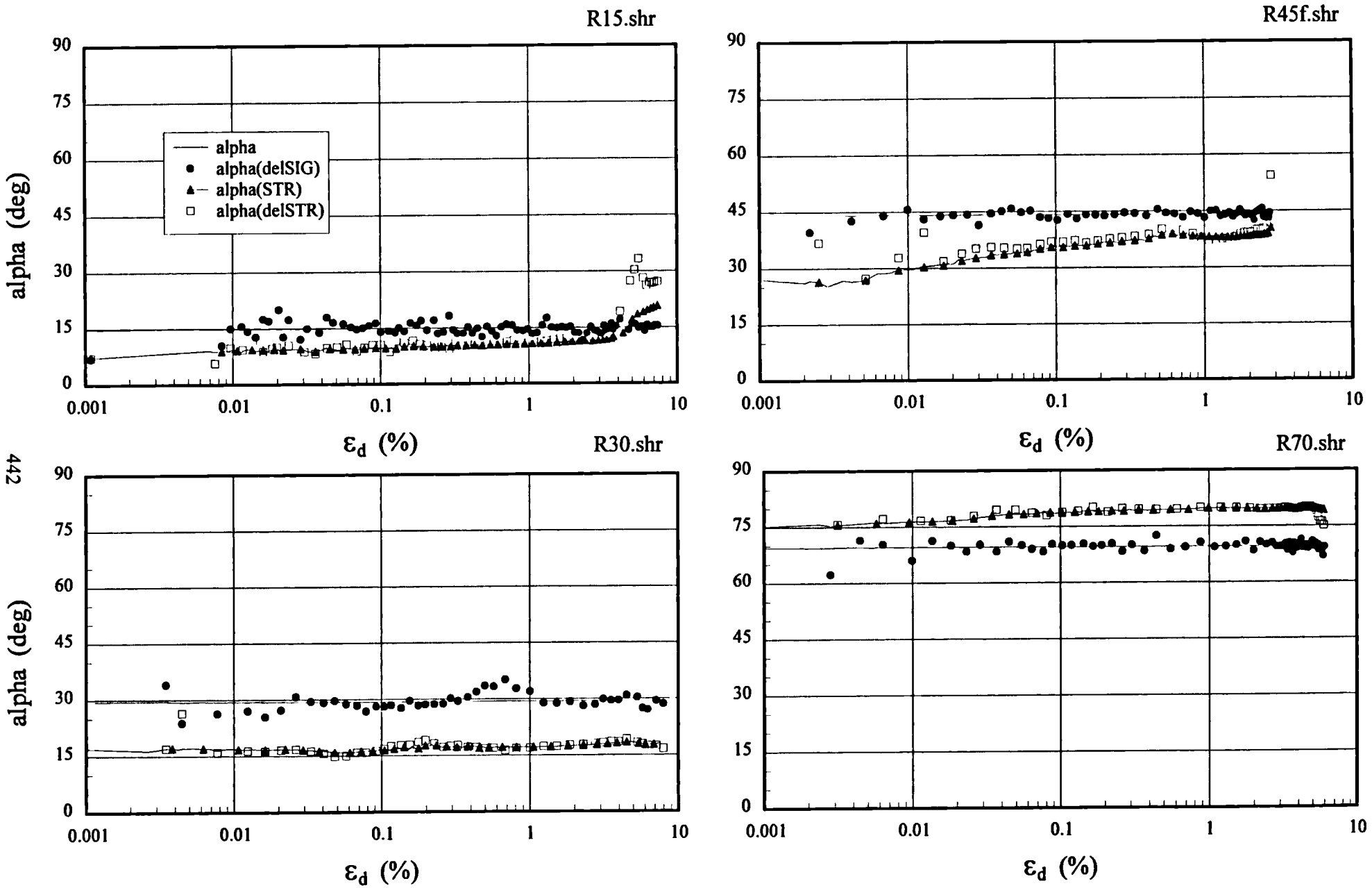


Fig.7.56 - Directions of stresses and strains and their increments during undrained shearing

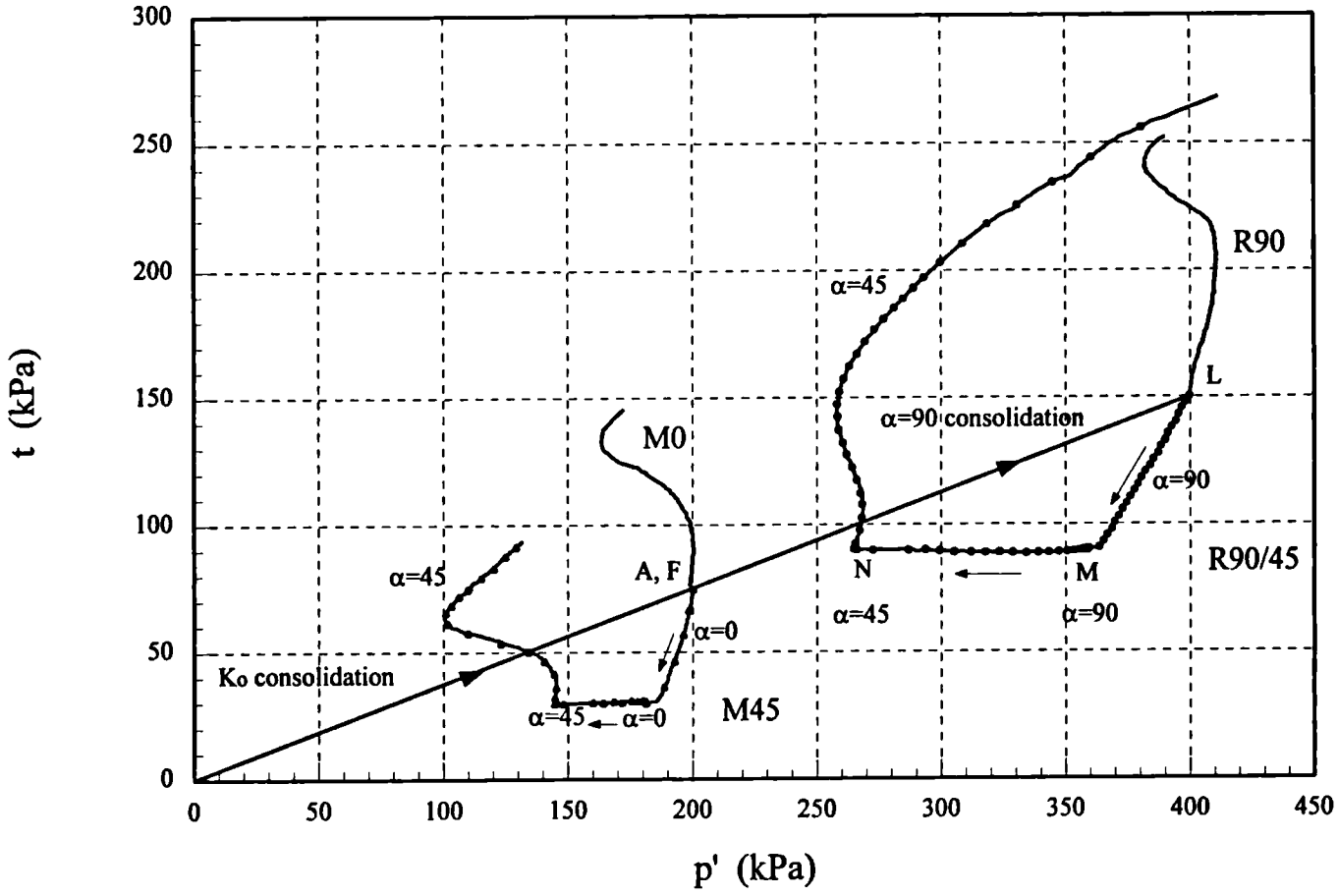


Fig.7.57 - Comparison of effective stress paths for Ko consolidated and inclined consolidated samples

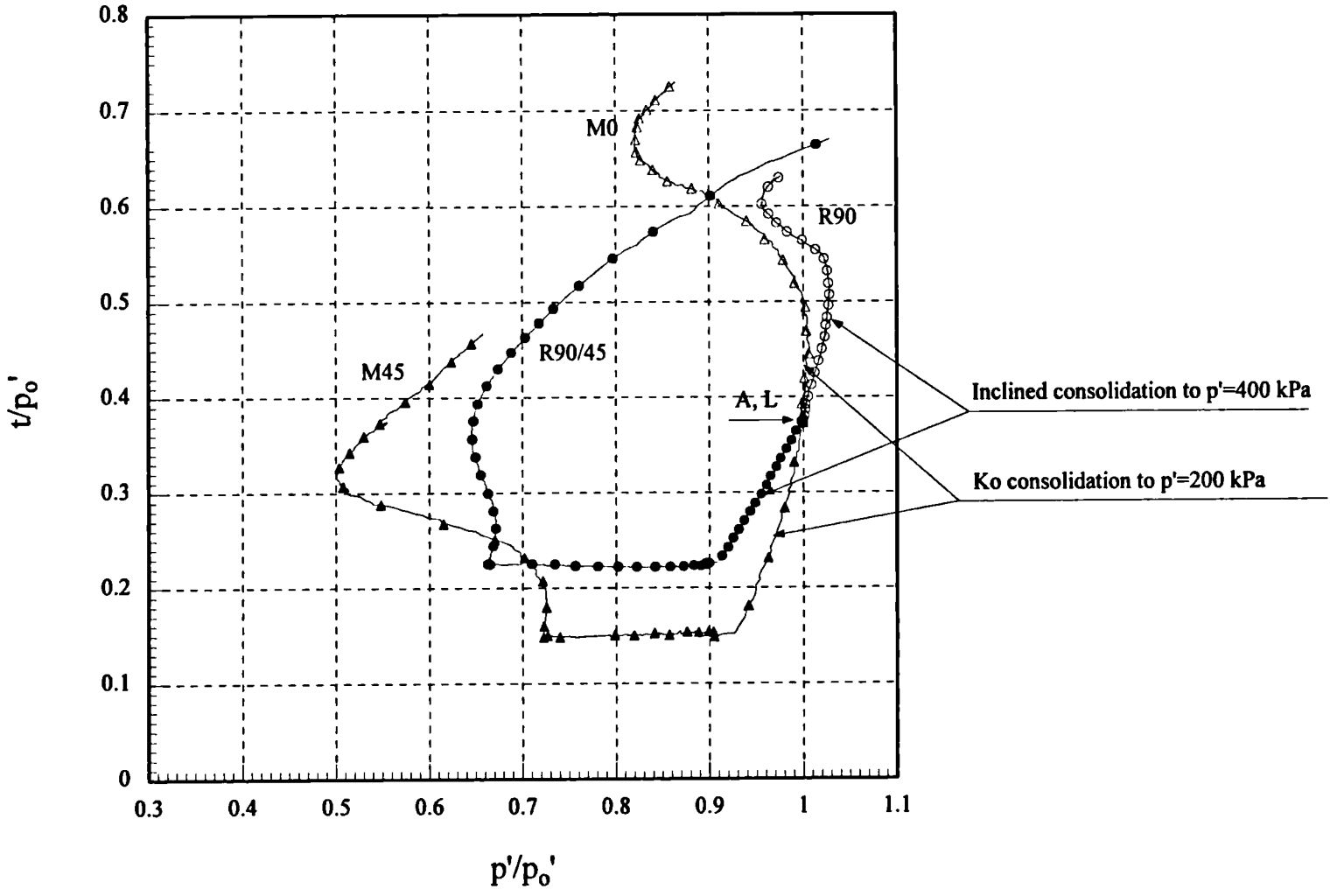


Fig.7.58 - Normalized effective stress paths for tests M45 and R90/45

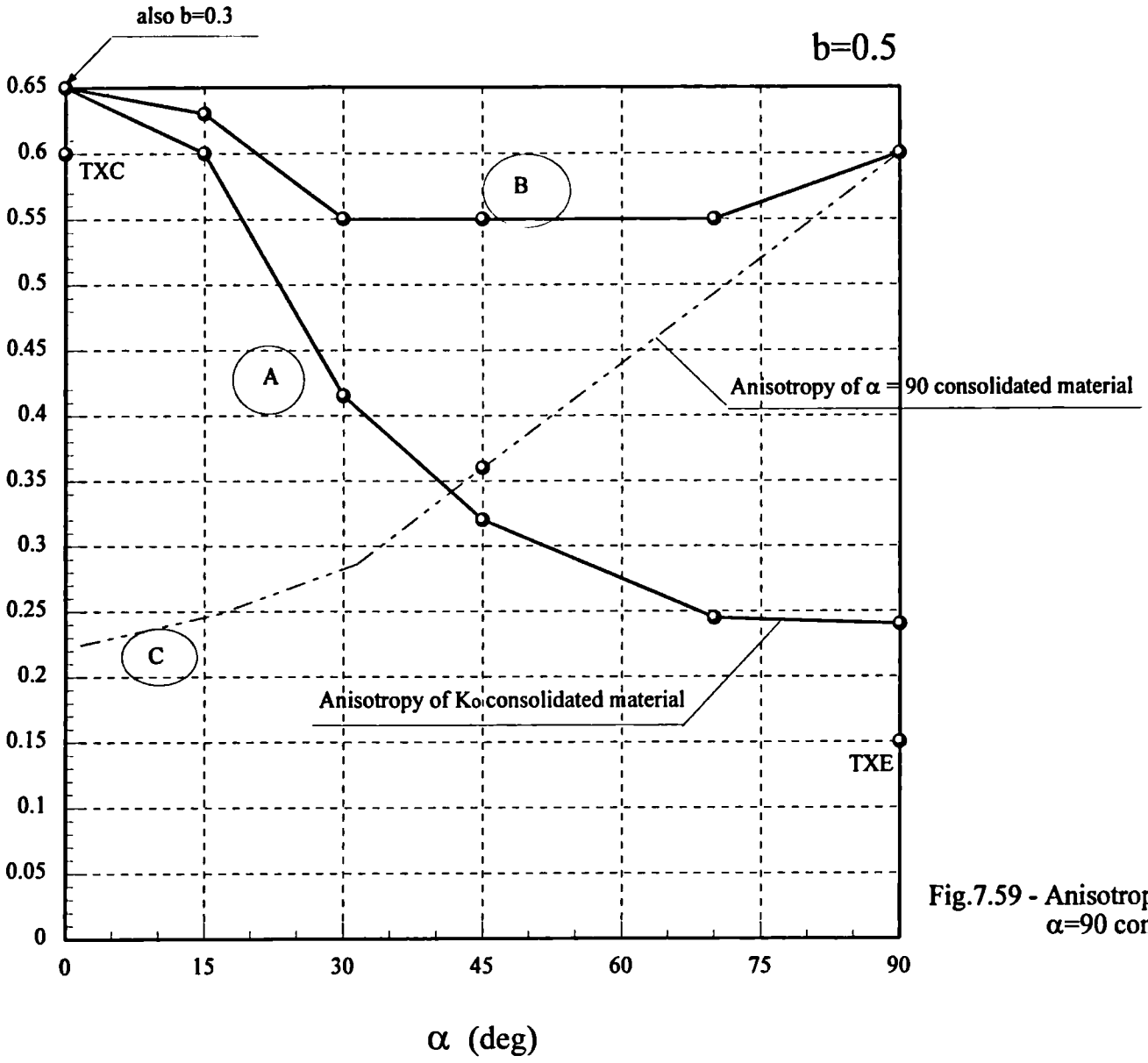


Fig.7.59 - Anisotropy of Ko consolidated and α=90 consolidated samples, b=0.5

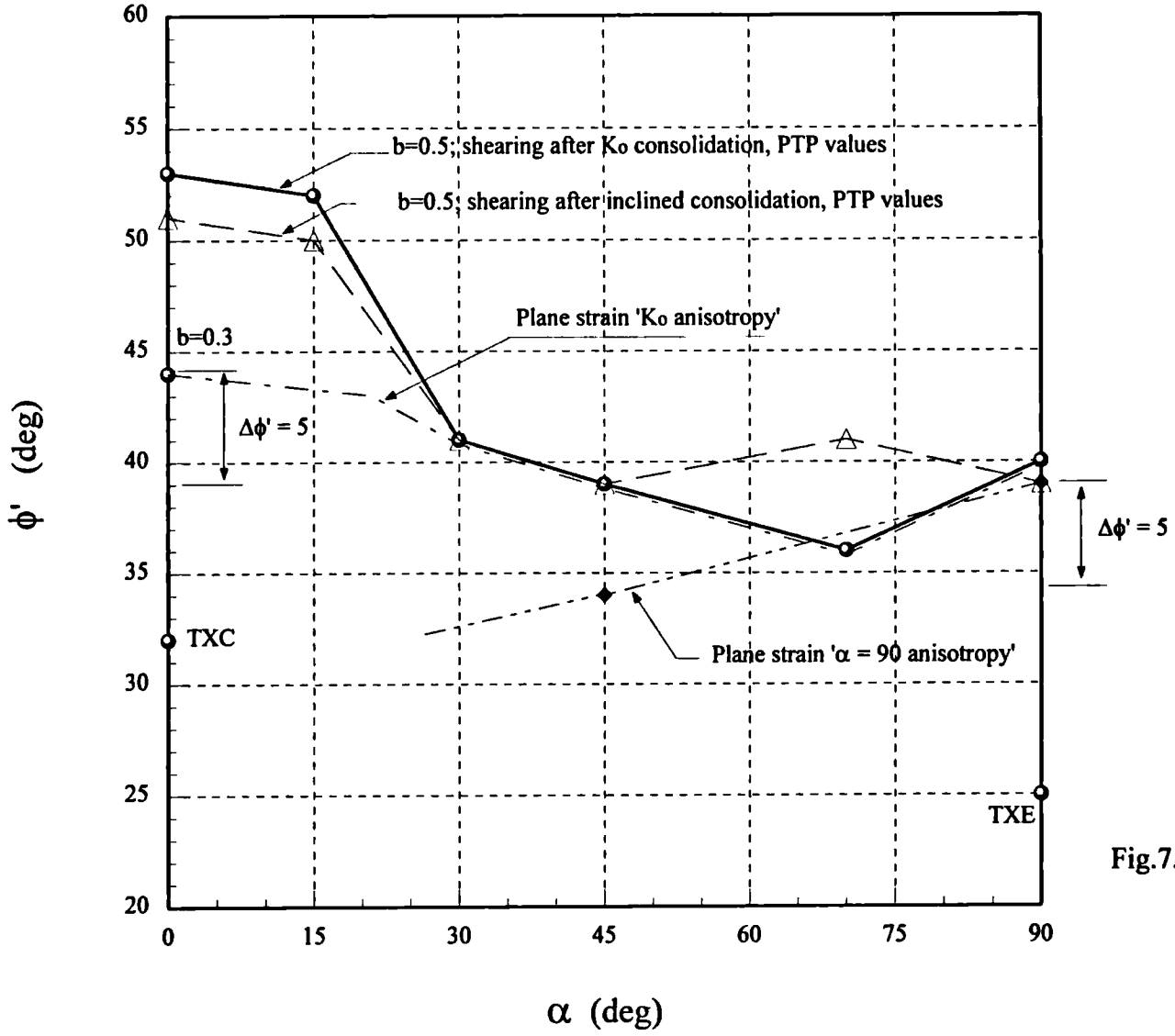


Fig.7.60 -Anisotropy in mobilized frictional resistance

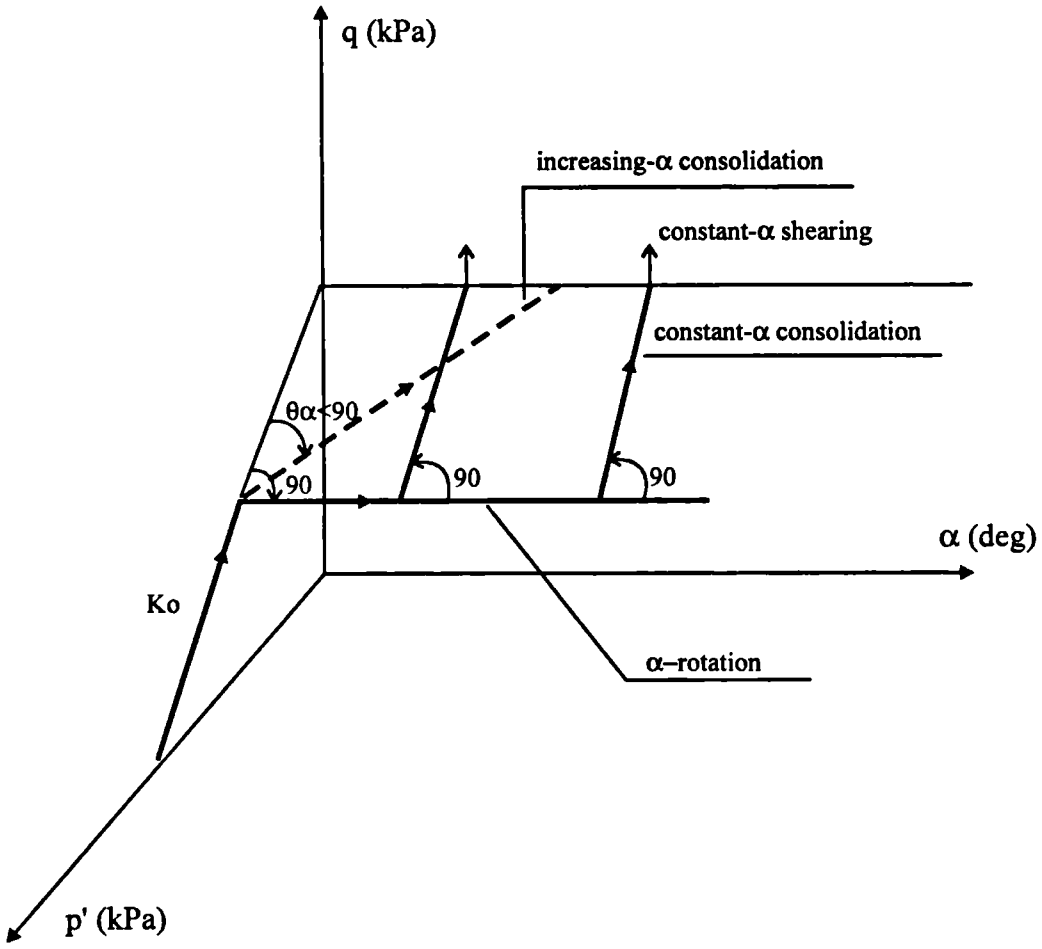


Fig.7.61 - Orientation of stress paths in α direction

Chapter 8

SUMMARY, PRACTICAL IMPLICATIONS AND RECOMMENDATIONS FOR FURTHER RESEARCH

8.1. Summary and conclusions

8.1.1. Review of previous work

A review of the literature published on the topic of soil anisotropy was presented in Chapter 2. The stress-strain-strength anisotropy was addressed as a characteristic of soil behaviour encountered in many geotechnical engineering problems, but, unfortunately, not fully understood. Laboratory experiments have been used to investigate the effects of anisotropy. These studies have involved testing mainly reconstituted soils in hollow cylinder devices, directional shear cells and other cubical testing devices with flexible boundaries.

General anisotropy has been sub-divided into two component parts, inherent and induced anisotropy: the inherent component is due to the sedimentation process, previous stress history and soil composition; induced anisotropy is associated with the strains generated from any applied loading. The interaction of inherent and induced anisotropy is relevant to many engineering problems, but is still poorly understood.

The main aims of this thesis have been:

- To broaden the data-base on soil anisotropy by testing silt, a material that has not been tested intensively in the past.

- To describe the observed anisotropic behaviour in terms of: a) small strain Kinematic Sub Yield surfaces; b) a conceptual large strain Bounding Surface; c) the particulate nature of granular materials, i.e. soil fabric and particle shape.

- To relate the experimental observations to some practical geotechnical problems.

8.1.2. Testing equipment and material

Two types of test equipment have been used in this research: a) the standard triaxial stress path cell and b) the Imperial College large hollow cylinder apparatus.

The main testing material was an artificial quartz based silt called HPF4. This had an e_{min}=0.563 and e_{max}=1.332. All HPF4 samples were prepared from a slurry which was poured through water into moulds and then K_o consolidated to the desired stress level. This preparation method simulated natural sedimentation of particles and produced initially dense samples, with D_r=89% (e_o=0.65). Loose HPF4 silt, with e_o=0.95 obtained by moist tamping, was tested by Ovando-Shelley (1986), but this technique does not resemble the natural sedimentation of particles.

Also, reports on the static and dynamic behaviour of some natural sea-bed quartz based clean silts, such as Valdez silts in Alaska, showed that this soil exhibited gradual deformation to large strains without catastrophic loss of strength, which is a pattern seen in tests performed in this thesis. Loose pure quartz based silts may not be common in the field and the Author's sedimented dense samples may provide a reasonable model for some natural rock-flour sediments.

However, HPF4 is an artificial, man made material, obtained by crushing quartz stone and is, therefore, highly angular and elongated, with an average roundness of 0.11 and average sphericity of 0.625. These particle characteristics were demonstrated to have a significant influence on the overall behaviour of HPF4, particularly the mobilized angle of shearing resistance. The following observations were made:

- Highly angular particles have very strong interlocking potential when consolidated by straining in one direction. This results in a very strong K_o consolidated structure in the vertical direction, which is comparatively weak in the radial direction.

- When such a K_o structure is sheared under conditions that offer more restraint in the radial then in the circumferential direction (with b>0), it can develop a remarkably high mobilized ϕ' value.

From this point of view, many natural silts, which have been deposited after some wind or water erosion and transportation process, have less angular particles and will not exhibit such

a dramatic variation of ϕ' with α and b. However, they may well possess similar degrees of undrained strength anisotropy. For example, sub-rounded Ham River Sand was shown to have similar anisotropy in c_u as HPF4.

8.1.3. Testing programme

Five Series of tests have been performed. The first Series involved tests performed in the stress path cell. Samples were K_o consolidated to overconsolidation ratios of 1.0, 1.3, 2.0 and 4.0. Conventional undrained compression and extension tests were then performed for each OCR, making a total of eight tests. The objective of this Series of tests was to quantify the basic soil properties and establish the behaviour of HPF4 in triaxial compression and extension.

The remaining four test Series were performed in the hollow cylinder apparatus. The objective of the second, M-Series was to investigate the general undrained strength and yielding anisotropy of K_o normally consolidated HPF4. Samples were initially K_o consolidated to a mean effective stress of 200 kPa. Keeping p, t and α fixed, b was then changed to 0.5. The samples were then unloaded undrained, before α was changed keeping p, t and b constant. Undrained shearing at the end was performed maintaining constant p, b and α. Tests were performed with α equal to 0°, 15°, 30°, 45°, 70° and 90°. An additional test with b=0.3 and α=0° was also performed.

The Q-A Series of tests was aimed at investigating the directionally dependent undrained shear stiffness characteristics of low OCR HPF4. Tests were performed on identical samples, starting from K_o stresses, with an overconsolidation ratio of 1.3 and b=0.0. The tests differed in that each was sheared undrained with a different $\Delta t/\Delta\alpha$ ratio, but in all tests the incremental b-value, Δb, was kept equal to 0.5. Drained probing tests were also performed in the D-Series, in order to investigate the material response, at small strains, to uni-directional effective stress changes applied on different orthogonal axes. For a cross-anisotropic material such tests would be sufficient to define the five classical anisotropic elastic parameters.

The R-Series tests were performed to investigate how different anisotropies could be induced in HPF4. These tests were motivated by the problems arising in the design and construction of multi-stage embankments. In these tests the samples were K_o normally consolidated to p'=200 kPa, at which point α was changed keeping p and t constant and b=0. The samples were then consolidated further to p'=400 kPa, with the same stress ratio as that

used for K_o consolidation, and keeping α constant. This second stage of consolidation is referred to as constant α consolidation or inclined consolidation. Parameter b was then changed to 0.5 before the samples were sheared undrained to failure.

8.1.4. Consolidation characteristics of HPF4

The following observations concerning the consolidation characteristics of HPF4 were made from the test results:

- HPF4 is relatively free draining, with an estimated coefficient of permeability of 2.5×10^{-7} m/s.

- HPF4 has a multitude of normal consolidation lines, each depending on the initial void ratio of the soil.

- For the engineering range of stresses (up to 1.0 MPa), the relative position of HPF4 is on the "dry" side of the critical state line. This is evident from the consolidation curves shown in Fig.8.1, which shows the estimated position of the possible critical state line and the back-projection of the K_o virgin consolidation line observed at high values of p'.

In this respect the HPF4 samples showed behaviour similar to that of dense granular materials. However, the compressibility of HPF4 was approximately 50% greater than that of Ham River Sand (HRS) and HK (Ham River Sand with 10% Kaolin), at the same stress level. But it was much less compressible than clayey soils like KSS (a mixture of 50% Kaolin, 25% silt and 25% sand), natural Pentre clay silt, or natural Bothkennar clay.

An interesting result form the R-Series tests, which involved inclined consolidation with constant values of t/p' and $\alpha=\alpha_c$, after initial K_o consolidation, was that after principal stress axis rotation the consolidation characteristics were not influenced by α_c, i.e. all paths generated approximately the same volume change (~1.0%) and Δe (~0.1), when the values of p' were increased by 100% (Fig.8.2).

8.1.5. Observed undrained strength anisotropy of HPF4

a) Initial anisotropy of K_o consolidated HPF4

A common feature of both the triaxial and hollow cylinder undrained shearing stress paths was that neither showed a distinct peak in the deviator stress. The stress strain curves indicated a monotonic increase in deviator stress with increase in strain. After reaching Phase Transformation, the samples continued to dilate, generating negative pore water pressures, but never reached a stable state (i.e. critical state) for the range of stresses considered (up to 1.0 MPa). This is, again, a characteristic of granular materials. To evaluate the influence of principal stress rotation, the values of c_u and ϕ' mobilised at the Phase Transformation points have been used to compare different tests.

The results from the M-Series tests in which samples were K_o consolidated to p'=200 kPa and then sheared with α=0° to 90°, at b=0.5, exhibited the following strength anisotropy:

- A 65% decrease in the PTP value of c_u when α changes from 0° to 90° (Fig.8.3).

- A 17° decrease in the PTP value of ϕ', from a maximum of 53° at α=0° to a minimum of 36° at α=70° (Fig.8.4).

- A major drop of 12° in the PTP value of ϕ' between α=0° to 15° (ϕ'=53°) and α=30° (ϕ'=41°), Fig.8.4.

The strain components observed in these tests showed that shearing with α=30° to 90°, at b=0.5, practically satisfied the plane strain condition, i.e. ε_r=0. However, this was not the case for shearing with α=0° and 15°. For these two values of α, shearing at b=0.3 modelled plane strain conditions more accurately. It may therefore be concluded that:

- The plane strain anisotropy of the mobilized ϕ' at the PTP was only 8° (from ϕ'=44° at α=0°, to ϕ'=36° at α=70°), Fig.8.4.

Comparing α=0° compression stress paths at b=0.0, 0.3 and 0.5 showed that:

- The b value does not significantly influence the PTP values of c_u, but has a large influence on the PTP value of ϕ'.

These two conclusions are also confirmed for other values of b and α by the results of the Q-A test Series.

- Generally, the ϕ' value mobilised at the PTP decreases with a decrease of b.

b) Induced anisotropy

The induced undrained strength anisotropy of HPF4 was examined in test Series R where samples were subjected to a second consolidation stage (after initial K_o consolidation to p_o'=200 kPa), with a constant value of $\alpha=\alpha_c$, to p'=400 kPa. The samples were then sheared undrained with the same value of α_c, at b=0.5. The strength characteristics of these samples were as follows:

- The samples sheared with $\alpha=\alpha_c$ gave similar PTP values of c_u: the difference between c_u values at $\alpha=0°$ to 15° and $\alpha=30°$ to 70° was reduced to only 15% (Fig.8.5a).

- This was not the case for the ϕ' values at the PTP. A significant difference (i.e. $\Delta\phi$'~10°) remained between the tests with $\alpha=0°$ and $\alpha=30°$ (Fig.8.5b). However, for $\alpha>30°$ the mobilized ϕ' values were more uniform (~40° on average). Again it was inferred that the tests with $\alpha<30°$ might not be reproducing plane strain conditions. If tests with a different b value had been performed which approximated more closely to plane strain conditions, then it is likely that the difference in ϕ' would be smaller (as in the M-Series).

It was clear that inclined consolidation changed the undrained strength anisotropy of HPF4. This was further investigated by testing a sample consolidated with $\alpha_c>0°$ and sheared under conditions where $\alpha\neq\alpha_c$. A sample consolidated to p'=400 kPa with $\alpha_c=90°$, was subsequently sheared undrained with $\alpha=45°$ and its behaviour compared with one tested with $\alpha=45°$, $\alpha_c=0°$. It was found that:

- The relationship between the PTP value of c_u was that $c_u(\alpha=\alpha_c=90°)$ exceeded that for $c_u(\alpha=45°, \alpha_c=90°)$ by ~40%, mirroring the trend seen with K_o consolidated samples where $c_u(\alpha=\alpha_c=0°)>c_u(\alpha=45°, \alpha_c=0°)$ by a similar amount. The inclined consolidation shifted the material's axis of c_u anisotropy from an inclination 0° to 90° (Fig.8.6a).

- The relationship between ϕ' values mobilized at the PTP in plane strain conditions was that $\phi'(\alpha=\alpha_c=90°)$ exceeded that for $\phi'(\alpha=45°, \alpha_c=90°)$ by ~5°, which is the same amount for which $\phi'(\alpha=\alpha_c=0°)$ exceeded $\phi'(\alpha=45°, \alpha_c=0°)$, Fig.8.6b.

This leads to a confirmation of a hypothesis put forward in Chapter 2 that inclined consolidation forms a new material which has an anisotropy similar to K_o consolidated material. In terms of c_u, the "new" material develops nearly the same normalized undrained strength and diagram shown in Fig.8.7 can be postulated. For the mobilized friction angle, however, inclined consolidation does not erase the inherent K_o differences in ϕ', when sheared with $\alpha=\alpha_c$. But, the anisotropy in ϕ' of a "new" material is similar to the K_o one.

All these results showed that the initial anisotropy, in terms of c_u and ϕ', of K_o consolidated HPF4 is broadly similar to that seen for other granular materials (Shibuya & Hight, 1996; Menkiti, 1995). The anisotropy in ϕ' seems to be more pronounced because of the particle shape of HPF4, which is highly angular and elongated. However, this behaviour, typical for granular materials, can be expected for other silt-type soils with low plasticity index and with hard mineral grains.

The above conclusions summarize the classical soil mechanics parameters of HPF4, i.e. compressibility and strength (c_u and ϕ'). The following findings describe HPF4 behaviour in a different framework that attempts to encompass the materials yielding and stiffness characteristics.

8.1.6. Bounding surface (BS)

The undrained shearing tests on HPF4 showed clear signs of yielding from which a Bounding Surface (BS) could be tentatively identified. The experiments on samples consolidated to p'=200 kPa, showed the following features:

- The normalised BS obtained for normally consolidated HPF4 (OCR=1.0) shrinks with increase in OCR. This is evident from the Series of triaxial tests performed in the stress path cell where it was noted that the effective stress paths for the overconsolidated samples did not engage the NC stress path immediately after the Y_3 yield points, but only came together after Phase Transformation had been reached (Fig.8.8).

- The shape of the local BS depends on the value of b in the sense that it becomes more contractant with increasing b (Fig.8.8).

- The BS expands proportionally with an increase in the consolidation stress level

(Fig.8.9). This indicates that the effective stress paths developed by samples of given OCRs are normalisable by the consolidation stresses.

- For the dense HPF4 tested, the local BS was not fully repeatable, i.e. a sample which had been unloaded inside the BS and then loaded to failure, yielded before reaching the BS indicated by samples loaded directly from K_o stresses. The two surfaces only coincided at Phase Transformation.

8.1.7. Undrained small strain yielding

The following conclusions can be drawn from the current research programme:

- The soil response was non-linear from a very early stage of any shear test. No reliable limit could be ascribed to the end of the elastic range (Y_1 yielding).

- All K_o consolidated and inclined consolidated HPF4 samples experienced undrained Y_2 yield at deviatoric strains, ε_d, between 0.01% and 0.02%. As the current test programme consisted of mainly undrained tests, where deviatoric shear strain was dominant, this strain had been adopted as generalized value to estimate yield. However this value can be zero for certain testing conditions and it would then be necessary to express yield in terms of some other strain measure, such as the magnitude of principal strain or the length of the strain vector.

- The shapes of the projections of the Y_2 and Y_3 yield boundaries onto the t-p' plane are similar to those observed before for other materials: elongated in the t-direction and narrow in the p'-direction (Fig.8.10).

- The projection of the yield boundaries onto the t-α plane showed how the Y_2 and Y_3 yield surfaces can be identified in another dimension by tests involving a range of $\Delta t/\Delta\alpha$ stress path inclinations (Fig.8.10).

8.1.8. Stiffness

The results of the experiments reported in this thesis have been used to calculate soil stiffness. The stiffness characteristics have been interpreted in terms of Kinematic Sub-Yield

Surfaces, with quantitative measurements being reported in terms of non-linear "Youngs modulus", "Poisson's ratio", "Octahedral shear stiffness" and "Torsional shear stiffness". A complex set of characteristics has been observed, but it is possible to make the following list of main points in relation to K_o consolidated samples:

a) Undrained Young's moduli

The undrained triaxial compression and extension tests on HPF4 showed trends in undrained vertical triaxial stiffness, E_u, declining steeply with strain, which are similar to those seen before at Imperial College for other clays and sands. As found previously:

- The undrained stiffness is smaller in compression than in extension for normally consolidated (NC) HPF4, while the opposite is true at OCR≥1.3.

- The normalised compression stiffness (E_u/p_c') increases with OCR, while the extension stiffness decreases with OCR at a fixed strain level (Fig.8.11).

- E_u in both undrained compression and extension increases with stress level, p', at a fixed strain level (Fig.8.12).

- The true undrained compression and extension Young's moduli developed in HCA tests on HPF4 with OCR=1.0 and b=0.5, are similar to those from comparable triaxial tests (where b=0.0 and 1.0)

b) Drained Young's moduli and Poisson's ratios

Research by Tatsuoka & Shibuya (1992), Porovic (1995) and others shows that granular materials are likely to show non-linear behaviour at strain levels ε_d>0.001%. The uncertainties of stiffness measurement at very small strains were reported in Chapter 3, where it was shown that individual stiffness components could be established at ε_d=0.001% to an accuracy of no greater than ±10% in HCA tests, and to ±30% in triaxial experiments. Bearing these restrictions in mind, the following can be concluded:

- At OCR=1.0 the vertical unloading stiffness is approximately double that for horizontal unloading, i.e $E_z'^{unld}/E_h'^{unld}$=2.0 (as observed in the *b* stages of the M-test Series).

Drained tests (forming a D-Series) performed at OCR=1.3, p'=165 kPa, showed that:

- Drained vertical loading led to transversely isotropic behaviour (i.e. $\varepsilon_r=\varepsilon_\theta$), giving $\nu_{zr}\approx0.46$ and $E_z'\approx200$ kPa, at $\varepsilon_d\sim0.001\%$.

- Drained circumferential loading showed a collapsible structure in the radial direction, so that the Poisson's ratio ν_{rz} was negative (≈-0.3). Poisson's ratio $\nu_{r\theta}\approx0.4$ and $E_H'\approx100$ kPa, at $\varepsilon_d\sim0.001\%$.

- These results lead to a conclusion that at very small strains HPF4 in drained loading is also twice as stiff in the vertical as in the horizontal direction, i.e. $E_z'^{load}/E_h'^{load}=2.0$, for $0.001\%\leq\varepsilon_d\leq0.1\%$.

- The vertical torsional shear stiffness, G_{vh}, is relatively stiff in comparison to the drained normal loading stiffnesses (Fig.8.13). The horizontal torsional shear stiffness, G_{hh}, which is not an independent parameter (i.e. it is calculated from E_h' and ν_{hh}'), is nearly three times softer than G_{vh} (Fig.8.13), for $0.001\%\leq\varepsilon_d\leq0.1\%$.

- The above parameters resulted in a non-symmetrical compliance matrix which is not in agreement with the symmetric form suggested by elasticity theory.

- Also, when drained elastic parameters were used to predict the behaviour of undrained tests (i.e. stress path inclination and stiffness), poor agreement was found between the predictions and the experimental observations. The Author's interpretation of the test data indicates that loading and unloading E' values and Poisson's ratios may be different for granular materials, even at very small strains, when attempting to predict undrained behaviour.

c) Octahedral shear stiffness, G

A) A high directional dependence of octahedral shear stiffness was observed when lightly overconsolidated samples were sheared undrained with different $\Delta t/\Delta\alpha$ directions (i.e loading in $\tau_{\theta z}$ while unloading in $(\sigma_z-\sigma_\theta)$), from the same in-situ stress point:

- Stress paths with $\Delta t/\Delta\alpha=0$, i.e. initially horizontal, exhibit the highest stiffness, G. The

stiffness decreases with increase in the inclination of the stress path with respect to horizontal (Fig.8.14).

- When considering stiffness in the light of the small strain yield surface Y_2, it is concluded that a stiffer response is associated with a higher degree of principal stress rotation (Fig.8.14).

B) When samples were subjected to inclined consolidation to the same stress level (R-Series tests), with $\alpha_c \neq 0°$, and then sheared with the same constant inclination, $\alpha=\alpha_c$, "new" materials were formed such that all samples had a similar octahedral shear stiffness, *G*, Fig.8.15.

- Stress level dependence of *G*, when comparing samples consolidated to *p'* and to *2p'*, was found to match the model proposed by Porovic (1995) for Ham River Sand: $G=A(p'/p_a)^n$. Exponent *n* showed strain level dependence similar to that found by Porovic (Fig.8.16).

d) Torsional shear stiffness, $G_{\theta z}$

For K_o consolidated HPF4, torsional shearing resulted in relatively stiff mode of deformation. That is $3G_{\theta z} \geq E_u^{com}$ or E_u^{ext} at compatible values of deviatoric shear strain.

- When K_o consolidated samples were sheared undrained from the same (t, p', b, α) stress point (i.e. Q-A tests), but with different $\Delta t/\Delta\alpha$ directions, all samples exhibited approximately the same initial value of $G_{\theta z}$ at a strain level of $\gamma_{\theta z} \sim 0.001\%$ (Fig.8.17). Strain cross-coupling developed in most cases, leading to differences of up to 20% for the $G_{\theta z}$ values developed on different stress paths. The maximum $G_{\theta z}$ stiffness in this region was observed for samples tested with $\Delta t/\Delta\alpha=0$. These results are compared with a similar test performed by Porovic (1995) (Fig.8.18): loose Ham River Sand sample ($e_o=0.77$), K_o consolidated to p'=200 kPa and swelled back to OCR=1.3, was then exposed to undrained torsional shearing. His values of $G_{\theta z}$ have been corrected to the porosity of the HPF4 samples ($e_o=0.65$), and the corrected curve plotted onto a diagram of $G_{\theta z}$ values from Q-A tests. The two soils show very similar torsional shear stiffness curves.

The R-Series tests showed the following small strain stiffness characteristics:

- When samples are loaded in both drained and undrained conditions from the same (t, p', b) stress point, but with different constant α_c inclinations of the principal stress axes, they also exhibit approximately the same value of $G_{\theta z}$ at a strain level of $\gamma_{\theta z}$~0.001%. A maximum difference of ~25% occurs between different α_c stress paths over the range $0.001\% \leq \gamma_{\theta z} \leq 0.1\%$. Figs.8.19 and 8.20 illustrate this using data from (i) drained inclined consolidation stress paths, which all start from (t, p, b=0.0) stresses, but different α_c, and (ii) undrained shearing stress paths, which all start from (2t, 2p', b=0.5) stresses, but also different α_c. The maximum stiffnesses have been observed for α_c=45° in both cases, because it involves the least strain cross-coupling.

- The average $G_{\theta z}$ curves for both cases are plotted in Fig.8.21, showing the stress level dependence of $G_{\theta z}$. However, the value of the exponent n at $\gamma_{\theta z}$~0.001% is small - only ~0.33.

Overall, the main conclusions drawn from the five test Series performed, are that the HPF4 behaves, under general stress conditions, in a similar way to most granular soils. It shows highly non-linear stress-strain curves; it is non-elastic even at very small strains; highly anisotropic at small strains as well as at failure; its stress-strain behaviour is history dependent, with strain increment directions being related to Kinematic Sub Yield Surfaces. The best description for such a material is likely to be provided by a theory based on anisotropic plasticity, involving small strain sub-yield surfaces, with an anisotropic bounding surface that may evolve as effective stress conditions change, depending on t/p', b, α and OCR. Such a model currently does not exist because of the lack of experimental data and this research should help to provide the basis for future development.

8.2. Practical implications

The laboratory experiments described in Chapters 4 to 7 show that the stress-strain and strength properties of HPF4 are highly anisotropic. A review of the literature shows that such behaviour has also been observed for both dense and loose sands and clay silts. Research shows that the tendency to lose strength dramatically when the principal stress axes rotate is strongest among non-plastic soils. However such trends in behaviour still remain significant in clays. Anisotropy affects not only the undrained strength of soils, but also has a strong influence on

their dilation/contraction characteristics and stiffness behaviour.

This Section draws attention to some practical implications of the present research, by illustrating the role that principal stress rotation can play in certain geotechnical engineering problems. Although the current work has not encompassed stress analyses of such problems, results from work performed by others can be used to support the statement made in the Introduction that "almost all geotechnical engineering problems involve rotations of the principal stresses acting in the ground".

The practical example of principal stress rotation in the ground under a single footing was analyzed by Hight (1983) and presented in Chapter 1. Some other examples are mentioned below:

8.2.1. Multi stage embankments

The potential effects of principal stress rotation on the behaviour of multi-stage embankment construction was the motivation for the R-Series tests presented in Chapter 7. Numerical analyses by Yeats (1983) and Smith (1984) on single stage embankments on soft clays showed that the direction of the principal stresses in the foundation soils rotates from 0° to 90° under the shoulders of the embankment. For multi staged construction the embankment is constructed in a series of lifts allowing pause periods in between. During these pause periods the soil will consolidate under various inclinations of the major principal stress and it is commonly assumed that the associated gain in undrained strength is the same as that in a laboratory triaxial test in which the direction of the major principal stress remains vertical. At first sight such an approach may seem unconservative, as tests indicate that there could be a considerable amount of undrained strength anisotropy. However, the results presented in Chapter 7 of this thesis have shown that such an assumption is likely to be reasonable as such consolidation involves a significant amount of induced undrained strength.

8.2.2. Behaviour of piles

Many of the offshore structures placed in the UK sector of the North Sea are supported on friction piles. The installation and loading processes involved with such piles give rise to important rotations of the σ_1 directions, as illustrated by the shaft loading - shear transfer mechanism sketched in Fig.8.22.

Information gathered in a field study reported by Lehane et al. (1993) indicated that principal stress rotation was responsible for the σ_r' values (developed on the shaft of piles installed in sand) reducing during the early stages of load testing. Data from tests performed in medium dense to loose Labenne sand, with the Imperial College instrumented pile, are presented in Fig.8.23, while Figs.8.24 and 8.25 show (i) the configuration of the test pile and (ii) the Labenne site's geotechnical profile. Fig.8.23 reproduces the effective stress paths (shaft shear stress vs. radial effective stress) developed at three levels on the shaft, for two identical piles tested to failure - one in compression and the other in tension. At all instrumentation positions initial reductions of σ_r' were observed, but the effect is clearly more significant under tension loading, where the σ_1 direction is rotated away from that acting during either pile installation or in the static, unloaded, state. The latter feature led to the overall shaft capacity being significantly lower under tension.

The orientation of the major principal stress, α, under shaft loading can only be deduced from the field measurements if some additional assumptions are made. Fig.8.26 shows one such analysis of the rotation of the major principal stress in the *z-r* plane (and the associated Mohr circle) for the peak capacity case from the compression test (at the leading instrument cluster). The assumptions made are that the interface friction angle, δ_f, is close to the mobilised angle of shearing resistance of the soil, ϕ', that the plane of maximum stress obliquity is vertical, that $\sigma_r'<\sigma_z'$ and that the simple Coulomb failure criterion applies:

$$\tau_{rz,f}=\sigma'_{r,f}\tan\delta_f \qquad (8.1)$$

The value of α is then found to be 31° at the failure point.

8.2.3. Submarine slopes

The formation, by deposition or erosion, of natural submarine slopes leads to rotations of the principal stress directions, in a similar way to that described in Chapter 1 for gravity based foundations. Further sudden rotations may take place if a failure is induced in the slope by any external perturbation. Rough assessments of the values of α applying around any potential failure surface can be made by the approximate approach outlined above for pile loading. We need first to estimate the mobilized ϕ' value. As shown in Fig.8.27, a ϕ' value of 30° implies that the major principal stress is inclined to the failure surface at an angle of 60°. We can then sketch the potential range of σ_1 orientations. It appears that α ranges from 0° to ±90°, so induced strength anisotropy is likely to have an important influence on stability. Readers

are referred to Kovacevic (1994) for examples of how more rigorous numerical analyses can be made of the stress regimes applying in slope stability problems.

8.2.4. Tunnels

Recently (Simpson et al., 1996) soil shear stiffness anisotropy has been recognized as a factor which can influence the width of the surface settlement trough above tunnels. This work considers tunnelling in London clay and presents results from laboratory experiments using bender element technique, which imply that G_{vh}/G_{hh}~0.65. However, experiments described in this thesis on low OCR granular material showed the opposite trend, i.e. G_{vh}/G_{hh}~3.0, and would, therefore, lead to a relative spreading of the settlement trough.

8.3. Future research

In the Author's opinion the most important direction for any future research oriented towards offshore engineering applications would be to advance Hollow Cylinder research into soil anisotropy and brittleness in step with developments in soil modelling and numerical methods. This would then enable the analyses of real geotechnical problems to be performed so that the role of soil anisotropy can be quantified.

Recent developments in foundation design, and moves into new provinces for oil and gas exploration, are raising such requirements. For example:

- Surveys in the West of Shetlands and other regions such as the Caspian sea, show that large scale slides have developed in the soft sediments found on relatively flat submarine slopes (Paul, 1994; Sweeny, 1994). Undrained strength reductions due to anisotropy may play a role in such slope instabilities and such effects need to be better understood.

- The recent use in Norwegian waters and other areas of concrete suction caissons for floating Tension Leg Platforms, and steel "bucket" foundations for fixed jacket structures, raises the need for improved theoretical models to both explore how anisotropy may affect these foundations, and to help provide design tools for site specific studies.

On the other hand, most of the currently available soil models do not incorporate soil anisotropy in a satisfactory manner. The MIT models are some of the best efforts to date. However, they are highly complex and need to be verified by comparison with the results of element tests which involve principal stress rotation. Consequently,

- There is a need for further fundamental experimental studies to help extend and test the theoretical frameworks for anisotropic soils, and to aid the development of more representative soil models. In particular the research presented in this thesis could be extended to investigate the effects of other stress path directions and to investigate the cyclic behaviour of HPF4. Some of the tests presented here could also be usefully applied to other soils. There is a need for further sophisticated hollow cylinder tests on clay soils.

- There is also a need to validate and improve existing models through comparisons with data from sophisticated element tests which can induce controlled principal stress rotation.

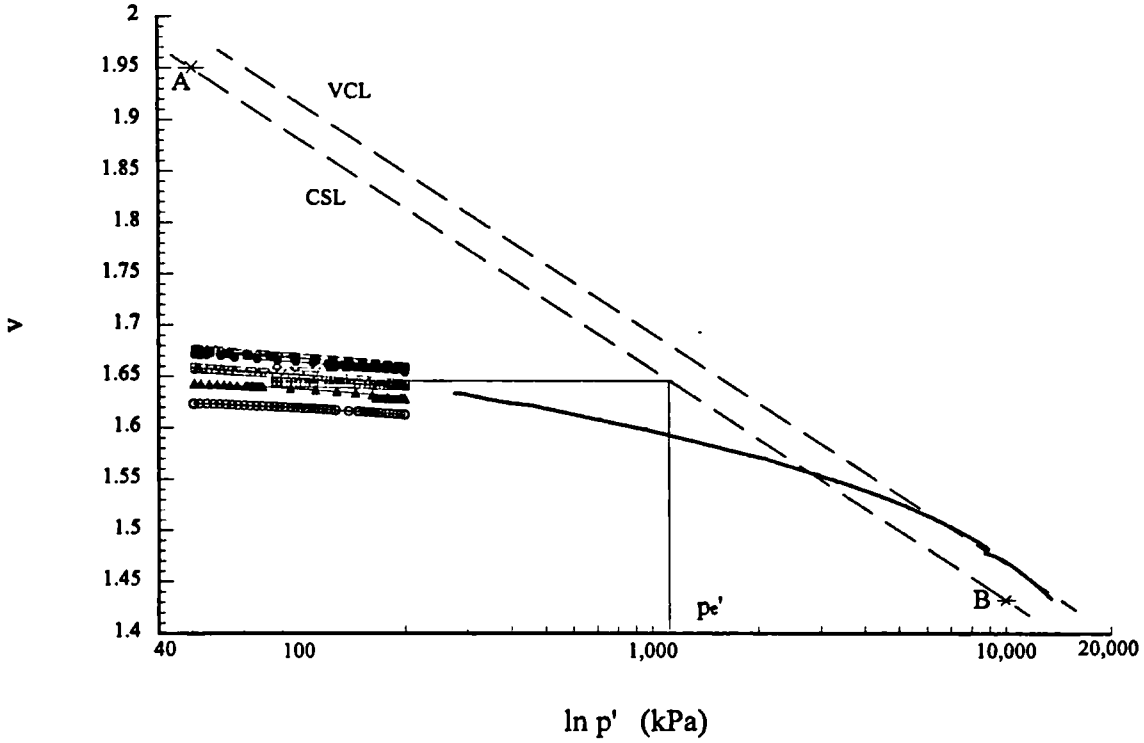


Fig.8.1 - HPF4 consolidation curves in relation to the tentative critical state line and virgin consolidation line

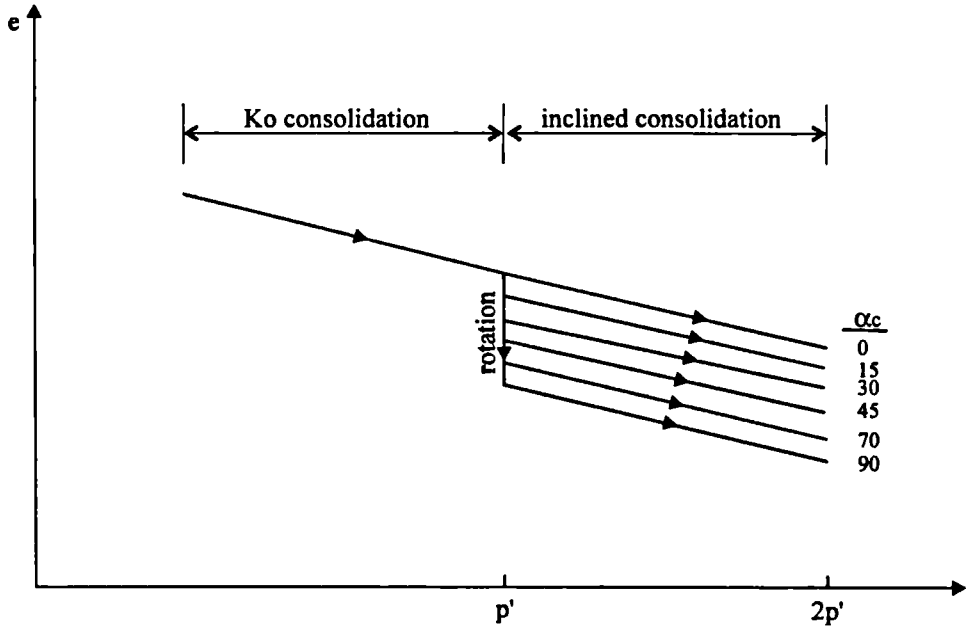


Fig.8.2 - Volumetric changes during consolidation with constant α

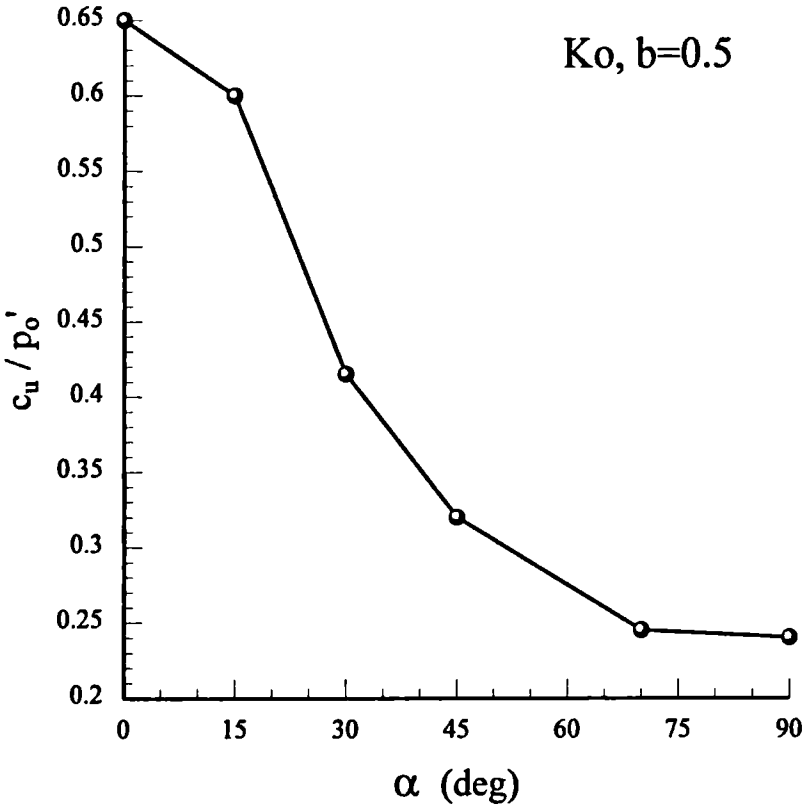


Fig.8.3 - Undrained strength anisotropy at PTP

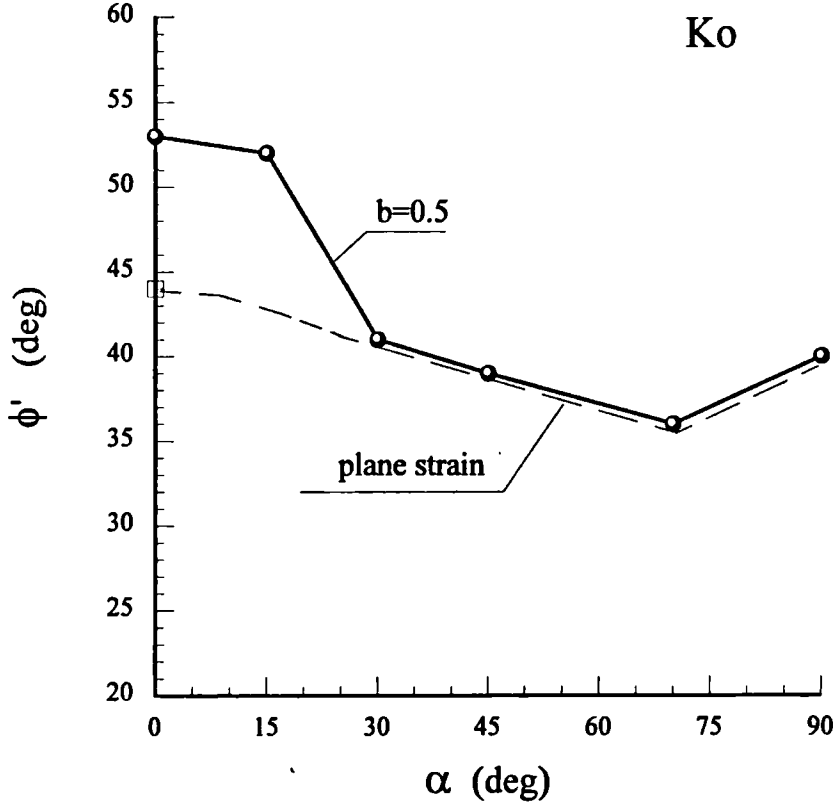


Fig.8.4 - Undrained mobilized ϕ' anisotropy at PTP

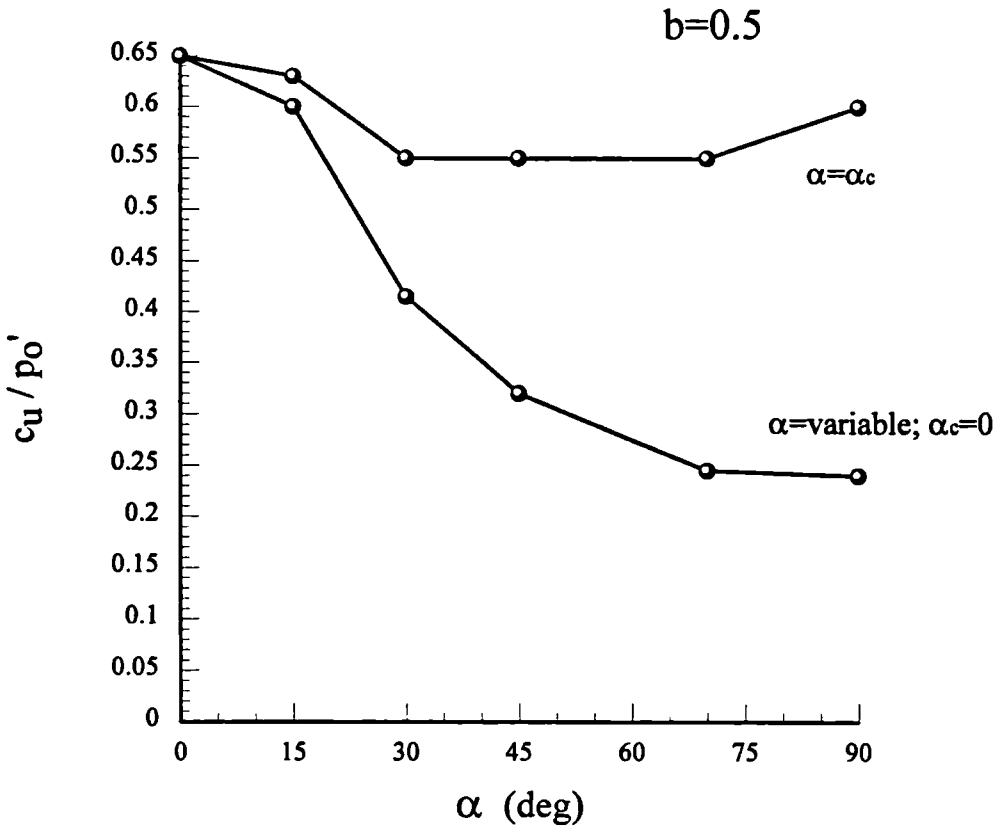


Fig.8.5a - Undrained PTP strength of samples consolidated and sheared with $\alpha=\alpha_c$

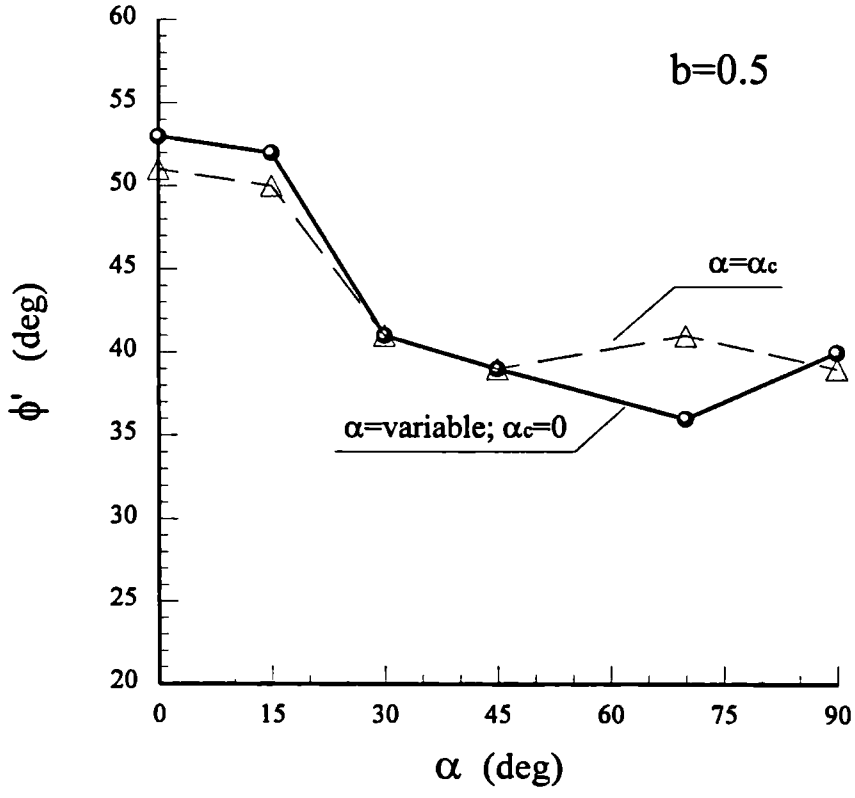


Fig.8.5b - Mobilized ϕ' at the PTP for samples consolidated and sheared with $\alpha=\alpha_c$

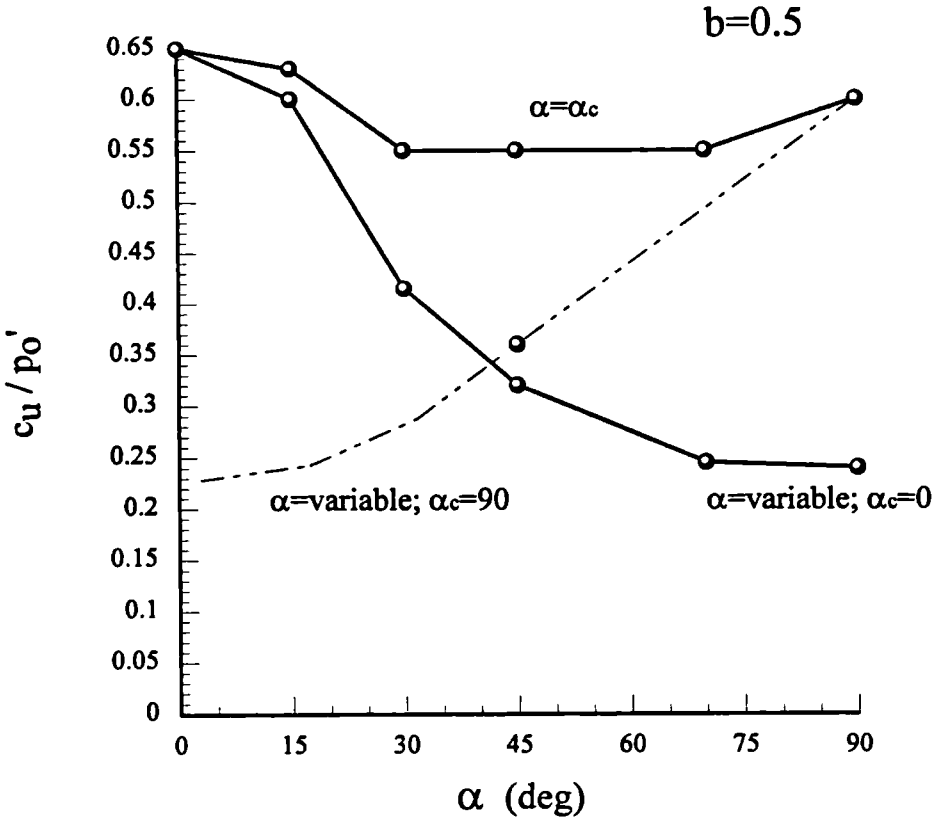


Fig.8.6a - Undrained PTP strength anisotropy of Ko and inclined consolidated samples

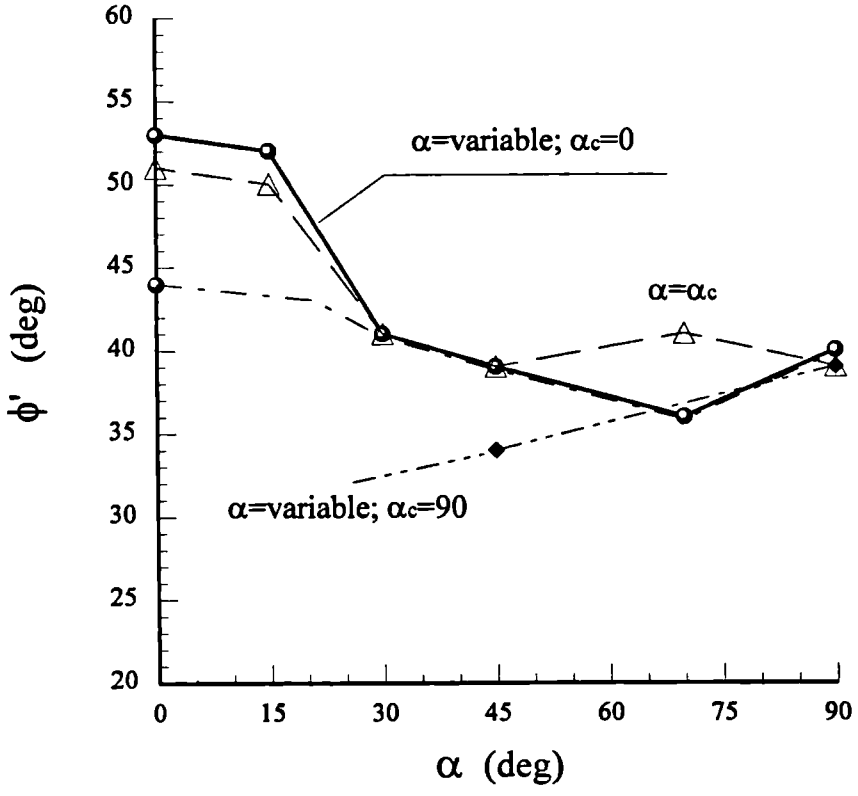


Fig.8.6b - Plane strain anisotropy of mobilized PTP values of ϕ' for Ko and inclined consolidated samples

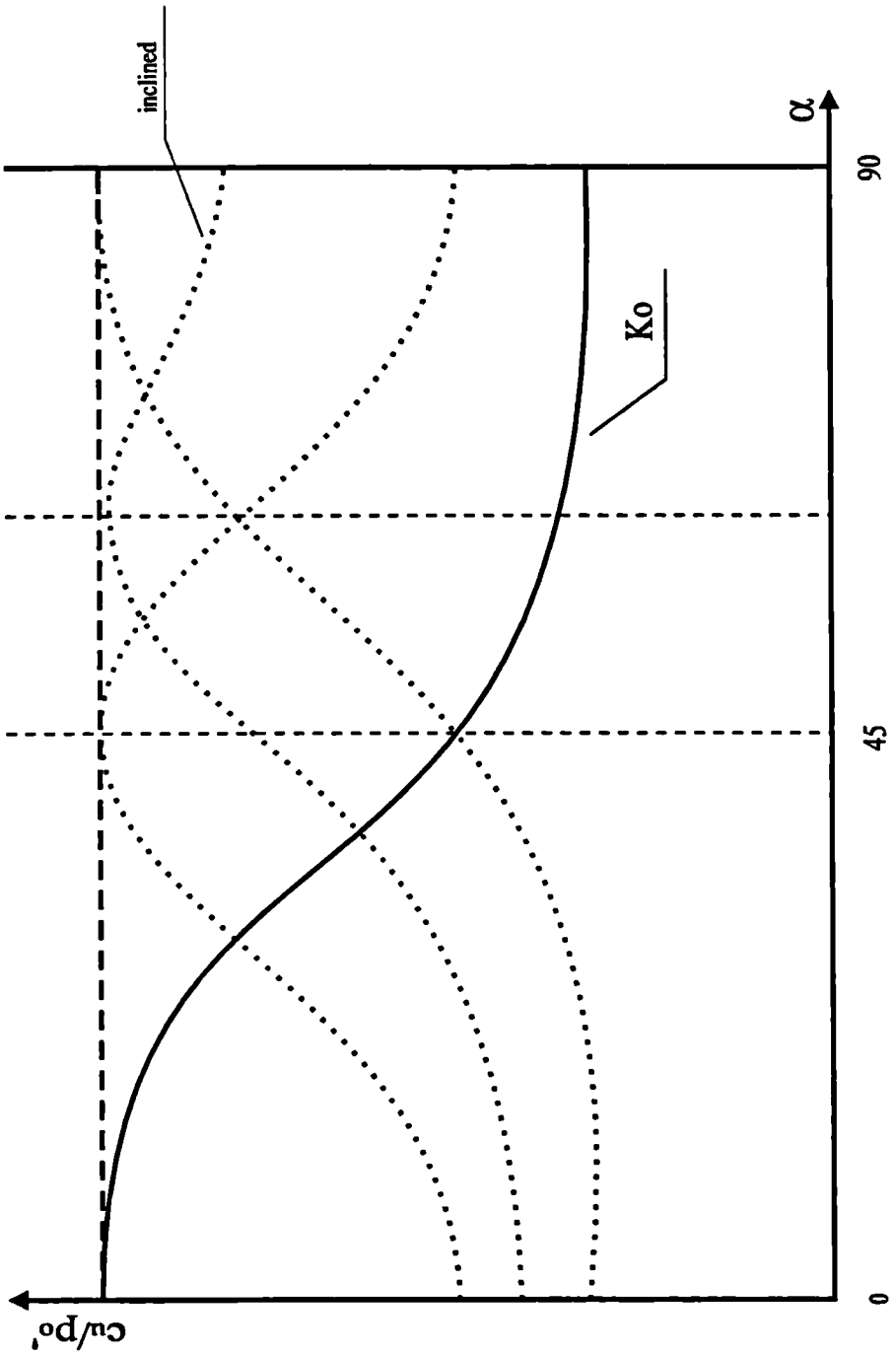


Fig.8.7 - Undrained strength anisotropy of inclined consolidated samples

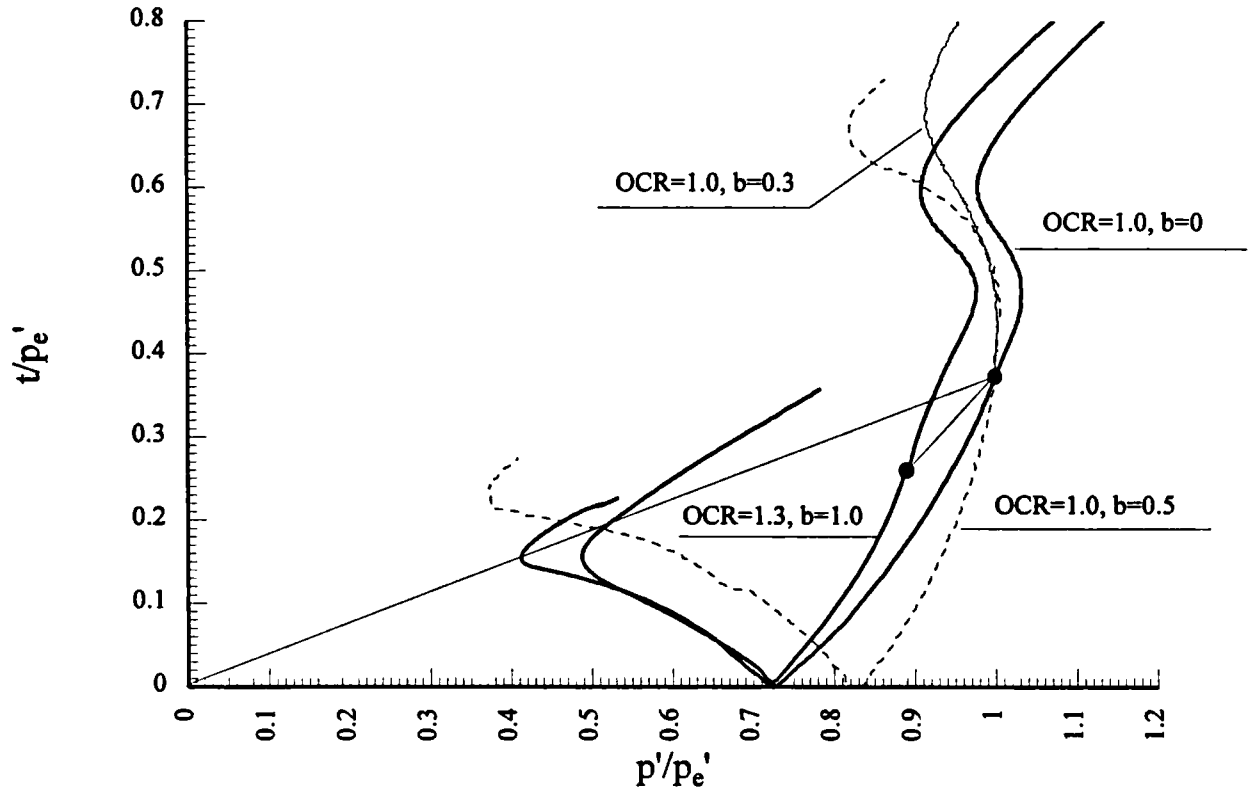


Fig.8.8 - Summary of the Bounding Surface characteristics

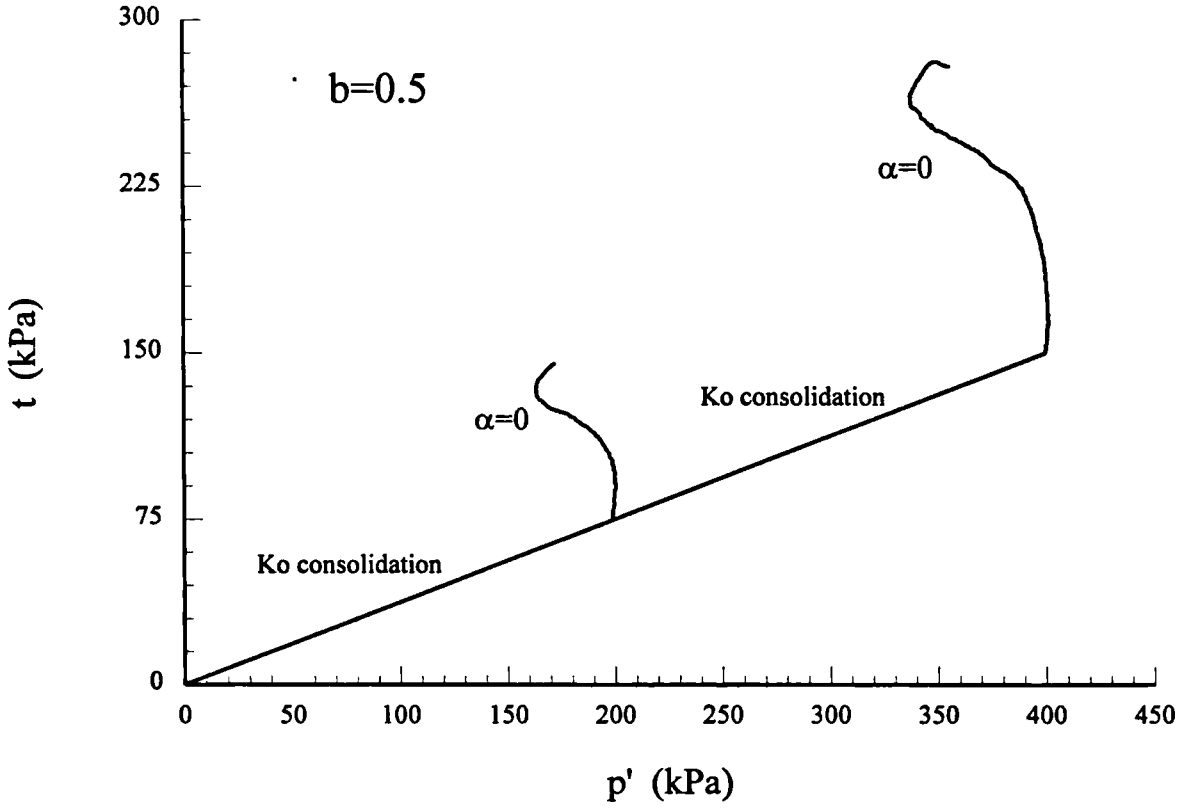


Fig.8.9 - Dependence of the Bounding Surface on stress level

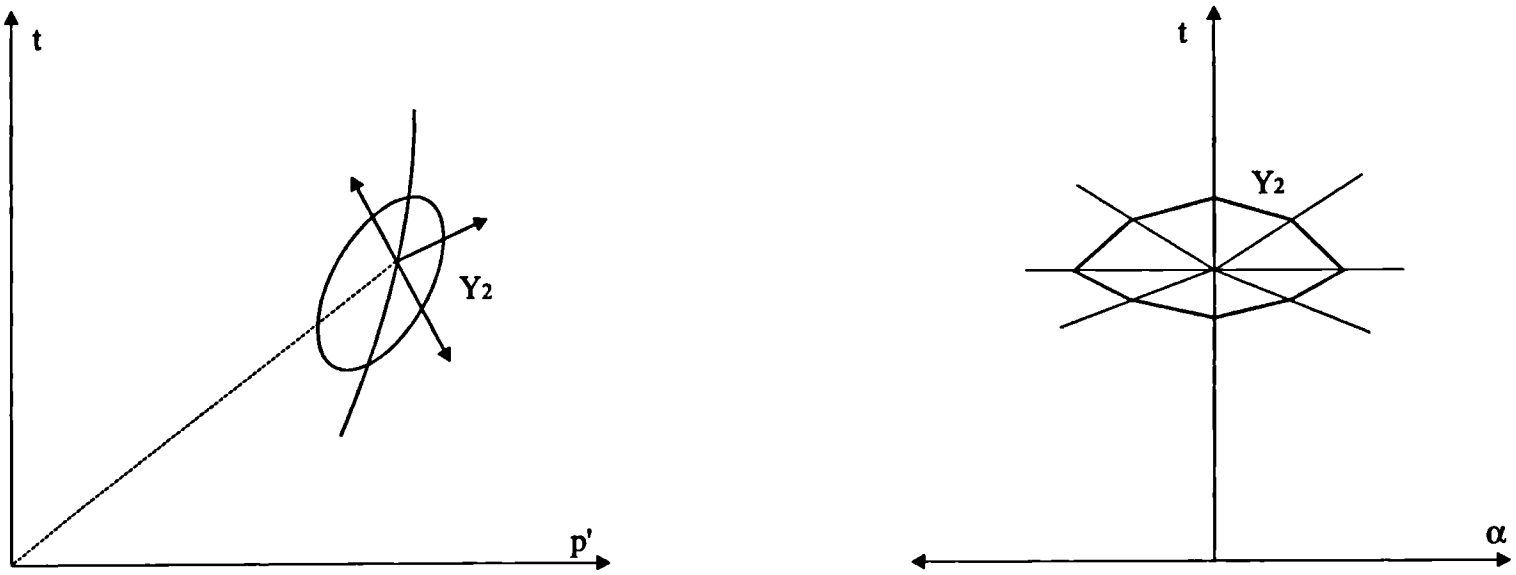


Fig.8.10 - Schematic presentation of the projection of Y2 surface on t-p' and t-α planes

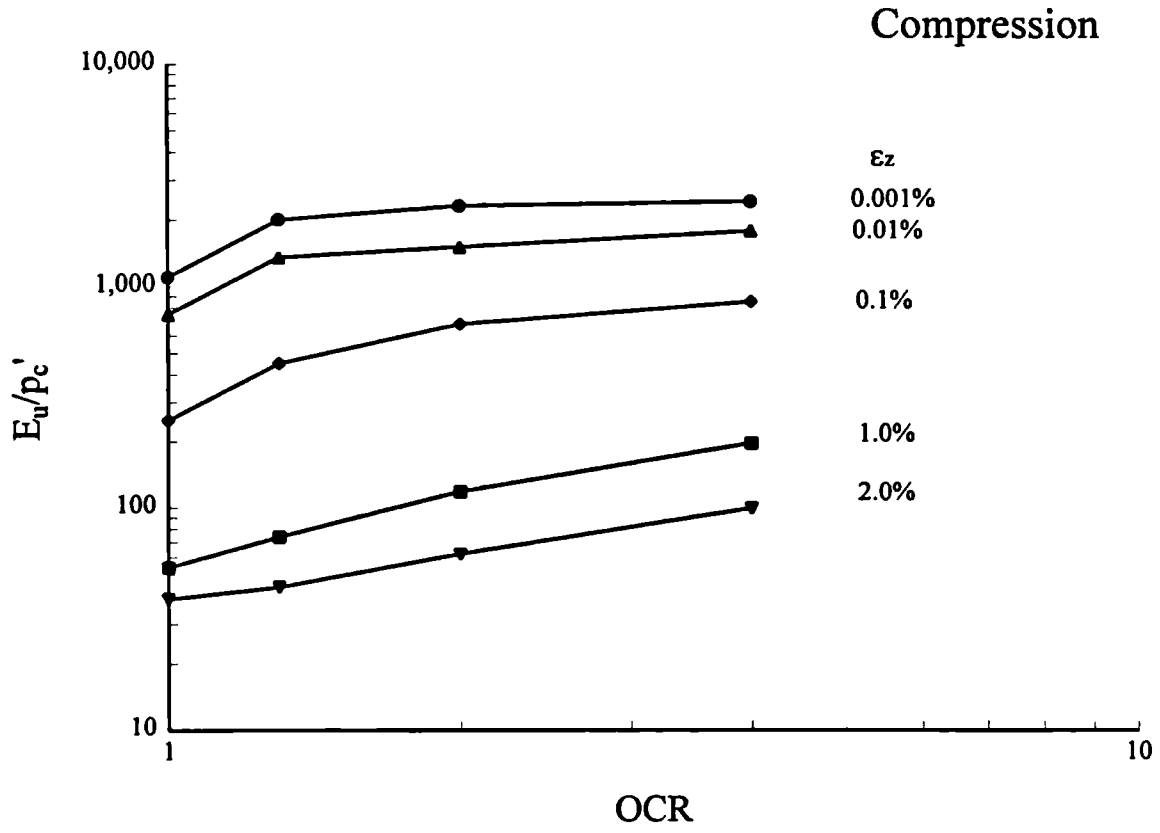


Fig.8.11a - Variation of compression Young modulus with OCR at fixed strain levels

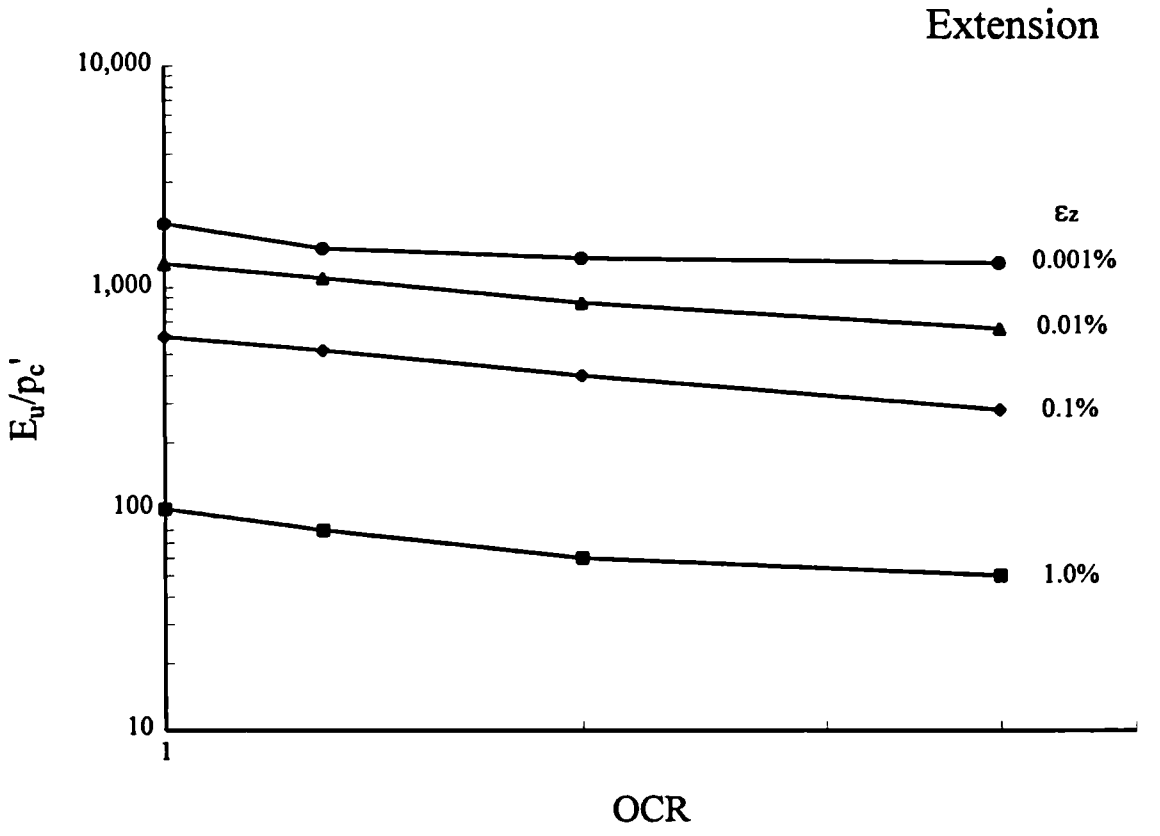


Fig.8.11b - Variation of extension Young modulus with OCR at fixed strain levels

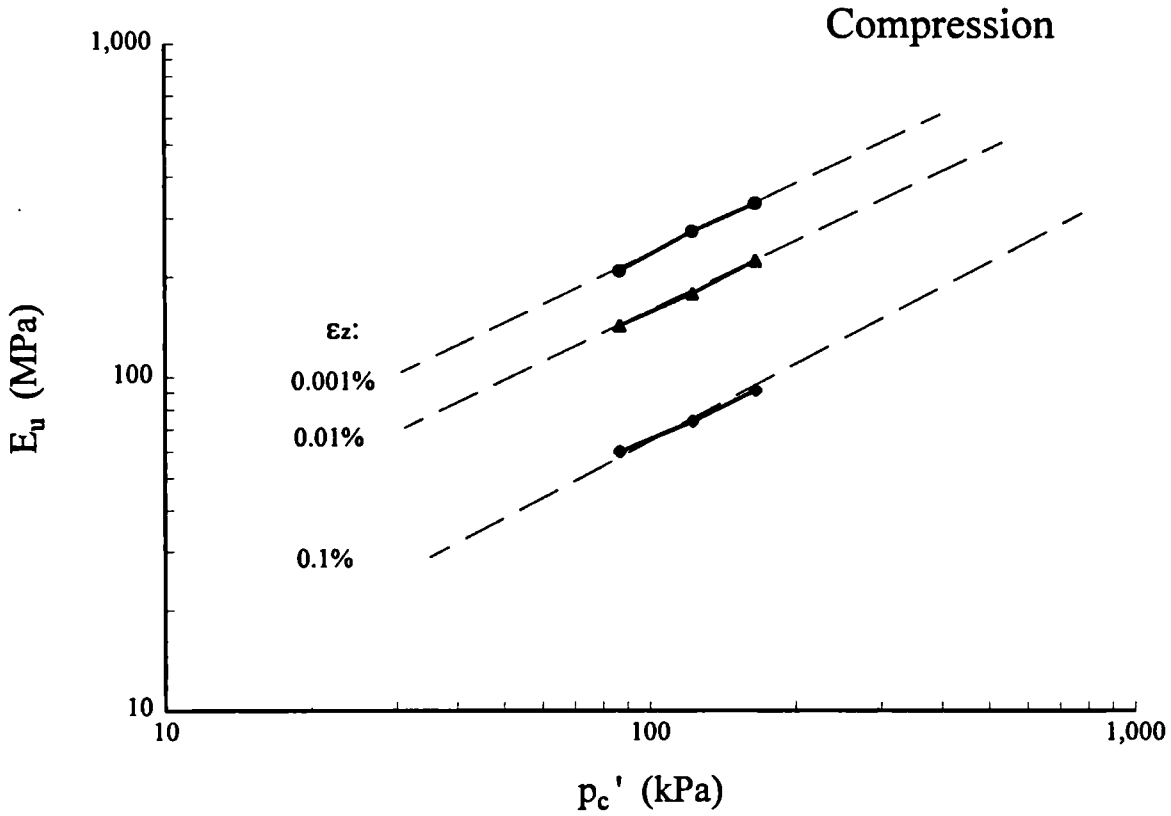


Fig.8.12a - Dependance of compression Young modulus on p' at fixed strain levels

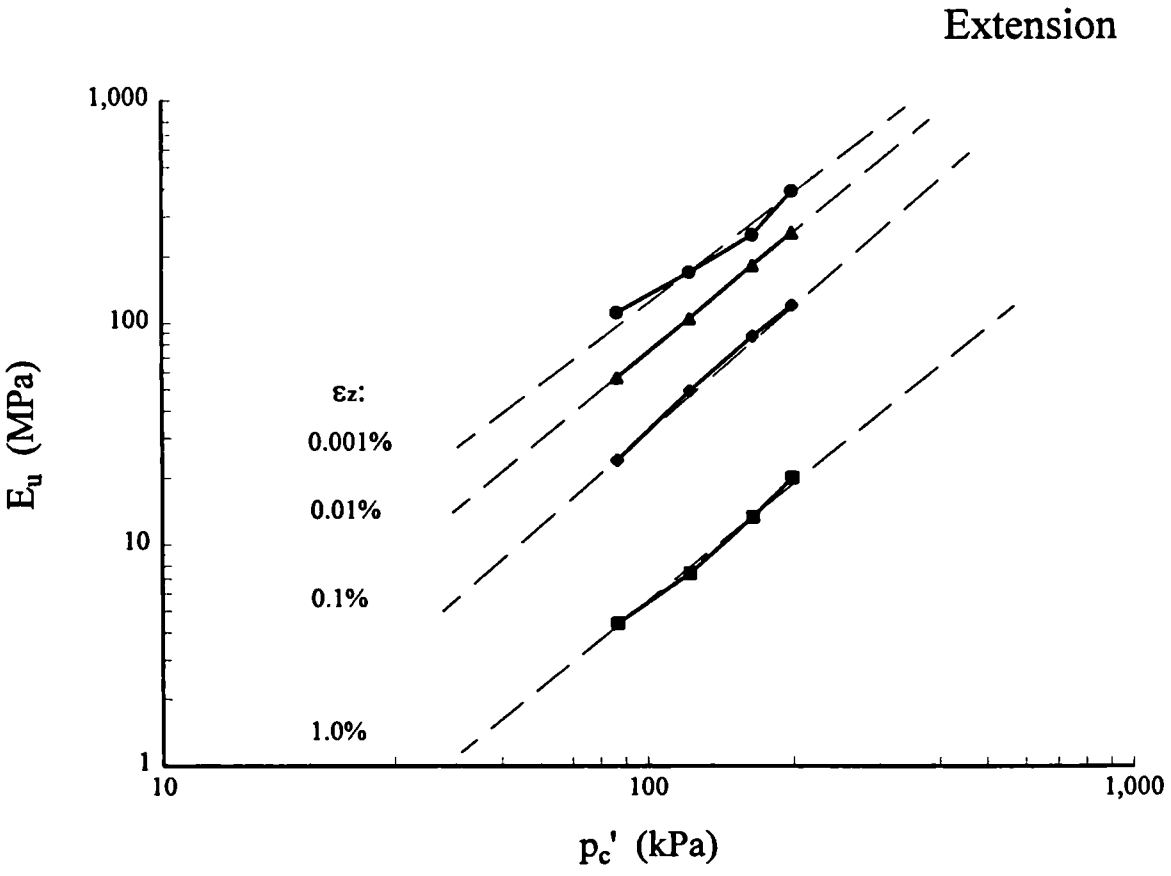


Fig.8.12b - Dependance of extension Young modulus on p' at fixed strain levels

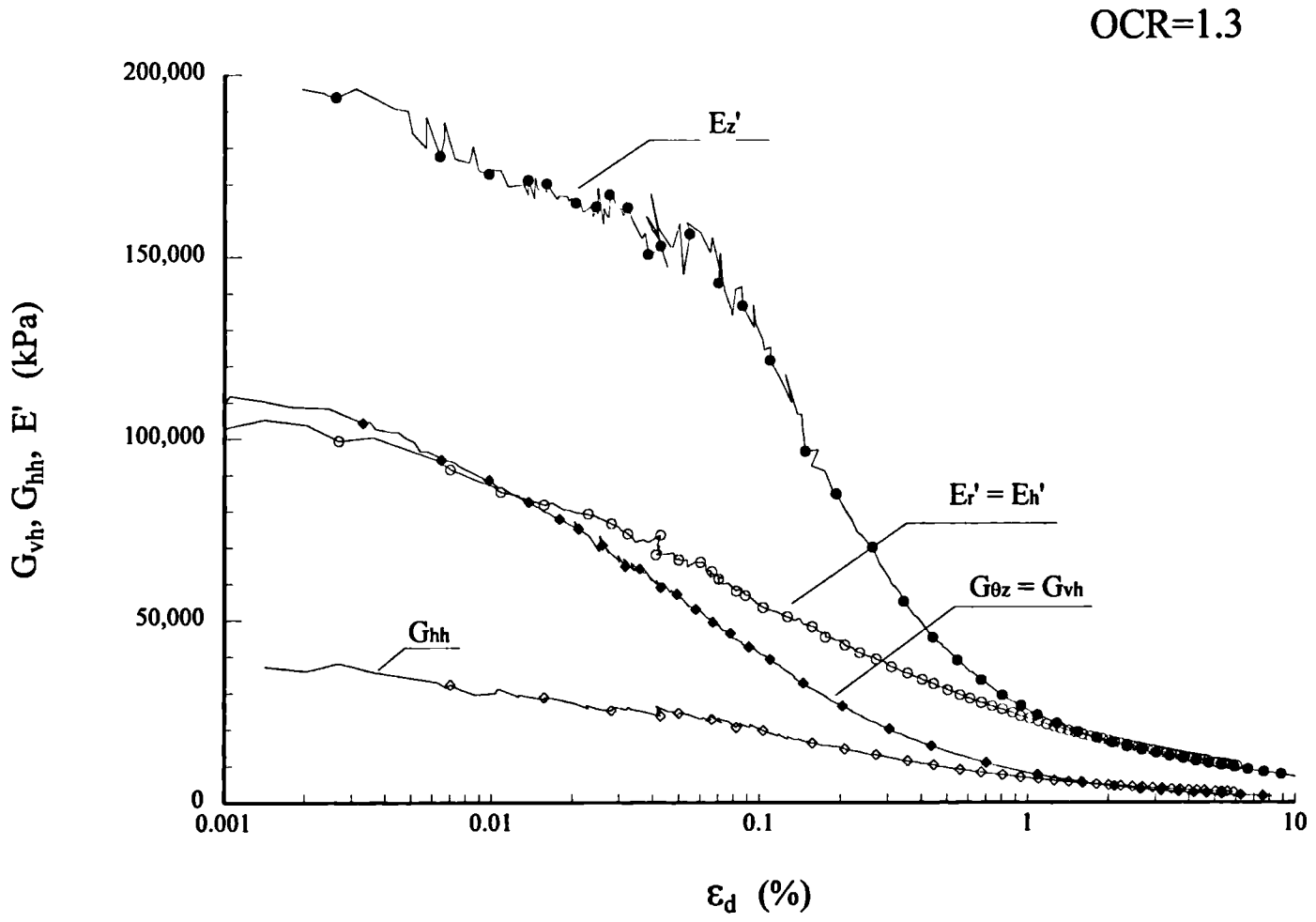


Fig.8.13 - Drained shear moduli of HPF4 sheared from OCR=1.3

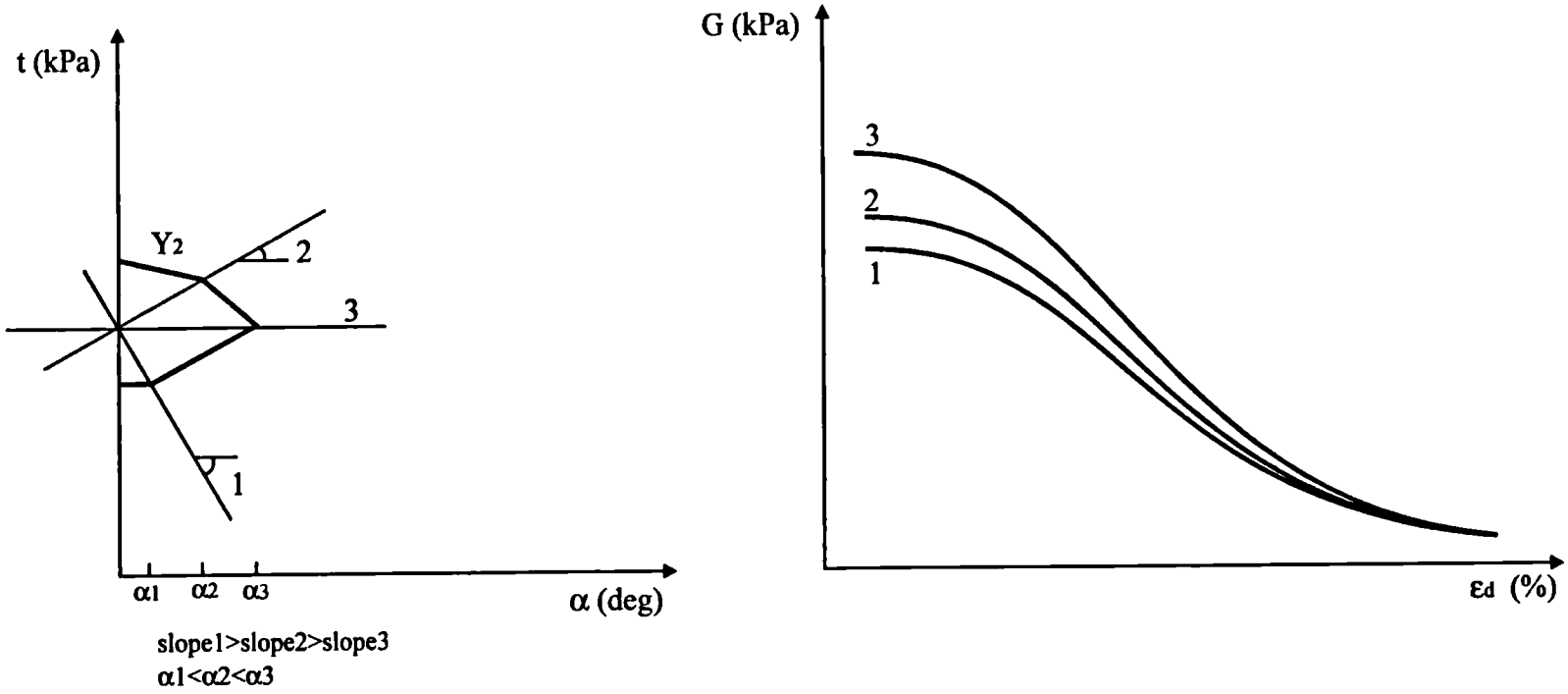


Fig.8.14 - Schematic presentation of the dependence of G on stress path inclination and angle of principal stress rotation

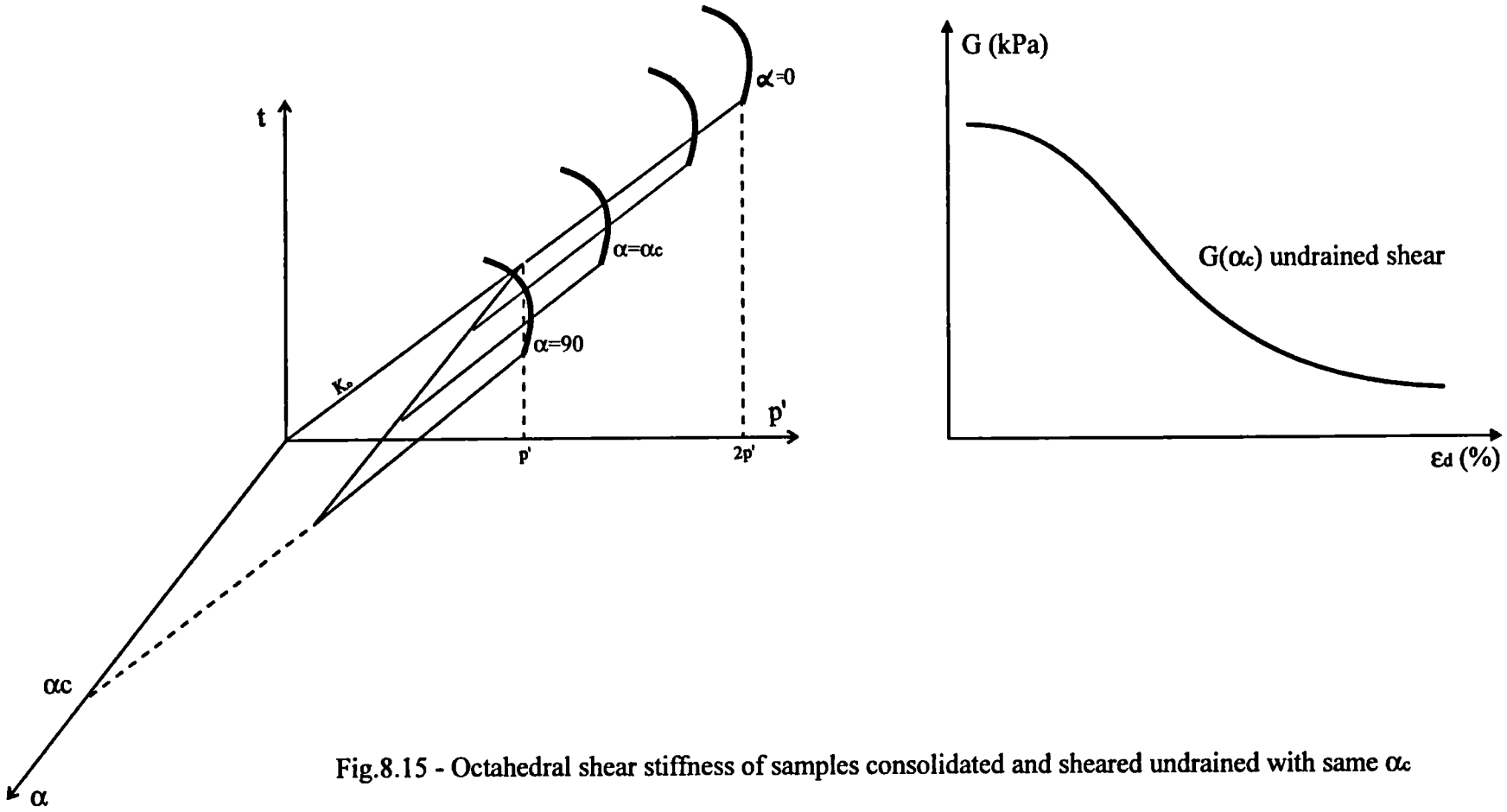


Fig.8.15 - Octahedral shear stiffness of samples consolidated and sheared undrained with same α_c

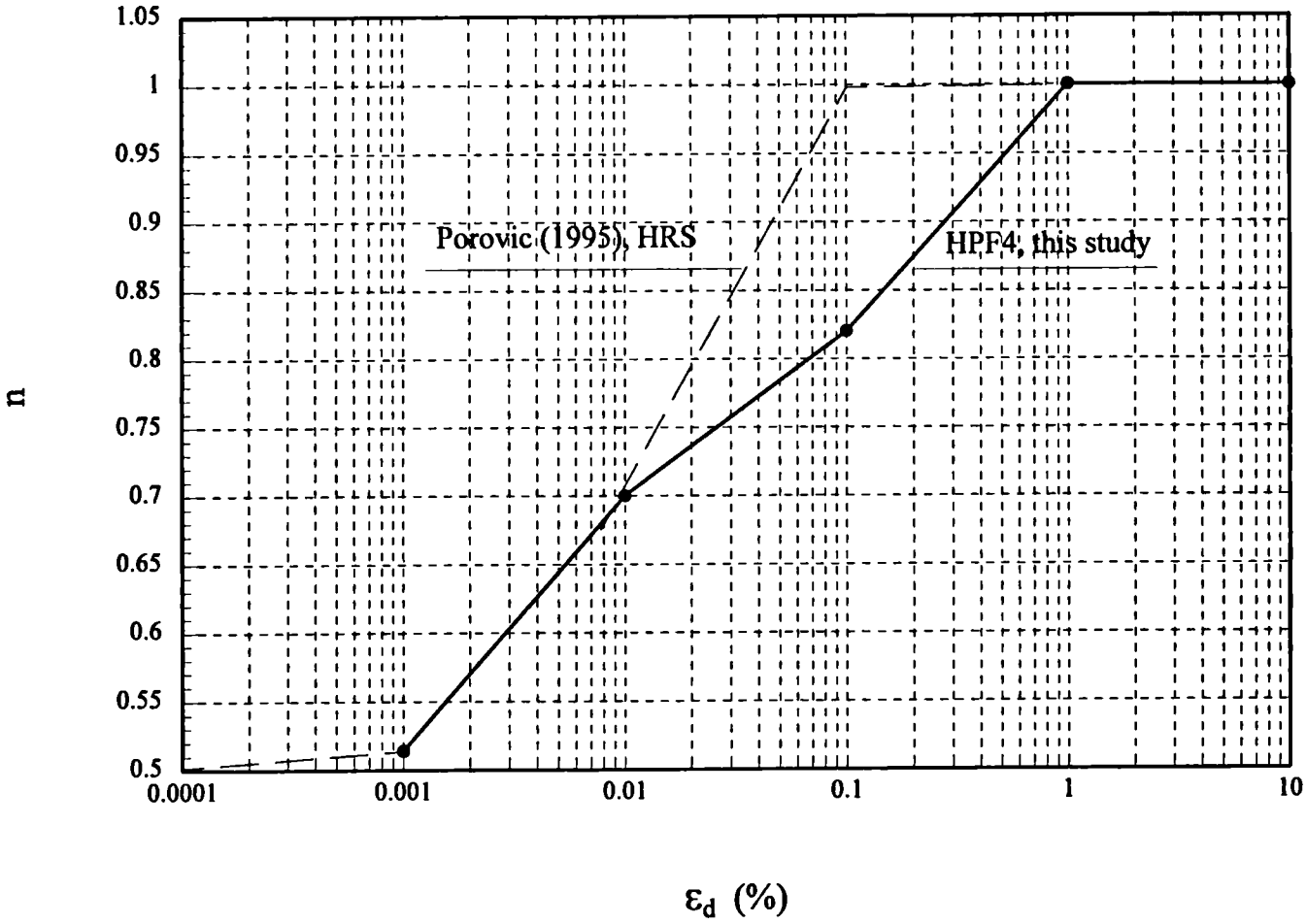


Fig.8.16 - Dependence of 'n' on the strain level

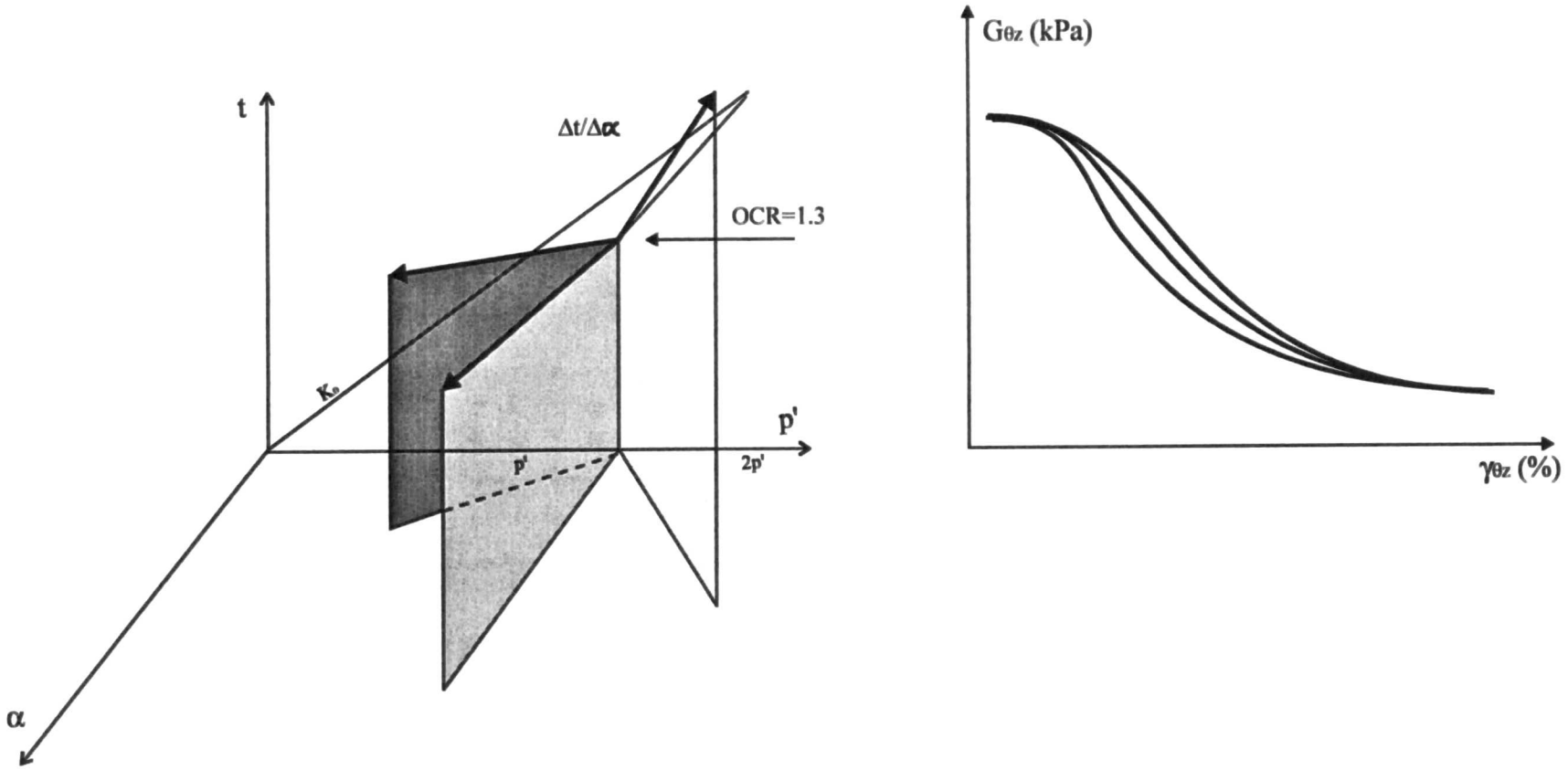


Fig.8.17 - Schematic view of the conditions for $G_{\theta z}$ in Q-A test Series

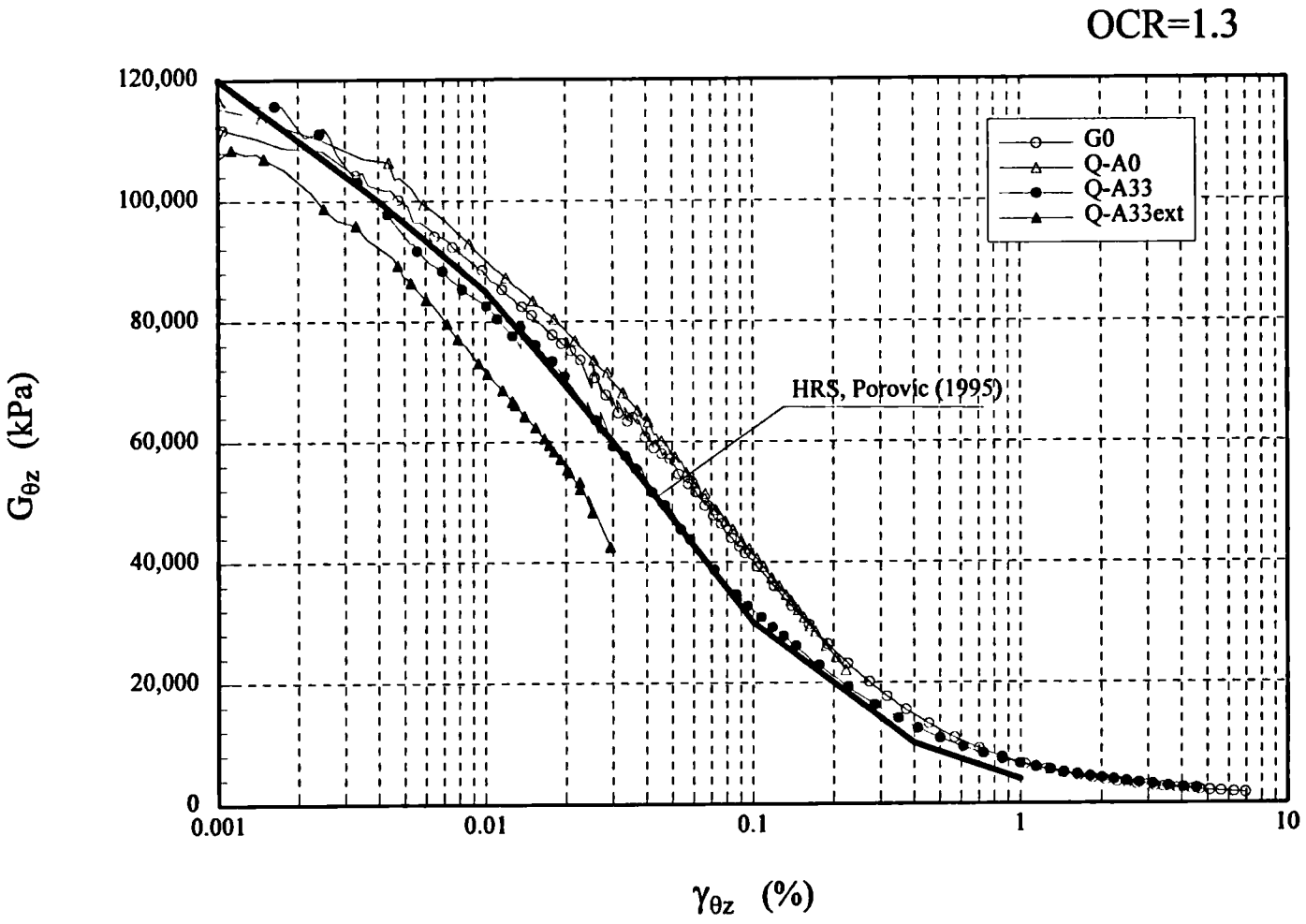


Fig.8.18 - Torsional shear moduli of HPF4 for undrained probing tests from OCR=1.3

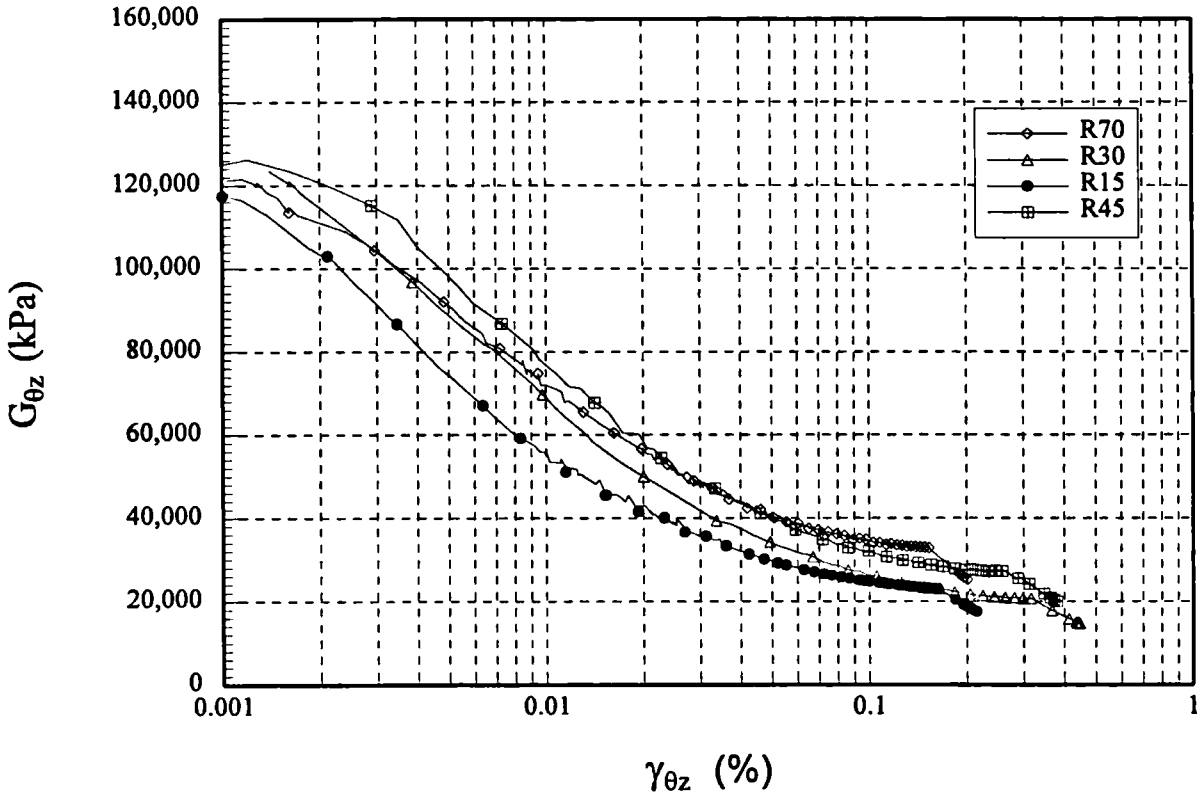


Fig.8.19a - Variation of torsional shear stiffness during drained inclined consolidation

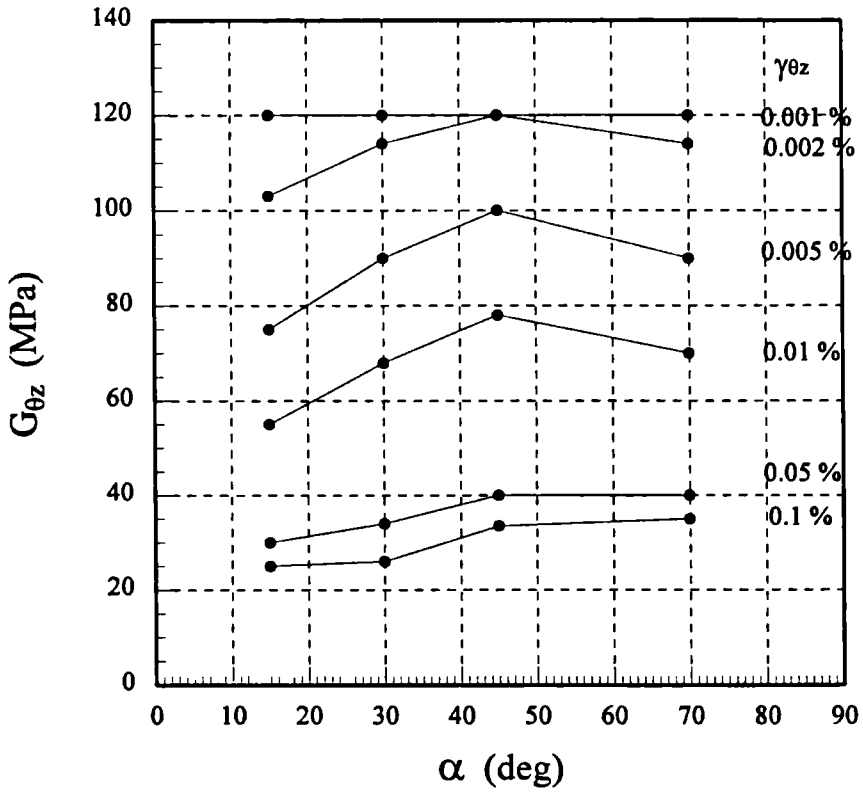


Fig.8.19b - Distribution of $G_{\theta z}$ with α, at different strain levels, during drained inclined consolidation

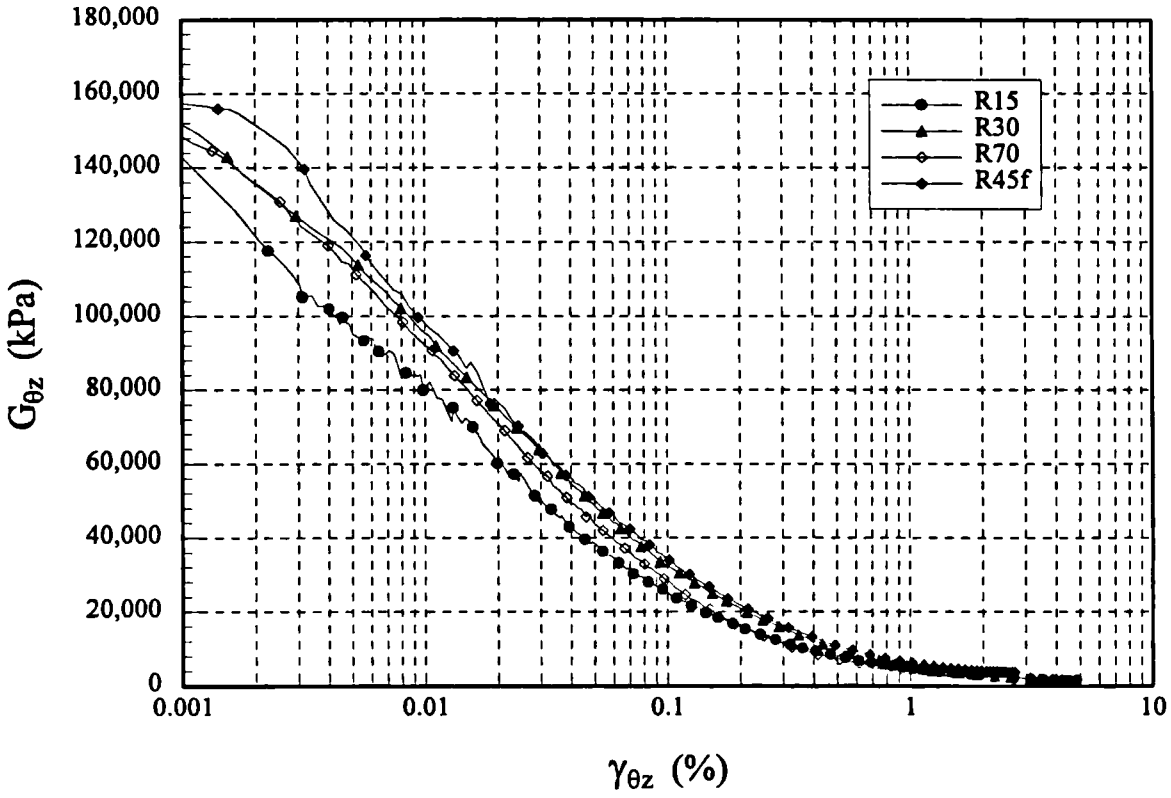


Fig.8.20a - Variation of torsional shear stiffness during undrained shearing stage of R-Series tests

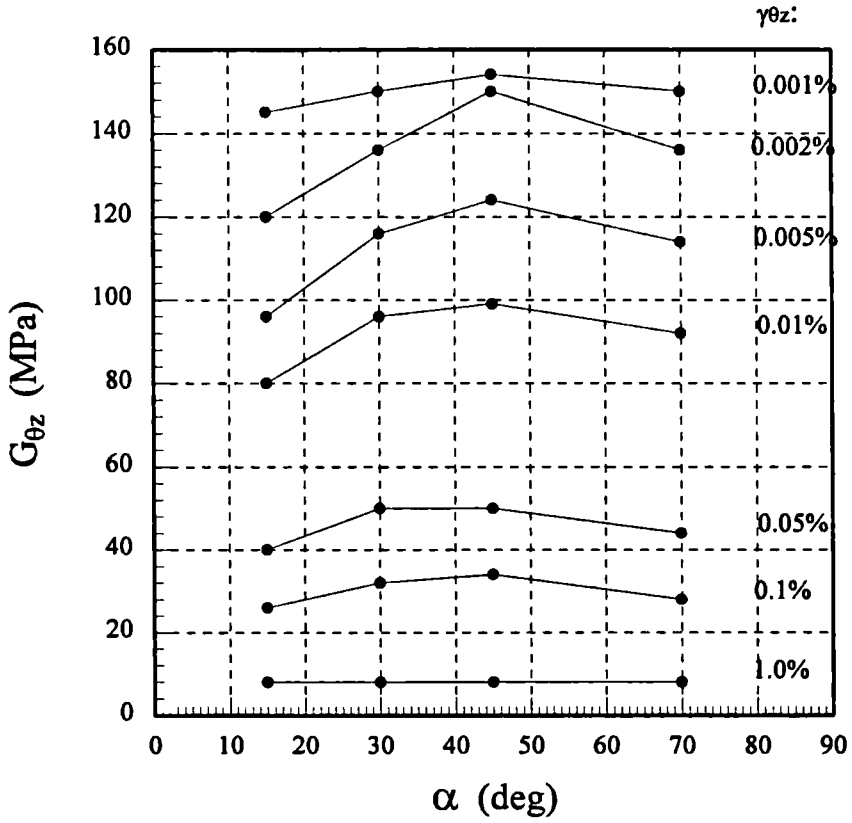


Fig.8.20b - Distribution of $G_{\theta z}$ with α, at different strain levels, during undrained shearing

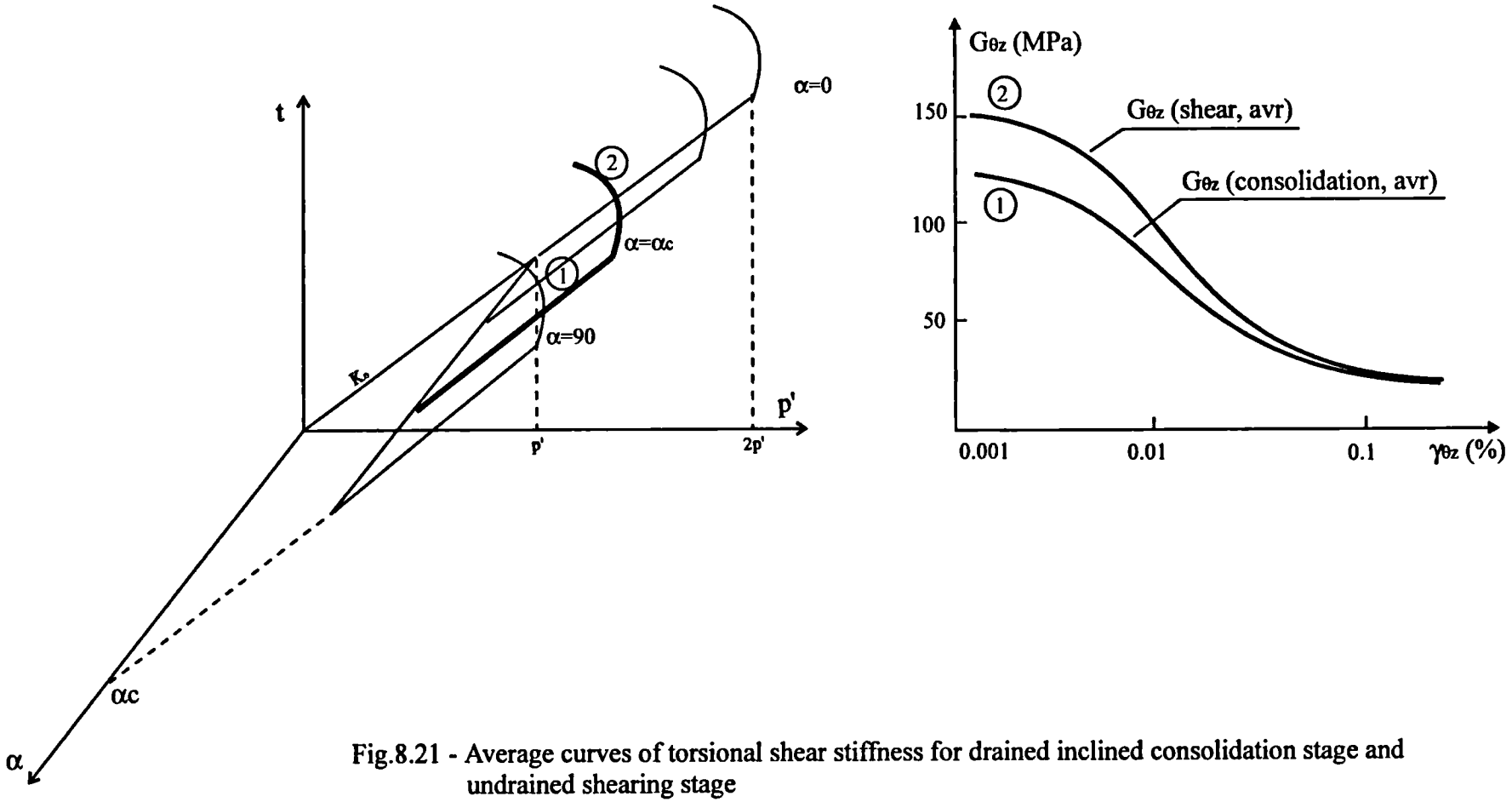


Fig.8.21 - Average curves of torsional shear stiffness for drained inclined consolidation stage and undrained shearing stage

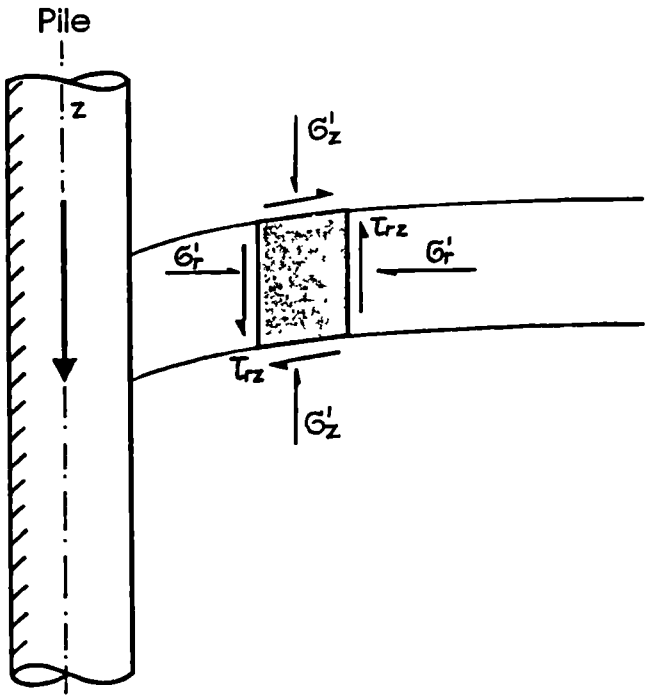


Fig.8.22 - Soil element close to axially loaded pile

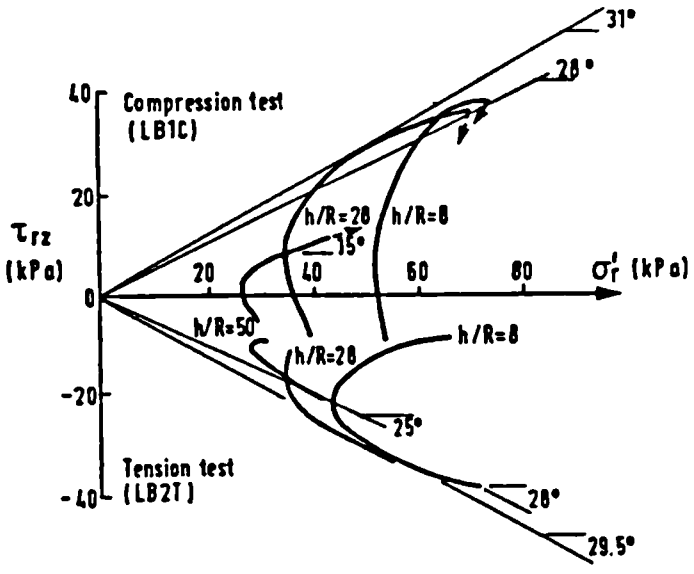


Fig.8.23 - Stress paths in compression and extension load tests at Labenne

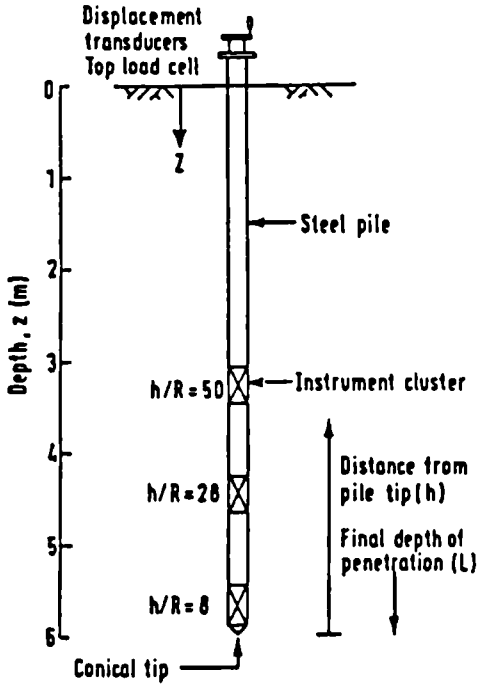
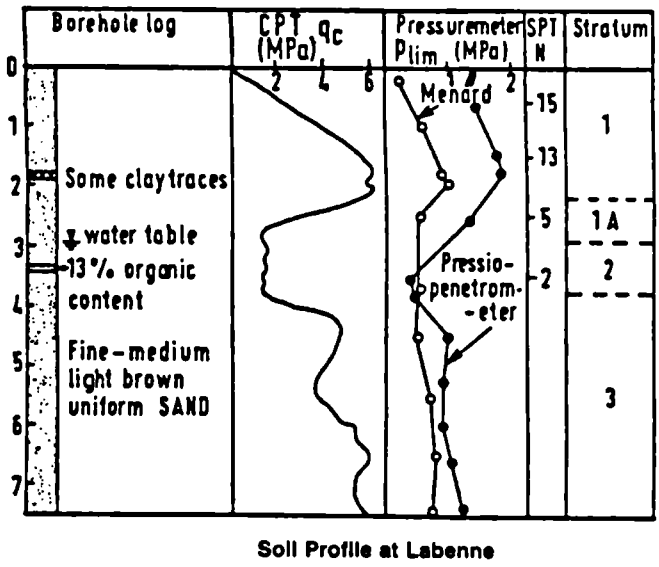


Fig.8.24 - Configuration of the Imperial College instrumented pile

Soil Properties at Labenne, by Layer

Layer number (1)	Depth, z (m) (2)	Relative density, D_r (%) (3)	Void ratio, e (4)	Bulk density, γ_b (kN/m³) (5)
1	0–2.2	60	0.60	16.9
1A	2.2–2.8	transition zone	transition zone	transition zone
2	2.8–3.8	25	0.72	19.2
3	3.8–6.0	40	0.67	19.5



Soil Profile at Labenne

Fig.8.25 - Soil profile at Labenne

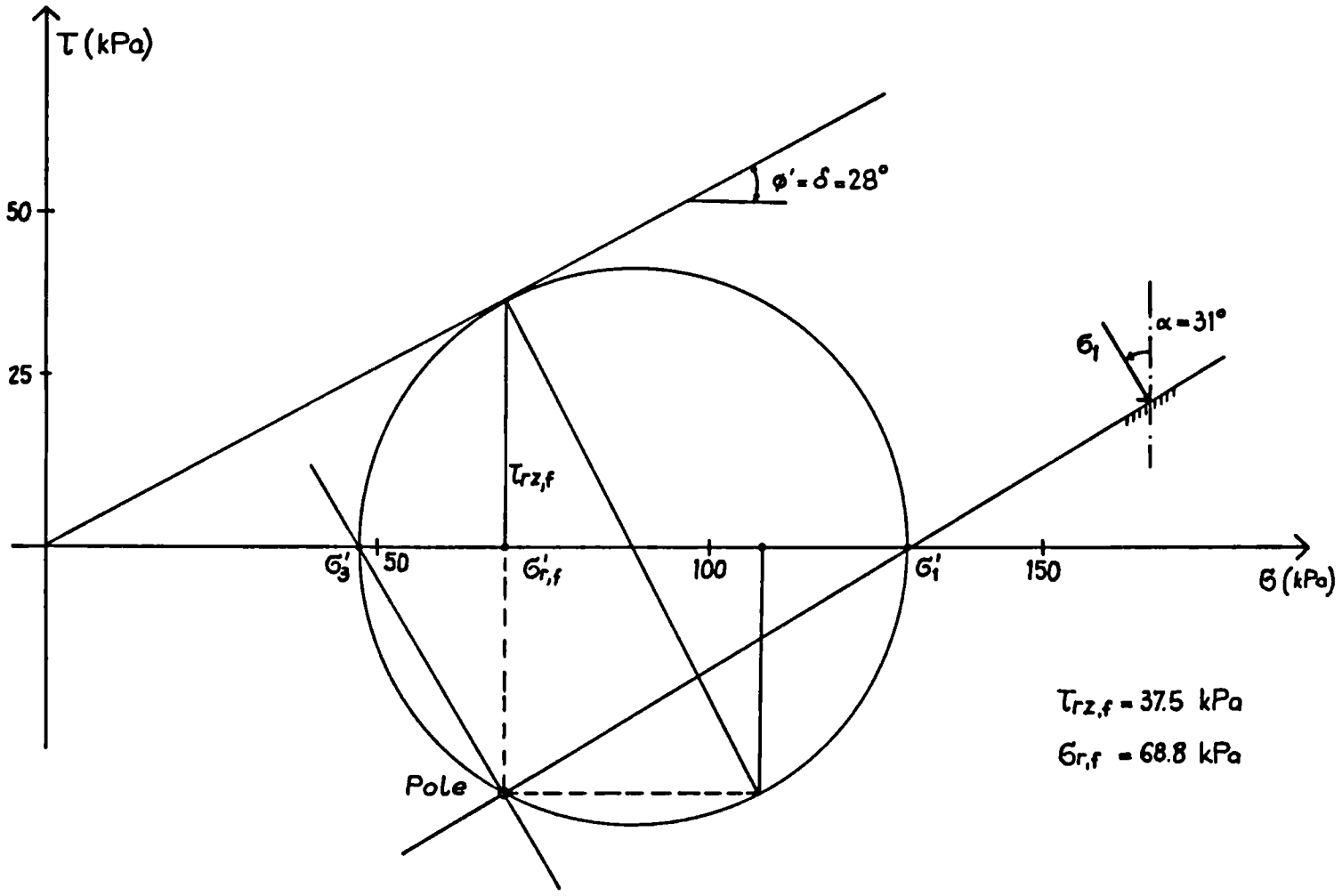


Fig.8.26 - Principal stress rotation in a soil element close to axially loaded pile

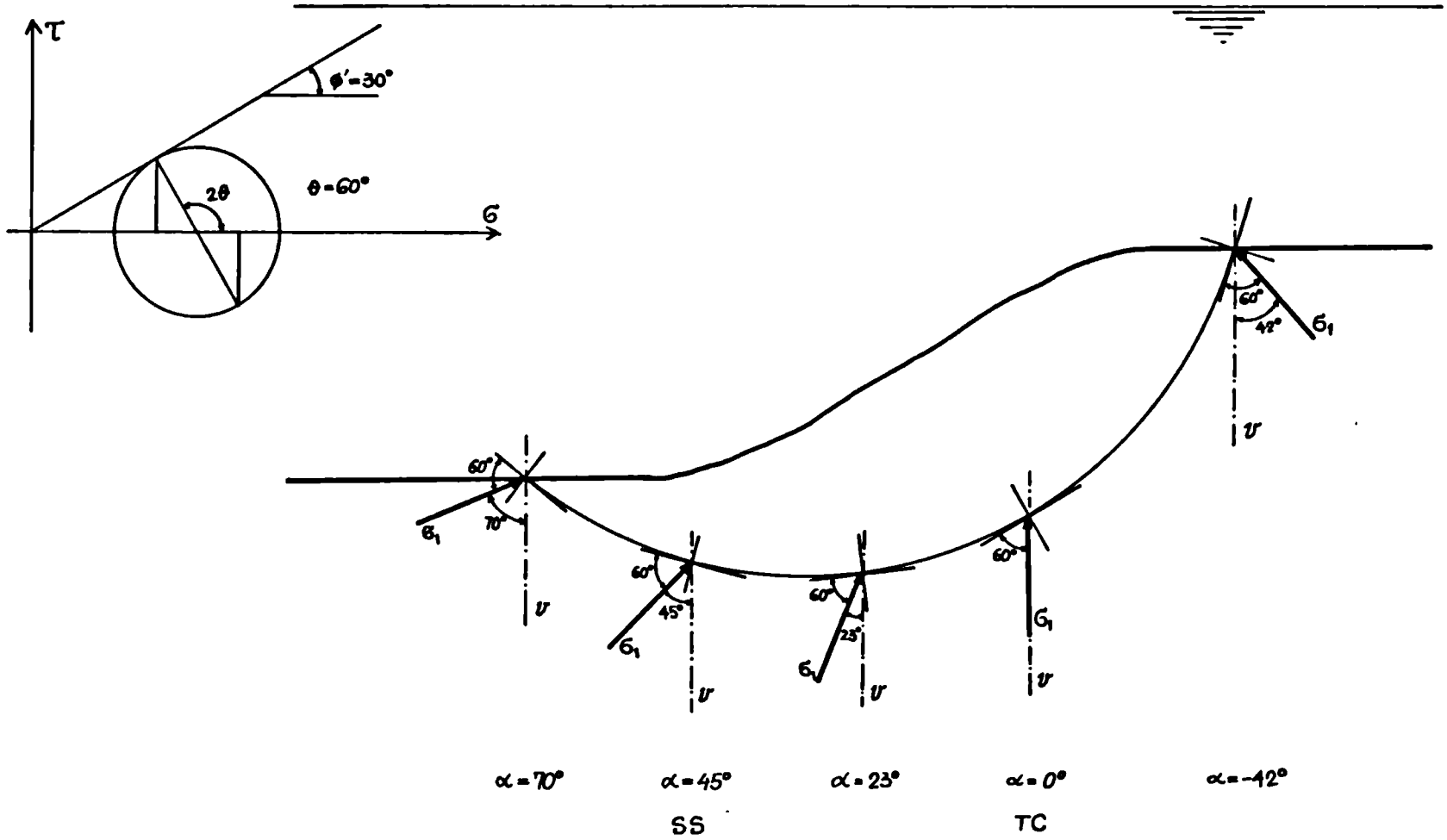


Fig.8.27 - Principal stress rotations in the failure surface of a slope

Appendix III

III.1. Thin sections

To gain a qualitative insight into the mechanical behaviour of HPF4, its microstructural characteristics were observed from thin sections. Fabric analyses from this sections at Imperial College have been done in the past mainly on clayey materials (Tchalenko, 1968; Menkiti, 1995). For this study thin sections were obtained from two triaxial samples prepared in stress path cell.

The usual procedure of submerging the sample in Carbowax (polyethyleneglycol), melted to 60°C, was used (Tchalenko, 1967). One of the triaxial samples was impregnated with wax after it had just been set up in a split mould and saturated with a mean effective stress of ~30 kPa. This sample therefore represents the "initial structure" (IN) of HPF4. The other sample had been subjected to K_o consolidation with p'=200 kPa and then quickly unloaded undrained before taken out from the cell and submerged in Carbowax. This sample therefore represents the structure after it has been anistropically consolidated. The samples were left in Carbowax for four weeks, so that the wax had sufficient time to fully penetrate into the samples pores. Subsequently the samples were taken out of the wax bath and left for 24 hours for the carbowax to cool down and harden. Thin sections from both samples were cut following the scheme shown in Fig.III.1, where *V1* and *V2* are vertical sections in two orthogonal directions and *H* is a horizontal cross section.

The thin sections are first used to quantify the particle shape and size of HPF4 silt by some standard methods.

Plate III.1 shows the silt particles at 400 times magnification. One division on the scale shown with the photographs represents 0.01 mm. On the basis of 50 particles seen against Krumbein's chart (Chart III.1) and Rittenhouse's chart (Chart III.2), the following are estimated:

- The roundness of the silt particles ranges from 0.0 to 0.2 and on average is 0.11.
- The sphericity of the particles is in the range 0.45 to 0.8, being on average 0.625.

These parameters show that HPF4 silt particles are highly angular and elongated.

For comparison, free Ham River Sand particles, at 63 times magnification, are presented in Plate III.3. According to this classical particle shape classification, the roundness is 0.4 and sphericity 0.772 (Kolbuszewski, 1948), characterizing HRS particles as subrounded and subangular.

The third parameter used in this study to characterize particle shape of HPF4 is the axial dimension ratio $\bar{n}$, defined by Oda (1972). As discussed in Chapter 2 (Section 2.7.5), $\bar{n}$ is the average sum of the shortest and longest axis ratio, measured for a certain number of particles. The average $\bar{n}$ value for 50 particles of silt HPF4, as measured from the thin sections, is 0.484. Recalling that $\bar{n}$=1.0 indicates spherical particles, while $\bar{n}$=0.0 corresponds to an infinitely thin bar, the $\bar{n}$=0.484 result corresponds to elongated particles.

It was not intended in this research to study in detail microstructure of HPF4. The minimum magnification of 63 times was not sufficient to show the picture of structural chains of particle contacts from the top to the bottom of the sample. However, thin sections have been looked at 250 times magnification to gain an impression of the local distribution of interparticle contacts. Plate III.2 shows a vertical thin section of K_o consolidated sample. On a diagram are drawn the observed interparticle contacts: the particular feature of this structure are clusters of contacts joined at one point. This is consequence of the angularity of the particles and indicates interlocking potential of HPF4, which can have a significant influence on material strength.

III.2. Improvement of the electrolevel devices

Electrolevel devices record changes in tilt and are used in the HCA for measuring axial and torsional shear strains. Their operating range is ±30° of tilt. For the axial device, the reference length between the pads attached to the sample (Fig.3.8) is approximately 120 mm and the output signal sensitivity is typically ~0.030 V/mm.

The old electrolevel wiring and signal conditioning system inherited by the Author at the beginning of this research programme were reaching the end of their useful life and the Analog to Digital conversion circuits and computer logging facilities were replaced completely. However, the new arrangements produced an unacceptable scatter of up to ±10 mV in the electrolevel output signals. For the axial strain devices this resulted in a scatter in strain of ±0.3%, i.e.

$$0.030\ V \equiv 1.0\ mm$$

$$\pm 0.010\ V \equiv \pm 0.33 mm$$

$$\Delta\varepsilon_a = \pm\frac{0.33}{120}x100 \simeq 0.3\%$$

They also showed occasional extreme voltage "spikes". A series of steps was taken to

improve their performance.

III.2.1. Scatter

In order to reduce the data scatter it was first necessary to establish whether it was the sensor itself or the signal conditioning/data acquisition system that was unstable. To achieve this, resistors were plugged into the instrument sockets instead of the electrolevel devices. The high level of output scatter remained, indicating that the signal conditioning arangements were 'unstable'. The first step in solving the problem was to improve data transmission facilities. In the old set up all analogue output signals from the electrolevel M/D box were transmitted to the A/D converter via a single multi-core cable. This resulted in electrical 'cross-talk' between the various wires in the cable which in turn resulted in high output scatter. To cure this, the multi-core cable was replaced by individual cables linking each of the 6 transmission cards in the M/D box with the A/D unit. This resulted in the output scatter reducing to ±0.4 mV, giving a stability of axial strain measurement of ±0.01%, i.e.

$$\pm\ 0.00040\ \text{V} \equiv \pm\ 0.0132\text{mm}$$

$$\Delta\varepsilon_a = \pm\frac{0.0132}{120}\text{x}100 \simeq 0.01\%$$

Further improvement of the output signal was achieved through the computer control program by introducing numerical averaging. For each reading of the electrolevel transducers a number of sequential readings was taken and the average value found. Fig.III.2 shows how scatter reduces as the number of readings contained in each average value is increased. Set of 10 readings was adopted for each average because this gives typical repeatability in voltage of ±0.05 mV over a period of hours, which amounts to ±0.0014% strain, while keeping a total reading time for the whole suite of transducers to an acceptable 23 sec. Although an increase in the number of readings taken for the averaging would reduce scatter further, the time taken for each data set to be recorded would severely slow the system down and would affect the required testing rates.

III.2.2. Spikes

Jardine (1988) observed that electrolevel devices can produce an unstable "spiky" response even when the energisation voltage applied to the electrolyte capsule is well within the manufacturers recommended working range (which allows up to 12V to be applied). The electrolyte warms-up and condenses on the electrodes. Small droplets form and eventually drop

from the electrode back into the reservoir of electrolyte. This causes a sudden jump in the output reading. Reducing the voltage avoids this problem and in the new system the energisation current was set at only 0.5 V, with the modulator/demodulator amplifier setting being increased to avoid any overall loss of sensitivity.

Another problem causing spikes was found in the modulator/demodulator signal conditioning unit. The relay switching (Section 3.4.4) between the two electrolevel axes was initially powered from the power supply in the M/D box itself. Unfortunately this was not always sufficient to open or close all the relays completely at the same time. To overcome this problem the relays were powered from the power supply on the PC I/O card. Power was transferred to the M/D via a cable and a transistor driver installed on the I/O card.

The above changes completely solved the problem of the occurrence of irregular spikes from the output signals.

III.2.3. Assessment of strain measurement

A typical stress-strain curve from the HCA test, in which the strains are plotted in terms of the raw voltage output, is presented in Fig.III.3a. An enlarged view of the early part of this curve is given in Fig.III.3b. At the end of a stage of the stress path (i.e. consolidation, shearing, b_change or α_change) the loads applied to the sample are maintained constant for sufficient time for any creep to stabilise. Only when the creep rate has reduced to 0.05 %/day was the next stage of the stress path activated. Before the first load step of a new stage is applied, several readings of the transducers are taken so that the start of the new stage can be accurately established. This is necessary as there is some small scatter in the readings (here ±0.02 mV) and the average value is more accurate. Such readings can be seen in Fig.III.3b as the group of data points at the beginning of the stress-strain curve. Such scatter in the readings also occurs during subsequent loading. As the scatter is of an almost constant magnitude, it has a greater affect on the early readings than those taken later. Consequently, for the small strain region, typically for changes in strain <0.1% from the start of any stage, an averaging process is implemented. This is performed manually. The data is plotted, as shown in Fig.III.3b, and the best fitting trend line is drawn through the data points by eye. The accuracy of individual readings is given by the maximum deviation of the data points about the average curve. The data in Fig.III.3b indicates scatter of ±0.02 mV, which is equivalent to $\Delta\varepsilon \approx \pm 0.00055\%$. This is typical for the results presented in this thesis. It is estimated that the trend line is reliable to within 1/5 of the scatter,

i.e. 0.00011% strain. If the load cell is assumed to be perfect (i.e. there is no scatter in load application), then the stiffness may be calculated from the trend line with 11% accuracy at 0.001% strain, and 1.1 % accuracy at 0.01% strain.

The same conclusion applies to electrolytic torsional shear strain devices.

Triaxial stress-strain data are interpreted in the same way, Fig.III.4. However, the scatter produced by pendulum devices is bigger than of electrolytic transducers, being typically ±0.0006 mm for ~40 mm gauge length (i.e. $\Delta\varepsilon_z$=±0.0015%). Reliability of the averaged trend line is also estimated to 1/5 of the scatter, i.e. 0.0003% strain. If so, with the same assumption as above about the load cell, stiffness at 0.001% strain is determined with ~30% accuracy, while at 0.01% strain with 3% accuracy.

III.3. Computer control and data acquisition system

III.3.1. The electronic instrument system

As described in many electronics text books (for example, Dally et al., 1993), a complete electronic instrument system usually consists of all or some of the following elements:

A *transducer* is an analogue device which converts the physical quantity being measured into an electrical quantity. For example, a strain gauge sensor attached to a sample converts a change in strain into the change in electrical resistance of the gauge. This change in resistance is then converted into a change of voltage.

A *power supply* generates the energy to drive the transducers. Two types of power supply can be used, depending on the energy required to drive a transducer: constant DC (direct) current source and AC (alternating) current source.

A *signal conditioner* is an electronic circuit that converts, or manipulates, the output from the transducer into a more usable electrical quantity. A Wheatstone bridge is, for example, used to convert change in resistance from a strain gauge sensor into a change of voltage. Other types of signal conditioners are filters, modulators, demodulators, compensators, etc.

Amplifiers are required in the system when the voltage output from the transducer's signal conditioning circuit is low and needs to be increased before being measured with the

voltage measuring devices used in the system.

Recorders are voltage measuring devices used to display the measurement in a form that can be read and interpreted. Recorders may be analogue or digital. An oscilloscope is an example of a analogue recorder. Digital recorders take an analogue signal and covert it to a digital code which is then numerically displayed. These recorders have their own analogue to digital converter which takes the voltage from the acquisition system as an input and converts it to an equivalent digital code. Once digitized, the signal can be displayed, processed, stored or transmitted.

III.3.2. Conversion process

Digital systems contain many logic switches which can have only two states, *on* or *off*. Therefore, a digital word is a combination of binary elements (bits) which are either 0, for *off*, or 1 for *on*. The first bit in a digital word is the Most Significant Bit (MSB) and the last is the Least Significant Bit (LSB). For example, a four-bit digital word can have a combination of bits like *1010*. The LSB has a weight of 2^0, the next bit 2^1, the next 2^2, and the MSB (with position m in a word) has a weight 2^{m-1}. The sum of all the weights for given binary combination of 0s and 1s in a digital word is its count (C) for that combination. The maximum number of combinations (counts) of 0s and 1s in an n-bit digital word is 2^n, ranging from C=0 (where all bits in a word are 0) to $C_{max}=2^n-1$ (where all bits in a word are 1). Table III.1 shows an example of all combinations for a 4-bit digital word, which are 16 in total, ranging from 0 to 15 (Dally et al., 1993).

The resolution R of a digital word containing n bits can be written as:

$$R = \frac{2^0}{2^n - 1} = \frac{1}{C_{max}} \times 100 \quad (\%) \qquad \text{(III.1)}$$

When an analog signal is converted into a digital number, the maximum resolution that can be achieved with an n-bit digital word is R times the full scale analog signal input (FSV). According to Eq.III.1 this resolution reduces in magnitude with increasing number of bits in a digital word.

Table III.1: Equivalent Count for a 4-Bit Binary Code

MSB	Bit 2	Bit 3	LSB	MSB		Bit 2		Bit 3		LSB		Count
0	0	0	0	0	+	0	+	0	+	0	=	0
0	0	0	1	0	+	0	+	0	+	2^0	=	1
0	0	1	0	0	+	0	+	2^1	+	0	=	2
0	0	1	1	0	+	0	+	2^1	+	2^0	=	3
0	1	0	0	0	+	2^2	+	0	+	0	=	4
0	1	0	1	0	+	2^2	+	0	+	2^0	=	5
0	1	1	0	0	+	2^2	+	2^1	+	0	=	6
0	1	1	1	0	+	2^2	+	2^1	+	2^0	=	7
1	0	0	0	2^3	+	0	+	0	+	0	=	8
1	0	0	1	2^3	+	0	+	0	+	2^0	=	9
1	0	1	0	2^3	+	0	+	2^1	+	0	=	10
1	0	1	1	2^3	+	0	+	2^1	+	2^0	=	11
1	1	0	0	2^3	+	2^2	+	0	+	0	=	12
1	1	0	1	2^3	+	2^2	+	0	+	2^0	=	13
1	1	1	0	2^3	+	2^2	+	2^1	+	0	=	14
1	1	1	1	2^3	+	2^2	+	2^1	+	2^0	=	15

The analogue to digital conversion process will be shown by using the example of 4-bit digital word. Fig.III.5 presents an analog-to-digital converter (A/D), with the analog voltage ranging as the independent variable from zero to the full scale analog voltage, FSV. If this is to be represented by a digital word consisting of 4 bits then we have 16 discrete values. Since all voltages between 0 and FSV can exist, they must be subdivided into successive subranges each of which is associated with one of the 16 discrete digital values. Consequently each subrange contains a band of voltages of length equal to FSVxLSB, where LSB=2^{-n}. In the present 4-bit A/D, each subrange is of length equal to 0.0625 FSV (i.e. (1/16)FSV). All analog voltages within the same subrange are represented by the same value of the digital word. Fig.III.5 shows that the value of the digital word corresponds to the midpoint of each subrange. So, the uncertainty of the conversion process, which replaces the linear analog output with a staircase function, is ±(1/2)(LSB) and this conversion error is shown at the top of Fig.III.5. Clearly the conversion error decreases with increasing number of bits in the binary word, because the subranges become smaller and the conversion process is closer to a linear analog function.

For a 16-bit resolution system employed in the HCA, absolute accuracy limit is 1/65535 of the full scale range (compared to 1/16 for 4-bit resolution).

III.3.3. Data distribution

After conversion from an analogue voltage to a digital code is completed, the digital code is stored in a register until it is needed by the system. The transmission of the digital code from the A/D register to another component in the digital system is performed via a data bus. This bus can either be of a parallel or serial type.

A parallel data bus consists of a series of parallel wires, one wire for each bit, which connects the register to the display driver. The use of such a parallel bus structure is the preferred approach if the analogue instrument is close to the processor. However, sometimes the A/D and the processor are too far apart for a parallel bus structure to be effective and single wire transmission is required. In this case the data are transmitted in a serial manner.

One of the most common serial bus structures is called RS232. Here a single transmitter sends one bit (0 or 1) of information at a time to a single receiver. This method is used when data transfer rates are low or when data must be transferred over long distances. It is popular to use because most personal computers have at least one RS232 port and the A/D is then simply "plugged in" as a printer, for example. Transmission of data with this serial protocol is illustrated in Fig.III.6 by a train of bits that include the leading idle bits, the start bit, the character bits, the parity bit, the stop bit and the trailing idle bits. The start bit is the first bit in the transmission sequence; the parity bit ensures that the correct number of character bits have been sent and received; the stop bit signifies the end of transmission. In addition to this, for RS232 transfer, baud rate, hardware and software handshakes have to be defined too.

The major disadvantage of the RS232 is its relatively low baud rate (i.e. transmission rate). For the Datascans the maximum rate is only 19K bits per second.

For the HCA system, Datascan baud rate is 9.6K, which is satisfactory for the rates of testing required.

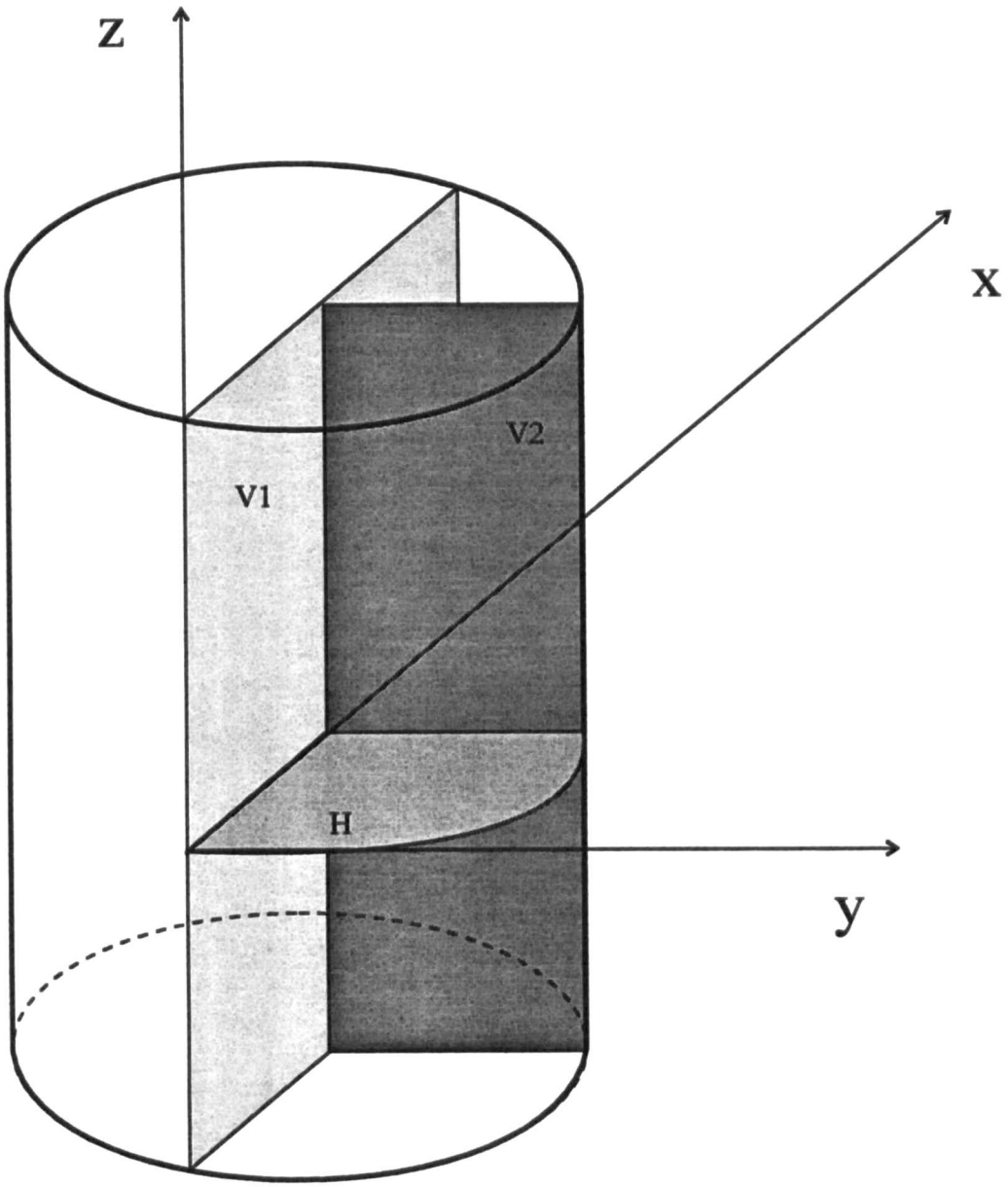


Fig.III.1 - Scheme for cutting thin sections from triaxial sample

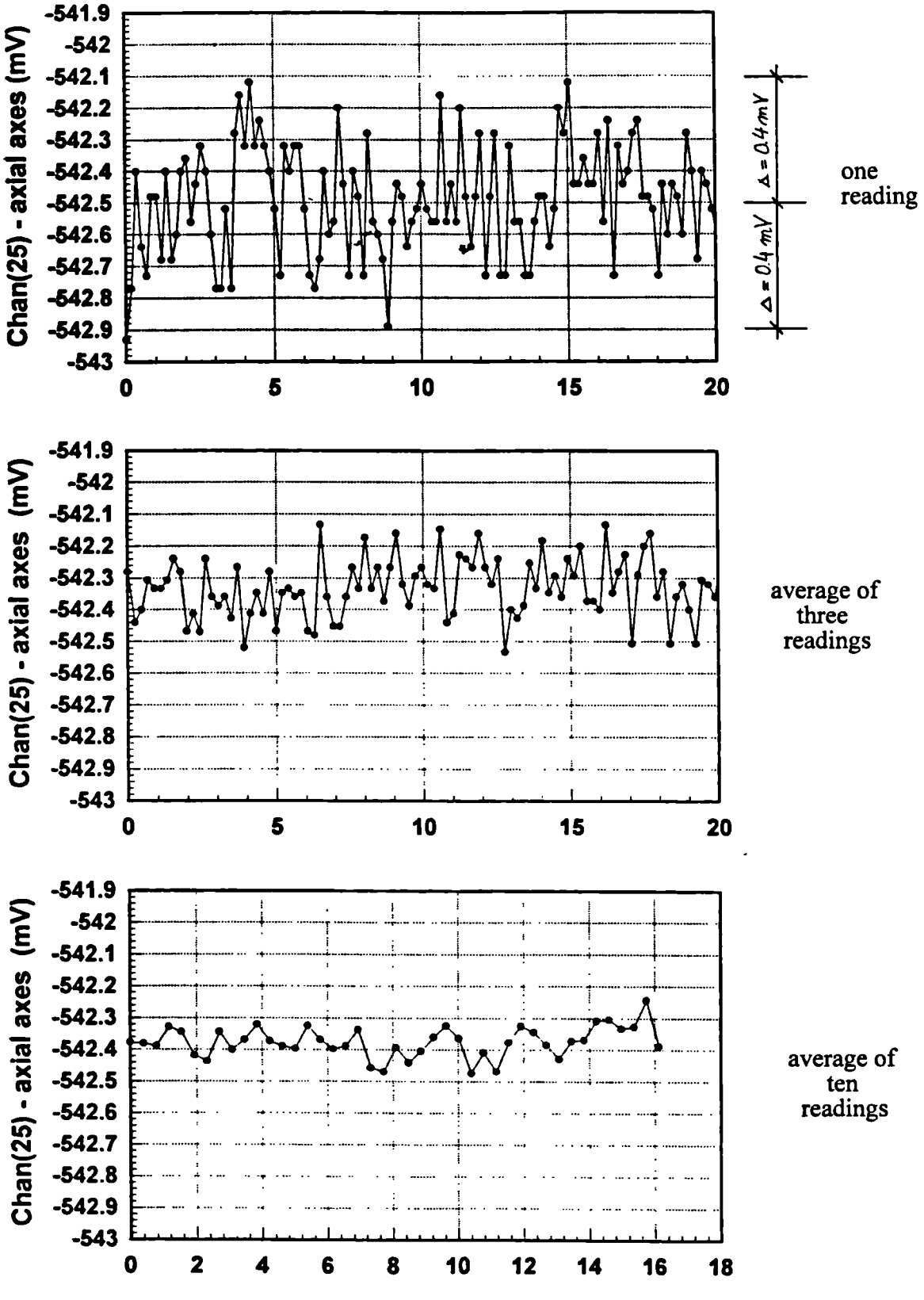


Fig.III.2 - Influence of numerical averaging on the scatter of electrolytic transducers

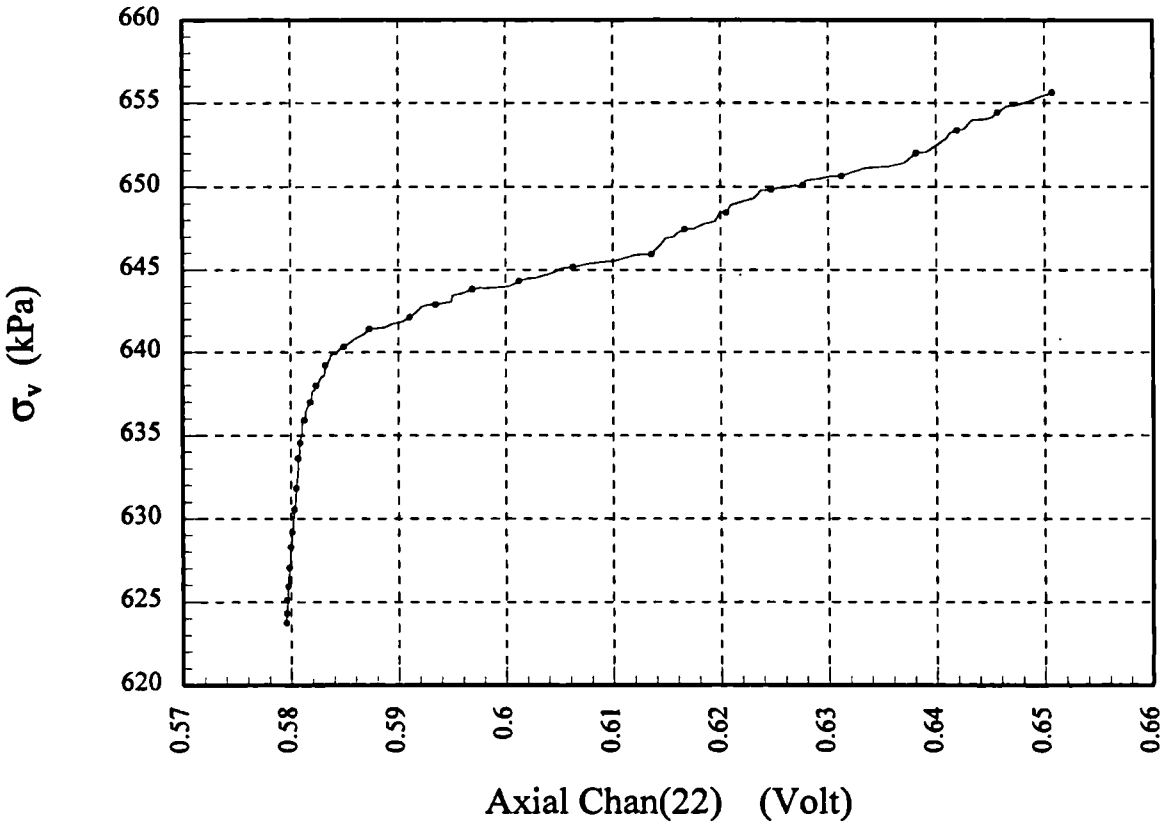


Fig.III.3a - Typical scatter of stress-strain curve for electrolytic type transducers

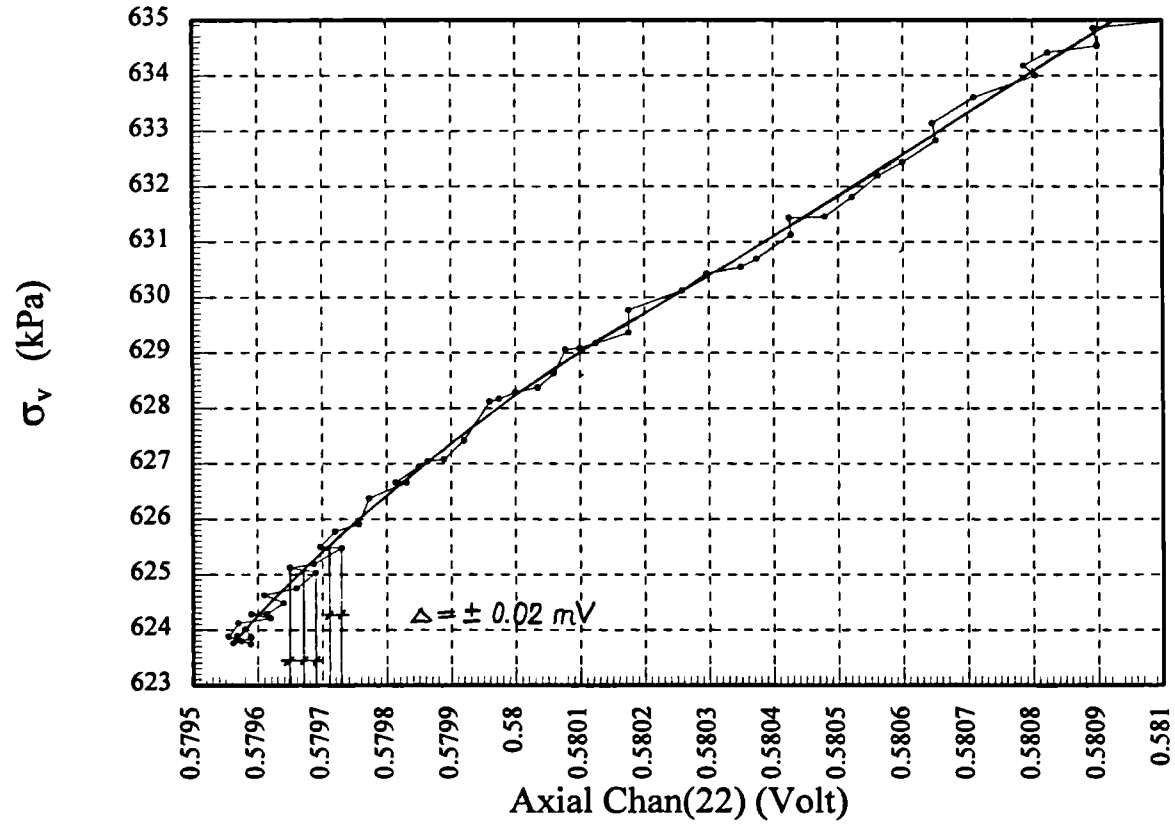


Fig.III.3b - Typical scatter of stress-strain curve for electrolytic type transducers, enlarged small strain view

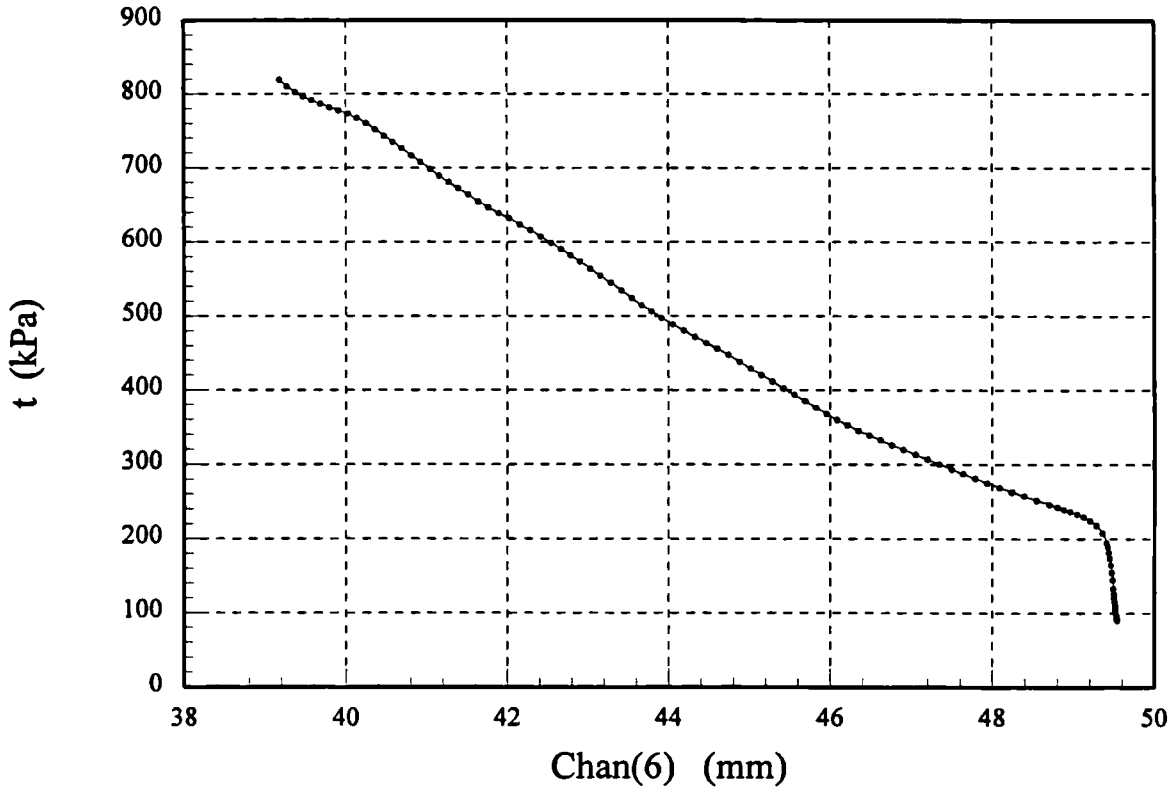


Fig.III.4a - Typical scatter of stress-strain curve for pendulum devices

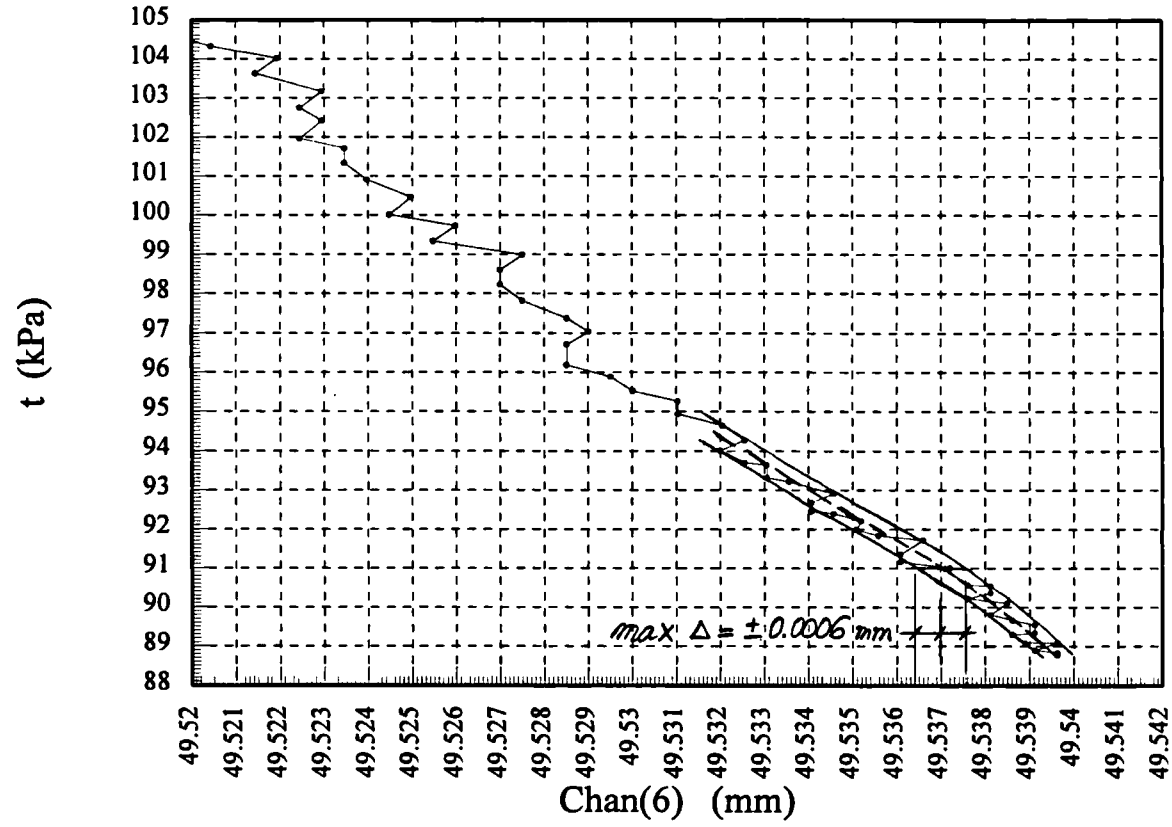


Fig.III.4a - Typical scatter of stress-strain curve for pendulum devices, enlarged small strain view

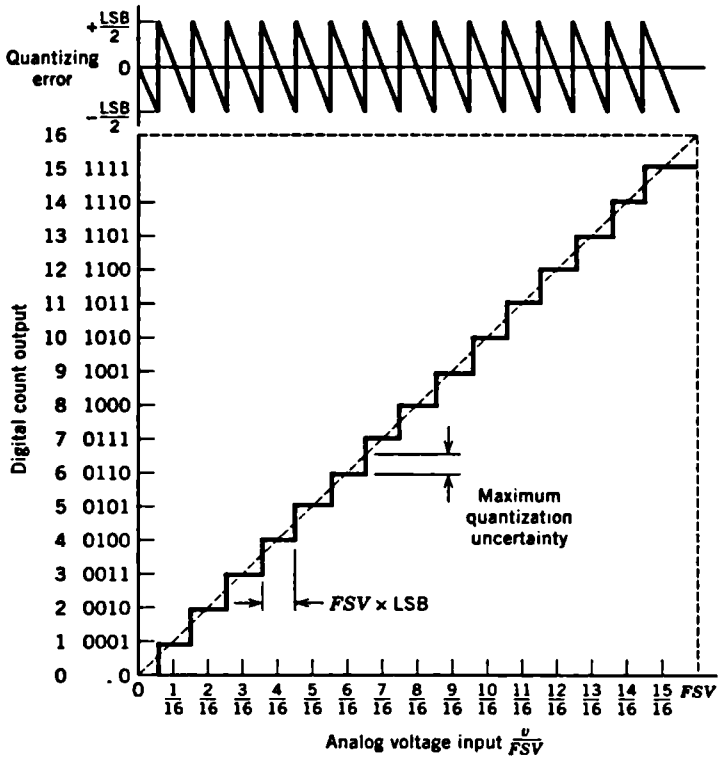


Fig.III.5 - Analog to Digital conversion proces
(from Dally et al., 1993)

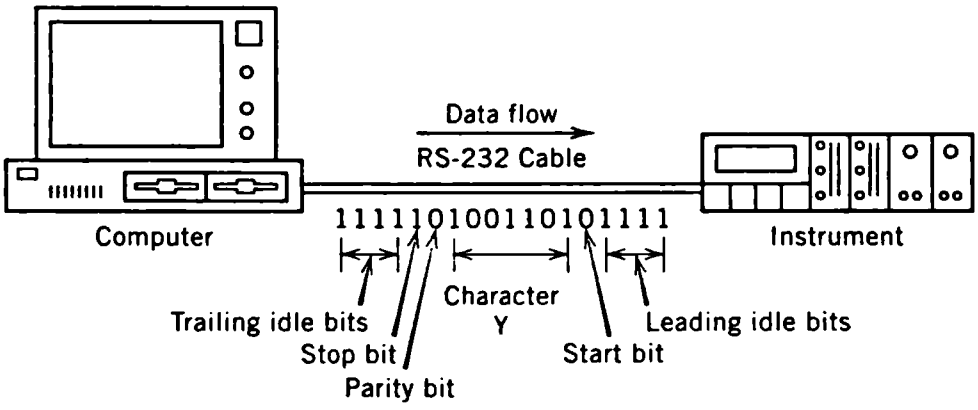
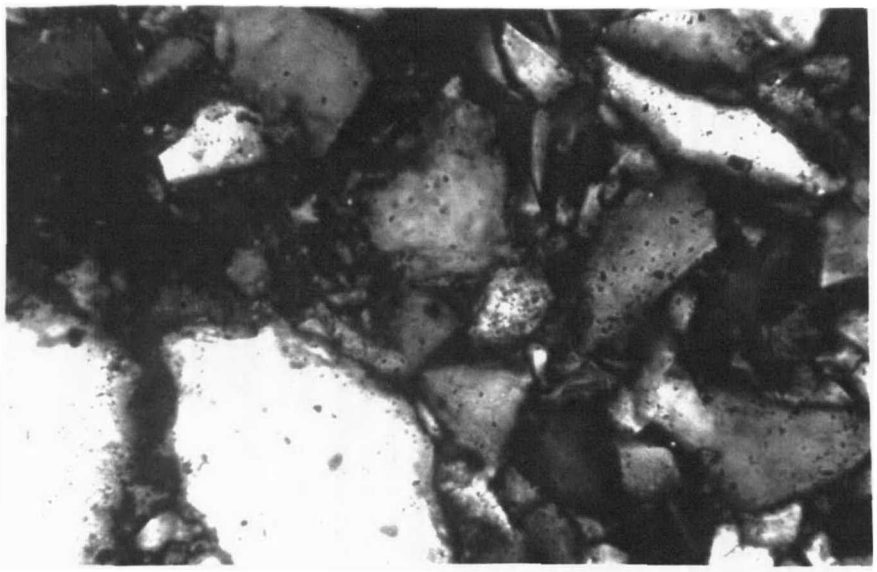
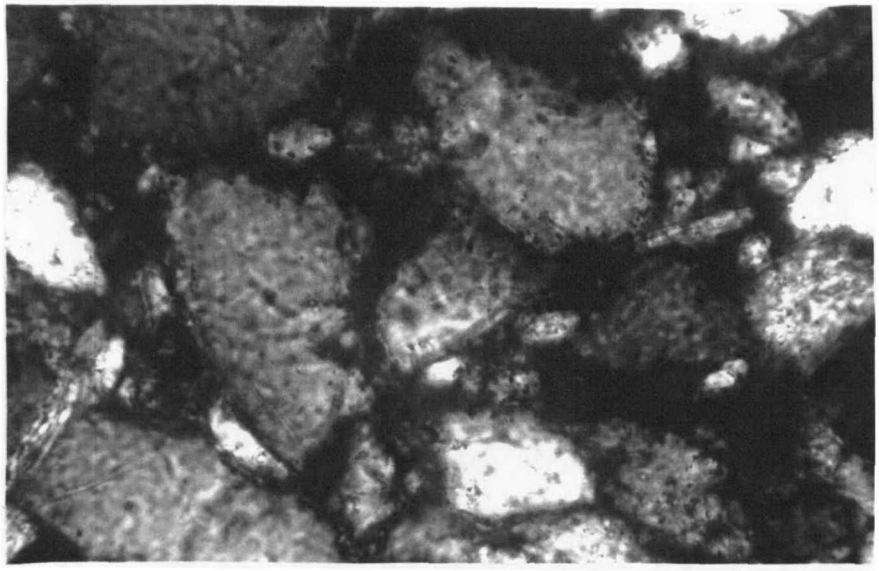


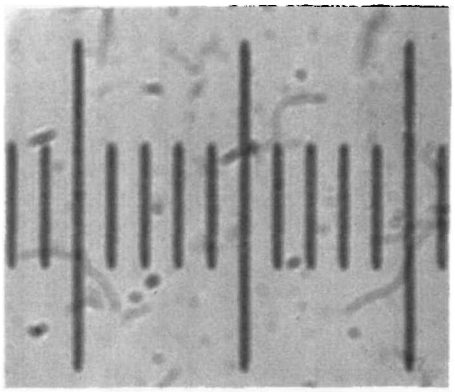
Fig.III.6 - Transmission of data with serial protocol
(from Dally et al., 1993)



IN-V1

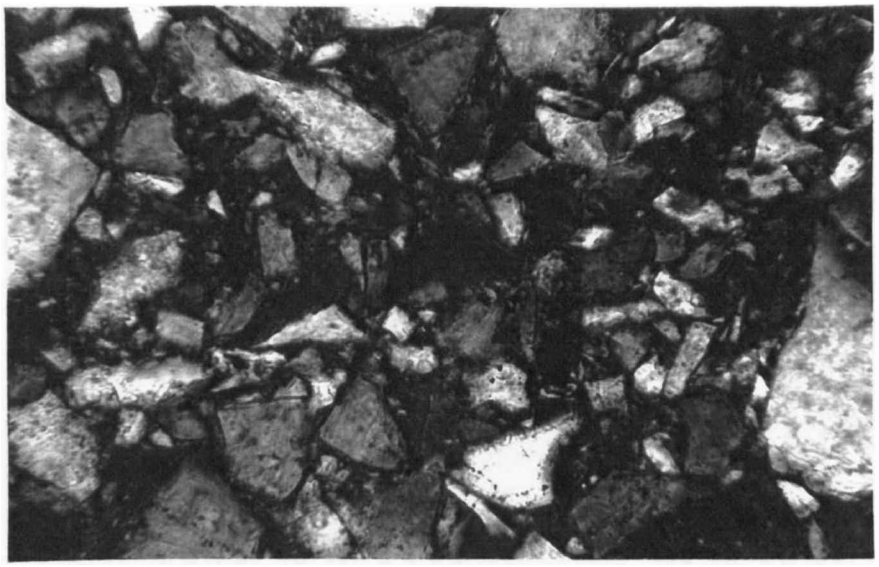


IN-V2

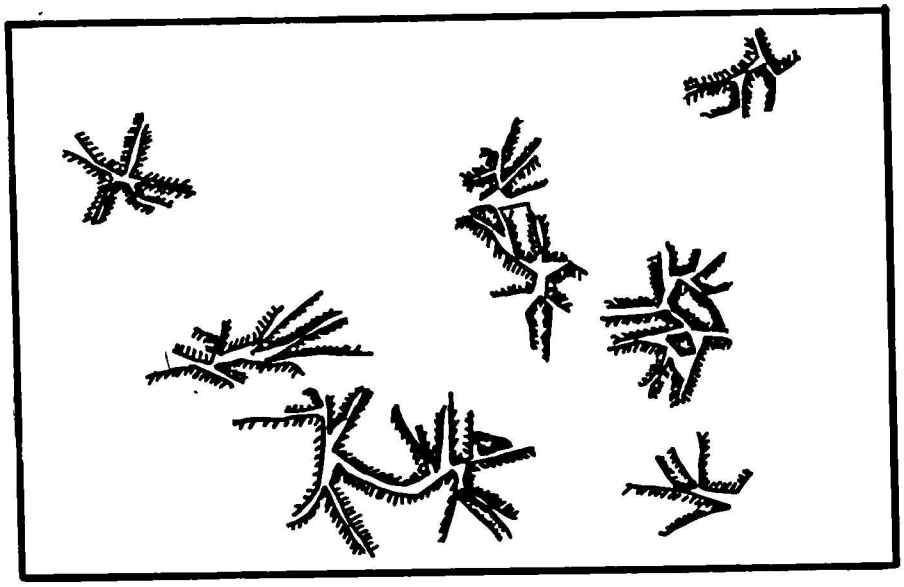


scale
400x magnification
1 div = 0.01 mm

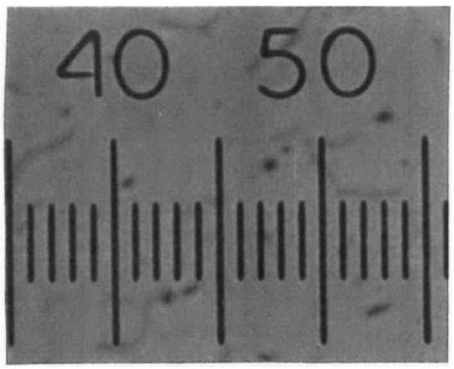
Plate III.1 - HPF4 particles at 400 times magnification,
(from two vertical cross-sections)



Ko-V1

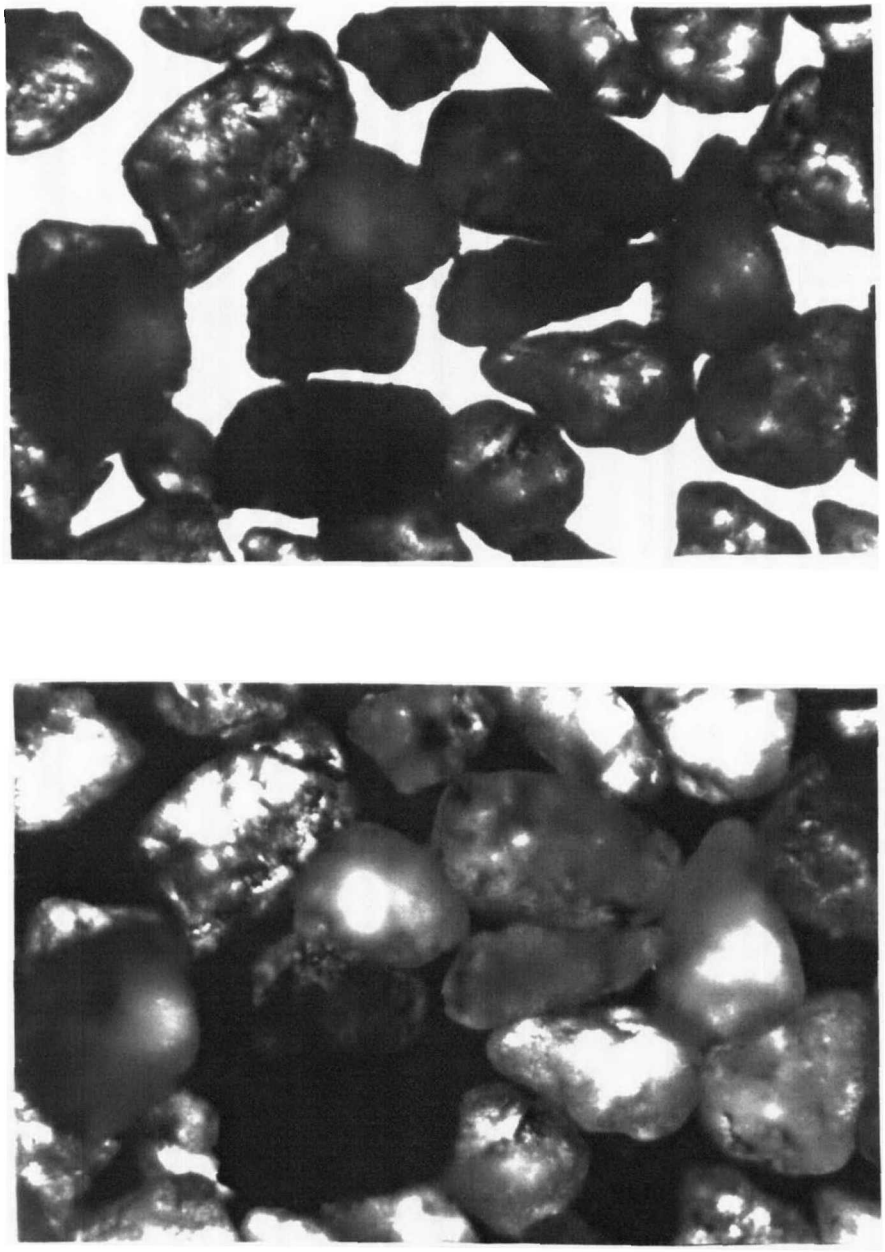


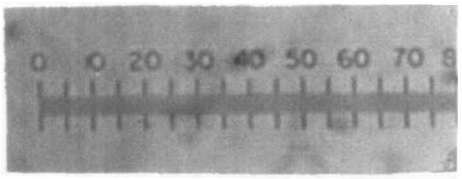
Tracing of particle contacts from the above image



scale
250x magnification
1 div = 0.01 mm

Plate III.2 - HPF4 particles at 250 times magnification,
(from vertical cross-sections)





scale
63x magnification
1 div = 0.01 mm

Plate III.3 - HRS particles at 63 times magnification,
at two orthogonal polarizing lights

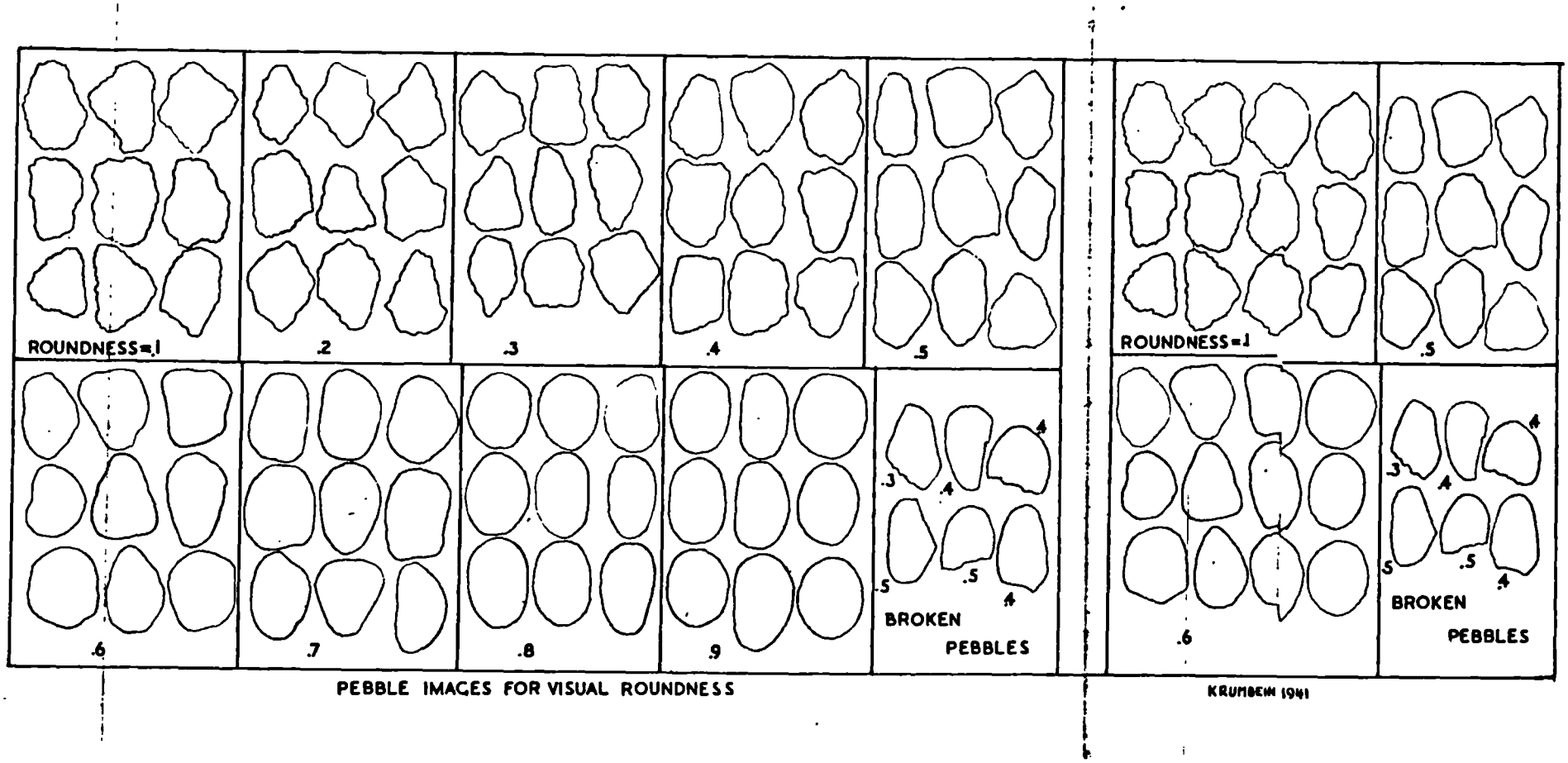


Chart III.1 - Chart for determining visually roundness of projected particles (Krumbein, 1941)

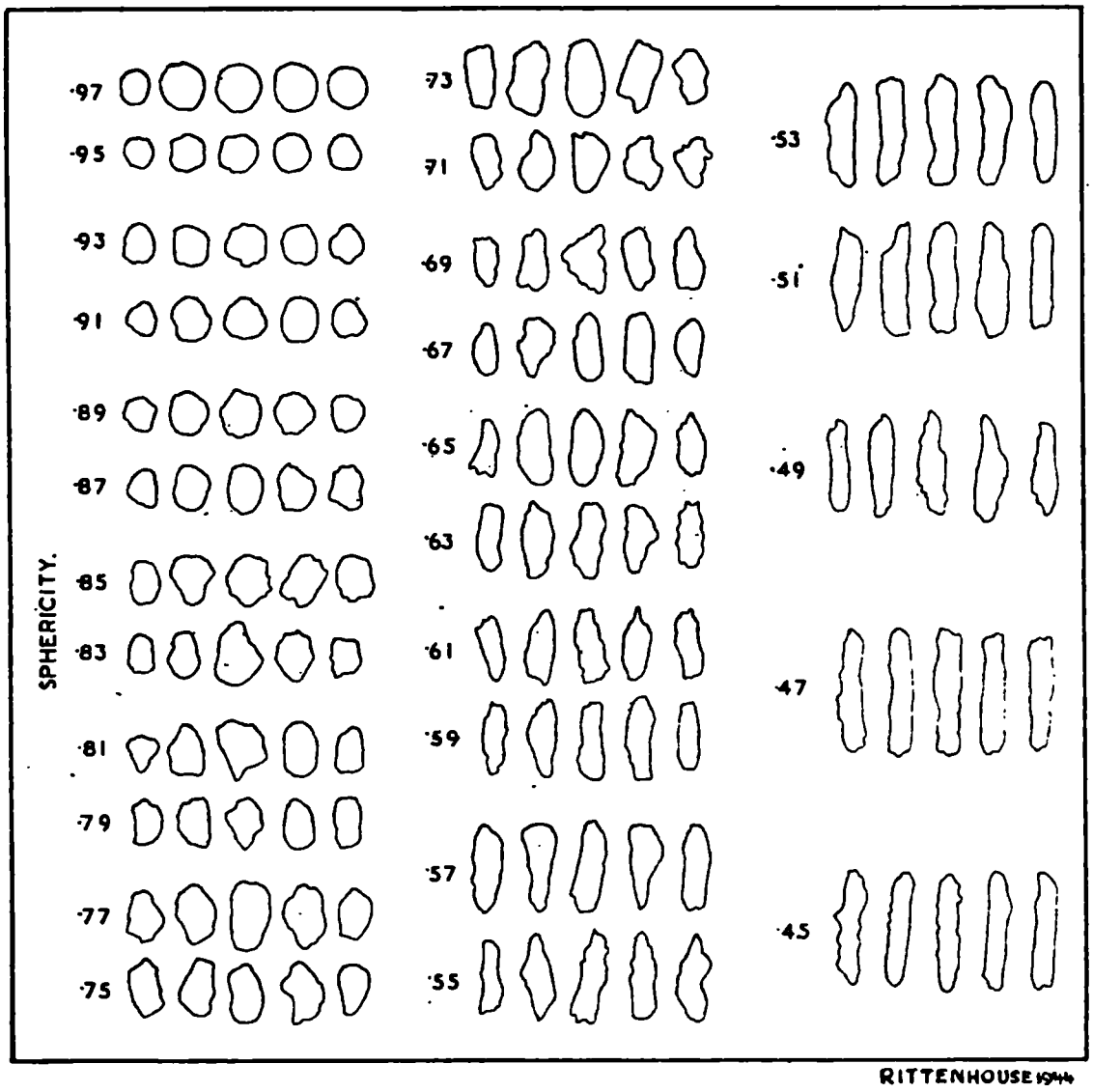


Chart III.2 - Chart for determining visually the projection sphericity of sands and other particulate materials (Rittenhouse, 1944)

Appendix V

Appendix V.1. Principal stress increment direction in α_rotation stage

The principal stress increment direction is defined from the stress components in the form:

$$\alpha_\sigma = \frac{1}{2}\operatorname{atan}\frac{2d\tau_{\theta z}}{d\sigma_z - d\sigma_\theta} \tag{V.1}$$

In an α-rotation stage, the control parameters are held such that:

$$p = \text{const}$$

$$t = \text{const}$$

$$b = \text{const}$$

$$\alpha_\sigma \text{ is changing}$$

The component stresses are expressed in terms of the control parameters:

$$\begin{aligned} \sigma_z &= p - t\left[\frac{2b-1}{3} - \cos 2\alpha_\sigma\right] \\ \sigma_\theta &= p - t\left[\frac{2b-1}{3} + \cos 2\alpha_\sigma\right] \\ \tau_{\theta z} &= t \sin 2\alpha_\sigma \end{aligned} \tag{V.2}$$

Their derivatives are:

$$\frac{d\sigma_z}{d\alpha_\sigma} = -2t \sin 2\alpha_\sigma \tag{V.3}$$

$$\frac{d\sigma_\theta}{d\alpha_\sigma} = 2t \sin 2\alpha_\sigma \tag{V.4}$$

$$\frac{d\tau_{\theta z}}{d\alpha_\sigma} = 2t \cos 2\alpha_\sigma \tag{V.5}$$

Substituting (V.3) to (V.5) into (V.1) gives:

$$\tan 2\alpha_\sigma = -\frac{1}{\tan 2\alpha_\sigma} \tag{V.6}$$

or:

$$\frac{\sin 2\alpha_{\dot{\sigma}}}{\cos 2\alpha_{\dot{\sigma}}}\frac{\sin 2\alpha_{\sigma}}{\cos 2\alpha_{\sigma}}=-1 \qquad (V.7)$$

If:

$$\sin 2\alpha_{\sigma}\sin 2\alpha_{\sigma}=-\frac{1}{2}[\cos(2\alpha_{\dot{\sigma}}+2\alpha_{\sigma})-\cos(2\alpha_{\dot{\sigma}}-2\alpha_{\sigma})]$$
$$\cos 2\alpha_{\dot{\sigma}}\cos 2\alpha_{\sigma}=\frac{1}{2}[\cos(2\alpha_{\dot{\sigma}}+2\alpha_{\sigma})+\cos(2\alpha_{\dot{\sigma}}-2\alpha_{\sigma})] \qquad (V.8)$$

then substituting (V.8) into (V.7) leads to:

$$\cos(2\alpha_{\dot{\sigma}}-2\alpha_{\sigma})=0 \qquad (V.9)$$

and

$$\alpha_{\dot{\sigma}}=\alpha_{\sigma}\pm\frac{\pi}{4} \qquad (V.10)$$

V.2. Simulation of triaxial tests in the HCA

Undrained compression and extension tests of K_o consolidated Ham River Sand (HRS) were performed in the Hollow Cylinder Apparatus in order to be compared with appropriate stress path triaxial tests performed by Ovando-Shelley (1986).

V.2.1. Consolidation

The initial void ratio achieved in the HCA was 0.75. Ovando-Shelley's tests performed in the stress path cell were slightly looser, with e_o=0.79.

Samples were consolidated under the same conditions as in the stress path cell: 200 kPa mean effective stress, under a back pressure of 400 kPa. The K_o was 0.5 for both soils.

V.2.2. Stress paths and strength

The effective stress paths for two HCA tests are presented in Fig.V.1 and, for comparison, effective stress paths from stress path cell are shown in Fig.V.2. At first sight, HCA stress path in compression seems to be slightly more contractant then the TXL one.

However, both sets of tests generate similar frictional resistances ϕ' at the PTPoints (Table V.1).

Table V.1: Comparison of HCA and SPC triaxial tests

TEST	HCA		TXL	
	e_o	ϕ'	e_o	ϕ'
K_o-com	0.75	32.8°	0.79	33.4°
K_o-ext	0.75	26°	0.79	26.4°

* SPC stands for stress path cell

V.3. Undrained triaxial compression of isotropically consolidated HPF4

Only one isotropically consolidated HPF4 sample was tested in the triaxial stress path cell, to give a brief comparison of the influence of isotropic and K_o consolidated structure on a subsequent shear. The sample was formed in the same way, from slurry, as in the main triaxial test series on K_o consolidated samples.

V.3.1. Isotropic consolidation

An HPF4 sample of initial void ratio 0.66 was isotropically consolidated to a mean effective stress, p', of 200 kPa, under a back pressure of 400 kPa (the same conditions as for K_o consolidated samples).

The same rate of volumetric strain during consolidation was applied (~1.0 %/day). Its relation to axial strain in Fig.V.3, i.e. $\varepsilon_{vol}/\varepsilon_z=3$, shows that consolidation was essentially isotropic.

The compressibility plot in Fig.V.4, *e-lnp'*, is compared with the curve for K_o consolidated sample to OCR=1.0. The changes in *e* are the same for both consolidation paths; the curves are closely parallel to each other.

V.3.2.Stress path and strength of isotropically consolidated sample

The compression effective stress path in Fig.V.5 shows similarly dilatant behaviour to the K_o normally consolidated sample, without exhibiting a distinct peak. However, it shows a

markedly larger reduction in p' (~40%) with increasing t, than the corresponding K_o consolidated sample (Chapter 4).

The mobilised frictional resistance at the PTPoint is ~31°, compared to 32° for the K_o consolidated sample.

V.4. Mechanism of fabric evolution in granular media

V.4.1. Development of Distinct Element Method

A granular medium is composed of distinct particles which displace independently from one another and interact only at contact points. This discrete character of the medium results in a complex behaviour during loading and unloading, which makes it difficult for constitutive relationships to be established.

The main feature of a granular medium is that particles form a structure which is in equilibrium with initial stage of external forces and then continuously changes under applied loads. The difficulty is that the stresses inside the sample, i.e. on particle's contacts, cannot be measured and have to be estimated from boundary conditions, although strains may be measured nowadays using X-ray techniques.

To reduce the level of uncertainties regarding the internal stresses in granular media, models have been developed which treat geometrically simpler particles whose stresses and strains can be calculated and measured. These models consist of assemblies of discs or spheres and can be analyzed physically or numerically.

One of the models which deals with ideal discs is the Distinct Element Method (DEM), developed by Cundall (1978) and Cundall & Strack (1979). In the DEM, the equilibrium forces and displacement at contacts of a stressed assembly of discs are found through a series of calculations tracing the movements of the individual particles. This movement is defined to be a dynamic process as a result of the propagation through the medium of disturbances originated at the boundaries.

If described as a dynamic process, it is obviously dependent on time over which velocities and accelerations are assumed to be constant. So, the idea is that time step can be chosen to be so small that during a single time step disturbances cannot propagate from any disc further than its immediate neighbours. Then, at all times, the resultant forces on any disc are determined exclusively by its interaction with the discs with which it is in contact. The calculations are made using Newton's second law for the discs and a force-displacement law for

contacts: the former gives the motion of a particle resulting from the forces acting on it; the latter finds contact forces from displacements, i.e:

$$\Delta F_n = k_n(\Delta n)_{t1} \qquad (V.11)$$

$$\Delta F_t = k_t(\Delta f)_{t1} \qquad (V.12)$$

Here, ΔF_n and ΔF_t are increments of normal and tangential contact force; k_n and k_t are the normal and tangential stiffness of particle contacts; $(\Delta n)_{t1}$ and $(\Delta f)_{t1}$ are normal and tangential components of displacement in time *t1*. This relationship models a contact by normal and shear springs with stiffness components k_n and k_p that are independent of particle size and act in compression only. Slip is assumed to occur when shear force, F_t, reaches a limiting value of $F_n tan\phi_\mu$. The detailed process of calculation of contact forces and displacements is given in Cundal (1978) and Cundal & Strack (1979).

This method was incorporated in program BALL (Cundall & Strack, 1979) and fabric generation through particle contacts was validated by comparison with photoelastic analysis on similar disc assembly (de Josselin de Jong & Verrujit, 1979). In photoelastic analysis the assembly of discs was placed between two vertical plexiglas plates and was loaded by means of two horizontal and two vertical rigid beams (see Chapter 2).

The purpose of verification was to compare force vector plots produced by BALL with those presented by de Jong & Verrujit. The verification is primarily qualitative, and, in interpreting the results, emphasis is placed upon visual comparison: Fig.V6 shows force vector plots obtained by photoelastic test, while Fig.V7 shows numerical reproduction of the same assembly by program BALL.

The results show good matching and prove that the DEM is a valid tool for fundamental research into the behaviour of granular assemblies.

V.4.2. Extension of program BALL to elliptical particles

Rothenberg & Bathurst (1989, 1992) used the same approach of plane discs to simulate, numerically and experimentally, mechanism of fabric evolution in granular media. They showed the effect of particle shape on the behaviour of planar granular assemblies by changing it from circular to elliptical disc assembly, as shown in Fig.V.8.

The core of their work is a stress-force-fabric relationship which links basic parameters of fabric (a, a_i and a_n) with indicator of material strength, ϕ':

$$\frac{\sigma_1-\sigma_2}{\sigma_1+\sigma_2} = \frac{1}{2}\frac{a+a_n+a_t}{1+\frac{aa_n}{2}} \qquad (V.13)$$

Parameter "a" defines anisotropy in contact orientations, i.e. ratio of number of vertical to number of horizontal contacts. The degree of anisotropy in granular assembly is a function of the geometrical particle arrangement which varies with strain. When deviatoric load is applied (without principal stress rotation) it preferentially increases the forces on contacts oriented perpendicularly to the major principal stress direction, while those on contacts oriented in the direction perpendicular to minor principal stress are reduced. If they go into tension, there is a contact loss. This formation of contacts in the direction of compressive strain and contact disintegration in the direction of tensile strain results in the development of oriented conglomerates of interlocked particles that move as rigid blocks, forming stiff load paths within the assembly. So, the parameter "a", which reflects the difference in the number of vertical and horizontal contacts, is also a representative of the number and size of blocks that move as a rigid units.

Another two parameters, a_n and a_t, define the orientational variation of average contact forces, F_n, (normal contact force) and F_t (tangential contact force). Fig.V.9 represents the evolution of these parameters, i.e. the evolution of the fabric and contact forces. Fig.V.9a presents the monotonic increase in the degree of anisotropy with shear strain, which, eventually, reaches a limiting value as there is a limiting number of contacts that can be lost.

The increase in a_t with shear strain, i.e. increase in tangential forces (Fig.V.9b), continues only up to a point when particle rotation starts to occur, tending afterwards to release tangential forces.

Normal forces, on the other side (Fig.V.9b), grow steadily in the direction of σ_1, along stiff load paths in the assembly. When the density of the assembly drops due to the dilatancy, these forces reduce, i.e. a_n reduces. Macroscopically, this corresponds to material softening.

This evolution of microstructure of granular medium with shear strain bears qualitative resemblance to stress-strain curves for granular material and represents a basis for the above relation between microscopic parameters and deviatoric load.

This set up has been used to see the influence of particle shape on material strength: circular discs have been transformed with different eccentricity to ellipses. Fig.V.10 presents data for three eccentricities (0.0, 0.05 and 0.20) from both numerical and experimental biaxial test. It is shown that ideal circular particles (e=0.0) have the lowest strength and that it increases with changing their shape to elliptical.

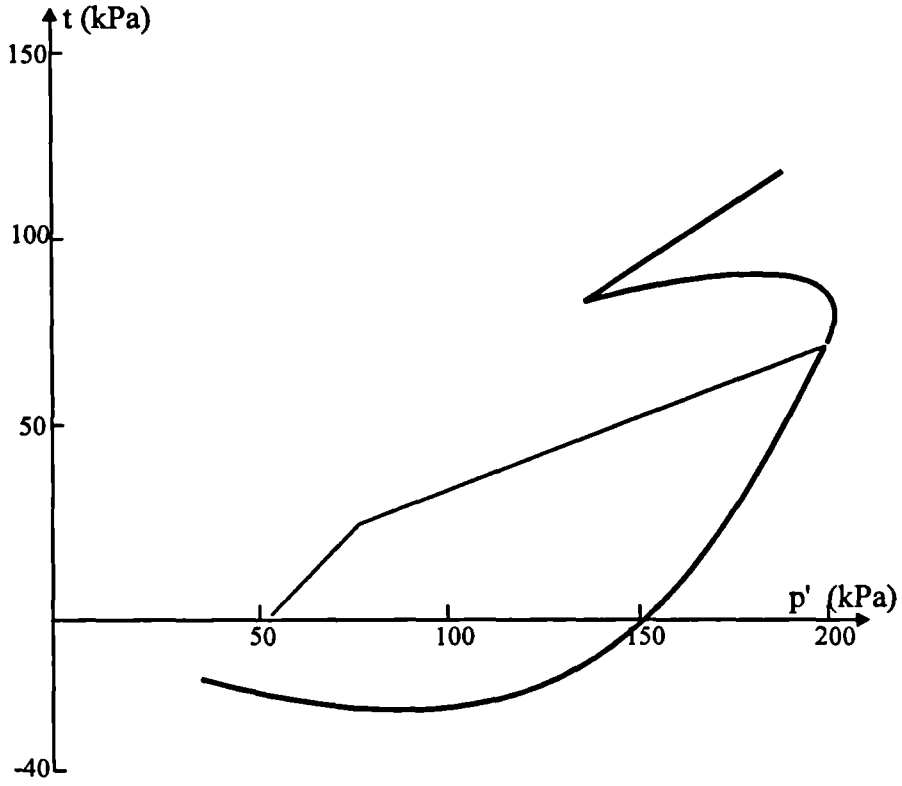


Fig.V.1 - Triaxial compression and extension tests on HRS, performed in HCA (e_o=0.8, this study)

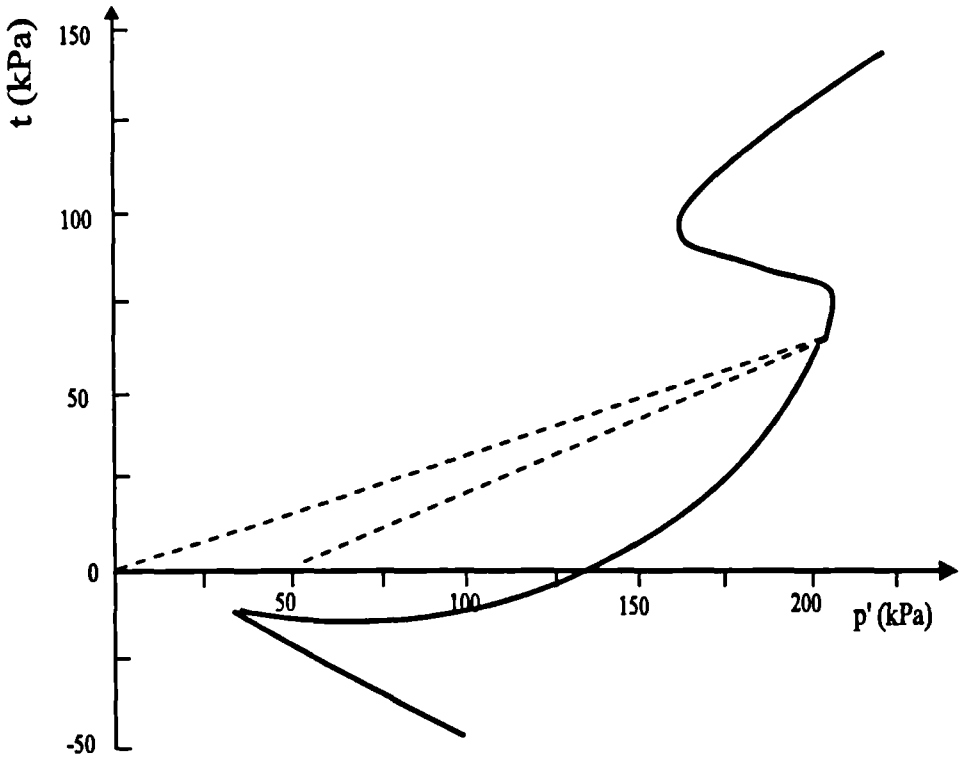


Fig.V.2 - Triaxial compression and extension tests on HRS, performed in SPC (e_o=0.77, Ovando-Shelley, 1986)

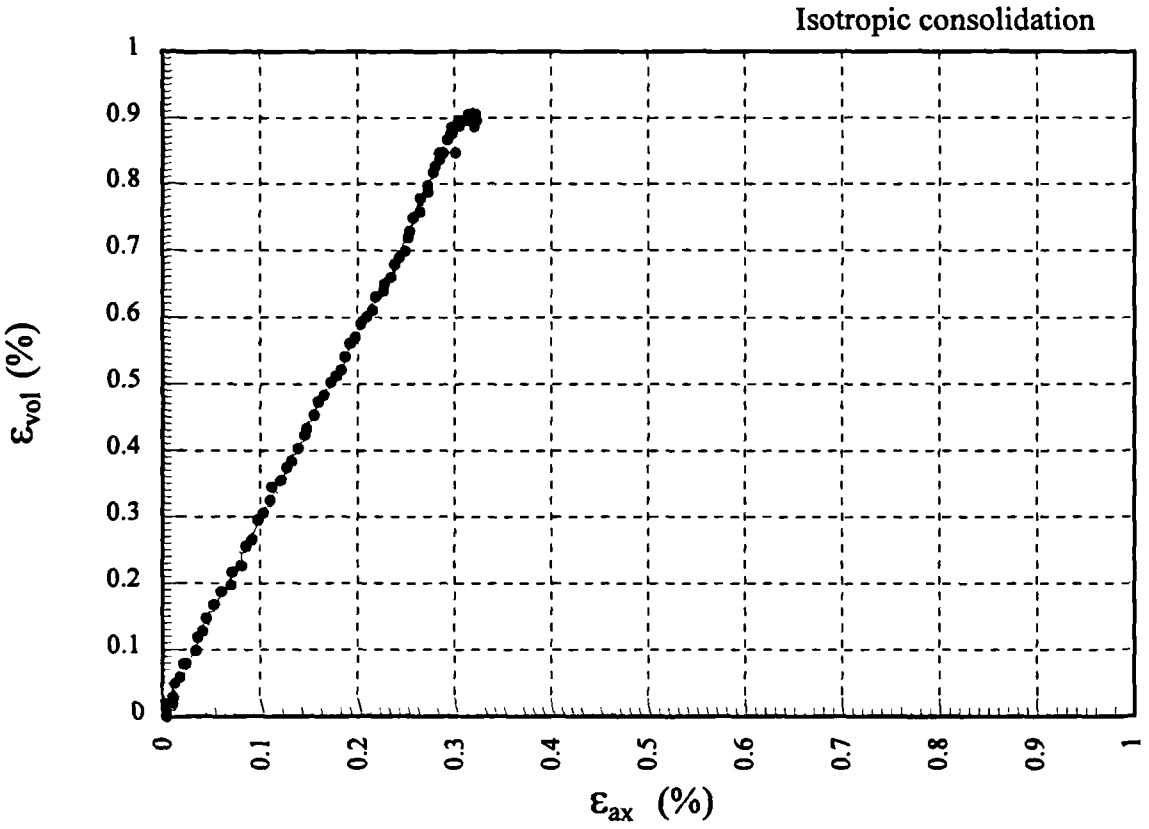


Fig.V.3 - Volumetric vs. axial strain during isotropic consolidation of HPF4

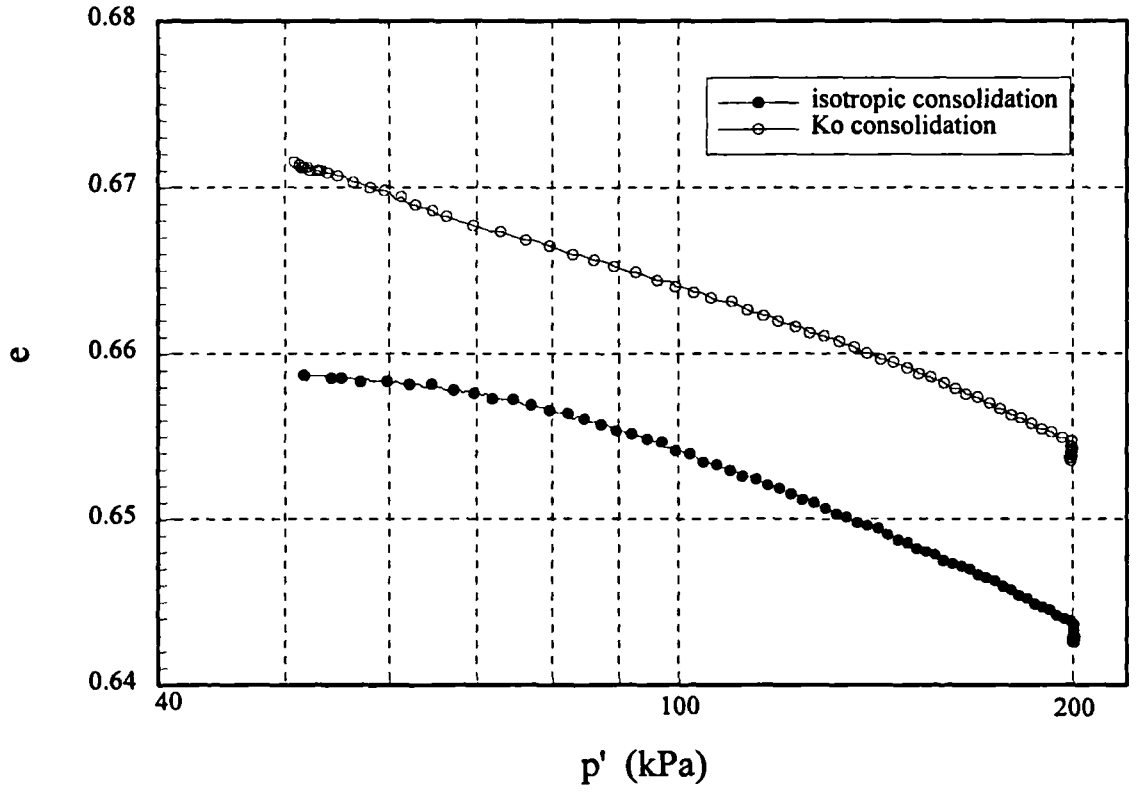


Fig.V.4 - Comparison of isotropic and Ko compressibility curves

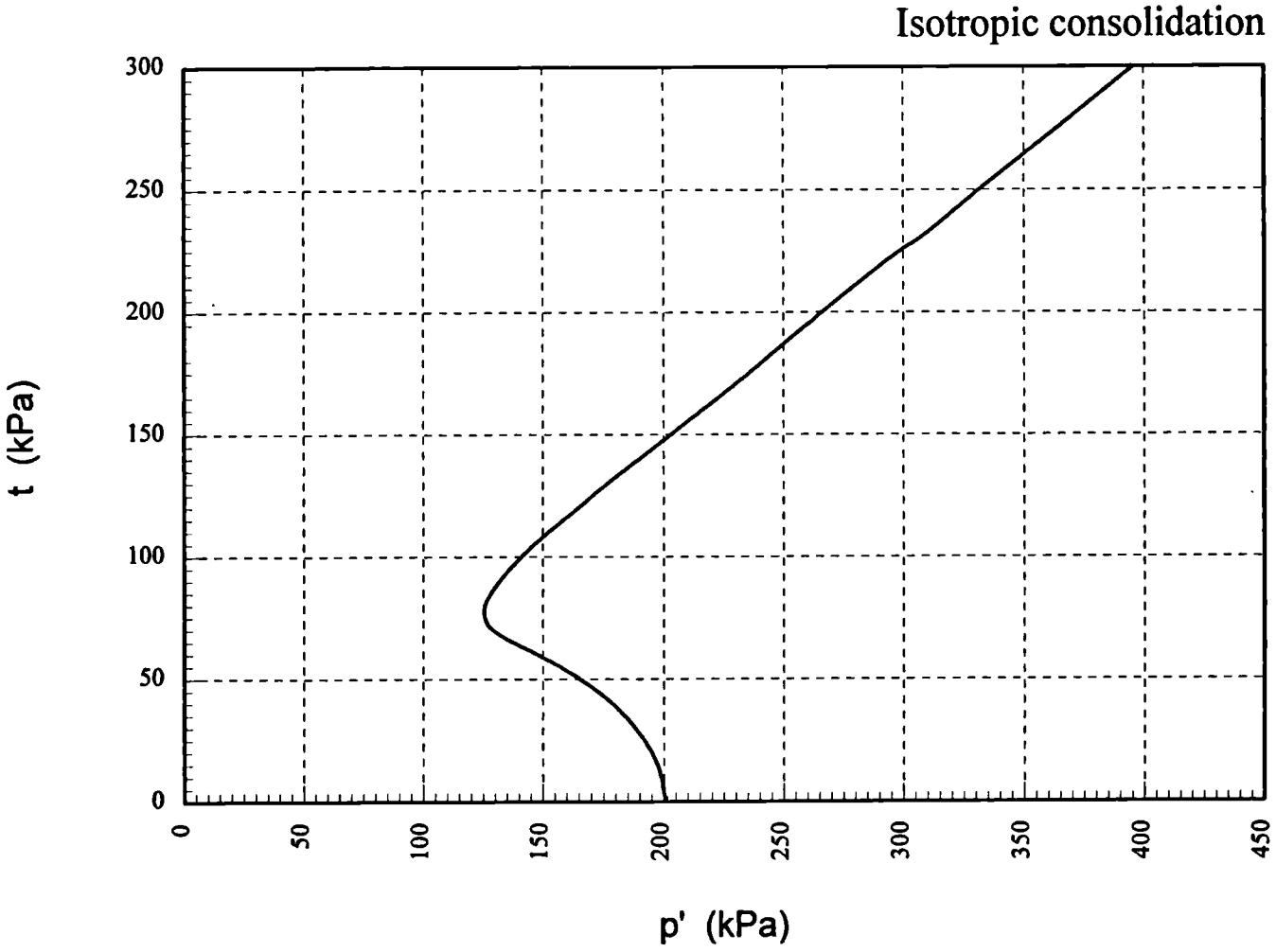


Fig.V.5 - Effective stress path in triaxial compression of isotropically consolidated HPF4

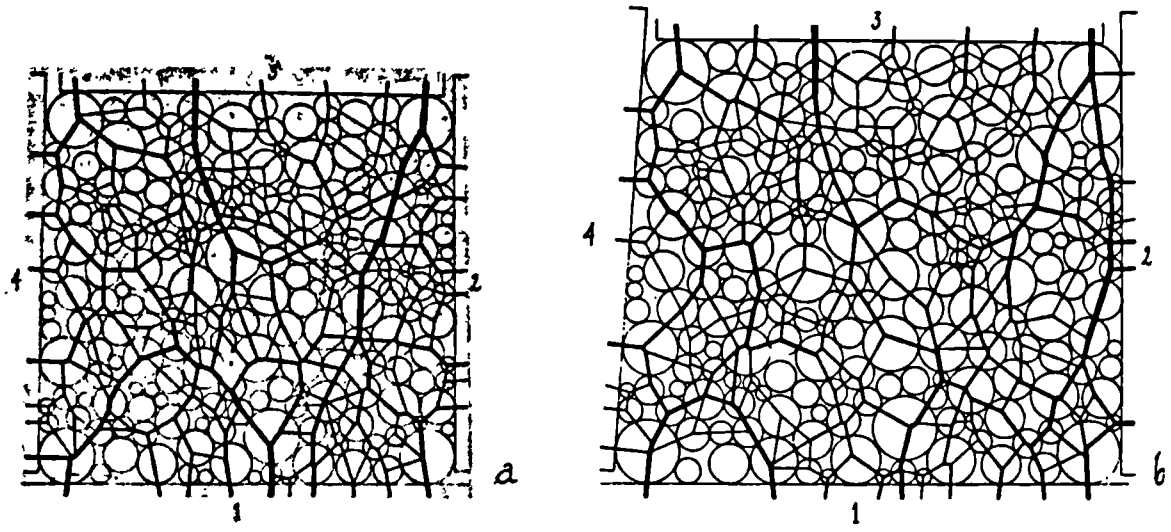


Fig.V.6 - Force vector plots obtained by De Jong & Verruijt (1969):
a) Fh/Fv=0.39; b) Fh/Fv=0.33

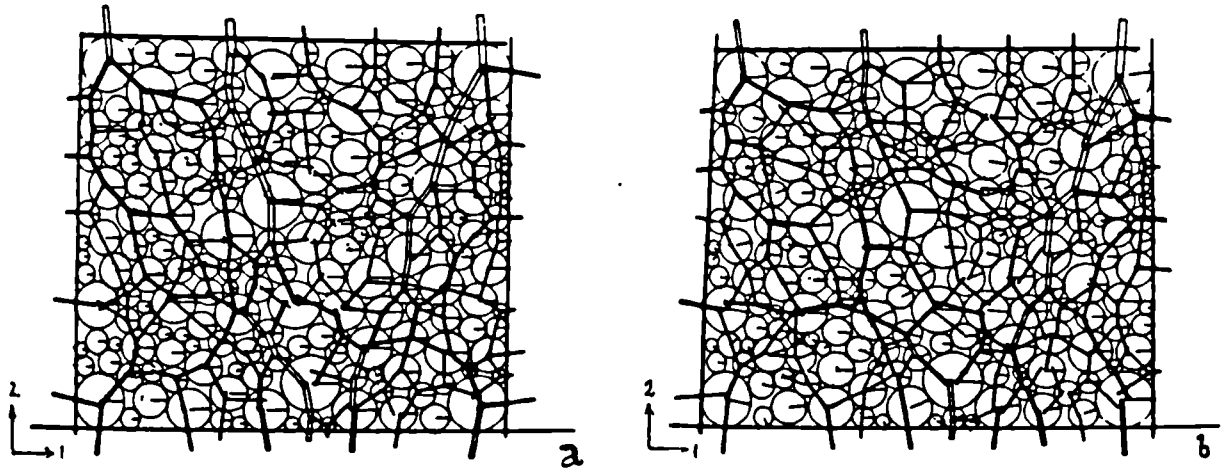


Fig.V.7 - Numerical reproduction of the above experiments:
a) Fh/Fv=0.43; b) Fh/Fv=0.40 (Cundall & Strack, 1979)

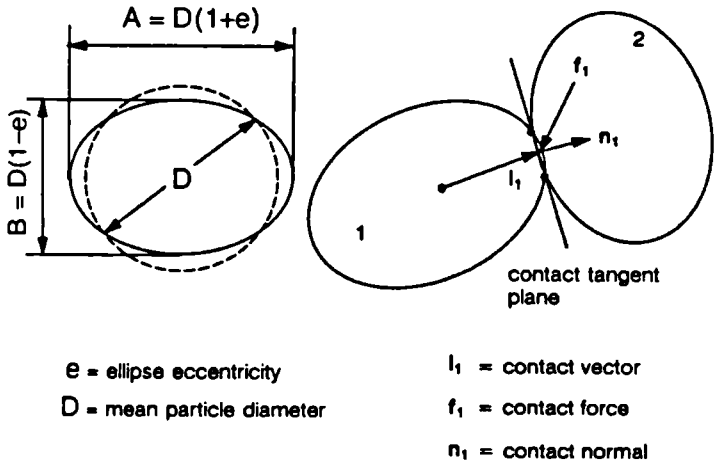


Fig.V.8 - Transformation of circular into elliptical particle

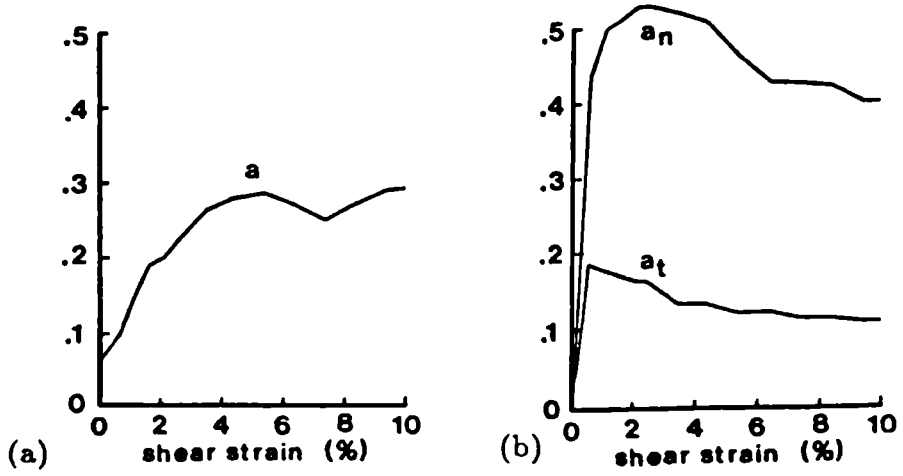


Fig.V.9 - a) Evolution of anisotropy in contact orientations;
b) Evolution of parameters of contact force anisotropy

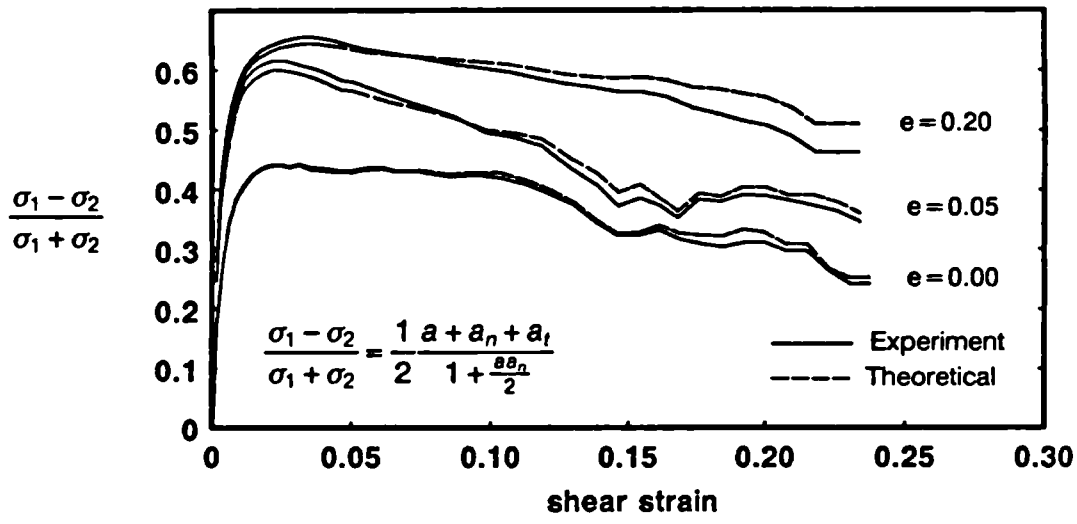


Fig.V.10 - Variation of strength factor with different eccentricities of ellipse

Appendix VI

VI.1 - Anisotropic elasticity

It is widely recognized that soil is not linearly elastic. However, it is often convenient to treat it as such, even if only for small load increments. In such a case linear relationships must be found between the 6 independent stress and strain components, giving a 6x6 matrix of moduli (Eq.VI.1). If a material is fully anisotropic, i.e. if its elastic properties depend on the orientation of the sample compared to the directions of applied loading, then, from the above consideration, 36 elastic parameters C_{ij} are required to describe its elastic response.

$$\begin{bmatrix} \varepsilon_x \\ \varepsilon_y \\ \varepsilon_z \\ \gamma_{xz} \\ \gamma_{yz} \\ \gamma_{xy} \end{bmatrix} = \begin{bmatrix} C_{11} & C_{12} & C_{13} & C_{14} & C_{15} & C_{16} \\ C_{21} & C_{22} & C_{23} & C_{24} & C_{25} & C_{26} \\ C_{31} & C_{32} & C_{33} & C_{34} & C_{35} & C_{36} \\ C_{41} & C_{42} & C_{43} & C_{44} & C_{45} & C_{46} \\ C_{51} & C_{52} & C_{53} & C_{54} & C_{55} & C_{56} \\ C_{61} & C_{62} & C_{63} & C_{64} & C_{65} & C_{66} \end{bmatrix} \begin{bmatrix} \sigma_x \\ \sigma_y \\ \sigma_z \\ \tau_{xz} \\ \tau_{yz} \\ \tau_{xy} \end{bmatrix} \qquad \text{(VI.1)}$$

However, thermodynamic strain energy considerations by Love, 1927, showed that an anisotropic elastic matrix (Eq.VI.1) must be symmetrical, i.e. $C_{ij} = C_{ji}$, for $i \neq j$. The total number of independent anisotropic parameters therefore reduces to 21.

Many materials, however, show more limited forms of anisotropy. For soil deposits, for example, it is often assumed that their anisotropic characteristics depend on the mode of deposition and stress history. Soils that are deposited vertically onto horizontal planes, are likely to exhibit a vertical axis of symmetry, i.e. their characteristics will not vary in the horizontal plane. This assumption is adopted for many soils, although certain natural occurrences, like deposition on a submarine slope, erosion or solifluction, can modify the horizontal layering and make such an assumption invalid.

For the type of anisotropy described above, the matrix of elastic moduli can be further reduced from 21 to only 5 independent parameters. This can be shown by considering the effect of a transformation of cartesian axes on the strains and maintaining the condition that the strain energy function does not change. The transformation is such that the *z* - axis remains vertical while the *x* and *y* axes rotate by an angle θ in the horizontal plane, i.e. plane of isotropy (see Fig.VI.1).

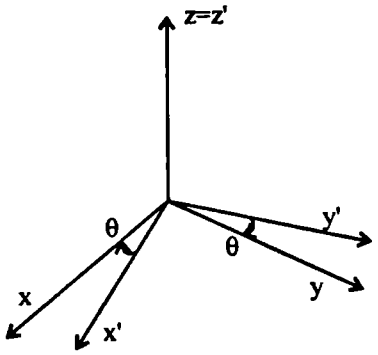


Fig.VI.1 - Coordinate axes

The transformation of coordinates is governed by the following relationships:

$$x' = x\cos\theta + y\sin\theta$$

$$y' = -x\sin\theta + y\cos\theta \qquad \text{(VI.2)}$$

$$z' = z$$

and the formulae that connect the components of strain of the two systems of axes are:

$$\varepsilon_x' = \varepsilon_x\cos^2\theta + \varepsilon_y\sin^2\theta + \gamma_{xy}\sin\theta\cos\theta$$

$$\varepsilon_y' = \varepsilon_x\sin^2\theta + \varepsilon_y\cos^2\theta - \gamma_{xy}\sin\theta\cos\theta$$

$$\varepsilon_z' = \varepsilon_z \qquad \text{(VI.3)}$$

$$\gamma_{y'z'} = \gamma_{yz}\cos\theta - \gamma_{zx}\sin\theta$$

$$\gamma_{z'x'} = \gamma_{yz}\sin\theta + \gamma_{zx}\cos\theta$$

$$\gamma_{x'y'} = -2\varepsilon_x\sin\theta\cos\theta + 2\varepsilon_y\sin\theta\cos\theta + \gamma_{xy}(\cos^2\theta - \sin^2\theta)$$

The algebraic manipulations which consist of expressing Eq.VI.1 through new C_{ij} parameters with the above transformations, brings into consideration sets of equations which will not be derived here. From them, the following coefficients must vanish:

C_{14}, C_{15}, C_{16}, C_{24}, C_{25}, C_{26}, C_{34}, C_{35}, C_{36}, C_{45}, C_{46}, C_{56}

and the remaining coefficients must satisfy the following relations:

$$C_{11} = C_{22},\ C_{13} = C_{23},\ C_{44} = C_{55},\ C_{66} = (C_{11} - C_{12})/2 \qquad \text{(VI.4)}$$

So finally, the behaviour of a transversely isotropic material can be represented by 5 independent constants and the full matrix takes the following form:

$$\begin{bmatrix} \varepsilon_x \\ \varepsilon_y \\ \varepsilon_z \\ \gamma_{xz} \\ \gamma_{yz} \\ \gamma_{xy} \end{bmatrix} = \begin{bmatrix} \frac{1}{E'_H} & -\frac{\nu'_{HH}}{E'_H} & -\frac{\nu'_{VH}}{E'_V} & 0 & 0 & 0 \\ -\frac{\nu'_{HH}}{E'_H} & \frac{1}{E'_H} & -\frac{\nu'_{VH}}{E'_V} & 0 & 0 & 0 \\ -\frac{\nu'_{HV}}{E'_H} & -\frac{\nu'_{HV}}{E'_H} & \frac{1}{E'_V} & 0 & 0 & 0 \\ 0 & 0 & 0 & \frac{1}{G_{VH}} & 0 & 0 \\ 0 & 0 & 0 & 0 & \frac{1}{G_{VH}} & 0 \\ 0 & 0 & 0 & 0 & 0 & \frac{1}{G_{HH}} \end{bmatrix} \begin{bmatrix} \sigma_x \\ \sigma_y \\ \sigma_z \\ \tau_{xz} \\ \tau_{yz} \\ \tau_{xy} \end{bmatrix} \qquad \text{(VI.5)}$$

Considering the requirements of Eq.VI.4,

$$\frac{\nu'_{VH}}{E'_V} = \frac{\nu'_{HV}}{E'_H}$$

$$G_{HH} = \frac{E'_H}{2(1 + \nu'_{HH})}$$

and therefore:

$$\begin{bmatrix} \varepsilon_x \\ \varepsilon_y \\ \varepsilon_z \\ \gamma_{xz} \\ \gamma_{yz} \\ \gamma_{xy} \end{bmatrix} = \begin{bmatrix} \frac{1}{E'_H} & -\frac{\nu'_{HH}}{E'_H} & -\frac{\nu'_{HV}}{E'_H} & 0 & 0 & 0 \\ -\frac{\nu'_{HH}}{E'_H} & \frac{1}{E'_H} & -\frac{\nu'_{HV}}{E'_H} & 0 & 0 & 0 \\ -\frac{\nu'_{HV}}{E'_H} & -\frac{\nu'_{HV}}{E'_H} & \frac{1}{E'_V} & 0 & 0 & 0 \\ 0 & 0 & 0 & \frac{1}{G_{VH}} & 0 & 0 \\ 0 & 0 & 0 & 0 & \frac{1}{G_{VH}} & 0 \\ 0 & 0 & 0 & 0 & 0 & \frac{E'_H}{2(1 + \nu'_{HH})} \end{bmatrix} \begin{bmatrix} \sigma_x \\ \sigma_y \\ \sigma_z \\ \tau_{xz} \\ \tau_{yz} \\ \tau_{xy} \end{bmatrix} \qquad \text{(VI.6)}$$

If triaxial stress conditions are considered, then the shear moduli G_{VH} and G_{HH} vanish from the matrix VI.6 and, because of the symmetry of the horizontal stresses, Eq.VI.6 reduces to the form:

$$\begin{bmatrix} \varepsilon_z \\ \varepsilon_H \end{bmatrix} = \begin{bmatrix} \frac{1}{E'_V} & -2\frac{\nu'_{HV}}{E'_H} \\ -\frac{\nu'_{HV}}{E'_H} & \frac{1-\nu'_{HH}}{E'_H} \end{bmatrix} \begin{bmatrix} \Delta\sigma'_z \\ \Delta\sigma'_H \end{bmatrix} \qquad \text{(VI.7)}$$

In terms of invariants, i.e: mean effective stress, p'; deviatoric stress, q; volumetric strain, ε_{vol} and shear strain, ε_d; equation VI.7 can be re-written in the form:

$$\begin{bmatrix} \delta p' \\ \delta q \end{bmatrix} = \begin{bmatrix} K^* & J \\ J & 3G^* \end{bmatrix} \begin{bmatrix} \delta\varepsilon_{vol} \\ \delta\varepsilon_d \end{bmatrix} \qquad \text{(VI.8)}$$

Here, K^* and G^* are marked with an asterisk to emphasize that these moduli are functions of the transversely isotropic parameters E_H', E_V', ν_{HH}' and ν_{HV}'. Modulus J is a parameter expressing the dependence of the shear strain on the mean pressure and volumetric strain on the shear stress. These moduli are then given by the following equations:

$$K^* = \frac{1}{9}\frac{4E_H'^2 + 2E_V'E_H'(1 + 4\nu'_{HV} - \nu'_{HH})}{2E_H'(1 - \nu'_{HH}) - 4E_V'\nu'^2_{HV}}$$

$$3G^* = \frac{E_H'^2 + 2E_V'E_H'(1 - 2\nu'_{HV} - \nu'_{HH})}{2E_H'(1 - \nu'_{HH}) - 4E_V'\nu'^2_{HV}} \qquad \text{(VI.9)}$$

$$J = \frac{2}{3}\frac{E_V'E_H'(1 + \nu'_{HV} - \nu'_{HH}) - E_H'^2}{2E_H'(1 - \nu'_{HH}) - 4E_V'\nu'^2_{HV}}$$

It should be remembered that for an isotropic elastic material, the stiffness matrix from Eq.VI.8 is of the form:

$$\begin{bmatrix} K^* & 0 \\ 0 & 3G^* \end{bmatrix} \qquad \text{(VI.10)}$$

where K = f(E, ν) and G = f(E, ν).

REFERENCE LIST

ACKERLEY S.K., HELLINGS J.E. & JARDINE R.J. (1987), Discussion on Clayton C.R.I. & Khatrush S.A. (1986) - "A new device for measuring local axial strains on triaxial specimens"; Geotechnique, Vol.37, No.3, pp 413-417

ADDENBROOKE T.I. (1996), "Numerical analysis of tunnelling in stiff clay", PhD thesis, Imperial College of Science, Technology and Medicine; University of London

ARTHUR J.R.F. & MENZIES B.K. (1972), "Inherent anisotropy in a sand", Geotechnique, Vol.22, No.1, pp 115-128

ARTHUR J.R.F. & PHILLIPS A.B. (1975), "Homogeneous and layered sand in triaxial compression", Geotechnique, Vol.25, No.4, pp 799-815

ARTHUR J.R.F., CHUA K.S. & DUNSTAN T. (1977a), "Induced anisotropy in a sand", Geotechnique, Vol.27, No.1, pp 13-30

ARTHUR J.R.F., DUNSTAN T., AL-ANI Q.A.J.L. & ASSADI A. (1977b), "Plastic deformation and failure in granular media", Geotechnique, Vol.27, No.1, pp 53-74

ARTHUR J.R.F. & ASSADI A. (1977), "Ruptured sand sheared in plane strain", IXth ICSMFE, Tokyo, Vol.1, pp 19-22

ARTHUR J.R.F., CHUA K.S., DUNSTAN T. & RODRIGUEZ del CAMINO F.I. (1980), "Principal stress rotation: a missing parameter", J. Geotech. Eng. Div., ASCE, Vol.106, GT4, pp 419-433.

ARTHUR J.R.F. & DUNSTAN T. (1982), "Rupture layers in granular media", IUTAM Conference on Deformation and Failure of Granular Materials, Delft, pp 453-459.

ARTHUR J.R.F. (1988), "Cubical devices: Versatility and constraints", Advanced triaxial testing of soil and rock - ASTM STP 977, Edt. Donaghe R.T., Chaney R.C and Silver M.L., pp 743-765

ATKINSON J.H., RICHARDSON D. & WOODS R.I. (1986), "Technical note on the determination of tangent stiffness parameters from soil test data", Computers and Geotechnics, Vol.2, pp 131-140

ATKINSON J.H., RICHARDSON D. & STALLEBRASS S.E. (1990), "Effects of recent stress history on the stiffness of overconsolidated soil", Geotechnique, Vol.40, No.4, pp.531-540

BELLOTI R., JAMIOLKOWSKI M., LO PRESTI D.C.F. & O'NEILL D.A. (1996), "Anisotropy of small strain stiffness in Ticino sand", Geotechnique, Vol.46, No.1, pp 115-131

BISHOP A.W. & HENKEL D.J. (1962), "Test measurement of soil properties in the triaxial test", 2nd Ed., Arnold, London.

BISHOP A.W. & GREEN G.E. (1965), "The influence of end restraint on the compression strength of a cohesionless soil", Geotechnique, Vol.15, No.3, pp 243-266

BISHOP A.W. (1966), "The strength of soils as engineering materials", Geotechnique, Vol.16,

No.1, pp 91-128

BISHOP A.W. (1969), Discussion, VIIth ICSMFE, Mexico, Vol.3, pp 182-185

BISHOP A.W. & WESLEY L.D. (1975), "A hydraulic triaxial apparatus for controlled stress path testing", Geotechnique, Vol.25, No.4, 657-670

BISHOP A.W. & HIGHT D.W. (1977), "The value of Poisson's ratio in saturated soils and rocks stressed under undrained conditions", Geotechnique, Vol.27, No.3, pp.369-384

BJERRUM L. & LANDVA A. (1966), "Direct simple-shear tests on a Norwegian quick clay", Geotechnique, Vol.16, No.1, pp 1-20

BJERRUM L. (1973), "Problems of soil mechanics and construction on soft clays and structurally unstable soils (collapsible, expansive and others). State-of-the-Art Report, Session 4, Proc. 8th ICSMFE, Moscow, Vol.3, pp 109-159

BOLTON M.D. (1986), "The strength and dilatancy of sands", Geotechnique, Vol.36, No.1, pp 65-78

BOLTON M.D. & WILSON J.M.R. (1989), "An experimental and theoretical comparison between static and dynamic torsional soil tests", Geotechnique, Vol.39, No.4, pp 585-599

BRANDON T.L., CLOUGH G.W. & RAHARDJO P.P. (1991), "Fabrication of silty sand specimens for large- and small-scale tests", Geotechnical Testing Journal, GTJODJ, Vol.14, No.1, pp 46-55.

BROMS B.B. & CASBARIAN A.O. (1965), "Effects of rotation of the principal stress axes and the intermediate principal stress on the shear strength", Proc. 6th ICSMFE, Montreal, Vol.1, pp 179-183.

BRUCY F., NAUROY J.F., LE TIRANT P. & MEUNIER J. (1991), "Comparison of static and dynamic tests of piles in sand", Proc. Int. Conf. on Deep Foundatins, Paris, Presses Ponts et chaussees, pp 369-378.

BURLAND J.B. (1971), " A method of estimating the pore pressures and displacements beneath embankments on soft natural clay deposits", Roscoe Mem. Conf. Stress-strain behaviour of soils, Cambridge University; pp 505-536

BURLAND J.B. & SYMES M. (1982), "A simple axial displacement gauge for use in the triaxial apparatus", Technical note, Geotechnique, Vol.32, No.1, pp 62-65.

BURLAND J.B. (1989), "Small is beautifull - the stiffness of soils at small strains" - IXth Laurits Bjerrum Memorial Lecture, Canadian Geotechn. Jnl, Vol 26, pp 499-516

BURLAND J.B. & GEORGIANNOU V.N. (1991), "Small strain stiffness under generalised stress changes", Xth European Conf. SMFE, Florence, Vol.1, pp 41-44.

CASAGRANDE A. & CARRILLO N. (1944), "Shear failure of anisotropic materials", Proc. Boston Soc. of Civil Eng., Vol.31, pp 74-87.

CASAGRANDE A. (1976), "Liquefaction and cyclic deformation of sands - A critical review", Harvard Soil Mechanics Series No.88, Harvard University, Cambridge, Mass

CHANG N.Y., YEY S.T. & KAUFMAN L.P. (1982), "Liquefaction potential of clean and silty sands", Proc. Third Microzonation Conf., Seattle, pp 1018-1032

CHOW F.C. (1995), PhD thesis, Imperial College of Science, Technology and Medecine; University of London (in preparation)

CLARE D. (1994), "Industry response and future research needs", Discussion in the Seminar on Recent Research in Offshore Geotechnics and Geophysics, MTD/SUT projects, November 1994, London

CLARKE J. (1992), "Large scale pile testing in clay", Proc. of Conference held at ICE, Thomas Telford, London

CLAYTON C.R. & KHATRUSH S.A. (1986), "A new device for measuring local axial strains on triaxial specimens", Technical Note, Geotechnique, Vol.36, No.4, pp 593-598

CONNOLLY T.M. (1995), Internal Imperial College Report and personal communication

COOLING & SMITH (1936), "The shear resistance of soils", Proc. Inst. Civil Eng., London, Vol.3, pp 333-343

COOP M.R. (1990), " The mechanics of uncemented carbonate sands", Geotechnique, Vol.40, No.4, pp 607-626

COOP M.R. & ATKINSON J.H. (1993), "The mechanics of cemented carbonate sands", Geotechnique, Vol.43, No.1, pp 53-67

CORNFORTH D.H. (1964), "Some experiments on the influence of strain conditions on the strength of sand", Geotechnique, Vol.14, No.2, pp 143-167

COSTA FILHO L. de M. (1985), "Measurement of axial strains in triaxial tests on London clay", Geotechnical Testing Jnrl, GTJODJ, Vol.8, No.1, pp 3-13

COTECCHIA F. (1996), "The effects of structure on properties of an Italian pleistocene clay", PhD thesis, Imperial College of Science, Technology and Medicine; University of London

CUNDALL P.A. (1978), "BALL - A program to model granular media using the distinct element method", Technical Note, Advanced Technology Group, Dames & Moore, London

CUNDALL P.A. & STRACK O.D.L. (1979), "A discrete numerical model for granular assemblies", Geotechnique Vol.29, No.1, pp 47-65

DALLY J.W., RILEY W.F. & McCONNELL K.G. (1993), "Instrumentation for engineering measurements", Secon edition, John Wiley & Sons

DE JOSSELIN DE JONG G. & VERRUIJT A. (1969), "Etude photo-elastique d'un empilement de disques", Cah. Grpe fr. Etud. Rheol. 2, pp 73-86

DOUNIAS G.T. & POTTS D.M. (1993), "Numerical analyses of drained direct and simple shear tests", Journal of Geotechnical Engineering, ASCE, Vol.119, No.12, pp 1870-1891

DRNEVICH V.P. & MASSARSCH K.R. (1979), "Sample disturbance and stress-strain behaviour", Journal of Geotechnical Div., ASCE, Vol.105, GT9, pp 1001-1016

DUNCAN J.M. & SEED B. (1966a), "Anisotropy and stress reorientation in clay", Journal of the Soil Mechanics and Foundation Div, ASCE, Vol.92, SM5

DUNCAN J.M. & SEED B. (1966b), "Strength variation along failure surfaces in clay", Journal of the Soil Mechanics and Foundation Div, ASCE, Vol.92, SM6

DUNCAN J.M. & CHANG C.Y. (1970), "Non-linear analysis of stress and strain in soils", Journal of Soil Mechanics and Foundations Div., Vol.96, SM5, pp 1629-1653

DUSSEAULT M.B. (1981), "A versatile hollow cylinder triaxial device", Canadian Geotechnical Journal, Vol.18, pp 1-7.

ERBRICH C.T. (1994), "Modelling of a novel Foundation for offshore structures", Presented at meeting of Offshore Engineering Group, ICE, 30th November 1994.

EVERTON S.J. (1991), "Experimental study of frictional shearing resistance between non-cohesive soils and construction materials", MSc thesis, Imperial College of Science, Technology and Medicine; University of London

FOLKES D.J. & CROOKS J.H.A. (1985), "Effective stress paths and yielding in soft clays below embankments", Canadian Geotechnical Journal, Vol.22, pp 357-374

FROSSARD E. (1979), "Effect of sand grain shape on interparticle friction; indirect measurements by Rowe's stress dilatancy theory", "Geotechnique, Vol.29, No.3, pp 341-350

GENS A. (1982), "Stress-strain and strength of a low plasticity clay", PhD thesis, Imperial College of Science, Technology and Medicine; University of London

GENS A. & POTTS D.M. (1982), "A theoretical model for describing the behaviour of soils not obeying Rendulic's principle", Int. Symp. on Numerical Models in Geomechnics, Zurich, pp 24-32

GENS A. & POTTS D.M. (1984), "Formulation of quasi-axisymmetric boundary value problems for finite element analysis", Eng. Comput., Vol.1, pp 144-150.

GENS A. (1985), "A state boundary surface for soils not obeying Rendulic's principle", Proc. 11th ICSMFE, San Francisco, Vol.2, pp 473-476.

GEORGIANNOU V.N. (1988), "The behaviour of clayey sands under monotonic and cyclic loading", PhD thesis, Imperial College of Science, Technology and Medicine, University of London.

GEORGIANNOU V.N., BURLAND J.B. & HIGHT D.W. (1990), "The undrained behaviour of clayey sands in triaxial compression and extension", Geotechnique, Vol.40, No.3, pp 431-449.

GIBBS C.E., McCAULEY J., MIRZA U.A. & COX W.R. (1992), "Reduction of field data and interpretation of results for axial load tests of two 762 mm diameter pipe piles in clay", Proc. Conf. on Recent Large Scale Fully Instrumented Pile Tests in Clay, London, pp 285-345.

GOTO S., TATSUOKA F., SHIBUYA S., KIM Y.S. & SATO T. (1991), "A simple gauge for local small strain measurements in the laboratory", Soils and Foundations, Vol.31, No.1, pp 169-180.

GRAHAM J. (1979), "Embankment stability on anisotropic soft clays", Canadian Geotechnical Journal, Vol.16, pp 295-308

GRAHAM J., NOONAN M.L. & LEW K.V. (1983), "Yield states and stress-strain relationships in a natural plastic clay", Canadian Geotechn. Journal, Vol.20, pp.502-516

GRAHAM J. & HOULSBY G.T. (1983), "Anisotropic elasticity of natural clay", Geotechnique, Vol.33, No.2, pp.165-180

GREEN G.E. & READES D.W. (1975), " Boundary conditions, anisotropy and sample shape effects on the stress-strain behaviour of sand in triaxial compression and plane strain", Geotechnique, Vol.25, No.2, pp 333-356

HARDIN B.O. & RICHART F.E. (1963), "Elastic wave velocities in granular soils", Journal of Soil Mech. and Foundation Div., ASCE, Vol.89, No. SM1, pp.33-65

HARDIN B.O. & BLACK.W. (1966), "Sand stiffness under various triaxial stresses", Journal of Soil Mech. and Foundation Div., ASCE, Vol.92, No. SM2, pp.27-42

HARDIN B.O. & DRNEVICH V.P. (1972), "Shear modulus and damping in soils: measurement and parameter effects", Journal of the Soil Mechanics and Foundations Div., ASCE, Vol.98, SM6, pp 603-624

HARDIN B.O. & DRNEVICH V.P. (1972), "Shear modulus and damping in soils: design equations and curves", Journal of the Soil Mechanics and Foundations Div., ASCE, Vol.98, SM7, pp 667-692

HARDIN B.O. (1978), "The nature of stress-strain behaviour of soils", Erthquake engineering and soil dynamics, Pasadena, Vol.1, pp 3-90

HARDIN B.O. & BLANDFORD G. (1989), "Elasticity of particulate materials", Journal of Geotechn. Eng., ASCE, Vol.115, No.6, pp.788-804

HELLINGS J.E. (1988), "The strength and stiffness of soils associated with excavations", PhD thesis, Imperial College of Science, Technology and Medicine; University of London

HENKEL D.J. (1970), "The role of waves in causing submarine landslides", Geotechnique 20, No.1, pp 75-80

HENKEL D.J. (1971), "The relevance of laboratory-measured parameters in field studies", Roscoe Memorial Symposium, Cambridge University, Edt. R.H.G.Parry

HIGHT D.W. (1983), "Laboratory investigation of sea-bed clays", PhD thesis, Imperial College of Science, Technology and Medicine, University of London.

HIGHT D.W., GENS A. & SYMES M.J. (1983), "The development of a new hollow cylinder apparatus for investigating the effects of principal stress rotation in soils", Geotechnique, Vol.33, No.4, pp 355-384

HIGHT D.W., GENS A. & JARDINE R.J. (1985), "Evaluation of geotechnical parameters from triaxial tests on offshore clay", Proc. of an International Conference organised by the Society of Underwater Technology, London, Vol.3, pp 253-268

HIGHT D.W., JARDINE R.J. & GENS A. (1987), "The behaviour of soft clays", Embankments on soft clays, Bulletin of the Public works research center, Athens, pp 33-158

HIGHT D.W. & SHIBUYA S. (1991), "Undrained stability of offshore gravity structures", GEO-COAST '91, Yokohama, pp 561-566

HIGHT D.W. (1993), "A review of sampling effects in clays and sands", Society for Underwater Technology, Offshore site investigation and foundation behaviour, Vol.28, pp 115-146

HIGHT D.W. (1993), Personal communication; Shear box report for TRRL

HIGHT D.W. & HIGGINS K.G. (1994), "An approach to the prediction of ground movements in engineering practice: background and application", First Int. Conf. on Pre-Failure Deformation of Geomaterials, Sapporo, Vol.2, pp 909-945

HIRD C.C. & YUNG.P.C.Y. (1989), "The use of proximity transducers for local strain measurements in triaxial tests", Technical Note, Geotechnical Testing Journal, GTJODJ, Vol.12, No.4, pp 292-296

HOULSBY G.T. (1991), "How the dilatancy of soils affects their behaviour", Proc. Xth ECSMFE, Florence, Vol.4, pp 1189-1202

ISHIBASHI I. & MEHMET A.S. (1974), "Soil liquefaction by torsional simple shear device", Journal of the Geotechnical Eng. Div, ASCE, Vol.100, GT8, pp 871-888

ISHIHARA K., TATSUOKA F. & YASUDA S. (1975), "Undrained deformation and liquefaction of sand under cyclic stresses", Soils and Foundations, Vol.15, No.1, pp 29-44

ISHIHARA K. & YASUDA S. (1975), "Sand liquefaction in hollow cylinder torsion under irregular excitation", Soils and Foundations, Vol.15, No.1, pp 45-59

ISHIHARA K. & TOWHATA I. (1983), "Sand response to cyclic rotation of principal stress directions as induced by wave loads", Soils and Foundations, Vol.23, No.4, pp 11-26

ISHIHARA K. & YAMAZAKI A. (1984), "Analysis of wave-induced liquefaction in seabed deposits of sand", Soils and Foundations, Vol.24, No.3, pp 85-100

JAMAL A.K. (1971), "Triaxial extension tests on hollow cylinder sand specimens", Canadian Geotechnical Journal, Vol.8, pp 119-133.

JAMIOLKOWSKI M., LADD C.C., GERMAINE J.T. & LANCELLOTTA R. (1985), "New developments in field and laboratory testing of soil", Theme lecture 2, XIth ICSMFE, San Francisco, Vol.1, pp 57-153

JAMIOLKOWSKI M., LEROUEIL S. & LO PRESTI D.C.F. (1991), "Design parameters from theory to practice", Geo-Coast '91 Conf., Yokohama

JAMIOLKOWSKI M., LANCELLOTTA R. & LO PRESTI D.C.F. (1994), "Remarks on the stiffness at small strains of six Italian clays", First Int. Conf. on pre-failure deformation characteristics of geomaterials, Sapporo-Japan; Vol.2, pp 817-836

JARDINE R.J., SYMES M.J. & BURLAND J.B. (1984), "The measurement of soil stiffness in the triaxial apparatus", Geotechnique, Vol.34, No.3, pp 323-340.

JARDINE R.J. (1985), "Investigation of pile-soil behaviour, with special reference to the foundations of offshore structure", PhD thesis, Imperial College of Science, Technology and Medicine; University of London.

JARDINE R.J., POTTS D.M., FOURIE A.B. & BURLAND J.B. (1986), "Studies of the influence of non-linear stress-strain characteristics in soil-structure interaction problems", Geotechnique, Vol.36, No.3, pp 337-396.

JARDINE R.J. & HIGHT D.W. (1987), "The behaviour and analysis of embankments on soft clay", Embankments on soft clays, Bulletin of the Public works research center, Athens, pp 159-244

JARDINE R.J. & HIGHT D.W. (1987), "Laboratory and field techniques for obtaining design parameters", Embankments on soft clays, Bulletin of the Public works research center, Athens, pp 245-296

JARDINE R.J. & POTTS D.M. (1988), "Hutton Tension Leg Platform Foundations: an approach to the prediction of pile behaviour", Geotechnique, Vol.38, No.2, pp 231-252.

JARDINE R.J., POTTS D.M., ST.JOHN H.D. & D.W.HIGHT (1991), "Some practical applications of a non-linear ground model", Xth ECSMFE, pp 223-228

JARDINE R.J. & SMITH P.R. (1991), "Evaluating design paramteres for multi-stage construction", GEO-COAST '91, Yokohama, pp 197-202

JARDINE R.J. (1992a), "Some observations on the kinematic nature of soil stiffness", Soil and Foundations, Vol.32, No.2, pp 111-124.

JARDINE R.J. (1992b), "Nonlinear stiffness parameters from undrained pressuremeter tests", Canadian Geotechn. Journal, Vol.29, pp.436-447

JARDINE R.J. (1994), "One perspective of the pre-failure deformation characteristics of some geomaterials", Keynote lecture, Proc. of the First Int. Conf. on pre-failure deformation characteristics of geomaterials, Sapporo-Japan, Vol.2, pp 855-885

JEFFERSON L.S. (1994), "The numerical analysis of the NGI shear apparatus", MSc dissertation, Imperial College of Science, Technology and Medicine; University of London

JOVICIC V. (1995), First year PhD transfer report - City University; and personal communication

JUAREZ BADILLO E. (1963), "Pore pressure functions in saturated soils", ASTM STP 361

JUAREZ BADILLO E. (1977), "Deviatoric stress-strain theory for soils", IXth ICSMFE, Tokyo

KIM D.S. & STOKOE K.H. (1995), "Deformational characteristics of soils at small to medium strains", First Int. Conf. on Erthquake Geotechnical Eng., Tokyo, Vol.1, pp 89-94

KING M.S. (1970), "Static and dynamic elastic moduli of rocks under pressure", Rock Mechanics - Theory and Practice, 11th Symposium on Rock Mech., AIME, New York, pp 329-351

KIRKGARD M.M. & LADE P.V. (1991), "Anisotropy of normally consolidatet San Francisco

Bay Mud", Geotechnical Testing Journal, Vol.14, No.3, pp.231-246

KJELLMAN W. (1950), "Testing the shear strength of clay in Sweden", Geotechnique, Vol.2, No.1, pp 225-235

KOHATA Y., TATSUOKA F., MUKABI J.N. & SUZUKI M. (1995), "Effects of strain rate and drainage on deformation characteristics at small strains", First Int. Conf. on Earthquake Geotechnical Eng., Tokyo, Vol.1, pp 151-156

KOLBUSZEWSKI J.J. (1948), "Research on packing and density of sands", PhD thesis, Imperial College of Science and Technology, University of London

KONISHI J. (1972), "On the deformation mechanism of granular material", Proc. 27th Anual Meeting of Japan. Soc. Civil Eng., Vol.3, pp 69-70

KOVACEVIC N. (1994), "Numerical analyses of rockfill dams, cut slopes and road embankments", PhD thesis, Imperial College of Science, Technology and Medecine; University of London.

KRUMBEIN W.C. (1941), "Measurement and geological significance of shape and roundness of sedimentary particles", Journal of Sedimentary Petrology, Vol.11, No.2, pp 64-72

KUERBIS R., NEGUSSEY D. & VAID Y.P. (1988a), "Effect of gradation and fines content on the undrained response of sand", prepared for the Conference on Hydraulic Fill Structures, Fort Collins, Colorado

KUERBIS R. & VAID Y.P. (1988b), "Sand sample preparation - the slurry deposition method", Soils and Foundations, Vol.28, No.4, pp 107-118

KUWANO R.I. (1995), Internal Imperial College Report and personal communication

LADD C.C. & EDGERS L. (1972), "Consolidated undrained direct simple shear tests on saturated clays", Research report R72-87, No.284, Dpt. of Civil Eng., MIT, Cambridge, Mass

LADD C.C (1991), "The 22nd Terzaghi lecture: Stability evaluation during staged construction", Journal of Geotechnical Eng. Div., ASCE, Vol.117, GT4, pp 537-615

LADE P.V. & DUNCAN J.M. (1973), "Cubical triaxial tests on cohesionless soil", Journal of Soil Mechanics and Foundations Div., ASCE, Vol.99, SM10, pp 793-812

LADE P.V. (1982), "Localization effects in triaxial tests on sand", IUTAM Conf. on Deformation and Failure of Granular materials, Delft, pp 461-471

LAM W.K. & TATSUOKA F. (1988a), "Effects of initial anisotropic fabric and σ_2 on strength and deformation characteristics of sand", Soils and Foundations, Vol.28, No.1, pp 89-106.

LAM W.K. & TATSUOKA F. (1988b), "Triaxial compressive and extension strength of sand affected by strength anisotropy and sample slenderness", Advanced triaxial testing of soil and rock - ASTM STP 977, Edt. Donaghe R.T., Chaney R.C. & Silver M.L., pp 655-666

LAMBSON M.D., CLARE D.G. & SEMPLE R.M. (1992), "Investigation and interpretation of Pentre and Tilbrook Grange soil conditions", Proc. Conf. on Recent Large Scale Fully Instrumented Pile Tests in Clay, London, pp 134-196.

LEE K.L. (1970), "Comparison of plane strain and triaxial tests on sand", JSMFED, ASCE, Vol.96, SM3, pp 901-923.

LEE S.H.H. (1985), "Investigation of low-amplitude shear wave velocity in anisotropic material", PhD thesis, University of Texas, Austin

LEHANE B.M., JARDINE R.J., BOND A.J. & FRANK R. (1993), "Mechanisms of shaft friction in sand from instrumented pile tests", Journal of Geotechnical Eng., ASCE, Vol.119, No.1, pp 19-35.

LEUSSINK H. & WITTKE W. (1964), "Difference in triaxial and plane strain shear strength", Laboratory shear testing of soils, ASTM STP 361, pp77-89

LO PRESTI D.C.F. & O'NEIL D.A. (1991), "Laboratory investigation of small strain modulus anisotropy in sands", Proc. ISOCCT1, Potsdam, Elsevier, pp 213-224

LO PRESTI D.C.F., PALLARA O., LANCELLOTTA R., ARMANDI M. & MANISCALCO R. (1993), "Monotonic and cyclic loading behaviour of two sands at small strains", Geotechnical Testing Journal, Vol.16, No.4, pp.409-424

LO PRESTI D.C.F., PALLARA O., COSTANZO D. & IMPAVIDO M. (1994), "Small strain measurements during triaxial tests: many problems, some solutions", First Int. Conf. on pre-failure deformation characteristics of geomaterials, Sapporo-Japan, Vol.1, pp 11-16

LO PRESTI D.C.F. (1994), "Measurement of shear deformation of geomaterials in the laboratory", General Report, First Int. Conf. on pre-failure deformation characteristics of geomaterials, Sapporo-Japan, Vol.2, pp 1067-1088

LOVE A.E.H. (1927), "A treatise on the mathematical theory of elasticity", Chapters III & VI; Edt. Dover Publications, New York

MAHMOOD A., MITCHELL J.K. & LINDBLOM U. (1976), "Effect of specimen preparation method on grain arrangement and compressibility in sand", Soil Specimen Preparation for Laboratory Testing, ASTM STP 599, American Society for Testing and Materials, pp 169-192.

MARACHI N.D., DUNCAN J.M. CHAN C.K. & SEED H.B. (1981), "Plane-strain testing of sand", Laboratory shear strength of soil, ASTM STP 740; Eds. R.N. Yong & F.C. Townsend, pp 294-302

MATSUOKA H. (1974), "A microscopic study on shear mechanism of granular materials", Soils and Foundations, Vol.14, No.1, pp 29-43

MATSUOKA H. & SAKAKIBARA K. (1987), "A constitutive model for sands and clays evaluating principal stress rotation", Soils and Foundations, Vol.27, No.4, pp 73-88

MAYNE P.W. & KULHAWY F.H. (1982), "Ko-OCR relationship in soils", Journal of the Geotechnical Eng. Div., ASCE, Vol.108, GT6, pp 851-872

MENKITI C.O. (1995), "Behaviour of clay and clayey-sand, with particular reference to principal stress rotation", PhD thesis, Imperial College of Science, Technology and Medecine; University of London

MIURA S. & TOKI S. (1982), "A sample preparation method and its effect on static and cyclic

deformation-strength properties of sand", Soils and Foundatins, Vol.22, No.1, pp 61-77

MIURA K., MIURA S. & TOKI S. (1986), "Deformation behaviour of anisotropic dense sand under principal stress axes rotation", Soils and Foundations, Vol.26, No.1, pp 36-52

MROZ Z. (1967), "On the description of anisotropic work hardening", Jnl. Mech. Phys. Solids, Vol.15, pp 163-175

MULILIS P., SEED B., CHAN C., MITCHELL J.K. & ARULANANDAN K. (1977), "Effects of sample preparation on sand liquefaction", Journal of the Geotechnical Eng. Div., ASCE, Vol.103, GT2, pp 91-108

NACCI V.A. & D'ANDREA R.A. (1976), "A technique for the preparation of specimens of loose layered silts", Soil Specimen Preparation for Laboratory Testing, ASTM STP 599, American Society for Testing and Materials, pp 193-201

NEWLAND P.L. & ALLELY B.H. (1957), "Volume changes in drained triaxial tests on granular materials", Geotechnique, Vol.7, pp 17-34

NICHOLSON D.P. & JARDINE R.J. (1981), "Performance of vertical drains at Queenborough Bypass", Geotechnique, Symposium in print, Vol.31, No.1, pp 67-90

OCHIAI H. & LADE P.V. (1983), "Three-dimensioanl behaviour of sand with anisotropic fabric", Journal of Geotechnical Eng., ASCE, Vol.109, No.10, pp 1313-1328

ODA M. (1972a), "Initial fabrics and their relations to the mechanical properties of granular materials", Soils and Foundations, Vol.12, No.1, pp 17-36.

ODA M. (1972b), "The mechanism of fabric changes during the compressional deformation of sand", Soils and Foundations, Vol.12, No.2, pp 1-18.

ODA M. (1972c), "Deformation mechanism of sand in triaxial compression tests", Soils and Foundations, Vol.12, No.4, pp 45-63.

ODA M. (1974), "A mechanical and statistical model of granular material", Soils and Foundations, Vol.14, No.1, pp 13-27

ODA M. & KONISHI J. (1974a), "Microscopic deformation mechanism of granular materials in simple shear", Soils and Foundations, Vol.14, No.4, pp 25-38

ODA M. & KONISHI J. (1974b), "Rotation of principal stresses in granular material during simple shear", Soils and Foundations, Vol.14, No.4, pp 39-53

ODA M., KOISHIKAWA I. & HIGUCHI T. (1978), "Experimental study of anisotropic shear strength of sand by plane strain test", Soils and Foundations, Vol.18, No.1, pp 25-38

ODA M. (1981), "Anisotropic strength of cohesionless sands", Journal of the Geotechnical Engineering Division, ASCE, Vol.107, GT9, pp 1219-1231

ODA M., NEMAT-NASSER S. & KONISHI J. (1985), "Stress induced anisotropy in granular masses", Soils and Foundations, Vol.25, No.3, pp 85-97

OVANDO-SHELLEY E. (1986), "Stress-strain behaviour of granular soils tested in the triaxial

cell", PhD thesis, Imperial College of Science, Technology and Medicine, University of London.

PARATHIRAS A.N. (1994), "Displacement rate effects on the residual strength of soils", PhD thesis, Imperial College of Science, Technology and Medicine; University of London

PAUL M.A. (1994), "Geotechnical and seismic analysis of sediments from the UK continental margin", Seminar on Recet Research in Offshore Geotechnics and Geophysics, MTD/SUT projects, November 1994, London

PICKERING, D.J. (1970), "Anisotropic elastic parameters for soil", Geotechnique, Vol.20, No.3, pp.271-276

PETERS J.F., LADE P.V. & BRO A. (1988), "Shear band formation in triaxial and plane strain tests", Advanced triaxial testing of soil and rock - ASTM STP 977, Edt. Donaghe R.T., Chaney R.C. and Marxhall L.S., pp 604-627

POROVIC E. & JARDINE R.J. (1994), "Some observations on the static and dynamic shear stiffness of Ham River Sand", First Int. Conf. on Pre-failure Deformation of Geomaterials, Sapporo-Japan, Vol.1, pp 25-30

POROVIC E. (1995), "Investigation of soil behaviour using a resonant-column torsional-shear hollow cylinder apparatus", PhD thesis, Imperial College of Science, Technology and Medicine, University of London.

POTTS D.M., DOUNIAS G.T. & VAUGHAN P.R. (1987), "Finite element analysis of the direct shear box test", Geotechnique, Vol.37, No.1, pp 11-23

PUZRIN A.M. & BURLAND J.B. (1996), "A logarithmic stress-strain function for rocks and soils", Technical Note, Geotechnique, Vol.46, No.1, pp 157-164

PUZRIN A.M. & BURLAND J.B. (1996), "Non-linear model of small strain behaviour of soils", submitted to Geotechnique

RAHMAN M.S., SEED B.H. & BOOKER J.R. (1977), "Pore pressure development under offshore gravity structures", Journal of the Geotech. Eng. Div., ASCE, Vol.103, GT12, pp 1419-1436.

RANDOLPH M.F. & WROTH C.P. (1981), "Application of the failure state in undrained simple shear to shaft capacity of driven piles", Geotechnique, Vol.31, No.1, pp 143-157.

RENDULIC L. (1936), "Relation between void ratio and effective principal staresses for a remoulded, silty clay", Discussion, 1st ICSMFE, Harvard, pp 48-51

RITTENHOUSE G. (1944), "A visual method of estimating two dimensional sphericity", Journal of Sedimentary Petrology, Vol.13, No.2, pp 79-81

RODRIGUEZ DEL CAMINO J.I. (1977), "Induced anisotropy in a loose sand", PhD thesis, University College London

ROESLER S.K. (1979), "Anisotropic shear modulus due to stress anisotropy", Journal of the Geotech. Eng. Div., ASCE, Vol.105, GT7, pp. 871-880

ROSCOE K.H., SCHOFIELD A.N. & WROTH C.P. (1958), "On the yielding of soil",

Geotechnique, Vol.8, No.1, pp 27-53.

ROSCOE K.H. & BURLAND J.B. (1968), "On the generalised stress-strain behaviour of 'wet' clay", Engineering Plasticity, Cambridge Univ. Press., Cambridge.

ROSENGREN K.J. & JAEGER J.C. (1968), "The mechanical properties of an interlocked low-porosity aggregate", Geotechnique Vol.18, pp 317-326

ROSSATO G. (1992), "Il comportamento tensioni-deformazioni nella prova di taglio semplice diretto", PhD thesis, University of Padova, Italy (in Italian)

ROTHENBURG L. & BATHURST R.J. (1989), "Analytical study of induced anisotropy in idealized granular materials", Geotechnique Vol.39, No.4, pp 601-614

ROTHENBURG L., BATHURST R.J. & MATYAS E.L. (1989), "Mechanisms of fabric evolution in granular media", 12th ICSMFE, Rio de Janeiro; Vol.1, pp753-756

ROTHENBURG L. & BATHURST R.J. (1992), "Micromechanical features of granular assemblies with planar elliptical particles", Geotechnique, Vol.42, No.1, pp 79-95

ROWE P.W. (1962), "The stress dilatancy relation for static equilibrium of an assembly of particles in contact", Journal of the Royal Society, Series A, pp 500-527

SAADA A.S. (1970), "Testing of anisotropic clay soils", Journal of Soil Mechanics and Foundations Div., ASCE, Vol.96, SM5, pp 1837-1852

SAADA A.S. & CHIN-DER OU (1973), "Strain-stress relations and failure of anisotropic clays", Journal of Soil Mech. and Foundation Div., ASCE, Vol.99, No.SM12, pp.1091-1111

SAADA A.S. & BIANCHINI G.F. (1975), "Strength of one dimensionally consolidated clays", Journal of Geotechnical Eng. Div., ASCE, Vol.101, GT11, pp 1151-1164

SAADA A.S. & TOWNSEND F.C. (1981), "State of the art: Laboratory strength testing of soils", Laboratory shear strength of soils - ASTMSTP 740, Edt. Young R.N. and Townsend F.C., pp 7-77

SAYAO A. & VAID Y.P. (1991), "A critical assessment of stress nonuniformities in hollow cylinder test specimens", Soils and Foundations, Vol.31, No.1, pp 60-72

SCARPELLI G. & WOOD.D.M (1982), "Experimental observations of shear band patterns in direct shear tests", IUTAM Conference on Deformation and Failure of Granular Materials, Delft, pp 473-483

SCHULTHEISS P.J. (1981), "Simultaneous measurement of P & S wave velocities during conventional laboratory soil testing procedures", Marine Geotechnology, Vol.4, No.4, pp 343-367

SHIBUYA S. (1985), "Undrained behaviour of granular materials under principal stress rotation", PhD thesis, Imperial College of Science, Technology and Medicine; University of London

SHIBUYA S. & HIGHT D.W. (1987a), "On the stress path in simple shear", Geotechnique, Vol.37, No.4, pp 511-515

SHUBUYA S. & HIGHT D.W. (1987b), "A bounding surface for granular materials", Soils and Foundations, Vol.27, No.4, pp 123-136

SHIBUYA S. & HIGHT D.W. (1987c), "Patterns of cyclic principal stress rotation and liquefaction", 8th Asian Regional Conf. on SMFE, Japan, Vol.1, pp 265-268

SHIBUYA S. (1988), "A servo system for hollow cylinder testing of soils", Geotechnical Testing Journal, GTJODJ, Vol.11, No.2, pp 109-118

SHIBUYA S., (1989), "Predictions of pore pressure under undrained cyclic principal stress rotation", 12th ICSMFE, Rio de Janeiro, Vol.1, pp 123-126

SHIBUYA S., KONG X.J. & TATSUOKA F. (1990), "Deformation characteristics of gravels subjected to monotonic and cyclic loading - with particular reference to their small strain behaviour", Proc. Japan Sym. on Erthquake Eng., Tokyo, pp 771-776

SHIBUYA S., TATSUOKA F., ABE F., KIM Y.S., PARK C.S. & MUKABI J.N. (1991), "A new look at stress-strain relations of soils and soft rocks", IXth ICSMFE, Bangkok, Vol.1, pp 63-66

SHIBUYA S., MITACHI T., KITAJIMA A. & TAKADA M. (1993), "Strength of sand as observed in a newly developed direct shear box apparatus", Bulletin of the Faculty of Engineering No. 166, Hokkaido University

SHIBUYA S., PARK C.S., TATSUOKA F., ABE F., TECHAVORASINSKUN S., KOHATA Y. & SATO T. (1994), "The significance of local lateral-strain measurement of soil specimens for a wide range of strain", Soils and Foundations, Vol.34, No.2, pp 95-105

SHIBUYA S., MITACHI T., YAMASHITA S. & TANAKA H. (1995), "Effects of sample disturbance on Gmax of soils - A case study", First Int. Conf. on Erthquake Geotechnical Eng., Tokyo, Vol.1, pp 77-82

SHIBUYA S. & HIGHT D.W. (1996), "Anisotropy of K_o-consolidated sand", in preparation

SHIRLEY D.J. (1978), "Improved shear wave transducer", Acoustic Society of America, 63(5), pp 1643-1645

SHIRLEY D.J. & HAMPTON L.D. (1978), "Shear wave measurements in laboratory sediments", Acoustic Society of America, 63(2), pp 607-613

SIMPSON B., O'RIORDAN N.J. & CROFT D.D. (1979), "A computer model for the analysis of ground movements in London Clay", Geotechnique, Vol.29, No.2, pp 149-175

SIMPSON B. (1992), "Retaining structures - displacement and design", 32nd Rankine Lecture, Geotechnique, Vol.42

SIMPSON B., ATKINSON J.H. & JOVICIC V. (1996), " The influence of anisotropy on calculations of ground settlements above tunnels", Geotechnical aspects on underground construction in soft ground - Int. Symp., City University, London, pp 511-514

SINGH J.P. & QUIGLEY D.W. (1983), "Valdez silts: a challenge in design of offshore facilities", Geotechnical practice in offshore engineering, ASCE, Edt. S.G.Wright

SKEMPTON A.W. (1954), "The pore pressure coefficients A and B", Geotechnique, Vol.4, No.4, pp 143-147

SKINNER A.E. (1969), "A note on the influence of interparticle friction on the shearing strength of a random assembly of spherical particles", Geotechnique, Vol.19, No.1, pp 150-157

SKINNER A.E. (1975), "The effect of high pore water pressures on the mechanical behaviour of sediments", PhD thesis, Imperial College of Science, Technology and Medicine; University of London.

SMITH P.R. (1984), "The construction of multi-stage embankments on soft clay", MSc dissertation, Imperial College of Science, Technology and Medicine; University of London.

SMITH P.R. (1992), "The properties of high compressibility clay with special reference to construction on soft ground", PhD thesis, Imperial College of Science, Technology and Medicine; University of London.

SMITH P.R., JARDINE R.J. & HIGHT D.W. (1992), "The yielding of Bothkennar clay", Geotechnique, Vol.42, No.2, pp 257-274

SOGA K., NAKAGAWA K. & MITCHEL J.K. (1995), "Measurement of stiffness degradation characteristics of clay using a torsional shear device", First Int. Conf. on Earthquake Geotechnical Eng., Tokyo, Vol.1, pp 107-112

SWEENEY M. (1994), Contribution to the Seminar on Recent Research in Offshore Geotechnics and Geophysics, MTD/SUT projects, November 1994, London

SYMES M.J. (1983), "Rotation of principal stresses in sand", PhD thesis, Imperial College of Science, Technology and Medicine; University of London.

SYMES M.J. & BURLAND J.B. (1984), "Determination of local displacement on soil samples", Geotechnical Testing Jnl, Vol.7, No.2, pp 49-59

SYMES M.J., GENS A. & HIGHT D.W. (1984), "Undrained anisotropy and principal stress rotation in saturated sand", Geotechnique, Vol.34, No.1, pp 11-27.

SYMES M.J., GENS A. & HIGHT D.W. (1988), "Drained principal stress rotation in saturated sand", Geotechnique, Vol.38, No.1, pp 59-81

TANI K. (1994), "General report: Measurement of shear deformation of geomaterials - Field tests", First Int. Conf on Pre-failure Deformation of Geomaterials, Sapporo-Japan, Vol.2, pp 1115-1131

TATSUOKA F. & ISHIHARA K. (1974), "Yielding of sand in triaxial conmpression", Soils and Foundations", Vo.14, No.2, pp 63-76

TATSUOKA F. (1980), "Stress-strain behaviour of an idealized anisotropic granular material", Soils and Foundations, Vol.20, No.3, pp 75-90

TATSUOKA F., SAKAMOTO M., KAWAMURA T. & FUKUSHIMA S. (1986), "Strength and deformation characteristics of sand in plane strain compression at extremely low pressures", Soils and foundations, Vol.26, No.1 pp 65-84

TATSUOKA F., NAKAMURA S., HUANG C.C. & TANI K. (1990), "Strength anisotropy and shear band direction in plane strain tests on sand", Soils and Foundations, Vol.30, No.1, pp 35-54

TATSUOKA F. & SHIBUYA S. (1992), "Deformation characteristics of soils and rocks from field and laboratory tests", Report of the Inst. of Industrial Sci., Tokio University, Vol.37, No.1

TATSUOKA F., SATO T., PARK C.S., KIM Y.S., MUKABI J.N. & KOHATA Y. (1994), "Measurements of elastic properties of geomaterials in laboratory compression test", Geotechnical Testing Jnl., GTJODJ, Vol.17, No.1, pp 80-94

TATSUOKA F. & KOHATA Y. (1995), "Stiffness of hard soils and soft rocks in engineering applications", Report of the Inst. of Industrial Sci., Tokio University, Vol.38, No.5

TCHALENKO J.S. (1967), "The influence of shear and consolidation on the microscopic structure of some clays", PhD thesis, Imperial College of Science and Technology; University of London

THORNTON C. (1979), "The conditions for failure of a face-centered cubic array of uniform rigid spheres", Geotechnique, Vol.29, No.4, pp 441-459

TOLL D. (1988), TRIAX - a computer program for controling triaxial stress path tests

TOMBS S.G. (1969), "Strength and deformation characteristics of roskfill", PhD thesis, Imperial College of Science and Technology; University of London

TOOLAN F.E. (1992), "Geotechnical Design and engineering for the 90's", BOSS Conference 1992, Supplement

VAID Y.P. & NEGUSSEY D. (1984), "Relative density of air and water pluviated sand", Soils and Foundations, Vol.24, No.2, pp 101-105

VAID Y.P., SAYAO A., HOU E. & NEGUSSEY D. (1990), "Generalized stress path dependent soil behaviour with a new hollow cylinder torsional apparatus", Canadian Geotechnical Journal, Vol.27, No.5, pp 601-606.

VAID Y.P. & SAYAO A. (1995), "Proportional loading behaviour of sand under multiaxial stresses", Soils and Foundations, Vol.35, No.3, pp 23-29

VARDOULAKIS I.G. & GRAF B. (1982), "Imperfection sensitivity of the biaxial test on dry sand", IUTAM Conference on Deformation and Failure of Granular Materials, Delft, pp 485-491.

VERMEER P.A. (1982), "A simple shear-band analysis using compliances", IUTAM Conference on Deformation and Failure of Granular Materials, Delft, pp 493-499.

VESIC A.S. & CLOUGH G.W. (1968), "Behaviour of granular materials under high stresses", Journal of the Soil Mechanics and Foundationss Div., ASCE, Vol.94, SM3, pp 661-688

VIGGIANI G., (1992), "Small strain stiffness of fine grained soils", PhD Thesis, The City University, London

VIGGIANI G. & ATKINSON J.H. (1995), "Interpretation of bender element tests", Geotechnique, Vol.45, No.1, pp 149-154

VIGGIANI G. & ATKINSON J.H. (1995), "Stiffness of fine-grained soil at very small strains", Geotechnique, Vol.45, No.2, pp 249-265

WIJEWICKREME D. & VAID Y.P. (1991), "Stress non-uniformities in hollow cylinder torsional shear specimens", Geotechnical Testing Journal, GTJODJ, Vol.14, No.4, pp 349-362.

WIJEWICKREME D. & VAID Y.P. (1993), "Behaviour of loose sand under simultaneous increase in stress ratio and principal stress rotation", Canadian Geotechnical Journal, Vol.30, pp 953-964.

WONG R.K.S. & ARTHUR J.R.F. (1985), "Induced and inherent anisotropy in sand", Geotechnique, Vol.35, No.4, pp 471-481.

WROTH P., (1971), "Some aspects of the elastic behaviour of overconsolidated clay", Roscoe Memorial Symposium, Cambridge University; Edt. R.H.G.Parry

YAMASHITA S., SHIBUYA S., TOKI S. & INAHARA H. (1995), "Cyclic deformation properties of a man-made loose sand deposit", First Int. Conf on Erthquake geotechnical eng., Tokyo, Vol.1, pp 71-76

YEATS, J.A. (1983), "The stability of single and multistage embankments on soft clay", MSc dissertation, Imperial College of Science, Technology and Medicine; University of London.

YOSHIMI Y., TOKIMATSU K. & HOSAKA Y. (1989), "Evaluation of liquefacton resistance of clean sands basd on high-quality undisurbed samples", Soils and Foundations, Vol.29, No.1, pp 93-104

YOSHIMI Y., TOKIMATSU K. & OHARA J. (1994), "In situ liquefaction resistance of clean sands over a wide density range", Geotechnique, Vol.44, No.3, pp 479-494

YU P. & RICHART F.E. (1984), "Stress ratio effects on shear modulus of dry sand", Journal of Geotechn. Eng., ASCE, Vol.110, No.3, pp. 331-345

ZDRAVKOVIC L. & JARDINE R.J. (1995), "The stress-strain-strength anisotropy of sea-bed sediments under general stress conditions", Offshore technology report OTO 95 029